Excited States of Atmospheric Molecules: Spectra, Structures, and Interactions

A thesis submitted for the degree
of Doctor of Science of
the University of Adelaide

Brenton R. Lewis
Research School of Physical Sciences and Engineering
The Australian National University

July 22, 2000

Contents

Abstract

The experimental, analytical and computational research achievements of the author, relating to the study of the interaction of vacuum ultraviolet (VUV) radiation with molecules of particular atmospheric, aeronomic, or astrophysical significance, are described. These achievements follow from the further development and application of the experimental techniques of quantitative VUV spectroscopy, and ultra-high-resolution VUV laser spectroscopy, together with the close-coupling technique for the computation of molecular photodissociation cross sections. The research described addresses the principal aims of the author, namely to (i) elucidate details of molecular structure and dynamics through comparison between precise experimental measurements and quantum-mechanical calculations, and (ii) provide benchmark experimental molecular data and develop molecular modelling techniques intended to contribute to the solution of problems in the photochemistry of the terrestrial and planetary atmospheres, aeronomy, and astrophysics.

In this thesis, the research achievements of the author, the consequent publications, and the recognition of this research, are summarized in the Preface (Section 1). Following the author's *curriculum vitae* (Section 2), and full list of publications (Section 3), a detailed description of the author's research is given in Section 4, which comprises reprints of 41 selected publications in refereed journals, totalling some 421 journal pages. These selected publications address the research theme defined by the thesis title *Excited states of atmospheric molecules: spectra, structures, and interactions*, and cover the period 1983–2000, following the establishment of the author's first laboratory at The Australian National University.

This work contains no material which has been accepted for the award of any other degree or diploma in any university or other tertiary institution, and no material previously published or written by another person, except where due reference has been made in the text.

Consent is given to this copy of the thesis, when deposited in the University Library, being available for loan and photocopying.

22/07/00

Brenton R. Lewis

July 22, 2000

Acknowledgements

The research achievements described in this thesis would not have been possible without the collaboration and support of a significant number of individuals. First, the author would like to thank the many local, interstate, and international collaborators, including graduate students, who have made valuable contributions to his research. Most of these collaborators are listed specifically as coauthors on the selection of published work described in Section 4. In particular, within the ANU, the author is grateful to Professor J. H. Carver for previous leadership and continuing inspiration; Dr. S. T. Gibson, for his development and maintenance of the coupled-channel Schrödinger equations computational code; and Dr. K. G. H. Baldwin, for his development of experimental techniques for the generation of tunable, narrow-bandwidth coherent VUV radiation. Within Australia, the author acknowledges valuable ongoing collaborations with Drs. L. W. Torop. D. G. McCoy, and A. J. Blake, of The University of Adelaide. One such collaborative project has been formalized with the award of an ARC Large Grant administered by that institution. Of his many international colleagues, the author would particularly like to thank Professor M. L. Ginter, of the University of Maryland, for his unflagging collaborative efforts; and Professor H. Lefebvre-Brion, of the Université de Paris-Sud, for her long-term and continuing advice and support. Second, the author is grateful to his technical staff, K. J. Lonsdale and C. J. Dedman, for their skill and dedication in contributing to the success of his experiments. Third, the author acknowledges the budgetary and administrative support provided to his research programme by the ANU, particularly through successive RSPhysSE Directors, Professors J. H. Carver and E. Weigold, and AMPL Heads of Department, Professor R. W. Crompton, Dr. M. T. Elford, and Professor S. J. Buckman. Finally, the author sincerely thanks his parents, Ray and Eileen, and wife Elizabeth, for their continuous encouragement and support over the years, without which his achievements would not have been possible.

1. Preface

1.1 Summary

The author has made a sustained, coherent, and significant contribution of high-quality original research which has advanced knowledge in the general field of atomic, molecular and optical physics. Summaries of this research, the resultant publications and research recognition are given below in Sections 1.2, 1.3, and 1.4, respectively. A selection of 41 refereed publications which encapsulate the main research theme, *Excited states of atmospheric molecules: spectra, structures, and interactions*, appears in Section 4, representing the bulk of this thesis.

1.2 Research

The author has established world-class experimental laboratories for the pursuit of quantitative vacuum-ultraviolet (VUV) spectroscopy, ultra-high-resolution laser VUV spectroscopy, and, recently, coincidence photofragment spectroscopy, together with a computational laboratory devoted to the study of excited molecular states and their interactions through the use of coupled-channel Schrödinger-equation (CSE) calculations (designated "close-coupled spectroscopy" by F. H. Mies). The overall emphasis of his research has been on the interaction of VUV radiation with molecules of particular atmospheric, aeronomic, or astrophysical importance, with the twin aims of (i) elucidating details of molecular structure and dynamics through comparisons between precise experimental measurements and quantum-mechanical calculations, and (ii) providing benchmark experimental molecular data and developing molecular modelling techniques intended to contribute to the solution of problems in the photochemistry of the terrestrial and planetary atmospheres, aeronomy, and astrophysics.

Two significant developments in technique have enhanced the pursuit of these goals. First, in 1987, in collaboration with Dr. K. G. H. Baldwin, of the Laser Physics Centre at The Australian National University (ANU), the author initiated a major experimental programme in the generation of tunable, coherent, ultra-narrow bandwidth VUV radiation using nonlinear, laser-based techniques. This effort has proven highly successful. A major contribution of the author has been in the *application* of these widely-tunable laser-based sources to high-resolution,

quantitative spectroscopy of atmospheric and astrophysical molecules. A resolving power of 10^6 was achieved in the VUV by using the four-wave mixing technique for wavelength downconversion: this is the best reported in this spectral region for a widely tunable source. Second, in collaboration with Dr. S. T. Gibson who wrote 90% of the associated code, starting in 1988, the author has made significant progress in the *application* of the CSE computational technique to elucidate the complex interactions between molecular excited states.

While detailed research results are not given here, since they are more properly gleaned from an examination of the published works in Section 4, it is appropriate to summarize and give a few highlights.[1] The author's major contributions have been in the elucidation of the structure and photodissociation dynamics of molecular oxygen. In particular, he has published 22 papers on the Schumann-Runge (SR) bands, which play a central role in the atmospheric photochemistry, describing measurements taken using a variety of instruments, and culminating in a series of definitive, high-resolution cross sections which have led to an unsurpassed understanding of photodissociation in this system [45,47,49,50,53]. Based on these results, he is developing a new CSE-based description of the SR system for use in photochemical models of the terrestrial atmosphere [52]. In addition, the author has made considerable progress in unravelling the complexities caused by Rydberg-valence interactions in the "window region" of the molecular-oxygen spectrum [30,31,38–44,48,55,56,58,59,62], thereby detecting three electronic states of O_2 for the first time [40,47,59] and demonstrating the first known example of a window resonance in molecular predissociation [40]. Finally, his studies on other atmospheric and astrophysical molecules have had an impact: his temperature-dependent CO_2 photoabsorption cross sections [19] have resolved a long-standing problem of "excessive" CO_2 stablility in the Martian atmosphere,[2] and his high-resolution CO oscillator strengths [54] have shown that values commonly adopted by the astrophysical community,[3] and used for the determination of CO abundance in interstellar space, need significant revision.

1.3 Publications

The author has published widely, with a total of over 130 refereed and conference papers (see Sections 3.1 and 3.5, respectively). His research, which is of cross-disciplinary significance, has resulted in more than 60 articles published in a wide range of top-quality international refereed journals, including *The Physical Review A*, *The Journal of Physics B*, *The Journal of Chemical Physics*, *Physical Review Letters*, *The Journal of Geophysical Research*, *Geophysical Research Letters*, *The Astrophysical Journal*, *Applied Optics*, and *The Journal of the Optical Society of America B*. Of his conference papers, $\sim$ 70% have been presented at significant

[1] Numbers in square brackets refer to the author's list of publications in refereed journals (Section 3.1).

[2] A. D. Anbar, M. Allen, and H. A. Nair, *Journal of Geophysical Research* **98**, 10925 (1993).

[3] D. C. Morton and L. Noreau, *Astrophysical Journal (Supplement Series)* **95**, 301 (1994).

international meetings.

The refereed journal publications of the author have been cited by a significant number of researchers in a range of physics, chemical physics, geophysics, and astrophysics journals, achieving a mean citation rate, averaged over the ten-year period 1989–1998, of 34.4 citations per annum.[1] The work of the author has also been well cited in the scientific monograph literature, e.g.; *Constants of Diatomic Molecules*, by K. P. Huber and G. Herzberg (Van Nostrand Reinhold, New York, 1979) [1,2,3]; *Perturbations in the Spectra of Diatomic Molecules*, by H. Lefebvre-Brion and R. W. Field (Academic, Orlando, 1986) [1,14, and further citations in new edition]; and *The Role of Rydberg States in Spectroscopy and Photochemistry*, edited by C. Sándorfy (Kluwer, Dordrecht, 1999) [30,31,38].

A selection of 41 representative articles in refereed journals, comprising 421 journal pages, forms the bulk of this thesis (see Section 4). These articles have been marked with asterisks in the full list of refereed journal publications in Section 3.1. The work described in Section 4 covers the period 1983–2000, following the establishment of the author's first laboratory at the ANU. Consistent with the title of this thesis, *Excited states of atmospheric molecules: spectra, structures, and interactions*, all of the publications in Section 4 present original research on atmospheric (or astrophysical) molecules (principally O_2 and its isotopomers, H_2O, CO_2, CO, NO), and all results stemming from both of the significant developments in technique described in Section 1.2 are included: 16 of the publications [33,36,37,39–42,44,45,47–50,53,54,60] contain high-resolution laser-spectroscopic measurements; while 10 publications [38,41,43,44,52, 55,56,58,59,62] contain CSE calculations. The work highlighted in Section 4 reflects the two principal research aims stated above: 17 papers [34,36,38–44,48,49,51,56–59,62] contribute primarily to an elucidation of molecular structure and dynamics; 4 papers [18,19,54,60] contribute primarily to benchmark data for atmospheric and astrophysical problems; while 18 papers [20,21,23–31,37,45–47,50,52,55] contribute to both. Two papers [33,53] are primarily instrumental. A subset of 11 of the submitted papers [36,38,40,41,47,49,51,55,56,59,62] perhaps best reflects the desire of the author to publish works which deal simultaneously at a high level with the experimental, analytical, and theoretical aspects of specific problems in molecular physics.

Since all of the work in Section 4 is of joint authorship, as is quite usual in this field, it is important to list the contributions of the author. His estimated contributions to each of the publications in Section 4 are given in the list of refereed publications in Section 3.1. Overall, they amount to $\sim$ 60% of the submitted work, $\sim$ 68% of which has been fully written by him. The general contributions of the author include: the establishment of laboratories, experiment design, many early experimental measurements, most data analysis, most theoretical analysis and computation, and most of the insight. The main exceptions to this assessment include the significant and important technique contributions of colleagues Gibson and Baldwin, described in Section 1.2, and the substantial experimental measure-

[1] Total citations in the ten-year period of all refereed publications, regardless of date of publication, divided by 10. Data obtained from printed ISI Science Citation Index, corrected downwards for self-citation

ments undertaken by ANU PhD students (Berzins, Dooley, Banerjee) and PDFs (England). In addition, the instigation and experimental work for [51] and [55] came from the international collaborators, van der Zande *et al.*, and Slanger *et al.*, respectively. Two-thirds of the material for the comparative instrumental paper [53] came from Cosby *et al.*, and Thorne, Yoshino *et al.*, while the experimental spectrum analyzed and explained in [56] came from Copeland *et al.* Other significant contributions to the theoretical parts of the work described in Section 4 are in: [18] (due to former ANU colleague, Vardavas); [36,43] (due to Gibson); [46] (due to England); [38] (Appendix due to international collaborator, Lefebvre-Brion); [47] (*ab initio* calculations due to international collaborator, Partridge); [49] (due to Adelaide collaborator Torop); and [62] (due to Lefebvre-Brion). For the most part, other coauthors had roles which were either minor, and/or limited mainly to suggestions, advice, and inspiration. Significant parts of [25–28], and some of [20–24] have been included in the ANU PhD thesis of L. Berzins; significant parts of [45,50], some of [47,53], and a very minor part of [37] in the ANU PhD thesis of P. M. Dooley; and significant parts of [44], some of [38], and a very minor part of [40] in the ANU PhD thesis of S. S. Banerjee. The estimated contributions of the author given in Section 3.1 have had taken into account the particular details given in this paragraph of the contributions of others.

1.4 Recognition

International recognition of the author's research achievements is evident from the following broad range of indicators:
(1) Appointment as an Associate Editor of the international refereed journal: *Journal of Quantitative Spectroscopy and Radiative Transfer* (1986–);
(2) Election to Membership of the International Advisory Board for the *International Conferences on VUV Radiation Physics* (1992–);
(3) Presentation of solicited talks at international physics and geophysics conferences (e.g., *Oji International Seminar on Atomic and Molecular Photoionization*, Tsukuba, 1995; *XXV General Assembly of the European Geophysical Society*, Nice, 2000);
(4) Chairing of sessions at international physics and geophysics conferences (*Eleventh International Conference on VUV Radiation Physics*, Tokyo, 1995; *XXV General Assembly of the European Geophysical Society*, Nice, 2000);
(5) Presentation of invited international seminars (e.g., UK: Edinburgh University, Daresbury Laboratory, Imperial College; The Netherlands: FOM; USA: SRI International, Harvard University, Naval Research Laboratory; Japan: Tohoku University).
(6) Research with international collaborators, facilitated by funded bilateral visits and appointments to Visiting Fellowships in the Ultraviolet Physics Unit of the ANU. Of The author's 24 refereed journal publications since 1995, 16 have involved collaborations with international researchers. Those appointed to Visiting Fellowships include: Professor J. A. R. Samson, University of Nebraska; Professor

R. J. Donovan, University of Edinburgh; Dr. W. J. van der Zande, FOM, The Netherlands; Professor H. Lefebvre-Brion and Professor R. Lefebvre, Université de Paris-Sud; Dr. F. H. Mies, NIST, USA; and Dr. J. B. West, Daresbury Laboratory, UK. Visits and sabbaticals funded by the NSF (US) have also been hosted for Professor G. Stark, Wellesley College; Professor M. L. Ginter and Professor T. J. McIlrath, University of Maryland; Dr. K. Yoshino, Harvard-Smithsonian Center for Astrophysics; and Dr. P. C. Cosby, SRI International.

National recognition of the author's research achievements is evident from his election to Fellowship of the Australian Institute of Physics in 1999, and by the competitive funding of ARC Large Grants for collaboration with researchers from The University of Adelaide (1998) and Macquarie University (2000).

2. Curriculum vitae

Brenton Raymond LEWIS
Head, Ultraviolet Physics Unit
Atomic and Molecular Physics Laboratories
Research School of Physical Sciences and Engineering
Institute of Advanced Studies
The Australian National University
Canberra, ACT 0200
Australia

Personal

Date of birth	16 December, 1945
Citizenship	Australian

Academic Qualifications

1973	Ph.D. (Physics), The University of Adelaide
Thesis title	*Oscillator Strength Measurements for Several Band Systems of Molecular Hydrogen*
1967	B.Sc. (Hons. I), The University of Adelaide
1966	B.Sc., The University of Adelaide

Main Research Interests

Experimental : The development of nonlinear laser-based techniques for the production of tunable, narrow-bandwidth coherent VUV radiation, and the application of those techniques to high-resolution VUV spectroscopy. Single- and multi-photon

quantitative molecular spectroscopy using conventional and laser sources in photoabsorption, photodissociation and fluorescence-excitation studies. Photofragment translational spectroscopy, multi-photon ionization, double-resonance techniques. In particular, the application of such techniques to problems of atmospheric, aeronomic, and astrophysical significance.
Theoretical : Elucidation of molecular structure, dynamics and interactions using coupled-channel Schrödinger equation techniques. Semi-empirical characterization of excited-state potential-energy curves, Rydberg-valence interactions, and other perturbations. Development of quantum-mechanical models for the interaction of VUV radiation with molecules, with a view to applications in atmospheric photochemistry, aeronomy, and astrophysics.

Present Appointment

Senior Fellow in the Research School of Physical Sciences and Engineering at The Australian National University since July 1989; Head, Ultraviolet Physics Unit, Atomic and Molecular Physics Laboratories, since October 1992.

Previous Appointments

6/79–7/89	Fellow	Research School of Physical Sciences, The Australian National University
6/77–6/79	Lecturer	Department of Physics, Bendigo College of Advanced Education
5/75–5/77	QEII Fellow	Department of Physics, The University of Adelaide
3/74–5/75	Senior Teaching Fellow	Department of Physics, The University of Adelaide
9/72–3/74	Postdoctoral Fellow	School of Physical Sciences, Flinders University
1/71–8/72	Demonstrator	Department of Physics, The University of Adelaide

Professional Affiliations

American Physical Society
American Geophysical Union
Optical Society of America
Australian Institute of Physics (Fellow)

Other Professional Activities

1987–1990	Member	LYMAN Science Working Group
1980–1982	Special Advisor	STARLAB Joint Science Working Group

Honours, Awards, and Fellowships

2000	Session Chair, XXV General Assembly of the European Geophysical Society, Nice
1999	Elected to Fellowship of the Australian Institute of Physics
1995	Session Chair, Eleventh International Conference on VUV Radiation Physics, Tokyo
1992	Elected to Membership of the International Advisory Board for the International Conferences on VUV Radiation Physics
1986	Appointed as an Associate Editor of the *Journal of Quantitative Spectroscopy and Radiative Transfer*
1975	A Queen Elizabeth II Fellowship
1967	A CSIRO Postgraduate Studentship
1966	A CSIRO Junior Postgraduate Studentship
1963–1966	The four Philips Prizes for physics
1962	The Shell Scholarship, the BHP Prize, the Alliance Française Prize, the Institute of Physics Prize, and the Advertiser Prize
1961	The Thomas Price Scholarship and the Advertiser Prize
1960	An Intermediate Exhibition and a Shell Scholarship

Grants[1]

2000	\$153,000	ARC Large Grant: *Pulsed nonlinear-optical spectroscopic sources: tunable narrowband and multiwavelength applications*, (with Macquarie University)
1999	\$154,800	IAS Fellowship (C. Tian)
1998	\$133,000	ARC Large Grant: *Development of an innovative quantum-mechanical model for the interaction of solar VUV radiation with the earth's atmosphere* (with the University of Adelaide)
1998	\$200,000	share of DETYA RIEF Grant for purchase of YAG laser (led by B. J. Orr, Macquarie University and K. G. H. Baldwin)
1998	\$4,955	DIST International Conference Support Scheme Grant to fund presentation of bid to host VUV13 Conference in Australia
1997	\$250,000	ANU Major Equipment Committee Grant for construction of Coincidence Photodetachment and Photofragment Spectrometer (led by S. T. Gibson)
1996	\$10,000	DIST Bilateral Science and Technology Program Grant: *Radiative interactions with atoms and molecules*

[1]Since the Institute of Advanced Studies (IAS) is block-funded, it has not been permissible to apply for ARC grants as Chief Investigator. Only recently has it been possible to be a coinvestigator in proposals submitted by other universities.

1994	$130,000	ANU Major Equipment Committee Grant for purchase of dye laser
1993	$10,800	DIST Bilateral Science and Technology Program Grant: *Atmospheric molecular laser spectroscopy* (led by K. G. H. Baldwin)
1991	$152,100	ARC Postdoctoral Fellowship (J. P. England)

3. List of publications

3.1 Publications in refereed journals[1]

[1] A. J. D. Farmer, W. Fabian, B. R. Lewis, K. H. Lokan, and G. N. Haddad, "Experimental oscillator strengths for the Schumann-Runge band system in oxygen", *Journal of Quantitative Spectroscopy and Radiative Transfer* **8**, 1739–1746 (1968).

[2] W. Fabian and B. R. Lewis, "Experimentally determined oscillator strengths for molecular hydrogen: I. The Lyman and Werner bands above 900 Å", *Journal of Quantitative Spectroscopy and Radiative Transfer* **14**, 523–535 (1974).

[3] B. R. Lewis, "Experimentally determined oscillator strengths for molecular hydrogen: II. The Lyman and Werner bands below 900 Å, the $B' - X$ and the $D - X$ bands", *Journal of Quantitative Spectroscopy and Radiative Transfer* **14**, 537–546 (1974).

[4] B. R. Lewis, "Experimentally determined oscillator strengths for molecular hydrogen: III. Rotational variation of band strength", *Journal of Quantitative Spectroscopy and Radiative Transfer* **14**, 723–729 (1974).

[5] C. R. Lloyd, P. J. O. Teubner, E. Weigold, and B. R. Lewis, "Differential cross sections for the elastic scattering of electrons from atomic hydrogen: II. Medium energies", *Physical Review A* **10**, 175–181 (1974).

[6] B. R. Lewis, J. B. Furness, P. J. O. Teubner, and E. Weigold, "The elastic scattering of electrons from argon", *Journal of Physics B* **7**, 1083–1090 (1974).

[7] B. R. Lewis, I. E. McCarthy, P. J. O. Teubner, and E. Weigold, "The elastic scattering of electrons from krypton, neon and xenon", *Journal of Physics B* **7**, 2549–2556 (1974).

[8] B. R. Lewis, E. Weigold, and P. J. O. Teubner, "The inelastic scattering of electrons from argon and krypton", *Journal of Physics B* **8**, 212–218 (1975).

[1] Those refereed journal publications appearing in Section 4 are marked with an asterisk. The estimated contributions of the author are given as percentages within the parentheses following his name.

[9] J. H. Carver, H. P. F. Gies, T. I. Hobbs, B. R. Lewis, and D. G. McCoy, "Temperature dependence of the molecular oxygen photoabsorption cross section near the hydrogen Lyman-alpha line", *Journal of Geophysical Research* **82**, 1955–1960 (1977).

[10] J. H. Carver, B. H. Horton, M. Ilyas, and B. R. Lewis, "Molecular oxygen densities and the atmospheric absorption of solar Lyman-alpha radiation", *Journal of Geophysical Research* **82**, 2613–2618 (1977).

[11] J. H. Carver, G. N. Haddad, T. I. Hobbs, B. R. Lewis, and D. G. McCoy, "A vacuum-ultraviolet six metre monochromator", *Applied Optics* **17**, 420–429 (1978).

[12] B. R. Lewis, J. H. Carver, T. I. Hobbs, D. G. McCoy, and H. P. F. Gies, "Experimentally determined oscillator strengths and linewidths for the Schumann-Runge band system of molecular oxygen: I. The (6,0)–(14,0) bands", *Journal of Quantitative Spectroscopy and Radiative Transfer* **20**, 191–203 (1978).

[13] B. R. Lewis, J. H. Carver, T. I. Hobbs, D. G. McCoy, and H. P. F. Gies, "Experimentally determined oscillator strengths and linewidths for the Schumann-Runge band system of molecular oxygen: II. The (2,0)–(5,0) bands", *Journal of Quantitative Spectroscopy and Radiative Transfer* **22**, 213–221 (1979).

[14] B. R. Lewis, J. H. Carver, T. I. Hobbs, D. G. McCoy, and H. P. F. Gies, "Rotational variation of predissociation linewidth for the Schumann-Runge bands of molecular oxygen", *Journal of Quantitative Spectroscopy and Radiative Transfer* **24**, 365–369 (1980).

[15] H. P. F. Gies, S. T. Gibson, D. G. McCoy, A. J. Blake, and B. R. Lewis, "Experimentally determined oscillator strengths and linewidths for the Schumann-Runge band system of molecular oxygen: III. The (7,0)–(19,0) bands", *Journal of Quantitative Spectroscopy and Radiative Transfer* **26**, 469–481 (1981).

[16] B. R. Lewis, "Focussing cam design for normal incidence VUV monochromators", *Applied Optics* **21**, 2523–2526 (1982).

[17] B. R. Lewis, "Measurement of absorption line intensities with VUV monochromators", *Applied Optics* **22**, 1546–1550 (1983).

*[18] B. R. Lewis (50%), I. M. Vardavas, and J. H. Carver, "The aeronomic dissociation of water vapour by solar Lyman-alpha radiation", *Journal of Geophysical Research* **88**, 4935–4940 (1983).

*[19] B. R. Lewis (90%) and J. H. Carver, "Temperature dependence of the carbon dioxide photoabsorption cross section between 1200 and 1970 Å", *Journal of Quantitative Spectroscopy and Radiative Transfer* **30**, 297–309 (1983).

*[20] B. R. Lewis (90%), L. Berzins, and J. H. Carver, "Decomposition of the photoabsorption continuum underlying the Schumann-Runge bands of $^{16}O_2$: I. Role of the $B\,^3\Sigma_u^-$ state; a new dissociation limit", *Journal of Quantitative Spectroscopy and Radiative Transfer* **33**, 627–643 (1985).

*[21] B. R. Lewis (80%), L. Berzins, J. H. Carver, S. T. Gibson, and D. G. McCoy, "Decomposition of the photoabsorption continuum underlying the Schumann-Runge bands of $^{16}O_2$: II. Role of the $1\,^3\Pi_g$ state and collision-induced absorption", *Journal of Quantitative Spectroscopy and Radiative Transfer* **36**, 405–415 (1985).

[22] B. R. Lewis, L. Berzins, and J. H. Carver, "Vacuum UV absorption cross sections for enflurane and isoflurane", *Applied Optics* **25**, 2647–2648 (1986).

*[23] B. R. Lewis (80%), L. Berzins, and J. H. Carver, "Oscillator strengths for the Schumann-Runge bands of $^{16}O_2$", *Journal of Quantitative Spectroscopy and Radiative Transfer* **36**, 209–232 (1986).

*[24] B. R. Lewis (80%), L. Berzins, J. H. Carver, and S. T. Gibson, "Rotational variation of predissociation linewidth in the Schumann-Runge bands of $^{16}O_2$", *Journal of Quantitative Spectroscopy and Radiative Transfer* **36**, 187–207 (1986).

*[25] B. R. Lewis (50%), L. Berzins, and J. H. Carver, "Oscillator strengths for the Schumann-Runge bands of $^{16}O^{18}O$", *Journal of Quantitative Spectroscopy and Radiative Transfer* **37**, 219–228 (1987).

*[26] B. R. Lewis (50%), L. Berzins, and J. H. Carver, "Predissociation linewidths for the Schumann-Runge bands of $^{18}O_2$", *Journal of Quantitative Spectroscopy and Radiative Transfer* **37**, 229–241 (1987).

*[27] B. R. Lewis (50%), L. Berzins, and J. H. Carver, "Predissociation linewidths for the Schumann-Runge bands of $^{16}O^{18}O$", *Journal of Quantitative Spectroscopy and Radiative Transfer* **37**, 243–254 (1987).

*[28] B. R. Lewis (50%), L. Berzins, and J. H. Carver, "Oscillator strengths for the Schumann-Runge bands of $^{18}O_2$", *Journal of Quantitative Spectroscopy and Radiative Transfer* **37**, 255–266 (1987).

*[29] B. R. Lewis (80%), L. Berzins, C. J. Dedman, T. T. Scholz, and J. H. Carver, "Pressure-broadening in the Schumann-Runge bands of molecular oxygen", *Journal of Quantitative Spectroscopy and Radiative Transfer* **39**, 271–282 (1988).

*[30] B. R. Lewis (90%), S. T. Gibson, M. Emami, and J. H. Carver, "Resonances in the photodissociation of isotopic molecular oxygen: I. The longest band.", *Journal of Quantitative Spectroscopy and Radiative Transfer* **40**, 1–13 (1988).

*[31] B. R. Lewis (90%), S. T. Gibson, M. Emami, and J. H. Carver, "Resonances in the photodissociation of isotopic molecular oxygen: II. The second and third bands", *Journal of Quantitative Spectroscopy and Radiative Transfer* **40**, 469–477 (1988).

[32] M. A. Dopita, I. R. Tuohy, M. Cropper, R. W. Hunstead, B. R. Lewis, D. S. Mathewson, C. J. Mitchell, R. P. Norris, J. O'Mara, M. Pettini, E. R. Roberts, and M. D. Waterworth, "LYMAN: A new window on the universe", *Proceedings of the Astronomical Society of Australia* **7**, 243–342 (1988).

*[33] B. R. Lewis (60%), S. T. Gibson, K. G. H. Baldwin, and J. H. Carver, "Vacuum-ultraviolet absorption linewidth measurement using high-order anti-Stokes Raman-shifted radiation", *Journal of the Optical Society of America B* **6**, 1200–1208 (1989).

*[34] B. R. Lewis (90%) and S. T. Gibson, "Rotational line strengths in $^3\Sigma^+ - {}^3\Sigma^-$ electronic transitions. The $\beta\,{}^3\Sigma_u^+ - X\,{}^3\Sigma_g^-$ and $A\,{}^3\Sigma_u^+ - X\,{}^3\Sigma_g^-$ systems of molecular oxygen", *Canadian Journal of Physics* **68**, 231–237 (1990).

[35] B. R. Lewis and S. T. Gibson, Comment on "The potential energy function for $O_2(X\,{}^3\Sigma_g^-)$ and the transition dipole moment of the Schumann-Runge band near X-state dissociation", *Journal of Chemical Physics* **93**, 7532–7533 (1990).

*[36] S. T. Gibson, B. R. Lewis (40%), K. G. H. Baldwin, and J. H. Carver, "Rotational features in the fluorescence excitation spectrum of $O(^1D_2)$ from vacuum-ultraviolet laser photodissociation of O_2", *Journal of Chemical Physics* **94**, 1060–1068 (1991).

*[37] B. R. Lewis (90%), S. T. Gibson, and P. M. Dooley, "Fine-structure dependence of predissociation linewidth in the Schumann-Runge bands of molecular oxygen", *Journal of Chemical Physics* **100**, 7012–7035 (1994).

*[38] B. R. Lewis (80%), S. S. Banerjee, and S. T. Gibson, "Asymmetric lineshapes in the indirect predissociation of the $f^1\Sigma_u^+$ Rydberg state of O_2", *Journal of Chemical Physics* **102**, 6631–6640 (1995).

*[39] J. P. England, B. R. Lewis (50%), and M. L. Ginter, "Identification of the $4p\sigma_u\,{}^1\Pi_u$ Rydberg state of O_2", *Journal of Chemical Physics* **103**, 1727–1731 (1995).

*[40] B. R. Lewis (80%), J. P. England, R. J. Winkel, Jr., S. S. Banerjee, P. M. Dooley, S. T. Gibson, and K. G. H. Baldwin, "Experimental observation of the lowest $^1\Sigma_u^+$ valence state of O_2", *Physical Review A* **52**, 2717–2733 (1995).

*[41] J. P. England, B. R. Lewis (60%), S. T. Gibson, and M. L. Ginter, "Assignment of the $^3\Pi_u - X^3\Sigma_g^-$ bands of O_2 observed in the region 1040–1200 Å", *Journal of Chemical Physics* **104**, 2765–2772 (1996).

*[42] J. P. England, B. R. Lewis (40%), and M. L. Ginter, "Spin-orbit interactions between Rydberg states of O_2", *Journal of Electron Spectroscopy and Related Phenomena* **79**, 449–452 (1996).

*[43] S. T. Gibson, and B. R. Lewis (40%), "Understanding diatomic photodissociation with a coupled-channel Schrödinger equation model", *Journal of Electron Spectroscopy and Related Phenomena* **80**, 9–12 (1996).

*[44] S. S. Banerjee, B. R. Lewis (40%), S. T. Gibson, J. P. England, and K. G. H. Baldwin, "Indirect predissociation of the $3p\pi_u f\,^1\Sigma_u^+$ state of O_2", *Journal of Electron Spectroscopy and Related Phenomena* **80**, 17–20 (1996).

*[45] P. M. Dooley, B. R. Lewis (40%), S. T. Gibson, and K. G. H. Baldwin, "Narrow-bandwidth VUV laser measurements of fine-structure predissociation linewidths in the Schumann-Runge bands of O_2", *Journal of Electron Spectroscopy and Related Phenomena* **80**, 29–32 (1996).

*[46] J. P. England, B. R. Lewis (50%), and S. T. Gibson, "Electronic transition moments for the Herzberg I bands of O_2", *Canadian Journal of Physics* **74**, 185–193 (1996).

*[47] B. R. Lewis (80%), P. M. Dooley, J. P. England, K. Waring, S. T. Gibson, K. G. H. Baldwin, and H. Partridge, "Observation of the second $^3\Pi_u$ valence state of O_2", *Physical Review A* **54**, 3923–3938 (1996).

*[48] J. P. England, B. R. Lewis (50%), and M. L. Ginter, "Identification of two $^3\Sigma_u^- \leftarrow X\,^3\Sigma_g^-$ transitions of O_2 near 88930 and 90780 cm^{-1}", *Journal of Chemical Physics* **105**, 1754–1763 (1996).

*[49] B. R. Lewis (60%), P. M. Dooley, J. P. England, S. T. Gibson, K. G. H. Baldwin, and L. W. Torop, "Non-Lorentzian line shapes for interfering rotational resonances in the predissociation of O_2", *Physical Review A* **55**, 4164–4167 (1997).

*[50] P. M. Dooley, B. R. Lewis (50%), K. Waring, S. T. Gibson, and K. G. H. Baldwin, "Fine-structure-resolved collisional broadening in the Schumann-Runge bands of O_2", *Journal of Quantitative Spectroscopy and Radiative Transfer* **58**, 93–100 (1997).

*[51] B. Buijsse, W, J. van der Zande, A. T. J. B. Eppink, D. H. Parker, B. R. Lewis (50%), and S. T. Gibson, "Angular distributions for photodissociation of O_2 in the Herzberg continuum", *Journal of Chemical Physics* **108**, 7229–7243 (1998).

*[52] B. R. Lewis (90%), S. T. Gibson, L. W. Torop, and D. G. McCoy, "Quantum interference in the Schumann-Runge bands of molecular oxygen", *Geophysical Research Letters* **25**, 2457–2460 (1998).

*[53] P. M. Dooley, B. R. Lewis (40%), S. T. Gibson, K. G. H. Baldwin, P. C. Cosby, J. L. Price, R. A. Copeland, T. G. Slanger, A. P. Thorne, J. E. Murray, and K. Yoshino, "A comparative high-resolution study of predissociation linewidths in the Schumann-Runge bands of O_2", *Journal of Chemical Physics* **109**, 3856–3867 (1998).

*[54] G. Stark, B. R. Lewis (40%), S. T. Gibson, and J. P. England, "High-resolution oscillator-strength measurements for high-v' bands of the $A\,^1\Pi(v') - X\,^1\Sigma^+(v'' = 0)$ system of carbon monoxide", *The Astrophysical Journal* **505**, 452–458 (1998).

*[55] J. Lacoursière, S. A. Meyer, G. W. Faris, T. G. Slanger, B. R. Lewis (50%), and S. T. Gibson, "The $O(^1D)$ yield from O_2 photodissociation near H Lyman-α (121.6 nm)", *Journal of Chemical Physics* **110**, 1949–1958 (1999).

*[56] B. R. Lewis (80%), S. T. Gibson, R. A. Copeland, and C. G. Bressler, "Missing bands in the multiphoton excitation of coupled molecular states", *Physical Review Letters* **82**, 4212–4215 (1999).

*[57] B. R. Lewis (90%), S. T. Gibson, T. G. Slanger, and D. L. Huestis, "The $B\,^3\Sigma_u^- \leftarrow b\,^1\Sigma_g^+$ transition of molecular oxygen", *Journal of Chemical Physics* **110**, 11129–11132 (1999).

*[58] J. S. Morrill, M. L. Ginter, B. R. Lewis (50%), and S. T. Gibson, "The $(X\,^2\Pi_g)\,ns\sigma_g\,^{1,3}\Pi_g$ Rydberg states of O_2: Spectra, structures and interactions", *Journal of Chemical Physics* **111**, 173–185 (1999).

*[59] B. R. Lewis (80%), S. T. Gibson, J. S. Morrill, and M. L. Ginter, "Perturbations in the $3s\sigma_g\,^{1,3}\Pi_g$ Rydberg states of O_2: bound-bound interactions with the second $^1\Pi_g$ and $^1\Delta_g$ valence states", *Journal of Chemical Physics* **111**, 186–197 (1999).

*[60] G. Stark, B. R. Lewis (40%), S. T. Gibson, and J. P. England, "High-resolution oscillator-strength measurements of the CO $B\,^1\Sigma^+ - X\,^1\Sigma^+$ (0,0) and (1,0) vibrational bands", *The Astrophysical Journal* **520**, 732–736 (1999).

[61] B. R. Lewis, S. T. Gibson, and K. Yoshino, Comment on "*Ab initio* dynamic polarizabilities for O_2, its photoabsorption spectrum in the Schumann-Runge region, and long-range interaction coefficients for its dimer", *Journal of Chemical Physics* **111**, 11236–11237 (1999).

*[62] B. R. Lewis (40%), S. T. Gibson, S. S. Banerjee, and H. Lefebvre-Brion, "Relations between Rydberg-valence interactions in the O_2 molecule", *Journal of Chemical Physics* **113**, 2214–2223 (2000).

[63] B. R. Lewis, S. T. Gibson, F. T. Hawes, and L. W. Torop, "A new model for the Schumann-Runge bands of O_2", *Physics and Chemistry of the Earth*, submitted (May, 2000).

[64] F. T. Hawes, L. W. Torop, B. R. Lewis, and S. T. Gibson, "An asymmetry sum rule for molecular predissociation", *Physical Review A*, submitted (July, 2000).

[65] B. R. Lewis, J. P. England, S. T. Gibson, M. J. Brunger, and M. Allan, "Electron energy-loss spectra of coupled electronic states: effects of Rydberg-valence interactions in O_2", *Physical Review A*, submitted (July, 2000).

3.2 Other refereed publications

[1] K. G. H. Baldwin, S. T. Gibson, B. R. Lewis, J. H. Carver, and T. J. McIlrath, "Four-wave difference-frequency generation at 124 nm for high-resolution photoabsorption studies of O_2", *Proceedings on Short-Wavelength Coherent Radiation*, eds. P. H. Bucksbaum and N. M. Ceglio (Optical Society of America, 1991), pp. 12–17.

[2] B. R. Lewis, S. T. Gibson, J. P. England, P. M. Dooley, S. S. Banerjee, and K. G. H. Baldwin, "Narrow-bandwidth VUV laser measurements of photodissociation in O_2", *Atomic and Molecular Photoionization*, eds. A. Yagishita and T. Sasaki (Universal Academy Press, Tokyo, 1996), pp. 177–185.

3.3 Other publications

[1] B. R. Lewis, "A low noise preamplifier", *Electronics Australia*, November 1970, p. 109.

[2] B. R. Lewis and T. I. Hobbs, "A high-voltage, high-current supply", *Electronics Today International*, December 1976, p. 26.

[3] B. R. Lewis and T. I. Hobbs, "Remote control tuner and IF strip", *Electronics Today International*, March 1977, p. 27.

[4] B. R. Lewis, "Add-on FM tuner", *Electronics Today International*, September 1977, p. 31.

[5] E. R. Roberts, W. Vincent, P. Martin, and B. R. Lewis, "Development of the LYMAN ultraviolet detectors", *Proceedings of the 4th National Space Engineering Symposium*, (National Conference Publication 1988/10), pp. 113–117.

[6] K. G. H. Baldwin, B. R. Lewis, and S. T. Gibson, "UV and VUV laser spectroscopy", *Lambda Physik Highlights No. 26*, ed. U. Brinkmann (Lambda Physik, 1990).

[7] B. R. Lewis, Book Review: "Free-Electron Lasers", by C. A. Brau (Academic, San Diego, 1990), *Australian Physicist* **27**, 252–253 (1990).

[8] B. R. Lewis (Editor), *RSPhysSE Annual Report*, 1992, 402 pp.

[9] B. R. Lewis (Editor), *RSPhysSE Annual Report*, 1993, 307 pp.

3.4 Unpublished reports

[1] B. R. Lewis, L. Berzins, and J. H. Carver, "Report on VUV cross section measurements for enflurane and isoflurane", 1983, 10 pp.

[2] B. R. Lewis, "Optical behaviour of materials in the 900–2000 Å range"

[3] B. R. Lewis, S. T. Gibson, C. J. Dedman, and K. J. Lonsdale, "Determination of quantum efficiency for channel intensifier tube ITT 19-667/1"

[4] B. R. Lewis, S. T. Gibson, C. J. Dedman, and K. J. Lonsdale, "Quantum efficiency measurement for reconstructed image tube ITT 19-667/2R", 1987, 6 pp.

3.5 Conference papers

[1] B. R. Lewis, J. B. Furness, P. J. O. Teubner, and E. Weigold, "The elastic scattering of electrons from argon", *Australian Institute of Physics Conference*, Adelaide, May, 1974.

[2] B. R. Lewis, I. E. McCarthy, P. J. O. Teubner, and E. Weigold, "The elastic scattering of electrons from krypton, neon and xenon", *Australian Institute of Physics Conference*, Adelaide, May, 1974.

[3] B. R. Lewis, E. Weigold, and P. J. O. Teubner, "The inelastic scattering of electrons from argon and krypton", *Australian Institute of Physics Conference*, Adelaide, May, 1974.

[4] C. R. Lloyd, P. J. O. Teubner, E. Weigold, and B. R. Lewis, "Differential cross sections for the elastic scattering of electrons from atomic hydrogen", *Eighth International Conference on the Physics of Electronic and Atomic Collisions*, Belgrade, 1975.

[5] B. R. Lewis and J. H. Carver, "Absorption of VUV radiation in the Schumann-Runge bands of molecular oxygen", *Sixth International Conference on Vacuum Ultraviolet Radiation Physics*, Charlottesville, 2–6 June, 1980.

[6] B. R. Lewis, L. Berzins, and J. H. Carver, "Decomposition of the photoabsorption continuum underlying the Schumann-Runge bands of $^{16}O_2$: Role of the $B\,^3\Sigma_u^-$ state; a new dissociation limit", *Fourteenth Australian Spectroscopy Conference*, Canberra, February, 10–14 February, 1985.

[7] B. R. Lewis, L. Berzins, S. T. Gibson, and J. H. Carver, "The Schumann-Runge bands of isotopic molecular oxygen", *Eighth International Conference on Vacuum Ultraviolet Radiation Physics*, Lund, 4–8 August, 1986.

[8] S. T. Gibson, B. R. Lewis, L. Berzins, and J. H. Carver, "Semi-empirical Franck-Condon model applied to the Schumann-Runge spectrum of molecular oxygen", *Seventh National Congress of the Australian Institute of Physics*, Adelaide, 25–29 August, 1986.

[9] S. T. Gibson, B. R. Lewis, L. Berzins, and J. H. Carver, "Decomposition of the VUV absorption spectrum of O_2 from measurements of $O(^1D)$ fluorescence",

invited talk, *Australian Conference on Lasers and Spectroscopy*, Surfers Paradise, 11–15 May, 1987.

[10] B. R. Lewis, L. Berzins, C. J. Dedman, T. T. Scholz, and J. H. Carver, "Pressure broadening in the Schumann-Runge bands of molecular oxygen", *Australian Conference on Lasers and Spectroscopy*, Surfers Paradise, 11–15 May, 1987.

[11] S. T. Gibson and B. R. Lewis, "Absorption into coupled states of molecular oxygen", *Ninth International Conference on Vacuum Ultraviolet Radiation Physics*, Honolulu, 17–21 July, 1989.

[12] B. R. Lewis, S. T. Gibson, K. G. H. Baldwin, and J. H. Carver, "VUV absorption linewidth measurement using high-order anti-Stokes Raman-shifted radiation", *Ninth International Conference on Vacuum Ultraviolet Radiation Physics*, Honolulu, 17–21 July, 1989.

[13] S. T. Gibson, B. R. Lewis, K. G. H. Baldwin, and J. H. Carver, "Excitation spectrum of $O(^1D)$ produced from laser VUV photodissociation of O_2", *Ninth International Conference on Vacuum Ultraviolet Radiation Physics*, Honolulu, 17–21 July, 1989.

[14] K. G. H. Baldwin, S. T. Gibson, B. R. Lewis, and J. H. Carver, "High-resolution VUV laser spectroscopy of O_2", *Australian Conference on Lasers and Spectroscopy*, Adelaide, 25–29 September, 1989.

[15] S. T. Gibson, B. R. Lewis, K. G. H. Baldwin, and J. H. Carver, "Photoabsorption into coupled electronic states of isotopic O_2 measured using laser-generated vacuum-ultraviolet radiation", *Seventeenth International Conference on the Physics of Electronic and Atomic Collisions*, Brisbane, 10–16 July, 1991.

[16] K. G. H. Baldwin, S. T. Gibson, and B. R. Lewis, "VUV generation by difference-frequency mixing for high-resolution O_2 spectroscopy", *Australian Conference on Optics, Lasers and Spectroscopy*, Canberra, 30 September–4 October, 1991.

[17] B. R. Lewis and S. T. Gibson, "A study of lineshape asymmetry in the Schumann-Runge bands of O_2 by the coupled-equations method", *Tenth International Conference on Vacuum Ultraviolet Radiation Physics*, Paris, 27–31 July, 1992.

[18] B. R. Lewis, J. P. England, R. J. Winkel, Jr., S. S. Banerjee, P. M. Dooley, K. G. H. Baldwin, and S. T. Gibson, "Observation of the $^1\Sigma_u^+$ valence state of O_2", *Tenth International Conference on Vacuum Ultraviolet Radiation Physics*, Paris, 27–31 July, 1992.

[19] P. C. Hill, B. R. Lewis, and S. T. Gibson, "Measurement and coupled-equations analysis of the photoabsorption spectrum of $O_2(a\,^1\Delta_g)$", *Tenth International Conference on Vacuum Ultraviolet Radiation Physics*, Paris, 27–31 July, 1992.

[20] S. T. Gibson, B. R. Lewis, and J. H. Carver, "Fluorescence excitation spectrum of $O(^1D_2)$ from the photodissociation of O_2 between 115 nm and 180 nm", *Tenth International Conference on Vacuum Ultraviolet Radiation Physics*, Paris, 27–31 July, 1992.

[21] S. S. Banerjee, P. M. Dooley, B. R. Lewis, K. G. H. Baldwin, and S. T. Gibson, "Laser-spectroscopic measurements of isotopic effects in the longest band of O_2", *Australian Conference on Optics, Lasers and Spectroscopy*, Melbourne, 6–10 December, 1993.

[22] P. M. Dooley, B. R. Lewis, K. G. H. Baldwin, and S. T. Gibson, "Narrow-bandwidth VUV laser measurements of fine-structure predissociation linewidths in the Schumann-Runge bands of O_2", *Australian Conference on Optics, Lasers and Spectroscopy*, Melbourne, 6–10 December, 1993.

[23] J. P. England, B. R. Lewis, and S. T. Gibson, "A high-resolution study of the $^3\Pi_u$ states of O_2", *Nineteenth International Quantum Electronics Conference*, Anaheim, 8–13 May, 1994.

[24] S. S. Banerjee, B. R. Lewis, K. G. H. Baldwin, and S. T. Gibson, "A spectroscopic investigation of the $f\,^1\Sigma_u^+$ Rydberg state of O_2", *Advanced Workshop on Atomic and Molecular Physics*, Canberra, 13–15 February, 1995.

[25] P. M. Dooley, B. R. Lewis, K. G. H. Baldwin, and S. T. Gibson, "Narrow-bandwidth VUV laser measurements of fine-structure predissociation linewidths in the Schumann-Runge bands of O_2", *Advanced Workshop on Atomic and Molecular Physics*, Canberra, 13–15 February, 1995.

[26] J. P. England, B. R. Lewis, and M. L. Ginter, "Identification of the $4p\sigma_u\,^1\Pi_u$ Rydberg state of O_2", *Advanced Workshop on Atomic and Molecular Physics*, Canberra, 13–15 February, 1995.

[27] S. T. Gibson and B. R. Lewis, "Photodissociation viewed as an atomic collision", *Advanced Workshop on Atomic and Molecular Physics*, Canberra, 13–15 February, 1995.

[28] J. P. England, B. R. Lewis, and M. L. Ginter, "Identification of the $4p\sigma_u\,^1\Pi_u$ Rydberg state of O_2", *50th Ohio State University International Symposium on Molecular Spectroscopy*, Columbus, 12–16 June, 1995.

[29] J. P. England, B. R. Lewis, and S. T. Gibson, "Interactions between Rydberg and valence states of O_2", *50th Ohio State University International Symposium on Molecular Spectroscopy*, Columbus, 12–16 June, 1995.

[30] S. S. Banerjee, B. R. Lewis, K. G. H. Baldwin, and S. T. Gibson, "An investigation of the interactions of the $np\pi_u\,^1\Sigma_u^+(n = 3, 4)$ Rydberg states of O_2", *Tenth Conference of the Australian Optical Society*, Brisbane, 5–7 July, 1995.

[31] P. M. Dooley, B. R. Lewis, K. G. H. Baldwin, and S. T. Gibson, "Predissociation in the Schumann-Runge bands of O_2", *Tenth Conference of the Australian Optical Society*, Brisbane, 5–7 July, 1995.

[32] K. Waring, B. R. Lewis, K. G. H. Baldwin, and S. T. Gibson, "Is pressure broadening in molecular oxygen a myth?", *Tenth Conference of the Australian Optical Society*, Brisbane, 5–7 July, 1995.

[33] P. M. Dooley, B. R. Lewis, S. T. Gibson, and K. G. H. Baldwin, "Narrow-bandwidth VUV laser measurements of fine-structure predissociation linewidths in the Schumann-Runge bands of O_2", *Eleventh International Conference on Vacuum Ultraviolet Radiation Physics*, Tokyo, 27 August–1 September, 1995.

[34] B. R. Lewis, S. T. Gibson, P. M. Dooley, S. S. Banerjee, and K. G. H. Baldwin, "Quantum interference and lineshape asymmetry in the VUV photodissociation spectrum of molecular oxygen", *Eleventh International Conference on Vacuum Ultraviolet Radiation Physics*, Tokyo, 27 August–1 September, 1995.

[35] S. S. Banerjee, B. R. Lewis, S. T. Gibson, and K. G. H. Baldwin, "Indirect predissociation of the $3p\pi_u\, f\, {}^1\Sigma_u^+$ state of O_2", *Eleventh International Conference on Vacuum Ultraviolet Radiation Physics*, Tokyo, 27 August–1 September, 1995.

[36] S. T. Gibson, B. R. Lewis, and J. P. England, "Understanding diatomic photodissociation with a coupled-channel Schrödinger equation model", *Eleventh International Conference on Vacuum Ultraviolet Radiation Physics*, Tokyo, 27 August–1 September, 1995.

[37] J. P. England, B. R. Lewis, and M. L. Ginter, "Spin-orbit interactions between Rydberg states of O_2", *Eleventh International Conference on Vacuum Ultraviolet Radiation Physics*, Tokyo, 27 August–1 September, 1995.

[38] B. R. Lewis, "Narrow-bandwidth VUV laser measurements of photodissociation in O_2", invited talk, *Oji International Seminar on Atomic and Molecular Photoionization*, Tsukuba, 4–7 September, 1995.

[39] S. T. Gibson, B. R. Lewis, and P. C. Cosby, "Excitation of coupled electronic states", *51st International Symposium on Molecular Spectroscopy*, Columbus, 9–14 June, 1996.

[40] K. Waring, P. M. Dooley, B. R. Lewis, J. P. England, S. T. Gibson, and K. G. H. Baldwin, "Perturbations in the Schumann-Runge bands of molecular oxygen", *Twentieth International Quantum Electronics Conference*, Sydney, 14–19 July, 1996.

[41] J. S. Morrill, M. L. Ginter, B. R. Lewis, and S. T. Gibson, "The electronic structure of molecular oxygen", *Fall Meeting of the American Geophysical Union*, San Francisco, 15–19 December, 1996.

[42] P. M. Dooley, B. R. Lewis, K. Waring, K. G. H. Baldwin, and S. T. Gibson, "High-resolution cross sections for atmospheric photochemistry using laser-generated VUV radiation", *Conference on Lasers and Electro-Optics: Quantum Electronics and Laser Science Conference*, Baltimore, 18–23 May, 1997.

[43] S. T. Gibson and B. R. Lewis, "Partial photodissociation cross sections for O_2 in the 1205 Å region", *52nd International Symposium on Molecular Spectroscopy*, Columbus, 16–20 June, 1997.

[44] L. J. Coin, B. R. Lewis, and S. T. Gibson, "A new collision-induced transition in the vacuum-ultraviolet spectrum of O_2", *52nd International Symposium on Molecular Spectroscopy*, Columbus, 16–20 June, 1997.

[45] K. Waring, P. M. Dooley, B. R. Lewis, S. T. Gibson, and K. G. H. Baldwin, "Rotational perturbations in the Schumann-Runge bands near the dissociation limit" *52nd International Symposium on Molecular Spectroscopy*, Columbus, 16–20 June, 1997.

[46] B. R. Lewis and S. T. Gibson, "Modelling photoabsorption in the Schumann-Runge bands of molecular oxygen", invited talk, *Joint Assemblies of the International Association of Meteorology and Atmospheric Sciences and the International Association for Physical Sciences of the Oceans*, Melbourne, 1–9 July, 1997.

[47] B. R. Lewis, J. P. England, S. T. Gibson, M. J. Brunger, and M. Allan, "Electron energy-loss spectra of coupled electronic states: Rydberg-valence interactions in O_2" *20th International Conference on the Physics of Electronic and Atomic Collisions*, Vienna, 23–29 July, 1997.

[48] J. S. Morrill, M. L. Ginter, B. R. Lewis, and S. T. Gibson, "Review of the electronic structure of molecular oxygen", *International Conference on Atomic and Molecular Data and their Applications*, Gaithersburg, 29 September–2 October, 1997.

[49] J. S. Morrill, M. L. Ginter, B. R. Lewis, and S. T. Gibson, "Electronic Rydberg and valence states of molecular oxygen", *Fall Meeting of the American Geophysical Union*, San Francisco, 8–12 December, 1997.

[50] K. Waring, P. M. Dooley, B. R. Lewis, S. T. Gibson, and K. G. H. Baldwin, "Oxygen: Isn't that what ozone is made from?", *Eleventh Australian Optical Society Conference*, Adelaide, 10–12 December, 1997.

[51] B. Buijsse, W. J. van der Zande, A. T. J. B. Eppink, D. H. Parker, B. R. Lewis, and S. T. Gibson, "A photodissociation study of the O_2 Herzberg continuum", *Faraday Discussion No. 108: Dynamics of Electronically-Excited States in Gaseous, Cluster and Condensed Media*, Brighton, 15–17 December, 1997.

[52] G. Stark, B. R. Lewis, S. T. Gibson, and J. P. England, "High-resolution oscillator-strength measurements of the CO $B\,^1\Sigma^+ - X\,^1\Sigma^+$ (0,0) and (1,0) vibrational bands", *Twelfth International Conference on Vacuum Ultraviolet Radiation Physics*, San Francisco, 3–7 August, 1998.

[53] S. T. Gibson and B. R. Lewis, "Competing pathways for molecular dissociation", *Twelfth International Conference on Vacuum Ultraviolet Radiation Physics*, San Francisco, 3–7 August, 1998.

[54] J. Lacoursière, S. A. Meyer, G. W. Faris, T. G. Slanger, B. R. Lewis, and S. T. Gibson, "The $O(^1D)$ yield from O_2 photodissociation near Lyman-alpha (121.6 nm)", *Twelfth International Conference on Vacuum Ultraviolet Radiation Physics*, San Francisco, 3–7 August, 1998.

[55] K. Waring, B. R. Lewis, S. T. Gibson, and K. G. H. Baldwin, "The dissociation-limit region of the Schumann-Runge bands of O_2", *Twelfth International Conference on Vacuum Ultraviolet Radiation Physics*, San Francisco, 3–7 August, 1998.

[56] B. R. Lewis, S. T. Gibson, J. S. Morrill, and M. L. Ginter, "Perturbations in the $3s\sigma_g$ Rydberg states of O_2", *Twelfth International Conference on Vacuum Ultraviolet Radiation Physics*, San Francisco, 3–7 August, 1998.

[57] B. R. Lewis, S. T. Gibson, W. J. van der Zande, and P. C. Cosby, "Product branching ratios in the dissociation of N_2", *Twelfth International Conference on Vacuum Ultraviolet Radiation Physics*, San Francisco, 3–7 August, 1998.

[58] J. Lacoursière, S. A. Meyer, G. W. Faris, T. G. Slanger, B. R. Lewis, and S. T. Gibson, "The $O(^1D)$ yield from O_2 photodissociation near Lyman-alpha (121.6 nm)", *Spring Meeting of the American Geophysical Union*, Boston, 26–29 May, 1998.

[59] J. S. Morrill, M. L. Ginter, B. R. Lewis, S. T. Gibson, E. S. Hwang, R. A. Copeland, and T. G. Slanger, "The rotational structure of the $d\,^1\Pi_g$ Rydberg state of O_2", *Fall Meeting of the American Geophysical Union*, San Francisco, 6–10 December, 1998.

[60] J. S. Morrill, M. L. Ginter, B. R. Lewis, and S. T. Gibson, "The electronic Rydberg and valence structures of molecular oxygen", *NASA Office of Space Science: Laboratory Space Science Workshop*, Cambridge, 1–3 April, 1998.

[61] G. Stark, B. R. Lewis, S. T. Gibson, and J. P. England, "High-resolution oscillator strength measurements for high-v' bands of the $A(v') - X(0)$ system of carbon monoxide", *NASA Office of Space Science: Laboratory Space Science Workshop*, Cambridge, 1–3 April, 1998.

[62] B. R. Lewis, S. T. Gibson, T. G. Slanger, and D. L. Huestis, "The $B\,^3\Sigma_u^- \leftarrow b\,^1\Sigma_g^+$ transition of molecular oxygen", *54th International Symposium on Molecular Spectroscopy*, Columbus, 14–18 June, 1999.

[63] K. Waring, B. R. Lewis, S. T. Gibson, and K. G. H. Baldwin, "VUV laser spectroscopy of the O_2 Schumann-Runge system near the dissociation limit", *Twelfth Australian Optical Society Conference*, Sydney, 7–9 July, 1999.

[64] A. Tucay, R. Robertson, R. A. Copeland, and B. R. Lewis, "REMPI spectroscopy of the 9.5–10.5 eV states of oxygen", *Fall Meeting of the American Geophysical Union*, San Francisco, 13–17 December, 1999.

[65] B. R. Lewis, S. T. Gibson, F. T. Hawes, and L. W. Torop, "A new model for the Schumann-Runge bands of O_2", invited talk, *XXV General Assembly of the European Geophysical Society*, Nice, 25–29 April, 2000.

4. Selected published work

4.1 The aeronomic dissociation of water vapour by solar Lyman-alpha radiation

[18] B. R. Lewis, I. M. Vardavas, and J. H. Carver,
Journal of Geophysical Research **88**, 4935–4940 (1983).

JOURNAL OF GEOPHYSICAL RESEARCH, VOL. 88, NO. A6, PAGES 4935–4940, JUNE 1, 1983

The Aeronomic Dissociation of Water Vapor by Solar H Lyman α Radiation

B. R. LEWIS, I. M. VARDAVAS, AND J. H. CARVER

Research School of Physical Sciences, Australian National University, Canberra ACT 2600, Australia

The photoabsorption cross sections of molecular oxygen and water vapor have been measured as a function of temperature at 0.1 Å intervals between 1214 and 1219 Å. Over the width of the solar Lyman α line there is no fine structure apparent in the cross sections which were measured with 0.05 Å resolution. A large wavelength and temperature dependence is seen in the molecular oxygen cross sections, but the variations are much smaller in the case of water vapor. The measured cross sections are used in calculations of the rate of photodissociation of atmospheric water vapor by solar Lyman α radiation, taking full account of both the temperature and wavelength dependences. It is found that the photodissociation rates may be accurately reproduced at altitudes above those where Lyman α ceases to dominate the dissociation by using molecular oxygen and water vapor cross sections corresponding to fixed temperatures near 200 K. Analytical models for these cross sections are presented for use in photochemical calculations.

INTRODUCTION

The aeronomic photodissociation of water vapor,

$$H_2O + h\nu(\lambda < 2000\ \text{Å}) \rightarrow H + OH$$

by solar UV radiation in the region of Lyman α and the Schumann-Runge bands, is a major source of the chemically active hydroxyl radical OH in the mesosphere. In the stratosphere the reaction

$$H_2O + O(1D) \rightarrow OH + OH^* \qquad v \leq 2$$

becomes the dominant water vapor dissociation mechanism leading to the formation of OH. The hydroxyl radical's affinity for reactions with pollution products such as CO and CH_4 and its reaction with odd oxygen to produce molecular oxygen and odd hydrogen [*Hunt*, 1966] underlines the importance of the dissociation of water vapor to the evolution of the atmosphere [*Carver*, 1981].

Above 70 km the destruction of water vapor in the atmosphere is dominated by solar Lyman α photodissociation which is limited by absorption mainly due to molecular oxygen. (With an overhead sun the dissociation fraction due to Lyman α varies from 50% near 70 km to 75% near 100 km.) Thus accurate photodissociation rates above 70 km can only be obtained if the true solar Lyman α profile is used together with the wavelength and temperature dependent Lyman α cross sections of water vapor and molecular oxygen, as was noted by *Frederick and Hudson* [1980]. These authors used the solar Lyman α profile of *Meier and Prinz* [1970], the high-resolution wavelength dependent molecular oxygen cross sections of *Ogawa* [1968] and a wavelength dependent water vapor cross section model based on the low-resolution measurements of *Watanabe and Zelikoff* [1953].

Carver et al. [1977] measured the temperature dependence of the molecular oxygen cross section near Lyman α and discussed the importance of this dependence in deducing reliable oxygen concentrations from Lyman α extinction measurements in the atmosphere. No studies have yet been reported on the effect of atmospheric temperature on water vapor dissociation rates. The only high-resolution measurements of the water vapor cross section which include the Lyman α region are those of *Gürtler et al.* [1977], but these authors do not provide detailed results near Lyman α. There have been no measurements of the temperature dependence of the water vapor cross section.

This work presents molecular oxygen and water vapor cross sections measured at 0.05 Å resolution as a function of temperature and wavelength in the vicinity of solar Lyman α. There is no fine structure over the width of the solar Lyman α line in either cross section. The molecular oxygen cross section is very temperature dependent above 1215 Å, but the water vapor cross section shows little variation with temperature.

Calculations of the photodissociation rate of atmospheric water vapor have been performed using the new cross sections and the same solar irradiance data used by *Frederick and Hudson* [1980]. The present photodissociation rates at an altitude corresponding to the peak water vapor photodestruction rate are about 30% larger than those calculated using the cross sections assumed by Frederick and Hudson because of the combined effect of smaller molecular oxygen cross sections, larger water vapor cross sections, and the neglect of temperature variations by Frederick and Hudson.

It is found that the atmospheric water vapor photodissociation rates due to Lyman α resulting from a full calculation may be reproduced to better than 3% down to an altitude where the total dissociation rate becomes dominated by radiation in the Schumann-Runge bands and collisional dissociation due to O(1D) by adopting molecular oxygen and water vapor cross section profiles corresponding to fixed temperatures near 200 K. We have obtained polynomial fits to these wavelength-dependent cross sections in order that the photodissociation rate may be rapidly computed as a function of altitude for use in atmospheric chemistry models.

EXPERIMENTAL METHOD

Photoabsorption cross sections for molecular oxygen and water vapor were measured in the laboratory using a 2.2 m VUV monochromator and a temperature-controlled absorption cell. The light source was an argon continuum discharge lamp operated in the windowless mode at a pressure of 400 torr and powered by a pulser based on the Argonne design [*Berkowitz*, 1979]. The radiation was dispersed by a Minute-

Paper number 3A0258.
0148-0227/83/003A-0258$05.00

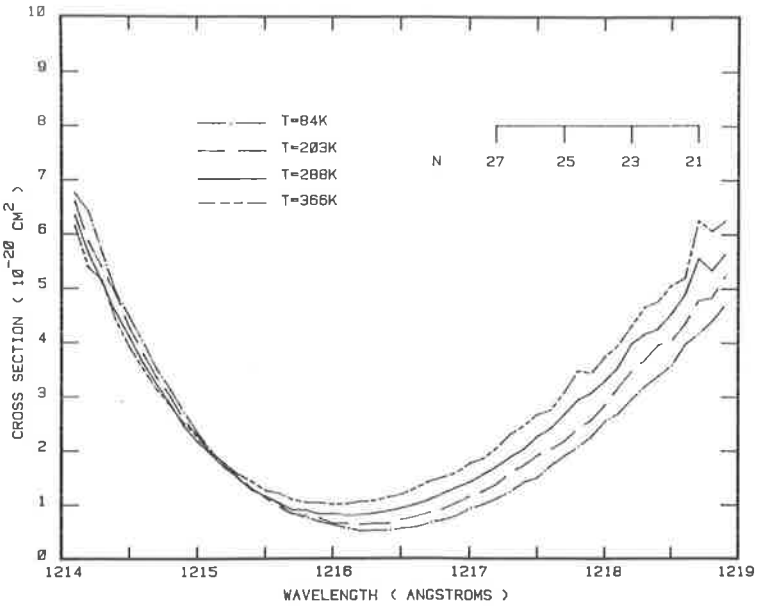

Fig. 1. Molecular oxygen photoabsorption cross sections measured near H Lyman α as a function of wavelength and temperature. Positions of some of the high rotational lines of the forbidden band $\alpha^1\Sigma_u^+$–$X^3\Sigma_g^-$ of molecular oxygen are also shown [*Ogawa*, 1968].

man 320 NIV normal incidence VUV scanning monochromator with 10 μ fixed slits giving a resolution of about 0.05 Å. An ARC VUV beamsplitter set at 45° served as the front window of the 1.2 m absorption cell and also allowed monitoring of the incident radiation. EMI solar blind photomultipliers type G-26E315, operated in the pulse counting mode, served to measure simultaneously the incident and transmitted radiation. With this arrangement the dark count rate was very low and no corrections were necessary for stray light.

The temperature of the gas in the cell could be altered by circulating heated or cooled liquids through an integral jacket, and the temperature was monitored by thermocouples placed at several points along the jacket. The cell was filled with either medical grade oxygen (2.5–30 torr) which had been carefully dried by passing through suitable cold traps, or water vapor (0.03–0.04 torr) purified from a distilled liquid sample by repeated freezing and pumping. These gases entered the cell through a Balzers RME 010 electromagnetic leak valve and the pressure was monitored by a Datametrics Barocel 570/1173 variable capacitance manometer. In the case of oxygen the pressure was servo controlled by a Datametrics 1404 valve controller. At the temperatures (83–370 K) and pressures used in the experiment no corrections were necessary for thermal transpiration.

The scanning routine was completely controlled by a Commodore PET 2001 microcomputer and HP3497A data acquisition/control unit. Wavelengths were set accurately by calibrating a shaft encoder on the monochromator at H Lyman α. At each wavelength the light entering and leaving the absorption cell was measured by the two photomultipliers with the cell alternately empty, then full, then empty. This enabled the calculation of a transmission value which was independent of lamp fluctuations and other background drifts. The absorption cross section corresponding to the transmission was calculated from Beer's law using the measured gas pressure, temperature, and cell length, and this value was stored on floppy disc. The wavelength was then advanced and the above process repeated until the desired wavelength interval had been covered. The wavelength was recalibrated periodically during a scan to eliminate the possible effects of thermal drifts. All of the above operations were executed under software control.

Experimental Results

Cross sections for molecular oxygen were measured from 1214 to 1219 Å at 0.1 Å intervals at temperatures of 84, 203, 288, and 366 K. The pressure dependence of the room temperature cross section was measured at several wavelengths from 1215 to 1218 Å at pressures up to 64 torr and was found to be approximately constant at $(1.5 \pm 0.2) \times 10^{-23}$ cm^2/Torr, in good agreement with the values of *Ogawa and Yamawaki* [1970], *Shardanand* [1967], and *Preston* [1940], all taken at H Lyman α and at higher pressures. This value was used to correct all cross sections to zero pressure, the maximum correction involved being about 5%. The results so obtained are shown in Figure 1 and Table 1. The errors due to counting statistics are better than 2% for all points and there is an additional error of about 3% arising from uncertainties in pressure, temperature, and cell length.

The room temperature cross sections of this work are consistently lower than those of *Ogawa* [1968] by about 15% but agree very well at 1215.7 Å with the pressure-corrected value of *Dose et al.* [1975]. The only previous measurements of the cross section as a function of temperature [*Carver et al.*, 1977] agree well with the current results near H Lyman α and near the absorption minima but become progressively lower than the present results as the cross section increases toward the scan extremities. Figure 1 shows that the cross section increases as the temperature decreases below about

1215.1 Å where there is virtually no temperature effect and then decreases markedly as the temperature decreases above 1215.1 Å. The structure due to the high rotational lines of the $\alpha^1\Sigma_u^+$–$X^3\Sigma_g^-$ band of molecular oxygen is also seen to decrease as the temperature decreases.

Cross sections for water vapor were measured at 0.1 Å intervals between 1214 and 1219 Å at temperatures of 235, 292, and 367 K and the results are presented in Table 1 and Figure 2. The statistical error of the results is better than 2%, and there is an additional error of 5% due to uncertainties in pressure, temperature, and cell length. (These cross sections are less accurate than those for molecular oxygen because of problems in stabilizing the small water vapor pressure.)

The observed temperature dependence of the water vapor cross section is small and passes through a minimum near H Lyman α. There have been no previous measurements as a function of temperature or indeed with this wavelength detail in this region but the present results are about 8% higher than the room temperature H Lyman α values of *Watanabe and Zelikoff* [1953] and *Preston* [1940]. No fine structure is observable in Figure 2. According to *Bell* [1965] the spectrum in this region consists of a narrow (010) α_2-X band (origin 1219.35 Å) overlapping a broad and diffuse (000) β_1-X band (origin 1218.95 Å). Some diffuse structure is observable above 1217 Å in Figure 2, and the absorption line at 1219.35 Å was observed in an extended scan to have a full width at half maximum (FWHM) comparable with the instrumental resolution of about 0.05 Å.

COMPUTATION OF THE PHOTODISSOCIATION RATE

The photodissociation rate of $J(s^{-1})$ of water vapor at altitude z due to solar Lyman α radiation is given by

$$J(z) = \int_{Ly\alpha} \sigma_{H_2O}(\lambda, T) I_\lambda(\infty) e^{-\tau(\lambda, z)}\, d\lambda \qquad (1)$$

where $I_\lambda(\infty)$ is the incident solar Lyman α irradiance at the top of the atmosphere and $\tau(\lambda, z)$ is the atmospheric optical depth which may closely be approximated by the expression

$$\tau(\lambda, z) \approx \tau_{O_2}(\lambda, z) = \sec\theta \int_z^\infty \sigma_{O_2}(\lambda, T) n_{O_2}(z')dz' \qquad (2)$$

since molecular oxygen is responsible for most of the absorption of solar Lyman α radiation at the altitudes of interest. n_{O_2} (cm^{-3}) is the number density of molecular oxygen, $\sigma_{O_2}(\lambda, T)$ and $\sigma_{H_2O}(\lambda, T)$ are the wavelength λ and temperature T dependent absorption cross sections in cm^2, and θ is the solar zenith angle. As we wish to compare the present computations with those of *Frederick and Hudson* [1980], we have taken the solar Lyman α profile from *Meier and Prinz* [1970] and normalized this to the integrated value of 3×10^{11} photons $cm^{-2}\ s^{-1}$ [*Ackerman*, 1971]. The integral in equation (1) is then evaluated over the wavelength region $\lambda_0 \pm 1$ Å, where $\lambda_0 = 1215.67$ Å. The molecular oxygen number density and atmospheric temperature profile were taken from the *U.S. Standard Atmosphere* (1976) and spline interpolation was used between the experimental values of $\sigma_{O_2}(\lambda, T)$.

We have also computed the water vapor photodestruction rate $n_{H_2O}J$ (molecules $cm^{-3}\ s^{-1}$) in order to isolate the altitude region of maximum water vapor destruction. For this we have taken a constant stratospheric-mesospheric water vapor mixing ratio of 2 ppm, which gives a water vapor height profile close to the winter profile computed by *Shimazaki and Laird* [1972] for the region $120 \geq z \geq 50$ km. The choice of 2 ppm mixing ratio is not critical in determining the altitude of maximum photodestruction, since the photodestruction rates are merely scaled at all altitudes with the water vapor mixing ratio.

In order to isolate the dependence of J on the various competing effects due to the wavelength and temperature dependences of the cross sections, we have computed J by sequentially suppressing the wavelength and temperature dependences of σ_{O_2} and σ_{H_2O} in turn. For comparison reasons we have also computed J by using the *Ogawa* [1968]

TABLE 1. Photoabsorption Cross Sections σ Measured Near H Lyman α for Molecular Oxygen and Water Vapor at Several Temperatures

Wavelength, Å	$\sigma(O_2) \times 10^{20}$, cm^2 Temperature, K				$\sigma(H_2O) \times 10^{17}$, cm^2 λ		
	84	203	288	366	235	292	367
1214.0	7.74	7.45	7.04	6.80	1.16	1.23	1.25
1214.1	6.76	6.61	6.34	6.15	1.18	1.25	1.24
1214.2	6.42	5.86	5.65	5.39	1.16	1.23	1.24
1214.3	5.66	5.39	5.11	5.14	1.21	1.27	1.29
1214.4	4.94	4.89	4.56	4.42	1.21	1.30	1.31
1214.5	4.48	4.29	4.11	3.92	1.24	1.29	1.30
1214.6	4.03	3.81	3.63	3.52	1.26	1.33	1.33
1214.7	3.52	3.36	3.23	3.14	1.30	1.34	1.35
1214.8	3.14	3.02	2.87	2.84	1.32	1.36	1.37
1214.9	2.74	2.59	2.46	2.53	1.32	1.41	1.40
1215.0	2.35	2.31	2.18	2.25	1.35	1.44	1.43
1215.1	2.01	1.99	1.94	1.97	1.38	1.45	1.46
1215.2	1.74	1.77	1.69	1.78	1.39	1.45	1.48
1215.3	1.49	1.54	1.51	1.57	1.43	1.46	1.45
1215.4	1.29	1.31	1.28	1.44	1.48	1.55	1.48
1215.5	1.17	1.13	1.16	1.27	1.50	1.52	1.52
1215.6	1.03	0.97	1.04	1.22	1.49	1.57	1.50
1215.7	0.84	0.83	0.91	1.10	1.51	1.57	1.57
1215.8	0.77	0.82	0.91	1.05	1.57	1.59	1.55
1215.9	0.70	0.76	0.83	1.04	1.57	1.60	1.57
1216.0	0.63	0.66	0.83	1.01	1.62	1.64	1.60
1216.1	0.58	0.66	0.81	1.02	1.65	1.66	1.58
1216.2	0.52	0.64	0.82	1.06	1.72	1.62	1.61
1216.3	0.53	0.66	0.84	1.08	1.66	1.67	1.61
1216.4	0.53	0.66	0.88	1.14	1.70	1.70	1.62
1216.5	0.57	0.74	0.94	1.19	1.72	1.70	1.60
1216.6	0.60	0.79	1.00	1.30	1.74	1.69	1.61
1216.7	0.67	0.86	1.08	1.42	1.71	1.70	1.63
1216.8	0.71	0.91	1.20	1.50	1.76	1.70	1.63
1216.9	0.80	1.03	1.32	1.59	1.74	1.72	1.61
1217.0	0.93	1.16	1.42	1.77	1.73	1.77	1.62
1217.1	1.02	1.26	1.57	1.86	1.79	1.74	1.67
1217.2	1.13	1.39	1.72	2.06	1.76	1.75	1.69
1217.3	1.25	1.60	1.89	2.31	1.82	1.78	1.67
1217.4	1.43	1.73	2.04	2.47	1.86	1.82	1.70
1217.5	1.51	1.92	2.27	2.68	1.81	1.80	1.71
1217.6	1.73	2.03	2.42	2.76	1.72	1.71	1.64
1217.7	1.91	2.18	2.68	3.09	1.69	1.72	1.66
1217.8	2.07	2.42	2.95	3.48	1.75	1.70	1.67
1217.9	2.27	2.58	3.08	3.45	1.72	1.76	1.72
1218.0	2.56	2.86	3.30	3.75	1.79	1.80	1.73
1218.1	2.70	3.18	3.56	3.96	1.83	1.84	1.76
1218.2	2.97	3.49	3.99	4.32	1.88	1.86	1.80
1218.3	3.20	3.68	4.17	4.67	1.80	1.81	1.75
1218.4	3.39	3.96	4.26	4.77	1.80	1.81	1.78
1218.5	3.58	4.04	4.54	5.07	1.85	1.92	1.83
1218.6	3.98	4.35	4.90	5.21	1.91	1.95	1.88
1218.7	4.17	4.79	5.56	6.26	1.93	1.98	1.95
1218.8	4.40	4.84	5.34	6.07	2.14	2.13	2.04
1218.9	4.71	5.23	5.64	6.25	2.26	2.25	2.18
1219.0	4.80	5.56	5.89	6.44	2.28	2.31	2.20

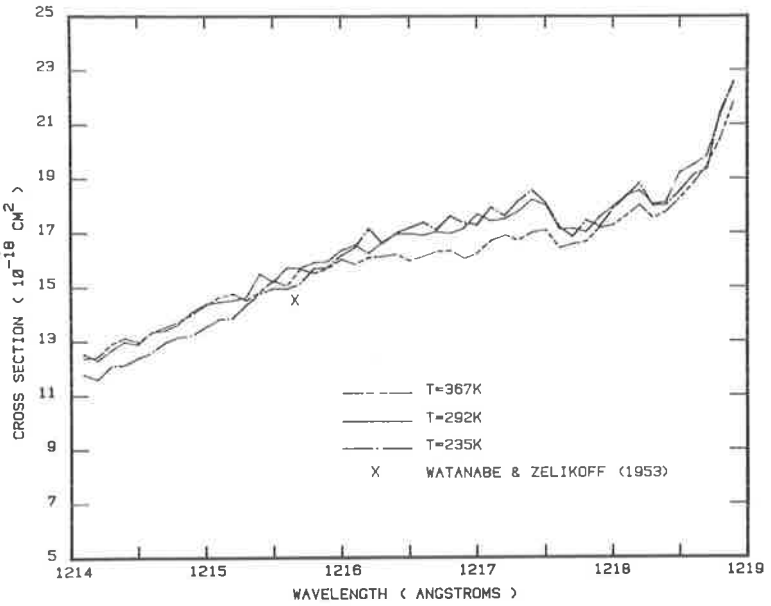

Fig. 2. Water vapor photoabsorption cross sections measured near H Lyman α as a function of wavelength and temperature. The room temperature measurement of *Watanabe and Zelikoff* [1953] at H Lyman α is also shown.

room temperature σ_{O_2} used by *Frederick and Hudson* [1980] together with their discontinuous wavelength dependent σ_{H_2O}.

Discussion

In Table 2 we give the Lyman α photodissociation rate J as a function of altitude both for an overhead sun and for a zenith angle of 85°. Our values are compared with calculations using the cross sections of *Frederick and Hudson* [1980]. It can be seen that using the present wavelength and temperature dependent cross sections results in higher J values, especially at the lower altitudes. In the region where the photodestruction of water vapor is important, the differences between our computations and those of Frederick and Hudson are about 30%. This is clearly shown in Figures 3 and 4, which give the water vapor photodestruction rate $n_{H_2O}J$ as a function of altitude. At the peaks of the curves we find differences of ~30% which can be reconciled with the following wavelength and temperature behavior of σ_{O_2} and σ_{H_2O}. The neglect of the temperature dependence of σ_{O_2}, i.e., using $\sigma_{O_2}(\lambda, T = 288\ K)$ reduces J_p (J at the peak) by ~8–9%. Neglecting both the wavelength and temperature dependence by using $\sigma_{O_2}(\lambda_0, T = 288\ K)$ results in an increase in J_p by ~14%. Similarly, using $\sigma_{H_2O}(\lambda, T = 288\ K)$ increases J_p by ~3–4%, while using $\sigma_{H_2O}(\lambda_0, T = 288\ K)$ decreases J_p by ~1–2%. When we consider the cross sections of *Frederick and Hudson* [1980] we see that they have neglected the temperature dependence of σ_{O_2}, so J_p is reduced by 8–9%. They also have an ~7% lower $\sigma_{H_2O}(\lambda, T)$ and an ~15% higher $\sigma_{O_2}(\lambda)$ resulting in an overall decrease in J_p by ~30%.

TABLE 2. Calculated Water Vapor Photodissociation Rates s^{-1} due to Lyman α

Altitude, km	Solar Zenith Angle 0°		Solar Zenith Angle 85°	
	Present Work	After *Frederick and Hudson* [1980]	Present Work	After *Frederick and Hudson* [1980]
120	4.58 − 6*	4.31 − 6	4.58 − 6	4.31 − 6
115	4.65 − 6	4.31 − 6	4.63 − 6	4.29 − 6
110	4.57 − 6	4.30 − 6	4.50 − 6	4.23 − 6
105	4.50 − 6	4.29 − 6	4.31 − 6	4.07 − 6
100	4.44 − 6	4.25 − 6	3.93 − 6	3.65 − 6
95	4.33 − 6	4.14 − 6	3.13 − 6	2.75 − 6
90	4.10 − 6	3.87 − 6	1.82 − 6	1.38 − 6
85	3.61 − 6	3.28 − 6	5.77 − 7	2.97 − 7
80	2.72 − 6	2.29 − 6	5.55 − 8	1.15 − 8
75	1.53 − 6	1.10 − 6	4.33 − 10	1.23 − 11
70	5.14 − 7	2.65 − 7	1.72 − 14	7.83 − 18
65	6.73 − 8	1.87 − 8	1.68 − 23	3.23 − 30
60	1.49 − 9	1.37 − 10		
55	1.18 − 12	1.69 − 14		
50	2.26 − 18	1.62 − 21		

*Read 4.58 − 6 as 4.58×10^{-6}.

In order to facilitate the computation of J we have explored the possibility of using σ_{H_2O} and σ_{O_2} values which are wavelength dependent but are evaluated at some specific temperature which reproduces the full wavelength and temperature dependent computations of J. It was found that $\sigma_{H_2O}(\lambda, T = 240\ K)$ and $\sigma_{O_2}(\lambda, T = 195\ K)$ reproduced the $J(z)$ profile to better than 3% down to the altitude where photodissociation of water vapor is dominated by solar radiation in the region of the Schumann-Runge bands. This is not surprising, since the atmospheric temperature in the region of the molecular oxygen absorption from 105 km down to 75 km is near 195 K, and the difference between this and the 240 K optimum found for σ_{H_2O} is not significant since the water vapor cross section is not too temperature dependent.

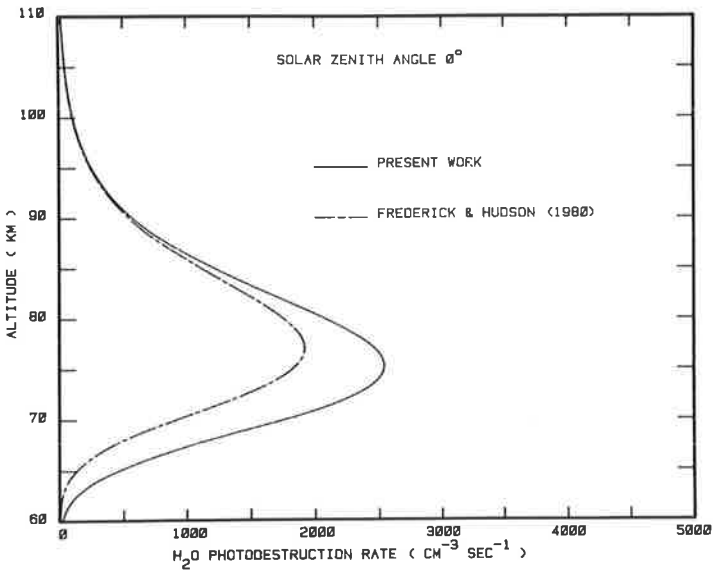

Fig. 3. The Lyman α photodestruction rate of atmospheric water vapor as a function of altitude for an overhead sun. A calculation performed using the cross sections of *Frederick and Hudson* [1980] is also shown. A water vapor mixing ratio of 2 ppm is assumed in each case, but curves can be deduced for another constant mixing ratios by simple scaling of the photodestruction rate $n_{H_2O}J$.

In addition, we have obtained polynomial fits to the wavelength dependences of the above cross sections of the form

$$\sigma_\lambda\ (\text{cm}^2) = C_4(\Delta\lambda)^4 + C_3(\Delta\lambda)^3 + C_2(\Delta\lambda)^2 + C_1\Delta\lambda + C_0 \quad (3)$$

where $\Delta\lambda = \lambda - \lambda_0(\text{Å})$, $|\Delta\lambda| \leq 1$, and the coefficients for water vapor and molecular oxygen are given in Table 3. The major part of computer execution time needed to obtain $J(z)$ is taken by the evaluation of the integral in equation (2) when σ_{O_2} is wavelength and temperature dependent. On using the above temperature independent fit, the column density $\int_z^\infty n_{O_2}(z')dz'$ can be precomputed and τ_{O_2} evaluated rapidly.

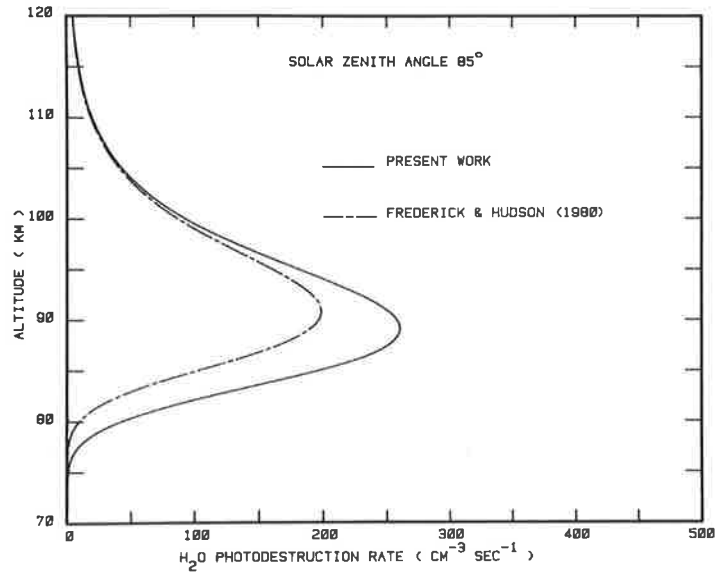

Fig. 4. The Lyman α photodestruction rate of atmospheric water vapor as a function of altitude for a solar zenith angle of 85°. A calculation performed using the cross sections of *Frederick and Hudson* [1980] is also shown. A water vapor mixing ratio of 2 ppm is assumed in each case, but curves can be deduced for other constant mixing ratios by simple scaling of the photodestruction rate $n_{H_2O}J$.

TABLE 3. Polynominal Coefficients for Evaluating σ_λ cm^2 for Water Vapor and Molecular Oxygen Using Equation (3)

	H_2O	O_2
C_4	−1.2199025 − 18*	−2.0319808 − 21
C_3	−8.2043638 − 19	−2.1569135 − 21
C_2	1.1857752 − 18	1.4286004 − 20
C_1	2.8891091 − 18	−1.1441759 − 20
C_0	1.5037800 − 17	8.9470039 − 21

*Read −1.2199025 − 18 as $-1.2199025 \times 10^{-18}$.

CONCLUSION

We have obtained experimentally the full wavelength and temperature dependence of the water vapor and molecular oxygen cross sections in the Lyman α region. Although the oxygen cross sections exhibit a strong temperature dependence, the water vapor cross sections are only weakly temperature dependent. In particular both the molecular oxygen and water vapor cross sections exhibit little fine structure in the vicinity of Lyman α. These new cross sections have been used to evaluate the water vapor photodissociation rate due to solar Lyman α radiation in the stratosphere and mesosphere. Differences of approximately 30% have been found between our photodissociation rates at the altitude of peak photodestruction and those calculated using the cross sections used by *Frederick and Hudson* [1980]. These differences arise because of the different magnitudes of the cross sections and the previous neglect of the temperature dependence of the molecular oxygen cross section in particular. Simple wavelength dependent polynomial expressions for both the water vapor and molecular oxygen cross sections have been obtained, allowing the rapid computation of the atmospheric water vapor photodissociation rate.

Acknowledgments. The editor thanks R. R. Meier and R. D. Hudson for their assistance in evaluating this paper.

REFERENCES

Ackerman, M., Ultraviolet solar radiation related to mesospheric processes, in *Mesospheric Models and Related Experiments*, edited by G. Fiocco, pp. 149–159, D. Reidel, Hingham, Mass., 1971.

Bell, S., The spectra of H_2O and D_2O in the vacuum ultraviolet, *J. Mol. Spectrosc., 16*, 205–213, 1965.

Berkowitz, J., *Photoabsorption, Photoionization, and Photoelectron Spectroscopy*, p. 413, Academic, New York, 1979.

Carver, J. H., Prebiotic atmospheric oxygen levels, *Nature, 292*, 136–138, 1981.

Carver, J. H., H. P. Gies, T. I. Hobbs, B. R. Lewis, and D. G. McCoy, Temperature dependence of the molecular oxygen photoabsorption cross section near the H Lyman α line, *J. Geophys. Res., 82*, 1955–1960, 1977.

Dose, V., U. Schmocker, and G. Sele, Photoabsorption coefficient of molecular oxygen in the vicinity of the hydrogen Lyman-Alpha line, *Z. Phys. A, 274*, 1–8, 1975.

Frederick, J. E., and R. D. Hudson, Atmospheric opacity in the Schumann-Runge bands and the aeronomic dissociation of water vapour, *J. Atmos. Sci., 37*, 1088–1098, 1980.

Gürtler, P., V. Saile, and E. E. Koch, Rydberg series in the absorption spectra of H_2O and D_2O in the vacuum ultraviolet, *Chem. Phys. Lett., 51*, 386–391, 1977.

Hunt, B. G., Photochemistry of ozone in a moist atmosphere, *J. Geophys. Res., 71*, 1385–1398, 1966.

Meier, R. R., and D. K. Prinz, Absorption of the solar Lyman alpha line by geocoronal atomic hydrogen, *J. Geophys. Res., 75*, 6969–6979, 1970.

Ogawa, M., Absorption coefficients of O_2 at the Lyman alpha line and its vicinity, *J. Geophys. Res., 73*, 6759–6763, 1968.

Ogawa, M., and K. R. Yamawaki, Absorption coefficients of O_2 at the Lyman α line and of other O_2 transmission windows, *Appl. Opt., 9*, 1709–1711, 1970.

Preston, W. M., The origin of radio fade-outs and the absorption coefficient of gases for light of wavelength 1215.7 Å, *Phys. Rev., 57*, 887–894, 1940.

Shardanand, Absorption coefficients of O_4 at oxygen windows, *NASA Tech. Note, TN D-4225*, 1967.

Shimazaki, T., and A. R. Laird, Seasonal effects on distributions of minor neutral constituents in the mesosphere and lower thermosphere, *Radio Sci., 7*, 23–43, 1972.

Watanabe, K., and M. Zelikoff, Absorption coefficients of water vapour in the vacuum ultraviolet, *J. Opt. Soc. Am., 43*, 753–755, 1953.

(Received December 20, 1982;
revised February 11, 1983;
accepted February 14, 1983.)

4.2 Temperature dependence of the carbon dioxide photoabsorption cross section between 1200 and 1970 Å

[19] B. R. Lewis and J. H. Carver,
Journal of Quantitative Spectroscopy and Radiative Transfer **30**, 297–309 (1983).

J. Quant. Spectrosc. Radiat. Transfer Vol. 30, No. 4, pp. 297–309, 1983
Printed in Great Britain.

0022-4073/83 $3.00 + .00

TEMPERATURE DEPENDENCE OF THE CARBON DIOXIDE PHOTOABSORPTION CROSS SECTION BETWEEN 1200 AND 1970 Å

B. R. Lewis and J. H. Carver
Research School of Physical Sciences, The Australian National University, Canberra, Australia 2600

(*Received* 27 *January* 1983)

Abstract—Photoabsorption cross sections have been measured for carbon dioxide at 0.5Å intervals between 1200 and 1970Å. The instrumental resolution was about 0.05Å and measurements were performed using relatively low pressures at temperatures near 200, 300, and 370 K. The room temperature cross sections are found to be in good agreement with previous measurements and a temperature effect is found which is small at the shorter wavelengths, passing through a minimum near 1400Å. At longer wavelengths the temperature effect increases steadily until at some fixed wavelengths above 1900 A the cross section increases by a factor of about 20 as the temperature is increased from 200 to 370 K. This behaviour is of particular significance to calculations of carbon dioxide photodissociation rates at low altitudes in the Martian atmosphere.

INTRODUCTION

Accurate knowledge of the VUV photoabsorption cross sections of carbon dioxide is essential if reliable calculations of photodissociation rates in the Martian atmosphere are to be undertaken. McElroy and Hunten[1] were the first to point out the importance of the 1670–2000 Å wavelength band as a source of atomic oxygen below 40 km but they only had room temperature cross sections available for use in their photodissociation rate calculations. Julienne *et al.*[2] have calculated a small temperature effect in the carbon dioxide photoabsorption cross section integrated between 1200 and 1750 Å, and De More and Patapoff[3] have measured a significant cross section temperature dependence between 1750 and 1860 Å. Nevertheless even the more recent Martian atmospheric models, for example Kong and McElroy,[4] still employ room temperature carbon dioxide cross sections despite the low temperatures prevailing at low altitudes in the atmosphere of Mars.

The photoabsorption cross sections of room temperature carbon dioxide have been measured by several investigators: Sun and Weissler (370–1310 Å),[5] Nakata *et al.* (580–1670 Å),[6] Wilkinson and Johnston (1440–1670 Å),[7] Inn *et al.* (1050–1750 Å),[8] Heimerl (1655–1825 Å),[9] Ogawa (1718–2160 Å),[10] Thompson *et al.* (1850–1960 Å),[11] and Shemansky (1700–3000 Å).[12] The only reported measurement of the temperature dependence of the cross section[3] was performed with poor wavelength resolution and at very high pressures of carbon dioxide in the wavelength range 1750–1860 Å. The authors[3] comment on the need for more measurements at lower pressures and with better resolution. No measurements of the temperature dependence of the cross section have been reported in the range 1200–1750 Å and thus no comparisons are possible with the theoretical calculations.[2]

We present measurements of the photoabsorption cross section of carbon dioxide at 0.5 Å intervals between 1200 and 1970 Å. The wavelength resolution was about 0.05 Å and measurements were taken at three gas temperatures near 200, 300, and 370 K. The pressure of the absorbing carbon dioxide varied from 0.5 to 850 torr. The room temperature cross sections are in excellent agreement with those of Nakata *et al.*[6] between 1250 and 1670 Å and those of Ogawa[10] between 1670 and 1970 Å. The present cross section temperature dependences are in good agreement with those of De More and Patapoff,[3] except for a small number of high values measured in the earlier work.[3]

At short wavelengths, the temperature effect is small, passing through a minimum near 1400 Å but, as the cross section falls at longer wavelengths, the relative variation with temperature increases steadily until, at some fixed wavelengths above 1900 Å, the cross section increases by a factor of about 20 when the temperature is raised from 200 to 370 K. Since the

temperature at low altitudes (<50 km) in the Martian atmosphere ranges between 140 and 220 K and since only radiation of wavelength greater than ~1800 Å penetrates this far, the use of room temperature carbon dioxide cross sections in lower Martian atmosphere photodissociation rate calculations will produce significant errors.

EXPERIMENTAL PROCEDURE

Photoabsorption cross sections for carbon dioxide were measured using a 2.2 m VUV monochromator and a temperature-controlled absorption cell. Below about 1300 Å the light source was an argon continuum discharge lamp powered by a pulser based on the Argonne design.[13] The lamp was operated in the windowless mode at a pressure of 400 torr of argon and a pulse repetition frequency of about 80 kHz. Above 1300 Å the lamp was run with 1–10 torr of molecular hydrogen and a d.c. discharge at 1 A. The resultant background spectrum in the range 1400–1700 Å is shown in Fig. 1, where the points have been taken at 0.3 Å intervals. The 0.05 Å resolution enables it to be clearly seen that the many-line spectrum is underlaid by a continuum with oscillating structure. This continuum was first noticed by Herzberg[14] and was first reported by Dalgarno *et al*[14] who attributed it to transitions from various vibrational levels of the $B\ ^1\Sigma_u^+$ state into the continuum of the $X\ ^1\Sigma_g^+$ state as distinct from the comparatively well known continuum in the region 1700–5000 Å which results from a $^3\Sigma_g^+ - {}^3\Sigma_u^+$ transition. The continuum between 1300 and 1700 Å provides a useful background for absorption measurements in association with the line spectrum, but below 1300 Å the argon source is preferable because of the strong continuum and absence of stray light.

The radiation was dispersed by a Minuteman 320 NIV normal incidence VUV scanning monochromator equipped with a 1200 g/mm grating blazed at 1500 Å. With 10 μ fixed slits a resolution of about 0.05 Å was obtained. An ARC VUV beamsplitter set at 45° served as the

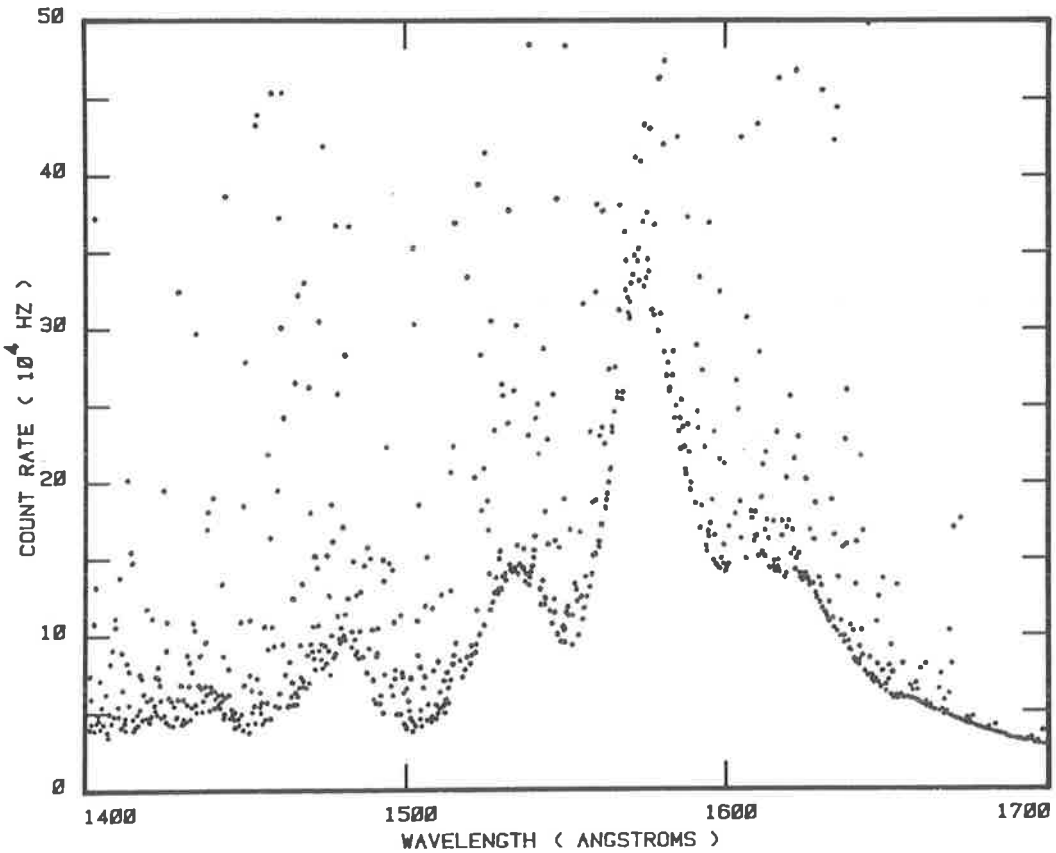

Fig. 1. Background spectrum of a molecular hydrogen lamp between 1400 and 1700 Å. Points were taken every 0.3 Å with an instrumental resolution of 0.05 Å. Many emission lines are off scale and the lower limit of the points represents the profile of the H_2 B–X continuum first reported by Dalgarno *et al.*[14]

front window of the 1.2 m absorption cell and also allowed monitoring of the incident radiaton. EMI photomultipliers type G-26E 315 (CsI photocathode) or type G-26H 315 (CsTe photocathode) were used at shorter and longer wavelengths respectively in the pulse counting mode in order to measure simultaneously the incident and transmitted radiation. The MgF_2 window of the rear photomultiplier also served as the rear window of the cell. Corrections for stray light were applied where necessary but never exceeded 2%.

The temperature of the gas in the cell could be altered by circulating heated or cooled liquids through an integral jacket and the temperature was monitored by several thermocouples. The cell was filled with anaerobic carbon dioxide (0.5–850 torr), carefully dried by passing through suitable cold traps, via a Balzers RME 010 electromagnetic leak valve. The pressure was monitored by a Datametrics Barocel 570/1173 variable capacitance manometer and was controlled by a Datametrics 1404 valve controller and a fixed leak, but at pressures near one atmosphere the cell was simply filled and closed off. At the temperatures (200–370 K) and pressures used in the experiment, no corrections were necessary for thermal transpiration.

The scanning routine was completely controlled by a Commodore PET 2001 microcomputer and an HP 3497A data acquisition/control unit. Two distinct scanning procedures were used. In regions where there was no background line structure, 100 Å scans with 0.5 Å steps were performed over the same region with the cell empty, then full, then empty and the photoabsorption cross sections were subsequently calculated by the microcomputer from the stored photomultiplier counts and other parameters. In the region of the many-line spectrum this was not possible due to the difficulty of accurately matching the positions of narrow emission lines in independent scans. In this case, the light entering and leaving the absorption cell was measured at each wavelength by the two photomultipliers with the cell alternately empty, then full, then empty. This procedure enabled the calculation of a transmission value which was independent of lamp fluctuations and other background drifts and eliminated the emission line position matching problem. The absorption cross section corresponding to the transmission was calculated from Beer's law using the measured gas pressure, temperature and cell length and was stored on floppy disc. The wavelength was then advanced and the above procedure repeated until the desired wavelength interval had been covered. In this mode all of the operations were executed under software control and the system could be left unattended for long periods.

RESULTS

The photoabsorption cross sections measured for temperatures near 200, 300, and 370 K at 0.5 Å intervals between 1200 and 1970 Å are shown in Figs. 2–9, where the points have been joined by straight line segments. The statistical accuracy of the cross sections is generally better than 5% with an additional absolute error of 2% due to uncertainties in pressure, temperature and cell length but, for cross sections below about 10^{-23} cm^2, the accuracy worsens considerably because of the low absorption at the maximum allowable cell pressure of about 850 torr. The cross sections below 10^{-23} cm^2 shown in Fig. 9 have been smoothed. Also shown in Figs. 2–9 is the explicit cross section (σ) temperature dependence (%/°C) for the lower and higher ranges of temperature (T). The ordinate is given by $100(\sigma_2-\sigma_1)/(0.5(\sigma_2+\sigma_1)(T_2-T_1))$ where the subscripts refer to the higher and lower temperatures respectively, but the values have been smoothed before plotting to minimize the incidence of false structure due to the increased statistical errors produced by the subtraction of the cross sections. Typical error bars are shown.

The overall absorption spectrum consists of two broad peaks near 1340 and 1480 Å which exhibit a certain amount of diffuse band structure. According to the calculations of Winter *et al.*,[15] the low wavelength peak corresponds to excitation to a $^1\pi_g$ state while the high wavelength peak corresponds to excitation to a $^1\Delta_u$ state. The latter assignment is consistent with the conclusions of Dixon,[16] who established that the emitting state of the carbon monoxide flame bands was a $^1B_2$ state of bent (122°) carbon dioxide correlating with the $^1\Delta_u$ state of the linear molecule, and that the same state was responsible for the 1480 Å absorption peak. Unfortunately, the irregular spacings of the complicated diffuse vibrational structure in the absorption spectrum make it difficult to contribute to a detailed understanding of the spectroscopy of carbon dioxide by purely optical methods.

In the range 1200–1670 Å the present room-temperature cross sections agree well with those

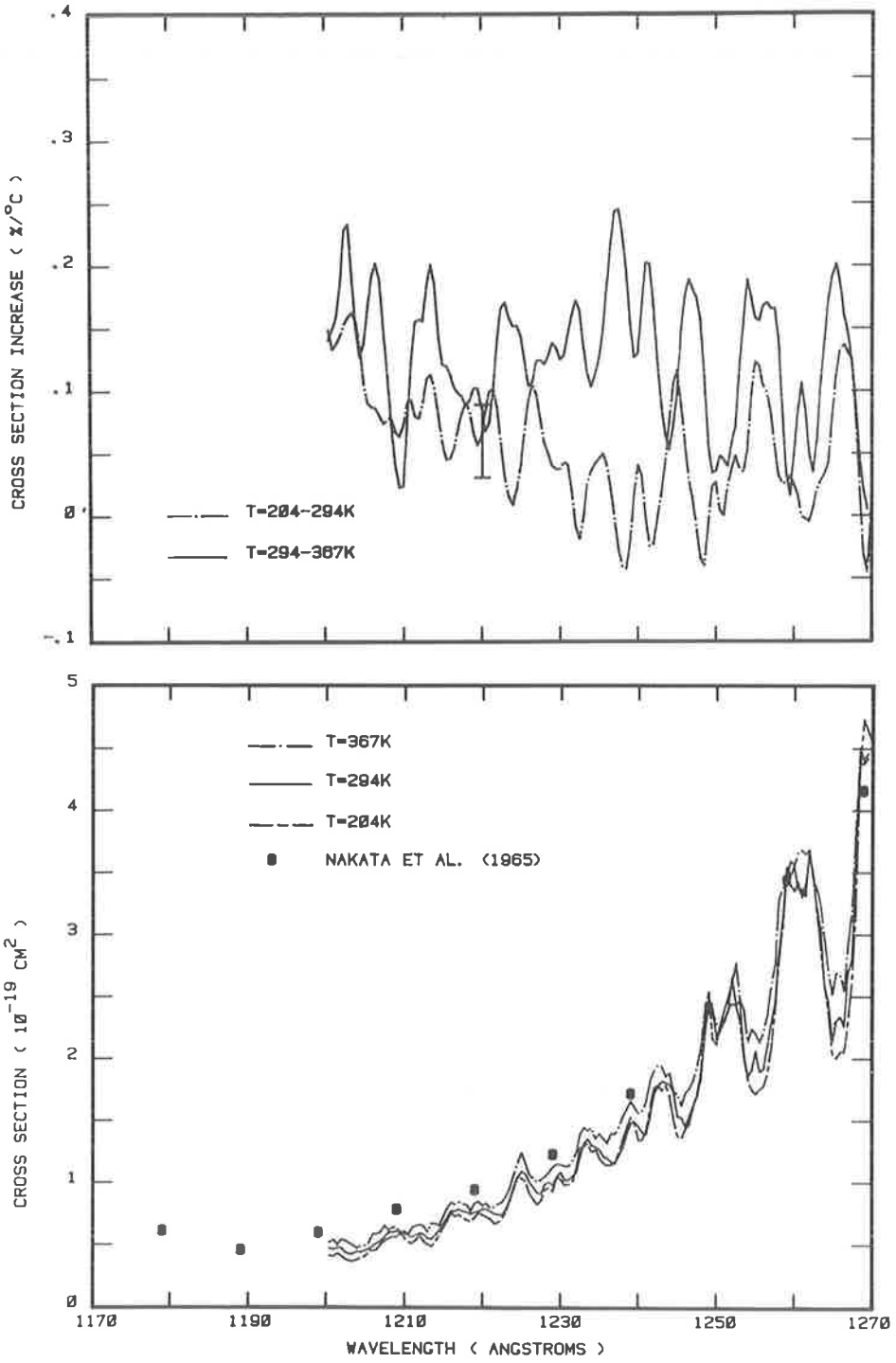

Fig. 2. Carbon dioxide photoabsorption cross sections from 1200 to 1270 Å at 204, 294, and 367 K compared with the room temperature results of Nakata *et al.*[6] Explicit cross section temperature dependences are also shown.

of Nakata *et al.*,[6] except in the range 1200–1240 Å where the present results are up to 20% lower. Nakata *et al.*[6] used a hydrogen source even in this region and may have had problems due to stray light. It was necessary to apply wavelength shifts of up to 2 Å to the graphed results of Nakata *et al.*[6] in order to match up positions of the absorption structure. Figures 2–6 show only selected cross sections taken from Nakata *et al.*[6] compared with the present results for diagrammatic simplicity. The agreement is good not only in absolute magnitude but also in the

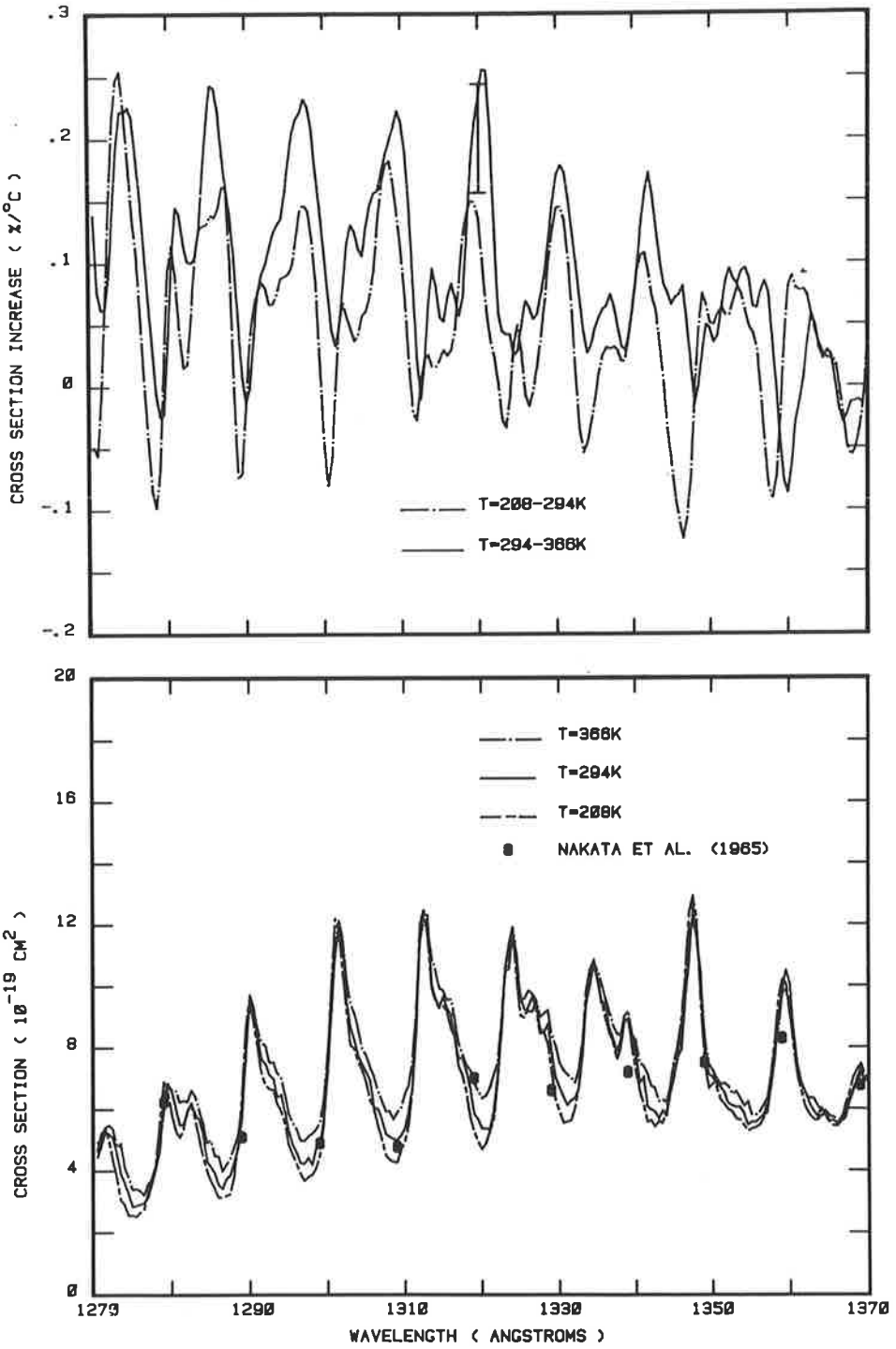

Fig. 3. Carbon dioxide photoabsorption cross sections from 1270 to 1370 Å at 208, 294, and 366 K compared with the room temperature results of Nakata *et al.*[6] Explicit cross section temperature dependences are also shown.

size and shape of the structure. Separate fine scans performed in this work yield the values $7.4\times10^{-20}\,cm^2$, $7.6\times10^{-20}\,cm^2$, $8.0\times10^{-20}\,cm^2$ for the cross section at Lyman α centre at temperatures of 205, 292 and 366 K respectively. The room temperature value should be compared with $7.3\times10^{-20}\,cm^2$ and $8.2\times10^{-20}\,cm^2$ obtained by Inn *et al.*[8] and Nakata *et al.*[6] respectively.

In the range 1670–1970 Å, the present room temperature cross sections agree well with those

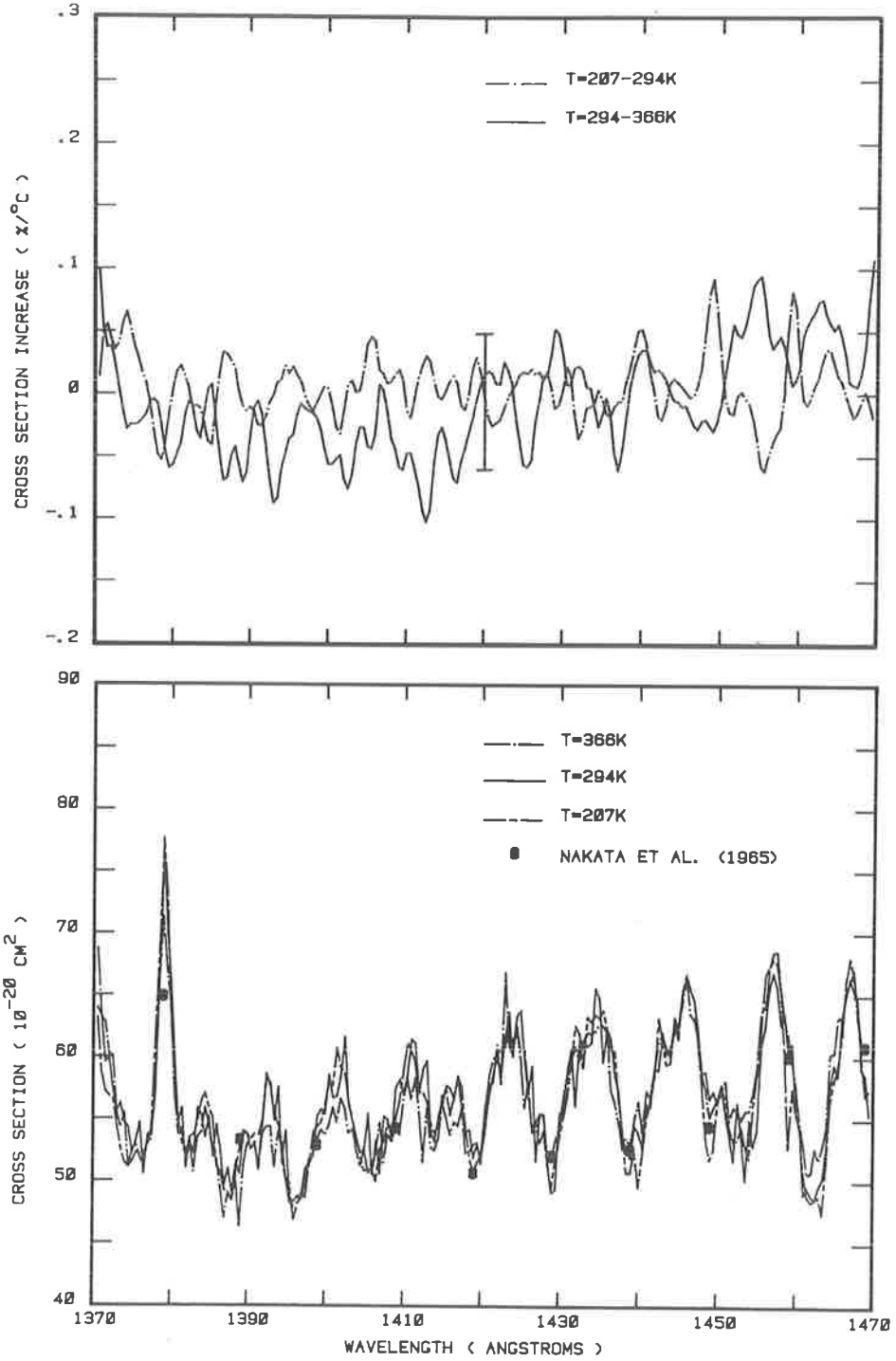

Fig. 4. Carbon dioxide photoabsorption cross sections from 1370 to 1470 Å at 207, 294, and 366 K compared with the room temperature results of Nakata *et al.*[6] Explicit cross section temperature dependences are also shown.

of Ogawa[10] and Shemansky[12] but, because of the high resolution, tend to favour those of Ogawa,[10] particularly with regard to the positions and characteristics of the fine structure. Cross sections of Ogawa[10] at the more prominent minima and of Shemansky[12] at maxima and minima are compared with the present results in Figs. 7–9.

The dependence of the cross section on temperature exhibits different behaviour in different wavelength regions. In the range 1200–1250 Å, the cross section increases only slowly with

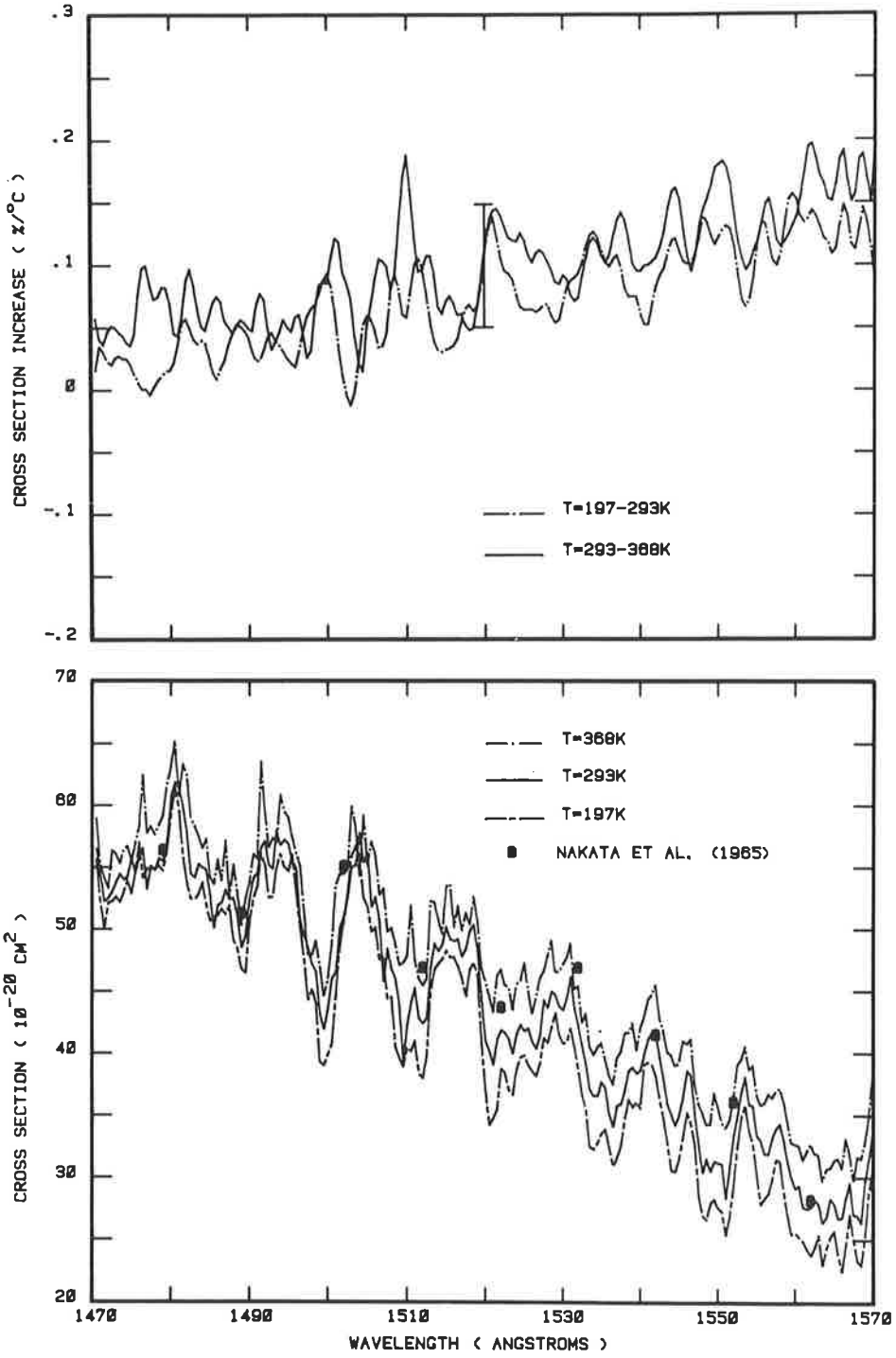

Fig. 5. Carbon dioxide photoabsorption cross sections from 1470 to 1570 Å at 197, 293, and 368 K compared with the room temperature results of Nakata *et al.*[6] Explicit cross section temperature dependences are also shown.

temperature at ~0.1%/°C. From 1250–1350 Å, the peaks of the vibrational structure show essentially no temperature dependence while the minima increase with temperature at ~0.2%/°C. From 1350–1450 Å, the region between the two major cross section peaks, there is effectively no temperature dependence at either the maxima or minima of the structure. At wavelengths greater than ~1450 Å, the mean temperature dependence increases steadily reaching ~1.2%/°C at ~1950 Å. In this region, the cross section always exhibits a greater

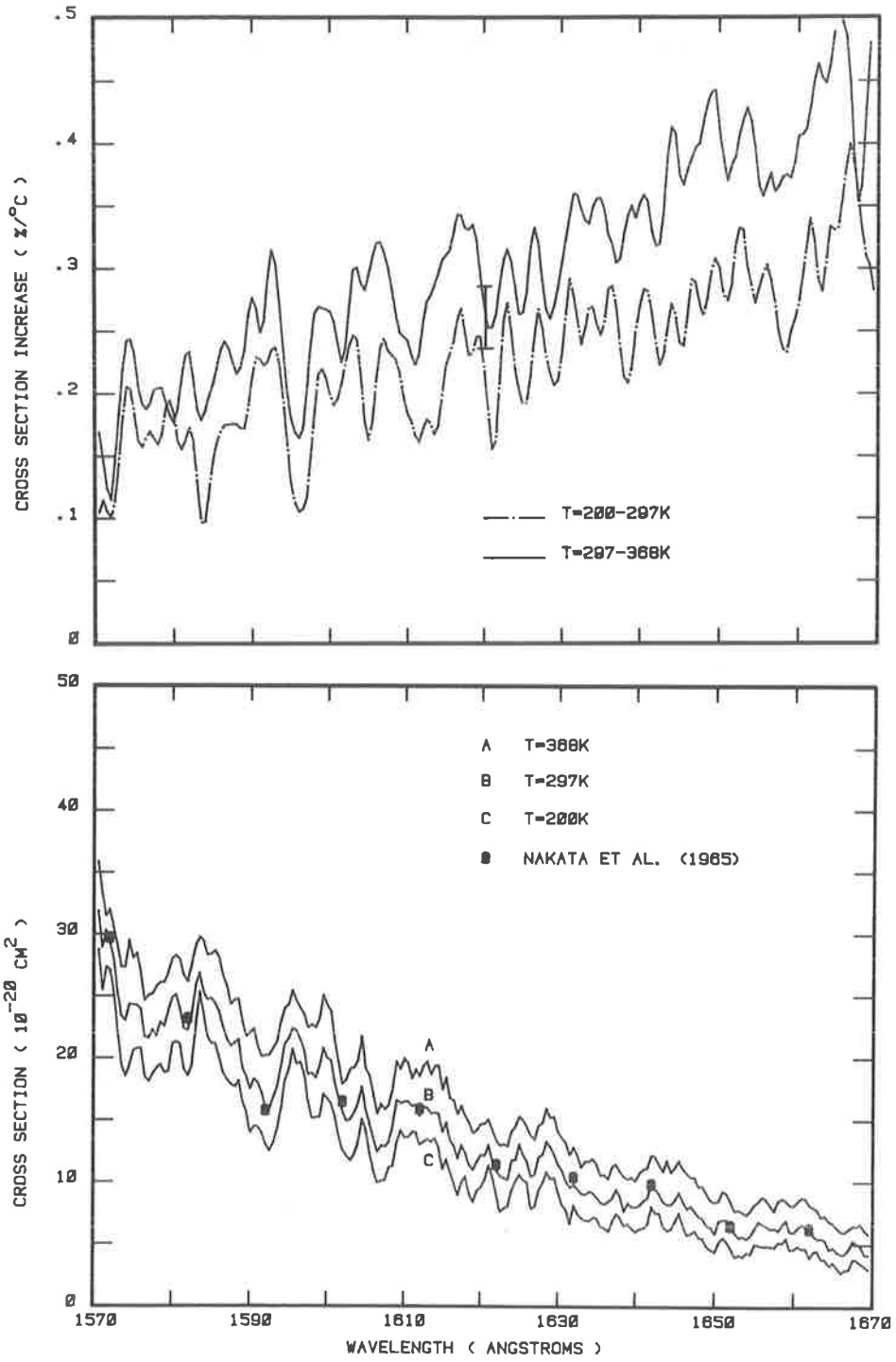

Fig. 6. Carbon dioxide photoabsorption cross sections from 1570 to 1670 Å at 200, 297, and 368 K compared with the room temperature results of Nakata *et al.*[6] Explicit cross section temperature dependences are also shown.

temperature dependence at the structural minima than at the maxima, and Figs. 8 and 9 dramatically show the greatly enhanced structure in the cross section as the temperature is decreased. At 1926.5 Å, a minimum in the low temperature cross section, a twenty fold increase in cross section occurs when the temperature is raised from 199 to 368 K. Table 1 gives values of the cross section as a function of temperature for some of the more prominent minima.

The only previous cross section temperature dependence measurements are those of De

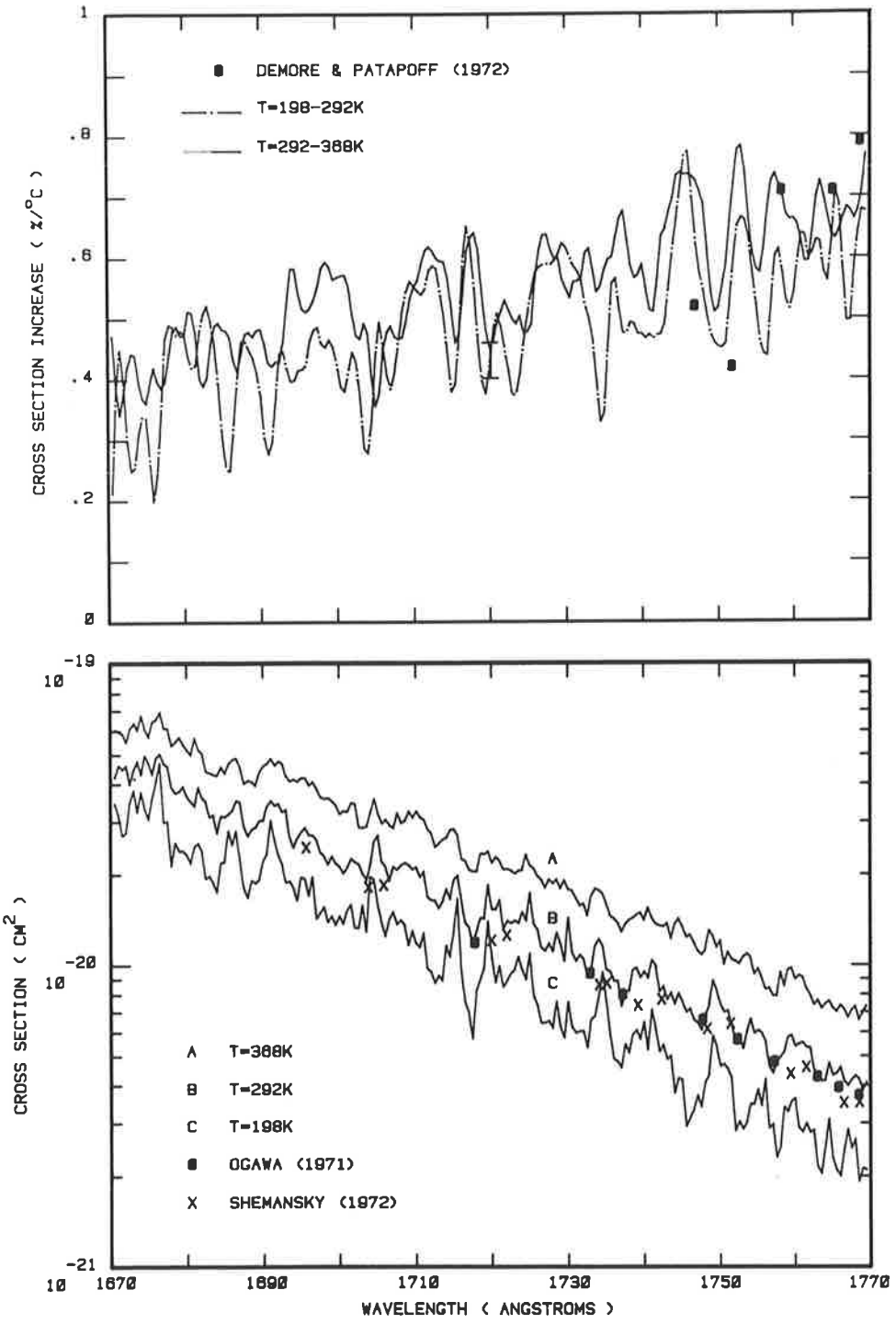

Fig. 7. Carbon dioxide photoabsorption cross sections from 1670 to 1770 Å at 198, 292, and 368 K compared with the room temperature results of Ogawa[10] and Shemansky.[12] Explicit temperature dependences are also shown compared with the results of De More and Patapoff.[3]

More and Patapoff[3] and are shown in Figs. 7 and 8. For the most part, the agreement with the present results is good apart from some high points in their work[3] in the 1800–1825 Å region. The present results are much more extensive than those of De More and Patapoff[3] and have been taken with much higher resolution and at much lower pressures.

Julienne *et al.*[2] calculated the temperature dependence of the integrated absorption coefficient for carbon dioxide between 1200 and 1750 Å, and it is possible to compare their

Table 1. Carbon dioxide photoabsorption cross sections $\sigma(T)\,\mathrm{cm}^2$ measured near deep local absorption minima at temperatures T near 200, 300, and 370 K. Values were measured at 0.5 Å intervals and hence will not coincide exactly with minima in most cases.

λ, Å	σ(~200)	σ(~300)	σ(~370)	λ, Å	σ(~200)	σ(~300)	σ(~370)
1213.5	4.86-20†	5.45-20	6.70-20	1536.5	3.09-19	3.41-19	3.75-19
1221.5	6.71-20	7.50-20	8.05-20	1551.0	2.54-19	2.83-19	3.40-19
1227.0	8.24-20	9.18-20	1.00-19	1566.0	2.25-19	2.68-19	3.08-19
1236.0	1.14-19	1.20-19	1.32-19	1574.0	1.85-19	2.30-19	2.74-19
1245.5	1.36-19	1.53-19	1.62-19	1582.0	1.86-19	2.23-19	2.62-19
1255.0	1.72-19	2.07-19	2.20-19	1592.5	1.25-19	1.59-19	2.03-19
1265.5	2.00-19	2.30-19	2.69-19	1606.5	9.92-20	1.24-19	1.55-19
1275.5	2.53-19	2.87-19	3.42-19	1622.5	7.59-20	1.05-19	1.30-19
1286.0	3.14-19	3.54-19	4.48-19	1640.0	6.01-20	8.01-20	1.01-19
1297.0	3.68-19	4.24-19	4.98-19	1653.5	3.99-20	5.63-20	7.60-20
1309.0	4.27-19	5.01-19	5.91-19	1666.0	2.74-20	4.19-20	6.04-20
1320.0	4.71-19	5.37-19	6.35-19	1684.0	1.75-20	2.75-20	4.27-20
1330.5	5.56-19	6.40-19	7.26-19	1688.0	1.68-20	2.69-20	4.11-20
1342.5	5.43-19	5.92-19	6.68-19	1717.5	5.69-21	1.18-20	2.05-20
1354.5	5.29-19	5.49-19	6.24-19	1737.0	4.56-21	7.29-21	1.29-20
1365.5	5.44-19	5.62-19	5.74-19	1745.5	2.92-21	6.99-21	1.24-20
1376.0	5.21-19	5.47-19	5.18-19	1752.0	2.83-21	5.61-21	1.03-20
1388.0	4.83-19	4.90-19	4.84-19	1757.5	2.31-21	4.76-21	7.91-21
1396.0	4.69-19	4.83-19	4.79-19	1763.5	2.04-21	4.14-21	7.20-21
1406.5	5.00-19	5.33-19	5.25-19	1766.0	2.00-21	4.59-21	7.35-21
1419.0	5.05-19	5.19-19	5.30-19	1768.5	1.92-21	4.18-21	6.56-21
1429.0	4.94-19	4.91-19	5.16-19	1774.0	1.39-21	3.48-21	5.93-21
1440.0	4.96-19	5.40-19	5.65-19	1783.5	1.04-21	2.29-21	4.22-21
1454.0	5.19-19	5.51-19	5.58-19	1805.5	3.43-22	1.05-21	2.57-21
1463.5	4.75-19	5.02-19	5.28-19	1827.0	1.73-22	5.00-22	1.38-21
1471.5	5.00-19	5.22-19	5.42-19	1844.5	9.11-23	3.12-22	9.11-22
1489.5	4.65-19	4.95-19	5.25-19	1863.5	4.56-23	1.66-22	5.28-22
1499.5	3.90-19	4.19-19	4.46-19	1883.5	2.36-23	9.74-23	3.17-22
1512.0	3.80-19	4.24-19	4.55-19	1902.5	1.23-23	5.82-23	1.98-22
1520.5	3.42-19	4.02-19	4.46-19	1926.5	4.59-24	2.57-23	9.58-23

†Read $4.86-20$ as 4.86×10^{-20}.

calculations with the present measurements. If we define the integrated cross section as

$$S(T)=\int \sigma(\lambda, T)\,\mathrm{d}\left(\frac{1}{\lambda}\right), \tag{1}$$

where $\sigma(\lambda, T)\,\mathrm{cm}^2$ is the wavelength-and temperature-dependent photoabsorption cross section and $1/\lambda\ \mathrm{cm}^{-1}$ is the wavenumber, then we find from the present results that $S(\sim300)=9.97\times10^{-15}$ cm, $S(\sim200)=9.60\times10^{-15}$ cm, $S(\sim370)=10.53\times10^{-15}$ cm, where all integrations are taken between 1200 and 1750 Å. That is, the integrated cross section changes by −3.7 and +5.6% as the temperature is changed from ≈300 to ~200 K and ~370 K respectively. The results of Julienne *et al.*[2] imply changes in $S(T)$ of ~ −9% and ~ +10% for the same conditions. Using the relation $f=1.130\times10^{12}S(T)$, the oscillator strength f for the 1200–1750 Å region is calculated as 0.011 from the present room temperature results. The value calculated by Julienne *et al.*[2] is $\sim6\times10^{-4}$, whereas that measured by Inn *et al.*[8] is 0.0096 (continuum only). Clearly, some factors have been neglected in the calculations of Julienne *et al.*[2] as noted by Winter *et al*,[15] and new calculations of the temperature dependence would be appropriate. Integrations of the present cross sections in the range 1750–1970 Å show that $S(\sim300)=7.35\times10^{-18}$ cm, $S(\sim200)=3.94\times10^{-18}$ cm (−46%), $S(\approx370)=13.7\times10^{-18}$ cm (+86%), emphasizing the much greater temperature effect at high wavelengths, the important region when considering photodissociation low in the Martian atmosphere.

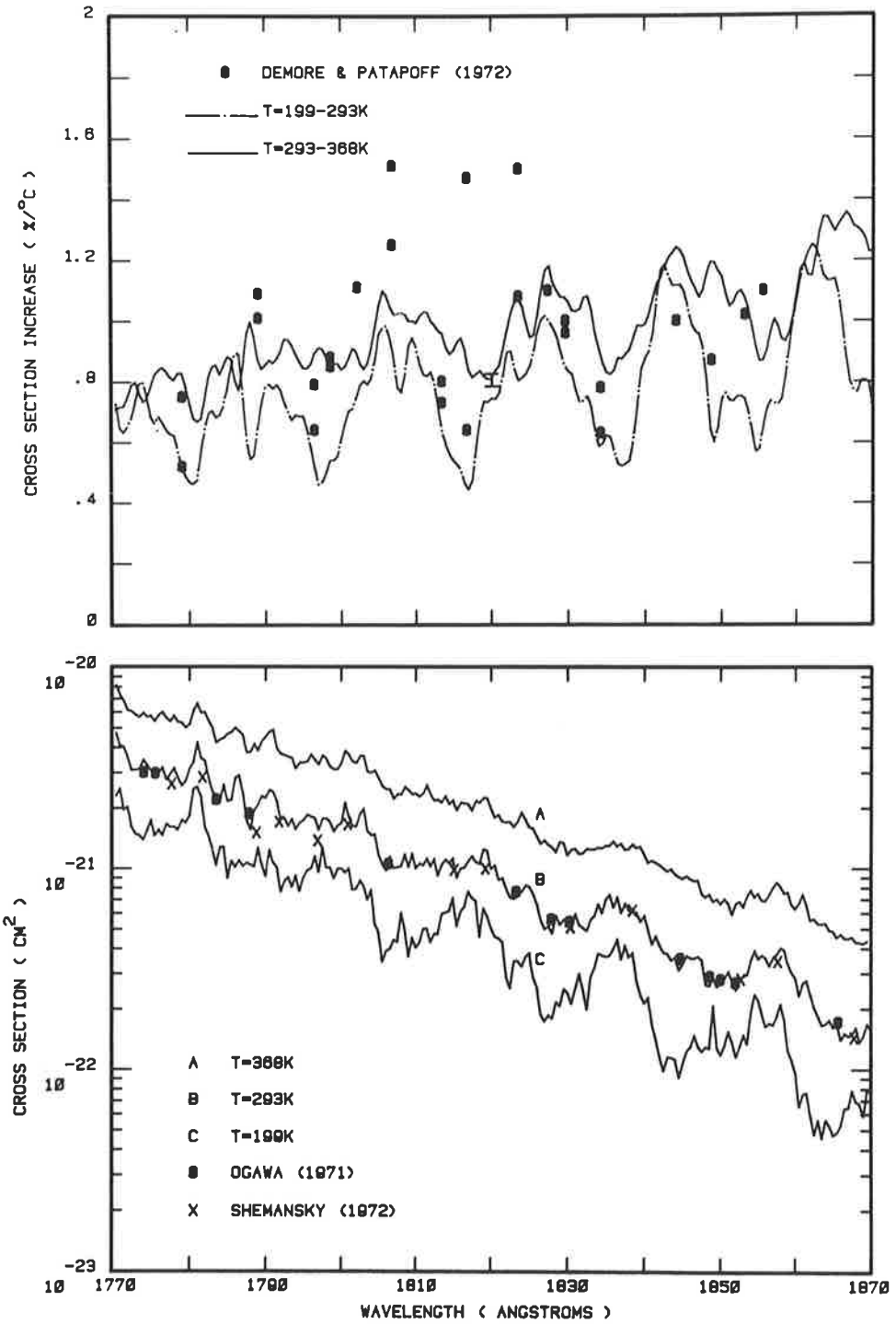

Fig. 8. Carbon dioxide photoabsorption cross sections from 1770 to 1870 Å at 199, 293, and 368 K compared with the room temperature results of Ogawa[10] and Shemansky.[12] Explicit temperature dependences are also shown compared with the results of De More and Patapoff.[3]

CONCLUSIONS

The present work shows that, while the room temperature carbon dioxide photoabsorption cross sections were generally well known,[6,10,12] much theoretical work remains to be done in order to understand the temperature dependence of the cross section. The very large temperature dependence at the higher wavelengths is significant with regard to calculations of atomic oxygen and carbon monoxide production rates at low altitudes in the Martian atmos-

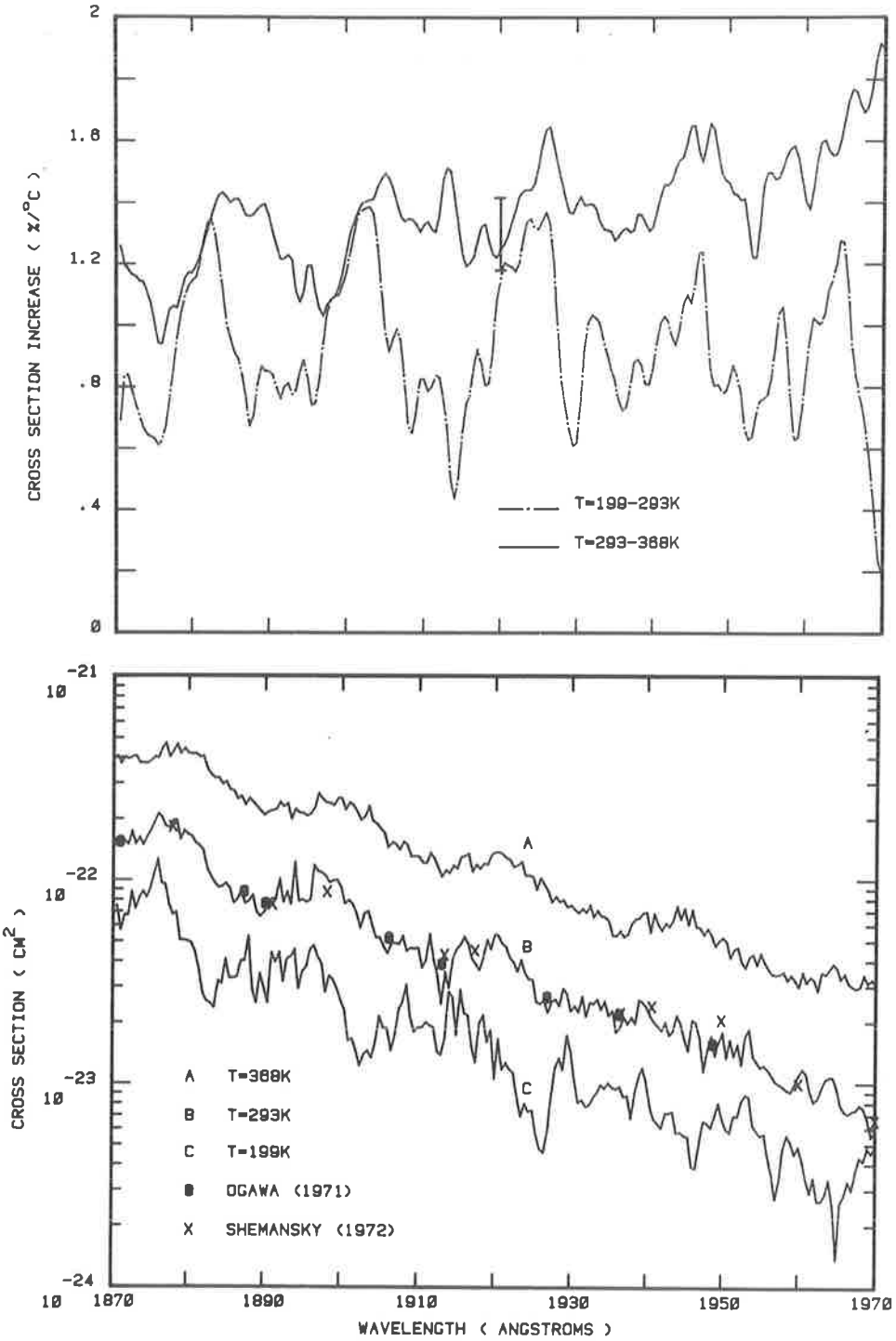

Fig. 9. Carbon dioxide photoabsorption cross sections from 1870 to 1970 Å at 199, 293, and 368 K compared with the room temperature results of Ogawa[10] and Shemansky.[12] Explicit temperature dependences are also shown.

phere. Full tabulations of cross sections at 0.5 Å intervals between 1200 and 1970 Å are available from the authors.

REFERENCES

1. M. B. McElroy and D. M. Hunten, *J. Geophys. Res.* **75**, 1188 (1970).
2. P. S. Julienne, D. Neumann, and M. Krauss, *J. Atmos. Sci.* **28**, 833 (1971).
3. W. B. De More and M. Patapoff, *J. Geophys. Res.* **77**, 6291 (1972).

4. T. Y. Kong and M. B. McElroy, *Icarus* **32**, 168 (1977).
5. H. Sun and G. L. Weissler, *J. Chem. Phys* **23**, 1625 (1955).
6. R. S. Nakata, K. Watanabe, and F. M. Matsunaga, *Sci. Light* **14**, 54 (1965).
7. P. G. Wilkinson and H. L. Johnston, *J. Chem. Phys.* **18**, 190 (1950).
8. E. C. Y. Inn, K. Watanabe, and M. Zelikoff, *J. Chem. Phys.* **21**, 1648 (1953).
9. J. Heimerl, *J. Geophys. Res.* **75**, 5574 (1970).
10. M. Ogawa, *J. Chem. Phys.* **54**, 2550 (1971).
11. B. A. Thompson, P. Harteck, and R. R. Reeves, Jr., *J. Geophys. Res.* **68**, 6431 (1963).
12. D. E. Shemansky, *J. Chem. Phys.* **56**, 1582 (1972).
13. J. Berkowitz, *Photoabsorption, Photoionization, and Photoelectron Spectroscopy*, p. 413. Academic Press, New York (1979).
14. A. Dalgarno, G. Herzberg, and T. L. Stephens, *Astrophys. J.* **162**, L49 (1970).
15. N. W. Winter, C. F. Bender, and W. A. Goddard, *Chem. Phys. Letts.* **20**, 489 (1973).
16. R. N. Dixon, *Proc. Roy. Soc.* **A275**, 431 (1963).

4.3 Decomposition of the photoabsorption continuum underlying the Schumann-Runge bands of $^{16}O_2$: I. Role of the $B\,^3\Sigma_u^-$ state; a new dissociation limit

[20] B. R. Lewis, L. Berzins, and J. H. Carver,
Journal of Quantitative Spectroscopy and Radiative Transfer **33**, 627–643 (1985).

J. Quant. Spectrosc. Radiat. Transfer Vol. 33, No. 6, pp. 627–643, 1985
Printed in Great Britain.

0022-4073/85 $3.00 + .00

DECOMPOSITION OF THE PHOTOABSORPTION CONTINUUM UNDERLYING THE SCHUMANN–RUNGE BANDS OF $^{16}O_2$—I. ROLE OF THE $B\ ^3\Sigma_u^-$ STATE: A NEW DISSOCIATION LIMIT

B. R. LEWIS, L. BERZINS and J. H. CARVER
Research School of Physical Sciences, The Australian National University, Canberra, ACT 2600, Australia

and

S. T. GIBSON
Physics Department, University of Adelaide, Adelaide, SA 5000, Australia

(*Received* 11 *September* 1984)

Abstract—Extensive measurements are presented of O_2 photoabsorption cross-sections taken at selected minima between rotational lines of the Schumann–Runge band system. Both room temperature and liquid nitrogen temperature results are presented from 1750 to 1800 Å and corrections are applied for the effect of the wings of the rotational lines. Step-like structure in the underlying continuum, due to absorption from rotationally excited levels of the ground state into the $B\ ^3\Sigma_u^-$ state, is verified experimentally for the first time, and the observation is used to deduce a definitive dissociation limit of 57136.0 ± 0.5 cm^{-1} for the B state.

INTRODUCTION

The absorption of solar ultraviolet radiation in the region of the Schumann–Runge (SR) bands of O_2 plays an important role in atmospheric photochemistry. In order to understand fully the processes involved it is necessary to separate absorption due to the bands from the underlying continuum and to divide that continuum into constituent parts.

Of previous continuum photoabsorption measurements in the wavelength range 1750–1950 Å,[1–7] only those of Gies *et al.*[6] are corrected for absorption due to the wings of neighbouring lines although Hudson and Mahle[8] applied wing corrections to the measurements of Ogawa[4] when developing their SR absorption model.

It is now well established[3,5,9,10] that most of the underlying continuum near 1750 Å is due to absorption from rotationally or vibrationally excited ground state oxygen molecules into the $B\ ^3\Sigma_u^-$ state. This dissociation mechanism is significant as the only one able to produce metastable oxygen atoms in the mesosphere and stratosphere with radiation of wavelength greater than 1750 Å.[11] Models for the absorption of radiation by vibrationally excited O_2 have been developed by Allison *et al.*[11] and Hudson and Mahle.[8] Blake[9] extended the model of Allison *et al.*[11] to include rotational effects and pointed out that discrete steps are expected in the continuum due to the onset of absorption from particular rotationally excited levels of the ground state. The most comprehensive model is that of Gies *et al.*[6] which corrects the rotational thresholds of Blake[9] by including the effect of the centrifugal barrier in the B-state potential for the rotating molecule, and demonstrates that the threshold cross-sections decrease with increasing rotation. The experimental measurements of Gies *et al.*[6] are, however, of insufficient number and quality to verify the finer points of their model.

In the region above 1950 Å the $X\ ^3\Sigma_g^- \rightarrow A\ ^3\Sigma_u^+$ Herzberg I transition is the main contributor to the observed cross-section, and this transition also provides a relatively less significant contribution as the wavelength decreases. There is considerable disagreement in the literature over possible contributions from other states, with Fang *et al.*[12] and Ogawa[4] invoking II states to explain some of the continuum, while Blake[9] concludes that a composite absorption cross-section comprising his vibrationally and rotationally excited SR model and a Jarmain and Nicholls[13] Herzberg continuum model fitted to the measurements of Ditchburn and Young[2] is sufficient to explain all the underlying

continuum in the region of the SR bands. That this conclusion is incorrect can be seen by examining the differences between the SR continuum models of Blake[9] and Gies *et al.*[6] The later model[6] predicts lower cross-sections at most wavelengths above 1750 Å because of the lower rotational threshold wavelengths due to the centrifugal potential barrier, changes in shape of the partial cross-sections with rotation, and the decrease in threshold cross-sections with increasing rotation. The difference in absorption must therefore be explained by transitions to another state.

In view of the detailed predictions of the rotationally and vibrationally excited SR continuum model of Gies *et al.*[6] and uncertainty regarding contributions from states other than $B\ ^3\Sigma_u^-$ and $A\ ^3\Sigma_u^+$, we decided to reinvestigate in detail the continuum underlying the SR bands between 1750 and 1950 Å. Cross-section measurements were made with a resolution of about 0.04 Å at many minima between rotational lines and corrections were applied where necessary for absorption due to line wings. The measurements were taken at temperatures of 295 and 83 K.

This paper presents results from 1750 to 1800 Å where the measured cross-sections at each temperature clearly exhibit step-like structure, verifying experimentally for the first time the predictions of Gies *et al.*[6] regarding absorption into the B state from rotationally excited levels of the $v'' = 0$ ground state. Indeed the size of the threshold cross-section is observed to decrease with rotation, also in agreement with the model. A new dissociation limit of $57136.0 \pm 0.5\ cm^{-1}$ is deduced from the observed wavelengths of the thresholds corresponding to lowest rotation, and the model of Gies *et al.*[6] is modified accordingly.

Results from 1800 to 1950 Å and a discussion of absorption into states other than $B\ ^3\Sigma_u^-$ will be presented in a future paper.[14]

EXPERIMENTAL

The O_2 photoabsorption cross-sections were measured using apparatus similar to that described previously.[15] The radiation source was a windowless d.c. discharge in H_2 operated at a pressure of about 10 torr and a current of 1 A. The radiation was dispersed by a Minuteman 320 NIV normal incidence VUV scanning monochromator equipped with a 1200 g/mm grating blazed at 1500 Å. Fixed slits were set to give a resolution of about 0.04 Å.

An ARC VUV beamsplitter served as the front window of the 1.2-m absorption cell and also allowed monitoring of the incident radiation. EMI photomultipliers type G-26H 315 (CsTe photocathode) were used in the pulse counting mode to measure simultaneously the incident and transmitted radiation. The MgF_2 window of the rear photomultiplier also served as the rear window of the cell. The temperature of the gas in the cell could be lowered by filling a stainless steel jacket with liquid nitrogen. Most of the absorbing gas was then at 77 K but there were temperature gradients at each end of the cell since both windows were maintained at room temperature. This necessitated small corrections in the data analysis to allow for the temperature gradients, and the effective temperature could be taken as 83 K.

The cell was filled with medical grade oxygen (0.5–800 torr), carefully dried by passing through suitable cold traps, via a Balzers RME010 electromagnetic leak valve. The pressure was monitored by a Datametrics Barocel 570/1173 variable capacitance manometer and was controlled by a Datametrics 1404 valve controller. At the temperatures and pressures used in the experiment no corrections were necessary for thermal transpiration.

The experimental routine was controlled by a Commodore 8032 microcomputer and an HP 3497A data acquisition/control unit. In the region 1750–1800 Å, and at temperatures of 295 and 83 K, scans were performed in 3 Å segments at a fixed pressure and with wavelength increments of 5.3 mÅ. Backgrounds were taken before and after each segment and absolute absorption cross-sections were calculated at the deeper minima using Beer's law. Above 1800 Å the availability of deep minima for study becomes severely restricted because of the predissociation broadening of the lines of the SR bands with $v' \leq 12$. Cross-sections presented in this paper have been extrapolated to zero pressure where appropriate by using pressure coefficients measured in an associate work.[14]

This correction was only necessary at $T = 83$ K for wavelengths greater than 1770 Å and the maximum value was about 20% near 1800 Å.

THEORETICAL CONSIDERATIONS

(a) *Threshold wavelengths for the Schumann–Runge continuum*

For oxygen molecules with rotational or vibrational excitation the threshold for absorption into the SR continuum lies at a greater wavelength than the limit of the band system at ~1750 Å. The threshold may be calculated by using the well-known[16] ground state energy levels for O_2 and estimating the height of the centrifugal barrier in the B-state potential as a function of rotation.

For the purposes of this calculation the B-state potential shape is taken from the CI calculations of Saxon and Liu[17] for $r < 5.3$ Å, normalized at ~3.5 Å to the RKR curve of Gibson *et al.*,[18] with an extrapolation of the form $V = 0.00348/2^{(1.89r-8)}$ eV for $r > 5.3$ Å. The extrapolation affects results for $J' \leq 17$. On adding the centrifugal potential $2.61 \times 10^{-4}\, J'(J'+1)/r^2$ eV, where r is in Å and J' represents rotation in the upper state, to the B-state potential, it is straightforward to calculate the height of the centrifugal barrier. This is found to vary from 0.03 cm^{-1} at $J' = 1$ to 90.5 cm^{-1} at $J' = 31$, the full results being shown as part of Table 1.

The fine structure of the threshold regions may now be understood by reference to Fig. 1 which gives energy level diagrams for $N'' = 1, 3, 5, 29$ including both the triplet splitting of the ground state[19] and the centrifugal effects on the upper state as calculated

Table 1. Calculated centrifugal barriers $\Delta F'$ (cm^{-1}) for the $B\,^3\Sigma_u^-$ state of O_2 and corresponding threshold wavelengths λ_{th} (Å) for the R_3P_1 component of continuum transitions from various rotational levels of the ground state ($v'' = 0$). A dissociation limit $D = 57136.0$ cm^{-1} is assumed for the B state, and the ground state energy levels[19] $F'' = F_1''$ ($N'' = 1$) or $(F_1'' + F_3'')/2$ ($N'' \geq 3$). Note that the R_3P_1 component is expected to be the strongest threshold for $N'' > 1$ (see text).

N" (=J')	ΔF', cm^{-1}	F", cm^{-1}	D+ΔF'-F"	λ_{th}, Å
1	0.03	1.0	57135.0	1750.241
3	0.24	15.2	57121.0	1750.668
5	0.68	41.1	57095.6	1751.449
7	1.64	78.5	57059.1	1752.568
9	3.1	127.4	57011.7	1754.025
11	5.2	187.7	56953.5	1755.820
13	7.9	259.5	56884.4	1757.952
15	11.5	342.8	56804.7	1760.419
17	16.0	437.5	56714.5	1763.217
19	21.7	543.6	56614.1	1766.345
21	28.9	661.1	56503.8	1769.794
23	37.9	790.1	56383.8	1773.559
25	48.5	930.5	56254.0	1777.652
27	60.8	1082.1	56114.7	1782.066
29	74.8	1245.2	55965.6	1786.813
31	90.5	1419.5	55807.0	1791.890

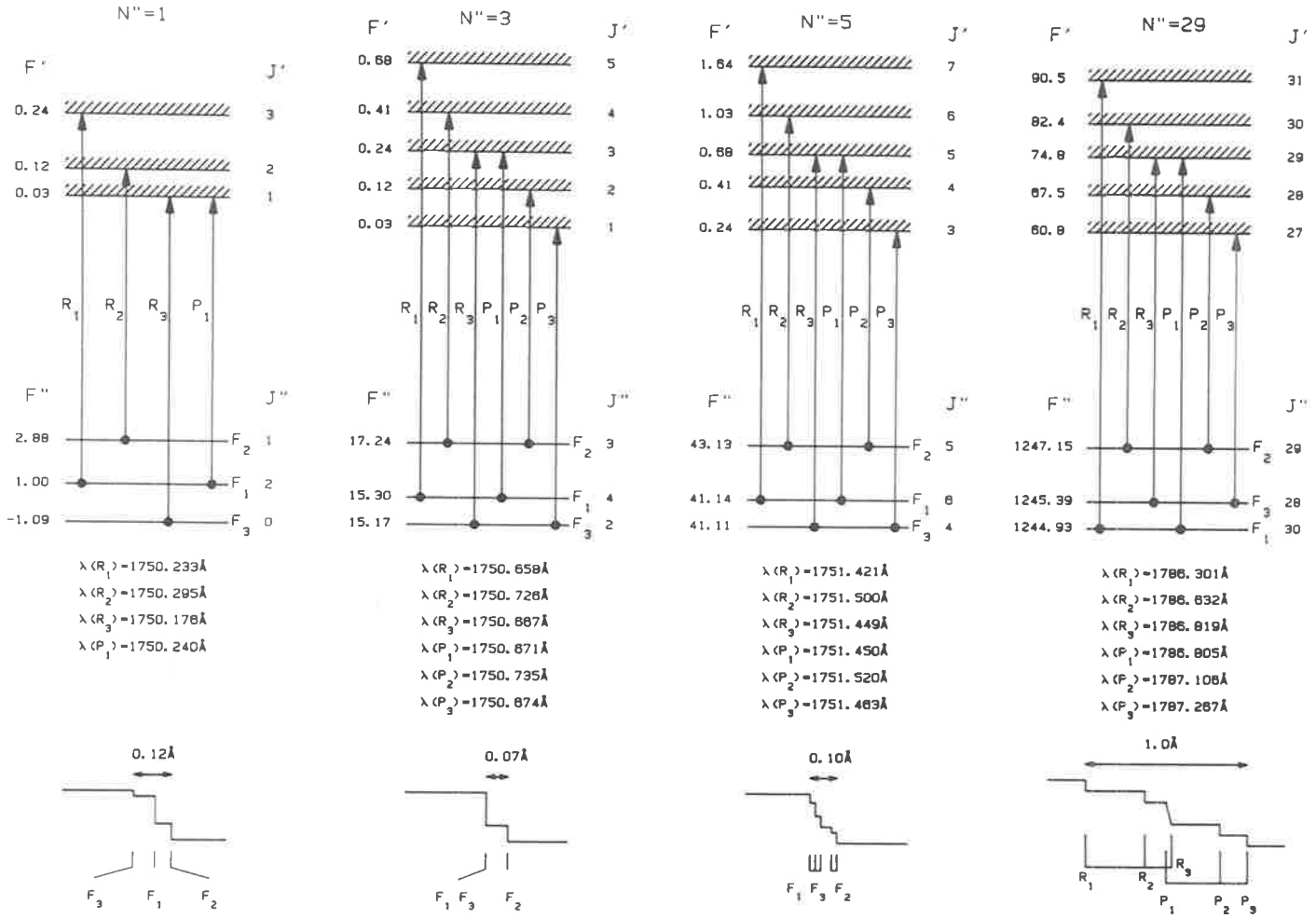

Fig. 1. Energy level diagrams showing the fine structure of the threshold Schumann–Runge continuum transitions from the $v'' = 0$ ground state for rotations $N'' = 1, 3, 5, 29$. Energy levels (cm^{-1}) for the ground state[19] are referred to the nonexistent $N'' = 0$, $J'' = 0$ level while the centrifugal barriers (cm^{-1}) of the $B\,^3\Sigma_u^-$ state are referred to the dissociation limit of 57136.0 cm^{-1}. Also shown are threshold cross-sections predicted using the calculated fine structure wavelengths and Boltzmann factors for $T = 83$ K (vertical scale arbitrary).

above. Only the main branches of the continuum threshold transitions are shown, and the dissociation limit is taken as 57136.0 cm^{-1} (see later discussion for the determination of this quantity). For the lowest values of rotation it is seen that the centrifugal barrier is very small and thus the fine structure of the continuum thresholds is determined mainly by the ground state triplet splitting. At higher rotation the difference in height of the centrifugal barrier in the B state for successive values of J' becomes larger than the ground state splitting and the threshold fine structure is then dominated by centrifugal effects. From Fig. 1 it is evident that for $N'' > 1$, since the F_3 and F_1 levels of the ground state are close together and since $J' = N''$ for both the R_3 and P_1 transitions, the strongest fine structure threshold will be associated with the R_3P_1 transition which will for medium and higher rotation always be fairly centrally placed among all the fine structure components. For $N'' = 1$ the P_1R_1 transition gives rise to the strongest component.

In an experimental situation it is likely that only the strongest fine structure components will be observable and on the basis of the above discussion, threshold wavelengths are calculated for the R_3P_1 components with $J' = N''$ for comparison with experimental measurements where fine structure is not resolved. Table 1 summarizes the calculation of threshold wavelengths for rotational levels up to $N'' = 31$ of the $v'' = 0$ ground state. Here $\Delta F'$ represents the centrifugal barrier of the B state, F'' is the mean term value for the F_1 and F_3 components of the ground state of O_2,[19] (except for $N'' = 1$ where it is F_1 only) and D is the dissociation limit for the B state (57136.0 cm^{-1}). It is found that for $N'' \lesssim 31$ the threshold wavelengths may be represented by the empirical equation

$$\lambda_{th}(v'' = 0) = 1750.157 + 0.0422N''(N'' + 1). \tag{1}$$

A similar calculation gives the relation:

$$\lambda_{th}(v'' = 1) = 1799.161 + 0.0442N''(N'' + 1) \tag{2}$$

for excitation from rotational levels of the $v'' = 1$ vibrational level of the ground state.

(b) *Calculation of Schumann–Runge continuum cross-sections*

The calculation of the continuum cross-sections follows the procedure of Gies *et al.*[6] The cross-section $\sigma_{v''N''}(\lambda)$ for absorption from a particular rovibrational level of the ground state is given by

$$\sigma_{v''N''}(\lambda) = \frac{2\pi^2}{3\epsilon_0 hcg''\lambda}\left|\int_0^\infty \psi_{v''N''}(r)R_e(r)\psi_{\lambda N''}(r)\,dr\right|^2 \tag{3}$$

where $g'' = (2 - \delta_{0\Lambda''})(2S + 1)$ is the statistical weight of the initial state, $\psi_{v''N''}$ and $\psi_{\lambda N''}$ are the normalised initial and final state vibrational wavefunctions for the rotating molecule, R_e is the electronic transition moment, r is the internuclear distance, and all other symbols have their usual meanings.

Vibrational wavefunctions are found by solving the Schrödinger equation using the potential for a rotating molecule:

$$V(r) = V_0(r) + N''(N'' + 1)h^2/8\pi^2\mu r^2 \tag{4}$$

where $V_0(r)$ is the potential for no rotation and μ is the reduced mass of the molecule. Values of $V_0(r)$ for the $X\ ^3\Sigma_g^-$ and $B\ ^3\Sigma_u^-$ states and $R_e(r)$ were taken from Gibson *et al.*,[18] but new spectroscopic constants derived from the accurate wavenumbers of Yoshino *et al.*[20] were used to make slight improvements to the B-state potential curve.

Examples of partial cross-sections $\sigma_{v''N''}(\lambda)$ for $v'' = 0$ and $N'' = 1$, 13, 25 and 51 are shown in Fig. 2 where the rapid increase in cross-section towards shorter wavelengths and the decrease in threshold cross-section as N'' increases are both evident.

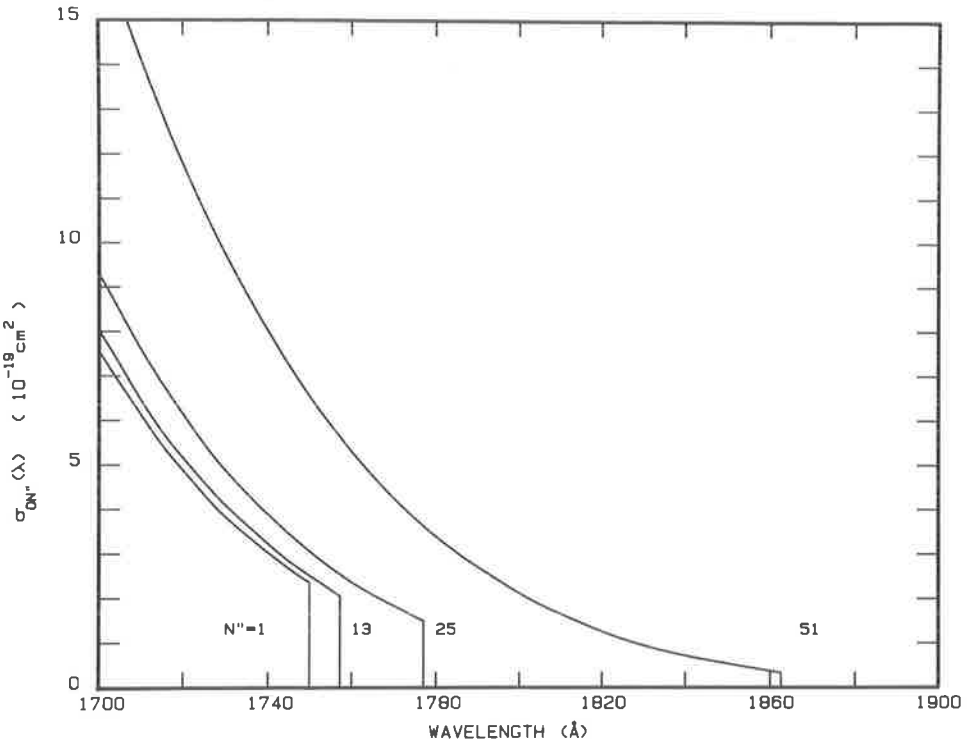

Fig. 2. Calculated partial Schumann–Runge continuum cross-sections $\sigma_{v''N''}(\lambda)$ for molecules in initial states with $v'' = 0$ and $N'' = 1, 13, 25, 51$.

The total continuum cross-section at any wavelength λ and temperature T is computed by summing over all initial states which contribute, with each partial cross-section being weighted according to the population of the initial state in the absorbing gas. The total cross-section is given by

$$\sigma_T(\lambda) = \frac{\sum_{v''=0}^{2} \sum_{N''} (2N'' + 1)\sigma_{v''N''}(\lambda) \exp(-F_{v''N''}/kT)}{\sum_{v''=0}^{2} \sum_{N''} (2N'' + 1) \exp(-F_{v''N''}/kT)} \quad (5)$$

where $F_{v''N''}$ is the energy of the initial state of the molecule and N'' is summed over all values which give a threshold for absorption at a wavelength greater than λ.

A detailed discussion of the above calculations is given by Gibson[21] who also predicts shape resonances in some rotational thresholds due to the centrifugal barriers in the B state.

EXPERIMENTAL RESULTS

(a) *Cross-sections*

Experimental cross-sections of this work, extrapolated to zero pressure where necessary, are given in Tables 2 and 3 for minima from 1750 to 1800 Å and at temperatures of 295 and 83 K respectively. Corrections for the wings of neighbouring lines and the nett underlying continuum cross-sections are also given at each wavelength.

Wing corrections were calculated with the aid of the SR band absorption model of Lewis *et al.*[22] which is similar to earlier models,[23–26] but with some improvement in oscillator strengths, predissociation linewidths and pressure broadening coefficients. Because of the sensitivity of the wing corrections to the instrument resolution function, careful measurements were performed on isolated narrow absorption lines in order to define

Table 2. Experimental photoabsorption cross-sections σ_M for O_2 measured at selected absorption minima in the range 1750–1800 Å at T = 295 K. Wing corrections σ_W and resultant underlying continuum cross-sections σ_T are also given. All cross-sections are in units of 10^{-21} cm^2, and errors in σ_T can be deduced by assuming σ_M and σ_W to be accurate to 5% and 20%, respectively. Daggers signify that observed but unclassified lines have been included in the wing correction calculation in order to match the observed spectrum.

λ, Å	σ_M	σ_W	σ_T	λ, Å	σ_M	σ_W	σ_T
1750.05	256	0	256	1766.03†	28	6	22
1750.30	256	0	256	1766.62†	25	5	20
1750.40	249	0	249	1767.20	27	16	11
1750.60	244	0	244	1768.01†	17	4	13
1750.70	246	0	246	1768.18	18	6	12
1750.80	234	0	234	1768.99	33	21	12
1751.03	223	0	223	1769.59	31	19	12
1751.20	222	0	222	1769.73	28	16	12
1751.50	206	0	206	1770.03	31	20	11
1751.67	189	0	189	1770.18	28.8	19.7	9.1
1751.83	189	0	189	1770.62	16.1	8.0	8.1
1752.54	183	2	181	1771.14	15.5	6.8	8.7
1752.90	180	28	152	1771.88	11.6	3.9	7.7
1753.23†	159	6	153	1772.40	14.1	5.6	8.5
1753.60†	159	10	149	1773.08	9.9	1.7	8.2
1754.00	171	28	143	1773.33	9.5	2.1	7.4
1754.15	129	6	123	1774.01	7.0	1.2	5.8
1754.53	123	12	111	1774.76	8.2	2.8	5.4
1754.73†	118	3	115	1776.15	11.4	6.3	5.1
1755.52†	121	11	110	1776.70	8.2	3.0	5.2
1756.03†	105	23	82	1777.00	7.8	2.3	5.5
1756.39†	94	21	73	1778.25†	6.4	2.3	4.1
1756.80	98	17	81	1779.00†	5.5	1.4	4.1
1757.08	84	6	78	1780.24†	5.0	1.3	3.7
1757.70	86	10	76	1780.47	4.0	0.5	3.5
1758.03	85	14	71	1781.12†	5.5	2.0	3.5
1758.25†	63	8	55	1781.23†	4.6	0.7	3.9
1758.40†	65	12	53	1781.47	4.1	0.9	3.2
1759.06	75	23	52	1782.15	4.7	1.0	3.7
1759.53	68	14	54	1782.50	5.3	1.7	3.6
1759.74	72	19	53	1782.85	7.3	5.1	2.2
1760.11	74	18	56	1783.92	5.8	3.4	2.4
1760.46†	52	7	45	1784.56	6.1	4.1	2.0
1761.03†	55	18	37	1785.03†	5.2	3.0	2.2
1761.48†	39	2	37	1785.57	4.4	2.5	1.9
1761.86	46	10	36	1785.66	4.5	1.9	2.6
1762.28	41	6	35	1786.83	3.3	1.0	2.3
1762.63†	38	3	35	1787.73	3.8	1.8	2.0
1762.97	42	7	35	1788.12	3.0	1.1	1.9
1763.78	44	16	28	1789.18	2.7	0.8	1.9
1764.57†	39	18	21	1789.88†	2.6	0.8	1.8
1764.95	42	17	25	1790.16	2.4	0.6	1.8
1765.31†	37	15	22	1791.85	3.0	1.2	1.8
1765.55†	31	12	19				

accurately the slit function. Allowance was also made for the lines of the isotopic molecule $O^{16}O^{18}$ which can produce significant effects at some minima in oxygen of normal isotopic composition. The background continuum in the model was set to zero and the predicted spectrum around the minimum of interest was generated. The effective cross-section at that minimum was then calculated, representing absorption due to the spectral lines only. In some cases, due to inadequate knowledge of line classifications, perturbations and so on,[20,27] the predicted spectrum did not match the observed, and observed but unclassified lines were included in the model with strengths and widths adjusted to match the observed spectrum. These cases are explicitly marked in Tables 2 and 3.

Table 3. Experimental photoabsorption cross-sections σ_M for O_2 measured at selected absorption minima in the range 1750–1800 Å at T = 83 K. The cross-sections have been extrapolated to zero pressure where necessary. Wing corrections σ_W and resultant underlying continuum cross-sections σ_T are also given. All cross-sections are in units of 10^{-21} cm^2, and errors in σ_T can be deduced by assuming σ_M and σ_W to be accurate to 5% and 20%, respectively. Daggers signify that observed but unclassified lines have been included in the wing correction calculation in order to match the observed spectrum.

λ, Å	σ_M	σ_W	σ_T	λ, Å	σ_M	σ_W	σ_T
1749.92	232	0	232	1758.28†	7.9	6.4	1.5
1750.11	230	0	230	1760.47†	8.9	7.9	1.0
1750.21	224	0	224	1761.55†	4.1	2.9	1.2
1750.25	214	0	214	1762.29	4.8	4.2	0.6
1750.32	209	0	209	1762.61	3.3	2.4	0.9
1750.48	196	0	196	1766.65	2.6	1.8	0.8
1750.57	196	0	196	1766.92	2.3	1.7	0.6
1750.73	160	0	160	1771.69	2.4	1.8	0.6
1750.96	140	1	139	1772.01	1.80	1.31	0.49
1751.19	146	1	145	1772.47	1.22	0.73	0.49
1751.42	136	3	133	1773.10	1.02	0.51	0.51
1751.51	126	5	121	1778.20	1.46	0.73	0.73
1751.65	88	15	73	1778.97	0.95	0.35	0.60
1752.35	88	11	77	1779.50	0.94	0.39	0.55
1752.47	81	3	78	1779.70	0.93	0.36	0.57
1752.63	80	33	47	1780.47	0.65	0.14	0.51
1752.91	81	41	40	1781.24	0.61	0.16	0.45
1753.25†	54	15	39	1781.52	0.74	0.22	0.52
1753.62†	56	15	41	1781.95	0.88	0.30	0.58
1754.17	30	9	21	1785.56	1.28	0.94	0.34
1754.55	31	20	11	1786.26	1.54	1.04	0.50
1754.76†	22	6	16	1786.61	1.35	0.93	0.42
1754.92†	23	8	15	1786.90	0.62	0.38	0.24
1755.52†	24	10	14	1787.60	0.61	0.39	0.22
1756.37	24.1	19.3	4.8	1788.21	0.43	0.21	0.22
1756.80	24.9	16.9	8.0	1789.04	0.65	0.41	0.24
1757.10	11.5	8.3	3.2	1789.18	0.55	0.21	0.34
1757.41	15.7	10.4	5.3	1789.89	0.58	0.24	0.34
1757.72†	14.4	7.8	6.6	1790.14	0.62	0.24	0.38
1758.14	13.0	11.1	1.9	1790.64	0.82	0.40	0.42

An example of a wing correction calculation is given in Fig. 3 which displays transmissions near the absorption minimum at 1755.52 Å measured at T = 83 K together with several model estimates. The strongest lines in this region have known assignments[20,27] but the three weaker lines, although listed by Yoshino *et al.*,[20] are yet to be assigned. Curve A represents the model transmission calculated assuming the prevailing experimental conditions, but ignoring the weaker three lines and assuming no underlying continuum. Agreement with experiment is seen to be poor. Curve B is calculated as for A but with the inclusion of three lines at the wavelengths given in Fig. 3,[20] with relative strengths adjusted to agree with the observed scan. Curves C and D are calculated as for B except that underlying continua of 1.4×10^{-20} and 2.9×10^{-20} cm^2 are assumed. It is seen that curve C gives good agreement with the observed spectrum and thus a value of 1.4×10^{-20} cm^2 follows for the underlying continuum at this wavelength (measured cross-section 2.4×10^{-20} cm^2, wing correction 1.0×10^{-20} cm^2). It is not possible to support significantly different values for the underlying cross-section without assuming relative line strengths disagreeing with the observed values.

The above example is intended to represent a worst-case situation. In most cases unassigned lines are not present and thus no strength adjustments are needed. At room temperature the unassigned lines are generally not as significant and extra uncertainties due to their presence are less important.

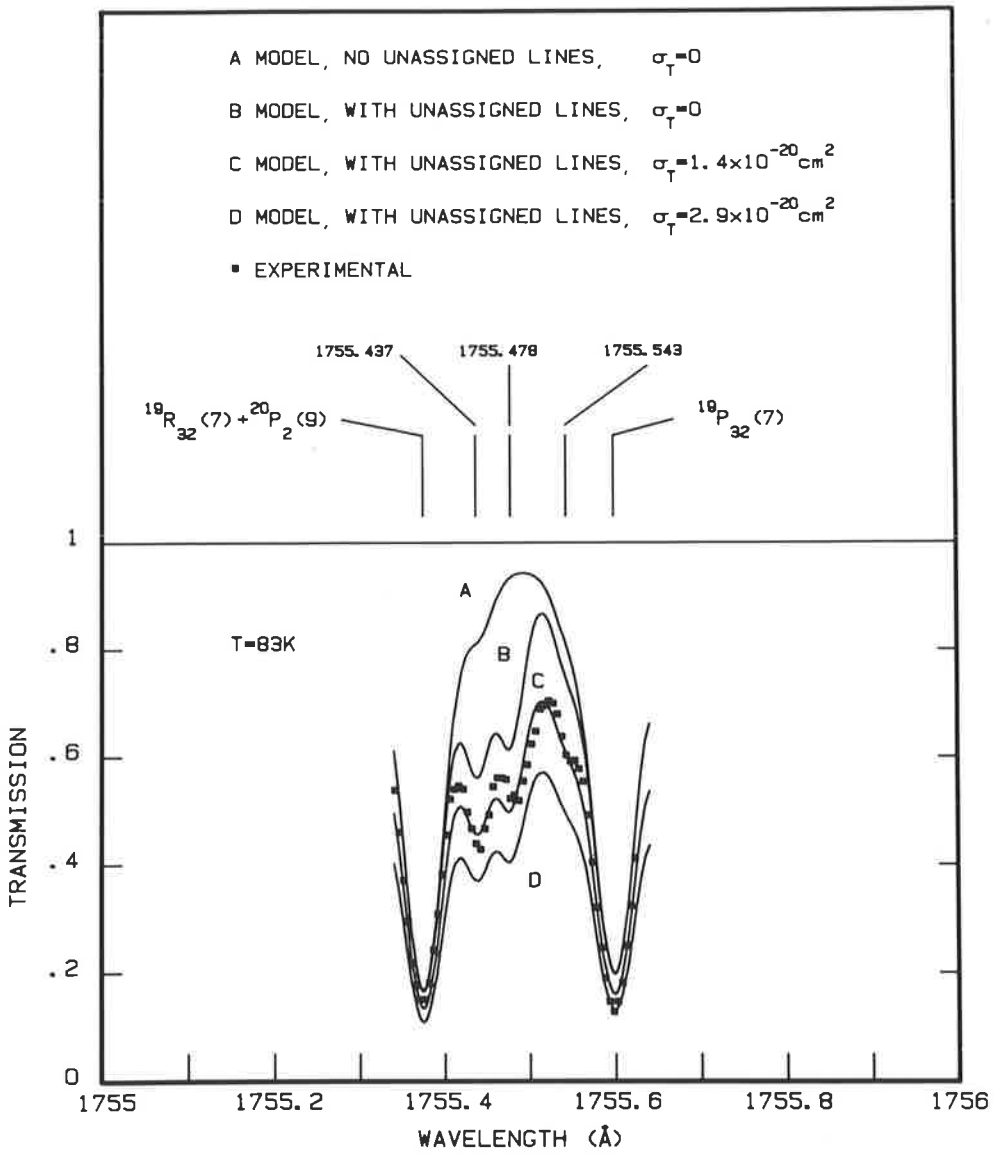

Fig. 3. Measured transmissions near the cross-section minimum at 1755.52 Å compared with various model transmissions. The temperature was 83 K.

Errors in the nett cross-section can normally be estimated by assuming a 5% error in the experimentally measured cross-section due to uncertainties in pressure, temperature and cell length and errors due to counting statistics, together with an estimated 20% error in the wing correction. Thus it is only in cases where the correction approaches the measured cross-section that the resultant error becomes large. Where unassigned lines are present the error in the wing correction is estimated to be 30%.

The wing-corrected cross-sections are shown graphically in Fig. 4 in the range 1750–1800 Å at both temperatures, together with SR continuum cross-sections calculated according to the procedures outlined earlier, neglecting fine structure and shape resonances. The step-like structure in the measurements at both temperatures is immediately apparent as is the good agreement with the calculations. The steps can be followed up to $N'' = 29$ at $T = 295$ K and up to $N'' = 13$ at $T = 83$ K. The region 1750–1760 Å is shown on a linear scale in Fig. 5 where the agreement between experiment and theory is even more apparent. At $T = 295$ K in this region the wing corrections are small compared with the measured cross-sections and the steps are readily observable in the raw data (σ_M of Table

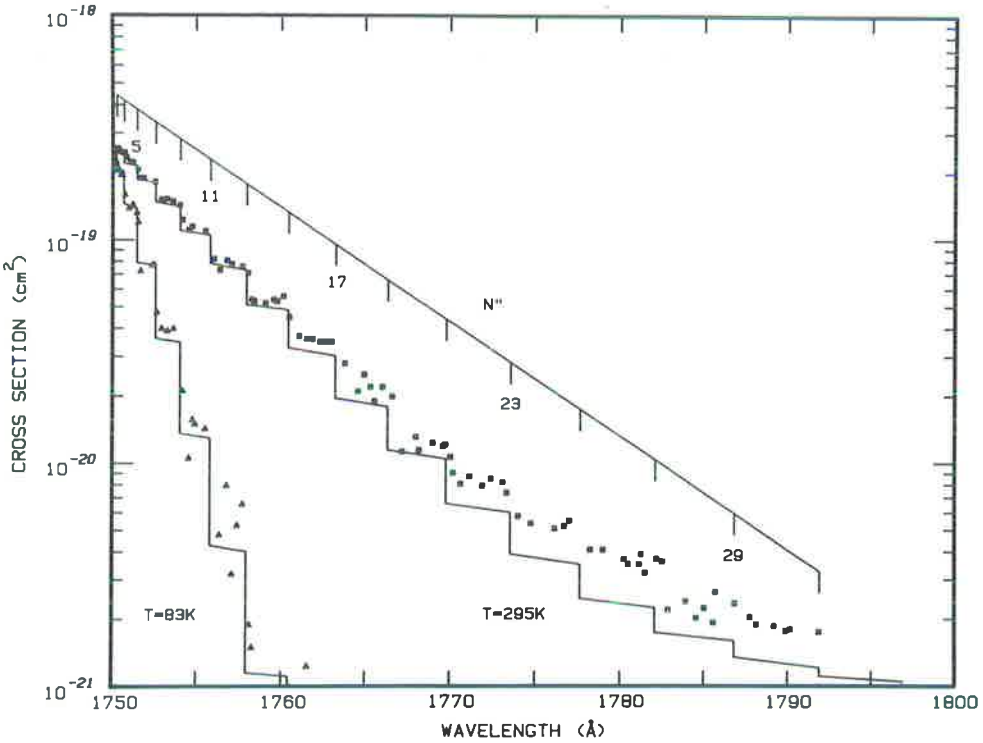

Fig. 4. Wing-corrected continuum absorption cross-sections underlying the Schumann–Runge bands of O_2 in the range 1750–1800 Å at temperatures of 295 and 83 K. The measurements of this work are shown together with the calculated Schumann–Runge continuum arising from rotationally and vibrationally excited ground state O_2.

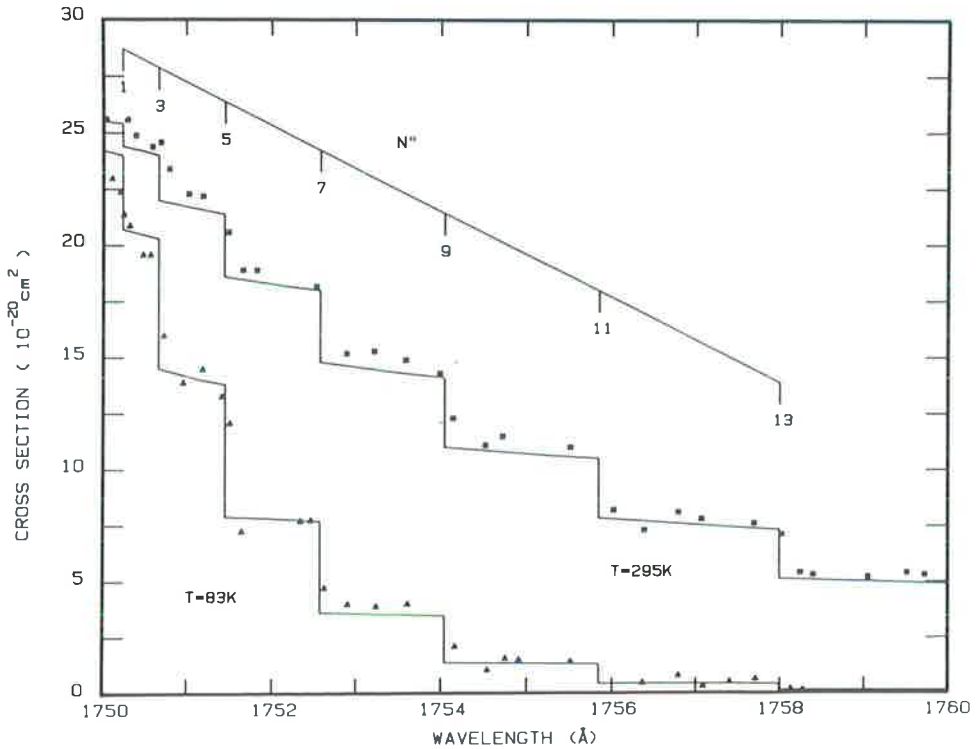

Fig. 5. Wing-corrected continuum absorption cross-sections underlying the Schumann–Runge bands of O_2 in the range 1750–1760 Å at temperatures of 295 K and 83 K, the linear scale highlighting the rotational thresholds. The measurements of this work are shown together with the calculated Schumann–Runge continuum arising from rotationally and vibrationally excited ground state O_2.

2). The results of Gies *et al.*,[6] not plotted for clarity, are less extensive, exhibit more scatter and are systematically higher than the present results at longer wavelengths. At $T = 83$ K the measured cross-sections decrease much more slowly, above about 1760 Å, than the theoretical predictions for the SR continuum. The significance of this will be fully discussed in a future publication.[14]

(b) *Threshold wavelengths*

Threshold wavelengths estimated from the data of Table 2 by graphical interpolation, knowing the general form of the cross-section, are listed in Table 4. It should be noted that the wavelengths corresponding to the first three steps ($N'' = 1, 3, 5$) result from direct measurements of edges (further discussion later; see also Fig. 7), and are thus considerably more accurate than the other values. When corrections are applied for the ground state energy levels[19] appropriate to each step, it is possible to obtain estimates of the upper-state threshold energies. These values are shown in Table 4 and Fig. 6 together with the values calculated earlier assuming a dissociation limit of 57136.0 cm^{-1}. The effects of barrier tunneling are expected to be small for O_2.[28] Figure 6 is in effect a limiting curve of dissociation[28] for the $B\ ^3\Sigma_u^-$ state of O_2. Despite the larger uncertainties in the wavelengths of steps corresponding to higher rotation, there is good agreement between the measured and calculated values. This implies that the previous assumptions regarding the shape of the B-state potential curve were realistic. It should also be noted that the data of Fig. 6 are not consistent with a linear dependence on $J'(J' + 1)$ but tend to asymptote to a horizontal line as $J' \rightarrow 0$. This implies[28] that the rotationless B-state potential curve does not have a maximum (at least for $r < 10$ Å), and that the dissociation limit ($J' = 0$ intercept) for the B state is 57136.0 cm^{-1}. The previous "definitive" dissociation limit for this state was determined by Brix and Herzberg,[27] and is shown in Fig. 6 for comparison.

Table 4. Measured threshold wavelengths λ_{th} for $v'' = 0$ and $N'' = 1$ to 29. Also shown are energies F' of the centrifugal barrier in the $B\ ^3\Sigma_u^-$ state inferred from λ_{th} assuming ground state energy levels[18] $F'' = F_1''$ ($N'' = 1$) and $F'' = (F_1'' + F_3'')/2$ ($N'' \geq 3$). A comparison is made with barriers calculated using a dissociation limit $D = 57136.0$ cm^{-1} and the $\Delta F'$ values of Table 1. The errors in F' may be taken as equal to those in ν_{th}, the measured threshold wavenumbers.

N"=J'	λ_{th}, Å	ν_{th}, cm^{-1}	F", cm^{-1}	F', cm^{-1}	D+ΔF', cm^{-1}
1	1750.244	57134.9 ± 0.5	1.0	57135.9	57136.0
3	1750.667	57121.1 ± 0.5	15.2	57136.3	57136.2
5	1751.455	57095.4 ± 0.5	41.1	57136.5	57136.7
7	1752.72	57054.2 ± 4	78.5	57133	57137.6
9	1754.1	57009.3 ± 4	127.4	57137	57139.1
11	1755.8	56954.1 ± 8	187.7	57142	57141.1
13	1758.1	56879.6 ± 5	259.5	57139	57143.9
15	1760.46	56803.3 ± 5	342.8	57146	57147.5
17	1763.6	56702.2 ± 10	437.5	57140	57152.0
19	1766.9	56596.3 ± 10	543.6	57140	57157.7
21	1770.1	56494.0 ± 5	661.1	57155	57164.9
23	1773.5	56385.7 ± 10	790.1	57176	57173.9
25	1777.7	56252.5 ± 10	930.5	57183	57184.5
27	1782.7	56094.7 ± 10	1082.1	57177	57196.8
29	1787.2	55953.4 ± 10	1245.2	57199	57210.8

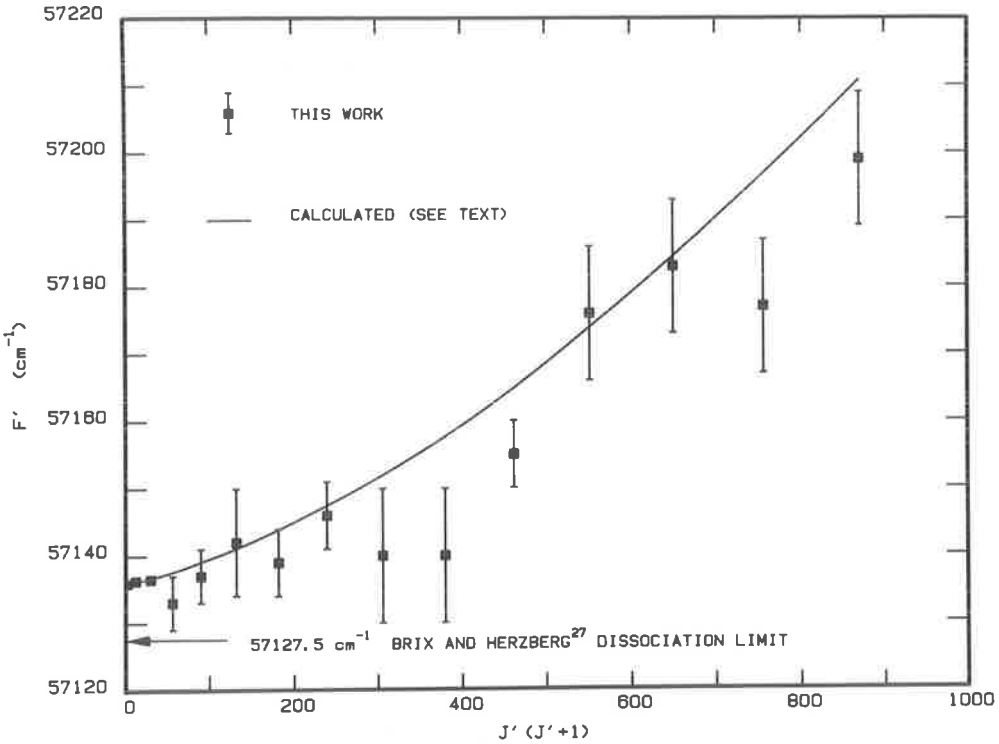

Fig. 6. Theoretical and measured limiting curves of dissociation[28] for the $B\ ^3\Sigma_u^-$ state of O_2 compared with the previously accepted dissociation limit.[27]

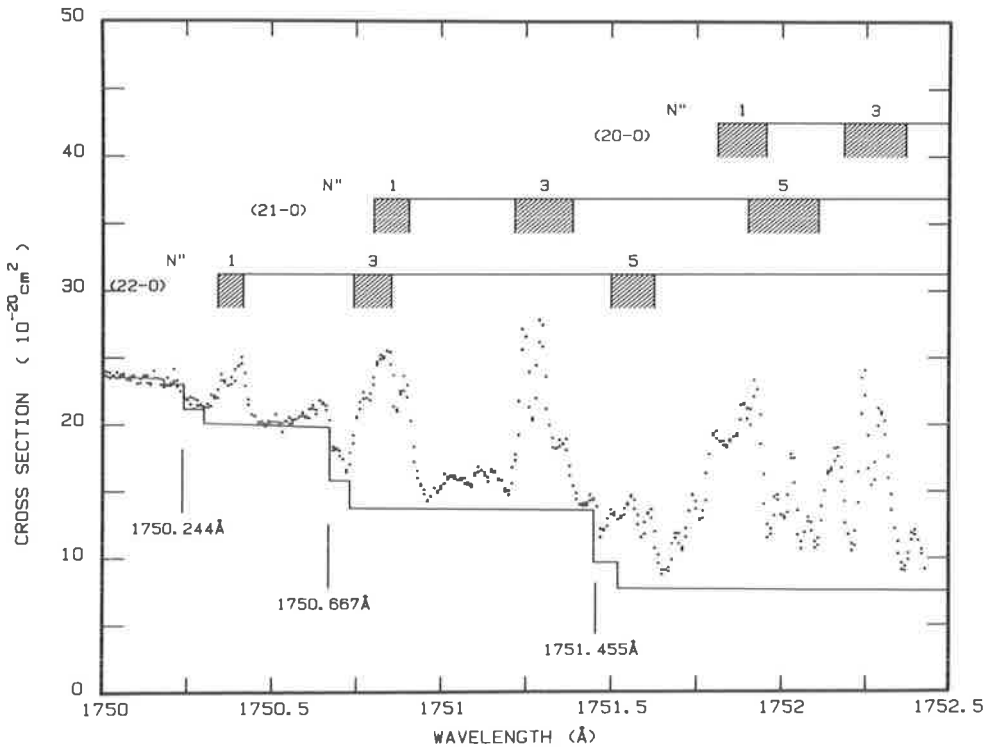

Fig. 7. Experimental photoabsorption cross-section from 1750 to 1752.5 Å for O_2 at T = 83 K. Groups of lines arising from the lowest rotational levels of the ground state are indicated for the (20–0) to (22–0) Schumann–Runge bands. Also shown (continuous line) is the theoretical underlying Schumann–Runge continuum cross-section including the main fine structure features for the first three thresholds.

(c) *Dissociation limit*

Figure 7 shows the measured absorption spectrum between 1750 and 1752.5 Å taken at 83 K with wavelength steps of 5.3 mÅ and a resolution of better than 0.04 Å. No corrections have been applied. Discrete structure in the spectrum starting at 1750.3 Å comprises lines from the (20–0) to (22–0) SR bands of O_2. Near 1750 Å the cross-section is only a slowly varying function of wavelength since we are beyond the dissociation limit of the B state in the rotationless SR continuum. At 1750.244 Å there is a sudden drop in the cross-section which does not appear to be associated with discrete absorption lines. In view of the previous theoretical discussion this is interpreted as the P_1R_1 component of the $N'' = 1$ threshold in the rotationally excited SR continuum for $v'' = 0$. From Fig. 1 the mean of the P_1 and R_1 components should lie at $(D - 0.87)$ cm^{-1} where D is the dissociation limit. Hence $D = 57135.8$ cm^{-1} with a maximum error of about 0.5 cm^{-1} due to possible measurement errors in the wavelength of the step. The theoretical cross-section of Fig. 5 has been adjusted downwards by 2.5%, within the experimental error, to agree accurately with the measurement at 1750 Å plotted in Fig. 7, and step wavelengths as in Fig. 1 have been used to predict the SR continuum cross-section in this region. The main fine structure features have been included and the relative intensity of the fine structure components have been estimated from the Boltzmann factors of the appropriate ground state levels at 83 K. No attempt has been made to include the effects of instrument resolution. It is apparent from Fig. 7 that not only are there downward steps in the

Table 5. Difference table for the Schumann–Runge band origins with $v' = 15$ to 22. Bracketed values are extrapolated.

v'	G'	$\Delta G'$	$-\Delta^2 G'$	$\Delta^3 G'$
15	56550.70 ± 0.05			
		168.86 ± 0.1		
16	56719.56 ± 0.05		35.86 ± 0.25	
		133.00 ± 0.15		4.9 ± 0.6
17	56852.56 ± 0.1		30.99 ± 0.35	
		102.01 ± 0.2		4.7 ± 0.8
18	56954.57 ± 0.1		26.29 ± 0.4	
		75.72 ± 0.2		3.2 ± 0.8
19	57030.29 ± 0.1		23.12 ± 0.4	
		52.60 ± 0.2		2.4 ± 0.8
20	57082.89 ± 0.1		20.68 ± 0.4	
		31.92 ± 0.2		4.7 ± 1.5
21	57114.81 ± 0.1		16.02 ± 1.1	
		15.9 ± 0.9		(4.0)
22	57130.7 ± 0.8		(12.0)	
		(3.9)		(4.0)
23			(8.0)	
		(-4.1)		

measured cross-section at the wavelengths predicted for the strongest components of the $N'' = 3, 5$ thresholds, but there is excellent agreement between the predicted cross-sections between steps and the base lines of the measured discrete line structure. The measured wavelengths for the $N'' = 3, 5$ steps are 1750.667 and 1751.455 Å, respectively, and from Fig. 1 the energies for these thresholds (mean R_3P_1) should be 14.9 and 40.3 cm^{-1} below the dissociation limit. Together with the previous estimate for $N'' = 1$, this gives 57135.8, 57136.0 and 57135.7 cm^{-1} for the dissociation limit from measurement of the step wavelengths for $N'' = 1, 3, 5$, (assuming the previous centrifugal barrier calculations, the maximum barrier being only 0.7 cm^{-1} for $N'' = 5$). It is proposed that the value 57136.0 $\pm$ 0.5 cm^{-1} be adopted as the definitive dissociation limit for the $B\ ^3\Sigma_u^-$ state of O_2.

The above determination relies essentially on the direct measurement of the wavelengths of distinct features in the spectrum of Fig. 7 and this measurement is easily performed within the stated accuracy. The previously accepted dissociation limit was that of Brix and Herzberg,[27] 57127.5 $\pm$ 5 cm^{-1}, obtained, far more indirectly than the present method, from an extrapolation of band origins for the SR-band system. It might be said that both values are not too far apart once the error estimates are considered, but it is instructive to pursue the cause of the difference. As stated by Brix and Herzberg[27] in the conclusion to their paper, the extrapolation technique for the SR bands had often been quoted to illustrate safe and precise spectroscopic methods of determining dissociation limits when only 15 bands were known. When 21 bands were known[27] the old value was found to be low by 260 cm^{-1}, thus demonstrating the difficulty with long extrapolations. It is proposed here that the group of lines at 1750.4 Å in Fig. 7, associated with an unassigned vibrational quantum number n by Brix and Herzberg,[27] are the lowest rotational members of the (22–0) band. This seems reasonable on intensity grounds after examination of Fig. 7. It is also proposed on intensity grounds that the line listed by Brix and Herzberg[27] at 57129.50 cm^{-1} is in fact the $^{22}R_2(1)$ line, that is the unassigned triplet component $i = 2$ in the notation of Brix and Herzberg.[27] This then enables a limited analysis of the small number of lines from the (22–0) band[27] and it follows that the corresponding band origin

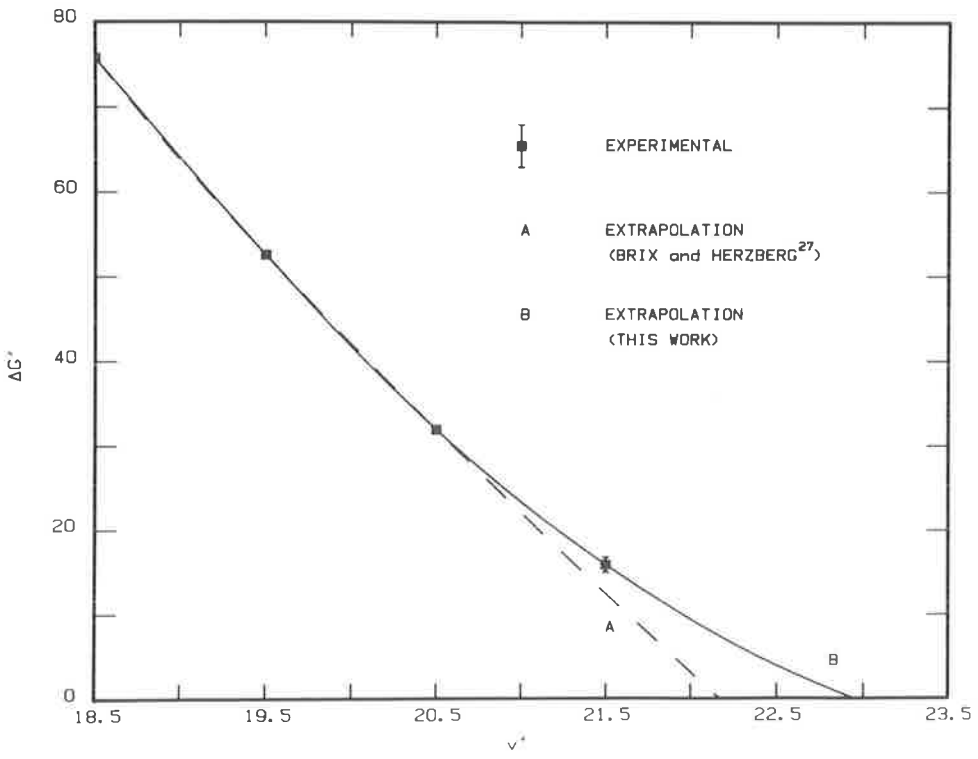

Fig. 8. $\Delta G'$ curve for the $B\ ^3\Sigma_u^-$ state of O_2 showing the suggested extrapolation of this work. The extrapolation of Brix and Herzberg[27] is also shown.

is $G_{22} = 57130.7 \pm 0.8\ \text{cm}^{-1}$. The new band origin enables an even shorter extrapolation than that performed by Brix and Herzberg.[27]

The band origins of Creek and Nicholls[29] for $v' = 15$ to 21 are used together with the above value for $v' = 22$ to form a difference table (Table 5). The errors become significant by the third difference which is averaged from $v' = 16.5$ to 20.5 to give $4.0\ \text{cm}^{-1}$ as an extrapolated value for higher v'. Extending the table by extrapolation implies that $\Delta G = 0$ at $v' = 22.95$ and the corresponding ΔG curve is shown in Fig. 8. The predicted dissociation limit is:

$$G_{22} + \int_{22}^{22.95} \Delta G\, dv' = \begin{cases} 57130.7 + 4.4, \\ 57135 \pm 3\ \text{cm}^{-1}. \end{cases}$$

The Brix and Herzberg[27] extrapolation is shown in Fig. 8 for comparison. It is seen that the new extrapolation agrees well with the new dissociation limit $57136.0 \pm 0.5\ \text{cm}^{-1}$ of this work. The above analysis is not intended to be rigorous but does clearly demonstrate that where the ΔG curve starts to curve upwards near the dissociation limit, as in the case of O_2, any extrapolation must be very short indeed if an accurate dissociation limit is to be deduced.

Table 6. Measured Schumann–Runge cross-section steps $\Delta\sigma$ as a function of ground state rotation for temperatures $T = 83$ and 295 K. Absolute threshold cross-sections σ_{th} calculated according to the relation $\sigma_{th} = \Delta\sigma/\alpha_{N''}$, where $\alpha_{N''}$ is the Boltzmann factor, are also given together with errors arising from the measurement inaccuracies in $\Delta\sigma$.

	T=83K			T=295K		
N''	$\Delta\sigma, 10^{-20}\text{cm}^2$	$\alpha_{N''}$	$\sigma_{th}, 10^{-19}\text{cm}^2$	$\Delta\sigma, 10^{-20}\text{cm}^2$	$\alpha_{N''}$	$\sigma_{th}, 10^{-19}\text{cm}^2$
1	3.2	0.141	2.3 ± 0.5	1.0	0.0414	2.4 ± 0.5
3	4.9	0.256	1.9 ± 0.4	2.2	0.0899	2.4 ± 0.5
5	5.8	0.257	2.3 ± 0.5	3.2	0.125	2.2 ± 0.3
7	3.6	0.184	2.0 ± 0.3	2.8	0.142	2.0 ± 0.3
9	2.1	0.100	2.1 ± 0.6	2.8	0.141	2.0 ± 0.3
11	0.7	0.042	1.7 ± 0.7	2.8	0.127	2.2 ± 0.3
13	0.3	0.014	2.1 ± 0.7	1.8	0.105	1.7 ± 0.3
15				1.4	0.081	1.7 ± 0.3
17				1.1	0.057	1.9 ± 0.2
19				0.75	0.038	2.0 ± 0.3
21				0.35	0.024	1.5 ± 0.2
23				0.22	0.014	1.6 ± 0.2
25				0.11	0.0076	1.4 ± 0.4
27				0.09	0.0039	2.3 ± 0.5
29				0.03	0.0019	1.6 ± 0.6

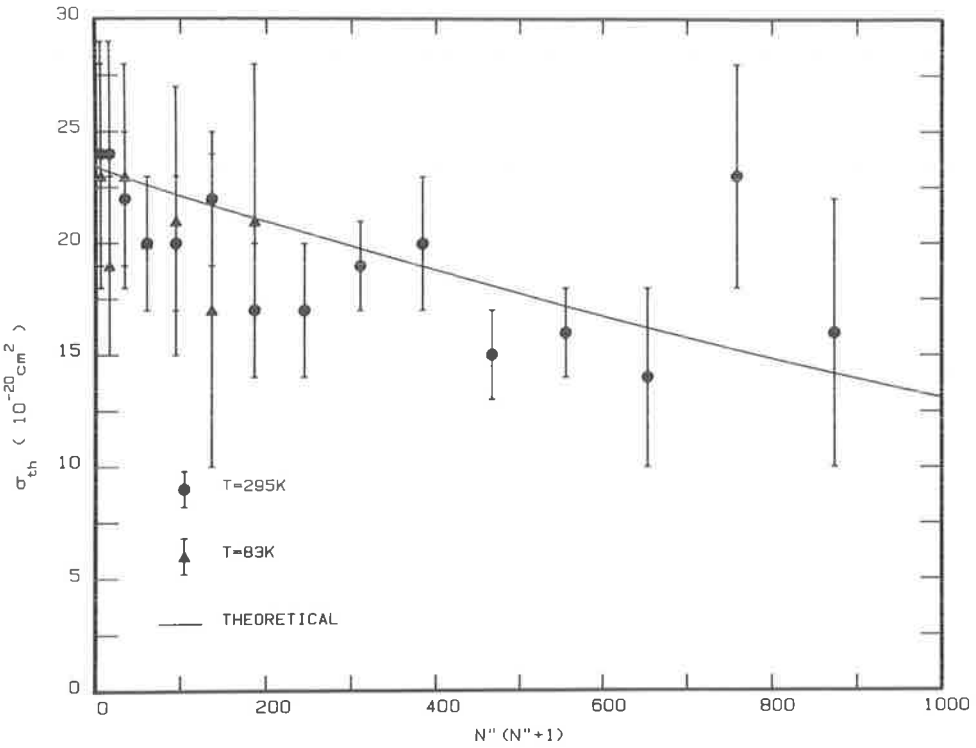

Fig. 9. Measured absolute Schumann–Runge threshold cross-sections for T = 83 K and 295 K as a function of $N''(N''+1)$ together with the theoretical predictions.

(d) *Magnitude of threshold cross-sections*

Threshold cross-sections for various rotations may be estimated from the data of Tables 2 and 3 by fitting straight lines to the measured cross-sections σ_T between thresholds and measuring the difference in cross-section $\Delta\sigma$ between successive lines at the calculated threshold wavelengths. Values so obtained at T = 83 and 295 K are listed in Table 6 together with Boltzmann factors appropriate to the temperature and ground state rotation of interest. Absolute threshold cross-sections σ_{th} for all observable values of N'' are obtained by dividing the measured cross-section steps $\Delta\sigma$ by the appropriate Boltzmann factor. The estimated threshold cross-sections for T = 83 and 295 K are plotted in Fig. 9, together with values calculated according to the theory discussed previously, ignoring shape resonances near threshold.

Despite the relatively poor accuracy of the measured values, the predicted decline in the threshold cross-section with N'' is clearly observed and the overall agreement with the theory is very good.

CONCLUSIONS

The extensive measurements of the photoabsorption cross-section underlying the Schumann–Runge bands of O_2 presented in this paper are the first to exhibit the step-like structure associated with absorption from rotationally excited levels of the ground state to the $B\ ^3\Sigma_u^-$ state continuum. Both the wavelengths and the magnitudes of the threshold cross-sectoins are seen to agree well with the theoretical calculations of this work. A new dissociation limit of 57136.0 ± 0.5 cm^{-1} for the B state is obtained from direct measurements of the wavelengths of the lowest rotational thresholds, and this supersedes the previously accepted value of 57127.5 ± 5 cm^{-1}.[27]

Acknowledgements—The authors would like to thank C. Dedman and K. Lonsdale for valuable technical assistance.

REFERENCES

1. P. G. Wilkinson and R. S. Mulliken, *Astrophys. J.* **125,** 594 (1957).
2. R. W. Ditchburn and P. A. Young, *J. Atmos. Terrest. Phys.* **24,** 127 (1962).
3. R. D. Hudson, V. L. Carter and J. A. Stein, *J. Geophys. Res.* **71,** 2295 (1966).
4. M. Ogawa, *J. Chem. Phys.* **54,** 2550 (1971).
5. V. Hasson and R. W. Nicholls, *J. Phys. B: Atom. Molec. Phys.* **4,** 1789 (1971).
6. H. P. F. Gies, S. T. Gibson, A. J. Blake and D. G. McCoy, *J. Geophys. Res.* **87,** 8307 (1982).
7. P. L. Smith, H. E. Griesinger, J. H. Black, K. Yoshino and D. E. Freeman, *Astrophys. J.* **277,** 569 (1984).
8. R. D. Hudson and S. H. Mahle, *J. Geophys. Res.* **77,** 2902 (1972).
9. A. J. Blake, *J. Geophys. Res.* **84,** 3272 (1979).
10. R. D. Hudson and V. L. Carter, *J. Opt. Soc. Am.* **58,** 1621 (1968).
11. A. C. Allison, A. Dalgarno and N. W. Pasachoff, *Planet. Space Sci.* **19,** 1463 (1971).
12. T. M. Fang, S. C. Wofsy and A. Dalgarno, *Planet. Space Sci.* **22,** 413 (1974).
13. W. R. Jarmain and R. W. Nicholls, *Proc. Phys. Soc.* **90,** 545 (1967).
14. B. R. Lewis, L. Berzins, J. H. Carver, S. T. Gibson and D. G. McCoy, *JQSRT*, to appear.
15. B. R. Lewis and J. H. Carver, *JQSRT* **30,** 297 (1983).
16. H. D. Babcock and L. Herzberg, *Astrophys. J.* **108,** 167 (1948).
17. R. P. Saxon and B. Liu, *J. Chem. Phys.* **67,** 5432 (1977).
18. S. T. Gibson, H. P. F. Gies, A. J. Blake, D. G. McCoy and P. J. Rogers, *JQSRT* **30,** 385 (1983).
19. L. Veseth and A. Lofthus, *Molec. Phys.* **27,** 511 (1974).
20. K. Yoshino, D. E. Freeman and W. H. Parkinson, *J. Phys. Chem. Ref. Data* **13,** 207 (1984).
21. S. T. Gibson, Ph.D. Thesis, University of Adelaide (1983).
22. B. R. Lewis, L. Berzins, J. H. Carver and S. T. Gibson, to appear.
23. B. R. Lewis, J. H. Carver, T. I. Hobbs, D. G. McCoy and H. P. F. Gies, *JQSRT* **20,** 191 (1978).
24. B. R. Lewis, J. H. Carver, T. I. Hobbs, D. G. McCoy and H. P. F. Gies, *JQSRT* **22,** 213 (1979).
25. B. R. Lewis, J. H. Carver, T. I. Hobbs, D. G. McCoy and H. P. F. Gies, *JQSRT* **24,** 365 (1981).
26. H. P. F. Gies, S. T. Gibson, D. G. McCoy, A. Blake and B. R. Lewis, *JQSRT* **26,** 469 (1981).
27. P. Brix and G. Herzberg, *Can. J. Phys.* **32,** 110 (1954).
28. G. Herzberg, *Spectra of Diatomic Molecules.* Van Nostrand, New York (1950).
29. D. M. Creek and R. W. Nicholls, *Proc. Roy. Soc. Lond.* **A341,** 517 (1975).

4.4 Decomposition of the photoabsorption continuum underlying the Schumann-Runge bands of $^{16}O_2$: II. Role of the $1\,^3\Pi_g$ state and collision-induced absorption

[21] B. R. Lewis, L. Berzins, J. H. Carver, S. T. Gibson, and D. G. McCoy, *Journal of Quantitative Spectroscopy and Radiative Transfer* **36**, 405–415 (1985).

J. Quant. Spectrosc. Radiat. Transfer Vol. 34, No. 5, pp. 405–415, 1985
Printed in Great Britain

0022-4073/85 $3.00+.00

DECOMPOSITION OF THE PHOTOABSORPTION CONTINUUM UNDERLYING THE SCHUMANN–RUNGE BANDS OF $^{16}O_2$—II. ROLE OF THE $1\,^3\Pi_g$ STATE AND COLLISION-INDUCED ABSORPTION

B. R. LEWIS, L. BERZINS, and J. H. CARVER
Research School of Physical Sciences, The Australian National University, Canberra, ACT 2600, Australia

and

S. T. GIBSON and D. G. MCCOY
Physics Department, University of Adelaide, Adelaide, SA 5000, Australia

(*Received* 13 *February* 1985)

Abstract—Measurements are presented of molecular oxygen photoabsorption cross-sections and pressure coefficients taken at selected minima between rotational lines of the Schumann–Runge band system. Both room-temperature and liquid-nitrogen–temperature results are presented from 1760–1980 Å, and corrections are applied for the effect of the wings of the rotational lines. Absorption into the $B\,^3\Sigma_u^-$ and $A\,^3\Sigma_u^+$ states is found to be insufficient to account for the total observed cross-section, and it is proposed that transitions to the $1\,^3\Pi_g$ valence state account for the remainder. The pressure dependence of the cross-sections is consistent with collision-induced enhancement of the intensities of the forbidden transitions $X\,^3\Sigma_g^- \rightarrow A\,^3\Sigma_u^+$ and $X\,^3\Sigma_g^- \rightarrow 1\,^3\Pi_g$, while the temperature dependence of the pressure coefficients is not consistent with absorption due to stable $(O_2)_2$ dimers.

INTRODUCTION

The previous paper in this series[1] contained measurements of the continuum underlying the Schumann–Runge (SR) bands of O_2 between 1750 and 1800 Å, and noted the importance of this absorption to atmospheric photochemical processes. The desirability of assigning the different transitions comprising the total cross-section was explained,[1] and a detailed discussion was given on the major role played by absorption from rotationally and vibrationally excited ground-state molecules into the $B\,^3\Sigma_u^-$ continuum for wavelengths longer than 1750 Å. This component of the cross-section will not be discussed further in this paper.

Of previous continuum photoabsorption measurements[2–8] in the range 1760–1980 Å, only those of Gies *et al.*[6] are corrected for absorption due to the wings of neighboring lines, although Hudson and Mahle[9] applied wing corrections to the measurements of Ogawa[4] when developing their SR absorption model.

The underlying continuum at wavelengths longer than 1950 Å, where wing corrections are small, is about 10^{-23} cm^2 and only slowly varying[3–5,9–11] and is attributed to the $X\,^3\Sigma_g^- \rightarrow A\,^3\Sigma_u^+$ Herzberg I forbidden transition. Ditchburn and Young[3] and Jarmain and Nicholls[12] have modeled this part of the continuum. Cross-sections in this region are pressure dependent,[3–5,9–11] and this has been attributed to the formation of $(O_2)_2$ dimers by some authors.[3,5,10]

At middle wavelengths (1800–1900 Å) the only detailed measurements of absorption underlying the SR bands are those of Ogawa[4] who claimed that there was definite structure in the continuum in this region despite having made no allowance for the wings of nearby lines, and attributed some of the cross-section to absorption into repulsive II states. Fang *et al.*[13] also deduced an excess continuum which they suggested might be due to the $X\,^3\Sigma_g^- \rightarrow 1\,^3\Pi_u$ transition. *Ab initio* calculations by Guberman and Dalgarno[14] and Allison *et al.*[15] on photoabsorption into the $^3\Pi_u$ state have shown that, at those wavelengths, this cross-section is expected to be significantly less than the Herzberg I continuum cross-section. Blake,[10] the first to model rotational effects in the B–X transition, claimed that the B–X

ORS1 34/5-E

and $A-X$ transitions were sufficient to account for all the underlying continuum above 1750 Å but, as shown in the previous work,[1] this conclusion does not hold if an improved model for the $B-X$ component is used.

We decided to extend the measurements reported in the previous work[1] to about 1950 Å, where the $A-X$ transition is dominant, in order to assess critically the wavelength dependence of transition components other than $B-X$ and $A-X$. This was made possible by the detailed confirmation of the accuracy of the $B-X$ transition model.[1]

Cross-section and pressure coefficient measurements were made at selected minima between rotational lines, and corrections were applied for absorption due to line wings. The measurements were taken at room and liquid nitrogen temperatures, and this paper presents results from 1760 to 1980 Å. Once wing and pressure corrections are applied to the present data, and the model SR and Herzberg continua are subtracted, there still remains a definite contribution which decreases from about $1\text{-}2 \times 10^{-21}$ cm^2 at 1760 Å to a negligible value near 1900 Å with some structure being shown between these wavelengths.

Transitions to the $1\,^3\Pi_g$ valence state of O_2 were mentioned briefly by Ogawa[4] as possible contributors to the underlying continuum above 1750 Å, and potential curves for this state have been calculated by some workers,[16,17] but there remains very little experimental information on the $1\,^3\Pi_g$ state. Cartwright *et al.*[18] attempted to decompose the SR continuum at wavelengths shorter than 1750 Å by analyzing electron scattering data and deduced that there was a component centred at 7.5 ± 0.1 eV which contributed to the total photoabsorption continuum. They assigned this component to the $1\,^3\Pi_g$ state, but Lee *et al.*[19] claimed no evidence of such a contribution in an experiment examining quantum yields for O (^1D) from photodissociation of O_2 between 1160 and 1770 Å. Examination of the results of Lee *et al.*[19] shows, however, that contributions of the order of a few percent would be masked by the experimental scatter.

In this work, semiempirical numerical calculations are performed using model $1\,^3\Pi_g$ potentials, and these indicate that the observed extra continuum including structure could arise from the forbidden $X\,^3\Sigma_g^- \rightarrow 1\,^3\Pi_g$ transition. This interpretation is consistent with the results of Cartwright *et al.*[18] This paper also presents the first low-temperature measurement of pressure coefficients for O_2 in this spectral region. It appears that, provided the coefficients are presented in terms of number density rather than pressure, there is no significant temperature dependence. This is not what would be expected if the interpretation of the pressure dependence of the absorption in terms of $(O_2)_2$ dimer absorption were valid (Shardanand and Rao[20]).

EXPERIMENTAL

A detailed discussion of the experimental method has been given elsewhere.[1] Briefly, an H_2 discharge, 2.2-m monochromator and temperature-controlled absorption cell were used to measure, photoelectrically, absorption cross-sections and pressure coefficients for O_2 with a resolution of about 0.04 Å. Measurements were taken between 1760 and 1980 Å at room (295 K) and liquid nitrogen temperatures. Cell lengths of 1.2 m and 10 cm were used, and the temperature gradients associated with the construction of the longer cell[1] resulted in an effective low temperature of 83 K, compared with 77 K for the 10-cm cell.

The deepest cross-section minima in each SR band were located during preliminary scanning, and the wavelength was then kept fixed while the transmission of the cell was measured at a number of pressures. Backgrounds were taken before and after each full cell transmission measurement in order to correct for the effects of detector drifts. At liquid nitrogen temperatures the pressure was kept below about 150 torr in order to avoid inaccuracies due to condensation of O_2, but at room temperature, pressures up to 1000 torr were used provided this did not produce transmission measurement inaccuracies due to absorption saturation. The effective absorption cross-section at each pressure was then calculated from Beer's law using the known pressure, cell length, transmission and temperature.

RESULTS

The results of a typical cross-section determination are given in Fig. 1. The minimum under study was at 1773.1 Å, and the 10-cm cell was used at liquid nitrogen temperature. The linear dependence of the effective cross-section on pressure is apparent. The cross-section extrapolated to zero pressure is 1.14×10^{-21} cm^2, and the slope, or pressure coefficient of the cross-section, is 8.1×10^{-24} cm^2/torr. Linear pressure dependence was observed at all wavelengths, provided that the experimental conditions were such that saturation of absorption did not occur at low pressures. This is consistent with the results of other workers at higher wavelengths.[3-5,11,20]

The full results of this work are summarized in Tables 1 and 2 for temperatures of 295 and ~80 K, respectively. The extrapolated cross-sections σ_M, and pressure coefficients $(d\sigma/dP)_M$ have been obtained in a similar manner to the above example. It is necessary to correct the cross-sections for the effect of the wings of the neighboring SR lines, σ_W, the wing correction procedure having been fully discussed previously.[1] Pressure broadening of the rotational lines of the SR bands also provides a pressure-dependent cross-section contribution, and the measured pressure coefficients are corrected for this effect, $(d\sigma/dP)_W$. The residual cross-sections σ_T and pressure coefficients $(d\sigma/dP)_T$ are given in Tables 1 and 2, together with error estimates arising from statistical errors in the measured values and assumed errors of about 20% in the corrections. At the longer wavelengths the values become quite inaccurate because of comparatively small absorption, especially at the lower temperature. The shorter cell and the lower temperature enable the measurements to be usefully extended to a significantly shorter wavelength than would have been possible with the 1.2-m cell at room temperature. The gaps in Table 1 correspond to measurements taken with the 1.2-m cell, where it was not possible to measure a pressure coefficient because of absorption saturation at relatively low pressures.

The largest uncertainty in the interpretation of the present work lies in the line-pressure-broadening correction applied to the measured pressure coefficients. In this work we have adopted the pressure-broadening coefficient

$$\Delta\nu/P = 0.3\,(273.2/T)^{0.7}\ , \tag{1}$$

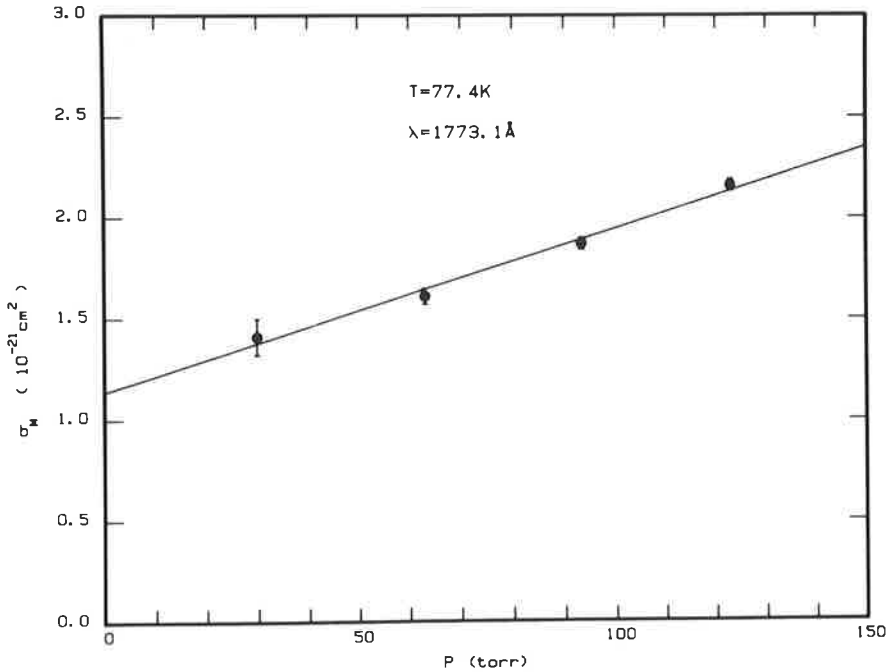

Fig. 1. Photoabsorption cross-section for O_2 at 1773.1 Å measured as a function of pressure. Measurements were taken at 77.4 K using a 10-cm cell.

Table 1. Cross-sections σ_M and pressure coefficients $(d\sigma/dP)_M$ at minima in the Schumann–Runge bands of O_2 measured at $T = 295$ K. Wing corrections σ_W, $(d\sigma/dP)_W$, Schumann–Runge cross-sections σ_{SR} and net results σ_T, $(d\sigma/dP)_T$ are also given. All cross-sections are in units of 10^{-23} cm^2, and pressure coefficients are in units of 10^{-26} cm^2/torr. The net pressure coefficients are also given in terms of number density as $(d\sigma/dN)_T$, units 10^{-43} cm^5/mol.

λ, Å	σ_M	σ_W	σ_T	σ_{SR}	$\left(\frac{d\sigma}{dP}\right)_M$	$\left(\frac{d\sigma}{dP}\right)_W$	$\left(\frac{d\sigma}{dP}\right)_T$	$\left(\frac{d\sigma}{dN}\right)_T$
1780.5	403	49	354 ± 30	229	188	164	24 ± 43	
1790.2	238	56	182 ± 22	124	106	101	5 ± 25	
1799.5	248	125	123 ± 40	96				
1801.1	246	142	104 ± 40	72	69	74	−5 ± 19	
1802.4	248	145	103 ± 40	56				
1812.4	118	104	14 ± 26	12				
1814.4	78	59	19 ± 16	8	29	24	5 ± 7	
1824.5	71	56	15 ± 16	2				
1825.1	78	52	26 ± 14	2				
1827.1	60	38	22 ± 11	1	26	23	3 ± 6	
1828.8	39	23	16 ± 6	1	24	14	10 ± 4	31 ± 8
1841.1	28	19	9 ± 5	0	12.4	9.3	3.1 ± 2.5	10 ± 8
1843.0	20	13	7 ± 4	0	12.0	5.3	6.7 ± 1.6	20 ± 5
1858.4	21	19	2 ± 5	0	8.8	4.6	4.2 ± 1.5	13 ± 5
1861.1	13.3	12.8	0.5 ± 3.1	0	7.3	2.9	4.4 ± 1.0	13 ± 3
1873.2	20.9	15.4	5.5 ± 4.0	0	10.0	4.0	6.0 ± 1.3	18 ± 4
1880.4	8.4	5.4	3.0 ± 1.5	0	3.8	1.4	2.4 ± 0.5	7.3 ± 1.5
1899.4	2.9	1.9	1.0 ± 0.5	0	2.8	0.4	2.4 ± 0.3	7.3 ± 1.0
1918.9	2.2	1.0	1.2 ± 0.4	0	2.7	0.2	2.5 ± 0.4	7.6 ± 1.2
1942.9	1.9	0.8	1.1 ± 0.4	0	2.2	0.1	2.1 ± 0.4	6.4 ± 1.2
1969.0	1.0	0.1	0.9 ± 0.4	0	1.5	0.0	1.5 ± 0.4	4.6 ± 1.2
1981.7	1.1	0.0	1.1 ± 0.4	0	1.4	0.0	1.4 ± 0.4	4.3 ± 1.2

where $\Delta\nu(\text{cm}^{-1})$ is the full width at half maximum (FWHM) linewidth, P(atm) is the pressure and T(K) the temperature, as deduced by Cann *et al.*[21] (An exponent sign correction should be noted.) Equation (1) is not inconsistent with preliminary measurements of SR linewidth pressure broadening made by us, but these measurements are very inaccurate, and further work in this area is in progress. Even Eq. (1) is not based directly on measurements of the self-broadening of SR lines of O_2, and predicts linewidth pressure broadening well in excess of the value obtained by assuming kinetic theory collision diameters for O_2. The pressure-broadening uncertainty is most important at room temperature and at the shorter wavelengths as can be seen in Tables 1 and 2.

Tables 1 and 2 also list the theoretical SR continuum cross-section component, σ_{SR}, as calculated by Lewis *et al.*[1] for the appropriate experimental conditions. Values of $(\sigma_T - \sigma_{SR})$ are plotted for room and liquid nitrogen temperatures in Fig. 2, and it is seen that the results at both temperatures exhibit qualitatively similar behavior. The cross-section falls from 1-2 $\times$ 10^{-21} cm^2 at 1760 Å down to $\sim$1 $\times$ 10^{-23} cm^2, the Herzberg continuum level, near 1900 Å. There is a suggestion of some structure between 1810 and 1900 Å, but in view of the broad absorption lines and consequent large wing corrections, the resultant cross-section accuracy is poor in this region. Nevertheless it is clear that even after allowing for the SR and Herzberg continua, as well as the wings of the SR lines, there still remains

Table 2. Cross-sections σ_M and pressure coefficients $(d\sigma/dP)_M$ at minima in the Schumann–Runge bands of O_2 measured at $T \sim 80$ K. Wing corrections σ_W, $(d\sigma/dP)_W$, Schumann–Runge cross-sections σ_{SR} and net results σ_T, $(d\sigma/dP)_T$ are also given. All cross-sections are in units of 10^{-23} cm^2, and pressure coefficients are in units of 10^{-25} cm^2/torr. The net pressure coefficients are also given in terms of number density as $(d\sigma/dN)_T$, units 10^{-43} cm^5/mol.

λ, Å	σ_M	σ_W	σ_T	σ_{SR}	$\left(\frac{d\sigma}{dP}\right)_M$	$\left(\frac{d\sigma}{dP}\right)_W$	$\left(\frac{d\sigma}{dP}\right)_T$	$\left(\frac{d\sigma}{dN}\right)_T$
1762.6	335	232	103 ± 63	18	200	77	123 ± 25	1020 ± 200
1766.9	212	134	78 ± 40	1	128	34	94 ± 15	780 ± 125
1773.1	114	47	67 ± 15	0	81	20	61 ± 10	510 ± 85
1780.5	69	14	55 ± 6	0	56	9	47 ± 5	390 ± 40
1788.2	47	20	27 ± 7	0	47	8	39 ± 5	320 ± 40
1800.4	36	33	3 ± 9	0	22	3	19 ± 2	160 ± 20
1812.4	11.3	17.4	-6 ± 5	0	10	2	8 ± 1	66 ± 10
1824.8	12.7	7.3	5.4 ± 2.2	0	8.4	0.9	7.5 ± 1.0	62 ± 10
1826.3	14.1	7.5	6.6 ± 2.2	0	6.4	0.9	5.5 ± 1.5	46 ± 15
1838.8	7.7	6.2	1.5 ± 1.7	0	3.2	0.6	2.6 ± 1.0	22 ± 10
1841.0	9.1	6.2	2.9 ± 2.2	0	3.1	0.4	2.7 ± 1.0	22 ± 10
1856.7	3.0	3.3	-0.3 ± 1.3	0	1.8	0.2	1.6 ± 1.0	13 ± 8
1858.9	4.3	3.7	0.6 ± 1.2	0	2.1	0.3	1.8 ± 0.8	15 ± 7
1874.0	4.7	1.9	2.8 ± 1.2	0	1.4	0.0	1.4 ± 1.0	12 ± 9
1875.7	3.5	1.8	1.7 ± 1.2	0	2.3	0.0	2.3 ± 1.3	19 ± 11
1892.4	1.1	1.1	0.0 ± 0.8	0	1.2	0.0	1.2 ± 0.9	10 ± 8
1894.4	1.9	0.8	1.1 ± 0.8	0	0.9	0.0	0.9 ± 0.9	7.5 ± 7.5
1914.7	1.1	0.4	0.7 ± 0.7	0	0.9	0.0	0.9 ± 0.9	7.5 ± 7.5

a definite component of the continuum between 1760 and 1900 Å which must correspond to a transition other than A–X or B–X.

Ogawa[4] has measured room-temperature cross-sections and pressure coefficients at certain minima between 1814 and 2050 Å, while Cheung *et al.*[11] have done likewise from 1935 to 2040 Å. Their results have been wing corrected for the appropriate experimental conditions, and the resultant cross-sections are also plotted in Figure 2; the SR continuum cross-section having been subtracted where appropriate.

The cross-sections of Ogawa[4] agree with those of this work within the combined experimental errors. Cheung *et al.*[11] claim that interference from the SR lines is negligible in their continuum measurements, presumably because of their excellent wavelength resolution. This is not true for the shortest wavelengths of their work, because there is a resolution-independent pseudo-continuum due to the combined effect of the Lorentzian wings of neighboring broad lines, which must be considered out to a large distance each side of the wavelength of interest. For example, under the experimental conditions of Cheung *et al.*[11] at 1935.8 Å, we calculate a wing correction of 1.1×10^{-23} cm^2 to their measured cross-section of 1.4×10^{-23} cm^2. As can be seen from Fig. 2, the corrections result in a downturn of their cross-section below 1970 Å, inconsistent with the other results. The wing corrections of this work are fairly consistent in this region with those of Hudson and Mahle,[9] who calculate for the experimental conditions of Ogawa[4] a wing correction of 1.0×10^{-23} cm^2 at 1935.8 Å. Unfortunately we cannot resolve the discrepancy between the results of Ogawa[4] and Cheung *et al.*[11] because of the small absorption in this region and consequent large uncertainty in the present results. Two points from Shardanand and Rao[20] are also shown in Fig. 2, and these merge smoothly with the results of Ogawa.[4]

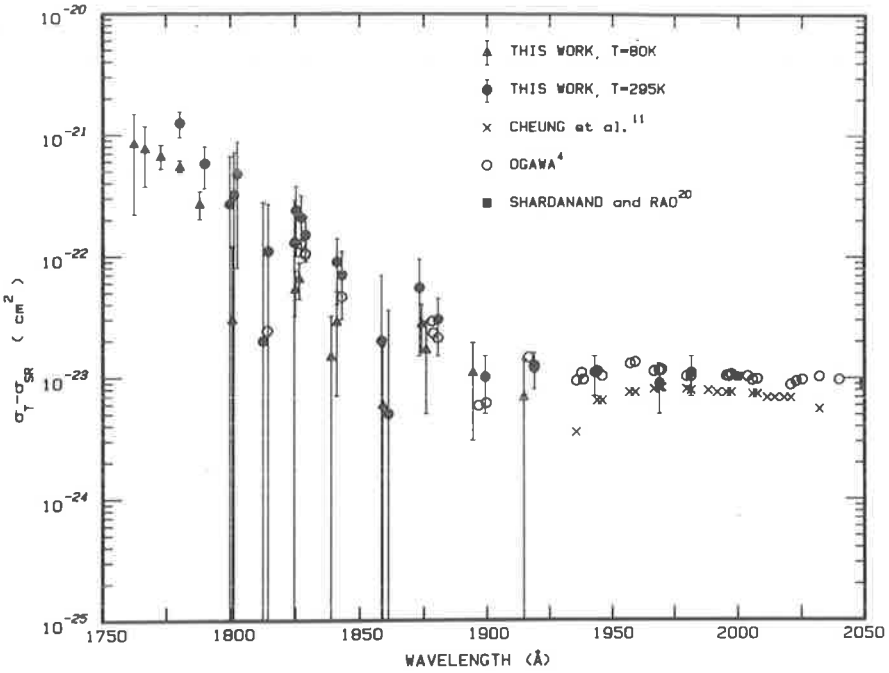

Fig. 2. Underlying O_2 continuum cross-sections measured at 295 and $\sim$ 80 K, corrected for the effects of line wings and the Schumann-Runge continuum. The room-temperature results of other workers[4,11,20] are also shown after the application of similar corrections.

The room-temperature pressure coefficients of this work $(d\sigma/dP)_T$ are shown in Fig. 3, together with those of Ogawa[4], Cheung *et al.*[11] and Shardanand and Rao[20]; all results having been corrected where necessary for pressure-broadening effects as described above. As seen from Table 1, the corrections are largest at the shorter wavelengths, and in fact points where the correction is larger than the net pressure coefficient have been omitted from the figure.

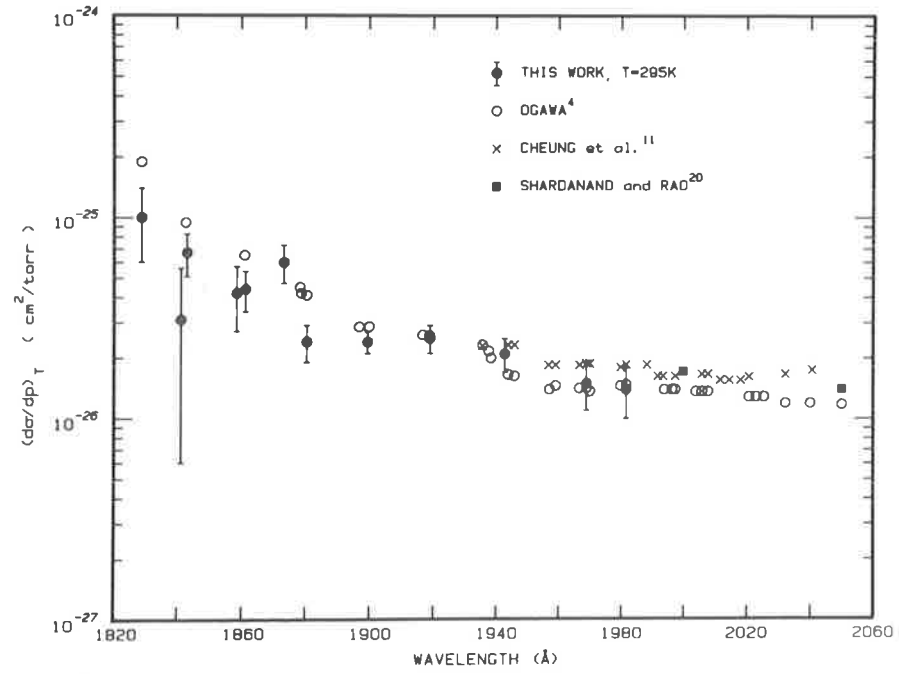

Fig. 3. The room-temperature pressure coefficients of this work, after correction for pressure broadening, together with the similarly corrected results of other workers.[4,11,20]

Once again there is agreement between the pressure coefficients of this work and those of Ogawa within the combined experimental errors, but with our results tending to be slightly lower at wavelengths shorter than 1880 Å. The pressure coefficients of Cheung *et al.*[11] and Shardanand and Rao[20] represent virtually their published values. Similarly, as for the cross-sections, we cannot distinguish between the pressure coefficients of Cheung *et al.*[11] and Ogawa[4] above 1935 Å because of the fairly large statistical error in the results of the present work.

DISCUSSION

(i) *Continuum cross-section*

As noted earlier, our results show a definite continuum cross-section component, in addition to the $B-X$ and $A-X$ transitions, which decreases from 1-2 $\times$ 10^{-21} cm^2 at 1760 Å to a small value at $\sim$1900 Å. What are the possible origins of this component?

If the room-temperature results were the only ones available, it would be possible to explain the extra cross-section component as the result of a systematic error in the calculated SR continuum from rovibrationally excited ground-state molecules,[1] which has an influence below $\sim$ 1820 Å (Table 1). The low-temperature results rule out this possibility, however, since in this case the SR continuum plays a significant role only below $\sim$ 1765 Å, yet a definite underlying continuum between 10^{-22} and 10^{-21} cm^2 is still measured from 1765 to 1790 Å.

Absorption into the $^3\Pi_u$ state is an unlikely explanation since *ab initio* calculations[14,15] have shown that $^3\Pi_u - X$ absorption should have a cross-section significantly less than 10^{-23} cm^2 in this spectral region. We must thus look toward transitions to another state to explain the observed absorption.

Cartwright *et al.*[18] attempt to decompose electron energy-loss spectra for O_2 under various conditions of electron energy and scattering angle, and deduce that there is a small contribution from a state at 7.5 $\pm$ 0.1 eV which they classify as a $^3\Pi_g$ valence state on the basis of *ab initio* calculations. Lee *et al.*[19] examined quantum yields for O (^1D) from photodissociation of O_2 between 1160 and 1770 Å and found no evidence for a contribution from the $^3\Pi_g$ state of the magnitude predicted by Cartwright *et al.*[18] which does seem too large in the electron scattering case analogous to photoabsorption. However, careful inspection of the results of Lee *et al.*[19] shows that $^3\Pi_g$ contributions of a few percent of the total cross-section cannot be ruled out. The present results imply an unclassified underlying cross-section of the order of 1% of the SR cross-section at 1750 Å, and this is clearly quite consistent with an assignment to the $1\,^3\Pi_g$ state and also with the results of Lee *et al.*[19]

In order to test this hypothesis fully, it is necessary to perform some calculations. There is little quantitative information available for the $1\,^3\Pi_g$ state. An *ab initio* potential curve for this state has been calculated by Saxon and Liu,[17] and a small portion of the curve near the Franck–Condon region has been determined experimentally by Cartwright *et al.*[18] For the purposes of this work, the curve of Saxon and Liu[17] is shifted to lower energies by 0.1 eV and to smaller internuclear separation by 0.09 Å in order to agree with the Cartwright *et al.*[18] curve in both slope and vertical excitation energy ($\sim$ 7.5 eV). These shifts are in the usual direction required to force agreement between experimental and *ab initio* potential curves, and are relatively small (see, for example, Cartwright *et al.*[18]). The $1\,^3\Pi_g$ potential curve so obtained is shown in Fig. 4, together with RKR potential curves for the $X\,^3\Sigma_g^-$ and $B\,^3\Sigma_u^-$ states, [22] and an *ab initio* potential curve for the $A\,^3\Sigma_u^+$ state[17] shifted to coincide with the Cartwright *et al.*[18] Franck–Condon region determination. The $1\,^3\Pi_g$ curve contains a plateau resulting from an avoided crossing with the $2\,^3\Pi_g$ state.

The Schrödinger equation for no rotation was solved numerically for the X and $1\,^3\Pi_g$ states using the Numerov integration method,[23,24] and the relative cross-section for absorption into the $1\,^3\Pi_g$ state from the lowest vibrational level of the ground state was evaluated from

$$\sigma_{v''=0} \propto \frac{1}{\lambda}\left|\int \psi_{v''=0}\,\psi_\lambda \mathrm{d}r\right|^2, \qquad (2)$$

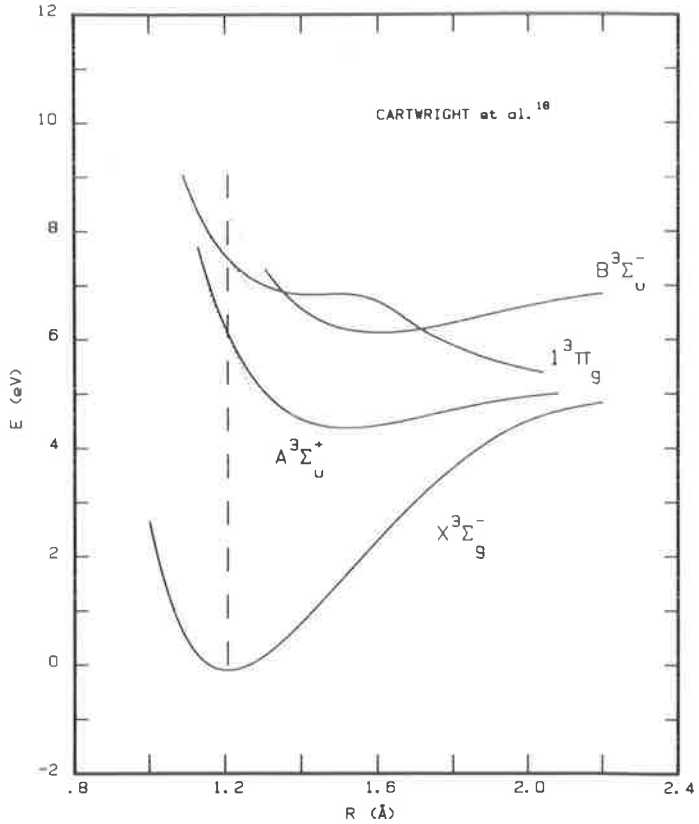

Fig. 4. Potential curve diagram for O_2. The X and B curves are RKR,[22] and the A and $1\,^3\Pi_g$ curves are *ab initio*[17] shifted to agree with experimental Franck–Condon region determinations.[18]

where $\psi_{v''=0}$ and ψ_λ are the normalized initial and final-state wave functions, and λ is the wavelength of the transition. The electronic transition moment has been assumed independent of internuclear separation in the absence of any existing calculation.

Figure 5 shows the $X - 1\,^3\Pi_g$ cross-section so obtained as a function of wavelength above 1550 Å, together with the values deduced from some of the results of Lewis *et al.*,[1] and the underlying continuum cross-sections of this work; all experimental results being taken at liquid nitrogen temperatures, the most valid comparison with the rotationless calculations. The theoretical cross-section has been normalized to the experimental results near 1770 Å. Also shown is an approximate Herzberg continuum based on the measurements of Cheung *et al.*[11] and the theoretical extrapolation of Ditchburn and Young.[3]

It is seen that the wavelength dependence of the experimental results from 1760 – 1800 Å is well matched by the theoretical calculations. Above 1800 Å the experimental results flatten off into the Herzberg continuum. Figure 5 provides strong support for the assignment of the extra underlying continuum of this work to absorption into the $1\,^3\Pi_g$ state, in agreement with the general conclusions of Cartwright *et al.*[18] if not in actual continuum strength. The theoretical continuum peaks at $\sim$ 1660 Å with a magnitude of about 6×10^{-21} cm^2, a factor of about 2300 weaker than the allowed B–X continuum peak. Magnetic dipole allowed transitions such as the $^3\Pi_g$–X are generally expected to be about a factor of 10,000 weaker than allowed electric dipole transitions (Herzberg[25]).

If the results of Lee *et al.*[19] are examined, one can assign a lower limit of about 0.95 to the O (^1D) yield near 1730 Å. Using a value of 4.2×10^{-19} cm^2 for the SR continuum[22] at 300 K, it then follows that $\sim 2 \times 10^{-20}$ cm^{-2} is an upper limit for the $X \rightarrow 1\,^3\Pi_g$ cross-section. This is well above the value implied by the present measurements and thus the results of Lee *et al.*[19] are not inconsistent with this work. Further experiments similar to those of Lee *et al.*[19] are planned to clarify the matter.

The rapid fall-off in cross-section towards 1810 Å is also of some interest. This is caused essentially by the avoided crossing plateau in the $1\,^3\Pi_g$ potential curve. It is conceivable

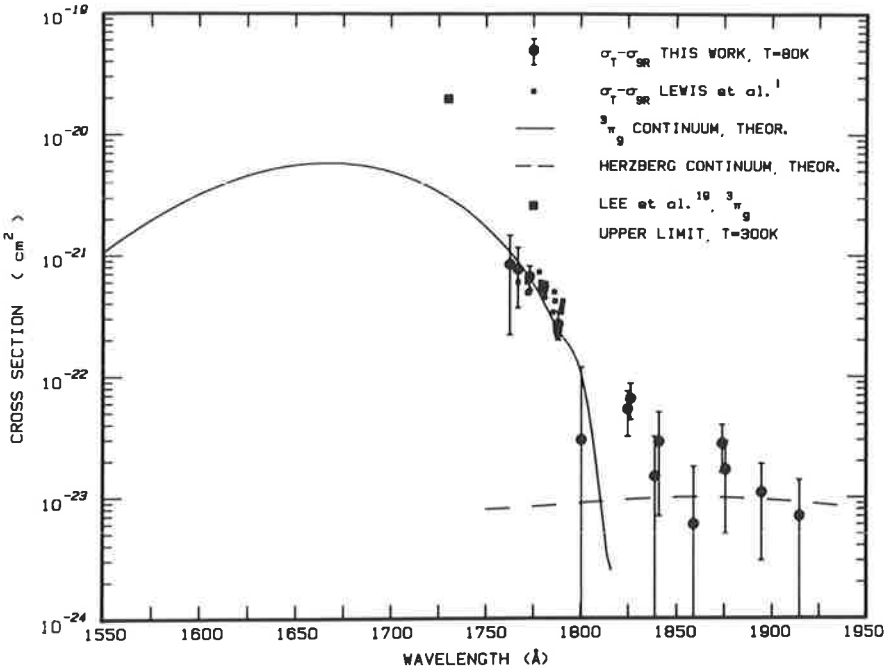

Fig. 5. Theoretical cross-section for the $X \rightarrow 1\,^3\Pi_g$ transition, calculated according to the procedure discussed in the text, normalized to the low-temperature results of this work and Lewis *et al.*[1] A theoretical curve for the Herzberg continuum is also shown as is an upper limit for the cross-section near 1730 Å deduced from the work of Lee *et al.*[19]

also that there may be a slight minimum in this region of the potential curve which could produce resonance effects due to bound or quasi-bound states. These could provide subsidiary peaks in the cross-section above 1800 Å; a possibility according to the current results. Brief calculations have indicated that this can indeed occur under certain conditions, but no quantitative fitting has been pursued because of the poor accuracy of the present results above 1800 Å.

(ii) Collision-induced absorption

In his well-known papers[20,26] on the pressure dependence of O_2 absorption above 2000 Å, Shardanand attributes the increase in absorption with pressure to absorption of the dimer $(O_2)_2$ via the equation

$$\sigma_{\text{eff}}(\lambda) = \sigma_1(\lambda) + K\,\sigma_2(\lambda)\,N\,, \tag{3}$$

where $\sigma_{\text{eff}}(\lambda)$ is the measured cross-section, $\sigma_1(\lambda)$ is the cross-section of O_2, $\sigma_2(\lambda)$ is the cross-section of $(O_2)_2$, N is the number density of O_2, and K is the equilibrium constant governing formation of the dimer, given by the second virial coefficient for O_2. For $T =$ 300 K, $K = 2.6 \times 10^{-23}$ cm^3/mol. This interpretation has been questioned by some authors.[4,11,27]

As noted recently by Cheung *et al.*,[11] it is not possible to deduce much information on the properties of the species responsible for the pressure-dependent cross-section from room-temperature measurements of the type mentioned. While a formulation such as Eq. (3) is certainly consistent with the measurements, uncertainties in K and the assumption that only bound-state dimers are involved make any deduced values of dimer cross-section extremely dubious. Another recent study by Johnston *et al.*[27] also concludes that the extra absorption is more likely to be due to O_2 transitions perturbed by nearby O_2 molecules rather than absorption by the species $(O_2)_2$. In a broader sense, the controversy over the significance of bound dimers has been well summarized by Krupenie.[28]

The pressure coefficient measurements of this work enable the hypothesis of Shardanand[20,26] to be examined more critically because of the extra information obtained

by varying the temperature. The present pressure coefficients are expressed in terms of number density as $(d\sigma/dN)_T$ cm^5/mol in Tables 1 and 2 where the statistical error is not too large, and these values are plotted in Fig. 6 for temperatures of 295 K and $\sim$ 80 K. It is seen that the two data sets merge fairly smoothly in the range of overlap from 1830 to 1910 Å. The temperature dependence is small; certainly less than a factor of two. Unfortunately this region corresponds with the least accurate of the data points for both temperatures, so it is not possible to be more precise. Shardanand[29] has measured the temperature dependence of the pressure coefficients at wavelengths longer than 2050 Å and at temperatures from 200 to 348 K. He obtains a small negative dependence which is not inconsistent with the present results which merge smoothly with his near 2000 Å.

These new measurements indicate that the assumptions of Shardanand[20,26,29] regarding absorption by $(O_2)_2$ dimers must be in error. Let us assume the Shardanand[20,26,29] theory, that is, $d\sigma_{eff}/dN = K\sigma_2$. The rate coefficient K, equal to the second virial coefficient of O_2, is expected to increase markedly on decreasing the temperature from 295 to $\sim$ 80 K,[27] and in fact a judicious extrapolation of tables of the virial coefficients for O_2 (Ref. 30) would indicate an increase of about a factor of 20. The current results then would imply that σ_2, the dimer absorption cross-section, should decrease by a factor of 20 at all wavelengths on going from room temperature to liquid nitrogen temperature! This seems unlikely, and thus the initial assumption of the Shardanand[20,26,29] theory is equally unlikely. In fact, Johnston *et al.*[27] have also recently noted that the observed small increases in pressure coefficient for decreasing temperature[29] above 2050 Å are much smaller than the increase in the equilibrium constant K and have reached similar conclusions to ours.

It thus follows that there really is no evidence at all for the existence of stable $(O_2)_2$ dimers from photoabsorption measurements in this spectral region. From Fig. 6, $(d\sigma/dN)_T$ is not significantly temperature dependent, and the wavelength dependence approximately follows that of the underlying forbidden $A-X$ and $^3\Pi_g-X$ cross-sections. The pressure effects can thus be modeled fairly easily, and the simple assumption that the increased absorption is due to unbound collision pairs enhancing the probabilities of the $A-X$ and $^3\Pi_g-X$ transitions, without invoking the ubiquitous bound dimer, seems appropriate.

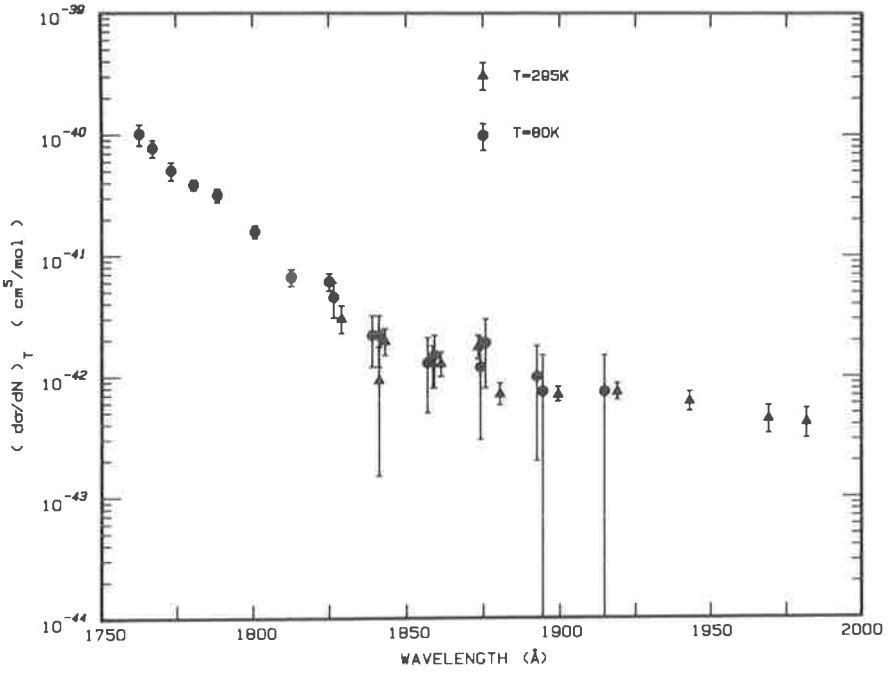

Fig. 6. The measured number density dependence of the underlying continuum cross-section, after correction for pressure broadening, at 295 and $\sim$ 80 K.

CONCLUSIONS

The present measurements, especially those taken at liquid nitrogen temperatures, clearly indicate a component of the continuum underlying the SR bands arising from transitions to a state other than $B\,^3\Sigma_u^-$ or $A\,^3\Sigma_u^+$. This component is assigned to the electric dipole forbidden $X - 1\,^3\Pi_g$ transition, and the observed wavelength dependence is found to be consistent with a $1\,^3\Pi_g$ potential curve based on previous experimental[18] and *ab initio*[17] work. The observed strength of the transition, although greater than expected for the magnetic dipole allowed case, is still consistent with the results of Lee *et al.*[19] The observed pressure coefficient temperature dependence strongly suggests that bound $(O_2)_2$ dimers play no significant part in the absorption, and thus that the interpretation of Shardanand[20,26,29] is wrong.

Acknowledgements—The authors would like to thank C. Dedman and K. Lonsdale for valuable technical assistance.

REFERENCES

1. B. R. Lewis, L. Berzins, J. H. Carver and S. T. Gibson, *JQSRT* **33**, 627 (1985).
2. P. G. Wilkinson and R. S. Mulliken, *Astrophys. J.* **125**, 594 (1957).
3. R. W. Ditchburn and P. A. Young, *J. Atoms. Terrest. Phys.* **24**, 127 (1962).
4. M. Ogawa, *J. Chem. Phys.* **54**, 2550 (1971).
5. V. Hasson and R. W. Nicholls, *J. Phys. B.* **4**, 1789 (1971).
6. H. P. F. Gies, S. T. Gibson, A. J. Blake and D. G. McCoy, *J. Geophys. Res.* **87**, 8307 (1982).
7. P. L. Smith, H. E. Griesinger, J. H. Black, K. Yoshino and D. E. Freeman, *Astrophys. J.* **277**, 569 (1984).
8. R. D. Hudson, V. L. Carter and J. A. Stein, *J. Geophys. Res.* **71**, 2295 (1966).
9. R. D. Hudson and S. H. Mahle, *J. Geophys. Res.* **77**, 2902 (1972).
10. A. J. Blake, *J. Geophys. Res.* **84**, 3272 (1979).
11. A. S. C. Cheung, K. Yoshino, W. H. Parkinson and D. E. Freeman, *Geophys. Res. Lett.* **11**, 580 (1984); *Can. J. Phys.* **62**, 1752 (1984).
12. W. R. Jarmain and R. W. Nicholls, *Proc. Phys. Soc.* **90**, 545 (1967).
13. T. M. Fang, S. C. Wofsy and A. Dalgarno, *Planet. Space. Sci.* **22**, 413 (1974).
14. S. L. Guberman and A. Dalgarno, *J. Geophys. Res.* **84**, 4437 (1979).
15. A. C. Allison, S. L. Guberman and A. Dalgarno, *J. Geophys. Res.* **87**, 923 (1982).
16. H. F. Schaefer III and F. E. Harris, *J. Chem. Phys.* **48**, 4946 (1968).
17. R. P. Saxon and B. Liu, *J. Chem. Phys.* **67**, 5432 (1977).
18. D. C. Cartwright, N. A. Fiamengo, W. Williams and S. Trajmar, *J. Phys. B.* **9**, L419 (1976).
19. L. C. Lee, T. G. Slanger, G. Black and R. L. Sharpless, *J. Chem. Phys.* **67**, 5602 (1977).
20. Shardanand and A. D. Prasad Rao, *JQSRT* **17**, 433 (1977).
21. M. W. P. Cann, R. W. Nicholls, W. F. J. Evans, J. L. Kohl, R. Kurucz, W. H. Parkinson and E. M. Reeves, *Appl. Opt.* **18**, 964 (1979).
22. S. T. Gibson, H. P. F. Gies, A. J. Blake, D. G. McCoy and P. J. Rogers, *JQSRT* **30**, 385 (1983).
23. J. K. Cashion, *J. Chem. Phys.* **39**, 1872 (1963).
24. A. C. Allison, *Comp. Phys. Com.* **1**, 21 (1969).
25. G. Herzberg, *Spectra of Diatomic Molecules.* Van Nostrand, New York (1950).
26. Shardanand, *Phys. Rev.* **186**, 5 (1969).
27. H. S. Johnston, M. Paige and F. Yao, *J. Geophys. Res.* **89**, 11661 (1984).
28. P. H. Krupenie, *J. Phys. Chem. Ref. Data* **1**, 423 (1972).
29. Shardanand, *JQSRT* **20**, 265 (1978).
30. J. M. H. L. Sengers, M. Klein and J. S. Gallagher, *American Institute of Physics Handbook* (Edited by D. E. Gray), 3rd Edn., p. 4–211. McGraw-Hill, New York (1972).

4.5 Oscillator strengths for the Schumann-Runge bands of $^{16}O_2$

[23] B. R. Lewis, L. Berzins, and J. H. Carver,
Journal of Quantitative Spectroscopy and Radiative Transfer **36**, 209–232 (1986).

J. Quant. Spectrosc. Radiat. Transfer Vol. 36, No. 3, pp. 209–232, 1986
Printed in Great Britain.

0022-4073/86 $3.00 + 0.00

OSCILLATOR STRENGTHS FOR THE SCHUMANN–RUNGE BANDS OF $^{16}O_2$

B. R. LEWIS, L. BERZINS and J. H. CARVER
Research School of Physical Sciences, The Australian National University, Canberra, Australia 2600

(*Received* 11 *November* 1985)

Abstract—Experimental oscillator strengths are presented for the (1–0)–(22–0) and (3–1)–(17–1) Schumann–Runge bands of $^{16}O_2$. A wavelength resolution of ~0.04 Å enabled individual rotational lines to be studied and an equivalent width data analysis method was used. The now established decrease in equivalent band oscillator strength with increased rotation is observed. The mean band oscillator strengths of this work for the (1–0)–(12–0) bands are in excellent agreement with recent ultra-high resolution absolute measurements, and the oscillator strength density is found to be continuous across the dissociation limit. The dipole moment deduced from the present oscillator strengths agrees well with recent *ab initio* and semi-empirical determinations.

INTRODUCTION

The oscillator strengths and linewidths for rotational lines in the Schumann–Runge bands of $^{16}O_2$ are important parameters determining the penetration into the atmosphere of solar radiation in the range 1750–2000 Å, and also affect the photodissociation rates for various atmospheric species. Many atmospheric transmission and photodissociation calculations[1–19] have been performed and the recent study by Nicolet[20] stresses the importance of an accurate knowledge of Schumann–Runge band oscillator strengths and linewidths. Measurements of predissociation linewidths taken in association with this work are presented in a companion paper,[21] and oscillator strengths only will be considered here.

Since the pioneering work of Schumann,[22] the Schumann–Runge bands have been photographed in absorption and emission and analyzed many times.[23,24] The accurate measurements of Brix and Herzberg[29] demonstrated the triplet splitting, forbidden lines and perturbations for $v' \geqslant 16$. The recent wavenumber measurements of Yoshino *et al.*[34] are the best resolved and most comprehensive available for the $(v'-0)$ and $(v'-1)$ bands.

Several experimental approaches have been used in determinations of Schumann–Runge band intensities. Low resolution photoelectric measurements[35,36] yielded only qualitative information because of an inability to determine the true cross section. Shock tube measurements[37,38] were of poor accuracy. Attempts to obtain quantitative oscillator strengths from photographic[39] and medium resolution photoelectric[40] measurements failed because of errors in the data analysis models. The first reasonably successful measurements of oscillator strength for the $(v'-0)$ series of bands were obtained by a low resolution pressure broadening technique,[41,42] the results of Bethke[41] for the (2–0)–(17–0) bands being commonly accepted until recently. Huebner *et al.*[43] have determined oscillator strengths for the (1–0)–(20–0) bands from electron energy loss spectra, but the available resolution does not approach that of the optical methods. Hasson *et al.*[44] successfully obtained oscillator strengths for the (0–0)–(3–0) and (2–1)–(5–1) bands by a photographic method. Ackerman *et al.*[2,45] measured absorption cross sections at spot wavelengths in the Schumann–Runge bands and deduced oscillator strengths by means of a data analysis model which assumed a Lorentz profile for each line with a constant half width of 1.4 cm^{-1}. This assumption is now known to be incorrect.[21]

Hudson and Carter[46] made the first line by line absorption measurements of the Schumann–Runge bands with good wavelength resolution (0.075 Å). From these measurements they obtained oscillator strengths and predissociation linewidths by applying a least-squares fitting procedure to the observed line profiles. Their measurements were taken at temperatures of 300,

600 and 900 K and oscillator strengths were published for the (5–1)–(13–1) and (6–2)–(13–2) bands. Oscillator strengths and linewidths deduced from their measurements were later published by Hudson and Mahle[6] for the (2–0)–(16–0) bands, and the same data was later reanalyzed by Frederick and Hudson[47] who presented new oscillator strengths and linewidths for the (2–0)–(13–0) bands. The results of Hudson and coworkers[6,46,47] suffer from a rather large scatter which is probably a result of fast monochromator scanning in the original measurements, and they exhibit an inverse correlation between the deduced oscillator strengths and linewidths due to the method of data analysis. Nevertheless, their pioneering application of least-squares data analysis techniques to high resolution line by line measurements has provided considerable impetus to later work in the field.

The construction of a 6.65 m scanning monochromator in Adelaide[48] led to a new series of line by line, high resolution (0.06 Å) absorption measurements by Lewis *et al.*[49,50] and Gies *et al.*[51] for the (2–0)–(19–0) bands using an equivalent width fitting procedure for the extraction of oscillator strengths and linewidths. These results generally exhibited less scatter than the previous high resolution oscillator strengths.[6,47] Lewis *et al.*[49,50] were the first to measure the decrease in effective band oscillator strength with increase in rotation which had been predicted theoretically by Allison.[52]

Yoshino *et al.*[53] measured ultra-high resolution (0.013 Å) absorption cross sections for the Schumann–Runge bands from 1793–2015 Å and, for the first time, these cross sections were absolute rather than effective since the predissociation linewidths were considerably in excess of the instrument resolution for the (1–0)–(12–0) bands studied. Oscillator strengths were determined for these bands by direct numerical integration of the measured cross sections with small corrections for high rotation lines not included in the integration. The measurements of Yoshino *et al.*[53] are basically independent of instrument resolution and the data analysis model assumptions necessary for the fitting procedures,[6,46,47,49–51] and thus serve as a yardstick for comparison with results so obtained. In general, the oscillator strengths of Yoshino *et al.*[53] lie between those of Frederick and Hudson[47] and Gies *et al.*[51] Smith *et al.*[54] extended the results of Yoshino *et al.*[53] from the (13–0) band to the (16–0) band, but these results were obtained using fitting procedures similar to those of Frederick and Hudson,[47] and are thus not absolute in the same sense as the (1–0)–(12–0) band results.

We have recently installed and modified a 2.2 m scanning VUV monochromator[55] to provide accurate linear scanning at an instrumental resolution of 0.04–0.05 Å. The aim of this work is to provide new line by line measurements of oscillator strength for the $(v' - 0)$ series on an independent instrument so that the reliability of the equivalent width fitting technique can be gauged by comparison with the absolute oscillator strengths of Yoshino *et al.*[53] The oscillator strength measurements obtained here are also essential to the companion study of the rotational dependence of predissociation linewidth.[21] Oscillator strengths are presented for as many rotational lines as possible from the (1–0)–(22–0) and (3–1)–(17–1) bands. Agreement between our oscillator strengths for the (1–0)–(12–0) bands and those of Yoshino *et al.*[53] is found to be excellent, except for the (11–0) band, and the hot band oscillator strengths presented here are considerably more reliable than the relatively few earlier determinations.[44,46]

EXPERIMENTAL

The experimental apparatus was similar to that used earlier for CO_2 absorption cross section measurements.[56] Equivalent widths were measured photoelectrically using a 2.2 m VUV monochromator and a 1.2 m temperature controlled absorption cell.

Background radiation from 1750–2010 Å was provided by a windowless d.c. discharge in molecular hydrogen. Typical operating conditions were a discharge current of 1 A and pressure of H_2 of 10 Torr. The radiation was dispersed by a Minuteman 320 NIV normal incidence VUV scanning monochromator fitted with a 1200 g/mm grating blazed at 1500 Å. With $\sim 10\,\mu$ slits a resolution of 0.04–0.05 Å was obtained. The scanning system of the monochromator was rebuilt and rigorous temperature control was employed in order to provide linear scanning and good wavelength stability.[55] These characteristics were essential for the accurate measurement of the equivalent widths of lines which were not generally substantially broader than the instrument

resolution. In fact, the resolution and stability of the present monochromator are significantly better than those of the Adelaide 6.65 m instrument[48] on which the earlier measurements[49–51] were taken.

An ARC VUV beamsplitter set at 45°C to the incident radiation acted as the front window of the absorption cell and also allowed monitoring of the incoming intensity. EMI photomultipliers type G-26H315 (CsTe photocathode) were used in the pulse counting mode in order to measure simultaneously the incident and transmitted radiation. The MgF_2 window of the rear photomultiplier also acted as the rear window of the absorption cell. Photomultiplier count rates were generally greater than 1 kHz allowing individual lines to be measured fairly quickly, but completion of the measurements took a considerable time because of the large number of lines studied.

All measurements on absorption lines were performed at room temperature but, in order to examine the continuity of oscillator strength density across the dissociation limit, the Schumann–Runge continuum below 1750 Å was measured also at liquid nitrogen temperature. The cell was filled with medical grade O_2 (0.1–850 Torr), passed through suitable cold traps, by means of a Balzers RME010 electromagnetic leak valve. The pressure was controlled by a Datametrics 1404 valve controller and a fixed leak, and was measured by a Datametrics Barocel 570/1173 variable capacitance manometer. A cold finger was connected remotely to the cell to ensure the removal of any condensible impurities which might have accumulated during the scans.

The scanning procedure was completely controlled by a Commodore 8032 microcomputer and an HP 3479A data acquisition/control unit. The absorption line of interest was scanned several times with a wavelength increment of 3–10 mÅ depending on the appropriate linewidth. Scans were performed alternately with the cell empty and then full, and the absolute transmission so obtained at each wavelength from the photomultiplier counts was corrected for the small dark count rate and for incident intensity fluctuations. The statistical accuracy of near unity transmissions was typically 1%. The integrated absorption over the line was then calculated as an equivalent width W (mÅ) from the recorded transmission values as a function of wavelength and the known wavelength increment. A small correction ($\lesssim 2\%$) was applied to the equivalent width values to account for the small 43 Å period error in wavelength due to inaccuracies in the main drive screw of the monochromator.[55] Each absorption line was generally studied at two widely differing pressures in order to allow the determination of both oscillator strength and predissociation linewidth as described below.

DATA ANALYSIS

Rotational lines in the Schumann–Runge system exhibit a mixture of Doppler and Lorentz lineshapes due to both thermal and predissociation broadening.[46] The Doppler HWHM b_D (cm^{-1}) is given by

$$b_D = 6.331 T^{1/2}/\lambda_0, \tag{1}$$

where T(K) is the temperature of the absorbing gas and λ_0 (Å) is the wavelength of the line centre. The relative importance of the two effects is defined in terms of a dimensionless mixing parameter a,[57] where

$$a = \Gamma(\ln 2)^{1/2}/(2b_D). \tag{2}$$

Γ (cm^{-1}) is the Lorentz FWHM, and a varies between 0.8 and 25 for the range of bands studied. Mixing between the Doppler and Lorentz components is described by the Voigt lineshape

$$\frac{P(v)}{P'} = \frac{a}{\pi}\int_{-\infty}^{\infty} \frac{\exp(-x^2)}{a^2 + (v-x)^2}\,dx, \tag{3}$$

where the dimensionless wavenumber is given by

$$v = (\nu - \nu_0)(\ln 2)^{1/2}/b_D. \tag{4}$$

ν_0 (cm^{-1}) is the wavenumber of the line centre, P is the absorption coefficient at wavenumber ν, and P' is the absorption coefficient at the centre of the equivalent Doppler line.[57] In this work we use the second approximation of Whiting[58] to represent the Voigt profile.

The equivalent width W (cm^{-1}) of an absorption line is given by

$$W = \int_{-\infty}^{\infty} \{1 - \exp[-P(v)X]\}\, dv, \tag{5}$$

where X is the amount of absorbing gas[57] (in units such that PX is dimensionless), and $P(v)$ followed from equations (3) and (4). A dimensionless equivalent width may be defined by the relation

$$W' = (W/b_D)(\ln 2/\pi)^{1/2}, \tag{6}$$

and W' as a function of $P'X$ for various values of a form a family of curves of growth, given for example by Penner.[57] The effective band oscillator strength for the line of interest is given by

$$f(v', N'') = \frac{1.577 \times 10^{-6} T^{3/2}(P'X)}{pl\lambda_0 \alpha S} \tag{7}$$

where p (Torr) is the pressure of O_2, l(cm) is the absorbing path length, α is the weighted Boltzmann factor for the ground state rotational level giving rise to the line of interest and S is the correctly normalized Hönl–London factor.

In an ideal case, for a known value of a an experimental equivalent width leads to a value for W', and $P'X$ may be read off the appropriate curve of growth, the oscillator strength following from equation (7). In practice, this is not possible due to such factors as limited integration ranges, limited experimental resolution, fine structure, underlying continua and absorption line overlap, but the above theory forms the basis of the computer data analysis model used in this work. A discussion of the model parameters follows, considerable improvements having been made to those used previously.[49–51]

Spectroscopic constants for the $X\ ^3\Sigma_g^-$ state of O_2 were taken from Veseth and Lofthus[59] and we were able to confirm the ground state energy levels tabulated there[59] for $v'' = 0$–1. The weighted Boltzmann factors α were calculated from these levels. The valuable and extensive recent wavenumber measurements of Yoshino *et al.*[34] were used in conjunction with the above constants for the ground state to generate spectroscopic constants for the $B^3\Sigma_u^-$ state. For $v' > 11$ we found it necessary to perform a six-parameter fit including a centrifugal contribution to the spin-rotation splitting constant of the form $\mu = \mu_0 + \mu_J J(J+1)$. Five-parameter fits were of insufficient accuracy to match the precision of the measurements. The spectroscopic constants obtained are given in Table 1 for $v' = 0$–15 and these were used to generate model wavelengths to a high degree of accuracy. For $v' = 0$–2, it is possible to fit the fine structure parameters λ and μ and interpolated values are forced for $v' = 3$–8. The constant D is not accurately determined for $v' = 0$–9 and the values obtained by Creek and Nicholls[33] are forced into the fit for these bands. For $v' \geqslant 16$, rotational perturbations severely compromise the accuracy of the spectroscopic constants, and in this case line wavelengths were taken directly from the measurements[34] or calculated from combination differences. Only if there were no direct or indirect experimental data were calculated wavelengths used for $v' \geqslant 16$ and the uncertainty in these calculations provided the most serious limitation of the model in this spectral region. Line wavelengths for $v'' = 1$ were calculated from the $v'' = 0$ wavelengths and the known ground state energy levels. Hönl–London factors S were taken from Tatum and Watson[60] for $^3\Sigma^- – ^3\Sigma^-$ transitions with coupling intermediate between Hund's cases (a) and (b). The transformation coefficients were determined from the energy levels obtained above. It is important to use the mixed coupling factors for $v' > 14$ where forbidden lines become prominent.[29]

Since the study of absorption lines with high rotational excitation is of priority in this work, it is very important to characterize weak absorption features as accurately as possible. Figure 1 shows a region of the absorption spectrum of O_2 between the $R(19)$ and $P(19)$ lines of the (9–0) band. Lines from the (13–1) and (14–1) bands are visible as is the $R(17)$ line from the (9–0) band of the isotope $^{16}O^{18}O$. It is apparent that a model which neglects the isotopic bands could result in significant errors in equivalent width for both hot band lines and the high rotational lines of the normal bands when oxygen of normal isotopic composition is measured. In this work, we model the Schumann–Runge bands of $^{16}O^{18}O$ using wavelengths, oscillator strengths and predissociation

Table 1. Spectroscopic constants (cm^{-1}) for the $B^3\Sigma_u^-$ state of $^{16}O_2$ obtained from the wavenumber measurements of Yoshino *et al.*[34] The errors are 3σ determined from the fitting procedure, and constants in parentheses are interpolated or extrapolated and then forced into the fit. Values of D for $v' = 0$–9 are taken from Creek and Nicholls[33] and forced into the fit

v'	ν_o	B	Dx10^6	λ	$-\mu_o$	$-\mu_J$x10^5
0	49358.01±0.22	0.8134±0.0001	4.66	1.80±0.30	0.033±0.006	(0.0)
1	50045.45±0.17	0.7998±0.0001	4.88	1.67±0.23	0.025±0.005	(0.0)
2	50710.73±0.23	0.7856±0.0001	5.09	1.74±0.31	0.029±0.005	(0.0)
3	51351.99±0.08	0.7706±0.0002	5.35	(1.78)	(0.030)	(0.0)
4	51969.36±0.32	0.7550±0.0007	5.97	(1.81)	(0.030)	(0.0)
5	52561.06±0.19	0.7380±0.0003	6.26	(1.85)	(0.031)	(0.0)
6	53122.55±0.16	0.7206±0.0003	7.12	(1.88)	(0.031)	(0.0)
7	53656.11±0.15	0.7002±0.0003	7.75	(1.92)	(0.032)	(0.0)
8	54156.08±0.14	0.6785±0.0003	8.78	(1.95)	(0.032)	(0.0)
9	54622.08±0.22	0.6541±0.0002	9.16	1.98±0.24	0.033±0.003	(0.0)
10	55050.97±0.13	0.6269±0.0003	10.3±0.2	2.10±0.09	0.034±0.001	(0.7)
11	55439.05±0.20	0.5966±0.0005	11.2±0.5	2.12±0.16	0.040±0.002	(1.4)
12	55784.56±0.06	0.5627±0.0002	13.8±0.2	2.33±0.05	0.0533±0.0004	2.32±0.02
13	56085.44±0.03	0.5242±0.0001	16.3±0.1	2.48±0.02	0.0834±0.0003	2.45±0.03
14	56340.44±0.04	0.4833±0.0001	20.9±0.1	2.81±0.03	0.1148±0.0004	4.13±0.03
15	56550.62±0.06	0.4396±0.0002	26.0±0.1	3.27±0.04	0.1653±0.0006	6.33±0.05

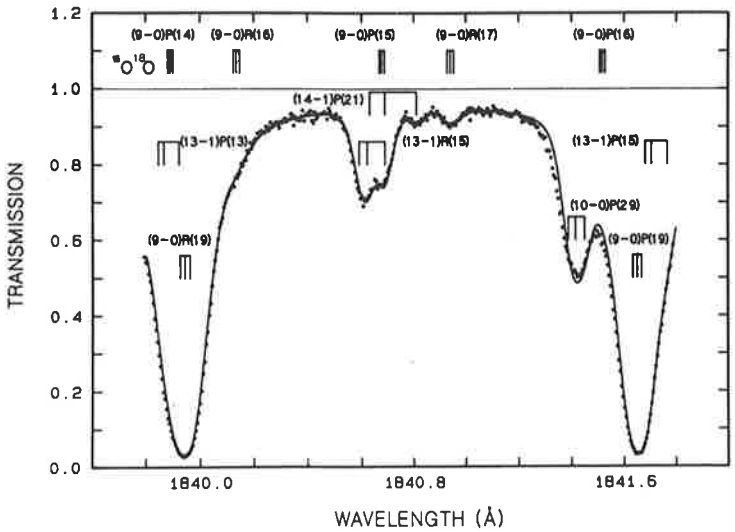

Fig. 1. The measured absorption spectrum near 1840 Å for O_2 of normal isotopic composition. The pressure was 55 Torr, the temperature 295 K, and the instrument resolution was 0.06 Å. The predicted model spectrum for these conditions is also shown.

linewidths based on measurements made by us on isotopically enriched O_2 samples[61] and, where necessary, the predictions of Blake *et al.*[62]

Oscillator strengths and linewidths are necessary to the model in order to account for the effects of distant, neighbouring or overlapping lines. Initially the oscillator strengths of Allison,[52] including centrifugal distortion explicitly, were used and linewidths were taken from Lewis *et al.*[49,50] and Gies *et al.*[51] As measurements proceeded, the initial values were replaced by actual measured values and reanalysis was performed. The model also included the variation of predissociation linewidth with rotation,[21] the initial rotational dependences being taken from the calculations detailed in the companion work.[21] The final oscillator strengths (and widths) were not sensitive to the initial estimates.

A Gaussian instrument function of FWHM 0.04–0.05 Å was folded into the analysis in order to reproduce the observed scan profiles. (The resolution varied a little because of clogging of the entrance slit by the windowless discharge.) Theoretically, the equivalent width of an isolated line is independent of the instrument resolution,[63] but small errors can occur by neglecting the instrument function for scans where the range of integration is limited.

Underneath the Schumann–Runge bands there is a continuous background comprising the Herzberg continuum (important at longer wavelengths) and the Schumann–Runge and X-$^3\Pi_g$ continua[64,65] (important at shorter wavelengths). The underlying continuum is pressure dependent. The model continuum and pressure coefficient used in this work are shown in Figs 2 and 3 and are based on the earlier work by Lewis *et al.*[64,65] including the observed steps[64] in the Schumann–Runge continuum from rotationally excited ground state molecules. It might be thought that there is a certain amount of correlation between the oscillator strengths and linewidths determined using the model and the underlying continuum determined from the model, but such correlation is minimal since most of the measured bandhead oscillator strengths and widths are essentially independent of the continuum, and the continuum itself is generally determined well away from the bandheads to minimize interference from the stronger lines. The oscillator strengths determined for both the weakest and highest vibrational hot bands are, however, sensitive to the assumed value of the underlying continuum.

An additional pseudo-continuum arises because of the summation of the Lorentzian wings of the distant lines. In our model lines having a significant contribution to the absorption in the scan range are explicitly included, while the weaker and more distant lines have the effects of their wings estimated over the scanned region. A parabolic fit with wavelength is made to the sum of these wings and this is then treated as a pseudo-continuum in the analysis. Lines were considered up to ± 5 Å from the wavelength of interest for the highest vibrational bands and this range increased to ± 30 Å for the lowest vibrational bands which generally had larger predissociation widths.[21]

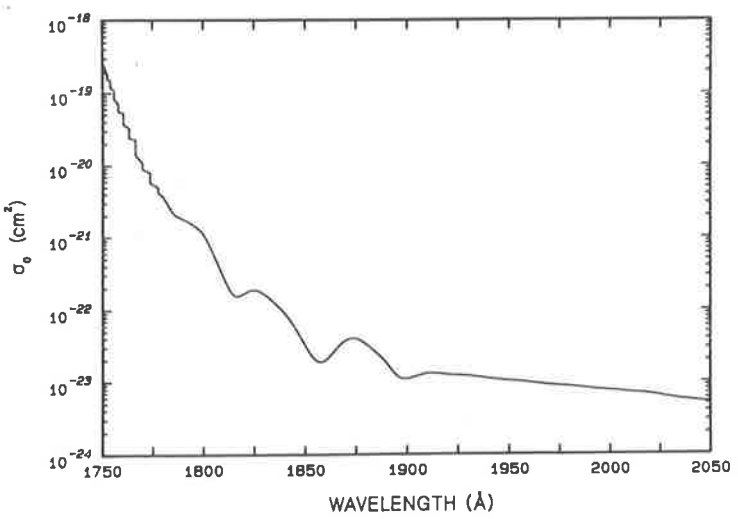

Fig. 2. The model underlying continuum cross section extrapolated to zero pressure, σ_0 cm^2, assumed in this work.

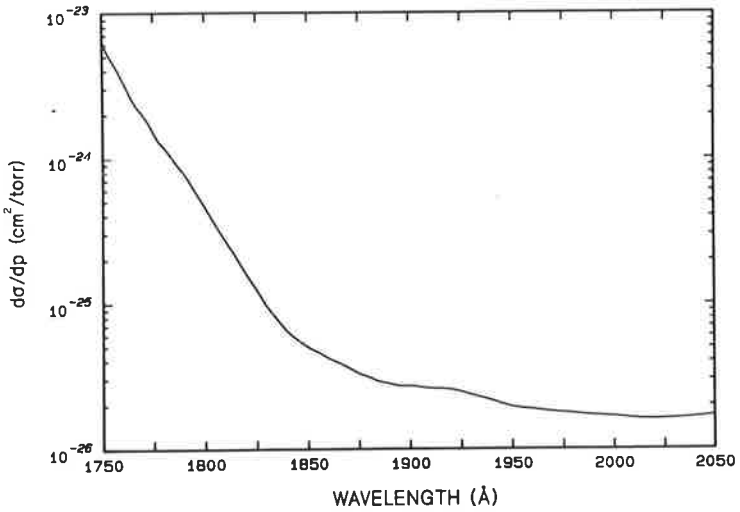

Fig. 3. The model pressure coefficient of the underlying continuum cross section, $d\sigma/dp$ cm^2/Torr, assumed in this work.

It was also necessary to consider the pressure-broadening coefficients for the Schumann Runge lines themselves and, in fact, the derived widths for the lower bands are sensitive to this parameter.[21] The earlier model[49,50] used the gas-kinetic pressure-broadening coefficient of $\sim 0.02\ cm^{-1}$/atm, while Lewis *et al.*[65] used the value $0.28\ cm^{-1}$/atm, after the discussion of Cann *et al.*[66] This latter value was not based on direct measurement of the O_2 self-broadening coefficient and measurements performed in our laboratory[67] indicate that a pressure broadening coefficient of $0.21\ cm^{-1}$/atm is appropriate to the lower Schumann–Runge bands. This value is adopted here. The effective collision diameter for self-broadening of O_2 is thus seen to be 3–4 times larger than the actual molecular diameter.

The specified factors were included in the data analysis model, which allowed calculation of the value of $P'X$ for a reference line in a scan group given the total experimental equivalent width for the scan (lines and continuum). This value was then converted to an oscillator strength using equation (7) and a predicted transmission as a function of wavelength was generated. The result could then be compared with the experimental data as in Fig. 1, where the model is seen to be capable of accurately predicting the normal band, hot band and isotopic band lines as well as the underlying continuum. (The monochromator slits were a little wider than usual for this scan, resulting in a resolution of ~ 0.06 Å.)

In normal experimental operation, a scan was performed at a comparatively low pressure, approaching the linear region where the curves of growth for different values of the mixing parameter a bunch together.[57] Assuming an initial approximation for a, an oscillator strength was obtained from the measured equivalent width and the above model. A second scan was performed over the same wavelength range but at a much higher pressure where the absorption is much more sensitive to a. The oscillator strength obtained from the low pressure scan was assumed and a new value of a obtained from the equivalent width of the second scan and the model. The interaction was continued until the pair of results f, a converged to values consistent with the results of each scan. In the case of hot bands, predissociation widths for the upper levels were assumed equal to those determined for the $v'' = 0$ bands,[21] and the oscillator strengths were determined from single low pressure scans.

RESULTS

Some 409 independent oscillator strength measurements are presented in this work. Tables 2–5 list oscillator strengths for rotational lines from the P and R branches of the (1–0)–(22–0) Schumann–Runge bands. It should be noted that these are effective band oscillator strengths deduced from the particular rotational lines studied. Tables 6–7 give oscillator strengths for rotational lines from the (3–1)–(17–1) bands.

Table 2. Measured oscillator strengths $f(v', N'') \times 10^x$ for the R branches of the (1–0)–(11–0) Schumann–Runge bands

N'' \ v'	1	2	3	4	5	6	7	8	9	10	11
1											
3	2.87±0.12	1.84±0.06									
5	3.10±0.12	1.97±0.06	8.09±0.20	2.78±0.09	8.01±0.21	1.66±0.05	3.40±0.09	6.04±0.15	8.94±0.30	1.42±0.04	1.96±0.04
7	3.29±0.14	2.01±0.06	7.91±0.20	2.71±0.09	7.39±0.15	1.70±0.05	3.60±0.09	6.15±0.18	9.48±0.30	1.45±0.04	1.92±0.04
9	3.10±0.14	1.99±0.06	7.93±0.20	2.73±0.09	7.17±0.18	1.63±0.05	3.37±0.09	5.84±0.12	9.15±0.30	1.47±0.04	1.99±0.04
11	3.06±0.18	1.93±0.06	8.56±0.20	2.59±0.06	7.46±0.18	1.61±0.05	3.41±0.09	6.32±0.15	9.54±0.30	1.54±0.04	1.95±0.04
13	3.11±0.18	1.95±0.06	7.98±0.20	2.77±0.06	7.17±0.24	1.66±0.05	3.39±0.09	6.25±0.15	10.20±0.30	1.45±0.04	1.90±0.04
15	2.65±0.18	1.86±0.06	7.82±0.20	2.64±0.06	7.01±0.24	1.57±0.05	3.42±0.09	5.73±0.18	10.30±0.30	1.45±0.05	1.82±0.04
17	3.16±0.32	1.79±0.10	7.88±0.20	2.63±0.06	7.11±0.24	1.59±0.05	3.15±0.09	5.83±0.15	9.40±0.50	1.40±0.05	1.95±0.06
19	2.63±0.38	1.89±0.10	7.89±0.25	2.54±0.06	6.94±0.27	1.68±0.05	3.15±0.09	5.60±0.15	9.18±0.50	1.26±0.05	1.76±0.06
21		1 69±0.10	7.28±0.35	2.50±0.06	6.74±0.27	1.44±0.05	2.91±0.09	5.29±0.15	8.89±0.50	1.29±0.07	1.78±0.08
23			6.74±0.35	2.35±0.09	6.24±0.27	1.52±0.05	2.90±0.12	5.02±0.21	8.91±0.50	1.14±0.10	
25		1.75±0.20			5.68±0.27	1.46±0.05	2.79±0.15	5.10±0.24		1.22±0.10	
27			6.02±0.60			1.42±0.05	2.62±0.15		6.89±0.80	1.17±0.10	
29									7.56±0.80	1.03±0.15	1.28±0.20
31										0.71±0.15	
33											
35								3.2 ± 0.5			
x	9	8	8	7	7	6	6	6	6	5	5

Table 3. Measured oscillator strengths $f(v', N'') \times 10^x$ for the P branches of the (1–0)–(11–0) Schumann–Runge bands. Values in parentheses refer to measurements on unresolved lines which are not independent of the R branch values

N'' \ v'	1	2	3	4	5	6	7	8	9	10	11
1		(1.86±0.06)									
3	(3.15±0.12)	(2.00±0.06)	(8.22±0.20)	(2.83±0.09)	(8.14±0.21)	(1.69±0.05)	(3.46±0.09)	(6.14±0.15)	(9.08±0.30)	(1.44±0.04)	(2.00±0.04)
5	3.26±0.16	(2.06±0.06)	(8.10±0.20)	(2.77±0.09)	(7.57±0.15)	(1.74±0.05)	(3.69±0.09)	(6.30±0.18)	(9.72±0.30)	(1.49±0.04)	(1.97±0.04)
7	3.18±0.16	(2.05±0.06)	(8.18±0.20)	(2.82±0.09)	(7.40±0.18)	(1.68±0.05)	(3.48±0.09	(6.03±0.12)	(9.44±0.30)	(1.52±0.04)	2.07±0.04
9	2.97±0.18	(2.00±0.06)	(8.89±0.20)	(2.69±0.06)	(7.76±0.18)	(1.67±0.05)	(3.54±0.09)	(6.57±0.15)	10.40±0.30	1.55±0.04	2.08±0.04
11	3.00±0.18	(2.04±0.06)	(8.35±0.20)	(2.90±0.06)	(7.51±0.24)	(1.74±0.05)	(3.55±0.09)	(6.55±0.15)	9.41±0.30	1.45±0.04	1.99±0.04
13	3.10±0.18	2.02±0.06	(8.24±0.20)	(2.78±0.06)	(7.40±0.24)	(1.66±0.05)	(3.61±0.09)	(6.05±0.18)	9.80±0.30	1.56±0.04	1.90±0.04
15	3.12±0.24	1.97±0.10	(8.36±0.20)	(2.79±0.06)	(7.56±0.24)	(1.69±0.05)	(3.35±0.09)	(6.20±0.15)	10.30±0.30	1.58±0.05	1.98±0.04
17	2.87±0.30	1.89±0.10	(8.43±0.25)	(2.72±0.06)	(7.43±0.27)	(1.80±0.05)	(3.37±0.09)	(6.00±0.15)	9.65±0.50	1.44±0.05	1.91±0.06
19		1.74±0.10	7.75±0.35	(2.69±0.06)	(7.27±0.27)	(1.55±0.05)	(3.14±0.09)	(5.71±0.15)	9.06±0.50	1.34±0.05	1.94±0.06
21		1.70±0.10	7.63±0.35	(2.55±0.09)	(6.78±0.27)	(1.65±0.05)	(3.15±0.12)	(5.46±0.21)	9.38±0.50	1.43±0.07	
23			6.73±0.35		(6.22±0.27)	(1.60±0.05)	(3.06±0.15)	(5.60±0.24)			1.93±0.10
25		1.77±0.20	6.71±0.50			(1.57±0.05)	(2.90±0.15)			1.40±0.10	1.87±0.10
27			6.10±0.60								
29										1.39±0.15	1.71±0.20
31										1.21±0.15	
33							2.30±0.23	4.7 ±0.5			
x	9	8	8	7	7	6	6	6	6	5	5

Table 4. Measured oscillator strengths $f(v', N'') \times 10^5$ for the R branches of the (12–0)–(22–0) Schumann–Runge bands

N'' \ v'	12	13	14	15	16	17	18	19	20	21	22
1	2.50±0.06										3.1±0.4
3	2.61±0.06	2.79±0.10			2.87±0.10		1.88±0.10			6.6±0.6	
5	2.60±0.06				3.10±0.10	2.40±0.10		1.40±0.06	0.99±0.10		
7	2.53±0.06	2.86±0.10	2.81±0.15	2.82±0.10	2.91±0.10		1.58±0.10				
9	2.50±0.06	2.69±0.10	2.83±0.15	2.79±0.10	2.51±0.10	2.06±0.10			0.88±0.10		
11	2.36±0.06	2.67±0.10	2.68±0.15	2.80±0.10	2.33±0.10			1.40±0.10			
13	2.57±0.06	2.55±0.10	2.60±0.10	2.61±0.10				0.49±0.15		4.5±1.0	
15	2.35±0.06		2.46±0.10		2.37±0.10	2.00±0.10	1.28±0.15				
17	2.17±0.06	2.34±0.10									
19	2.09±0.10			2.48±0.15		1.61±0.10					
21			2.53±0.15	2.43±0.15	2.05±0.15	1.55±0.15	1.35±0.20				
23	1.99±0.20	2.01±0.20	2.24±0.15	2.00±0.15	1.73±0.15						
25	1.85±0.20	2.00±0.20	1.83±0.20			1.46±0.20	1.04±0.20				
27			1.73±0.20	2.17±0.20	1.62±0.20						
29			1.88±0.15								
31				1.40±0.20							
x	5	5	5	5	5	5	5	5	5	6	6

Table 5. Measured oscillator strengths $f(v', N'') \times 10^x$ for the P branches of the (12–0)–(22–0) Schumann–Runge bands. Values in parentheses refer to measurements on unresolved lines which are not independent of the R branch values

N'' \ v'	12	13	14	15	16	17	18	19	20	21	22
1	(2.51±0.06)				(2.86±0.10)						
3	2.78±0.06	2.95±0.10			2.88±0.10	2.88±0.10	1.91±0.10		0.98±0.10	6.8±0.6	
5	2.48±0.06	3.15±0.10	3.11±0.10		2.83±0.10	2.42±0.10	2.09±0.10	1.22±0.06			3.0±0.5
7	2.48±0.06	2.59±0.10	3.09±0.10	2.93±0.10	2.91±0.10	2.35±0.10		1.36±0.08			
9	2.63±0.06	2.74±0.10	2.93±0.10	2.66±0.10	2.70±0.10				1.05±0.10		
11	2.35±0.06	2.55±0.10	2.91±0.10	2.67±0.10	2.73±0.10			1.58±0.10			
13	2.40±0.06	3.05±0.10	3.20±0.10	2.77±0.10		1.97±0.10	1.20±0.15	1.27±0.10			
15	2.36±0.06		2.67±0.10				1.39±0.15				
17			3.13±0.15		2.25±0.10	1.71±0.10	1.24±0.15	0.59±0.15			
19			2.82±0.15	2.78±0.18		1.62±0.10					
21			2.34±0.15		2.02±0.15		1.34±0.20				
23				2.13±0.20	2.15±0.15		1.16±0.20				
25	2.07±0.20	2.60±0.20		2.18±0.20	2.21±0.15	1.38±0.20	1.25±0.20				
27			1.95±0.20								
x	5	5	5	5	5	5	5	5	5	6	6

Table 6. Measured oscillator strengths $f(v', N'') \times 10^x$ for the R branches of the (3–1)–(17–1) Schumann–Runge bands. Values in parentheses refer to measurements on unresolved lines which are not independent of the other values

v' / N''	3	4	5	6	7	8	9	10	11	12	13	14	16	17
1	(1.72±0.12)		(1.25±0.06)		(5.29±0.20)	(8.86±0.30)			(2.00±0.10)					(2.03±0.15)
3	1.71±0.12		1.24±0.06		5.27±0.20	8.82±0.30		1.76±0.10	1.99±0.10		3.33±0.15			2.01±0.15
5		5.14±0.30	1.25±0.06		5.12±0.20	8.85±0.40		1.80±0.06	2.04±0.10	2.65±0.12				
7			1.22±0.06	2.81±0.12			1.20±0.06			2.54±0.12			2.28±0.20	1.68±0.20
9	1.83±0.10	4.96±0 30	1.28±0.06	2.81±0.09	4.98±0.25			1.76±0.10	2.28±0.12			3.20±0.15		
11		4.85±0.30	1.19±0.06	2.50±0.15					2.20±0.12		2.72±0.12			
13	1.75±0.24		1.26±0.06	2.72±0.12			1.24±0.05	1.53±0.12	1.90±0.12	2.57±0.12				
15		4.89±0.30	1.14±0.06	2.37±0.09			1.05±0.05	1.69±0.10			2.26±0.15			
17		5.08±0.40	1.22±0.06	2.58±0.09		8.09±0.40	1.12±0.05	1.60±0.10		2.25±0.18	2.46±0.15			
19			1.22±0.06			6.82±0.80	1.23±0.06			2.05±0.15				
21						6.79±0.80	1.23±0.05	1.39±0.12						
23				2.13±0.18		7.86±0.90	0.93±0.06							
x	6	6	5	5	5	5	4	4	4	4	4	4	4	4

Table 7. Measured oscillator strengths $f(v', N'') \times 10^x$ for the P branches of the (3–1)–(17–1) Schumann–Runge bands. Values in parentheses refer to measurements on unresolved lines which are not independent of the R branch values

N'' \ v''	3	4	5	6	7	8	9	10	11	12	13	14	15	16	17
1	(1.72±0.12)		(1.25±0.06)		(5.31±0.20)	(8.89±0.30)		(1.77±0.10)	(2.01±0.10)						(2.04±0.15)
3		(5.22±0.30)	(1.27±0.06)		(5.19±0.20)	(8.98±0.40)		(1.82±0.06)	2.23±0.12	2.70±0.18	2.69±0.21				
5			(1.25±0.06)	(2.87±0.12)			(1.23±0.06)		2.47±0.12	2.87±0.18		2.67±0.15		1.98±0.18	
7	(1.88±0.10)	(5.10±0.30)	(1.32±0.06)	(2.89±0.12)	(5.11±0.25)			1.72±0.12	2.10±0.12	2.75±0.15					(1.73±0.20)
9		(5.02±0.30)	(1.23±0.06)	(2.59±0.15)			1.28±0.06		2.11±0.15		2.42±0.15	3.26±0.15		2.26±0.18	
11	1.77±0.20		(1.31±0.06)	(2.83±0.12)			1.28±0.05	1.65±0.12	2.27±0.12				2.67±0.12		
13		(5.13±0.30)	(1.20±0.06)	(2.49±0.09)			1.15±0.05	1.78±0.10	1.98±0.15	2.77±0.15			2.49±0.18		
15		(5.36±0.40)	(1.29±0.06)	(2.72±0.09)		(8.53±0.49)	1.17±0.06						2.43±0.18		
17			(1.30±0.06)			8.14±0.70	1.18±0.05	1.64±0.10				2.83±0.21	2.17±0.21		
19						7.95±0.60	1.11±0.05	1.53±0.10							
21						7.55±0.60	1.22±0.05					2.16±0.36		1.77±0.21	
23						7.32±0.90									
x	6	6	5	5	5	5	4	4	4	4	4	4	4	4	4

When scans were performed across unresolved PR doublets, the calculated oscillator strength was referred to the R component and the oscillator strength for the P component was calculated by using the predicted P/R strength ratios of Allison.[52] It is also expected[52] that the oscillator strength will vary with the fine structure component, but this effect is too small to verify here and all results have been averaged over the individual fine structure components where these have been separately measured. The errors given in Tables 2–7 are due essentially to counting statistics. Additional errors due to uncertainties in pressure, temperature and cell length are expected to be $\sim 3\%$. For lines near the bandheads of the stronger bands, the oscillator strengths are generally accurate to $\sim 5\%$ and are essentially independent of the data analysis model parameters. For very weak lines [(1–0) and (3–1) bands, higher rotational lines, (16–1), (17–1), (21–0) and (22–0) bands], the error in the oscillator strength increases. In such cases, there is an enhanced dependence of the oscillator strength on the assumed values for the underlying continuum cross section. When the underlying continuum was observed to be comparable in strength to the line being studied, it was allowed to become a free parameter in the data analysis model so that excellent fits to the observed scans could be obtained. This technique produced far more accurate oscillator strengths than did forcing the model continuum, since variations of the model continuum within the appropriate uncertainty could produce exaggerated changes in the deduced oscillator strength. Because of extensive rotational perturbations in the spectrum above the (15–0) band, resultant line classification uncertainties and genuine intensity perturbations, full characterization of the model is difficult in this region. This fact leads to an additional uncertainty for $v' \geqslant 16$ which is difficult to quantify.

From Tables 2–5, one can see the well known peak in the $v'' = 0$ vibrational oscillator strength at $v' = 14$ and the decrease in oscillator strength with rotation which is expected theoretically[52] and was first measured by Lewis *et al.*[49] In cases where the P and R branches are resolved, the P branch oscillator strengths exceed those of the R branch, in agreement with earlier measurements.[49] In Fig. 4, oscillator strengths are presented graphically for the (10–0) band. The P and R branches are resolved for most rotations in this band and many high rotation lines are accessible. The approximately linear decrease in oscillator strength with increase in $N''(N''+1)$ is evident, as is the excess in oscillator strength of the P branch over the R branch. Agreement with the predictions of Allison[52] is good considering the increased scatter of the higher rotation measurements.

The rotational band oscillator strengths may be expressed approximately in the form

$$f(v', N'') = f_0(v') - \beta(v')N''(N''+1), \tag{8}$$

where $f_0(v')$ is the rotationless band oscillator strength needed for comparison with theoretical calculations, and $\beta(v')$ is a parameter indicating the degree of decrease in oscillator strength with

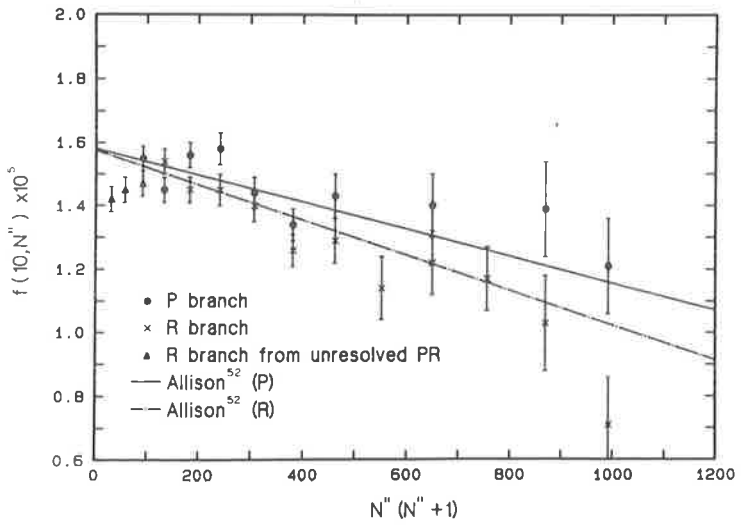

Fig. 4. Measured oscillator strengths for rotational lines from the (10–0) Schumann–Runge band showing the decrease in oscillator strength with rotation and the difference in strength between the P and R branches. The calculations of Allison[52] are also shown.

rotation.[49] Table 8 gives values of f_0 and β obtained by fitting equation (8) to the oscillator strength measurements of this work for the (1–0)–(17–0) bands which could be followed to fairly high values of rotation. Because of the small magnitude of the β values and the resultant large uncertainty, although the P and R branches were fitted separately, the tabulated results are averaged over the P and R branches. The rotationless oscillator strengths given for $v' = 18$–21 in Table 8 were obtained by assuming the β values implied from the calculations of Allison,[52] while $f_0(22)$ is an average of the two low rotation measurements of this work. The statistical error in the f_0 values is $\sim 3\%$ for $v' = 2$–16 and increases for the other bands for the reasons stated earlier. The measured values of β have in general quite a large uncertainty (30% r.m.s.).

For $v' = 5$–16, the present values of f_0 and β are compared in Table 8 with the best measurements of the Adelaide group.[49–51] Our rotationless oscillator strengths vary between 83–98% of the earlier values,[49–51] with a mean of 92% and an r.m.s. scatter in the ratio of 5%. Our values of β have a weighted average of 63% of the Adelaide values, but here the r.m.s. scatter in the ratio is $\sim 40\%$, emphasizing the difficulty of accurately obtaining this parameter. Presented here for the first time are measurements of β for the (1–0)–(4–0) and (17–0) bands, and an oscillator strength for the (22–0) band. The theoretical values of f_0 and β calculated by Allison[52] are also given in Table 8.

Table 8. Rotationless oscillator strengths f_0 and rotational dependences β for the $(v' - 0)$ bands. The f_0 values marked with an asterisk are determined from the present measurements by assuming the β values of Allison[52]

		$f_0(v') \times 10^x$				$\beta(v') \times 10^y$		
v'	x	This work	Refs. 49-51	Ref. 52	y	This work	Refs. 49-51	Ref. 52
1	9	3.09±0.15		3.30	13	7.2±6.0		7.0
2	8	1.99±0.06		2.03	12	3.8±2.0		4.4
3	8	8.44±0.25		8.61	11	2.1±0.8		2.0
4	7	2.81±0.09		2.86	11	5.2±1.8		6.9
5	7	7.76±0.25	7.90±0.15	7.86	10	2.4±0.5	2.2±0.6	2.0
6	6	1.71±0.05	1.83±0.03	1.84	10	2.7±1.0	6.1±0.8	4.8
7	6	3.60±0.11	3.84±0.07	3.74	9	1.2±0.2	1.5±1.0	1.0
8	6	6.33±0.20	7.16±0.14	6.70	9	1.7±0.5	2.5±2.1	1.8
9	6	9.68±0.30	11.6±0.3	10.76	9	0.6±1.5	3.1±0.2	3.0
10	5	1.52±0.05	1.61±0.04	1.58	9	3.7±1.2	7.8±0.6	4.9
11	5	2.02±0.06	2.27±0.05	2.13	9	4.0±2.0	8.6±1.5	7.3
12	5	2.60±0.08	2.91±0.05	2.66	8	1.1±0.3	1.2±0.2	1.0
13	5	2.87±0.09	3.00±0.07	3.06	8	1.0±0.6	1.0±0.3	1.3
14	5	3.01±0.10	3.54±0.10	3.24	8	1.3±0.3	1.8±0.3	1.6
15	5	2.91±0.10	3.23±0.07	3.17	8	1.2±0.3	2.0±0.3	1.8
16	5	2.88±0.10	2.97±0.07	2.92	8	1.7±0.3	2.4±0.5	1.8
17	5	2.46±0.15		2.55	8	2.1±0.5		1.9
18	5	1.91±0.15*		2.08	8			1.8
19	5	1.56±0.16*		1.59	8			1.8
20	5	1.07±0.11*		1.05	8			1.6
21	6	6.9 ±0.7*		6.7	8			1.5
22	6	3.1 ±0.4**						

Our rotationless oscillator strengths vary from 90–99% of the theoretical values,[52] with a weighted mean of 96% and an r.m.s. scatter of 3%. Our values of β average 86% of the theoretical values with an r.m.s. scatter of ~30%. The low experimental β for the (9–0) band follows from the low measured bandhead oscillator strengths which result in a non-linear f vs $N''(N''+1)$ dependence. If the experimental β were determined by neglecting points for $N''(N''+1) < 100$ much better agreement would be obtained for this band.

The values of f_0 and β listed in Table 8 are sufficient, together with equation (8), to model the oscillator strengths of the rotational lines of the Schumann–Runge bands. Most reliable values would be obtained by using the f_0 values measured here and the theoretical β values.[52] It is also possible to deduce mean band oscillator strengths $\bar{f}(v)$ by summing individual line oscillator strengths from equation (8), weighted with appropriate Boltzmann factors. These quantities are of dubious significance, especially for bands near the dissociation limit where only a few rotational lines may exist, but it is necessary to obtain them for comparison with earlier measurements obtained by different techniques.

Our mean band oscillator strengths are given in Table 9 for the (1–0)–(16–0) bands which are well developed rotationally. The oscillator strengths of Frederick and Hudson[47] are in disagreement with ours for seven of the common twelve bands. Although their measurements are obtained on individual rotational lines by a fitting procedure, they do not notice a variation in oscillator strength with rotation. The scatter in their results is larger, and there is an inverse correlation between the oscillator strengths and predissociation linewidths obtained from their fitting procedure. The large

Table 9. Mean band oscillator strengths $\bar{f}$ for the (1–0)–(16–0) bands. The values marked with an asterisk[54] are deduced as described in the text

v'	x	$\bar{f}(v') \times 10^x$ This work	Refs. 53, 54	Ref. 47	Refs. 49-51	Ref. 52
1	9	3.04±0.15	3.15±0.32			3.19
2	8	1.94±0.06	1.89±0.19	$2.77^{+0.07}_{-0.05}$	2.26±0.05	1.97
3	8	8.14±0.25	8.45±0.42	$7.51^{+0.13}_{-0.09}$	9.7 ±0.2	8.33
4	7	2.74±0.09	2.82±0.14	$3.04^{+0.02}_{-0.03}$	2.65±0.05	2.76
5	7	7.42±0.25	7.42±0.37	$7.39^{+0.90}_{-0.50}$	7.7 ±0.2	7.57
6	6	1.67±0.05	1.62±0.08	$1.62^{+0.05}_{-0.03}$	1.74±0.03	1.77
7	6	3.44±0.11	3.43±0.17	$3.15^{+0.10}_{-0.07}$	3.68±0.10	3.59
8	6	6.08±0.20	6.31±0.32	$5.78^{+0.04}_{-0.04}$	6.92±0.20	6.43
9	6	9.65±0.30	10.0 ±0.5	$10.4^{+3.6}_{-2.0}$	11.3 ±0.5	10.3
10	5	1.47±0.05	1.54±0.08	$2.60^{+0.47}_{-0.20}$	1.52±0.04	1.51
11	5	1.96±0.06	2.26±0.11	$1.80^{+0.53}_{-0.08}$	2.16±0.05	2.02
12	5	2.44±0.08	2.43±0.12	$2.09^{+0.08}_{-0.08}$	2.74±0.06	2.51
13	5	2.73±0.09	2.48±0.25*	$2.69^{+0.36}_{-0.20}$	2.87±0.12	2.85
14	5	2.82±0.10	2.79±0.28*		3.21±0.14	3.00
15	5	2.73±0.10	2.94±0.29*		2.95±0.12	2.91
16	5	2.63±0.10	2.66±0.27*		2.63±0.08	2.66

oscillator strength and correspondingly small linewidth obtained by them for the (10–0) band are not possible within the framework of our results.

Our mean band oscillator strengths disagree with the earlier best Adelaide values[49–51] for eight of the common fifteen bands are in general a little lower. The error estimates on the previous results[49–51] were probably a little optimistic and the current results are expected to be more reliable. Most other earlier measurements have been tabulated by Yoshino *et al.*[53] and will not be discussed further.

Of particular interest are the oscillator strengths obtained by Yoshino *et al.*[53] and Smith *et al.*[54] listed in Table 9. For the (1–0)–(12–0) bands, Yoshino *et al.*[53] directly integrated very high resolution absolute absorption cross section measurements to obtain essentially absolute band oscillator strengths. For the (13–0)–(16–0) bands, Smith *et al.*[54] used fitting procedures similar to those of Frederick and Hudson[47] to obtain oscillator strengths for a few lines near the bandheads. We have converted these measurements[54] to mean band oscillator strengths by noting the average ratio of these oscillator strengths compared with the theoretical values of Allison,[52] and then multiplying by the mean band oscillator strengths of Allison[52] obtained by procedures similar to those discussed above. Our results are in excellent agreement with those of Yoshino *et al.*[53] and Smith *et al.*[54] The only disagreement occurs for the (11–0) band for which they obtain a value 15% larger than ours. Our values average ~99% of those of Yoshino *et al.*[53] [excluding the (11–0) band] with an r.m.s. scatter in the ratio of ~3%.

Table 9 also gives mean band oscillator strengths obtained from the calculations of Allison.[52] Our results average ~96% of the theoretical values[52] with an r.m.s. scatter of only ~2% in the ratio. It is instructive to compare the minor fluctuations of our results and those of Yoshino *et al.*[53] These are shown in Fig. 5 relative to the theoretical oscillator strengths,[47] and several things are immediately apparent. Firstly, the theoretical predictions of the relative dependence of oscillator strength on vibration match our observations remarkably well, although our results are ~4% lower. Secondly, the small-scale variations in oscillator strength with vibration from the results of Yoshino *et al.*[53] are curiously similar to those observed by us, with the exception of their rather large point at $v' = 11$. The statistical scatter in the ratios is ~3% for our results and ~5% for Yoshino *et al.*[53] of about the same order as the structure seen in Fig. 5, but there does appear to be a dip in the ratio at $v' = 6$–9. The associate paper on predissociation linewidths shows that this region coincides with a maximum in the $^3\Pi_u$ partial width. If this inner limb potential curve crossing were to result in slightly non-Lorentzian lineshapes for the $^3\Pi_u$ component, then it might be possible to explain the dip in the oscillator strength since our data analysis assumes Lorentzian lineshapes and the experimental integration is over a finite range. This view is, of course, speculative and does not necessarily explain the corresponding dip in the results of Yoshino *et al.*[53]

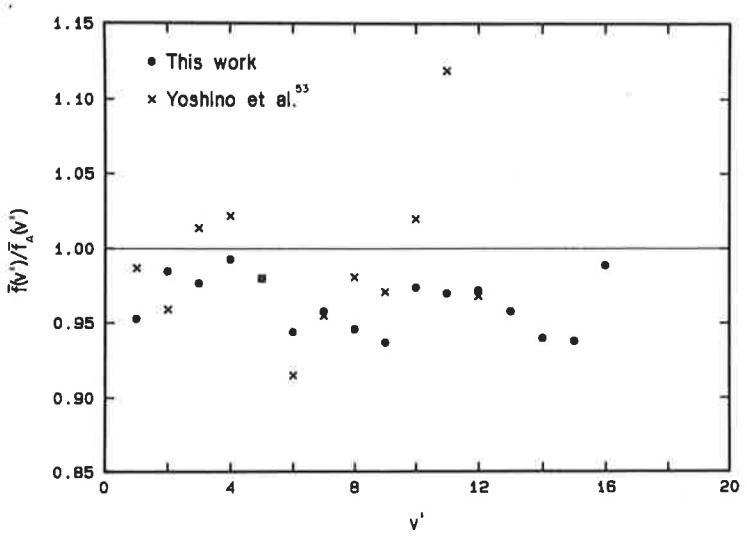

Fig. 5. The present mean band oscillator strengths and those of Yoshino *et al.*[53] each divided by the theoretical mean band oscillator strengths of Allison,[52] $\bar{f}_A(v')$.

Table 10. Rotationless (f_0) and mean ($\bar{f}$) oscillator strengths for the (3–1)–(17–1) bands. The f_0 values marked with an asterisk are determined from the present measurements by assuming the β values of Allison[52]

		$f_0(v') \times 10^x$		$\bar{f}(v') \times 10^x$			
v'	x	This work	Ref. 52	This work	Ref. 46	Ref. 44	Ref. 52
3	6	1.81±0.12*	1.77	1.76±0.12		1.8 ±0.5	1.72
4	6	5.20±0.25*	5.35	5.03±0.25		5.55±1.11	5.17
5	5	1.25±0.07	1.34	1.24±0.07	1.5 ±0.2	1.23±0.18	1.30
6	5	2.86±0.14	2.88	2.68±0.14	3.0 ±0.2		2.78
7	5	5.20±0.25*	5.38	5.03±0.25	4.8 ±0.4		5.20
8	5	8.95±0.40	8.86	8.57±0.40	8.2 ±0.4		9.23
9	4	1.23±0.10	1.31	1.20±0.10	1.6 ±0.1		1.26
10	4	1.81±0.10	1.79	1.71±0.10	1.97±0.24		1.72
11	4	2.15±0.10*	2.27	2.05±0.10	2.21±0.20		2.16
12	4	2.77±0.14*	2.66	2.61±0.14	2.76±0.35		2.52
13	4	2.74±0.30*	2.89	2.58±0.30	2.32±0.25		2.72
14	4	3.10±0.30*	2.92	2.93±0.30			2.71
15	4	2.75±0.20*	2.74	2.52±0.20			2.51
16	4	2.27±0.25*	2.45	2.09±0.25			2.22
17	4	1.97±0.20*	2.09				

Oscillator strengths for the hot bands (3–1)–(17–1) are presented in Table 10. The f_0 values were obtained as for the $v'' = 0$ series except that most β values were fixed at the theoretical values[52] because of the poor accuracy of the experimental β values. Nevertheless, several of the hot bands ($v' = 6, 8, 10, 12$) can be followed to sufficiently high values of rotation to demonstrate clearly the decrease in oscillator strength with increasing rotation. This result has been verified by us for the first time for the hot bands.

Agreement with the f_0 values of Allison[52] is curiously better than for the $v'' = 0$ bands, our values averaging ~99% of the theoretical values with ~5% scatter in the ratio. There have been very few previous measurements of hot band oscillator strengths for the Schumann–Runge bands and our results are the most accurate and extensive available. Mean band oscillator strengths deduced from our measurements are compared with the measurements of Hudson and Carter[46] and Hasson *et al.*[44] in Table 10. All measurements are in agreement within the combined experimental errors except for the (9–0) band, but the statistical scatter is lowest for our results.

OSCILLATOR STRENGTH DENSITY CONTINUITY

Theoretical investigations of the continuity of oscillator strength, Franck–Condon density and transition moment have been performed by several workers.[68–70] Marr,[68] using Morse potentials, found continuity of the transition moment through the $B^3\Sigma_u^-$ dissociation limit with a slope discontinuity, but noted that Morse potentials were not a good representation for the $B^3\Sigma_u^-$ state. Jarmain and Nicholls,[69] using the oscillator strengths of Bethke[41] and realistic Franck–Condon factors, found approximate transition moment continuity across the dissociation limit, but also obtained an unexpected secondary maximum due to the poor experimental data available. Allison *et al.*[70] compared theoretically $f_0(v')\,(dv'/dv)$ in the bands with $df/dv = 1.13 \times 10^{12}\sigma$ in the continuum (σ, cm^2 is the continuum cross section) and found continuity.

Table 11. The calculation of the experimental oscillator strength densities for Schumann–Runge transitions from the $v'' = 0$ state. Below the dissociation limit the wavenumbers are the band origins for the (1–0)-(22–0) bands and $df/d\nu$ is calculated as $f_0(v')/\Delta G'$ where $f_0(v')$ is the rotationless oscillator strength and $\Delta G'$ is the first vibrational difference. Above the dissociation limit $df/d\nu$ is calculated as $1.13 \times 10^{12}\sigma(\nu)$ where $\sigma(\nu)\text{cm}^2$ is the measured low temperature absorption cross section. The smoothed oscillator strength densities and discrete oscillator strengths are also shown

v'	ν, cm^{-1}	f_o (v') for ν<57136cm^{-1} σ(ν), cm^2 for ν>57136cm^{-1}	ΔG', cm^{-1}	f_o(v')/ΔG', cm for ν<57136cm^{-1} 1.13x10^{12}σ(ν), cm for ν>57136cm^{-1}	smoothed df/dν, cm	smoothed f_o(v')
1	50045.45	3.09-9*	676.36	4.57-12	4.66-12	3.15-9
2	50710.73	1.99-8	653.27	3.05-11	2.95-11	1.92-8
3	51351.99	8.44-8	629.32	1.34-10	1.34-10	8.42-8
4	51969.36	2.81-7	604.54	4.65-10	4.69-10	2.84-7
5	52561.06	7.76-7	576.60	1.35-9	1.34-9	7.72-7
6	53122.55	1.71-6	547.53	3.12-9	3.23-9	1.77-6
7	53656.11	3.60-6	516.77	6.97-9	6.85-9	3.54-6
8	54156.08	6.33-6	482.99	1.31-8	1.30-8	6.29-6
9	54622.08	9.68-6	447.45	2.16-8	2.26-8	1.01-5
10	55050.97	1.52-5	408.49	3.72-8	3.65-8	1.49-5
11	55439.05	2.02-5	366.80	5.51-8	5.48-8	2.01-5
12	55784.56	2.60-5	323.20	8.04-8	7.74-8	2.50-5
13	56085.44	2.87-5	277.94	1.03-7	1.03-7	2.87-5
14	56340.44	3.01-5	232.59	1.29-7	1.31-7	3.04-5
15	56550.62	2.91-5	189.56	1.54-7	1.58-7	2.99-5
16	56719.56	2.88-5	150.97	1.91-7	1.83-7	2.76-5
17	56852.56	2.46-5	117.51	2.09-7	2.05-7	2.40-5
18	56954.57	1.91-5	88.87	2.15-7	2.23-7	1.98-5
19	57030.29	1.56-5	64.16	2.43-7	2.37-7	1.52-5
20	57082.89	1.07-5	42.26	2.53-7	2.48-7	1.05-5
21	57114.81	6.9 -6	23.90	(2.89-7)	2.53-7	6.06-6
22	57130.69	3.1 -6	9.9	(3.1 -7)	2.57-7	2.54-6
	57142.85	2.30-19		2.60-7	2.60-7	
	57306.59	2.57-19		2.90-7	2.97-7	
	57471.26	2.91-19		3.29-7	3.37-7	
	57636.88	3.36-19		3.80-7	3.82-7	
	57803.46	3.76-19		4.25-7	4.31-7	
	57971.01	4.22-19		4.77-7	4.85-7	
	58139.53	4.85-19		5.48-7	5.44-7	
	58309.03	5.41-19		6.11-7	6.08-7	
	58479.53	5.93-19		6.70-7	6.75-7	
	58651.02	6.76-19		7.64-7	7.47-7	

*For 3.09-9 read 3.09×10^{-9}

The extent and accuracy of the present oscillator strengths make it possible to examine experimentally the continuity of the oscillator strength density defined by Allison *et al.*[70] across the dissociation limit. Table 11 shows the results for transitions from the $v'' = 0$ level. Band origins (Table 1 for $v' = 1$–15, Creek and Nicholls[33] for $v' = 16$–21, Lewis *et al.*[64] for $v' = 22$) were taken as the wavenumber ν, cm^{-1} appropriate to the rotationless oscillator strengths f_0, and the density of states $dv'/d\nu$ was taken as $1/\Delta G'$ where the differences $\Delta G'(cm^{-1})$ were obtained from the band origins. The oscillator strength density $df/d\nu$ was thus approximated by $f_0/\Delta G'$ for the bands. Measurements of the Schumann–Runge continuum cross section σ, cm^2 were taken at ~80 K near 1750 Å in order to approximate the rotationless continuum as closely as possible (cross sections were ~10% lower than those at room temperature); $df/d\nu$ in the continuum was then calculated as $1.13 \times 10^{12}\sigma$. The hot bands were treated similarly except that, since it was impossible to measure the $v'' = 1$ continuum, theoretical values were taken from Gibson.[71] Oscillator strength densities for the hot bands are given in Table 12.

The oscillator-strength densities are plotted as a function of wavenumber in Fig. 6. Continuity is observed across the $B^3\Sigma_u^-$ dissociation limits for transitions from the $v'' = 0$ and $v'' = 1$ states. For the $v'' = 0$ bands, only the $v' = 21$, 22 densities vary significantly from a smooth behaviour, and this is quite understandable considering the lower accuracy of the f_0 values for these bands and also the uncertainties in the small $\Delta G'$ values.

Table 12. The calculation of the experimental oscillator strength densities for Schumann–Runge transitions from the $v'' = 1$ state. The method is as described in Table 11 except that the continuum cross sections listed here are theoretical[71]

v'	ν, cm^{-1}	$f_0(v')$ for ν<55580cm^{-1} σ(ν), cm^2 for ν>55580cm^{-1}	ΔG', cm^{-1}	$f_0(v')/\Delta G'$, cm for ν<55580cm^{-1} 1.13×10^{12} σ(ν), cm for ν>55580cm^{-1}	smoothed df/dν, cm	smoothed $f_0(v')$
3	49795.60	1.81-6*	629.32	2.88-9	2.86-9	1.80-6
4	50412.97	5.20-6	604.54	8.60-9	8.67-9	5.24-6
5	51004.67	1.25-5	576.60	2.17-8	2.24-8	1.29-5
6	51566.16	2.86-5	547.53	5.22-8	5.02-8	2.75-5
7	52099.72	5.20-5	516.77	1.01-7	9.99-8	5.16-5
8	52599.69	8.95-5	482.99	1.85-7	1.79-8	8.63-5
9	53065.69	1.23-4	447.45	2.75-7	2.92-7	1.30-4
10	53494.58	1.81-4	408.49	4.43-7	4.39-7	1.79-4
11	53882.66	2.15-4	366.80	5.86-7	6.17-7	2.26-4
12	54228.17	2.77-4	323.20	8.57-7	8.16-7	2.64-4
13	54529.05	2.74-4	277.94	9.86-7	1.02-6	2.84-4
14	54784.05	3.10-4	232.59	1.33-6	1.22-6	2.85-4
15	54994.23	2.75-4	189.56	1.45-6	1.41-6	2.67-4
16	55163.17	2.27-4	150.97	1.50-6	1.57-6	2.37-4
17	55296.17	1.97-4	117.51	1.68-6	1.70-6	2.00-4
	55580.11	1.75-18		1.98-6	2.01-6	
	55944.05	2.17-18		2.45-6	2.45-6	
	56338.02	2.64-18		2.98-6	2.98-6	
	56737.58	3.20-18		3.62-6	3.56-6	
	57142.85	3.68-18		4.16-6	4.19-6	

*For 1.81-6 read 1.81×10^{-6}

Equations of the form

$$\frac{df}{dv} = \exp\left(\sum_{i=0}^{4} a_i v^i\right), \tag{9}$$

where the coefficients a_i are given in Table 13, were fitted to the oscillator strength densities for $v'' = 0$–1, excluding $v' = 21$–22 and the resultant smoothed values are given in Tables 11–12 and are plotted in Fig. 6 also. The region near the $B^3\Sigma_u^-$ dissociation limit, for transitions from the $v'' = 0$ level, is shown in more detail in Fig. 7, where the continuity is remarkably demonstrated considering that all points are based purely on experimental data.

The observed continuity of the oscillator strength density enables the confident interpolation of oscillator strength in regions of poor experimental accuracy. Smoothed rotationless oscillator strengths $f_0(v')$ for $v'' = 0$–1 are obtained from the smoothed df/dv values in Tables 11–12 and are also presented there. Smoothed values for the (21–0) and (22–0) bands in particular are expected to be more reliable than the original measured values.

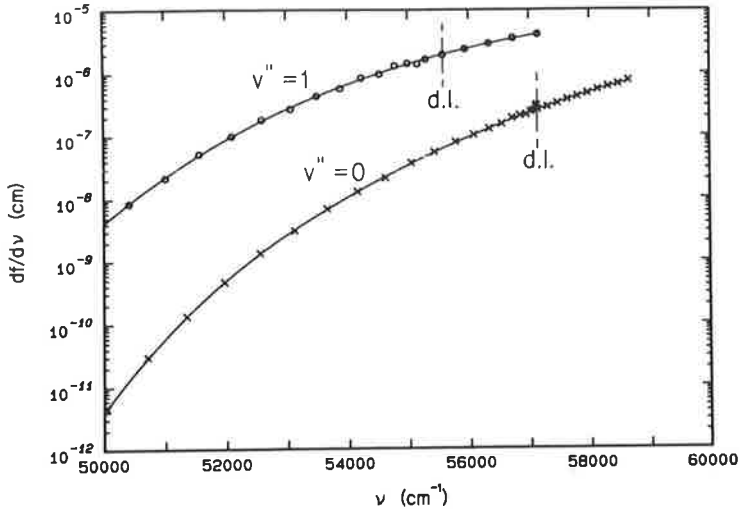

Fig. 6. Oscillator strength densities obtained from the current measurements for Schumann–Runge transitions from the $v'' = 0$ and $v'' = 1$ states.

THE DIPOLE MOMENT

It is possible to calculate dipole moments from the current oscillator strengths given potential curves for the $X^3\Sigma_g^-$ and $B^3\Sigma_u^-$ states. In this work, the ground state potential is taken from Gibson,[71] and the B state potential is derived using RKR techniques from the spectroscopic constants in Table 1 which are based on the accurate wavenumber measurements of Yoshino *et al.*[34] A Morse extension from the inner $v' = 14$ turning point is optimized to be consistent with the Schumann–Runge continuum temperature coefficients of Gibson *et al.*[72] Wavefunctions for $v'' = 0$, $v' = 1$–22 and $v'' = 1$, $v' = 3$–17 are calculated by numerical integration of the Schrödinger equation and the dipole moment $D(r)$ is expressed as a power series in the internuclear separation r. The coefficients of this power series are determined by a weighted least-squares procedure which compares the calculated with the smoothed measured rotationless oscillator strengths for $v'' = 0$–1. Such a procedure avoids the assumption of the r centroid approximation. The dipole moment so obtained is, for $1.306\ \text{Å} \leqslant r \leqslant 1.370\ \text{Å}$,

$$D(r) = 1.56734 + 0.058397r - 0.48285r^2, \tag{10}$$

where $D(r)$ is in atomic units and r is in Å. Our form for the dipole moment is consistent with the recommendations of Whiting *et al.*[73] and is a factor of $\sqrt{3}$ smaller than some forms adopted in the literature. The inclusion of a cubic term does not improve the fit which gives an r.m.s.

Table 13. Coefficients a_i to be used with equation (9) to calculate the smoothed oscillator strength densities as a function of v for Schumann–Runge transitions from the $v'' = 0$ and $v'' = 1$ states

a_i	v"=0	v"=1
a_0	-1.334733669 x 10^{4}	-2.598946355 x 10^{3}
a_1	9.356569994 x 10^{-1}	1.642677290 x 10^{-1}
a_2	-2.473098864 x 10^{-5}	-3.943483384 x 10^{-6}
a_3	2.915103723 x 10^{-10}	4.243417343 x 10^{-11}
a_4	-1.291691134 x 10^{-15}	-1.726872661 x 10^{-16}

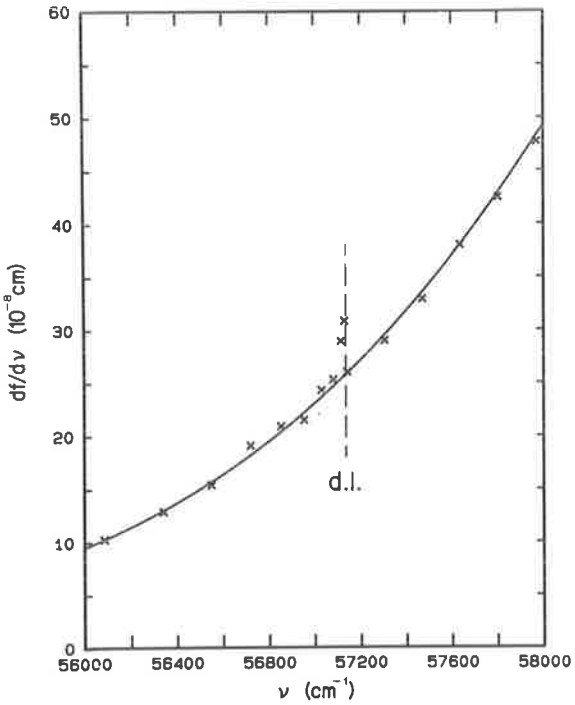

Fig. 7. Oscillator strength densities obtained from the current band and continuum measurements near the $v'' = 0$ dissociation limit. Continuity is observed across this limit.

deviation from the experimental results of 3.2%. The fitting procedure demonstrates that the (11–1)–(17–1) oscillator strengths are ~5% larger than would be implied by a perfect fit. This result is about the same as the experimental uncertainty for these bands and merely reflects the experimental difficulties in measuring weak lines which occur near strong neighbouring structure.

In Fig. 8, our dipole moment is compared with the empirical exponential best fit obtained by Kuz'menko *et al.*[74] in their review, and with shifted *ab initio* calculations and an empirically adjusted dipole moment curve obtained very recently by Allison *et al.*[75] Excellent agreement is obtained with the empirical curve of Allison *et al.*[75] The current results are lower than, and have a greater slope than the Kuz'menko *et al.*[74] fit, but the discrepancy is probably within the combined

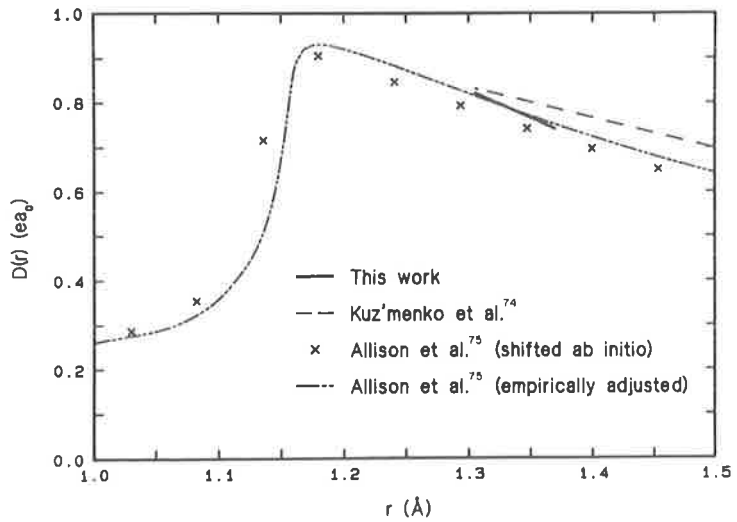

Fig. 8. The variation of dipole moment obtained by us compared with the *ab initio* and empirical determinations of Allison *et al.*[75] and the best exponential fit from the review of Kuz'menko *et al.*[74]

errors. It should be noted that, with experimental data of the quality presented here, uncertainties in Franck–Condon factors arising from potential curves calculated from different sets of spectroscopic constants can produce dipole moment uncertainties of ~5% which can exceed the experimental scatter. In fact, Kuz'menko *et al.* use the Franck–Condon factors of Harris *et al.*[76] which differ from ours by enough to explain a major part of the difference between our dipole moment and the Kuz'menko *et al.*[74] fit.

CONCLUSIONS

Experimental oscillator strengths presented here for the (1–0)–(22–0) and (3–1)–(17–1) Schumann–Runge bands of $^{16}O_2$ are the most extensive and the most accurate currently available. We also present in the first experimental oscillator strengths for the (22–0) and (14–1)–(17–1) bands. The decrease of equivalent band oscillator strength with increasing rotation is confirmed for the $v'' = 0$ bands and observed for the $v'' = 1$ bands for the first time. Line-by-line modelling of the Schumann–Runge bands is best performed by using the smoothed rotationless oscillator strengths f_0 obtained here together with the theoretical rotational dependences β obtained by Allison.[52] The modelling of the predissociation linewidth is discussed in an associate paper.[21] The mean band oscillator strengths obtained here for the (1–0)–(12–0) bands are in excellent agreement with the recent model-independent absolute oscillator strengths obtained by Yoshino *et al.*[53] and the hot band oscillator strengths agree well with the few previous measurements.[44,46] The present $v'' = 0$ oscillator strengths are about 4% lower than the theoretical values of Allison,[52] probably a significant amount in view of the low scatter in the experimental measurements. Continuity of the oscillator strength density across the $B^3\Sigma_u^-$ dissociation limit is verified for transitions from the $v'' = 0$ and $v'' = 1$ states and this enables more reliable high v' oscillator strengths to be obtained by interpolation and smoothing. The dipole moment $D(r)$ found by us agrees very well with recent *ab initio* and semi-empirical determinations.[75]

Acknowledgements—The authors would like to thank C. Dedman and K. Lonsdale for valuable technical assistance. Some of the programs needed for the dipole moment calculations were kindly provided by S. T. Gibson.

REFERENCES

1. R. D. Hudson, V. L. Carter and E. L. Brieg, *J. Geophys. Res.* **74,** 4079 (1969).
2. M. Ackerman, F. Biaume and G. Kockarts, *Planet. Space Sci.* **18,** 1639 (1970).
3. G. Kockarts, in *Mesopheric Models and Related Experiments* (Edited by G. Fiocco), pp. 160–176. D. Reidel, Dordrecht, The Netherlands (1971).
4. M. Ackerman, in *Mesospheric Models and Related Experiments* (Edited by G. Fiocco), pp. 149–159. D. Reidel, Dordrecht, The Netherlands, (1971).
5. R. T. Brinkman, in *Mesopheric Models and Related Experiments* (Edited by G. Fiocco), pp. 89–102. D. Reidel, Dordrecht, The Netherlands, (1971).
6. R. D. Hudson and S. H. Mahle, *J. Geophys. Res.* **77,** 2902 (1972).
7. T. M. Fang, S. C. Wofsy and A. Dalgarno, *Planet. Space Sci.* **22,** 413 (1974).
8. J. H. Park, *J. Atmos. Sci.* **31,** 1893 (1974).
9. H. Muramatsu, *Pap. Met. Geophys.* **26,** 219 (1973).
10. R. P. Turco, *Geophys. Surv.* **2,** 153 (1975).
11. G. Kockarts, *Planet. Space Sci.* **24,** 589 (1976).
12. A. J. Blake, *J. Geophys. Res.* **84,** 3272 (1979).
13. J. E. Frederick and R. D. Hudson, *J. Atmos. Sci.* **37,** 1099 (1980).
14. J. E. Frederick and R. D. Hudson, *J. Atmos. Sci.* **37,** 1088 (1980).
15. M. Nicolet and W. Peetermans, *Planet. Space Sci.* **28,** 85 (1980).
16. M. Allen and J. E. Frederick, *J. Atmos. Sci.* **39,** 2066 (1982).
17. S. Cieslik and M. Nicolet, *Planet. Space Sci.* **21,** 925 (1973).
18. M. Nicolet, *J. Geophys. Res.* **86,** 5203 (1981).
19. R. J. Cicerone and J. L. McCrumb, *Geophys. Res. Lett.* **7,** 251 (1980).
20. M. Nicolet, *J. Geophys. Res.* **89,** 2573 (1984).
21. B. R. Lewis, L. Berzins, J. H. Carver and S. T. Gibson, *JQSRT*, In press (1986).
22. V. Schumann, *Akad. Weiss. Wein* **102,** 625 (1893).
23. C. Runge, *Physica* **1,** 254 (1921).
24. W. Lochte-Holtgreven and G. H. Dieke, *Ann. Phys.* **3,** 937 (1929).
25. J. Curry and G. Herzberg, *Ann. Phys.* **19,** 800 (1934).
26. H. P. Knauss and S. S. Ballard, *Phys Rev.* **48,** 796 (1935).
27. L. Lal, *Nature* **161,** 477 (1948).
28. M. Feast, *Proc. phys. Soc. Lond.* **63,** 549 (1950).

29. P. Brix and G. Herzberg, *Can. J. Phys.* **32,** 110 (1954).
30. M. Ogawa, *Sci. Lt.* **15,** 97 (1966).
31. M. Ackerman and F. Biaume, *J. molec. Spectrosc.* **35,** 73 (1970).
32. V. Snopko, *Optika Spektrosk.* **29,** 445 (1970).
33. D. Creek and R. W. Nicholls, *Proc. R. Soc.* (*Lond. Ser.*) **341,** 517 (1975).
34. K. Yoshino, D. E. Freeman and W. H. Parkinson, *J. phys. chem. Ref. Data* **13,** 207 (1984).
35. K. Watanabe, E. C. Y. Inn and M. Zelikoff, *J. chem. Phys.* **21,** 1026 (1953).
36. A. J. Blake, J. H. Carver and G. N. Haddad, *JQSRT* **6,** 451 (1966).
37. J. Keck, J. Camm and B. Kivel, *J. chem. Phys.* **28,** 723 (1958).
38. C. E. Treanor and W. H. Wurster, *J. chem. Phys.* **32,** 758 (1960).
39. R. W. Ditchburn and D. W. O. Heddle, *Proc. R. Soc.* (*Lond. Ser.*) **A226,** 509 (1954).
40. A. J. D. Farmer, B. R. Lewis, K. H. Lokan and G. N. Haddad, *JQSRT* **8,** 1739 (1968).
41. G. W. Bethke, *J. chem. Phys.* **31,** 669 (1959).
42. M. Halmann, *J. chem. Phys.* **44,** 2406 (1966).
43. R. H. Huebner, R. J. Celotta, S. R. Mielczarek and C. E. Kuyatt, *J. chem. Phys.* **63,** 241 (1975).
44. V. Hasson, G. R. Hebert and R. W. Nicholls, *J. Phys. B: Atom. molec. Phys.* **3,** 1188 (1970).
45. M. Ackerman, F. Biaume and M. Nicolet, *Can. J. Chem.* **47,** 1834 (1969).
46. R. D. Hudson and V. L. Carter, *J. opt. Soc. Am.* **58,** 1621 (1968).
47. J. E. Frederick and R. D. Hudson, *J. molec. Spectrosc.* **74,** 247 (1979).
48. J. H. Carver, G. N. Haddad, T. I. Hobbs, B. R. Lewis and D. G. McCoy, *Appl. Opt.* **17,** 420 (1978).
49. B. R. Lewis, J. H. Carver, T. I. Hobbs, D. G. McCoy and H. P. F. Gies, *JQSRT* **20,** 191 (1978).
50. B. R. Lewis, J. H. Carver, T. I. Hobbs, D. G. McCoy and H. P. F. Gies, *JQSRT* **22,** 213 (1979).
51. H. P. F. Gies, S. T. Gibson, D. G. McCoy, A. J. Blake and B. R. Lewis, *JQSRT* **26,** 469 (1981).
52. A. C. Allison, Private communication (1975).
53. K. Yoshino, D. E. Freeman, J. R. Esmond and W. H. Parkinson, *Planet. Space Sci.* **31,** 339 (1983).
54. P. L. Smith, H. E. Griesinger, J. H. Black, K. Yoshino and D. E. Freeman, *Astrophys. J.* **277,** 569 (1984).
55. B. R. Lewis, *Appl. Opt.* **22,** 1546 (1983).
56. B. R. Lewis and J. H. Carver, *JQSRT* **30,** 297 (1983).
57. S. S. Penner, *Quantitative Molecular Spectroscopy and Gas Emissivities*. Addison–Wesley, Reading, Mass. (1959).
58. E. E. Whiting, *JQSRT* **8,** 1379 (1968).
59. L. Veseth and A. Lofthus, *Molec. Phys.* **27,** 511 (1974).
60. J. B. Tatum and J. K. G. Watson, *Can. J. Phys.* **49,** 2693 (1971).
61. B. R. Lewis, L. Berzins and J. H. Carver, submitted to *JQSRT*.
62. A. J. Blake, S. T. Gibson and D. G. McCoy, *J. Geophys. Res.* **89,** 7277 (1984).
63. R. M. Goody, *Atmospheric Radiation: I. Theoretical Basis*. Oxford University Press, London (1964).
64. B. R. Lewis, L. Berzins, J. H. Carver and S. T. Gibson, *JQSRT* **33,** 627 (1985).
65. B. R. Lewis, L. Berzins, J. H. Carver, S. T. Gibson and D. G. McCoy, *JQSRT* **34,** 405 (1985).
66. M. W. P. Cann, R. W. Nicholls, W. F. J. Evans, J. L. Kohl, R. Kurucz, W. H. Parkinson and E. M. Reeves, *Appl. Opt.* **18,** 964 (1979).
67. B. R. Lewis, L. Berzins, T. Scholz, C. J. Dedman and J. H. Carver, in preparation.
68. G. V. Marr, *Can. J. Phys.* **42,** 382 (1964).
69. W. R. Jarmain and R. W. Nicholls, *Proc. phys. Soc.* **84,** 417 (1964).
70. A. C. Allison, A. Dalgarno and N. W. Pasachoff, *Planet. Space Sci.* **19,** 1463 (1971).
71. S. T. Gibson, Ph.D. thesis, University of Adelaide (1983).
72. S. T. Gibson, H. P. F. Gies, A. J. Blake, D. G. McCoy and P. J. Rogers, *JQSRT* **30,** 385 (1983).
73. E. E. Whiting, A. Schadee, J. B. Tatum, J. T. Hougen and R. W. Nicholls, *J. molec. Spectrosc.* **80,** 249 (1980).
74. N. E. Kuz'menko, L. A. Kuznetsova, A. P. Monyakin and Yu. Ya. Kuzyakov, *JQSRT* **24,** 29 (1980).
75. A. C. Allison, S. L. Guberman and A. Dalgarno, *J. Geophys. Res.* A, In press.
76. R. Harris, M. Blackledge and J. Generosa, *J. molec. Spectrosc.* **30,** 506 (1969).

4.6 Rotational variation of predissociation linewidth in the Schumann-Runge bands of $^{16}O_2$

[24] B. R. Lewis, L. Berzins, J. H. Carver, and S. T. Gibson,
Journal of Quantitative Spectroscopy and Radiative Transfer **36**, 187–207 (1986).

J. Quant. Spectrosc. Radiat. Transfer Vol. 36, No. 3, pp. 187–207, 1986
Printed in Great Britain.

0022-4073/86 $3.00 + 0.00

ROTATIONAL VARIATION OF PREDISSOCIATION LINEWIDTH IN THE SCHUMANN–RUNGE BANDS OF $^{16}O_2$

B. R. LEWIS,[1] L. BERZINS,[1] J. H. CARVER[1] and S. T. GIBSON[2]*

[1]Research School of Physical Sciences, The Australian National University, Canberra, Australia 2600
and [2]Department of Physics, University of Adelaide, Australia 5001

(*Received* 11 *November* 1985)

Abstract—Extensive high resolution photoabsorption measurements have been performed on most of the experimentally accessible rotational lines in the Schumann–Runge band system of $^{16}O_2$. Predissociation linewidths are inferred from these measurements for as many lines as possible from the (1–0) to (19–0) bands. A model of the predissociation is developed, which includes the interactions of the $B^3\Sigma_u^-$ state with repulsive $^5\Pi_u$, $^3\Pi_u$, $^1\Pi_u$ and $^3\Sigma_u^+$ states, and molecular parameters for these interactions are determined by least-squares fitting the model to the experimental vibrational widths for the (1–0) to (18–0) bands. These parameters are then used, in conjunction with the model, to predict the variation of predissociation linewidth with rotation for each Schumann–Runge band. The experimental linewidths are found to exhibit systematic variation with rotation for most of the bands studied, and agreement with the model predictions of rotational variation is excellent. Polynomial fits to the model rotational linewidths are also presented in order to facilitate atmospheric modelling applications.

INTRODUCTION

In order to calculate the transmission of solar radiation in the range 1750–2000 Å through the atmosphere it is necessary to know accurately both oscillator strengths and linewidths for individual rotational lines of the Schumann–Runge band system of $^{16}O_2$. Atmospheric transmission is also important in calculations of photodissociation rates for various atmospheric constituents. There have been many atmospheric transmission and photodissociation models[1–19] developed in the past, and the most recent work of Nicolet[20] emphasises the need to know Schumann–Runge band oscillator strengths and linewidths with a high degree of accuracy. New measurements of oscillator strength are presented by Lewis *et al.*[21] in a companion work, but this paper is restricted to a discussion of predissociation linewidths.

Flory[22] attributed the observed diffuseness of the rotational Schumann–Runge lines on photographic plates to predissociation of the $B^3\Sigma_u^-$ state by a repulsive $^3\Pi_u$ state, but Feast[23] observed B–X emission from bands with $v > 2$ and claimed that this refuted Flory's argument. Volman[24] provided the first photochemical evidence for predissociation. Since that time several workers[25–28] have observed qualitative broadening of absorption lines in some bands and have attributed this to predissociation due to the $^3\Pi_u$ state and possibly others. A full summary of the situation to 1972 is given by Krupenie.[29]

Quantitative linewidth measurements are few. Ackerman and Biaume[30] estimated linewidths from photographic plates of the (0–0) to (13–0) bands, but no allowance was made for fine structure splitting and these results should only be regarded as semi-quantitative. Hudson and Mahle[6] obtained linewidths for the (2–0) to (16–0) bands by applying a least-squares profile fitting technique to the measurements of Hudson and Carter,[31,32] and the same data for the (2–0) to (13–0) bands was reanalysed by Frederick and Hudson,[33] who presented a few measurements as a function of rotation for the (8–0) to (13–0) bands. In a series of experiments, Lewis *et al.*[34,35] and Gies *et al.*[36] obtained individual rotational linewidths from the (2–0) to (19–0) bands by using an iterative equivalent width method of analysis. Prompted by the conclusion of Frederick and Hudson[33] that

*Present address: Argonne National Laboratory Argonne, IL 60439, U.S.A.

the linewidth tended to increase with rotation, although they[33] cautioned that their results should be viewed with reservation due to uncertainties in the triplet splitting parameters, Lewis *et al.*[37] re-examined their previous measurements.[34–36] They concluded that, of the 12 bands studied, only the (9–0) and (12–0) bands showed a statistically significant increase in linewidth with rotation, no variation being observed in the remainder. Recently, Smith *et al.*[38] presented bandhead measurements of linewidth for the (13–0) to (16–0) bands obtained by data analysis methods similar to those of Frederick and Hudson.[33]

Theories explaining the observed predissociation have developed considerably in the last 20 years. Schaefer and Harris[39] performed *ab initio* calculations and interpreted the predissociation in terms of interaction between the $B^3\Sigma_u^-$ state and a repulsive $^3\Pi_u$ state. More reliable calculations were then performed by Schaefer and Miller[40] who stated that spin-orbit coupling was the principal interaction responsible for the predissociation, and then noted that the four repulsive states $^1\Pi_u$, $^3\Pi_u$, $^5\Pi_u$ and $^5\Sigma_u^-$ would be expected to predissociate $B^3\Sigma_u^-$ to about the same degree. Riess and Ben-Aryeh,[41] using Morse eigenfunctions for the bound states of $B^3\Sigma_u^-$ and an asymptotic sinusoidal form for the unbound wavefunction, found that overlap between the bound and unbound wavefunctions for the $^3\Pi_u$ state had several maxima and was thus possibly sufficient to account for all the observed predissociation. A more sophisticated calculation by Murrell and Taylor[42] produced a similar conclusion, and another by Child[43] gave results similar to those of Murrell and Taylor.[42] Durmaz and Murrell[44] were the first to consider the effect of centrifugal distortion on the Franck–Condon density. For most vibrational levels, they found considerable J dependence, but their work suffers through only considering the $^3\Pi_u$ state. It was not until the work of Julienne and Krauss[45] and Julienne[46] that theoretical calculations started to reproduce the observed linewidths. These authors used *ab initio* calculations to obtain an initial range for the parameters describing the potential curve interactions and then refined this qualitative picture of the predissociation through a detailed comparison between the calculated level shifts and linewidths and the available experimental data. Julienne and Krauss[45] found significant differences between the couplings to each repulsive state and concluded that the dominant state causing the predissociation was the $^5\Pi_u$ with the $^3\Pi_u$ and $^1\Pi_u$ playing minor roles. Coupling to the $2^3\Sigma_u^+$ state was initially thought to be zero,[45] but Julienne later found that this was not so and showed that including this coupling resulted in an improved fit to the experimental measurements. Julienne[46] also discussed several of the factors causing J dependence of the calculated widths but did not perform detailed calculations because of the lack of available experimental data for comparison. Sink and Bandrauk[47] have made the most recent calculation of predissociation linewidths based upon an analytical scattering model. Their results show a similar trend to those of Julienne and Krauss[45] but are not of the same accuracy.

Let us briefly summarize the situation. Sufficient quantitative measurements of predissociation linewidth as a function of vibration[33–36] exist to enable an assessment of the predissociation theories. It is found[33–36] that only the theory of Julienne[46] is capable of explaining the observed predissociation maxima at $v = 4$, 7, 11, and thus the predissociation is caused primarily by the $^5\Pi_u$ interaction with lesser roles being played by the $2^3\Sigma_u^+$, the $^3\Pi_u$ and the $^1\Pi_u$ states. This conclusion is in direct contrast to the earlier reliance on the $^3\Pi_u$ state to explain most of the predissociation.

There have been no experiments performed explicitly to measure the rotational dependence of the linewidth. The work of the Frederick and Hudson[33] and Lewis *et al.*[37] relies upon re-examination of old measurements and is not very comprehensive. The theoretical techniques exist[46] enabling calculation of the J dependence of the linewidth, but there are several contributions to this effect and the complicated nature of the processes involved, together with the lack of comprehensive experimental data, has inhibited extensive calculations. Krupenie[29] and Julienne[46] have both commented on the need for experimental measurements of the J dependence of predissociation linewidth.

This work presents the results of an extensive experimental study of the predissociation linewidths of the (1–0) to (19–0) Schumann–Runge bands of $^{16}O_2$ as a function of rotation. The measurements of the vibrational widths are fitted by adjusting the interaction parameters of the Julienne[46] model, and these parameters are then used in a modified theoretical model to predict the J dependence of the predissociation widths. Excellent agreement is found between the measured and theoretical v and J dependences.

EXPERIMENTAL METHOD AND DATA ANALYSIS

A detailed discussion of the experimental method has been given elsewhere.[21] Radiation from a d.c. H_2 continuum discharge was dispersed by a 2.2 m monochromator and monitored by two u.v. photomultipliers, operating in the pulse counting mode, before entering and after leaving the 1.2 m absorption cell. Extensive modifications to the monochromator,[48] and close temperature control of the environment, enabled good scanning linearity at the wavelength resolution of 0.04–0.05 Å and excellent absolute wavelength reproducibility. These characteristics were essential for the accurate measurements required of this work and also for the routine computer control of the experiment.

Scans were performed across the absorption line of interest at two widely differing O_2 pressures and the resultant line profiles and equivalent widths were recorded. This technique allowed the simultaneous determination of both oscillator strength and predissociation linewidth by an iterative procedure first applied to O_2 by Lewis *et al.*[34] The model parameters assumed in the data analysis program have been discussed previously,[21] but it should be emphasized that the assumed pressure broadening coefficient particularly affects the linewidths deduced for the low v bands which are measured at pressures near one atmosphere. The low-pressure scan approaches the linear region of the curve of growth and results in an equivalent width much more sensitive to oscillator strength than to the mixing parameter a (proportional to the predissociation linewidth).[21] Assuming an initial approximation for a, the oscillator strength is then calculated for this scan. In the case of the high-pressure scan there is a considerably enhanced dependence of the equivalent width on a and thus a refined value for a can be determined using the oscillator strength obtained from the low-pressure scan. This procedure is repeated until a consistent pair of results for oscillator strength and a is produced. Absorption spectra calculated using these results are then compared with the experimental scan profile as a final check on the accuracy of the procedure.

For the (1–0) band and for higher rotational lines in the (2–0) and (3–0) bands, pressures necessary to accurately apply the equivalent width method were experimentally inaccessible. In these cases predissociation linewidths were obtained by a two parameter least-squares fit to the observed line profiles at a single pressure, a variant of the method used by Frederick and Hudson.[33] Linewidths obtained in this way were found to merge smoothly with those obtained by the equivalent width method, and were consistent where both methods were compared for a given line.

It is seen from the above that the fitted experimental linewidths are closely related to the fitted oscillator strengths in an inverse fashion. This behaviour can be seen in the results of Hudson and Mahle[6] and Frederick and Hudson,[33] where oscillator strengths which are anomalously large are correlated with small linewidths and vice versa. The low scatter in the oscillator strengths of the companion work,[21] together with the excellent agreement with the model-independent oscillator strengths obtained by Yoshino *et al.*[49] for the (1–0) to (12–0) bands, implies that this problem has been minimized in this work and that the predissociation linewidths obtained here should be very reliable.

THEORETICAL

The theoretical predissociation model used in this work is based on that of Julienne and Krauss[45] and Julienne,[46] and similar notation will be used here.

An absorption line to the bound triplet level F_i with vibrational and rotational quantum numbers v and J is broadened by an amount

$$\Gamma(vJi) = 2\pi \sum_{\alpha} [T_{vJi\alpha}(E_{vJi})]^2, \tag{1}$$

where the sum is over α ($\alpha = {}^5\Pi_u, {}^3\Sigma_u^+, {}^3\Pi_u, {}^1\Pi_u$), the repulsive potential curves which cross the $B^3\Sigma_u^-$ state. The quantities T^2 are the matrix elements for interaction between the bound state and the continuum and are given in Table 2 of Julienne and Krauss[45] or Table 1 of Julienne.[46] In this work we ignore the small electronic-rotation interaction which contributes to the $B^3\Sigma_u^- - {}^3\Pi_u$ coupling and use the spin-orbit matrix elements only, with a mixed case (a)–(b) representation of the $B^3\Sigma_u^-$ state. These matrix elements are given in Table 1 of Julienne[46] and are reproduced here

Table 1. Matrix elements T^2 for $^3\Sigma_u^-$ predissociation through spin-orbit coupling. A mixed-case (a)–(b) representation of the $^3\Sigma_u^-$ state is assumed. ξ is defined in equation (3), while a and b are defined in equation (2)

Coupling to	$^3\Sigma_u^+$, $^1\Pi_u$	$^5\Pi_u$	$^3\Pi_u$
Level			
F_1	$b^2\xi^2$	$(1+b^2/6)\xi^2$	$(1+a^2)\xi^2$
F_2	ξ^2	$(7/6)\xi^2$	ξ^2
F_3	$a^2\xi^2$	$(1+a^2/6)\xi^2$	$(1+b^2)\xi^2$

in Table 1.The mixing coefficients for the $B^3\Sigma_u^-$ state are given by[50]

$$\left.\begin{aligned} a(vJ) &= \left[\frac{F_2(vJ)-F_1(vJ)}{F_3(vJ)-F_1(vJ)}\right]^{1/2}, \\ \text{and} \qquad b(vJ) &= \left[\frac{F_3(vJ)-F_2(vJ)}{F_3(vJ)-F_1(vJ)}\right]^{1/2}. \end{aligned}\right\} \tag{2}$$

If we initially consider the zero rotation case, the matrix element ξ in Table 1 is the vibrational-electronic overlap integral

$$\xi_{v\alpha}(E) = \langle \psi_v | A_\alpha(r) | \psi_{E\alpha} \rangle, \tag{3}$$

where ψ_v and $\psi_{E\alpha}$ are the respective bound vibrational and energy-normalized continuum wavefunctions, $A_\alpha(r)$ is the electronic spin-orbit matrix element and, for calculations of linewidth, E is the energy of the bound vibrational level v.

In this work, the B state potential is derived using standard RKR techniques from spectroscopic constants fitted to the recent wavenumber measurements of Yoshino *et al.*[51] with a Morse extension from the inner $v = 14$ turning point optimized to be consistent with the Schumann–Runge continuum temperature coefficients of Gibson *et al.*[52] This procedure is adequate to describe bound vibrational levels up to $v = 21$. After Julienne and Krauss,[45] the repulsive potentials are assumed to take the form

$$V_\alpha(r) = V_{\alpha x} \exp[-(M_{\alpha x}/V_{\alpha x})(r - R_{\alpha x})] + V_\infty, \tag{4}$$

where V_∞ is the energy of the $O(^3P) + O(^3P)$ asymptote, $R_{\alpha x}$ is the crossing point and $V_{\alpha x}$ is the energy at which the repulsive potential α crosses the $B^3\Sigma_u^-$ potential. $M_{\alpha x}$ is the slope of the repulsive potential α at the crossing point. The electronic matrix element is assumed to be independent of r and to have a constant value $A_{\alpha x} = A_\alpha(R_{\alpha x})$, after the discussion by Julienne.[46] The wavefunctions in equation (3) are calculated by numerical integration of the Schrödinger equation.

Calculations of rotationless F_2 linewidths were performed for $v = 0$–16 using equations (1) and (3) and Table 1, with repulsive state parameters identical with those of Julienne.[46] Essentially identical linewidths were obtained, indicating that any small differences between the assumed $B^3\Sigma_u^-$ state potentials were insignificant in terms of such predissociation linewidth calculations.

In the case of explicit calculations of linewidth as a function of rotation, the centrifugal energy term is added to the bound and unbound potentials and the above procedure is followed. In this work, the major contributor to the rotational dependence is found to be centrifugal distortion with secondary effects due to the J dependences of the $B^3\Sigma_u^-$ state mixing coefficients and the intermediate case $(a)-(b)$ coupling factors of Table 1 for the F_1 and F_3 levels.

In order to give a valid comparison with unresolved experimental triplet widths, the full set of partial widths $\Gamma(vJi)$ are calculated using the above procedure. They must then be averaged over the fine-structure parameter i for a fixed N ($J = N$, $N \pm 1$), since this is the way that the triplets occur in practice. The procedure is somewhat less convenient than the neat sum rules that develop[45,46] when the averaging is performed for fixed J, but is more appropriate for most

experimental comparisons. From now on for simplicity the predissociation linewidths will be denoted by $\bar{\Gamma}$ to indicate the fine structure averaging although some of the experimental widths to be presented are of resolved triplet components.

RESULTS

Some 285 distinct linewidth measurements are presented in this work, each measurement generally resulting from multiple scans at two different pressures, as explained earlier. The oscillator strengths associated with these linewidths have been discussed elsewhere[21] and have been found to be in excellent agreement with the model-independent measurements of Yoshino *et al.*[49] for the (1–0) to (12–0) bands. This result supports the reliability of the predissociation linewidths presented here.

As noted earlier, the measured linewidth is mainly dependent on the equivalent width of the higher pressure scan. Figure 1 shows the experimentally measured transmission values for a scan of the R(15)P(13) lines of the (4–0) band at a pressure of 466 Torr. The absorbing gas was at a temperature of 295 K, the instrument resolution was 45 mÅ and the wavelength increment between steps was 10.67 mÅ. The statistical error in each data point is $\sim 1\%$ in the line wings. Also shown in Fig. 1 is the theoretical data-analysis model profile for the above conditions with an oscillator strength $f = 2.64 \times 10^{-7}$ and predissociation linewidth $\bar{\Gamma} = 3.52\ \text{cm}^{-1}$, the measured values of this and the previous work,[21] obtained by the equivalent width technique. The theoretical profile is in excellent agreement with the observed, verifying that an analysis based on equivalent widths will give accurate line profiles provided that there are no local line classification problems. (The equivalent width is basically independent of the instrumental resolution and thus the method does not require accurate knowledge of this parameter, in contrast with line profile fitting methods of analysis.) Figure 1 also shows theoretical line profiles calculated as above, but with $\bar{\Gamma}$ changed by $\pm 25\%$. As expected, the maximum difference occurs in the line wings. Although the difference in wing transmission is not large, it is still far in excess of the $\sim 1\%$ scatter of the experimental measurements, and it is thus possible to determine linewidths quite accurately by either data

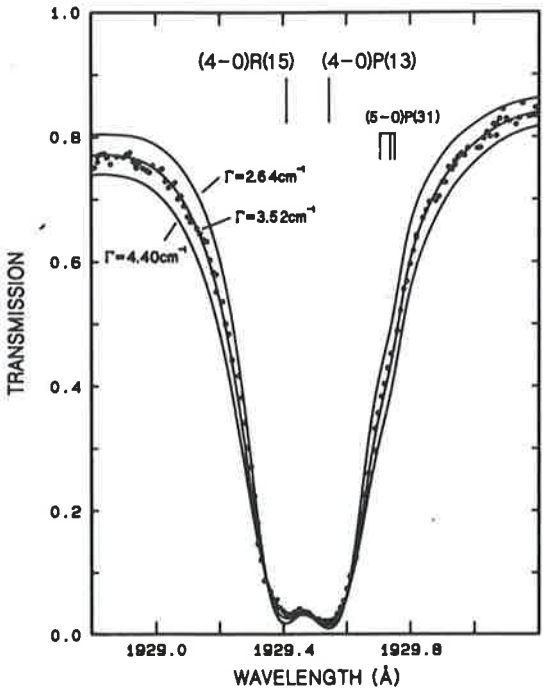

Fig. 1. An experimental scan across the $R(15)P(13)$ lines of the (4–0) band, together with model predictions for several predissociation linewidths. The pressure of O_2 was 466 Torr, the temperature 295 K, and an oscillator strength of 2.64×10^{-7} was assumed for the model calculations.

analysis technique if the oscillator strength is known. The equivalent width over the 1.4 Å experimental scan range varies by +5.6, −7.0% as $\bar{\Gamma}$ is changed by ±25%. The P(31) line of the (5–0) band is seen as an inflection on the long wavelength wing in Fig. 1 and the theoretical profile is in excellent agreement with the experiment in this region also, but such overlapping weak features clearly must be well modelled if accurate linewidths are to be obtained. In this work, both the hot bands and the isotopic $^{16}O^{18}O$ bands are accurately modelled.[21] The need to have accurate oscillator strengths for the line of interest is also demonstrated clearly by the above example.

Our measured linewidths are presented in Tables 2 and 3 as functions of v and J. In cases where the $P(I-1)$ and $R(I+1)$ branches were unresolved, the appropriate mean $J = I$, for fine structure unresolved $P(I)$ measurements $J = I-1$, and for similar $R(I)$ measurements $J = I+1$. (The bracketed quantities I, $I \pm 1$ refer to the rotation N'' of the ground state level from which the absorption line originates; the primes are omitted for simplicity from the upper state quantum numbers throughout this work.) For $v \geqslant 13$ many measurements were taken on resolved triplet fine structure components. In general, it was not possible to distinguish reliably systematic width variations as a function of the triplet sub-level due to limited available lines and the increased statistical error for measurements on the higher rotational lines. Width measurements on resolved single and double fine structure components account for the odd and non-integral mean J values assigned to some of the measurements in Table 3. The widths marked with an asterisk in Table 2 were obtained from scans taken at a single high pressure by a profile fitting technique, as mentioned above. This technique resulted in larger errors, especially for the (1–0) band.

The errors listed in Tables 2 and 3 are statistical only. There will be an additional error of about 3% due to possible systematic errors in pressure, cell length and temperature. The errors introduced due to inaccuracies in model parameters such as spectroscopic constants, underlying continuum and pressure broadening coefficients are not considered explicitly, but the best possible values are used for these parameters. The bandhead widths of the (3–0) to (17–0) bands are particularly reliable and are effectively independent of the analytical model parameters apart from the fine structure splitting. The (1–0) and (2–0) results are sensitive to the pressure-broadening coefficient, the underlying continuum and the pressure coefficient of the underlying continuum[21] and, for $v \geqslant 18$, weak-line classification problems provide an additional source of error. Widths for the weaker, high rotational lines can become quite inaccurate in relative terms, but are still significant in determining the general rotational behaviour of some bands (in particular for $v \geqslant 14$).

The linewidths in Tables 2 and 3 were smoothed and extrapolated to $J = 0$ and these results are presented in Table 4, together with previously published vibrational linewidths.[33–36,38] Predissociation maxima are observed at $v = 4$, 7, 11, 16 in agreement with previous observations and measurements. The recent bandhead width measurements of Smith *et al.*[38] are in good agreement with the present values except for $v = 13$. It should be noted that Smith *et al.*[38] use a fitting procedure similar to that of Frederick and Hudson[33] and that they[38] obtain an oscillator strength for the (13–0) band which is about 12% lower than expected from the trend of the $v = 0$–12 oscillator strengths of Yoshino *et al.*[49] Because of the inverse coupling between the f and Γ values inherent in the fitting procedure, an increased f would imply a decreased Γ, resulting in better agreement with the present results for $v = 13$. The bandhead widths measured by Frederick and Hudson[33] agree reasonably well with ours except for $v = 2$, 3, 4, 10, 12. These discrepancies can be resolved, except for $v = 4$, by noting that their oscillator strengths[33] for $v = 2$, 3, 10, 12 are in error[21] in an inverse fashion to the width discrepancies. This indicates a problem in their data analysis for these bands.

Agreement with the measured widths of Gies *et al.*[36] is also reasonably good, except for $v = 10$, 12, 13, 17. Their linewidths are averaged over all rotational lines measured and are not therefore necessarily directly comparable with our bandhead measurements. In fact, for the indicated bands, the deviations from our results are of the same sign as our observed rotational dependence for these bands. Scatter in their[36] associated oscillator strengths may account for some of the discrepancy for $v = 13$, 17 but, in general, their f values are much less scattered than those of Frederick and Hudson.[33] The (13–0) band linewidth of Gies *et al.*[36] is 0.20 cm^{-1}, nearly twice our value, and this remains the most serious discrepancy. The earlier linewidths measured by Lewis *et al.*[34,35] are shown for completeness. Their values for $v = 2$,3 should be ignored because of incorrect analytical model parameters. As noted by Gies *et al.*,[36] the oscillator strengths of Lewis *et al.*[34,35] for $v \geqslant 7$ were too

Table 2. Measured FWHM predissociation linewidths Γ (cm^{-1}) for rotational lines from the (1–0) to (10–0) Schumann–Runge bands. Unmarked values are derived from measurements of unresolved *PR* doublets, while values marked *P* and *R* are derived from measurements of *P* and *R* branch lines, respectively. Values marked with an asterisk were obtained from a scan profile fitting technique. No resolved triplet components were measured for these bands

J \ v	1	2	3	4	5	6	7	8	9	10
2	0.62±0.20 *	0.38±0.08								
4	0.73±0.20 P*									
4	0.66±0.20 *	0.40±0.06	1.60±0.10	2.99±0.30	1.82±0.10	1.44±0.08	1.83±0.09	1.62±0.06	0.71±0.06	1.07±0.08
6	0.76±0.20 P*	0.42±0.06	1.63±0.10	3.00±0.30	1.93±0.06	1.33±0.08	1.86±0.06	1.63±0.06	0.58±0.06	0.92±0.08
8	0.57±0.20 P*	0.29±0.10 P							0.07±0.06 P	0.89±0.08 P
8	0.83±0.20 R*	0.41±0.06	1.62±0.10	3.17±0.30	1.92±0.10	1.60±0.08	2.03±0.09	1.78±0.06	0.76±0.06	0.93±0.08
10	0.59±0.20 P*	0.42±0.10 P								
10	0.73±0.20 R*	0.39±0.06	1.73±0.10	3.53±0.20	1.93±0.10	1.53±0.08	1.74±0.06	1.71±0.06	0.65±0.06 P	0.82±0.08 P
12		0.37±0.10 R								
12	0.81±0.30 P*	0.41±0.10 P*							0.65±0.06 P	0.71±0.08 P
12	0.80±0.20 R*	0.42±0.06	1.84±0.15	3.30±0.20	1.79±0.10	1.69±0.08	1.74±0.09	1.59±0.06	0.69±0.06 R	0.86±0.08 R
14	0.61±0.30 P*	0.38±0.10 R	1.89±0.25 P*						0.69±0.06 P	0.87±0.08 P
14	0.93±0.30 R*	0.45±0.10 P*	1.68±0.15	3.49±0.20	1.82±0.10	1.78±0.08	1.72±0.09	1.75±0.09	0.75±0.06 R	0.92±0.08 R
16	0.98±0.50 P*		1.66±0.25 P*						0.75±0.06 P	0.79±0.08 P
16	0.52±0.30 R*	0.40±0.10 R*	1.51±0.20	3.46±0.20	1.80±0.12	1.73±0.08	1.73±0.09	1.79±0.09	0.87±0.06 R	0.83±0.08 R
18			1.69±0.25 P*						0.80±0.10 P	0.72±0.08 P
18	1.14±0.50 R*	0.35±0.10 R*	1.82±0.25 R*	3.35±0.20	1.90±0.12	1.86±0.08	1.85±0.12	2.05±0.09	0.71±0.06 R	0.72±0.08 R
20			2.00±0.30 P*						0.83±0.15 P	0.80±0.08 P
20	0.57±0.50 R*		1.90±0.25 R*	3.24±0.30	1.72±0.12	2.05±0.10	1.43±0.12	1.77±0.09	0.69±0.10 R	0.85±0.08 R
22			1.68±0.30 P*							
22			1.75±0.30 R*	3.04±0.40	1.66±0.12	1.97±0.10	1.44±0.12	1.95±0.21	0.92±0.15 R	0.64±0.08 R
24			2.06±0.40 P*							0.35±0.15 P
24			1.97±0.35 R*		1.62±0.21	2.04±0.10	1.62±0.15	1.67±0.15	0.99±0.15 R	0.83±0.25 R
26			1.91±0.40 P*			2.10±0.10	1.17±0.15			0.51±0.10 R
28										0.52±0.10 P
28			1.89±0.40 R*							0.54±0.28 R
30										0.60±0.26 P
30										0.14±0.25 R

Table 3. Measured FWHM predissociation linewidths $\bar{\Gamma}$ (cm^{-1}) for rotational lines from the (11–0) to (19–0) Schumann–Runge bands. Unmarked values are derived from measurements of unresolved *PR* doublets, while values marked *P* and *R* are derived from measurements of *P* and *R* branch lines, respectively. Widths referring to resolved triplet components are given an appropriate subscripted marking, and for fully resolved single triplet components $\bar{\Gamma}$ should be replaced by Γ

J \ v	11	12	13	J	v=14	J	v=15	J	v=16	J	v=17	J	v=18	J	v=19
1		0.47±0.04						2.7	0.24±0.03						
2		0.51±0.05P	0.11±0.01P					2.7	0.25±0.03						
								3	0.43±0.03P_1	3	0.31±0.03P_1	3	0.22±0.03	3.5	0.24±0.06P_{32}
4		0.43±0.04P	0.10±0.01P												
4	1.07±0.06	0.35±0.03R	0.12±0.01R	4	0.15±0.02P			4	0.33±0.03P	4	0.31±0.03				
												5	0.18±0.03P_1	5.5	0.25±0.03P_{32}
6	1.26±0.06P	0.61±0.05P						6	0.31±0.03P						
6	1.16±0.06	0.49±0.05R	0.10±0.01P	6	0.15±0.02P	6	0.31±0.03P	6	0.42±0.03R	5.5	0.34±0.03R_{32}				
										7	0.26±0.03P_1	7.5	0.21±0.03R_{32}	7	0.20±0.06R_1
8		0.54±0.05P	0.14±0.01P	8	0.13±0.03R	8	0.24±0.03P	8	0.27±0.03P						
8	1.25±0.06P	0.55±0.05R	0.12±0.01R	8	0.15±0.02P	8	0.24±0.03R	8	0.38±0.03R						
										9.5	0.33±0.03R_{32}				
10	1.19±0.10P	0.72±0.05P	0.13±0.01P	10	0.15±0.03R	10	0.22±0.03P	10	0.36±0.03P					10	0.17±0.03P_2
10	1.33±0.06R	0.61±0.05R	0.12±0.01R	10	0.12±0.02P	10	0.32±0.03R	10	0.27±0.03R						
										11.5	0.24±0.03P_{32}				
12	1.27±0.15P	0.77±0.05P	0.16±0.02P	12	0.11±0.03R	12	0.25±0.03P								
12	1.27±0.06R	0.72±0.05R	0.12±0.01R	12	0.14±0.02P	12	0.24±0.03R	12	0.24±0.03R					12	0.26±0.06R_2
												13	0.11±0.03P_1	13	0.28±0.07P_1
14	1.27±0.06P	0.62±0.05P		14	0.11±0.03R										
14	1.25±0.06R	0.79±0.06R	0.13±0.02R	14	0.12±0.02P	14	0.22±0.03R							13	0.26±0.06R_1
								15.5	0.26±0.03P_{32}	15	0.15±0.03P_3				
16	1.30±0.10P			15.5	0.11±0.02P_{32}			15.5	0.27±0.03R_{32}	15	0.15±0.03R_3	15	0.10±0.03P_3		
16	1.23±0.06R	0.86±0.07R		16	0.12±0.03R							15.5	0.11±0.03P_2R_1		
										17	0.17±0.03P_1				
18	1.40±0.15P			17.5	0.14±0.02P_{32}										
18	1.24±0.10R	0.74±0.07R	0.21±0.02R			19	0.09±0.03P_1			18	0.08±0.03P_2				
						19.5	0.12±0.03R_{32}			21	0.11±0.03R_3				
20	1.03±0.10R	0.94±0.07R													
				21	0.06±0.02P_1	21.5	0.16±0.03R_{32}	21	0.14±0.03P_1	21	0.07±0.03R_1	21	0.05±0.03P_1		
22	1.05±0.15P														
22	1.37±0.20R			22	0.12±0.02R			22	0.16±0.03P_2			22	0.05±0.03R_2		
						23	0.06±0.03P_1	23	0.06±0.03P_1						
24		0.96±0.15P													
24	1.08±0.15P	0.88±0.10R	0.36±0.03R	24	0.14±0.02R_2	25	0.02±0.03P_1	23	0.06±0.03R_1	24	0.06±0.03P_2				
25			0.29±0.03P_1			25	0.03±0.03R_1	25	0.02±0.03P_1						
								25	0.06±0.03R_1						
26		0.74±0.15R	0.36±0.03R												
				27	0.16±0.03P_1			27	0.10±0.03R_3	27	0.10±0.03R_1				
28	0.82±0.15P					28	0.09±0.03R_2								
				29	0.22±0.04R_1			29	0.01±0.03R_1						
30	0.76±0.20R			30	0.20±0.04R_2										
				31	0.13±0.05R_1										

Table 4. Measured FWHM predissociation linewidths Γ (cm^{-1}) extrapolated to zero rotation, for the (1–0) to (19–0) Schumann–Runge bands. The comparable values of other workers[33–36,38] are also given

v	This work	Smith *et al.*[38]	Frederick and Hudson[33]	Gies *et al.*[36]	Lewis *et al.*[34,35]
1	0.66±0.10				
2	0.39±0.03		0.24±0.02		0.62±0.08
3	1.61±0.08		1.84±0.08		1.2 ± 0.1
4	2.99±0.20		4.18±0.10		3.0 ± 0.4
5	1.91±0.10		2.34±0.50		1.9 ± 0.3
6	1.38±0.10		1.11±0.20		1.41±0.07
7	1.87±0.10		1.70±0.15	1.62±0.10	1.47±0.08
8	1.61±0.10		1.43±0.15	1.36±0.09	1.23±0.09
9	0.67±0.05		0.76±0.40	0.67±0.04	0.56±0.07
10	0.95±0.05		0.42±0.07	0.70±0.04	0.78±0.07
11	1.18±0.10		1.27±0.45	0.94±0.06	0.98±0.07
12	0.42±0.05		0.81±0.07	0.66±0.03	0.57±0.03
13	0.11±0.01	0.16±0.02	0.13±0.01	0.20±0.01	0.14±0.01
14	0.18±0.02	0.18±0.02		0.16±0.02	0.09±0.01
15	0.33±0.03	0.33±0.01		0.32±0.04	
16	0.35±0.05	0.40±0.01		0.33±0.03	
17	0.34±0.03			0.25±0.03	
18	0.22±0.03			0.16±0.03	
19	0.23±0.04			0.22±0.12	

large due to a pressure gradient in the experimental apparatus, and the corresponding linewidths will therefore be too small.

The measurements of Ackerman and Biaume[30] are not tabulated here since they were apparent photographic widths, not deconvoluted linewidths, and are about 0.5 cm^{-1} larger than the entries in Table 4 for all bands. The widths of Hudson and Mahle[6] are not considered since their data has been reanalysed by Frederick and Hudson.[33]

MODEL PARAMETERS

Our empirical predissociation linewidth model is based on the interaction of the $B^3\Sigma_u^-$ state with four repulsive states α ($\alpha = {}^5\Pi_u$, $2^3\Sigma_u^+$, ${}^3\Pi_u$, ${}^1\Pi_u$). The repulsive states are described by equation (4) and there are three undetermined parameters $A_{\alpha x}$, $M_{\alpha x}$, $R_{\alpha x}$ for each state, a total of 12. Julienne and Krauss[45] approximately determined the parameters for the ${}^5\Pi_u$ state by a remarkable deperturbation of the observed band origins of Ackerman and Biaume.[30] The unique behaviour of the 19 vibrational widths measured here enables all 12 parameters to be determined to quite a high degree of accuracy. A least-squares routine was written in order to fit the predissociation model of this work to our observed linewidths by adjustment of the 12 parameters.

It was necessary to choose the most reliable widths from each band for inclusion in the fit, and smoothed values for $N = 10$ were used for $v = 1$–15 and $N = 6$ for $v = 16$–18. The less accurate (19–0) band widths were not included in the fit since this considerably improved the reduced value

Table 5. Calculated best fit partial and total FWHM predissociation widths (cm^{-1}) for the (1–0) to (18–0) Schumann–Runge bands compared with the measured values of this work ($N = 10$ for $v = 1$–15, $N = 6$ for $v = 16$–18). The deviations between the measured and model values are also shown as a percentage. All theoretical widths are averaged over the fine structure components

v \ α	$^5\Pi_u$	$^3\Sigma_u^+$	$^3\Pi_u$	$^1\Pi_u$	$\bar{\Gamma}$ (theor.)	$\bar{\Gamma}$ (meas.)	Deviation, %
1	0.002	0.000	0.075	0.714	0.792	0.724	-9.4
2	0.081	0.000	0.153	0.178	0.412	0.405	-1.7
3	0.918	0.000	0.236	0.440	1.595	1.67	4.5
4	3.051	0.005	0.307	0.072	3.435	3.31	-3.8
5	1.425	0.065	0.352	0.026	1.867	1.89	1.2
6	0.712	0.336	0.366	0.166	1.580	1.57	-0.6
7	0.810	0.484	0.355	0.234	1.881	1.81	-3.9
8	1.112	0.014	0.323	0.203	1.652	1.71	3.4
9	0.002	0.270	0.278	0.136	0.686	0.689	0.5
10	0.605	0.000	0.230	0.075	0.910	0.897	-1.4
11	0.835	0.157	0.181	0.035	1.208	1.23	1.8
12	0.339	0.113	0.139	0.013	0.605	0.617	2.0
13	0.019	0.005	0.103	0.004	0.132	0.126	-4.5
14	0.040	0.020	0.075	0.001	0.136	0.134	-1.3
15	0.147	0.057	0.054	0.000	0.257	0.256	-0.6
16	0.226	0.064	0.037	0.001	0.327	0.329	0.6
17	0.211	0.045	0.026	0.001	0.284	0.308	7.9
18	0.169	0.028	0.018	0.001	0.216	0.197	-9.7

of χ^2. The results of the fitting procedure are shown in Table 5, where the best fit model linewidths are compared with the measured values. The model widths are averaged over all triplet components for a fixed N, the most valid comparison with the experimental measurements. The overall fit is seen to be excellent, with an r.m.s. deviation of only 4.4%. The maximum deviation for $v = 2$–16 is only $\pm 4.5\%$. That the results for $v = 1$, 17, 18 are least well fitted is entirely expected since these are the least accurate measurements for the reasons mentioned earlier.

The best-fit model parameters are shown in Table 6, where the quoted errors are 3σ values determined from the fitting procedure. The $^5\Pi_u$ parameters assumed by Julienne[46] were obtained from a deperturbation of the second differences of the band origins of Ackerman and Biaume[30] by Julienne and Krauss,[45] who claimed errors of 10% in $A_{\alpha x}$ and $M_{\alpha x}$ and 0.002 Å in $R_{\alpha x}$. They later noted however that a deperturbation of the data of Curry and Herzberg[53] implied that $A_{\alpha x} \sim 75\ cm^{-1}$ and concluded that a cautious interpretation of the deperturbation with more liberal error estimates may have been warranted. Julienne's[46] parameters for the other repulsive states were estimated mainly from *ab initio* calculations with extra restraints being applied through qualitative observation of linewidth and lineshift trends. Where no errors are given in Table 6 the values are regarded as uncertain.

From Table 5, it is clear that the $^5\Pi_u$ interaction is the most important overall, and thus the $^5\Pi_u$ parameters are the most accurately determined by the fit. Within the error estimates there is agreement with the $A_{\alpha x}$ and $M_{\alpha x}$ of Julienne,[46] but not with the crossing point $R_{\alpha x}$. Agreement could readily be obtained by applying a more liberal error estimate to Julienne's[46] crossing point. A full *ab initio* calculation of the matrix element for the $^5\Pi_u$ state has been performed by Lefebvre-Brion[54] who obtains the value $68\ cm^{-1}$ at $r = 1.852$ Å.

The parameters for the $^1\Pi_u$ state are the next best determined by the fit. These rely heavily on the experimental width for the (1–0) band, but we have found that, even if this result is excluded from the fit, similar parameters result. Agreement is excellent between our values for $M_{\alpha x}$ and $R_{\alpha x}$ and those of Julienne,[46] but our matrix element is a little larger as exemplified by our observed width

Table 6. The best fit model parameters of this work compared with those adopted by Julienne[46]

	α	$A_{\alpha x}$, cm^{-1}	$M_{\alpha x}$, cm^{-1} Å^{-1}	$R_{\alpha x}$, Å
This work	$^5\Pi_u$	70.9±1.5	39700±1000	1.880±0.001
	$2^3\Sigma_u^+$	38.8±4.2	42300±8000	1.996±0.008
	$^3\Pi_u$	25.8±2.8	62700±5000	1.441±0.006
	$^1\Pi_u$	32.2±3.0	22400±1300	1.731±0.003
Julienne[46]	$^5\Pi_u$	65±7	40000±4000	1.875±0.002
	$2^3\Sigma_u^+$	55±6	45000±2500	2.000±0.010
	$^3\Pi_u$	30	80000	1.425
	$^1\Pi_u$	25±3	23000	1.730

for the (1–0) band. As implied earlier, the $^1\Pi_u$ parameters are sensitive to the assumed pressure broadening coefficient.

Our fitting procedure enables the $^3\Pi_u$ parameters to be reasonably well determined. Our matrix element is found to be fairly close to the rough estimate of Julienne,[46] but we obtain significantly different values for the slope and crossing point. This follows basically since we measure quite low widths ($\sim 0.13\ cm^{-1}$) for the (13–0) and (14–0) bands at $N = 10$. Julienne's parameters would imply widths of about $0.2\ cm^{-1}$ for these bands.

The $2^3\Sigma_u^+$ state is the least well determined by our procedure, the ~20% error in $M_{\alpha x}$ being the largest for any of the 12 parameters. Nevertheless, we find good agreement with the slope and crossing point of Julienne,[46] although our matrix element is significantly lower than his *ab initio* estimate.

Overall, there is quite good agreement for the 12 parameters, but the present experimenally based values are significantly more accurate than the previous estimates.[46] It does appear that the 10% uncertainty attributed by Julienne[46] to the *ab initio* matrix element calculations may be optimistic.

ROTATIONAL DEPENDENCE

The measured predissociation linewidths of this work are presented in Figs 2–20 as functions of rotation for the (1–0) to (19–0) bands. Also presented are model calculations made according to the method discussed earlier with the best fit parameters given in Table 6. The few rotational linewidths obtained by Frederick and Hudson[33] for the (8–0) to (13–0) bands are also shown.

The present results show a clear increase in linewidth with rotation for $v = 3$, 6, 8, 9, 12, 13, a decrease for $v = 5$, 7, 10, 11, 15–18, and no well defined behaviour for $v = 1$, 2, 4, 19. Widths from the (14–0) band appear to decrease slightly at first and then increase for the highest values of rotation studied. Lewis *et al.*[37] determined a significant increase in linewidth with rotation for $v = 9$, 12, in agreement with the trends observed here for these bands. The higher rotational linewidths of Frederick and Hudson[33] are in reasonable agreement with our measurements for $v = 8$, 9, 12, 13, all cases where an increase in width with rotation is observed. The sudden increase in linewidth at $J = 17$ observed by Frederick and Hudson[33] in the (11–0) band is not observed here, consistent with the measurements of Lewis *et al.*[37] The linewidths observed by Frederick and Hudson[33] for the (10–0) band are totally at variance with the current observations where we measure a decrease, rather than an increase, with rotation. This disagreement is consistent with that noted earlier for the bandhead width and oscillator strength for this band.

Apart from some minor discrepancies in the (4–0) and (5–0) bands, the measured and calculated rotational dependences of linewidth are in excellent agreement for $v = 1$–16. For higher values of

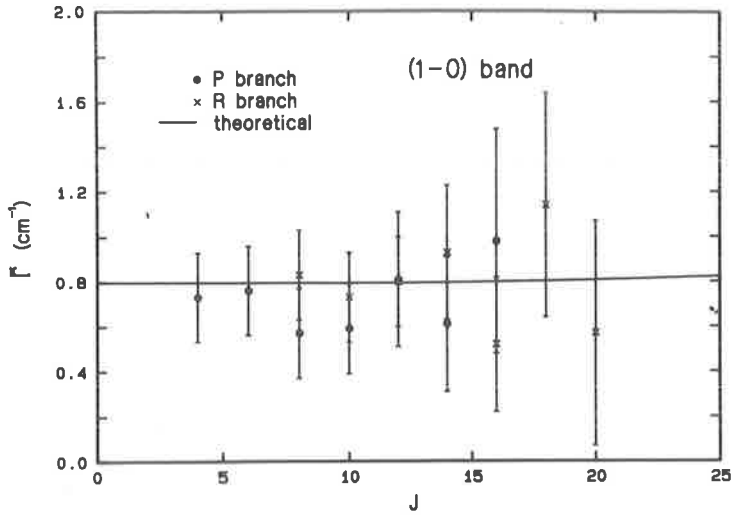

Fig. 2. The variation of FWHM predissociation linewidth with rotation for the (1–0) Schumann–Runge band of O_2.

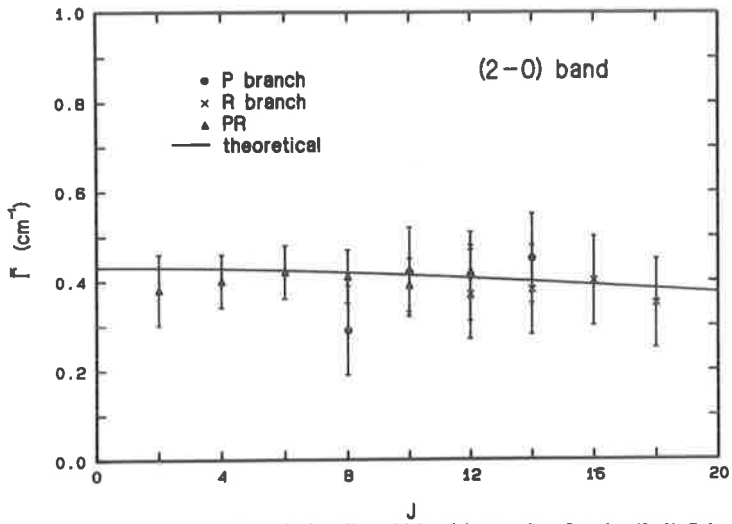

Fig. 3. The variation of FWHM predissociation linewidth with rotation for the (2–0) Schumann–Runge band of O_2.

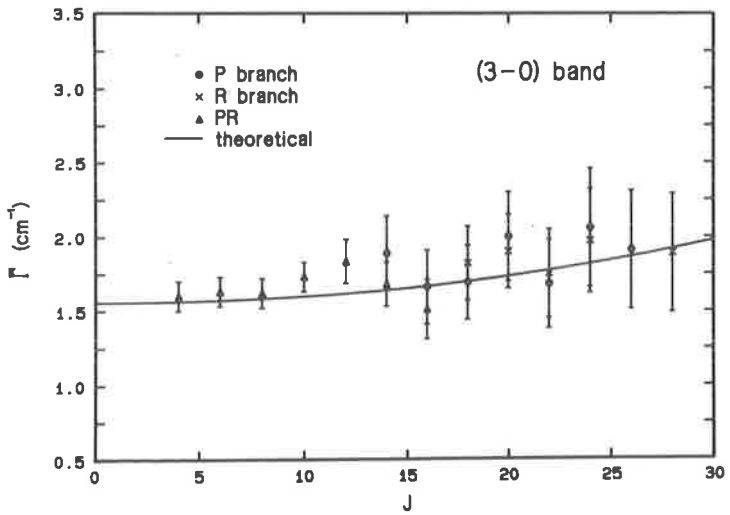

Fig. 4. The variation of FWHM predissociation linewidth with rotation for the (3–0) Schumann–Runge band of O_2.

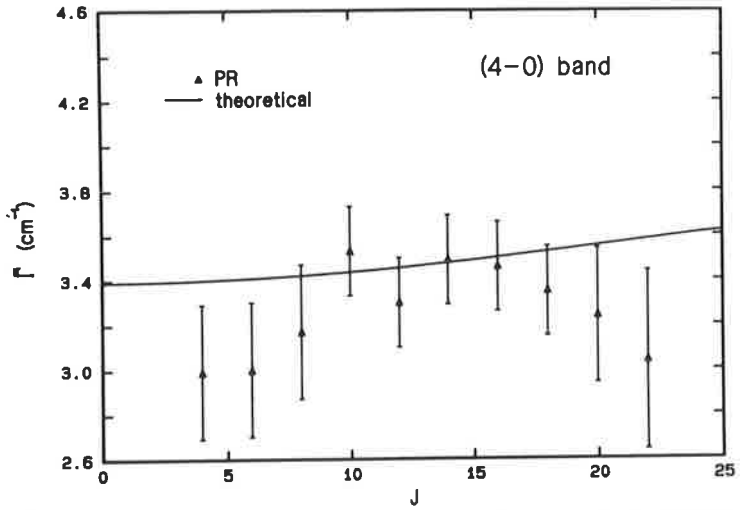

Fig. 5. The variation of FWHM predissociation linewidth with rotation for the (4–0) Schumann–Runge band of O_2.

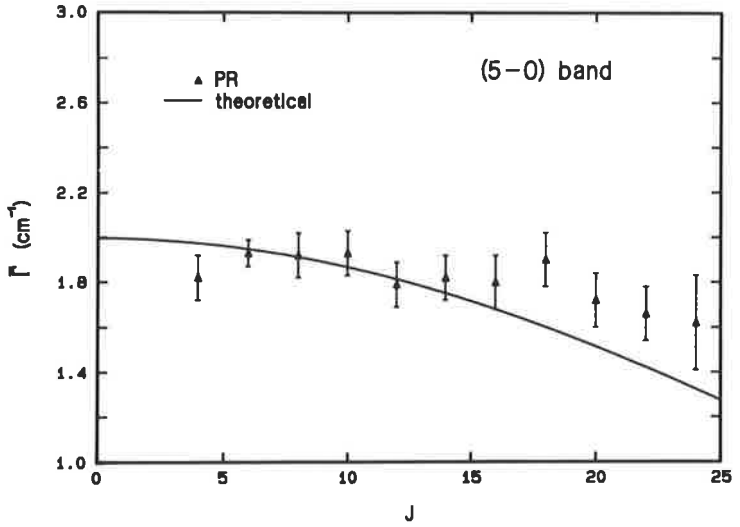

Fig. 6. The variation of FWHM predissociation linewidth with rotation for the (5–0) Schumann–Runge band of O_2.

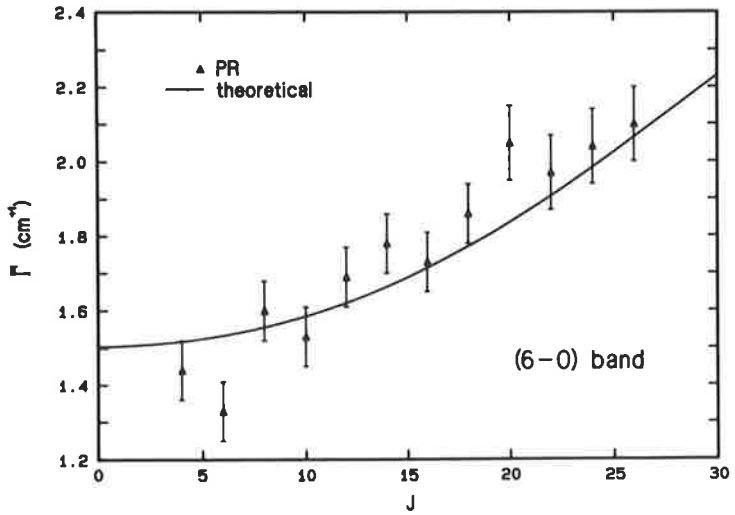

Fig. 7. The variation of FWHM predissociation linewidth with rotation for the (6–0) Schumann–Runge band of O_2.

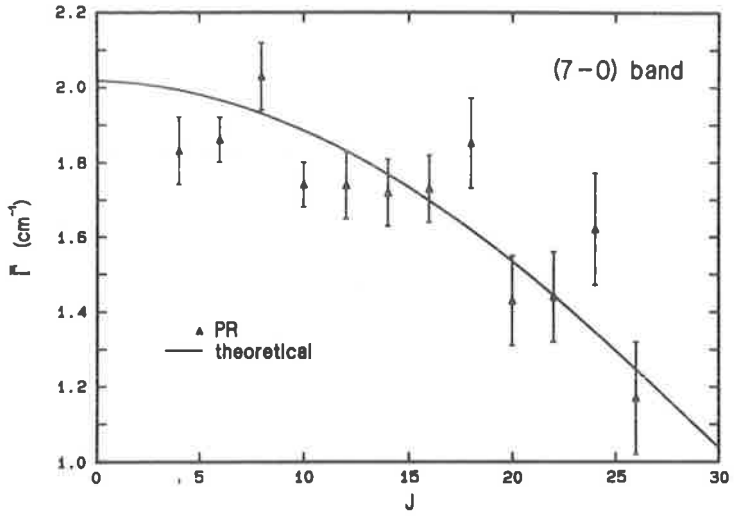

Fig. 8. The variation of FWHM predissociation linewidth with rotation for the (7–0) Schumann–Runge band of O_2.

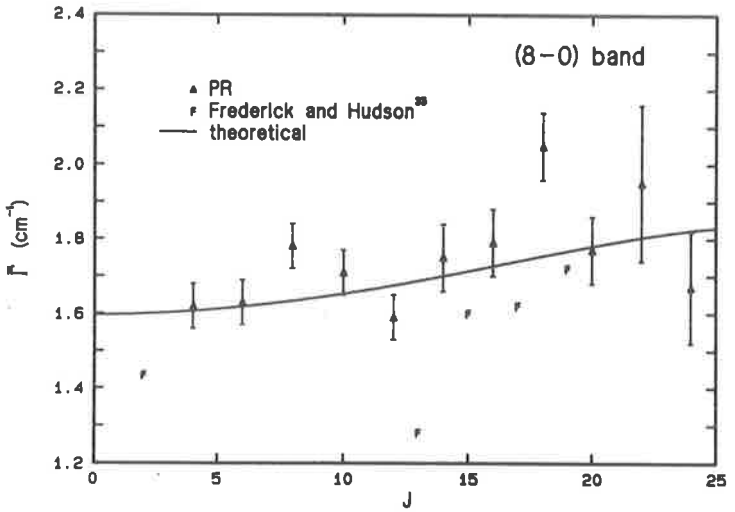

Fig. 9. The variation of FWHM predissociation linewidth with rotation for the (8–0) Schumann–Runge band of O_2.

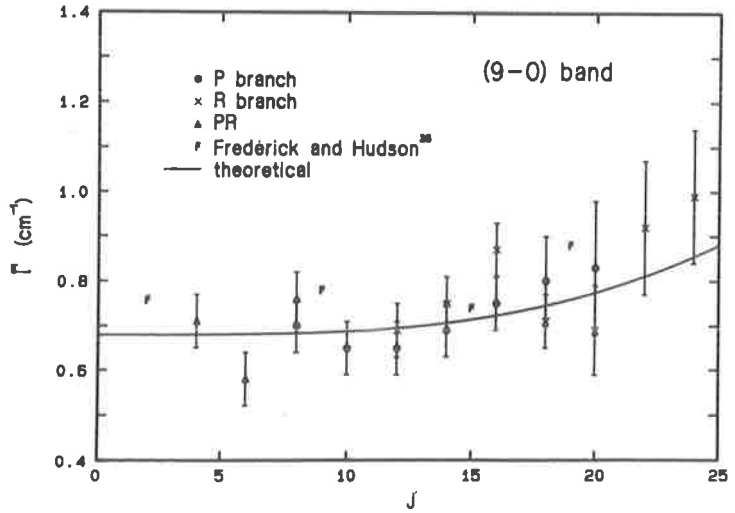

Fig. 10. The variation of FWHM predissociation linewidth with rotation for the (9–0) Schumann–Runge band of O_2.

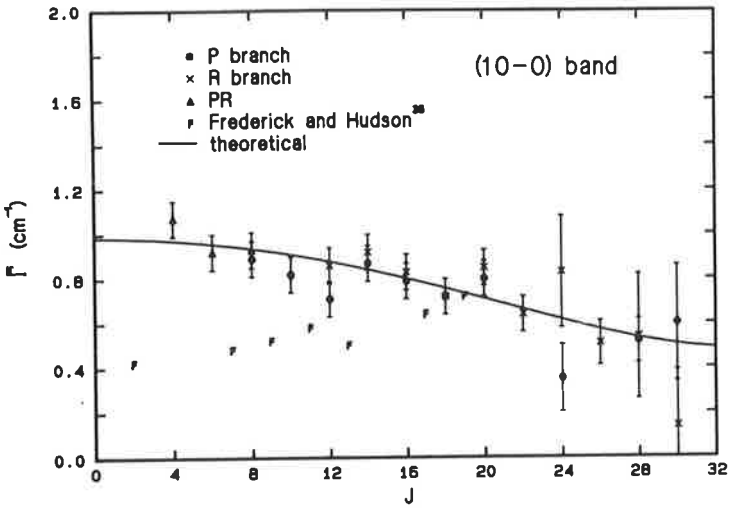

Fig. 11. The variation of FWHM predissociation linewidth with rotation for the (10–0) Schumann–Runge band of O_2.

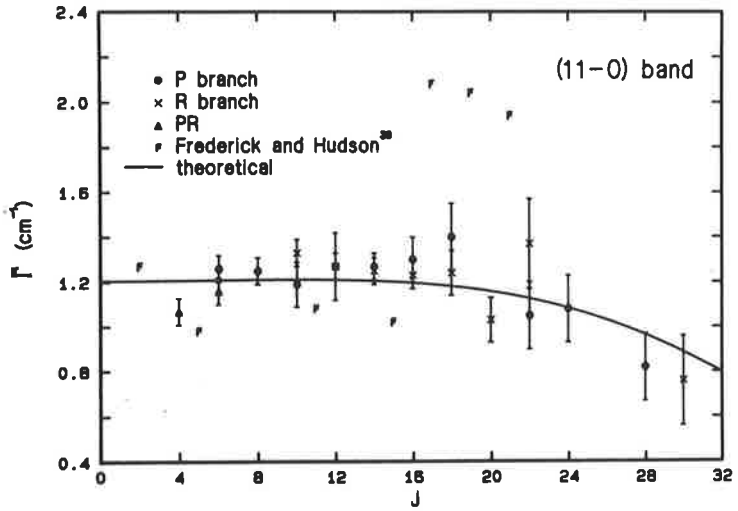

Fig. 12. The variation of FWHM predissociation linewidth with rotation for the (11–0) Schumann–Runge band of O_2.

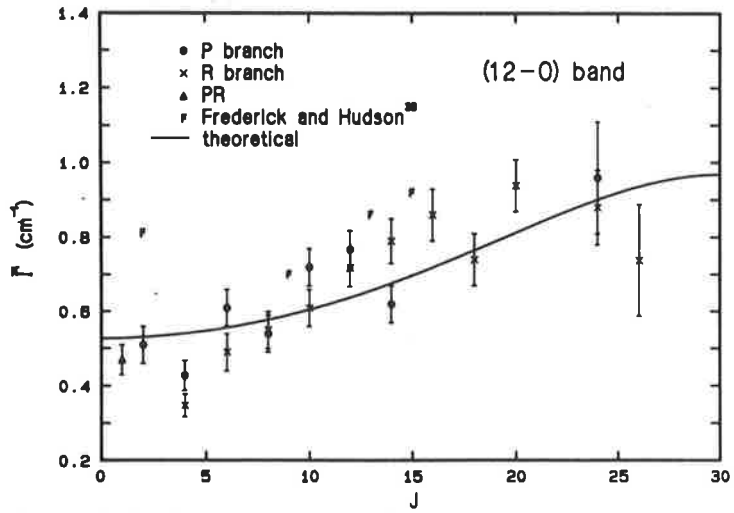

Fig. 13. The variation of FWHM predissociation linewidth with rotation for the (12–0) Schumann–Runge band of O_2.

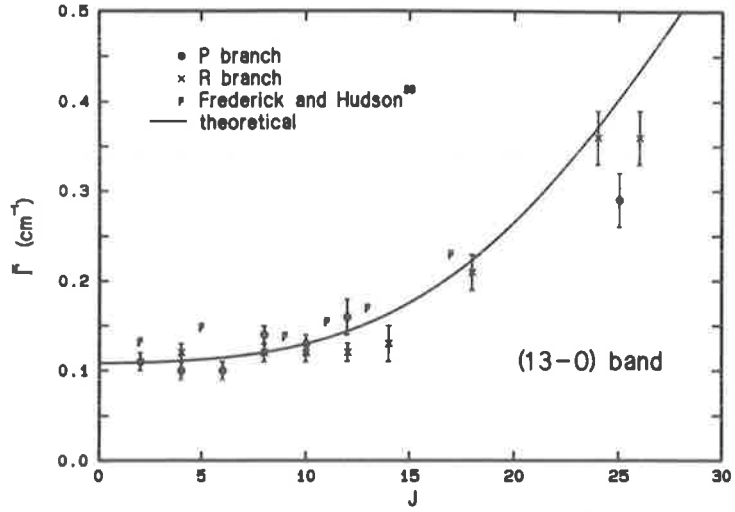

Fig. 14. The variation of FWHM predissociation linewidth with rotation for the (13–0) Schumann–Runge band of O_2.

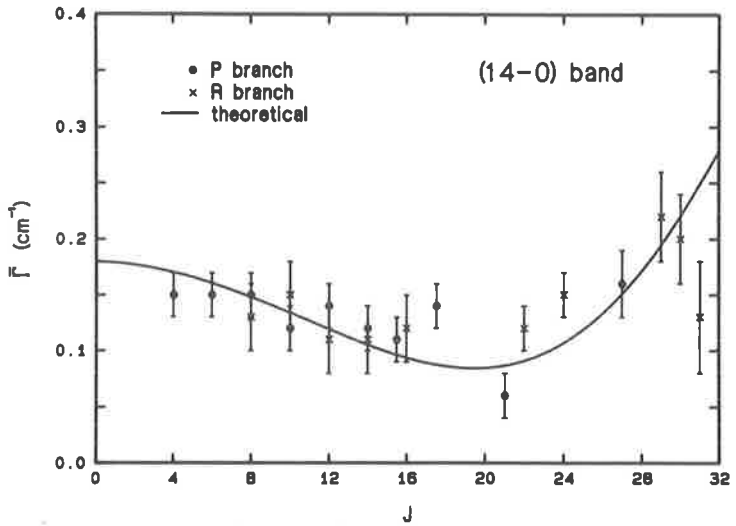

Fig. 15. The variation of FWHM predissociation linewidth with rotation for the (14–0) Schumann–Runge band of O_2.

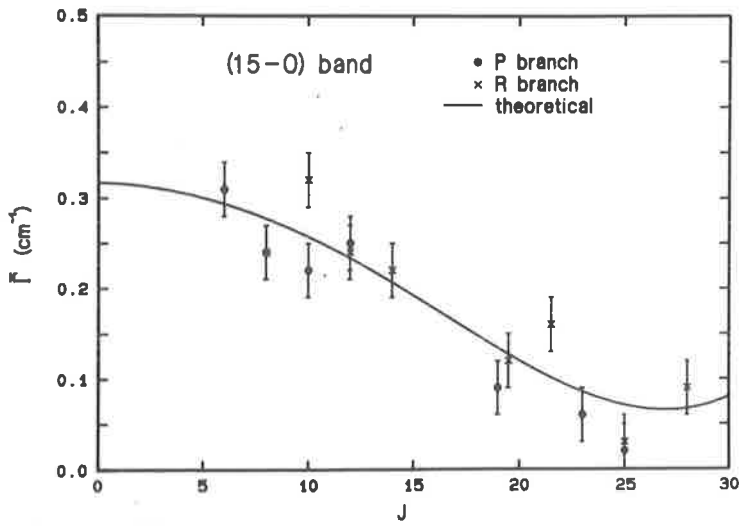

Fig. 16. The variation of FWHM predissociation linewidth with rotation for the (15–0) Schumann–Runge band of O_2.

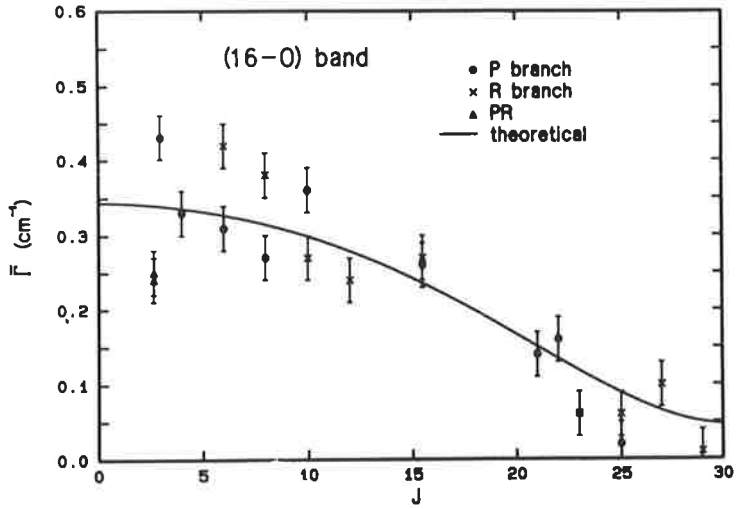

Fig. 17. The variation of FWHM predissociation linewidth with rotation for the (16–0) Schumann–Runge band of O_2.

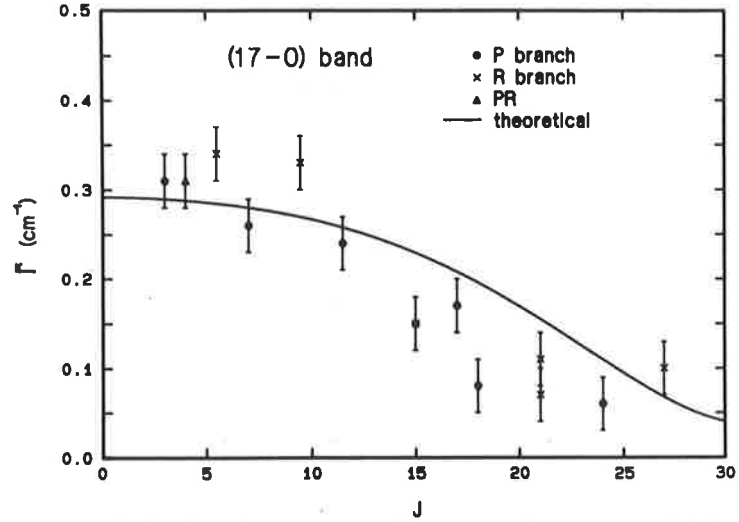

Fig. 18. The variation of FWHM predissociation linewidth with rotation for the (17–0) Schumann–Runge band of O_2.

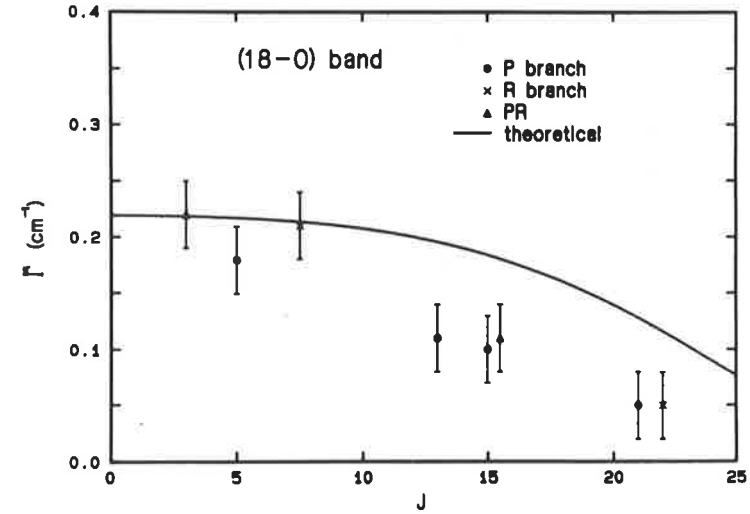

Fig. 19. The variation of FWHM predissociation linewidth with rotation for the (18–0) Schumann–Runge band of O_2.

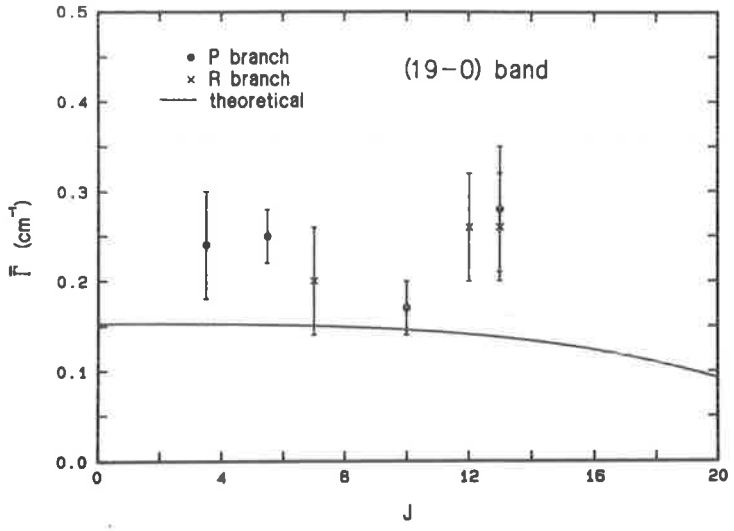

Fig. 20. The variation of FWHM predissociation linewidth with rotation for the (19–0) Schumann–Runge band of O_2.

rotation the measurements fall a little below the model values for $v = 17$, 18, and the (19–0) band widths are significantly larger than the predictions. That the biggest discrepancies occur in this region is not surprising considering both the difficulties of fully characterizing the spectrum in this region and also possible errors in the RKR $B^3\Sigma_u^-$ potential for turning points at higher v. Some of the discrepancies may also occur because the theoretical results are averaged over the fine structure while some of the experimental results are for resolved triplet components.

Since the model calculations have been effectively only normalized to the measurements for a fixed value of rotation, the agreement between the measured and calculated rotational dependences over such a range of vibration is a totally independent phenomenon providing powerful evidence that the predissociation model is correct in detail. The use of the mixed case (a)–(b) representation of the $B^3\Sigma_u^-$ state provides only small changes of linewidth for low values of rotation in bands where

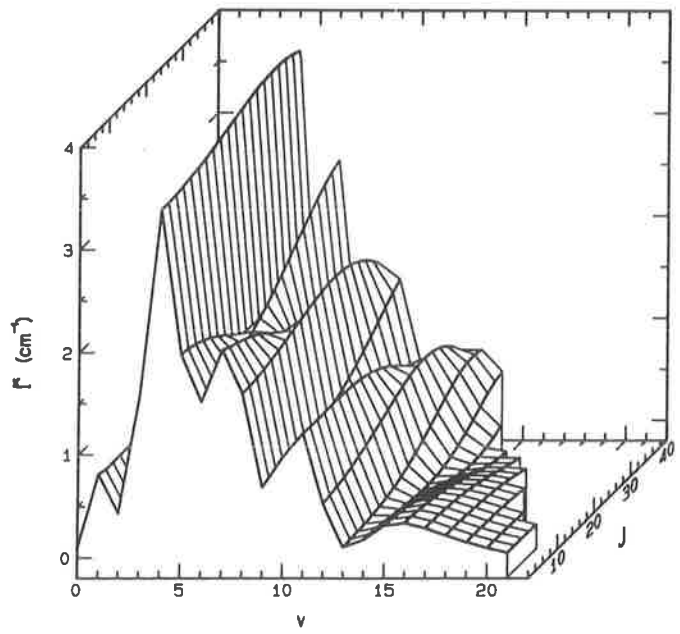

Fig. 21. A three-dimensional plot of the best fit model predissociation linewidths $\Gamma(vJ)$. The widths are averaged over the fine structure components for a given N.

Table 7. Polynomial coefficients $a_i(v)$ enabling the generation of model predissociation linewidths $\Gamma(vJ)$ using equation (5)

v	$a_1(v)$	$a_2(v)$	$a_3(v)$	$a_4(v)$	$a_5(v)$
0	0.100	1.7957-5*	3.5649-8	-2.1721-11	5.9110-15
1	0.798	-4.4677-5	2.5043-7	-2.2125-10	5.9972-14
2	0.431	-1.7124-4	9.6445-8	-2.7822-11	9.8534-15
3	1.557	3.5845-4	2.0714-7	-1.4908-10	3.8520-14
4	3.391	4.2616-4	-4.4225-8	-1.2254-10	2.4210-14
5	1.998	-1.1956-3	7.1429-8	8.9515-11	-3.8001-15
6	1.504	7.0758-4	3.2647-7	-3.1715-10	5.5516-14
7	2.018	-1.2253-3	1.9585-7	-5.8604-11	4.9873-14
8	1.597	5.3849-4	-1.4892-7	-2.3699-10	6.8732-14
9	0.679	1.4933-5	6.0852-7	-2.5064-10	1.9906-14
10	0.984	-6.7816-4	-6.0261-8	3.2007-10	-7.2881-14
11	1.205	1.1501-4	-5.5759-7	-2.0676-12	7.6844-14
12	0.527	7.0618-4	1.5578-7	-5.8527-10	1.6190-13
13	0.108	1.1204-4	8.1889-7	-4.8307-10	4.4999-14
14	0.180	-4.8661-4	6.1547-7	5.3847-11	-1.1040-13
15	0.317	-5.4893-4	1.4810-8	5.0776-10	-1.9647-13
16	0.344	-3.8944-4	-2.1801-7	3.5812-10	-4.5558-14
17	0.292	-1.9102-4	-3.5550-7	2.6219-10	3.0071-14
18	0.219	-6.7914-5	-3.9820-7	2.5275-10	0.0
19	0.153	-2.9441-5	-3.2100-7	1.1435-10	0.0
20	0.097	-2.7365-5	-3.9977-7	3.6219-10	0.0
21	0.051	-4.0120-5	-3.2188-7	-1.4023-9	0.0

*For 1.7957-5 read 1.7957×10^{-5}

interaction with the $^5\Pi_u$ state is not dominant, and so it seems that centrifugal distortion is the major contributor to the observed rotational dependences, contrary to the fears of Julienne[46] regarding the complexity of the situation. Nevertheless, some improvement may be obtained for the bands with $v > 16$ by refinements to the model.

Since the model widths represent the measurements well, we have performed polynomial fits of the form

$$\Gamma(vJ) = a_1(v) + a_2(v)x + a_3(v)x^2 + a_4(v)x^3 + a_5(v)x^4, \tag{5}$$

to the model values for $v = 0$–21, where $x = J(J+1)$, $J \leqslant 40$. The resulting coefficients are given in Table 7 and these should be useful in creating accurate atmospheric absorption models. It should be noted that, for $v > 15$, the maximum value of J for which equation (5) is applicable decreases below 40 because of the dissociation of the molecule.

The best fit model linewidths of this work for $v = 0$–21 are summarized neatly in Fig. 21 which emphasises the complexity of both the v and J dependences.

Note that, although the rotational axes in Figs 2–21 are labelled with J, this is in effect a mean J equal to N because of the averaging over the fine structure components in the model calculations. Separate calculations for each triplet component are not shown in Figs 2–21 since they would only be relevant for comparison with a small number of experimentally resolved triplet widths presented in Table 3. Nevertheless, the mixing of widths for unresolved and different resolved triplet components in Table 3 for $v \geqslant 15$ may result in a small increase in the apparent scatter of the measurements since the predissociation model shows that the individual fine structure widths for a fixed N can vary significantly. The largest predicted effect in this region is 25% near the bandhead of the (16–0) band.

CONCLUSIONS

Predissociation linewidth measurements presented here for the (1–0) to (19–0) Schumann–Runge bands of O_2 are the most extensive and the most accurate currently available. Systematic variation of linewidth with rotation is unambiguously demonstrated for the first time, with 15 out of the 19 bands studied showing such variation. The conclusions of Frederick and Hudson,[33] from their fragmentary measurements, that there is a tendency for the linewidth to increase with rotation is not verified, since a greater number of bands exhibit a decrease than an increase. The conclusions of Lewis *et al.*[37] that there is in general no measurable variation with rotation appears to be merely a reflection on the statistical accuracy of the earlier measurements which were in fact not originally designed to detect rotational variation of linewidth. A theoretical predissociation model of the kind developed by Julienne,[46] with interaction between the $B^3\Sigma_u^-$ state and four repulsive states, $^5\Pi_u$, $2^3\Sigma_u^+$, $^3\Pi_u$ and $^1\Pi_u$, is found to be excellent in explaining the observed vibrational and rotational variation of linewidth. Centrifugal distortion seems to be the major contributor to the observed dependence of linewidth on rotation. Repulsive state parameters resulting from a model fit to the observed vibrational widths are the most accurate currently available and agree reasonably well with the assumed values of Julienne,[46] but the *ab initio* matrix elements exhibit a 25% r.m.s. deviation from the current determinations. Polynomial fits are presented to the best fit model rotational linewidths of this work in order to enable accurate transmission calculations by atmospheric modellers.

Acknowledgements—The authors would like to thank C. Dedman and K. Lonsdale for valuable technical assistance.

REFERENCES

1. R. D. Hudson, V. L. Carter and E. L. Brieg, *J. Geophys. Res.* **74,** 4079 (1969).
2. M. Ackerman, F. Biaume and G. Kockarts, *Planet. Space Sci.* **18,** 1639 (1970).
3. G. Kockarts, in *Mesospheric Models and Related Experiments* (Edited by G. Fiocco), pp. 160–176. D. Reidel, Dordrecht, The Netherlands (1971).
4. M. Ackerman, in *Mesospheric Models and Related Experiments* (Edited by G. Fiocco), pp. 149–159. D. Reidel, Dordrecht, The Netherlands (1971).
5. R. T. Brinkman, in *Mesospheric Models and Related Experiments* (Edited by G. Fiocco), pp. 89–102. D. Reidel, Dordrecht, The Netherlands (1971).
6. R. D. Hudson and S. H. Mahle, *J. Geophys. Res.* **77,** 2902 (1972).
7. T. M. Fang, S. C. Wofsy and A. Dalgarno, *Planet. Space Sci.* **22,** 413 (1974).
8. J. H. Park, *J. Atmos. Sci.* **31,** 1893 (1974).
9. H. Muramatsu, *Pap. Met. Geophys.* **26,** 219 (1973).
10. R. P. Turco, *Geophys. Surv.* **2,** 153 (1975).
11. G. Kockarts, *Planet. Space Sci.* **24,** 589 (1976).
12. A. J. Blake, *J. Geophys. Res.* **84,** 3272 (1979).
13. J. E. Frederick and R. D. Hudson, *J. Atmos. Sci.* **37,** 1099 (1980).
14. J. E. Frederick and R. D. Hudson, *J. Atmos. Sci.* **37,** 1088 (1980).
15. M. Nicolet and W. Peetermans, *Planet. Space Sci.* **28,** 85 (1980).
16. M. Allen and J. E. Frederick, *J. Atmos. Sci.* **39,** 2066 (1982).
17. S. Cieslik and M. Nicolet, *Planet. Space Sci.* **21,** 925 (1973).
18. M. Nicolet, *J. Geophys. Res.* **86,** 5203 (1981).
19. R. J. Cicerone and J. L. McCrumb, *Geophys. Res. Lett.* **7,** 251 (1980).
20. M. Nicolet, *J. Geophys. Res.* **89,** 2573 (1984).
21. B. R. Lewis, L. Berzins and J. H. Carver, *JQSRT* (1986) In press.
22. P. J. Flory, *J. chem. Phys.* **4,** 23 (1936).
23. M. W. Feast, *Proc. phys. Soc. Lond.* **A62,** 114 (1949).
24. D. H. Volman, *J. chem. Phys.* **24,** 122 (1956).

25. P. G. Wilkinson and R. S. Mulliken, *Astrophys. J.* **125,** 594 (1957).
26. D. Rakotoarijimy, S. Weniger and H. Grenat, *C.r. Acad. Sci., Paris* **246,** 2883 (1958).
27. L. Herman, R. Herman and D. Rakotoarijimy, *J. Phys. Radium* **22,** 1 (1961).
28. P. K. Carroll, *Astrophys. J.* **129,** 794 (1959).
29. P. H. Krupenie, *J. phys. chem. Ref. Data* **1,** 423 (1972).
30. M. Ackerman and F. Biaume, *J. molec. Spectrosc.* **35,** 73 (1970).
31. R. D. Hudson and V. L. Carter, *J. opt. Soc. Am.* **58,** 1621 (1968).
32. R. D. Hudson and V. L. Carter, *Can. J. Phys.* **47,** 1840 (1969).
33. J. E. Frederick and R. D. Hudson, *J. molec. Spectrosc.* **74,** 247 (1979).
34. B. R. Lewis, J. H. Carver, T. I. Hobbs, D. G. McCoy and H. P. F. Gies, *JQSRT* **20,** 191 (1978).
35. B. R. Lewis, J. H. Carver, T. I. Hobbs, D. G. McCoy and H. P. F. Gies, *JQSRT* **22,** 213 (1979).
36. H. P. F. Gies, S. T. Gibson, D. G. McCoy, A. J. Blake and B. R. Lewis, *JQSRT* **26,** 469 (1981).
37. B. R. Lewis, J. H. Carver, T. I. Hobbs, D. G. McCoy and H. P. F. Gies, *JQSRT* **24,** 365 (1980).
38. P. L. Smith, H. E. Griesinger, J. H. Black, K. Yoshino and D. E. Freeman, *Astrophys. J.* **277,** 569 (1984).
39. H. F. Schaefer and F. E. Harris, *J. chem. Phys.* **48,** 4946 (1968).
40. H. F. Schaefer and W. H. Miller, *J. chem. Phys.* **55,** 4107 (1971).
41. I. Riess and Y. Ben-Aryeh, *JQSRT* **9,** 1463 (1969).
42. J. N. Murrell and J. M. Taylor, *Molec. Phys.* **16,** 609 (1969).
43. M. S. Child, *J. molec. Spectrosc.* **33,** 487 (1970).
44. S. Durmaz and J. N. Murrell, *Molec. Phys.* **21,** 209 (1971).
45. P. S. Julienne and M. Krauss, *J. molec. Spectrosc.* **56,** 270 (1975).
46. P. S. Julienne, *J. molec. Spectrosc.* **63,** 60 (1976).
47. M. L. Sink and A. D. Bandrauk, *J. chem. Phys.* **66,** 5313 (1977).
48. B. R. Lewis, *Appl. Opt.* **22,** 1546 (1983).
49. K. Yoshino, D. E. Freeman, J. R. Esmond and W. H. Parkinson, *Planet. Space Sci.* **30,** 339 (1983).
50. J. B. Tatum and J. K. G. Watson, *Can. J. Phys.* **49,** 2693 (1971).
51. K. Yoshino, D. E. Freeman and W. H. Parkinson, *J. phys. chem. Ref. Data* **13,** 207 (1984).
52. S. T. Gibson, H. P. F. Gies, A. J. Blake, D. G. McCoy and P. J. Rogers, *JQSRT* **30,** 385 (1983).
53. J. Curry and G. Herzberg, *Ann. Phys.* **19,** 800 (1934).
54. H. Lefebvre-Brion, private communication (see Ref. 46).

J. Quant. Spectrosc. Radiat. Transfer Vol. 37, No. 3, pp. 219–228, 1987
Printed in Great Britain

0022-4073/87 $3.00 + 0.00
Pergamon Journals Ltd

OSCILLATOR STRENGTHS FOR THE SCHUMANN–RUNGE BANDS OF $^{16}O^{18}O$

B. R. LEWIS, L. BERZINS and J. H. CARVER
Research School of Physical Sciences, The Australia, National University, Canberra, Australia 2600

(*Received* 21 *May* 1986)

Abstract—Oscillator strengths were measured for the (2–0)–(15–0) Schumann–Runge bands of $^{16}O^{18}O$. Individual rotational lines were studied at a resolution of ~0.05 Å. Band oscillator strengths decrease with increasing rotation at a rate intermediate between those for $^{16}O_2$ and $^{18}O_2$. Our measurements are in good agreement with oscillator strengths calculated using potential curves and dipole moments derived from $^{16}O_2$ measurements, and support conclusions that $^{16}O^{18}O$ plays only a minor role in the photodissociation of atmospheric O_2. Dipole moments deduced from our oscillator strengths agree well with those obtained for $^{16}O_2$, $^{18}O_2$, as well as with recent *ab initio* and semi-empirical determinations.

INTRODUCTION

We have recently reported extensive measurements on the vibrational and rotational variation of oscillator strength and predissociation linewidth in the Schumann–Runge bands of $^{16}O_2$ and $^{18}O_2$.[1–4] $^{16}O^{18}O$ constitutes 0.408% of atmospheric oxygen[5] and many absorption lines of this species can be seen in the spectrum of normal O_2.[1] A knowledge of the oscillator strengths and predissociation linewidths of $^{16}O^{18}O$ is therefore necessary to the construction of accurate line-by-line absorption models for atmospheric O_2.[1] Cicerone and McCrumb[6] suggested that $^{16}O^{18}O$ may be an important contributor to the photodissociation of atmospheric O_2, due to isotope effects resulting in some $^{16}O^{18}O$ lines lying between those of $^{16}O_2$, but their conclusions were not verified in the extensive theoretical modelling of the $^{16}O^{18}O$ absorption spectrum by Blake *et al.*[7] The complete lack of experimental data on the absorption intensities of the Schumann–Runge bands of $^{16}O^{18}O$ suggests that such measurements should be performed to resolve this disagreement. Julienne,[8] in his important work outlining the theoretical basis of the predissociation observed in the Schumann–Runge bands of O_2, concluded that linewidth measurements on isotopically substituted O_2 would be very useful in obtaining a more complete understanding of the predissociation. With instruments of limited resolution it is necessary to have a knowledge of the oscillator strengths before linewidths can be determined.[1]

The existence of $^{16}O^{18}O$ in the atmosphere was first discovered by Dieke and Babcock[9] who observed an extremely weak band near the (0–0) band of the $b^1\Sigma_g^+ - X^3\Sigma_g^-$ system of O_2 at 7596 Å. The analysis of Giauque and Johnston[10] confirmed that the band originated from the $^{16}O^{18}O$ molecule. Babcock and Herzberg[11] investigated this system of forbidden bands and derived spectroscopic constants for the B and X states of $^{16}O^{18}O$. The only Schumann–Runge wavenumbers for $^{16}O^{18}O$ were obtained by Hecht *et al.*[12] who tabulated the positions of 89 lines in the (6–0), (8–0)–(10–0) bands and determined some spectroscopic constants. Steinbach and Gordy[13] measured rotational transitions in the microwave spectrum of $^{16}O^{18}O$ and derived precise spectroscopic constants for the ground state. Edwards *et al.*[14] determined rotational constants and bond lengths for the ground states of $^{16}O_2$, $^{16}O^{18}O$ and $^{18}O_2$ from an analysis of pure rotational Raman spectra. No experimental oscillator strengths or predissociation linewidths are available for the Schumann–Runge bands of $^{16}O^{18}O$.

This work aims to provide extensive line-by-line measurements of oscillator strength for $^{16}O^{18}O$. Predissociation linewidths measured in association with this work are presented in a companion paper.[15] We present oscillator strengths for as many rotational lines as possible from the (2–0)–(15–0) Schumann–Runge bands of $^{16}O^{18}O$, and good agreement is found with values calculated using the potential curves and dipole moment of our previous $^{16}O_2$ work.[1]

EXPERIMENTAL METHOD

The experimental system was identical with that used for the $^{18}O_2$ measurements.[3] Briefly, background radiation from an H_2 continuum was dispersed by a 2.2 m scanning VUV monochromator at a resolution of ~ 0.05 Å, and was detected photoelectrically before entering and after leaving the 10 cm sealed quartz cells[3] containing the isotopically enriched samples.

The individual cells were filled with pressures in the range 2 Torr–2 atm using the technique described in detail[3] for $^{18}O_2$, and were mounted on a carousel[3] which enabled concurrent scans of different samples to be taken as desired. The scanning system was microcomputer controlled.

The isotopically enriched samples were obtained from Amersham (U.K.) and had an ^{18}O abundance of 20%, implying a statistical mixture of 64% $^{16}O_2$, 32% $^{16}O^{18}O$ and 4% $^{18}O_2$. Preliminary absorption measurements indicated that the amount of $^{16}O^{18}O$ present was considerably $< 32\%$, indicating a non-statistical mixture, so we irradiated the samples for several hours with a mercury lamp to promote dissociation and statistical recombination. This procedure rapidly increased the proportion of $^{16}O^{18}O$, and we were able to confirm approximately the manufacturer's enrichment figure.

Lengthy absorption scans were performed on all samples with wavelength increments of 5–10 mÅ depending on the linewidths, and the absorption data was stored on disc. The statistical error of the unnormalized transmissions (detector signal/monitor signal) was better than 1%.

The presence of a significant proportion of $^{16}O_2$ in the isotopic mixture resulted in two advantages over the nearly pure $^{18}O_2$ sample used previously.[3] Firstly, the strong $^{16}O_2$ absorption lines provided an inbuilt wavelength calibration in association with the wavenumber tables of Yoshino *et al.*,[16] and secondly, it was possible to check the partial pressure of $^{16}O_2$, and hence the total pressure, by observing the $^{16}O_2$ absorption and applying the known strengths[1,2] for this species. The individual cell pressures were 4.0, 29, 204, 771 and 1573 Torr.

There are considerable difficulties in the measurement of the $^{16}O^{18}O$ absorption spectrum. For a mixture with $^{16}O_2$ and $^{18}O_2$ there are effectively four times the number of rotational lines as there are for a homogeneous sample of one of the homonuclear species. The problems of analysis caused by overlapping lines are thus greatly increased, and the knowledge of line strengths[1-4] for $^{16}O_2$ and $^{18}O_2$ is clearly important. The 20% ^{18}O enriched mixture was close to ideal in minimizing the difficulties. While a 50% ^{18}O enrichment would result in the maximum (50%) concentration of $^{16}O^{18}O$, it would also result in equal (25%) concentrations of $^{16}O_2$ and $^{18}O_2$, and the resolution of $^{16}O^{18}O$ lines would be more difficult than in the 20% ^{18}O mixture where the $^{18}O_2$ lines are much weaker than the $^{16}O^{18}O$ lines.

DATA ANALYSIS

The data-analysis procedures and the O_2 absorption model have been discussed in detail previously.[1,3] Briefly, absorption profiles and equivalent widths were recorded for all lines of interest

Table 1. Spectroscopic constants (cm^{-1}) for the $B\,^3\Sigma_u^-$ state of $^{16}O^{18}O$ determined from our wavenumber measurements. The errors are 3σ determined from the fitting procedure and values in parentheses are either estimates or calculations based on the constants for $^{16}O_2$

v'	ν_0	B	$D \times 10^6$	λ	$-\mu_0$	$-\mu_J \times 10^5$
0	(49369.22)	(0.7864)	(4.1)	(1.74)	(0.029)	(0.0)
1	(50038.37)	(0.7560)	(4.4)	(1.74)	(0.029)	(0.0)
2	(50686.44)	(0.7434)	(4.5)	(1.74)	(0.029)	(0.0)
3	51311.63 ± 0.29	0.7294 ± 0.0012	(4.7)	(1.77)	(0.030)	(0.0)
4	51914.26 ± 0.55	0.7137 ± 0.0020	(5.3)	(1.81)	(0.030)	(0.0)
5	52493.00 ± 0.37	0.6991 ± 0.0009	(5.5)	(1.84)	(0.031)	(0.0)
6	53043.26 ± 0.67	0.6855 ± 0.0017	(6.2)	(1.88)	(0.031)	(0.0)
7	53567.50 ± 0.27	0.6654 ± 0.0007	(6.7)	(1.91)	(0.032)	(0.0)
8	54060.94 ± 0.31	0.6457 ± 0.0010	(7.8)	(1.94)	(0.032)	(0.0)
9	54522.92 ± 0.21	0.6230 ± 0.0007	(7.9)	(1.98)	(0.033)	(0.0)
10	54949.60 ± 0.32	0.6012 ± 0.0012	(8.8)	(2.05)	(0.034)	(0.6)
11	55338.72 ± 0.63	0.5740 ± 0.0028	(9.7)	(2.10)	(0.039)	(1.2)
12	55689.87 ± 0.26	0.5425 ± 0.0010	(12.0)	(2.25)	(0.047)	(2.1)
13	55998.18 ± 0.23	0.5095 ± 0.0009	(14.4)	(2.42)	(0.067)	(3.2)
14	56263.78 ± 0.24	0.4729 ± 0.0007	(17.8)	(2.74)	(0.087)	(4.9)
15	56485.72 ± 0.40	0.4350 ± 0.0017	(21.0)	(3.11)	(0.129)	(6.2)
16	56668.00 ± 0.41	0.3893 ± 0.0028	(24.0)	(3.61)	(0.195)	(8.0)
17	(56813.09)	(0.3489)	(29.0)	(4.54)	(0.272)	(10.0)

at several pressures, and an equivalent width analysis technique allowed the simultaneous determination of both oscillator strength and predissociation linewidth[15] by an iterative procedure. Absolute backgrounds, which could not be obtained experimentally, were determined as in the case[3] of $^{18}O_2$. The model parameters used for the $^{16}O_2$ and $^{18}O_2$ constituents have been given previously,[1,3] and only those relevant to $^{16}O^{18}O$ will be discussed here.

Spectroscopic constants for the $X^3\Sigma_g^-$ state of $^{16}O^{18}O$ were taken from the microwave work of Steinbach and Gordy,[13] and were used to generate the manifold of rovibrational levels for the ground state and the corresponding weighted Boltzmann factors. The gas mixture was characterized as 64% $^{16}O_2$, 32% $^{16}O^{18}O$ and 4% $^{18}O_2$ and the overall level populations for the mixture were determined from the species Boltzmann factors and the above proportions, consistent with correct overall normalization. As noted earlier, the known wavenumbers[16] of the $^{16}O_2$ absorption lines in the scans of our gas mixture enabled us to interpolate wavenumbers for all the observable $^{16}O^{18}O$ lines. Spectroscopic constants obtained from our measurements were used for the (3–0)–(16–0) bands. These constants are shown in Table 1 for $0 \leqslant v' \leqslant 17$. Values in parentheses are either calculated in the manner of Blake *et al.*,[7] estimated or extrapolated. The G and B values in Table 1 agree reasonably well with totally calculated values and represent the observed spectrum well, but it should be stressed that the constants that we have obtained should be treated as a guide only, in the absence of any extensive and reliable spectrographic measurements. Line wavelengths for $v'' = 1$ were calculated from the $v'' = 0$ wavelengths and the known ground state energy levels. Hönl–London factors were taken from Tatum and Watson[17] for $^3\Sigma^- - ^3\Sigma^-$ transitions with coupling intermediate between Hund's cases (a) and (b), and with transformation coefficients determined from the energy levels obtained above.

Oscillator strengths and linewidths are necessary to the model in order to account for the effects of distant, neighbouring or overlapping lines. The initial oscillator strengths for $^{16}O^{18}O$ were calculated using the potential curves and dipole moment from the previous $^{16}O_2$ work.[1] The linewidths were calculated using the curve crossing parameters deduced previously[2] for $^{16}O_2$. The model included the rotational variation of both oscillator strength and linewidth and the final oscillator strengths (and widths) were not sensitive to the initial estimates.

A Gaussian instrument function of FWHM ~ 0.05 Å was folded into the analysis in order to check the reproducibility of the observed scan profiles. Theoretically, the equivalent width of an isolated line is independent of the instrument resolution,[18] but small errors can occur when the instrument function is neglected for scans with limited range of integration.

The underlying continuum and its pressure coefficients are set equal to zero in this model, but the method used for background determination automatically compensates for this.[3] The pseudo-continuum arising from the summation of Lorentzian wings of absorption lines is included[1] as for $^{16}O_2$. The pressure broadening coefficient for $^{16}O^{18}O$ is taken to be 0.20 cm^{-1}/atm, as for $^{16}O_2$, with a small mass correction factor.

Because of the limited number of pressures and the fixed cell length, the ideal pairs of pressures for application of the full equivalent width method were not always available. In these cases a least-squares profile fitting technique similar to that used for $^{16}O_2$ by Frederick and Hudson[19] was employed. While this procedure introduces a direct dependence on the instrument function, it does enable oscillator strength and width values to be determined from scans taken at a single pressure.

RESULTS

The nuclei of the $^{16}O^{18}O$ molecule are distinguishable, unlike those of $^{16}O_2$ and $^{18}O_2$, and therefore the symmetry conditions which result in alternate rotational levels being missing in the homonuclear species no longer apply. Thus all rotational levels occur, and a system of $^{16}O^{18}O$ molecules occupies twice as many states as a $^{16}O_2$ or $^{18}O_2$ system, and has approximately half as many molecules in any given state. The spectrum of $^{16}O^{18}O$ should then have twice as many lines as that of $^{16}O_2$ or $^{18}O_2$, but the lines should be only approximately half as strong as those of corresponding transitions in the homonuclear species. These conclusions are verified beautifully in Fig. 1, an experimental scan of our isotopic sample in the region of the (6–0) Schumann–Runge band. The dominant feature is the (6–0) band of $^{16}O_2$, with a band origin near 1882Å and a classical Boltzmann rotational envelope. Starting at an isotopically shifted band origin near 1885Å is the

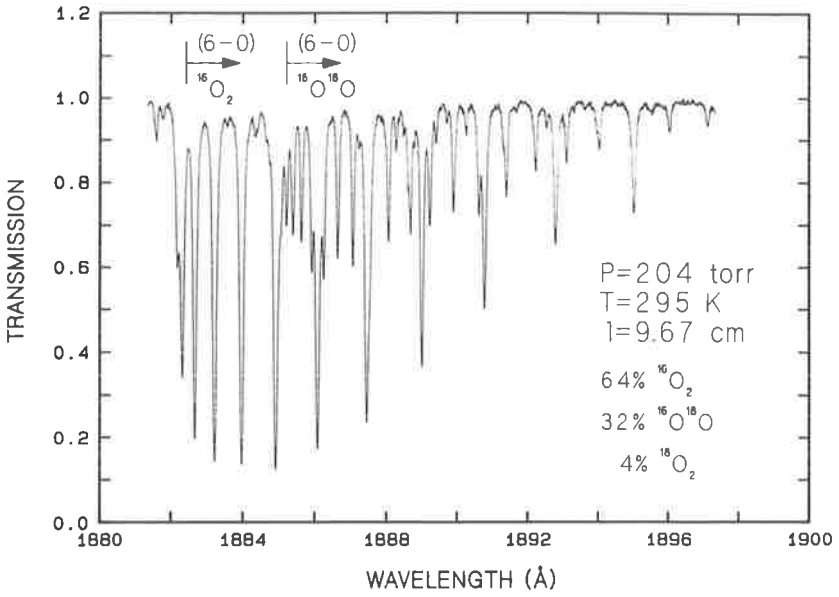

Fig. 1. The measured absorption spectrum of the 20% ^{18}O enriched oxygen mixture in the wavelength region 1880–1900Å. The (6–0) bands of both $^{16}O_2$ and $^{16}O^{18}O$ are clearly seen and the isotopic shift of the band origin and the occurrence of twice as many rotational lines for $^{16}O^{18}O$ are also evident.

(6–0) band of $^{16}O^{18}O$. It is clear that the density of lines for $^{16}O^{18}O$ is twice that of $^{16}O_2$, and the line intensities are about one-quarter of those for $^{16}O_2$. Half of this intensity drop arises as described above, and the other half because there is twice as much $^{16}O_2$ as $^{16}O^{18}O$ in our sample. The wisdom of the chosen 20% ^{18}O enrichment is clear when one notes the small intensities of the $^{18}O_2$ lines above 1888Å.

Some 158 independent oscillator strength measurements are presented here. Tables 2 and 3 list oscillator strengths for rotational lines from the P and R branches of the (2–0)–(15–0) Schumann–Runge bands of $^{16}O^{18}O$. These are effective band oscillator strengths deduced from the particular rotational lines studied. Results were obtained from the single scan equivalent width method (linewidth fixed theoretically) for $v' = 2$, $v' = 9$ ($N'' \geqslant 20$), $v' = 14$($N'' = 25$), and from the simple scan profile fitting method for $v' = 3$–5, $v' = 6$ ($N'' \geqslant 20$), $v' = 7$ ($N'' \geqslant 9$), $v' = 8$, $v' = 9$ ($N'' = 18,19$), $v' = 10$($N'' \geqslant 18$). In all other cases the full two scan equivalent width method of data analysis was used. When scans were performed on unresolved PR doublets the deduced oscillator strength was referred to the R component, and the oscillator strength for the P component was calculated using theoretical P/R strength ratios. It is also expected[20] that the oscillator strength will vary with the fine-structure component, but this effect is too small to verify here and all results have been averaged over the individual fine-structure components where these have been measured separately. The errors given in Tables 2 and 3 are essentially due to counting statistics. Additional errors due to uncertainties in pressure, temperature and cell length are expected to be $\sim 5\%$. Oscillator strengths for the stronger lines near the bandheads are robust, while those for the weaker lines show an increasing sensitivity to the interpolated backgrounds and other model parameters. The much greater density of lines in the 20% ^{18}O gas sample makes it impossible to follow the development of the $^{16}O^{18}O$ Schumann–Runge bands to a high a vibration as we have done for $^{16}O_2$ and $^{18}O_2$, and the overall reliability of these results is a little less for the same reasons.

The results in Tables 2 and 3 show that the vibrational oscillator strengths increase up to $v' = 14$–15, but the extent of the present work does not allow us to determine unambiguously the position of the maximum. The decrease in oscillator strength with rotation due to centrifugal distortion[3] is observed here at a rate intermediate between those observed[1,3] for $^{16}O_2$ and $^{18}O_2$, as expected theoretically. In cases where the P and R branches are resolved, the P branch oscillator strengths exceed those of the R branch by an amount intermediate between those observed[1,3] for $^{16}O_2$ and $^{18}O_2$. In Fig. 2 our measured oscillator strengths are presented graphically for the (9–0) Schumann–Runge band of $^{16}O^{18}O$. The approximately linear decrease in oscillator strength with

Table 2. Measured oscillator strengths $f(v', N'') \times 10^x$ for the R branches of the (2–0)–(15–0) Schumann–Runge bands of $^{16}O^{18}O$

v'	2	3	4	5	6	7	8	9	10	11	12	13	14	15
N''														
1														
2							4.74 ± 0.30							
3							4.33 ± 0.44							
4					1.16 ± 0.08		4.72 ± 0.30					2.31 ± 0.15		
5	1.21 ± 0.09				1.18 ± 0.09		4.59 ± 0.30				1.85 ± 0.10			
6		5.42 ± 0.30		4.87 ± 0.27	1.14 ± 0.08							2.21 ± 0.15	2.64 ± 0.15	
7				4.82 ± 0.23										2.89 ± 0.20
8	1.14 ± 0.11		1.75 ± 0.10			2.38 ± 0.10	4.51 ± 0.31	7.16 ± 0.40	1.21 ± 0.08	1.48 ± 0.09		2.17 ± 0.15		
9		4.98 ± 0.30			1.15 ± 0.10	2.41 ± 0.10	4.62 ± 0.30	7.78 ± 0.40	1.10 ± 0.08	1.63 ± 0.09	2.04 ± 0.10			
10				4.71 ± 0.25	1.08 ± 0.08					1.76 ± 0.09				2.39 ± 0.20
11	1.16 ± 0.11		1.70 ± 0.12			2.32 ± 0.23	4.61 ± 0.30	7.31 ± 0.40	1.16 ± 0.08	1.58 ± 0.09		2.25 ± 0.15		
12		5.38 ± 0.51			1.19 ± 0.08	2.28 ± 0.12	4.58 ± 0.30	7.68 ± 0.40	1.10 ± 0.08	1.55 ± 0.09	1.97 ± 0.10		2.66 ± 0.15	
13	1.05 ± 0.14		(1.68 ± 0.10)	4.78 ± 0.50	1.25 ± 0.08					1.62 ± 0.09		2.39 ± 0.15	2.43 ± 0.15	
14			(1.41 ± 0.22)		1.20 ± 0.10	2.32 ± 0.31	4.37 ± 0.30	6.54 ± 0.40	1.03 ± 0.08	1.62 ± 0.09				
15				4.42 ± 0.19	0.99 ± 0.10	2.24 ± 0.13	4.17 ± 0.37	7.06 ± 0.40	1.12 ± 0.08	1.60 ± 0.09	2.00 ± 0.10	2.18 ± 0.17		
16			1.60 ± 0.12	4.20 ± 0.20				6.43 ± 0.41			1.86 ± 0.10			
17		5.87 ± 0.82			1.09 ± 0.10	2.09 ± 0.25	4.05 ± 0.73	6.57 ± 0.40			1.81 ± 0.10		2.36 ± 0.15	
18				4.14 ± 0.41	1.10 ± 0.08				1.04 ± 0.17					
19					1.01 ± 0.10	2.20 ± 0.15	4.00 ± 0.30	6.26 ± 0.84						
20				4.39 ± 0.43	0.90 ± 0.17	1.99 ± 0.12	3.63 ± 0.35	6.76 ± 0.40	0.88 ± 0.16					
21							3.46 ± 0.37	6.37 ± 0.40						
22				4.82 ± 0.60	0.93 ± 0.19	1.89 ± 0.15	3.91 ± 0.30	6.25 ± 0.40						
23				3.77 ± 0.65	1.10 ± 0.15									
24				4.34 ± 0.72	0.95 ± 0.15	1.81 ± 0.12								
25					0.83 ± 0.31								2.15 ± 0.41	
x	8	8	7	7	6	6	6	6	5	5	5	5	5	5

Table 3. Measured oscillator strengths $f(v', N'') \times 10^x$ for the P branches of the (2–0)–(15–0) Schumann–Runge bands of $^{16}O\,^{18}O$. Values in parentheses refer to measurements on unresolved lines which are not independent of the R branch values

v'	2	3	4	5	6	7	8	9	10	11	12	13	14	15
N''														
1							(4.37 ± 0.44)							
2					(1.18 ± 0.08)		(4.76 ± 0.30)							
3	(1.23 ± 0.09)				(1.20 ± 0.09)		(4.67 ± 0.30)					(2.35 ± 0.15)		
4		(5.51 ± 0.30)		(4.95 ± 0.27)	(1.16 ± 0.08)						(1.88 ± 0.10)			
5				(4.93 ± 0.23)								(2.26 ± 0.15)	(2.71 ± 0.15)	
6	1.34 ± 0.12		(1.80 ± 0.10)			(2.44 ± 0.10)	(4.62 ± 0.31)	(7.33 ± 0.40)	1.13 ± 0.08		2.04 ± 0.11			(2.98 ± 0.20)
7		(5.13 ± 0.30)			(1.18 ± 0.10)	(2.48 ± 0.10)	(4.76 ± 0.30)	(8.03 ± 0.40)	1.20 ± 0.08	1.65 ± 0.09		(2.24 ± 0.15)		
8	1.14 ± 0.12			(4.89 ± 0.25)	(1.11 ± 0.08)						(2.10 ± 0.10)			
9			(1.76 ± 0.12)			(2.41 ± 0.23)	(4.79 ± 0.30)	(7.60 ± 0.40)	1.15 ± 0.08					(2.50 ± 0.20)
10		5.21 ± 0.56			(1.24 ± 0.08)	(2.37 ± 0.12)	(4.76 ± 0.30)	(7.99 ± 0.40)	1.19 ± 0.08	1.59 ± 0.09		(2.34 ± 0.15)		
11			1.76 ± 0.10	(4.99 ± 0.50)	(1.31 ± 0.08)						1.94 ± 0.10		(2.80 ± 0.15)	
12		5.58 ± 0.39	1.48 ± 0.22		(1.26 ± 0.10)	(2.44 ± 0.31)	(4.57 ± 0.30)	7.54 ± 0.40	1.16 ± 0.08				(2.56 ± 0.15)	
13				(4.65 ± 0.19)	(1.04 ± 0.10)	(2.36 ± 0.13)	(4.40 ± 0.37)	7.96 ± 0.40	1.13 ± 0.08		2.09 ± 0.10			
14		5.73 ± 0.50	1.64 ± 0.12	(4.42 ± 0.20)					1.11 ± 0.08		2.01 ± 0.10	2.02 ± 0.15		
15		5.19 ± 0.41			(1.16 ± 0.10)	(2.22 ± 0.25)	4.40 ± 0.30	6.86 ± 0.40	1.10 ± 0.08	1.54 ± 0.09				
16			1.64 ± 0.28	(4.42 ± 0.41)	(1.17 ± 0.08)				1.12 ± 0.08	1.65 ± 0.09	1.80 ± 0.10		(2.53 ± 0.15)	
17		3.78 ± 1.06			(1.08 ± 0.10)	(2.35 ± 0.15)	4.41 ± 0.30	6.95 ± 0.40		1.48 ± 0.09				
18			1.59 ± 0.16	(4.72 ± 0.43)	(0.96 ± 0.17)	(2.13 ± 0.12)	4.30 ± 0.45	6.84 ± 0.62	1.00 ± 0.10					
19									0.96 ± 0.12					
20				(5.22 ± 0.60)	(1.01 ± 0.19)	(2.03 ± 0.15)	3.71 ± 0.32	6.96 ± 0.40						
21				(4.08 ± 0.65)	(1.19 ± 0.15)									
22				(4.70 ± 0.72)	(1.03 ± 0.15)	(1.96 ± 0.12)						1.97 ± 0.19		
23					(0.91 ± 0.31)									
24													(2.39 ± 0.41)	
x	8	8	7	7	6	6	6	6	5	5	5	5	5	5

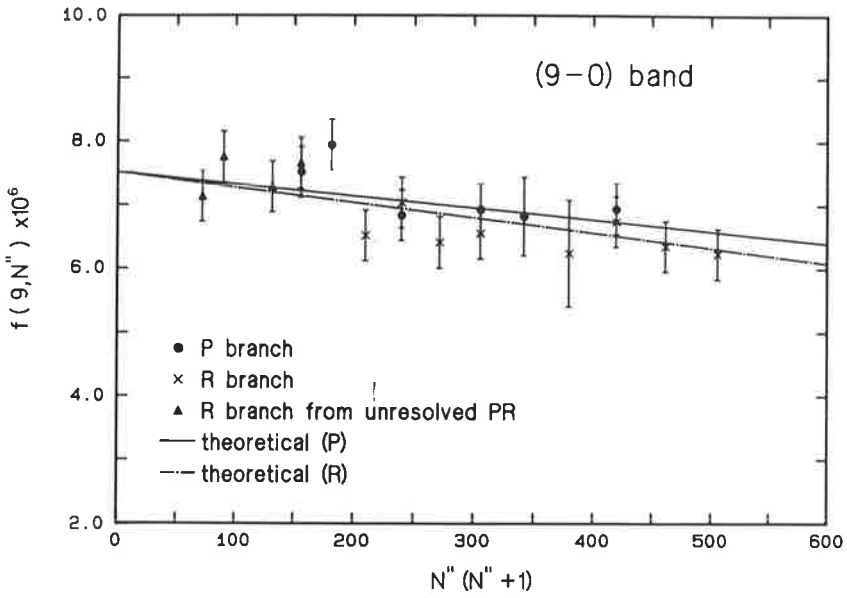

Fig. 2. Measured oscillator strengths for rotational lines from the (9–0) Schumann–Runge band of $^{16}O^{18}O$ together with the predicted rotational dependences.

$N''(N''+1)$ can be seen clearly, while the resolved P branch values exceed those for the R branch. Considering the scatter in the measurements, agreement with theoretical predictions based on our $^{16}O_2$ results[1] is good.

Rotational band oscillator strengths of the form[1]

$$f(v',N'') = f_0(v') - \beta(v')\,N''(N''+1) \tag{1}$$

were least-squares fitted to our measurements for the (2–0)–(15–0) bands, and the resultant values of f_0 and β are given in Table 4 together with the corresponding theoretical values. Because of the small magnitude of the β values and the resultant large uncertainty, although the P and R branches were fitted separately, the tabulated results are averaged over the P and R branches. In view of the small number of lines studied in the (15–0) band, the f_0 value was determined using the theoretical β value. The f_0 values for $2 \leqslant v' \leqslant 14$ average about 2% larger than the theoretical values, with an r.m.s. scatter of 3–4% in the ratio. The measured β values for $3 \leqslant v' \leqslant 14$ average about 20% larger than the theoretical values, with an r.m.s. scatter or about 50% in the ratio, indicating the difficulty of following the bands to high rotation in an isotopic mixture of the type used. The errors quoted in Table 4 are statistical errors determined by the least-squares fitting procedure, but there is an additional uncertainty of about 5% in f_0, due mainly to the determination of the pressure in the isotopic cells. In cases where the measured β values differ greatly from the

Table 4. Rotationless oscillator strengths $f_0(v')$, rotational dependences $\beta(v')$ and mean band oscillator strengths $\bar{f}(v')$ for the (2–0)–(15–0) Schumann–Runge bands of $^{16}O^{18}O$. Values marked with an asterisk were determined from the measurements by assuming the theoretical β values. The statistical errors implied by the fitting procedure are also given

		$\beta(v') \times 10^y$			$f_0(v') \times 10^x$		$\bar{f}(v') \times 10^x$	
v'	y	Measured	Theor.	x	Measured	Theor.	Measured	Theor.
2	12	9.6 ± 15.5	2.6	8	1.25 ± 0.14	1.20	1.11 ± 0.14	1.16
3	11	1.0 ± 2.1	1.2	8	5.28 ± 0.43	5.24	5.33 ± 0.43	5.06
4	11	8.2 ± 3.6	4.1	7	1.82 ± 0.09	1.78	1.70 ± 0.09	1.72
5	10	1.4 ± 0.5	1.2	7	4.87 ± 0.14	4.95	4.67 ± 0.14	4.77
6	10	3.1 ± 1.3	2.9	6	1.20 ± 0.04	1.17	1.15 ± 0.04	1.13
7	10	10.9 ± 1.0	6.2	6	2.51 ± 0.05	2.44	2.34 ± 0.05	2.35
8	9	1.9 ± 0.3	1.2	6	4.76 ± 0.10	4.52	4.47 ± 0.10	4.34
9	9	2.8 ± 0.8	2.1	6	7.79 ± 0.36	7.52	7.37 ± 0.36	7.20
10	9	5.8 ± 1.7	3.5	5	1.22 ± 0.04	1.15	1.13 ± 0.04	1.10
11	9	2.6 ± 4.3	5.2	5	1.63 ± 0.13	1.59	1.61 ± 0.13	1.51
12	9	3.1 ± 4.6	7.2	5	2.00 ± 0.11	2.03	1.95 ± 0.11	1.92
13	9	4.5 ± 3.9	9.3	5	2.28 ± 0.11	2.39	2.22 ± 0.11	2.25
14	8	0.9 ± 0.2	1.1	5	2.74 ± 0.11	2.60	2.60 ± 0.11	2.43
15	8		1.3	5	2.79 ± 0.25*	2.63	2.59 ± 0.25*	2.43

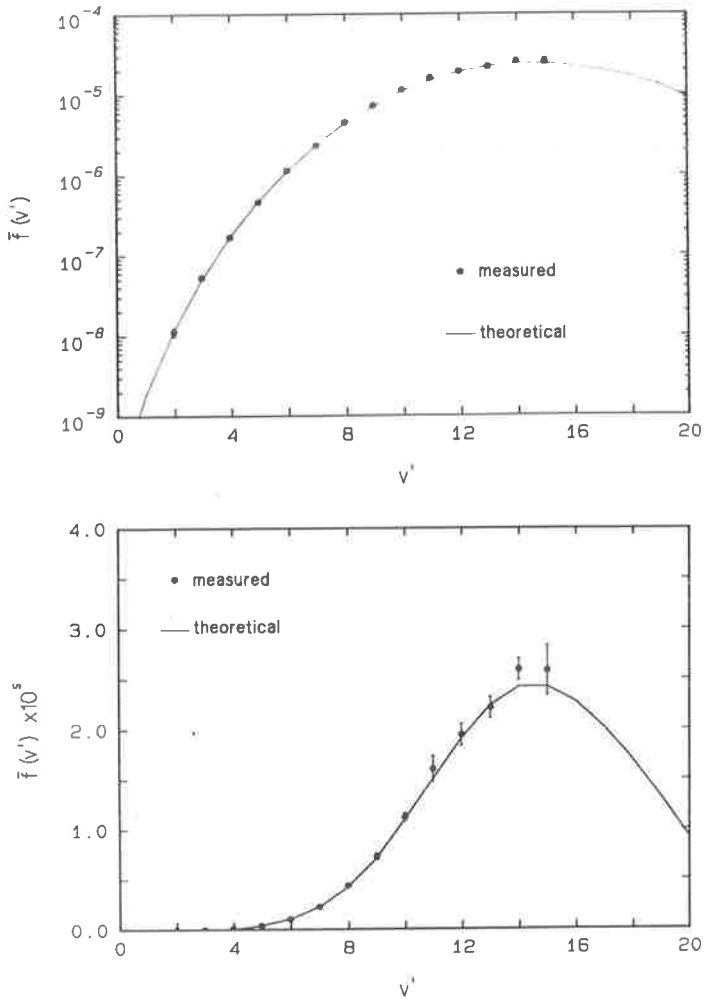

Fig. 3. Measured mean band oscillator strengths for the (v'–0) Schumann–Runge bands of $^{16}O^{18}O$ together with the theoretical predictions.

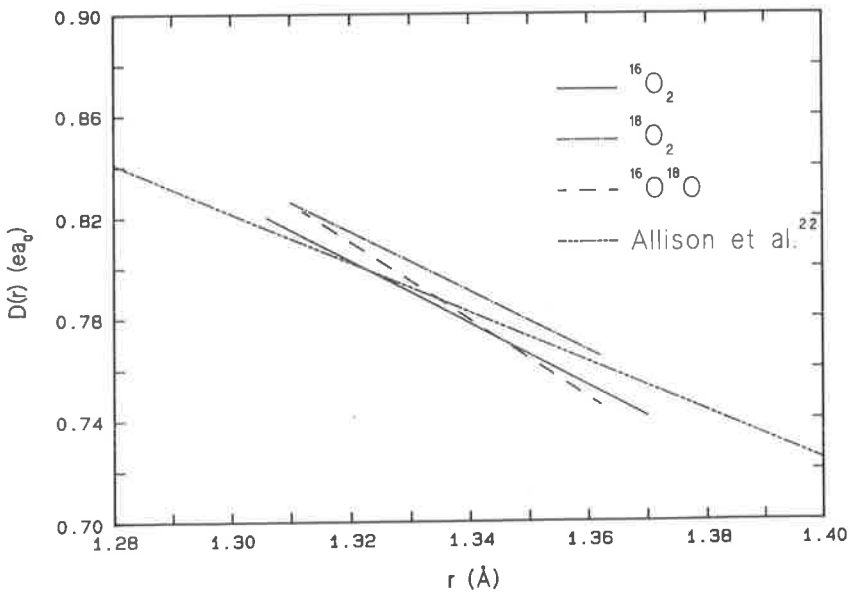

Fig. 4. The dipole moment obtained here for the B–X transition in $^{16}O^{18}O$ compared with those previously determined for $^{16}O_2$ and $^{18}O_2$ and the semi-empirical calculations of Allison *et al.*[22]

theoretical values, the corresponding f_0 value may be affected, but if theoretical β values are forced into the fit to equation (1), the f_0 values are observed to change only up to $\pm 3\%$.

Measured and theoretical mean band oscillator strengths $\bar{f}(v')$, determined[1] by summing individual line oscillator strengths weighted with appropriate Boltzmann factors, are also listed in Table 4 and shown in Fig. 3. The oscillator strengths for $^{16}O^{18}O$ are intermediate between those for $^{16}O_2$ and $^{18}O_2$.[1,3] Agreement between the measured and theoretical values is excellent, as for the rotationless values. No other experimental values are available for comparison, but theoretical rotationless oscillator strengths have been calculated by Blake *et al.*[7] These are 2–5% greater than our theoretical values because of the different potential curves and dipole moment used. Nevertheless, there is fairly good agreement between our measured parameters and those used in the photodissociation model of Blake *et al.*[7] who conclude that the $^{16}O^{18}O$ atmospheric dissociation rate contributes a maximum of 3% to the total photodissociation of O_2, an order of magnitude less than the estimate of Cicerone and McCrumb[6] whose analysis contains several dubious assumptions.[7]

THE DIPOLE MOMENT

A dipole moment was calculated for $^{16}O^{18}O$ using our oscillator strength measurements and the potential curves of Lewis *et al.*[1] for the $X^3\Sigma_g^-$ and $B^3\Sigma_u^-$ states. Wavefunctions for $v'' = 0$, $v' = 2$–15 were calculated by numerical integration of Schrödinger equation and the dipole moment $D(r)$ was expressed as a power series in the internuclear separation r. The coefficients of this series were determined by a weighted least-squares procedure which compared the calculated and measured rotationless oscillator strengths, avoiding the r-centroid approximation. The dipole moment obtained is, for $1.312\text{Å} \leqslant r \leqslant 1.362\text{Å}$,

$$D(r) = 1.77534 + 0.054137r - 0.59478r^2, \tag{2}$$

where $D(r)$ is in atomic units and r is in Å. Our form for the dipole moment is consistent with the recommendations of Whiting *et al.*,[21] but is a factor of $\sqrt{3}$ smaller than some forms adopted in the literature. The r.m.s. deviation of the fit is 2.8%. The dipole moment is compared in Fig. 4 with those obtained[1,3] for $^{16}O_2$ and $^{18}O_2$, and with the semi-empirical determinations of Allison *et al.*[22] All the dipole moments agree to within 2% over the ranges of applicability, well within the statistical uncertainties of the fitting procedures. This is a testament to the reliability of the oscillator strength measurements, and shows that the dipole moment is not significantly affected by isotopic substitution.

CONCLUSIONS

Experimental oscillator strengths for the Schumann–Runge bands of $^{16}O^{18}O$ are presented for the first time. The (2–0)–(15–0) bands have been studied on a line-by-line basis and the equivalent band oscillator strength is observed to decrease with increasing rotation at a rate intermediate between those measured[1,3] for $^{16}O_2$ and $^{18}O_2$. The mean band oscillator strengths also lie between the corresponding values for the homonuclear isotopes.[1,3] Line-by-line modelling of the Schumann–Runge bands of $^{16}O^{18}O$ is best performed by using the rotationless oscillator strengths f_0 obtained here together with the theoretical rotational dependences β listed in Table 4. Our oscillator strengths are in excellent agreement with theoretical values based on our $^{16}O_2$ measurements,[1] and are in good agreement with the values calculated by Blake *et al.*[7] whose atmospheric O_2 photodissociation model predicts that Cicerone and McCrumb[6] have overestimated the importance of $^{16}O^{18}O$ to total atmospheric O_2 photodissociation by about an order of magnitude. The dipole moment found here for $^{16}O^{18}O$ agrees well with our $^{16}O_2$ and $^{18}O_2$ dipole moments[1,3] and also with recent semi-empirical determinations.[22]

Acknowledgements—The authors would like to thank C. Dedman and K. Lonsdale for valuable technical assistance. Some of the programs for the dipole moment calculations were kindly provided by S. T. Gibson.

REFERENCES

1. B. R. Lewis, L. Berzins and J. H. Carver, *JQSRT* **36,** 209 (1986).
2. B. R. Lewis, L. Berzins, J. H. Carver and S. T. Gibson, *JQSRT* **36,** 187 (1986).
3. B. R. Lewis, L. Berzins and J. H. Carver, *JQSRT* **37,** 229 (1987).
4. B. R. Lewis, L. Berzins and J. H. Carver, *JQSRT* **37,** 243 (1987).
5. A. O. Nier, *Phys. Rev.* **77,** 789 (1950).
6. R. J. Cicerone and J. L. McCrumb, *Geophys. Res. Lett.* **7,** 251 (1980).
7. A. J. Blake, S. T. Gibson and D. G. McCoy, *J. Geophys. Res.* **89,** 7277 (1984).
8. P. S. Julienne, *J. molec. Spectrosc.* **63,** 60 (1976).
9. G. H. Dieke and H. D. Babcock, *Proc. natn. Acad. Sci. U.S.A.* **13,** 670 (1927).
10. W. F. Giauque and H. L. Johnston, *Nature* **123,** 318 (1929).
11. H. D. Babcock and L. Herzberg, *Astrophys. J.* **108,** 167 (1948).
12. H. G. Hecht, S. W. Rabideau and R. Engleman, Report LA-5871-MS, 10pp., Los Alamos Sci. Lab., Los Alamos, N.M. (1975).
13. W. Steinbach and W. Gordy, *Phys. Rev.* **A11,** 729 (1975).
14. H. G. M. Edwards, E. A. M. Good and D. A. Long, *J. chem. Soc. Faraday II* **72,** 865 (1976).
15. B. R. Lewis, L. Berzins and J. H. Carver, *JQSRT* **37,** 255 (1987).
16. K. Yoshino, D. E. Freeman and W. H. Parkinson, *J. phys. chem. Ref. Data* **13,** 207 (1984).
17. J. B. Tatum and J. K. G. Watson, *Can J. Phys.* **49,** 2693 (1971).
18. R. M. Goody, *Atmospheric Radiation: I. Theoretical Basis.* Oxford University Press, London (1964).
19. J. E. Frederick and R. D. Hudson, *J. molec. Spectrosc.* **74,** 247 (1979).
20. S. T. Gibson, Ph.D. thesis, University of Adelaide (1983).
21. E. E. Whiting, A. Schadee, J. B. Tatum, J. T. Hougen and R. W. Nicholls, *J. molec. Spectrosc.* **80,** 249 (1980).
22. A. C. Allison, S. L. Guberman and A. Dalgarno, *J. Geophys. Res. A*, paper 5A8157 (1986).

4.8 Predissociation linewidths for the Schumann-Runge bands of $^{18}O_2$

[26] B. R. Lewis, L. Berzins, and J. H. Carver,
Journal of Quantitative Spectroscopy and Radiative Transfer **37**, 229–241 (1987).

J. Quant. Spectrosc. Radiat. Transfer Vol. 37, No. 3, pp. 229–241, 1987
Printed in Great Britain.

0022-4073/87 $3.00 + 0.00

PREDISSOCIATION LINEWIDTHS FOR THE SCHUMANN–RUNGE BANDS OF $^{18}O_2$

B. R. LEWIS, L. BERZINS and J. H. CARVER
Research School of Physical Sciences, The Australian National University, Canberra, Australia 2600

(*Received* 27 *May* 1986)

Abstract—Predissociation linewidths were measured for rotational lines from the (2–0)–(19–0) Schumann–Runge bands of $^{18}O_2$. While the qualitative behaviour of the vibrational linewidths is similar to that observed for $^{16}O_2$, with four maxima at various vibrations, for a given band the linewidth may vary significantly between isotopes. As in the case of $^{16}O_2$, the experimental linewidths are found to exhibit systematic variation with rotation for most of the bands studied. A model of the predissociation, including the interactions of the $B\,^3\Sigma_u^-$ state with repulsive $^5\Pi_u$, $^3\Pi_u$, $^1\Pi_u$ and $^3\Sigma_u^+$ states, and with molecular interaction parameters determined by a least-squares fit to experimental $^{16}O_2$ linewidths, is found to predict accurately the observed vibrational and rotational dependences of linewidth for $^{18}O_2$.

INTRODUCTION

In order to characterize accurately the absorption spectrum of the Schumann–Runge bands of $^{18}O_2$ one must have a knowledge of the oscillator strengths and the widths of individual rotational lines. New measurements of oscillator strength are presented by Lewis *et al.*[1] in a companion work and this paper discusses the associated predissociation linewidths.

Since Flory[2] first observed the diffuseness of rotational lines in the Schumann–Runge bands of $^{16}O_2$ on photographic plates and attributed this to predissociation of the $B\,^3\Sigma_u^-$ state by a repulsive $^3\Pi_u$ state, there have been many experimental and theoretical investigations of the problem. The historical development to 1972 has been summarized by Krupenie,[3] and a detailed discussion of the work since that time has been given by Lewis *et al.*[4]

The only experimental linewidth measurements on individual rotational lines for $^{16}O_2$ are those of Lewis *et al.*,[4–6] Gies *et al.*,[7] and Frederick and Hudson[8] who reanalysed the measurements of Hudson and Carter.[9,10] Of these, only the measurements of Lewis *et al.*[4] were comprehensive enough to demonstrate unambiguously the systematic variation of predissociation linewidth with rotation.

It was not until the work of Julienne and Krauss[11] and Julienne[12] that theoretical calculations started to reproduce the observed linewidths. These authors used *ab initio* calculations to obtain an initial range for the parameters describing interactions between the $B\,^3\Sigma_u^-$ state and various repulsive potential curves, and then refined their qualitative picture of the predissociation through a detailed comparison between calculated level shifts and linewidths and the available experimental data. Julienne[12] found that the predissociation is caused primarily by interactions with a $^5\Pi_u$ state, with lesser roles being played by $^3\Sigma_u^+$, $^3\Pi_u$ and $^1\Pi_u$ states. In this way the observed predissociation maxima at $v' = 4,7,11$ for $^{16}O_2$ could be explained.

Julienne[12] stressed the need for experimental measurements of the dependence of predissociation linewidth on rotation and isotopic substitution. Lewis *et al.*[4] found that the theoretical model of Julienne[12] was capable of explaining both the vibrational and rotational variations of linewidth observed for $^{16}O_2$, and a refined set of model parameters was obtained by a least-squares fit to the experimental results.[4] Julienne[12] calculated the vibrational linewidths expected for $^{18}O_2$ using $^{16}O_2$ model parameters, but the only experimental measurements for this isotope are microdensitometer tracings of the photographs of Tilford[13] for $v' = 9$–14. These linewidths include fine-structure splitting in some cases and are in general larger than the predicted values.[12]

In this work we present the results of an extensive experimental study of the predissociation linewidths of the (2–0)–(19–0) Schumann–Runge bands of $^{18}O_2$, including variation with rotation. Model linewidths calculated according to the theory of Julienne,[12] but with model parameters taken from a fit to our previous $^{16}O_2$ results,[4] agree very well with our $^{18}O_2$ measurements. Model parameters obtained by a least-squares fit to our $^{18}O_2$ linewidths agree fairly well with those obtained from our $^{16}O_2$ linewidths.[4]

EXPERIMENTAL METHOD AND DATA ANALYSIS

A detailed discussion of the experimental method has been given elsewhere.[1] Briefly, background radiation from an H_2 continuum was dispersed by a modified[14] 2.2 m scanning VUV monochromator at a resolution of ~ 0.05 Å, and was detected photoelectrically before entering and after leaving the 10 cm sealed quartz cells containing 99.6% $^{18}O_2$. The individual cells were filled[1] with pressures in the range 2 Torr–2 atm and were mounted on a carousel[1] which enabled concurrent scans of different samples to be taken as desired. The scanning system was microcomputer controlled.

Concurrent absorption scans over the region of the Schumann–Runge bands were performed for each cell, including a wavelength reference cell filled with $^{16}O_2$. A few short scans were performed using a refillable 10 cm cell and these were used to calibrate accurately the sealed cell pressures.[1] It was not possible to determine backgrounds experimentally using the sealed cells,[1] and an interpolation was performed between experimentally determined transmissions at deeper minima between absorption lines, after correction for adjacent and distant line wings.[1] This procedure did not require a knowledge of the underlying continuum for $^{18}O_2$, but resulted in less accurate oscillator strengths and linewidths for this species.

The general data analysis procedures and model parameters have been discussed in detail previously.[1,15] Line profiles and equivalent widths were recorded for all lines of interest at several pressures, and the equivalent width data analysis technique allowed the simultaneous determination of both oscillator strength and predissociation linewidth by an iterative procedure.[1,5,15]

Because of the limited number of pressures and the fixed cell length, the ideal pairs of pressures for application of the full equivalent width method were not always available. In these cases oscillator strengths and predissociation linewidths were obtained by a two parameter least-squares fit to the observed line profile at a single pressure, a variant of the method used by Frederick and Hudson.[8] Linewidths obtained in this way were found to be consistent with those obtained by the two scan equivalent width method when it was possible to compare both for a given line. While the equivalent width method is to be preferred because a knowledge of the instrument function is not strictly required,[16] the profile fitting method does allow more scans to be analysed for a given set of experimental conditions.

THEORETICAL METHOD

The predissociation model used in this work is based on that of Julienne and Krauss[11] and Julienne,[12] and similar notation is used here. Full details of our implementation of this model have been given previously[4] for the case of $^{16}O_2$.

Briefly, the predissociation of the $B\,^3\Sigma_u^-$ state of O_2 is described in terms of the interactions of this state with four repulsive states $\alpha = {}^5\Pi_u$, $2\,^3\Sigma_u^+$, $^3\Pi_u$, $^1\Pi_u$, whose potentials take the form

$$V_\alpha(r) = V_{\alpha x} \exp[-(M_{\alpha x}/V_{\alpha x})(r - R_{\alpha x})] + V_\infty, \tag{1}$$

where V_∞ is the energy of the $O(^3P) + O(^3P)$ asymptote, $R_{\alpha x}$ is the crossing point and $V_{\alpha x}$ is the energy at which the repulsive potential α crosses the $B\,^3\Sigma_u^-$ potential. $M_{\alpha x}$ is the slope of the repulsive potential α at the crossing point.

The $B\,^3\Sigma_u^-$ state is described in mixed case (a)–(b) representation and the B state potential curve is that used by Lewis *et al.*[4] Spin-orbit interaction only is considered and the electronic matrix element is assumed independent of r and to have a constant value $A_{\alpha x} = A_\alpha(R_{\alpha x})$, after the discussion by Julienne.[12]

The predissociation linewidth due to a single curve crossing is related to the product of the matrix element $A_{\alpha x}$ and the overlap of the wavefunctions of the bound and unbound states at the vibrational energy of interest.[12] The linewidths are determined as the sum of the contributions from each curve crossing and are dependent on the fine-structure component i and the rotation, mainly due to centrifugal distortion.[4] In this work we assume the twelve repulsive curve parameters ($A_{\alpha x}$, $R_{\alpha x}$, $M_{\alpha x}$, $\alpha = {}^5\Pi_u$, $2\,^3\Sigma_u^+$, $^3\Pi_u$, $^1\Pi_u$) determined previously[4] for $^{16}O_2$ and calculate the full manifold of partial widths $\Gamma(v'J'i)$ using the procedure described by Lewis *et al.*[4] In order to give a valid comparison with unresolved triplet experimental widths, the partial widths are averaged over the fine structure for each N' ($J' = N', N' \pm 1$). Henceforth the linewidths will be denoted by $\bar{\Gamma}$ to

indicate fine-structure averaging although some of the experimental widths refer to resolved triplet components.

RESULTS

Some 248 distinct linewidth measurements from the (2–0)–(19–0) Schumann–Runge bands of $^{18}O_2$ are presented here. The corresponding oscillator strengths, which have been given elsewhere,[1] are in good agreement with theoretical expectations, supporting the reliability of our predissociation linewidths.

The measured linewidths for each band studied are given in Figs 1–18 as functions of upper state rotation J'. In the case of experimentally unresolved lines (P and R branch triplets, PR sextuplets) an appropriate mean J' is assigned to each measurement. For $v' \geqslant 15$ some measurements were taken of resolved fine-structure components. In general it was not possible to distinguish reliably systematic width variations as a function of triplet sub-level due to limited availability of lines and increased statistical error for measurements on the higher rotational lines. Width measurement on resolved single and double fine-structure components account for the odd and non-integral mean J' values assigned to some of the widths in Figs 1–18. In some cases ($v' = 2$–5; $v' = 6,7,10,11$ for

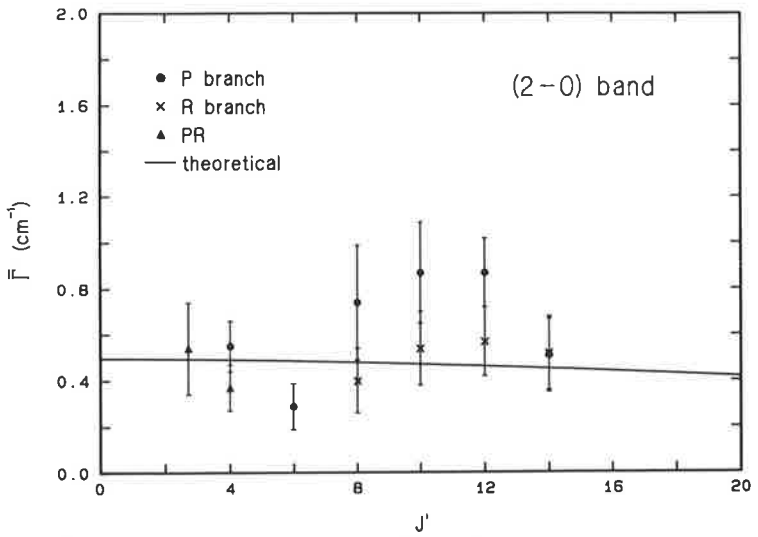

Fig. 1. The variation of FWHM predissociation linewidth with rotation for the (2–0) Schumann–Runge band of $^{18}O_2$.

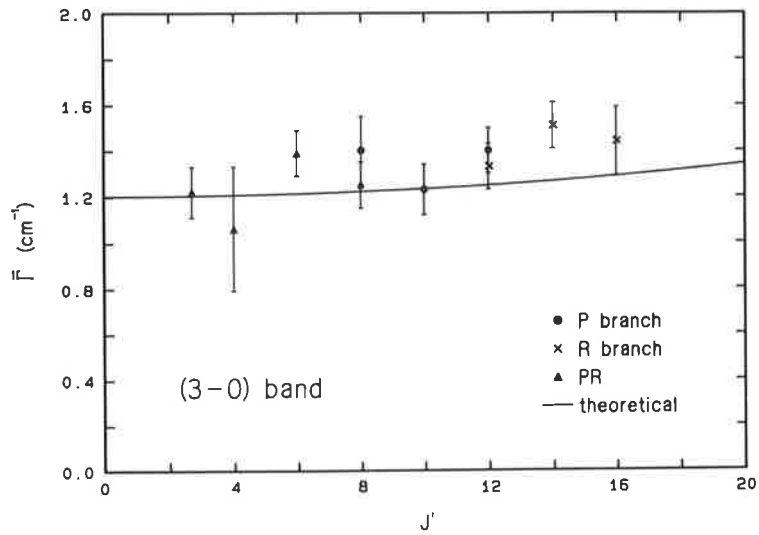

Fig. 2. The variation of FWHM predissociation linewidth with rotation for the (3–0) Schumann–Runge band of $^{18}O_2$.

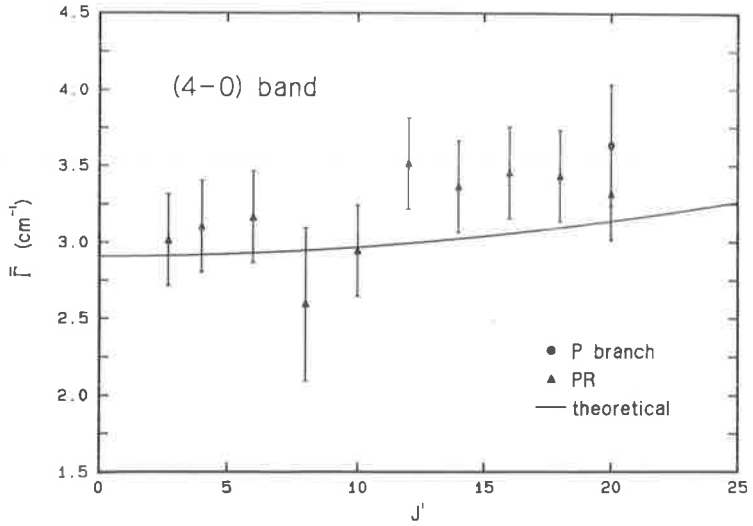

Fig. 3. The variation of FWHM predissociation linewidth with rotation for the (4–0) Schumann–Runge band of $^{18}O_2$.

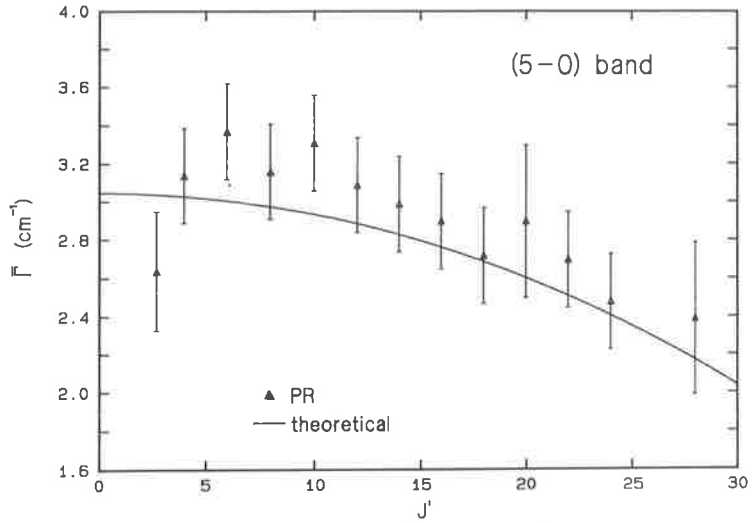

Fig. 4. The variation of FWHM predissociation linewidth with rotation for the (5–0) Schumann–Runge band of $^{18}O_2$.

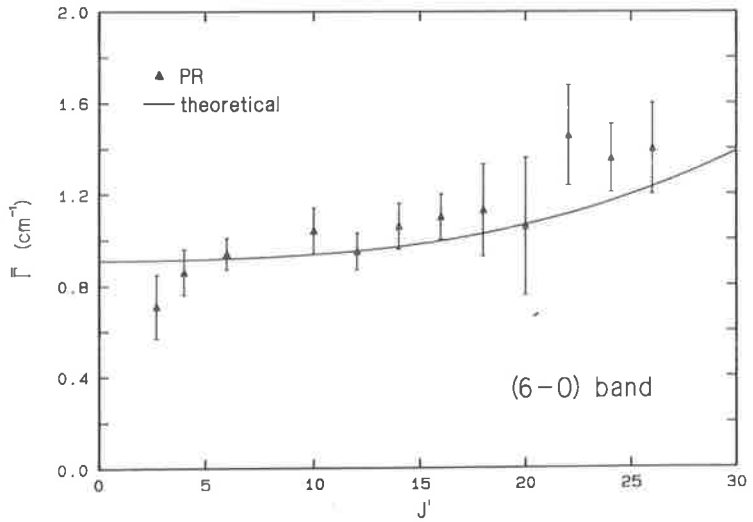

Fig. 5. The variation of FWHM predissociation linewidth with rotation for the (6–0) Schumann–Runge band of $^{18}O_2$.

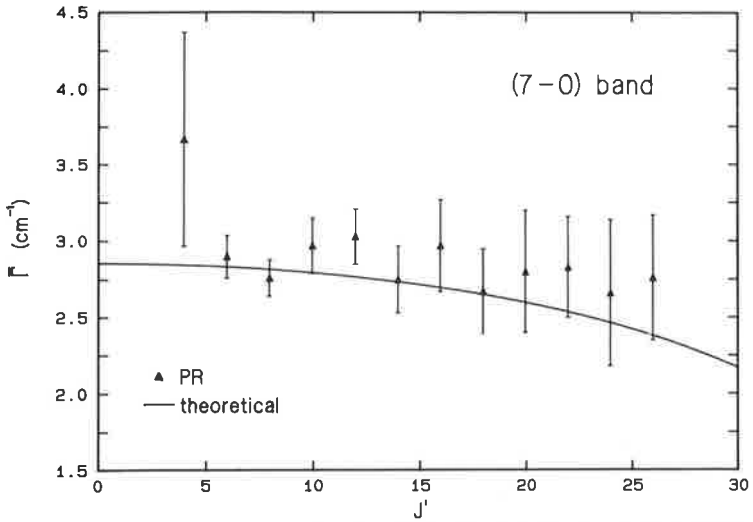

Fig. 6. The variation of FWHM predissociation linewidth with rotation for the (7–0) Schumann–Runge band of $^{18}O_2$.

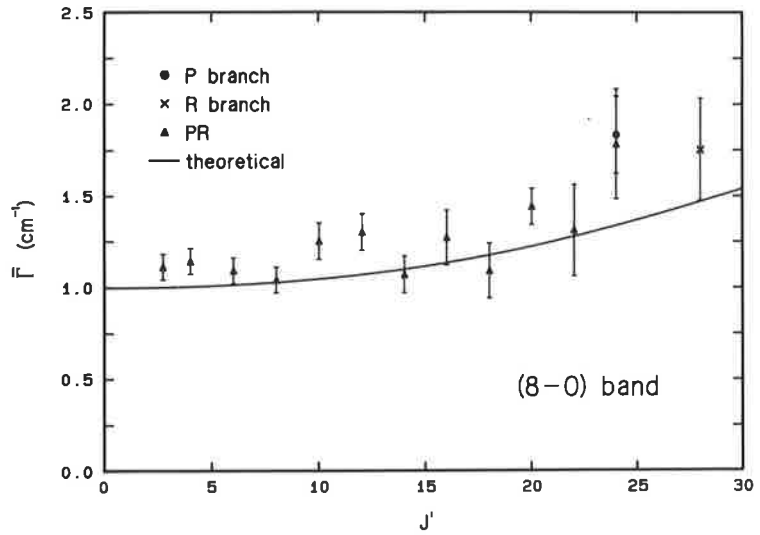

Fig. 7. The variation of FWHM predissociation linewidth with rotation for the (8–0) Schumann–Runge band of $^{18}O_2$.

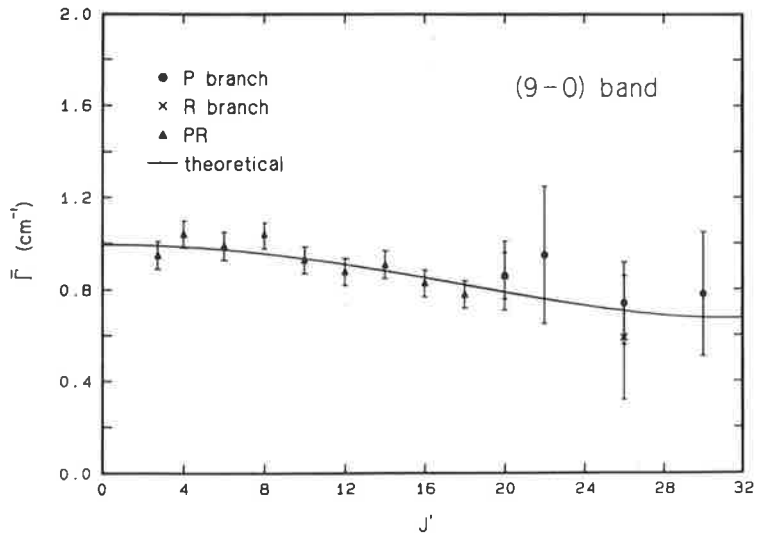

Fig. 8. The variation of FWHM predissociation linewidth with rotation for the (9–0) Schumann–Runge band of $^{18}O_2$.

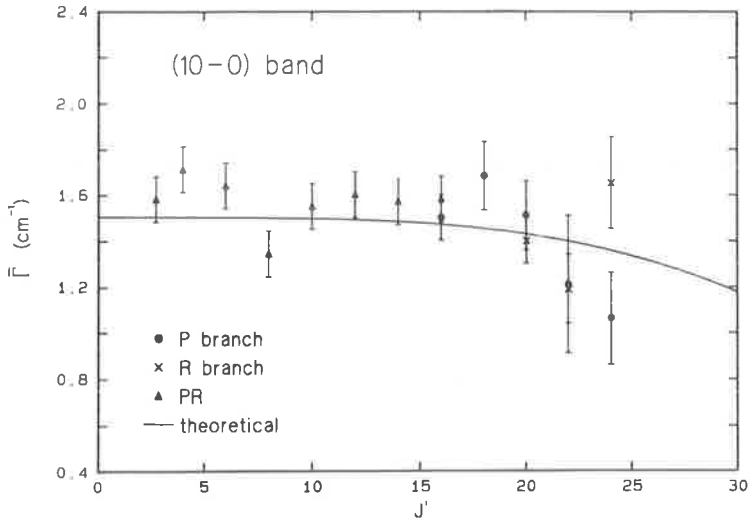

Fig. 9. The variation of FWHM predissociation linewidth with rotation for the (10–0) Schumann–Runge band of $^{18}O_2$.

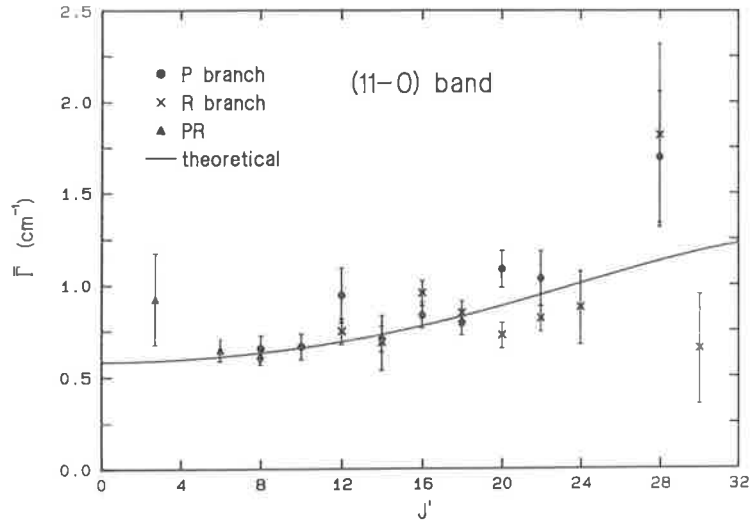

Fig. 10. The variation of FWHM predissociation linewidth with rotation for the (11–0) Schumann–Runge band of $^{18}O_2$.

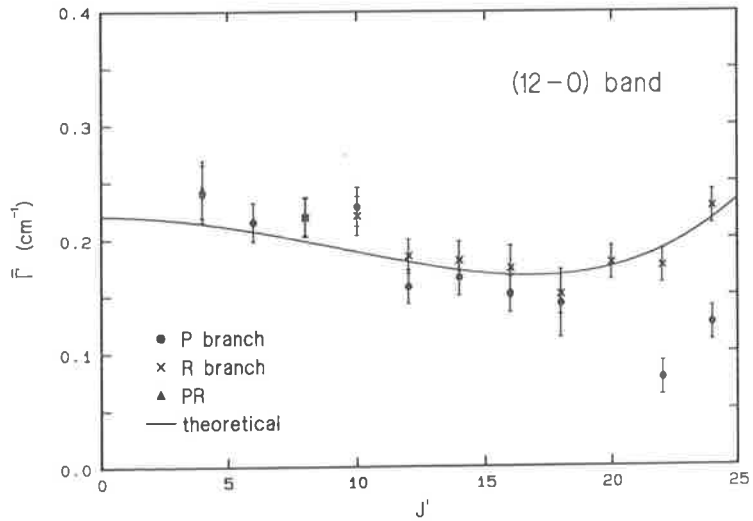

Fig. 11. The variation of FWHM predissociation linewidth with rotation for the (12–0) Schumann–Runge band of $^{18}O_2$.

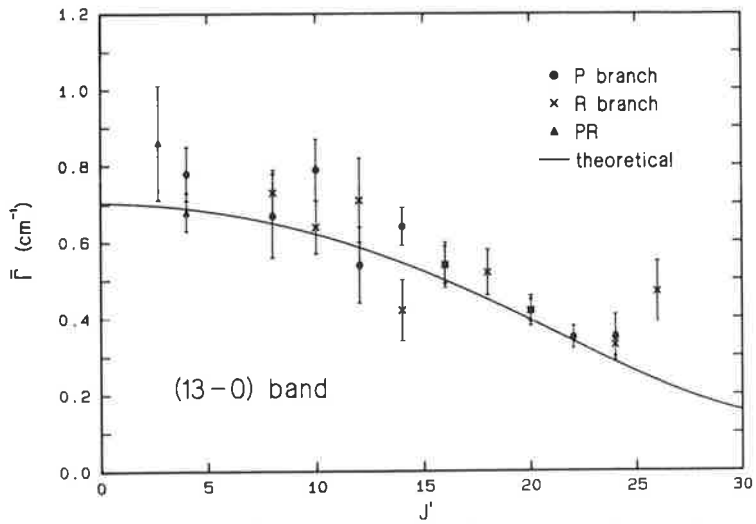

Fig. 12. The variation of FWHM predissociation linewidth with rotation for the (13–0) Schumann–Runge band of $^{18}O_2$.

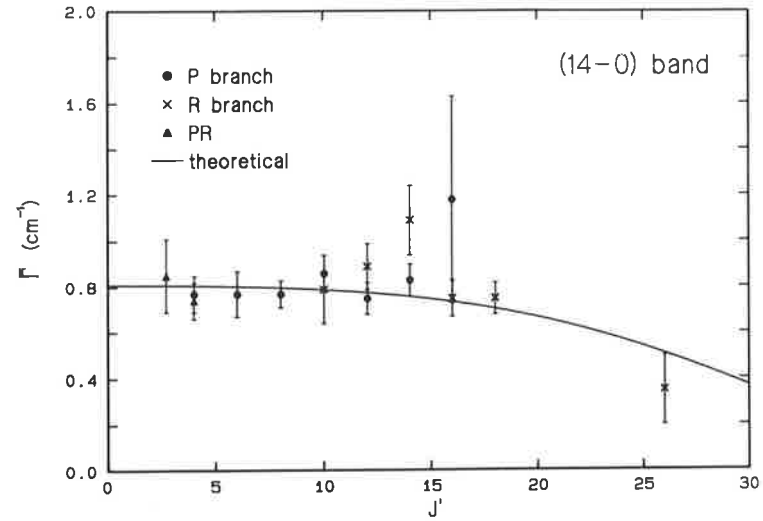

Fig. 13. The variation of FWHM predissociation linewidth with rotation for the (14–0) Schumann–Runge band of $^{18}O_2$.

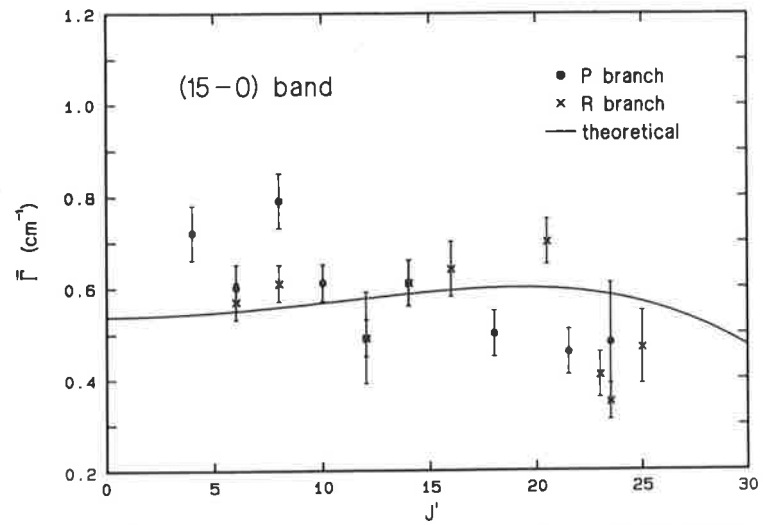

Fig. 14. The variation of FWHM predissociation linewidth with rotation for the (15–0) Schumann–Runge band of $^{18}O_2$.

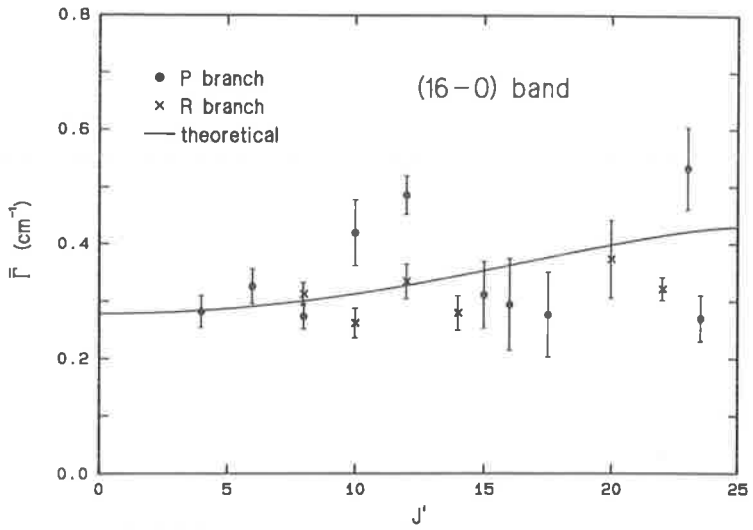

Fig. 15. The variation of FWHM predissociation linewidth with rotation for the (16–0) Schumann–Runge band of $^{18}O_2$.

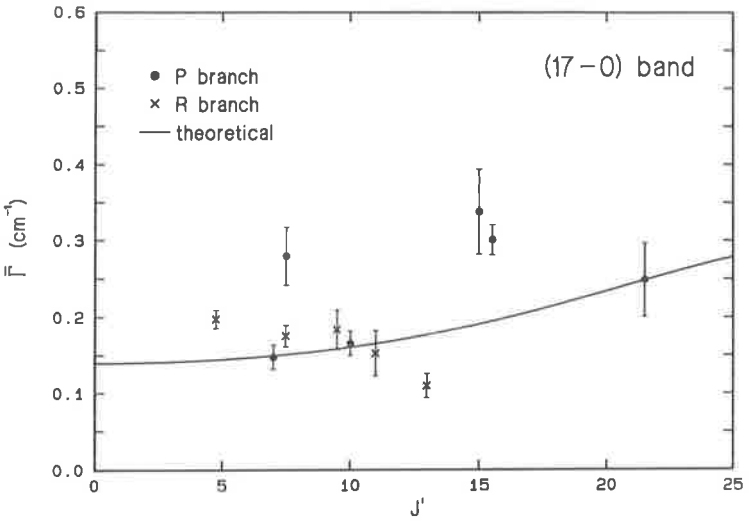

Fig. 16. The variation of FWHM predissociation linewidth with rotation for the (17–0) Schumann–Runge band of $^{18}O_2$.

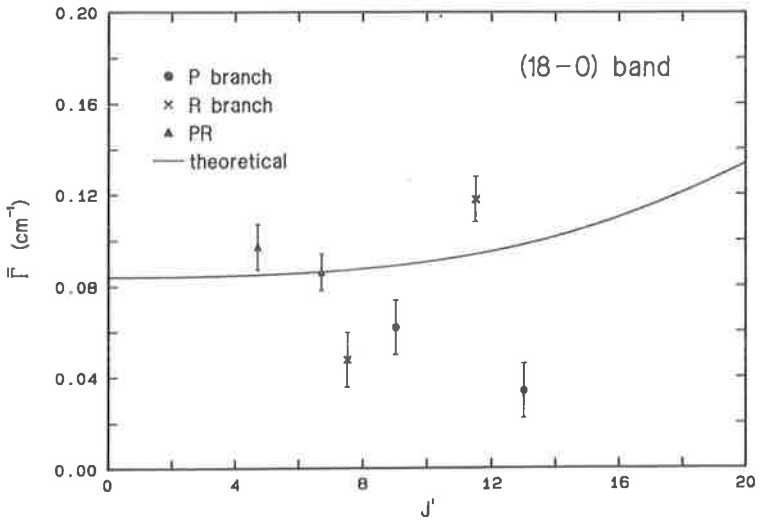

Fig. 17. The variation of FWHM predissociation linewidth with rotation for the (18–0) Schumann–Runge band of $^{18}O_2$.

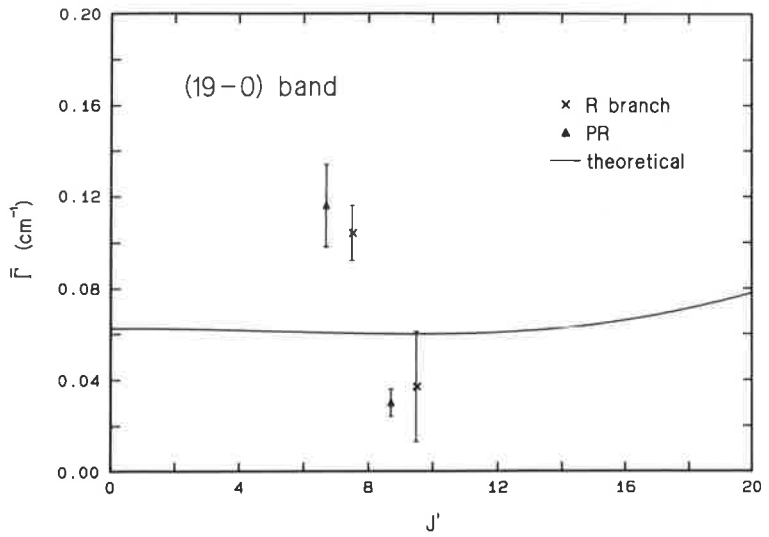

Fig. 18. The variation of FWHM predissociation linewidth with rotation for the (19–0) Schumann–Runge band of $^{18}O_2$.

$J' \geqslant 22$; $v' = 8$ for $J' \geqslant 24$; $v' = 9$ for $J' \geqslant 26$) widths were obtained from a single scan by the profile fitting method mentioned earlier. This technique generally results in larger errors, especially for the weak lines of the (2–0) band.

The errors shown in Figs 1–18 are statistical only. There is an additional uncertainty of about 5% due to possible systematic errors in pressure, cell length and temperature. The errors introduced by uncertainties in model parameters are not considered explicitly here, but our $^{16}O_2$ results[4] indicate the soundness of these parameters. Because of the lack of experimental backgrounds for $^{18}O_2$, although the bandhead widths are quite robust, the high J' widths are more sensitive to the model parameters and, as a result, are less accurate than the corresponding widths[4] for $^{16}O_2$.

Our linewidths were smoothed and extrapolated to $J' = 0$ and these results are compared in Table 1 and Fig. 19 with rotationless widths calculated using the model interaction parameters determined by Lewis *et al.*[4] for $^{16}O_2$. There is excellent agreement between the present measurements and the model predictions. The best-fit linewidths[4] for $^{16}O_2$ are also shown in Fig. 19. For $^{18}O_2$ we observe peaks at $v' = 4$–5,7,10,14, in accordance with the predictions, compared with $v' = 4,7,11,16$ for $^{16}O_2$. Although the patterns are qualitatively similar for the two isotopes, there are dramatic differences for certain bands, for example $v' = 13$ where the measured rotationless width increases from 0.11 cm^{-1} for $^{16}O_2$ to 0.75 cm^{-1} for $^{18}O_2$.

Table 1. Measured FWHM predissociation linewidths $\Gamma_0(cm^{-1})$, extrapolated to zero rotation, for the (2–0)–(19–0) Schumann–Runge bands of $^{18}O_2$. Our model calculations are also shown, together with those of Julienne[12] and the apparent photographic widths of Tilford[13]

v'	Measured	Theoretical	Julienne[12] (theor.)	Tilford[13]
2	0.55 ± 0.10	0.50	0.29	
3	1.16 ± 0.09	1.20	0.96	
4	2.88 ± 0.20	2.91	2.63	
5	3.18 ± 0.14	3.05	2.21	
6	0.75 ± 0.05	0.91	1.05	
7	2.88 ± 0.13	2.86	2.69	
8	1.15 ± 0.04	1.00	1.65	
9	1.00 ± 0.03	1.00	0.73	1.28 ± 0.17
10	1.60 ± 0.06	1.50	1.55	1.85 ± 0.15
11	0.67 ± 0.04	0.58	0.95	1.35 ± 0.30
12	0.26 ± 0.01	0.22	0.24	0.70 ± 0.32
13	0.75 ± 0.03	0.70	0.61	0.79 ± 0.32
14	0.82 ± 0.04	0.81	0.71	1.07 ± 0.32
15	0.57 ± 0.03	0.54	0.54	
16	0.29 ± 0.02	0.28	0.39	
17	0.18 ± 0.02	0.14		
18	0.07 ± 0.03	0.08		
19	0.08 ± 0.03	0.06		

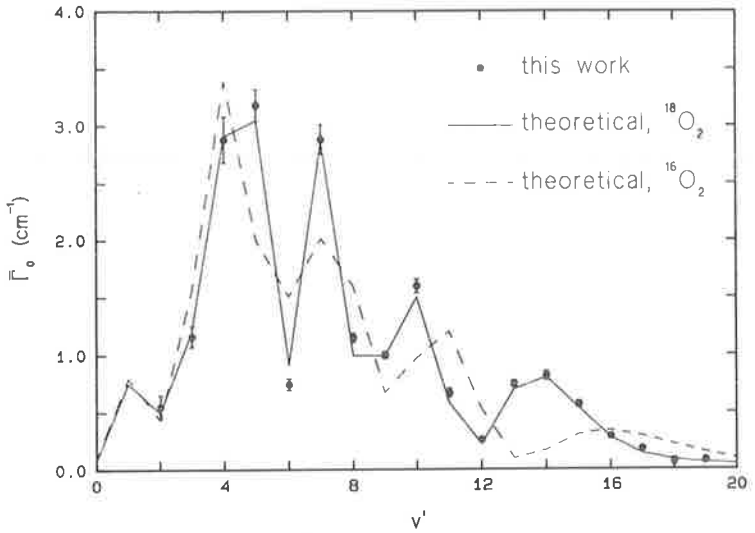

Fig. 19. Measured FWHM predissociation linewidths, extrapolated to zero rotation, for the (2-0)–(19-0) Schumann–Runge bands of $^{18}O_2$. The model predictions for $^{18}O_2$ and $^{16}O_2$, with the model parameters determined from a fit to our $^{16}O_2$ linewidths,[4] are also shown.

The predissociation linewidths for $^{18}O_2$ predicted by Julienne[12] are also given in Table 1. These were calculated using a method similar to ours, but the model parameters used were mainly estimates[12] rather than the fitted values used here. His widths[12] are the average of the three fine-structure components with the same J', rather than the same N', and are thus not rigorously comparable with experimental results. As a result their values differ from our model predictions in detail. Our calculations are in much better agreement with the measurements. For example, Julienne[12] predicts that the rotationless width for $v' = 5$ is less than that for $v' = 4$, whereas the reverse is true for our measurements and calculations. The actual behaviour near $v' = 8,9$ is also significantly different from Julienne's predictions.

The apparent photographic linewidths of Tilford[13] for $v' = 9$–14 are also given in Table 1 for completeness. As would be expected, these widths are consistently larger than ours, the excess averaging $\sim 0.3\ \text{cm}^{-1}$, although their relative behaviour is consistent with our predictions. No other experimental widths are available for $^{18}O_2$.

MODEL PARAMETERS

It is quite clear that predictions based on the model parameters determined for $^{16}O_2$ by Lewis *et al.*[4] are in excellent agreement with our measurements, and that these parameters are significantly better than the estimates of Julienne.[12] It is also possible to determine the twelve parameters ($A_{\alpha\nu}$, $R_{\alpha\nu}$, $M_{\alpha\nu}$ for the states $\alpha = {}^5\Pi_u$, $2\,{}^3\Sigma_u^+$, ${}^3\Pi_u$, ${}^1\Pi_u$) by least-squares fitting the predissociation model to the 18 vibrational widths determined here, as we have done[4] for $^{16}O_2$.

It was necessary to choose the most reliable widths from each band for inclusion in the fit, and smoothed values for $N' = 8$ were used for $v' = 2$–19, rather than the less reliable extrapolated zero rotation values. The results of the fitting procedure are shown in Table 2 where the best fit model linewidths are compared with the measured values and the partial linewidths are also shown. The model widths are averaged over all triplet components for the fixed N', the most valid comparison with the experimental measurements. The r.m.s. deviation of the fit is 7.4%, more than that[4] for $^{16}O_2$ because of the increased difficulty of measurement for this isotope, but for $v' = 2$–15 the r.m.s. deviation is only 1.4%. The worsening accuracy for $v' \geqslant 16$ is merely a reflection of the problem of accurate background determination in the crowded high v' region of $^{18}O_2$.

Our best-fit model parameters for $^{18}O_2$ are given in Table 3 where the quoted errors are 3σ values determined from the fitting procedure, and the parameters[4] obtained for $^{16}O_2$ and the estimates of Julienne[12] are also shown. The ${}^5\Pi_u$ parameters of Julienne[12] were obtained from a deperturbation of the second differences of the $^{16}O_2$ band origins of Ackerman and Biaume[17] by Julienne and

Table 2. Calculated best-fit partial and total FWHM predissociation linewidths (cm^{-1}) for the (2–0)–(19–0) Schumann–Runge bands of $^{18}O_2$ compared with the measured values of this work for $N' = 8$. The deviations between the measured and fitted values are also shown as a percentage. All theoretical widths are averaged over the fine-structure components

v'	$^5\Pi_u$	$2\,^3\Sigma_u^+$	$^3\Pi_u$	$^1\Pi_u$	$\bar{\Gamma}$ (theor.)	$\bar{\Gamma}$ (meas.)	Dev. (%)
2	0.040	0.000	0.398	0.188	0.626	0.63	0.7
3	0.562	0.000	0.473	0.265	1.300	1.31	0.8
4	2.587	0.001	0.499	0.015	3.101	3.09	−0.4
5	2.524	0.021	0.487	0.050	3.081	3.11	0.9
6	0.062	0.190	0.451	0.149	0.853	0.84	−1.5
7	1.682	0.615	0.406	0.165	2.868	2.86	0.3
8	0.321	0.356	0.357	0.122	1.157	1.16	0.2
9	0.494	0.088	0.308	0.070	0.960	0.96	0.0
10	1.091	0.229	0.264	0.033	1.617	1.60	−1.1
11	0.282	0.171	0.222	0.012	0.687	0.70	1.9
12	0.028	0.006	0.185	0.003	0.222	0.22	−1.0
13	0.385	0.145	0.153	0.000	0.684	0.70	2.3
14	0.560	0.146	0.125	0.000	0.831	0.81	−2.6
15	0.435	0.052	0.100	0.001	0.589	0.60	1.9
16	0.239	0.004	0.079	0.002	0.323	0.31	−4.2
17	0.101	0.003	0.061	0.002	0.168	0.19	11.8
18	0.034	0.015	0.047	0.002	0.097	0.08	−21.1
19	0.008	0.021	0.035	0.002	0.066	0.08	17.3

Krauss,[11] and his other parameters were estimated mainly from *ab initio* calculations with extra restraints being applied through qualitative observation of linewidth and lineshift trends.

Conclusions drawn from the $^{16}O_2$ results[4] are confirmed here for $^{18}O_2$. The $^5\Pi_u$ interaction is the strongest and its parameters are very well determined by the fitting procedure, the $^{18}O_2$ values obtained being in excellent agreement with the $^{16}O_2$ values. The $2\,^3\Sigma_u^+$ interaction is important for $v' = 7$–14 and, while the matrix elements and slopes are in good agreement, the crossing points for the two isotopes disagree by a little more than the combined error estimates. The $^1\Pi_u$ interaction is important only for $v' \leqslant 3$, but there is good agreement between the parameters determined for each isotope. The smoothly varying $^3\Pi_u$ contribution is difficult to determine for $^{18}O_2$. While the matrix elements agree for the two isotopes, the slopes and crossing points are in poor agreement. The $^3\Pi_u$ contribution is most significant for $v' = 6,12$ and $v' \geqslant 17$, and the poor agreement between the $^{16}O_2$ and $^{18}O_2$ parameters may be a consequence of the decreasingly reliable $^{18}O_2$ measurements for $v' \geqslant 17$.

Although estimates of the interaction parameters by Julienne[12] were remarkably good considering the paucity of experimental information available to him, either set of our fitted parameters for $^{16}O_2$ or $^{18}O_2$ is to be preferred for the generation of theoretical linewidths.

ROTATIONAL DEPENDENCE

Together with the experimental linewidths of Figs 1–18, we also show model calculations based on our $^{16}O_2$ best-fit parameters.[4]

Table 3. The best-fit model parameters for $^{18}O_2$ compared with those for $^{16}O_2$ and those adopted by Julienne[12]

	α	$A_{\alpha\gamma}$(cm^{-1})	$M_{\alpha\gamma}$(cm^{-1} Å^{-1})	$R_{\alpha\gamma}$(Å)
$^{18}O_2$ This work	$^5\Pi_u$	70.1 ± 2.2	38,700 ± 1100	1.881 ± 0.001
	$2\,^3\Sigma_u^+$	39.8 ± 3.7	34,000 ± 4000	2.004 ± 0.004
	$^3\Pi_u$	21.1 ± 3.0	39,000 ± 3000	1.482 ± 0.009
	$^1\Pi_u$	25.2 ± 7.1	21,000 ± 2000	1.733 ± 0.008
$^{16}O_2$ (Ref. [4])	$^5\Pi_u$	70.9 ± 1.5	39,700 ± 1000	1.880 ± 0.001
	$2\,^3\Sigma_u^+$	38.8 ± 4.2	42,300 ± 8000	1.996 ± 0.008
	$^3\Pi_u$	25.8 ± 2.8	62,700 ± 5000	1.441 ± 0.006
	$^1\Pi_u$	32.2 ± 3.0	22,400 ± 1300	1.731 ± 0.003
$^{16}O_2$ Julienne[12]	$^5\Pi_u$	65 ± 7	40,000 ± 4000	1.875 ± 0.002
	$2\,^3\Sigma_u^+$	55 ± 6	45,000 ± 2500	2.000 ± 0.010
	$^3\Pi_u$	30	80,000	1.425
	$^1\Pi_u$	25 ± 3	23,000	1.730

Table 4. Polynominal coefficients $a_i(v')$ enabling the generation of model predissociation linewidths $\bar{\Gamma}(v'J')$ for $^{18}O_2$ using equation (2)

v'	$a_1(v')$	$a_2(v')$	$a_3(v')$	$a_4(v')$	$a_5(v')$
0	0.084	1.2491 × 10	3.3278 − 8	−2.0917 − 11	5.5504 − 15
1	0.754	−5.1833 − 5	2.9412 − 7	−2.5191 − 10	6.8363 − 14
2	0.497	−2.3480 − 4	1.4455 − 7	−9.0934 − 11	2.7124 − 14
3	1.200	2.7168 − 4	2.1354 − 7	−1.5674 − 10	4.2873 − 14
4	2.909	5.4723 − 4	4.3470 − 8	−8.1767 − 11	1.1393 − 14
5	3.047	−1.0349 − 3	−5.9412 − 8	−1.4324 − 11	2.3203 − 14
6	0.911	1.9798 − 4	4.8578 − 7	−1.7918 − 10	2.4220 − 14
7	2.857	−5.7519 − 4	−1.4702 − 8	−2.7704 − 10	1.1013 − 13
8	0.997	4.2105 − 4	3.8464 − 7	−2.5986 − 10	3.5493 − 14
9	0.995	−5.7241 − 4	1.4508 − 7	1.4517 − 10	−3.7153 − 14
10	1.504	−1.2274 − 5	−3.7878 − 7	−3.9319 − 11	5.8679 − 14
11	0.582	6.6947 − 4	2.9160 − 7	−4.0850 − 10	7.5689 − 14
12	0.221	−3.5103 − 4	5.7028 − 7	5.9580 − 11	−8.3819 − 14
13	0.704	−7.4362 − 4	−1.4286 − 7	4.2305 − 10	−9.5621 − 14
14	0.809	−1.3459 − 4	−5.7776 − 7	2.1027 − 10	2.0281 − 14
15	0.538	3.0909 − 4	−3.1923 − 7	−2.0775 − 10	1.2052 − 13
16	0.278	3.1698 − 4	9.9303 − 8	−4.4568 − 10	1.4741 − 13
17	0.140	1.6596 − 4	2.8373 − 7	−3.6993 − 10	7.2519 − 14
18	0.084	2.8261 − 5	3.1484 − 7	−2.4142 − 10	4.4131 − 15
19	0.062	−5.2932 − 5	2.9801 − 7	−1.9930 − 10	0.0
20	0.049	−7.3660 − 5	1.6441 − 7	−3.5012 − 11	0.0
21	0.038	−6.9174 − 5	2.9654 − 8	1.5844 − 10	0.0
22	0.024	−6.1194 − 5	−1.6628 − 7	8.5242 − 10	0.0

The present results show an increase in linewidth with rotation for $v' = 3,4,6,8,11,16,17$, a decrease for $v' = 5,9,12,13,15$ and no well defined behaviour for $v' = 2,7,10,14,18,19$. No previous measurements of rotational variation are available. Agreement with the predictions is good, the largest discrepancies occurring for relatively scattered measurements with $v' \geqslant 17$. This corresponds to the region of greatest experimental uncertainty and some of the differences may occur because the theoretical results are averaged over the fine-structure, while some of the experimental results in this region are for resolved triplet components.

In the case of $^{16}O_2$, our measured linewidths[4] show an increase with rotation for $v' = 3,6,8,9,12,13$, a decrease for $v' = 5,7,10,11,15$–18, and no discernible variation for $v' = 1,2,4,19$, vastly different behaviour from the present $^{18}O_2$ results. For example, the $^{16}O_2$ model linewidth for $v' = 13$ increases from 0.11 cm^{-1} at $J' = 0$ to 0.43 cm^{-1} at $J' = 26$, while over the same range of rotation the model linewidth for $^{18}O_2$ decreases from 0.71 to 0.24 cm^{-1}. The dramatic changes in rotational linewidth behaviour observed in some cases can be explained qualitatively by noting that the linewidth depends on the overlap integral between multi-lobed wavefunctions, a quantity which is very sensitive to slight isotopic displacements.

The excellent agreement between the full manifold of experimental rovibrational linewidths for $^{18}O_2$ and theoretical predictions based on model parameters determined from $^{16}O_2$ linewidths,[4] provides powerful evidence that the predissociation model is correct in detail. The basic model of Julienne,[12] with the includion of centrifugal distortion to explain the rotational dependences, and with experimentally determined parameters, has indeed been proved appropriate.

Model widths based on the best-fit parameters for $^{18}O_2$ differ only in detail from those calculated with our $^{16}O_2$ parameters[4] and shown in Figs 1–18. We have performed polynomial fits of the form

$$\bar{\Gamma}(v'J') = a_1(v') + a_2(v')x + a_3(v')x^2 + a_4(v')x^3 + a_5(v')x^4 \qquad (2)$$

to our $^{18}O_2$ model widths for $v' = 0$–22, where $x = J'(J' + 1)$, $J' \leqslant 40$. The resulting coefficients are given in Table 4. For $v' > 16$, the maximum value of J' for which equation (2) is applicable decreases below 40 because of dissociation of the molecule.

The theoretical linewidths of this work are summarized in Fig. 20 which emphasizes the complexity of both the v' and J' dependences. Although the rotational axes in Figs 1–18, 20 are labelled with J', this is in effect a mean J' equal to N' because of averaging over the fine-structure components in the model calculations.

CONCLUSIONS

Predissociation linewidth measurements for the (2–0)–(19–0) Schumann–Runge bands of $^{18}O_2$ are presented here for the first time. Systematic variation of linewidth with rotation, observed

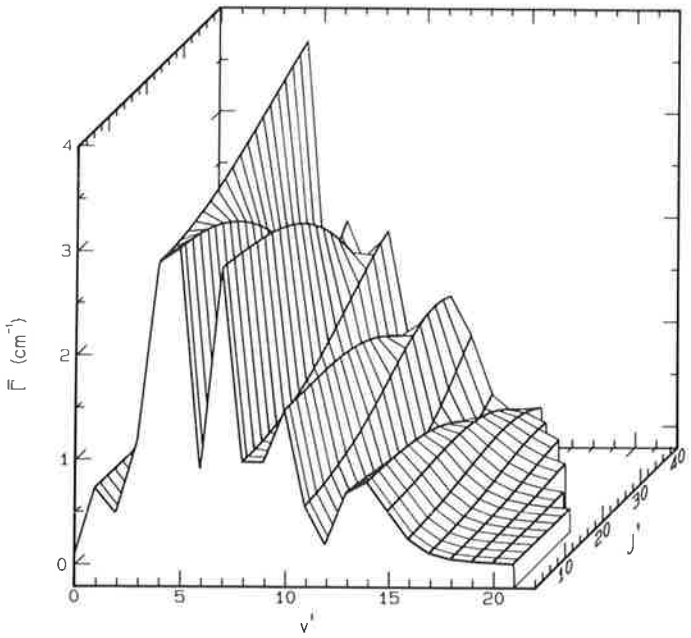

Fig. 20. A three dimensional plot of the model predissociation linewidths $\bar{\Gamma}(v'J')$ for the Schumann–Runge bands of $^{18}O_2$. The widths are averaged over the fine-structure components for a given N'.

previously[4] for $^{16}O_2$, is also found for 12 out of the 18 bands studied here. The vibrational widths and the rotational dependences vary significantly between the $^{16}O_2$ and $^{18}O_2$ isotopes. A theoretical predissociation model of the kind developed by Julienne,[12] with interaction between the $B\,^3\Sigma_u^-$ state and four repulsive states $^5\Pi_u$, $2\,^3\Sigma_u^+$, $^3\Pi_u$, $^1\Pi_u$, and with model parameters determined from previous linewidth measurements[4] for $^{16}O_2$, is found to be capable of explaining the observed vibrational and rotational variation of linewidth for $^{18}O_2$. Repulsive state parameters resulting from a least-squares fit to the observed vibrational widths for $^{18}O_2$ agree well with the corresponding values[4] for $^{16}O_2$, except for the slope and crossing point of the $^3\Pi_u$ potential.

Acknowledgements—The author would like to thank C. Dedman and K. Lonsdale for valuable technical assistance. Some of the programs needed for the model linewidth calculations were kindly provided by S. T. Gibson.

REFERENCES

1. B. R. Lewis, L. Berzins and J. H. Carver, *JQSRT* **37,** 219 (1987).
2. P. J. Flory, *J. chem. Phys.* **4,** 23 (1936).
3. P. H. Krupenie, *J. phys. chem. Ref. Data* **1,** 423 (1972).
4. B. R. Lewis, L. Berzins, J. H. Carver and S. T. Gibson, *JQSRT* **36,** 187 (1986).
5. B. R. Lewis, J. H. Carver, T. I. Hobbs, D. G. McCoy and H. P. F. Gies, *JQSRT* **20,** 191 (1978).
6. B. R. Lewis, J. H. Carver, T. I. Hobbs, D. G. McCoy and H. P. F. Gies, *JQSRT* **22,** 213 (1979).
7. H. P. F. Gies, S. T. Gibson, D. G. McCoy, A. J. Blake and B. R. Lewis, *JQSRT* **26,** 469 (1981).
8. J. E. Frederick and R. D. Hudson, *J. molec. Spectrosc.* **74,** 247 (1979).
9. R. D. Hudson and V. L. Carter, *J. opt. Soc. Am.* **58,** 1621 (1968).
10. R. D. Hudson and V. L. Carter, *Can. J. Phys.* **47,** 1840 (1969).
11. P. S. Julienne and M. Krauss, *J. molec. Spectrosc.* **56,** 270 (1975).
12. P. S. Julienne, *J. molec. Spectrosc.* **63,** 60 (1976).
13. S. Tilford, private communication, see Ref. [12].
14. B. R. Lewis, *Appl. Opt.* **22,** 1546 (1983).
15. B. R. Lewis, L. Berzins and J. H. Carver, *JQSRT* **37,** 243 (1987).
16. R. M. Goody, *Atmospheric Radiation: I. Theoretical Basis. Oxford University Press, London* (1964).
17. M. Ackerman and F. Biaume. *J. molec. Spectrosc.* **35,** 73 (1970).

4.9 Predissociation linewidths for the Schumann-Runge bands of $^{16}O^{18}O$

[27] B. R. Lewis, L. Berzins, and J. H. Carver,
Journal of Quantitative Spectroscopy and Radiative Transfer **37**, 243–254 (1987).

J. Quant. Spectrosc. Radiat. Transfer Vol. 37, No. 3, pp. 243–254, 1987
Printed in Great Britain.

0022-4073/87 $3.00 + 0.00

PREDISSOCIATION LINEWIDTHS FOR THE SCHUMANN–RUNGE BANDS OF $^{16}O^{18}O$

B. R. LEWIS, L. BERZINS and J. H. CARVER
Research School of Physical Sciences, The Australia, National University, Canberra, Australia 2600

(*Received* 20 *May* 1986)

Abstract—We have measured predissociation linewidths for rotational lines from the (2–0)–(15–0) Schumann–Runge bands of $^{16}O^{18}O$. The behaviour of the vibrational widths is intermediate between those observed previously for $^{16}O_2$ and $^{18}O_2$, with predissociation maxima at $v' = 4, 7, 10, (15)$. Our experimental linewidths are found to exhibit systematic variation with rotation for some of the bands studied. A model of the predissociation, including the interactions of the $B^3\Sigma_u^-$ state with repulsive $^5\Pi_u$, $^3\Pi_u$, $^1\Pi_u$ and $^3\Sigma_u^+$ states, and with molecular interaction parameters determined by a least-squares fit to previous $^{16}O_2$ linewidths, is found to predict accurately the observed vibrational and rotational dependences of linewidth for $^{16}O^{18}O$.

INTRODUCTION

We have recently presented extensive measurements[1-4] of the vibrational and rotational variation of oscillator strength and predissociation linewidth in the Schumann–Runge bands of $^{16}O_2$ and $^{18}O_2$, and, in an associate paper,[5] oscillator strength measurements for $^{16}O^{18}O$. Since $^{16}O^{18}O$ constitutes 0.408% of atmospheric oxygen,[6] and since its absorption lines are visible in the spectrum of normal O_2,[1] it is necessary to know the oscillator strengths and linewidths for this species in order to construct accurate line-by-line atmospheric absorption models.

It has been suggested[7] that atmospheric $^{16}O^{18}O$ may be a significant absorber and have a disproportionate effect on the O_2 photodissociation rate due to isotope effects in the Schumann–Runge bands, but Blake *et al.*[8] have recently produced a theoretical model of the $^{16}O^{18}O$ absorption which discounts that suggestion. Our measurements of the $^{16}O^{18}O$ oscillator strengths[5] support those used by Blake *et al.*,[8] but there have been no experimental predissociation linewidths to compare with their model calculations. Julienne,[9] in his important work modelling predissociation in the Schumann–Runge bands of O_2, noted the desirability of having linewidth measurements on isotopically substituted O_2 in order to obtain a more complete understanding of the predissociation.

$^{16}O^{18}O$ was first discovered in the atmosphere by Dieke and Babcock.[10] Spectroscopic constants have been determined for the $b^1\Sigma_g^+$ state,[11] and the ground state $X^3\Sigma_g^-$ by several methods,[11-13] but the $B^3\Sigma_u^-$ state has been studied little.[5,14]

The historical development of the study of predissociation in O_2 has been given by Krupenie,[15] and a detailed discussion of the work since that time has been given by Lewis *et al.*[2] Our recent measurements[2,4] of the vibrational and rotational variation of predissociation linewidth for $^{16}O_2$ and $^{18}O_2$ were found to be in excellent agreement with predictions based on the theoretical model of Julienne and Krauss,[16] later updated by Julienne,[9] but with model parameters slightly different from those used by those authors.[9,16] The observed predissociation can be explained in terms of the interaction of the $B^3\Sigma_u^-$ state with four repulsive states $^5\Pi_u$, $2^3\Sigma_u^+$, $^3\Pi_u$, $^1\Pi_u$. The only existing calculations of linewidth for $^{16}O^{18}O$ are those of Blake *et al.*[8]

In this work, the final in this series on isotopic effects in O_2, we present the first experimental study of predissociation linewidths for the (2–0)–(15–0) Schumann–Runge bands of $^{16}O^{18}O$, including variation with rotation. Model linewidths calculated according to the theory of Julienne,[9] but with model parameters taken from a fit to our previous $^{16}O_2$ results,[2] agree well with our $^{16}O^{18}O$ measurements, as do the model linewidths of Blake *et al.*[8] Model parameters obtained by a least-squares fit to the $^{16}O^{18}O$ linewidths agree fairly well with those obtained from the $^{16}O_2$ linewidths.[2]

EXPERIMENTAL METHOD AND DATA ANALYSIS

A detailed discussion of the experimental method has been given elsewhere.[3,5] Background radiation from an H_2 continuum was dispersed by a modified[17] 2.2 m scanning VUV monochromator at a resolution of ~ 0.05 Å, and was detected photoelectrically before entering and after leaving the 10 cm sealed quartz cells containing 64% $^{16}O_2$, 32% $^{16}O^{18}O$ and 4% $^{18}O_2$. The individual cells were filled[3] with pressures in the range 2 Torr–2 atm and were mounted on a carousel[3] which enabled concurrent scans of different samples to be taken as desired. The scanning system was microcomputer controlled.

Absorption scans over the region of the Schumann–Runge bands were performed for each cell, the $^{16}O_2$ lines acting as built in wavelength calibrators. It was not possible to determine backgrounds experimentally using the sealed cells, and an interpolation was performed between experimentally determined transmissions at the deeper minima between absorption lines, after correction for adjacent and distant line wings.[5]

The general data analysis procedures have been discussed in detail previously.[1,5] Briefly, line profiles and equivalent widths were recorded for all lines of interest and the equivalent width data analysis technique allowed simultaneous determination of both oscillator strength and linewidth by an iterative procedure.[18] The model parameters assumed in the data analysis program have been described previously[1,3,5] and will not be discussed further here except to note that, due to the significant proportions of $^{16}O_2$ and $^{18}O_2$ inevitably present in the statistical gas mixture used in this work, an accurate knowledge of the oscillator strengths and linewidths for these isotopes is required. This knowledge is provided by our previous studies.[1–4]

When possible, scans of a given line at two widely separated pressures were analysed by the equivalent width method,[1] but, because of the limited number of pressures in the sealed cells and the fixed cell length, the ideal pairs of pressures for application of the full equivalent width method were not always available. In these cases oscillator strengths[5] and linewidths were obtained by a two parameter least-squares fit to the observed line profiles at a single pressure, a variant of the method used for $^{16}O_2$ by Frederick and Hudson.[19] Linewidths found in this way were consistent with those obtained by the two scan equivalent width method when it was possible to compare the two for a given line.

THEORETICAL METHOD

The predissociation model used here is based on the work of Julienne and Krauss[16] and Julienne,[9] and has been fully discussed by Lewis *et al.*[2] Only a brief outline will be given here.

The predissociation of the $B^3\Sigma_u^-$ state is described in terms of the interactions of this state with four repulsive states $\alpha = {}^5\Pi_u$, $2^3\Sigma_u^+$, ${}^3\Pi_u$, ${}^1\Pi_u$, described by exponential potentials.[2] The B state potential is taken from Lewis *et al.*[2] The individual interactions α are described by three parameters, the curve crossing point $R_{\alpha v}$, the slope of the repulsive potential at crossing $M_{\alpha v}$, and the matrix element of the interaction $A_{\alpha v}$. The predissociation linewidth due to a single curve crossing is related to the product of $A_{\alpha v}$ and the overlap of the wavefunctions of the bound and unbound states at the vibrational energy of interest.[9] The total linewidths are determined as the sum of the contributions from each curve crossing and are dependent on the fine-structure component i and the rotation.

In this work we assume the twelve repulsive curve parameters $A_{\alpha v}$, $R_{\alpha v}$, $M_{\alpha v}$, determined previously[2] for $^{16}O_2$, and calculate the full manifold of partial widths $\Gamma(v'J'i)$ using the procedure outlined above. We have averaged the widths over the fine-structure parameter i for a fixed $N'(J' = N', N' \pm 1)$, as this gives a valid comparison with the experimental measurements. Henceforth the predissociation widths will be denoted by $\bar{\Gamma}$ to indicate the fine-structure averaging.

RESULTS

Some 147 distinct linewidth measurements from the (2–0)–(15–0) Schumann–Runge bands of $^{16}O^{18}O$ are presented here. As in the cases[1–4] of $^{16}O_2$ and $^{18}O_2$, the oscillator strengths measured in association with this work[5] are in good agreement with theoretical expectations, supporting the reliability of the predissociation linewidths presented here.

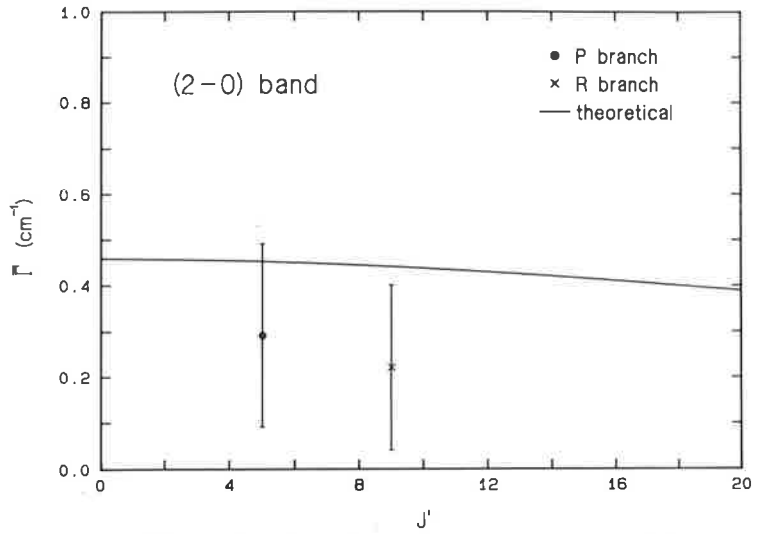

Fig. 1. The variation of FWHM predissociation linewidth with rotation for the (2–0) Schumann–Runge band of $^{16}O^{18}O$.

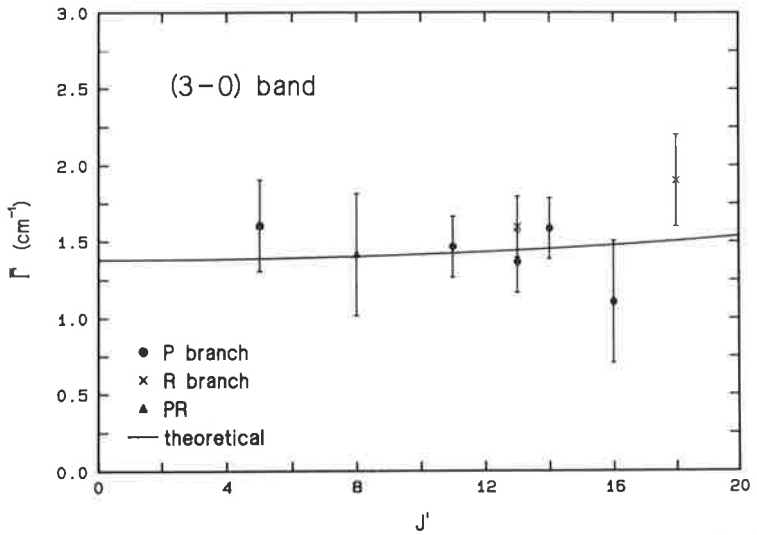

Fig. 2. The variation of FWHM predissociation linewidth with rotation for the (3–0) Schumann–Runge band of $^{16}O^{18}O$.

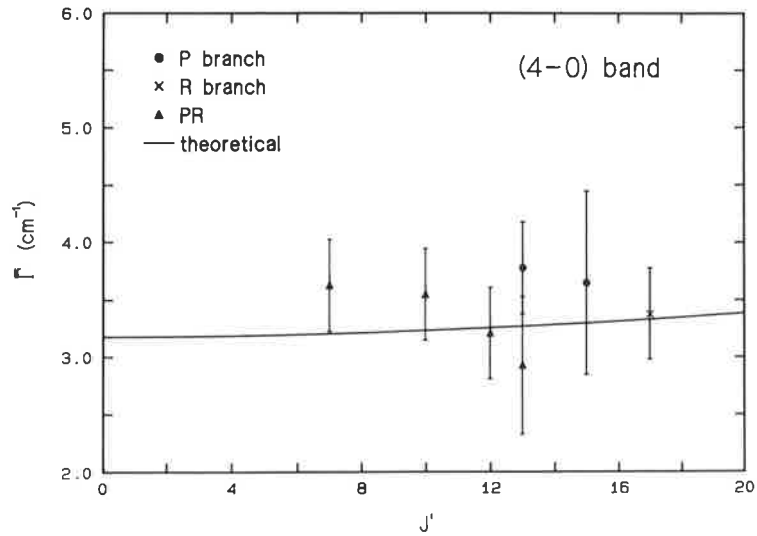

Fig. 3. The variation of FWHM predissociation linewidth with rotation for the (4–0) Schumann–Runge band of $^{16}O^{18}O$.

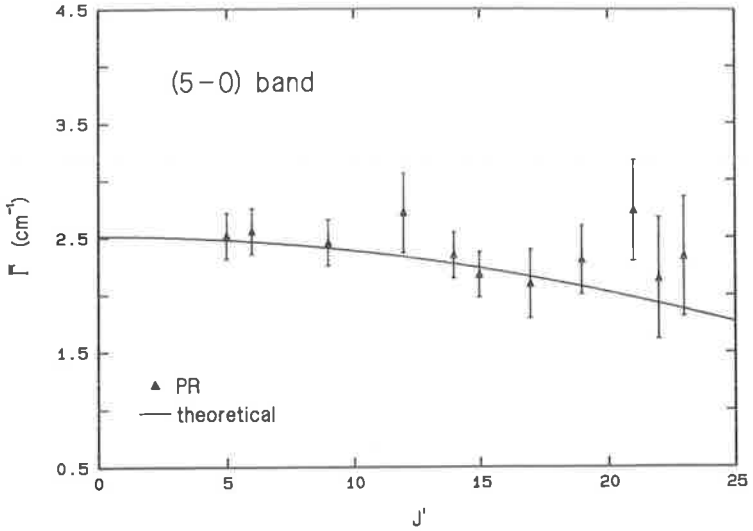

Fig. 4. The variation of FWHM predissociation linewidth with rotation for the (5–0) Schumann–Runge band of $^{16}O^{18}O$.

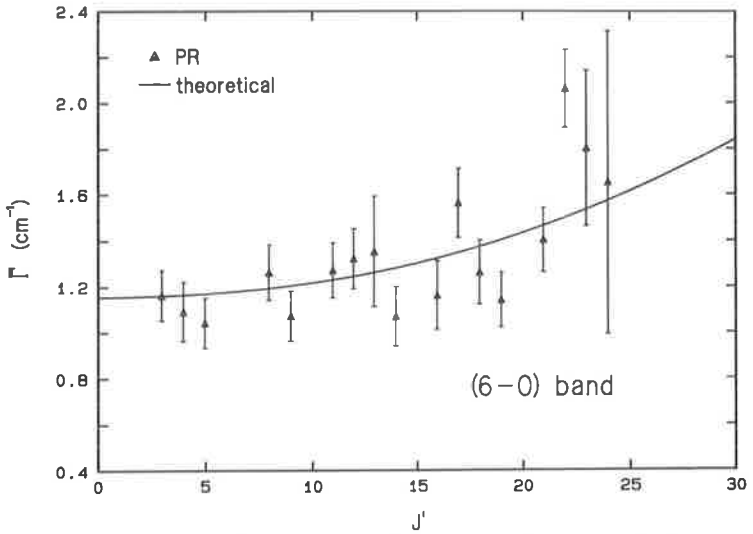

Fig. 5. The variation of FWHM predissociation linewidth with rotation for the (6–0) Schumann–Runge band of $^{16}O^{18}O$.

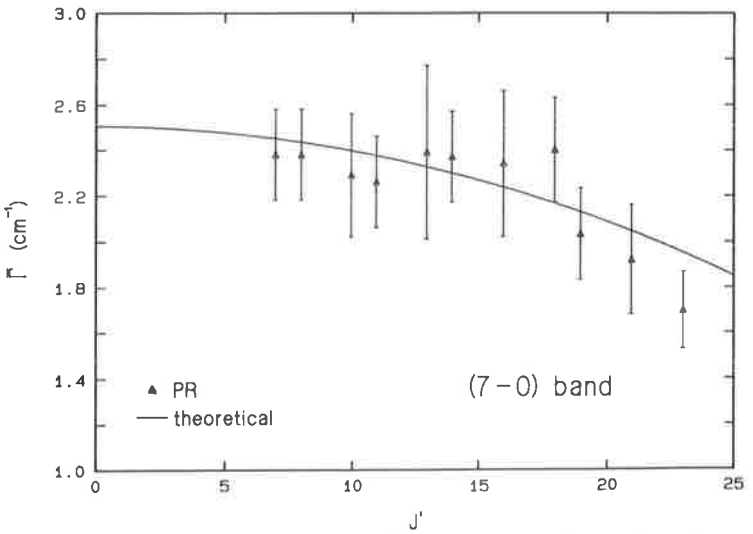

Fig. 6. The variation of FWHM predissociation linewidth with rotation for the (7–0) Schumann–Runge band of $^{16}O^{18}O$.

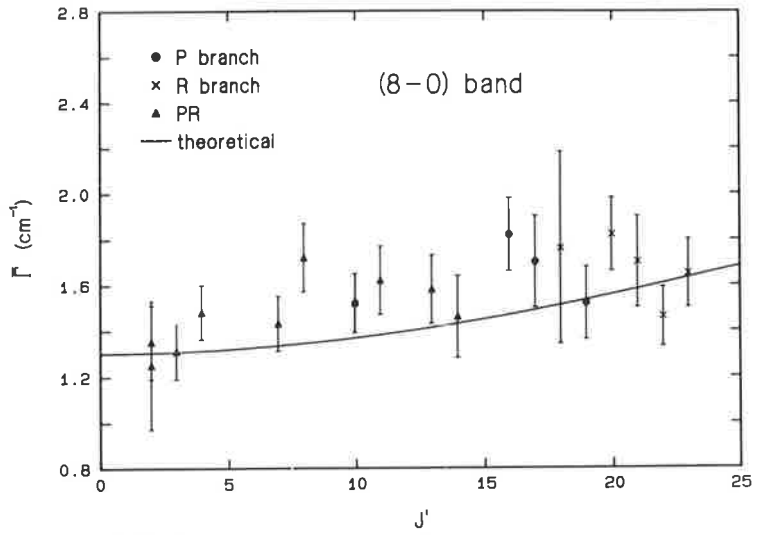

Fig. 7. The variation of FWHM predissociation linewidth with rotation for the (8–0) Schumann–Runge band of $^{16}O^{18}O$.

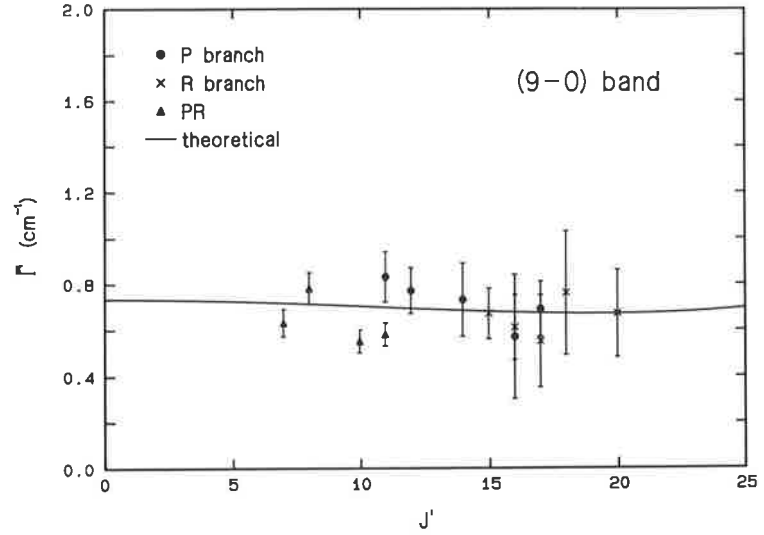

Fig. 8. The variation of FWHM predissociation linewidth with rotation for the (9–0) Schumann–Runge band of $^{16}O^{18}O$.

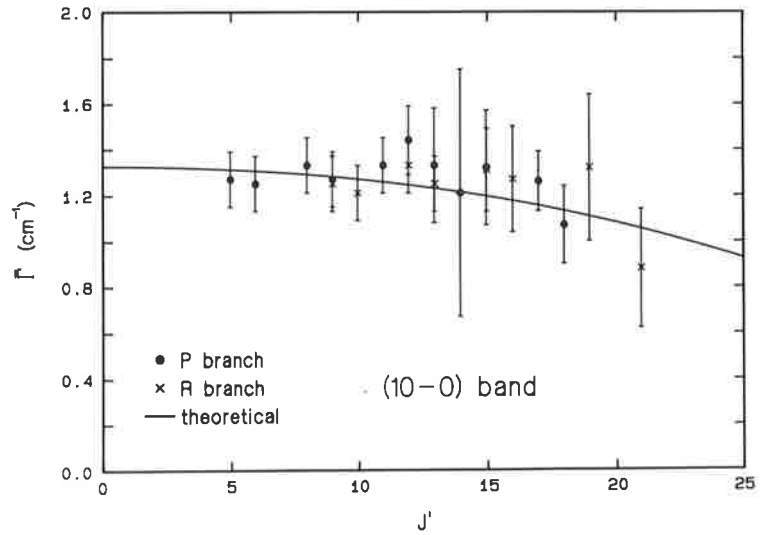

Fig. 9. The variation of FWHM predissociation linewidth with rotation for the (10–0) Schumann–Runge band of $^{16}O^{18}O$.

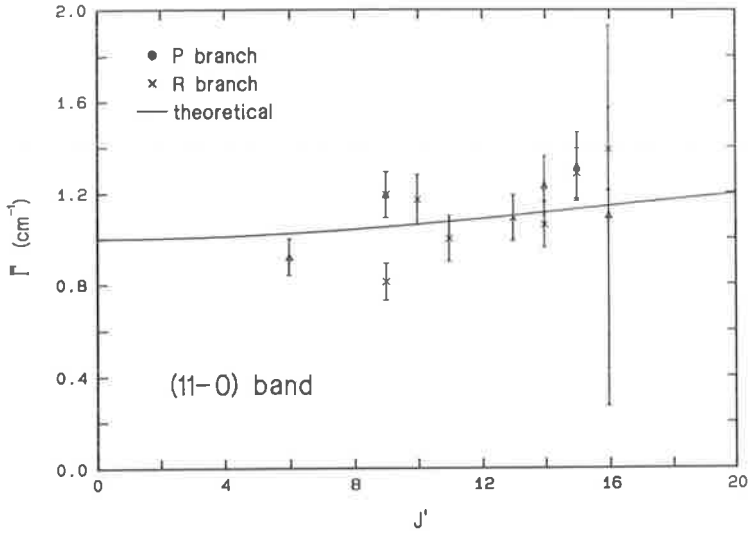

Fig. 10. The variation of FWHM predissociation linewidth with rotation for the (11–0) Schumann–Runge band of $^{16}O^{18}O$.

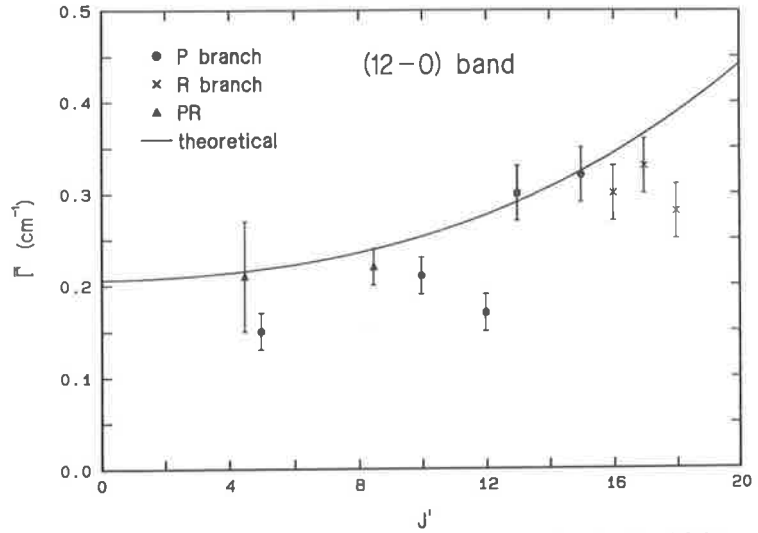

Fig. 11. The variation of FWHM predissociation linewidth with rotation for the (12–0) Schumann–Runge band of $^{16}O^{18}O$.

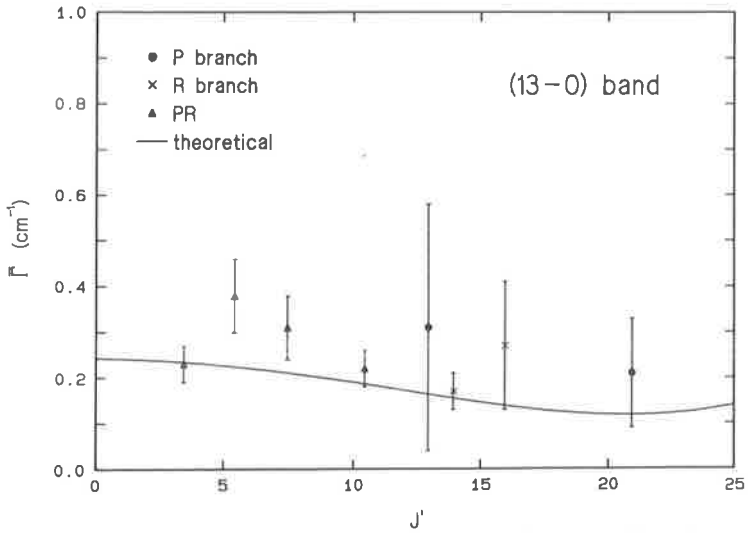

Fig. 12. The variation of FWHM predissociation linewidth with rotation for the (13–0) Schumann–Runge band of $^{16}O^{18}O$.

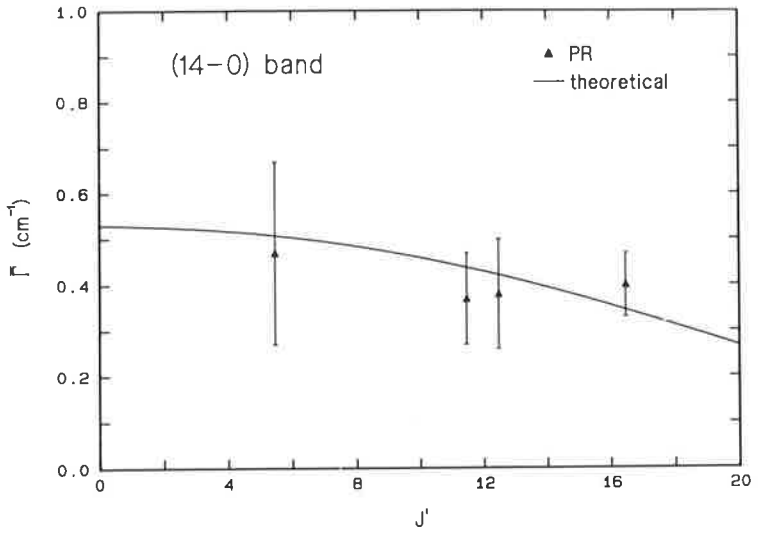

Fig. 13. The variation of FWHM predissociation linewidth with rotation for the (14–0) Schumann–Runge band of $^{16}O^{18}O$.

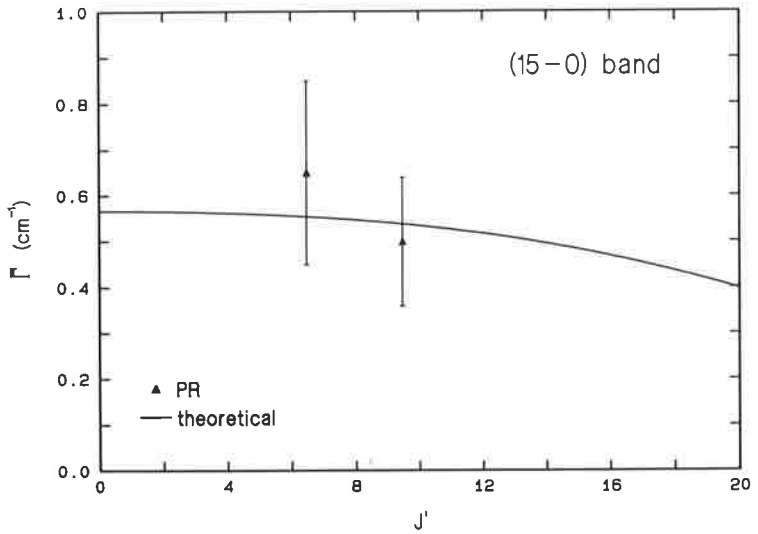

Fig. 14. The variation of FWHM predissociation linewidth with rotation for the (15–0) Schumann–Runge band of $^{16}O^{18}O$.

The linewidths measured by us for each band are given in Figs 1–14 as functions of upper state rotation J'. In the case of unresolved lines (P, R branch triplets, PR sextuplets) an appropriate mean J' is assigned to the measurement. In only one case [(13–0), $P_1(22)$] was the width of a resolved fine-structure component measured. For the heteronuclear molecule $^{16}O^{18}O$ all rotations are allowed, and there are twice as many lines[5] as in the absorption spectra of the homonuclear species $^{16}O_2$ and $^{18}O_2$. For low vibration the $P(N'')$ and $R(N''+2)$ branches may overlap, as for $^{16}O_2$ and $^{18}O_2$, but for $^{16}O^{18}O$ the $P(N'')$ and $R(N''+1)$ branches may also overlap for $v' > 11$. This accounts for the half integral values of J' assigned to some measurements. For this isotope, in many cases ($v' = 2$–8; $v' = 9$, $J' \geqslant 17$; $v' = 10$, $J' \geqslant 15$) the widths were obtained from a single scan using the profile fitting technique, while the remainder were obtained using the two scan equivalent width method.

The errors given in Figs 1–14 are statistical only. There is an additional uncertainty of about 6% due to possible systematic errors in pressure, cell length and temperature. Because of the nature of the istopic sample used in this work, some of the widths obtained here depend on the previously determined parameters[1–4] for $^{16}O_2$ and $^{18}O_2$. These parameters are thought to be sound, but the more

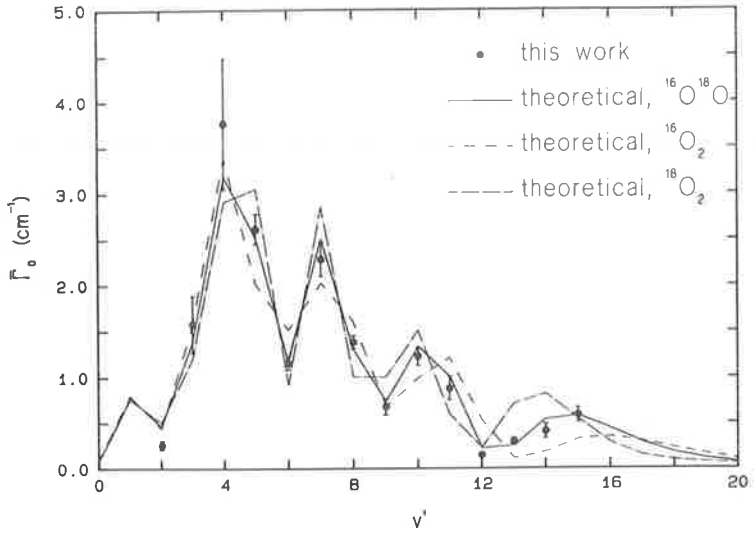

Fig. 15. Measured FWHM predissociation linewidths, extrapolated to zero rotation, for the (2–0)–(15–0) Schumann–Runge bands of $^{16}O^{18}O$. The model predictions for $^{16}O^{18}O$, $^{16}O_2$ and $^{18}O_2$, with the model parameters determined from a fit to our $^{16}O_2$ linewidths,[2] are also shown.

complicated spectrum for the statistical isotopic mixture generally results in the $^{16}O^{18}O$ widths being a little less reliable than those for the other isotopes,[2–4] especially for the weaker lines.

Our linewidths were smoothed and extrapolated to $J' = 0$ and these results are compared in Table 1 and Fig. 15 with model predictions based on the model parameters determined by Lewis *et al.*[2] for $^{16}O_2$. There is excellent agreement between the present measurements and the model predictions. The model linewidths for $^{16}O_2$ and $^{18}O_2$ are also shown in Fig. 15 and the $^{16}O^{18}O$ widths generally lie between those for the other isotopes. For $^{16}O^{18}O$ we observe peaks at $v' = 4$, 7, 10, (15) compared with $v' = 4$, 7, 11, 16 for $^{16}O_2$. Although the vibrational width patterns are qualitatively similar for the different isotopes, there are significant differences for certain bands, for example $v' = 12$ where the measured rotationless width for $^{16}O^{18}O$ is 0.14 cm^{-1} compared with[2] 0.42 cm^{-1} for $^{16}O_2$ and with[4] 0.26 cm^{-1} for $^{18}O_2$.

The predissociation linewidths for $^{16}O^{18}O$ calculated by Blake *et al.*[8] are also presented in Table 1. These were obtained using a model similar to ours, but with slightly different model parameters not based on measurements. The relatively small differences between the widths of Blake *et al.*[8] and our values is not expected to affect significantly their calculations[8] of the atmospheric $^{16}O^{18}O$ photodissociation rate. No experimental widths other than those presented here are available for $^{16}O^{18}O$.

Table 1. Measured FWHM predissociation linewidths Γ_0 (cm^{-1}), extrapolated to zero rotation, for the (2–0)–(15–0) Schumann–Runge bands of $^{16}O^{18}O$. Our model calculations are also shown together with those of Blake *et al.*[8]

	Γ_0 (cm^{-1})		
v'	Measured	Theoretical	Blake *et al.*[8]
2	0.25 ± 0.20	0.46	0.47
3	1.57 ± 0.31	1.38	1.29
4	3.76 ± 0.72	3.18	2.80
5	2.61 ± 0.17	2.51	2.04
6	1.15 ± 0.07	1.16	1.41
7	2.28 ± 0.19	2.51	2.06
8	1.38 ± 0.07	1.30	1.19
9	0.67 ± 0.09	0.73	0.68
10	1.22 ± 0.10	1.33	1.05
11	0.87 ± 0.13	1.00	0.98
12	0.14 ± 0.02	0.21	0.37
13	0.29 ± 0.04	0.24	0.20
14	0.40 ± 0.10	0.53	0.43
15	0.58 ± 0.14	0.57	0.52

Table 2. Calculated best-fit partial and total FWHM predissociation widths for the (3–0)–(15–0) Schumann–Runge bands of $^{16}O^{18}O$ compared with the measured values of this work for $N' = 8$. The deviations between the measured and fitted values are also shown as a percentage. All theoretical values were averaged over the fine-structure components

v'	$^5\Pi_u$	$2^3\Sigma_u^+$	$^3\Pi_u$	$^1\Pi_u$	$\bar{\Gamma}$ (theor.)	$\bar{\Gamma}$ (meas.)	Dev. (%)
3	0.717	0.000	0.433	0.298	1.448	1.45	0.2
4	2.773	0.003	0.515	0.308	3.598	3.56	−1.1
5	1.875	0.037	0.542	0.027	2.481	2.49	0.4
6	0.339	0.223	0.519	0.053	1.134	1.14	0.5
7	1.216	0.472	0.463	0.198	2.349	2.34	−0.4
8	0.745	0.131	0.389	0.213	1.477	1.48	0.2
9	0.094	0.136	0.308	0.122	0.659	0.66	0.2
10	0.917	0.096	0.234	0.035	1.282	1.28	−0.1
11	0.644	0.155	0.169	0.001	0.969	0.98	1.1
12	0.071	0.000	0.118	0.009	0.198	0.20	−1.8
13	0.054	0.076	0.080	0.030	0.241	0.26	7.5
14	0.268	0.103	0.053	0.046	0.470	0.42	−12.0
15	0.365	0.047	0.035	0.051	0.498	0.58	14.2

MODEL PARAMETERS

As in the cases[2,4] of $^{16}O_2$ and $^{18}O_2$, we have determined the twelve parameters ($A_{\alpha v}$, $R_{\alpha v}$, $M_{\alpha v}$ for the states $\alpha = {}^5\Pi_u$, $2^3\Sigma_u^+$, $^3\Pi_u$, $^1\Pi_u$) by least-squares fitting the predissociation model to our vibrational widths for $^{16}O^{18}O$.

Rather than use the less reliable extrapolated zero rotation values, we used smoothed widths for $N' = 8$ and $v' = 3$–15. The uncertain (2–0) width was omitted from the fit. The results of the fitting procedure are shown in Table 2 where the best-fit model linewidths are compared with the measured values, and the partial linewidths are also shown. The model widths are averaged over all triplet components for a fixed N', the most valid comparison with the experimental measurements. The r.m.s. deviation of the fit is about 6% and the worsening accuracy for $v' \geqslant 13$ reflects the problems of accurate background determination in the crowded high v' region of $^{16}O^{18}O$.

The best-fit model parameters determined for $^{16}O^{18}O$ are given in Table 3 where the quoted errors are 3σ values determined from the fitting procedure, and the corresponding values obtained previously[2,4] for $^{16}O_2$ and $^{18}O_2$ are also shown, together with the estimates of Julienne.[9] It is surprising that the error estimates for the $^{16}O^{18}O$ parameters compare favourably with those for $^{16}O_2$, but this is probably due to the inclusion of the less reliable (1–0), (2–0) and high rotation bands for the latter isotope. The $^{16}O^{18}O$ parameters are not expected to be inherently as reliable as those for $^{16}O_2$.

General conclusions drawn from the results for $^{16}O_2$ and $^{18}O_2$ are confirmed for $^{16}O^{18}O$. The $^5\Pi_u$ interaction is the strongest and its parameters are very well determined from the fitting procedure, the $^{16}O^{18}O$ values obtained being in excellent agreement with the $^{16}O_2$ and $^{18}O_2$ values. The $2^3\Sigma_u^+$

Table 3. The best-fit model parameters for $^{16}O^{18}O$ compared with those for $^{16}O_2$ and $^{18}O_2$ and those adopted by Julienne[9]

	α	$A_{\alpha v}$(cm^{-1})	$M_{\alpha v}$(cm^{-1} Å^{-1})	$R_{\alpha v}$(Å)
$^{16}O^{18}O$	$^5\Pi_u$	69.2 ± 1.8	39,000 ± 1000	1.880 ± 0.001
This work	$2^3\Sigma_u^+$	40.7 ± 5.0	53,000 ± 12,000	1.999 ± 0.005
	$^3\Pi_u$	28.1 ± 1.8	55,000 ± 2000	1.458 ± 0.003
	$^1\Pi_u$	37.3 ± 6.1	34,000 ± 2000	1.695 ± 0.004
$^{18}O_2$ (Ref. [4])	$^5\Pi_u$	70.1 ± 2.2	38,700 ± 1100	1.881 ± 0.001
	$2^3\Sigma_u^+$	39.8 ± 3.7	34,000 ± 4000	2.004 ± 0.004
	$^3\Pi_u$	21.1 ± 3.0	39,000 ± 3000	1.482 ± 0.009
	$^1\Pi_u$	25.2 ± 7.1	21,000 ± 2000	1.733 ± 0.008
$^{16}O_2$ (Ref. [2])	$^5\Pi_u$	70.9 ± 1.5	39,700 ± 1000	1.880 ± 0.001
	$2^3\Sigma_u^+$	38.8 ± 4.2	42,300 ± 8000	1.996 ± 0.008
	$^3\Pi_u$	25.8 ± 2.8	62,700 ± 5000	1.441 ± 0.006
	$^1\Pi_u$	32.2 ± 3.0	22,400 ± 1300	1.731 ± 0.003
$^{16}O_2$ Julienne[9]	$^5\Pi_u$	65 ± 7	40,000 ± 4000	1.875 ± 0.002
	$2^3\Sigma_u^+$	55 ± 6	45,000 ± 2500	2.000 ± 0.010
	$^3\Pi_u$	30	80,000	1.425
	$^3\Pi_u$	25 ± 3	23,000	1.730

Table 4. Polynomial coefficients $a_i(v')$ enabling the generation of model predissociation linewidths $\bar{\Gamma}(v'J')$ for $^{16}O^{18}O$ using equation (1)

v'	$a_1(v')$	$a_2(v')$	$a_3(v')$	$a_4(v')$	$a_5(v')$
0	0.092	1.7521 × 10^{-5}	2.9722-8	−1.7792-11	4.8210-15
1	0.778	−4.4778-5	2.6554-7	−2.3132-10	6.2871-14
2	0.459	−2.0377-4	1.1004-7	−4.7705-11	1.4565-14
3	1.379	3.1851-4	2.0298-7	−1.4582-10	3.9132-14
4	3.178	5.1628-4	−2.2602-8	−7.5891-11	8.7836-15
5	2.514	−1.1648-3	−1.0051-8	4.0911-11	1.1181-14
6	1.156	5.2788-4	4.2718-7	−2.5372-10	4.0107-14
7	2.508	−1.0044-3	6.7335-8	−1.7699-10	8.9690-14
8	1.302	6.0479-4	1.4199-7	−2.9463-10	5.9195-14
9	0.735	−3.3422-4	4.4378-7	−1.3786-11	−2.5849-14
10	1.327	−4.6613-4	−3.7964-7	2.4069-10	−1.5959-14
11	1.001	5.9905-4	−1.8595-7	−3.6094-10	1.2739-13
12	0.206	3.6682-4	6.3168-7	−4.1399-10	4.0580-14
13	0.242	−5.3418-4	5.2867-7	1.5676-10	−1.1755-13
14	0.530	−6.2693-4	−2.0019-7	5.4399-10	−1.4981-13
15	0.566	−2.4843-4	−5.0046-7	3.1847-10	−8.8951-15
16	0.428	7.1026-5	−4.4612-7	−3.2580-12	1.1104-13
17	0.278	1.8564-4	−2.5577-7	−2.2778-10	1.7214-13
18	0.170	1.7386-4	−4.4244-8	−4.4859-10	2.6820-13
19	0.102	1.3137-4	−4.5571-8	−1.9403-10	0.0
20	0.060	8.2617-5	−9.3334-9	−2.9214-10	0.0

interaction is important for $v' = 7$–14 and the parameters obtained for $^{16}O^{18}O$ are in good agreement with those for $^{16}O_2$. The $^1\Pi_u$ interaction is poorly determined for $^{16}O^{18}O$ because accurate widths for $v' < 3$ are not available. While the matrix element agrees with that determined from the $^{16}O_2$ measurements within the combined experimental errors, the crossing points and slopes are in poor agreement for the $^1\Pi_u$ state. As we observed[4] for $^{18}O_2$, the smoothly varying $^3\Pi_u$ contribution for $^{16}O^{18}O$ is difficult to determine accurately. While the matrix element is in agreement with that for $^{16}O_2$, the crossing points and slopes are in only fair agreement. The $^3\Pi_u$ contribution is most significant for $v' = 6$, 12 of the bands measured, and perhaps accurate measurements for bands with $v' > 13$ are required in order to determine more accurately the parameters for this state.

Although the estimates of the interaction parameters by Julienne[9] were remarkably good considering the paucity of experimental information available to him, any of the sets of fitted parameters for $^{16}O^{18}O$, $^{16}O_2$ or $^{18}O_2$ is to be preferred for the generation of model linewidths.

ROTATIONAL DEPENDENCE

Because of the experimental difficulties noted earlier, it is difficult to determine rotational dependences of linewidth for $^{16}O^{18}O$. Nevertheless, Figs 1–14 show a definite increase in linewidth with rotation for $v' = 6$, 8, 11, 12, and a decrease for $v' = 7$, 10. Agreement with our model predictions of rotational variation of linewidth is good for all bands studied.

The observed rotational variation of linewidth varies greatly between the different isotopes. For example, the $^{16}O^{18}O$ model linewidth for $v' = 13$ decreases from 0.24 cm^{-1} at $J' = 2$ to 0.15 cm^{-1} at $J' = 26$, while the $^{16}O_2$ width for $v' = 13$ increases from 0.11 to 0.43 cm^{-1}, and the $^{18}O_2$ width decreases from 0.71 to 0.24 cm^{-1} for the same range of rotation. This dramatic change in behaviour between isotopes of comparatively small mass differences can be explained qualitatively by noting that the linewidth depends on the overlap integral between multilobed wavefunctions, a quantity very sensitive to slight isotopic displacements.

As has already been noted[4] for $^{18}O_2$, the excellent agreement between the full manifold of experimental rovibrational linewidths for $^{16}O^{18}O$ and the model predictions, provides powerful evidence that the predissociation model of Julienne[9] used here is correct in detail.

Model widths based on the best-fit parameters for $^{16}O^{18}O$ differ only in detail from those calculated from the best-fit parameters[2] for $^{16}O_2$. We have performed polynomial fits of the form

$$\bar{\Gamma}(v'J') = a_1(v') + a_2(v')x + a_3(v')x^2 + a_4(v')x^3 + a_5(v')x^4 \quad (1)$$

to the $^{16}O^{18}O$ model widths for $v' = 0$–22, where $x = J'(J'+1)$, $J' \leqslant 40$, and the resulting coefficients are given in Table 4. For $v' \geqslant 16$, the maximum value of J' for which equation (1) is applicable decreases below 40 because of dissociation of the molecule.

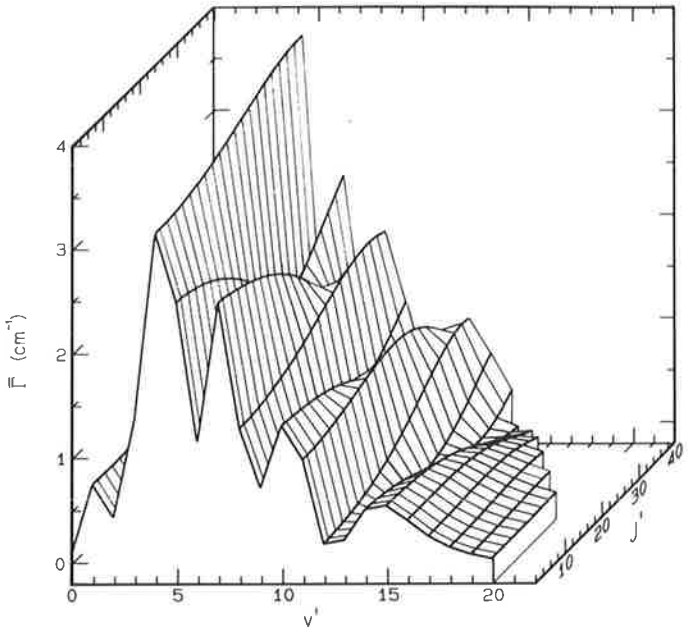

Fig. 16. A three dimensional plot of the model predissociation linewidths $\bar{\Gamma}(v'J')$ for the Schumann–Runge bands of $^{16}O^{18}O$. The widths are averaged over the fine-structure components for a given N'.

The theoretical linewidths of this work are summarized in Fig. 16 which emphasizes the complexity of both the v' and J' dependences. Although the rotational axes in Figs 1–14 and 16 are labelled with J', this is in effect a mean J' equal to N' because of averaging over the fine-structure components.

CONCLUSIONS

Predissociation linewidth measurements for the (2–0)–(15–0) Schumann–Runge bands of $^{16}O^{18}O$ are presented here for the first time. Systematic variation of linewidth with rotation, observed previously[2,4] for $^{16}O_2$ and $^{18}O_2$, is seen also for $^{16}O^{18}O$ with 6 of the 14 bands studied clearly showing such variation. The vibrational widths and rotational dependences measured for $^{16}O^{18}O$ differ significantly from those observed for the other isotopes. A theoretical predissociation model of the kind developed by Julienne,[9] with interaction between the $B^3\Sigma_u^-$ state and four repulsive states $^5\Pi_u$, $2^3\Sigma_u^+$, $^3\Pi_u$, $^1\Pi_u$, using model parameters determined from previous linewidth measurements[2] for $^{16}O_2$, is found to be capable of explaining the observed vibrational and rotational variation of linewidth for $^{16}O^{18}O$. The present linewidths agree quite well with those calculated by Blake *et al.*[8] whose atmospheric O_2 photodissociation model predicts that Cicerone and McCrumb[7] have overestimated the importance of $^{16}O^{18}O$ to total atmospheric O_2 photodissociation by about an order of magnitude.

Acknowledgements—The authors would like to thank C. Dedman and K. Lonsdale for valuable technical assistance. Some of the programs needed for the model linewidth calculations were kindly provided by S. T. Gibson.

REFERENCES

1. B. R. Lewis, L. Berzins and J. H. Carver, *JQSRT* **36,** 209 (1986).
2. B. R. Lewis, L. Berzins, J. H. Carver and S. T. Gibson, *JQSRT* **36,** 187 (1986).
3. B. R. Lewis, L. Berzins and J. H. Carver, *JQSRT* **37,** 219 (1987).
4. B. R. Lewis, L. Berzins and J. H. Carver, *JQSRT* **37,** 229 (1987).
5. B. R. Lewis, L. Berzins and J. H. Carver, *JQSRT* **37,** 255 (1987).
6. A. O. Nier, *Phys. Rev.* **77,** 789 (1950).
7. R. J. Cicerone and J. L. McCrumb, *Geophys. Res. Lett.* **7,** 251 (1980).
8. A. J. Blake, S. T. Gibson and D. G. McCoy, *J. Geophys. Res.* **89,** 7277 (1984).
9. P. S. Julienne, *J. molec. Spectrosc.* **63,** 60 (1976).

10. G. H. Dieke and H. D. Babcock, *Proc. natn. Acad. Sci. U.S.A.* **13,** 670 (1927).
11. H. D. Babcock and L. Herzberg, *Astrophys. J.* **108,** 167 (1948).
12. W. Steinbach and W. Gordy, *Phys. Rev.* **A11,** 729 (1975).
13. H. G. M. Edwards, E. A. M. Good and D. A. Long, *J. chem. Soc. Faraday II* **72,** 865 (1976).
14. H. G. Hecht, S. W. Rabideau and R. Engleman, Report LA-5871-MS, 10pp., Los Alamos, Sci. Lab., Los Alamos, N.M. (1975).
15. P. H. Krupenie, *J. phys. chem. Ref. Data* **1,** 423 (1972).
16. P. S. Julienne and M. Krauss, *J. molec. Spectrosc.* **56,** 270, (1975).
17. B. R. Lewis, *Appl. Opt.* **22,** 1546 (1983).
18. B. R. Lewis, J. H. Carver, T. I. Hobbs, D. G. McCoy and H. P. F. Gies, *JQSRT* **20,** 191 (1978).
19. J. E. Frederick and R. D. Hudson, *J. molec. Spectrosc.* **74,** 247 (1979).

4.10 Oscillator strengths for the Schumann-Runge bands of $^{18}O_2$

[28] B. R. Lewis, L. Berzins, and J. H. Carver,
Journal of Quantitative Spectroscopy and Radiative Transfer **37**, 255–266 (1987).

J. Quant. Spectrosc. Radiat. Transfer Vol. 37, No. 3, pp. 255–266, 1987
Printed in Great Britain.

0022-4073/87 $3.00 + 0.00

OSCILLATOR STRENGTHS FOR THE SCHUMANN–RUNGE BANDS OF $^{18}O_2$

B. R. LEWIS, L. BERZINS and J. H. CARVER
Research School of Physical Sciences, The Australian National University, Canberra, Australia 2600

(*Received* 19 *May* 1986)

Abstract—Oscillator strengths were measured for the (2–0)–(19–0) and (5–1)–(15–1) Schumann–Runge bands of $^{18}O_2$. Individual rotational lines were studied with a wavelength resolution of ~0.05Å. Band oscillator strengths decrease with increasing rotation, but not as rapidly as for $^{16}O_2$. Our results agree well with oscillator strengths calculated using potential curves and dipole moments derived from our $^{16}O_2$ measurements. The oscillator strength density for the (v'–0) bands is continuous across the dissociation limit. Dipole moments deduced from our oscillator strengths agree well with those for $^{16}O_2$, as well as with recent *ab initio* and semi-empirical determinations.

INTRODUCTION

We have recently presented extensive measurements of the vibrational and rotational variation of oscillator strength[1] and predissociation linewidth[2] in the Schumann–Runge bands of $^{16}O_2$. It was noted[1] that knowledge of the oscillator strengths and linewidths for $^{16}O^{18}O$ is required for construction of accurate atmospheric u.v. absorption models, especially near the weak high rotational lines of $^{16}O_2$. Since in practice $^{16}O^{18}O$ is obtainable only in statistical mixtures with $^{16}O_2$ and $^{18}O_2$, one needs to know oscillator strengths and linewidths for these species before $^{16}O^{18}O$ parameters can be extracted from the measurements. Julienne,[3] in his important work outlining the theoretical basis of the predissociation observed in the Schumann–Runge bands of molecular oxygen, concluded that measurements on isotopically substituted O_2 would be very useful in obtaining a more complete understanding of the predissociation. With instruments of limited wavelength resolution, it is not possible to separate oscillator strengths and linewidths without a data-analysis model,[1,2] and it is thus necessary to obtain the oscillator strengths of $^{18}O_2$ (and $^{16}O^{18}O$) simultaneously with the predissociation linewidths.

There are few experimental data available on the Schumann–Runge bands of $^{18}O_2$. The best wavenumber measurements are unpublished results of Howard and Tilford,[4] who classified lines from the (12–0)–(20–0) bands. Hecht *et al.*[5] made a photographic study of the Schumann–Runge bands of all six isotopic species ($^{16}O_2$, $^{17}O_2$, $^{18}O_2$, $^{16}O^{17}O$, $^{16}O^{18}O$, $^{17}O^{18}O$) including a tabulation of wavenumbers for 151 rotational lines from the (5–0)–(13–0) bands of $^{18}O_2$. Halmann and Laulicht[6] measured integrated absorption intensities for the (4–0)–(11–0) bands of $^{16}O_2$ and $^{18}O_2$ and compared their ratios with the corresponding ratios of Franck–Condon factors. They reported that the $^{16}O_2$ bands were about 1.5 times more intense than the corresponding $^{18}O_2$ bands, and that the Franck–Condon factors for $^{16}O_2$ were two to four times larger than those for $^{18}O_2$. It was suggested[6] that these differences could be interpreted as a dependence of the r-centroid and transition moment on isotopic substitution. Halmann[7] remeasured the integrated absorption for the (2–0)–(10–0) bands of $^{16}O_2$ and $^{18}O_2$ using an argon pressure-broadening technique similar to that used by Bethke[8] on $^{16}O_2$. For the (2–0)–(6–0) bands, he found that the isotope effect on the integrated absorption intensities was equal to the calculated isotope effect on the Franck–Condon factors. The deviations found for the (7–0)–(10–0) bands were thought to result from the failure of the Morse potential at these higher v' values, or from experimental difficulties due to overlapping of bands. Halmann and Laulicht[9–12] also published results of later calculations of the isotopic effects on the Franck–Condon factors for several transitions, including the Schumann–Runge bands of $^{16}O_2$ and $^{18}O_2$.

Julienne[3] presented linewidth measurements for the (9–0)–(14–0) bands of $^{18}O_2$ obtained from microdensitometer tracings of the unpublished photographic work of Tilford.[13] The linewidths had

large relative errors and also included fine-structure splitting, but they were in reasonable agreement with the predictions of Julienne's[3] predissociation model.

Precise spectroscopic constants for the ground state of $^{18}O_2$ have been determined by Steinbach and Gordy[14] from measurements of the microwave spectrum. Edwards *et al.*[15] determined rotational constants and bond lengths for the ground states of $^{16}O_2$, $^{16}O^{18}O$ and $^{18}O_2$ from the analysis of pure rotational Raman spectra.

In view of the relatively poor state of knowledge of intensities for the Schumann–Runge bands of $^{18}O_2$ and for the other reasons discussed, the aim of this work is to provide extensive line-by-line measurements of oscillator strength for $^{18}O_2$. Measurements of predissociation linewidth taken in association with this work are presented in a companion paper.[16] We measure oscillator strengths for as many rotational lines as possible from the (2–0)–(19–0) and (5–1)–(15–1) bands of $^{18}O_2$, and our results agree well with theoretical values derived from the potential curves and dipole moment of our previous $^{16}O_2$ work.[1] The oscillator strengths of this work are considerably more extensive and reliable than the relatively few earlier measurement.[6,7]

EXPERIMENTAL METHOD

Apart from the absorption cell proper, the apparatus was identical to that described elsewhere for the $^{16}O_2$ work.[1] Briefly, background radiation from 1750–1980 Å was provided by a windowless d.c. discharge in molecular hydrogen (10 Torr, 1A). The radiation was dispersed by a modified[17] Minuteman 320 NIV normal incidence VUV scanning monochromator fitted with a 1200 g/mm grating blazed at 1500 Å. The operating resolution was typically 0.05 Å and scanning linearity and temperature stability were exemplary,[17] as is required in the study of narrow rotational lines. An ARC VUV beam splitter set at 45° to the incident radiation allowed monitoring of the incident intensity. EMI photomultipliers type G26H315 (CsTe photocathode) were used in the pulse-counting mode in order to measure simultaneously the incident and transmitted radiation. The scanning system was microcomputer controlled.

The study of isotopic molecular oxygen requires a technique different from that used previously[1] for $^{16}O_2$ due to the much greater cost of the isotopically enriched gas. In this work, the gas was sealed in 10 cm quartz cells. Cell filling was performed on an all glass vacuum system equipped with a mercury manometer for pressure measurements in the range 2–800 Torr and a McLeod gauge for pressures below 2 Torr. Each cell was attached to the vacuum system and baked out overnight at a temperature of 150–200°C before being filled to the required pressure of gas via a cold trap. A glass tap on the cell stem was then closed and the cell was detached from the vacuum system and sealed by melting a pinched section of the stem with a gas torch. Cell pressures of 1 atm and greater were obtained by partially immersing the cell in liquid nitrogen during the sealing process. The isotopically enriched gas samples were obtained from Amersham (U.K.) in 400 ml lecture bottles and they had an ^{18}O abundance of better than 99%.

The individual sealed cells, filled to pressures in the range 2 Torr–2 atm, were mounted on a specially designed carousel which could accommodate six cells and could be mounted in the same vacuum chamber as the normal 10 cm cell described previously.[18] The motion of the carousel was controlled by a stepper motor, which allowed any of the cells to be positioned quickly in the beam path while the housing chamber remained under vacuum. Concurrent scans of different samples were taken as desired.

It was not possible to obtain accurate experimental backgrounds for the $^{18}O_2$ scans because of window-transmission degradation during cell filling and some impurity outgassing after filling. For this reason, lengthy absorption scans were performed on all samples, starting at a wavelength where the strongest lines were fully absorbed and ending where the lines were too weak to measure. All scans were performed continously with wavelength increments of 5–10 mÅ depending on the linewidths. Transmission data were stored on disc. The statistical error of the unnormalized transmissions (detector counts/monitor counts) was better than 1%.

Since the pressures of $^{18}O_2$ in the various cells were measured at filling only, and since some of these estimates relied on plausible assumptions, a few short scans were performed in selected regions using the normal 10 cm cell[18] and a known pressure of $^{18}O_2$. This enabled the determination of some absolute backgrounds, and a comparison of the observed absorption with the absorption

of the sealed cells enabled the cell pressures to be checked. Cell pressures for $^{18}O_2$ were 1.88, 21.4, 200, 809, and 1576 Torr, with the lower two values having been adjusted by $\sim 10\%$ as specified. The adjustments indicate either some problem in the low-pressure measurement of the cell-filling apparatus or that the assumption that the pressure on both sides of the seal was equal after sealing was incorrect at low pressures. The higher pressures were found to be accurate within the limits of this method of verification.

DATA ANALYSIS

Backgrounds could not be determined experimentally at all wavelengths, and it was necessary to infer these by using the absorption model. Since we had no knowledge of the underlying continuum for $^{18}O_2$ it was set equal to zero in the model, which was then used to predict the absolute transmission at every deep absorption minimum between rotational absorption lines. The actual measured non-absolute transmissions at the absorption minima were then divided by these model values. Backgrounds obtained by this technique were then plotted as a function of wavelength for each cell. For the most part they varied smoothly with wavelength, decreasing at lower wavelengths to reflect the decreasing transmission of the cell windows and the increasing underlying continuum. Backgrounds at any wavelength were then obtained by interpolation. These were then used as the base levels for comparison between the observed and modelled spectra, and the resultant oscillator strengths are thus free of contributions from the underlying continuum.

The data-analysis procedures and the molecular oxygen absorption model have been discussed in detail previously[1] for $^{16}O_2$. Briefly, absorption profiles and equivalent widths were recorded for all lines of interest at several pressures, and an equivalent width analysis technique allowed the simultaneous determination of both oscillator strength and predissociation linewidth[16] by an iterative procedure. A discussion of the appropriate model parameters follows.

Since our isotopically enriched gas sample was better than 99% ^{18}O, the main constitutents were $^{18}O_2$ (>98%), $^{16}O^{18}O$ (<2%), and a negligible amount of $^{16}O_2$. Measurements on the sample near the (9–0) band indicated, in conjuction with theoretical $^{16}O^{18}O$ line strengths, that the actual purity of the sample was higher than indicated (99.6% $^{18}O_2$, 0.4% $^{16}O^{18}O$). Parameters used for a small $^{16}O^{18}O$ correction were calculated from the known $^{16}O_2$ values[1] using techniques similar to those discussed by Blake *et al.*[19] A more detailed discussion of these is given in a companion work[20] on $^{16}O^{18}O$. The following discussion refers only to $^{18}O_2$.

Spectroscopic constants for the $X^3\Sigma_g^-$ state of $^{18}O_2$ were taken from the microwave work of Steinbach and Gordy[14] and were used to generate the manifold of rovibrational levels for the ground state and the corresponding weighted Boltzmann factors. The unpublished wavenumber measurements of Howard and Tilford[4] were used to generate spectroscopic constants for the $v' = 12$–20 levels of the $B^3\Sigma_u^-$ state. Constants derived from the wavenumbers of Hecht *et al.*[5] proved to be unreliable. Therefore, we scanned samples of $^{16}O_2$ and $^{18}O_2$ concurrently and interpolated wavelengths for the $^{18}O_2$ lines between the known $^{16}O_2$ lines.[21] Spectroscopic constants obtained from our measurements were used for the (2–0)–(11–0) bands. The constants used in this work are shown in Table 1 for $0 \leqslant v' \leqslant 19$. Values shown in brackets are either calculated in the manner of Blake *et al.*[19] or extrapolated. Numerous rotational perturbations set in for $v' \geqslant 19$ (vs $v' \geqslant 16$ for $^{16}O_2$). The G and B values in Table 1 agree quite well with totally calculated values and represent the observed spectrum well. Our instrument has no spectrographic capability and was not designed for very accurate wavelength measurement. The constants in Table 1 should therefore be treated as a guide only, in the absence of other experimental information. Extensive, accurate wavenumber measurements, of the nature of those of Yoshino *et al.*[21] for $^{16}O_2$, are urgently needed for $^{18}O_2$. Line wavelengths for $v'' = 1$ were calculated from the $v'' = 0$ wavelengths and the known ground state energy levels. As for $^{16}O_2$, Hönl–London factors were taken from Tatum and Watson[22] for $^3\Sigma^- - ^3\Sigma^-$ transitions with coupling intermediate between Hund's cases (a) and (b) and with transformation coefficients determined from the energy levels obtained above.

Oscillator strengths and linewidths are necessary in order to account for the effects of distant, neighbouring or overlapping lines. The initial oscillator strengths were calculated using the potential curves and dipole moment of the previous $^{16}O_2$ work.[1] The linewidths were calculated by using the curve-crossing parameters deduced previously[2] for $^{16}O_2$. The model included the

Table 1. Spectroscopic constants (cm^{-1}) for the $B^3\Sigma_u^-$ state of $^{18}O_2$ obtained from our wavenumber measurements and those of Howard and Tilford.[4] The errors are 3σ determined from the fitting procedure, and constants in parentheses are either extrapolated or calculated from corresponding $^{16}O_2$ values

v'	ν_0	B	$D \times 10^6$	λ	$-\mu_0$	$-\mu_J \times 10^5$
0	(49383.00)	(0.7226)	(3.6)	(1.74)	(0.029)	(0.0)
1	(50032.28)	(0.7113)	(3.8)	(1.74)	(0.029)	(0.0)
2	50661.28 ± 0.17	0.7006 ± 0.0007	(4.0)	(1.74)	(0.029)	(0.0)
3	51269.67 ± 0.14	0.6881 ± 0.0004	(4.14)	(1.77)	(0.030)	(0.0)
4	51856.86 ± 0.31	0.6749 ± 0.0009	(4.71)	(1.80)	(0.030)	(0.0)
5	52421.98 ± 0.46	0.6616 ± 0.0012	(4.87)	(1.83)	(0.031)	(0.0)
6	52961.37 ± 0.21	0.6449 ± 0.0005	(5.44)	(1.86)	(0.031)	(0.0)
7	53475.36 ± 0.34	0.6297 ± 0.0007	(5.83)	(1.91)	(0.032)	(0.0)
8	53961.04 ± 0.20	0.6124 ± 0.0004	(6.63)	(1.94)	(0.032)	(0.0)
9	54418.10 ± 0.15	0.5921 ± 0.0003	(6.71)	(1.96)	(0.033)	(0.0)
10	54841.69 ± 0.15	0.5724 ± 0.0003	(7.37)	(2.00)	(0.033)	(0.5)
11	55232.11 ± 0.20	0.5474 ± 0.0004	(8.25)	(2.07)	(0.037)	(1.0)
12	55586.76 ± 0.16	0.5211 ± 0.0003	(10.2)	(2.20)	(0.040)	(2.0)
13	55901.79 ± 0.10	0.4936 ± 0.0005	12.5 ± 0.5	2.35 ± 0.14	0.0506 ± 0.0085	(4.0)
14	56176.51 ± 0.12	0.4614 ± 0.0005	14.7 ± 0.7	2.67 ± 0.09	0.0594 ± 0.0027	5.66 ± 0.37
15	56410.66 ± 0.11	0.4255 ± 0.0005	16.0 ± 0.6	2.94 ± 0.08	0.0918 ± 0.0022	6.25 ± 0.29
16	56605.30 ± 0.10	0.3878 ± 0.0005	19.1 ± 0.9	3.23 ± 0.07	0.1479 ± 0.0034	4.93 ± 0.72
17	56763.71 ± 0.14	0.3502 ± 0.0008	24.1 ± 1.2	4.07 ± 0.08	0.2085 ± 0.0022	8.22 ± 0.21
18	56889.96 ± 0.19	0.3091 ± 0.0008	22.8 ± 1.0	5.05 ± 0.12	0.3006 ± 0.0050	10.81 ± 0.48
19	56989.12 ± 0.39	0.2716 ± 0.0019	26.4 ± 1.5	7.05 ± 0.33	0.394 ± 0.031	(12.0)

rotational variation of both oscillator strength and linewidth. As measurements proceeded, the initial values were replaced by measured values and a reanalysis was performed. The final oscillator strengths (and widths) were not sensitive to the initial estimates.

A Gaussian instrument function of FWHM 0.04–0.05 Å was folded into the analysis in order to reproduce the observed scan profiles. The resolution varied a little because of the clogging of the entrance slit by the windowless discharge. Theoretically, the equivalent width of an isolated line is independent of instrumental resolution,[23] but small errors can occur when the instrument function is neglected for scans with limited range of integration.

The underlying continuum and its pressure coefficient are set equal to zero in this model, but the method used for background determination automatically compensates for this step, provided that individual lines are analysed with an identical model. When the model estimates of transmission between lines become unreliable due to perturbations ($v' \geqslant 19$), backgrounds become unobtainable and the results cannot be analysed successfully.

The pseudo-continuum arising from the summation of Lorentzian wings of absorption lines is included as described for $^{16}O_2$.[1] The pressure broadening coefficient for $^{18}O_2$ is taken to be 0.20 cm^{-1}/atm, as[1] for $^{16}O_2$, with a small mass correction factor.

In the case of the hot bands, predissociation widths for the upper levels were assumed equal to those determined for the $v'' = 0$ bands,[16] and oscillator strengths were determined from single low pressure scans. Because of the limited number of pressures and the fixed cell length, ideal pairs of pressures for application of the full equivalent width method were not always available. In these cases the theoretical predissociation width values were assumed and a single low pressure scan was analysed to yield an oscillator strength.

THEORETICAL CONSIDERATIONS

It is instructive to consider qualitatively the isotope effects expected on theoretical grounds. The ground and upper state potential curves for O_2 are not expected to be sensitive to isotopic substitution, but the vibtrational and rotational constants will be smaller for the heavier isotopes. In the case of the $B^3\Sigma_u^-$ state, 24 vibrational levels are expected for $^{18}O_2$ compared with 22 for $^{16}O_2$, given the dissociation limit previously determined for $^{16}O_2$.[1] Figure 1 is a low temperature scan of the dissociation limit region for $^{18}O_2$ in which bands up to the (24–0) are clearly visible.

Widely differing r_e values for the ground and upper state potential curves of O_2 lead to the Franck–Condon region occurring in the Schumann–Runge continuum and the oscillator strength density[1] rapidly decreasing as $v' \to 0$ in the bands. As has been noted by Lewis *et al.*,[1] the oscillator strength density in the region of the bands, df/dv, may be approximated by $f_0/\Delta G'$ where f_0 is the rotationless oscillator strength and $\Delta G'$ is the first difference of the band origins for the band of

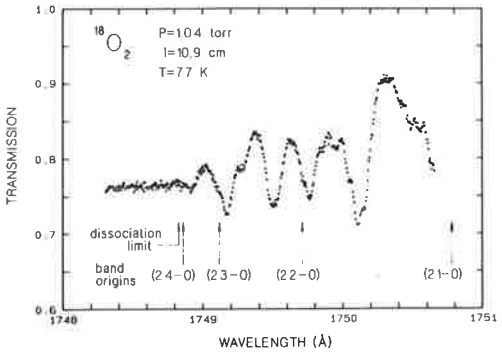

Fig. 1. A low temperature scan of the $B^3\Sigma_u^-$ dissociation limit region in $^{18}O_2$ showing bands up to the (24–0).

interest. The oscillator strength for that band can thus be thought of as the product of $\Delta G'$, a monotonically decreasing function of wavenumber (Table 2 of Ref. [1]), and df/dv, a monotonically increasing function of wavenumber (Fig. 6 of Ref. [1]). In the case of $^{16}O_2$ this product has a maximum at $v' = 14$,[1] and for $^{18}O_2$ the position of this maximum might be expected to change depending on the detailed behaviour of the $\Delta G'$ and df/dv functions.

The depression of vibrational levels of the upper and lower states for the heavier isotope, $^{18}O_2$, results in reduced wavefunction overlap and smaller Franck–Condon factors and oscillator strengths. The widely differing shapes and r_e values for the $X^3\Sigma_g^-$ and $B^3\Sigma_u^-$ potential curves result in significant centrifugal distortion effects in O_2. When the centrifugal energy term is added to the X and B potentials there is a displacement of each vibrational wavefunction to larger internuclear distances, but the displacement is greater for the wavefunction of the upper state because of the broader potential curve, and for the higher vibrational levels near the dissociation limit the displacement is greater still. This results in reduced wavefunction overlap and lower oscillator strength with increasing rotation, the effect being greater for the higher vibrational bands. This is just what is observed for $^{16}O_2$.[1] In the case of $^{18}O_2$, the rotational constants and centrifugal energy term are reduced and the effects of the centrifugal distortion will be reduced correspondingly. For similar reasons, since an R branch line corresponds to an upper state rotation larger than that for an associated P branch line, the increased displacement of the upper state wavefunction for the R branch line results in an oscillator strength smaller than that for the P branch line, but this difference will be smaller for the heavier isotope.

RESULTS

Some 305 independent oscillator strength measurements are presented in this work. Tables 2–5 list oscillator strengths for rotational lines from the P and R branches of the (2–0)–(19–0)

Table 2. Measured oscillator strengths $f(v', N'') \times 10^x$ for the R branches of the (2–0)–(10–0) Schumann-Runge bands of $^{18}O_2$

v' / N''	2	3	4	5	6	7	8	9	10
1									
3	7.6 ± 0.4	3.13 ± 0.15	1.14 ± 0.05	3.29 ± 0.15	8.17 ± 0.40		3.25 ± 0.15	5.80 ± 0.25	8.82 ± 0.40
5	6.9 ± 0.4	3.37 ± 0.15	1.11 ± 0.05	3.15 ± 0.15	7.78 ± 0.40	1.74 ± 0.10	3.11 ± 0.15	5.88 ± 0.25	9.12 ± 0.40
7	7.0 ± 0.4	3.18 ± 0.15	1.11 ± 0.05	3.00 ± 0.15	8.00 ± 0.40	1.66 ± 0.10	3.51 ± 0.15	5.41 ± 0.25	8.85 ± 0.40
9	6.9 ± 0.4	3.09 ± 0.15	1.13 ± 0.05	3.16 ± 0.15	7.97 ± 0.40	1.67 ± 0.10	3.10 ± 0.15	5.46 ± 0.25	8.37 ± 0.40
11	7.5 ± 0.4	3.13 ± 0.15	1.08 ± 0.05	3.02 ± 0.15	7.58 ± 0.40	1.64 ± 0.10	2.99 ± 0.15	5.34 ± 0.25	8.46 ± 0.40
13	6.8 ± 0.4	3.06 ± 0.15	1.14 ± 0.05	3.11 ± 0.15	7.61 ± 0.40	1.64 ± 0.10	3.15 ± 0.15	5.04 ± 0.25	8.14 ± 0.40
15	6.4 ± 0.4	3.14 ± 0.15	1.11 ± 0.05	2.98 ± 0.15	7.48 ± 0.40	1.51 ± 0.10	2.96 ± 0.15	5.42 ± 0.25	8.25 ± 0.40
17	6.5 ± 0.6	2.84 ± 0.20	1.10 ± 0.08	2.93 ± 0.20	7.55 ± 0.40	1.49 ± 0.10	2.97 ± 0.15	5.19 ± 0.25	7.89 ± 0.40
19		2.76 ± 0.25	1.02 ± 0.08	2.84 ± 0.20	7.15 ± 0.40	1.46 ± 0.10	2.87 ± 0.15	5.08 ± 0.25	8.60 ± 0.50
21		2.47 ± 0.25	1.02 ± 0.15	2.68 ± 0.20	6.95 ± 0.40	1.47 ± 0.10	2.89 ± 0.20	4.76 ± 0.25	7.31 ± 0.50
23			0.97 ± 0.20	2.71 ± 0.25	6.28 ± 0.50	1.42 ± 0.15	2.76 ± 0.20		7.32 ± 0.60
25				2.55 ± 0.25	6.45 ± 0.50	1.24 ± 0.15	2.69 ± 0.20	4.16 ± 0.40	
27					6.01 ± 0.50	1.23 ± 0.15	2.47 ± 0.20		
29				2.62 ± 0.40					
x	9	8	7	7	7	6	6	6	6

Table 3. Measured oscillator strengths $f(v', N'') \times 10^c$ for the P branches of the (2–0)–(10–0) Schumann–Runge bands of $^{18}O_2$. Values in parentheses refer to measurements on unresolved lines which are not independent of the R branch values

v' / N''	2	3	4	5	6	7	8	9	10
1	(7.7 ± 0.4)	(3.15 ± 0.15)	(1.15 ± 0.05)	(3.32 ± 0.15)	(8.24 ± 0.40)		(3.28 ± 0.15)	(5.85 ± 0.25)	(8.90 ± 0.40)
3	(7.0 ± 0.4)	(3.42 ± 0.15)	(1.13 ± 0.05)	(3.20 ± 0.15)	(7.90 ± 0.40)	(1.76 ± 0.10)	(3.16 ± 0.15)	(5.98 ± 0.25)	(9.27 ± 0.40)
5	(7.2 ± 0.4)	(3.25 ± 0.15)	(1.13 ± 0.05)	(3.07 ± 0.15)	(8.18 ± 0.40)	(1.69 ± 0.10)	(3.59 ± 0.15)	(5.54 ± 0.25)	(9.06 ± 0.40)
7	(7.1 ± 0.4)	(3.18 ± 0.15)	(1.16 ± 0.05)	(3.25 ± 0.15)	(8.20 ± 0.40)	(1.71 ± 0.10)	(3.19 ± 0.15)	(5.63 ± 0.25)	(8.63 ± 0.40)
9	(7.8 ± 0.4)	(3.24 ± 0.15)	(1.11 ± 0.05)	(3.13 ± 0.15)	(7.86 ± 0.40)	(1.69 ± 0.10)	(3.10 ± 0.15)	(5.54 ± 0.25)	(8.79 ± 0.40)
11	(7.1 ± 0.4)	(3.19 ± 0.15)	(1.19 ± 0.05)	(3.24 ± 0.15)	(7.94 ± 0.40)	(1.70 ± 0.10)	(3.29 ± 0.15)	(5.27 ± 0.25)	(8.52 ± 0.40)
13	(6.7 ± 0.4)	(3.30 ± 0.15)	(1.17 ± 0.05)	(3.13 ± 0.15)	(7.86 ± 0.40)	(1.64 ± 0.10)	(3.11 ± 0.15)	(5.71 ± 0.25)	(8.70 ± 0.40)
15	(6.9 ± 0.4)	(3.00 ± 0.20)	(1.16 ± 0.08)	(3.10 ± 0.20)	(7.99 ± 0.40)	(1.57 ± 0.10)	(3.15 ± 0.15)	(5.51 ± 0.25)	(8.39 ± 0.40)
17		(2.94 ± 0.25)	(1.09 ± 0.08)	(3.02 ± 0.20)	(7.62 ± 0.40)	(1.55 ± 0.10)	(3.06 ± 0.15)	(5.43 ± 0.25)	8.42 ± 0.50
19		(2.65 ± 0.25)	(1.09 ± 0.15)	(2.87 ± 0.20)	(7.46 ± 0.40)	(1.57 ± 0.10)	(3.11 ± 0.20)	(5.13 ± 0.25)	8.21 ± 0.50
21			(1.05 ± 0.20)	(2.93 ± 0.25)	(6.79 ± 0.50)	(1.52 ± 0.15)	(2.99 ± 0.20)	5.08 ± 0.30	7.88 ± 0.50
23				(2.77 ± 0.25)	(7.02 ± 0.50)	(1.34 ± 0.15)	(2.94 ± 0.20)	5.24 ± 0.30	7.65 ± 0.60
25					(6.59 ± 0.50)	(1.34 ± 0.15)	(2.72 ± 0.20)		6.87 ± 0.60
27				(2.89 ± 0.40)				4.64 ± 0.40	
29									
31								3.67 ± 0.50	
x	9	8	7	7	7	6	6	6	6

Table 4. Measured oscillator strengths $f(v', N'') \times 10^5$ for the R branches of the (11–0)–(19–0) Schumann–Runge bands of $^{18}O_2$

v' / N''	11	12	13	14	15	16	17	18	19
1									
3	1.23 ± 0.06		2.09 ± 0.10	2.26 ± 0.10					
5		1.52 ± 0.08	2.21 ± 0.10	2.12 ± 0.10	2.53 ± 0.10		(2.30 ± 0.10)	(2.10 ± 0.15)	
7	1.16 ± 0.06	1.62 ± 0.08	1.95 ± 0.10		2.28 ± 0.10	2.21 ± 0.10	2.17 ± 0.10	1.69 ± 0.15	1.15 ± 0.12
9	1.13 ± 0.06	1.55 ± 0.08	1.85 ± 0.10	2.15 ± 0.10		2.03 ± 0.10	1.66 ± 0.10		0.90 ± 0.15
11	1.27 ± 0.06	1.41 ± 0.08	1.82 ± 0.10	2.11 ± 0.10	2.11 ± 0.10	2.08 ± 0.10	1.91 ± 0.15	1.99 ± 0.15	
13	1.07 ± 0.06	1.46 ± 0.08	1.71 ± 0.10	2.16 ± 0.10	1.95 ± 0.10	2.09 ± 0.10			
15	1.16 ± 0.06	1.50 ± 0.08	1.67 ± 0.10	1.81 ± 0.10	1.84 ± 0.10				
17	1.04 ± 0.08	1.53 ± 0.08	1.56 ± 0.10	2.17 ± 0.10					
19	1.05 ± 0.08	1.36 ± 0.08	1.65 ± 0.10		1.86 ± 0.10	1.54 ± 0.15			
21	1.10 ± 0.08	1.32 ± 0.08			1.98 ± 0.10	1.66 ± 0.15			
23	1.01 ± 0.08	1.35 ± 0.08	1.47 ± 0.10		1.75 ± 0.10				
25			1.30 ± 0.10	1.50 ± 0.15					
27	0.93 ± 0.10								
29	1.03 ± 0.15	1.02 ± 0.25							

Schumann–Runge bands of $^{18}O_2$. These are effective band oscillator strengths deduced from the particular rotational lines studied. Tables 6–7 give oscillator strengths for rotational lines from the (5–1)–(15–1) bands.

Results in Tables 2–5 were obtained from single scans for $v' = 2, 3, 4\,(N'' \geqslant 7)$, $5(N'' \geqslant 21)$, $6(N'' \geqslant 21)$, $7(N'' \geqslant 23)$ and $12(N'' \geqslant 29)$. When scans were performed on unresolved PR doublets, the deduced oscillator strength was referred to the R component and the oscillator strength for the P component was calculated using theoretical P/R strength ratios. It is also expected[24] that the oscillator strength will vary with the fine-structure component, but this effect is too small to verify

Table 5. Measured oscillator strengths $f(v', N'') \times 10^5$ for the P branches of the (11–0)–(19–0) Schumann–Runge bands of $^{18}O_2$. Values in parentheses refer to measurements on unresolved lines which are not independent of the R branch values

v' / N''	11	12	13	14	15	16	17	18	19
1	(1.24 ± 0.06)		(2.11 ± 0.10)	(2.28 ± 0.10)					
3		(1.55 ± 0.08)	(2.25 ± 0.10)	(2.16 ± 0.10)					
5	(1.19 ± 0.06)	1.54 ± 0.08	2.30 ± 0.10	2.25 ± 0.10	2.43 ± 0.10	2.26 ± 0.10	2.35 ± 0.10	2.15 ± 0.15	
7		1.52 ± 0.08		2.12 ± 0.10	2.31 ± 0.10	2.22 ± 0.10	2.33 ± 0.15	1.96 ± 0.15	1.07 ± 0.10
9	1.16 ± 0.06	1.70 ± 0.08	1.89 ± 0.10	2.21 ± 0.10	2.31 ± 0.10	2.16 ± 0.10	1.91 ± 0.10	2.35 ± 0.40	1.04 ± 0.12
11	1.16 ± 0.06	1.62 ± 0.08	2.03 ± 0.10	2.25 ± 0.10	2.30 ± 0.10	2.03 ± 0.10	2.03 ± 0.10		
13	1.21 ± 0.06	1.45 ± 0.08	1.80 ± 0.10	1.96 ± 0.10	2.02 ± 0.10	2.44 ± 0.12		1.37 ± 0.15	
15	1.13 ± 0.06	1.64 ± 0.08	1.80 ± 0.10	2.20 ± 0.10	2.00 ± 0.10	2.17 ± 0.20	2.17 ± 0.20		
17	1.12 ± 0.08	1.62 ± 0.08	1.81 ± 0.10	2.22 ± 0.15		1.83 ± 0.10	1.78 ± 0.10		
19	1.12 ± 0.08	1.31 ± 0.08			2.13 ± 0.10	1.74 ± 0.15			
21	1.11 ± 0.08		1.81 ± 0.10						
23	1.12 ± 0.08	1.24 ± 0.08	1.48 ± 0.10		2.15 ± 0.10	1.91 ± 0.15	1.26 ± 0.20		
25		1.38 ± 0.10	1.44 ± 0.10		1.92 ± 0.15	1.83 ± 0.15			
27									
29	0.95 ± 0.15	1.22 ± 0.25							

Table 6. Measured oscillator strengths $f(v', N'') \times 10^4$ for the R branches of the (5–1)–(15–1) Schumann-Runge bands of $^{18}O_2$

v' / N''	5	6	7	8	9	10	11	12	13	14	15
1											
3				4.40 ± 0.25			1.37 ± 0.08	1.68 ± 0.10			
5		1.33 ± 0.08		4.39 ± 0.25		1.16 ± 0.07	1.38 ± 0.08	1.70 ± 0.10			
7	5.90 ± 0.40	1.23 ± 0.08		4.50 ± 0.25				1.73 ± 0.10		2.10 ± 0.10	1.99 ± 0.10
9	5.69 ± 0.40	1.25 ± 0.08	2.37 ± 0.15			0.99 ± 0.07	1.37 ± 0.08	1.60 ± 0.10			
11	4.96 ± 0.40	1.27 ± 0.08	2.42 ± 0.15		7.1 ± 0.4			1.51 ± 0.10			
13	5.46 ± 0.40	1.32 ± 0.08	2.49 ± 0.15		6.6 ± 0.4		1.44 ± 0.08	1.45 ± 0.10		1.63 ± 0.15	
15		1.22 ± 0.08	2.42 ± 0.15		6.8 ± 0.4	0.93 ± 0.07	1.11 ± 0.10			1.65 ± 0.15	
17		1.20 ± 0.08			6.5 ± 0.4	0.95 ± 0.07			1.51 ± 0.15		
19					6.2 ± 0.4	0.99 ± 0.07	1.15 ± 0.20		1.76 ± 0.25		
21					5.2 ± 0.6						
23					5.7 ± 0.6						
25					3.8 ± 1.2						
x	6	5	5	5	5	4	4	4	4	4	4

Table 7. Measured oscillator strengths $f(v', N'') \times 10^4$ for the P branches of the (5–1)–(15–1) Schumann–Runge bands of $^{18}O_2$. Values in parentheses refer to measurements on unresolved lines which are not independent of the R branch values

v' / N''	5	6	7	8	9	10	11	12	13	14	15
1				(4.43 ± 0.25)			(1.38 ± 0.08)				
3		(1.35 ± 0.08)		(4.45 ± 0.25)		(1.18 ± 0.07)	(1.40 ± 0.08)	(1.73 ± 0.10)			
5	(6.02 ± 0.40)	(1.25 ± 0.08)		(4.59 ± 0.25)				1.76 ± 0.10		(2.15 ± 0.10)	
7	(5.84 ± 0.40)	(1.28 ± 0.08)	(2.43 ± 0.15)			(1.02 ± 0.07)	(1.41 ± 0.08)				2.00 ± 0.10
9	(5.12 ± 0.40)	(1.31 ± 0.08)	(2.50 ± 0.15)		(7.3 ± 0.4)			1.74 ± 0.10			
11	(5.67 ± 0.40)	(1.37 ± 0.08)	(2.59 ± 0.15)		(6.9 ± 0.4)	1.00 ± 0.07)	(1.50 ± 0.08)				
13		(1.28 ± 0.08)	(2.53 ± 0.15)		(7.1 ± 0.4)	0.99 ± 0.07					
15		(1.26 ± 0.08)			(6.8 ± 0.4)	1.01 ± 0.07	1.43 ± 0.10			2.15 ± 0.15	
17					6.3 ± 0.4		1.34 ± 0.10				
19					6.0 ± 0.6						
21					7.6 ± 0.6						
23					6.6 ± 0.6						
x	6	5	5	5	5	4	4	4	4	4	4

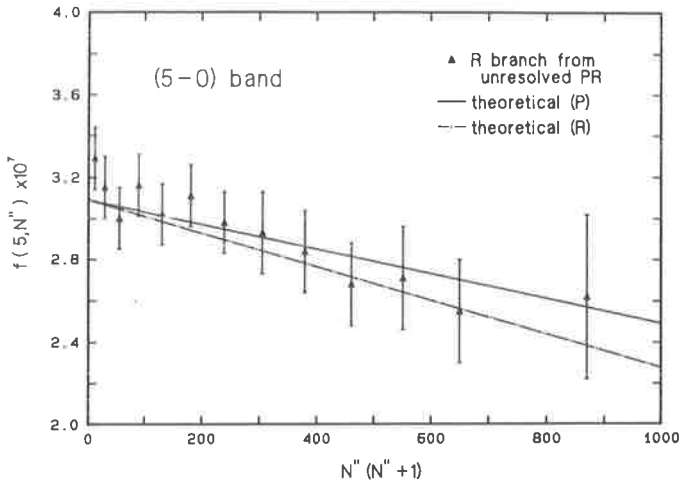

Fig. 2. Measured oscillator strengths for rotational lines from the (5–0) Schumann–Runge band of $^{18}O_2$ together with predicted rotational dependences.

here and all results have been averaged over the individual fine-structure components where these have been measured separately. The errors given in Tables 2–7 are essentially due to counting statistics. Additional errors due to uncertainties in pressure, temperature and cell length are expected to be $\sim 5\%$. Oscillator strengths for the stronger lines near the bandheads are robust while those for the weaker lines show an increasing sensitivity to the interpolated backgrounds and other model parameters. For $v' \geqslant 17$, model characterization becomes more difficult due to uncertainties in the positions of high rotational lines from bands with $v' \geqslant 19$. From Tables 2–5 one can see a maximum in the $v'' = 0$ vibrational oscillator strength at $v' = 15$ and the decrease in oscillator strength with rotation which is expected theoretically, although this effect is not as great as that for $^{16}O_2$. In cases where the P and R branches are resolved, the P branch oscillator strengths exceed those of the R branch, but not as clearly as in the case of $^{16}O_2$ where the expected effect is greater. In Fig. 2 our measured oscillator strengths are presented graphically for the (5–0) band. The measurements do not resolve the P and R branches for this band but the approximately linear decrease in oscillator strength with increased $N''(N''+1)$ is seen clearly. Agreement with theoretical predictions based on our $^{16}O_2$ results[1] is good.

Rotational band oscillator strengths of the form[1]

$$f(v', N'') = f_0(v') - \beta(v')N''(N''+1) \tag{1}$$

were least-squares fitted to our measurements for the (2–0)–(19–0) bands and the resultant values of f_0 and β are given in Table 8 together with corresponding theoretical values. Because of the small magnitude of the β values and the resultant large uncertainty, although the P and R branches were fitted separately, the tabulated results are averaged over the P and R branches. In view of the large errors in β for $v' \geqslant 17$, the rotationless oscillator strengths for $v' \geqslant 17$ were deduced from our measurements using the theoretical β values. The measured f_0 values for $v' < 17$ average $\sim 6\%$ larger than the theoretical values with an r.m.s. scatter of $\sim 3\%$, while the β values for $v' < 17$ average $\sim 20\%$ larger than the theoretical values, but with an r.m.s. scatter of $\sim 40\%$. The errors quoted in Table 8 are statistical errors determined by the least-squares fitting procedure, but there is an additional uncertainty of about 5% in f_0 due mainly to the determination of pressure in the isotopic cells.

Measured and theoretical mean band oscillator strengths $\bar{f}(v')$, determined[1] by summing individual line oscillator strengths from equation (1), weighted with appropriate Boltzmann factors, are shown in Fig. 3 together with values deduced from the integrated absorption intensities (K_0) of Halmann and Laulicht[6] and Halmann[7] using the relation $\bar{f} = 4.203 \times 10^{-8} K_0$. As for the f_0 values, the present mean band oscillator strengths for $v' < 17$ average 6% larger than the theoretical values with an r.m.s. scatter of better than 3%. The other measurements[6,7] are in poor agreement with ours, averaging 15% less, and with significant r.m.s. scatters of ~ 40[6] and $\sim 20\%$,[7]

Table 8. Rotationless oscillator strengths $f_0(v')$ and rotational dependences $\beta(v')$ for the (2–0)–(19–0) Schumann–Runge bands of $^{18}O_2$. The values marked with an asterisk were determined from the present measurements using the theoretical β values. The statistical errors implied by the fitting procedure are also given

		$f_0(v') \times 10^5$			$\beta(v') \times 10^4$	
v'	x	Measured	Theoretical	y	Measured	Theoretical
2	9	7.37 ± 0.24	6.85	12	2.7 ± 1.5	1.5
3	8	3.30 ± 0.08	3.09	12	12.5 ± 4.0	6.7
4	7	1.14 ± 0.02	1.08	11	1.1 ± 0.8	2.4
5	7	3.22 ± 0.06	3.09	11	8.0 ± 1.4	7.1
6	7	8.15 ± 0.13	7.53	10	2.5 ± 0.3	1.8
7	6	1.73 ± 0.04	1.61	10	6.2 ± 0.6	3.9
8	6	3.28 ± 0.07	3.07	10	8.6 ± 2.0	7.9
9	6	5.75 ± 0.12	5.25	9	1.8 ± 0.3	1.4
10	6	8.98 ± 0.23	8.23	9	2.8 ± 0.6	2.3
11	5	1.21 ± 0.03	1.18	9	2.8 ± 0.9	3.6
12	5	1.60 ± 0.07	1.55	9	4.8 ± 1.6	5.1
13	5	2.09 ± 0.12	1.89	9	11.4 ± 2.0	6.8
14	5	2.23 ± 0.10	2.14	9	6.2 ± 3.8	8.6
15	5	2.31 ± 0.10	2.25	9	8.1 ± 3.5	10.0
16	5	2.26 ± 0.08	2.21	8	1.1 ± 0.4	1.1
17	5	2.11 ± 0.25*	2.05	8	1.8 ± 0.5	1.1
18	5	1.95 ± 0.30*	1.80	8	5.3 ± 1.3	1.1
19	5	1.13 ± 0.30*	1.52	8	3.5 ± 5.0	1.1

respectively. The present results are to be preferred because of greater extent, superior accuracy, and good agreement with theoretical predictions based on accurate $^{16}O_2$ measurements.[1]

Mean band oscillator strengths for the hot bands (5–1)–(15–1) are shown in Fig. 4. Values were obtained as for the $v'' = 0$ series except that the β values were fixed theoretically because of poor accuracy in their experimental determination. Our results for $v' < 13$ average 3% larger than the

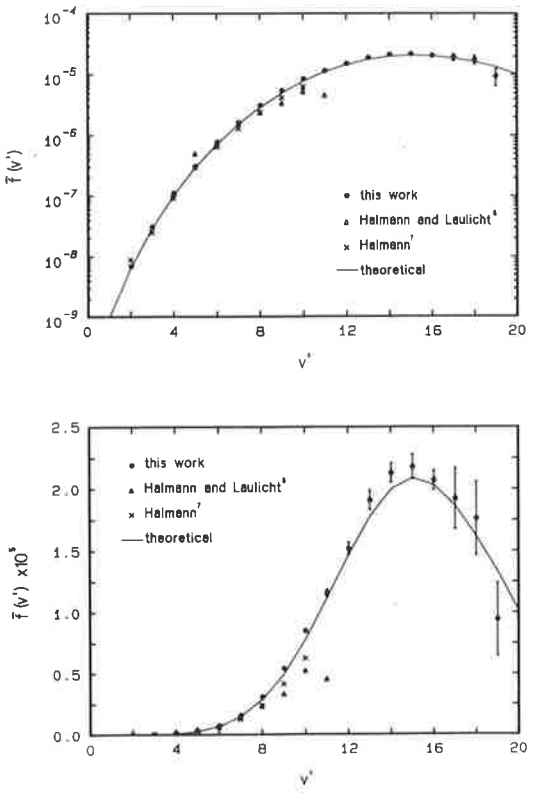

Fig. 3. Measured mean band oscillator strengths $\bar{f}(v')$ for the $(v'–0)$ Schumann–Runge bands of $^{18}O_2$ together with the results of other workers[6,7] and our theoretical values. Note that the band oscillator strengths are a little smaller than the rotationless oscillator strengths of Table 8 because of the decrease in f with increasing rotation.

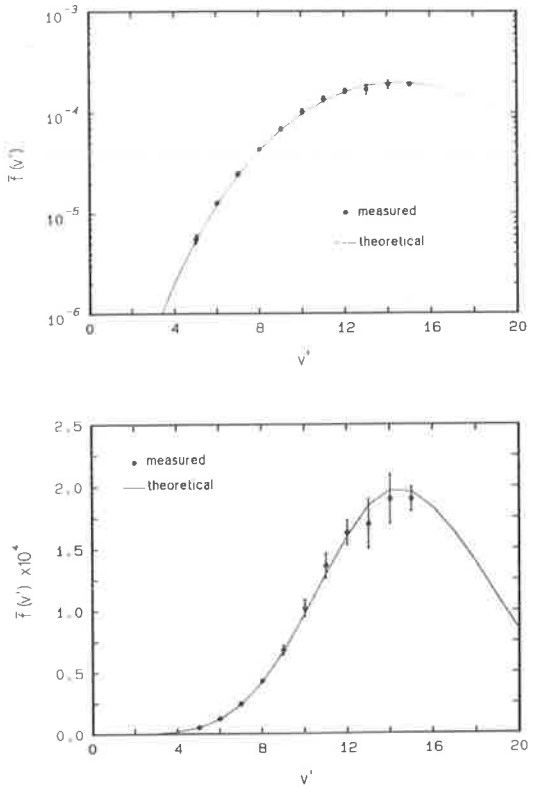

Fig. 4. Measured mean band oscillator strengths $\bar{f}(v')$ for the $(v'-1)$ Schumann–Runge bands of $^{18}O_2$ together with our theoretical values.

theoretical values with an r.m.s. scatter in the ratio of ~2%. No other experimental oscillator strengths are available.

OSCILLATOR STRENGTH DENSITY CONTINUITY

Theoretical investigations of the continuity of oscillator strength, Franck–Condon density and transition moment for O_2 have been performed by several workers.[25–27] Lewis *et al.*[1] summarized their work and found that the experimental oscillator strength density was continuous across the dissociation limit for $^{16}O_2$ by comparing $f_0(v')(dv'/dv)$ in the bands with $df/dv = 1.13 \times 10^{12}\sigma$ in the continuum, after Allison *et al.*[32] (σ, cm^2 is the continuum cross section).

We have performed a similar investigation for the $v'' = 0$ transitions of $^{18}O_2$. Band origins from Table 1 were taken as the wavenumbers v, cm^{-1} associated with our rotationless oscillator strengths f_0, and the density of states dv'/dv was taken as $1/\Delta G'$, where the differences $\Delta G'$, cm^{-1} were obtained from the band origins. The oscillator strength density df/dv was thus approximated by $f_0/\Delta G'$ for the bands. Measurements of the Schumann–Runge continuum cross section σ, cm^2 for $^{18}O_2$ were taken using a non-sealed 10 cm cell at 77K in order to approximate the rotationless continuum as nearly as possible. df/dv in the continuum was calculated as $1.13 \times 10^{12}\sigma$.

Our experimental oscillator strength density is plotted as a function of wavenumber in Fig. 5. Bands with $v' > 17$ have been ignored because of poor experimental accuracy. Continuity is observed across the $B^3\Sigma_u^-$ dissociation limit as for $^{16}O_2$. It would be possible to obtain more experimental points for $v' > 17$ with an improved knowledge of the rotational perturbations, and by using non-sealed cells to avoid background problems. An equation of the form

$$df/dv = \exp\left(\sum_{i=0}^{4} a_i v^i\right) \tag{2}$$

was fitted to the measured oscillator strength densities and the resultant smoothed values are shown

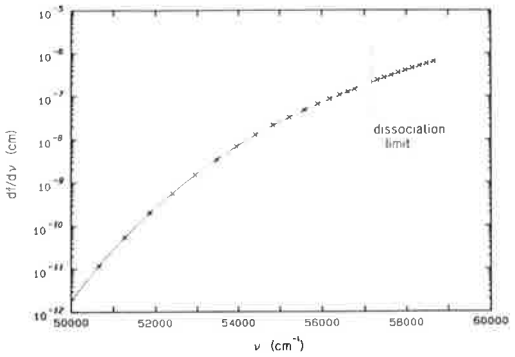

Fig. 5. Oscillator strength densities obtained from our measurements of $^{18}O_2$ transitions from the $v'' = 0$ level of the ground state. Continuity across the dissociation limit is observed. The solid line represents the fitted equation (2).

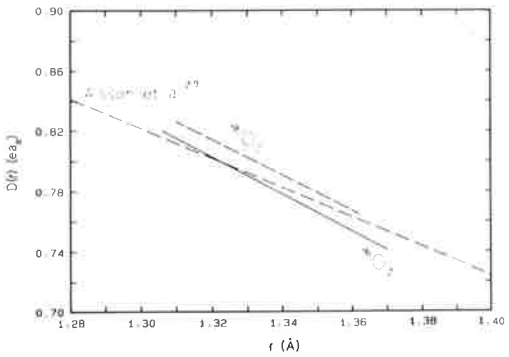

Fig. 6. The dipole moment obtained here for the B–X transition in $^{18}O_2$ compared with that previously determined[1] for $^{16}O_2$ and the semi-empirical calculations of Allison *et al.*[29]

in Fig. 5 also. Values for the coefficients in equation (2) were found to be $a_0 = -7247.998927$, $a_1 = 0.4857503692$, $a_2 = -1.231109229 \times 10^{-5}$, $a_3 = 1.393969849 \times 10^{-10}$, $a_4 = -5.941533405 \times 10^{-16}$. The observed continuity of oscillator strength density allows the interpolation of oscillator strength in regions of poor experimental accuracy ($v' = 18$–24).

THE DIPOLE MOMENT

A dipole moment was calculated for $^{18}O_2$ using the measured oscillator strengths and the potential curves of Lewis *et al.*[1] for the $X^3\Sigma_g^-$ and $B^3\Sigma_u^-$ states. Wavefunctions for $v'' = 0$, $v' = 2$–17 and $v'' = 1$, $v' = 5$–15 were calculated by numerical integration of the Schrödinger equation and the dipole moment $D(r)$ was expressed as a power series in the internuclear separation r. The coefficients of this power series were determined by a weighted least-squares procedure, which compared the calculated and measured rotationless oscillator strengths for $v'' = 0, 1$, avoiding the r-centroid approximation. The dipole moment obtained is, for $1.310\ \text{Å} \leqslant r \leqslant 1.362\ \text{Å}$,

$$D(r) = 1.54952 + 0.050258r - 0.45990r^2, \tag{3}$$

where $D(r)$ is in atomic units and r is in Å. Our form for the dipole moment is consistent with the recommendations of Whiting *et al.*[28] but is a factor of $\sqrt{3}$ smaller than some forms adopted in the literature. The r.m.s. deviation of the fit is 3.3%. The dipole moment is compared in Fig. 6 with that obtained[1] for $^{16}O_2$ and the semi-empirical determinations of Allison *et al.*[29] Our dipole moments for the two isotopes agree within 1–2%, well within the ~3% statistical uncertainty of each fitting procedure. Agreement with the results of Allison *et al.*[29] is also good. There is therefore no evidence that the dipole moment is affected by isotopic substitution.

CONCLUSIONS

Experimental oscillator strengths presented here for the (2–0)–(19–0) and (5–1)–(15–1) Schumann–Runge bands of $^{18}O_2$ are the most extensive and accurate currently available. Our measurements include the first experimental oscillator strengths for the (12–0)–(19–0) and (5–1)–(15–1) bands. We observe two more vibrational levels in the $B^3\Sigma_u^-$ state of $^{18}O_2$ ($v'_{max} = 24$) than in the case of $^{16}O_2$ ($v'_{max} = 22$), and the band oscillator strengths are smaller for the heavier isotope. The peak in the vibrational oscillator strength for $^{18}O_2$ lies at $v' = 15$, compared with $v' = 14$ for $^{16}O_2$. The band oscillator strength is observed to decrease with increased rotation, but not as quickly as for $^{16}O_2$. Our oscillator strengths agree well with theoretical values based on a fit to our $^{16}O_2$ measurements.[1] Continuity of the oscillator strength density across the $B^3\Sigma_u^-$ dissociation limit is verified for the $v'' = 0$ transitions. The dipole moment found here for $^{18}O_2$ agrees well with our $^{16}O_2$ dipole moment[1] and also with recent semi-empirical determinations.[29]

Acknowledgements—The authors would like to thank C. Dedman and K. Lonsdale for valuable technical assistance. Some of the programs needed for the dipole moment calculations were kindly provided by S. T. Gibson. We would also like to thank C. Brown of NRL for providing the unpublished wavenumbers of R. A. Howard and S. Tilford for the (12–0)–(20–0) Schumann–Runge bands of $^{18}O_2$.

REFERENCES

1. B. R. Lewis, L. Berzins and J. H. Carver, *JQSRT* **36,** 209 (1986).
2. B. R. Lewis, L. Berzins, J. H. Carver and S. T. Gibson, *JQSRT* **36,** 187 (1986).
3. P. S. Julienne, *J. molec. Spectrosc.* **63,** 60 (1976).
4. R. A. Howard and S. G. Tilford, private communication (1980).
5. H. G. Hecht, S. W. Rabideau and R. Engleman, Report LA-5871-MS, 10 pp., Los Alamos Sci. Lab., Los Alamos, N.M. (1975).
6. M. Halmann and I. Laulicht, *J. chem. Phys.* **42,** 137 (1965).
7. M. Halmann, *J. chem. Phys.* **44,** 2406 (1966).
8. G. W. Bethke, *J. chem. Phys.* **31,** 669 (1959).
9. M. Halmann and I. Laulicht, *J. chem. Phys.* **43,** 438 (1965).
10. M. Halmann and I. Laulicht, *J. chem. Phys.* **43,** 1503 (1965).
11. M. Halmann and I. Laulicht, *J. chem. Phys.* **44,** 2398 (1966).
12. M. Halmann and I. Laulicht, *J. chem. Phys.* **46,** 2684 (1967).
13. S. Tilford, private communication, see Ref. [3].
14. W. Steinbach and W. Gordy, *Phys. Rev.* **A8,** 1753 (1973).
15. H. G. M. Edwards, E. A. M. Good and D. A. Long, *J. chem. Soc. Faraday II* **72,** 865 (1976).
16. B. R. Lewis, L. Berzins and J. H. Carver, *JQSRT* **37,** 219 (1987).
17. B. R. Lewis, *Appl. Opt.* **22,** 1546 (1983).
18. B. R. Lewis, L. Berzins, J. H. Carver, S. T. Gibson and D. G. McCoy, *JQSRT* **34,** 405 (1985).
19. A. J. Blake, S. T. Gibson and D. G. McCoy, *J. geophys. Res.* **89,** 7277 (1984).
20. B. R. Lewis, L. Berzins and J. H. Carver, *JQSRT* **37,** 229 (1987).
21. K. Yoshino, D. E. Freeman and W. H. Parkinson, *J. phys. chem. Ref. Data* **13,** 207 (1984).
22. J. B. Tatum and J. K. G. Watson, *Can. J. Phys.* **49,** 2693 (1971).
23. R. M. Goody, *Atmospheric Radiation: I. Theoretical Basis.* Oxford University Press, London (1964).
24. S. T. Gibson, Ph.D. thesis, University of Adelaide (1983).
25. G. V. Marr, *Can. J. Phys.* **42,** 382 (1964).
26. W. R. Jarmain and R. W. Nicholls, *Proc. Phys. Soc.* **84,** 417 (1964).
27. A. C. Allison, A. Dalgarno and N. W. Pasachoff, *Planet. Space Sci.* **19,** 1463 (1971).
28. E. E. Whiting, A. Schadee, J. B. Tatum, J. T. Hougen and R. W. Nicholls, *J. molec. Spectrosc.* **80,** 249 (1980).
29. A. C. Allison, S. L. Guberman and A. Dalgarno, *J. geophys. Res.* In press (1987).

4.11 Pressure-broadening in the Schumann-Runge bands of molecular oxygen

[29] B. R. Lewis, L. Berzins, C. J. Dedman, T. T. Scholz, and J. H. Carver, *Journal of Quantitative Spectroscopy and Radiative Transfer* **39**, 271–282 (1988).

J. Quant. Spectrosc. Radiat. Transfer Vol. 39, No. 4, pp. 271–282, 1988
Printed in Great Britain.

0022-4073/88 $3.00 + 0.00

PRESSURE-BROADENING IN THE SCHUMANN–RUNGE BANDS OF MOLECULAR OXYGEN

B. R. LEWIS, L. BERZINS,† C. J. DEDMAN, T. T. SCHOLZ,‡ and J. H. CARVER
Research School of Physical Sciences, The Australian National University, Canberra, Australia 2600

(*Received* 10 *August* 1987)

Abstract—The pressure-broadened widths for selected rotational lines from the (2–0) to (15–0) Schumann–Runge bands of O_2 have been measured at pressures up to 60 atm. The self-broadening coefficient exhibits no dependence on rotation and a small dependence on vibration, in agreement with theoretical expectations, and may be taken as 0.20 cm^{-1}/atm FWHM, implying an optical collision diameter of 6.2 Å. The broadened absorption lines are shifted towards longer wavelengths and are asymmetric with a steeper blue wing, both of these effects increasing with pressure.

INTRODUCTION

A knowledge of the pressure-broadening coefficients for spectral lines in the Schumann–Runge system of O_2 is essential to the accurate modelling of the atmospheric transmission of solar radiation[1,2] and to the reliable determination of oscillator strengths and predissociation linewidths from laboratory measurements at pressures near 1 atm.[3,4] The determination of the continuum underlying the Schumann–Runge bands can be particularly sensitive to the value of the pressure-broadening coefficient.[5]

An enormous amount of experimental effort has gone into the measurement of pressure-broadening coefficients for rotational lines of various gases in the i.r. region of the spectrum, and a body of data exists for microwave and visible transitions. Comparatively few measurements have been performed, however, in the u.v. region, especially for self-broadening. Because of the generally close spacing of the rotational lines, even where measurements exist in the u.v. region, pressure-broadening coefficients often are determined as parameters of an overall band model rather than from direct observations of the broadening of individual lines.[6,7] Dodge et al[8] have made direct measurements of the broadening of lines in the γ(0–0) band of NO by various foreign gases and have noted the inconsistency of collision diameters obtained from the indirect methods.

Measurements of the self-broadening of O_2 in the red atmospheric system $b^1\Sigma_g^+ - X^3\Sigma_g^-$ have been performed by several investigators,[9–14] and pressure-induced shifts to the red have been observed in the (0–0) band by Galkin.[15] Measurements[16–22] of self-broadening in the microwave spectrum of O_2 gave results similar to those obtained for the atmospheric system: the broadening coefficients (FWHM) decreased from $\sim 0.06\ cm^{-1}\ atm^{-1}$ at $N'' = 1$ to $\sim 0.04\ cm^{-1}\ atm^{-1}$ at $N'' = 25$.

As has been noted by Cann et al,[1] there appear to have been no previous measurements of pressure-broadening coefficients for the Schumann–Runge bands of O_2 at normal temperatures. They[1] deconvoluted some of the strongly pressure-broadened spectra of Bethke[23] to obtain an FWHM linewidth of 0.32 cm^{-1} at 1 atm, but this value relates to broadening by argon, not self-broadening. Shock-tube studies[24–26] have yielded self-broadening coefficients for O_2 at temperatures near 3000 K and these results were extrapolated to 0 K using a $T^{-0.7}$ dependence by Cann et al[1] who chose a final form $0.3P(273/T)^{0.7}\ cm^{-1}$ for the FWHM linewidth; the exponent sign correction to their Eq. (10) should be noted. This result implies a broadening coefficient (FWHM) of 0.28 cm^{-1}/atm at room temperature.

†Present address: School of Chemistry, University of New South Wales, Sydney, Australia 2033.
‡Present address: Department of Mathematics and Theoretical Physics, Queens University of Belfast, Belfast BT7 1NN, Northern Ireland.

Although there is a vast body of literature dealing with the theoretical basis of the broadening of spectral lines, there are relatively few calculations dealing with the self-broadening of electronic transitions for non-polar molecules such as O_2. As far as we can tell, the only calculation dealing specifically with the broadening of lines in the Schumann–Runge system of O_2 is that of Breene,[27] who considered the van der Waals broadening of O_2 in the impact approximation by equilibrium air above 1000 K. Using the van der Waals constants calculated by Breene,[27] it is possible to deduce an optical collision diameter of ~ 5.6 Å for the self-broadening of the Schumann–Runge bands of O_2. Breene's theory[27] also implies that there is expected to be little dependence of the broadening coefficient on rotation or vibration, although his tables suggest a small decrease in the broadening coefficient with increased upper state vibration. The high-temperature shock-tube measurements of Treanor and Wurster[24] also support the lack of a noticeable dependence of linewidth on rotational quantum number.

For the reasons mentioned in the preceding paragraphs, we decided to measure room-temperature self-broadening coefficients for the Schumann–Runge bands of O_2 by as direct a method as possible.

EXPERIMENTAL STUDIES

The experimental apparatus employed in this work was identical to that used in our extensive study of the oscillator strengths and predissociation linewidths for isotopic O_2,[4,5,28–33] with the exception of the high-pressure absorption cells used for this work. Background radiation from an H_2 continuum was dispersed by a modified[34] 2.2 m scanning VUV monochromator with a resolution of ~ 0.05 Å and was detected photoelectrically before entering and after leaving the absorption cell. The scanning system and data collection were microcomputer-controlled.

The high-pressure absorption cells were machined from a solid block of stainless steel and the MgF_2 windows (1 in. dia, 1.5 in. length) used were obtained from Harshaw and held in place by appropriate flanges. A number of cells were constructed, and absorbing paths of 10 cm, 5 mm, 0.5 mm, and ~ 0.05 mm were used, depending on the strength of the band being studied. The shorter path lengths were defined by copper shims. At the high pressures (up to ~ 60 atm) used in this work, it was essential that the cells be constructed accurately and that assembly be performed in a clean environment in order to avoid surface cracking near the edges of the windows.

Medical grade oxygen was admitted manually to the cells through a stainless steel valve and the cell pressure was measured by an 8.5 in. Heise type cc precision stainless steel, bourdon-tube dial-gauge with a pressure range of 0–1500 lb/in^2. Evacuation of the cells was performed in two stages: firstly, the pressure was reduced to atmospheric by opening a second valve to the air and, secondly, this valve was shut and a third valve was opened to allow pumping of the cell down to the base pressure of $\sim 10^{-6}$ torr.

In practice, a cell of path length appropriate to the strength of the band of interest and to the 0–60 atm pressure range was selected, and a wavelength scan of relative transmission (detector counts/monitor counts) was performed over the line(s) of interest at the highest desired pressure. The pressure was then reduced by bleeding gas from the cell and the scan was repeated. This procedure was continued down to the lowest feasible pressure. A few scans performed with increasing pressures verified that there were no systematic errors introduced by the chosen experimental procedure. Scans taken with an empty cell were used to normalize the transmission scale, and results were recorded as values of $-ln$ (absolute transmission) as a function of wavelength.

DATA ANALYSIS

In the Schumann–Runge bands, absorption lines generally occur as unresolved triplets and, near $v' = 6$, the P and R branches overlap producing groups of six unresolved lines. The low-pressure linewidths vary from ~ 0.1 to 3 cm^{-1} due to predissociation.[28] Complications also occur in the form

of overlapping lines from other bands and a pressure dependent underlying continuum.[5,33] Full details of the modelling of the Schumann–Runge bands at low pressures have been given by Lewis et al.[4]

Since the pressure-broadening coefficient for O_2 is $\sim 0.2\,cm^{-1}$/atm, we require pressures of ~ 10 atm in order to obtain linewidths clearly in excess of the instrumental resolution of $\sim 1.3\,cm^{-1}$ FWHM. Only under these conditions can one make relatively unambiguous direct measurements of the pressure-broadened linewidths. Even then, it is still necessary to use a model in order to deduce successfully the linewidths for the experimentally inaccessible individual rotational components of the group of lines studied.

A Schumann–Runge band model of the type described earlier[4] is used to analyse the absorption scans measured here, but several simplifications are made. At the pressures used in this work, it is possible to neglect the Doppler component of the lineshape and it is therefore not necessary to use a Voigt profile. Use of a Lorentzian lineshape to describe both the predissociation and collision processes in the impact approximation[35] proved to be inadequate to describe the asymmetry that we observe at high pressures. In this work, we adopt the asymmetric lineshape discussed in the Appendix, $J(\alpha, x)$, where $x = 2(\nu - \nu_0 - \Delta\nu_s)/\Delta\nu$. Here, ν cm^{-1} is the wavenumber, ν_0 is the wavenumber of the line centre at zero pressure, $\Delta\nu_s$ is the shift of the line centre, $\Delta\nu$ is an FWHM linewidth parameter, and α is an asymmetry parameter. The zero pressure line centre wavenumbers were taken from the comprehensive measurements of Yoshino et al,[36] and the relative strengths of the individual lines in a group were calculated using the Hönl–London factors of Tatum and Watson,[37] the oscillator strengths of Lewis et al[4] and Boltzmann factors determined by the procedure described previously.[4]

It was assumed that the parameters α, $\Delta\nu_s$ and $\Delta\nu$ were the same for each component line of a given group from the same band and the function

$$F(\nu) = B(\nu) + A \sum_{i=1}^{N} R_i J(\alpha, x_i), \tag{1}$$

where $x_i = 2(\nu - \nu_{0i} - \Delta\nu_s)/\Delta\nu$, after convolution with the instrument slit function, was fitted in a least-squares fashion to the experimentally-observed absorption profile. In Eq. (1), N is the number of individual rotational lines considered explicitly, A is an amplitude constant, and ν_{0i} and R_i are the line centre wavenumber and the relative strength of the ith line. Normally, lines up to 10 half widths from the group of lines of interest were included in Eq. (1).

The function $B(\nu)$ includes the underlying pressure-dependent continuum and the effects of distant lines not explicitly included in Eq. (1). Normally, especially near a bandhead, $B(\nu) =$ constant was not a suitable form for the background and it was necessary to use the linear form $B(\nu) = B_0(1 + B_1\nu)$. The relative background slopes B_1 were generally found to be small at low pressures, with an increase at higher pressures.

In this work, we are interested only in the parameters pertaining to the pressure-broadened part of the lineshape, yet the indicated fitting procedure inevitably results in parameters which include the effects of the predissociation linewidth for the line under consideration. We correct the observed widths $\Delta\nu$ by subtracting the accurately known predissociation linewidths,[28] which vary with both vibration and rotation. These corrections are largest for the strongly predissociated lines of the (4–0) band for which the predissociation width is comparable with the pressure-broadened width at ~ 15 atm. Surprisingly, extensive computation showed that it was not necessary to correct the asymmetry parameters for the effects of predissociation given the lineshape used in this work. As will be seen later, the linear dependence of α on density supports this conclusion. The shifts $\Delta\nu_s$ were not corrected.

Use of the indicated procedure results in values for the parameters $\Delta\nu$, $\Delta\nu_s$ and α which are related to the width, shift and asymmetry of the pressure-broadened part of the individual rotational lines comprising the group of lines under study at the pressure of interest. It should be noted that the deduced parameters $\Delta\nu$, $\Delta\nu_s$ and α are not identical to the normally defined experimental width, shift and asymmetry (e.g. Royer[38]), but they may bear simple relationships to these. This aspect will be discussed in the next section.

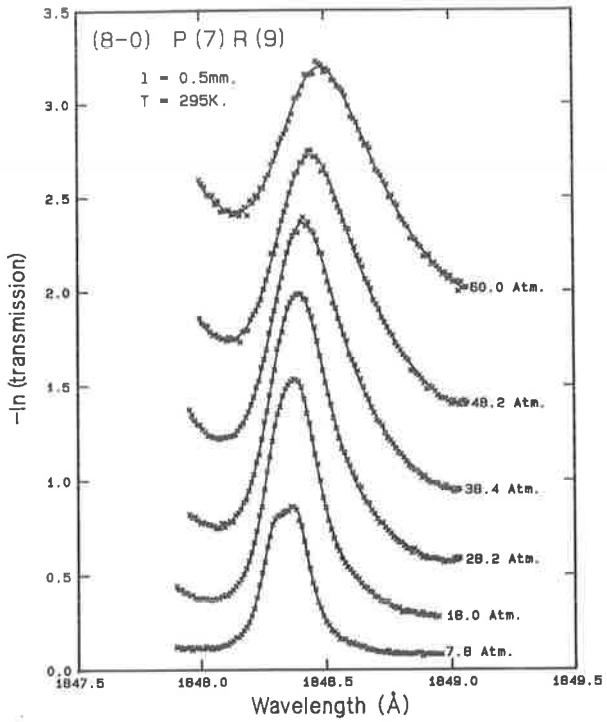

Fig. 1. Absorption in the P(7)R(9) lines of the (8–0) Schumann–Runge band as a function of pressure. The solid lines represent model fits to the experimental data points. The broadening, asymmetry and red shift are seen to increase with pressure.

RESULTS AND THEORETICAL DISCUSSION

All measurements in this work were taken at room temperature (295 K). We have examined a selection of lines from the (2–0) to (15–0) Schumann–Runge bands of O_2 using cell lengths from $\sim$0.05 mm to 10 cm and pressures up to 60 atm in order to see how the lineshape parameters vary with vibration and rotation, as well as pressure.

Pressure dependence

In Fig. 1, we present raw experimental results for the P(7)R(9) line group of the (8–0) band for pressures up to 60 atm. The observed behaviour is representative of the lines studied in this work, the broadening, red shift and asymmetry resulting from pressure increases being immediately obvious.

Before proceeding, it is important to note that, since the relevant variable in pressure-broadening is actually density and since real gas effects need to be taken into account at the pressures used in these experiments, we have converted pressures to number densities by interpolating tables in the *American Institute of Physics Handbook*.[39] In this work, the densities n are given as multiples of the STP density $2.69 \times 10^{19}\,\mathrm{cm}^{-3}$.

In Figs. 2–4, we present asymmetry, width and shift parameters for the $P(5)R(7)$ line group of the (6–0) band as a function of relative density. Each parameter is a linear function of density and this behaviour is typical of all of the lines studied here.

Royer[38] has obtained theoretical impact lineshapes in the Anderson–Talman[38,40,41] approximation which are applicable at intermediate densities; his second-order lineshape expansion, Eq. (8.4), is identical to our lineshape in the low-density limit, if we are in wavenumber space rather than angular frequency space, and if we make the transformations $\alpha = -na$, $\Delta\nu = 2nb$, and $\Delta\nu_s = nd$, where a, b, d are the lineshape constants of the Royer[38] theory. While it is not necessarily expected that ours is the appropriate lineshape to use at the higher densities of this work, the excellent agreement between the fitted solid line of Fig. 1 and the experimental points, together with the

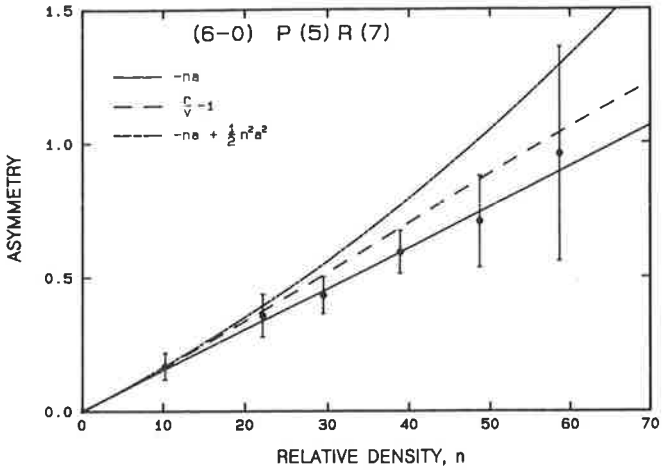

Fig. 2. The density dependence of asymmetry for the P(5)R(7) lines of the (6–0) Schumann–Runge band. Asymmetry parameters (experimental points), deduced from the least-squares fitting procedure, may be represented in the form $\alpha = -na$, where n is the relative density and $a = -0.0152 \pm 0.003$ r.d.$^{-1}$ The corresponding perceived asymmetries $\alpha' = (r/v) - 1$, where r and v are the red and blue halfwidths, are also shown together with the Royer[38] expression $-na + 0.5n^2a^2$ which is seen to be a good approximation only below ~25 r.d.

observed linear dependences of α, $\Delta\nu$ and $\Delta\nu_s$ on the density, support our choice of lineshape and the fact that a, b and d are constants. For the particular case of the $P(5)R(7)$ lines of the (6–0) band, illustrated in Figs. 2–4, $a = -0.0152$/r.d., $b = 0.110$ cm^{-1}/r.d. and $d = -0.0548$ cm^{-1}/r.d., where r.d. represents the unit of relative density described earlier.

It is appropriate to discuss here the relationships between the lineshape parameters and the normal, experimentally observable quantities of shift, width and asymmetry as defined, for example, by Royer.[38] In this work, we use least-squares to fit Eq. (1) to the experimentally observed absorption profile in order to obtain the lineshape parameters $\Delta\nu$, $\Delta\nu_s$ and α (and hence b, d and a), but these parameters are not directly observable experimentally. Let us assume that we can observe directly the pressure-broadened absorption lineshape of a single rotational line. The experimental lineshift $\Delta\nu_s'$ is the difference in wavenumber between the line peak at the pressure of interest and that at zero pressure, and this has a component due to the shift of the line centre $\Delta\nu_s$ and a component due to the increasing displacement of the line peak from the line centre

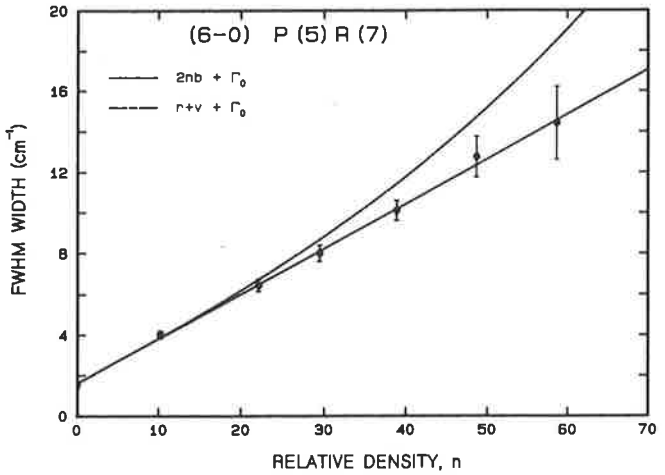

Fig. 3. The density dependence of linewidth for the P(5)R(7) lines of the (6–0) Schumann–Runge band. FWHM linewidth parameters (experimental points), deduced from the least-squares fitting procedure, may be represented in the form $\Delta\nu = 2nb + \Gamma_0$, where $b = 0110 \pm 0.002$ cm^{-1}/r.d. and $\Gamma_0 = 1.61$ cm^{-1}, in good agreement with the measured predissociation linewidth[28] plotted at $n = 0$. The corresponding perceived linewidths $\Delta\nu' = r + v + \Gamma_0$ are seen to deviate from a linear dependence on density above ~25 r.d.

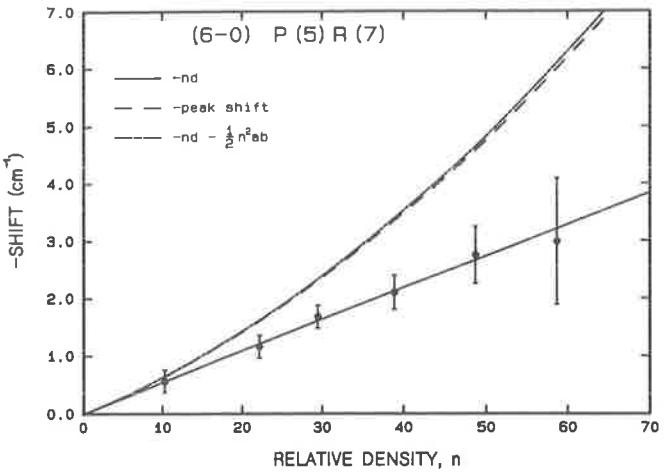

Fig. 4. The density dependence of shift for the P(5)R(7) lines of the (6–0) Schumann–Runge band. Shift parameters (experimental points), deduced from the least-squares fitting procedure, may be represented in the form $\Delta\nu_s = nd$, where $d = -0.0548 \pm 0.002\,\mathrm{cm}^{-1}$/r.d. Corresponding peak shifts $\Delta\nu_s'$ are seen to be in good agreement with the Royer[38] expression $nd + 0.5n^2ab$ to the maximum density used in this work, ~60 r.d.

because of increasing asymmetry at higher densities. The FWHM linewidth $\Delta\nu'$ can be easily measured, but is not exactly equal to $\Delta\nu$. Similarly, the line asymmetry α', defined as $(r/v) - 1$, where r and v are the red and blue half-widths, respectively, is not equal to α.

Given the form of $J(\alpha, x)$, it is possible to obtain $\Delta\nu_s'$, $\Delta\nu'$ and α' from the corresponding $\Delta\nu_s = nd$, $\Delta\nu = 2nb$ and $\alpha = -na$. We have presented the results of such transformations in Figs. 2–4. The experimental parameters, denoted by the primed symbols, are seen to exhibit a non-linear density dependence at higher pressures.

Royer[38] has obtained general expansions of the experimentally observable shifts, widths and asymmetries in powers of the density, which are expected to apply at low to intermediate densities. His results are:

$$\Delta\nu_s' = nd + 0.5n^2ab + \mathrm{O}(n^4), \tag{2}$$

$$\Delta\nu = 2nb + \mathrm{O}(n^3), \tag{3}$$

$$\alpha' = -na + 0.5n^2a^2 + \mathrm{O}(n^3). \tag{4}$$

To the second order, similar expressions follow from the low-density limit of our lineshape. We have plotted Eq. (2) on Fig. 4 using values for a, b and d obtained from Figs. 2–4. Good agreement is found with the experimentally-measured peak shifts at densities up to the maximum used by us. This agreement is quite general for the lines studied in this work and we therefore support the experimental verification of Eq. (2) noted by Royer[38] in measurements of the broadening of Cs lines[42–46] at pressures up to 100 atm. From Eq. (3), we see that the second order width correction is zero. This result means that observed widths are expected to be a linear function of density up to higher densities than are normally expected to apply to the impact approximation. The same is not true of the shift, for example. This fact is useful in experimental work which yields widths directly at somewhat limited resolution. Thus, widths measured at relatively high pressures can be extrapolated linearly to lower pressures with confidence. From Fig. 3, we see that the experimental widths $\Delta\nu' = r + v$ obtained by us deviate from linear behaviour only above ~25 r.d. We have plotted Eq. (4) on Fig. 2 and find good agreement with our values of the asymmetry $(r/v) - 1$ below ~25 r.d.

To summarize, we find that the expansions of the shift, width and asymmetry obtained by Royer[38] to the second order in n accurately represent our measurements below ~25 r.d. The shift expression, Eq. (2), is accurate to even higher densities, and we interpret this as confirming the lack of a third-order term in this equation. If we consider the Cs–rare-gas measurements[42–46] examined by Royer,[38] we find that similar conclusions to ours may be drawn but that the applicable density

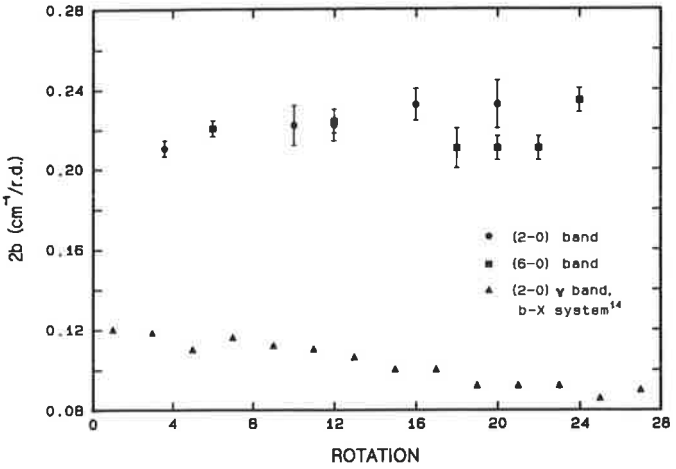

Fig. 5. Fitted FWHM linewidth coefficients $2b$ for the (2–0) and (6–0) Schumann–Runge bands. There is seen to be little dependence on rotation, in contrast to broadening coefficients measured for the (2–0)γ band of the b–X atmospheric system of O_2 by Melières et al.[14]

range is $\lesssim$3–4 r.d. The difference in the range of application can be understood by noting that the asymmetry coefficient a in the Cs–rare-gas case is typically 6–8 times larger than that measured here for O_2 self-broadening. The range of applicability of the expansions is largely dependent on the size of na and hence the density range is 6–8 times larger for O_2.

Rotation dependence

In Fig. 5, we present measured values of the FWHM broadening coefficient $2b$ as a function of rotation for the (2–0) and (6–0) bands. It is observed that there is no significant dependence on rotation and the same observation holds for the other bands and other coefficients a and d. As we shall see shortly, at normal temperatures this result is consistent with theoretical expectations for self-broadening of an allowed electronic transition in a non polar molecular such as O_2. For comparative purposes we have also shown in Fig. 5 the rotational dependence of the coefficient for self-broadening in the (2–0)γ band of the forbidden $b^1\Sigma_g^+ - X^3\Sigma_g^-$ atmospheric red system at 6280 Å as measured by Melières et al.[14] Here, there is a noticeable variation in broadening with rotation, and the extent of the broadening is about half of that observed by us for the u.v. Schumann–Runge transitions.

Vibration dependence

As far as we are aware, the only theoretical study of pressure-broadening in the Schumann–Runge bands of O_2 is due to Breene,[27] who calculated the broadening by equilibrium air at temperatures >1000 K. Before proceeding, we shall briefly discuss those of his considerations which are relevant to self-broadening.

Watson[47] noted that dispersion (van der Waals) forces appear to predominate in the self-broadening of non-polar molecular lines. If the normal resonance forces between like atoms were present, we would expect a significant rotational dependence of the broadening, but this is not observed. At normal temperatures, the Maxwell–Boltzmann distribution of molecules over the many closely-spaced rotational levels is so extensive that there are not enough molecules in any given rotational level to induce detectable resonance broadening. We thus restrict ourselves to a consideration of van der Waals interactions of the form $\Delta E = -\beta/R^6$, where R is the intermolecular distance, and the van der Waals constant β for the A state of a molecule perturbed by another molecule in its B state is given by[27,48]

$$\beta = \text{const.} \sum_{a,b} \frac{f_{Aa} f_{Bb}}{(E_A - E_a)(E_B - E_b)(E_A - E_a + E_B - E_b)}, \tag{5}$$

where f_{li} is the dipole oscillator strength for the transition $l \rightarrow i$, while $E_l - E_i$ is the corresponding

energy difference. As has been pointed out by Breene,[27] since the rotational energies are small compared with the vibrational and electronic energies, the oscillator strengths may be taken as electronic–vibrational and rotational excitation may be ignored altogether. Thus, β is independent of rotation and would be expected to change only slowly with vibration since the vibrational energies are small compared with the electronic energies. Breene[27] calculated van der Waals constants β for the $B^3\Sigma_u^-$ and $X^3\Sigma_g^-$ states of O_2 for self-broadening and obtained values varying from (68 to 60) $\times 10^{-60}$ erg-cm^6 for $v' = 0$–12 and (42 to 39) $\times 10^{-60}$ erg-cm^6 for $v'' = 0$–12, variations of the order of 10% over this range of vibration.

From the classical Fourier integral theory of interruption broadening due to Lindholm,[35] it follows that, in the limit of low pressure, the FWHM van der Waals broadening and lineshift parameters (cm^{-1}) are given by

$$\Delta\nu = 2.68\ (n_0/c)(\bar{v})^{3/5}(\Delta\beta/h)^{2/5}n, \tag{6}$$

$$\Delta\nu_s = -0.363\,\Delta\nu, \tag{7}$$

while the asymmetry parameter is given by

$$\alpha = -10.6\,n_0\,(\bar{v})^{-3/5}\,(\Delta\beta/h)^{3/5}n; \tag{8}$$

n_0 is Loschmidt's number, n is the relative density, $\Delta\beta$ (erg-cm^6) is the difference in the van der Waals constants between the upper and lower states, $\bar{v}$ is the mean relative velocity between the perturbed and perturbing molecules, and the other symbols have their usual meanings. Since the width, shift and asymmetry parameters are directly related to the van der Waals constants, we expect no variation with rotation and only slight variation with vibration.

In Fig. 6, we present our FWHM linear broadening coefficients for the Schumann–Runge bands as a function of vibration. Each point is a weighted average over values obtained for the rotational lines studied in a given band. We observe a small decrease in $2b$ with increased vibration, consistent with qualitative expectations. Theoretical broadening coefficients calculated from Eq. (6) using the van der Waals constants obtained by Breene[27] are also shown in Fig. 6. The agreement is fair, the theoretical values being ~20% smaller than our measurements, and the observed decrease with vibration is consistent with that predicted.

The experimentally-weighted average values of the linear shift coefficient d are given in Fig. 7 as a function of vibration, together with theoretical values from Eq. (7). The measured shift coefficients are ~30% smaller than the predictions. Our asymmetry coefficients, given in Fig. 8, are ~25% larger than the theoretical values given by Eq. (8).

The errors in the coefficients shown in Figs. 6–8 are statistical, representing the goodness of fit of the model to the experimental data. Systematic errors which may arise due to model

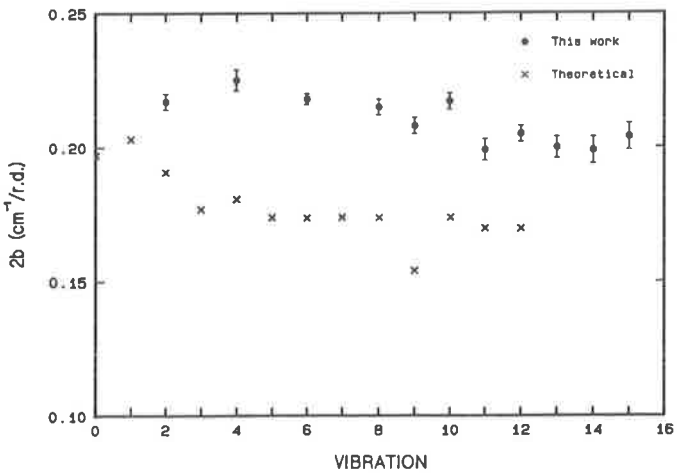

Fig. 6. Mean FWHM linewidth coefficients $2b$ for the Schumann-Runge system of O_2 as a function of upper state vibration, together with theoretical values calculated using the van der Waals constants of Breene[27] and the van der Waals broadening lineshapes of Lindholm.[35]

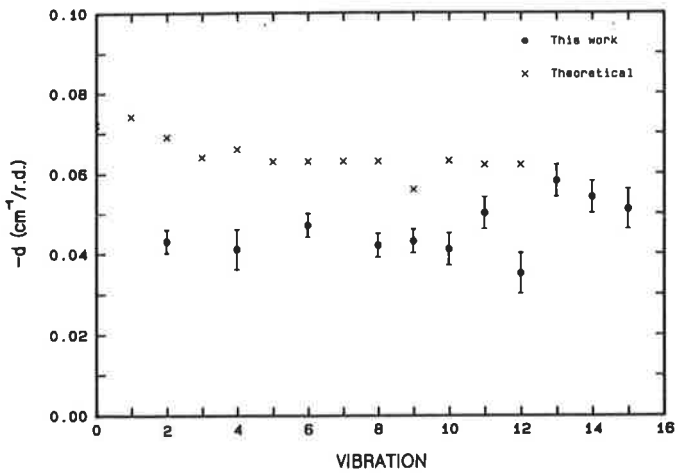

Fig. 7. Mean shift coefficients d for the Schumann–Runge system of O_2 as a function of upper state vibration, together with theoretical values calculated using the van der Waals constants of Breene[27] and the van der Waals broadening lineshapes of Lindholm.[35]

oversimplifications are not shown. The fitting procedure was carried out for several different lineshapes and the following observations were made. Firstly, the linewidth coefficient b was very robust in the sense that its value was almost independent of lineshape. For this reason, the small decrease in b with increasing rotation seen in Fig. 6 is significant. Secondly, the asymmetry and, especially, shift coefficients were considerably less consistent than the width coefficients, and the values of a, d and the slope of the underlying contributions to the absorption coupled together fairly strongly in the fitting procedure, resulting in less reliable determinations. If Figs. 7 and 8 are examined, it is seen that d increases slightly at large vibrations and that a decreases fairly strongly with vibration. We believe that the inverse coupling between a and d in the fitting procedure, together with model inadequacies in the crowded region of the spectrum for $v' \geqslant 13$, has resulted in values of d which are a little high and values of a which are correspondingly a little low. Ignoring values for $v' \geqslant 13$, we then conclude that, within the accuracy of our measurements, the shift coefficient does not show any dependence on vibration, while the asymmetry coefficient decreases with increasing vibration. For $v' = 2$–12, there is fair agreement with theory, which implies a decrease of 10% in d and 16% in a.

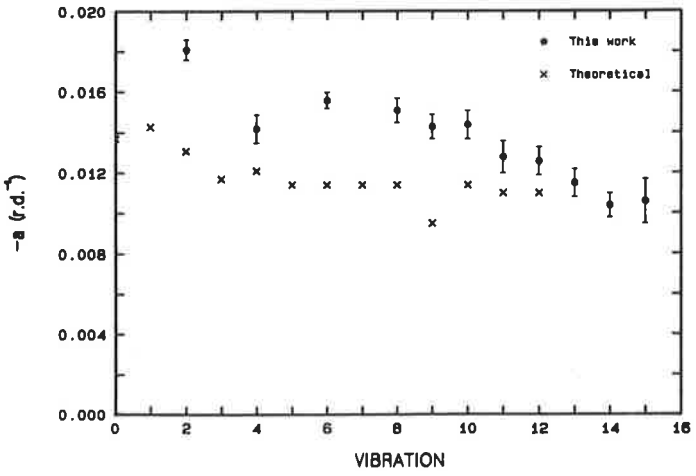

Fig. 8. Mean asymmetry coefficients a for the Schumann–Runge system of O_2 as a function of upper state vibration, together with theoretical values calculated using the van der Waals constants of Breene[27] and the van der Waals broadening lineshapes of Lindholm.[35]

CONCLUSIONS

The main purpose of this work was to measure self-pressure-broadening coefficients at room temperature for the Schumann–Runge bands by a direct method. Our FWHM broadening coefficients are model-independent and may be represented by $2b = (0.227 \pm 0.003) - (1.72 \pm 0.27) \times 10^{-3} v'$, where $2b$ is in cm^{-1}/r.d. No other such measurements exist, but our values may be compared with those adopted by Cann et al,[1,2] who suggest a vibration-independent broadening coefficient of 0.284 cm^{-1}/atm at 295 K. Our best broadening coefficient for $v' = 8$ is 0.213 cm^{-1}/r.d., or 0.197 cm^{-1}/atm at low pressures. The corresponding billiard ball collision diameter is 6.2 Å. The previous 44% overestimate of the broadening will result in significant errors in oxygen absorption coefficients calculated according to the methods of Cann et al[1,2] in some spectral regions.

The red shifts and asymmetries observed here at high pressures, together with the broadening, exhibit a non-linear density dependence which is described well by the general formulae of Royer.[38] The linearized coefficients a, b and d show no dependence on rotation and no (d) or a small negative (a, b) dependence on vibration, and their values are within 30% of theoretical estimates obtained by assuming van der Waals broadening, the van der Waals constants of Breene,[27] and the Lindholm[35] theory of interruption broadening. Our experimental shift/width ratio of ~0.20, compared with 0.363 for this theory, indicates that more sophisticated interaction potentials and theories will be required in order to obtain better agreement with experiment.

Acknowledgement—The authors would like to thank K. Lonsdale for valuable technical assistance.

REFERENCES

1. M. W. P. Cann, R. W. Nicholls, W. F. J. Evans, J. L. Kohl, R. Kurucz, W. H. Parkinson, and E. M. Reeves, *Appl. Opt.* **18,** 964 (1979).
2. M. W. P. Cann, J. B. Shin, and R. W. Nicholls, *Can. J. Phys.* **62,** 1738 (1984).
3. B. R. Lewis, J. H. Carver, T. I. Hobbs, D. G. McCoy, and H. P. F. Gies, *JQSRT* **22,** 213 (1979).
4. B. R. Lewis, L. Berzins, J. H. Carver, and S. T. Gibson, *JQSRT* **36,** 209 (1986).
5. B. R. Lewis, L. Berzins, J. H. Carver, S. T. Gibson, and D. G. McCoy, *JQSRT* **34,** 405 (1985).
6. M. J. Pilling, A. M. Bass, and W. Braun, *JQSRT* **11,** 1593 (1971).
7. D. E. Shemansky, *J. Chem. Phys.* **51,** 5487 (1969).
8. L. G. Dodge, J. Dusek, and M. F. Zabielski, *JQSRT* **24,** 237 (1980).
9. D. E. Burch and D. A. Gryvnak, *Appl. Opt.* **8,** 1493 (1969).
10. J. H. Miller, R. W. Boese, and L. P. Giver, *JQSRT* **9,** 1507 (1969).
11. V. D. Galkin, S. N. Zhukov, and L. A. Mitrofanova, *Opt. Spektrosk.* **33,** 837 (1972).
12. L. P. Giver, R. W. Boese, and J. H. Miller, *JQSRT* **14,** 793 (1974).
13. T. G. Adiks and V. I. Dianov-Klokov, *Bull. Acad. Sci. USSR, Atm. Ocean. Phys.* **4,** 605 (1968).
14. M. A. Melières, M. Chenevier, and F. Stoeckel, *JQSRT* **33,** 337 (1985).
15. V. D. Galkin, *Opt. Spektrosk.* **46,** 192 (1978).
16. R. S. Anderson, W. V. Smith, and W. Gordy, *Phys. Rev.* **87,** 561 (1952).
17. R. W. Zimmerer and M. Mizushima, *Phys. Rev.* **121,** 152 (1961).
18. R. M. Hill and W. Gordy, *Phys. Rev.* **93,** 1019 (1954).
19. J. O. Artman and J. P. Gordon, *Phys. Rev.* **96,** 1237 (1954).
20. J. H. Burkhalter, R. S. Anderson, W. V. Smith, and W. Gordy, *Phys. Rev.* **79,** 651 (1950).
21. B. V. Gokhale and M. W. P. Strandberg, *Phys. Rev.* **84,** 844 (1951).
22. H. J. Liebe, G. G. Gimmestad, and J. D. Hopponen, *IEEE Trans.* **AP25,** 327 (1977).
23. G. W. Bethke, *J. Chem. Phys.* **31,** 669 (1959).
24. C. E. Treanor and W. H. Wurster, *J. Chem. Phys.* **32,** 758 (1960).
25. N. I. Krindach, N. N. Sobolev, and L. N. Tunitskii, *Opt. Spectrosc.* **15,** 326 (1963).
26. D. E. Buttrey, *JQSRT* **9,** 1527 (1969).
27. R. G. Breene, *Appl. Opt.* **6,** 141 (1967).
28. B. R. Lewis, L. Berzins, J. H. Carver, and S. T. Gibson, *JQSRT* **36,** 187 (1986).
29. B. R. Lewis, L. Berzins, and J. H. Carver, *JQSRT* **37,** 219 (1987).
30. B. R. Lewis, L. Berzins, and J. H. Carver, *JQSRT* **37,** 243 (1987).
31. B. R. Lewis, L. Berzins, and J. H. Carver, *JQSRT* **37,** 255 (1987).
32. B. R. Lewis, L. Berzins, and J. H. Carver, *JQSRT* **37,** 229 (1987).
33. B. R. Lewis, L. Berzins, J. H. Carver, and S. T. Gibson, *JQSRT* **33,** 627 (1985).
34. B. R. Lewis, *Appl. Opt.* **22,** 1546 (1983).
35. E. Lindholm, *Ark. Math. Astron. Fys.* **32A,** 17 (1945).
36. K. Yoshino, D. E. Freeman, and W. H. Parkinson, *J. Phys. Chem. Ref. Data* **13,** 207 (1984).

37. J. B. Tatum and J. K. G. Watson, *Can. J. Phys.* **49,** 2693 (1971).
38. A. Royer, *Phys. Rev.* **A22,** 1625 (1980).
39. D. E. Gray (Ed.), *American Institute of Physics Handbook*, 3rd ed., McGraw-Hill, New York, NY (1972).
40. P. W. Anderson, *Phys. Rev.* **86,** 809 (1952).
41. P. W. Anderson and J. D. Talman, Bell Teleph. Syst. Tech. Publ. No. 3117 (1956).
42. S. Y. Ch'en and R. O. Garrett, *Phys. Rev.* **144,** 59 (1966).
43. R. O. Garrett and S. Y. Ch'en, *Phys. Rev.* **144,** 66 (1966).
44. S. Y. Ch'en, E. C. Looi, and R. O. Garrett, *Phys. Rev.* **155,** 38 (1967).
45. R. O. Garrett, S. Y. Ch'en, and E. C. Looi, *Phys. Rev.* **156,** 48 (1967).
46. S. Y. Ch'en, D. E. Gilbert, and D. K. L. Tan, *Phys. Rev.* **184,** 51 (1969).
47. W. W. Watson, *J. Phys. Chem.* **41,** 61 (1937).
48. H. Margenau, *Rev. Mod. Phys.* **11,** 1 (1939).
49. S. Y. Ch'en and M. Takeo, *Rev. Mod. Phys.* **29,** 20 (1957).
50. W. Lenz, *Z. Phys.* **80,** 423 (1933).

APPENDIX

In this work, we require an asymmetric lineshape, preferably with a single asymmetry parameter, in order to fit the experimentally observed absorption profiles. The lineshape should fit the observations over a fairly wide range of pressures (asymmetries). We chose the lineshape developed by Lindholm[35] as our starting point. This shape may be expressed as $f_L(l, k)$, where l is a shape (asymmetry) parameter, and k is a wavenumber parameter. For our purposes, there are several disadvantages in Lindholm's[35] shape: firstly, there are fixed relationships between the width, shift and asymmetry; secondly, numerical techniques are required for the evaluation of $f_L(l, k)$. We generalize the shape by making the transformations $\alpha = 0.227\, l$, $x = (k + 0.577\, l)/0.795\, l$, where α is an asymmetry parameter, and x is a dimensionless wavenumber parameter. By the second of these transformations, the fixed relationships between the Lindholm[35] width, shift and asymmetry have been removed. It also follows that $f_L(\alpha, x)$ reduces to the Lorentzian shape, const./$(1 + x^2)$, in the case of zero asymmetry ($\alpha = 0$), and to the form const. $(1 - \alpha x)/(1 + x^2)$ for small asymmetries. The second form is identical to the second-order impact approximation lineshape of Royer[38] and is similar to the Lenz[50] lineshape, but it is limited in range of applicability to regions where $\alpha x \leqslant 1$, i.e., for low asymmetries and near the line centre. We initially used this form in fitting

Table A1. Polynomial coefficients b_{ij} which, together with the equations of the Appendix, allow the construction of an analytic approximation to the generalized Lindholm[35] lineshape $f_L(\alpha, x)$.

i \ j	0	1	2	3	4	region
0	-0.42978	0.24478	-5.17552-2	5.25359-3	-2.07398-4	-5.0<αx<-0.6
1	1.39976	0.40629	-0.11545	1.33640-2	-5.86992.4	
2	0.36050	8.33750-2	-3.26663-2	4.85013-3	-2.44953-4	
3	3.67526-2	2.57971-3	-2.43233-3	4.93260-4	-2.80261-5	
0	1.0	0.0	0.0	0.0	0.0	-0.6<αx<0.0
1	1.00475	6.98054-4	-8.08826-3	7.93155-4	-2.82810-5	
2	0.19905	9.03683-2	-1.75709-2	1.30201-3	-3.49840-5	
3	-0.22501	0.10459	-1.73435-2	1.52773-3	-6.07640-5	
0	1.0	0.0	0.0	0.0	0.0	0.0<αx<0.7
1	1.00804	-4.01533-3	-6.94704-3	6.76344-4	-2.35239-5	
2	9.45870-2	0.13062	-2.27189-2	1.51170-3	-3.21701-5	
3	-0.16883	-1.61079-2	1.60651-2	-2.34367-3	1.15806-4	
0	0.98338	-5.78610-2	2.21590-2	-2.78855-3	1.24300-4	0.7<αx<2.0
1	1.15033	0.15863	-8.07711-2	1.07302-2	-5.01304-4	
2	-0.20998	1.00462-2	5.55196-2	-1.04029-2	5.78083-4	
3	2.41257-2	-6.68355-3	-9.67488-3	2.27475-3	-1.41757-4	
0	1.43058	2.28710-2	-7.93850-2	8.19300-3	-2.65440-4	αx>2.0
1	0.66719	0.12271	5.02260-2	-8.40530-3	3.71430-4	
2	-3.37400-2	-5.31650-3	-4.70220-3	1.18690-3	-6.10360-5	
3	8.99710-4	1.15450-4	1.63112-4	-4.51920-5	2.55410-6	

our measurements and the results were reasonable below ~ 25 r.d., but the resulting parameters exhibited non-linear density dependence above this point because of the unrealistic wing behaviour of the chosen lineshape. We therefore decided to use the full generalized Lindholm[35] lineshape $f_L(\alpha, x)$, but had to introduce an analytic approximation to this function in order to obviate repeated numerical calculations in the final application of the function.

Our lineshape was expressed in the form $J(\alpha, x) = F(\alpha x)/(1 + x^2)$ and fitted to $f_L(\alpha, x)$ over a wide range of values of α and x. The results are

$$\left.\begin{aligned} \alpha x < -5\text{: } & F(\alpha x) = 0.25, \\ -5 < \alpha x < -0.6\text{: } & F(\alpha x) = 0.2 + \exp\left(\sum_{i=0}^{3} a_i(-\alpha x)^i\right), \\ \alpha x > -0.6\text{: } & F(\alpha x) = \sum_{i=0}^{3} a_i(-\alpha x)^i, \end{aligned}\right\} \tag{A1}$$

where

$$a_i = \sum_{j=0}^{4} b_{ij}(\alpha/0.227)^j.$$

Values of b_{ij} appropriate to various ranges of αx are given in Table A1. Inspection of the table shows that $J(\alpha, x) = 1/(1 + x^2)$ for $\alpha = 0$, and that $J(\alpha, x) \approx (1 - \alpha x)/(1 + x^2)$ for small α.

4.12 Resonances in the photodissociation of isotopic molecular oxygen: I. The longest band

[30] B. R. Lewis, S. T. Gibson, M. Emami, and J. H. Carver,
Journal of Quantitative Spectroscopy and Radiative Transfer **40**, 1–13 (1988).

J. Quant. Spectrosc. Radiat. Transfer Vol. 40, No. 1, pp. 1–13, 1988
Printed in Great Britain.

0022-4073/88 $3.00 + 0.00

RESONANCES IN THE PHOTODISSOCIATION OF ISOTOPIC MOLECULAR OXYGEN—I. THE LONGEST BAND

B. R. LEWIS, S. T. GIBSON, M. EMAMI†, and J. H. CARVER
Research School of Physical Sciences, The Australian National University, Canberra, Australia 2600

(*Received* 8 *January* 1988)

Abstract—We present detailed photoabsorption cross section measurements of the (0–0) and (0–1) bands of the $E^3\Sigma_u^- - X^3\Sigma_g^-$ transition of molecular oxygen. The isotopes $^{16}O_2$, $^{16}O^{18}O$ and $^{18}O_2$ were studied at 79 and 295 K, with an instrumental resolution of 0.04–0.06 Å FWHM. Our results show clearly that these bands provide one of the rarely observed examples of Beutler–Fano resonances in molecular photodissociation. With the aid of empirical modelling, we show that the widths and asymmetries of individual lines vary significantly with rotation and isotopic mass, but the oscillator strengths show no isotope effect.

INTRODUCTION

In the region from the LiF cutoff to the short wavelength side of the Schumann–Runge continuum (1050–1300 Å), the photoabsorption spectrum of $^{16}O_2$ consists of a number of strong bands separated by windows of relatively weak absorption. Cross sections in this region have been measured by several investigators,[1–4] especially near the solar Lyman-α line.[5–10]

The diffuse bands were first observed spectrographically by Price and Collins.[11] In this and associated works,[12,13] we are concerned with Tanaka's progression I,[14] consisting of bands at 1244 Å (longest), 1206 Å (second), 1172 Å (third), and 1269 Å, classified by Tanaka[14] as the hot band associated with the longest band. The assignment of these bands has been in doubt until quite recently. On the basis of isotope shift measurements, Ogawa et al[15] classified the longest band as the (1–0) transition of a progression with upper state $E^3\Sigma_u^-$, and the 1269 Å band as the corresponding (0–0) band. Ogawa[16] showed spectrographically that rotational and fine structure was visible in the longest band of $^{18}O_2$, confirming identification of the upper state as $^3\Sigma_u^-$, but he persisted with the vibrational assignments of Ogawa et al.[15]

Ab initio calculations of the mixing of valence and Rydberg $^3\Sigma_u^-$ states of O_2, by Buenker and Peyerimhoff[17–19] and Yoshimine,[20] showed that the longest, second and third bands could be explained as transitions to the *lowest* three vibrational levels of the resulting upper mixed valence-Rydberg state, $E^3\Sigma_u^-$. Reasonable agreement was found between calculated and observed energy levels, and between calculated[20] and observed[21] oscillator strengths. This reclassification was supported by the arguments of Katayama et al,[22] who suggested that the anomalous isotope shift of the longest band[15] might be explained by the strong configuration interaction which produced the $E^3\Sigma_u^-$ state. Black et al[23] measured the absorption spectrum of $^{16}O_2$ at 930 K, discovering new hot bands at 1229 and 1195 Å, associated with the second and third bands, and confirming the classification of the 1269 Å band as (0–1).

At this time, it is clear that the longest, second, third, and 1269 Å bands are all part of the same progression, as originally envisaged by Tanaka.[14] They are the (0–0), (1–0), (2–0), and (0–1) transitions to the mixed valence-Rydberg $E^3\Sigma_u^-$ state (labelled B' by some authors[20,22]). What remain to be explained are the anomalous isotope shift for the (0–0) band, and the large variations of width with vibration and isotopic mass. Using the methods of Fano,[24] Cimiraglia et al[25] showed theoretically that isotopic shifts and widths of the order of 100 cm^{-1} were possible. They[25] noted that this was sufficiently large to explain the observations, but emphasized that their calculations

†Permanent address: Department of Physics, College of Arts and Sciences, Shiraz University, Iran.

were extremely sensitive to the assumed potential curves, and that they had no ambition of fitting the scanty experimental data.

Resonances in molecular photodissociation due to absorption into mixed states, such as the $E^3\Sigma_u^-$ state of O_2, may be treated theoretically by a full solution of the coupled Schrödinger equations. This method has been applied, for example, to coupled $^2\Pi$ states in OH by van Dishoeck et al,[26] who also give a brief review of the technique. Torop et al[27] have developed a similar treatment which has been applied by Wang et al[28] to an interpretation of the temperature dependence of the O_2 cross section in the region 1300–1600 Å.

The aim of the present work is to obtain detailed experimental cross sections for the (0–0) and (0–1) E–X bands of $^{16}O_2$, $^{16}O^{18}O$ and $^{18}O_2$, so that accurate potential curves and coupling parameters may be deduced by comparison with the predictions of the coupled-equations model of Torop et al.[27] This fitting procedure will be discussed in detail in an associate work.[13] Previously, cross sections have been measured only for $^{16}O_2$, and they are of insufficient detail[25] for an accurate determination of the theoretical parameters. The (1–0) and (2–0) E–X bands will be discussed in a future work.[12]

EXPERIMENTAL METHOD

The experimental apparatus was similar to that used in our study of oscillator strengths and predissociation linewidths for the Schumann–Runge bands of isotopic O_2.[29–36] Background radiation was provided by an argon continuum discharge lamp powered by a pulser based on the Argonne design.[37] The lamp was operated in the windowless mode at a pressure of 400 torr of argon and a pulse repetition frequency of ~80 kHz. The radiation was dispersed by a modified[38] 2.2 m scanning VUV monochromator, operating in the first or second order with FWHM resolutions of ~0.06 and ~0.04 Å, respectively. Radiation was detected photoelectrically before entering and after leaving the 10 cm, controlled-temperature absorption cell. The scanning system and data collection were controlled by an IBM AT microcomputer.

We studied three gas samples, 99.8% ^{16}O, 53% ^{18}O, and 99% ^{18}O, the latter two being supplied by ICON. For a previous 20% ^{18}O sample from another manufacturer,[32] it had proved necessary to dissociate the gas with radiation from a mercury lamp in order to achieve a statistical molecular mixture, but this procedure was not required for the ICON samples. The cell was filled from the gas cylinders through an electromagnetic leak valve to pressures in the range 0.01–10 torr, monitored by a variable capacitance manometer. Cold traps used with the $^{16}O_2$ sample were not found to alter the measured cross sections, even in regions of low absorption. Their use was abandoned, therefore, for the 53% ^{18}O sample, since repeated observations of the absorption spectrum implied a noticeable variation of the isotopic molecular composition in the cell when the cold traps were used.

Scans were performed with cell temperatures of 295 and 79 K and with wavelength increments from 5 to 100 mÅ, depending on the scale of the structure being studied. Wavelengths were calibrated by the NI lines present in the lamp spectrum. The longest band was studied at pressures near 0.01 torr, while the weaker structures were measured at pressures up to 10 torr. Corrections to the pressure for the effects of thermal transpiration were necessary at 79 K for pressures <0.05 torr. The magnitude of the correction was determined by measuring the temperature dependence of the effective $^{16}O_2$ Schumann–Runge continuum cross section at 1400 Å, a wavelength where the actual cross section is known to have a very small temperature coefficient.[39] A stray light correction of 0.4% and a small dark count correction were necessary also. For scans over a small wavelength range, empty-cell background ratios (detector/monitor) were taken at the initial wavelength before the scan, at the final wavelength after the scan, and were linearly interpolated at intermediate wavelengths. For longer scans, empty runs over the wavelength range of interest were taken before and after the full run, and were averaged to provide the reference background ratios.

Using the known pressure, temperature, cell length and absolute transmission, absorption cross sections were calculated using Beer's law. Statistical errors in the cross sections, except in the case of very weak absorption, were normally $\leqslant 2\%$, with an extra ~2% uncertainty due to uncertainties in cell length, pressure, and temperature. Additional uncertainties arose in the case of the 79 K

measurements because of increased temperature measurement error, thermal transpiration correction, and increased background drifts, but every precaution was taken to minimize these.

Cross sections of $^{16}O^{18}O$ were deduced from measured total cross sections for the 53% ^{18}O sample by performing a weighted subtraction using the known isotopic enrichments and the previously measured cross sections for the nearly pure $^{16}O_2$ and $^{18}O_2$ samples. This procedure, at some wavelengths, can produce $^{16}O^{18}O$ cross sections with dramatically increased relative uncertainties due to the subtraction, but this occurs only over very limited wavelength ranges, and where the cross section is quite small.

EMPIRICAL MODEL

Although the E–X bands in $^{16}O_2$ are all diffuse,[14] and thus seem to offer no hope of rotational analysis, the remarkable appearance[15,16] of rotational and fine structure in the longest band of $^{18}O_2$, and the rotational analysis of Ogawa,[16] enable the development of an empirical band model from which it is possible to obtain some information on the behaviour of rotational linewidths and asymmetries, even for the diffuse bands.

Spectroscopic constants for the $X^3\Sigma_g^-$ state were taken from Veseth and Lofthus[40] and Steinbach and Gordy,[41,42] for $^{16}O_2$, $^{18}O_2$, and $^{16}O^{18}O$, respectively. These were used to generate the manifold of rovibrational levels for the ground state and the corresponding weighted Boltzmann factors.

For $^{18}O_2$, except for D', spectroscopic constants for the $v' = 0$ level of the $E^3\Sigma_u^-$ state were taken from Ogawa.[16] The splitting constants λ and μ were taken as the same for all isotopes. Band origins for $^{16}O^{18}O$ and $^{16}O_2$ were obtained by fitting the model absorption spectrum to our measurements. The remaining rotational constants B' were obtained from preliminary calculations of Wang,[43] normalized to the measurements of Ogawa[16] for $^{18}O_2$. Centrifugal distortion constants D' were calculated from the rotational constants for $^{18}O_2$ and an approximate value for ω_e', with appropriate isotope correction.[44] Line wavenumbers for $v'' = 1$ were calculated from the $v'' = 0$ wavenumbers and the known ground state energy levels. Hönl–London factors were taken from Tatum and Watson[45] for $^3\Sigma^-$–$^3\Sigma^-$ transitions with coupling intermediate between Hund's cases (a) and (b). The transformation coefficients were determined from the energy levels obtained previously. The forbidden $^NP_{13}$ branch of the (0–0) $E^3\Sigma_u^-$–$X^3\Sigma_g^-$ transition, seen experimentally by Ogawa,[16] and also studied by us in this work, is well described by the mixed coupling factors.

As we shall see later, the longest bands of all three isotopes are asymmetric, and there is clear evidence of absorption minima associated with one wing of each band. Therefore, we described each rotational line by a Fano[24] lineshape, given by

$$F(\epsilon) = (q + \epsilon)^2/(1 + \epsilon^2), \tag{1}$$

where

$$\epsilon = (\nu - \nu_0)/\Gamma, \tag{2}$$

q is an asymmetry parameter, Γ is the HWHM linewidth, and ν_0 is the wavenumber of the line centre. Initially, Γ and q were assumed to be independent of rotation, but it was not possible to fit the experimental cross sections in this way. The model was generalized, therefore, to allow the linewidths and asymmetries to change systematically with rotation so that

$$\Gamma(J') = \Gamma_0 + \Gamma_J J'(J' + 1), \tag{3}$$

and

$$q(J') = q_0 + q_J[J'(J' + 1)]^2. \tag{4}$$

In reality, of course, the variation of Γ and q with rotation is unlikely to be described by such simple expressions, and we experimented with other forms. Equations (3) and (4) were found to be the most appropriate two parameter expressions which were consistent with the measurements.

The model band profile was built up by adding the Fano profiles of individual rotational lines at the positions and with the relative strengths determined by the technique described previously. The effects of interference between resonance profiles, allowed for some pairs of band branches, are expected to be small, for reasons similar to those given by Julienne[46] regarding predissociation

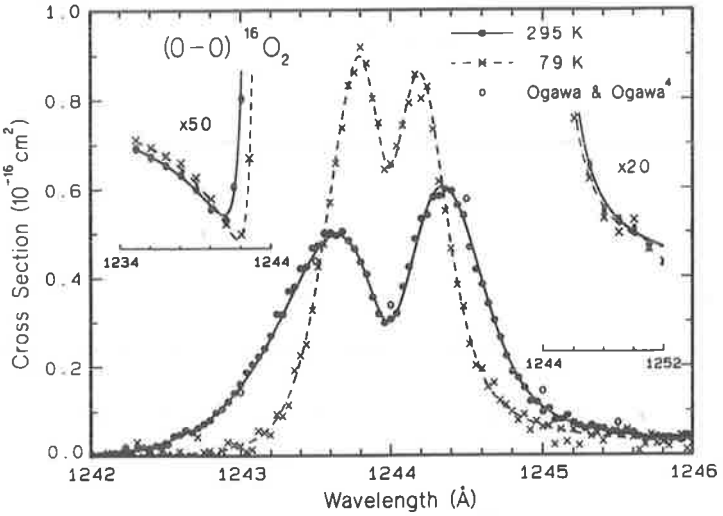

Fig. 1. Measured photoabsorption cross sections for the longest band of $^{16}O_2$ at room and liquid nitrogen temperature, together with the measurements of Ogawa and Ogawa,[4] and model cross sections (lines) generated with $\nu_0 = 80{,}382.8\ \text{cm}^{-1}$, $f = 0.00625$, $\Gamma_0 = 5.6\ \text{cm}^{-1}$, $\Gamma_J = 0.018\ \text{cm}^{-1}$, $q_O = -19.2$, $q_J = 2.8 \times 10^{-5}$.

of the $B^3\Sigma_u^-$ state of O_2. The overall band oscillator strength and the width and asymmetry parameters were determined by least-squares fitting the model cross section, after convolution with a Gaussian instrument function, to the experimental measurements.

RESULTS AND DISCUSSION

In Fig. 1, we present measured cross sections for the longest band of $^{16}O_2$ at 295 and 79 K, together with model cross sections calculated with a fixed set of parameters ($\nu_0 = 80{,}382.8\ \text{cm}^{-1}$, $f = 0.00625$, $\Gamma_0 = 5.6\ \text{cm}^{-1}$, $\Gamma_J = 0.018\ \text{cm}^{-1}$, $q_0 = -19.2$, $q_J = 2.8 \times 10^{-5}$). The measurements of Ogawa and Ogawa[4] are in excellent agreement with ours provided that they are displaced by ~ 0.07 Å towards shorter wavelengths.

The observed cross sections are not resolution dependent since the rotational linewidths are larger than the rotational line spacing, but there is a substantial temperature dependence of the cross section since the linewidths are smaller than the extent of the band. The relative enhancement of the R branch at liquid nitrogen temperature occurs essentially because the Hönl–London factors for the R branch exceed those for the P branch at low rotation. The band profile is noticeably asymmetric, with a stronger long wavelength wing, and structure reminiscent of a Fano minimum is evident near 1241 Å.

The model cross sections generated with the single set of parameters listed previously are in excellent agreement with the measurements in all respects. The choice of Fano lineshapes in the model is vindicated by the observed asymmetry and the cross section minimum near 1241 Å, which is correctly reproduced by the model at both temperatures. As mentioned previously, if the linewidth is taken to be independent of rotation there is a noticeable systematic discrepancy between the observed and fitted cross sections. Despite the diffuse nature of this band, there is clear evidence from the model that the linewidth increases strongly with rotation. Although the cross section near the band centre is relatively insensitive to the asymmetry parameter q, it is possible to accurately determine this parameter by fitting in the wings of the band. Using model simulations, the values of q found by this method at each temperature can be associated with an effective rotation. The functional form given previously for the variation of q with rotation, Eq. (4), is then fitted to the results. The value of q_J obtained by this technique, while being somewhat uncertain, indicates unambiguously that rotational lines in the longest band of $^{16}O_2$ become more asymmetric for high values of rotation.

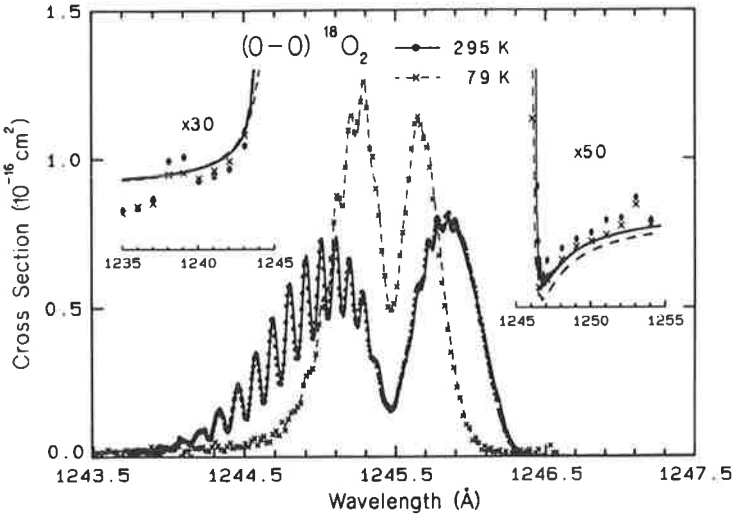

Fig. 2. Measured photoabsorption cross sections for the longest band of $^{18}O_2$ at room and liquid nitrogen temperature, together with model cross sections (lines) generated with $\nu_0 = 80{,}286.3\ \text{cm}^{-1}$, $f = 0.00629$, $\Gamma_0 = 1.7\ \text{cm}^{-1}$, $\Gamma_J = -0.0028\ \text{cm}^{-1}$, $q_O = 41$, $q_J = 1.9 \times 10^{-4}$. The room temperature spectrum was taken in the second order (0.04 Å FWHM).

In Fig. 2, we present measured effective cross sections for the longest band of $^{18}O_2$ at 295 and 79 K, together with model cross sections calculated with a fixed set of parameters ($\nu_0 = 80{,}286.3\ \text{cm}^{-1}$, $f = 0.00629$, $\Gamma_0 = 1.7\ \text{cm}^{-1}$, $\Gamma_J = -0.0028\ \text{cm}^{-1}$, $q_0 = 41$, $q_J = 1.9 \times 10^{-4}$). The observed cross sections are resolution dependent. The room temperature measurements were taken in the second order (0.04 Å FWHM), while the liquid nitrogen temperature results were taken in the first order (0.06 Å FWHM).

Although the general characteristics of the $^{18}O_2$ cross sections are similar to those for $^{16}O_2$, there are three obvious differences. Firstly, the rotational structure seen in Ogawa's plate[16] is also seen in our cross sections; secondly, the observed asymmetry is smaller than, and in the opposite sense to, that observed in $^{16}O_2$; thirdly, the Fano minimum appears on the long wavelength side (~1247 Å), compared with the short wavelength side (~1241 Å) for $^{16}O_2$. Detailed first order cross sections near the minimum are given in Fig. 3. Part of the forbidden $^NP_{13}$ branch also occurs in this region.

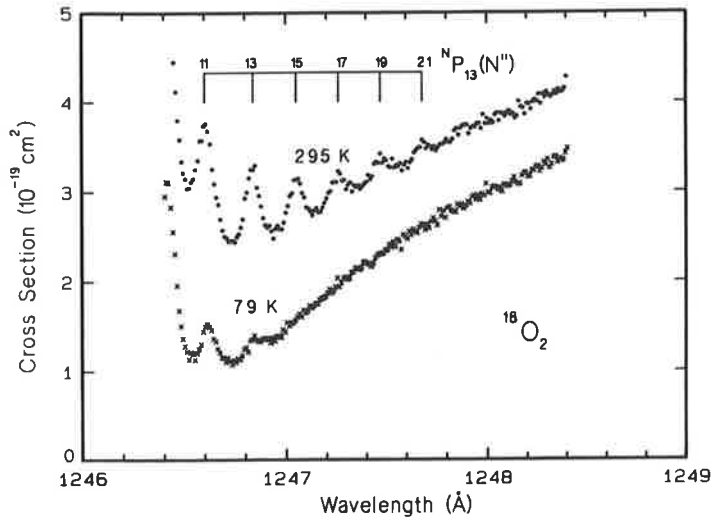

Fig. 3. Measured photoabsorption cross sections near the Fano minimum for $^{18}O_2$ at room and liquid nitrogen temperature. Individual rotational lines from the forbidden $^NP_{13}$ branch are indicated.

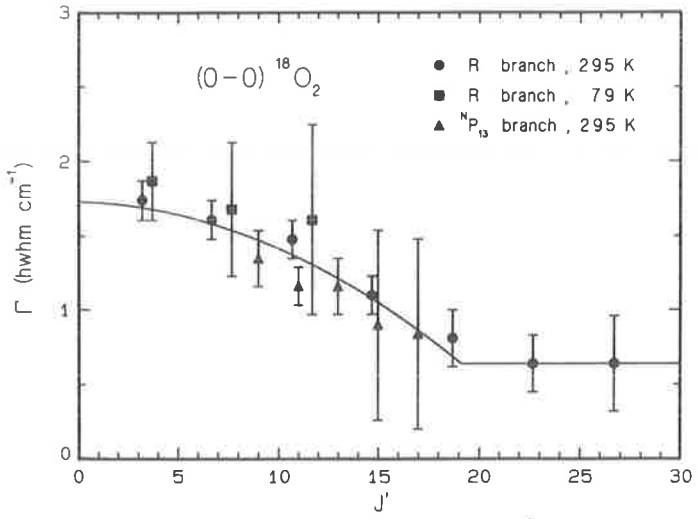

Fig. 4. Rotational linewidths for the longest band of $^{18}O_2$, obtained from the R branch structure at room and liquid nitrogen temperature, and the forbidden $^NP_{13}$ branch at room temperature. The solid line indicates the fitted model rotational linewidth.

The model cross sections generated with the single set of parameters listed previously are in good agreement with the measurements except in the more distant wings. More direct evidence of the variation of linewidth with rotation is obtainable in the case of $^{18}O_2$. The linewidths in Fig. 4 were obtained by fitting individually to small regions of rotational structure in the R branch, and by deconvoluting the instrument function from first and second order spectra of the $^NP_{13}$ branch. The lines of the $^NP_{13}$ branch are single, and are broader than even the first order instrument function. The solid line in Fig. 4 represents the model width function assumed for the longest band of $^{18}O_2$. The previous functional form, Eq. (3), is used for $J' \leqslant 19$, and the width is held constant for $J' \geqslant 19$. Widths which are significantly less than the instrumental width are difficult to determine accurately, and thus those for $J' \geqslant 19$ have a large relative uncertainty. Nevertheless, it is clear that the linewidth decreases strongly with rotation for $^{18}O_2$, opposite behaviour to that deduced for $^{16}O_2$.

Because of the smaller asymmetries for $^{18}O_2$, the values deduced for q are less accurate than those for $^{16}O_2$ but, using the method described previously, we have ascertained that the rotational asymmetry decreases with rotation for $^{18}O_2$, once again opposite behaviour to that observed for $^{16}O_2$.

It is clear from Fig. 2 that the model overestimates the cross section in the short wavelength wing and underestimates the cross section in the long wavelength wing. The structures near 1238 and 1253 Å are forbidden bands, which we shall ignore for the purposes of this discussion. It is possible to optimize the fit for each wing separately, but the corresponding best values of q exhibit a small systematic difference. This may be interpreted as a breakdown of the applicability in the wings of a Fano lineshape which assumes energy-independent q, Γ, and continuum. It should be noted that, in the case of the wings for $^{18}O_2$ at $\pm \sim 5$ Å from band centre, the dimensionless energy parameter $\epsilon \approx 200$, while for $^{16}O_2$ $\epsilon \approx 60$.

We could not find a single set of parameters which resulted in model cross sections in agreement with the observed room and liquid nitrogen temperature cross sections at the minimum near 1247 Å, but we could obtain the correct relative behaviour at a level of cross section less than that observed. This suggests that there may be a non-negligible contribution to the cross section in this region from another state, the $^3\Pi_u$ valence state, for example.

In Fig. 5, we present measured cross sections for the longest band of $^{16}O^{18}O$ at 295 and 79 K, together with model cross sections calculated with a fixed set of parameters ($\nu_0 = 80{,}334.4\,\text{cm}^{-1}$, $f = 0.00611$, $\Gamma_0 = 0.90\,\text{cm}^{-1}$, $\Gamma_J = 0.0064\,\text{cm}^{-1}$, $q_O = -45$, $q_J = 6.1 \times 10^{-5}$). The data have been obtained from raw cross sections for the 53% ^{18}O mixture, corrected for the previously determined contributions of $^{16}O_2$ and $^{18}O_2$. As a result, the reduced cross sections are less accurate in some

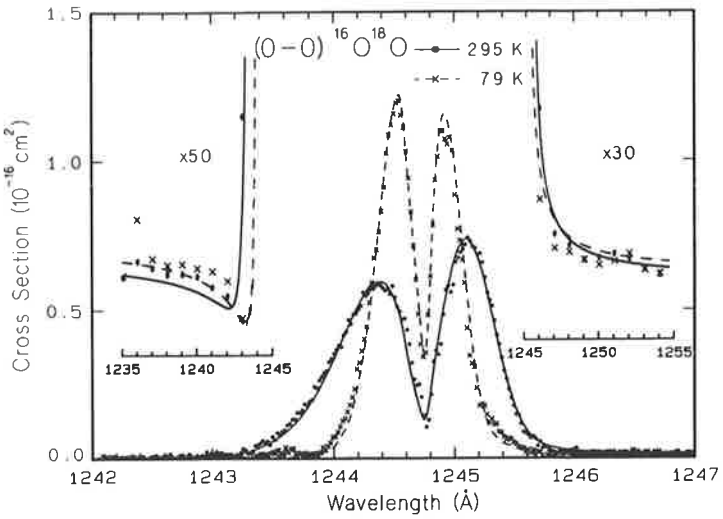

Fig. 5. Measured photoabsorption cross sections for the longest band of $^{16}O^{18}O$ at room and liquid nitrogen temperature, together with model cross sections (lines) generated with $\nu_0 = 80{,}334.4\,\text{cm}^{-1}$, $f = 0.00611$, $\Gamma_0 = 0.90\,\text{cm}^{-1}$, $\Gamma_J = 0.0064\,\text{cm}^{-1}$, $q_O = -45$, $q_J = 6.1 \times 10^{-5}$.

wavelength regions than those for the homonuclear molecules, and weak artefacts can appear due to uncertainties in wavelength registrations and isotopic abundances.

There is no rotational structure visible in the $^{16}O^{18}O$ cross sections, and the general characteristics are similar to those for $^{16}O_2$. There is a weak asymmetry, with a stronger long wavelength wing, and a weak Fano minimum near 1243 Å. The depth of the cross section minimum between the R and P branches is greater for $^{16}O^{18}O$ than for either of the homonuclear molecules. This implies that the rotational linewidth for $^{16}O^{18}O$, at least near the band head, is smaller than that for $^{16}O_2$ and $^{18}O_2$. Rotational structure is not seen in the cross section because, due to the occurrence of even, as well as odd rotational levels in the ground state, there are twice as many rotational lines in the spectrum of $^{16}O^{18}O$ as there are for $^{16}O_2$ or $^{18}O_2$, with a correspondingly closer line spacing. We could not detect rotational structure, even in a second order scan, but such a structure should be readily observable near the band head with a higher resolution experiment.

The model cross sections generated with the single set of parameters are in quite good agreement with the measured cross sections except in the more distant wings, as observed for $^{18}O_2$. We find that the rotational linewidth increases with rotation, but the values of Γ_O and Γ_J are quite uncertain, both because most rotational linewidths are significantly less than the instrumental width, and because of the poorer quality data for $^{16}O^{18}O$. The model overestimates the cross section of the stronger wing, and underestimates that of the weaker wing, just as we observe for $^{18}O_2$. The dimensionless energy parameter $\pm \sim 5$ Å from band centre is $\epsilon = 360$ for $^{16}O^{18}O$.

In Fig. 6, we present the measured cross section in the region of the (0–1) band of $^{16}O_2$ at 295 K, together with the measurements of Ogawa and Ogawa.[4] We fitted a cubic polynomial to the background cross section and subtracted this from the data in order to estimate the contribution due to the (0–1) band alone. This result is given also in Fig. 6, together with a model prediction based on the parameters given earlier for $^{16}O_2$, with the exception that the oscillator strength $f = 0.0112$. The agreement is seen to be excellent. The asymmetry parameter q for the (0–1) band may be different from that for the (0–0) band, but it is not possible to obtain a significant value of q by fitting to the (0–1) data since it is difficult to separate the background cross section from the (0–1) band wings. In any case, the difference does not appear to be great.

In Fig. 7, we present measured total and reduced first order cross sections in the region of the (0–1) band of $^{18}O_2$ at 295 K, together with a model prediction using the parameters given previously for $^{18}O_2$, but with an oscillator strength $f = 0.0112$. This spectral region is complicated by the adjacent (2–0) band of the forbidden $\beta^3\Sigma_u^+ - X^3\Sigma_g^-$ transition, but we were able to determine the oscillator strength by fitting to the P branch only. The degree of structure in the R branch is well predicted by the model.

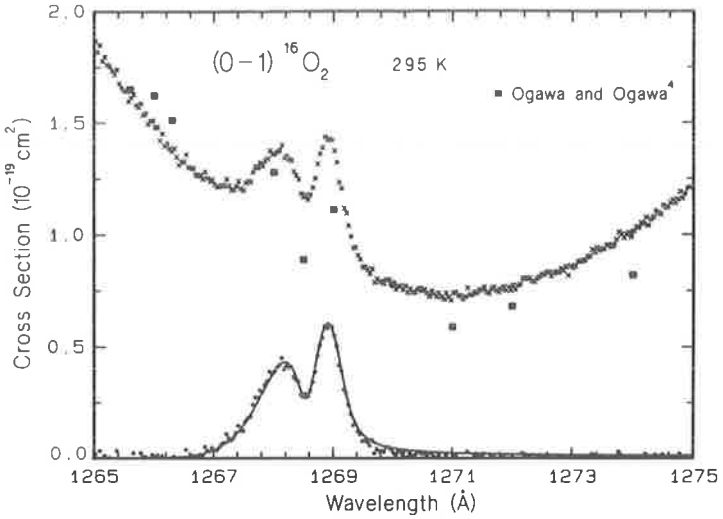

Fig. 6. Measured room temperature photoabsorption cross section near the (0–1) band of $^{16}O_2$, together with the measurements of Ogawa and Ogawa.[4] The cross section obtained by subtracting the background is also shown, together with a model cross section (line) generated with the parameters of Fig. 1, but with $f = 0.0112$.

For completeness, we present in Fig. 8 total and reduced cross sections in the region of the (0–1) band of $^{16}O^{18}O$ at 295 K, together with a model prediction based on the parameters given previously for $^{16}O^{18}O$, but with an oscillator strength $f = 0.0105$. The necessity to subtract the contributions of the homonuclear molecules, as well as the continuum, from the raw data, leads to a quite scattered reduced cross section, but the agreement between the measurements and the model is good. In particular, the cross section minimum between the P and R branches is deeper than for either of the other isotopes.

Figure 9 summarizes the rotational widths obtained from the model fits to the measurements of this work. The experimental points were obtained by fitting a constant width to the strongest parts of the (0–0) bands for $^{16}O_2$ and $^{16}O^{18}O$ at 295 and 79 K. The corresponding effective values of rotation ($\sim$5 at 79 K, $\sim$10 at 295 K) were deduced by model simulations. The experimental points are consistent with the model widths based on the chosen functional form, Eq. (3). Individual widths for $^{18}O_2$ are given in Fig. 4.

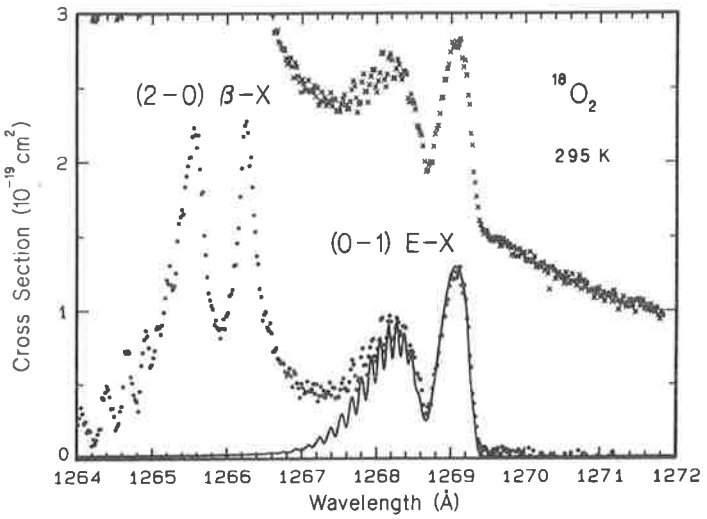

Fig. 7. Measured room temperature photoabsorption cross section near the (0–1) band of $^{18}O_2$. The background-subtracted cross section includes the (2–0) band of the $\beta^3\Sigma_u^+ - X^3\Sigma_g^-$ transition and is compared with a model cross section (line) generated with the parameters of Fig. 2, but with $f = 0.0112$.

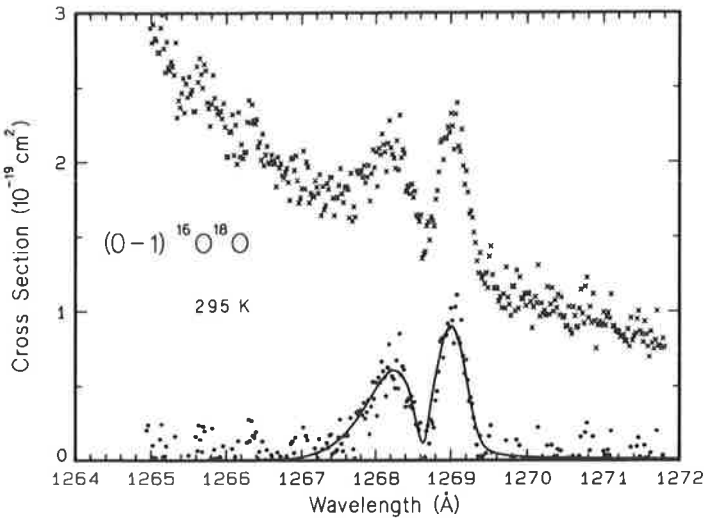

Fig. 8. Measured room temperature photoabsorption cross section near the (0–1) band of $^{16}O^{18}O$. The background-subtracted cross section is compared with a model cross section (line) generated with the parameters of Fig. 5, but with $f = 0.0105$.

Figure 10 summarizes the limited amount of data on the variation with rotation of the asymmetry parameter q. In this case, the experimental points are the only data available. Except in the case of $^{16}O_2$, where it is possible to obtain a reasonable value for q from the strong region of the band, the points in Fig. 10 result from fits to the wings. The corresponding effective values of rotation, deduced by model simulations, depend both on the actual form of the rotational dependence of q, and also on the distance of the fitting region from the band centre. Equation (4) was fitted to the experimental data to give the model parameters q_o and q_J. Because of the interaction between the chosen functional form and the effective rotations, the values of q_J are very uncertain, but the general behaviour of q with rotation is clear. The most strongly varying asymmetry occurs for $^{18}O_2$, where the narrowest lines are nearly symmetric. The systematic difference between q values obtained from the Fano minimum region and the stronger wing, for both $^{18}O_2$ and $^{16}O^{18}O$, is clear in Fig. 10. The relative behaviour with rotation, however, is similar for each region.

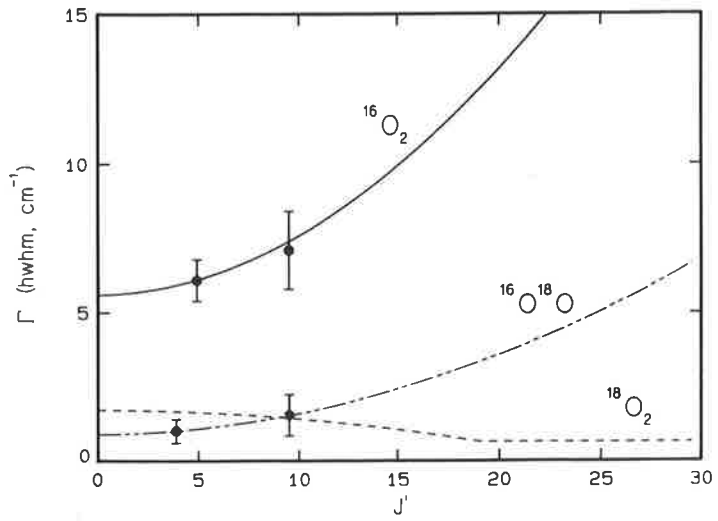

Fig. 9. A summary of rotational widths for the longest band of isotopic O_2. The lines represent the best model fits to the measurements, with $\Gamma(J') = \Gamma_o + \Gamma_J J'(J'+1)$, while the points are effective widths fitted to the 79 and 295 K measurements, with $\Gamma(J') =$ constant. The full data for $^{18}O_2$ are given in Fig. 4.

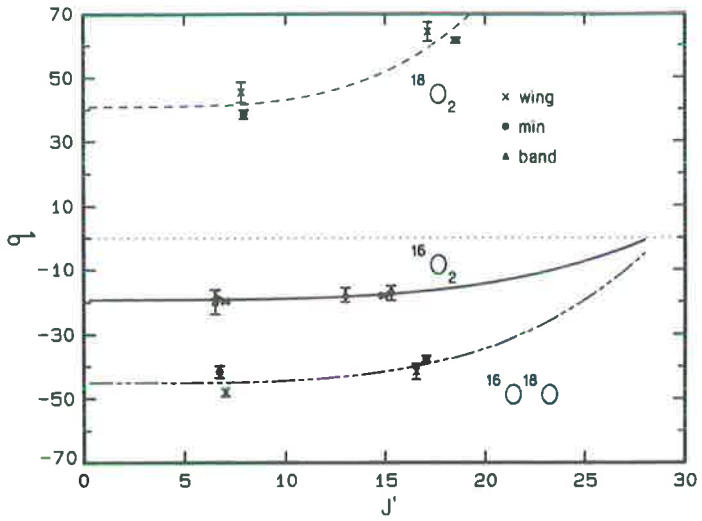

Fig. 10. A summary of rotational asymmetries for the longest band of isotopic O_2. The points are effective values of q fitted to 79 and 295 K cross sections near the band centre, the strong wing, or the Fano minimum, with $q(J') = \text{constant}$. The lines are best values of the function $q(J') = q_0 + q_J[J'(J'+1)]^2$ fitted to the data points.

From Figs. 9 and 10, we see that Γ and q vary with rotation in an inverse fashion, and, indeed, the product $|q|\Gamma^{0.5} \approx 50\,\text{cm}^{-0.5}$, within experimental error, independent of isotopic mass or rotation. This type of behaviour is to be expected if a Fano profile with energy-independent parameters is applicable. From Fig. 10 the maximum variation in the effective value of q across the resonance is only $\sim 15\%$.

In Table 1, we have summarized the spectroscopic constants, oscillator strengths, widths, and asymmetries obtained from our measurements of the (0–0) and (0–1) bands of the isotopes $^{16}O_2$, $^{16}O^{18}O$ and $^{18}O_2$. Using the tabulated parameters together with our model, it is possible to generate accurately the (0–0) and (0–1) cross sections for all isotopes to a distance of several Å from the band centres. Our measured oscillator strengths show no significant isotope effect for either the (0–0) or (0–1) bands, but the (0–1) oscillator strength is nearly twice that of the (0–0) band. The only previous measurement of oscillator strength for these bands is from the electron energy loss

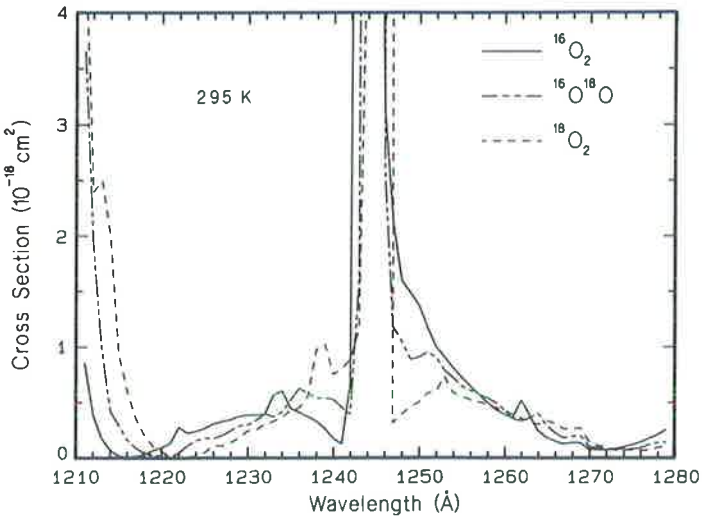

Fig. 11. Measured room temperature photoabsorption cross sections for isotopic O_2 in the range 1210–1280 Å, emphasizing the isotopic shifts, the Fano minima, and the oscillatory behaviour of the continuum.

Table 1. A summary of the results of this work. Band origins, widths, asymmetries, and oscillator strengths which include error estimates have been determined by fitting an empirical model to the measured cross sections. Values refer to the (0–0) band of the $E^3\Sigma_u^- - X^3\Sigma_g^-$ transition unless otherwise indicated. Other spectroscopic constants for the upper level of this transition are also given. Units are cm^{-1}, except for q_O, q_J, and f, which are dimensionless.

	$^{16}O_2$	$^{16}O^{18}O$	$^{18}O_2$
ν_o	80382.8±1.0	80334.4±1.5	80286.3†
B'	1.4701‡	1.3838‡	1.3072†
D'	1.93×10^{-6}§	1.66×10^{-6}§	1.47×10^{-6}§
λ'	-3.3725†	-3.3725†	-3.3725†
μ'	0.045†	0.045†	0.045†
Γ_0	5.6±0.4	0.9±0.4	1.7±0.2
Γ_J	$(1.8\pm0.3)\times10^{-2}$	$(6.4\pm2.6)\times10^{-3}$	$-(2.8\pm0.3)\times10^{-3}$
q_o	-19.2±1.0	-45±8	41±4
q_J	$(2.8\pm0.8)\times10^{-5}$	$(6.1\pm3.0)\times10^{-5}$	$(1.9\pm0.7)\times10^{-4}$
$f(0-0)$	$(6.25\pm0.08)\times10^{-3}$	$(6.11\pm0.16)\times10^{-3}$	$(6.29\pm0.08)\times10^{-3}$
$f(0-1)$	$(11.2\pm0.5)\times10^{-3}$	$(10.5\pm0.8)\times10^{-3}$	$(11.2\pm0.5)\times10^{-3}$

† Measurements of Ogawa.[16] Zero isotope effect is assumed for λ', μ'.

‡ Calculations of Wang,[43] normalized to B' for $^{18}O_2$. (Close to values obtained by applying an isotope correction[44] to the measured B' for $^{18}O_2$.)

§ Calculated from B' for $^{18}O_2$ and aproximate value for ω_e, with appropriate isotope correction.[44] Measured $D'=1.8\times10^{-6}$ for $^{18}O_2$.[16]

measurements of Huebner et al,[21] who obtained the value 0.010 for the oscillator strength of the longest band of $^{16}O_2$. The optical values are to be preferred.

Room temperature cross sections measured at 1 Å intervals for the three isotopes are presented in Fig. 11 from 1210 to 1280 Å. The Fano minima are apparent in each case, but it is clear that a simple Fano profile model is not consistent with the observed peaked continuum between ~1220 and 1270 Å. Distorted Fano profiles which allow for the energy dependences of Γ, q and the continuum, such as those discussed by Bandrauk and Laplante,[47,48] will be needed in order to explain the more distant wings of the resonance, and adjacent resonances, such as the (1–0) band, will have to be considered, but we will not pursue these aspects here. A theoretical intepretation of the spectrum in this region, using coupled Schrödinger equations, will be given in an associate work.[13]

CONCLUSIONS

We have presented the most detailed photoabsorption cross section measurements available for the (0–0) and (0–1) bands of the $E^3\Sigma_u^- - X^3\Sigma_g^-$ transition of $^{16}O_2$, and the first such measurements

for $^{18}O_2$ and $^{16}O^{18}O$. The bands exhibit significant broadening and asymmetry, strongly dependent on isotopic mass, due to configuration interaction. An empirical band model, based on Beutler–Fano lineshapes, is capable of accurate cross section prediction out to several Å from the band centres, including minima observed in the wings of the longest band for all isotopes.

Although the resonance phenomenon arising from interacting molecular states is quite general, asymmetric Fano profiles in molecular photodissociation have been observed previously only for H_2 in absorption,[49–53] and OD in emission.[54,55] Berkowitz[37] notes this paradox and discusses some possible explanations. It is clear from our work that the longest band of O_2 provides a second classical example of a Beutler–Fano resonance due to predissociation in photoabsorption. The rotationally smeared Fano minimum of the band falls fortuitously in a region of the spectrum which allows ready observation.

With the aid of our empirical model, we have obtained band origins, oscillator strengths, rotational linewidths and asymmetries. Our measurements provide the first optical oscillator strengths for these bands. We find no isotope effect, and our oscillator strength for the longest band of $^{16}O_2$ is significantly less than the electron-impact value.[21] Directly, in the case of $^{18}O_2$, and from the model otherwise, we find that linewidth changes strongly with rotation, and that the asymmetry parameter changes in an inverse fashion such that $|q|\Gamma^{0.5} \approx 50\,\mathrm{cm}^{-0.5}$, almost independent of isotopic mass or rotation. The (1–0) and (2–0) bands of the $E^3\Sigma_u^- - X^3\Sigma_g^-$ transition will be discussed in a future work.[12]

Acknowledgements—The authors would like to thank C. Dedman and K. Lonsdale for valuable technical assistance. We are also grateful to A. Dalgarno, A. Blake, D. McCoy, L. Torop, and J. Wang for illuminating discussions on resonances in molecular photodissociation.

REFERENCES

1. K. Watanabe, E. C. Y. Inn, and M. Zelikoff, *J. Chem. Phys.* **21,** 1026 (1953).
2. K. Watanabe, *Advances in Geophysics*, Vol. 5, p. 153, Academic Press, New York, NY (1958).
3. P. H. Metzger and G. R. Cook, *JQSRT* **4,** 107 (1969).
4. S. Ogawa and M. Ogawa, *Can. J. Phys.* **53,** 1845 (1975).
5. M. Ogawa, *J. Geophys. Res.* **73,** 6759 (1968).
6. M. Ogawa and K. R. Yamawaki, *Appl. Opt.* **9,** 1709 (1970).
7. V. Dose, U. Schmocker, and G. Sele, *Z. Phys.* **A274,** 1 (1975).
8. J. H. Carver, H. P. Gies, T. I. Hobbs, B. R. Lewis, and D. G. McCoy, *J. Geophys. Res.* **82,** 1955 (1977).
9. B. R. Lewis, I. M. Vardavas, and J. H. Carver, *J. Geophys. Res.* **88,** 4935 (1983).
10. D. Kley, *J. Atmos. Chem.* **2,** 203 (1984).
11. W. C. Price and G. Collins, *Phys. Rev.* **48,** 714 (1938).
12. B. R. Lewis, S. T. Gibson, and J. H. Carver, *JQSRT*, in press (1988).
13. J. Wang, A. J. Blake, D. G. McCoy, and L. Torop, *JQSRT*, in press (1988).
14. Y. Tanaka, *J. Chem. Phys.* **20,** 1728 (1952).
15. M. Ogawa, K. R. Yamawaki, A. Hashizume, and Y. Tanaka, *J. Molec. Spectrosc.* **55,** 425 (1975).
16. M. Ogawa, *Can. J. Phys.* **53,** 2703 (1975).
17. R. J. Buenker and S. D. Peyerimhoff, *Chem. Phys.* **8,** 324 (1975).
18. R. J. Buenker and S. D. Peyerimhoff, *Chem. Phys. Lett.* **34,** 225 (1975).
19. R. J. Buenker and S. D. Peyerimhoff, *Chem. Phys. Lett.* **36,** 415 (1975).
20. M. Yoshimine, *J. Chem. Phys.* **64,** 2254 (1976).
21. R. H. Huebner, R. J. Celotta, S. R. Mielczarek, and C. E. Kuyatt, *J. Chem. Phys.* **63,** 241 (1975).
22. D. H. Katayama, S. Ogawa, M. Ogawa, and Y. Tanaka, *J. Chem. Phys.* **67,** 2132 (1977).
23. G. Black, R. L. Sharpless, T. G. Slanger, and M. R. Taherian, *Chem. Phys. Lett.* **113,** 311 (1985).
24. U. Fano, *Phys. Rev.* **124,** 1866 (1961).
25. R. Cimiraglia, M. Persico, and J. Tomasi, *Chem. Phys.* **42,** 297 (1979).
26. E. F. van Dishoeck, M. C. van Hemert, A. C. Allison, and A. Dalgarno, *J. Chem. Phys.* **81,** 5709 (1984).
27. L. Torop, D. G. McCoy, A. J. Blake, J. Wang, and T. Scholz, *JQSRT* **38,** 9 (1987).
28. J. Wang, D. G. McCoy, A. J. Blake, and L. Torop, *JQSRT* **38,** 19 (1987).
29. B. R. Lewis, L. Berzins, J. H. Carver, and S. T. Gibson, *JQSRT* **36,** 209 (1986).
30. B. R. Lewis, L. Berzins, J. H. Carver, S. T. Gibson, and D. G. McCoy, *JQSRT* **34,** 405 (1985).
31. B. R. Lewis, L. Berzins, J. H. Carver, and S. T. Gibson, *JQSRT* **36,** 187 (1986).
32. B. R. Lewis, L. Berzins, and J. H. Carver, *JQSRT* **37,** 219 (1987).
33. B. R. Lewis, L. Berzins, and J. H. Carver, *JQSRT* **37,** 243 (1987).
34. B. R. Lewis, L. Berzins, and J. H. Carver, *JQSRT* **37,** 255 (1987).
35. B. R. Lewis, L. Berzins, and J. H. Carver, *JQSRT* **37,** 229 (1987).
36. B. R. Lewis, L. Berzins, J. H. Carver, and S. T. Gibson, *JQSRT* **33,** 627 (1985).

37. J. Berkowitz, *Photoabsorption, Photoionization, and Photoelectron Spectroscopy*, Academic Press, New York, NY (1979).
38. B. R. Lewis, *Appl. Opt.* **22,** 1546 (1983).
39. S. T. Gibson, H. P. Gies, A. J. Blake, D. G. McCoy, and P. J. Rogers, *JQSRT* **30,** 385 (1983).
40. L. Veseth and A. Lofthus, *Molec. Phys.* **27,** 511 (1974).
41. W. Steinbach and W. Gordy, *Phys. Rev.* **A8,** 1753 (1973).
42. W. Steinbach and W. Gordy, *Phys. Rev.* **A11,** 729 (1975).
43. J. Wang, private communication (1987).
44. G. Herzberg, *Molecular Spectra and Molecular Structure, I. Spectra of Diatomic Molecules*, Van Nostrand–Reinhold, New York, NY (1950).
45. J. B. Tatum, and J. K. G. Watson, *Can. J. Phys.* **49,** 2693 (1971).
46. P. S. Julienne, *J. Molec. Spectrosc.* **63,** 60 (1976).
47. A. D. Bandrauk and J. P. Laplante, *J. Chem. Phys.* **65,** 2602 (1976).
48. A. D. Bandrauk and J. P. Laplante, *J. Chem. Phys.* **65,** 2592 (1976).
49. G. Herzberg, *Topics in Modern Physics—A Tribute to Edward U. Condon*, p. 191, Colorado Associated University, Boulder, CO (1971).
50. F. J. Comes and G. Schumpe, *Z. Naturforsch.* **26,** 538 (1971).
51. M. Rothschild, H. Egger, R. T. Hawkins, H. Plummer, and C. K. Rhodes, *Chem. Phys. Lett.* **72,** 404 (1980).
52. M. Rothschild, H. Egger, R. T. Hawkins, J. Bokor, H. Plummer, and C. K. Rhodes, *Phys. Rev.* **A23,** 206 (1981).
53. M. Glass-Maujean, J. Breton, and P. M. Guyon, *Chem. Phys. Lett.* **63,** 591 (1979).
54. C. Carlone, *Phys. Rev.* **A9,** 606 (1974).
55. C. Carlone, *Phys. Rev.* **A12,** 2464 (1975).

4.13 Resonances in the photodissociation of isotopic molecular oxygen: II. The second and third bands

[31] B. R. Lewis, S. T. Gibson, M. Emami, and J. H. Carver,
Journal of Quantitative Spectroscopy and Radiative Transfer **40**, 469–477 (1988).

J. Quant. Spectrosc. Radiat. Transfer Vol. 40, No. 4, pp. 469–477, 1988
Printed in Great Britain.

0022-4073/88 $3.00 + 0.00

RESONANCES IN THE PHOTODISSOCIATION OF ISOTOPIC MOLECULAR OXYGEN—II. THE SECOND AND THIRD BANDS

B. R. LEWIS, S. T. GIBSON, M. EMAMI,† and J. H. CARVER
Research School of Physical Sciences, The Australian National University, Canberra, Australia 2600

(*Received* 13 *April* 1988)

Abstract—We present detailed photoabsorption cross-section measurements for the (1–0) and (2–0) bands of the $E^3\Sigma_u^- - X^3\Sigma_g^-$ transition of molecular oxygen. The isotopic molecules $^{16}O_2$, $^{16}O^{18}O$ and $^{18}O_2$ were studied at 79 and 295 K, with an instrumental resolution of 0.06 Å FWHM. We find that the bands are further examples of Beutler–Fano resonances in molecular photodissociation.

INTRODUCTION

The photoabsorption spectrum of $^{16}O_2$ from 1165 to 1320 Å is dominated by Tanaka's progression I,[1] consisting of strong, diffuse bands at 1244 Å (longest), 1206 Å (second), and 1172 Å (third). These are the (0–0), (1–0) and (2–0) transitions from the ground state to the mixed valence–Rydberg $E^3\Sigma_u^-$ state (labelled B' by some authors[2,3]). A weak band at 1269 Å is the (0–1) band of the same progression.

In an earlier work,[4] hereafter referred to as I, we reviewed previous experimental and theoretical studies of the $E^3\Sigma_u^- - X^3\Sigma_g^-$ transition, and presented detailed photoabsorption cross section measurements for the (0–0) and (0–1) bands of the molecules $^{16}O_2$, $^{16}O^{18}O$ and $^{18}O_2$. These bands exhibit significant broadening and asymmetry, strongly dependent on isotopic mass, due to configuration interaction with the continuum of the $B^3\Sigma_u^- - X^3\Sigma_g^-$ transition. We found that an empirical band model, based on Beutler–Fano lineshapes, was capable of accurate cross section prediction out to several Å from the band centres, including minima observed in the wings of the (0–0) band for all isotopes. It was clear that the longest band of O_2 was a rare example of a Beutler–Fano resonance due to predissociation in photoabsorption.

At large distances from the band centre, there is some evidence from I that the model cross sections deviate from the measurements due to the effects of neighbouring resonances and the energy-dependences of the Fano parameters. A more complete theoretical description is required. Potential energy curves for the $E^3\Sigma_u^-$ and $B^3\Sigma_u^-$ states undergo an avoided crossing in accordance with the adiabatic non-crossing rule,[5–8] and coupling of the two excited states by the radial component of the nuclear kinetic energy operator is expected to be large in the avoided-crossing region, leading to significant non-adiabatic effects on the molecular energy eigenstates and the corresponding photoabsorption.[9] Resonances due to absorption into mixed states can be treated theoretically by solving the coupled Schrödinger equations. This method has been applied to coupled $^2\Pi$ states in OH by van Dishoeck et al,[10] who noted that individual resonances were well described by Beutler–Fano profiles. Torop et al[9] have developed a similar treatment which has been applied by Wang et al[11] to an interpretation of the temperature dependence of the O_2 photoabsorption cross section in the region 1300–1600 Å.

Wang et al,[12] using the diabatic form of the coupled equations given by Torop et al,[9] recently calculated photoabsorption cross sections for O_2 in the region of the longest band. Using an iterative procedure, they[12] found potential curves for the Rydberg and valence states which mix to form the $B^3\Sigma_u^-$ and $E^3\Sigma_u^-$ states, and a value of 0.469 eV for the diabatic electronic coupling constant, by fitting their calculations to the experimental cross sections of I. The anomalous isotope shift for the longest band and the observed[4] variations in width and asymmetry with rotation were

†Permanent address: Department of Physics, College of Arts and Science, Shiraz University, Iran.

predicted correctly by the coupled-equations model. The complex variations in linewidth and line profile for each isotopic form of the molecule were reproduced correctly by calculations with a single set of potentials, and a single coupling constant, changing only the reduced mass of the molecule. The coupled-equations model, however, underestimates the cross section in the region of the minimum near 1247 Å for $^{18}O_2$, and it was in just this region that our empirical band model[4] failed to fit the experimental cross sections at 79 and 295 K with a single set of parameters. Similar conclusions were reached in both papers,[4,12] namely that a weak, underlying continuum due to another state contributes to the cross section near 1247 Å.

It is clear that the experimental cross sections of I, together with widths and asymmetries obtained from our empirical band model,[4] provide significant data against which the coupled-equations calculations may be tested. It is also seen from the work of Wang et al[12] that almost all of the observed absorption in the region of the longest band may be attributed to transitions into the coupled $^3\Sigma_u^-$ states. The sensitivity of the calculations to the precise form of the potential curves and strength of the coupling is such that it is unlikely that realistic cross sections can be produced by *ab initio* calculations without reference to experimental data.[12] In this work we extend the cross section measurements of I to the (1–0) and (2–0) bands and examine whether an empirical band model, based on Beutler–Fano lineshapes, is consistent with the measurements. Comparison between the experimental cross sections and the results of coupled-equations calculations will enable the refinement of the potential energy curves of Wang et al[12] to higher energies. The most comprehensive previous cross section measurements for the (1–0) and (2–0) bands of $^{16}O_2$ are those of Ogawa and Ogawa,[13] but they are of insufficient detail for an accurate determination of the theoretical parameters.[14] Cross sections for $^{16}O^{18}O$ and $^{18}O_2$ have not been measured previously.

EXPERIMENTAL METHOD

The apparatus and experimental technique were discussed in detail in I. Briefly, background radiation from a pulsed discharge in argon was dispersed by a 2.2 m scanning monochromator[15] operating in the first order with a FWHM resolution of $\sim$0.06 Å. Radiation was detected photoelectrically before entering and after leaving the 10 cm, controlled-temperature absorption cell.

We studied three gas samples, 99.8% ^{16}O, 53% ^{18}O, 99% ^{18}O, with cell temperatures of 295 and 79 K, and with wavelength increments of 50–160 mÅ, depending on the scale of the structure in the cross section. Cell pressures were in the range 0.04–30 torr. Statistical errors in the resultant photoabsorption cross sections were normally $\leqslant$2%, with an extra $\sim$2% uncertainty due to uncertainties in cell length, pressure and temperature. Additional uncertainties arose in the case of the 79 K measurements because of increased temperature measurement error and increased empty-cell transmission drifts. Cross sections for $^{16}O^{18}O$ were deduced from measured total cross sections of the 53% ^{18}O sample by performing a weighted subtraction using the known isotopic enrichments and the previously-measured cross sections for the nearly pure $^{16}O_2$ and $^{18}O_2$ samples. This procedure increased the relative uncertainty in the $^{16}O^{18}O$ cross section, dramatically in some wavelength regions.

EMPIRICAL MODEL

Most of the $E^3\Sigma_u^- - X^3\Sigma_u^-$ bands are diffuse, but, remarkably, the occurrence[4,16,17] of rotational and fine structure in the longest band of $^{18}O_2$ enables the development of an empirical band model from which it is possible to obtain some information on the behaviour of linewidths and asymmetries, even for the diffuse bands. The details of the empirical band model were discussed in I.

Band origins for $v' = 1, 2$ were obtained by fitting the model absorption spectrum to our measurements. Rotational constants B' were obtained from preliminary calculations of Wang,[18] normalized to the measurements of Ogawa[17] for the longest band of $^{18}O_2$. Centrifugal distortion constants D' were calculated from the rotational constants for $^{18}O_2$ and an approximate value for ω_e', with appropriate isotope correction.[19] The splitting constants λ and μ were taken as the values

measured by Ogawa[17] for $v' = 0$, $^{18}O_2$ for all bands of all isotopic molecules. Ground state spectroscopic constants and Hönl–London factors for the $^3\Sigma^- - ^3\Sigma^-$ transition were given in I.

For the reasons discussed previously,[4] each rotational line was described by a Fano[20] lineshape, given by

$$F(\epsilon) = (q + \epsilon)^2/(1 + \epsilon^2), \tag{1}$$

where

$$\epsilon = (\nu - \nu_0)/\Gamma, \tag{2}$$

q is an asymmetry parameter, Γ the HWHM linewidth, and ν_0 the wavenumber of the line centre. The linewidth was taken to vary systematically with rotation[4] according to the relation

$$\Gamma(J') = \Gamma_0 + \Gamma_J J'(J' + 1); \tag{3}$$

contrary to I, q was taken to be independent of rotation, since the extreme broadness of the (1–0) and (2–0) bands made it impossible to determine any variation. The model band profile was built up by adding the Fano profiles of individual lines at the positions and with the relative strengths determined by the technique described above and in I. Oscillator strengths, linewidths and asymmetry parameters were determined by least-squares fitting the model cross section, after convolution in transmission with a Gaussian instrument function, to the experimental measurements.

RESULTS AND DISCUSSION

In Fig. 1, we present measured photoabsorption cross sections for the (2–0) band of the isotopic molecules $^{16}O_2$, $^{16}O^{18}O$ and $^{18}O_2$ at 295 K, together with model cross sections. The measurements of Ogawa and Ogawa[13] for $^{16}O_2$ agree well with ours except near the band centre where they[13] significantly underestimate the true cross section. It is not possible to construct a $^3\Sigma_u^- - ^3\Sigma_g^-$ band model which is consistent with the band profile of Ogawa and Ogawa.[13]

The (2–0) band is diffuse for all molecules, but a double head, corresponding to the P and R branches, can be seen in the case of $^{18}O_2$. The width of the band increases significantly from $^{18}O_2$ to $^{16}O_2$, but there is a strong asymmetry of the same sign for all molecules, the long wavelength wing being stronger. The isotopic shift, based on peak positions, is significantly smaller from $^{16}O_2$ to $^{16}O^{18}O$ than from $^{16}O^{18}O$ to $^{18}O_2$.

Similar conclusions can be drawn from the cross sections measured at 79 K which are given in Fig. 2. At the lower temperature, the band widths become smaller and the peak cross sections larger

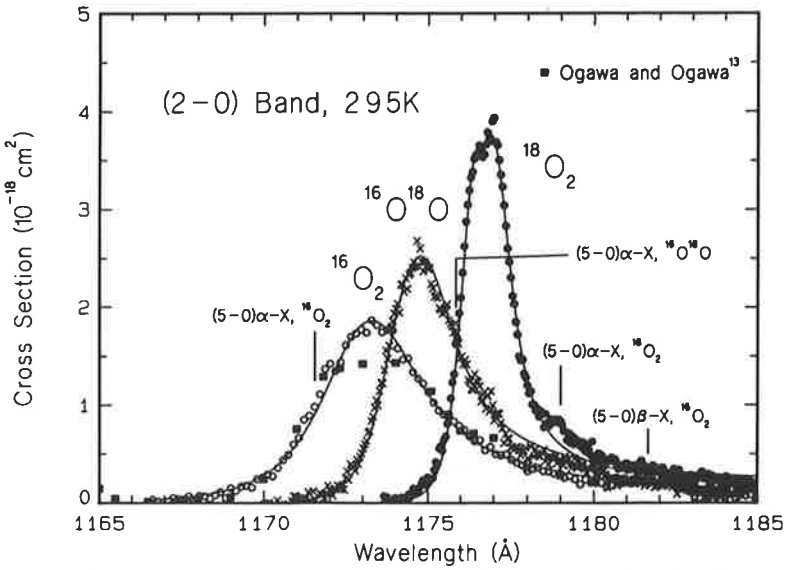

Fig. 1. Measured photoabsorption cross sections for the third bands of $^{16}O_2$, $^{16}O^{18}O$ and $^{18}O_2$ at room temperature, together with the measurements of Ogawa and Ogawa[13] for $^{16}O_2$, and model cross sections (lines) generated with the parameters given in the text.

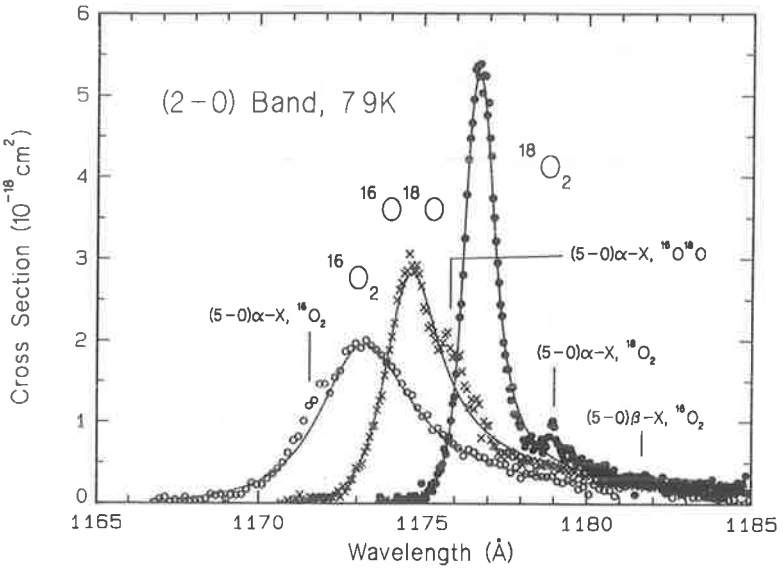

Fig. 2. Measured photoabsorption cross sections for the third bands of $^{16}O_2$, $^{16}O^{18}O$ and $^{18}O_2$ at liquid-nitrogen temperature, together with model cross sections (lines) generated with the parameters of Fig. 1.

due to restriction of the rotational structure of the band. This effect is largest for $^{18}O_2$ which has the narrowest (2–0) band, and the double head is no longer in evidence at 79 K.

Superimposed on the (2–0) band of the $E^3\Sigma_u^- - X^3\Sigma_g^-$ transition are weak structures due to the (5–0) band of the forbidden transition $\alpha\,^1\Sigma_u^+ - X^3\Sigma_g^-$, and, in the case of $^{16}O_2$, the (5-0) band of the forbidden transition $\beta^3\Sigma_u^+ - X^3\Sigma_g^-$. These forbidden bands also become more localized and more prominent at the lower temperature, but they are not of concern to us in this work. Regions where the forbidden bands occur were excluded from the empirical band model fitting procedure.

The solid curves given in Figs. 1 and 2 are model fits to the experimental cross sections based on the following parameters: for $^{16}O_2$, $\nu_0 = 85{,}245.8\ \text{cm}^{-1}$, $f = 8.3 \times 10^{-4}$, $\Gamma = 121\ \text{cm}^{-1}$, $q = -7.5$; for $^{16}O^{18}O$, $\nu_0 = 85{,}141.7\ \text{cm}^{-1}$, $f = 6.6 \times 10^{-4}$, $\Gamma = 68\ \text{cm}^{-1}$, $q = -4.6$; for $^{18}O_2$, $\nu_0 = 84{,}983.9\ \text{cm}^{-1}$, $f = 6.3 \times 10^{-4}$, $\Gamma_0 = 26\ \text{cm}^{-1}$, $\Gamma_J = 2.6 \times 10^{-4}\ \text{cm}^{-1}$, $q = -7.4$. The good agreement observed between

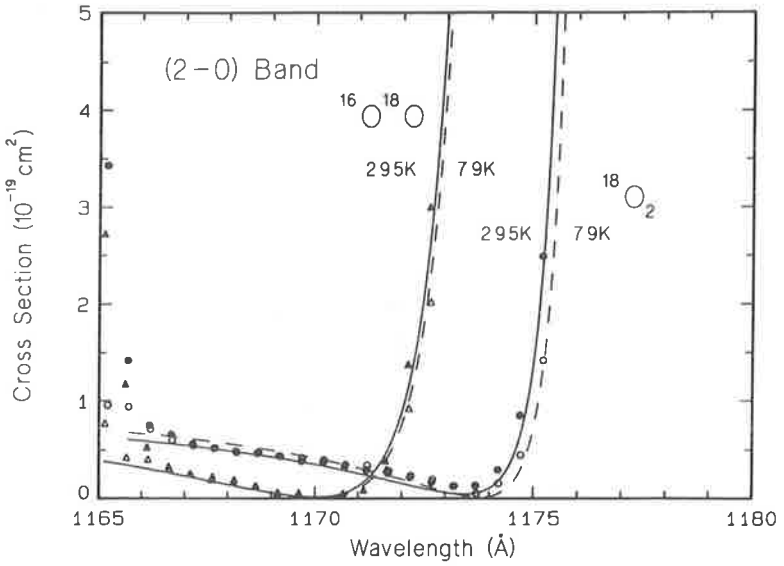

Fig. 3. Measured photoabsorption cross sections, taken at 295 and 79 K, in the region of the short-wavelength wings of the third bands of $^{18}O_2$ and $^{16}O^{18}O$, together with model cross sections (lines) generated with the parameters of Fig. 1.

the measured cross sections at both temperatures and model cross sections calculated with a single set of parameters supports the validity of the $^3\Sigma_u^- - ^3\Sigma_g^-$ band model. The narrowest linewidths for the (2–0) band are five times larger than the broadest linewidths measured in I for the longest band. This greater diffuseness makes it extremely difficult to detect any systematic variation in Γ or q with rotation. Nevertheless, as implied by the parameters listed previously, it appears that linewidths in the (2–0) band of $^{18}O_2$ increase slightly with rotation.

In Fig. 3, we present experimental cross sections in the region of the short wavelength wing of the (2–0) bands of $^{18}O_2$ and $^{16}O^{18}O$ at 79 and 295 K, together with model cross sections based on the parameters given previously. Deep cross section minima are observed near 1174 Å for $^{18}O_2$ and near 1170 Å for $^{16}O^{18}O$, despite decreased accuracy for the latter molecule. The increased cross section near 1165 Å is due to the (0–0) band of a Rydberg transition $^3\Pi_u - X^3\Sigma_g^-$ which is not heavily predissociated. The good agreement between the measured cross sections in this region, at both temperatures and model calculations based on fits performed over the band centres, is a conclusive vindication of the empirical band model. As in the case of the longest band presented in I, we have unambiguous Fano minima associated with the (2–0) bands of $^{18}O_2$ and $^{16}O^{18}O$. The third band is thus another example of a Beutler–Fano resonance in molecular photodissociation. It is impossible to detect the minimum for the (2–0) band of $^{16}O_2$, since, from Eqs. (1) and (2) and the model values of q and Γ given previously for this molecule, the minimum would be expected to occur near the centre of the strong $^3\Pi_u - X^3\Sigma_g^-$ transition mentioned earlier.

In Figs. 4 and 5, we present measured photoabsorption cross sections for the (1–0) band of the isotopic molecules $^{16}O^{18}O$ and $^{18}O_2$ at 295 and 79 K, together with model cross sections. There is little isotopic or temperature dependence of the band widths or asymmetries, and, together with the (2–0) band of $^{16}O_2$, these are the broadest of the bands studied here or in I. For both molecules, the bands appear nearly symmetric. The only irregularities visible in Figs. 4 and 5 are due to the (4–0) bands of the forbidden transitions $\alpha\,^1\Sigma_u^+ - X^3\Sigma_g^-$ and $\beta\,^3\Sigma_u^+ - X^3\Sigma_g^-$. We have not presented cross sections for the (1–0) band of $^{16}O_2$ because strong interference from the (4–0) $\beta\,^3\Sigma_u^+ - X^3\Sigma_g^-$ band makes the measured cross sections useless for the fitting of either the empirical band model or the coupled-equations calculations. The interference will be discussed in detail elsewhere.[21]

The solid curves given in Figs. 4 and 5 are model fits to the experimental cross sections based on the following parameters: for $^{18}O_2$, $\nu_0 = 82{,}786.1\ cm^{-1}$, $f = 7.9 \times 10^{-3}$, $\Gamma = 109\ cm^{-1}$, $q = \ldots 140$; for $^{16}O^{18}O$, $\nu_0 = 82{,}858.7\ cm^{-1}$, $f = 8.0 \times 10^{-3}$, $\Gamma = 106\ cm^{-1}$, $q = -60$. The forbidden bands have been excluded from the fit. Due to the extreme broadness of the (1–0) band, it is not possible to determine the dependence on rotation of any parameter, and the values of q are very uncertain

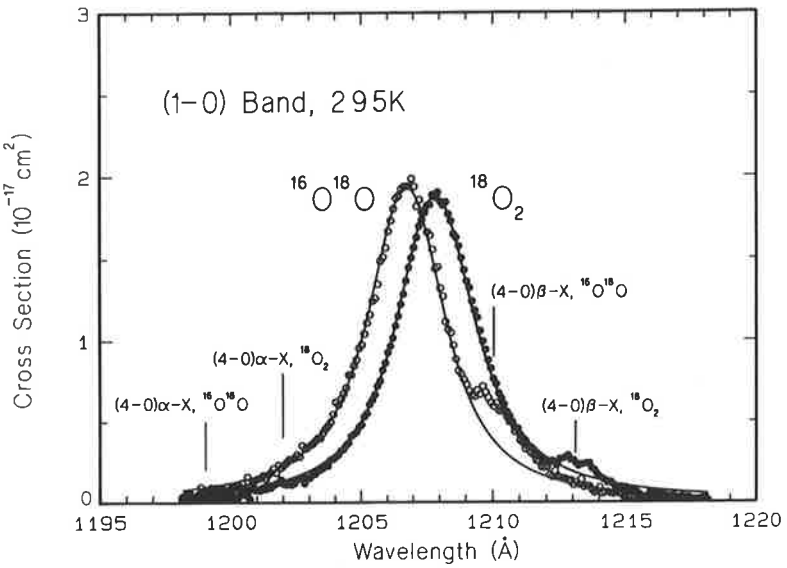

Fig. 4. Measured photoabsorption cross sections for the second bands of $^{18}O_2$ and $^{16}O^{18}O$ at room temperature, together with model cross sections (lines) generated with the parameters given in the text.

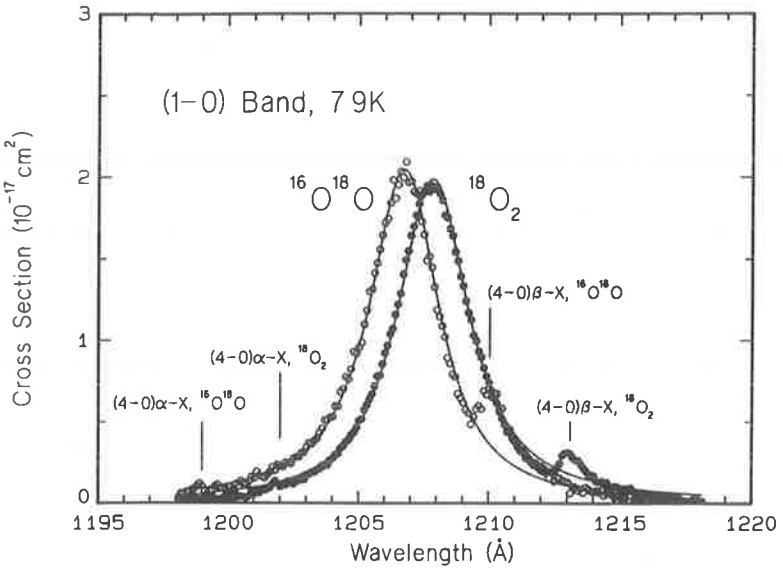

Fig. 5. Measured photoabsorption cross sections for the second bands of $^{18}O_2$ and $^{16}O^{18}O$ at liquid-nitrogen temperature, together with model cross sections (lines) generated with the parameters of Fig. 4.

because of interference from the forbidden bands, possible energy dependence of the Fano parameters, and interaction with adjacent $E^3\Sigma_u^- - X^3\Sigma_g^-$ resonances. No Fano minima are visible for the (1–0) band for reasons similar to those mentioned previously for the (2–0) band of $^{16}O_2$. The product $|q|\Gamma$ is much larger for the (1–0) band than for any other band studied here or in I. For these reasons, the good agreement between the model and our experimental cross sections for the (1–0) band is not, in itself, a verification of the lineshape used in our empirical model. For example, a Lorentzian shape may fit nearly as well, but, when taken together with the results for the (0–0)[4] and (2–0) bands, it is seen that a model based on Fano lineshapes is the only one capable of fitting all bands.

In Tables 1 and 2, we have summarized the spectroscopic constants, oscillator strengths, widths, and asymmetries obtained from our measurements of cross sections for the (1–0) and (2–0) bands of the isotopic molecules $^{16}O_2$, $^{16}O^{18}O$ and $^{18}O_2$. Using the tabulated parameters together with our model, it is possible to generate accurately the (1–0) and (2–0) cross sections to a distance of several Å from the band centres, with the exception of the regions where the forbidden bands occur.

It is necessary to discuss the meaning of the oscillator strengths presented in Tables 1 and 2. Because of the intimate mixing of the $B^3\Sigma_u^-$ and $E^3\Sigma_u^-$ states and consequent spreading of the strength of the bound state into the underlying continuum, the concept of a bound state oscillator strength is difficult to define and the total (bound + continuum) $^3\Sigma_u^-$ oscillator strength becomes wavelength interval dependent.

The oscillator strengths mentioned previously in this paper and in I are bound state oscillator strengths of the fit, calculated effectively by integrating the fitted Fano lineshape *less the continuum contribution*. In the case of the longest band[4] q is relatively large (continuum small), Γ is small, and the model is a good fit to the observed cross section out to a large number of halfwidths from the band centre. As a result, the oscillator strength of the fit is nearly equal to that obtained by integrating the experimental cross section. This result does not obtain for the (1–0) and (2–0) bands. In the case of the (2–0) bands of the $^{18}O_2$ and $^{16}O^{18}O$, there is an extended continuum component of the cross section which may include contributions from adjacent resonances, and thus the integrated oscillator strength exceeds the fitted bound oscillator strength. For the remaining broad bands, the (2–0) for $^{16}O_2$ and the (1–0) for $^{18}O_2$ and $^{16}O^{18}O$, the fitted cross section significantly overestimates the actual cross section in the more distant wings, and the continuum components are less prominent. For this reason the oscillator strength obtained by integrating the cross section is less than the fitted oscillator strength. Both estimates are given in Tables 1 and 2.

The only previous measurement of oscillator strength for the (1–0) and (2–0) bands is from the electron energy-loss measurements of Huebner et al,[22] who obtained the values 8.04×10^{-3} and

Table 1. A summary of the results of this work for the (2–0) band of the $E^3\Sigma_u^- - X^3\Sigma_g^-$ transition. Band origins, widths, asymmetries and oscillator strengths which include error estimates have been determined by fitting an empirical model to the measured cross sections. Other spectroscopic constants for the upper level of the transition are given also. The splitting constants for all isotopic molecules were taken as $\lambda = -3.3725\,\text{cm}^{-1}$ and $\mu = 0.045\,\text{cm}^{-1}$.[17] Units are cm^{-1}, except for q and f, which are dimensionless.

	$^{16}O_2$	$^{16}O^{18}O$	$^{18}O_2$
ν_o	85245.8±2	85141.7±4	84983.9±2
B'	1.4271†	1.3439†	1.2702†
D'	4.50×10^{-6} ‡	3.76×10^{-6} ‡	3.27×10^{-6} ‡
Γ_o	121±5§	68±3§	26.0±1.5
Γ_J	0§	0§	$(2.6\pm1.3)\times10^{-4}$
q	−7.5±1.0	−4.6±0.4	−7.4±0.5
f¶	$(8.3\pm0.3)\times10^{-4}$	$(6.6\pm0.3)\times10^{-4}$	$(6.3\pm0.2)\times10^{-4}$
f‖	7.8×10^{-4}	7.6×10^{-4}	7.7×10^{-4}

† Calculations of Wang,[18] normalized to B' for v'=0, $^{18}O_2$.[17]

‡ Calculated from B' and an approximate value for ω_e'.

§ Γ_J=0 was forced in the fit since this parameter could not be determined accurately.

¶ Fitted oscillator strengths (see text).

‖ Integrated oscillator strengths, λ = 1166.6-1187.4Å ($^{16}O_2$), λ=1170.0-1185.0Å ($^{16}O^{18}O$), λ=1173.6-1185.1Å ($^{18}O_2$). Contributions from forbidden bands have been removed.

1.47×10^{-3} for the second and third bands of $^{16}O_2$, respectively. The electron energy-loss oscillator strength[22] is only slightly larger than our integrated optical value for the second band, but, as was observed in I for the longest band, the electron energy-loss oscillator strength for the third band is nearly double our optical value. The optical oscillator strengths should be regarded as superseding the electron energy-loss values. Because of the difficulties mentioned previously, and the presence of the forbidden bands, it is difficult to determine accurately the isotopic dependence of oscillator strength for the (2–0) band, but there may be a small decrease in f with increasing isotopic mass. There is no significant isotopic dependence for the (1–0) band.

CONCLUSIONS

We have presented the most detailed photoabsorption cross section measurements available for the (2–0) band of the $E^3\Sigma_u^- - X^3\Sigma_g^-$ transition of $^{16}O_2$ and the first such measurements for the (1–0)

Table 2. A summary of the results of this work for the (1–0) band of the $E^3\Sigma_u^- - X^3\Sigma_g^-$ transition. Band origins, widths, asymmetries and oscillator strengths which include error estimates have been determined by fitting an empirical model to the measured cross sections. Other spectroscopic constants for the upper level of the transition are given also. The splitting constants for each isotopic molecule were taken as $\lambda = -3.3725\,\mathrm{cm}^{-1}$ and $\mu = 0.045\,\mathrm{cm}^{-1}$.[17] Units are cm^{-1} except for q and f, which are dimensionless.

	$^{16}O^{18}O$	$^{18}O_2$
ν_o	82858.7±4	82786.1±2
B'	1.3596 †	1.2848†
D'	2.53×10^{-6} ‡	2.21×10^{-6} ‡
Γ	106±3	109±2
q	~60	-140
f §	$(8.0\pm0.2)\times10^{-3}$	$(7.9\pm0.1)\times10^{-3}$
f ¶	7.1×10^{-3}	7.0×10^{-3}

† Calculations of Wang,[18] normalized to B' for v'=0, $^{18}O_2$.[17]

‡ Calculated from B' and an approximate value for ω_e'.

§ Fitted oscillator strengths (see text).

¶ Integrated oscillator strengths, λ = 1198.1-1217.1Å. Contributions from forbidden bands have been removed.

and (2–0) bands of $^{18}O_2$ and $^{16}O^{18}O$. The broadening of the bands, caused by configuration interaction with the $B^3\Sigma_u^- - X^3\Sigma_g^-$ continuum, is significantly greater than that observed previously[4] for the longest band, and the (2–0) band is the most asymmetric of the bands studied here and in I. An empirical band model, based on Beutler–Fano lineshapes, is capable of accurate cross section prediction out to several Å from the band centres, including minima observed in the short-wavelength wing of the (2–0) band for $^{18}O_2$ and $^{16}O^{18}O$. As we found in I, the $E^3\Sigma_u^- - X^3\Sigma_g^-$ transition provides a comparatively rare example of Beutler–Fano resonances due to predissociation in photoabsorption.

With the aid of our empirical model, we have obtained band origins, oscillator strengths, linewidths and asymmetries which will enable the refinement of the potential curves and electronic coupling constant which may be deduced from a coupled-Schrödinger equation treatment of the resonances.[23] Our oscillator strengths, the first optical values published, are in reasonable

agreement with the electron-impact values[22] for the (1–0) band, but are substantially smaller for the (2–0) band.

Acknowledgements—The authors would like to thank C. Dedman and K. Lonsdale for valuable technical assistance. We are also grateful to A. Dalgarno, A. Blake, D. McCoy, L. Torop, and J. Wang for discussions on the theoretical aspects of resonances in molecular photodissociation.

REFERENCES

1. Y. Tanaka, *J. Chem. Phys.* **20,** 1728 (1952).
2. M. Yoshimine, *J. Chem. Phys.* **64,** 2254 (1976).
3. D. H. Katayama, S. Ogawa, M. Ogawa, and Y. Tanaka, *J. Chem. Phys.* **67,** 2132 (1977).
4. B. R. Lewis, S. T. Gibson, M. Emami, and J. H. Carver, *JQSRT* **40,** 1 (1988).
5. R. J. Buenker and S. D. Peyerimhoff, *Chem. Phys.* **8,** 324 (1975).
6. R. J. Buenker and S. D. Peyerimhoff, *Chem. Phys. Lett.* **34,** 225 (1975).
7. R. J. Buenker and S. D. Peyerimhoff, *Chem. Phys. Lett.* **36,** 415 (1975).
8. M. Yoshimine, *J. Chem. Phys.* **64,** 2254 (1976).
9. L. Torop, D. G. McCoy, A. J. Blake, J. Wang, and T. Scholz, *JQSRT* **38,** 9 (1987).
10. E. F. van Dishoeck, M. C. van Hemert, A. C. Allison, and A. Dalgarno, *J. Chem. Phys.* **81,** 5709 (1984).
11. J. Wang, D. G. McCoy, A. J. Blake, and L. Torop, *JQSRT* **38,** 19 (1987).
12. J. Wang, A. J. Blake, D. G. McCoy, and L. Torop, *JQSRT* **40,** 501 (1988).
13. S. Ogawa and M. Ogawa, *Can. J. Phys.* **53,** 1845 (1975).
14. R. Cimiraglia, M. Persico, and J. Tomasi, *Chem. Phys.* **42,** 297 (1979).
15. B. R. Lewis, *Appl. Opt.* **22,** 1546 (1983).
16. M. Ogawa, K. R. Yamawaki, A. Hashizume, and Y. Tanaka, *J. Molec. Spectrosc.* **55,** 425 (1975).
17. M. Ogawa, *Can. J. Phys.* **53,** 2703 (1975).
18. J. Wang, private communication (1987).
19. G. Herzberg, *Molecular Spectra and Molecular Structure, Vol. I. Spectra of Diatomic Molecules*, Van Nostrand-Reinhold, New York, NY (1950).
20. U. Fano, *Phys. Rev.* **124,** 1866 (1961).
21. B. R. Lewis, S. T. Gibson, and J. H. Carver, in preparation (1988).
22. R. H. Huebner, R. J. Celotta, S. R. Mielczarek, and C. E. Kuyatt, *J. Chem. Phys.* **63,** 241 (1975).
23. J. Wang, A. J. Blake, D. G. McCoy, and L. Torop, in preparation (1988).

4.14 Vacuum-ultraviolet absorption linewidth measurement using high-order anti-Stokes Raman-shifted radiation

[33] B. R. Lewis, S. T. Gibson, K. G. H. Baldwin, and J. H. Carver, *Journal of the Optical Society of America B* **6**, 1200–1208 (1989).

Vacuum-ultraviolet absorption linewidth measurement using high-order anti-Stokes Raman-shifted radiation

B. R. Lewis, S. T. Gibson, K. G. H. Baldwin, and J. H. Carver

Research School of Physical Sciences, The Australian National University, Canberra ACT 2600, Australia

Received August 31, 1988; accepted December 19, 1988

We assess the suitability of a tunable, coherent source of VUV radiation, based on stimulated Raman scattering in compressed H_2, for quantitative high-resolution spectroscopy. The ~360-nm output of an excimer-pumped dye laser was used as a pump source. The high-order anti-Stokes components (AS6–AS9, ~150–~190 nm) show a power-dependent bandwidth, a FWHM of ~0.15 cm^{-1} being attainable at low pump power. Measurements of predissociation linewidth for rotational lines from the (17–0) Schumann–Runge band of $^{16}O_2$ were made by using the seventh anti-Stokes component of the source. These are currently the most accurate measurements available and are in good agreement with theoretical predictions.

INTRODUCTION

Since the first measurement of the stimulated Raman effect in gases by Minck *et al.*,[1] there have been numerous experimental studies[2–13] of the generation of coherent VUV radiation by anti-Stokes Raman scattering (ASRS) of laser radiation in compressed H_2. A large $Q_{01}(1)$ vibrational Raman shift (4155.255 cm^{-1}),[14] a favorable Raman cross section,[15] a small wavelength dependence of dispersion,[16] and transparency in the VUV[17] combine to make H_2 an excellent nonlinear medium for generation of VUV radiation by ASRS. The four-wave mixing processes responsible for the generation of anti-Stokes radiation have been discussed, for example, by Döbele *et al.*[10] and the references listed therein.

Experiments using excimer-laser pump radiation have given the shortest wavelengths obtained by ASRS in H_2. Döbele *et al.*[13] generated 117-nm radiation as the eighth anti-Stokes component (AS8) of ArF pump radiation and 116 nm as AS11 from a KrF pump. Takahashi *et al.*[12] achieved 121.5 nm as AS12 from a XeCl pump. The suitability of ASRS for tunable VUV spectroscopy was shown by Schomburg *et al.*[9] and by Baldwin *et al.*,[11] who Raman shifted continuously tunable dye-laser radiation into the VUV. Using excimer-pumped butyl-PBD dye, Baldwin *et al.*[11] demonstrated the advantage of shorter dye wavelengths in improving the VUV output efficiency and generated the shortest widely tunable ASRS wavelengths that were then obtainable at 136.2 nm in AS11. Recently Wallmeier and Zacharias,[18] with a similar configuration but using DMQ dye and cooled H_2, obtained ~100 W in AS12 at 129 nm.

Very narrow linewidths, of the order of 0.01 cm^{-1}, have been measured for the $Q_{01}(1)$ vibrational transition of H_2 in experiments[19–21] involving the stimulated Raman scattering (SRS) of low-power cw laser radiation. Using stimulated Raman gain spectroscopy, Bischel and Dyer[19] made accurate measurements of the temperature and density dependences of the Raman linewidth and line shift for the $Q_{01}(1)$ and $Q_{01}(0)$ transitions, but only a small amount of inconsistent data exists on the spectral characteristics of the high-order anti-Stokes (AS) components produced by using the pulsed laser systems mentioned above. The temporal behavior of these components, including pulse shortening, was discussed by Wilke and Schmidt.[3,4] Schomburg *et al.*[8,9] concluded that the bandwidth of their AS8 component near 195 nm was <1 cm^{-1} by observation of absorption lines in the Schumann–Runge bands of O_2.[22] Bischel *et al.*[23] and Zacharias *et al.*[24] reported bandwidths of ~0.3 cm^{-1} in an AS3 component near 220 nm from an examination of NO spectra. However, Bischel *et al.*[23] observed no broadening, whereas Zacharias *et al.*[24] noted that considerable broadening may occur in the ASRS process, depending on intensity and AS order. In a recent publication, Glab and Hessler[25] reported the observation of bandwidths of 0.3–0.8 cm^{-1} in the AS4 component near 209 nm when they used a narrow-band pump laser. They also reported an intensity-dependent line shift and an asymmetric line shape, that they explained in terms of the ac Stark effect.[26–28]

The high conversion efficiency,[4] continuous tunability,[4] and relatively narrow spectral bandwidth[23,24] obtainable by the ASRS of dye-laser radiation from compressed H_2 make a source based on this process highly desirable for high-resolution spectroscopy and photochemistry. Fluorescence[18,23,29–32] and photoionization[24] experiments using such a source have already been reported. In particular, Bogen *et al.*[32] used a laser-induced fluorescence technique involving the AS8 component at 166 nm of dye-laser radiation, Raman scattered in H_2, to measure the velocity distribution of C atoms sputtered from C and TiC targets by impinging Ar ions. Their reported bandwidth of ~0.1 cm^{-1} appears to be the narrowest yet attained for a high-order AS component.

Our current interests include high-resolution photoabsorption and excitation spectroscopy of O_2 in the VUV. The best previous absorption cross sections for the Schumann–Runge bands[22,33,34] (175–200 nm) were measured with resolutions of ~0.4–1.5 cm^{-1} by using conventional techniques. The improvement in resolution obtainable with an ASRS source should allow us to obtain significantly improved cross sections for bands with $v' \geq 13$, where the predissociation linewidths[22] are as narrow as ~0.1 cm^{-1}. In this paper, therefore, we set out to examine the spectral characteristics of the high-order AS components of a source based on the ASRS in H_2 of excimer-pumped dye laser radiation. We

0740-3224/89/061200-09$02.00

illustrate the application of the source to the measurement of narrow rotational linewidths by an experimental examination of predissociation linewidths for the (17–0) Schumann–Runge band of O_2. The results obtained are significantly more accurate than the best previous linewidths,[22] and the ASRS source realizes its potential as an invaluable tool for high-resolution VUV spectroscopy.

EXPERIMENT

The experimental arrangement was similar to that used by Baldwin *et al.*[11] A three-stage dye laser with intracavity étalon (Lambda Physik FL3002E) was pumped transversely by a XeCl excimer laser (Lambda Physik EMG 201 MSC). When operated with DMQ dye at 363 nm, the dye laser produced ~30-mJ pulses of ~20-nsec duration in a beam of D-shaped cross section, resulting in a peak power of ~1.5 MW. The DMQ/dioxane dye/solvent combination used was significantly superior in efficiency and lifetime[35] to the butyl-PBD/methanol combination used in the same spectral region by Baldwin *et al.*[11] With daily running at 10 Hz, the half-energy lifetime of an excimer gas fill was as great as 2×10^6 shots, and the dye/solvent lifetime was significantly greater. The dye laser bandwidth specified by the manufacturer was 0.04 cm^{-1} with the intracavity étalon installed and ~0.3 cm^{-1} when the grating was the only tuning element; our measured values were <0.08 and 0.3 cm^{-1}, respectively.

The dye-laser output beam was expanded with a telescope and focused into a 1-m-long Raman cell with a cone angle of ~0.03 rad in order to enhance the phase matching of the higher-order AS components.[11] The entrance and exit windows of the Raman cell were 1.96-cm-thick quartz and 0.64-cm-thick MgF_2, respectively. The cell was operated at room temperature with 500–2500 kPa of ultrahigh-purity H_2 (99.999%). Use of high-purity grade (99.98%) resulted in unacceptably large absorption of the high-order AS components (135–175 nm) in the 10-parts-in-10^6 O_2 impurity. The forward-scattered AS cones[10] of the desired order were focused near the entrance slit of a 0.2-m VUV scanning monochromator (ARC VM502) by an adjustable 0.1-m focal-length MgF_2 lens contained in a vacuum housing. The VUV radiation was dispersed by a 1200-groove/mm grating with a reciprocal dispersion of 40 Å/mm.

The backward-scattered Stokes components (S1–S3) were monitored simultaneously with an étalon (Burleigh RC140), and it was found that the bandwidth of S2 (~520 nm) was ~0.3 or ~0.1 cm^{-1}, depending on the absence or presence of the dye-laser intracavity étalon. The monitor étalon was also used to optimize the grating-étalon tracking of the dye laser by observation of S1 fringes.

The dispersed VUV radiation was detected before entering and after leaving a MgF_2-windowed, 30-cm-long absorption cell with the aid of a VUV beam splitter and two solar-blind photomultipliers (EMI type 9413, CsI photocathode). In most AS orders severe attenuation (~10^{-2}) was employed by means of neutral-density filters in order to ensure linear operation of the detectors. There was a large amount of stray primary laser radiation measurable in the absorption cell with a CsTe photocathode photomultiplier, but this was not detected at all by the CsI tubes. Small amounts of scattered VUV radiation from unwanted AS orders were measurable in some circumstances; however, provided that relatively narrow monochromator slits (≤100 μm) were employed, this did not affect quantitative measurements. We observed pulse shortening in the higher AS orders that was qualitatively similar to that seen previously by Wilke and Schmidt.[4]

The photomultiplier outputs were processed by an EGG/PARC 4400 series boxcar averaging system in the alternate-trigger baseline-subtract mode. The lasers were normally triggered at 10 Hz, and 100 shots were taken at each data point. The detector signal was divided by the beam-split monitor signal to provide a measure of protection against intensity fluctuations, which become significant in high AS orders, as noted by Döbele *et al.*[13]

All measurements on absorption lines were taken at room temperature. The cell was filled with ultrahigh-purity O_2 (99.99%, 1–1000 Torr), NO (99.0%, 0.01–10 Torr), or CO (99.5%, 0.01–10 Torr), which was passed through suitable cold traps, by means of a Balzers RME 010 electromagnetic leak valve. The pressure was controlled by a Datametrics 1404 valve controller and was measured by a Datametrics Barocel 570/1173 variable capacitance manometer. Burst scans using the intracavity étalon were performed over the rotational line of interest with increments of ≥0.018 cm^{-1}. If we wanted to measure an absolute absorption coefficient, empty-cell reference points were taken.

RESULTS AND DISCUSSION

Spectral Characteristics of Anti-Stokes Raman Scattering Source

We observed generated AS radiation to AS11 (~137 nm), as did Baldwin *et al.*,[11] but bandwidth and linewidth measurements in the present paper were restricted to the AS6–AS9 components (~150–~190 nm).

In Fig. 1 we present measurements of AS6 (190.36 nm) and AS7 (176.04 nm) obtained under various conditions by scanning the monochromator (~0.2-nm resolution) with a fixed pump wavelength. The detector was unattenuated, and, in the case of AS6, the main vibrational transition was strongly absorbed by O_2 [$P(5)R(7)$ lines, (5–0) Schumann–Runge band] contained in the absorption cell. Under these conditions a number of weak sidebands are evident. Appearing in each scan are equally spaced Stokes sidebands and a single AS sideband, with a mean separation of (234 ± 10) cm^{-1}, arising from excited-state SRS involving transitions from $v = 1$ to $v = 2$ levels.[5,36] The energy difference between the $Q_{01}(1)$ and $Q_{12}(1)$ vibrational quanta[14] is (4155.255 − 3920.056) = 235.199 cm^{-1}, in good agreement with our measured spacing. The sidebands may be considered vibrational modulation signals at combinational frequencies $m_1Q_{01}(1) \pm m_2Q_{12}(1)$, where m_1 and m_2 are positive integers and $m_1 + m_2 = n$, which is the AS order. So far as we are aware, the AS sidebands due to this process have not been seen previously.

Apparent also in the AS7 scan in Fig. 1 are two additional sidebands, ±(565 ± 10) cm^{-1} from the main transition, which we attribute to SRS involving a rotational excitation from $J = 1$ to $J = 3$. The energy difference between the $S_{01}(1)$ and $Q_{01}(1)$ quanta[14] is (4712.905 − 4155.255) = 557.650 cm^{-1}, in reasonable agreement with our measured spacing. Whether one or two steps are involved in the rotational/vibrational excitation is not clear, and it is possible to assign the sidebands to combinational frequencies $nQ_{01}(1) \pm$

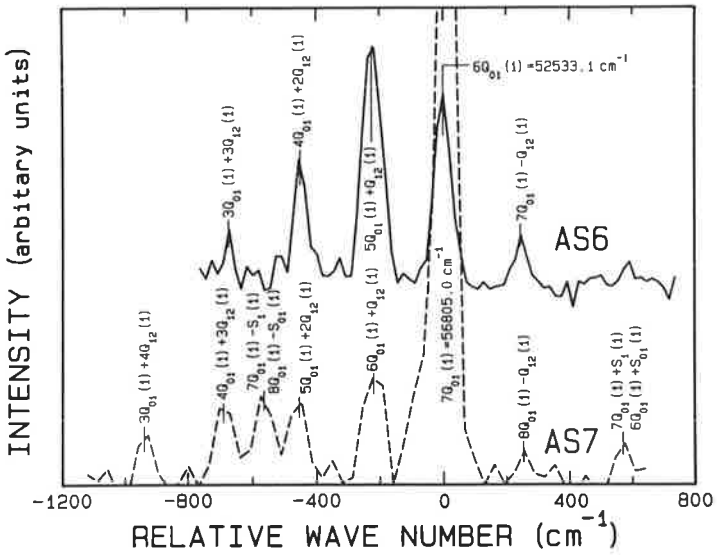

Fig. 1. Spectra of sixth and seventh AS components of the ASRS source obtained by scanning the VUV monochromator for fixed dye-laser wavelengths. The main vibrational transition for AS6 is strongly absorbed by O_2, and the intensity scale is nonlinear because of the absence of detector attenuation. The sidebands observed are caused by SRS involving excitation from $v = 1$ to $v = 2$ and from $J = 1$ to $J = 3$. The assignments are explained in the text.

$mS_1(1)$ or $m_1Q_{01}(1) \pm m_2S_{01}(1)$, where m, m_1, and m_2 are positive integers and $m_1 + m_2 = n$, which is the AS order. Döbele *et al.*,[13] using elliptically polarized radiation, observed similar rotational sidebands, which they assigned to processes of the type $nQ_{01}(1) \pm mS_0(1)$, where $S_0(1) = 587$ cm^{-1}, which is the pure rotational transition from $J = 1$ to $J = 3$. Our measured spacing does not favor this assignment, and further research in this area is desirable under a variety of experimental conditions.

Sidebands similar to those observed by us have been found to be quite strong for some conditions of excitation.[5,13] For accurate absorption spectroscopy their effects should be suppressed. The separation of the closest sideband from the main component varies from 0.56 nm for AS9 to 0.85 nm for AS6. Therefore keeping the monochromator slit width below ~100 μm will guard against measurement errors due to their presence.

The detection linearity and stray-light characteristics of the experimental system were checked by careful O_2 absorption measurements in regions of continuum absorption or where the line structure was broad compared with the VUV bandwidth. At 164.04 nm (AS8) in the Schumann–Runge continuum it was necessary to attenuate the VUV signal by a factor of ~10 to avoid detector saturation. Under these conditions we found a linear dependence of $\ln(I_0/I)$ on O_2 pressure, where I_0 and I are the incident and transmitted fluxes, and an absorption cross section of $(2.53 \pm 0.13) \times 10^{-18}$ cm^2, in good agreement with an interpolation of the measurements of Gibson *et al.*[37] (2.49×10^{-18} cm^2). At 190.264 nm (AS6), in the center of the $R(3)P(1)$ line complex of the (5–0) Schumann–Runge band (linewidths of ~2 cm^{-1}),[22] with attenuation of the VUV signal by a factor of ~100 we observed similar linearity and measured an absorption cross section of $(1.13 \pm 0.05) \times 10^{-20}$ cm^2, in excellent agreement with the measurements of Yoshino *et al.*[34] (1.13×10^{-20} cm^2), which were taken with an instrumental resolution of ~0.4 cm^{-1}. In both cases deviations from linearity occurred only for very strong absorption, and stray-light corrections were not necessary when the measured cell transmission exceeded ~8%. It was quite clear that, provided that care was taken to avoid detector saturation, accurate absorption cross sections were attainable with the ASRS source, at least for spectral features with widths broader than the VUV bandwidth (~0.15 cm^{-1}).

We deduced the ASRS source bandwidth by carefully measuring the absorption due to Doppler-limited rotational lines in the VUV spectra of NO and CO. The apparent linewidths were found to be functions of pump-laser power, focal conditions, and beam alignment, in accordance with previous bandwidth measurements for SRS in metal vapors[38] and H_2.[25]

In Fig. 2 we present absorption measurements of the single Λ-doubling component $R_{21}(8.5)$ of the δ(0–0) band of NO, corresponding to the $C\ ^2\Pi$–$X\ ^2\Pi$ transition, taken with the AS6 component (~190 nm) of the ASRS source. The line center[39] is at 52 453.1 cm^{-1}, the Doppler width at 297 K is 0.118 cm^{-1} FWHM, and the predissociation width[40] is ~0.01 cm^{-1}, resulting in a nearly Doppler-limited linewidth. The NO pressure was 0.02 Torr, and the focal conditions and beam alignments were the same for each scan. We observed a symmetric line with noticeable apparent broadening at the higher pump power.

The solid curves in Fig. 2 were obtained as follows. The absorption line was represented by a Voigt profile,[33] the characteristics of which were defined by the Gaussian and Lorentzian widths given above. The Voigt transmission was then convolved with a normalized Gaussian source function and compared with the measured transmission in an iterative least-squares procedure, resulting in values of the source bandwidth and the absorption oscillator strength. The

best-fit absorption curves obtained by this procedure are given in Fig. 2, where we can see that a Gaussian source function is capable of good agreement with the measurements.

In Fig. 3 we present similar measurements of the $P(17)$ line of the (0–0) band of the CO fourth positive system, $A\,^1\Pi$–$X\,^1\Sigma^+$, taken with the AS9 component (~155 nm) of the ASRS source. The line center[41] is at 64 589.58 cm^{-1}, the Doppler width at 297 K is 0.150 cm^{-1} FWHM, and the pressure of CO was 0.012 Torr. Once again an essentially symmetric line with broadening at higher pump power is observed.

Source bandwidths (FWHM) obtained from NO and CO measurements by using the procedure described above are

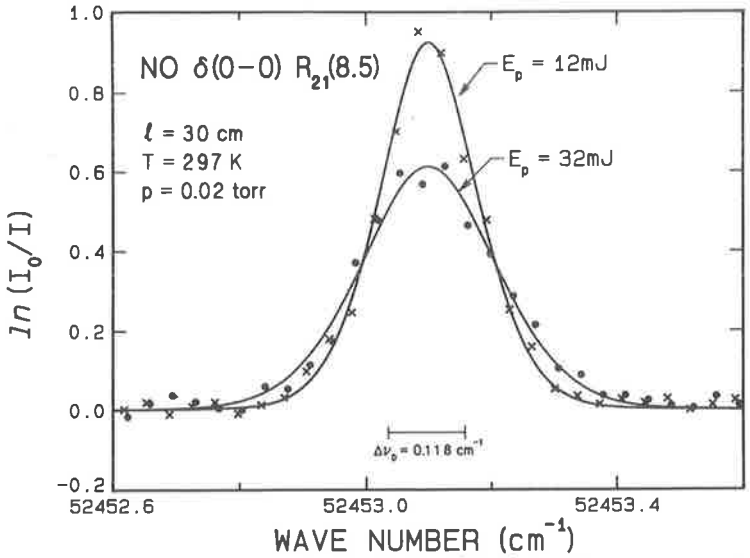

Fig. 2. Absorption measurements of the R_{21} (8.5) line of the δ(0–0) band of the $C\,^2\Pi$–$X\,^2\Pi$ transition of NO for two different pump energies, illustrating the power dependence of bandwidth for the AS6 component. The fitted solid curves represent the expected absorption profiles of a near-Doppler line of 0.118-cm^{-1} FWHM width and 1.3×10^{-5} oscillator strength, convolved in transmission with Gaussian instrument functions of FWHM widths 0.15 and 0.24 cm^{-1}.

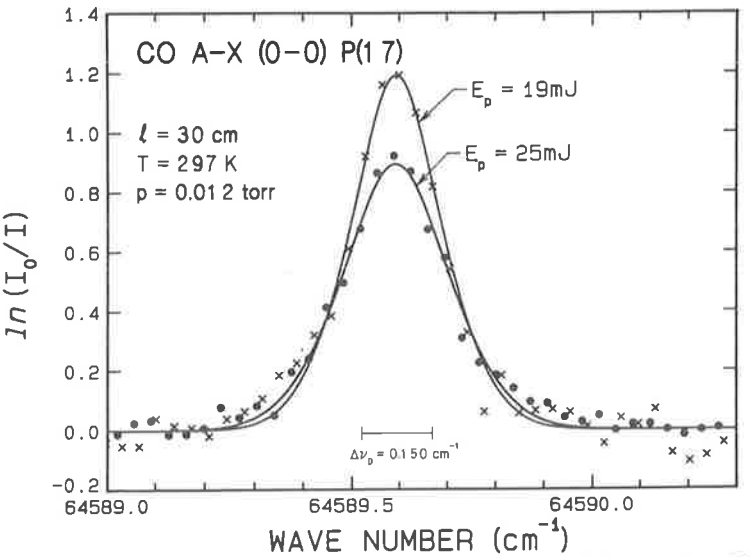

Fig. 3. Absorption measurements of the $P(17)$ line of the (0–0) band of the fourth positive $A\,^1\Pi$–$X\,^1\Sigma^+$ transition of CO for two different pump energies, illustrating the power dependence of bandwidth for the AS9 component. The fitted solid curves represent the expected absorption profiles of Doppler lines of 0.150-cm^{-1} FWHM width and oscillator strengths of 3.9×10^{-5} and 3.5×10^{-5}, convolved in transmission with Gaussian instrument functions of FWHM widths 0.20 and 0.24 cm^{-1}.

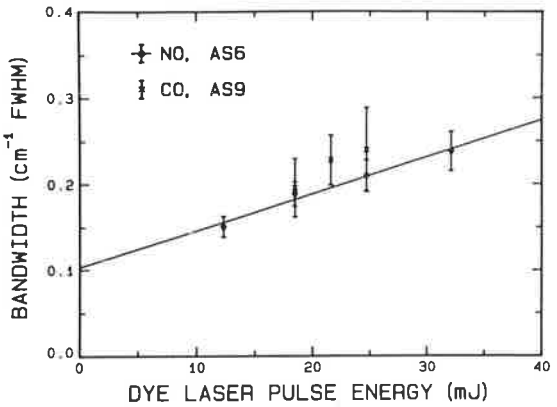

Fig. 4. Measured bandwidths for the sixth and ninth AS components of the ASRS source as a function of dye-laser pulse energy. The solid line is a least-squares fit to the measurements for AS6.

shown in Fig. 4. The laser intensity was varied by blocking a fraction of the dye amplifier pump beam, which may also have simultaneously altered the beam quality slightly. The focal conditions and the beam alignment procedures were otherwise identical for all scans, but the CO results are less accurate because of the significantly greater pulse-to-pulse fluctuations in the AS9 output. The H_2 pressure was optimized separately at each pump power level, but we observed no pressure dependence of the bandwidth under our experimental conditions. We did, however, measure a pressure shift of the AS components that was in reasonable agreement, per order, with previous measurements for the $Q_{01}(1)$ transition[19] but including, possibly, a small intensity-dependent shift.[25] From Fig. 4 we can see that the measured source bandwidths increase linearly with dye-laser pulse energy in the range of energies available for our experiment and the AS9 bandwidths are only marginally greater than those for AS6. To achieve a bandwidth approaching 0.1 cm^{-1}, it is necessary to operate at a low pulse energy. However, this must be balanced against the requirement that the pulse energy must be large enough to exceed the threshold of the Raman process and provide reasonable pulse-to-pulse stability of the output of the desired AS order. We found that an energy of ~12 mJ gave a bandwidth of ~0.15 cm^{-1} FWHM with adequate pulse repeatability in the case of AS6. This was the primary operating condition used for the O_2 linewidth measurements, for which the bandwidth of AS7 was assumed to be intermediate between the almost identical values measured for AS6 and AS9.

Because the bandwidth obtainable with the ASRS source is comparable with the Doppler widths for transitions of light molecules in the VUV, measured cross sections will approach the real values. It is possible to obtain oscillator strengths relatively quickly and directly, provided that saturation of the real line center is avoided [$\ln(I_0/I)_{\text{real}} \leq 2.5$]. From a number of scans of the R_{21} (8.5) line of the $\delta(0\text{–}0)$ band of NO at different pressures and by using the procedure described above, we obtained a mean line oscillator strength of $(1.22 \pm 0.06) \times 10^{-5}$ (single component of Λ doublet). Using the Hönl–London factors and Boltzmann factors calculated by Cieslik,[39] with an allowance for the temperature difference, we obtain a band oscillator strength of $(2.4 \pm 0.2) \times 10^{-3}$, in good agreement with literature values[39] [$(2.2\text{–}2.5) \times 10^{-3}$] obtained at inferior resolution with rather indirect techniques. From a few scans of the $P(17)$ line of the $A\text{–}X$ (0–0) band of CO at 0.012 Torr, we found a line oscillator strength of $(3.8 \pm 0.5) \times 10^{-5}$. Using the Hönl–London factors given by Herzberg[42] for $^1\Pi\text{–}^1\Sigma$ transitions and Boltzmann factors calculated from the

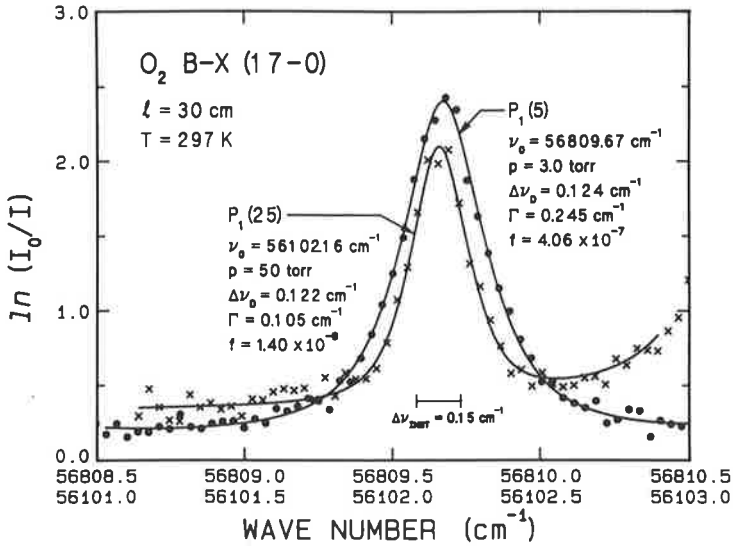

Fig. 5. Absorption measurements of the $P_1(5)$ and $P_1(25)$ lines of the (17–0) band of the Schumann–Runge $B\,^3\Sigma_u^- \text{–} X\,^3\Sigma_g^-$ transition of O_2 made by using the AS7 component of the ASRS source with a resolution of 0.15 cm^{-1} FWHM. The decrease in linewidth with increasing rotation and the Lorentzian wings of the Voigt profile of the $P_1(5)$ line are clearly evident. The fitted solid curves represent the expected absorption profiles of Voigt lines, with the Doppler and Lorentzian widths (FWHM) and oscillator strengths given in the figure, convolved in transmission with the instrument function. Allowances were made for neighboring strong lines and the underlying continuum absorption.

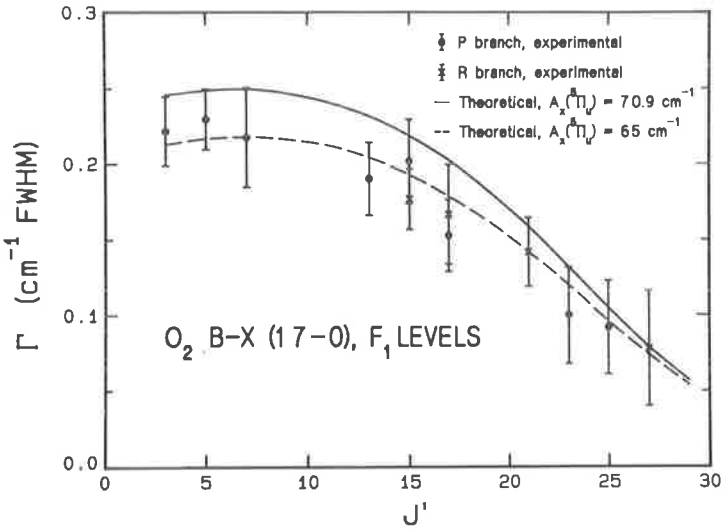

Fig. 6. Measured predissociation linewidths for P_1 and R_1 lines from the (17–0) band of the Schumann–Runge $B\,^3\Sigma_u^- - X\,^3\Sigma_g^-$ transition of O_2 as a function of upper-state rotation $J' = N' + 1$. Two model predictions are also shown.

known spectroscopic constants[41] for the ground state, $X\,^1\Sigma^+$, we obtained a band oscillator strength of $(8.9 \pm 1.2) \times 10^{-3}$. According to the comprehensive study of perturbations in the $A\,^1\Pi$ state of CO by Le Floch *et al.*,[43] the $P(17)$ transition loses 39.6% of its strength to the perturbing transition $e\,^3\Sigma^- - X\,^1\Sigma^+$. Therefore our measurement implies an unperturbed band oscillator strength of $(14.7 \pm 2.0) \times 10^{-3}$. Experimental and theoretical literature values[44,45] for this transition range from 9.6×10^{-3} to 23.0×10^{-3}.

Predissociation Linewidth Measurements for O_2

The Schumann–Runge bands of O_2, as well as being important in studies of the photochemistry of the terrestrial atmosphere, are also of great spectroscopic interest. All bands exhibit predissociation[22] with FWHM linewidths varying from $\sim 0.1\ cm^{-1}$ ($v' = 13$) to $\sim 3\ cm^{-1}$ ($v' = 4$), caused by the mixing of the $B\,^3\Sigma_u^-$ state with four repulsive[46,47] states, $^5\Pi_u$, $^3\Pi_u$, $^1\Pi_u$, and $^3\Sigma_u^+$. Individual rotational lines therefore have a Voigt profile[33] resulting from a combination of the Lorentzian predissociation contribution and a Gaussian Doppler line shape ($\sim 0.1\ cm^{-1}$ FWHM at room temperature). The predissociation linewidth varies in a complex manner with upper-state vibration and rotation.[22]

The interpretation of experimental O_2 spectra is also complicated by the occurrence of triplet fine structure, unresolved in manay cases; underlying continua,[48,49] some of which are pressure dependent; overlapping of bands and lines; and collision broadening[50] of weaker lines, which must be measured at relatively high pressures. In an extensive experimental study at $\sim 1.5\ cm^{-1}$ resolution, Lewis *et al.*[22,23] obtained oscillator strengths and predissociation linewidths for the Schumann–Runge bands by taking absorption measurements at two widely separated pressures and applying a complex computer model of the O_2 spectrum, including the factors mentioned above, in an iterative fashion.

The order-of-magnitude improvement in resolution obtained with the ASRS source allows us to obtain such results more directly. In Fig. 5 we present absorption scans over the $P_1(5)$ and $P_1(25)$ lines of the (17–0) Schumann–Runge band by using the AS7 component of the ASRS source with a resolution of $0.15\ cm^{-1}$. Several observations can be made. First, the $P_1(5)$ line is noticeably broader than the $P_1(25)$ line, which is qualitatively consistent with the indirectly obtained results of Lewis *et al.*[22] Second, in the case of the strong $P_1(5)$ line the Lorentzian wings are clearly visible despite the narrow apparent linewidth of $\sim 0.3\ cm^{-1}$, in contrast to the Gaussian wings observed for NO and CO in Figs. 2 and 3. The sloping background for the $P_1(25)$ line is the Lorentzian wing of the strong (15–0) $R_2(21)$ line at 56 103.34 cm^{-1}, and the continuum components of the cross sections are also evident.

Predissociation linewidths and oscillator strengths can be obtained from single absorption scans by a simple fitting procedure similar to that described in the previous section. Line centers ν_0 (in inverse centimeters) are taken from Yoshino *et al.*,[51] and Doppler widths (in inverse centimeters, FWHM) are given by $\Delta\nu_D = 1.266 \times 10^{-7}\,\nu_0\sqrt{T}$, where T (in kelvins) is the temperature. Each line is described by a Voigt profile, the Lorentzian width component and strength of which are to be determined. The Voigt transmission profile is convolved with a normalized Gaussian instrument function of $0.15\text{-}cm^{-1}$ FWHM width, and the result is compared with experimental transmission measurements in an iterative least-squares fashion. Because of the continuum absorption, the baseline is permitted to float in the fitting procedure. In cases in which an adjacent line contributes to the cross section in the region of interest, such as the $P_1(25)$ scan of Fig. 5, the Voigt profile of the adjacent line is included in the analysis explicitly, with the oscillator strength and linewidth given by Lewis *et al.*[22,23]

The method just described results in a determination of the true Voigt profile of the absorption line of interest. The predissociation linewidth (in inverse centimeters, FWHM) is given by $\Gamma = \Gamma_L - 2.63 \times 10^{-4} p$, where Γ_L is the Lorentzian component of the width resulting from the fitting procedure, the second term is a correction,[50] normally negligible, for the

collision-broadened component of the Lorentzian width, and p (Torr) is the pressure of the absorbing gas. Using the relation $\sigma(\nu) = 1.036 \times 10^{-21} \ln[I_0(\nu)/I(\nu)]T/(lp)$ {where $\sigma(\nu)$ (in square centimeters) is the true absorption cross section, $\ln[I_0(\nu)/I(\nu)]$ is the instrument-corrected absorption determined by the fitting procedure, and l (centimeters) is the cell length}, the true Voigt profile is converted into units of cross section. The rotational line oscillator strength is then calculated from the relation $f(N', N'') = 1.13 \times 10^{12} \int_{-\infty}^{\infty} \sigma(\nu) d\nu$. The equivalent vibrational band oscillator strength is given by $f(v', v'', N', N'') = (2N'' + 1)\, \nu_{v'v''} f(N', N'')/(\nu_{J'J''} \alpha_{N''} S_{N''})$, where $\nu_{v'v''}$ and $\nu_{N'N''}$ are wave numbers for the vibrational and rotational transitions ($\nu_{v'v''}/\nu_{N'N''} \approx 1$), $\alpha_{N''}$ is the Boltzmann factor giving the relative population of the ground-state rotational level giving rise to the line of interest, and $S_{N''}$ is the Hönl–London factor, properly normalized, determining the sharing of strength between the rotational branches. Boltzmann factors were calculated from the known[52] ground-state energy levels of O_2, and the Hönl–London factors were taken from Tatum and Watson[53] for $^3\Sigma^- - ^3\Sigma^-$ transitions with a coupling intermediate between Hund's cases (a) and (b).

Predissociation widths Γ measured for the F_1 triplet sublevels of the $v' = 17$ level of the $B\,^3\Sigma_u^-$ state of O_2 are given in Fig. 6 as a function of upper-state rotation J' ($=N' + 1$ for the F_1 levels studied here). The widths are weighted means determined from several scans over individual $P_1(N'')$ and $R_1(N'')$ lines of the (17–0) Schumann–Runge band. Widths given in Fig. 5 for the $P_1(5)$ and $P_1(25)$ lines were determained from single scans and thus differ slightly from those of Fig. 6. Statistical uncertainties (3σ) determined by the fitting routine are also shown in Fig. 6, but there is an additional uncertainty of ~3%, which is due to uncertainties in cell length, temperature, and pressure.

The widths for F_1, $v' = 17$ determined by Lewis *et al.*[22] were sparser and more scattered than the present measurements, but the predictions of the theoretical model fit to their measurements[22] are in quite good agreement with our results. This fact thus supports the validity of the fitting procedure used by Lewis *et al.*[22] to obtain oscillator strengths and linewidths from relatively poor resolution measurements. Widths for low rotation are determined mainly by interaction of the $B\,^3\Sigma_u^-$ state with the $^5\Pi_u$ repulsive state,[22] and an interaction matrix element $A_x(^5\Pi_u) = 70.9\ \text{cm}^{-1}$ was determined by Lewis *et al.*[22] by fitting a theoretical model to measurements of linewidth for 20 bands. Julienne and Krauss[46] and Julienne[47] used the value $A_x(^5\Pi_u) = 65\ \text{cm}^{-1}$, determined from a deperturbation of measured band origins for $v' = 1$–12, in their theoretical calculations. In Fig. 6 we also show model F_1 linewidths calculated for both values of $A_x(^5\Pi_u)$, but with other interaction parameters set at the values determined by Lewis *et al.*[22] $A_x(^5\Pi_u) = 65\ \text{cm}^{-1}$ gives better agreement with the current measurements; however, definitive comment must await further measurements on other bands and a consideration of all 12 interaction parameters.

Vibrational oscillator strengths involving F_1 levels, $f(17, 0, N', N'') = f(17, N'')$, measured concurrently with the predissociation linewidths, are given in Fig. 7 as a function of $N''(N'' + 1)$. The results are in good agreement with the measurements of Lewis *et al.*[33] and theoretical expectations.

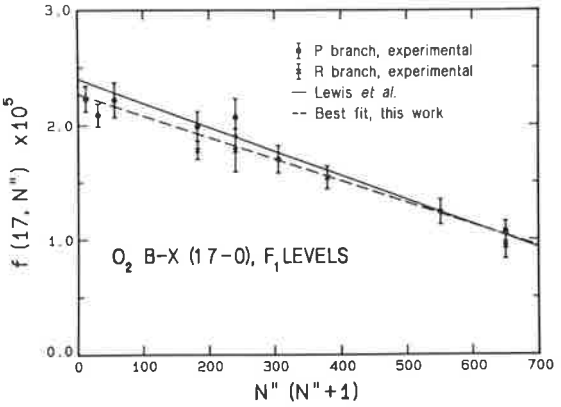

Fig. 7. Measured equivalent band oscillator strengths for P_1 and R_1 lines from the (17–0) band of the Schumann–Runge $B\,^3\Sigma_u^- - X\,^3\Sigma_g^-$ transition of O_2 as a function of $N''(N'' + 1)$. The best estimates of Lewis *et al.*[33] are also shown.

The effective band oscillator strength decreases significantly with rotation because of the effects of centrifugal distortion on upper- and lower-state potential curves of significantly different equilibrium internuclear distances. If we let $f(v', N'') = f(v', 0) - \beta(v')N''(N'' + 1)$, then a weighted least-squares fit to our measurements gives $f(17, 0) = (2.27 \pm 0.06) \times 10^{-5}$ and $\beta(17) = (1.89 \pm 0.14) \times 10^{-8}$, compared with the best measured estimates of $f(17, 0) = (2.40 \pm 0.15) \times 10^{-5}$ and $\beta(17) = (2.1 \pm 0.5) \times 10^{-8}$ by Lewis *et al.*[33] Theoretical calculations by Allison[54] give $f(17, 0) = 2.55 \times 10^{-5}$ and $\beta(17) = 1.9 \times 10^{-8}$. In agreement with previous observations,[33] we find that R-branch oscillator strengths are a little less than the corresponding P-branch strengths. This arises because $N_R' = N_P' + 2$ for a fixed N'', and the greater centrifugal distortion of the upper state results in reduced wave-function overlap for the R branch.

CONCLUSIONS

The potential of a tunable, coherent source of VUV radiation, based on SRS of dye-laser radiation by compressed H_2, for quantitative high-resolution spectroscopy has been realized. The high-order AS components (AS6–AS9, ~150–~190 nm) of Raman-shifted radiation from UV dyes exhibit Gaussian spectral profiles with bandwidths down to ~0.15 cm^{-1}. The AS bandwidth appears to increase linearly with increasing pump power, and consistent narrow-bandwidth performance is attainable only at relatively low power with carefully fixed focal conditions and beam alignment. Care must also be taken to avoid detector saturation and the effects of spurious sidebands of the AS orders. The main limitation of the source is the relatively large variation of AS energy from pulse to pulse, an effect that increases with AS order and with decreased pump power. We have limited the consequences of the energy variation by using a dual detector–monitor system, but further improvements, such as the low-temperature operation of the H_2 cell studied by Wallmeier and Zacharias,[18] may be necessary for the measurement of weak absorptions with greater accuracy.

We have illustrated the spectroscopic utility of such a

source by using the seventh AS component to measure linewidths of some rotational lines from the (17–0) Schumann–Runge band of O_2 at 0.15-cm^{-1} resolution. The predissociation linewidths that we obtain are currently the most accurate linewidths available, and an extension of the measurements to other bands will permit the determination of definitive interaction parameters between the $B\ ^3\Sigma_u^-$ state and the repulsive $^5\Pi_u$, $^3\Pi_u$, $^1\Pi_u$, and $^3\Sigma_u^+$ states causing the predissociation. Oscillator strengths measured concurrently with the linewidths agree well with previous measurements, thereby tending to confirm the reliability of the predissociation linewidths measured here.

ACKNOWLEDGMENTS

We thank B. Luther-Davies for a considerable amount of time spent setting up the laser system, the loan of equipment, and a critical reading of the manuscript. We are also grateful to C. Dedman and K. Lonsdale for valuable technical assistance.

REFERENCES

1. R. W. Minck, R. W. Terhune, and W. G. Rado, "Laser-stimulated Raman effect and resonant four-photon interactions in gases H_2, D_2, and CH_4," Appl. Phys. Lett. **3,** 181–184 (1963).
2. T. R. Loree, R. C. Sze, and D. L. Barker, "Efficient Raman shifting of ArF and KrF laser wavelengths," Appl. Phys. Lett. **31,** 37–39 (1977).
3. V. Wilke and W. Schmidt, "Tunable UV-radiation by stimulated Raman scattering in hydrogen," Appl. Phys. **16,** 151–154 (1978).
4. V. Wilke and W. Schmidt, "Tunable coherent radiation source covering a spectral range from 185 to 880 nm," Appl. Phys. **18,** 177–181 (1979).
5. T. R. Loree, R. C. Sze, D. L. Barker, and P. B. Scott, "New lines in the UV: SRS of excimer laser wavelengths," IEEE J. Quantum Electron. **QE-15,** 337–341 (1979).
6. R. S. Hargrove and J. A. Paisner, "Tunable, efficient VUV generation using ArF-pumped, stimulated Raman scattering in H_2," in *Digest of Topical Meeting on Excimer Lasers* (Optical Society of America, Washington, D.C., 1979), paper ThA6.
7. D. J. Brink and D. Proch, "Efficient tunable ultraviolet source based on stimulated Raman scattering of an excimer-pumped dye laser," Opt. Lett. **7,** 494–496 (1982).
8. H. Schomburg, H. F. Döbele, and B. Rückle, "Tunable narrow line amplification in ArF^* and anti-Stokes production around 179 nm," Appl. Phys. B **28,** 201 (1982).
9. H. Schomburg, H. F. Döbele, and B. Rückle, "Generation of tunable narrow-bandwidth VUV radiation by anti-Stokes SRS in H_2," Appl. Phys. B **30,** 131–134 (1983).
10. H. F. Döbele, M. Röwekamp, and B. Rückle, "Amplification of 193 nm radiation in argon fluoride and generation of tunable VUV radiation by high-order anti-Stokes Raman scattering," IEEE J. Quantum Electron. **QE-20,** 1284–1287 (1984).
11. K. G. H. Baldwin, J. P. Marangos, D. D. Burgess, and M. C. Gower, "Generation of tunable coherent VUV radiation by anti-Stokes Raman scattering of excimer-pumped dye laser radiation," Opt. Commun. **52,** 351–354 (1985).
12. A. Takahashi, O. Matsumoto, M. Maeda, and Y., Miyazoe, "Tunable VUV generation by anti-Stokes stimulated Raman conversion of XeCl laser radiation," Jpn. J. Appl. Phys. **26,** L954–L956 (1987).
13. H. F. Döbele, M. Hörl, and M. Röwekamp, "Tuning ranges of KrF and ArF excimer laser amplifiers and of associated vacuum ultraviolet anti-Stokes Raman lines," Appl. Phys. B **42,** 67–72 (1987).
14. S. L. Bragg, J. W. Brault, and W. H. Smith, "Line positions and strengths in the H_2 quadrupole spectrum," Astrophys. J. **263,** 999–1004 (1982).
15. H. W. Schrötter and H. W. Klöckner, "Raman scattering cross sections in gases and liquids," in *Raman Spectroscopy*, A. Weber, ed., Vol. 11 of Topics in Current Physics (Springer, Berlin, 1979), pp. 123–197.
16. H. H. Landolt and R. Börnstein, *Zahlenwerte und Funktionen* (Springer-Verlag, Berlin, 1962), Vol. 2, Part 8, pp. 6–884.
17. H. Okabe, *Photochemistry of Small Molecules* (Wiley, New York, 1978), p. 162.
18. H. Wallmeier and H. Zacharias, "Continuously tunable VUV radiation (129–210 nm) by anti-Stokes Raman scattering in cooled H_2," Appl. Phys. B **45,** 263–272 (1988).
19. W. K. Bischel and M. J. Dyer, "Temperature dependence of the Raman linewidth and lineshift for the $Q(1)$ and $Q(0)$ transitions in normal and para-H_2," Phys. Rev. A **33,** 3113–3123 (1986).
20. G. G. Bret and M. M. Denariez, "Study of hydrogen stimulated Raman emission," Phys. Lett. **22,** 583–585 (1966).
21. A. Owyoung, "High-resolution cw stimulated Raman spectroscopy in molecular hydrogen," Opt. Lett. **2,** 91–93 (1978).
22. B. R. Lewis, L. Berzins, J. H. Carver, and S. T. Gibson, "Rotational variation of predissociation linewidth in the Schumann-Runge bands of $^{16}O_2$," J. Quant. Spectrosc. Radiat. Transfer **36,** 187–207 (1986).
23. W. K. Bischel, B. E. Perry, and D. R. Crosley, "Detection of fluorescence from O and N atoms induced by two-photon absorption," Appl. Opt. **21,** 1419–1429 (1982).
24. H. Zacharias, H. Rottke, and K. H. Welge, "Sensitivity and mass selectivity of NO detection by stepwise photoionization," Appl. Phys. **24,** 23–28 (1981).
25. W. L. Glab and J. P. Hessler, "Frequency shift and asymmetric line shape of the fourth anti-Stokes component from a hydrogen Raman shifter," submitted to Appl. Opt.
26. L. A. Rahn, R. L. Farrow, M. L. Koszykowski, and P. L. Mattern, "Observation of an optical Stark effect on vibrational and rotational transitions," Phys. Rev. Lett. **45,** 620–623 (1980).
27. R. L. Farrow and L. A. Rahn, "Optical Stark splitting of rotational Raman transitions," Phys. Rev. Lett. **48,** 395–398 (1982).
28. R. A. Hill, A. Owyoung, and P. Esherick, "Optical Stark effects in the stimulated Raman spectrum of molecular oxygen," J. Mol. Spectrosc. **112,** 233–251 (1985).
29. H. F. Döbele, M. Hörl, M. Röwekamp, and B. Reimann, "Detection of atomic oxygen by laser-induced fluorescence spectroscopy at 130 nm," Appl. Phys. B **39,** 91–95 (1986).
30. H. F. Döbele, M. Hörl, and M. Röwekamp, "Two-photon excitation of molecular hydrogen and stimulated emission in the vacuum ultraviolet," Appl. Phys. Lett. **49,** 925–926 (1986).
31. U. Czarnetzki, H. F. Döbele, M. Hörl, B. Reimann, M. Röwekamp, and V. Schulz-Von-Der-Gathen, "Fluorescence spectroscopy of low-Z materials: application of Raman-converted VUV-radiation to beryllium and oxygen," J. Nucl. Mater. **145–147,** 438–442 (1987).
32. P. Bogen, H. F. Döbele, and P. Mertens, "Measurement of velocity distributions of sputtered carbon atoms using laser-induced fluorescence in the vacuum UV," J. Nucl. Mater. **145–147,** 434–437 (1987).
33. B. R. Lewis, L. Berzins, and J. H. Carver, "Oscillator strengths for the Schumann–Runge bands of $^{16}O_2$," J. Quant. Spectrosc. Radiat. Transfer **36,** 209–232 (1986).
34. K. Yoshino, D. E. Freeman, J. R. Esmond, and W. H. Parkinson, "High resolution absorption cross section measurements and band oscillator strengths of the (1–0)–(12–0) Schumann–Runge bands of O_2," Planet. Space Sci. **31,** 339–353 (1983).
35. V. S. Antonov and K. L. Hohla, "Dye stability under excimer laser pumping II. Visible and UV dyes," Appl. Phys. B **32,** 9–14 (1983).
36. M. Audibert and J. Lukasik, "Observations of stimulated Raman scattering between $v = 1$ and $v = 2$ levels in hydrogen gas," Opt. Commun. **21,** 137–138 (1977).
37. S. T. Gibson, H. P. F. Gies, A. J. Blake, D. G. McCoy, and P. J. Rogers, "Temperature dependence in the Schumann–Runge photoabsorption continuum of oxygen," J. Quant. Spectrosc. Radiat. Transfer **30,** 385–393 (1983).
38. D. C. Hanna, M. A. Yuratich, and D. Cotter, *Nonlinear Optics of Free Atoms and Molecules* (Springer-Verlag, Berlin, 1979), pp. 200–201.
39. S. Cieslik, "Sections efficaces d'absorption intégrées des raies

des bandes δ et ϵ de la molécule NO," Bull. Cl. Sci. Acad. R. Belg. **64,** 265–281 (1978).
40. A. B. Callear and M. J. Pilling, "Fluorescence of nitric oxide. Part 6. Predissociation and cascade quenching in NO $D\,^2\Sigma^+$ ($v = 0$) and NO $C\,^2\Pi$ ($v = 0$), and the oscillator strengths of the $\epsilon(0, 0)$ and $\delta(0, 0)$ bands," Trans. Faraday Soc. **66,** 1886–1906 (1970).
41. J. D. Simmons, A. M. Bass, and S. G. Tilford, "The fourth positive system of carbon monoxide observed in absorption at high resolution in the vacuum ultraviolet region," Astrophys. J. **155,** 345–358 (1969).
42. G. Herzberg, *Molecular Spectra and Molecular Structure I. Spectra of Diatomic Molecules* (Van Nostrand, Princeton, N.J., 1950), p. 208.
43. A. C. LeFloch, F. Launay, J. Rostas, R. W. Field, C. M. Brown, and K. Yoshino, "Reinvestigation of the CO $A\,^1\Pi$ state and its perturbations: the $v = 0$ level," J. Molec. Spectrosc. **121,** 337–379 (1987).
44. L. C. Lee and J. A. Guest, "Quantitative absorption and fluorescence studies of CO from 1060 to 1550 Å," J. Phys. B **14,** 3415–3421 (1981).
45. T. A. Carlson, N. Durić, P. Erman, and M. Larsson, "Correlation between perturbation and collision transfers in the A, B, C and b states of CO as revealed by high resolution lifetime measurements," Z. Phys. A **287,** 123–136 (1978).
46. P. S. Julienne and M. Krauss, "Predissociation of the Schumann–Runge bands of O_2," J. Molec. Spectrosc. **56,** 270–308 (1975).
47. P. S. Julienne, "$^3\Sigma_u^-$–$^3\Sigma_u^+$ coupling in the O_2 $B\,^3\Sigma_u^-$ predissociation," J. Molec. Spectrosc. **63,** 60–79 (1976).
48. B. R. Lewis, L. Berzins, J. H. Carver, and S. T. Gibson, "Decomposition of the photoabsorption continuum underlying the Schumann–Runge bands of $^{16}O_2$—I. Role of the $B\,^3\Sigma_u^-$ state: a new dissociation limit," J. Quant. Spectrosc. Radiat. Transfer **33,** 627–643 (1985).
49. B. R. Lewis, L. Berzins, and J. H. Carver, "Decomposition of the photoabsorption continuum underlying the Schumann–Runge bands of $^{16}O_2$—II. Role of the $1\,^3\Pi_g$ state and collision-induced absorption," J. Quant. Spectrosc. Radiat. Transfer **34,** 405–415 (1985).
50. B. R. Lewis, L. Berzins, C. J. Dedman, T. T. Scholz, and J. H. Carver, "Pressure-broadening in the Schumann–Runge bands of molecular oxygen," J. Quant. Spectrosc. Radiat. Transfer **39,** 271–282 (1988).
51. K. Yoshino, D. E. Freeman, and W. H. Parkinson, "Atlas of the Schumann–Runge absorption bands of O_2 in the wavelength region 175–205 nm," J. Phys. Chem. Ref. Data **13,** 207–227 (1984).
52. L. Veseth and A. Lofthus, "Fine structure and centrifugal distortion in the electronic and microwave spectra of O_2 and SO," Mol. Phys. **27,** 511–519 (1974).
53. J. B. Tatum and J. K. G. Watson, "Rotational line strengths in $^3\Sigma^\pm$–$^3\Sigma^\pm$ transitions with intermediate coupling," Can. J. Phys. **49,** 2693–2703 (1971).
54. A. C. Allison, Department of Computing Science, Glasgow University, Glasgow, Scotland (personal communication, 1975).

4.15 Rotational line strengths in $^3\Sigma^+ - {}^3\Sigma^-$ electronic transitions. The $\beta\,{}^3\Sigma_u^+ - X\,{}^3\Sigma_g^-$ and $A\,{}^3\Sigma_u^+ - X\,{}^3\Sigma_g^-$ systems of molecular oxygen

[34] B. R. Lewis and S. T. Gibson,
Canadian Journal of Physics **68**, 231–237 (1990).

Rotational line strengths in $^3\Sigma^+ - ^3\Sigma^-$ electronic transitions. The $\beta^3\Sigma_u^+ - X^3\Sigma_g^-$ and $A^3\Sigma_u^+ - X^3\Sigma_g^-$ systems of molecular oxygen

B. R. LEWIS AND S. T. GIBSON

Research School of Physical Sciences, The Australian National University, P.O. Box 4, Canberra ACT 2600, Australia

Received October 3, 1989

Rotational line strengths are given for $^3\Sigma^+$(int) – $^3\Sigma^-$(int) transitions arising from spin–orbit coupling. Observed branch intensities for the forbidden $\beta^3\Sigma_u^+ - X^3\Sigma_g^-$ transition of O_2 may be explained by assuming spin–orbit mixing of $\beta^3\Sigma_u^+$ with the $B^3\Sigma_u^-$ and $E^3\Sigma_u^-$ states. On the other hand, observed branch intensities for the Herzberg I $A^3\Sigma_u^+ - X^3\Sigma_g^-$ transition of O_2 may be explained only by assuming mixing with $^3\Sigma$ and $^3\Pi$ states. In neither case do earlier formulae, derived assuming a single $^3\Pi$ perturber, apply.

On donne les forces des raies rotationnelles pour les transitions $^3\Sigma^+$(int.) – $^3\Sigma^-$(int.) dues au couplage spin–orbite. Les intensités des branches observées pour la transition défendue $\beta^3\Sigma_u^+ - X^3\Sigma_g^-$ de O_2 peuvent être expliquées en supposant que le couplage spin–orbite mélange l'état $\beta^3\Sigma_u^+$ avec les états $B^3\Sigma_u^-$ et $E^3\Sigma_u^-$. Par ailleurs, les intensités des branches observées pour la transition Herzberg I $A^3\Sigma_u^+ - X^3\Sigma_g^-$ de O_2 ne peuvent s'expliquer qu'en supposant un mélange avec les états $^3\Sigma$ et $^3\Pi$. Les formules dérivées antérieurement en supposant un seul état perturbateur $^3\Pi$ ne s'appliquent dans aucun des cas.

[Traduit par la revue]

Can. J. Phys. **68**, 231 (1990)

1. Introduction

$^3\Sigma^+ - ^3\Sigma^-$ transitions occur with measurable intensity, despite being electric dipole forbidden by the reflection symmetry selection rule (1), when spin–orbit or orbit–rotation couplings are nonzero. Present (2) has given rotational line strengths for $^3\Sigma^+ - ^3\Sigma^-$ transitions arising from spin–orbit and orbit–rotation coupling in the case of a $^3\Pi$ perturber and his formulae have been repeated by Kovacs (3).

Attempts to reconcile the line strengths of Present (2) with measurements of the weak Herzberg I system of O_2, $A^3\Sigma_u^+ - X^3\Sigma_g^-$, have failed. While the N dependence of the Q-form branch intensity measured by Hasson and Nicholls (4) is in agreement with the predictions of Present (2), the measured distribution of intensity (4, 5) among the resolved rotational branches is in considerable disagreement with the predictions of Present (2) for both spin–orbit and orbit–rotation couplings. Huestis and Slanger (6) correctly realized that an understanding of the Herzberg I rotational line strengths could only be achieved by considering simultaneously spin–orbit and orbit–rotation perturbations by a number of electronic states.

As part of an extensive experimental and theoretical study of the photoabsorption spectrum of O_2 in the window region (7–9), we made high-resolution measurements of several bands of the $\beta^3\Sigma_u^+ - X^3\Sigma_g^-$ system.[1] Although measured branch intensities for the β–X bands are significantly different from those of the Herzberg I system, it is impossible to explain them on the basis of the theory of Present (2). It is clear that a more general approach is necessary.

At this time, there do not appear to be any theoretical rotational line intensities in the literature suitable for application to the $\beta^3\Sigma_u^+ - X^3\Sigma_g^-$ system of O_2. Therefore, we present here rotational line strengths for $^3\Sigma^+ - ^3\Sigma^-$ transitions, where the $^3\Sigma$ states, arising from spin–orbit coupling to a number of perturbing states, are intermediate between Hund's cases *a* and *b*. It is found that, in general, three independent transition moments are necessary for an accurate description of the rotational line strengths.

We present, and discuss in some detail, photoabsorption cross-section measurements for the (3–0) band of the $\beta^3\Sigma_u^+ - X^3\Sigma_g^-$ system, and find that a single parallel transition moment is sufficient to explain the observed branch intensities. We briefly contrast this result with the more complicated case of the Herzberg I system and deduce approximate parallel and perpendicular transition moments for the (10–0) band of the $A^3\Sigma_u^+ - X^3\Sigma_g^-$ system from the measured branch intensities of Herzberg (5). We have learned of a detailed study of rotational line intensities in the Herzberg I system by Huestis and Slanger,[2] who include the effects of orbit–rotation coupling to $^3\Pi$ states to explain the observed Q-branch intensities.

2. Intensity theory

General methods for the calculation of rotational line strengths are well known, a particularly clear review having been given by Hougen (10).

The intensity of the rotational transition $F_i'(J')$–$F_j''(J'')$ is related to the line strength

$$[1] \qquad S(F_i'(J') - F_j''(J'')) = \sum_{fM'M''} |\langle F_i'(J'), M'| \times \mu_f | F_j''(J''), M'' \rangle|^2$$

where the μ_f are the laboratory-fixed components of the dipole-moment operator, related to the molecule-fixed components by

$$[2] \qquad \mu_f = \lambda_{fx}\mu_x + \lambda_{fy}\mu_y + \lambda_{fz}\mu_z$$

where λ_{fx}, λ_{fy}, and λ_{fz} are direction cosines between the laboratory- and molecule-fixed axes. In the case of unpolarised radiation, an isotropic absorber, and a lack of external fields all spatial directions are equivalent and the summations in [1] are simplified (11). The line strength is then expressible in the form

$$[3] \qquad S(F_i'(J') - F_j''(J'')) = |\langle F_i'(J') | \mu_{eff} | F_j''(J'') \rangle|^2$$

[1] B. R. Lewis, S. T. Gibson, and J. H. Carver; manuscript in preparation.

[2] D. L. Huestis and T. G. Slanger; manuscript in preparation.

Printed in Canada/Imprimé au Canada

where

$$[4] \quad \mu_{eff} = \frac{\phi_+\mu_-}{2} + \frac{\phi_-\mu_+}{2} + \phi_z\mu_z$$

and

$$[5] \quad \phi_\pm = \phi_x \pm i\phi_y$$

$$[6] \quad \mu_\pm = \mu_x \pm i\mu_y$$

The μ_α are the molecule-fixed components of the electric dipole-moment operator and the ϕ_α are rotational operators the nonzero matrix elements of which have been given, for example, by Tatum and Watson (12) in the (Ω, J) representation. If the wave functions in [3] are expressed in terms of suitable vibronic basis functions the resulting vibronic transition moments become the fundamental intensity parameters of the rotational line strength analysis. Formal expressions for this representation of the transition moment have been given by Kerr and Watson (13).

We now consider the $^3\Sigma^+ - {}^3\Sigma^-$ transition in detail. The selection rule $\Delta\Omega = 0, \pm 1$ for the nonrotating molecule allows six vibronic transition moments between the signed Ω components, but these are related in pairs by reflection symmetry. With a choice of phases consistent with those of Condon and Shortley (14) and Hougen (10), the $^3\Sigma$ vibronic functions transform according to (15)

$$[7] \quad \sigma_{xz}|^3\Sigma_\Omega^\pm\rangle = \pm(-1)^{\Omega+1}|^3\Sigma_{-\Omega}^\pm\rangle$$

under the reflection symmetry operator σ_{xz}. Thus, the three independent vibronic transition moments can be shown to be

$$[8] \quad iY_0 = 2^{-1/2}\langle^3\Sigma_0^+|\mu_-|^3\Sigma_1^-\rangle = 2^{-1/2} \times \langle^3\Sigma_0^+|\mu_+|^3\Sigma_{-1}^-\rangle$$

$$[9] \quad iY_1 = 2^{-1/2}\langle^3\Sigma_1^+|\mu_+|^3\Sigma_0^-\rangle = 2^{-1/2} \times \langle^3\Sigma_{-1}^+|\mu_-|^3\Sigma_0^-\rangle$$

$$[10] \quad iZ_1 = \langle^3\Sigma_1^+|\mu_z|^3\Sigma_1^-\rangle = -\langle^3\Sigma_{-1}^+|\mu_z|^3\Sigma_{-1}^-\rangle$$

since $\sigma_{xz}\mu_z = \mu_z$ and $\sigma_{xz}\mu_\pm = \mu_\mp$ (11). Equations [8]–[10] are normalized according to the recommendations of Whiting and Nicholls (11). The complex conjugates of the vibronic transition moments are obtained by time reversal. With the same phase conventions used to obtain [7], the $^3\Sigma$ vibronic functions transform according to (11)

$$[11] \quad \theta|^3\Sigma_\Omega^\pm\rangle = (-1)^\Omega|^3\Sigma_{-\Omega}^\pm\rangle$$

under the time reversal operator θ. It follows from [7]–[11] that Y_0, Y_1, and Z_1 are all purely real, the same conclusions as may be reached by an examination of the general formulae of Whiting and Nicholls (11).

Y_0, Y_1, and Z_1 vanish in the absence of spin–orbit coupling owing to the reflection symmetry selection rule (1). To the first order in the spin–orbit coupling, it is only $^3\Pi$ states that contribute as perturbers and in the case of $^3\Sigma_u^+ - {}^3\Sigma_g^-$ transitions in homonuclear diatomic molecules such as O_2 intensity is stolen from the perpendicular transitions $^3\Pi_u - {}^3\Sigma_g^-$ and $^3\Sigma_u^+ - {}^3\Pi_g$. The parallel transition moment $Z_1 = 0$ and the perpendicular transition moments Y_0 and Y_1 may be expressed explicitly in terms of the spin–orbit matrix elements between the $^3\Sigma$ and $^3\Pi$ states, according to the manner of Kerr and Watson (13). It follows that $Z_1 = 0$ and $Y_0 = Y_1 = Y$. The case of first-order perturbations is the one treated by Present (2), but, as noted above, his results are inadequate to explain observed rotational line stengths for $^3\Sigma_u^+ - {}^3\Sigma_g^-$ transitions of O_2.

TABLE 1. Rovibronic transition moment operators in case (a)

$\Omega(^3\Sigma^+)$	$\Omega(^3\Sigma^-) = 1$	$\Omega(^3\Sigma^-) = 0$	$\Omega(^3\Sigma^-) = -1$
1	$Z_1\phi_z$	$Y_1\phi_-/\sqrt{2}$	0
0	$Y_0\phi_+/\sqrt{2}$	0	$Y_0\phi_-/\sqrt{2}$
−1	0	$Y_1\phi_+/\sqrt{2}$	$-Z_1\phi_z$

In the second and higher orders we must consider a large number of electronic states as possible perturbers of the ground and upper states of the transition. In this case we may have $Z_1 \neq 0$ and $Y_0 \neq Y_1$. Thus, in general, three independent vibronic transition moments will be necessary to describe rotational line strengths in $^3\Sigma^+ - {}^3\Sigma^-$ transitions. In particular transitions single perturbers may dominate owing to close coincidences in energy or large spin–orbit matrix elements, but, as we shall see, these will not necessarily be $^3\Pi$ perturbers.

Having obtained the vibronic parameters [8]–[10], we are now in a position to write down a set of rovibronic transition moment operators by including the rotational operators of [3]–[6]. The results in case a are given in Table 1.

The energy levels and eigenfunctions for $^3\Sigma$ states are well known (10, 12, 15). Using the phase conventions of Hougen (10) and Watson (15), we have taken the $^3\Sigma$ eigenfunctions to be

$$[12] \quad |F_1(J)\rangle = c_J|^3\Sigma_0, J\rangle + 2^{-1/2}\, s_J\,(|^3\Sigma_1, J\rangle + |^3\Sigma_{-1}, J\rangle)$$

$$[13] \quad |F_2(J)\rangle = 2^{-1/2}\,(|^3\Sigma_1, J\rangle - |^3\Sigma_{-1}, J\rangle)$$

$$[14] \quad |F_3(J)\rangle = s_J|^3\Sigma_0, J\rangle - 2^{-1/2}\, c_J\,(|^3\Sigma_1, J\rangle + |^3\Sigma_{-1}, J\rangle)$$

for upper and lower states. Equations [12]–[14] hold for coupling that is intermediate between cases a and b, the coupling coefficients being given by (15)

$$[15] \quad c_J = ((F_2(J) - F_1(J))/(F_3(J) - F_1(J)))^{1/2}$$

$$[16] \quad s_J = ((F_3(J) - F_2(J))/(F_3(J) - F_1(J)))^{1/2}$$

if centrifugal distortion is neglected.
In case b,

$$[17] \quad c_J = (J/(2J+1))^{1/2}$$

$$[18] \quad s_J = ((J+1)/(2J+1))^{1/2}$$

We are now in a position to evaluate the rotational line strengths for $^3\Sigma^+ - {}^3\Sigma^-$ transitions. If we substitute the wave functions [12]–[14] into the line strength expression [3] and use the rovibrational operators of Table 1 and the well-known matrix elements of the rotational operators (Table 1 of ref. 12 and Table 7 of ref. 10), after considerable algebra we obtain the rotational line strengths of Table 2 where J is to be taken as J''.

The sum of the line strengths over all branches is $(2J+1)(Z_1^2 + Y_0^2 + Y_1^2)$, in accordance with the normalization recommendations of Whiting and Nicholls (11), and the individual line strengths in case b reduce to those of Present (2) when $Z_1 = 0$ and $Y_0 = Y_1$. Case b line strengths may be obtained from Table 2 by applying [17] and [18]. For nonzero values of the vibronic transition moments there is the possibility of

TABLE 2. Rotational line strengths in $^3\Sigma^+ - {}^3\Sigma^-$ transitions for coupling cases intermediate between (*a*) and (*b*)

Line	Line strength
$^sR_{21}(J)$	$\frac{(J+2)}{2(J+1)}\left[s''_J\sqrt{J}Z_1 - c''_J\sqrt{(J+1)}\,Y_1\right]^2$
$^sR_{32}(J)$	$\frac{J}{2(J+1)}\left[-c'_{J+1}\sqrt{(J+2)}\,Z_1 + s'_{J+1}\sqrt{(J+1)}\,Y_0\right]^2$
$^sQ_{31}(J)$	$\frac{(2J+1)}{2J(J+1)}\left[-c'_Js''_J\,Z_1 - c'_Jc''_J\sqrt{J(J+1)}\,Y_1 + s'_Js''_J\sqrt{J(J+1)}Y_0\right]^2$
$^oP_{12}(J)$	$\frac{(J+1)}{2J}\left[s'_{J-1}\sqrt{(J-1)}\,Z_1 - c'_{J-1}\sqrt{J}\,Y_0\right]^2$
$^oP_{23}(J)$	$\frac{(J-1)}{2J}\left[-c''_J\sqrt{(J+1)}\,Z_1 + s''_J\sqrt{J}\,Y_1\right]^2$
$^oQ_{13}(J)$	$\frac{(2J+1)}{2J(J+1)}\left[-s'_Jc''_J\,Z_1 + s'_Js''_J\sqrt{J(J+1)}\,Y_1 - c'_Jc''_J\sqrt{J(J+1)}\,Y_0\right]^2$
$^qQ_1(J)$	$\frac{(2J+1)}{2J(J+1)}\left[s'_Js''_J\,Z_1 + s'_Jc''_J\sqrt{J(J+1)}\,Y_1 + c'_Js''_J\sqrt{J(J+1)}\,Y_0\right]^2$
$^qQ_2(J)$	$\frac{(2J+1)}{2J(J+1)}Z_1^2$
$^qQ_3(J)$	$\frac{(2J+1)}{2J(J+1)}\left[c'_Jc''_J\,Z_1 - c'_Js''_J\sqrt{J(J+1)}\,Y_1 - s'_Jc''_J\sqrt{J(J+1)}\,Y_0\right]^2$
$^qR_{12}(J)$	$\frac{J}{2(J+1)}\left[s'_{J+1}\sqrt{(J+2)}\,Z_1 + c'_{J+1}\sqrt{(J+1)}\,Y_0\right]^2$
$^qR_{23}(J)$	$\frac{(J+2)}{2(J+1)}\left[-c''_J\sqrt{J}\,Z_1 - s''_J\sqrt{(J+1)}\,Y_1\right]^2$
$^qP_{32}(J)$	$\frac{(J+1)}{2J}\left[-c'_{J-1}\sqrt{(J-1)}\,Z_1 - s'_{J-1}\sqrt{J}\,Y_0\right]^2$
$^qP_{21}(J)$	$\frac{(J-1)}{2J}\left[s''_J\sqrt{(J+1)}\,Z_1 + c''_J\sqrt{J}Y_1\right]^2$
Total	$(2J+1)(Z_1^2 + Y_1^2 + Y_0^2)$

destructive and constructive interference between the parallel and perpendicular components leading to a great range of possibilities for the branch strength ratios of different $^3\Sigma^+ - {}^3\Sigma^-$ transitions.

3. The $\beta^3\Sigma_u^+ - X^3\Sigma_g^-$ system of O_2

Although the Rydberg system of bands $\beta^3\Sigma_u^+ - X^3\Sigma_g^-$ may be interpreted in terms of a single transition moment, the single-perturber formulae of Present (2) are not applicable to this transition.

The forbidden series of bands $\beta^3\Sigma_u^+ - X^3\Sigma_g^-$ was photographed first by Tanaka (16) (progression I), and later by Alberti *et al.* (17) and Ogawa and Yamawaki (18), those for $^{18}O_2$ were photographed by Ogawa (19). Rotational analyses have been performed (17–19) for the (2–0) and (3–0) bands and the upper state, classified as $^3\Sigma_u^+$ by quantum defect arguments (18), is a Rydberg state converging to the $X^2\Pi_g$ ground state of O_2^+ (17, 18). All bands exhibit varying degrees of diffuseness owing to predissociation. The rotational structure is clearly visible for the (2–0) and (3–0) bands, but the triplet fine structure is not resolvable in any band.

In considering the origin of the strength of the $\beta^3\Sigma_u^+ - X^3\Sigma_g^-$ bands, we must examine other local features in the spectrum. It has been shown recently (7, 8) that most of the cross section from 1165–1320 Å (1Å = 10^{-10} m) consists of a series of predissocating resonances that result from the configuration interaction between the valence and the Rydberg $B,E^3\Sigma_u^-$ states of O_2. Tanaka (16) has noted, and we discuss in more detail elsewhere (see footnote 1), that the $v' = 4$ level of the $\beta^3\Sigma_u^+$ state almost coincides with the $v' = 1$ level of the $E^3\Sigma_u^-$ state, and that the intensity of the (4-0) $\beta^3\Sigma_u^+ - X^3\Sigma_g^-$ band is anomalously enhanced owing to the coincidence in energy. Anomalous broadening is also observed. Clearly, the $\beta^3\Sigma_u^+$ and $B, E^3\Sigma_u^-$ states are interacting through spin–orbit coupling. The importance of $^3\Sigma^+ - {}^3\Sigma^-$ interactions in O_2 has been noted also by Klotz and Peyerimhoff (20), in relation to the origin of the strength of the Herzberg I bands, and by Julienne (21) in relation to the predissociation of the Schumann–Runge $B^3\Sigma_u^- - X^3\Sigma_g^-$ system. Interactions with the $1^3\Pi_u$ state may also play a part, especially at longer wavelengths, but they are expected to be secondary because of the low-transition strength (22–24) of the $1^3\Pi_u - X^3\Sigma_g^-$ system.

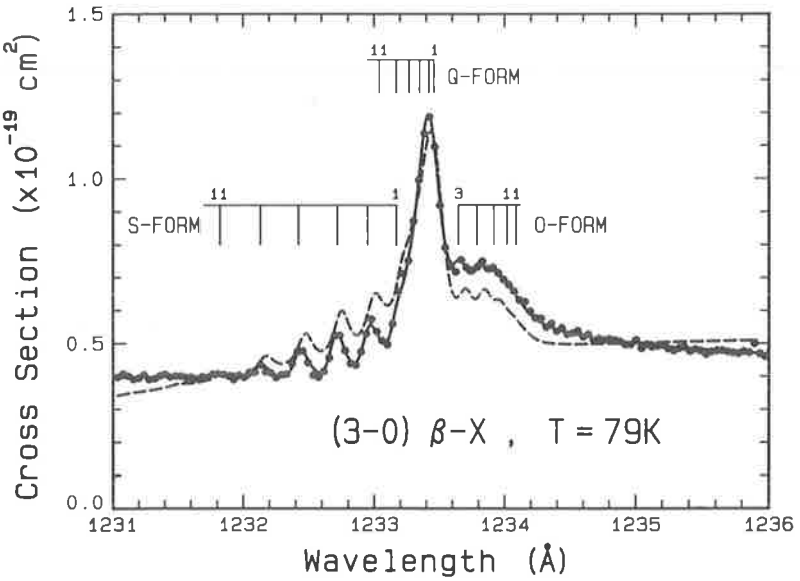

FIG. 1. Photoabsorption cross section of molecular oxygen in the region of the (3–0) $\beta^3\Sigma_u^+ - X^3\Sigma_g^-$ band. Measurements (•) were taken at a temperature of 79 K and with a wavelength resolution of ~0.06 Å FWHM. Least-squares fitted model cross sections assuming Fano (solid line) and Lorentzian (– – –) rotational line shapes are also shown.

In Fig. 1 we present measured absorption cross sections for $^{16}O_2$ in the region of the (3–0) $\beta^3\Sigma_u^+ - X^3\Sigma_g^-$ band at 79 K and with a wavelength resolution of ~0.06 Å FWHM. An Ar continuum light source, a 2.2 m VUV monochromator, a 10 cm absorption cell, and a photoelectric detection system were employed. Full details of the apparatus are given elsewhere (7). The (3–0) band lies between the longest and second bands, (0–0) and (1–0) $E^3\Sigma_u^- - X^3\Sigma_g^-$, which occur at 1244 and 1205 Å, respectively. It is seen from Fig. 1 that the *S*- and *O*-form branches are much stronger than in the case of the Herzberg I bands.

The case *b* rotational line strengths of Present (2) were calculated on the basis of intensity borrowing from perpendicular transitions, $^3\Pi - {}^3\Sigma$, and the same formulae follow from Table 2 and [17] and [18] if we put $Z_1 = 0$ and $Y_0 = Y_1 \neq 0$. In this case the limiting branch strengths become (2) $S{:}Q{:}O$ = 1:6:1 (Hund's case *b*, $N \rightarrow \infty$), insufficient to explain the strong *O*- and *S*-form branches observed in Fig. 1. In the case of intensity stealing from parallel transitions, $^3\Sigma - {}^3\Sigma$, we have $Z_1 \neq 0$ and $Y_0 = Y_1 = 0$ and it follows that the relative branch strengths for Hund's case *b*, summed over the fine-structure components, become

$$[19] \quad S(N) = (2N^3 + 5N^2 + N - 2)/[(2N - 1)(2N + 3)]$$

$$[20] \quad Q(N) = (4N^3 + 6N^2 - 1)/[(2N - 1)(2N + 3)]$$

$$[21] \quad O(N) = (2N^3 + N^2 - 3N)/[(2N - 1)(2N + 3)]$$

leading to limiting ratios $S{:}Q{:}O$ = 1:2:1 as $N \rightarrow \infty$. These ratios are in much better agreement with our observations. It should be noted that, apart from the factor of three in the *Q*-form branches, the rotation dependences of [19]–[21] are almost identical to those of the analogous equations given by Present (2) and used by Hasson and Nicholls (4) in a successful analysis of their measurements of the Herzberg I system. In summary, qualitatively it appears that the strength of the $\beta^3\Sigma_u^+ - X^3\Sigma_g^-$ transition is stolen from the strongly allowed B, $E^3\Sigma_u^- - X^3\Sigma_g^-$ transition by spin–orbit interaction, the rotational intensities being attributable to a single parallel transition moment, Z_1.

To test this conclusion quantitatively we performed band model fits to the measured cross section at 79 K. Using the well-known energy levels (25) for the ground state, we obtained spectroscopic constants for $v' = 3$, $\beta^3\Sigma_u^+$ from a least-squares fit to the observed line positions of Ogawa and Yamawaki (18). In the case of $^3\Sigma^+ - {}^3\Sigma^-$ coupling, it is expected, from Table 2, that there will be eight dominant branches in the spectrum; $^SR_{21}$, $^SR_{32}$, $^OP_{12}$, $^OP_{23}$, $^QR_{12}$, $^QR_{23}$, $^QP_{32}$, and $^QP_{21}$. Therefore, the observed lines of the *S*-form branch, for example, will consist of unresolved doublets. Assuming this scheme, we obtained the following constants: $\nu_0 = 81071.5 \pm 1.6$; $B = 1.639 \pm 0.007$; $D = (2.1 \pm 1.5) \times 10^{-5}$; $\lambda = -2.7 \pm 3.4$; and $\mu = 0.07 \pm 0.10$ where all units are cm^{-1} and the errors are 3σ. Apart from a different definition of the band origin, our values for ν_0, B, and D agree well with those of Ogawa and Yamawaki (18). The values of the effective spin–spin and spin–rotation constants λ and μ are extremely approximate since the triplet structure is not resolvable experimentally, but values for these parameters are needed to construct realistic band profiles.

Line positions were generated using the above constants and relative line strengths were fixed, as the products of appropriate Boltzmann factors and normalized rotational strengths from Table 2, assuming intermediate coupling and a single parallel transition moment. Coupling factors c_j and s_j were determined for the upper and lower states from the calculated triplet energy levels. In view of the evident asymmetry of the measured band profile in Fig. 1, each rotational line was described by a Fano profile (26). The continuum in the absence

TABLE 3. Theoretical and observed relative intensities for branches of the (10–0) band of the $A^3\Sigma_u^+ - X^3\Sigma_g^-$ system of O_2 for $N'' = 3$, 13*†

Branch	I_{obs} ($N''=3$)	I_{calc} ($N''=3$)	I_{obs} ($N''=13$)	I_{calc} ($N''=13$)
$^Q P_{32}$	2‡	1.6	4	3.4
$^Q R_{12}$	3	3.7	4	4.4
$^Q P_{21}$ }	5	2.6 }	6	3.1
$^Q R_{23}$ }		2.3 }		3.0
$^O P_{12}$	2‡	1.5	2	0.89
$^O P_{23}$	1‡	0.36	0.5	0.69
$^O Q_{13}$	0.2	0.09	0.3	0.02
$^S Q_{31}$	0.5‡	0.35	‡	0.16
$^S R_{21}$	‡	0.66	0.5	0.75
$^S R_{32}$	‡	0.04	—	0.07

*I_{obs} are the measured relative intensities of Herzberg (5).
†I_{calc} are calculated from the fitted parameters given in the text.
‡These lines are blended (5).

of the predissociating state was described as a quadratic function of energy. The band oscillator strength f, the predissociation linewidth Γ, the Fano asymmetry parameter q, the Fano overlap parameter ρ, and the coefficients describing the energy dependence of the continuum were parameters of the fitting procedure. Γ, q, and ρ were taken to be independent of rotation and upper or lower state fine-structure levels. Although these assumptions are not strictly correct for $^3\Sigma^+ - {}^3\Sigma^-$ transitions, where the relative widths of the upper fine-structure levels are given by (21) $\Gamma_1:\Gamma_2:\Gamma_3 = (s_J')^2:1:(c_J')^2$, for example, little error is expected in the model band profile since the fine-structure components are not resolvable experimentally.

The solid line in Fig. 1 represents the result of a least-squares fit of the model to the measured cross section at 79 K with $f = (2.9 \pm 0.2) \times 10^{-5}$, $\Gamma = 7.3 \pm 0.6$ cm^{-1} FWHM, $q = -3.7 \pm 0.2$, and $\rho^2 = 0.40 \pm 0.05$. The errors are 3σ determined by the fitting procedure. The agreement is seen to be excellent. The fitted oscillator strength refers to the discrete transition only and the Fano parameters are effective mean values, as described above. The results of a model fit to the measurements in the case of Lorentzian lines superimposed on a noninteracting continuum are given by the broken line of Fig. 1. In this case the fit is very poor, emphasizing the necessity of assuming an asymmetric line shape to explain the measurements.

Of particular interest is the parameter ρ^2, which represents the proportion of the continuum with which the predissociating resonance interacts. In the case of spin–orbit coupling between $^3\Sigma^+$ and $^3\Sigma^-$, it is only the $\Omega = \pm 1$ components that interact and one might then expect $\rho^2 \leq 2/3$ depending on whether other inactive continua are present. From the results of model fits to the (3–0) and other $\beta^3\Sigma_u^+ - X^3\Sigma_g^-$ bands at a number of temperaures, we find a mean value $\rho^2 \approx 0.5$. For spin–oribit coupling between $^1\Sigma^+$ and $^3\Sigma^-$ states, it is only the $\Omega = 0$ components that interact, implying that $\rho^2 \leq 1/3$. Our measured value for ρ^2 is, therefore, an independent piece of evidence supporting the classification of the β state (18) as $^3\Sigma^+$ rather than $^1\Sigma^+$ (17).

Excellent fits are also obtained to cross sections measured at room temperature for the (3–0) band using similar model parameters. The modelling evidence thus supports our earlier conclusion that the $\beta^3\Sigma_u^+ - X^3\Sigma_g^-$ rotational intensities can be described in terms of a single parallel transition moment giving limiting branch intensities $S:Q:O = 1:2:1$. The transition moment can be determined using the relation (4,11),

$$[22] \qquad \Sigma R_e^2 = 3.29 \times 10^5 \frac{g'' f_{v'v''}}{\nu_{v'v''} q_{v'v''}}$$

where g'' is the electronic degeneracy of the lower state, $f_{v'v''}$ the oscillator strength, $\nu_{v'v''}$ the transition energy in cm^{-1}, and $q_{v'v''}$ the Franck–Condon factor. The sum ΣR_e^2, in the manner of Whiting and Nicholls (11), is taken over the distinct nonzero transition moments. In the case of the (3–0) $\beta^3\Sigma_u^+ - X^3\Sigma_g^-$ transition, we have $\Sigma R_e^2 = Z_1^2$, $g'' = 3$, $f_{30} = 2.9 \times 10^{-5}$, and $\nu_{30} = 81\,071.5$ cm^{-1} from above. We determined the Franck–Condon factor $q_{30} = 0.172$ by overlapping appropriate wave functions obtained by numerical integration of the Schrödinger equation with Rydberg–Klein–Rees potentials for the $X^3\Sigma_g^-$ and $\beta^3\Sigma_u^+$ states. The latter potential was approximate owing to the broadness and irregularity of the experimental $\beta^3\Sigma_u^+$ levels (16–19). The transition moment obtained by this procedure is $|Z_1| = 0.045$ a.u., a very large value for a forbidden transition mainly due to the relatively close proximity in energy of the $\beta^3\Sigma_u^+$ and $B,E^3\Sigma_u^-$ states at internuclear separations near 1.2 Å.

The clearly asymmetric band profile and the accurate modelling using Fano line shapes indicate that the $\beta^3\Sigma_u^+ - X^3\Sigma_g^-$ transition is another rare example of an asymmetric predissociating resonance (7, 8). The (3–0) and other bands of this transition will be discussed elsewhere (see footnote 1) in more detail.

The $A^3\Sigma_u^+ - X^3\Sigma_g^-$ system of O_2

Several independent transition moments are necessary to explain rotational line intensities in the Herzberg I system of O_2, $A^3\Sigma_u^+ - X^3\Sigma_g^-$, which provides an interesting contrast to the $\beta^3\Sigma_u^+ - X^3\Sigma_g^-$ system of the same molecule.

Since its discovery (27) the Herzberg I system has been measured in absorption several times (4, 5, 28) and detailed assignments have been given. Observations in emission (29) showed that the original vibrational numbering (5) of the $A^3\Sigma_u^+$ state needed to be increased by one. The bands of the Herzberg I system are much weaker (4) than those of the $\beta^3\Sigma_u^+ - X^3\Sigma_g^-$ system, their rotational lines are neither predissociated nor asymmetric, and the S- and O-form branches are significantly weaker, relative to the Q-form branches, than those of the $\beta^3\Sigma_u^+ - X^3\Sigma_g^-$ system (4, 5).

It has only recently been shown that first-order perturbations by $^3\Pi$ states are not the main contributors to the strength of the Herzberg I system. In a detailed *ab initio* study, Klotz and Peyerimhoff (20) found that the strength of the $A^3\Sigma_u^+ - X^3\Sigma_g^-$ transition is governed primarily by the $B^3\Sigma_u^- - X^3\Sigma_g^-$ transition, whereby the $B^3\Sigma_u^-$ state is a perturber in the $A^3\Sigma_u^+$ wave function. Huestis and Slanger (6), in a study of rotational line strengths, found that approximately equal contributions from $B^3\Sigma_u^-$ and $^3\Pi$ states were necessary to explain measured *O*- and *S*-form branch intensities, while orbit–rotation coupling was necessary to explain the *Q*-form branch strengths.

In Table 3 we present the results of a least-squares fit of the intensity formulae of Table 2, normalized and multiplied by Boltzmann factors appropriate to $T = 300$ K, to the semiquantitative relative line strength measurements of Herzberg (5) for $v' = 10$ and $N'' = 3,13$, the only measurements available that include some *S*- and *O*-form intensities. Coupling coefficients were calculated according to [15] and [16] with energy levels determined using appropriate spectroscopic constants for the upper (28) and lower (25) states. We omittted the Q_Q branches from consideration since these are expected to be strongly affected by orbit–rotation couplings to $^3\Pi$ states (2). The quality of the resultant fit is quite good when one considers the inaccuracies inherent in the estimation of intensities from photographic plates. We find that $|Z_1| = (0.90 \pm 0.13) \times 10^{-3}$ a.u., $|Y_1| = (0.31 \pm 0.16) \times 10^{-3}$ a.u., and $|Y_0| = (0.49 \pm 0.18) \times 10^{-3}$ a.u. where all transition moments are of the same sign and the errors are 3σ determined by the fitting procedure. We have normalized the relative transition moments to the value $\sqrt{\Sigma R_e^2} = (1.07 \pm 0.11) \times 10^{-3}$ a.u. at $r = 1.291$ Å, which follows from the measured band strength of Hasson and Nicholls (4) for $v' = 10$ and the Franck–Condon factors and r centroids given by Krupenie (30) for the $A^3\Sigma_u^+ - X^3\Sigma_g^-$ transition. The transition moments which we have determined should be compared with the *ab initio* calculations of Klotz and Peyerimhoff (20) who obtained $|Z_1| = 1.04 \times 10^{-3}$ a.u., $|Y_0| = |Y_1| = 0.24 \times 10^{-3}$ a.u., and $\sqrt{\Sigma R_e^2} = 1.09 \times 10^{-3}$ a.u. at $r = 1.217$ Å.

Transition moments deduced from measured rotational line strengths for the $A^3\Sigma_u^+ - X^3\Sigma_g^-$ transition of O_2 are thus seen to be in qualitative agreement with the *ab initio* calculations, although the empirical value $Y/Z \sim 0.45$ is significantly larger than the calculated value $|Y/Z| = 0.23$. More definitive experimental determinations of Y/Z and Y_0/Y_1 will not be possible until new highly accurate photoelectric intensity measurements are made on rotational lines from the bands of the Herzberg I system. Our analysis may also be improved by the inclusion of orbit–rotation coupling, which will affect the *Q*-branch intensities. Huestis and Slanger (see footnote 2) have such a study in progress.

5. Conclusions

Rotational line strength formulae have been given for $^3\Sigma^+$(int) – $^3\Sigma^-$(int) transitions arising from spin–orbit coupling. In the general case, it is found that three independent transition moments are required for a correct description of the branch strengths, contrary to the earlier formulae of Present (2) and repeated later by Kovacs (3), which assumed perturbation by $^3\Pi$ states only.

Indeed, both parallel and perpendicular transition moments are needed to explain observed branch intensities in the important $A^3\Sigma_u^+ - X^3\Sigma_g^-$ transition of O_2. For $v' = 10$, we find a mean ratio of perpendicular to parallel transition moments, $Y/Z \sim 0.45$, implying that 71% of the transition strength arises from an allowed parallel transition. This is in qualitative agreement with recent *ab initio* calculations (20) that give $|Y/Z| = 0.23$ and imply that most of the $A^3\Sigma_u^+ - X^3\Sigma_g^-$ transition strength is stolen from the Schumann–Runge transition, $B^3\Sigma_u^- - X^3\Sigma_g^-$, with lesser contributions arising from perturbations by $^3\Pi$ states.

On the other hand, branch intensities observed by us for the (3–0) band of the Rydberg $\beta^3\Sigma_u^+ - X^3\Sigma_g^-$ transition of O_2 may be explained in terms of a single parallel transition moment $|Z_1| = 0.045$ a.u. by assumig spin–orbit mixing of $\beta^3\Sigma_u^+$ with the valence Rydberg $B,E^3\Sigma_u^-$ configuration. Partly because of the close approach of the potentials of the $\beta^3\Sigma_u^+$ and the $B,E^3\Sigma_u^-$ states, the $\beta^3\Sigma_u^+ - X^3\Sigma_g^-$ bands are much stronger than the $A^3\Sigma_u^+ - X^3\Sigma_g^-$ bands (oscillator strengths of order 10^{-5} compared with 10^{-10} (4)) and perturbations of the ground state become unimportant. It is also necessary to assume Fano line shapes to correctly model the $\beta^3\Sigma_u^+ - X^3\Sigma_g^-$ cross section, demonstrating that this transition provides a rare documented example of an asymmetric predissociating resonance.

Acknowledgements

The authors would like to thank D. L. Huestis and J. K. G. Watson for informative discussions on the problem addressed in this work. We are grateful to J. K. G. Watson for a critical reading of the manuscript and we would also like to thank C. J. Dedman and K. J. Lonsdale for their valuable technical assistance.

1. G. Herzberg. Spectra of diatomic molecules. D. Van Nostrand Company Inc., New York. 1950. p. 129.
2. R. D. Present. Phys. Rev. **48**, 140 (1935).
3. I. Kovacs. Rotational structure in the spectra of diatomic molecules. Hilger & Watts Ltd., London, 1969. p. 135.
4. V. Hasson and R. W. Nicholls. J. Phys. B, **4**, 1778 (1971).
5. G. Herzberg. Can. J. Phys. **30**, 185 (1952).
6. D. L. Huestis and T. G. Slanger. The 38th Symposium on Molecular Spectroscopy, Columbus, OH. 1983. Paper WF3.
7. B. R. Lewis, S. T. Gibson, M. Emami, and J. H. Carver. J. Quant. Spectrosc. Radiat. Transfer, **40**, 1 (1988).
8. B. R. Lewis, S. T. Gibson, M. Emami, and J. H. Carver. J. Quant. Spectrosc. Radiat. Transfer, **40**, 469 (1988).
9. J. Wang, A. J. Blake, D. G. McCoy, and L. Torop. J. Quant. Spectrosc. Radiat. Transfer, **40**, 501 (1988).
10. J. T. Hougen. N. B. S. Monogr. (U.S.) n. 115 1970.
11. E. E. Whiting and R. W. Nicholls. Astrophys. J. Suppl. **27**, 1 (1974).
12. J. B. Tatum and J. K. G. Watson, Can. J. Phys. **49**, 2693 (1971).
13. C. M. L. Kerr and J. K. G. Watson, Can. J. Phys. **64**, 36 (1986).
14. E. U. Condon and G. H. Shortley. The theory of atomic spectra. Cambridge University Press, London, 1935.
15. J. K. G. Watson. Can. J. Phys. **46**, 1637 (1968).
16. Y. Tanaka. J. Chem. Phys. **20**, 1728 (1952).
17. F. Alberti, R. A. Ashby, and A. E. Douglas. Can. J. Phys. **46**, 337 (1968).
18. M. Ogawa and K. R. Yamawaki. Can. J. Phys. **47**, 1805 (1969).
19. M. Ogawa. Can. J. Phys. **53**, 2703 (1975).
20. R. Klotz and S. D. Peyerimhoff. Mol. Phys. **57**, 573 (1986).
21. P. S. Julienne. J. Mol. Spectrosc. **63**, 60 (1976).
22. R. J. Buenker, S. D. Peyerimhoff, and M. Peric. Chem. Phys. Lett. **42**, 383 (1976).

23. S. L. GUBERMAN and A. DALGARNO. J. Geophys. Res. A, **84**, 4437 (1979).
24. P. S. JULIENNE, D. NEUMANN, and M. KRAUSS. J. Chem. Phys. **64**, 2990 (1976).
25. L. VESETH and A. LOFTHUS. Mol. Phys. **27**, 511 (1974).
26. U. FANO and J. W. COOPER. Rev. Mod. Phys. **40**, 441 (1968).
27. G. HERZBERG. Naturwissenschaften, **20**, 577 (1932).
28. P. M. BORRELL, P. BORRELL, and D. A. RAMSAY. Can. J. Phys. **64**, 721 (1986).
29. H. P. BROIDA and A. G. GAYDON. Proc. R. Soc. London, A, **222**, 181 (1954).
30. P. H. KRUPENIE. J. Phys. Chem. Ref. Data **1**, 423 (1972).

4.16 Rotational features in the fluorescence excitation spectrum of $O(^1D_2)$ from vacuum-ultraviolet laser photodissociation of O_2

[36] S. T. Gibson, B. R. Lewis, K. G. H. Baldwin, and J. H. Carver, *Journal of Chemical Physics* **94**, 1060–1068 (1991).

Rotational features in the fluorescence excitation spectrum of $O(^1D_2)$ from vacuum ultraviolet laser photodissociation of O_2

S. T. Gibson, B. R. Lewis, K. G. H. Baldwin, and J. H. Carver
Research School of Physical Sciences, The Australian National University, Canberra, ACT 2600, Australia

(Received 20 August 1990; accepted 1 October 1990)

Seventh-order anti-Stokes Raman-shifted ultraviolet laser radiation is used to dissociate O_2 in the 175–177 nm region of the Schumann–Runge band system, $B\,^3\Sigma_u^- - X\,^3\Sigma_g^-$. A cross section for the production of $O(^1D_2)$ is deduced from the 762 nm fluorescence of $O_2(b\,^1\Sigma_g^+)$, a collisional de-excitation product of $O(^1D_2)$ and $O_2(X\,^3\Sigma_g^-)$. Step structure observed in the spectrum is attributed to rotational thresholds for absorption from $X\,^3\Sigma_g^-$ to energies above the $B\,^3\Sigma_u^-$ dissociation limit. The threshold energies define a limiting rotationless dissociation energy of 57 136.4 $\pm$ 0.9 cm^{-1}. Shape resonances, quasibound by the rotational barrier of $B\,^3\Sigma_u^-$, are observed for the first time in O_2. A theoretical calculation of the cross section is in agreement with the measured cross section when the near-dissociation outer limb of the $B\,^3\Sigma_u^-$ potential has an R^{-5} long range form. The shape of the adopted potential is consistent with an avoided crossing with another $^3\Sigma_u^-$ state near $R = 4.6$ Å.

I. INTRODUCTION

Molecular oxygen is a strong absorber of vacuum ultraviolet (VUV) radiation at wavelengths shorter than 200 nm. It has an important role in atmospheric photochemistry, limiting the depth of penetration of solar ultraviolet light and, through photodissociation, is also an important source of atomic oxygen. The spectrum of O_2 provides a number of examples of interesting quantum-mechanical phenomena. Recent studies,[1] for example, have revealed bound-continuum interference features that are rarely observed in diatomic photoabsorption at energies below the first ionization limit.

The Schumann–Runge bands, $B\,^3\Sigma_u^- - X\,^3\Sigma_g^-$, 175–200 nm, are bounded by two continua.[2] The Schumann–Runge continuum, below 175 nm, is six orders of magnitude stronger than the Herzberg continuum, mainly $A\,^3\Sigma_u^+ - X\,^3\Sigma_g^-$, visible above 200 nm. Early photographic measurements[3] of the Schumann–Runge band photoabsorption spectrum indicated the presence of a weak continuum underlying the complex band structure. The continuum was initially thought to be a consequence of a $^3\Pi_u - X\,^3\Sigma_g^-$ transition. However, *ab initio* calculations of the $^3\Pi_u - X\,^3\Sigma_g^-$ transition[4,5] found that it should be extremely weak in the region of the Schumann–Runge bands. Further measurements of the absorption cross section, made between rotational lines, demonstrated a strong temperature dependence[6] and revealed wavelength structure indicative of overlapping continua.[7]

The strength of the adjacent Schumann–Runge continuum suggested the possibility of photodissociation from thermally excited molecules[8] and the limited experimental data[6,7] were described by two exponential functions,[9] representing the thermal $v'' = 0$ and 1 (for wavelengths longer than 180 nm) excitations of the molecule. A theoretical calculation of the cross section associated with each ground state vibrational excitation by Allison *et al.*[10] reproduced the available experimental data. The thermal excitation concept was extended by Blake[11] to include rotation, where the rotational cross sections were calculated by wavelength shifting and scaling the vibrational cross sections of Allison *et al.*[10] The resultant cross section has a step-like structure where each edge represents a rotational threshold for a transition into the Schumann–Runge continuum.

It is now clear that most of the continuum underlying the O_2 Schumann–Runge bands near 175 nm is due to absorption by thermally excited molecules to energies above the $B\,^3\Sigma_u^-$ dissociation limit. Direct absorption measurements of the continuum underlying the Schumann–Runge bands are difficult because the wings of predissociated lines overlap to form a pseudocontinuum and, in addition, the limited resolution of VUV dispersion instruments blends the line structure, particularly at short wavelengths where the bands converge to the dissociation limit. Gies *et al.*[12] applied wing corrections to their photoabsorption measurements, but the data were not of sufficient quantity and accuracy to provide evidence of any step structure. Their theoretical calculation, which included the effects of the rotational centrifugal barrier in the $B\,^3\Sigma_u^-$ potential, demonstrated that the cross section at threshold is reduced as rotational excitation of the molecule increases. High resolution (0.0013 nm FWHM) measurements made by Smith *et al.*[13] at three wavelengths determined cross sections less than the corresponding values of Gies *et al.*,[12] illustrating the difficulties in estimating the resolution-dependent Schumann–Runge band contributions to the total photoabsorption cross section.

The most extensive measurements and comprehensive theoretical calculation of the continuum underlying the Schumann–Runge bands have been made by Lewis *et al.*[14] Regions of their photoabsorption spectra show evidence of absorption edges similar to those observed in H_2 by Herzberg.[15,16] However, in O_2 the absorption edges are more substantially masked by the discrete band spectrum and a correction for the discrete structure is required. A cross section for the wing pseudocontinuum was calculated[14] from a synthetic absorption model based on extensive measurements of

 0021-9606/91/021060-09$03.00

line oscillator strengths and predissociation line widths for the Schumann–Runge band system.[17,18] The resulting continuum cross section exhibited clear evidence of the step structure associated with rotational thresholds for absorption into the Schumann–Runge continuum. A limiting curve of dissociation[19] formed from the measured threshold energies gave a rotationless limit for dissociation via the $B\,^3\Sigma_u^-$ state of 57 136.0 $\pm$ 0.5 cm^{-1}. This value is 8.5 cm^{-1} higher than the 57 127.5 $\pm$ 5 cm^{-1} determined for O_2 by Brix and Herzberg,[20] who used the more indirect technique of extrapolation of band origins measured from the discrete structure of the Schumann–Runge system. A cyclic determination of the dissociation limit from independent measurements, by Albritton *et al.*,[21] has given a value closer to the Brix and Herzberg limit, 57 130 $\pm$ 10 cm^{-1}, but the Lewis *et al.*[14] and Albritton *et al.*[21] limits agree to within experimental error.

In O_2, the masking of the continuum edges by discrete line structure is a major limitation to the determination of an accurate dissociation limit. An alternative technique enables the direct observation of dissociation edges without the masking effect of predissociating transitions. Dissociation of O_2 via the Schumann–Runge continuum results in the atomic products $O(^1D_2) + O(^3P_2)$, whereas Schumann–Runge band predissociation results in two ground state atoms, $O(^3P_2) + O(^3P_2)$. The detection of $O(^1D_2)$ provides a method to follow one dissociation channel of molecular oxygen, direct dissociation via the $B\,^3\Sigma_u^-$ continuum, completely separated from the strong absorption into the Schumann–Runge bands which predissociate into ground state atomic products.

$O(^1D_2)$ is metastable, with a lifetime of 147 s,[22] and is observed to fluoresce at 630 nm in the atmosphere. In the laboratory, the long lifetime of the $^1D_2$ state allows the oxygen atom to be quenched by collision with other species. Quenching by a ground state oxygen molecule results in the $b\,^1\Sigma_g^+$ state,[22] itself metastable with a lifetime of 11 s.[22] This species fluoresces, producing radiation at 762 nm [$(0\text{–}0)\,b\,^1\Sigma_g^+ \sim X\,^3\Sigma_g^-$].[22] Lee *et al.*,[23] in laboratory investigations, used the 762 nm radiation as a measure of the quantum yield of $O(^1D_2)$ from 116–177 nm. Their investigation was concerned predominantly with wavelengths below 175 nm, however, the two points in their measurements that define the Schumann–Runge band region indicate that the production of $O(^1D_2)$ falls off rapidly towards the long wavelength end of the spectrum.

In this work we measure the fluorescence associated with the production of $O(^1D_2)$ to determine the Schumann–Runge continuum cross section from rotationally excited molecules in the energy region of the Schumann–Runge bands. The rotational thresholds lead to an independent measurement of the $B\,^3\Sigma_u^-$ dissociation limit. In addition, the measurements provide a critical test of the accuracy of theoretical calculations which suggest the presence of shape resonance features associated with rotational barriers to dissociation.[24,25] The continuum cross section is also of atmospheric interest as a source of $O(^1D_2)$ from O_2 absorption of solar wavelengths in the Schumann–Runge band region. There has also been some recent interest in $O_2(\,b\,^1\Sigma_g^+\,)$ as a lasing state,[26] the production of this state from dissociation of O_2 may be of some interest.

II. EXPERIMENTAL

A schematic diagram of the apparatus is given in Fig. 1. VUV light was generated using the anti-Stokes Raman-shifted excimer/dye laser source employed by Lewis *et al.*[27] for high resolution [$\sim$0.15 cm^{-1} full width at half maximum (FWHM)] photoabsorption measurements. The 356–373 nm output from a DMQ dye laser, when frequency shifted in molecular hydrogen to the 7th anti-Stokes component, matches the wavelength region of interest, 174.9–178.9 nm. The dye laser was operated without an intracavity etalon, producing a bandwidth of $\sim$0.3 cm^{-1}, but this was degraded to $\sim$0.55 cm^{-1} by the Raman process at the 10 mJ dye laser energy output levels used.[27]

The 330 nm stainless steel absorption chamber is similar in design to that used by Lee *et al.*[23] Two solar blind photomultipliers (type EMI 9413, CsI photocathodes) were used to detect the incident and transmitted UV radiation, which was attenuated at each photomultiplier by a factor of approximately 1500 using neutral density filters. The photomultiplier pulses were gated with a box car integrator (EG&G PARC 4400/4421) set in alternate-trigger baseline-subtract mode. The fluorescence radiation was detected using a cooled photomultiplier (EMI 9658R), located at right angles to the beam axis, in combination with a filter (Kodak Wratten 89B) to isolate the 762 nm radiation. The output signal was pulse counted (Canberra 2071A) during operation of the laser.

It was found, as has been previously reported,[23,28] that the 762 nm fluorescence intensity was weak and that the signal decayed with time. The initial intensity and rate of decay were dependent on the vacuum history of the absorption cell,[28] with long pumping periods between gas fills improving the initial fluorescence intensity and reducing the rate of decay. Decay occurred even during periods of no O_2 photolysis and was, therefore, not simply associated with ozone formation. The decay rate was found also to be temperature dependent, with a more rapid loss of fluorescence if

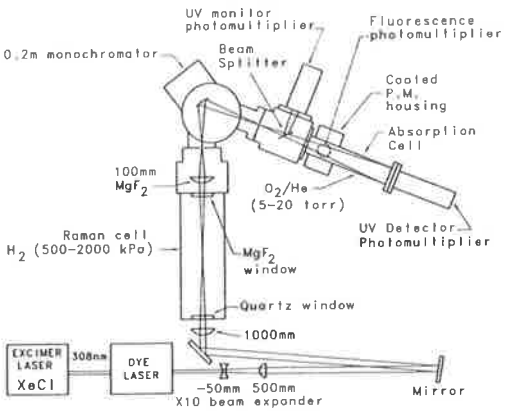

FIG. 1. Schematic diagram of the experimental apparatus.

the absorption cell were heated. It is interesting to note that the quenching efficiency should also decrease as the temperature is increased, although this effect is small.[29] Contamination from the stainless steel walls was the most probable cause for the decay, with hydrogen, having a high quenching rate,[30] the most likely candidate. The decay rate was substantially reduced by using a helium buffer gas and by coating the absorption cell walls with colloidal graphite. High purity oxygen in helium (O_2:He = 0.498:0.502) was passed through a 220 K cold trap, to remove water vapor, prior to admittance to the absorption cell by a servocontrolled electromagnetic leak valve. The experiment was controlled by an IBM AT clone PC which synchronized gas filling, wavelength stepping, and data acquisition.

For scans of less than about 20 min, measurement of the fluorescence intensity as a function of time indicated that, after a short period, the decay curve was approximately a linear function which could be corrected by remeasuring the starting wavelength fluorescence intensity, as shown in Fig. 2. A typical scan employed 0.0125 nm(~ 1 cm^{-1}) wavelength steps, with each data point the result of 200 laser pulses at 10 Hz. Smaller step-size scans were performed in regions requiring high detail (0.002 nm, ~ 0.16 cm^{-1}). Energy calibration was obtained by the simultaneous measurement of the O_2 Schumann–Runge band absorption lines which were referenced to the assignments of Yoshino *et al.*.[31] The relative calibrations between scans agree to better than 0.2 cm^{-1}.

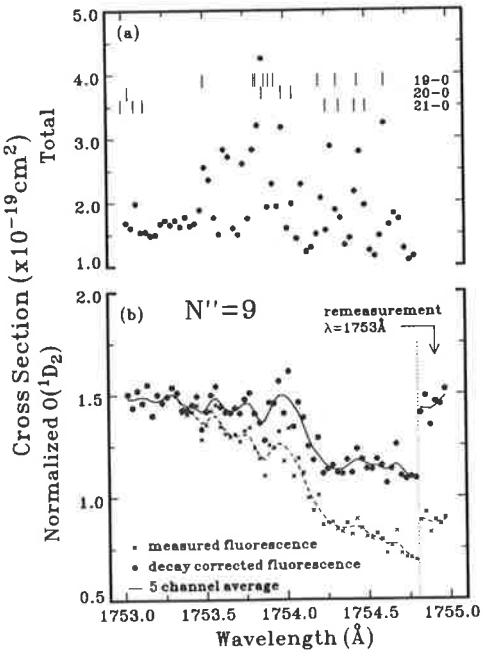

FIG. 2. Scan over the wavelength region of the $N'' = 9$ absorption edge near the (19–0) band head. Each point corresponds to an average of 200 laser shots. The VUV radiation has an effective bandwidth of ~ 0.55 cm^{-1}. (a) Measured total photoabsorption cross section. The wavelength increment (~ 1 cm^{-1}) is too coarse to map the profile of individual absorption lines, some of which have been indicated by the vertical lines. (b) Fluorescence intensity expressed in terms of an effective $O(^1D_2)$ excitation cross section. Decay in the fluorescence signal is evident from a comparison of the initial effective cross section, at 1753 Å, with the value measured at the same wavelength after the scan. The decay is adequately corrected by a linear function. Note the absence of any structure associated with the Schumann–Runge band absorption and also the clearly defined $N'' = 9$ absorption edge.

The relative $O(^1D_2)$ cross section was calculated from

$$\sigma_{\text{relative}}[O(^1D_2)] \propto \frac{(F - F_0)\sigma_{\text{total}}}{I_0[\tau^{l_1/L} - \tau^{l_2/L}]}, \tag{1}$$

where F is the number of fluorescence quanta, F_0 the dark signal, σ_{total} the total photoabsorption cross section, I_0 the number of incident VUV quanta, and the bracketed term corrects for the viewing region of the fluorescence detector, with τ the transmittance for absorption path L(= 330 mm), and l_1(= 20 mm), l_2(= 70 mm) defining the effective viewing region. The quantum efficiency of the VUV detector was constant over the narrow spectral region studied in this work. If the correction term is not included in Eq. (1), then, for strong absorption, structure associated with the absorption lines of the Schumann–Runge bands became apparent in the fluorescence spectrum. This was due purely to the attenuation of the VUV radiation producing the dissociation. The correction was verified over some strong absorption lines of the Schumann–Runge bands and is appropriate for a transmittance above 0.07. In general, the O_2 pressure was adjusted to ensure a transmittance greater than 0,07, however, at long wavelengths where the fluorescence signal was weak, higher pressures were required and in regions of strong Schumann–Runge band line absorption some fluorescence data were ignored. It is seen in Fig. 2 that the observation of fluorescence completely eliminates the strong, discrete absorption of the Schumann–Runge bands and, as a consequence, the absorption edge is clearly determined.

III. THEORETICAL

A. Cross section

Absorption by the Schumann–Runge bands is well described by a vibrational wave function overlap model.[17,18] In accordance with the Born–Oppenheimer approximation, the total molecular wave function is separated into electronic and nuclear parts and the transition strength is interpreted in terms of an overlap integral between vibrational wave functions of the initial and final states. The absorption cross section for a transition between the bound level $v''N''$ and continuum level EN' is given by

$$\sigma_{vN'v''N''} = \frac{2\pi^2\nu}{3\hbar\epsilon_0} g|\langle\chi_{EN'}(R)|D_e(R)|\chi_{v''N''}(R)\rangle|^2, \tag{2}$$

where ν is the transition energy in cm^{-1} and g is a degeneracy factor. The electronic part of the total wave function is included in the transition moment $D_e(R)$, where R is the internuclear separation, and the vibrational wave functions χ are solutions of the nuclear Schrödinger equation

$$\left[-\frac{\hbar^2}{2\mu}\frac{d^2}{dR^2} + V(R) - E\right]\chi(R) = 0, \tag{3}$$

where μ is the reduced mass of the O_2 molecule. The model parameters are thus the potential energy curves $V(R)$ for the

initial and final states and the electronic transition moment $D_e(R)$.

The total absorption cross section at a temperature $T(K)$ is obtained by summing over all possible initial states and weighting each cross section with the appropriate Boltzmann factor to give

$$\sigma(\nu,T)=\frac{\sum_{v''}\sum_{N''(\text{odd})}\sum_{P,R}\sigma_{vN'v''N''}(2N''+1)e^{-E_{v''N''}/kT}}{\sum_{v''}\sum_{N''(\text{odd})}(2N''+1)e^{-E_{v''N''}/kT}}, \quad (4)$$

where $E_{v''N''}$ is the energy of the initial state and k is Boltzmann's constant. Equation (4) contains explicitly a summation over the P and R branches of the continuum, but triplet fine structure has been ignored. Experimentally, fine structure becomes resolvable for the high-rotational absorption edges, however, a full treatment of the fine-structure problem would require a coupled-equations calculation involving the F_1 and F_3 levels,[32] which is beyond the scope of the present work.

B. Potential energy curves

Accurate rotationless Rydberg–Klein–Rees (RKR) potential energy curves were constructed following the description of Jarmain.[33] Spectroscopic constants for the $X\,^3\Sigma_g^-$ state were obtained from Creek and Nicholls[34] and for the $B\,^3\Sigma_u^-$ state from Lewis *et al.*[17] Although the spectroscopic constants of Creek and Nicholls[34] have come under question[35] they are still appropriate for low v'' levels and have the advantage of forming a complete set. Turning points were evaluated using Gauss–Mehler quadrature as described by Tellinghuisen.[36] Inversion using cubic splines produced a potential curve at 0.005 Å intervals and Morse functions[33] were used to extend the potential curves down to 0 Å and up to 50 Å. This outer limit was necessary to ensure a correct energy normalization for the unbound wave function of the upper state. The inner limb of the $B\,^3\Sigma_u^-$ state potential matches the adiabatic curve used by Gibson *et al.*[37] in order to reproduce the correct temperature dependence of the absorption cross section in the Schumann–Runge continuum.

Rotational potentials were calculated by adding a centrifugal energy term to the rotationless potential $V_0(R)$,

$$V_N(R)=V_0(R)+\frac{\hbar^2}{2\mu}\frac{N(N+1)}{R^2}. \quad (5)$$

Calculations near the dissociation limit are sensitive to the long-range form of the $B\,^3\Sigma_u^-$ potential which needs to be described more accurately than by a Morse function extension. The form of the potential energy curve applicable to the long-range interaction of atoms has been discussed by LeRoy.[38] Perturbation theory yields the power series,

$$V_0(R)=D-\sum_{m\geq n}\frac{C_m}{R^m}, \quad (6)$$

where D is the dissociation limit, the m are positive integer powers, n is the asymptotic power and the C_m are constants that may be obtained from the formal expressions of perturbation theory.[39] For a given range of internuclear separation of the atoms, if all significant contributions to the sum are attractive, the potential may be approximated by a single term,[40]

$$V_0(R)=D-\frac{C_{\bar n}}{R^{\bar n}}, \quad (7)$$

where $\bar n$ represents a weighted average of the powers associated with locally important terms. Adding the centrifugal energy term, as in Eq. (5), to Eq. (7), and taking the derivative with respect to the internuclear separation R, gives an expression for the position of the barrier maximum,

$$R_M(N)=\left[\frac{\bar n\mu C_{\bar n}}{N(N+1)\hbar^2}\right]^{1/(\bar n-2)}. \quad (8)$$

A simple relationship follows for the maximum of the potential barrier,

$$E_M(N)=D+S_{\bar n}[N(N+1)]^{\bar n/(\bar n-2)}, \quad (9)$$

where

$$S_{\bar n}=\frac{\bar n-2}{2}\left[\frac{\hbar^{2\bar n}}{(\bar n\mu)^{\bar n}(C_{\bar n})^2}\right]^{1/(\bar n-2)}. \quad (10)$$

Equation (9) was first derived by Bernstein,[40] and is termed the locus of barrier maxima (LBM) by LeRoy.[38] It relates rotational threshold energies for dissociation to the dissociation limit and the long range form of the potential.

C. Wave functions

Wave functions were calculated numerically by solving the Schrödinger equation (3) using the renormalization Numerov method of Johnson.[41] The closed channel wave functions of the ground state were normalized to unity. The open channel solutions of the upper state were energy normalized to the asymptotic form

$$\chi_{EN'}\sim\left(\frac{2\mu}{\pi^2E'}\right)^{1/4}\sin\left(\left(\frac{2\mu E'}{\hbar^2}\right)^{1/2}R-\frac{N'\pi}{2}+\eta_N\right), \quad (11)$$

where E' is the energy above the dissociation threshold and η_N is an elastic scattering phase shift.

Calculated rotationless eigenvalues differ from the spectroscopic G_v values by less than 0.9 cm^{-1} for all vibrational levels of the $B\,^3\Sigma_u^-$ state and for the first 10 vibrational levels of the $X\,^3\Sigma_g^-$ state. The deviations arise because the spectroscopic constants are not totally deperturbed. Rotational energies in general agree to within 1 cm^{-1} with the experimental F_2 transition energies listed in Brix and Herzberg,[20] except in regions of perturbations. Within a band, the deviations become larger for the higher-rotational excitations, comparison with the listings of Yoshino *et al.*[31] revealing that transition energy differences for $v'=15$–17 may be as large as 3 cm^{-1} for $N'\sim20$.

Since this work is concerned primarily with the near dissociation energy region and as the wave function overlap between the lower and upper states extends only over a small range of R (a consequence of the large separation in R between the ground $X\,^3\Sigma_g^-$ and $B\,^3\Sigma_u^-$ states), the extended form of the transition moment $D_e(R)$ is not important. The diabatic transition moment of Wang *et al.*[42] was used and scaled by a factor 1.0325 to correct for the avoided crossing

with the $E\,^3\Sigma_u^-$ Rydberg state that has not been included explicitly in our calculation.

IV. RESULTS

A. Absorption edges

Short scans ($\sim$20 min) were performed over selected wavelength regions of the O_2 Schumann–Runge band spectrum, as illustrated in Fig. 2. Each scan was corrected for fluorescence decay, using a linear function, and then combined with adjacent scans. Figure 3 shows the measured relative $O(^1D_2)$ cross section from 56 685–57 150 cm^{-1}, which has been placed on an absolute scale by normalization to the total photoabsorption cross section at 57 143 cm^{-1}, 2.56×10^{-19} cm^2.[14] At this energy, dissociation of O_2 is expected to occur almost exclusively via the $O(^1D_2)$ channel.[23] In view of the uncertainty in correcting for the decay, the absolute magnitude of the measured cross section becomes increasingly uncertain at the lower transition energies, away from the initial scaling point. However, all measurements are in agreement, to within experimental error, with the cross section values determined by Lewis *et al.*[14]

From Fig. 3, it is evident that the experimental technique has completely eliminated the strong absorption structure of the Schumann–Runge bands, which predissociate to ground state oxygen atoms, enabling absorption edges in the $O(^1D_2)$ continuum to be seen clearly. Each edge represents a rotational threshold for absorption into the Schumann–Runge continuum and defines a corresponding centrifugal barrier in the $B\,^3\Sigma_u^-$ state. The measured edges are not sharp, having a slope associated with the bandwidth of the VUV light used to dissociate the molecule ($\sim$0.55 cm^{-1}), the spectral structure (in particular, the P and R branch transitions with associated fine-structure components) and the character of the near dissociation behavior of the $B\,^3\Sigma_u^-$ state. The complex nature of the absorption edges requires a much more detailed experimental and theoretical study which is currently in progress. For the purpose of this work, the midpoint of each edge was determined from the experimental data, effectively representing an average over the branch and fine-structure components. Each edge was assigned a corresponding ground state rotational quantum number N''. For the higher rotational excitations, separate absorption edges associated with the P and R branches become apparent. In these cases, the two edges were identified and an average position was used as an effective edge. Note that the $P(N''+2)$ and $R(N'')$ transitions define the same upper level and that the corresponding absorption edges, if resolved, should be separated by the ground state rotational spacing $F_i''(N''+2) - F_i''(N'')$.[43] The measured energies of the midpoints of each absorption edge are listed in Table I.

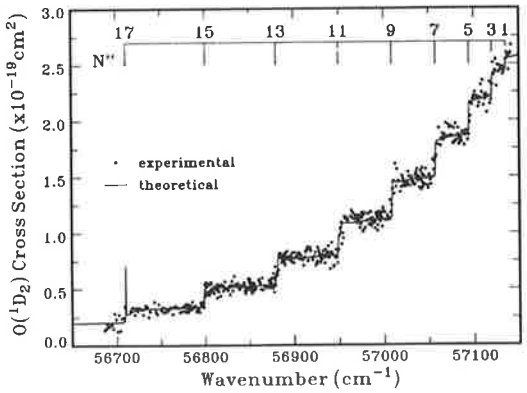

FIG. 3. Excitation spectrum for the production of $O(^1D_2) + O(^3P_2)$ from dissociation of O_2 in the spectral region of the high Schumann–Runge bands (16–0) to the dissociation limit. Each edge corresponds to a rotational threshold energy for absorption into the Schumann–Runge continuum. The experimental points are a composite of individual scans, spanning each absorption edge, which have been corrected for fluorescence decay and then scaled to match with an adjacent higher energy scan over the region of overlap. The cross section has been normalized to 2.56×10^{-19} cm^2 at 57 143 cm^{-1}. Experimental points are separated by $\sim$1 cm^{-1} and data corresponding to a transmittance $\leqslant$0.07 have been excluded. The theoretical calculation, including P- and R-branch transitions, but not the triplet fine structure, assumes a $B\,^3\Sigma_u^-$ potential energy curve with the long range form C_4/R^4. The line near the $N''=17$ edge is a quasibound shape resonance. Similar structure is observed in the region of the $N''=19$ edge as shown in Fig. 6.

The solid line in Fig. 3 is the model calculation described previously. In order to reproduce the experimental threshold energies it was necessary to modify the shape of the model $B\,^3\Sigma_u^-$ potential energy curve near the dissociation limit. For increasing rotational excitation of the molecule, the maximum of the centrifugal barrier moves to a smaller internuclear separation. Hence the measured threshold energies, when corrected for the centrifugal energy, are related to the $B\,^3\Sigma_u^-$ potential energy curve from near the dissociation limit down into the high vibrational levels. The region of the potential energy curve between the highest vibrational level and the dissociation limit is not defined by typical spectroscopic measurements.

A limiting curve of dissociation,[19] referenced to $v''=0$, $N''=0$, was derived from the experimental thresholds by addition of the ground state energy,[43] as shown in Fig. 4. It was assumed that each absorption edge contains all the fine-structure components so that an average triplet fine-

TABLE I. Experimentally determined rotational thresholds (midpoints) for absorption into the Schumann–Runge continuum of O_2 and corresponding barrier maxima (BM) referenced to the ground state $N''=0$, $v''=0$ energy level.

	Thresholds(cm^{-1})[a]				
N''	Mean	P branch	R branch	$\bar{F}''$[b]	BM
1	Not determined			0.932	
3	57 120.5			15.906	57 136.4
5	57 094.7			41.796	57 136.5
7	57 057.4			79.176	57 136.6
9	57 008.7			128.035	57 136.7
11	56 949.5			188.375	57 137.9
13	56 880.3			260.177	57 140.5
15	56 800.8	56 799.1	56 802.5	343.456	57 144.3
17	56 710.4	56 707.9	56 712.8	438.147	57 148.5
19	56 610.9	56 607.6	56 614.2	544.277	57 155.2

[a] Estimated experimental error $\sim \pm 1$ cm^{-1}.
[b] Average ground state triplet energy (Ref. 43).

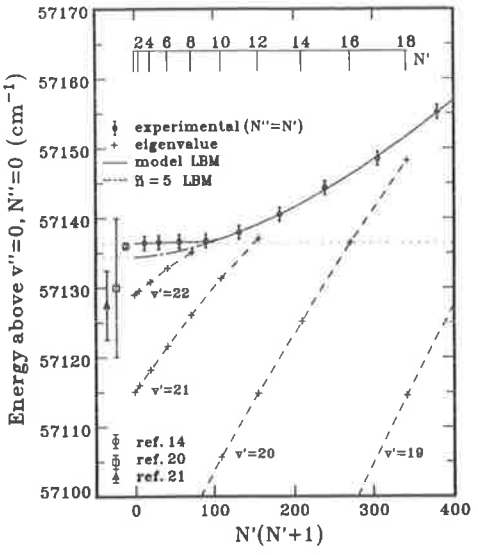

FIG. 4. Limiting curve of dissociation for the $B\,^3\Sigma_u^-$ state of O_2. The experimentally determined absorption edges for $N' > 9$ give a locus of barrier maxima (LBM) consistent with $\tilde{n} = 5$, resulting in an extrapolated energy limit of 57 134.4 $\pm$ 0.9 cm^{-1}. The initial linear behavior suggests a dissociation energy of 57 136.4 $\pm$ 0.9 cm^{-1} and a possible intrinsic barrier with a maximum located beyond 14 Å. Rovibrational energy levels above the 57 136.4 cm^{-1} dissociation limit are quasibound and may rotationally predissociate by tunneling through the centrifugal barrier. The eigenvalue at $v' = 20$, $N' = 18$ produces a resonance in the vicinity of the $N'' = 17$ and $N'' = 19$ edges.

structure energy was used as the ground state energy (Table I). The experimental points should asymptote to the zero-rotation dissociation limit if the potential energy curve has no intrinsic maximum. Conversely, a maximum in the rotationless potential should result in an initial linear behavior with a nonzero slope at the zero rotation intercept.[19] The experimental points define a LBM curve with a slope discontinuity at $N'' = 9$ indicative of two barrier maxima. The data for $N'' > 9$ follow an ordinary LBM of a centrifugal barrier. The data for $N'' \leqslant 9$ are almost constant which suggests a small intrinsic barrier in the $B\,^3\Sigma_u^-$ potential energy curve. A linear least-squares fit to the $N'' = 3$–9 threshold energies gives an intercept, or dissociation energy, of 57 136.4 $\pm$ 0.9 cm^{-1} and a slope 0.004 $\pm$ 0.02 cm^{-1}. The slope is not accurately determined due to the experimental uncertainty of the edges and would imply only that any intrinsic barrier in the potential energy curve is located about $R = 14$ Å.

For rotational excitations $N'' > 9$, the experimental thresholds follow a smooth curve. Applying the locus of barrier maxima expression, Eq. (9), for various trial values of $\tilde{n}$ yields the dissociation limit D and $S_{\tilde{n}}$ from a least-squares fit to the experimental thresholds. A value of $\tilde{n} = 5$, equal to the expected asymptotic power,[39] was found to give a good fit to the experimental measurements. This value for $\tilde{n}$ is probably more coincidental rather than of any physical significance since it would be expected that high-order terms would contribute at the smaller internuclear separations, corresponding to the high rotational excitation, so that $\tilde{n}$ would be expected to increase with N'. The LBM curve yields a dissociation limit of $D = 57\,134.4 \pm 0.9\ cm^{-1}$ and $S_5 = (1.04 \pm 0.08) \times 10^{-3}\ cm^{-1}$. The value of S_5 implies $C_5 = (3.59 \pm 0.39) \times 10^5\ cm^{-1}$ Å^5 and the position of the centrifugal barrier maximum is given by $R_M(N) = 3.49/[N(N+1)]^{1/3}$ Å which is beyond 4.7 Å for $N < 20$.

The LBM analysis indicates that the outer limb of the $B\,^3\Sigma_u^-$ potential curve is adequately represented by a power law, Eq. (7) with $\tilde{n} = 5$, for $R > 4.7$ Å. The potential energy curve for smaller internuclear separations is defined by the RKR curve, as derived from spectroscopic analysis, with the largest outer turning point of 5.4 Å corresponding to $v' = 22$. It was found that the C_5/R^5 curve intersects the RKR curve at $R = 4.6$ Å (Fig. 5) but there is a slope discontinuity between the two potential forms. An analysis of the experimental vibrational energy levels near the dissociation limit, in accordance with the mathematical techniques described by LeRoy,[38] implies that $\tilde{n} \geqslant 7$. Although the predominant power is expected to increase as R decreases, it is clear that there is a definite change in slope from the outer limb of the RKR potential energy curve to the long range form of the potential. This behavior is consistent with a potential that has an avoided crossing with another state, a concept which is supported by the *ab initio* calculations of Saxon and Liu[44] which imply that the $B\,^3\Sigma_u^-$ state suffers an avoided crossing with the $2\,^3\Sigma_u^-$ valence state near $R = 3.8$ Å.

A cautionary note must be added here. In the case of an avoided crossing, the parametrization embodied in Eqs. (6)–(10) remains a convenient description of the potential energy curve but, as noted by LeRoy,[38] the coefficients C_m

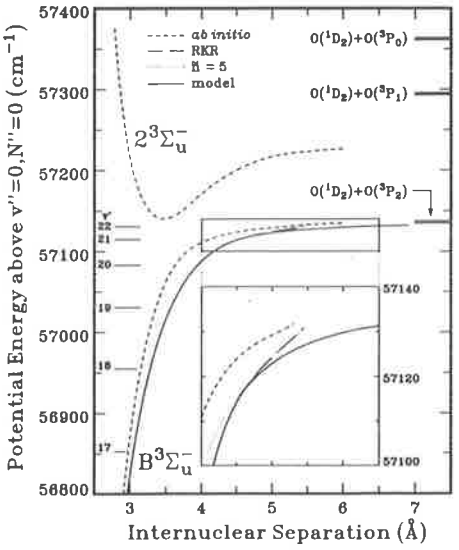

FIG. 5. Outer limb of the $B\,^1\Sigma_u$ potential curve, illustrating the matching of the long range form of the potential, $\tilde{n} = 5$, to the RKR potential. The slope discontinuity is consistent with an avoided crossing with the $2\,^1\Sigma_u$ state, as illustrated by *ab initio* calculations (Ref. 44).

no longer have the simple physical significance implied by perturbation theory. For this reason, the C_5 of this work should be treated as a parameter only.

The model $B\,^3\Sigma_u^-$ potential energy curve consists of an RKR curve joined smoothly, using a cubic spline function, to the C_5/R^5 curve at 4.6 Å. In order to emulate the behavior of the limiting curve of dissociation, a fixed barrier is required at large R. The barrier, the shape of which is unknown, may represent some form of avoided crossing between electronic states converging to the $O(^3P_2) + O(^1D_2)$ dissociation limit. A Gaussian function located at 30 Å with a FWHM of 20 Å and a maximum at 57 136.4 cm^{-1} was found adequately to reproduce the initial linear behavior of the limiting curve of dissociation. The fixed barrier needed to be as broad as possible in order to reduce the corresponding quantal effect. A consequence of the barrier on the calculated absorption cross section is to introduce resonant structure near the absorption edge, however, this structure is blended when convolved with the instrument bandpass and, therefore, does not appear in the calculated apparent cross section.

The model $B\,^3\Sigma_u^-$ potential energy curve reproduces the correct barrier height with rotation, as shown by the solid line in Fig. 4. The calculated absorption edges also yield center positions, evaluated from the maximum derivative, in agreement with the experimental threshold energies, indicating that the quantal effect of the centrifugal barrier is small and within the experimental error of the measured threshold energies. It is seen in Fig. 3 that the model calculation gives a good fit to the experimental measurements and it also defines a theoretical value for the $N'' = 1$ edge of 57 135.4 cm^{-1}.

The dissociation limit determined from the linear extrapolation, 57 136.4 ± 0.9 cm^{-1}, is in agreement with the independent determination of Lewis *et al.*,[14] 57 136.0 ± 0.5 cm^{-1}, but is 9 cm^{-1} above the dissociation limit determined by Brix and Herzberg,[20] 57 127.5 ± 5 cm^{-1}. As Lewis *et al.*[14] have explained, the lower value obtained by Brix and Herzberg[20] is consistent with the difficulties in nonlinear extrapolation of band origins to the dissociation limit. The cyclic determination of the dissociation limit by Albritton *et al.*,[21] 57 130 ± 10 cm^{-1}, is in agreement within the quoted error.

B. Rotational predissociation

At lower transition energies, in the region of high-rotational steps ($N'' \geqslant 17$), structure in addition to the absorption edges appears in the fluorescence spectra. This is most clearly identified in the region of the $N'' = 19$ step (Fig. 6), where the absence of band absorption structure enables the fluorescence signal to be enhanced by using a higher O_2 pressure. The strongest feature in the $O(^1D_2)$ cross section, at 56 603.86 cm^{-1}, is a quasibound shape resonance,[45] an example of rotational predissociation where dissociation occurs by tunneling through the centrifugal barrier of the $B\,^3\Sigma_u^-$ state. This feature is probably narrower than it appears since the observed width is approximately equal to the experimental bandwidth. A weak feature is also observed in the total absorption cross section at the same transition energy. The ratio of apparent line strengths between partial and total cross sections is ~0.5 ± 0.2, indicating an approximately equal probability of rotational and electronic predissociation resulting in the atomic products $O(^1D_2) + O(^3P_2)$ and $O(^3P_2) + O(^3P_2)$, respectively.

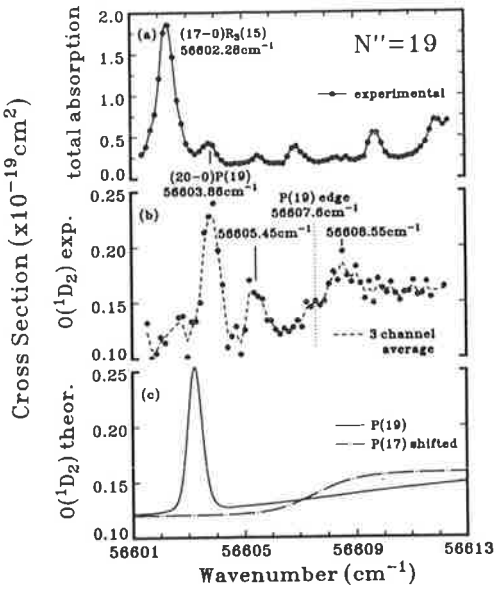

FIG. 6. A quasibound shape resonance, an example of rotational predissociation, located in the region of the $N'' = 19$ absorption edge. The experimental points are separated by 0.16 cm^{-1}. (a) Apparent total photoabsorption cross section. The (17–0)R_3(15) line provides an absolute energy calibration (Ref. 31). (b) Experimental $O(^1D_2)$ cross section revealing an absorption edge and discrete structure. The strongest feature is identified as a (20–0)P(19) transition. The weaker features are unclassified. (c) Model calculation in qualitative agreement with the observed resonance and edge features. Edge sharpness is intimately related to the $B\,^3\Sigma_u^-$ centrifugal barrier. Sharper edges occur for $N'' < 19$, as illustrated for P(17), due to the R^{-5} long range form of the potential. The $N'' = 19$ edge is shallow as its centrifugal barrier includes part of the RKR potential which does not have the correct overall shape.

A somewhat similar resonance feature is observed near the $N'' = 17$ edge where the strongest feature is at 56 709.9 cm^{-1}, separated by 106.1 cm^{-1} from the $N'' = 19$ feature. This separation is very close to the ground state F_2(106.134 cm^{-1}) or F_3(106.14 cm^{-1}) $N'' = 17$ to $N'' = 19$ spacing,[43] suggesting that the resonances are P and R branch transitions to the same upper level, $N' = 18$. The assignment is supported by the theoretical rovibrational eigenvalues, (plus symbols) in Fig. 4. A quasibound level occurs for $v' = 20$, $N' = 18$, just below the $N' = 18$ dissociation threshold.

The resonance adds extra constraints to the model $B\,^3\Sigma_u^-$ potential energy curve since its absolute position, width and separation from the absorption edge, are strongly dependent on the shape of the centrifugal barrier. The calculated rotational transition energies for our model $B\,^3\Sigma_u^-$ potential are systematically above the experimental values. In contrast the calculated transition energy for the $v' = 20$, $N' = 18$, quasibound resonance is 56 602.76 cm^{-1},

below the experimental energy of 56 603.86 cm^{-1}. This might suggest that the transition is an F_3 triplet component. However, energy differences $F_3 - F_2$, evaluated from the line positions of Brix and Herzberg,[19] are linear with $N'(N'+1)$ and extrapolation suggests that the $F_3 - F_2$ splitting for $v' = 20$, $N' = 18$ should be at least 3 cm^{-1}, which is greater than the calculated F_2 deviation from the experimental position. Interestingly, the $v' = 20$ band appears to suffer some form of perturbation in that the slope, $(F_3 - F_2)/N'(N''+1)$, is much less than one would anticipate judging from the slope trend for $v' = 14$–19. It is possible that the transition is perturbed and therefore shifted. For the purpose of this work, the transition was assumed to be an F_2 component. A calculation of the partial cross section for $N'' = 19$, $N' = 18$ produces a structure similar to the experimental measurements, consisting of a (20–0)$P(19)$ resonance and a $P(19)$ edge. The calculated FWHM of the resonance is 0.04 cm^{-1}.

Electronic predissociation of the Schumann–Runge bands of O_2 by the states $^5\Pi_u$,$2\,^3\Sigma_u^+$,$^3\Pi_u$, and $^1\Pi_u$ result in additional broadening and an energy shift of the resonance. The contribution of each predissociating state may also be evaluated from a coupled Schrödinger equation calculation[46] where the predissociating states are mixed with the $B\,^3\Sigma_u^-$ state. It is found that the $^5\Pi_u$ state contributes a width of 0.048 cm^{-1}, with a shift of 0.37 cm^{-1}, the $^3\Sigma_u^+$ state a width of 0.01 cm^{-1} and a shift of 0.10 cm^{-1}. The other two states give a negligible contribution to the total electronic predissociation. As a consequence of electronic predissociation the (20–0)$P(19)$ resonance is shifted by 0.46 cm^{-1}, to 56 603.22 cm^{-1}, from the unperturbed position and is broadened by 0.06 cm^{-1} to give a total width of 0.1 cm^{-1}. The ratio of rotational predissociation width to the total predissociation width is thus calculated to be 0.4, in agreement with the measured probability of dissociation via the $O(^1D_2) + O(^3P_2)$ channel, 0.5 ± 0.2, within experimental error.

As a comparison with the experimental measurements, the cross section excluding rotational excitations below $N'' = 19$, and therefore the discrete structure, has been calculated in the energy region of the $N'' = 19$ edge. The resonance has been scaled, in addition to the Boltzmann factor, by a Hönl–London factor and by 0.5 representing the proportion of molecules that rotationally predissociate. It is seen in Fig. 6(c) that the calculated spectrum is in qualitative agreement with the experimental data. However, the theoretical edge is somewhat shallower than the experimental data would imply and the resonance to edge separation is larger. The sharpness of the calculated edge is intimately related to the shape of the centrifugal barrier in the potential, as is illustrated by a sharper $P(17)$ edge. It happens that the centrifugal barrier for $N' = 18$ includes part of the RKR curve, forming a barrier of less width than the pure $\tilde{n} = 5$ barrier occurring for smaller N'. Extending the $\tilde{n} = 5$ curve to smaller R would sharpen the calculated edge and would require an adjustment of the inner RKR limb to smaller internuclear separation in order to preserve the bound energy levels. Such an adjustment is consistent with the well-known[24] anomalous outward turn of the inner RKR limb for $v' > 17$ and would also shift the avoided crossing region to smaller R in closer agreement with the *ab initio* calculation.[44] At the moment there is insufficient experimental information to determine the exact shape of the $B\,^3\Sigma_u^-$ potential energy curve.

Detailed measurements of each rotational edge are required to improve the model calculation. A study of the higher rotational edges would probe deeper into the $B\,^3\Sigma_u^-$ well, to a region where the outer limb is fully defined by the RKR potential curve, enabling a consistent description to be developed. Further, an examination of fine structure would provide information about the variation of spin–orbit coupling with internuclear separation. A full calculation of the $O(^1D_2)$ cross section in the Schumann–Runge band region requires an S-matrix treatment of the coupled equations resulting in partial cross sections into the open channels.[46] This is beyond the scope of this work.

The model does not account for other observed structure, a resonance at 56 605.45 cm^{-1} and a broad feature at 56 608.55 cm^{-1}. The former resonance could be a perturbation that splits the main resonance into two and the latter a shape dependence of the potential or perhaps an interference effect between the $2\,^3\Sigma_u^-$ and $B\,^3\Sigma_u^-$ valence states in the energy region of the avoided crossing.

V. CONCLUSIONS

The near-dissociation behavior of the $B\,^3\Sigma_u^-$ state of O_2 has been studied from measurements of the excitation spectrum of $O(^1D_2)$. The experimental technique removes the discrete structure of the Schumann–Runge bands that would otherwise mask the detail of the continuum absorption, resulting in the clear observation of rotational threshold absorption edges. Observation of absorption edges in a continuum as a method to determine a dissociation limit has been applied to only one other molecule H_2 by Herzberg.[15,16] In that study, the edges were observed in a measurement of the total absorption cross section and, unlike the present work, the major limitation to the observation of the rotational continuum thresholds was the presence of a large number of overlapping lines.

Our absorption edges define a locus of barrier maxima that is a composite of two curves. For $N'' \leqslant 9$, there is little change in the threshold energies which can be extrapolated to a zero-rotational dissociation limit of 57 136.4 $\pm$ 0.9 cm^{-1}, 9 cm^{-1} above the generally accepted value of 57 127.5 $\pm$ 5 cm^{-1} determined by Brix and Herzberg.[20] For $N'' > 9$, the data follow an ordinary centrifugal barrier curve which is consistent with the $B\,^3\Sigma_u^-$ state potential having the long-range form C_5/R^5. The threshold energies for $N'' > 9$ limit at an energy 2 cm^{-1} below the dissociation energy, suggesting the possibility of a small intrinsic barrier in the $B\,^3\Sigma_u^-$ potential energy curve at large internuclear separation.

A theoretical calculation of the absorption cross section, using a model $B\,^3\Sigma_u^-$ potential having an R^{-5} long range form and a fixed 2 cm^{-1} barrier, accurately reproduces the experimental cross section and absorption edge positions. A slope change evident between the long range form of the

$B\,^3\Sigma_u^-$ state and the inner (RKR) part of the potential well is consistent with an avoided crossing with another $^3\Sigma_u^-$ state near $R = 4.6$ Å. Qualitative support for this observation is provided by *ab initio* calculations.[44]

For the first time in O_2, we have observed rotational predissociation for some transitions near high-rotational absorption edges, corresponding to the tunneling of oxygen atoms through the centrifugal barrier. For the (20–0)$P(19)$ transition, the ratio of rotational predissociation to total predissociation is measured to be 0.5 ± 0.2, indicating an approximate equal probability of predissociation via the electronic and rotational channels.

ACKNOWLEDGMENTS

The authors would like to thank K. Lonsdale and C. Dedman for valuable technical assistance.

[1] B. R. Lewis, S. T. Gibson, M. Emami, and J. H. Carver, J. Quant. Spectrosc. Radiat. Transfer **40**, 1 (1988); **40**, 469 (1988).
[2] P. S. Krupenie, J. Phys. Chem. Ref. Data **1**, 423 (1972).
[3] P. G. Wilkinson and R. S. Mulliken, Astrophys. J. **125**, 594 (1957).
[4] P. S. Julienne, D. Neumann, and M. Krauss, J. Chem. Phys. **64**, 2990 (1976).
[5] A. C. Allison, S. L. Guberman, and A. Dalgarno, J. Geophys. Res. **87**, 923 (1982).
[6] R. D. Hudson, V. L. Carter, and J. A. Stein, J. Geophys. Res. **71**, 2295 (1966).
[7] M. Ogawa, J. Chem. Phys. **54**, 2550 (1971).
[8] V. Hasson and R. W. Nicholls, J. Phys. B **4**, 1789 (1971).
[9] R. D. Hudson and S. H. Mahle, J. Geophys. Res. **77**, 2902 (1972).
[10] A. C. Allison, A. Dalgarno, and N. W. Pasachoff, Planet. Space. Sci. **19**, 1463 (1971).
[11] A. J. Blake, J. Geophys. Res. **84**, 3272 (1979).
[12] H. P. F. Gies, S. T. Gibson, A. J. Blake, and D. G. McCoy, J. Geophys. Res. **87**, 8307 (1982).
[13] P. L. Smith, H. E. Griesinger, J. H. Black, K. Yoshino, and D. E. Freeman, Astrophys. J. **277**, 569 (1984).
[14] B. R. Lewis, L. Berzins, J. H. Carver, and S. T. Gibson, J. Quant. Spectrosc. Radiat. Transfer **33**, 627 (1985).
[15] G. Herzberg and A. Mofils, J. Mol. Spectrosc. **5**, 482 (1960).
[16] G. Herzberg, J. Mol. Spectrosc. **33**, 147 (1970).
[17] B. R. Lewis, L. Berzins, and J. H. Carver, J. Quant. Spectrosc. Radiat. Transfer **36**, 209 (1986).
[18] B. R. Lewis, L. Berzins, J. H. Carver, and S. T. Gibson, J. Quant. Spectrosc. Radiat. Transfer **36**, 187 (1986).
[19] G. Herzberg, *Molecular Spectra and Molecular Structure, The Spectra of Diatomic Molecules*, Vol. 1 (Van Nostrand, New York, 1950).
[20] P. Brix and G. Herzberg, Can. J. Phys. **32**, 110 (1954).
[21] D. L. Albritton, J. T. Moseley, P. C. Cosby, and M. Tadjeddine, J. Mol. Spectrosc. **70**, 326 (1978).
[22] L. C. Lee and T. G. Slanger, J. Chem. Phys. **69**, 4053 (1978).
[23] L. C. Lee, T. G. Slanger, G. Black, and R. L. Sharpless, J. Chem. Phys. **67**, 5602 (1977).
[24] S. T. Gibson, Ph.D. thesis, University of Adelaide, 1983.
[25] J. Tellinguisen, J. Chem. Phys. **89**, 6150 (1988).
[26] I. V. Dvornikov, V. A. Pivovar, and T. D. Sidorova, Opt. Spectrosc. (U.S.S.R.) **58**, 684 (1985).
[27] B. R. Lewis, S. T. Gibson, K. G. H. Baldwin, and J. H. Carver, J. Opt. Soc. Am. B **6**, 1200 (1989).
[28] J. F. Noxon, J. Chem. Phys. **52**, 1852 (1970).
[29] G. E. Streit, C. J. Howard, A. L. Schmeltekopf, J. A. Davidson, and H. I. Schiff, J. Chem. Phys. **65**, 4761 (1976).
[30] S. V. Filseth, A. Zia, and K. H. Welge, J. Chem. Phys. **52**, 5502 (1970).
[31] K. Yoshino, D. E. Freeman, and W. H. Parkinson, J. Phys. Chem. Ref. Data. **13**, 207 (1984).
[32] P. S. Julienne and M. Krauss, J. Mol. Spectrosc. **56**, 270 (1975).
[33] W. Jarmain, J. Quant. Spectrosc. Radiat. Transfer **11**, 421 (1971).
[34] D. M. Creek and R. W. Nicholls, Proc. Roy. Soc. Lond. **A341**, 517 (1975).
[35] P. C. Cosby and H. Helm, J. Chem. Phys. **90**, 1434 (1989).
[36] J. Tellinghuisen, Computer. Phys. Comm. **6**, 221 (1974).
[37] S. T. Gibson, H. P. F. Gies, A. J. Blake, D. G. McCoy, and P. J. Rogers, J. Quant. Spectrosc. Radiat. Transfer **30**, 385 (1983).
[38] R. J. LeRoy, *Molecular Spectroscopy*, Vol. 1 (a Specialist Periodical Report of the Chemical Society of London), edited by R. F. Barrow, D. A. Long, and D. J. Millen (Chemical Society, London, 1973), Chap. 3, pp. 113–176.
[39] T. Y. Chang, Rev. Mod. Phys. **39**, 911 (1967).
[40] R. B. Bernstein, Phys. Rev. Lett. **16**, 385 (1966).
[41] B. R. Johnson, J. Chem. Phys. **67**, 4086 (1977); **69**, 4678 (1978).
[42] J. Wang, D. G. McCoy, A. J. Blake, and L. Torop, J. Quant. Spectrosc. Radiat. Transfer **38**, 19 (1987).
[43] L. Veseth and A. Lofthus, Mol. Phys. **27**, 511 (1974).
[44] R. P. Saxon and B. Liu, J. Chem. Phys. **67**, 5432 (1977).
[45] R. J. LeRoy and R. B. Bernstein, J. Chem. Phys. **54**, 5114 (1971).
[46] B. R. Lewis, S. T. Gibson, and J. Mitroy (unpublished); F. H. Mies, Mol. Phys. **41**, 953 (1980).

4.17 Fine-structure dependence of predissociation linewidth in the Schumann-Runge bands of molecular oxygen

[37] B. R. Lewis, S. T. Gibson, and P. M. Dooley,
Journal of Chemical Physics **100**, 7012–7035 (1994).

Fine-structure dependence of predissociation linewidth in the Schumann–Runge bands of molecular oxygen

B. R. Lewis, S. T. Gibson, and P. M. Dooley
Research School of Physical Sciences and Engineering, The Australian National University, Canberra ACT 0200, Australia

(Received 8 December 1993; accepted 31 January 1994)

Fine-structure-specific predissociation linewidths have been calculated for the $v=0-18$, $N=0-40$ levels of the $B\ ^3\Sigma_u^-$ state of $^{16}O_2$ using a predissociation model which takes into account spin–orbit interactions between the $B\ ^3\Sigma_u^-$ state and the $1\ ^1\Pi_u$, $1\ ^3\Pi_u$, $1\ ^5\Pi_u$, and $2\ ^3\Sigma_u^+$ states, and spin-electronic and L-uncoupling interactions between the $B\ ^3\Sigma_u^-$ and $1\ ^3\Pi_u$ states. The model parameters were optimized by comparing the calculated widths with existing measurements of fine-structure linewidth for $v=0$, 14–18, and new determinations for $v=1$, 2, 5, 7, 9–13 which have been obtained from existing cross sections for the $(v,0)$ and $(v,1)$ Schumann–Runge bands using a fitting procedure which assumes unequal linewidths for the triplet fine-structure components. The L-uncoupling interaction is found to be important for all vibrational levels in determining the width ratios for the fine-structure components, even at quite low rotational levels. The calculated linewidths vary from 0.03 (for $v=16$, $N=30$, F_1) to 4.8 cm^{-1} (for $v=4$, $N=40$, F_3), and good agreement is found between the measurements and the model calculations for most vibrational levels. The calculations are expected to be useful in the construction of state-of-the-art models describing the photochemistry of the middle atmosphere. Greatly improved predissociation model parameters, in good agreement with *ab initio* calculations, have been obtained for the $^3\Pi_u$ and $^1\Pi_u$ states, while the $^3\Sigma_u^+$ parameters remain the most uncertain. The model parameters resulting in the best fit to the widths also give good agreement with observed perturbations in the Schumann–Runge band origins. It is found that the actual separations between triplet fine-structure levels consistently exceed values predicted from generally accepted spectroscopic constants for the $B\ ^3\Sigma_u^-$ state, suggesting that a reevaluation of those constants may be in order.

I. INTRODUCTION

Molecular oxygen plays an important role in the photochemistry of the terrestrial atmosphere. The photodissociation of O_2 by solar ultraviolet radiation between 1750 and 2420 Å is the source of ozone in the stratosphere and mesosphere and O_2 photoabsorption controls the depth of penetration of that radiation into the atmosphere, and the corresponding height profiles for the photodissociation of various trace species. A major source of odd oxygen in the stratosphere and the dominant one in the mesosphere is photodissociation in the Schumann–Runge (SR) band system of O_2, $B\ ^3\Sigma_u^- \leftarrow X\ ^3\Sigma_g^-$, 1750–2050 Å. Predissociation of the bound $B\ ^3\Sigma_u^-$ state by a number of repulsive states correlating with two ground-state oxygen atoms results in a virtual equivalence between the photoabsorption and $O(^3P)$ photodissociation cross sections.

As noted by Nicolet and Mange,[1] and reemphasized by Nicolet,[2] realistic photochemical modeling of the stratosphere and mesosphere is dependent on a precise knowledge of the positions, oscillator strengths, and predissociation linewidths of rovibrational lines from the SR system. Despite uncertainties in early measurements of these quantities, many models were developed[2–22] which have resulted in an increased understanding of the implications for atmospheric photochemistry of ultraviolet absorption in the SR bands. More recently, improved determinations of spectroscopic constants,[23,24] oscillator strengths,[23,25–27] and predissociation linewidths[28,29] have resulted in considerable refinement of the atmospheric models.[30–36] For example, Murtagh[31] and Minschwaner *et al.*[36] now incorporate the rotation dependence of oscillator strength[23] and predissociation linewidth[28] into their calculations.

The predissociation linewidth is crucial in defining the depth of penetration of solar ultraviolet radiation deep into the atmosphere in the regions of low absorption between the rovibrational lines of the SR system. Since Flory[37] first attributed the observed diffuseness of some rovibrational lines on photographic plates to predissociation of the $B\ ^3\Sigma_u^-$ state by a repulsive $^3\Pi_u$ state, there have been many experimental studies[8,38–50] of the predissociation, the situation to 1986 having been summarized by Lewis *et al.*[28] At present, there are two comprehensive sets of predissociation linewidth measurements available in the literature. Lewis *et al.*[28] employed measurements of equivalent width at low and high pressures, together with a complex modeling procedure, to obtain oscillator strengths and linewidths simultaneously for $v=1-19$. Despite an instrumental resolution of 0.045 Å full width half-maximum (FWHM), the equivalent width method resulted in the elimination of instrumental effects, except to the extent that the apparent cross sections failed to reach background between each group of lines studied. Accordingly, it was possible for them to determine predissociation linewidths significantly narrower than their instrumental bandwidth with reasonable accuracy. Lewis *et al.*[28] were the first to demonstrate unambiguously the systematic variation of predissociation linewidth with rotation for several vibrational bands. Yoshino *et al.*[25,27] and Cheung *et al.*[26] have

 0021-9606/94/100(10)/7012/24/$6.00

measured absolute photoabsorption cross sections in the SR system from 1795–2050 Å using a 6.65 m scanning spectrometer with an instrumental resolution of 0.013 Å FWHM. Cheung *et al.*[29] have obtained predissociation linewidths for $v=1-12$ from these measurements using a nonlinear least-squares fitting procedure and assumptions regarding the spacings, relative strengths, and relative widths of the triplet fine-structure components. They found linewidths exhibiting qualitative vibration and rotation dependences similar to those of Lewis *et al.*[28] with maxima at $v=4$, 7, 11, but found unacceptably large systematic differences in linewidth for $v=1$, 2, 4, 9, 10, 12, their values being larger than those of Lewis *et al.*[28]

There have been few measurements of fine-structure-specific predissociation linewidths in the SR band system. The *P*- and *R*-branch triplets are largely incompletely resolved because the splittings of the ground and upper state triplet components F_1, F_2, F_3 are similar and the predissociation linewidths are comparable in magnitude with the fine-structure splittings for many vibrational levels. A few fine-structure-specific linewidths were given by Lewis *et al.*[28] for $v>12$, but no inferences were drawn by those authors regarding the possible fine-structure dependence of linewidth because the number of such measurements was small and because of increased uncertainty in the narrow linewidths involved. Recently, however, Lewis *et al.*[51] have directly measured fine-structure-specific linewidths for the resolved F_1 levels, $v=17$, $N=2-26$, from high-resolution (0.15 $cm^{-1}\approx$0.005 Å FWHM) photoabsorption spectra obtained using a coherent vacuum ultraviolet source based on high-order anti-Stokes stimulated Raman scattering (ASRS) in H_2 of pulsed dye laser radiation.

The inspiration for this work was provided by the recent laser-induced fluorescence (LIF) measurements of Wodtke *et al.*,[52] Yang *et al.*,[53] and, especially, Cosby *et al.*[54] Whereas the photoabsorption analyses of Lewis *et al.*[28] and Cheung *et al.*[29] assumed equal widths for the individual components of the unresolved triplets, resulting in the determination of mean rovibrational linewidths, the LIF measurements demonstrate more clearly the unequal nature of the component linewidths for some vibrational levels, both through excitation from vibrationally excited ground-state levels with favorable triplet splitting constants, and through modification of the absorption profiles by an intensity factor dependent on the predissociation rates for the individual fine-structure components.[54] The LIF flame-based spectra of Wodtke *et al.*[52] show clearly unequal fine-structure linewidths for some rotational levels of the (11,2), (14,3), (15,3), and (16,3) bands, but no quantitative linewidths have been derived. The authors[52] have, however, attributed a $^3\Pi_u$ predissociative mechanism to the $v=11$ levels and a $^3\Sigma_u^+$ mechanism to the $v=14-16$ levels. Yang *et al.*[53] specifically modeled flame-based LIF spectra of high rotational lines from the (10,2) and (11,2) bands to obtain fine-structure-specific linewidths and deduced that an L-uncoupling interaction with a $^3\Pi_u$ state was necessary to explain their results. Cosby *et al.*[54] have obtained detailed rotation- and fine-structure-specific predissociation linewidths for $v=0$, 2 from LIF measurements of the (0,9), (0,10), (0,21), (2,10), and (2,22) SR bands where

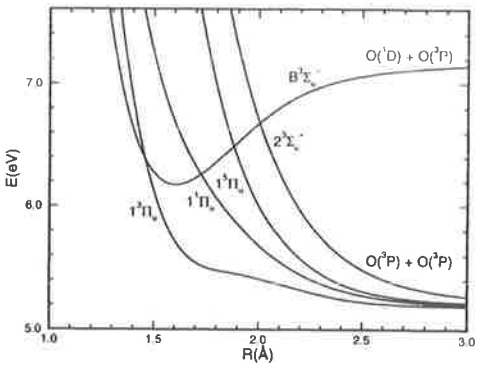

FIG. 1. Potential energy curves for electronic states relevant to the problem of predissociation in the Schumann–Runge bands of O_2. Energies are given relative to the minimum of the ground-state $X\ ^3\Sigma_g^-$ potential energy curve.

the vibrationally excited O_2 was provided by O_3 photodissociation in the Hartley band. They found considerable fine-structure dependence of the linewidths, with the F_1 levels being narrowest for each vibrational level studied. It was necessary for Cosby *et al.*[54] to assume an L-uncoupling interaction with a $^3\Pi_u$ state in order to fully explain their results, just as was done by Yang *et al.*[53]

Theories explaining the observed predissociation in the $B\ ^3\Sigma_u^-$ state of O_2 had developed considerably over several years,[55–60] but it was not until the detailed work of Julienne and Krauss[61] and Julienne[62] that theoretical calculations started to resemble the measured linewidths. They[61,62] found that the predissociation resulted from spin–orbit interactions between the $B\ ^3\Sigma_u^-$ state and repulsive $1\ ^5\Pi_u$, $1\ ^3\Pi_u$, $1\ ^1\Pi_u$, and $2\ ^3\Sigma_u^+$ states, the $B\ ^3\Sigma_u^- - 1\ ^5\Pi_u$ interaction dominating, while an L-uncoupling interaction between the $B\ ^3\Sigma_u^-$ and $1\ ^3\Pi_u$ states was expected to be important for $N>10$. Potential energy curves for the relevant electronic states of O_2 are given in Fig. 1 where the $B\ ^3\Sigma_u^-$ curve is an RKR potential determined by Lewis *et al.*[28] and the repulsive curves are *ab initio* calculations by Partridge *et al.*[63] ($^3\Pi_u$, $^5\Pi_u$) and Partridge[64] ($^1\Pi_u$, $^3\Sigma_u^+$).

The Julienne and Krauss[61]–Julienne[62] (JK) predissociation model, without L-uncoupling, has been applied by Lewis *et al.*[28,65,66] to explain their rovibration-specific predissociation linewidth measurements on $^{16}O_2$, $^{16}O^{18}O$, and $^{18}O_2$ and to obtain fitted values for the JK model parameters describing the repulsive potential energy curves and their spin–orbit interactions with the $B\ ^3\Sigma_u^-$ state. Chiu *et al.*[67] have performed a similar model analysis on the isotopic linewidth measurements of Cheung *et al.*[29] ($^{16}O_2$) and Chiu *et al.*[68] ($^{16}O^{18}O$ and $^{18}O_2$) and have obtained a similar set of parameters. The parameters describing the interaction between the $B\ ^3\Sigma_u^-$ and $1\ ^5\Pi_u$ states are very well determined by such procedures and there is excellent agreement between the two determinations and also with *ab initio* calculations. However, the interactions between the $B\ ^3\Sigma_u^-$ state and the $^3\Pi_u$, $^1\Pi_u$, and $^3\Sigma_u^+$ states are not at all well determined.

The JK predissociation model predicts that the difference in linewidth between the F_3 and F_1 fine-structure levels is

sensitive to the magnitude of the **L**-uncoupling interaction between the $B\ ^3\Sigma_u^-$ and $^3\Pi_u$ states, especially at high rotational excitation. Yang *et al.*[53] applied the JK model, with **L**-uncoupling, to their LIF measurements and determined rough estimates of the **L**-uncoupling interaction for $v=10$, 11. The ratio of the **L**-uncoupling interaction to the spin–orbit interaction for the $^3\Pi_u$ state was found to be ~0.03 by Cosby *et al.*[54] from an application of the JK model to their LIF measurements for $v=0$, 2. While both of the LIF analyses suffer from the need to make various assumptions, since there are only two vibrational levels to analyze, it is clear that a comprehensive analysis of fine-structure-specific linewidths would enable a much more accurate determination of the $B\ ^3\Sigma_u^- - ^3\Pi_u$ interaction than is possible from a fit to average linewidths.

The JK predissociation model has proved remarkably effective in explaining linewidth measurements taken well after its inception with only minor adjustments to the predissociation parameters. The model parameters determined by Lewis *et al.*[28] from a fit to their $N=10$ average linewidths of a JK model with only spin–orbit interaction serve to explain the full rovibrational behavior of the predissociation observed by those authors. After inclusion of the **L**-uncoupling interaction, it is possible to explain the relative fine-structure-specific linewidths measured by Yang *et al.*[53] and Cosby *et al.*[54]

Very recently, Cheung *et al.*[69] have calculated the rotational dependence of predissociation linewidth in the SR bands using a JK model together with a pure precession[70] estimate of the **L**-uncoupling interaction, but they have not addressed the problem of fine-structure-specific linewidths.

In this work, we perform band model fits to the room temperature SR band photoabsorption cross sections of Yoshino *et al.*,[71] assuming unequal linewidths for the individual fine-structure components, and obtain new estimates of the fine-structure-specific linewidths for $v=1$, 2, 5, 7, 9–13. The new linewidths and a selection of the previous determinations are fitted with a JK predissociation model including **L**-uncoupling. The new predissociation parameters determined by the fitting procedure are then used in a JK model to calculate the full manifold of fine-structure- and rovibration-specific predissociation linewidths for the SR bands of O_2.

II. PREDISSOCIATION MODEL

The predissociation model used here is based on that of Julienne and Krauss[61] and Julienne[62] who found that couplings between the $B\ ^3\Sigma_u^-$ state and four repulsive states, $1\ ^5\Pi_u$, $1\ ^3\Pi_u$, $1\ ^1\Pi_u$, and $2\ ^3\Sigma_u^+$, correlating with ground-state dissociation products, $O(^3P)+O(^3P)$, were primarily responsible for the $B\ ^3\Sigma_u^-$ state predissociation, leading to broadening of rovibrational lines from the SR bands and perturbations in the $B\ ^3\Sigma_u^-$ state spectroscopic constants.[61]

Our $B\ ^3\Sigma_u^-$ state potential energy curve $V_B(R)$ was taken from Lewis *et al.*,[28] and, following Julienne and Krauss,[61] the model repulsive potentials were taken as

$$V_k(R)=V_{kx}\exp[-(M_{kx}/V_{kx})(R-R_{kx})]+V_\infty, \tag{1}$$

where R is the internuclear separation, V_∞ is the energy of the $O(^3P)+O(^3P)$ asymptote, R_{kx} is the crossing point, and V_{kx} is the energy at which the repulsive potential V_k crosses the $B\ ^3\Sigma_u^-$ state potential V_B, and $M_{kx}>0$ is the magnitude of the (negative) slope of the repulsive potential V_k at the crossing point.

The interaction of a rovibrational level v, J of a bound state B with a continuum state k at an energy E is determined by the off-diagonal matrix element of the total Hamiltonian **H**:[70]

$$H_{vJE}^{Bk}=\langle\Psi_{Bv J}|\mathbf{H}|\Psi_{kEJ}\rangle$$
$$=\langle\Phi_B(r,R)\chi_{vJ}(R)|\mathbf{H}|\Phi_k(r,R)\chi_{EJ}(R)\rangle, \tag{2}$$

where r represents the electronic coordinates, the wave functions Ψ have been expressed as Born–Oppenheimer (BO) products of electronic Φ and vibrational χ wave functions, and the rotational wave functions have been suppressed. The bound and energy-normalized[70] continuum vibrational wave functions are solutions of the uncoupled radial Schrödinger equations,

$$\left\{-\frac{\hbar^2}{2\mu}\frac{d^2}{dR^2}+V_B(R)+\frac{\hbar^2}{2\mu R^2}\ [J(J+1)]-E\right\}\chi_{vJ}(R)=0, \tag{3}$$

$$\left\{-\frac{\hbar^2}{2\mu}\frac{d^2}{dR^2}+V_k(R)+\frac{\hbar^2}{2\mu R^2}\ [J(J+1)]-E\right\}\chi_{EJ}(R)=0, \tag{4}$$

where μ is the molecular reduced mass, and the J-independent centrifugal terms have been included in the electronic potentials $V(R)$.

In the case of an isolated level of the bound state, and when transitions from the ground state into the predissociating continuum do not carry an oscillator strength, the Fano[72,73] configuration-interaction theory predicts that the discrete level will be broadened into a Lorentzian profile of FWHM width:

$$\Gamma_k(v,J)=2\pi|H_{vJE}^{Bk}|^2, \tag{5}$$

similar to the well-known Fermi–Wentzel Golden Rule, where the interaction matrix element is evaluated at an energy equal to the rovibrational energy of the bound state. In the case of predissociation of the $B\ ^3\Sigma_u^-$ state of O_2, transitions from the ground state $X\ ^3\Sigma_g^-$ into all predissociating states are electric-dipole forbidden, except in the case of the $^3\Pi_u$ state. Absorption into this state, however, has been shown to be very weak in the region of the SR bands[74–76] and is not expected to produce significantly non-Lorentzian line shapes. Similarly, except in the case of some F_1 and F_3 levels of very low rotational excitation, discussed in detail by Julienne,[62] the isolated resonance approximation is expected to hold for the rovibrational lines of the SR bands which may, therefore, be represented as independent Lorentzian profiles, or Voigt profiles if the Doppler contribution to the line shape is included.

For predissociation of the bound state B by multiple continua k, the individual contributions to the broadening of the resonance are additive,[61]

$$\Gamma(v,J)=\sum_k \Gamma_k(v,J)=2\pi\sum_k |H^{Bk}_{vJE}|^2, \tag{6}$$

provided that the continua have no mutual interactions. From Fig. 1, it is evident that the repulsive states contributing to the predissociation of the $B\ ^3\Sigma_u^-$ state are well separated, implying negligible mutual vibrational Franck–Condon overlap factors. Therefore, it is not necessary to consider explicitly electronic interactions between the repulsive states and Eq. (6) may be applied to the study of predissociation in the SR bands of O_2.

Lefebvre-Brion and Field[70] discuss comprehensively the Hamiltonian terms neglected in the nonrelativistic BO approximation and summarize, in their Table 2.2, the corresponding off-diagonal matrix elements of the total Hamiltonian between BO product wave functions, together with appropriate selection rules for the various angular momenta and their projections. Terms important to this work which have been neglected in the BO approximation are the relativistic part of the Hamiltonian

$$\mathbf{H}^{\mathrm{REL}}=\mathbf{H}^{\mathrm{SO}}+\mathbf{H}^{\mathrm{SS}}+\mathbf{H}^{\mathrm{SR}}, \tag{7}$$

where $\mathbf{H}^{\mathrm{SO}}$, $\mathbf{H}^{\mathrm{SS}}$, and $\mathbf{H}^{\mathrm{SR}}$ contain the spin–orbit, spin–spin, and spin–rotation interactions, respectively, and the cross terms from the rotational part of the Hamiltonian

$$\mathbf{H}^{\mathrm{ROT}}=\frac{1}{2\mu R^2}\ [(\mathbf{J}^2-\mathbf{J}_z^2)+(\mathbf{L}^2-\mathbf{L}_z^2)+(\mathbf{S}^2-\mathbf{S}_z^2)]+\mathbf{H}^{SE}+\mathbf{H}^{JL}+\mathbf{H}^{JS}, \tag{8}$$

where

$$\mathbf{H}^{SE}=\frac{1}{2\mu R^2}\ (\mathbf{L}^+\mathbf{S}^-+\mathbf{L}^-\mathbf{S}^+), \tag{9}$$

$$\mathbf{H}^{JL}=-\frac{1}{2\mu R^2}\ (\mathbf{J}^+\mathbf{L}^-+\mathbf{J}^-\mathbf{L}^+), \tag{10}$$

and

$$\mathbf{H}^{JS}=-\frac{1}{2\mu R^2}\ (\mathbf{J}^+\mathbf{S}^-+\mathbf{J}^-\mathbf{S}^+) \tag{11}$$

contain the spin-electronic, **L**-uncoupling, and **S**-uncoupling interactions, respectively. The operators **J**, **L**, and **S** represent the total angular momentum exclusive of nuclear spin, the total electronic orbital angular momentum, and the total electron spin, respectively, $\mathbf{J}_z$, $\mathbf{L}_z$, and $\mathbf{S}_z$ their projections onto the internuclear axis, and $\mathbf{J}^\pm$, $\mathbf{L}^\pm$, and $\mathbf{S}^\pm$ the corresponding molecule-fixed raising and lowering operators. We adopt the approximation of Julienne and Krauss,[61] $\mathbf{H}^{\mathrm{REL}}\approx\mathbf{H}^{\mathrm{SO}}$, where the smaller terms $\mathbf{H}^{\mathrm{SS}}$ and $\mathbf{H}^{\mathrm{SR}}$ have been neglected. In this order of approximation, after applying the selection rules for perturbations between electronic states,[70] it has been shown[61,62] that predissociation of the $B\ ^3\Sigma_u^-$ state is caused by spin–orbit interaction with the $1\ ^5\Pi_u$, $1\ ^1\Pi_u$, and $2\ ^3\Sigma_u^+$ states, and a combination of spin–orbit, spin-electronic, and **L**-uncoupling interactions with the $1\ ^3\Pi_u$ state. The possibility of an **S**-uncoupling interaction between the $\Delta\Omega=\pm1$ components of the $B\ ^3\Sigma_u^-$ and $2\ ^3\Sigma_u^+$ states is ruled out by the $+\leftrightarrow-$ selection rule resulting from a consideration of the transformation properties of the relevant matrix elements under the σ_v symmetry operation.

TABLE I. Off-diagonal matrix elements of the spin–orbit and rotational operators between Hund's case (a) parity-basis wave functions for electronic states relevant to the predissociation of the $B\ ^3\Sigma_u^-$ state of O_2.

$^{2S+1}\Lambda_\Omega$	$\langle {}^3\Sigma_\Omega^-, J,v,f^e\vert\mathbf{H}^{\mathrm{SO}}+\mathbf{H}^{\mathrm{ROT}}\vert {}^{2S+1}\Lambda_\Omega, J,E,f^e\rangle$[a] $^3\Sigma_0^-(e)$	$^3\Sigma_1^-$
$^3\Sigma_1^+$	0	ξ_+
$^1\Pi_1$	0	ξ_1
$^3\Pi_0$	$\sqrt{2}(\xi_3+\sqrt{2}\eta)$	$\mp\eta\sqrt{J(J+1)}$
$^3\Pi_1$	$-\eta\sqrt{2J(J+1)}$	$\xi_3+\sqrt{2}\eta$
$^3\Pi_2$	0	$-\eta\sqrt{J(J+1)-2}$
$^5\Pi_0$	ξ_5	0
$^5\Pi_1(\vert\Sigma\vert=0)$	0	$\xi_5/\sqrt{6}$
$^5\Pi_1(\vert\Sigma\vert=2)$	0	ξ_5

[a] $\xi_k(v,J,E)=\langle v,J\vert A_k(R)\vert E,J\rangle$,
$A_+(R)=\langle {}^3\Sigma_1^-\vert\mathbf{H}^{\mathrm{SO}}\vert {}^3\Sigma_1^+\rangle$,
$A_1(R)=\langle {}^3\Sigma_1^-\vert\mathbf{H}^{\mathrm{SO}}\vert {}^1\Pi_1\rangle$,
$A_3(R)=\langle {}^3\Sigma_1^-\vert\mathbf{H}^{\mathrm{SO}}\vert {}^3\Pi_1\rangle$,
$A_5(R)=\langle {}^3\Sigma_1^-\vert\mathbf{H}^{\mathrm{SO}}\vert {}^5\Pi_1,\Sigma=2\rangle$,
$\eta(v,J,E)=\langle v,J\vert\langle {}^3\Sigma^-\vert\mathbf{BL}^-\vert {}^3\Pi\rangle\vert E,J\rangle$,

The nonzero interaction matrix elements of $\mathbf{H}^{\mathrm{SO}}+\mathbf{H}^{\mathrm{ROT}}$ needed for a calculation of the $B\ ^3\Sigma_u^-$ state predissociation are given in Table I with wave functions expressed in the Hund's case (a) (f^e) parity basis,[70] where the $^3\Sigma_0^-$ wave function consists of the single component of e parity, $\vert {}^3\Sigma_0^-,J,v,e\rangle$, and all others are given by

$$\vert {}^{2S+1}\Lambda_\Omega,J,v,f^e\rangle=\frac{1}{\sqrt{2}}\ [\vert\Lambda,S\Sigma,J\Omega,v\rangle\pm(-)^{-S+s}\times\vert-\Lambda,S-\Sigma,J-\Omega,v\rangle], \tag{12}$$

where Λ is the quantum number of the projection of the electronic orbital angular momentum onto the internuclear axis, S and Σ are the quantum numbers of the electron spin and its projection, J and $\Omega=\Lambda+\Sigma$ are the quantum numbers of the total angular momentum and its projection, and $s=1$ for Σ^- states but $s=0$ otherwise. The phase conventions used in obtaining the results in Table I are consistent with those used by Lefebvre-Brion and Field[70] and our matrix elements are equivalent to those of Johns and Lepard,[77] except that we have not used the macroscopic form $\mathbf{AL}\cdot\mathbf{S}$ of the spin–orbit operator $\mathbf{H}^{\mathrm{SO}}$. As emphasized by Lefebvre-Brion and Field,[70] the macroscopic form of $\mathbf{H}^{\mathrm{SO}}$ has led to many errors in the literature, including the prediction of zero interaction between $^3\Sigma^+$ and $^3\Sigma^-$ states. In fact, the $^3\Sigma_1^+$ and $^3\Sigma_1^-$ components can be shown to interact[62,70] by using the microscopic form of the spin–orbit operator, $\Sigma_i\hat{a}_i\mathbf{l}_i\cdot s_i$. The interaction matrix elements between the $^3\Sigma^-$ state and each other state k considered in Table I are given in terms of the phenomenological spin–orbit parameters $\xi_k(v,J,E)$. The relative interactions with specific Ω substates of a given electronic state have been determined using the Wigner–Eckart theorem.[70] In the case of the $^3\Sigma^- - {}^3\Pi$ interaction, the additional parameter $\eta(v,J,E)$ contains the $\Delta\Lambda=\pm1$ interactions resulting from the $\mathbf{L}^\pm$ operator, that is the spin-electronic and

TABLE II. Partial triplet fine-structure predissociation widths for the $B\ ^3\Sigma_u^-$ state of O_2 arising from interactions with each continuum electronic state contributing to the predissociation.

State, k	F_i	$\Gamma_k(^3\Sigma_u^-, J, v, F_i)^a$
$^3\Sigma_u^+$	F_1	$2\pi b^2\xi_+^2$
	F_2	$2\pi\xi_+^2$
	F_3	$2\pi a^2\xi_+^2$
$^1\Pi_u$	F_1	$2\pi b^2\xi_1^2$
	F_2	$2\pi\xi_1^2$
	F_3	$2\pi a^2\xi_1^2$
$^3\Pi_u$	F_1	$2\pi[(1+a^2)\xi_3^2+(4a^2+2x-8ab\sqrt{x})\eta^2$ $+2\sqrt{2}(1+a^2-2ab\sqrt{x})\eta\xi_3]$
	F_2	$2\pi(\xi_3^2+2x\eta^2+2\sqrt{2}\eta\xi_3)$
	F_3	$2\pi[(1+b^2)\xi_3^2+(4b^2+2x+8ab\sqrt{x})\eta^2$ $+2\sqrt{2}(1+b^2+2ab\sqrt{x})\eta\xi_3]$
$^5\Pi_u$	F_1	$2\pi(1+b^2/6)\xi_5^2$
	F_2	$7\pi\xi_5^2/3$
	F_3	$2\pi(1+a^2/6)\xi_5^2$

$^a x=J(J+1)$.

L-uncoupling interactions. The full **L**-uncoupling matrix elements are J-dependent and are expected to produce significant effects at high rotation.

The most general wave functions for the $B\ ^3\Sigma_u^-$ state are those intermediate between Hund's cases (a) and (b),

$$|^3\Sigma_u^-, F_1, J, v\rangle = a(v,J)|^3\Sigma_0^-, J, v, e\rangle + b(v,J)|^3\Sigma_1^-, J, v, e\rangle, \tag{13}$$

$$|^3\Sigma_u^-, F_2, J, v\rangle = |^3\Sigma_1^-, J, v, f\rangle, \tag{14}$$

$$|^3\Sigma_u^-, F_3, J, v\rangle = b(v,J)|^3\Sigma_0^-, J, v, e\rangle - a(v,J)|^3\Sigma_1^-, J, v, e\rangle. \tag{15}$$

The mixing parameters are given by

$$a(v,J)=\sqrt{[F_2(v,J)-F_1(v,J)]/[F_3(v,J)-F_1(v,J)]}, \tag{16}$$

$$b(v,J)=\sqrt{[F_3(v,J)-F_2(v,J)]/[F_3(v,J)-F_1(v,J)]}, \tag{17}$$

where $F_i(v,J)$ are the measured fine-structure term values of the $B\ ^3\Sigma_u^-$ state, provided that centrifugal distortion can be neglected.[78] Using Eqs. (2) and (5), with $\mathbf{H}=\mathbf{H}^{SO}+\mathbf{H}^{ROT}$, summing over the Ω substates with the interaction matrix elements given in Table I, and using the mixed case (a)–(b) $B\ ^3\Sigma_u^-$ wave functions of Eqs. (13)–(15), we have calculated expressions for the fine-structure partial widths for predissociation of the $B\ ^3\Sigma_u^-$ state by each repulsive state and the results are presented in Table II. As implied by Eq. (6), the total predissociation width for each fine-structure component F_i may be obtained by summing the contributions from the interactions with each electronic state. Following Julienne and Krauss,[61] we have assumed Hund's case (a) coupling for the $^5\Pi_u$ and $^3\Pi_u$ states. The results in Table II are independent of the $^5\Pi_u$ and $^3\Pi_u$ Hund's coupling cases, however, provided that the rovibrational overlap factors $\langle\chi_{vJ}(R)|\chi_{EJ}(R)\rangle$ can be taken to be independent of the Ω substate.

Julienne and Krauss[61] have given fine-structure partial width expressions for the predissociation of $^3\Sigma^-$ states with case (a) and case (b) coupling which include spin-electronic interaction and **L**-uncoupling between the $^3\Sigma^-$ and $^3\Pi$ states. Julienne[62] has extended these expressions to the case of $^3\Sigma^-$ states with coupling intermediate between cases (a) and (b), but has considered only spin–orbit interactions. The general expressions given in Table II reduce to those obtained by Julienne[62] for the case of spin–orbit interaction only, ($\eta=0$), and to those obtained by Julienne and Krauss[61] for case (a), ($a=1$, $b=0$). For a case (b) $^3\Sigma^-$ state,

$$a(v,J)=\sqrt{J/(2J+1)}, \quad b(v,J)=\sqrt{(J+1)/(2J+1)}, \tag{18}$$

and our expressions reduce to the case (b) expressions of Julienne and Krauss,[61] provided that we make the substitutions $J=N+1$, $J=N$, and $J=N-1$ for the F_1, F_2, and F_3 levels, respectively. However, our expressions for the F_1 and F_3 predissociation widths resulting from the $^3\Pi_u$ interaction differ from those obtained by Yang *et al.*,[53] repeated by Cosby *et al.*,[54] which appear to underestimate both the F_1 and F_3 widths relative to the F_2 width when $\eta\xi_3>0$. As we will show later, in the case of $B\ ^3\Sigma_u^-$ predissociation $\eta/\xi_3\approx 0.02$ and the discrepancy between our expression for the F_1 width, e.g., and that of Yang *et al.*[53] is in the range 6%–8% for $0<J<30$. The expressions of Yang *et al.* fail to reduce to those of Julienne and Krauss[61] for the limiting coupling cases (a) and (b).

Nevertheless, the general conclusions of Yang *et al.*[53] regarding the $^3\Sigma_u-{}^3\Pi_u$ interaction are valid. Although the main contribution to the rotationless width comes from the spin–orbit term proportional to ξ_3^2, a significant part of the width at high rotational excitation comes from the J-dependent cross terms proportional to $\eta\xi_3$ which result from constructive and destructive quantum interference between the spin–orbit and **L**-uncoupling interaction amplitudes. If $\eta\xi_3>0$, the F_3 width increases with rotation, while the F_1 width decreases. In the case of the F_1 levels, we have the counterintuitive result that the inclusion of an extra dissociation mechanism (**L**-uncoupling) results in an *increased* lifetime.

As is well known,[62,70] if the electronic part of the matrix element in Eq. (2) is independent of R, or varies linearly with R, then we may express the interaction matrix element as

$$H^{Bk}_{vJE}=H^{Bk}\langle v,J|E,J\rangle, \tag{19}$$

where we have represented the vibrational wave functions χ by their quantum numbers and H^{Bk} is the value of the electronic interaction matrix element at the R-centroid of the interaction, corresponding approximately to the crossing point of the predissociated and predissociating potential energy curves. If we adopt this approximation, the spin–orbit matrix elements defined in Table I may then be written

$$\xi_k(v,J,E)=A_{kx}\langle v,J|E,J\rangle, \tag{20}$$

where the electronic spin–orbit matrix elements $A_k(R)$ have been replaced by their values A_{kx} at the crossing points R_{kx}. Similarly, we may write

$$\eta(v,J,E)=\langle v,J|B(R)|E,J\rangle\langle {}^3\Sigma|\mathbf{L}^-|{}^3\Pi\rangle$$
$$=B_x\langle {}^3\Sigma|\mathbf{L}^-|{}^3\Pi\rangle\langle v,J|E,J\rangle, \quad (21)$$

where B_x is an effective rotational constant applying near the crossing point of the $B\ {}^3\Sigma_u^-$ and ${}^3\Pi_u$ potential energy curves. The ratio η/ξ_3 then becomes

$$p=\eta/\xi_3=B_x\langle {}^3\Sigma|\mathbf{L}^-|{}^3\Pi\rangle/A_{3x}. \quad (22)$$

For perturbations between any pair of electronic states, the R-centroid is nearly constant,[79] essentially independent of v and J, and it follows that p can also be taken as a constant. The results of Field *et al.*[79] have demonstrated this fact for a perturbation of the $a\ {}^3\Pi$ state of CO by the $a'\ {}^3\Sigma^+$ state. Cheung *et al.*,[69] by explicit calculation of η for the $B\ {}^3\Sigma_u^- - {}^3\Pi_u$ interaction in O_2 using the hypothesis of pure precession, have also shown that the ratio $p=\eta/\xi_3$ is nearly independent of vibration.

Thus, within the approximations of the model described above, the $B\ {}^3\Sigma_u^-$ predissociation is determined by a set of 13 parameters. The four exponential repulsive model potentials V_k [Eq. (1)] are each described by a crossing point R_{kx} and a slope M_{kx}, and their spin–orbit interactions with the $B\ {}^3\Sigma_u^-$ state are described by $A_{kx}\approx A_k(R_x)$ (Table I), while the single parameter $p=\eta/\xi_3$ [Eq. (22)] describes the spin-electronic and L-uncoupling interactions between the $B\ {}^3\Sigma_u^-$ and ${}^3\Pi_u$ states.

For a given set of predissociation parameters and for each rotation J, each pair of bound state and continuum vibrational wave functions is obtained from a numerical solution of Eqs. (3) and (4) using the Numerov method, as described by Johnson.[80] The corresponding partial widths [Eq. (5)] are calculated using the expressions given in Table II with the matrix elements defined in Table I. The F_2 partial widths are calculated directly and the implicit assumption that the vibrational overlap factors $\langle v,J|E,J\rangle$ are independent of the fine-structure level is made in the calculation of the F_1 and F_3 widths. The total predissociation widths $\Gamma(v,J,F_i)$ are obtained by summing the individual contributions according to Eq. (6), and the results are rearranged as $\Gamma(v,N,F_i)$, since the SR lines actually occur as N-triplets, in order to facilitate comparisons with experiment. Provided that sufficient experimental linewidths are available, optimum values of the 13 parameters of the predissociation model can be obtained by least-squares fitting the model to the measured widths.

Predissociation of the $B\ {}^3\Sigma_u^-$ state, in addition to broadening the rovibrational levels, results in measurable perturbations in the SR band origins.[61] It is of interest to see whether model parameters determined from a fit to observed predissociation linewidths serve to explain the measured band origin perturbations. Rather than use the perturbative technique whereby the shift of a resonance is given by a principal part integral,[61] we use the coupled-equations technique[70] as applied previously by Cheung *et al.*[81] Rather than solve the uncoupled Eqs. (3) and (4), we use the Numerov renormalization method of Johnson,[82] to solve the *coupled* equations

$$\left\{-\frac{\hbar^2}{2\mu}\frac{d^2}{dR^2}+V_B(R)+\frac{\hbar^2}{2\mu R^2}\ [J(J+1)]-E\right\}\chi'_{vJ}(R)$$
$$=H^{Bk}(R)\chi'_{EJ}(R), \quad (23)$$

$$\left\{-\frac{\hbar^2}{2\mu}\frac{d^2}{dR^2}+V_k(R)+\frac{\hbar^2}{2\mu R^2}\ [J(J+1)]-E\right\}\chi'_{EJ}(R)$$
$$=H^{Bk}(R)\chi'_{vJ}(R), \quad (24)$$

where the vibrational functions χ' are unknown exact solutions and $H^{Bk}(R)$ is the electronic part of the interaction matrix element between the bound state B and the repulsive state k. We treat interactions between the $B\ {}^3\Sigma_u^-$ state and each repulsive state separately, the resonance energy being determined from the scattering phase shift of the continuum state wave function χ'_{EJ}. The partial energy shift $S_k(v)$ is then the difference between the resonance energy and the eigenvalue for the uncoupled closed channel, Eq. (3). Provided that mutual interactions between the repulsive states can be ignored, the total energy shift is equal to the sum of the partial shifts,

$$S(v)=\sum_k S_k(v). \quad (25)$$

Since the band origin refers to the F_2 levels with $J=0$, we need only solve the *rotationless* Eqs. (23) and (24), with the electronic coupling matrix elements $H^{Bk}(R)$ given by the $A_{kx}=A_k(R_x)$ of Table I, except that, for the ${}^5\Pi_u$ state, we have used $H^{B5}(R)=\sqrt{7/6}A_{5x}$ because the effects of the ${}^5\Pi_1$ ($|\Sigma|=0$ and $|\Sigma|=2$) interactions have been condensed into a single interaction. This, of course, is equivalent to assuming that a single potential energy curve describes both ${}^5\Pi_1$ substates.

III. FITTING PROCEDURE

In order to obtain predissociation model parameters capable of reproducing the detailed rovibrational and fine-structure dependence of predissociation linewidth in the SR bands of O_2, it is necessary to have an extensive set of measured fine-structure linewidths with which comparisons can be made. Prior to this work, the only fine-structure linewidths available were for a few levels, mainly F_1, for $v\geq 13$ from Lewis *et al.*,[28] the F_1 levels for $v=17$ from Lewis *et al.*,[51] a small number of high rotational levels for $v=10$, 11 from Yang *et al.*,[53] and the recent extensive LIF measurements for F_1, F_2, and F_3 levels with $v=0$, 2 from Cosby *et al.*[54] who realized that insufficient data were available for the creation of a realistic fine-structure predissociation model.

Recently, Yoshino *et al.*[71] have published high-resolution photoabsorption cross sections for O_2 in the region of the (1,0)–(12,0) SR bands, combining their previous measurements[25,26] with new measurements at high column densities in the regions between the main branch absorption lines. The greatly improved statistical accuracy of these new results enables the study of many highly rotationally excited levels which provide valuable information on both the rovibrational and fine-structure dependence of the predissocia-

tion linewidth. In this work, we extract predissociation linewidths, including a significant proportion of fine-structure-specific widths, from the measurements of Yoshino *et al.*[71] using an iterative nonlinear least-squares procedure which compares the observed cross sections with a simple model cross section appropriate to the experimental conditions. Our approach, while similar to that of Cheung *et al.*[29] who fitted a Lorentzian profile model to their earlier measurements[25,26] and obtained fine-structure-averaged predissociation linewidths, differs in several important details.

As we shall see, the individual predissociation linewidths which we obtain range from ~0.2–4 cm^{-1} FWHM, while the Doppler linewidth, due to thermal molecular motion, is ~0.12 cm^{-1} FWHM near 50 000 cm^{-1} at room temperature. Since, in the case of the narrowest lines, the predissociation linewidth approaches the Doppler width, we represent each rotational line in our model with a Voigt profile which combines the effects of Doppler and predissociation broadening. We use the second approximation of Whiting[83] in calculations of the Voigt profile.

The nominal instrumental bandwidth for the 6.65 m scanning photoelectric spectrometer used by Yoshino *et al.*[71] is 0.013 Å FWHM, which is narrow enough to give absolute cross section measurements for most of the blended features of the (1,0)–(12,0) SR bands. It is possible, however, to also obtain information on some of the higher rotational lines from the less predissociated (13,0) band for which a knowledge of the instrumental function becomes important. By fitting instrumentally degraded Voigt profiles to several highly rotationally excited isolated fine-structure lines from the (14,0) band, which have very narrow predissociation linewidths and are thus totally instrument limited, we obtained an effective bandwidth of 0.0145 Å FWHM for the instrument function, which was assumed to be Gaussian. For the analysis of all other data, we degraded our model cross sections (in transmission) with this instrumental function before comparison with the measured cross sections of Yoshino *et al.*[71]

In the case of the (1,0)–(12,0) SR bands, since the predissociation linewidths are comparable with, or greater than, the triplet fine-structure splittings, no fully resolved fine-structure components occur. However, shoulders and asymmetries are observable in the combined cross sections of many of the N-triplets, allowing the determination of individual fine-structure predissociation linewidths from the incompletely resolved features in those cases. As far as is possible, we do not constrain the positions of the line centers of the triplet components in the fitting procedure. However, at low rotational excitation, and for $v \approx 6$, where the $P(N'')$ and $R(N''+2)$ features coincide, this approach becomes impractical and we calculate and constrain the splittings of the three (or six) components using the ground $X\ ^3\Sigma_g^-$ state spectroscopic constants of Veseth and Lofthus[84] and the $B\ ^3\Sigma_u^-$ state spectroscopic constants of Lewis *et al.*[23]

Except for some completely resolved triplets in the (13,0) band, in general we constrain the *relative* intensities of the three (or six) components of a spectral feature. The calculated line strength ratios are determined from the product of Boltzmann factors calculated from the ground-state energy levels[84] and Hönl–London factors taken from Tatum and Watson[85] for $^3\Sigma^- - ^3\Sigma^-$ transitions with coupling intermediate between Hund's cases (a) and (b). The constraint on the relative line strengths is not restrictive since they are known accurately. The variation of band oscillator strength with rotational excitation, reported by Lewis *et al.*,[23] is not important here since we are dealing only with *relative* line strengths and each line group studied consists of fine-structure lines of similar rotational excitation.

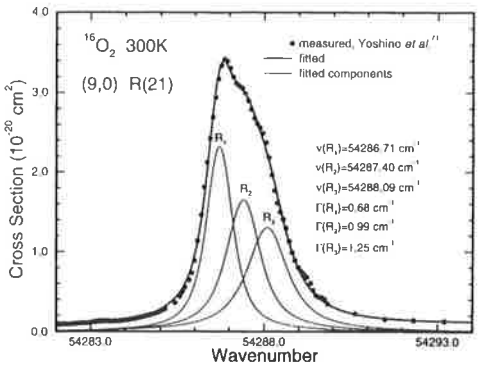

FIG. 2. The results of a Voigt profile fit to the partially resolved $R(21)$ triplet from the (9,0) Schumann–Runge band of O_2 assuming unequal predissociation linewidths for the individual triplet fine-structure components. The separate fine-structure contributions to the total cross section are also shown.

In the most favorable cases, each group of lines studied is represented as a sum of instrumentally degraded Voigt profiles with constrained relative strengths, but unconstrained line centers and unequal fine-structure predissociation linewidth components. The background pseudocontinuum due to the wings of neighboring lines not explicitly included in the fitting procedure is taken to be a quadratic function of energy. Weak features are allowed for by either explicit fitting, or a calculated correction if the interfering feature is not visible under the stronger lines being studied. In cases where the triplet features are completely unresolved and it becomes inappropriate to attempt to determine separate fine-structure linewidths, we constrain the multiplet splittings and assume equal widths for the fine-structure components, as did Cheung *et al.*[29]

Figures 2 and 3 illustrate the application of our model fitting procedure to the partially resolved (9,0) $R(21)$ and (11,0) $R(17)$ triplet cross sections of Yoshino *et al.*[71] It can be seen that the quality of the fits is excellent and that the triplet component predissociation linewidths are noticeably unequal in each case. In contrast, Figs. 4 and 5 of Cheung *et al.*[29] illustrate the rather poor quality of their fits, based on constrained triplet splittings and equal fine-structure linewidths, to the same groups of lines. Our fitted values for the triplet splittings significantly exceed the calculated splittings. For example, the fitted (9,0) $R_3(21)-R_1(21)$ splitting is 1.38 ± 0.07 cm^{-1}, compared with splittings of 1.19 and 1.14 cm^{-1} calculated from the spectroscopic constants of Lewis *et al.*[23] and Cheung *et al.*,[24] respectively. In the case of the

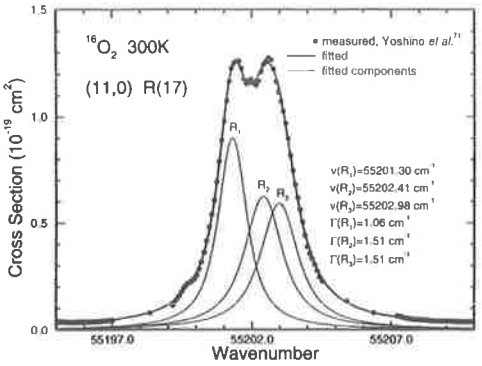

FIG. 3. The results of a Voigt profile fit to the partially resolved $R(17)$ triplet from the (11,0) Schumann–Runge band of O_2 assuming unequal predissociation linewidths for the individual triplet fine-structure components. The separate fine-structure contributions to the total cross section are also shown.

(11,0) $R_3(17)-R_1(17)$ splitting, the corresponding values are 1.68 ± 0.06, 1.31, and 1.25 cm^{-1}. These observations can be understood if we note that the $B\ ^3\Sigma_u^-$ state spin-splitting constants in the literature, relevant to high rotational lines in the (9,0) and (11,0) bands, result from spectrographic measurements[86] of features where the fine-structure wave numbers have been estimated from the positions of blended lines or shoulders. It is well known that such procedures underestimate the actual separations of the individual line centers. For example, Yoshino *et al.*[86] give a measured (9,0) $R_3(21)-R_1(21)$ separation of 0.88 cm^{-1}, considerably less than both the calculated and our fitted separation. More evidence for the inaccuracy of existing spin-splitting constants for the $B\ ^3\Sigma_u^-$ state of O_2 will be presented in Sec. IV.

IV. RESULTS AND DISCUSSION

A. Linewidths

1. Measurements

Predissociation linewidths which we have obtained from the measured cross sections of Yoshino *et al.*[71] for $v=1-13$ are given in Table III. Where possible, the tabulated widths are averages of separate determinations for P- and R-branch lines terminating on the same $B\ ^3\Sigma_u^-$ state level. Fine-structure-specific widths were obtained for some or all of the rovibrational lines studied for $v=1$, 2, 5, 7–13. With the exceptions of the LIF measurements of Cosby *et al.*[54] for $v=2$, $N\leq24$ and Yang *et al.*[53] for $v=10$, $N=16-20$ and $v=11$, $N=28-30$, ours are the first fine-structure-specific linewidths reported for $v=1-12$. In cases where it was not possible to obtain meaningful fine-structure-specific linewidths, we determined fine-structure-averaged widths according to the procedures described in Sec. III. For most such lines with $v=3-9$, this necessitated the constraint of the fine-structure splittings to the calculated values.

The error estimates given in Table III are statistical uncertainties determined by the least-squares fitting algorithm and are related to the overall quality of the fit and the sensitivity of the fit to the particular width of interest. Errors due to uncertainties in the experimental wavelength scale and cross sections, and the constraint of triplet relative line strengths to the theoretical values, are expected to be small compared with the tabulated error estimates. In the case of the fine-structure-averaged widths, however, it is not clear how to assess quantitatively possible additional errors resulting from the necessary, but incorrect, assumption of equal fine-structure linewidths and the constraint, when applied, of the fine-structure splittings to the theoretical values.

The linewidths in Table III for $v=1$, 2 have been corrected for the effects of pressure broadening using a broadening coefficient of 0.20 $cm^{-1}\ atm^{-1}$.[87] For $v=1$ and $v=2$, $N<24$, we have assumed that the experimental cross sections were measured at a pressure of 300 Torr,[29] while for the very weak lines with $v=2$, $N\geq24$, we have assumed a pressure of 760 Torr, the upper limit of the range given by Yoshino *et al.*[71]

Before discussing the experimental fine-structure linewidths, it is of interest to compare the present fine-structure-averaged linewidths with some previous results. Mean linewidths obtained from the present results and the room-temperature results of Cheung *et al.*[29] by averaging several rotational widths near $N=10$, are compared with the corresponding results of Lewis *et al.*[28] in Table IV. The widths of Cheung *et al.*[29] for $v=1$, 2 have been corrected downwards by 0.08 cm^{-1} to allow for the effects of pressure broadening, enabling a fair comparison with the present results. The results of Lewis *et al.*[28] already include corrections for pressure broadening.

Although each set of linewidths exhibits the usual dependence on vibration, with predissociation maxima at $v=4$, 7, 11, there are systematic differences in detail between the present results and both previous sets of linewidths.[28,29] The present mean predissociation linewidths for $N=10$ exceed those of Lewis *et al.*[28] by 0%–18% (mean 8%), but are narrower than those of Cheung *et al.*[29] by 2%–27% (mean 11%) despite the fact that the latter results are derived from essentially the same cross sections used in this work. The linewidths of Lewis *et al.*[28] were determined from a complex curve of growth analysis of equivalent width measurements of unresolved triplet features taken at high and low pressures, resulting in the simultaneous determination of mean linewidths and oscillator strengths. Thus, it is not surprising that differences may occur between the linewidths of Lewis *et al.*[28] and the present results which are obtained by the entirely different technique of line profile modeling, especially when it is considered that both data analysis techniques necessarily include the incorrect assumption that the fine-structure linewidths are equal, resulting in some uncertainty as to what is meant by the "mean" fine-structure linewidth in each case. In any event, the observed differences in linewidth exceed the combined experimental errors only for $v=4$, 9 and the overall agreement is quite good. More surprising is the slightly worse agreement between the present linewidths and those of Cheung *et al.*[29] which were obtained by similar techniques, especially for $v=3-9$ where both fitting procedures fix the relative fine-structure splittings. Evidently, even quite small fitting model differences, e.g., dif-

TABLE III. Fine-structure predissociation widths $\Gamma(F_i)$ and fine-structure-averaged widths Γ_{av} for rovibrational levels of the $B\ ^3\Sigma_u^-$ state of O_2, in cm^{-1} FWHM, deduced from the photoabsorption cross section measurements of Yoshino *et al.* (Ref. 71) using a Voigt profile fitting technique.

v	N	Γ_{av}	$\Gamma(F_1)$	$\Gamma(F_2)$	$\Gamma(F_3)$
1	4	0.80±0.09			
1	6		0.44±0.06	1.12±0.16	0.82±0.09
1	8		0.49±0.05	1.25±0.18	0.76±0.08
1	10		0.58±0.06	1.00±0.14	0.93±0.12
1	12		0.53±0.06	1.19±0.15	0.90±0.09
1	14		0.54±0.06	1.56±0.25	0.82±0.09
1	16		0.61±0.08	0.98±0.22	0.80±0.08
1	18		0.50±0.06	1.41±0.34	0.83±0.09
1	20		0.64±0.09	1.22±0.27	0.97±0.10
2	4	0.49±0.04			
2	6	0.45±0.03			
2	8	0.44±0.03			
2	10	0.46±0.04			
2	12		0.39±0.04	0.39±0.05	0.68±0.07
2	14		0.35±0.04	0.35±0.06	0.66±0.07
2	16		0.31±0.04	0.36±0.04	0.69±0.07
2	18		0.34±0.04	0.61±0.07	0.85±0.09
2	20		0.30±0.04	0.44±0.08	0.84±0.09
2	22		0.34±0.05	0.45±0.07	0.95±0.11
2	24		0.29±0.04	0.53±0.08	0.90±0.09
2	26		0.31±0.07	0.51±0.12	1.01±0.15
2	28		0.32±0.12	0.77±0.21	0.88±0.18
3	4	1.56±0.08			
3	6	1.67±0.09			
3	8	1.70±0.09			
3	10	1.71±0.09			
3	12	1.89±0.10			
3	14	1.87±0.10			
3	16	1.89±0.10			
3	18	1.89±0.10			
3	20	2.02±0.10			
3	22	2.02±0.11			
3	26	2.03±0.12			
3	28	2.23±0.35			
4	6	3.48±0.18			
4	8	3.66±0.18			
4	10	3.76±0.18			
4	12	3.89±0.19			
4	14	3.68±0.19			
4	16	3.81±0.19			
4	18	3.79±0.20			
4	20	3.97±0.20			
4	22	4.12±0.21			
4	24	4.11±0.21			
5	6	1.97±0.10			
5	8	1.93±0.10			
5	10	1.92±0.10			
5	12	1.93±0.10			
5	14	1.97±0.10			
5	16	1.91±0.10			
5	18		1.41±0.15	1.64±0.19	2.40±0.45
5	20		1.21±0.12	1.54±0.15	2.34±0.25
5	22		1.32±0.15	1.80±0.36	2.41±0.25
5	24		1.06±0.11	1.98±0.42	2.13±0.25
6	4	1.49±0.08			
6	6	1.52±0.08			
6	8	1.56±0.08			
6	10	1.58±0.08			
6	12	1.60±0.08			
6	14	1.70±0.09			
6	16	1.73±0.09			
6	18	1.86±0.10			
6	20	1.87±0.10			
6	22	2.11±0.11			
6	24	1.99±0.10			
6	26	2.25±0.12			

TABLE III. (*Continued.*)

v	N	Γ_{av}	$\Gamma(F_1)$	$\Gamma(F_2)$	$\Gamma(F_3)$
7	4	1.99 ± 0.10			
7	6	2.05 ± 0.11			
7	8	1.98 ± 0.10			
7	10	1.85 ± 0.10			
7	12	1.89 ± 0.10			
7	14	1.89 ± 0.10			
7	16	1.83 ± 0.10			
7	18	1.60 ± 0.10			
7	22		1.00 ± 0.10	1.40 ± 0.14	1.96 ± 0.20
7	24		0.99 ± 0.10	1.79 ± 0.30	1.96 ± 0.20
7	26		0.94 ± 0.10	1.89 ± 0.38	1.95 ± 0.31
7	28		0.83 ± 0.09	1.57 ± 0.29	2.05 ± 0.34
7	30		0.75 ± 0.14	0.95 ± 0.17	2.18 ± 0.25
7	32		1.22 ± 0.12	1.70 ± 0.21	2.44 ± 0.28
7	34		1.15 ± 0.15	1.51 ± 0.19	2.00 ± 0.25
7	36		1.08 ± 0.14	1.46 ± 0.23	1.91 ± 0.25
8	4	1.63 ± 0.09			
8	6	1.82 ± 0.10			
8	8	1.76 ± 0.09			
8	10	1.77 ± 0.09			
8	12	1.74 ± 0.09			
8	14	1.82 ± 0.10			
8	16	1.94 ± 0.10			
8	18	1.99 ± 0.10			
8	20	1.92 ± 0.10			
8	22	1.94 ± 0.10			
8	24	1.78 ± 0.10			
8	26	1.87 ± 0.10			
8	30		1.61 ± 0.21	2.26 ± 0.41	
8	36		1.73 ± 0.21	1.92 ± 0.31	2.59 ± 0.36
9	4	0.78 ± 0.05			
9	6	0.82 ± 0.05			
9	8	0.76 ± 0.05			
9	10	0.81 ± 0.05			
9	12		0.65 ± 0.07	0.82 ± 0.14	0.96 ± 0.10
9	14		0.53 ± 0.06	0.82 ± 0.08	1.08 ± 0.11
9	16		0.61 ± 0.06	0.84 ± 0.08	1.19 ± 0.12
9	18		0.65 ± 0.07	0.86 ± 0.09	1.18 ± 0.12
9	20		0.63 ± 0.07	0.89 ± 0.09	1.20 ± 0.12
9	22		0.68 ± 0.07	1.12 ± 0.11	1.37 ± 0.14
9	24		0.67 ± 0.07	1.02 ± 0.13	1.64 ± 0.29
9	28		0.86 ± 0.11		1.70 ± 0.38
9	30		0.79 ± 0.09	1.39 ± 0.17	1.73 ± 0.22
10	4	1.10 ± 0.06			
10	6	1.04 ± 0.06			
10	8	1.03 ± 0.06			
10	10	1.01 ± 0.08			
10	12	0.95 ± 0.05			
10	14	1.00 ± 0.07			
10	16		0.79 ± 0.08	1.02 ± 0.10	1.20 ± 0.12
10	18		0.74 ± 0.08	0.98 ± 0.10	1.22 ± 0.12
10	22		0.66 ± 0.07	0.97 ± 0.10	1.20 ± 0.12
10	24		0.69 ± 0.07	0.92 ± 0.09	1.45 ± 0.14
10	26		0.60 ± 0.07	0.85 ± 0.11	1.08 ± 0.14
10	28		0.47 ± 0.05	0.77 ± 0.08	1.24 ± 0.12
10	30		0.43 ± 0.05		
10	32		0.47 ± 0.05	0.87 ± 0.10	1.33 ± 0.14
11	6	1.28 ± 0.07			
11	8	1.19 ± 0.07			
11	10	1.23 ± 0.07			
11	12	1.18 ± 0.07			
11	14	1.23 ± 0.07			
11	16	1.31 ± 0.08			
11	18		1.06 ± 0.10	1.47 ± 0.14	1.48 ± 0.15
11	20		1.00 ± 0.10	1.39 ± 0.14	1.36 ± 0.15
11	22		1.05 ± 0.10	1.32 ± 0.14	1.59 ± 0.15
11	24		0.90 ± 0.11	1.19 ± 0.24	1.39 ± 0.21
11	28		0.78 ± 0.20		
12	6		0.55 ± 0.05	0.66 ± 0.07	0.66 ± 0.07

TABLE III. (*Continued.*)

v	N	Γ_{av}	$\Gamma(F_1)$	$\Gamma(F_2)$	$\Gamma(F_3)$
12	8		0.53 ± 0.05	0.62 ± 0.06	0.76 ± 0.08
12	10		0.50 ± 0.05	0.63 ± 0.06	0.71 ± 0.07
12	12		0.62 ± 0.06	0.77 ± 0.08	0.75 ± 0.07
12	14		0.63 ± 0.06	0.76 ± 0.08	0.87 ± 0.09
12	16		0.70 ± 0.07	0.84 ± 0.08	0.98 ± 0.10
12	18		0.71 ± 0.07	0.86 ± 0.09	0.91 ± 0.07
12	20		0.76 ± 0.08	0.94 ± 0.09	1.09 ± 0.11
12	24		0.77 ± 0.07	1.02 ± 0.10	1.27 ± 0.13
12	26		0.93 ± 0.09	1.23 ± 0.12	1.30 ± 0.13
13	18		0.23 ± 0.03	0.34 ± 0.04	0.45 ± 0.04
13	20			0.36 ± 0.05	0.47 ± 0.06
13	22		0.25 ± 0.03		
13	24		0.36 ± 0.04	0.48 ± 0.05	0.72 ± 0.06
13	26		0.33 ± 0.08	0.56 ± 0.09	0.73 ± 0.11

ferent spin-splitting constants, can significantly affect deduced mean linewidths. It is interesting that the worst agreement between the present results and those of Cheung *et al.*[29] occurs for the narrowest lines, $v=2$, 12. For $v=2$, we allow the fine-structure splittings to vary while Cheung *et al.*[29] do not, while for $v=12$ we have successfully obtained individual fine-structure linewidths near $N=10$ and have used $\Gamma_{av}=[\Gamma(F_1)+\Gamma(F_2)+\Gamma(F_3)]/3$. In each case, we expect our linewidth to be the more accurate. In the case of the narrowest lines for which the predissociation linewidths become comparable with, or smaller than, the fine-structure splittings, then the assumption of equal fine-structure linewidths and the constraint of the triplet splittings to calculated values which are possibly inaccurate are likely to lead to errors in deduced fine-structure-averaged linewidths.

The results listed in Table III enable conclusions to be drawn regarding the dependence of the predissociation linewidth on rotation. We observe definite increases in the mean or F_2 linewidths with rotation for $v=3$, 4, 6, 8, 9, 12, 13, a possible slight increase for $v=2$, definite decreases for $v=7$, 10, a possible slight decrease for $v=5$, and no clear trend for $v=1$, 11. These observations agree well with those of Lewis *et al.*[28] except for $v=2$, 4 where the quality of their measurements did not allow the observation of a trend, and for $v=11$ where they observed a decrease in mean linewidth for $N\geq 24$. Since our results for $v=11$, F_2 extend only to $N=24$, there is no real inconsistency. On the other hand, agreement with the rotational dependences observed by Cheung *et al.*[29] is quite poor. They found no clear trend for $v=3-5$, 7, a decrease for $v=1$, and a definite increase for $v=11$. The significant disagreement for $v=11$ supports the reservations expressed by those authors[29] regarding the adequacy of their model assumptions, especially for the bands of higher vibrational excitation where their fitting procedure did not successfully reproduce their experimental cross sections for higher rotations. Evidently, the rotational dependence of the predissociation linewidth is very sensitive to the details of the profile fitting model assumptions. Since our model makes fewer assumptions, we expect that our observed trends for the dependence of the predissociation linewidth on rotation will be more accurate than those of Cheung *et al.*[29] More puzzling, however, is the good agreement between our rotational trends and those of Lewis *et al.*[28] whose fitting model assumptions were essentially similar to those of Cheung *et al.*[29] It appears that a curve of growth analysis may be less sensitive than a profile fitting analysis to the model assumptions of equal fine-structure linewidths and fixed relative fine-structure line centers.

TABLE IV. Fine-structure-averaged widths $\Gamma_{av}(N=10)$, in cm^{-1} FWHM, deduced from the photoabsorption cross section measurements of Yoshino *et al.* (Ref. 71) compared with some previous measurements.

	$\Gamma_{av}(N=10)$		
v	This work[a]	Lewis *et al.*[d]	Cheung *et al.*[e]
1	0.85±0.06[b]	0.72±0.10	0.89±0.18[c]
2	0.46±0.03	0.41±0.03	0.63±0.04[c]
3	1.77±0.09	1.67±0.08	1.84±0.11
4	3.74±0.19	3.31±0.20	3.76±0.27
5	1.93±0.10	1.89±0.10	2.08±0.07
6	1.58±0.08	1.57±0.10	1.76±0.21
7	1.92±0.10	1.81±0.10	1.96±0.10
8	1.76±0.10	1.71±0.10	1.94±0.12
9	0.79±0.04	0.69±0.05	1.00±0.16
10	1.00±0.05	0.90±0.05	1.03±0.08
11	1.24±0.06	1.23±0.10	1.44±0.18
12	0.65±0.03[b]	0.62±0.05	0.85±0.14

[a]Deduced from the cross sections of Yoshino *et al.* (Ref. 71).
[b]$\Gamma_{av}=[\Gamma(F_1)+\Gamma(F_2)+\Gamma(F_3)]/3$.
[c]Corrected for pressure broadening.
[d]Reference 28.
[e]Reference 29.

The primary interest in the predissociation linewidths presented in Table III lies in the availability of a large number of fine-structure-specific widths for the first time. As noted by Wodtke *et al.*,[52] such data enables conclusions to be drawn regarding the symmetries of the electronic states responsible for the $B\ ^3\Sigma_u^-$ state predissociation.

Two general observations can be drawn from the fine-structure widths given in Table III for $v\geq 2$. First, $\Gamma(F_3)>\Gamma(F_2)>\Gamma(F_1)$, and second, the difference $\Gamma(F_3)-\Gamma(F_1)$ increases significantly as the rotational excitation increases. An inspection of the expressions given in

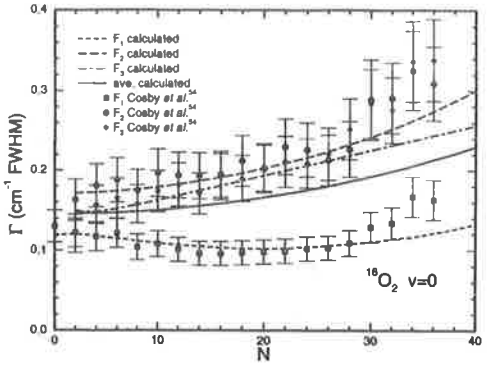

FIG. 4. Measured and calculated fine-structure predissociation widths for the $v=0$ levels of the $B\ ^3\Sigma_u^-$ state of O_2.

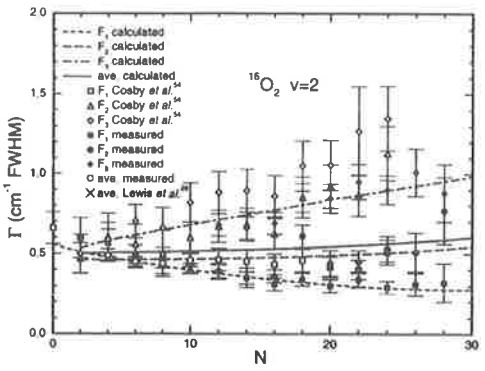

FIG. 6. Measured and calculated predissociation widths for the $v=2$ levels of the $B\ ^3\Sigma_u^-$ state of O_2.

Table II for fine-structure linewidths in $^3\Sigma_u^-$ predissociation, noting that $\eta\xi_3 \gg \eta^2$, leads to the conclusion that such observations can only be explained if a $^3\Pi_u$ state with $\eta\xi_3 \geq 0$ plays a significant role in the $B\ ^3\Sigma_u^-$ state predissociation. For the exceptional level $v=1$, we observe from Table III that all fine-structure widths differ significantly, with $\Gamma(F_2)>\Gamma(F_3)>\Gamma(F_1)$, and that $\Gamma(F_3)-\Gamma(F_1)$ does not increase significantly with rotation. From Table II, this implies that the $^3\Pi_u$ state does not play as significant a role in the $B\ ^3\Sigma_u^-$ state predissociation for $v=1$, but that a $^1\Pi_u$ or $^3\Sigma_u^+$ state dominates the predissociative mechanism for this level.

The present predissociation linewidths for $v=1-13$ are combined with a selection of other measurements for $v=0-18$ and presented in Figs. 4–22. From Fig. 6, it can be seen that the qualitative agreement between the present fine-structure linewidths for $v=2$ and the LIF measurements of Cosby *et al.*[54] is reasonable. The F_1 and F_3 linewidths from each data set exhibit similar dependences on rotation, but our widths are 0.1–0.2 cm^{-1} narrower than those of Cosby *et al.*[54] In the case of the F_2 widths, however, there is poor

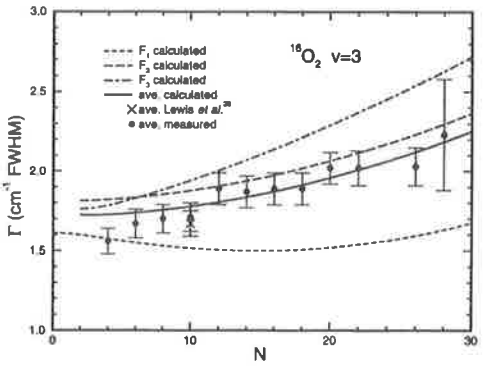

FIG. 7. Measured and calculated predissociation widths for the $v=3$ levels of the $B\ ^3\Sigma_u^-$ state of O_2.

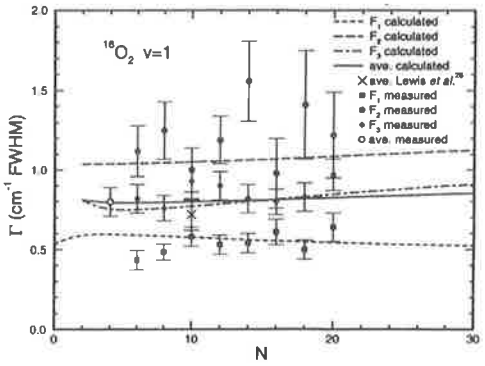

FIG. 5. Measured and calculated predissociation widths for the $v=1$ levels of the $B\ ^3\Sigma_u^-$ state of O_2.

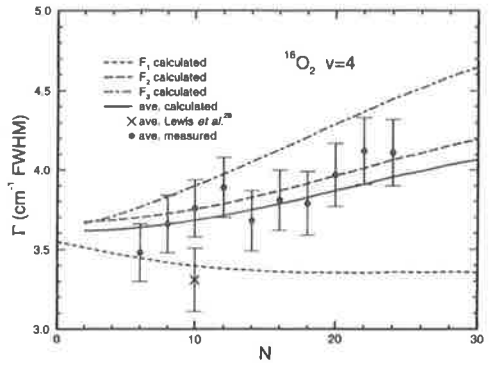

FIG. 8. Measured and calculated predissociation widths for the $v=4$ levels of the $B\ ^3\Sigma_u^-$ state of O_2.

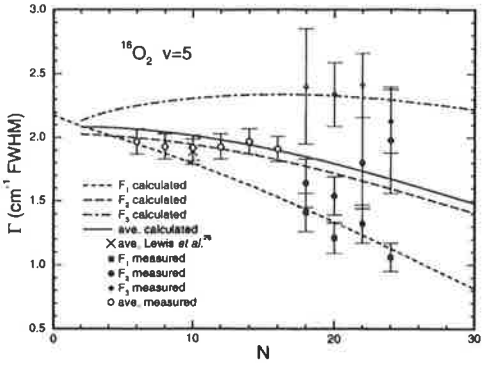

FIG. 9. Measured and calculated predissociation widths for the $v=5$ levels of the $B\ ^3\Sigma_u^-$ state of O_2.

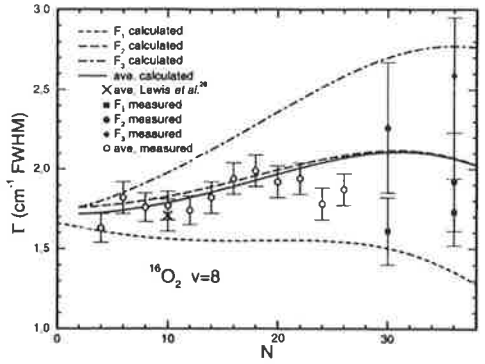

FIG. 12. Measured and calculated predissociation widths for the $v=8$ levels of the $B\ ^3\Sigma_u^-$ state of O_2.

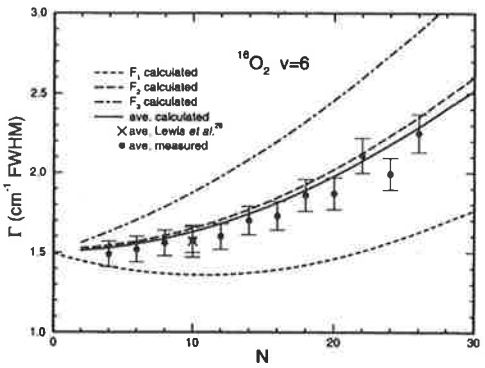

FIG. 10. Measured and calculated predissociation widths for the $v=6$ levels of the $B\ ^3\Sigma_u^-$ state of O_2.

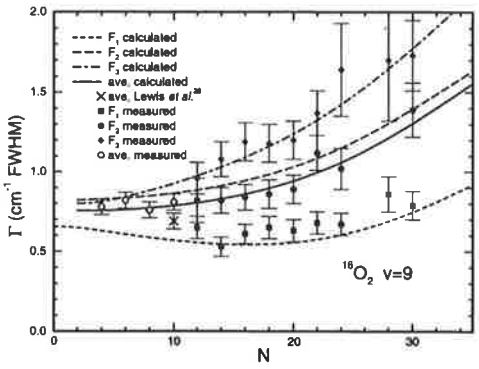

FIG. 13. Measured and calculated predissociation widths for the $v=9$ levels of the $B\ ^3\Sigma_u^-$ state of O_2.

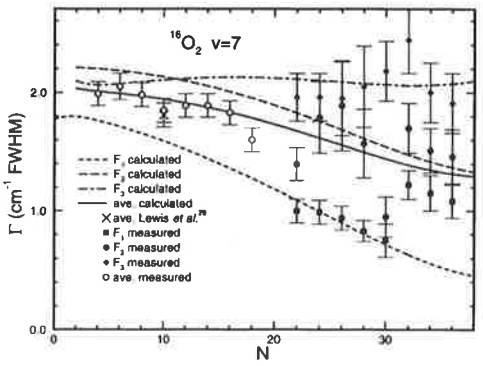

FIG. 11. Measured and calculated predissociation widths for the $v=7$ levels of the $B\ ^3\Sigma_u^-$ state of O_2.

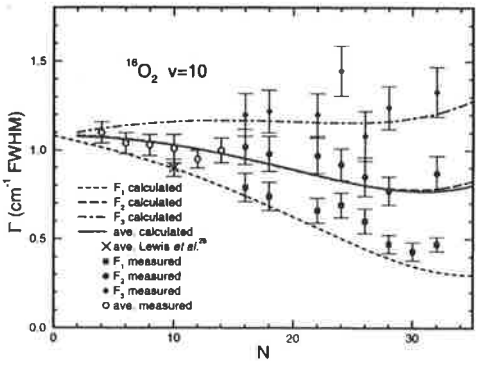

FIG. 14. Measured and calculated predissociation widths for the $v=10$ levels of the $B\ ^3\Sigma_u^-$ state of O_2.

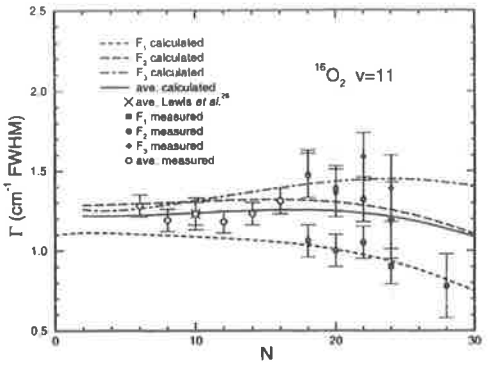

FIG. 15. Measured and calculated predissociation widths for the $v=11$ levels of the $B\ ^3\Sigma_u^-$ state of O_2.

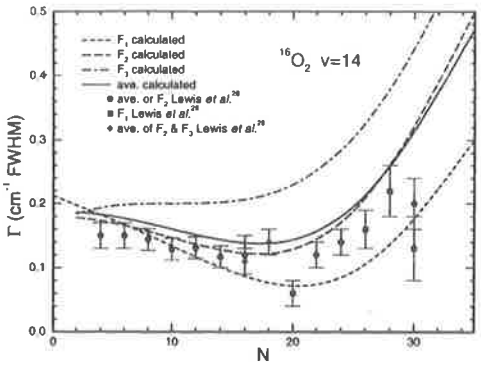

FIG. 18. Measured and calculated predissociation widths for the $v=14$ levels of the $B\ ^3\Sigma_u^-$ state of O_2.

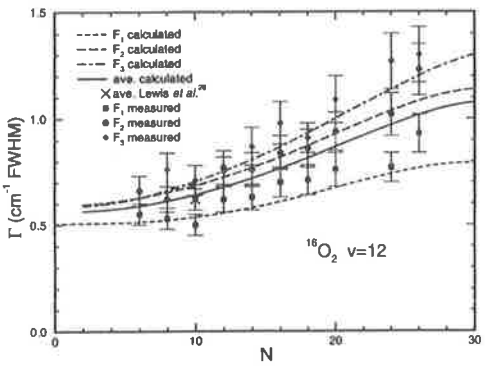

FIG. 16. Measured and calculated predissociation widths for the $v=12$ levels of the $B\ ^3\Sigma_u^-$ state of O_2.

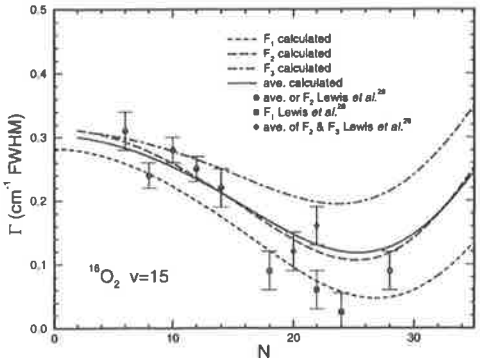

FIG. 19. Measured and calculated predissociation widths for the $v=15$ levels of the $B\ ^3\Sigma_u^-$ state of O_2.

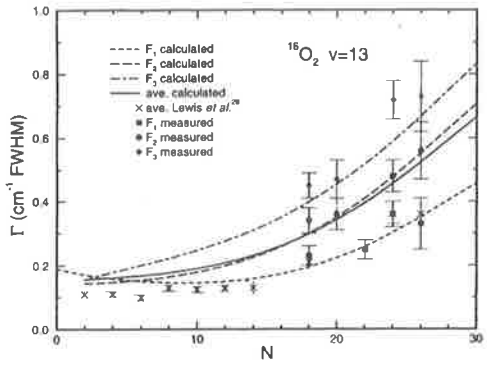

FIG. 17. Measured and calculated predissociation widths for the $v=13$ levels of the $B\ ^3\Sigma_u^-$ state of O_2.

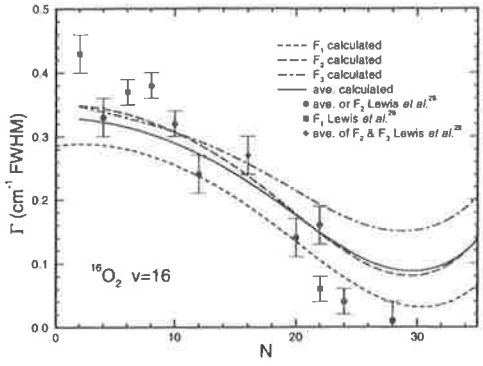

FIG. 20. Measured and calculated predissociation widths for the $v=16$ levels of the $B\ ^3\Sigma_u^-$ state of O_2.

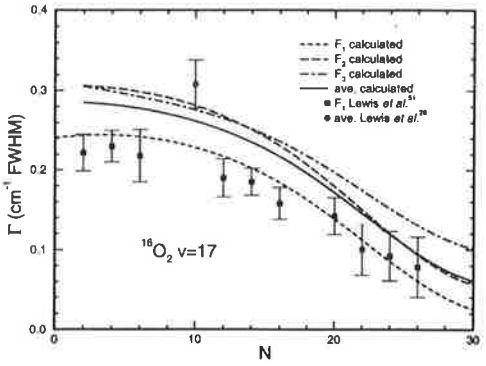

FIG. 21. Measured and calculated predissociation widths for the $v=17$ levels of the $B\ ^3\Sigma_u^-$ state of O_2.

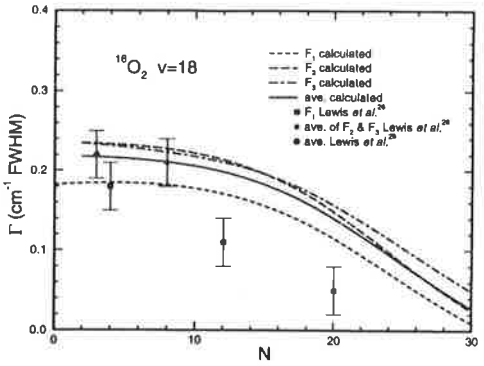

FIG. 22. Measured and calculated predissociation widths for the $v=18$ levels of the $B\ ^3\Sigma_u^-$ state of O_2.

agreement, our widths being considerably narrower. Yang *et al.*[53] have derived fine-structure linewidths from their LIF measurements for $v=10$, $N=16-20$ and $v=11$, $N=28$, 30, which can be directly compared with our photoabsorption linewidths for $v=10$, $N=16$, 18 and $v=11$, $N=28$, F_1. The widths of Yang *et al.*[53] are considerably in excess of ours, ranging from 17%–63% (mean 40%) broader, and we have not shown their widths in Figs. 14 and 15. The qualitative behaviour of their *relative* fine-structure widths, however, is similar to ours and their conclusions regarding the importance of L-uncoupling in the $^3\Pi_u$ predissociative mechanism are well taken. From Figs. 2 and 3 of Yang *et al.*,[53] it can be seen that the data to which they fit their model line profiles do not extend significantly into the wings of the lines. Linewidths, especially for the broader lines, retrieved from profile fitting are very sensitive to the cross section in the line wings and the treatment of backgrounds due to more distant lines or other effects. It is, perhaps, possible that a relatively small error in the background cross sections might explain their[53] anomalously large linewidths.

2. Predissociation model fitting

Our determination of the fine-structure-specific predissociation linewidths listed in Table III enables us to attempt a comprehensive fit of the 13-parameter JK predissociation model, described in Sec. II, to the measured linewidths for the first time. Although Lewis *et al.*[28,65,66] and Chiu *et al.*[67] have performed comprehensive fits of a 12-parameter model to fine-structure-averaged linewidth measurements for several isotopes of O_2, the only estimates[53,54] of the 13th parameter $p=\eta/\xi_3$, which contains the spin-electronic and L-uncoupling interactions between the $B\ ^3\Sigma_u^-$ and $^3\Pi_u$ states, are each derived from fine-structure-specific linewidths for only two vibrational levels.

In this work, we perform a weighted nonlinear least-squares fit of the 13-parameter predissociation model to a set of 80 representative linewidth measurements for $v=0-18$. For $v=0$, we use the fine-structure-specific LIF linewidths of Cosby *et al.*;[54] for $v=1-12$, the present fine-structure-specific and fine-structure-averaged linewidths; for $v=13$, the present fine-structure-specific linewidths and the fine-structure-averaged linewidths of Lewis *et al.*;[28] for $v=14-18$, the fine-structure-specific and fine-structure-averaged linewidths of Lewis *et al.*;[28] and, in addition, the F_1 linewidths of Lewis *et al.*[51] for $v=17$. In general, we include linewidths corresponding to two to four different rotations for each band and we average over several adjacent rotations to minimize the statistical uncertainties in the data to be fitted.

The results of our predissociation model fit are presented in Table V together with other empirical determinations[28,67] and *ab initio* calculations[63,64,88] of the relevant molecular parameters. The errors listed for our parameters are 3σ statistical uncertainties determined by the least-squares fitting algorithm.

As is well known,[61] the $^5\Pi_u$ state plays the major role in $B\ ^3\Sigma_u^-$ state predissociation, as evidenced by its relatively large spin–orbit interaction matrix element of 70 cm^{-1}. In particular, the outer limb crossing of the $^5\Pi_u$ and $B\ ^3\Sigma_u^-$ states results in a characteristic, rapidly varying pattern of predissociation with vibration, dominated by the ~ 4 cm^{-1} FWHM linewidth maximum at $v=4$. As a result, the $^5\Pi_u$ predissociation parameters are extremely well determined by the fitting procedure. Our matrix element, crossing point, and slope for the $^5\Pi_u$ state are in good agreement with the other empirical determinations[28,67] with the exception of the slope determined by Chiu *et al.*[67] which disagrees by almost twice the combined error estimates. Since the fine-structure linewidths for a $^5\Pi_u$ predissociative mechanism are approximately equal (Table II), and since the $^5\Pi_u$-dominated linewidths are generally broad, the inclusion of a significant number of fine-structure-specific linewidths in the fitting procedure has not resulted in the determination of $^5\Pi_u$ parameters significantly different from previous results[28,67] which were based entirely on fits to fine-structure-averaged linewidth measurements. The uncertainties in our $^5\Pi_u$ parameters are, however, a little less.

The $^1\Pi_u$ predissociative mechanism, also resulting from an outer limb crossing, dominates the $v=0$, 1 levels and is responsible for the predissociation maximum at $v=1$. From

TABLE V. Molecular parameters determined from a weighted least-squares fit of the predissociation model to a selection of fine-structure-specific and -averaged linewidth measurements. Previous empirical and *ab initio* determinations of the molecular parameters are also given.

Source	State, k	$\lvert A_{kx}\rvert$ (cm^{-1})	M_{kx} (cm^{-1} Å^{-1})	R_{kx} (Å)	p
This work	$^5\Pi_u$	69.9±1.0	41 000±800	1.8787±0.0007	
	$^3\Sigma_u^+$	29.7±2.1	27 600±4300	2.009±0.006	
	$^3\Pi_u$	30.8±1.5	55 600±1800	1.454±0.002	0.0189±0.0011
	$^1\Pi_u$	28.3±0.9	23 000±700	1.724±0.002	
Lewis *et al.*[f]	$^5\Pi_u$	70.9±1.5	39 700±1000	1.880±0.001	
	$^3\Sigma_u^+$	38.8±4.2	42 300±8000	1.996±0.008	
	$^3\Pi_u$	25.8±2.8	62 700±5000	1.441±0.006	
	$^1\Pi_u$	32.2±3.0	22 400±1300	1.731±0.003	
Chiu *et al.*[g]	$^5\Pi_u$	70±2	38 600±500	1.879±0.001	
	$^3\Sigma_u^+$	46±2	49 000±1000	1.999±0.001	
	$^3\Pi_u$	35±3	74 000±4000	1.429±0.010	0.029[a]
	$^1\Pi_u$	33±5	25 000±3000	1.711±0.010	
Ab initio	$^5\Pi_u$	65[b]	41 900[c]	1.880[c]	
	$^3\Sigma_u^+$	45[b]	40 800[d]	2.004[d]	
	$^3\Pi_u$	28[b]	58 700[c]	1.457[c]	0.018[e]
	$^1\Pi_u$	25[b]	23 000[d]	1.724[d]	

[a]From Cheung *et al.* (Ref. 69).
[b]From Julienne (Ref. 88), MCSCF+CI.
[c]From Partridge *et al.* (Ref. 63), MRCI+Q.
[d]From Partridge (Ref. 64), MRCI+Q.
[e]From Julienne (Ref. 88), $|A_{3x}|$, and Julienne (Ref. 62), $\langle {}^3\Sigma_u^-|\mathbf{L}^-|{}^3\Pi_u\rangle$.
[f]Reference 28.
[g]Reference 67.

Figs. 4 and 5, it can be seen that the measured F_2 width exceeds the F_3 width, marginally for $v=0$, significantly for $v=1$. As stated previously, this characteristic is consistent with a $^1\Pi_u$ predissociative mechanism. The availability, for the first time, of a good set of fine-structure-specific linewidths for $v=0-2$ ensures that the fitted $^1\Pi_u$ molecular parameters given in Table V are of very high accuracy. The previous empirical determinations[28,67] were hampered by a lack of experimental linewidths for $v=0$, a lack of fine-structure-specific linewidths, and, in the case of Chiu *et al.*,[67] inadequate modeling of the lower vibrational levels by Cheung *et al.*,[29] including a lack of correction for the effects of pressure broadening. The present $^1\Pi_u-B\ ^3\Sigma_u^-$ crossing point disagrees with both previous determinations,[28,67] lying between them. This is consistent with the qualitative observation of Cosby *et al.*[54] that an average of the Lewis *et al.*[28] and Chiu *et al.*[67] $^1\Pi_u$ potentials provides a better description of the $^1\Pi_u-B\ ^3\Sigma_u^-$ interaction than either one separately.

Since the $^3\Pi_u$ state crosses the inner limb of the $B\ ^3\Sigma_u^-$ state, the $^3\Pi_u$ contribution to predissociation linewidth varies only slowly with vibration. At low rotational excitations, the relatively small $^3\Pi_u-B\ ^3\Sigma_u^-$ spin–orbit interaction matrix element, coupled with the lack of a characteristic vibrational signature, make it difficult to extract accurate $^3\Pi_u$ molecular parameters from fine-structure-averaged linewidths. Accordingly, both previous empirical sets of $^3\Pi_u$ parameters[28,67] vary widely and have large uncertainties. In the present work, however, the inclusion of fine-structure-specific linewidths in the fit, especially at high rotation, enables the determination of $^3\Pi_u$ parameters of much higher accuracy than possible heretofore. As we have mentioned previously, the general observation in Figs. 4–22 of diverging F_3 and F_1 linewidths for increasing rotation is the signature of a $^3\Pi_u$ predissociative mechanism involving an L-uncoupling interaction with the $B\ ^3\Sigma_u^-$ state. Thus, ours is the first experimental determination of the parameter $p=\eta/\xi_3$, containing the spin-electronic and L-uncoupling interactions, which is based on an extensive set of measurements. Our value, $p=0.0189\pm0.0011$, supersedes the previous estimates of ~0.03, by Cosby *et al.*[54] from the application of a limited predissociation model to their $v=0$, 2 levels, and by Cheung *et al.*[69] assuming the hypothesis of pure precession.

Although the $2\ ^3\Sigma_u^+$ state crosses the outer limb of the $B\ ^3\Sigma_u^-$ state, resulting in a characteristic vibrational signature with a maximum at $v=7$, in practice the $2\ ^3\Sigma_u^+$ predissociative mechanism does not dominate for any vibrational level. Consequently, any relative experimental errors are likely to be magnified in the determination of the $2\ ^3\Sigma_u^+$ parameters. Our matrix element, slope, and crossing point for the $2\ ^3\Sigma_u^+$ state are not very well determined, with uncertainties significantly greater than those of the other predissociating states. Agreement is poor with both other empirical determinations.[28,67] Considering the great difficulty in characterizing the $2\ ^3\Sigma_u^+$ state, the extremely low uncertainties listed for the $2\ ^3\Sigma_u^+$ parameters determined by Chiu *et al.*[67] seem curious.

Our predissociation model parameters are also compared with *ab initio* calculations in Table V. Recently, very high quality potential curves for the $^3\Pi_u$ and $^5\Pi_u$ states have been calculated by Partridge *et al.*[63] using a multireference configuration-interaction (MRCI) treatment with a Davidson correction (+Q) in an extended basis set. Partridge[64] has also calculated potential curves for the $^1\Pi_u$ and $2\ ^3\Sigma_u^+$ states. Crossing points and slopes determined from the MRCI+Q potentials by spline fitting are given in Table V and are in

excellent agreement with our empirical values for the Π_u states, the maximum discrepancies being 0.003 Å in the crossing points and 5% in the slopes. Although our crossing point for the $2\ ^3\Sigma_u^+$ state agrees with the *ab initio* value[64] within our uncertainty estimate, our slope is in very poor agreement. In fact, the *ab initio* slope for the $2\ ^3\Sigma_u^+$ state is in much better agreement with the data of Lewis *et al.*[28] It is likely that agreement has been worsened by the inclusion of different sets of linewidth data in the fit performed in this work. As we have seen, the present widths are a little broader than those of Lewis *et al.*[28] and any inconsistencies are likely to be reflected in the determination of the $2\ ^3\Sigma_u^+$ parameters. The fit performed by Lewis *et al.*,[28] however, used a single self-consistent set of data. At this stage, we expect that the *ab initio* slope and crossing point[64] for the $2\ ^3\Sigma_u^+$ potential energy curve will reflect the actual behavior of that state better than the parameters obtained from the fitting of a predissociation model to measured linewidths.

Semiempirical spin–orbit interaction matrix elements relevant to the predissociation of the $B\ ^3\Sigma_u^-$ state were originally calculated by Julienne[62] who has recently obtained new *ab initio* values[88] based on a multiconfiguration self-consistent field (MCSCF) plus first-order configuration-interaction (CI) treatment. The *ab initio* matrix elements[88] applying at the relevant crossing points are given in Table V. Our matrix elements for the Π_u states are in good agreement with Julienne's calculations,[88] but consistently ~10% greater. Once again, however, agreement is very poor in the case of the $2\ ^3\Sigma_u^+$ state.

Lefebvre-Brion and Field[70] have pointed out the difficulty in obtaining semiempirical estimates of the matrix elements of the operator $\mathbf{L}^-$, especially for the valence states of nonhydride molecules. It is also well known[56,61,89] that the valence states of O_2 are not generally well represented by a single configuration. In the case of the $^3\Sigma_u^-$ and $^3\Pi_u$ states of O_2, Rydberg–valence interactions[90] also play a significant role at smaller internuclear separations. The leading configurations for the $B\ ^3\Sigma_u^-$ and $^3\Pi_u$ states, $(3\sigma_g)^2(1\pi_u)^3(1\pi_g)^3$ and $(3\sigma_g)^2(3\sigma_u)^1(1\pi_u)^4(1\pi_g)^1$, respectively, do not couple via the $\mathbf{L}^-$ operator, and so the **L**-uncoupling matrix element involving these states is dependent both on the configuration coefficients of secondary configurations which do couple, and on the extent to which the relevant σ and π molecular orbitals are formed from the $2p$ orbital of atomic oxygen. Thus, it is clear that the pure precession value of the **L**-uncoupling matrix element, $\sqrt{2}$, will not apply in this case. In fact, in an early *ab initio* calculation, Julienne[62] found that $|\langle {}^3\Sigma_u^-|\mathbf{L}^-|{}^3\Pi_u\rangle|=0.50$ at $R=1.21$ Å. Using Eq. (22), with $B_x=h/(8\pi^2\mu c R_{3x}^2)=0.997$ cm^{-1} at $R_{3x}=1.454$ Å, and Julienne's[88] *ab initio* $|A_{3x}|=28$ cm^{-1}, we find that $|p|=|\eta/\xi_3|=0.018$, in excellent agreement with our empirical determination of the same ratio. The quality of the agreement may be coincidental, however, since, as has been pointed out by Lefebvre-Brion and Field,[70] the matrix elements of $\mathbf{L}^-$ may vary significantly with R and no *ab initio* calculation of $\langle {}^3\Sigma_u^-|\mathbf{L}^-|{}^3\Pi_u\rangle$ is currently available at the $^3\Pi_u$–$B\ ^3\Sigma_u^-$ crossing point, $R_{3x}=1.454$ Å. The observed behavior of the fine-structure-specific linewidths, with $\Gamma(F_3)>\Gamma(F_1)$ and the difference $\Gamma(F_3)-\Gamma(F_1)$ increasing with rotational excitation, unambiguously defines $\eta\xi_3$ as positive (Table II). It follows that $p=\eta/\xi_3>0$ and one would expect that this could be verified by further *ab initio* calculations.

The linewidths of Figs. 4–22, together with the results of the predissociation model fitting procedure, confirm that the **L**-uncoupling interaction between the $^3\Pi_u$ and $B\ ^3\Sigma_u^-$ states is important in describing the $B\ ^3\Sigma_u^-$ predissociation fully, even at quite low rotational excitation. Although Julienne and Krauss[61] included an **L**-uncoupling formalism in their original predissociation model, it was not until the work of Yang *et al.*[53] and Cosby *et al.*[54] that the full effect of **L**-uncoupling on the F_1 and F_3 linewidths was understood. Previously, Lewis *et al.*[28] concluded from a comprehensive study of fine-structure-averaged predissociation linewidths in the SR bands that spin–orbit interaction and centrifugal distortion were the only mechanisms necessary to explain the observed dependence on vibration and rotation. The previous[28] and the current conclusions, however, are not incompatible, as can be seen from an examination of the $^3\Pi_u$ width expressions given in Table II. If we form the average width $\Gamma_{av}(J)=[\Gamma(F_1,J)+\Gamma(F_2,J)+\Gamma(F_3,J)]/3$, the J-dependent interference terms in $\eta\xi_3$ from the $^3\Pi_u$ F_1 and F_3 levels cancel, leaving only the much smaller terms in η^2. In other words, the importance of η in determining the rotation dependence of predissociation widths is greatly reduced if we consider fine-structure-averaged widths only. In practice, we are interested in N-triplets. If we assume the Hund's case (b) limit for the $B\ ^3\Sigma_u^-$ state levels, applicable for medium to high J, it can be shown from Table II that $\Gamma_{av}(N)=[\Gamma(F_1,N)+\Gamma(F_2,N)+\Gamma(F_3,N)]/3$ is given by

$$\frac{\Gamma_{av}(N)}{2\pi}\approx\frac{10}{9}\xi_5^2+\frac{2}{3}\xi_1^2+\frac{2}{3}\xi_+^2+\frac{4}{3}\xi_3^2+2N(N+1)\eta^2+\frac{4\sqrt{2}}{3}\xi_3\eta. \tag{26}$$

The terms involving η are small, resulting in corrections of only 9% and 25% of the small $^3\Pi_u$ partial width for $N=10$ and $N=20$, respectively. Thus, a model, such as that of Lewis *et al.*,[28] which neglects **L**-uncoupling ($p=0$) will reproduce essentially the correct rotational dependence of the *fine-structure-averaged* predissociation linewidth even if the F_1 and F_3 linewidths show dramatically the effects of **L**-uncoupling, as in the present case.

One of the most significant aspects of the current work is the greatly improved knowledge of the parameters governing the $^3\Pi_u$ predissociative mechanism. The inclusion of **L**-uncoupling in the predissociation model, together with fine-structure-specific linewidths, especially at high rotation, in the model fitting procedure, has led to the determination of the best $^3\Pi_u$ parameters currently available. It is instructive to consider the reasons for this in more detail.

From Table II, if we assume the case (b) limit for the $B\ ^3\Sigma_u^-$ state, and form the difference linewidth $\Gamma(F_3,N)-\Gamma(F_1,N)$, it follows that

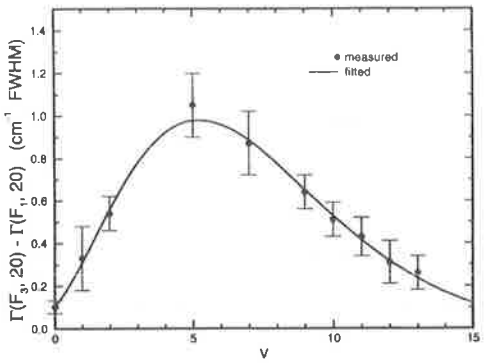

FIG. 23. Measured difference predissociation linewidths $\Gamma(F_3,N=20)-\Gamma(F_1,N=20)$ for the $B\ ^3\Sigma_u^-$ state of O_2, together with a fitted model based on predissociation by a single $^3\Pi_u$ state with $R_{3x}=1.457$ Å, $M_{3x}=52\ 400\ \text{cm}^{-1}\ \text{Å}^{-1}$, and $pA_{3x}^2=16.3\ \text{cm}^{-2}$.

$$\frac{[\Gamma(F_3,N)-\Gamma(F_1,N)]}{2\pi} = \frac{(2N+1)}{(2N-1)(2N+3)}\left(\xi_3^2-\frac{\xi_5^2}{6}-\xi_1^2-\xi_+^2\right) + 2\sqrt{2}(2N+1)\eta\xi_3. \quad (27)$$

As N increases, the difference width becomes dominated by the interference term in $\eta\xi_3$, and we may write

$$\Gamma(F_3,N)-\Gamma(F_1,N)\approx 4\sqrt{2}\pi(2N+1)\eta\xi_3. \quad (28)$$

By forming the difference width at high rotation, it is thus possible to isolate the effects of the $^3\Pi_u$ state from the effects of the other repulsive states which dominate the average and low rotational widths. For example, in the case of $B\ ^3\Sigma_u^-$ state predissociation with the parameters given in Table V, for $N=20$ the error in using the approximate form Eq. (28) is <2% for $v=2-18$, 2% for $v=0$, and 5% for $v=1$.

We illustrate these observations in Fig. 23 by forming the difference widths $\Gamma(F_3,20)-\Gamma(F_1,20)$ from the present fine-structure-specific linewidth measurements, averaging and interpolating where necessary. Remarkably, the measured difference widths have a smooth dependence on vibration with a maximum of $\sim 1\ \text{cm}^{-1}$ near $v=5$, a signature consistent with that expected for a $^3\Pi_u$ state crossing the inner limb of the $B\ ^3\Sigma_u^-$ state.[61] The well-known signatures of the other predissociating states which cross the outer limb, resulting in rapid width variation with vibration (see, e.g., Fig. 21 of Lewis *et al.*[28]) are totally absent. In addition, the $^3\Pi_u$ widths have been enhanced by considering the high rotation, $N=20$. The $^3\Pi_u$ contribution to the rotationless F_2 width, e.g., reaches a maximum of only $\sim 0.5\ \text{cm}^{-1}$ near $v=5$. The shape of the vibrational dependence of the difference width will, of course, be slightly different from the rotationless shape because of centrifugal distortion in the parameters $\eta(v,J,E)$ and $\xi_3(v,J,E)$.

We have fitted a modified predissociation model, including only a $^3\Pi_u$ mechanism, to the difference widths given in Fig. 23 and the results of the fit are also shown in that figure. The measured difference widths are well described by a $^3\Pi_u$ predissociative mechanism with the fitted parameters $R_{3x}=1.457\pm0.002$ Å, $M_{3x}=52400\pm1400\ \text{cm}^{-1}\ \text{Å}^{-1}$, and $pA_{3x}^2=16.3\pm0.9\ \text{cm}^{-2}$. From Eq. (28), it can be seen that the difference widths are determined by the product $\eta\xi_3$ and it is thus not possible to determine either parameter separately by this technique. The $^3\Pi_u$ parameters determined are in good agreement with those obtained from the full fitting procedure and given in Table V where $pA_{3x}^2=17.9\pm2.7\ \text{cm}^{-2}$.

3. Calculations

Model fine-structure-specific and -averaged predissociation linewidths have been calculated using the parameters given in Table V for $v=0-18$ and $N=0-40$. The results are presented in Table VI together with partial F_2 widths contributed by each predissociating state. Although the F_2 levels with $N=0$ are virtual, partial widths for this case are included so that the full rotational dependences of the repulsive state contributions can be seen. For $v\geq15$, some of the rotational levels with $N\leq40$ become unbound, so the maximum rotation considered for those bands is reduced accordingly (to $N=24$ for $v=18$, for example).

The model linewidths are also shown in Figs. 4–22 together with a selection of the measured linewidths discussed previously. In general, the model is in very good agreement with the fitted data sets, but some of the discrepancies are of interest. While there is excellent agreement between the model and the LIF linewidths of Cosby *et al.*[54] for $v=0$, except for $N\geq30$ where the measurements become more uncertain, agreement is quite poor for $v=2$, $N\geq10$ where the LIF measurements exceed the calculations by 0.1–0.4 cm^{-1}, the greatest discrepancies occurring for the F_2 levels of high rotation. While it is true that we have fitted the model to the present $v=2$ linewidths, rather than those of Cosby *et al.*,[54] even if we ignore the present $v=2$ measurements it is not possible to explain the $v=2$ measurements of Cosby *et al.*[54] within the constraints of the current model. This observation has been supported by Cheung *et al.*[69] who modified their $^1\Pi_u$ parameters to produce better agreement with the average widths of Cosby *et al.*[54] for $v=0$ and $v=2$, but could not reproduce the measured N dependences and created greater discrepancies for some of the other vibrational levels.

Agreement is excellent between the model and the present linewidths for $v=1-8$, 11, 13, except for the F_1 levels with $v=7$, $N\geq32$, but there are systematic discrepancies of the order of 0.1 cm^{-1} in some of the fine-structure-specific widths for $v=9$, 10, 12. For $v=9$, 12 the model does not fully reproduce the measured ratios of the fine-structure-specific linewidths, the calculated $F_2:F_3$ and $F_2:F_1$ linewidth ratios being larger in each case. Both of these vibrations correspond to peaks in the $2\ ^3\Sigma_u^+$ linewidth contribution and it may be possible to remove the discrepancies with a better $2\ ^3\Sigma_u^+$ model.

TABLE VI. Fine-structure-specific $\Gamma(F_i)$ and fine-structure-averaged Γ_{av} rovibrational predissociation widths for the $B\ ^3\Sigma_u^-$ state of O_2, in cm^{-1} FWHM, calculated using the predissociation model parameters given in Table V. Partial linewidths $\Gamma(F_2,k)$ contributed by each predissociating state k are also given.

v	N	$\Gamma(F_2,{}^5\Pi_u)$	$\Gamma(F_2,{}^3\Sigma_u^+)$	$\Gamma(F_2,{}^3\Pi_u)$	$\Gamma(F_2,{}^1\Pi_u)$	$\Gamma(F_1)$	$\Gamma(F_2)$	$\Gamma(F_3)$	Γ_{av}
0	0	0.000	0.000	0.048	0.123	0.118			
0	10	0.000	0.000	0.050	0.129	0.109	0.179	0.163	0.150
0	20	0.000	0.000	0.055	0.148	0.102	0.203	0.193	0.166
0	30	0.000	0.000	0.060	0.182	0.110	0.242	0.226	0.192
0	40	0.000	0.000	0.062	0.238	0.133	0.301	0.257	0.230
1	0	0.002	0.000	0.152	0.882	0.531			
1	10	0.003	0.000	0.159	0.890	0.577	1.051	0.772	0.800
1	20	0.004	0.000	0.176	0.908	0.542	1.087	0.847	0.825
1	30	0.006	0.000	0.196	0.923	0.524	1.124	0.910	0.853
1	40	0.011	0.000	0.211	0.917	0.514	1.139	0.935	0.863
2	0	0.080	0.000	0.280	0.101	0.557			
2	10	0.087	0.000	0.294	0.086	0.400	0.467	0.681	0.516
2	20	0.110	0.000	0.329	0.050	0.308	0.489	0.835	0.544
2	30	0.158	0.000	0.375	0.012	0.277	0.545	0.985	0.602
2	40	0.255	0.000	0.414	0.003	0.338	0.671	1.141	0.717
3	0	0.899	0.000	0.395	0.515	1.611			
3	10	0.949	0.000	0.416	0.511	1.515	1.877	1.941	1.778
3	20	1.099	0.000	0.472	0.494	1.519	2.065	2.291	1.959
3	30	1.373	0.000	0.548	0.446	1.674	2.366	2.719	2.253
3	40	1.798	0.000	0.621	0.347	1.990	2.767	3.203	2.653
4	0	3.025	0.002	0.472	0.171	3.545			
4	10	3.066	0.002	0.500	0.187	3.398	3.754	3.902	3.685
4	20	3.158	0.003	0.573	0.231	3.356	3.965	4.291	3.870
4	30	3.216	0.005	0.676	0.297	3.355	4.194	4.645	4.064
4	40	3.071	0.010	0.785	0.365	3.224	4.230	4.757	4.070
5	0	1.495	0.034	0.502	0.001	2.181			
5	10	1.375	0.037	0.534	0.000	1.797	1.946	2.308	2.017
5	20	1.043	0.049	0.620	0.005	1.335	1.717	2.329	1.794
5	30	0.555	0.076	0.745	0.033	0.816	1.408	2.223	1.482
5	40	0.102	0.131	0.882	0.101	0.424	1.217	2.138	1.260
6	0	0.641	0.282	0.490	0.109	1.496			
6	10	0.732	0.299	0.523	0.096	1.360	1.650	1.878	1.629
6	20	0.994	0.351	0.614	0.063	1.461	2.022	2.456	1.980
6	30	1.391	0.438	0.750	0.022	1.765	2.601	3.192	2.519
6	40	1.719	0.551	0.910	0.000	2.087	3.180	3.864	3.044
7	0	0.897	0.647	0.447	0.223	1.776			
7	10	0.795	0.645	0.480	0.212	1.592	2.132	2.106	1.943
7	20	0.519	0.624	0.570	0.180	1.184	1.893	2.122	1.733
7	30	0.160	0.551	0.709	0.124	0.714	1.544	2.067	1.442
7	40	0.007	0.378	0.879	0.053	0.433	1.318	2.144	1.298
8	0	1.040	0.088	0.385	0.243	1.661			
8	10	1.107	0.066	0.415	0.240	1.562	1.828	1.977	1.789
8	20	1.248	0.021	0.499	0.227	1.552	1.995	2.360	1.969
8	30	1.289	0.002	0.631	0.194	1.502	2.117	2.699	2.106
8	40	0.952	0.088	0.799	0.129	1.184	1.968	2.737	1.963
9	0	0.001	0.306	0.316	0.197	0.654			
9	10	0.002	0.320	0.342	0.201	0.569	0.864	0.926	0.786
9	20	0.067	0.342	0.416	0.207	0.556	1.031	1.240	0.942
9	30	0.341	0.315	0.537	0.202	0.747	1.395	1.774	1.305
9	40	0.814	0.175	0.695	0.167	1.093	1.852	2.448	1.798
10	0	0.699	0.004	0.249	0.136	1.082			
10	10	0.618	0.000	0.271	0.142	0.897	1.031	1.162	1.030
10	20	0.385	0.012	0.335	0.157	0.624	0.888	1.162	0.891
10	30	0.083	0.084	0.439	0.171	0.349	0.777	1.181	0.769
10	40	0.048	0.208	0.576	0.164	0.367	0.995	1.491	0.951
11	0	0.808	0.205	0.189	0.082	1.097			
11	10	0.827	0.186	0.207	0.088	1.086	1.308	1.313	1.236
11	20	0.815	0.125	0.258	0.106	1.007	1.303	1.433	1.248
11	30	0.598	0.031	0.346	0.128	0.748	1.103	1.405	1.085
11	40	0.151	0.012	0.463	0.139	0.328	0.765	1.227	0.773
12	0	0.255	0.151	0.140	0.045	0.504			
12	10	0.317	0.164	0.154	0.051	0.537	0.685	0.704	0.642
12	20	0.485	0.184	0.195	0.066	0.675	0.930	1.001	0.869
12	30	0.636	0.152	0.264	0.088	0.792	1.139	1.301	1.078
12	40	0.442	0.036	0.354	0.106	0.566	0.938	1.257	0.920

TABLE VI. (*Continued.*)

v	N	$\Gamma(F_2,{}^5\Pi_u)$	$\Gamma(F_2,{}^3\Sigma_u^+)$	$\Gamma(F_2,{}^3\Pi_u)$	$\Gamma(F_2,{}^1\Pi_u)$	$\Gamma(F_1)$	$\Gamma(F_2)$	$\Gamma(F_3)$	Γ_{av}
13	0	0.001	0.017	0.101	0.023	0.191			
13	10	0.012	0.028	0.111	0.027	0.146	0.179	0.247	0.191
13	20	0.099	0.070	0.142	0.039	0.224	0.351	0.455	0.343
13	30	0.327	0.127	0.195	0.058	0.457	0.707	0.833	0.666
13	40	0.448	0.092	0.260	0.075	0.560	0.875	1.071	0.835
14	0	0.089	0.009	0.071	0.011	0.213			
14	10	0.051	0.003	0.079	0.014	0.134	0.147	0.200	0.160
14	20	0.000	0.004	0.102	0.022	0.072	0.129	0.230	0.143
14	30	0.093	0.052	0.140	0.037	0.177	0.322	0.443	0.314
14	40	0.298	0.085	0.181	0.050	0.386	0.615	0.743	0.581
15	0	0.213	0.047	0.050	0.005	0.282			
15	10	0.164	0.033	0.055	0.007	0.223	0.259	0.278	0.253
15	20	0.049	0.005	0.072	0.013	0.096	0.139	0.207	0.147
15	30	0.010	0.011	0.097	0.023	0.060	0.142	0.242	0.148
15	34	0.059	0.031	0.108	0.028	0.115	0.226	0.324	0.222
16	0	0.251	0.063	0.035	0.002	0.286			
16	10	0.213	0.052	0.039	0.003	0.255	0.307	0.307	0.289
16	20	0.100	0.021	0.050	0.007	0.134	0.178	0.214	0.175
16	30	0.001	0.001	0.066	0.014	0.031	0.081	0.152	0.088
17	0	0.225	0.058	0.024	0.001	0.241			
17	10	0.201	0.052	0.027	0.002	0.229	0.281	0.276	0.262
17	20	0.114	0.027	0.034	0.004	0.138	0.179	0.197	0.171
17	28	0.020	0.003	0.041	0.008	0.040	0.071	0.113	0.075
18	0	0.174	0.045	0.017	0.000	0.183			
18	10	0.161	0.042	0.018	0.001	0.178	0.222	0.218	0.206
18	20	0.099	0.025	0.023	0.002	0.115	0.148	0.157	0.140
18	24	0.057	0.013	0.024	0.003	0.072	0.098	0.114	0.095

For the very narrow $v=13$, 14 levels, the measured fine-structure-averaged linewidths of Lewis *et al.*[28] are systematically narrower than the model linewidths. For $v=15$–18, with only a few exceptions, the agreement is good, even for the few F_1 linewidths measured by Lewis *et al.*[28] For $v=17$, there is excellent agreement between the model F_1 linewidths and the very high-resolution VUV laser photoabsorption linewidths of Lewis *et al.*[51]

It is also of interest to consider the work of Wodtke *et al.*[52] who measured LIF spectra of some (11,2), (14,3), (15,3), and (16,3) SR triplets in an atmospheric pressure flame. Although no linewidths were extracted from their spectra, it is possible to obtain information regarding the relative fine-structure linewidths for some of their almost resolved triplets. For example, perhaps the best resolved example in their spectra is the $R(17)$ line of the (15,3) band. Since their instrumental bandwidth was ~ 1 cm^{-1}, significantly broader than the actual linewidths for this band, the relative intensities of their fine-structure features should be inversely proportional to the corresponding relative fine-structure predissociation linewidths. From their Fig. 3, we obtain $\Gamma(F_1):\Gamma(F_2):\Gamma(F_3)=1:1.3:1.8$, in excellent agreement with our calculated ratio of 1:1.34:1.82 for $v=15$, $N=18$. However, despite the authors' claim to the contrary,[52] it is likely that a small, but significant amount of collision broadening will occur under the experimental conditions of $P=1$ atm, $T=1750$ K, perhaps compromising this excellent agreement. Nevertheless, the LIF experiments certainly have the potential to provide valuable information on relative fine-structure linewidths for the narrower levels with $v\geq 13$. We cannot, however, support the conclusions of Wodtke *et al.*[52] that a $^3\Sigma_u^+$ predissociative mechanism is dominant for $v=14$–16, and a $^3\Pi_u$ mechanism for $v=11$. For example, in the case of the $v=15$, $N=18$ level, from Table VI it can be seen that $^3\Pi_u$ and $^5\Pi_u$ mechanisms predominate. In the case of the $v=11$, $N=28$ level studied by Wodtke *et al.*,[52] the $^5\Pi_u$ mechanism is twice as important as the $^3\Pi_u$ mechanism. Freeman *et al.*[91] have also questioned the conclusions of Wodtke *et al.*[52] regarding the $v=11$ level.

The calculated fine-structure-specific rovibrational predissociation linewidths presented here in Figs. 4–22 and Table VI should provide a basis for the construction of sophisticated photochemical models of the terrestrial atmosphere. In particular, the ability of the predissociation model effectively to interpolate and extrapolate into experimentally difficult regions is valuable.

Despite the generally excellent agreement between the model and the measurements, several areas require further investigation. A reconciliation between the LIF linewidths[54] and the present linewidths for $v=2$ would be desirable, as would a resolution of the differences between the present linewidths for $v=1$–13, based on the measured cross sections of Yoshino *et al.*,[71] and the linewidths of Lewis *et al.*,[28] derived from a curve of growth analysis. A great amount of work also remains to be done on bands with $v\geq 13$ where it should be possible to obtain linewidths for completely resolved triplet components using photoabsorption techniques with narrow bandwidth VUV sources. A resolution of these matters is likely to result in better parameters describing the $2\,^3\Sigma_u^+$–$B\,^3\Sigma_u^-$ interaction and an improved predissociation model.

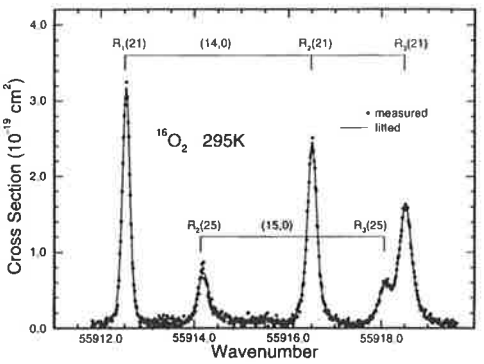

FIG. 24. Fine-structure photoabsorption cross sections for the $R(21)$ triplet of the (14,0) Schumann–Runge band measured at room temperature with a laser-based VUV source providing a bandwidth of 0.13 cm^{-1} FWHM. The results of a Voigt profile model fit are also shown.

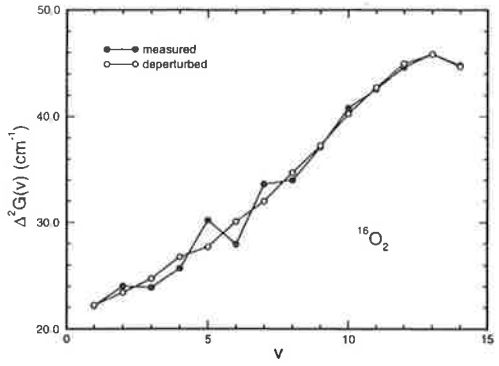

FIG. 25. A deperturbation of the measured second vibrational differences for the $B\ ^3\Sigma_u^-$ state of O_2 using a predissociation model with the parameters given in Table V.

To this end, we have begun a comprehensive photoabsorption study of the SR bands with $v \geqslant 9$ using a narrow bandwidth VUV laser source.[92] It is of interest to compare some preliminary experimental results from this study, obtained after the calculations described previously were performed, with our predicted fine-structure-specific linewidths. We have scanned the region of the $R(21)$ triplet from the (14,0) band with an instrumental bandwidth of ~0.13 cm^{-1} FWHM and the measured photoabsorption cross sections are shown in Fig. 24. The VUV radiation was generated by the technique of two-photon-resonant difference-frequency four-wave mixing in xenon using two dye lasers pumped by an excimer laser. From Fig. 24, it is clear that the apparent widths of the fine-structure components imply that $\Gamma(F_3)>\Gamma(F_2)>\Gamma(F_1)$, and, using the Voigt line shape fitting procedure described in Sec. III with an instrumental bandwidth of 0.13 cm^{-1} and a Doppler width of 0.12 cm^{-1}, we find experimental predissociation linewidths $\Gamma(F_1)=0.04\pm0.02$ cm^{-1}, $\Gamma(F_2)=0.119\pm0.019$ cm^{-1}, and $\Gamma(F_3)=0.234\pm0.020$ cm^{-1} for the $v=14$, $N=22$ components. Our model predictions for these levels are 0.074, 0.144, and 0.253 cm^{-1}, respectively. The model linewidths are in quite good agreement with the new observations, the observed discrepancies being of the order of the uncertainties which are due primarily to an incomplete knowledge of the instrumental bandwidth. Overall conclusions, of course, must await the completion of the new measurements.

B. Shifts

As was first demonstrated dramatically by Julienne and Krauss,[61] who used the experimental energy levels of Ackerman and Biaume,[44] it is possible to observe the shifts in SR band origins caused by the predissociating repulsive states, principally the $^5\Pi_u$, and to deperturb the measurements with the aid of a predissociation model. In order to magnify the effects of the perturbations, we form the second vibrational differences,

$$\Delta^2 G(v)=G(v-1)+G(v+1)-2G(v), \tag{29}$$

from the band origins given by Lewis *et al.*[23] Level shifts $S(v)$ are calculated according to the procedure described in Sec. II using the predissociation model parameters given in Table V and their second differences,

$$\Delta^2 S(v)=S(v-1)+S(v+1)-2S(v), \tag{30}$$

are formed also. The deperturbed second differences are given by

$$\Delta^2 G^0(v)=\Delta^2 G(v)-\Delta^2 S(v). \tag{31}$$

The perturbed and deperturbed second differences are shown in Fig. 25. It is clear that the predissociation model parameters which best describe the observed linewidths also result in a smooth deperturbation of the observed second vibrational differences. The quality of the deperturbation is superior to that obtained by Chiu *et al.*[67] using different predissociation model parameters, and is similar to those obtained by Julienne and Krauss[61] and Cheung *et al.*[81] who specifically fitted the observed perturbations with a predissociation model based solely on a $^5\Pi_u$ mechanism.

C. Spectroscopic constants

Although it is not our intention to dwell on matters involving the spectroscopic constants of the $B\ ^3\Sigma_u^-$ state, we must emphasize that the spin-splitting constants are in doubt, and that this may have a significant effect on linewidths extracted from unresolved features where it is necessary to constrain the line centers during the fitting procedure. In Sec. III, we determined that the fitted fine-structure line spacings for the (9,0) $R(21)$ and (11,0) $R(17)$ features shown in Figs. 2 and 3 significantly exceeded the calculated spacings. This tendency is quite general. In Fig. 26, we present fine-structure energy splittings $F_3(N=20)-F_1(N=20)$, extracted from the measured cross sections of Yoshino *et al.*[71] using the fitting procedure described in Sec. III and the known ground-state splittings. Our results are compared with splittings calculated from the Hamiltonian and spectroscopic constants of Cheung *et al.*[24] It can be seen that the measured

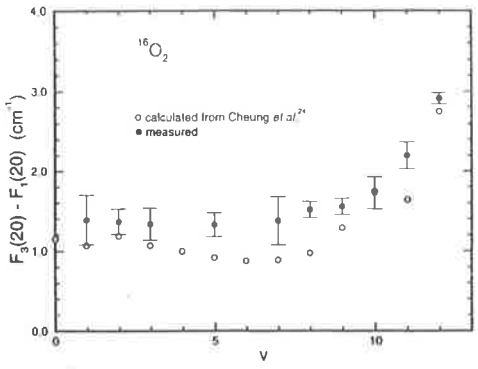

FIG. 26. Fine-structure energy splittings $F_3(N=20)-F_1(N=20)$ for the $B\ ^3\Sigma_u^-$ state of O_2. Values extracted from the measured Schumann–Runge band photoabsorption cross sections of Yoshino *et al.* (Ref. 71) using a Voigt profile fitting procedure are shown, together with splittings calculated from the Hamiltonian and spectroscopic constants of Cheung *et al.* (Ref. 24).

splittings exceed the calculations except for $v=10$, and that the minimum in the calculated splittings near $v=6-7$ is not reproduced in the measurements which asymptote towards a constant value as v decreases.

This observation suggests that it may be necessary to reevaluate the spin-splitting constants for the $B\ ^3\Sigma_u^-$ state before it is possible to obtain completely accurate fine-structure-averaged linewidths for the broader levels for which it is necessary to constrain the line centers during the fitting procedure.

V. CONCLUSIONS

We have determined a comprehensive set of fine-structure-specific and fine-structure-averaged predissociation linewidths for the $v=1-13$ levels of the $B\ ^3\Sigma_u^-$ state of $^{16}O_2$ from the room temperature photoabsorption cross sections of the $(v,0)$ and $(v,1)$ SR bands measured by Yoshino *et al.*[71] The use of a Voigt profile fitting procedure which assumes unequal linewidths for the triplet fine-structure components and unconstrained triplet splittings has resulted in the first extensive determination of fine-structure-specific predissociation linewidths for $v=1$, 5, 7, 9–13. Improvements to the fitting procedure employed by Cheung *et al.*[29] have considerably reduced the previously observed[29] disagreement with the fine-structure-averaged linewidths of Lewis *et al.*,[28] obtained from lower resolution measurements using a curve of growth analysis. We have found that the actual separations between triplet fine-structure levels consistently exceed values predicted from generally accepted spectroscopic constants[24] for the $B\ ^3\Sigma_u^-$ state, suggesting that a reevaluation of those constants may be necessary.

We have calculated realistic fine-structure-specific predissociation linewidths for the $v=0-18$, $N=0-40$ levels of the $B\ ^3\Sigma_u^-$ state of $^{16}O_2$ for the first time, using a predissociation model which takes into account spin–orbit interactions between the $B\ ^3\Sigma_u^-$ state and the $1\ ^1\Pi_u$, $1\ ^3\Pi_u$, $1\ ^5\Pi_u$, and $2\ ^3\Sigma_u^+$ states, together with spin-electronic and L-uncoupling interactions between the $B\ ^3\Sigma_u^-$ and $1\ ^3\Pi_u$ states. The calculated widths vary from 0.03 (for $v=16$, $N=30$, F_1) to 4.8 cm^{-1} (for $v=4$, $N=40$, F_3). Following the correction of an error in previous model expressions[53,54] for the F_1 and F_3 partial widths resulting from the $^3\Pi_u$ interaction, we have optimized the predissociation model parameters by comparing the calculated linewidths with the present determinations and previous[28,51,54] measurements. Our calculations are expected to be important in the construction of state-of-the-art models describing the photochemistry of the middle atmosphere.

The inclusion of fine-structure-specific predissociation linewidths for several rotational excitations in the predissociation model fitting procedure confirms previous determinations[28,29] of the molecular parameters for the dominant $^5\Pi_u$ predissociative state, but results in greatly improved parameters for the $^1\Pi_u$ and $^3\Pi_u$ states. Parameters for the $^3\Sigma_u^+$ state remain ill-determined since the $^3\Sigma_u^+$ mechanism does not dominate for any vibrational level. Parameters for the Π_u states are in good agreement with *ab initio* calculations.[62–64,88] The optimum parameters from the fitting procedure for the widths also results in a smooth deperturbation of the observed second vibrational differences. The particular predissociative mechanisms proposed by Wodtke *et al.*[52] to explain their LIF measurements on levels with $v=11$, 14–16 are not supported by our model.

The L-uncoupling interaction between the $B\ ^3\Sigma_u^-$ and $1\ ^3\Pi_u$ states is found to be important for most vibrational levels in determining width ratios for the fine-structure components, even at quite low rotational excitation. In particular, the observed increase in $\Gamma(F_3,N)-\Gamma(F_1,N)$ with increasing rotation for most levels, characteristic of the L-uncoupling interaction, can be used to determine $^3\Pi_u$ parameters free from the influence of any of the other predissociative mechanisms.

The present measured and model linewidths are generally narrower than those determined recently from LIF spectra.[54,53] It would be of interest to examine a particular set of levels, e.g. the totally resolved fine-structure levels with $v=14$, in associated studies using narrow bandwidth photoabsorption and LIF spectroscopies, in order to resolve any discrepancies between the techniques.

While some improvements may be possible in the determination of fine-structure-averaged linewidths for the unresolved triplet features of the broader levels, by using better spin-splitting constants, e.g., linewidths for these levels will always be dependent upon the profile fitting model and it may be impossible to obtain experimental fine-structure-specific values. On the other hand, it is quite possible to increase considerably the available set of fine-structure-specific widths by performing narrow bandwidth photoabsorption studies on the resolved triplet features with $v\geq 13$, after the manner of Lewis *et al.*[51] who examined the F_1 levels for $v=17$. Currently, we have such a study underway,[92] the preliminary results of which are in good agreement with our model predictions. The results of this further study, together with a reconciliation between various determinations of fine-structure-averaged linewidths, may enable the con-

struction of an improved predissociation model with more realistic 2 $^3\Sigma_u^+$ parameters.

ACKNOWLEDGMENTS

We thank Dr. H. Partridge for providing unpublished *ab initio* potential curves for the $^1\Pi_u$ and 2 $^3\Sigma_u^+$ states of O_2, and Dr. P. S. Julienne for the provision of unpublished *ab initio* spin–orbit matrix elements relevant to the $B\ ^3\Sigma_u^-$ state predissociation. We are grateful to Professor J. H. Carver, Professor H. Lefebure-Brion, Professor M. L. Ginter, Professor R. J. Donovan, Dr. P. C. Cosby, and Dr. J. P. England for critical readings of the manuscript. Valuable technical assistance was provided by K. J. Lonsdale and C. J. Dedman.

[1] M. Nicolet and P. Mange, J. Geophys. Res. **59**, 15 (1954).
[2] M. Nicolet, J. Geophys. Res. **89**, 2573 (1984).
[3] R. D. Hudson, V. L. Carter, and E. L. Brieg, J. Geophys. Res. **74**, 4079 (1969).
[4] M. Ackerman, F. Biaume, and G. Kockarts, Planet. Space Sci. **18**, 1639 (1970).
[5] G. Kockarts, *Mesospheric Models and Related Experiments*, edited by G. Fiocco (Reidel, Dordrecht, 1971), p. 160.
[6] M. Ackerman, *Mesospheric Models and Related Experiments*, edited by G. Fiocco (Reidel, Dordrecht, 1971), p. 149.
[7] R. T. Brinkmann, *Mesospheric Models and Related Experiments*, edited by G. Fiocco (Reidel, Dordrecht, 1971), p. 89.
[8] R. D. Hudson and S. H. Mahle, J. Geophys. Res. **77**, 2902 (1972).
[9] T. M. Fang, S. C. Wofsy, and A. Dalgarno, Planet. Space Sci. **22**, 413 (1974).
[10] J. H. Park, J. Atmos. Sci. **31**, 1893 (1974).
[11] H. Muramatsu, Papers Meteor. Geophys. **26**, 219 (1973).
[12] R. P. Turco, Geophys. Surveys **2**, 153 (1975).
[13] G. Kockarts, Planet. Space Sci. **24**, 589 (1976).
[14] A. J. Blake, J. Geophys. Res. **84**, 3272 (1979).
[15] J. E. Frederick and R. D. Hudson, J. Atmos. Sci. **37**, 1099 (1980).
[16] J. E. Frederick and R. D. Hudson, J. Atmos. Sci. **37**, 1088 (1980).
[17] M. Nicolet and W. Peetermans, Planet. Space Sci. **28**, 85 (1980).
[18] M. Allen and J. E. Frederick, J. Atmos. Sci. **39**, 2066 (1982).
[19] S. Cieslik and M. Nicolet, Planet. Space Sci. **21**, 925 (1973).
[20] M. Nicolet, J. Geophys. Res. **86**, 5203 (1981).
[21] R. J. Cicerone and J. L. McCrumb, J. Geophys. Res. Lett. **7**, 251 (1980).
[22] M. W. P. Cann, J. B. Shin, and R. W. Nicholls, Can. J. Phys. **62**, 1738 (1984).
[23] B. R. Lewis, L. Berzins, and J. H. Carver, J. Quant. Spectrosc. Radiat. Transfer **36**, 209 (1986).
[24] A. S.-C. Cheung, K. Yoshino, W. H. Parkinson, and D. E. Freeman, J. Mol. Spectrosc. **119**, 1 (1986).
[25] K. Yoshino, D. E. Freeman, J. R. Esmond, and W. H. Parkinson, Planet. Space Sci. **31**, 339 (1983).
[26] A. S.-C. Cheung, K. Yoshino, W. H. Parkinson, and D. E. Freeman, Can. J. Phys. **62**, 1752 (1984).
[27] K. Yoshino, D. E. Freeman, J. R. Esmond, and W. H. Parkinson, Planet. Space Sci. **35**, 1067 (1987).
[28] B. R. Lewis, L. Berzins, J. H. Carver, and S. T. Gibson, J. Quant. Spectrosc. Radiat. Transfer **36**, 187 (1986).
[29] A. S.-C. Cheung, K. Yoshino, J. R. Esmond, S. S.-L. Chiu, D. E. Freeman, and W. H. Parkinson, J. Chem. Phys. **92**, 842 (1990).
[30] K. Omidvar and J. E. Frederick, Planet. Space Sci. **35**, 769 (1987).
[31] D. P. Murtagh, Planet. Space Sci. **36**, 819 (1988).
[32] M. Nicolet, S. Cieslik, and R. Kennes, Aeronom. Acta (Brussels) **318**, 1 (1987).
[33] M. Nicolet, S. Cieslik, and R. Kennes, Planet. Space Sci. **36**, 1039 (1988).
[34] M. Nicolet, S. Cieslik, and R. Kennes, Planet. Space Sci. **37**, 427 (1989).
[35] M. Nicolet and R. Kennes, Planet. Space Sci. **37**, 459 (1989).
[36] K. Minschwaner, G. P. Anderson, L. A. Hall, and K. Yoshino, J. Geophys. Res. **97**, 10,103 (1992).
[37] P. J. Flory, J. Chem. Phys. **4**, 23 (1936).
[38] M. W. Feast, Proc. Phys. Soc. London Sect. A **62**, 114 (1949).
[39] D. H. Volman, J. Chem. Phys. **24**, 122 (1956).
[40] P. G. Wilkinson and R. S. Mulliken, Astrophys. J. **125**, 594 (1957).
[41] D. Rakotoarijimy, S. Weniger, and H. Grenat, C. R. Acad. Sci. (Paris) **246**, 2883 (1958).
[42] L. Herman, R. Herman, and D. Rakotoarijimy, J. Phys. Radium **22**, 1 (1961).
[43] P. K. Carroll, Astrophys. J. **129**, 794 (1959).
[44] M. Ackerman and F. Biaume, J. Mol. Spectrosc. **35**, 73 (1970).
[45] J. E. Frederick and R. D. Hudson, J. Mol. Spectrosc. **74**, 247 (1979).
[46] B. R. Lewis, J. H. Carver, T. I. Hobbs, D. G. McCoy, and H. P. F. Gies, J. Quant. Spectrosc. Radiat. Transfer **20**, 191 (1978).
[47] B. R. Lewis, J. H. Carver, T. I. Hobbs, D. G. McCoy, and H. P. F. Gies, J. Quant. Spectrosc. Radiat. Transfer **22**, 213 (1979).
[48] H. P. F. Gies, S. T. Gibson, D. G. McCoy, A. J. Blake, and B. R. Lewis, J. Quant. Spectrosc. Radiat. Transfer **26**, 469 (1981).
[49] B. R. Lewis, J. H. Carver, T. I. Hobbs, D. G. McCoy, and H. P. F. Gies, J. Quant. Spectrosc. Radiat. Transfer **24**, 365 (1980).
[50] P. L. Smith, H. E. Griesinger, J. H. Black, K. Yoshino, and D. E. Freeman, Astrophys. J. **277**, 569 (1984).
[51] B. R. Lewis, S. T. Gibson, K. G. H. Baldwin, and J. H. Carver, J. Opt. Soc. Am. B **6**, 1200 (1989).
[52] A. M. Wodtke, L. Hüwel, H. Schluter, H. Voges, G. Meijer, and P. Andresen, J. Chem. Phys. **89**, 1929 (1988).
[53] X. Yang, A. M. Wodtke, and L. Hüwel, J. Chem. Phys. **94**, 2469 (1991).
[54] P. C. Cosby, H. Park, R. A. Copeland, and T. G. Slanger, J. Chem. Phys. **98**, 5117 (1993).
[55] H. F. Schaefer and F. E. Harris, J. Chem. Phys. **48**, 4946 (1968).
[56] H. F. Schaefer and W. H. Miller, J. Chem. Phys. **55**, 4107 (1971).
[57] I. Riess and Y. Ben-Aryeh, J. Quant. Spectrosc. Radiat. Transfer **9**, 1463 (1969).
[58] J. N. Murrell and J. M. Taylor, Mol. Phys. **16**, 609 (1969).
[59] M. S. Child, J. Mol. Spectrosc. **33**, 487 (1970).
[60] S. Durmaz and J. N. Murell, Mol. Phys. **21**, 209 (1971).
[61] P. S. Julienne and M. Krauss, J. Mol. Spectrosc. **56**, 270 (1975).
[62] P. S. Julienne, J. Mol. Spectrosc. **63**, 60 (1976).
[63] H. Partridge, C. W. Bauschlicher, S. R. Langhoff, and P. R. Taylor, J. Chem. Phys. **95**, 8292 (1991).
[64] H. Partridge (private communication, 1993).
[65] B. R. Lewis, L. Berzins, and J. H. Carver, J. Quant. Spectrosc. Radiat. Transfer **37**, 243 (1987).
[66] B. R. Lewis, L. Berzins, and J. H. Carver, J. Quant. Spectrosc. Radiat. Transfer **37**, 229 (1987).
[67] S. S.-L. Chiu, A. S.-C. Cheung, M. Finch, M. J. Jamieson, K. Yoshino, A. Dalgarno, and W. H. Parkinson, J. Chem. Phys. **97**, 1787 (1992).
[68] S. S.-L. Chiu, A. S.-C. Cheung, K. Yoshino, J. R. Esmond, D. E. Freeman, and W. H. Parkinson, J. Chem. Phys. **93**, 5539 (1990).
[69] A. S.-C. Cheung, D. K.-W. Mok, M. J. Jamieson, M. Finch, K. Yoshino, A. Dalgarno, and W. H. Parkinson, J. Chem. Phys. **99**, 1086 (1993).
[70] H. Lefebvre-Brion and R. W. Field, *Perturbations in the Spectra of Diatomic Molecules* (Academic, Orlando, 1986), pp. 32–40, 55–56, 88, 107, 109–115, 166–168, 225–231, 344, 347.
[71] K. Yoshino, J. R. Esmond, A. S.-C. Cheung, D. E. Freeman, and W. H. Parkinson, Planet. Space Sci. **40**, 185 (1992).
[72] U. Fano, Phys. Rev. **124**, 1866 (1965).
[73] F. H. Mies, Phys. Rev. **175**, 164 (1968).
[74] P. S. Julienne, D. Neumann, and M. Krauss, J. Chem. Phys. **64**, 2990 (1975).
[75] S. L. Guberman and A. Dalgarno, J. Geophys. Res. **84**, 4437 (1979).
[76] A. C. Allison, S. L. Guberman, and A. Dalgarno, J. Geophys. Res. **87**, 923 (1982).
[77] J. W. C. Johns and D. W. Lepard, J. Mol. Spectrosc. **55**, 374 (1975).
[78] J. K. G. Watson, Can. J. Phys. **46**, 1637 (1968).
[79] R. W. Field, B. G. Wicke, J. D. Simmons, and S. G. Tilford, J. Mol. Spectrosc. **44**, 383 (1972).
[80] B. R. Johnson, J. Chem. Phys. **67**, 4086 (1977).
[81] A. S.-C. Cheung, K. Yoshino, D. E. Freeman, R. S. Friedman, A. Dalgarno, and W. H. Parkinson, J. Mol. Spectrosc. **134**, 362 (1989).
[82] B. R. Johnson, J. Chem. Phys. **69**, 4678 (1978).
[83] E. E. Whiting, J. Quant. Spectrosc. Radiat. Transfer **8**, 1379 (1968).
[84] L. Veseth and A. Lofthus, Mol. Phys. **27**, 511 (1974).

[85] J. B. Tatum and J. K. G. Watson, Can. J. Phys. **49**, 2693 (1971).
[86] K. Yoshino, D. E. Freeman, and W. H. Parkinson, J. Phys. Chem. Ref. Data **13**, 207 (1984).
[87] B. R. Lewis, L. Berzins, C. J. Dedman, T. T. Scholz, and J. H. Carver, J. Quant. Spectrosc. Radiat. Transfer **39**, 271 (1988).
[88] P. S. Julienne (private communication, 1991).
[89] R. J. Buenker and S. D. Peyerimhoff, Chem. Phys. **8**, 324 (1975).
[90] R. J. Buenker and S. D. Peyerimhoff, Chem. Phys. Lett. **34**, 225 (1975).
[91] D. E. Freeman, A. S.-C. Cheung, K. Yoshino, and W. H. Parkinson, J. Chem. Phys. **91**, 6538 (1989).
[92] P. M. Dooley, B. R. Lewis, S. T. Gibson, and K. G. H. Baldwin (unpublished).

4.18 Asymmetric lineshapes in the indirect predissociation of the $f^1\Sigma_u^+$ Rydberg state of O_2

[38] B. R. Lewis, S. S. Banerjee, and S. T. Gibson,
Journal of Chemical Physics **102**, 6631–6640 (1995).

Asymmetric line shapes in the indirect predissociation of the $f\ ^1\Sigma_u^+$ Rydberg state of O_2

B. R. Lewis, S. S. Banerjee, and S. T. Gibson
Research School of Physical Sciences and Engineering, The Australian National University, Canberra, ACT 0200, Australia

(Received 29 December 1994; accepted 23 January 1995)

Rotationally-resolved Beutler–Fano line shapes observed in the photoabsorption spectrum of the (2,0) band of the $3p\pi_u f\ ^1\Sigma_u^+ \leftarrow X\ ^3\Sigma_g^-$ Rydberg system of O_2 are interpreted using a coupled-channel Schrödinger equations model. It is found that the $f\ ^1\Sigma_u^+$ state is indirectly predissociated by the $B\ ^3\Sigma_u^-$ continuum, and that the $f \leftarrow X$ transition borrows oscillator strength primarily from dipole-allowed transitions into the mixed Rydberg-valence states of $^3\Sigma_u^-$ symmetry. Both the predissociation linewidth and oscillator strength of the (2,0) resonance are controlled by the spin-orbit interaction between the $^1\Sigma_u^+$ and $^3\Sigma_u^-$ components of the $3p$-complex. There is some evidence for a destructive quantum interference between the transition amplitude borrowed from the $3p\pi_u E\ ^3\Sigma_u^- \leftarrow X\ ^3\Sigma_g^-$ transition and that borrowed weakly from the $f\ ^1\Sigma_u^+ \leftarrow b\ ^1\Sigma_g^+$ transition through spin-orbit mixing between the $b\ ^1\Sigma_g^+$ and $X\ ^3\Sigma_g^-$ states. © *1995 American Institute of Physics.*

I. INTRODUCTION

As shown by Fano,[1] the interaction of a quasi-discrete state with an active continuum will normally result in an asymmetric line shape. Although such interactions are common among molecular excited states, there have been only a few reported cases of asymmetric line shapes in molecular predissociation below the first ionization limit. Beutler–Fano profiles have been observed in the photoabsorption[2–5] and fluorescence-excitation[6] spectra of H_2, HD, and D_2 ($3p\pi_u D\ ^1\Pi_u \leftarrow X\ ^1\Sigma_g^+$ and $4p\sigma_u B''\ ^1\Sigma_u^+ \leftarrow X\ ^1\Sigma_g^+$), the photoabsorption spectrum of O_2 ($3p\pi_u E\ ^3\Sigma_u^- \leftarrow X\ ^3\Sigma_g^-$ and $3p\pi_u D\ ^3\Sigma_u^+ \leftarrow X\ ^3\Sigma_g^-$),[7–9] and the photofragment-yield spectrum of Cs_2,[10] but rotational resolution has been achieved for only a few lines in the spectra of H_2 and its isotopomers. The most asymmetric rotationally-resolved predissociation line shape yet reported was that of the $R(2)$ line from the (5,0) $D\ ^1\Pi_u \leftarrow X\ ^1\Sigma_g^+$ band of D_2 for which Rothschild *et al.*[5] obtained a fitted Fano asymmetry parameter $q = -4 \pm 1$.

The oxygen molecule not only plays an important role in the photochemistry and aeronomy of the terrestrial atmosphere by controlling atmospheric opacity to solar vacuum ultraviolet (VUV) radiation from 1000 Å to 2000 Å, but also exhibits a rich spectrum containing several examples of asymmetric predissociating resonances,[7–9] particularly in the window region, 1100–1300 Å. This spectral region comprises a number of strong resonances of varying diffuseness, due to transitions into mixed Rydberg-valence $^3\Sigma_u^-$ and $^3\Pi_u$ states,[11,12] separated by regions of very weak absorption. Two weaker vibrational progressions, first observed by Tanaka,[13] have been assigned[14] as transitions into Rydberg states converging to the $X\ ^2\Pi_g$ state of O_2^+, $3p\pi_u f\ ^1\Sigma_u^+ \leftarrow X\ ^3\Sigma_g^-$ and $3p\pi_u D\ ^3\Sigma_u^+ \leftarrow X\ ^3\Sigma_g^-$ (where we have used the nomenclature f,D of Huber and Herzberg,[15] rather than the α,β of Alberti *et al.*[16]) Since, in the Fano formalism,[1] the degree of line shape asymmetry[17] of a predissociating resonance is inversely proportional to the transition moment into the quasi-bound state, it might be expected that such forbidden transitions will provide optimum conditions for the observation of highly asymmetric resonances. Indeed, Lewis *et al.*[9] have reported that it is impossible to model the measured photoabsorption cross section of the (3,0) $D\ ^3\Sigma_u^+ \leftarrow X\ ^3\Sigma_g^-$ band of O_2 without representing each rotational line by an asymmetric profile. They found a fine-structure-averaged asymmetry parameter $q = -3.7 \pm 0.2$ by fitting a Fano profile-based band model to their rotationally-unresolved measurements.

Several vibrational bands in the $f\ ^1\Sigma_u^+ \leftarrow X\ ^3\Sigma_g^-$ and $f\ ^1\Sigma_u^+ \leftarrow b\ ^1\Sigma_g^+$ systems have been observed photographically and rotationally analyzed,[14,16,18,19] but absolute photoabsorption cross sections have not been reported previously. The singlet nature of the upper state and the open character of the blue-degraded ^SR branch of the $3p\pi_u f\ ^1\Sigma_u^+ \leftarrow X\ ^3\Sigma_g^-$ transition suggest that it should be possible to observe rotationally-resolved predissociation profiles. In this work, we demonstrate the occurrence of asymmetric rotational lines in the $f \leftarrow X$ system and interpret our measurements using a coupled-channel Schrödinger equations (CSE) model of the $f\ ^1\Sigma_u^+$ state predissociation.

II. MEASUREMENTS AND DISCUSSION

In Fig. 1 we present photoabsorption cross sections for $^{16}O_2$ in the region of the (2,0) $f\ ^1\Sigma_u^+ \leftarrow X\ ^3\Sigma_g^-$ band, measured at a temperature of 79 K, with pressures in the range 1.1–1.5 Torr, and with a wavelength resolution of ~0.03 Å full-width-half-maximum (FWHM). An Ar continuum light source, a 2.2 m scanning VUV monochromator, a 10 cm absorption cell, and a photoelectric detection system were employed in taking the measurements. Full details of the apparatus and experimental method have been given elsewhere,[7] but the original monochromator grating has since been replaced with a 2400 grooves/mm version, resulting in an improved resolution. The wavelength scale of the monochromator was calibrated against known emission lines of

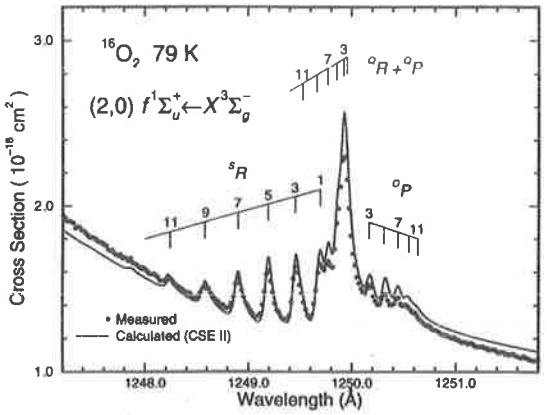

FIG. 1. The absolute photoabsorption cross section of $^{16}O_2$ in the region of the (2,0) band of the $f\,^1\Sigma_u^+ \leftarrow X\,^3\Sigma_g^-$ system. The measurements were taken at a temperature of 79 K with a wavelength resolution of ~0.03 Å FWHM. The results of a temperature-specific calculation of the cross section using a coupled-channel Schrödinger equations model (CSE II) are also shown.

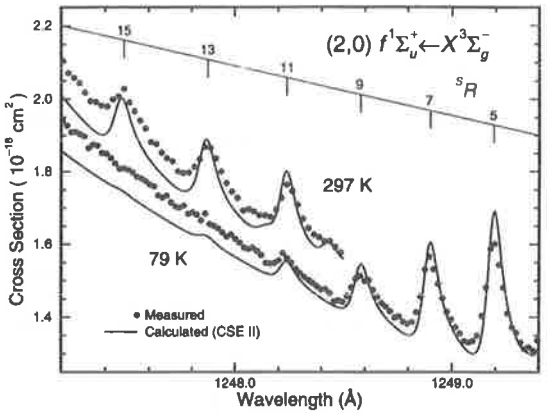

FIG. 2. The absolute photoabsorption cross section of $^{16}O_2$ in the ^SR branch of the (2,0) $f\,^1\Sigma_u^+ \leftarrow X\,^3\Sigma_g^-$ band. The measurements were taken at temperatures of 79 K and 297 K with a wavelength resolution of ~0.03 Å FWHM. The results of temperature-specific calculations using a coupled-channel Schrödinger equations model (CSE II) are also shown.

N I, O I, and C I, and absorption lines of the $A\,^1\Pi \leftarrow X\,^1\Sigma^+$ system of CO,[20] and is expected to be accurate to within ± 0.01 Å. The statistical variation in the measured cross sections is ~1% and there is an absolute uncertainty of ~3% due to uncertainties in cell length, pressure, temperature, and window transmittance degradation with time at 79 K. The measured cross section is only marginally degraded by instrumental effects since the predissociation linewidths significantly exceed the instrumental resolution.

As in the case of the (3,0) $D\,^3\Sigma_u^+ \leftarrow X\,^3\Sigma_g^-$ cross section reported by Lewis *et al.*,[9] it can be seen from Fig. 1 that it is not possible to draw a smooth curve which is consistent with the continuum backgrounds on each side of the discrete transition. This is an indication of the rotationally-averaged band shape asymmetry resulting from the discrete state-continuum interaction. In Fig. 2 we present cross sections measured at 297 K and 79 K in that region of the ^SR branch which is not overlapped by $^QR + {}^QP$-branch lines. It can be seen that lines in the rotationally-resolved ^SR branch are clearly asymmetric, the extent of their red wings being approximately twice that of the blue.

Spectroscopic and line shape parameters were obtained from the measured 79 K cross section by fitting an empirical band model similar to those described previously.[7–9] The known spectroscopic constants[21] for the $X\,^3\Sigma_g^-$ state were used to generate the manifold of rovibrational term values for the ground state and the corresponding weighted Boltzmann factors for $T=79$ K. Rotational line strengths for the five branches of a $^1\Sigma^+ \leftarrow {}^3\Sigma^-$ transition were taken from Watson,[22] for the case of a $^3\Sigma^-$ state intermediate between Hund's cases (a) and (b), where the ground-state coupling factors[22] were determined from the calculated term values, and the ratio of the perpendicular and parallel transition moments[22] z was a parameter of the fit. The band origin ν_0 and the rotational constant B for $f\,^1\Sigma_u^+(v=2)$ were also parameters of the fit. Rotational line centres ν_i were generated using the term values obtained from the upper- and lower-state spectroscopic constants, and relative line strengths r_i, where $\Sigma_i r_i = 1$, were proportional to the product of an appropriate Boltzmann factor and rotational line strength. Each rotational line was described by a profile of the form

$$\sigma_i(\nu) = \frac{1.77\times10^{-12} f_{\text{eff}} r_i}{\rho^2(1+q^2)\pi\Gamma}\left[1-\rho^2+\frac{\rho^2(q+x)^2}{1+x^2}\right] \times(1+a\Gamma x+b\Gamma^2x^2)\ \text{cm}^2, \quad (1)$$

based on the line shape of Fano and Cooper,[23] where $x=2(\nu-\nu_i)/\Gamma$, and the FWHM predissociation linewidth Γ cm^{-1}, the Fano line shape parameter q, the Fano overlap parameter ρ, the effective band oscillator strength f,[24] and the polynomial coefficients a and b which describe the energy dependence of the underlying continuum, were parameters of the fitting procedure. The total cross section was given by $\sigma(\nu)=\Sigma_i\sigma_i(\nu)$. After modification of $\sigma(\nu)$ to allow for the Doppler contribution to the line shapes, and convolution (in transmission) with a Gaussian instrument function, the model cross section appropriate to the experimental conditions was least-squares fitted to the measured cross section, enabling the determination of the spectroscopic and line shape parameters associated with the (2,0) $f\,^1\Sigma_u^+ \leftarrow X\,^3\Sigma_g^-$ transition. Due to the reduced rotational structure at 79 K, the assumption, implicit in Eq. (1), that the fitted parameters were rotation-independent was found to be valid except for the predissociation linewidth which was allowed to vary with upper-state rotation according to $\Gamma=\Gamma_0+\Gamma_J J(J+1)$.

The results of the fitting procedure are given in Table I. It was found that the transition moment ratio (not given in the Table) $z=0$ within the experimental uncertainty. This is consistent with the absence of ^QQ branches in spectrographic studies of the $f\,^1\Sigma_u^+ \leftarrow X\,^3\Sigma_g^-$ bands,[14,16,18] and shows that $f\,^1\Sigma_u^+ \leftarrow X\,^3\Sigma_g^-$ is a *parallel* transition. Within the combined experimental uncertainties, our measured spectroscopic constants are consistent with those of Ogawa and Yamawaki,[14]

TABLE I. Measured and calculated spectroscopic and line shape parameters for the (2,0) band of the $f\ ^1\Sigma_u^+ \leftarrow X\ ^3\Sigma_g^-$ system of O_2.

Parameter	Measured[a]	CSE I[b]	CSE III[c]
ν_0, cm^{-1}	80001.8±0.6	80001.6	80001.6
B, cm^{-1}	1.651±0.002	1.649[d]	1.649[d]
$f\times10^5$	3.4±0.1	3.9	3.3
Γ_0, cm^{-1}	4.4±0.2	4.2	4.2
$\Gamma_J\times10^3$, cm^{-1}	8.0±4.0[e]	3.3[d]	3.3[d]
ρ^2	0.32±0.03	0.33[f]	0.33[f]
q	−3.0±0.1	−3.4	−3.1

[a]Results of Fano band model fit to $T=79$ K cross section.
[b]Results of Fano profile fit to three-state model calculation.
[c]Results of Fano profile fit to three-state model calculation with additional transition moment.
[d]Effective value determined from energies for $J=0$ and $J=11$ calculated assuming $\mathbf{V}^{\mathrm{ROT}}(R)=J(J+1)\mathbf{I}/R^2$.
[e]A more accurate value 5.6±1.7 was obtained from a fit to a room-temperature cross section.
[f]Estimated from the calculated value $\rho^2=1.0$ for the $\Omega=0$ components of the cross section and a separate calculation of the $\Omega=1$ components.

who obtained $\nu_0=80000.6$ cm^{-1}, $B=1.653$ cm^{-1}, and $D=2.58\times10^{-5}$ cm^{-1}, provided it is noted (1) that we were unable to determine a significant value for D from our low-temperature cross section and (2) that our band origin refers to the *centre*, rather than the peak[14] of the asymmetric line, where $\nu_0(\mathrm{peak})=\nu_0(\mathrm{centre})+\Gamma/(2q)$. The magnitude of our fitted asymmetry parameter, $|q|=3.0$, is the smallest yet reported for a predissociating resonance. The fitted oscillator strength, much greater than that normally expected for a dipole-forbidden transition, and the relatively large predissociation linewidth suggest that a minimal-perturber model may be appropriate in the interpretation of the origins of the $f\ ^1\Sigma_u^+ \leftarrow X\ ^3\Sigma_g^-$ transition moment and the $f\ ^1\Sigma_u^+$ state predissociation. Another important clue to the predissociation mechanism is provided by the fitted value of ρ^2 which implies that the discrete state exhibits a quantum interference with only *one third* of the underlying continuum.

The $f\ ^1\Sigma_u^+$ state is a member of the Rydberg $3p$-complex, built on the ground $X\ ^2\Pi_g$ state of O_2^+, which comprises eight electronic states, $\ldots\pi_g 3p\pi_u(^{1,3}\Sigma_u^{\pm}, ^{1,3}\Delta_u)$ and $\ldots\pi_g 3p\sigma_u(^{1,3}\Pi_u)$. As shown in the Appendix, the diabatic[25] $^1\Sigma_0^+$ and $^3\Sigma_0^-$ Ω-substates from this complex exhibit a spin-orbit interaction $H_{f\hat{E}}^{\mathrm{SO}}=\langle\hat{f}\ ^1\Sigma_{0u}^+|\mathbf{H}^{\mathrm{SO}}|\hat{E}\ ^3\Sigma_{0u}^-\rangle \approx a_{\pi_g}/2$, where a_{π_g} is a one-electron integral over the π_g valence orbital. Lefebvre-Brion and Field[26] have shown that the spin-orbit constant of a $^3\Pi$ state arising from the $\pi\sigma$ molecular orbital configuration is given by $A(^3\Pi)=\langle^3\Pi_1|\mathbf{H}^{\mathrm{SO}}|^3\Pi_1\rangle=a_\pi/2$. In the case of the $3p$-complex of O_2, it follows that $H_{f\hat{E}}^{\mathrm{SO}}\approx A(\pi_g 3p\sigma_u\hat{F}\ ^3\Pi_u) \approx 96$ cm^{-1}.[27] A mechanism whereby the $f\ ^1\Sigma_u^+ \leftarrow X\ ^3\Sigma_g^-$ transition borrows oscillator strength from the dipole-allowed parallel sub-transition $E\ ^3\Sigma_{0u}^- \leftarrow X\ ^3\Sigma_{0g}^-$ via this spin-orbit interaction is consistent with the observed parallel nature of the $f\ ^1\Sigma_u^+ \leftarrow X\ ^3\Sigma_g^-$ transition ($z=0$).

Since Rydberg-valence interactions are expected to play an important role in the spectrum of O_2 in the window region,[11,12] it is necessary to consider the significance of valence states of $^1\Sigma_u^+$ symmetry to the $f\ ^1\Sigma_u^+$ state predissociation. The lowest $^1\Sigma_u^+$ valence state is high-lying, dissociating to $O(^1D)+O(^1S)$ at 11.37 eV, and is thus energetically incapable of directly predissociating $f\ ^1\Sigma_u^+(v=2)$ at 10.02 eV. Guberman and Giusti-Suzor[28] have calculated an *ab initio* potential energy curve for the bound $^1\Sigma_u^+$ valence state which has $T_e=10.08$ eV and $R_e=1.63$ Å, well separated from the $3p\pi_u\ ^1\Sigma_u^+$ potential which has $T_e=9.44$ eV and $R_e=1.11$ Å. They have also determined an *ab initio* electronic width which is related to the electrostatic coupling between the valence $^1\Sigma_u^+$ state and the Rydberg series $np\pi_u\ ^1\Sigma_u^+$. Their results imply that the coupling between the $3p\pi_u\hat{f}\ ^1\Sigma_u^+$ and valence $^1\Sigma_u^+$ states is $|H^e|\approx2200$ cm^{-1}. Although this coupling is substantial, the outer limb of the Rydberg potential crosses the inner limb of the valence potential at an energy well above that of $f\ ^1\Sigma_u^+(v=2)$ and a small Franck–Condon overlap ensures that the $^1\Sigma_u^+$ valence state does not play a role in the predissociation of this level even as an intermediary in second-order couplings to dissociative valence states.

Most of the absorption oscillator strength in the O_2 spectrum from 1170 Å to 2050 Å results from transitions into $^3\Sigma_u^-$ states, especially the Schumann–Runge system $B\ ^3\Sigma_u^- \leftarrow X\ ^3\Sigma_g^-$, ~1350–2050 Å. Although $^3\Pi_u$ states are also dipole-connected to the $X\ ^3\Sigma_g^-$ state, *ab initio* calculations[29] show that the electronic transition moment for the $B\ ^3\Sigma_u^- \leftarrow X\ ^3\Sigma_g^-$ system exceeds that for the lowest valence $^3\Pi_u \leftarrow X\ ^3\Sigma_g^-$ system by more than an order of magnitude. Explicit calculations by Allison *et al.*[30] predict a $^3\Pi_u \leftarrow X\ ^3\Sigma_g^-$ continuum cross section of $\sim6\times10^{-21}$ cm^2 near 1250 Å, <0.5% of our measured cross section. The measurements of Lee *et al.*,[31] who obtain a quantum yield of >0.9 for the production of $O(^1D)+O(^3P)$ in the photodissociation of O_2 near 1250 Å, also support the lack of importance of absorption into the repulsive $^3\Pi_u$ state which dissociates to $O(^3P)+O(^3P)$. Therefore, the contributions of other than $^3\Sigma_u^- \leftarrow X\ ^3\Sigma_g^-$ transitions to the continuum underlying the (2,0) $f\ ^1\Sigma_u^+ \leftarrow X\ ^3\Sigma_g^-$ band can be ignored.

It is well-known[11,12,32] that the lowest pure Rydberg and valence states of $^3\Sigma_u^-$ symmetry, which differ in two of the occupied orbitals, exhibit a strong electrostatic interaction ($|H^e|\approx4000$ cm^{-1}) resulting in the formation of the adiabatic $B\ ^3\Sigma_u^-$ and $E\ ^3\Sigma_u^-$ states which are mixtures of the $\pi_u^3\pi_g^3$ and $\pi_u^4\pi_g 3p\pi_u$ configurations at short internuclear distances. Transitions into the lowest vibrational level of $E\ ^3\Sigma_u^-$ give rise to the longest band,[13] (0,0) $E\ ^3\Sigma_u^- \leftarrow X\ ^3\Sigma_g^-$, a very strong and diffuse resonance near 1244 Å. The $^3\Sigma_u^-$ valence-Rydberg interaction causes the strong predissociation of $E\ ^3\Sigma_u^-(v=0)$, together with noticeable asymmetry and anomalous isotopic effects.[7,33] We propose that the bound state $f\ ^1\Sigma_u^+$ is indirectly predissociated by the $B\ ^3\Sigma_u^-$ continuum through a second-order interaction involving the electronic couplings $H_{f\hat{E}}^{\mathrm{SO}}$ and $H_{\hat{E}\hat{B}}^{\mathrm{e}}=\langle\hat{E}\ ^3\Sigma_{0u}^-|\mathbf{H}^{\mathrm{el}}|\hat{B}\ ^3\Sigma_{0u}^-\rangle$, where $\mathbf{H}^{\mathrm{el}}$ is the electrostatic part of the molecular Hamiltonian. In the case of $f\ ^1\Sigma_u^+(v=2)$, the relative proximity of $E\ ^3\Sigma_u^-(v=0)$ is responsible for the strong observed predissociation.[34] Since only the $\Omega=0$ component of the $^3\Sigma_u^-$ triplet is involved in the spin-orbit interaction, $f\ ^1\Sigma_u^+(v=2)$ will interact with

only one third of the $B\ ^3\Sigma_u^-$ continuum. Since the $^3\Pi_u$ continuum does not contribute appreciably to the cross section near 1250 Å, this picture is consistent with our observed value of $\rho^2=0.32$.

III. CALCULATIONS

A. Coupled-channel Schrödinger equations formalism

Although the Beutler–Fano profile[1] provides a convenient method of characterizing our experimental line shapes, the Fano discrete state-continuum configuration-interaction picture is inappropriate[26] for a quantitative study of the indirect predissociation described here, especially considering the strong $^3\Sigma_u^-$ Rydberg-valence coupling. The techniques of scattering theory[35,36] have been adapted recently to the calculation of molecular photodissociation cross sections. The coupled-channel Schrödinger equations approach, detailed by van Dishoeck *et al.*[37] and Torop *et al.*,[38] can be applied to the strong avoided crossing between the $B\ ^3\Sigma_u^-$ and $E\ ^3\Sigma_u^-$ states of O_2. Briefly, the partial photodissociation cross section from a given rovibrational level of an initial uncoupled electronic state Φ_i into the n coupled states Φ_k, which include n_o open channels, at an energy E and with rotation J is given by

$$\sigma_{EJ\leftarrow iv''J''\Omega''} = 1.225\times10^{-23} g\,\nu |\langle \chi_{EJ}(R)|\mathbf{M}|\chi_{iv''J''\Omega''}(R)\rangle|^2 \ \text{cm}^2, \tag{2}$$

where ν is the transition energy in cm^{-1}, the degeneracy factor $g=(2-\delta_{0,\Lambda+\Lambda''})/(2-\delta_{0,\Lambda''})$, and the transition matrix elements are in atomic units. $\chi_{EJ}(R)$ is the coupled-channel radial wave function matrix, of dimension $n\times n_o$, $\chi_{iv''J''\Omega''}(R)$ is the vibrational wave function of the initial state, and the elements of the $n\times1$ rotronic transition moment vector $\mathbf{M}$ are the products of appropriately normalized electronic transition moments and rotational matrix elements, $M_k=D_{ki}A_k$, where the elements of the electronic transition moment vector $\mathbf{D}$ are

$$D_{ki}=\langle\Phi_k|\boldsymbol{\mu}|\Phi_i\rangle, \tag{3}$$

and the rotational matrix elements

$$A_k=\langle J\Omega_k|\alpha_Z|J''\Omega''\rangle, \tag{4}$$

where $\boldsymbol{\mu}$ and α_Z are the electric dipole and direction-cosine operators, respectively. The coupled-channel radial wave function matrix $\chi_{EJ}(R)$ is the solution of the diabatic-basis coupled Schrödinger equations, expressed in matrix form,

$$\left\{\mathbf{I}\frac{d^2}{dR^2}+\frac{2\mu}{\hbar^2}[E\mathbf{I}-\mathbf{V}(R)-\mathbf{V}^{\text{ROT}}(R)]\right\}\chi_{EJ}(R)=0, \tag{5}$$

where μ is the molecular reduced mass, R is the internuclear separation, $\mathbf{I}$ is the identity matrix, $\mathbf{V}(R)$, of dimension $n\times n$, is the symmetric diabatic potential matrix, the diagonal elements of which are the diabatic electronic potential energy curves $V_k(R)=\langle\Phi_k|\mathbf{H}^{\text{el}}|\Phi_k\rangle$, and $\mathbf{V}^{\text{ROT}}(R)$ is a diagonal matrix with elements $V_{kk}^{\text{ROT}}(R)=\langle\Phi_k|\mathbf{H}^{\text{ROT}}|\Phi_k\rangle$, where $\mathbf{H}^{\text{ROT}}$ is the rotational part of the molecular Hamiltonian. The couplings between the interacting electronic states are given by the off-diagonal elements of $\mathbf{V}(R)$, $V_{kj}(R)=\langle\Phi_k|\mathbf{H}^{\text{el}}+\mathbf{H}^{\text{ROT}}+\mathbf{H}^{\text{SO}}|\Phi_j\rangle$, containing the effects of electrostatic, rotational and spin-orbit interactions.

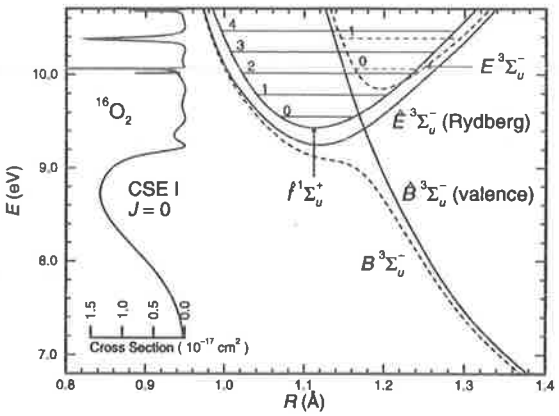

FIG. 3. Diabatic electronic potential energy curves (solid lines) for the three-state model (CSE I) of the $f\ ^1\Sigma_u^+$ state predissociation, together with the corresponding calculated rotationless photoabsorption cross section. Adiabatic potential energy curves (dashed lines) for the $B\ ^3\Sigma_u^-$ and $E\ ^3\Sigma_u^-$ states, which show a strong avoided crossing, are also shown. The $B\ ^3\Sigma_u^-$ potential, and the observed energy levels of the $f\ ^1\Sigma_u^+$ and $E\ ^3\Sigma_u^-$ states can be associated with features in the calculated cross section.

If the electronic wave functions are expressed in the Hund's case (a) e/f parity basis,[26] then the only non-zero elements of $\mathbf{D}$ arise from dipole-allowed parallel and perpendicular transitions between case (a) basis states, and forbidden transitions borrow strength via the explicitly calculated upper-state mixing processes. For a finite temperature, the total photodissociation cross section can be expressed as a sum of upper-state e- and f-level cross sections, each of which is calculated separately as a Boltzmann sum of Eq. (2) over the initial distribution of v'', J'', and, in the case of a multiplet, Ω''.

B. Basic model (CSE I)

The essentials relevant to the predissociation of $f\ ^1\Sigma_u^+(v=2)$ may be illustrated by considering a three-state model,

$$\mathbf{V}(R)=\begin{pmatrix} V_{\hat{B}}(R) & -4038 & 0 \\ -4038 & V_{\hat{E}}(R) & 96 \\ 0 & 96 & V_f(R) \end{pmatrix},$$
$$\mathbf{D}(R)=\begin{pmatrix} D_{\hat{B}X}(R) \\ D_{\hat{E}X}(R) \\ 0 \end{pmatrix}, \tag{6}$$

where the diabatic electronic potential energy curves $V_k(R)$ are shown in Fig. 3, the electrostatic Rydberg-valence coupling $H^e_{\hat{B}\hat{E}}=-4038\ \text{cm}^{-1}$, and the diabatic electronic transition moments, in a. u., are given by

$$D_{\hat{B}X}(R)=\langle\hat{B}\ ^3\Sigma_{0u}^-|\boldsymbol{\mu}_z|X\ ^3\Sigma_{0g}^-\rangle=-2.124+1.059R, \tag{7}$$

and

$$D_{\hat{E}X}(R)=\langle \hat{E}\ ^3\Sigma_{0u}^-|\mu_z|X\ ^3\Sigma_{0g}^-\rangle=-0.052-0.161R, \quad (8)$$

where R is in Å. These parameters have been determined by a least-squares procedure in which the results of CSE calculations were compared with the observed energies and rotational constants for $f\ ^1\Sigma_u^+(v=0-4)$[19] and $E\ ^3\Sigma_u^-(^{18}O_2,\ v=0)$,[18] the measured photoabsorption cross sections into $E\ ^3\Sigma_u^-(^{16}O_2,\ v=0-1)$,[7,8] and measured Schumann–Runge continuum $O(^1D)+O(^3P)$ photodissociation cross sections[31,39] which approximate the $B\ ^3\Sigma_u^-\leftarrow X\ ^3\Sigma_g^-$ photoabsorption cross section. The spin-orbit interaction $H_{\hat{f}\hat{E}}^{SO}$, fixed at 96 cm^{-1} as described previously, and the electrostatic Rydberg-valence interaction $H_{\hat{B}\hat{E}}^{e}$ were taken to be R-independent at small internuclear distances, as appropriate for the diabatic representation, but were decreased to zero at long range with a Gaussian form so that the diabatic and adiabatic potential energy curves became indistinguishable for large R. Tchang-Brillet *et al.*[40] have discussed the effects of different R-dependences for the coupling terms. Our calculated cross sections are sensitive only to the value of the constant coupling in the Franck–Condon region. It was found necessary to allow the electronic transition moments to vary with R in order to obtain a reasonable fit to the measured $^3\Sigma_u^-\leftarrow X\ ^3\Sigma_g^-$ cross sections between 1200 Å and 1750 Å, which correspond to effective R-centroids in the range ~1.1–1.3 Å. The calculated cross sections are insensitive to the transition moments given in Eqs. (7) and (8) for R values significantly outside of this Franck–Condon region.

Although it is not our intention to discuss the $^3\Sigma_u^-$ Rydberg-valence interaction in detail here, we note that our model diabatic $^3\Sigma_u^-$ potentials, $^3\Sigma_u^-\leftarrow X\ ^3\Sigma_g^-$ transition moments, and electrostatic Rydberg-valence coupling are in reasonable agreement with those of Wang *et al.*,[41] obtained principally by fitting the temperature-dependence of the O_2 cross section in the region 1300–1600 Å using a two-state CSE model. The magnitudes and R-dependences of the extrapolated zero-threshold *ab initio* diabatic electronic transition moments of Li *et al.*[32] are in good agreement with our model values, except for the Rydberg transition $\hat{E}\ ^3\Sigma_u^-\leftarrow X\ ^3\Sigma_g^-$ where their result is ~30% smaller, but with a similar R-dependence. We found that it was not possible to obtain good agreement with the observed $^3\Sigma_u^-\leftarrow X\ ^3\Sigma_g^-$ cross section for energies higher than $E\ ^3\Sigma_u^-(v\approx 1)$ unless Rydberg states $np\pi_u\ ^3\Sigma_u^-$ with $n>3$ were included in the model. More detailed CSE studies of the $^3\Sigma_u^-$ states will be reported elsewhere.[42]

C. Rotationless cross sections

A rotationless three-state CSE I cross section $\sigma_{E0\leftarrow X001}$ was calculated using Eqs. (2)–(5) with the degeneracy factor g and the direction-cosine matrix elements A_k set to unity, and ignoring the rotational potential term in Eq. (5). The diabatic coupled-channel radial wave functions $\chi_{E0}(R)$, normalized according to the method of Mies,[35] were calculated by solving Eq. (5) using the Numerov renormalization method of Johnson.[43] In the case of the ground state, the vibrational wave function $\chi_{X001}(R)$ was calculated using an RKR potential energy curve for the $X\ ^3\Sigma_g^-$ state constructed from the spectroscopic constants of Creek and Nicholls.[44]

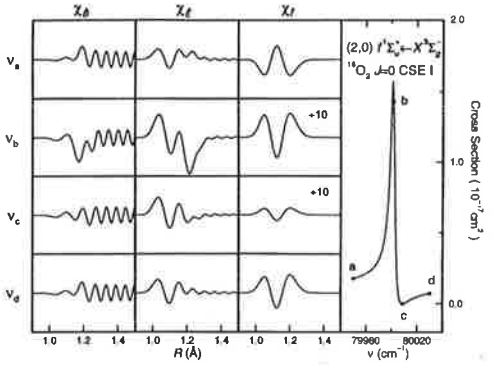

FIG. 4. Detail of the calculated three-state model (CSE I) rotationless cross section for the (2,0) $f\ ^1\Sigma_u^+\leftarrow X\ ^3\Sigma_g^-$ transition, together with corresponding coupled-channel diabatic radial wave functions calculated at four energies across the resonance.

The calculated rotationless cross section is shown in Fig. 3. In the uncoupled adiabatic picture, the essential features of the spectrum can be related to the avoided crossing between the adiabatic $B\ ^3\Sigma_u^-$ and $E\ ^3\Sigma_u^-$ states. The Schumann–Runge continuum which peaks near 8.7 eV, the rapid fall-off at higher energies, and the subsidiary maxima in the cross section are associated with the $B\ ^3\Sigma_u^-$ potential, while the longest and second bands arise from transitions into the lowest two vibrational levels of $E\ ^3\Sigma_u^-$. The CSE treatment, however, demonstrates the large predissociation widths of these two resonances. The spin-orbit coupling between the $\hat{f}\ ^1\Sigma_u^+$ and $\hat{E}\ ^3\Sigma_u^-$ states results in the appearance of $f\ ^1\Sigma_u^+$ resonances in the calculated cross section. In particular, the (2,0) $f\ ^1\Sigma_u^+\leftarrow X\ ^3\Sigma_g^-$ transition appears as a relatively sharp feature on the low-energy wing of the longest band, (0,0) $E\ ^3\Sigma_u^-\leftarrow X\ ^3\Sigma_g^-$. The other $f\leftarrow X$ resonances, even narrower, are not visible in Fig. 3 because of the energy step size chosen for the calculation.

The calculated rotationless cross section in the region of the (2,0) $f\ ^1\Sigma_u^+\leftarrow X\ ^3\Sigma_g^-$ transition is shown in more detail in Fig. 4, together with corresponding coupled-channel radial wave functions calculated at four energies across the highly asymmetric resonance. Since there is only one open channel ($\hat{B}\ ^3\Sigma_u^-$) in the three-state model, the wave function matrix $\chi_{E0}(R)$ reduces to a three-element column vector. In the Fano picture,[1] the quasi-bound level $f\ ^1\Sigma_u^+(v=2)$ undergoes a quantum interference with the underlying $^3\Sigma_u^-$ continuum, constructively at energies lower than the centre of the resonance, destructively at higher energies. In the CSE picture, this interference is implicit in the calculated coupled-channel wave function matrix, in particular $\chi_{\hat{B}}(R)$, and, to a lesser extent $\chi_{\hat{E}}(R)$, since $|D_{\hat{B}X}|\gg|D_{\hat{E}X}|$ and $|D_{\hat{f}X}|=0$. Van Dishoeck *et al.*[37] have shown numerically for the case of photodissociation of OH that resonances calculated using the CSE formalism generally exhibit Fano line shapes. Torop *et al.*[45] have formally established the CSE-Fano equivalence

in the case of the isolated-resonance approximation. Since the Fano line shape parameters provide a convenient means of comparison between experimental and theoretical line shapes, we have fitted a simplified form of Eq. (1) to the calculated cross section of Fig. 4, obtaining the results given in Table I. We found that the calculated resonance was well described by a Fano profile, with a root-mean-square deviation of the fit $<3\times10^{-23}$ cm^2. The simple three-state model (CSE I) is found to predict well all characteristics of the observed resonance, including oscillator strength, predissociation linewidth, and the degree and sense of the line shape asymmetry. It is noteworthy that such good agreement is found with a model $\hat{f}\ ^1\Sigma_u^+$ potential obtained from only the energies and rotational constants of $f\ ^1\Sigma_u^+(v=0-4)$, and using a spin-orbit coupling $H_{\hat{f}\hat{E}}^{SO}$ fixed on configurational grounds.

D. Temperature-specific model (CSE II)

Having verified the essentials of our predissociation model, we now need to calculate realistic cross sections for $T=79$ K and $T=297$ K. We adopt a five-state e-level model with

$$\mathbf{V}(R)=\begin{pmatrix} V_{\hat{B}}(R) & -4038 & -2\sqrt{x}B(R) & 0 & 0 \\ -4038 & V_{\hat{E}}(R) & 0 & -2\sqrt{x}B(R) & 0 \\ -2\sqrt{x}B(R) & 0 & V_{\hat{B}}(R) & -4038 & 0 \\ 0 & -2\sqrt{x}B(R) & -4038 & V_{\hat{E}}(R) & 96 \\ 0 & 0 & 0 & 96 & V_{\hat{f}}(R) \end{pmatrix}, \tag{9}$$

and

$$\mathbf{D}(R)=\begin{pmatrix} D_{\hat{B}X}(R) \\ D_{\hat{E}X}(R) \\ D_{\hat{B}X}(R) \\ D_{\hat{E}X}(R) \\ 0 \end{pmatrix}, \tag{10}$$

where the rows and columns of the diabatic potential matrix are labelled by the case (a) electronic substates, all of e-parity, $\hat{B}\ ^3\Sigma_1^-$, $\hat{E}\ ^3\Sigma_1^-$, $\hat{B}\ ^3\Sigma_0^-$, $\hat{E}\ ^3\Sigma_0^-$, and $\hat{f}\ ^1\Sigma_0^+$, respectively, and the S-uncoupling between the $^3\Sigma_u^-$ $\Omega=0$ and $\Omega=1$ substates has been included explicitly, with $x=J(J+1)$ and $B(R)=\hbar^2/(2\mu R^2)$. This treatment allows correct realization of the rotational structure for both the $^3\Sigma_u^-$ and $^1\Sigma_u^+$ states. The corresponding two-state f-level model has

$$\mathbf{V}(R)=\begin{pmatrix} V_{\hat{B}}(R) & -4038 \\ -4038 & V_{\hat{E}}(R) \end{pmatrix}, \quad \mathbf{D}(R)=\begin{pmatrix} D_{\hat{B}X}(R) \\ D_{\hat{E}X}(R) \end{pmatrix}, \tag{11}$$

where only the $\hat{B}\ ^3\Sigma_1^-$ and $\hat{E}\ ^3\Sigma_1^-$ substates of f-parity contribute to the cross section.

Energy levels of the $X\ ^3\Sigma_g^-$ ground state of O_2, intermediate between Hund's cases (a) and (b), occur as closely spaced N-triplets $F_i(N)$, $i=1-3$. The wave function for the F_2-level with $N=J$ is expressible as a single f-parity case (a) basis function,

$$|X\ ^3\Sigma_g^-,v'',J'',F_2\rangle=|^3\Sigma_1^-,f\rangle|J''1\rangle|\chi_{Xv''J''1}(R)\rangle, \tag{12}$$

while those for the e-parity F_1- and F_3-levels with $J=N\pm1$, respectively, may be expressed as linear combinations of $^3\Sigma_0^-$ and $^3\Sigma_1^-$ basis functions which interact through S-uncoupling.[22] In this work, we do not treat the ground-state mixing explicitly. Using the $X\ ^3\Sigma_g^-$ state RKR potential energy curve and the method described previously, we calculated the F_2 energy levels and vibrational wave functions $\chi_{Xv''J''1}(R)$. The corresponding F_1- and F_3-levels were treated approximately by calculating the $F_1(N)-F_2(N)$ and $F_3(N)-F_2(N)$ energy splittings using the known $X\ ^3\Sigma_g^-$ spectroscopic constants,[21] and assuming that the vibrational wave functions did not vary significantly within the N-triplet fine-structure.

E. Temperature-specific cross sections

Using this model, we calculated temperature-specific cross sections for transitions into the e- and f-levels of the coupled upper states, the lower-state sums over F_i'' reducing to equivalent Boltzmann sums of Eq. (2) over the case (a) basis states, or Ω''. The cross sections were then degraded marginally by convolution (in transmission) with a Gaussian instrumental function of appropriate FWHM before comparison with the measurements. As an example of the validity of our model of the $^3\Sigma_u^-$ Rydberg-valence interaction, it can be seen in Fig. 5 that our calculated total $(e+f)$ cross section for $T=297$ K in the region of the longest band, (0,0) $E\ ^3\Sigma_u^-\leftarrow X\ ^3\Sigma_g^-$, is in excellent agreement with the measured cross section of Lewis *et al.*[7] The calculated total cross section for $T=79$ K in the region of the (2,0) $f\ ^1\Sigma_u^+\leftarrow X\ ^3\Sigma_g^-$ transition, shown in Fig. 1, is in good agreement with our measurements. It is interesting that, following the CSE treatment of the final state, the correct branch stucture is obtained for the $\Delta S=1$ forbidden transition from a model in which the only non-zero rotational matrix elements are the $\Delta S=0$ allowed parallel terms $\langle J0|\alpha_Z^z|J''0\rangle$ and $\langle J1|\alpha_Z^z|J''1\rangle$. It can also be seen in Fig. 2 that the calculated $T=79$ K and $T=297$ K total cross sections describe well the observed strengths, widths and asymmetries of the rotationally-resolved lines of the ^SR branch. With a more

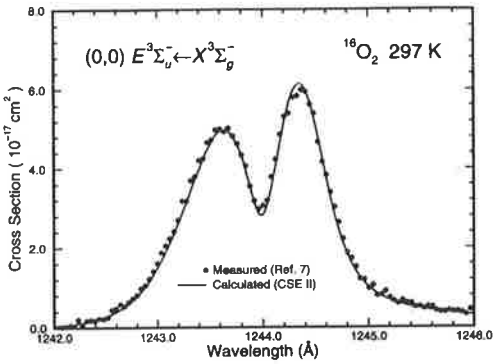

FIG. 5. The calculated (CSE II) room-temperature photoabsorption cross section in the region of the longest band, (0,0) $E\ ^3\Sigma_u^- \leftarrow X\ ^3\Sigma_g^-$, compared with the measurements of Lewis *et al.*[7]

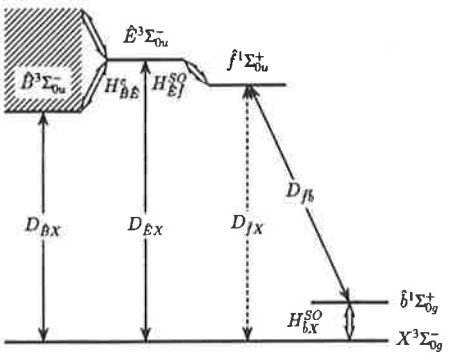

FIG. 6. A schematic view of the diabatic electronic interactions (double lines) and transition amplitudes (single lines) relevant to the predissociation of the $f\ ^1\Sigma_u^+$ state of O_2. In our CSE III model, the transition pathway involving the metastable state $b\ ^1\Sigma_g^+$ is condensed into an equivalent transition amplitude, $D_{\hat{f}X} \approx 0.003$ a. u. If $D_{\hat{f}X}$ is set equal to zero, our simplest model CSE I is obtained.

extensive theoretical treatment of the $^3\Sigma_u^-$ states, it may be possible to reduce further the very small disrepancies between the measured and calculated continuum backgrounds.

F. Further refinements

Before concluding, it is of interest to consider possible model improvements. The most striking feature of our model of the indirect predissociation of $f\ ^1\Sigma_u^+(v=2)$ is that a single spin-orbit parameter $H_{\hat{f}\hat{E}}^{SO}$ controls both the band oscillator strength and the predissociation linewidth. When that parameter is held fixed at a value determined from configurational considerations, both the calculated oscillator strength (+15%) and predissociation linewidth (−5%) are in fairly good agreement with our measurements, but it is impossible to remove the remaining 20% relative discrepancy within the constraints of our model. However, by introducing another source of oscillator strength whereby the forbidden transition $f\ ^1\Sigma_u^+ \leftarrow X\ ^3\Sigma_g^-$ borrows some strength from the dipole-allowed transition $f\ ^1\Sigma_u^+ \leftarrow b\ ^1\Sigma_g^+$ through a strong spin-orbit coupling $H_{bX}^{SO} = \langle \hat{b}\ ^1\Sigma_{0g}^+ | \mathbf{H}^{SO} | X\ ^3\Sigma_{0g}^- \rangle$ between the metastable and ground states, both arising from the π_g^2 configuration, it is possible to resolve the discrepancy. A schematic picture of the improved model is given in Fig. 6, where the possibility of quantum interference between the transition amplitudes involving upper- and lower-state mixing can be seen. Although we do not treat the ground-state mixing explicitly, an estimate of the effective electronic transition moment provided by the new pathway can be obtained from the perturbation theory expression,

$$D_{\hat{f}X} = \langle \hat{f}\ ^1\Sigma_{0u}^+ | \boldsymbol{\mu} | X\ ^3\Sigma_{0g}^- \rangle = \frac{\langle \hat{b}\ ^1\Sigma_{0g}^+ | \mathbf{H}^{SO} | X\ ^3\Sigma_{0g}^- \rangle}{E_0(X\ ^3\Sigma_{0g}^-) - E_0(\hat{b}\ ^1\Sigma_{0g}^+)} \langle \hat{f}\ ^1\Sigma_{0u}^+ | \boldsymbol{\mu} | \hat{b}\ ^1\Sigma_{0g}^+ \rangle. \tag{13}$$

Klotz and Peyerimhoff[46] have calculated *ab initio* a value of $H_{bX}^{SO} = 177$ cm^{-1} at $R = 2.3$ a. u. The unperturbed energy separation $E_0(X\ ^3\Sigma_{0g}^-) - E_0(\hat{b}\ ^1\Sigma_{0g}^+) \approx -T_e(b\ ^1\Sigma_g^+)$ ≈ -13200 cm^{-1}, and, as shown in the Appendix, in the single-configuration approximation the Rydberg electronic transition moment $D_{\hat{f}\hat{b}} = D_{\hat{E}X}$. Using our model value for $D_{\hat{E}X}$ [Eq. (8)] and neglecting R-dependence in the Franck–Condon region, it follows from Eq. (13) that $D_{\hat{f}X} \approx (177 \times -0.25)/(-13200) \approx +0.003$ a. u.

Using an improved three-state model (CSE III) which includes a modified diabatic electronic transition moment vector

$$\mathbf{D}(R) = \begin{pmatrix} D_{\hat{B}X}(R) \\ D_{\hat{E}X}(R) \\ 0.003 \end{pmatrix}, \tag{14}$$

we calculated a rotationless cross section for the (2,0) $f\ ^1\Sigma_u^+ \leftarrow X\ ^3\Sigma_g^-$ transition, obtaining the improved spectroscopic and line shape parameters given in Table I, where it can be seen that there has been *destructive* quantum interference between the transition amplitudes such that the calculated oscillator strength has been reduced from 3.9×10^{-5} to 3.3×10^{-5}, in better agreement with the measurements. The only other affected parameter is the q-value which has changed from −3.4 to −3.1, also in better agreement with the measurements.

Although the absolute sign of an off-diagonal matrix element between electronic wave functions has no physical meaning, it is often possible to determine the sign of the product of several such matrix elements from experimental observations of quantum-interference effects.[26] We have determined unambiguously that the product $D_{\hat{B}X} H_{\hat{B}\hat{E}}^e D_{\hat{E}X}$ is *negative* by fitting the $^3\Sigma_u^-$ part of the CSE model to the measured $^3\Sigma_u^- \leftarrow X\ ^3\Sigma_g^-$ cross section over a significant energy range. It was found that the measurements could only be explained if the transition amplitudes into the Rydberg and valence $^3\Sigma_u^-$ states interfered destructively. We suggest that the product $D_{\hat{E}X} H_{\hat{f}\hat{E}}^{SO} D_{\hat{f}X}$ is also negative, since a constructive interference between the transition amplitudes would make it impossible to explain simultaneously the ob-

served predissociation linewidth and oscillator strength for the (2,0) $f\,^1\Sigma_u^+ \leftarrow X\,^3\Sigma_g^-$ band. Because of the relatively small interference effect for the (2,0) band, however, an absolute confirmation of the latter conclusion must await a more detailed study of all vibrational bands in the $f\,^1\Sigma_u^+ \leftarrow X\,^3\Sigma_g^-$ system, since it is likely that the interference effect will be greater for the weaker bands. We show in the Appendix that the observed negative signs for the above two matrix-element products are confirmed theoretically in the single-configuration picture.

The only remaining unsatisfactory aspect of the results presented in Table I is that the CSE calculations underestimate the observed J-dependence of the predissociation linewidth. It is likely that this occurs because we have neglected L-uncoupling interactions between the $f\,^1\Sigma_u^+$ state and $^1\Pi_u$ states in our model. At present, knowledge of the $^1\Pi_u$ states of O_2, including a strong expected Rydberg-valence interaction,[11] is slight.

IV. CONCLUSIONS

Rotationally-resolved Beutler–Fano line shapes observed in the photoabsorption spectrum of the (2,0) band of the $3p\pi_u f\,^1\Sigma_u^+ \leftarrow X\,^3\Sigma_g^-$ Rydberg system of O_2 are found to be the most asymmetric yet reported for molecular dissociation, with fitted Fano asymmetry parameters $q=-3.0\pm0.1$. It has been established that the $f\,^1\Sigma_u^+$ state is indirectly predissociated by the $B\,^3\Sigma_u^-$ continuum, the $f\,^1\Sigma_u^+ \leftarrow X\,^3\Sigma_g^-$ transition borrowing oscillator strength primarily from the dipole-allowed mixed Rydberg-valence transitions $B,E\,^3\Sigma_u^- \leftarrow X\,^3\Sigma_g^-$. In this picture, a single spin-orbit interaction between the $f\,^1\Sigma_u^+$ and $\hat{E}\,^3\Sigma_u^-$ diabatic components of the Rydberg $3p$-complex controls both the predissociation linewidth and the oscillator strength of the (2,0) $f\,^1\Sigma_u^+ \leftarrow X\,^3\Sigma_g^-$ resonance. A coupled-channel Schrödinger equations treatment of the predissociation succeeds in explaining quantitatively the observed spectroscopic and line shape parameters. There is some evidence that a small portion of the $f \leftarrow X$ oscillator strength is borrowed from the dipole-allowed transition $f\,^1\Sigma_u^+ \leftarrow b\,^1\Sigma_g^+$ through spin-orbit mixing between the $b\,^1\Sigma_g^+$ and $X\,^3\Sigma_g^-$ states, and that this transition amplitude interferes destructively with the contribution from the $E\,^3\Sigma_u^- \leftarrow X\,^3\Sigma_g^-$ transition.

ACKNOWLEDGMENTS

The authors are extremely grateful to Dr. H. Lefebvre-Brion, whose advice led to the theoretical arguments contained in the Appendix, and Professor R. W. Field, for clarifications regarding the single-configuration expressions for molecular matrix elements. We also thank Professor M. L. Ginter and Dr. P. C. Cosby for their assistance, comments and suggestions made during visits to the ANU sponsored by the National Science Foundation (US) through a US Australia Cooperative Research Grant. The authors are also indebted to Professor J. H. Carver and Dr. J. P. England for critical readings of the manuscript, and K. J. Lonsdale and C. J. Dedman for valuable technical assistance.

APPENDIX THE SIGNS OF MATRIX-ELEMENT PRODUCTS (Ref. 47)

Using relatively simple arguments based on a single-configuration view of the relevant electronic matrix elements, it is possible to obtain theoretical support for the destructive nature of the interference effects observed in the present work. In order to achieve this, it is important to note that, while the absolute sign of an off-diagonal matrix element has no physical meaning, it is necessary to define consistently the phases of the determinantal wave functions used in calculating the signs of matrix-element products which can be determined experimentally.[26]

1. The sign of $D_{\hat{E}X}H^{SO}_{\hat{f}\hat{E}}D_{\hat{f}X}$

The ground $X\,^3\Sigma_g^-$ and second metastable $\hat{b}\,^1\Sigma_g^+$ valence states of O_2 arise from the primary molecular orbital configuration $...(1\pi_u)^4(1\pi_g)^2$, while the pure Rydberg states $\hat{f}\,^1\Sigma_u^+$ and $\hat{E}\,^3\Sigma_u^-$ are derived from the $...(1\pi_u)^4(1\pi_g)^1(3p\pi_u)$ configuration. Suppressing the closed shells, we choose the following representations of the molecular electronic wave functions:

$$|X\,^3\Sigma_{g0}^-\rangle = \frac{1}{\sqrt{2}}|\pi_g^+\pi_g^-(\alpha\beta+\beta\alpha)\rangle, \tag{A1}$$

$$|\hat{b}\,^1\Sigma_{g0}^+\rangle = \frac{1}{\sqrt{2}}|\pi_g^+\pi_g^-(\alpha\beta-\beta\alpha)\rangle, \tag{A2}$$

$$|\hat{E}\,^3\Sigma_{u0}^-\rangle = \tfrac{1}{2}|(\pi_g^+3p\pi_u^- - \pi_g^-3p\pi_u^+)(\alpha\beta+\beta\alpha)\rangle, \tag{A3}$$

and

$$|\hat{f}\,^1\Sigma_{u0}^+\rangle = \tfrac{1}{2}|(\pi_g^+3p\pi_u^- + \pi_g^-3p\pi_u^+)(\alpha\beta-\beta\alpha)\rangle, \tag{A4}$$

where the conventional notation of Lefebvre-Brion and Field[26] has been used to describe the spin-orbitals.

The mono-electronic form of the spin-orbit operator may be written[26]

$$\mathbf{H}^{SO} = \sum_i \hat{a}_i \mathbf{l}_i \cdot \mathbf{s}_i, \tag{A5}$$

where $\hat{a}_i$ is an operator acting only on the radial part of the wave functions and

$$\mathbf{l}_i \cdot \mathbf{s}_i = \mathbf{l}_{iz}\mathbf{s}_{iz} + \tfrac{1}{2}(\mathbf{l}_i^+\mathbf{s}_i^- + \mathbf{l}_i^-\mathbf{s}_i^+). \tag{A6}$$

When the spin-orbit operator Eq. (A5) is applied to the wave functions of Eqs. (A1) and (A2), the $\mathbf{l}_{iz}\mathbf{s}_{iz}$ term leads to the result

$$H^{SO}_{\hat{b}X} = \langle \hat{b}\,^1\Sigma_{g0}^+|\mathbf{H}^{SO}|X\,^3\Sigma_{g0}^-\rangle = a_{\pi_g}, \tag{A7}$$

where $a_{\pi_g} = \langle \pi_g|\hat{a}|\pi_g\rangle > 0$ is a molecular spin-orbit parameter which is expected to be of the order of the atomic spin-orbit parameter[26] $\zeta_O(2p) = 151$ cm^{-1}. *Ab initio* calculations[46,48] of $H^{SO}_{\hat{b}X}$ have yielded values ≈ 180 cm^{-1} at $R=2.3$ a. u. The result in Eq. (A7) is consistent with that obtained by Lefebvre-Brion and Field[26] for $^1\Sigma_0^+$ and $^3\Sigma_0^-$ states derived from the π^2 configuration.

Similarly, applying Eq. (A5) to the wave functions of Eqs. (A3) and (A4), we obtain

$$H^{SO}_{\hat{f}\hat{E}}=\langle \hat{f}\ ^1\Sigma^+_{u0}|\mathbf{H}^{SO}|\hat{E}\ ^3\Sigma^-_{u0}\rangle=\tfrac{1}{2}(a_{\pi_g}+a_{3p\pi_u}), \quad \text{(A8)}$$

where $a_{3p\pi_u}=\langle 3p\pi_u|\hat{a}|3p\pi_u\rangle>0$. This is consistent with the result of Loo *et al.*[49] for $^1\Sigma^+_0$ and $^3\Sigma^-_0$ states arising from the $\pi\pi'$ configuration, but is of the opposite sign to the earlier results of Lefebvre-Brion and Field[26,50] due to the adoption of different phase conventions for the wave functions. Since the operator $\hat{a}$ varies as $1/r^3$, where r represents the electron coordinates, the contribution from the Rydberg orbital is negligible compared with $a_{\pi_g}/2$. For the calculations in this work we have adopted the value $H^{SO}_{\hat{f}\hat{E}}=96\ \text{cm}^{-1}$, as justified in Sec. II.

Applying the electric-dipole transition operator $\vec{\mu}=e\Sigma_i\vec{r}_i$ to the wave functions of Eqs. (A1)–(A4), we obtain the following single-configuration estimates of the electronic transition moments into the Rydberg states:

$$D_{\hat{E}X}=\langle \hat{E}\ ^3\Sigma^-_{u0}|\mu_z|X\ ^3\Sigma^-_{g0}\rangle=\sqrt{2}\langle 3p\pi_u|\mu_z|\pi_g\rangle, \quad \text{(A9)}$$

and

$$D_{\hat{f}\hat{b}}=\langle \hat{f}\ ^1\Sigma^+_{u0}|\mu_z|\hat{b}\ ^1\Sigma^+_{g0}\rangle=\sqrt{2}\langle 3p\pi_u|\mu_z|\pi_g\rangle. \quad \text{(A10)}$$

Finally, from Eq. (13) of Sec. III F, we note that $D_{\hat{f}X}=D_{\hat{f}\hat{b}}H^{SO}_{\hat{b}X}/[E_0(X)-E_0(\hat{b})]$. Using this result together with Eqs. (A7)–(A10), and ignoring the contribution of the Rydberg orbital to Eq. (A8), it follows that

$$D_{\hat{E}X}H^{SO}_{\hat{f}\hat{E}}D_{\hat{f}X}\approx\langle 3p\pi_u|\mu_z|\pi_g\rangle^2 a^2_{\pi_g}/[E_0(X)-E_0(\hat{b})]<0. \quad \text{(A11)}$$

The negative sign of this matrix-element product supports our tentative observation of destructive interference between the two transition amplitudes.

2. The sign of $D_{\hat{B}X}H^{e}_{\hat{B}\hat{E}}D_{\hat{E}X}$

The molecular electronic wave function for the $\hat{B}\ ^3\Sigma^-_u$ valence state of O_2, which arises principally from the $\ldots(1\pi_u)^3(1\pi_g)^3$ molecular orbital configuration, may be written as

$$|\hat{B}\ ^3\Sigma^-_{u0}\rangle=\tfrac{1}{2}|\pi^+_u\alpha\pi^+_u\beta\pi^-_g\alpha\pi^-_g\beta[\pi^-_u\pi^+_g(\alpha\beta+\beta\alpha)]-\pi^-_u\alpha\pi^-_u\beta\pi^+_g\alpha\pi^+_g\beta[\pi^+_u\pi^-_g(\alpha\beta+\beta\alpha)]\rangle. \quad \text{(A12)}$$

Using Eq. (A12) together with Eq. (A1), but noting that it is now necessary to consider the closed $(1\pi_u)^4$ shell suppressed in Eq. (A1) since the operator sums span six, rather than two electrons, it follows that the $\hat{B}\leftarrow X$ electronic transition moment may be written as

$$D_{\hat{B}X}=\langle \hat{B}\ ^3\Sigma^-_{u0}|\mu_z|X\ ^3\Sigma^-_{g0}\rangle=\sqrt{2}\langle \pi_g|\mu_z|\pi_u\rangle. \quad \text{(A13)}$$

Although the valence and Rydberg states of $^3\Sigma^-_u$ symmetry differ in two of the occupied orbitals, they are coupled by the electronic Hamiltonian $\mathbf{H}^{el}$ which contains a two-electron operator $\Sigma_{i<j}e^2/r_{ij}$.[26] Applying this operator to Eqs. (A3) and (A2), but considering the closed $(1\pi_u)^4$ shell suppressed in Eq. (A3), we obtain

$$H^{e}_{\hat{B}\hat{E}}=\langle \hat{B}\ ^3\Sigma^-_{0u}|\mathbf{H}^{el}|\hat{E}\ ^3\Sigma^-_{0u}\rangle=2\langle \pi^+_u\pi^-_g|3p\pi^+_u\pi^-_g\rangle, \quad \text{(A14)}$$

where we have used the notation of Lefebvre-Brion and Field[26] to describe the two-electron orbital integral. It then follows from Eqs. (A9), (A13) and (A14) that the required matrix-element product can be expressed as

$$D_{\hat{B}X}H^{e}_{\hat{B}\hat{E}}D_{\hat{E}X}=4\langle \pi_g|\mu_z|\pi_u\rangle\langle \pi^+_u\pi^-_g|3p\pi^+_u\pi^-_g\rangle\times\langle 3p\pi_u|\mu_z|\pi_g\rangle \quad \text{(A15)}$$

in the single-configuration approximation. Since each molecular orbital appears exactly twice in Eq. (A5), the sign of the expression is independent of the choice of a molecular phase convention.

Unlike the situation in Sec. A 1, the sign of the matrix-element product in Eq. (A15) can only be determined from a specific consideration of the atomic-orbital composition of the relevant molecular orbitals. Using a $3p\pi_u$ Rydberg orbital obtained from *ab initio* calculations in the manner described in Ref. 51, and the basis set reported in Ref. 52, we obtain, at $R=2.582$ a. u.,

$$\langle \pi_g|\mu_z|\pi_u\rangle=-1.306\ \text{a. u.}, \quad \text{(A16)}$$

$$\langle 3p\pi_u|\mu_z|\pi_g\rangle=-0.0393\ \text{a. u.}, \quad \text{(A17)}$$

and

$$\langle \pi^+_u\pi^-_g|3p\pi^+_u\pi^-_g\rangle=-0.01849\ \text{a. u.} \quad \text{(A18)}$$

These expressions lead to single-configuration estimates of $D_{\hat{B}X}$, $H^{e}_{\hat{B}\hat{E}}$ and $D_{\hat{E}X}$ of the same sign as, but with magnitudes differing somewhat from the semi-empirical values adopted in this work.

The terms contributing to the matrix elements given in Eqs. (A16)–(A18) may be decomposed as follows. First, the valence orbitals can be approximated by[26,53]

$$|\pi_u\rangle=\frac{1}{\sqrt{2}}(|2p\pi_A\rangle+|2p\pi_B\rangle), \quad \text{(A19)}$$

and

$$|\pi_g\rangle=\frac{1}{\sqrt{2}}(|2p\pi_A\rangle-|2p\pi_B\rangle), \quad \text{(A20)}$$

where the overlap between the orbitals centred on the A and B atoms has been neglected in the normalization factor. In this case, it can be shown that $\langle \pi_g|\mu_z|\pi_u\rangle\approx -R/2<0$, in good agreement with the *ab initio* value given in Eq. (A16) when $R=2.582$ a. u. Second, if the Rydberg orbital is approximated by

$$|3p\pi_u\rangle=|3p\pi_G\rangle-S|\pi_u\rangle, \quad \text{(A21)}$$

where G is the centre of mass and S is the overlap between the $3p\pi_G$ Slater orbital and the π_u orbital, then

$$\begin{aligned}\langle 3p\pi_u|\mu_z|\pi_g\rangle&=\langle 3p\pi_G|\mu_z|\pi_g\rangle-S\langle \pi_u|\mu_z|\pi_g\rangle\\&=-0.2224-0.14\times(-1.306)\\&=-0.0396\ \text{a. u.},\end{aligned} \quad \text{(A22)}$$

in agreement with Eq. (A17). Similarly,

$$\begin{aligned}\langle \pi_u^+ \pi_g^- | 3p\pi_u^+ \pi_g^- \rangle &= \langle \pi_u^+ \pi_g^- | 3p\pi_G^+ \pi_g^- \rangle \\ &\quad - S\langle \pi_u^+ \pi_g^- | \pi_u^+ \pi_g^- \rangle \\ &= 0.0132 - 0.14 \times (0.2277) \\ &= -0.01865 \text{ a. u.}, \end{aligned} \tag{A23}$$

in agreement with Eq. (A18).

From Eqs. (A15)–(A18), it is clear that $D_{\hat{B}X} H^e_{\hat{B}\hat{E}} D_{\hat{E}X} < 0$, in agreement with our observation of destructive interference between the Rydberg and valence transition amplitudes.

[1] U. Fano, Phys. Rev. **124**, 1866 (1961).
[2] G. Herzberg, in *Topics in Modern Physics—A Tribute to E. U. Condon*, edited by W. E. Brittin and H. Odabasi (Colorado Association University Press, Boulder, 1971), p. 191.
[3] F. J. Comes and G. Schumpe, Z. Naturforsch. **26**, 538 (1971).
[4] M. Rothschild, H. Egger, R. T. Hawkins, H. Pummer, and C. K. Rhodes, Chem. Phys. Lett. **72**, 404 (1980).
[5] M. Rothschild, H. Egger, R. T. Hawkins, J. Bokor, H. Pummer, and C. K. Rhodes, Phys. Rev. A **23**, 206 (1981).
[6] M. Glass-Maujean, J. Breton, and P. M. Guyon, Chem. Phys. Lett. **63**, 591 (1979).
[7] B. R. Lewis, S. T. Gibson, M. Emami, and J. H. Carver, J. Quant. Spectrosc. Radiat. Transfer **40**, 1 (1988).
[8] B. R. Lewis, S. T. Gibson, M. Emami, and J. H. Carver, J. Quant. Spectrosc. Radiat. Transfer **40**, 469 (1988).
[9] B. R. Lewis and S. T. Gibson, Can. J. Phys. **68**, 231 (1990).
[10] B. Kim and K. Yoshihara, J. Chem. Phys. **99**, 1433 (1993).
[11] R. J. Buenker and S. D. Peyerimhoff, Chem. Phys. **8**, 324 (1975).
[12] R. J. Buenker and S. D. Peyerimhoff, Chem. Phys. Lett. **34**, 225 (1975).
[13] Y. Tanaka, J. Chem. Phys. **20**, 1728 (1952).
[14] M. Ogawa and K. R. Yamawaki, Can. J. Phys. **47**, 1805 (1969).
[15] K. P. Huber and G. Herzberg, *Molecular Spectra and Molecular Structure. IV. Constants of Diatomic Molecules* (Van Nostrand, New York, 1979), p. 494.
[16] F. Alberti, R. A. Ashby, and A. E. Douglas, Can. J. Phys. **46**, 337 (1968).
[17] For values of the Fano asymmetry parameter $|q| \gtrsim 1$, the line shape asymmetry can be related to $1/q$. As q approaches zero, however, the line shape approaches a symmetric window resonance.
[18] M. Ogawa, Can. J. Phys. **53**, 2703 (1975).
[19] D. H. Katayama, S. Ogawa, M. Ogawa, and Y. Tanaka, J. Chem. Phys. **67**, 2132 (1977).
[20] S. G. Tilford and J. D. Simmons, J. Phys. Chem. Ref. Data **1**, 147 (1972).
[21] L. Veseth and A. Lofthus, Mol. Phys. **27**, 511 (1974).
[22] J. K. G. Watson, Can. J. Phys. **46**, 1637 (1968).
[23] U. Fano and J. W. Cooper, Rev. Mod. Phys. **40**, 441 (1968).
[24] The discrete oscillator strength f_{FC} defined by Fano and Cooper (Ref. 23) is related to our oscillator strength by $f_{FC} = fq^2/(1+q^2)$. Our choice bears a more direct relationship to the apparent strength of the observed band structure.
[25] Throughout this work we use the *hat* to distinguish the pure diabatic state from the corresponding adiabatic state.
[26] H. Lefebvre-Brion and R. W. Field, *Perturbations in the Spectra of Diatomic Molecules* (Academic, Orlando, 1986), pp. 56, 59, 64, 67, 74–75, 88, 91–94, 108, 208–210, 217, 375.
[27] Although the $F\ ^3\Pi_u$ state is a mixture of the $\pi_g 3p\sigma_u$ Rydberg and $\pi_g \sigma_u$ valence configurations (Refs. 11, 12, and 26) its spin-orbit constant depends only on the valence orbital π_g which is common to each component of the mixture. Therefore, the single-configuration expression for A will still be valid. The value adopted in this work (96 cm^{-1}) applies at the R-centroid for the (2,0) $f\ ^1\Sigma_u^+ \leftarrow X\ ^3\Sigma_g^-$ transition and was determined from an analysis of the $(v',0)$ $F\ ^3\Pi_u \leftarrow X\ ^3\Sigma_g^-$ bands (J. P. England, manuscript in preparation, 1994). The slightly smaller value which is obtained from the (0,0) $F \leftarrow X$ band measurements (H. C. Chang and M. Ogawa, J. Mol. Spectrosc. **44**, 405 (1972)) applies at a larger R value since the $F\ ^3\Pi_u$ potential-energy curve exhibits a double minimum with the $v=0$ level contained in the outer minimum.
[28] S. L. Guberman and A. Giusti-Suzor, J. Chem. Phys. **95**, 2602 (1991).
[29] P. S. Julienne, D. Neumann, and M. Krauss, J. Chem. Phys. **64**, 2990 (1976).
[30] A. C. Allison, S. L. Guberman, and A. Dalgarno, J. Geophys. Res. **87**, 923 (1982).
[31] L. C. Lee, T. G. Slanger, G. Black, and R. L. Sharpless, J. Chem. Phys. **67**, 5602 (1977).
[32] Y. Li, M. Honigmann, K. Bhanuprakash, G. Hirsch, R. J. Buenker, M. A. Dillon, and M. Kimura, J. Chem. Phys **96**, 8314 (1992).
[33] J. Wang, A. J. Blake, D. G. McCoy, and L. Torop, J. Quant. Spectrosc. Radiat. Transfer **40**, 501 (1988).
[34] Despite the relative proximity of $f\ ^1\Sigma_u^+(v=2)$ and $E\ ^3\Sigma_u^-(v=0)$, with an energy separation of ~ 380 cm^{-1}, the remote-perturber rotational line strengths of Watson (Ref. 22) appear adequate to describe the measured 79 K cross section.
[35] F. H. Mies, Mol. Phys. **41**, 953 (1980).
[36] F. H. Mies, Mol. Phys. **41**, 973 (1980).
[37] E. F. van Dishoeck, M. C. van Hemert, A. C. Allison, and A. Dalgarno, J. Chem. Phys. **81**, 5709 (1984).
[38] L. Torop, D. G. McCoy, A. J. Blake, J. Wang, and T. Scholz, J. Quant. Spectrosc. Radiat. Transfer **38**, 9 (1987).
[39] S. T. Gibson and B. R. Lewis (unpublished).
[40] W. -Ü L. Tchang-Brillet, P. S. Julienne, J. -M. Robbe, C. Letzelter, and F. Rostas, J. Chem. Phys. **96**, 6735 (1992).
[41] J. Wang, D. G. McCoy, A. J. Blake, and L. Torop, J. Quant. Spectrosc. Radiat. Transfer **38**, 19 (1987).
[42] B. R. Lewis, S. T. Gibson, and J. P. England (in preparation, 1994).
[43] B. R. Johnson, J. Chem. Phys. **69**, 4678 (1978).
[44] D. Creek and R. W. Nicholls, Proc. R. Soc. Lond. Ser. **341**, 517 (1975).
[45] L. Torop, J. Wang, D. G. McCoy, and A. J. Blake, J. Quant. Spectrosc. Radiat. Transfer **43**, 457 (1990).
[46] R. Klotz and S. D. Peyerimhoff, Mol. Phys. **57**, 573 (1986).
[47] The material in this appendix is due to H. Lefebvre-Brion (private communication, 1994).
[48] F. D. Wayne and E. A. Colbourn, Mol. Phys. **34**, 1141 (1977).
[49] R. Ogorzalek Loo, W. J. Marinelli, P. L. Houston, S. Arepalli, J. R. Wiesenfeld, and R. W. Field, J. Chem. Phys. **91**, 5185 (1989).
[50] R. W. Field and H. Lefebvre-Brion, Acta Phys. Hung. **35**, 51 (1974).
[51] H. Lefebvre-Brion, in *Atomic and Molecular Physics and Quantum Optics*, edited by H.-A. Bachor, K. Kumar, and B. A. Robson (World Scientific, Singapore, 1992), pp. 396–398.
[52] H. Lefebvre-Brion, in *Abstracts of International Symposium: Molecules in Physics, Chemistry and Biology*, Vol. 2, edited by J. Maruani (Kluwer, Dordrecht, 1988), p. 257.
[53] P. S. Julienne, D. Neumann, and M. Krauss, J. Chem. Phys. **64**, 2990 (1976).

4.19 Identification of the $4p\sigma_u\,{}^1\Pi_u$ Rydberg state of O_2

[39] J. P. England, B. R. Lewis, and M. L. Ginter,
Journal of Chemical Physics **103**, 1727–1731 (1995).

Identification of the $4p\sigma_u\ ^1\Pi_u$ Rydberg state of O_2

J. P. England and B. R. Lewis
Research School of Physical Sciences and Engineering, The Australian National University, Canberra, ACT 0200, Australia

M. L. Ginter
Institute for Physical Science and Technology, University of Maryland, College Park, Maryland 20742

(Received 23 February 1995; accepted 24 April 1995)

New high-resolution measurements of the O_2 photoabsorption cross section in the 1147–1155 Å region are presented. The observation of three previously-unreported narrow lines in a band near 1148 Å has enabled unambiguous assignment of the band to a $^1\Pi_u \leftarrow X^3\Sigma_g^-$ transition which gains strength through a spin-orbit interaction with the upper state of a $^3\Pi_u \leftarrow X^3\Sigma_g^-$ transition appearing at 1153 Å. Other lines in the 1148 Å band are broadened by predissociation through a heterogeneous interaction with a nearly energetically coincident $^1\Delta_u$ level. The states, labelled $h^1\Pi_u$, $F^3\Pi_u$ and $i^1\Delta_u$, are predominantly of $4p\lambda$ Rydberg molecular orbital configurations although there are indications that the Π_u states interact strongly with valence states of the same symmetry. © *1995 American Institute of Physics.*

I. INTRODUCTION

Oxygen molecules in the atmosphere are the dominant absorbers of solar radiation in the 1000–2000 Å region. The importance of O_2 in the photochemistry and aeronomy of the terrestrial atmosphere has motivated a large number of experimental studies of the photoabsorption spectrum; however, the complexity of the spectrum in the window region (1100–1300 Å) and irregularities due to large Rydberg-valence state interactions have meant that there have been few definitive assignments of the features. A comprehensive review of the spectrum of molecular oxygen was published by Krupenie[1] and the importance of molecular oxygen in the absorption processes in the upper atmosphere has been discussed by Watanabe.[2] This paper, in which we discuss two bands near 1148 Å and 1153 Å, is part of a detailed study of photoabsorption in the O_2 window region involving high resolution measurements as well as theoretical modelling using coupled-channel Schrödinger equation (CSE) calculations.

Figure 1 shows the potential energy curves of the lowest states of O_2 as well as the diabatic potential energy curves of excited states relevant to the present work. The ground $X^3\Sigma_g^-$ state and the metastable $a^1\Delta_g$ and $b^1\Sigma_g^+$ states are associated with the molecular orbital configuration $(1\sigma_g)^2(1\sigma_u)^2(2\sigma_g)^2(2\sigma_u)^2(3\sigma_g)^2(1\pi_u)^4(1\pi_g)^2$. The bound valence states $B^3\Sigma_u^-$ and $^1\Delta_u$ arise from the configuration $(1\sigma_g)^2(1\sigma_u)^2(2\sigma_g)^2(2\sigma_u)^2(3\sigma_g)^2(1\pi_u)^3(1\pi_g)^3$, while the unbound $^3\Pi_u$ and $^1\Pi_u$ valence states arise from the configuration $(1\sigma_g)^2(1\sigma_u)^2(2\sigma_g)^2(2\sigma_u)^2(3\sigma_g)^2(3\sigma_u)^1(1\pi_u)^4(1\pi_g)^1$.

The lowest energy *ungerade* Rydberg states are the first members of the $np\lambda$ complexes ($n=3,4,5,...$) built on the $X^2\Pi_g$ state of O_2^+. These complexes consist of the molecular states $^1\Pi_u$ and $^3\Pi_u$ from the configurations $(1\sigma_g)^2(1\sigma_u)^2(2\sigma_g)^2(2\sigma_u)^2(3\sigma_g)^2(1\pi_u)^4(1\pi_g)^1np\sigma_u$ and $^1\Sigma_u^\pm$, $^3\Sigma_u^\pm$, $^1\Delta_u$ and $^3\Delta_u$ from the configurations $(1\sigma_g)^2(1\sigma_u)^2(2\sigma_g)^2(2\sigma_u)^2(3\sigma_g)^2(1\pi_u)^4(1\pi_g)^1np\pi_u$. The crossing of these states by valence states of the same symmetry which differ in one or two of the occupied molecular orbitals can result in strong electrostatic interactions,[3,4] and it is these interactions which are responsible for many of the irregularities in the absorption spectrum. In addition, in most cases the Rydberg states are at energies above the dissociation limits of the valence states and, therefore, Rydberg-valence coupling can give rise to predissociation of the Rydberg states.

The strongest transitions from the ground state seen in the photoabsorption spectrum of O_2 are dipole-allowed $^3\Sigma_u^- \leftarrow X^3\Sigma_g^-$ and $^3\Pi_u \leftarrow X^3\Sigma_g^-$ transitions. Transitions from the $X^3\Sigma_g^-$ state to the $B^3\Sigma_u^-$ state give rise to the well-known Schumann-Runge system. Transitions to the $E^3\Sigma_u^-$ state,[5] a potential well formed by the interaction of the $3p\pi_u$ Rydberg and the valence $^3\Sigma_u^-$ states,[6] give rise to Tanaka's Longest, Second and Third Bands.[7] The lowest energy $^3\Pi_u \leftarrow X^3\Sigma_g^-$ transition having discrete structure is at 1163 Å. A rotational analysis[9] of this band indicated that the upper state, labelled $F^3\Pi_u$ by Huber and Herzberg,[8] is a Rydberg-valence mixed state, analogous to the $E^3\Sigma_u^-$ state.

Transitions from the ground state to states of other multiplicities are electric-dipole forbidden, but they may be seen in the absorption spectrum if they gain strength through interactions of their upper states with $^3\Sigma_u^-$ or $^3\Pi_u$ states. For example, weak bands of the system $3p\pi_u\ f^1\Sigma_u^+ \leftarrow X^3\Sigma_g^-$ (1196–1280 Å), which have been studied in some detail,[10–12] gain strength through $^1\Sigma_u^+ - ^3\Sigma_u^-$ spin-orbit interactions.[12]

The ground-state absorption spectrum in the 1085–1165 Å region has been studied extensively by Ogawa and coworkers.[9,11,13–15] Assignments presented by Chang[13] and Ogawa *et al.*[15] contain several errors. For example, Chang[13] made the assignment of strong features at 1153 Å to $^1\Pi_u$, $^1\Sigma_u^-$, $^3\Sigma_u^-$ and $^1\Sigma_u^+$ upper states (the $^1\Pi_u$ subsequently labelled the $g^1\Pi_u$ state by Huber and Herzberg[8]). These assignments can be questioned on the basis of the strength of the absorption features and the absence of transitions to the same upper states in absorption from the metastable $a^1\Delta_g$ and $b^1\Sigma_g^+$ states,[10,16–18] some of which would be allowed transitions. The 1153 Å features were subsequently labelled

 0021-9606/95/103(5)/1727/5/$6.00

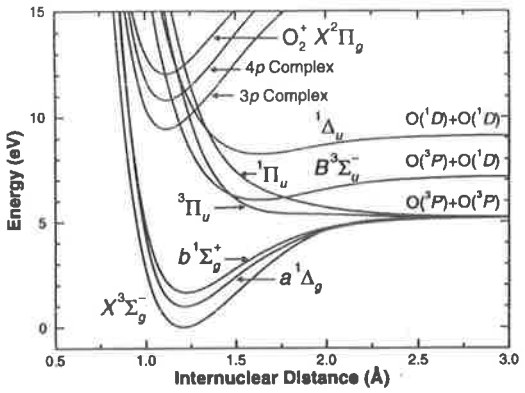

FIG. 1. Some O_2 potential energy curves relevant to the present work. The diabatic representations of the states involved in Rydberg-valence interactions are shown. Energies are given relative to the minimum in the $X^3\Sigma_g^-$ state potential energy curve.

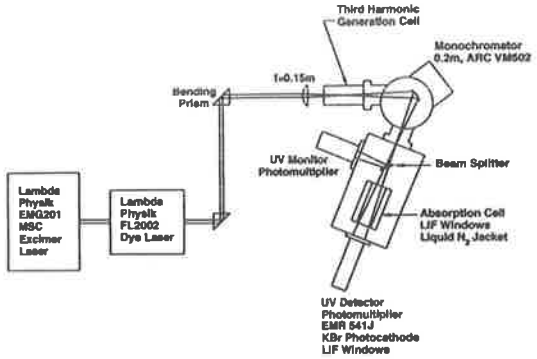

FIG. 2. Schematic diagram of the apparatus used for the photoabsorption measurements.

by Ogawa *et al.*[15] as a (0–0) $^3\Pi_u \leftarrow X^3\Sigma_g^-$ band although no justification was given. The assignment of the band to an allowed transition seems more in line with experimental observations than the assignments of Chang.[13]

Chang[13] also assigned a weak band near 1148 Å to a $^3\Sigma_u^+ \leftarrow X^3\Sigma_g^-$ transition and noted that the diffuseness and complex structure of the band made rotational analysis difficult. The isotopic shift of this band led to a vibrational level assignment[15] of $v'=0$. At the corresponding wavelength, ~1262 Å, in the $a^1\Delta_g$ spectrum, a strong transition to the $4p\pi_u$ $i^1\Delta_u(v=0)$ level has been observed[16] and the presence of an extra head in the spectrum led Yamawaki[16] to postulate the existence of a $4p\sigma_u$ $^1\Pi_u(v=0)$ level at about the same energy. Transitions to these levels are forbidden from the ground state but spin-orbit coupling of $^1\Pi_u$ with $^3\Pi_u$ states may mean that the (0–0) $4p\sigma_u$ $^1\Pi_u \leftarrow X^3\Sigma_g^-$ transition can be observed.

In this paper we present new high-resolution measurements of the ground-state $^{16}O_2$ photoabsorption cross section in the 1147–1155 Å region. The band at 1148 Å shows some novel features in linewidth variation which enable us to assign unambiguously both the upper state, $^1\Pi_u$, and its major sources of predissociation broadening. No comment on this linewidth variation appears in previous reports describing this band or the corresponding band in the $a^1\Delta_g$ metastable absorption spectrum. In addition, we will confirm the assignment of the 1153 Å band as a $^3\Pi_u \leftarrow X^3\Sigma_g^-$ transition and discuss the spin-orbit interaction of this $^3\Pi_u$ level with the $^1\Pi_u$ level.

II. EXPERIMENTAL METHOD

A schematic diagram of the apparatus is shown in Fig. 2. Tunable vacuum ultraviolet (VUV) radiation was generated[19] by focussing radiation from an excimer-pumped dye laser, using *p*-terphenyl in dioxane, in a cell containing Kr at a pressure of ~8 Torr. A 0.2 m monochromator was used to remove the fundamental from the third harmonic radiation before passage through an 11 cm absorption cell containing O_2 (99.9% with 99.8 atom% ^{16}O) at a pressure chosen to give transmittances in the range 10%–60%. The transmitted and incident radiation was detected using solar-blind photomultipliers operated at low gain to avoid dynode-saturation effects. Wavelengths were calibrated in the VUV using CO absorption lines.[20] The VUV bandwidth, estimated from measurements of the Xe absorption line at 1129.3 Å, was ~0.5 cm^{-1} full width at half maximum (FWHM) and ~0.1 cm^{-1} FWHM when the intracavity etalon in the dye laser was employed. The etalon was used when the measured absorption linewidths became comparable with the 0.5 cm^{-1} bandwidth. Therefore, the present technique yields the absolute photoabsorption cross section, not limited by instrumental bandwidth, except where linewidths are $\lesssim$0.1 cm^{-1} FWHM.

III. RESULTS AND DISCUSSION

The measured photoabsorption cross section from 1146.8 Å (87200 cm^{-1}) to 1155.0 Å (86580 cm^{-1}) is shown in Fig. 3. The strong features analysed by Chang[13] can be seen near 86700 cm^{-1} (1153 Å) while at higher energies near 87100 cm^{-1} (1148 Å) lies the much weaker band previously assigned[13] to a $^3\Sigma_u^+ \leftarrow X^3\Sigma_g^-$ transition. Strikingly, three very narrow lines, unreported in previous studies, appear near the centre of the weaker band (predissociation widths of $\lesssim$0.1 cm^{-1} FWHM) while all other lines in the band are considerably broader. The measured transition energies of the narrow lines, labelled *A*, *B* and *C* in Fig. 3, are 87095.3, 87109.5 and 87111.6 cm^{-1}, respectively, with an estimated uncertainty of $\pm$0.2 cm^{-1}. A comparison of their energy separations with the energies of the ground-state rotational levels[21] ($v''=0$) shows that the three lines arise from transitions from $J''=0$ and 2 levels of the $N''=1$ triplet and the $J''=2$ level of the $N''=3$ triplet to a single upper level with $J'=1$ (see Fig. 4). The rest of the lines in the band (those with $J'>1$) are broadened by predissociation of the upper state through an interaction with a state that does not have $J=1$ levels, *i.e.* a state with $\Omega=2$. The only transition which is consistent with the observed relative intensities[22] of the narrow lines and with the absence of multiplet structure,

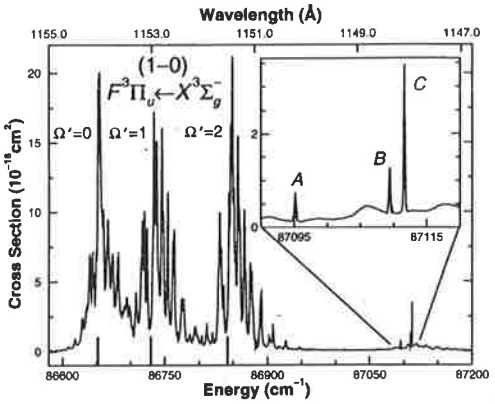

FIG. 3. The measured photoabsorption cross section of O_2 at 79 K showing the 86580–87200 cm^{-1} region. The insert shows an expanded view, 87090 – 87120 cm^{-1}, of sharp lines, labelled *A*, *B* and *C*, in an otherwise diffuse spectrum near 87100 cm^{-1}. The assignments shown for the strong features near 86700 cm^{-1} are discussed in the text. Rotationless term values (Ref. 23) for the three strong bands are indicated on the energy axis.

of transitions involving $J'=0$ and of a $J'=1 \leftarrow J''=1$ transition, is a $^1\Pi_u \leftarrow X^3\Sigma_g^-$ transition which borrows strength from a $^3\Pi_u \leftarrow X^3\Sigma_g^-$ transition. In the $^1\Pi_u$ state, $N=J$ and the branch lines of the transition to this state can be labelled using the notation $^{\Delta N}\Delta J(N'')$, so that lines labelled *A*, *B* and *C* in Fig. 4 become $^OP(3)$, $^QP(1)$ and $^QR(1)$, respectively.

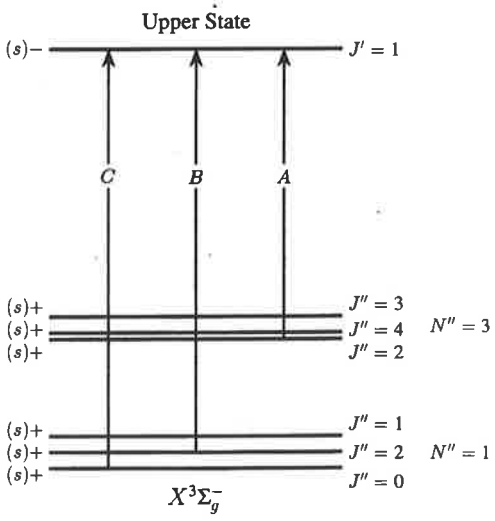

FIG. 4. Schematic diagram showing the transitions to a $J'=1$ level from the ground $X^3\Sigma_g^-$ state which give rise to the lines labelled *A*, *B* and *C* on Fig. 3. The *a*/*s* and +/− symmetries of the levels are indicated. For $^{16}O_2$, with identical nuclei having zero spins, only the symmetric levels of the ground state are populated and, therefore, antisymmetric levels of the excited state cannot be seen. The only other transition allowed by the ΔJ selection rules is the $J'=1 \leftarrow J''=1$ transition which has not been observed in the absorption cross section.

The closest bands to the $^1\Pi_u \leftarrow X^3\Sigma_g^-$ band identified above are the strong transitions near 86700 cm^{-1} (see Fig. 3), which consist of three nearly equally-spaced bands with rotationless term values[23] of 86652.0, 86729.5 and 86842.0 cm^{-1}. In general appearance, the rotational structure is characteristic of a $^3\Pi_u \leftarrow X^3\Sigma_g^-$ transition[23] with the upper state near case (a), and the average multiplet splitting of 95 cm^{-1} (half of the $^3\Pi_2 - ^3\Pi_0$ separation) is close to the value of 91.4 cm^{-1} measured by Chang and Ogawa[9] for the (0–0) $F^3\Pi_u \leftarrow X^3\Sigma_g^-$ band at 86000 cm^{-1} (1163 Å). Therefore, we conclude that the 86700 cm^{-1} band is a $^3\Pi_u \leftarrow X^3\Sigma_g^-$ transition.

One obvious feature of the 86700 cm^{-1} $^3\Pi_u \leftarrow X^3\Sigma_g^-$ band is the perturbation of its triplet structure. The $^3\Pi_1$ component shows a shift to lower energy from the expected unperturbed position[23] near the centre of the multiplet. This observation is what one would expect if the $^3\Pi_{1u}$ and $^1\Pi_{1u}$ states in the 86700 cm^{-1} and 87100 cm^{-1} transitions were spin-orbit coupled. Since such coupling is also likely to lead to the donation of strength to the forbidden $^1\Pi_u \leftarrow X^3\Sigma_g^-$ transition, we can test this supposition by using the observed energy shift and separation to calculate the relative intensities of the $^1\Pi_u \leftarrow X^3\Sigma_g^-$ and $^3\Pi_{1u} \leftarrow X^3\Sigma_g^-$ transitions and comparing the result with the observed relative transition intensities.

Assuming that the strength of the $^1\Pi_u \leftarrow X^3\Sigma_g^-$ transition gained from interactions with levels apart from the $^3\Pi_u$ level is negligible and that there are no significant perturbations caused by other levels, the relative intensity relation

$$R = \frac{I(^1\Pi_u \leftarrow X)}{I(^3\Pi_{1u} \leftarrow X)} = \frac{|S|}{|S| + \Delta E_0} \tag{1}$$

from two-level perturbation theory[24,25] can be used. Here $S=-20.6$ cm^{-1} is the shift of the $^3\Pi_1$ component and $\Delta E_0 = 336.4$ cm^{-1} is the unperturbed separation of the $^1\Pi_u$ and $^3\Pi_{1u}$ levels determined from the rotationless term values and the shift.[26] Using these values, we obtain $R=0.058$, in good agreement with the experimental value of 0.050 ± 0.007, obtained by integrating the measured cross section with a smooth background continuum cross section ($^3\Sigma_u^- \leftarrow X^3\Sigma_g^-$) subtracted. The correct prediction of the ratio of band intensities from observed energy levels lends strong support for our assignments of the excited states involved.

In addition, perturbation theory[24] allows us to calculate the value of the interaction matrix element, H_{12}, from the values of S and ΔE_0 given above. This yields $H_{12}=86$ cm^{-1}, which is ~90% of the value of the spin-orbit splitting of the $^3\Pi_u$ state. This strong spin-orbit coupling and the energy region of the states make it probable that the $^1\Pi_u$ and $^3\Pi_u$ states are associated with the $...(1\pi_u)^4(1\pi_g)^1 4p\sigma_u$ configuration.[27]

We noted above that the $^1\Pi_u$ ($J>1$) levels are predissociated by a state with $\Omega=2$. The only such state that has a first-order interaction with a $^1\Pi_{1u}$ state is a $^1\Delta_{2u}$ state, the interaction being rotational mixing ($\Delta\Omega=\pm 1$, sometimes referred to as L-uncoupling[3]). The appearance of the 87100 cm^{-1} band (Fig. 5) allows several qualitative deductions to be made. First, the large predissociation width of lines with $J'>1$, which arises from the sharing of the inherent $^1\Pi_u$ and

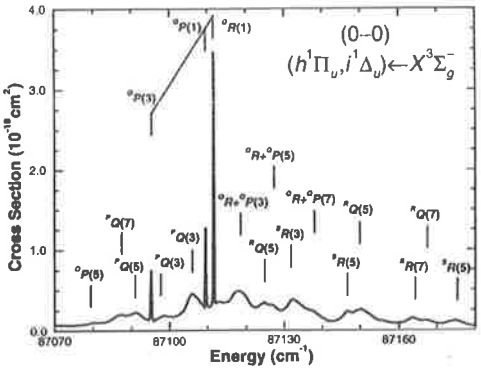

FIG. 5. An expanded view of the measured cross section showing the (0–0) $(h^1\Pi_u,\ i^1\Delta_u) \leftarrow X^3\Sigma_g^-$ band with some rotational line assignments. The three narrow lines result from transitions to the $h^1\Pi_u$ ($v=0$, $J=1$) level. Note that for $J'>1$, the strong mixing of the $h^1\Pi_u$ and $i^1\Delta_u$ upper states makes it meaningless to assign lines specifically to one or other of the states.

$^1\Delta_u$ widths,[28] implies that the inherent $^1\Delta_u$ width, due presumably to predissociation through valence channels, is very much larger than the $^1\Pi_u$ width of $\lesssim 0.1$ cm^{-1} FWHM measured for $J'=1$. Second, the rapid onset of broadening at $J'=2$ implies that the mixing is complete even at low J' values. The provisional rotational assignments in Fig. 5 are based on fits to the present spectrum and the measured line positions of Yamawaki,[16] who observed the $^1\Delta_u$ level in absorption from the $a^1\Delta_g$ state, using a two-level perturbation model with a coupling matrix element of $H_{12}=-1.4\sqrt{2(J(J+1)-2)}$ cm^{-1} and nearly coincident $^1\Pi_u$ and $^1\Delta_u$ unperturbed band origins. The assignments of rotational lines by Yamawaki were revised in light of this work. The rotational coupling suggested by the model is ~80% of the value expected for states of the same Rydberg p-complex, assuming pure precession.[3] Therefore, the $^1\Delta_u$ level is likely to consist dominantly of the $\ldots(1\pi_u)^4(1\pi_g)^1 4p\pi_u$ Rydberg configuration. This was also the conclusion of Yamawaki.[16]

The above transitions, as well as others in the 1100–1300 Å region, are currently undergoing extensive reanalysis using CSE calculations to model Rydberg-valence interactions. Preliminary results reinforce the observations and assignments presented above and indicate that the $^3\Pi_u \leftarrow X^3\Sigma_g^-$ transition is actually the (1–0) band of the $F^3\Pi_u \leftarrow X^3\Sigma_g^-$ system,[27] and that the $^1\Pi_u \leftarrow X$ and $^1\Delta_u \leftarrow X$ transitions are (0–0) bands of the $h^1\Pi_u \leftarrow X$ and $i^1\Delta_u \leftarrow X$ systems. We have found that it is not necessary to invoke the $g^1\Pi_u$ state listed by Huber and Herzberg[8] which resulted from an incorrect assignment by Chang[13] of the 86700 cm^{-1} features in the ground state spectrum. The preliminary CSE results are being refined and extended to other states and will be the subject of subsequent publications.

ACKNOWLEDGMENTS

The authors wish to acknowledge financial support from the Australian Research Council through a Post-Doctoral Research Fellowship (J.P.E.) and partial sponsorship (M.L.G.) from the United States National Science Foundation through a U.S.-Australia Cooperative Research Grant. Valuable technical assistance was provided by K. J. Lonsdale and C. J. Dedman. We also wish to thank Professor J. H. Carver and Dr S. T. Gibson for critically reading the manuscript.

[1] P. H. Krupenie, J. Phys. Chem. Ref. Data **1**, 423 (1972).
[2] K. Watanabe, Adv. Geophys. **5**, 153 (1958).
[3] H. Lefebvre-Brion and R. W. Field, *Perturbations in the Spectra of Diatomic Molecules* (Academic, Orlando, 1986), pp. 38, 208-211, 229.
[4] R. J. Buenker and S. D. Peyerimhoff, Chem. Phys. Lett. **34**, 225 (1975).
[5] B. R. Lewis, S. T. Gibson, M. Emami, and J. H. Carver, J. Quant. Spectrosc. Radiat. Transfer **40**, 1 (1988); **40**, 469 (1988).
[6] J. Wang, A. J. Blake, D. G. McCoy, and L. Torop, J. Quant. Spectrosc. Radiat. Transfer **40**, 501 (1988).
[7] Y. Tanaka, J. Chem. Phys. **20**, 1728 (1952).
[8] K. P. Huber and G. Herzberg, *Molecular Spectra and Molecular Structure, IV. Constants of Diatomic Molecules* (Van Nostrand Reinhold, New York, 1979), p. 493.
[9] H. C. Chang and M. Ogawa, J. Mol. Spectrosc. **44**, 405 (1972).
[10] F. Alberti, R. A. Ashby, and A. E. Douglas, Can. J. Phys. **46**, 337 (1968).
[11] M. Ogawa and K. R. Yamawaki, Can. J. Phys. **47**, 1805 (1969).
[12] B. R. Lewis, S. S. Banerjee, and S. T. Gibson, J. Chem. Phys. **102**, 6631 (1995).
[13] H. C. Chang, Ph.D. dissertation thesis, University of Southern California (1973).
[14] S. Ogawa and M. Ogawa, Can. J. Phys. **53**, 1845 (1975).
[15] M. Ogawa, K. R. Yamawaki, A. Hashizume, and Y. Tanaka, J. Mol. Spectrosc. **55**, 425 (1975).
[16] K. R. Yamawaki, Ph.D. dissertation thesis, University of Southern California (1972).
[17] R. J. Collins, D. Husain, and R. J. Donovan, J. Chem. Soc. Faraday Trans. 2 **69**, 145 (1973).
[18] D. H. Katayama, S. Ogawa, M. Ogawa, and Y. Tanaka, J. Chem. Phys. **67**, 2132 (1977).
[19] R. Mahon, T. J. McIlrath, V. P. Myerscough, and D. W. Koopman, IEEE J. Quantum Electron. **15**, 444 (1979).
[20] S. G. Tilford and J. D. Simmons, J. Phys. Chem. Ref. Data **1**, 147 (1972).
[21] C. Amiot and J. Verges, Can. J. Phys. **59**, 1391 (1981).
[22] Line intensities were calculated using the formulae of T. K. Balasubramanian and V. P. Bellary, Acta Phys. Hung. **63**, 249 (1988), assuming a ground state intermediate between Hund's cases (a) and (b). The relative line strengths, as determined from the present absorption spectrum, are in good agreement with calculated strength ratios of 1 : 0.26 : 0.17 : 0.0 for $^QR(1)$: $^QP(1)$: $^OP(3)$: $^QQ(1)$, where the notation $^{\Delta N}\Delta J(N'')$ is described in the text.
[23] A complete $^3\Pi_u \leftarrow X^3\Sigma_g^-$ band model fit to the spectrum, including the determination of spectroscopic constants, rotational line intensities and widths, will be published elsewhere as part of a larger work covering all of the $^3\Pi_u \leftarrow X$ absorption bands in the 85000–89300 cm^{-1} region. The effective Hamiltonian used to calculate the $^3\Pi_u$ rotational levels was that given by J. M. Brown and A. J. Merer, J. Mol. Spectrosc. **74**, 488 (1979). For this Hamiltonian, the rotationless term value of the $^3\Pi_{1u}$ level, in the absence of external perturbations, would be $2B=3.1$ cm^{-1} higher than the energy given by the average of the $^3\Pi_{2u}$ and $^3\Pi_{0u}$ rotationless term values.
[24] I. Kovács, *Rotational Structure in the Spectra of Diatomic Molecules* (Hilger, London, 1969), pp. 205 - 209.
[25] The theory of Mulliken [R. S. Mulliken, Phys. Rev. **57**, 500 (1940)] dealing specifically with the $^3\Pi$–$^1\Pi$ interaction for $\pi\sigma$ or $\pi^3\sigma$ configurations, gives the same result if one reverses the $^1\Pi_1$ and $^3\Pi_1$ states in the transition moment integrals.
[26] The shift of the $^3\Pi_1$ level is $S=-(17.5+3.1)$ cm^{-1} calculated from the $^3\Pi_u$ rotationless term values given in the text and assuming a value for B of 1.56 cm^{-1} (see Ref. 23). The term value of the $^1\Pi_u$ ($J=1$) level, 87110.5 cm^{-1}, was determined from the measured energies of the narrow lines and the ground $X^3\Sigma_g^-$ state term values of Ref. 21. This was converted to a rotationless term value of $\nu_0=87110.5-3.4$ cm^{-1} $=87107.1$ cm^{-1} using the relation $\nu=\nu_0+BJ(J+1)$ for the upper state term values with a rotational constant $B=1.7$ cm^{-1}, appropriate for a $4p$ Rydberg

state. Whence, the unperturbed energy separation can be calculated: $\Delta E_0 = 87107.1 - 86729.5 + 2S = 336.4\ \mathrm{cm}^{-1}$.

[27] We have begun analysis of the features in the window region of the spectrum using CSE calculations. Our results show that, as predicted by Buenker and Peyerimhoff (Ref. 4), the $n=3$ and 4 Rydberg and the unbound valence $^1\Pi_u$ and $^3\Pi_u$ states have large electrostatic interactions which result in adiabatic potential energy curves having double minima. The levels in the wells can be considered to be of mixed Rydberg-valence character and this mixing accounts for the anomalous B values and isotope shifts of the observed bands. The large spin-orbit interaction between $F^3\Pi_u$ $(v=1)$ and $h^1\Pi_u$ $(v=0)$ can be attributed to the considerable $v=0$, $n=4$ Rydberg character of each of these levels.

[28] By the term *inherent width* we mean the width which would be observed if the $^1\Pi_u - i^1\Delta_u$ interaction were absent.

4.20 Experimental observation of the lowest $^1\Sigma_u^+$ valence state of O_2

[40] B. R. Lewis, J. P. England, R. J. Winkel, Jr., S. S. Banerjee, P. M. Dooley, S. T. Gibson, and K. G. H. Baldwin,
Physical Review A **52**, 2717–2733 (1995).

Experimental observation of the lowest $^1\Sigma_u^+$ valence state of O_2

B. R. Lewis, J. P. England, R. J. Winkel, Jr.,* S. S. Banerjee, P. M. Dooley, S. T. Gibson, and K. G. H. Baldwin
Research School of Physical Sciences and Engineering, The Australian National University, Canberra, Australian Capital Territory 0200, Australia
(Received 4 May 1995)

Transitions into the lowest $^1\Sigma_u^+$ valence state of O_2, which we shall name $f'\ ^1\Sigma_u^+$, are observed. A total of nine weak absorption bands is found from the system $f'\ ^1\Sigma_u^+ \leftarrow X\ ^3\Sigma_g^-$ for the isotopes $^{16}O_2$ and $^{18}O_2$. The observed band origins and rotational constants are found to be significantly perturbed due to an electrostatic interaction between the valence state $f'\ ^1\Sigma_u^+$ and the Rydberg states $3p\pi_u\ f\ ^1\Sigma_u^+$ and $4p\pi_u\ j\ ^1\Sigma_u^+$. In addition, rotational perturbations observed in certain vibrational levels of the Rydberg states $f\ ^1\Sigma_u^+$ and $j\ ^1\Sigma_u^+$ are found to be caused by the $f'\ ^1\Sigma_u^+$ state through the same valence-Rydberg interaction. The $f' \leftarrow X$ bands are found to be predissociating resonances that exhibit Beutler-Fano line shapes of widely varying asymmetry. In particular, the (13,0) band of $^{18}O_2$ is an example of a window resonance in molecular dissociation.

PACS number(s): 33.20.Ni, 33.70.−w

I. INTRODUCTION

Although there have been no previous experimental observations of the $^1\Sigma_u^+$ valence states of O_2, such states are well known theoretically. The lowest molecular-orbital configuration for O_2, $(1\sigma_g)^2(1\sigma_u)^2(2\sigma_g)^2(2\sigma_u)^2(3\sigma_g)^2(1\pi_u)^4(1\pi_g)^2$, gives rise to three bound states $X\ ^3\Sigma_g^-$, $a\ ^1\Delta_g$, and $b\ ^1\Sigma_g^+$, dissociating to $O(^3P)+O(^3P)$, all of which have been observed. The first-excited molecular-orbital configuration $(1\sigma_g)^2(1\sigma_u)^2(2\sigma_g)^2(2\sigma_u)^2(3\sigma_g)^2(1\pi_u)^3(1\pi_g)^3$ gives rise to six states $c\ ^1\Sigma_u^-$, $A'\ ^3\Delta_u$, $A\ ^3\Sigma_u^+$, $B\ ^3\Sigma_u^-$, $^1\Delta_u$, and $^1\Sigma_u^+$, the first four of which have been found to be bound. The c, A', and A states dissociate to $O(^3P) + O(^3P)$ at 5.21 eV, the B state to $O(^3P) + O(^1D)$ at 7.18 eV, the $^1\Delta_u$ state to $O(^1D)+O(^1D)$ at 9.15 eV, and the $^1\Sigma_u^+$ state to $O(^1D)+O(^1S)$ at 11.37 eV [1]. Although neither of the latter two states has been observed experimentally, they were both predicted to be bound in the early semiempirical study of Gilmore [2]. Later *ab initio* calculations [3–7] of the $^1\Sigma_u^+$ state predicted well depths D_e from 0.74 eV to 1.65 eV and equilibrium internuclear distances R_e from 1.61 Å to 1.66 Å, similar to the values found for the other isoconfigurational states [6]. Unfavorable Franck-Condon overlaps with the ground state ($X\ ^3\Sigma_g^-$, $R_e = 1.21$ Å) and the second metastable state ($b\ ^1\Sigma_g^+$, $R_e = 1.23$ Å) explain why the $^1\Sigma_u^+$ state has not been observed previously, even in the electric-dipole-allowed transition $^1\Sigma_u^+ \leftrightarrow b\ ^1\Sigma_g^+$ [8]. In Fig. 1, we show O_2 potential-energy curves for valence and Rydberg states of interest to this work, including the most recent *ab initio* calculation [9] of the $^1\Sigma_u^+$ valence state, which indicates that the diabatic Rydberg and valence $^1\Sigma_u^+$ potential-energy curves cross at an internuclear distance near 1.34 Å.

The atomic oxygen green line at 5577 Å, arising from the forbidden transition $^1S \rightarrow {}^1D$, is a well-known feature of the night-sky emission spectrum. Following a suggestion of Kaplan [10] that dissociative recombination (DR) of O_2^+ with an electron might provide a significant channel for the production of ionospheric $O(^1S)$, Nicolet [11] showed that green-line emission could result from the DR of O_2^+. Guberman [12,13] showed theoretically that the $^1\Sigma_u^+$ valence state is the only significant channel enabling the generation of $O(^1S)$ from the lowest ten vibrational levels of $O_2^+(X\ ^2\Pi_g)$. Thus the relevant DR process is $O_2^+ + e^- \rightarrow O_2(^1\Sigma_u^+) \rightarrow O(^1S) + O(^1D)$. In addition, he showed that the $^1\Sigma_u^+$ potential-energy curve crosses that of the ion between $v^+ = 1$ and 2, resulting in DR rates that increase significantly as v^+ increases from 0 to 2 [14–16], in agreement with satellite-based results [17–19]. In a recent work, Guberman and Giusti-Suzor [9] treated both direct DR and indirect DR, which involves the temporary capture of the electron

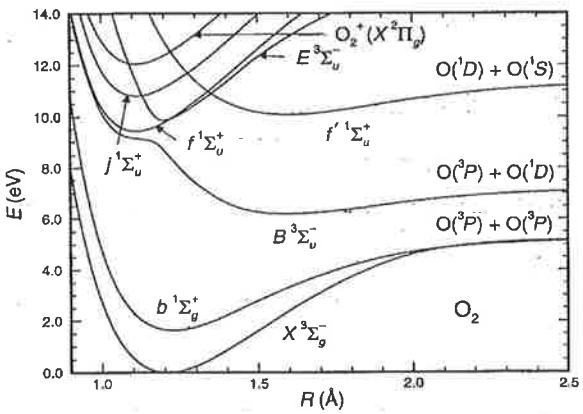

FIG. 1. Selected potential-energy curves for O_2, including the most recent *ab initio* calculation [9] of the $^1\Sigma_u^+$ valence state, which we have named $f'\ ^1\Sigma_u^+$ following the observations reported in this work.

*Permanent address: Department of Physics, United States Military Academy, West Point, NY 10996-1790.

into a neutral, vibrationally excited Rydberg state which then autoionizes or predissociates, by the methods of multichannel quantum-defect theory. In the course of that work, they calculated an *ab initio* diabatic potential-energy curve for the $^1\Sigma_u^+$ valence state, shown in Fig. 1, which is expected to be more accurate than previous calculations, obtaining $T_e=10.08$ eV, $D_e=1.31$ eV, $R_e=1.626$ Å, $\omega_e=752$ cm^{-1}, and $\omega_e x_e=7.98$ cm^{-1}. They also calculated an *ab initio* electronic width $\Gamma(R)$, which is related to the electrostatic coupling $H^e(R)$ between the valence $^1\Sigma_u^+$ state and the Rydberg series $np\pi_u\ ^1\Sigma_u^+$ by the relation $\Gamma(R)=2\pi\rho|H^e(R)|^2$, where ρ is a density of states. Their results imply [20] that the coupling between the $3p\pi_u\ f^1\Sigma_u^+$ and the valence $^1\Sigma_u^+$ states is $H^e=2242$ cm^{-1} at $R=2.2819a_0$, decreasing at larger internuclear distances. In comparison, the corresponding valence-Rydberg coupling for the $^3\Sigma_u^-$ states, isoconfigurational with the $^1\Sigma_u^+$ states, is approximately 4000 cm^{-1} [21–23]. The considerably weaker coupling between the $^1\Sigma_u^+$ states, together with the bound nature of the $^1\Sigma_u^+$ valence state below 11.37 eV, results in the observed $f\ ^1\Sigma_u^+$ levels being relatively sharp and regular when compared with the extremely diffuse and irregular $E\ ^3\Sigma_u^-$ levels.

In this work, we observe levels of the $^1\Sigma_u^+$ valence state, henceforth called the $f'\ ^1\Sigma_u^+$ state. We characterize rotational perturbations in the $^1\Sigma_u^+$ Rydberg states and show that they are caused by the $f'\ ^1\Sigma_u^+$ valence state through electrostatic Rydberg-valence coupling, contrary to the heterogeneous perturbation mechanism suggested by Katayama *et al.* [8] for the $v=4$ level of the $f\ ^1\Sigma_u^+$ state of $^{16}O_2$. The $f'\ ^1\Sigma_u^+\leftarrow X\ ^3\Sigma_g^-$ bands are found to be predissociating resonances that exhibit Beutler-Fano line shapes.

II. EXPERIMENTAL METHOD

Two distinct experimental systems were used to take the measurements presented here. Because of superior signal stability, a conventional light source and scanning monochromator system was used for the bulk of the measurements, which necessarily involved very weak bands of the $f'\ ^1\Sigma_u^+\leftarrow X\ ^3\Sigma_g^-$ system competing with relatively strong background continua. On the other hand, because of superior wavelength stability and narrower bandwidth, a laser-based system was employed in the precise measurements of rotational perturbations in the less diffuse bands of the $f\ ^1\Sigma_u^+\leftarrow X\ ^3\Sigma_g^-$ Rydberg system.

A. Monochromator system

The apparatus was similar to that used in our previous studies [24,25] of resonances in the window region of the O_2 spectrum. Background radiation was provided by an argon-dimer continuum discharge lamp powered by a pulser based on a design developed at the Argonne National Laboratory [26]. The lamp was operated in the windowless mode at a pressure of 400 Torr of argon, a pulse repetition frequency of approximately 80 kHz, and a current of 200 mA. The radiation was dispersed by a modified 2.2-m scanning vacuum ultraviolet (vuv) monochromator [27] operating in the first order of a 2400 grooves/mm grating, resulting in a full width at half maximum (FWHM) resolution of approximately 0.025 Å. Radiation was detected photoelectrically, using EMR LiF-windowed solar-blind photomultipliers operated in the pulse-counting mode, before entering and after leaving the 10-cm, temperature-controlled, LiF-windowed absorption cell. The scanning system and data collection were controlled by an IBM AT microcomputer.

The absorption cell was filled with molecular oxygen (BOC 99.9%, containing 99.8 at. % ^{16}O, or ICON, containing 99.5 at. % ^{18}O, 0.2 at. % ^{17}O, and 0.3 at. % ^{16}O), through an electromagnetically controlled leak valve, to pressures in the range 1–100 Torr, monitored by a Datametrics Barocel variable capacitance manometer. In order to concentrate the rotational structure of the weak bands studied here, most scans were performed with the absorption-cell surround filled with liquid nitrogen, providing an effective cell temperature of 79 K. Scans were generally performed over wavelength regions of width 1.2 Å, with wavelength increments of 0.01 Å, in the range 1100–1200 Å, but increments of 0.005 Å were used on a few occasions. The wavelength scale of the monochromator was calibrated against known emission lines of N I, O I, and C I and absorption lines of the $A\ ^1\Pi\leftarrow X\ ^1\Sigma^+$ system of CO [28]. This enabled pre-correction of the periodic wavelength error [27] caused by machining errors in the monochromator drive screw. Temporal wavelength drifts were corrected by monitoring the apparent wavelength of the impurity line of N I at 1134.980 Å before and after each scan. Small stray-light and dark-count corrections were applied to the photomultiplier signals. Empty-cell background ratios (detector to monitor) were taken at the initial wavelength before the scan and the final wavelength after the scan and a linear interpolation was applied to obtain the ratio for intermediate wavelengths. This procedure was found to be satisfactory since, although the transmittance of the cell windows decreased noticeably with time at 79 K, the decrease over the relatively short period of a scan, approximately 2 h, was observed to be linear to within 0.5%. Absolute cell transmittances were determined by dividing the full-cell ratios (detector to monitor) by the empty-cell ratios at each wavelength.

Using the known pressure, temperature, cell length, and absolute cell transmittance, absolute total photoabsorption cross sections were determined using the Beer-Lambert law. Since the bands of interest are rather weak, with peak cross sections approximately 1–10 % of the underlying continuum cross section, particular attention was paid to the statistical accuracy of the measurements. We aimed to obtain a statistical scatter of less than 20% of the peak of the band cross sections, equivalent to an absolute statistical accuracy of approximately 0.2–2.0 % in the total cross section. It is easy to show, using counting statistics and neglecting the monitor photomultiplier, that optimum relative statistical accuracy in the measured cross section is obtained at a transmittance near 0.1, the optimum being better by a factor 2 than that obtained at a transmittance of 0.5. Considering the complicating factors of stray light and photomultiplier dark counts, both of which increase the uncertainty in the measured cross section at low transmittances, we aimed to operate at a reasonable compromise transmittance of approximately 0.25, as far as was possible. Typically, by photon counting for 50 s at each wavelength, we obtained a root-mean-square (rms) statistical uncertainty of approximately 1% from a single scan, in some

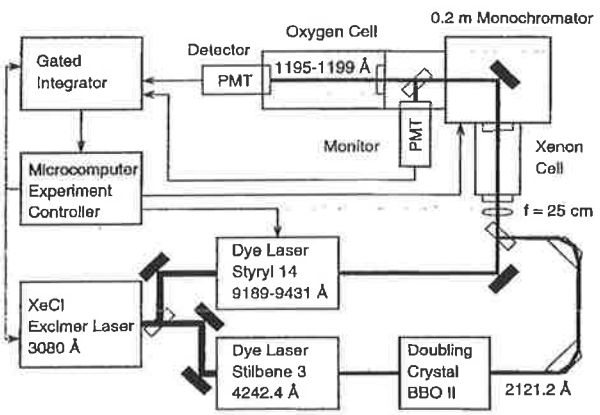

FIG. 2. Schematic diagram of the laser-based apparatus.

cases necessitating averaging over several scans in order to obtain the desired accuracy. In addition to the statistical uncertainty in the measured cross sections, an absolute uncertainty of less than 5% arose because of uncertainties in cell length, pressure, temperature, and window transmittance degradation at 79 K.

B. Laser system

The technique of four-wave frequency mixing in gases as a means of generating coherent radiation in the vuv has been used extensively in recent years and the resultant narrow-bandwidth radiation has been employed in a number of high-resolution spectroscopic studies [29]. In this work, we used two-photon-resonant difference-frequency four-wave mixing [30] in Xe to generate tunable vuv radiation near 1196 Å in order to study rotational perturbations in the (4,0) bands of the Rydberg systems $f\ ^1\Sigma_u^+ \leftarrow X\ ^3\Sigma_g^-$ of $^{16}O_2$ and $^{16}O^{18}O$ with a resolution of approximately 0.25 cm^{-1} FWHM.

The apparatus is shown schematically in Fig. 2. Radiation from a Lambda Physik EMG201 XeCl excimer laser (3080 Å, 450 mJ per pulse) was used to pump transversely two Lambda Physik FL3002 dye lasers, one of which was operated with the dye Styryl 14 in dimethyl sulfoxide (9040–9920 Å, 15 mJ per pulse), the other with Stilbene 3 in methanol (4120– 4430 Å, 21 mJ per pulse). The latter dye laser was operated with an intracavity étalon and its output was frequency doubled in a temperature-stabilized β-BaB_2O_4 (BBO II) crystal. The frequency-doubled output was tuned to be two-photon resonant with a chosen vuv transition of Xe by observing the (2+1)-photon ionization signal from a Xe cell and was combined, after removal of the fundamental radiation, with the tunable infrared (ir) laser output. The laser beams were then focused into a second Xe cell by a 25-cm focal length quartz lens. The approximately 25-cm-long cell was equipped with a quartz entrance window, a MgF_2 exit window, and an MKS Baratron gauge that monitored the pressure of Xe (ICON 99.999%). The generated vuv radiation was passed through an ARC VM502 0.2-m vuv scanning monochromator (1200 grooves/mm osmium-coated grating, reciprocal dispersion 40 Å/mm, 30–100 μ slit widths) acting as a comparatively broad bandpass filter, tuned synchronously with the ir dye laser, which discriminated against the fundamental and doubled dye-laser radiation. The vuv radiation leaving the monochromator was divided by a MgF_2 beam splitter into two beams. The reflected beam was monitored directly, while the transmitted beam passed through a 33-cm-long MgF_2-windowed absorption cell before being detected. Molecular oxygen (BOC 99.9%, containing 99.8 at. % ^{16}O, or ICON, containing 50.4 at. % ^{18}O, 49.0 at. % ^{16}O, and 0.6 at. % ^{17}O) was admitted to the cell through an electromagnetically controlled leak valve and cell pressure was monitored by a Datametrics Barocel variable capacitance manometer. Output pulses from the solar-blind monitor and detector photomultipliers (EMI type 9413, CsI photocathode) were processed by an EGG/PARC 4400 series boxcar averaging system operating in alternate base-line subtract mode. The apparatus was automated using an IBM AT microcomputer to control the triggering of the excimer laser, the scanning of the ir dye laser, the synchronous scanning of the monochromator, the pressure of O_2 in the absorption cell, and the acquisition of the shot-averaged detector and monitor signals from the boxcar system.

The level scheme for the two-photon-resonant difference-frequency four-wave mixing process used in the current experiment is shown in Fig. 3. The visible dye laser was tuned to a vacuum wavelength of 4242.428 Å so that the frequency-doubled radiation was two-photon resonant with the Xe transition, $5p^5(^2P^o_{3/2})9p[\frac{1}{2}]_0 \leftarrow 5p^6\ ^1S_0$. The production of vuv radiation between 1192 Å and 1200 Å using this scheme was verified by tuning the ir laser between 9130 Å and 9620 Å. The two-photon resonances used in early difference-frequency four-wave mixing experiments [30] were confined to relatively low-lying levels of Xe due to the limits for the production of the fundamental laser radiation in the ultraviolet. However, the development of the BBO II crystal has allowed two-photon access to high-lying states of Xe. An attempt by Miyazaki *et al.* [31] to use the $5p^5(^2P^o_{3/2})9p[\frac{1}{2}]_0$ level for two-photon-resonant third-harmonic generation led only to the production of very small signals. As far as we are aware, we are the first to demonstrate the effective generation of tunable vuv radiation using this level of Xe in a two-photon-resonant difference-frequency four-wave mixing experiment.

In order to obtain the measurements presented here, scans were performed over 0.5–1.0 Å ranges in the vuv from 1195 to 1199 Å with wavelength increments of 0.0015 Å. The phase matching was optimized by adjusting the pressure of Xe in the range 1–10 Torr to maximize the vuv signal for the appropriate scan range. Despite the use of the baffled monochromator and solar-blind photomultipliers as detectors, a residual signal due to scattered doubled radiation at 2121.2 Å was present. Accordingly, before and after each scan the ir laser beam was blocked and the scattered radiation measured. The monitor and detector signals were averaged over 200 laser shots for each data point during scans with the absorption cell empty and then filled with presssures of O_2 in the range 1.5–2.5 Torr. Division of the detector signal by the monitor signal, after correction for the scattered radiation, provided a measure of protection against the shot-to-shot fluctuations in the generated vuv signal, but the statistical performance of the laser-based system was still markedly inferior to that of the 2.2-m monochromator system and the very short lifetimes of the laser dyes used made it difficult to

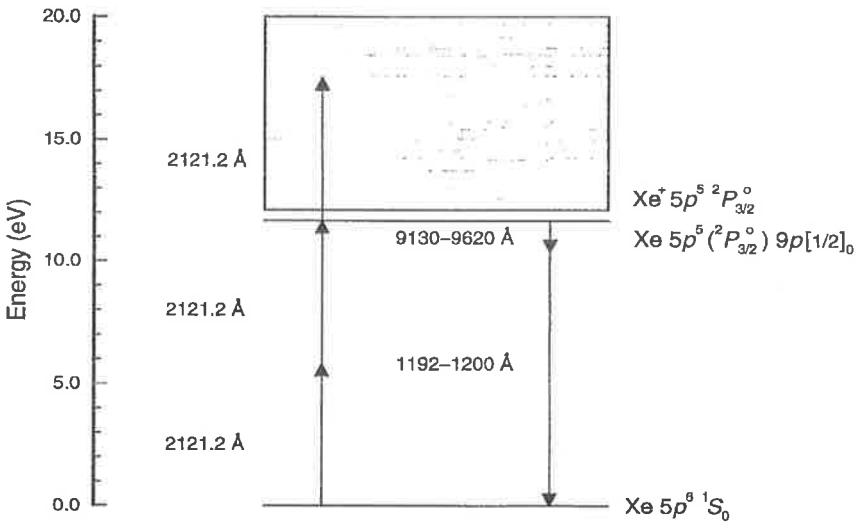

FIG. 3. Xe energy-level scheme for the two-photon-resonant difference-frequency four-wave mixing process.

improve the data by multiple scanning. We also observed a strong, reproducible component of the generated vuv signal that appeared to vary sinusoidally with wavelength, but that was not removable by dividing the detector and monitor signals, possibly being associated with polarization-dependent effects related to the MgF_2 beam-splitter. Thus it was necessary to perform complete empty-cell scans so that the effects of the periodic signal could be removed from the absolute cell transmittances that were obtained by dividing the full-cell ratios (detector to monitor) by the empty-cell ratios for each wavelength. Photoabsorption cross sections were calculated from the absolute transmittances using the Beer-Lambert law.

For high-resolution spectroscopic studies, it is essential to establish an accurate wavelength scale. In a previous study [32], which used four-wave mixing in Kr to generate vuv radiation near 1244 Å, the ir dye laser used here was fully calibrated against a Burleigh pulsed wavemeter. Not only was the nominal dye-laser wavelength observed to deviate from the correct value quadratically with wavelength, but a periodic error component of amplitude 0.17 Å and period 20 Å was found. The effects of the periodic error, due to machining or mounting imperfections in the dye-laser grating drive screw, were verified in the vuv domain by comparing the known positions of absorption lines of the CO $A\ ^1\Pi \leftarrow X\ ^1\Sigma^+$ system [28] with those measured using the four-wave mixing apparatus. In this work, the nominal vuv wavelength was calculated from

$$1/\lambda_{\mathrm{vuv}} = 1/\lambda_{2p} - 1/\lambda_{\mathrm{irv}}, \tag{1}$$

where λ_{vuv} is the vuv wavelength, λ_{2p} ($=1060.607$ Å) is half of the two-photon-resonant frequency-doubled vacuum-corrected wavelength, and λ_{irv} is the calibrated, vacuum-corrected ir dye laser wavelength. Final absolute calibration was achieved by comparing the measured $^{16}O_2$ absorption line positions with values deduced from spectrographic measurements [8] of the $f\ ^1\Sigma_u^+ \leftarrow b\ ^1\Sigma_g^+$ band system. The nominal vuv wavelength was generally within 0.003 Å of the final calibrated value and day-to-day wavelength drifts were less than 0.002 Å because of precise laboratory temperature control. The bandwidth of the generated vuv radiation was determined to be approximately 0.25 cm^{-1} FWHM by fitting an instrumentally-degraded Voigt profile to the very narrow (approximately 0.1 cm^{-1} FWHM) $^{16}O_2$ absorption lines near the (4,0) $f \leftarrow X$ bandhead.

III. EMPIRICAL BAND MODEL

Spectroscopic and line-shape parameters were obtained from the measured cross sections of the bands of the $f'\ ^1\Sigma_u^+ \leftarrow X\ ^3\Sigma_g^-$ system by fitting an empirical band model similar to those used in previous interpretations of the $E\ ^3\Sigma_u^- \leftarrow X\ ^3\Sigma_g^-$ resonances [24,25] and the $D\ ^3\Sigma_u^+ \leftarrow X\ ^3\Sigma_g^-$ bands [33] of O_2. As in those cases, it was found necessary to describe each rotational line by an *asymmetric* profile.

Spectroscopic constants for the $X\ ^3\Sigma_g^-$ states of $^{16}O_2$ and $^{18}O_2$ were taken from Veseth and Lofthus [34] and Steinbach and Gordy [35], respectively. These were used to generate the manifold of rovibrational term values for the ground state and the corresponding weighted Boltzmann factors for $T=79$ K. The band origins ν_0 and the rotational constants B' and D' for levels of the $f'\ ^1\Sigma_u^+$ state were parameters of the fit. Rotational line strengths for the five branches of a $^1\Sigma^+ \leftarrow\ ^3\Sigma^-$ transition, ^SR, ^QR, ^QQ, ^QP, and ^OP, were taken from Watson [36], for the case of a $^3\Sigma^-$ state intermediate between Hund's cases (a) and (b). The ground-state coupling factors c_J'' and s_J'' [36] were determined from the calculated term values and the ratio of the parallel and perpendicular transition moments z [36] was a parameter of the fit.

Rotational line centers ν_i were generated using the term

values obtained from the upper- and lower-state spectroscopic constants and relative line strengths r_i, where $\Sigma_i r_i = 1$, were proportional to the product of an appropriate Boltzmann factor and rotational line strength. The parameter z affected only the relative strengths of different branches. Each rotational line was described by a Fano profile [37] of the form

$$\sigma_i(\nu) = \frac{1.77\times 10^{-12} f_{\text{eff}}\, r_i}{\xi^2(1+q^2)\pi\Gamma}\left[1-\xi^2+\frac{\xi^2(q+x)^2}{1+x^2}\right] \times(1+a\Gamma x+b\Gamma^2x^2), \quad (2)$$

where $x=2(\nu-\nu_i)/\Gamma$ and the FWHM predissociation linewidth Γ cm^{-1}, the reciprocal of the Fano line-shape parameter q, the Fano overlap parameter ξ [38], the effective band oscillator strength f_{eff}, and the polynomial coefficients a and b, which describe the energy dependence of the underlying continuum, all of which were assumed to be independent of the particular rotational line under consideration, were parameters of the fitting procedure. The total cross section was given by $\sigma(\nu)=\Sigma_i\sigma_i(\nu)$. In view of the restricted rotational structure at 79 K, the constant-parameter assumption was generally adequate. However, in some cases it was not possible to obtain a good fit to the measured cross sections [39] unless the Fano parameters p were allowed to vary with rotation according to the relation

$$p=p_0+p_J J'(J'+1) \ . \quad (3)$$

After modification of $\sigma(\nu)$, to allow for the Doppler contribution to the line shapes, and convolution (in transmission) with a Gaussian instrument function, the model cross section appropriate to the experimental conditions was least-squares fitted to the measured cross section, enabling the determination of the spectroscopic and line-shape parameters associated with the $f'\leftarrow X$ transition.

The effective band oscillator strength f_{eff}, related to the amplitude-width product of the rapidly varying band structure, should be distinguished from the formal discrete oscillator strength defined by Fano and Cooper [37], $f=f_{\text{eff}}q^2/(1+q^2)$, which goes to zero in the case of a window resonance ($q=0$). The effective band oscillator strength used in this work bears a more direct relationship to the apparent strength of the band structure observed experimentally.

IV. RESULTS AND DISCUSSION

A. Rotational perturbations [40]

1. The (4,0) band of the $3p\pi_u f\ ^1\Sigma_u^+\leftarrow X\ ^3\Sigma_g^-$ system of $^{16}O_2$

A perturbation near $J'=9$ in the rotational structure of the (4,0) band of the forbidden Rydberg system $3p\pi_u f^1\Sigma_u^+\leftarrow X^3\Sigma_g^-$ of $^{16}O_2$ was first reported by Ogawa and Yamawaki [41], who noted that the rotational constant of the perturbing vibrational level must be smaller than that of $f\ ^1\Sigma_u^+(v=4)$. Katayama *et al.* [8], following observations of the (4,0) band of the allowed Rydberg system $f\ ^1\Sigma_u^+\leftarrow b\ ^1\Sigma_g^+$ in the photoabsorption spectrum of O_2 excited by a transformer discharge, reported the same upper-state perturbation for $^{16}O_2$, but no perturbation was observed for $^{18}O_2$. They [8] suggested that the perturbation was heterogeneous, but no extra lines from the perturbing state were observed and it was thus impossible to determine its rotational constant. The main impetus for the work presented here came from our observation of extra lines associated with the rotational perturbation discussed above. This enabled an accurate determination of the rotational constant of the perturbing level and consequent identification of the perturbing electronic state. Further measurements based on predictions suggested by these key observations enabled an extensive characterization of the perturbing state.

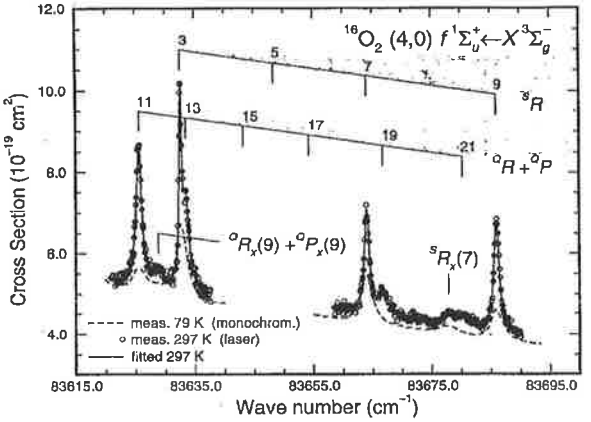

FIG. 4. Measured photoabsorption cross sections for selected regions in the (4,0) band of the $f\ ^1\Sigma_u^+\leftarrow X\ ^3\Sigma_g^-$ system of $^{16}O_2$, which show the extra lines with $J'=9$ associated with rotational perturbations in the ^sR and $^qR + {}^qP$ branches. Measurements were taken at room temperature with the laser-based system (resolution approximately 0.25 cm^{-1} FWHM) and at liquid-nitrogen temperature with the monochromator-based system (resolution approximately 1.7 cm^{-1} FWHM). A least-squares fit to the room-temperature results, based on Voigt line shapes, is also shown.

In Figs. 4 and 5 we present measured photoabsorption cross sections for small regions of the (4,0) $f\ ^1\Sigma_u^+\leftarrow X\ ^3\Sigma_g^-$ band of $^{16}O_2$. The cross sections show extra lines that are not part of the normal $f\leftarrow X$ band structure. Using the method of combination differences, these weak extra lines [42] can be assigned as $^sR_x(7)$, $^qR_x(9)+{}^qP_x(9)$, $^qR_x(11)+{}^qP_x(11)$, and $^oP_x(13)$. Their positions and strengths relative to the corresponding main $f\leftarrow X$ lines, the most perturbed in the (4,0) band, imply that the extra lines are associated with the $J=9$ and 11 rotational levels of the perturbing state [43].

We determined wave numbers, widths, and relative strengths for the observed extra lines by least-squares fitting to the measured cross sections a model, based on Voigt line shapes. In this case, asymmetric profiles were not necessary to obtain satisfactory fits. The results of the fitting procedure are presented in Table I. The parameters determined for $^oP_x(13)$ are more uncertain than those for the other lines because the height of the line is only a factor 2 greater than the measurement noise and no wavelength calibration lines are nearby. The extra lines have Lorentzian width components of approximately 2 cm^{-1} FWHM, considerably broader than the nearby lines of the $f\leftarrow X$ system, which

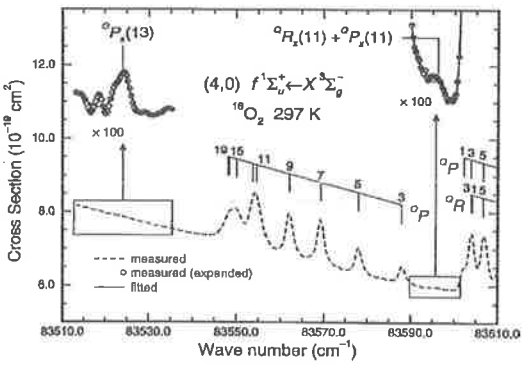

FIG. 5. Measured photoabsorption cross section for a selected region in the (4,0) band of the $f\,^1\Sigma_u^+ \leftarrow X\,^3\Sigma_g^-$ system of $^{16}O_2$, which shows the extra lines with $J'=11$ associated with rotational perturbations in the ^{O}P and $^{Q}R+^{Q}P$ branches. Measurements were taken at room temperature with the monochromator-based system (resolution approximately 1.7 cm^{-1} FWHM). The upper cross sections (open points) were obtained by subtracting the underlying continuum from the measured cross section, followed by an expansion of the vertical scale by the factors indicated and then a vertical displacement of the results, for clarity. Voigt-profile fits to the extra lines are shown.

have Lorentzian widths of approximately 1 cm^{-1} FWHM. Evidently, the perturbing electronic state is significantly predissociated by one or more repulsive states correlating with any of the lowest four dissociation limits of O_2.

The observation of two rotational levels of the perturbing state enables a rotational deperturbation to be performed on the $f\,^1\Sigma_u^+(v=4)$ levels using a simple two-level perturbation model [44,45]. We used term values $T_4^f(1-19)$ deduced from the R-branch measurements of the (4,0) $f \leftarrow b$ transition by Katayama *et al.* [8] and the level $T_4^f(21)=84341.4$ cm^{-1} determined from our fit to the high-resolution room-temperature cross section shown in Fig. 4, which contains the unresolved lines $^{Q}R(21)+^{Q}P(21)$. The perturber term value for $J=9$ was taken to be the weighted average of the separate determinations from the $^{S}R_x(7)$ and $^{Q}R_x(9)+^{Q}P_x(9)$ observations, while for $J=11$ we used the term value determined from the $^{Q}R_x(11)+^{Q}P_x(11)$ observation alone since the absolute wavelength calibration for the $^{O}P_x(13)$ line was inferior. Using an iterative least-squares technique, we deperturbed the above levels and obtained the results presented in Table II. The quality of the fit was excellent, with a rms deviation of approximately 0.1 cm^{-1}. The maximum perturbations for $f\,^1\Sigma_u^+(v=4)$ are -2.5 cm^{-1} for $J=9$ and $+1.0$ cm^{-1} for $J=11$, with a culmination [45] at $J=9.5$.

If we assume that the perturbed transition $f \leftarrow X$ carries an oscillator strength, but that the transition into the undetermined perturbing state x does not, it can be shown [44,45] that the ratio of the strengths of the extra and main lines of a particular branch are given by

$$\frac{I_x(J)}{I_f(J)} = \frac{2}{1+[\Delta E_0(J)/2]\{[\Delta E_0(J)/2]^2+H_{fx}^2\}^{-\frac{1}{2}}} - 1 = \frac{S(J)}{S(J)+\Delta E_0(J)}\,, \tag{4}$$

where $\Delta E_0(J)$ is the unperturbed energy separation between the perturbed and perturbing levels, H_{fx} is the interaction matrix element, and $S(J)>0$ is the shift in energy of each level due to the perturbation. Using Eq. (4) with the parameters obtained from the deperturbation of the observed energy levels, in the case of the most strongly perturbed lines we obtain $I_x(9)/I_f(9)=0.20$ and $I_x(11)/I_f(11)=0.034$, in good agreement with our observed values of 0.220 ± 0.015 and 0.047 ± 0.012, respectively. This agreement independently supports the validity of the simple perturbation model employed since line intensities were not included in the fitting procedure.

The Rydberg transition $f\,^1\Sigma_u^+ \leftarrow X\,^3\Sigma_g^-$ is nominally forbidden and borrows strength from the allowed transition between the ground state and the mixed Rydberg-valence state $E\,^3\Sigma_u^-$ by means of a spin-orbit coupling H_{fE} between the $f\,^1\Sigma_u^+$ and $E\,^3\Sigma_u^-$ states [46]. In this picture, the extra lines

TABLE I. Wave numbers, widths, relative strengths, and upper-state term values for the extra lines observed in association with rotational perturbations in the (4,0) band of the $f\,^1\Sigma_u^+ \leftarrow X\,^3\Sigma_g^-$ system of $^{16}O_2$, determined by least-squares fitting a model based on Voigt line shapes to the measured cross sections.

Line	ν (cm^{-1})	FWHM Γ (cm^{-1})	I_x/I_f [a]	T' (cm^{-1})
$^{S}R_x(7)$	83677.80±0.11	2.17±0.17	0.225±0.015	83756.29±0.11[b]
$^{Q}R_x(9)+^{Q}P_x(9)$	83628.74±0.17	2.37±0.39	0.192±0.040	83756.11±0.17
$J'=9$[c]		2.20±0.16	0.220±0.015	83756.24±0.10
$^{Q}R_x(11)+^{Q}P_x(11)$	83596.35±0.15	2.28±0.61	0.047±0.012	83783.88±0.15
$^{O}P_x(13)$	83523.98±0.30	2.90±0.50	0.040±0.008	83783.58±0.30
$J'=11$[c]		2.28±0.61	0.047±0.012	83783.88±0.15

[a]The intensities of the extra lines are expressed relative to the main line intensities, e.g., $^{S}R_x(7)/^{S}R(7)$.
[b]The quoted uncertainties in line positions and term values are 1σ statistical values determined by the fitting procedure. There is an additional absolute calibration uncertainty of approximately 0.2 cm^{-1}.
[c]Best estimates obtained from the measurements as described in the text.

TABLE II. Summary of the experimentally determined (deperturbed) spectroscopic constants, isotopic shifts, and interaction matrix elements relevant to rotational perturbations in the $np\pi_u\,^1\Sigma_u^+$ Rydberg states (R) caused by an electrostatic interaction with the valence state $f'\,^1\Sigma_u^+$.

	Rydberg $np\pi_u\,^1\Sigma_u^+$				Valence $f'\,^1\Sigma_u^+$	
Isotope	n	v	Parameters (cm^{-1})	$H_{Rf'}$ (cm^{-1})	v	Parameters (cm^{-1})
$^{16}O_2$	3	4	$\nu_0 = 83600.1 \pm 0.2$[a]	5.3 ± 0.1	5	$\nu_0 = 83687.1 \pm 0.6$
			$B = 1.6089 \pm 0.0006$			$B = 0.740 \pm 0.007$
			$D = (9.5 \pm 3.8) \times 10^{-6}$			
$^{16}O^{18}O$	3	4	$\nu_0 = 83400.7 \pm 0.2$	4.0 ± 0.1	5	$\nu_0 = 83612.3 \pm 1.4$[b]
			$B = 1.5208 \pm 0.0006$			
			$D = (4.4 \pm 1.5) \times 10^{-6}$			
			$^i\Delta G = 221.6 \pm 0.1$[c]			$^i\Delta G = 97.0 \pm 1.6$
$^{18}O_2$	3	4	$\nu_0 = 83194.9 \pm 0.2$	3.0 ± 0.9	5	$\nu_0 = 83539 \pm 9$[d]
			$B = 1.4338 \pm 0.0007$			
			$D = (6.6 \pm 1.1) \times 10^{-6}$			
			$^i\Delta G = 450.4 \pm 0.1$			$^i\Delta G = 193 \pm 9$
$^{16}O_2$	3	5	$\nu_0 = 85324.7 \pm 1.3$	41.3 ± 0.4	8	$\nu_0 = 85467.0 \pm 1.2$
			$B = 1.578 \pm 0.010$			$B = 0.701 \pm 0.005$
			$D = (5.6 \pm 1.6) \times 10^{-5}$			
$^{16}O_2$	4	1	$\nu_0 = 89263.8 \pm 0.4$	1.3 ± 0.4	17	
			$B = 1.712 \pm 0.003$			
			$D = (9.0 \pm 1.1) \times 10^{-5}$[e]			

[a]Band-origin uncertainties include statistical (1σ) and calibration uncertainties.
[b]Rotational constant fixed at the isotopic value $^{1618}B_5 \approx \rho_{1618}^2 B_5 = 0.699$.
[c]Uncertainties in the isotopic shifts are unaffected by the calibration uncertainty.
[d]Rotational constant fixed at the isotopic value $^{18}B_5 \approx \rho_{18}^2 B_5 = 0.658$.
[e]Rotational constants perturbed by a lower-lying $^1\Pi_u$ level. $H = (5.6 \pm 1.0) \times 10^{-8}$.

that we have observed borrow their strengths from the allowed $E\,^3\Sigma_u^- \leftarrow X\,^3\Sigma_g^-$ transition by a second-order process involving the H_{fE} and H_{fx} interactions and the $f\,^1\Sigma_u^+$ intermediate state.

The deperturbed rotational constant for the perturbing state (0.740 cm^{-1}) implies an internuclear distance of approximately 1.7 Å, characteristic of a valence state. This is in contrast to the approximately 1.1 Å internuclear distance for the f and other Rydberg states in this energy region that converge to the ground state of the ion. In order to produce the observed rotational perturbations in the $f\,^1\Sigma_u^+$ Rydberg state, the perturbing state must be bound at approximately 10.5 eV and the selection rules for perturbation [45] require that the perturbing state be of *ungerade* symmetry. Of the bound *ungerade* valence states predicted by *ab initio* calculations [5,6], only the $^1\Sigma_u^+$ state, arising from the first-excited molecular-orbital configuration and correlating with the $O(^1D) + O(^1S)$ dissociation limit at 11.37 eV, is energetically capable of rotationally perturbing the f state. In addition, the calculated equilibrium internuclear distance for the $^1\Sigma_u^+$ valence state [9] is in good agreement with the approximately 1.7 Å internuclear distance deduced from our measured rotational constant for the perturbing state [47]. Thus the present measurements have allowed the identification of the perturbing state as the valence state $f'\,^1\Sigma_u^+$.

Further support for our perturber assignment can be obtained by considering the interaction matrix elements. According to Lefebvre-Brion and Field [45], the valence and Rydberg $^1\Sigma_u^+$ states may interact electrostatically because their primary molecular-orbital configurations differ by two orbitals. Guberman and Giusti-Suzor [9,20] have calculated an electrostatic interaction strength $H^e \approx 2000$ cm^{-1} between the valence and $3p\pi_u$ Rydberg $^1\Sigma_u^+$ states. Such a strong interaction is necessary to explain our observation of a vibronic interaction $H_{ff'} = \langle v_f | H^e | v_{f'} \rangle \approx 5$ cm^{-1} between the $f\,^1\Sigma_u^+(v_f = 4)$ and the $f'\,^1\Sigma_u^+(v_{f'} = v_x)$ levels, since the vibrational overlap $\langle v_f | v_{f'} \rangle$ will be very small because of the large difference in R_e between the perturbed and perturbing states. In view of this, it is unlikely that the weaker spin-orbit or L-uncoupling interactions could explain the observed perturbation. We should also note that our deperturbation analysis assumed implicitly that the perturbation interaction $H_{ff'}$ was J independent. In view of our assignment for the perturbing state, this has proven to be a valid assumption.

In summary, our observation of extra levels associated with rotational perturbations in the $v = 4$ level of the $f\,^1\Sigma_u^+$ Rydberg state of $^{16}O_2$ has allowed a full rotational deperturbation, resulting in an accurate rotational constant for the perturbing state and an accurate determination of the strength of the perturbation. Together with information from *ab initio* calculations, this has allowed us to identify the perturbing state as the lowest $^1\Sigma_u^+$ valence state, which we denote as $f'\,^1\Sigma_u^+$. The perturbation occurs through an electrostatic

Rydberg-valence interaction, which may be quite strong. The extra lines that we have observed are experimental observations of the $f'\ ^1\Sigma_u^+$ valence state.

2. The (4,0) band of the $3p\pi_u$ $f\ ^1\Sigma_u^+ \leftarrow X\ ^3\Sigma_g^-$ system of $^{18}O_2$

In order to establish the vibrational numbering of the perturbing state $f'\ ^1\Sigma_u^+$, it is helpful to obtain isotopic shifts for the perturbing levels. Ogawa [48] measured wave numbers for the (4,0) band of the $f\ ^1\Sigma_u^+ \leftarrow X\ ^3\Sigma_g^-$ system of $^{18}O_2$, while Katayama *et al.* [8] measured those for the (4,0) band of the $f\ ^1\Sigma_u^+ \leftarrow b\ ^1\Sigma_g^+$ system of $^{18}O_2$, but neither author has reported any rotational perturbations for the heavier isotope.

We calculated rotational term values for the $f\ ^1\Sigma_u^+(v=4)$ level of $^{18}O_2$ from the R-branch measurements of Katayama *et al.* [8] and have found evidence for a weak rotational perturbation at $J=21$. We have not attempted to find extra lines associated with the perturbation by taking new measurements since the main lines for high rotational excitation are weak and exhibit predissociation linewidths that increase rapidly with rotation. Nevertheless, we rotationally deperturbed the $f\ ^1\Sigma_u^+$ levels for $^{18}O_2$ in the manner described previously, but with the additional assumptions that the same vibrational level is involved in the perturbation of each isotope and that the rotational constant for the perturbing state is $B=0.658$, obtained from our $^{16}O_2$ value using the normal isotopic relation [44] with $\rho_{18}=0.94268$. The results are presented in Table II. The derived band origin for the perturber and the interaction strength are, necessarily, approximate since no extra lines have been observed. The resultant deperturbation indicates a weak rotational perturbation of approximately 0.7 cm^{-1} for $J=21$. While the quality of the deperturbation is similar to that obtained for $^{16}O_2$, with a rms deviation of approximately 0.1 cm^{-1}, the weakness of the perturbation and the greater measurement uncertainty for the higher rotational levels suggest that further isotopic information would be desirable.

3. The (4,0) band of the $3p\pi_u f\ ^1\Sigma_u^+ \leftarrow X\ ^3\Sigma_g^-$ system of $^{16}O^{18}O$

We have measured room-temperature photoabsorption cross sections for an isotopic mixture of O_2 containing 50.4 at. % ^{18}O in the region of the (4,0) $f\ ^1\Sigma_u^+ \leftarrow X\ ^3\Sigma_g^-$ bands of $^{16}O^{18}O$ and $^{16}O_2$, using narrow-bandwidth vuv radiation produced with the laser system described in Sec. II B. Our measured cross section is shown in Fig. 6 for the region 83 420–83 575 cm^{-1}, which shows the ^SR branch of the (4,0) $f \leftarrow X$ band of $^{16}O^{18}O$. An abnormally large spacing is evident between the $^SR(13)$ and $^SR(14)$ lines and also between the $^QR(15)+{}^QP(15)$ and $^QR(16)+{}^QP(16)$ lines, which are partially obscured by the stronger $^SR(4)$ and $^SR(5)$ lines respectively. These observations suggest that the $J=15$ and $J=16$ levels of $f\ ^1\Sigma_u^+(v=4)$ are rotationally perturbed for $^{16}O^{18}O$. However, no extra lines associated with the perturbing state have been observed.

Our measured wave numbers for the $^QR+{}^QP$ and ^SR branches are given in Table III, together with $f\ ^1\Sigma_u^+$ term values derived from our measurements and the ground-state spectroscopic constants for $^{16}O^{18}O$ given by Steinbach and Gordy [49]. For $J<18$, our $T_4^f(J)$ are accurate to better than $\pm$ 0.1 cm^{-1} in a relative sense. The absolute wave-number scale has been established by calibration against $^{16}O_2$ term values deduced from the measurements of Katayama *et al.* [8], making use of the overlap between the $^{16}O^{18}O$, ^SR-branch lines of higher rotation and the $^{16}O_2$, ^OP-branch lines in our experimental scan. The additional calibration uncertainty is expected to be approximately 0.2 cm^{-1}.

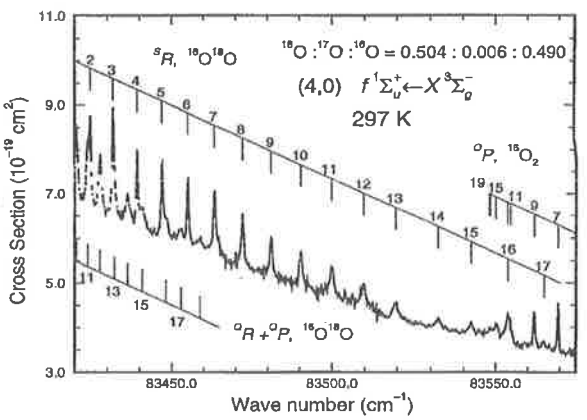

FIG. 6. Photoabsorption cross section for an isotopic mixture of O_2 in the region of the (4,0) $f\ ^1\Sigma_u^+ \leftarrow X\ ^3\Sigma_g^-$ bands of $^{16}O^{18}O$ and $^{16}O_2$, measured at room temperature with narrow-bandwidth (approximately 0.25 cm^{-1} FWHM) vuv radiation generated using the laser-based system. Anomalous separations between the $^SR(13)$ and $^SR(14)$ lines and the $^QR(15)+{}^QP(15)$ and $^QR(16)+{}^QP(16)$ lines indicate that the levels with $J'=15$ and 16 are rotationally perturbed.

We have performed a rotational deperturbation of the $^{16}O^{18}O$ levels $T_4^f(0-19)$, given in Table III, using our simple two-level perturbation model with the rotational constant of the perturbing f' level fixed at 0.699, determined using the normal isotopic relation with $\rho_{1618}=0.971\,77$. The results obtained are presented in Table II. The quality of the deperturbation, illustrated graphically in Fig. 7, is excellent, consistent with the very low uncertainties in the experimental measurements. The maximum perturbations are +1.2 cm^{-1} for $J=16$ and −1.0 cm^{-1} for $J=15$, with a culmination at $J=15.6$.

Using our deperturbed band origins for the unknown perturbing level v_x of the $f'\ ^1\Sigma_u^+$ valence state for $^{16}O_2$ and $^{16}O^{18}O$ and noting that the isotopic shift for the $v=0$ level of the $X\ ^3\Sigma_g^-$ state is 22.2 cm^{-1}, it follows that the isotopic shift for $f'\ ^1\Sigma_u^+(v_x)$ is $^{1618}\Delta G_{v_x}=97.0\pm1.6$ cm^{-1}. From the usual polynomial representation of the vibrational levels G_v of a potential well [44]

$$G_v=\omega_e(v+\tfrac{1}{2})-\omega_e x_e(v+\tfrac{1}{2})^2+\cdots, \tag{5}$$

it can be shown [44] that the isotopic shift is

$$\begin{aligned} {}^i\Delta G_v &= G_v - {}^iG_v \\ &= (1-\rho_i)G_v-\rho_i(1-\rho_i)\omega_e x_e(v+\tfrac{1}{2})^2+\cdots, \end{aligned} \tag{6}$$

TABLE III. Measured wave numbers for the ^SR and $^QR+^QP$ branches of the (4,0) band of the $f\,^1\Sigma_u^+ \leftarrow X\,^3\Sigma_g^-$ system of $^{16}O^{18}O$, together with the corresponding upper-state term values.

N''	^QP	^QR	^SR	J'	T'[a] (cm^{-1})
0	83402.41		83411.42	0	83400.60[c]
1	83402.79	83404.90[b]	83418.00	1	83403.63
2	83403.59[d]		83424.79	2	83409.69
3	83404.60[b,d]		83431.87	3	83418.82
4	83405.86[d]		83439.31	4	83431.01
5	83407.47[d]		83447.00	5	83446.20
6	83409.43[d]		83455.03	6	83464.47
7	83411.65[b,d]		83463.38	7	83485.74
8	83414.29[d]		83472.09	8	83510.04
9	83417.18[d]		83481.07	9	83537.38
10	83420.44[d]		83490.36	10	83567.78
11	83423.96[d]		83499.98	11	83601.17
12	83427.84[d]		83509.70	12	83637.60
13	83432.26[b,d]		83519.51	13	83677.08
14	83436.35[d]		83532.31	14	83719.34
15	83440.84[d]		83542.39	15	83764.42
16	83448.22[b,d]			16	83815.22
17	83452.86[d]		83564.97	17	83865.95
18	83458.81[d]			18	83920.71
19				19	83977.96

[a]Weighted averages determined from the separate branch wave numbers.
[b]Partial blend.
[c]Relative uncertainties less than 0.1 cm^{-1} for $J'<18$ and less than 0.2 cm^{-1} for $J'=18,19$. There is an additional calibration uncertainty of approximately 0.2 cm^{-1}.
[d]Unresolved ^QP and ^QR branches.

where i refers to the heavier isotope and $\rho_i=\sqrt{\mu/\mu_i}$. If we neglect terms in $(v+1/2)^2$ and higher powers, it follows from our f' isotopic shift measurement that $G_{v_x} \approx {}^{1618}\Delta G_{v_x}/(1-\rho_{1618})=3440\ cm^{-1}$. Since the dissociation limit for the f' state is 11.37 eV and, from Table II, $\nu_{v_x 0}=83\,687.1\ cm^{-1}$, it also follows that the minimum energy of the f' potential well $T_e \approx 10.05$ eV and that the well depth $D_e \approx 1.32$ eV. These values, estimated solely from experimental measurements, agree remarkably well with the latest *ab initio* values of Guberman and Giusti-Suzor [9], $T_e=10.08$ eV and $D_e=1.31$ eV. For the moment, there is not enough experimental information available to define v_x uniquely. However, if we assume the *ab initio* values [9] $\omega_e=752\ cm^{-1}$ and $\omega_e x_e=7.98\ cm^{-1}$, we may use Eqs. (5) and (6) with our experimental isotope shift to obtain an estimate for the vibrational excitation of the perturber, obtaining $v_x=4.6\approx 5$. Since the isotopic shift for $^{16}O^{18}O$ is approximately half of that for $^{18}O_2$, the above results suggest that a single level $f'\,^1\Sigma_u^+(v=5)$ is responsible for the rotational perturbations observed in the $f\,^1\Sigma_u^+(v=4)$ level of isotopic O_2, as foreshadowed in Table II. In addition, slightly modified experimental values for the $f'\,^1\Sigma_u^+$ valence-state-potential parameters $G_5=3670\ cm^{-1}$, $T_e=10.02$ eV, and $D_e=1.35$ eV can be determined.

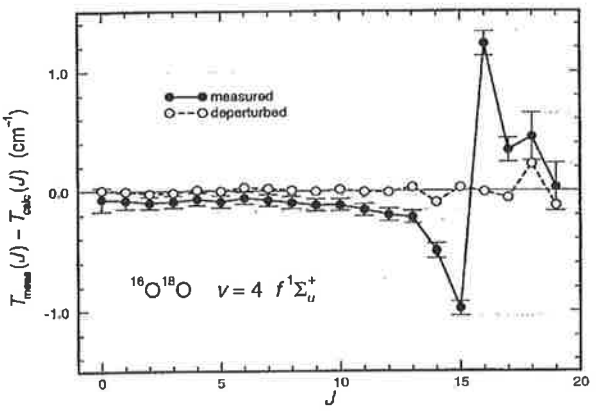

FIG. 7. Rotational deperturbation of the $v=4$ energy levels of the $f\,^1\Sigma_u^+$ Rydberg state of $^{16}O^{18}O$. The plotted differences between the measured term values and unperturbed (solid points) or perturbed (open points) term values calculated with the parameters given in Table II emphasize the rotational perturbations that culminate at $J=15.6$.

4. The (5,0) band of the $3p\pi_u f\,^1\Sigma_u^+ \leftarrow X\,^3\Sigma_g^-$ system of $^{16}O_2$

If our picture of the interaction between the Rydberg and valence $^1\Sigma_u^+$ states is correct, then stronger rotational perturbations might be expected at energies higher than $f\,^1\Sigma_u^+(v=4)$. Ogawa *et al.* [50] have assigned features observed spectrographically in the $^{16}O_2$ photoabsorption spectrum near 85 315 cm^{-1} and 85 382 cm^{-1} to the (5,0) $f \leftarrow X$ band. In Fig. 8 we present measured room-temperature pho-

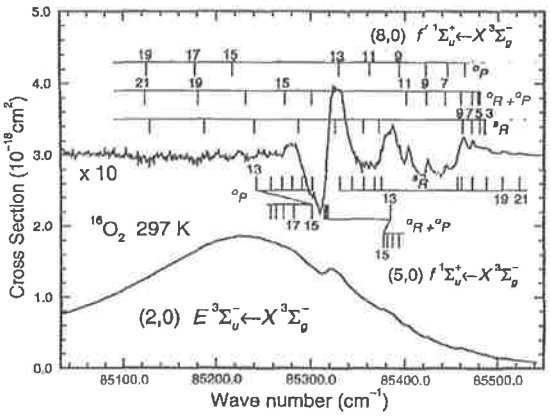

FIG. 8. Measured photoabsorption cross section in the region of the (5,0) band of the $f\,^1\Sigma_u^+ \leftarrow X\,^3\Sigma_g^-$ system, taken at room temperature with the monochromator-based system (resolution approximately 1.7 cm^{-1} FWHM). The expanded-scale upper trace, obtained by subtracting the smoothly varying component from the measured cross section, illustrates the asymmetric nature of the (5,0) $f \leftarrow X$ resonance, rotational perturbations in the $f \leftarrow X$ branch structure, and extra lines resulting from transitions into the perturbing level $v=8$ of the valence state $f'\,^1\Sigma_u^+$. Only the numbered lines (not necessarily resolved) have been assigned in Table IV.

toabsorption cross sections for $^{16}O_2$ in this region, obtained using the monochromator system. The dominant feature in the spectrum is a broad peak near 85 230 cm^{-1}, the third band of Tanaka [51], actually the (2,0) band of the $E\,^3\Sigma_u^- \leftarrow X\,^3\Sigma_g^-$ system discussed previously by Lewis *et al.* [25]. The (5,0) $f \leftarrow X$ band appears as a diffuse feature with a head near 85 320 cm^{-1}, on the high-energy wing of the third band. Of particular interest is the fact that the (5,0) $f \leftarrow X$ band is a Beutler-Fano resonance of quite high asymmetry. This can be seen clearly in the upper trace of Fig. 8, a difference cross section obtained by subtracting a smooth curve drawn through the measured cross section, ignoring the more rapid fluctuations, from the measured cross section, and expanding the vertical scale by a factor 10.

Apart from the feature near 85 380 cm^{-1}, also observed by Ogawa *et al.* [50], we have found a number of other irregularities in the spectrum, notably a group of rotational lines between 85 390 cm^{-1} and 85 490 cm^{-1}. We propose that these additional features arise because of a strong rotational perturbation caused by the interaction of the Rydberg level $f\,^1\Sigma_u^+(v=5)$ with another undetermined vibrational level of the valence state $f'\,^1\Sigma_u^+$. Assignments of features were made by the method of combination differences and by using characteristics such as linewidth and asymmetry. Extra lines have been assigned that are significantly narrower at low rotation than the (5,0) $f \leftarrow X$ lines. As rotation increases, the extra lines become broader and asymmetric, appearing as *dips* for $J \geq 17$. An iterative technique was used to aid the assignment of the weaker features. The initially assigned lines were used in a two-level deperturbation model, which was used to predict the positions of unassigned features.

Observed wave numbers for rotational features from the (5,0) $f \leftarrow X$ and the perturbing $f' \leftarrow X$ bands are given in Table IV, together with corresponding term values for the f and f' states. In each case, the tabulated wave numbers refer to the estimated line *centers*, which differ from the line peaks in the case of asymmetric features, for example, the broad, dispersion-profile-like features of the (5,0) $f \leftarrow X$ bandhead. Relative uncertainties in the tabulated term values range from approximately 0.5 cm^{-1} for the narrower low-rotational levels of the valence state to approximately 2 cm^{-1} for the broader levels of each state and there is an additional calibration uncertainty of approximately 0.7 cm^{-1}. The assignments given in Fig. 8 and Table IV for the extra lines $^sR_x(5)$, $^sR_x(7)$, $^sR_x(9)$, $^QR_x(7)+{}^QP_x(7)$, $^QR_x(9)+{}^QP_x(9)$, and $^QR_x(11)+{}^QP_x(11)$ can be verified explicitly from the observed combination differences. Most of the other assignments are tentative due to the problems in interpreting strongly perturbed spectra and difficulties due to weak, diffuse, asymmetric, and blended features.

The results of the final deperturbation of the term values given in Table IV are given in Table II. The deperturbation is illustrated in Fig. 9, where the culmination is seen to occur at $J=12.3$. The interaction matrix element $H_{ff'}$ ($=41.3$ cm^{-1}) is nearly an order of magnitude larger than that found for the $v_f=4$ perturbation. This is in accord with our qualitative picture of valence and Rydberg $^1\Sigma_u^+$ states exhibiting a strong electrostatic interaction, with a rapidly increasing vibrational overlap as the vibrational excitation increases and the crossing point of the Rydberg and valence potential-energy curves is approached from below.

The vibrational quantum number of the perturbing f' state may be estimated as follows. Experimentally, we have determined that $G_{5+\Delta v} - G_5 = 85\,467.0 - 83\,687.1 = 1779.9 \pm 1.3$ cm^{-1}, where Δv is the unknown difference in vibrational excitation between the levels of the valence state that perturb the $v=4$ and $v=5$ levels of the Rydberg state. Using the *ab initio* values for ω_e and $\omega_e x_e$ [9] in Eq. (5), we obtain $\Delta v = 2.8 \approx 3$, suggesting that the $v=8$ level of the f' state perturbs the $v=5$ level of the f state, as foreshadowed in Figs. 8 and 9 and Table II.

Before proceeding, we should note that the spectrum in the region of the (5,0) $f \leftarrow X$ band is complex, involving three interacting electronic states, one of which ($E\,^3\Sigma_u^-$) is a mixed Rydberg-valence state which is heavily predissociated. The correct theoretical treatment of such a situation requires the use of a coupled-Schrödinger-equations (CSE) technique [45], which is beyond the scope of this work. Therefore, it may be necessary to increase the uncertainties in the deperturbed parameters given in Table II to allow for the approximate nature of the two-level model.

5. The (1,0) band of the $4p\pi_u j\,^1\Sigma_u^+ \leftarrow b\,^1\Sigma_g^+$ system of $^{16}O_2$

Since the strong electrostatic interaction between the valence state $f'\,^1\Sigma_u^+$ and the Rydberg state $3p\pi_u f\,^1\Sigma_u^+$ is responsible for the rotational perturbations observed in the f levels, it is likely that a similar interaction between the $f'\,^1\Sigma_u^+$ and the higher-lying $4p\pi_u j\,^1\Sigma_u^+$ Rydberg state will produce perturbations in the j levels. Since the electrostatic interaction between the valence state and the Rydberg series is expected to decrease with increasing effective principal

TABLE IV. Measured wave numbers for the main (M) and extra (X) lines observed in association with strong rotational perturbations in the (5,0) band of the $f\,^1\Sigma_u^+ \leftarrow X\,^3\Sigma_g^-$ system of $^{16}O_2$, together with corresponding upper-state term values for the perturbed Rydberg and perturbing valence $^1\Sigma_u^+$ states.

N''	^OP	$^QR+^QP$	^SR	J'	T^f (cm^{-1})	$T^{f'}$ (cm^{-1})
3		85316.6M[a]	85486.0X	3	85331.8±2.0[b]	
5			85480.5X	5		85501.3±0.7
7		85442.6X	85472.2X	7		85521.4±0.5
9	85394.0X	85423.9X	85462.7X	9		85550.8±0.5
11	85362.6X[c]	85401.8X		11	85501.9±1.5	85589.7±0.5
13	85242.3M[a] 85330.1X[d]	85385.1M		13	85644.5±0.5	85561.5±1.5
15	85218.6X 85301.4M[a]	85270.8X 85376.8M[a]		15	85719.3±0.7	85614.9±1.5
17	85178.5X[e,f] 85281.4M			17		85667.3±2.0
19	85123.5X[e,f]	85178.5X[e,f]	85505.8M[a]	19		85722.1±2.0
21		85123.5X[e,f]	85522.6M[a]	21	86049.3±2.0	85784.7±2.0
23				23	86183.6±2.0	

[a]Broad, asymmetric.
[b]Estimated relative uncertainties are given for all term values. There is an additional calibration uncertainty of approximately 0.7 cm^{-1}.
[c]Weak.
[d]Shoulder.
[e]Dip.
[f]Blended.

quantum number as $(n^*)^{-3/2}$ [45], for a given vibrational overlap the perturbations will be weaker for the higher Rydberg member.

The only sharp levels of the j state are the lowest two. Katayama *et al.* [8] have observed spectrographically the (0,0) and (1,0) bands of the allowed system $j \leftarrow b$ and have listed the corresponding wave numbers. An examination of their results shows no irregularity in the structure of the (0,0) band, but there are indications of a weak rotational perturbation in the (1,0) band. The densitometer tracing taken from the (1,0) $j \leftarrow b$ spectrogram of Katayama *et al.* [8] shows that the $R(12)$ line is anomalously weak when compared with a smooth curve drawn through the transmittance minima of the other R-branch lines. We used the measured wave numbers of Katayama *et al.* [8], assumed to have *relative* uncertainties of approximately 0.1 cm^{-1}, to obtain the rotational term values of $j\,^1\Sigma_u^+(v=1)$. The term values and spectrogram suggest a very weak rotational perturbation of -0.3 ± 0.05 cm^{-1} at $J=13$, transitions into this level losing $(5\pm1)\%$ of their strength. Using Eq. (4) with $I_{f'}(13)/I_j(13)=0.05/0.95$ and $S(13)=0.3$ cm^{-1}, we obtain $H_{jf'}=1.3\pm0.4$ cm^{-1} and $\Delta E_0(13)=5.4\pm0.1$ cm^{-1}. These results, together with the measured [8] upper-state term value $T_1^j(13)=89\,572.3$ cm^{-1}, imply that the corresponding perturbing level is at $89\,578.3\pm1.1$ cm^{-1}. It is not possible to estimate the vibrational excitation of this perturbing level of the f' state using the techniques employed previously since this energy is approaching the dissociation limit where the polynomial expression Eq. (5) breaks down. We shall see in Sec. V that the perturbing level is likely to be $v=17$. The results of this section and the previous sections have been collected together and are presented in Table II, which provides a summary of the experimental results pertinent to the rotational perturbations caused in the $np\pi_u$ $^1\Sigma_u^+$ Rydberg states by the $f'\,^1\Sigma_u^+$ valence state.

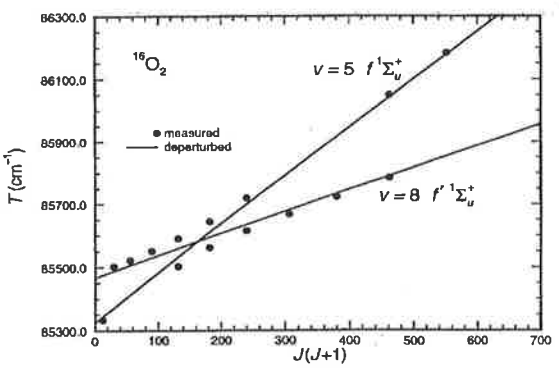

FIG. 9. Observed term values for the $f\,^1\Sigma_u^+(v=5)$ and $f'\,^1\Sigma_u^+(v=8)$ levels of $^{16}O_2$, illustrating a strong mutual perturbation. Deperturbed term values for the f and f' states, calculated with the parameters given in Table II, indicate a culmination of the rotational perturbations at $J=12.3$.

B. The $f'\,^1\Sigma_u^+ \leftarrow X\,^3\Sigma_g^-$ system

At energies higher than than those applying to the rotational perturbations discussed above and especially near the

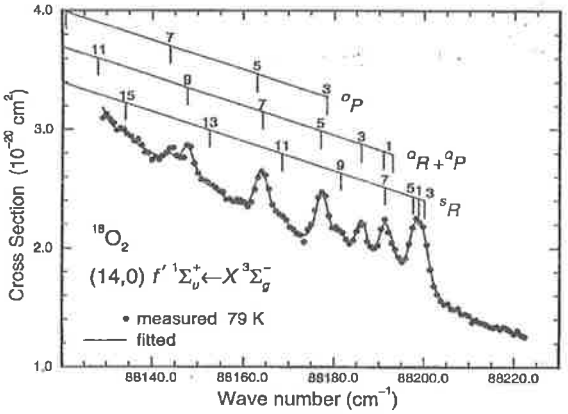

FIG. 10. Observed and fitted photoabsorption cross sections for the (14,0) $f'\ ^1\Sigma_u^+ \leftarrow X\ ^3\Sigma_g^-$ band of $^{18}O_2$.

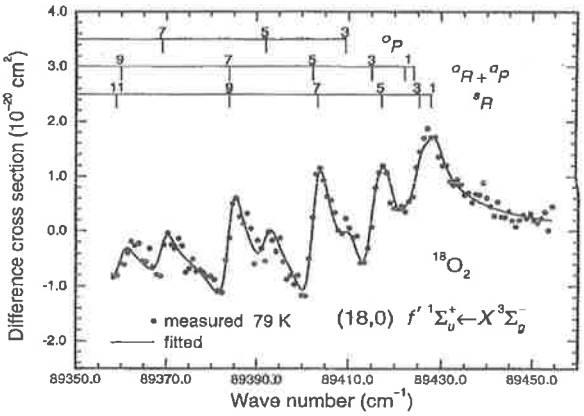

FIG. 12. Observed and fitted photoabsorption difference cross sections for the (18,0) $f'\ ^1\Sigma_u^+ \leftarrow X\ ^3\Sigma_g^-$ band of $^{18}O_2$.

crossing point of their potential-energy curves, the f and f' levels might be expected to interact strongly. This suggests the possibility of observing a few complete absorption bands from the $f \leftarrow X$ valence system, as distinct from the fragmentary extra lines observed in association with the rotational perturbations discussed in Sec. IV A. We have searched the photoabsorption spectrum of O_2 for signs of weak bands having branch structure consistent with a $^1\Sigma^+ \leftarrow ^3\Sigma^-$ transition and have found one partial ($v'=15$) and two complete such bands ($v'=14,19$) in the spectrum of $^{16}O_2$ and six complete bands ($v'=7,10,13,14,18,19$) in the spectrum of $^{18}O_2$. All measurements were taken with the monochromator-based system at a resolution of approximately 1.7 cm^{-1} FWHM and it was necessary to average over 3–40 separate scans in order to attain the desired accuracy. With the exception of the partial band observed for $^{16}O_2$, all measurements were taken at an effective temperature of 79 K in order to concentrate the rotational structure. Indeed, the (7,0) band of $^{18}O_2$, for example, could not be detected in room-temperature scans.

All observed bands exhibit a single head and relatively open rotational structure that is degraded to the red, consistent with an upper state having a rotational constant much smaller than that of the ground state. This characteristic appearance is in marked contrast with all other bands observed in this region of the O_2 spectrum, including those of the $f \leftarrow X$ Rydberg system that exhibit two heads due to the Q and returning ^OP branches and are degraded to the blue. The bands reported here vary widely in strength, with peak cross sections (excluding the continuum component) from approximately 1×10^{-21} cm^2 for (19,0) band of $^{16}O_2$ to approximately 6×10^{-20} cm^2 for the (13,0) band of $^{18}O_2$. The apparent rotational linewidths vary from a little greater than the instrumental bandwidth of 1.7 cm^{-1} to much broader, indicating a significant degree of predissociation in the upper state of these bands.

Perhaps the most dramatic aspect of the measured cross sections is the marked degree of line-shape asymmetry exhibited in some of the bands. While rotational lines from the (14,0) and (19,0) bands of $^{16}O_2$ and $^{18}O_2$ seem relatively symmetric, those from the (7,0), (10,0), (13,0), and (18,0) bands of $^{18}O_2$ display unusual line shapes. The measured photoabsorption cross section for the band containing the

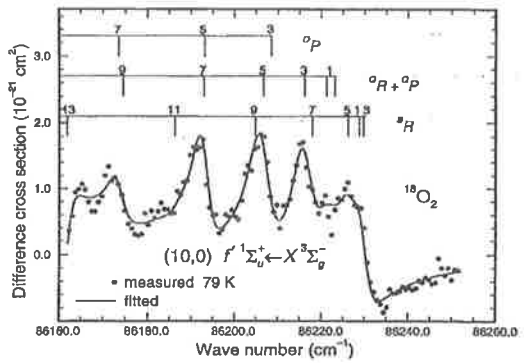

FIG. 11. Observed and fitted photoabsorption difference cross sections for the (10,0) $f'\ ^1\Sigma_u^+ \leftarrow X\ ^3\Sigma_g^-$ band of $^{18}O_2$.

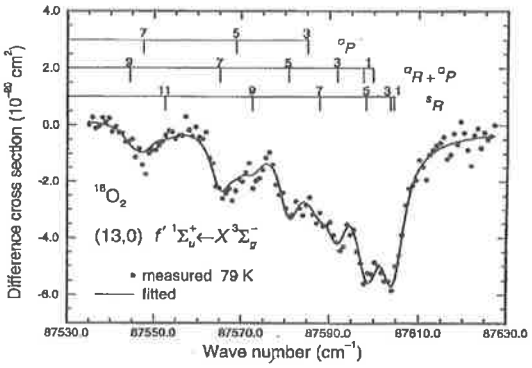

FIG. 13. Observed and fitted photoabsorption difference cross sections for the (13,0) $f'\ ^1\Sigma_u^+ \leftarrow X\ ^3\Sigma_g^-$ band of $^{18}O_2$. This band is an example of a window resonance in molecular photodissociation.

TABLE V. Summary of experimentally determined upper-state (perturbed) spectroscopic constants, oscillator strengths, and line-shape parameters for vibrational bands from the $f'\ ^1\Sigma_u^+ \leftarrow X\ ^3\Sigma_g^-$ valence systems of $^{16}O_2$ and $^{18}O_2$.

Isotope	v'	ν_0 (cm^{-1})	B (cm^{-1})	$10^4 D$ (cm^{-1})	$10^7 f_{eff}$	$1/q$	ξ^2	Γ (cm^{-1})
$^{16}O_2$	5	83687.5±0.6[a,b]	0.745±0.007[a,c]					2.20±0.16[a,c]
	8	85478.1±1.2[a]	0.770±0.005[a]					
	14	88313.7±1.0	0.723±0.006		1.94±0.14	0.029±0.004	~0.0	1.70±0.18
	15	88631.0±2.0[b]	0.840±0.015[d]	2.19±0.21[d]	1.07±0.11[d]			1.75±0.35[d]
	19	89975.4±1.0	0.499±0.006		0.224±0.024	0.080±0.006	~0.0	1.37±0.31
$^{18}O_2$	7	84686.5±1.0	0.665±0.006		1.76±0.11[e]	−0.345±0.033	0.0075±0.0013	2.73±0.21
	10	86220.3±1.0	0.766±0.009	2.06±0.24	0.644±0.053	−0.417±0.048	0.061±0.010	3.75±0.31[f]
	13	87597.1±1.0	0.670±0.006		24.6±1.9	−23.0±13.0	0.264±0.012	5.06±0.38
	14	88190.1±1.0	0.775±0.006	−1.21±0.12	1.58±0.10[g]	0.000±0.008[h]	~0.0	2.15±0.14
	18	89421.6±1.0	0.571±0.006		5.84±0.46	0.682±0.048	0.136±0.013	2.65±0.27
	19	89662.6±1.0	0.599±0.006	1.74±0.40	0.800±0.045	0.108±0.024	0.016±0.005	2.22±0.19

[a]Perturbed value derived from rotational deperturbation analysis.
[b]Extrapolated value.
[c]Derived primarily from data with $J \approx 9$.
[d]Derived primarily from data with $J \approx 13$.
[e]$f_J = (-1.30 \pm 0.15) \times 10^{-9}$.
[f]$\Gamma_J = (-6.7 \pm 3.1) \times 10^{-3}$ cm^{-1}.
[g]$f_J = (5.4 \pm 2.3) \times 10^{-10}$.
[h]$(1/q)_J = (7.7 \pm 2.2) \times 10^{-5}$.

most symmetric line shapes, the (14,0) band of $^{18}O_2$, is presented in Fig. 10, where the strength of the underlying continuum is evident. More interesting line shapes can be seen in Figs. 11–13, where, in order to emphasize the observed rotational structure, which is weak compared with the underlying continuum, we have shown the *difference cross section* that has been obtained by subtracting the slowly varying continuum contribution from the measured photoabsorption cross section. In particular, in Fig. 11 it is clear that the low-energy wings of the rotational lines are more prominent than the high-energy wings. The rotationally averaged effect of this asymmetry can be seen near the bandhead of the (10,0) band where the difference cross section is *negative* at energies higher than the bandhead. Precisely the opposite behavior is observed for the (18,0) band in Fig. 12, where the underlying difference cross section is negative at energies lower than the bandhead. Most spectacular of all is the (13,0) band of $^{18}O_2$, shown in Fig. 13, which appears to be a series of rotational window resonances. The entire difference cross section for this band is negative.

While asymmetric line shapes are commonplace in autoionization spectra, few examples have been observed in molecular photodissociation spectra. Until recently, the only reported examples occurred in the spectrum of H_2 [52,53], but other examples have since been observed in the $E\ ^3\Sigma_u^- \leftarrow X\ ^3\Sigma_g^-$, $D\ ^3\Sigma_u^+ \leftarrow X\ ^3\Sigma_g^-$, and $f\ ^1\Sigma_u^+ \leftarrow X\ ^3\Sigma_g^-$ bands of O_2 [24,25,33,46] and the photofragment-yield spectrum of Cs_2 [54]. The present observation of the (13,0) band of the $f'\ ^1\Sigma_u^+ \leftarrow X\ ^3\Sigma_g^-$ system of $^{18}O_2$ is a rare example of a window resonance in molecular photodissociation.

In order to put the foregoing discussion onto a quantitative basis, we have fitted the empirical $^1\Sigma^+ \leftarrow {}^3\Sigma^-$ band model described in Sec. III, based on asymmetric Fano predissociation line shapes, to the measured cross sections. Fitted cross sections are shown in Figs. 10–13, together with the measurements. Within the statistical uncertainties of the measured cross sections, the agreement is seen to be very good. Preliminary fits using a band model based on Lorentzian predissociation line shapes were incapable of reproducing the experimental measurements.

The ratio of the perpendicular and parallel transition moments is an important parameter controlling the rotational line strengths in a $^1\Sigma^+ \leftarrow {}^3\Sigma^-$ transition [36]. In particular, the perpendicular transition moment is solely responsible for the appearance of the ^QQ branches. As far as we can tell, no ^QQ lines occur in our measured spectra and preliminary fits to our measurements that allowed the transition moment ratio to vary consistently gave ratios near zero. Accordingly, we fixed the perpendicular transition moment to zero in performing the final fits. This result is consistent with an $f'\ ^1\Sigma_u^+ \leftarrow X\ ^3\Sigma_g^-$ transition that borrows strength from the $f\ ^1\Sigma_u^+ \leftarrow X\ ^3\Sigma_g^-$ transition through Rydberg-valence coupling. The spectrograms of Ogawa and Yamawaki [41] and Ogawa [48] show no evidence of ^QQ-branch lines in the vibrational bands of the $f\ ^1\Sigma_u^+ \leftarrow X\ ^3\Sigma_g^-$ system, implying a zero perpendicular transition moment for that system, which is known [46] to borrow its strength from the parallel transition $E\ ^3\Sigma_u^- \leftarrow X\ ^3\Sigma_g^-$ through spin-orbit coupling.

The upper-state spectroscopic constants, oscillator strengths, and line-shape parameters resulting from the empirical band-model fits to the measured cross sections are listed in Table V. The tabulated uncertainties include components due to uncertainty in the absolute wave-number calibration and a fitting uncertainty related to the statistical scatter in the data and the appropriateness of the empirical band model. Since its bandhead is overlapped by a stronger band at higher energy, parameters for the (15,0) band of $^{16}O_2$ were determined from an average of nine room-temperature cross-

section measurements encompassing more highly rotationally excited lines with $J'=11$–19. Consequently, the tabulated spectroscopic constants for the $v=15$ level of $^{16}O_2$ involve a certain degree of extrapolation and the oscillator strength and predissociation linewidth listed apply at $J\approx 13$. The parameters listed in Table V for the $v=5$ and 8 levels of $^{16}O_2$ are *perturbed* values determined from the rotational deperturbation analyses given in Sec. IV A.

The spectroscopic constants listed in Table V for the remaining vibrational levels are referred to the line *centers* rather than the peaks and have been used to determine the rotational-line assignments given in Figs. 10–13. The B values and, less obviously, the band origins exhibit irregular perturbations. The vibrational assignments of Table V were estimated by a trial-and-error procedure starting from the assignments of the $v=5$ and 8 levels of $^{16}O_2$ deduced in Sec. IV A from the rotational-perturbation data. Because of the remaining large perturbations in B and ν_0, the relative assignments cannot be regarded as completely definite. For some levels, the D values are significant, surprisingly in view of the restricted range of rotational levels observed in the 79 K cross sections. Indeed, for the $v=14$ level of $^{18}O_2$, D has a substantial *negative* value. Such behavior is consistent with a vibrational series subject to perturbation.

The observed effective oscillator strengths also vary in an irregular fashion over two orders of magnitude. For the (7,0) and (14,0) bands of $^{18}O_2$, it was necessary to include a J-dependent strength term f_J in the fitting procedure. Such a necessity can occur if the band under consideration gains strength primarily from a single, nearby vibrational band of the perturbing transition. The (7,0) band of $^{18}O_2$ is a particularly interesting case since we have observed significant rotational structure despite the fact that the level $f'\ ^1\Sigma_u^+(v=7)$ for $^{18}O_2$ lies between the $v=5$ and 8 levels for $^{16}O_2$, for which only fragmentary extra lines have been observed in association with rotational perturbations. This can be understood by noting that, for $^{18}O_2$, the level $f\ ^1\Sigma_u^+(v=5)$ lies only approximately 125 cm^{-1} higher than $f'\ ^1\Sigma_u^+(v=7)$. Therefore, the bandhead of the (7,0) $f'\leftarrow X$ band gains strength primarily from the (5,0) $f\leftarrow X$ band through the Rydberg-valence coupling $H_{ff'}$. However, since the rotational constant for $f\ ^1\Sigma_u^+(v=5)$ is approximately twice the value observed for $f'\ ^1\Sigma_u^+(v=7)$, the Rydberg and valence levels separate rapidly with increasing rotation, allowing less strength to be borrowed. This explains the negative value of f_J determined for the (7,0) $f'\leftarrow X$ band of $^{18}O_2$ and helps to explain the nonobservation of that band in room-temperature scans that favor higher rotational quantum numbers.

The observed predissociation linewidths vary from 1.4 to 5.1 cm^{-1} FWHM, the maximum occurring for the window-resonance (13,0) $f'\leftarrow X$ band of $^{18}O_2$. For the (10,0) band of $^{18}O_2$, it was necessary to include a J-dependent width Γ_J in the fitting procedure. In this case, the predissociation linewidths were observed to decrease with increasing rotation.

The fitted line shapes display a wide range of behaviors. At one extreme, the line shape for the (14,0) band of $^{18}O_2$ is indistinguishable from Lorentzian ($1/q\approx 0$); at the other extreme, the line shape for the (13,0) band of $^{18}O_2$, as we have already noted qualitatively, is a near-window resonance ($q\approx -0.04$). The other bands display varying degrees of asymmetry of either sign. The maximum asymmetry is reached for the (7,0), (10,0), and (18,0) bands of $^{18}O_2$, where $|q|$ is of the order of unity. For the (14,0) band of $^{18}O_2$, it was necessary to include a J-dependent line-shape parameter $(1/q)_J$ in the fitting procedure, implying that strict Lorentzian line shapes occur only near the bandhead for this band.

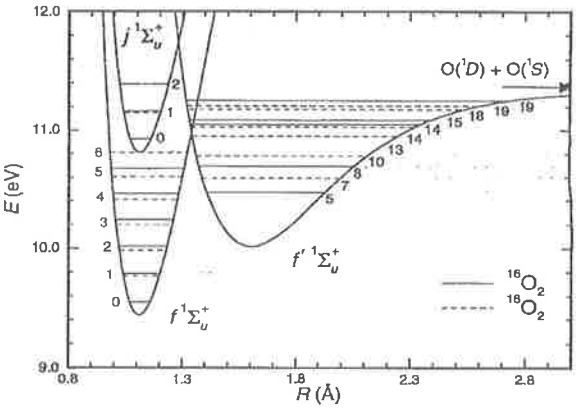

FIG. 14. Approximate diabatic potential-energy curves for the valence and Rydberg $^1\Sigma_u^+$ states of O_2. Known vibrational levels of the Rydberg states $3p\pi_u f\ ^1\Sigma_u^+$ and $4p\pi_u j\ ^1\Sigma_u^+$ are shown, together with the levels of the valence state $f'\ ^1\Sigma_u^+$ reported in this work.

The square of the Fano overlap parameter ξ^2 gives essentially the proportion of the underlying continuum with which the bound level interacts [see Eq. (2)]. The fitted values of ξ^2 vary from approximately 0 for the more Lorentzian lines to 0.26 for the window-resonance (13,0) band of $^{18}O_2$. The underlying continuum in the O_2 photoabsorption spectrum comprises contributions from allowed parallel transitions $^3\Sigma_u^-\leftarrow X\ ^3\Sigma_g^-$ and allowed perpendicular transitions $^3\Pi_u\leftarrow X\ ^3\Sigma_g^-$. In our proposed picture of the origin of the $f'\leftarrow X$ bands, described previously, the f' and f states interact through the electrostatic term $H_{ff'}$, while the $f\ ^1\Sigma_u^+$ and $E\ ^3\Sigma_u^-$ Rydberg states exhibit a spin-orbit interaction. According to the $\Delta\Omega=0$ selection rule for spin-orbit perturbations [45], only the $^3\Sigma_{0u}^-\leftarrow X\ ^3\Sigma_{0g}^-$ component of the parallel transition can donate strength to the discrete transition $f'\ ^1\Sigma_{0u}^+\leftarrow X\ ^3\Sigma_{0g}^-$. Therefore, the *maximum* proportion of the continuum available to interact, corresponding to the absence of a contribution from the $^3\Pi_u\leftarrow X\ ^3\Sigma_g^-$ transition, is $\xi^2=1/3$. This value is approached by the $\xi^2=0.26$ observed for the (13,0) $f'\ ^1\Sigma_u^+\leftarrow X\ ^3\Sigma_g^-$ band of $^{18}O_2$ that occurs near the peak of a broad resonance which appears to be part of the vibrational Rydberg series $E\ ^3\Sigma_u^-\leftarrow X\ ^3\Sigma_g^-$.

V. DISCUSSION

In Fig. 14 we present approximate diabatic potential-energy curves for the $^1\Sigma_u^+$ valence and Rydberg states of O_2 relevant to this study. Known vibrational levels of the Rydberg states $3p\pi_u f\ ^1\Sigma_u^+$ and $4p\pi_u j\ ^1\Sigma_u^+$ are shown

[8,55], as are levels of the valence state $f'\ ^1\Sigma_u^+$ measured in this work. The composite f' potential-energy curve comprises an anharmonic potential constructed to be consistent with the rotational perturbation data of Sec. IV A, together with a Morse extension above $v \approx 11$, which provides rough agreement with the perturbed band origins and rotational constants of Sec. IV B. However, because of the strong valence-Rydberg interaction and the need to apply a full CSE theoretical treatment in order to determine accurate potentials and interaction matrix elements for such strongly coupled states, the eigenvalues of our approximate potential-energy curves do not coincide exactly with the actual perturbed energies. Nevertheless, Fig. 14 provides a convenient summary of our results and aids in understanding the physical processes behind our observations. Our f' potential-energy curve is in good agreement with that recently calculated *ab initio* by Guberman and Giusti-Suzor [9] and shown in Fig. 1.

The large difference between the R_e values of approximately 1.1 Å for the Rydberg and approximately 1.6 Å for the valence potentials reflects the disparity in the corresponding observed rotational constants. The B values for the Rydberg levels are greater than the ground-state B value, while the B values for the valence levels reported here are considerably smaller, resulting in Rydberg bands $np\pi_u\ ^1\Sigma_u^+ \leftarrow X\ ^3\Sigma_g^-$ that are shaded to the blue and valence bands $f'\ ^1\Sigma_u^+ \leftarrow X\ ^3\Sigma_g^-$ that are shaded to the red.

In Fig. 14 it can be seen that the $v=4$ and 5 levels of the f state for $^{16}O_2$ lie slightly lower than the $v=5$ and 8 levels of the f' state, respectively. The greater rotational constants for the Rydberg levels ensure that the diabatic Rydberg and valence rotational term series will cross, resulting in rotational perturbations due to the Rydberg-valence interaction $H_{ff'}$ and the presence of extra lines from transitions into the valence levels. The outer-Rydberg and inner-valence turning points lie closer together for $f(v=5)$ and $f'(v=8)$ than for $f(v=4)$ and $f'(v=5)$, resulting in a much larger vibrational overlap and interaction matrix element $H_{ff'}$. Our measured values for $H_{ff'}$ and vibrational overlaps calculated using the potential-energy curves of Fig. 14 support an electrostatic Rydberg-valence interaction $H^e \approx 1500-2000\ \text{cm}^{-1}$ at $R=1.340$ Å, the crossing point of the diabatic f and f' potentials, but this is an indicative range of values only. The *ab initio* calculations of Guberman and Giusti-Suzor [9] imply an interaction of $H^e \approx 2000\ \text{cm}^{-1}$ at the crossing point.

The uncertainty in the absolute vibrational numbering for the lower levels of the f' state, estimated solely from the isotopic energy-level data of Sec. IV A, is approximately one unit. However, a consideration of the interaction matrix elements allows this uncertainty to be eliminated since the ratio of the $H_{ff'}$ values for the $f(v=5)-f'(v=8)$ and $f(v=4)-f'(v=5)$ interactions is very sensitive to the local slope of the f' potential-energy curve. The ratio of the vibrational overlaps for these levels, calculated using the potentials of Fig. 14, reproduces the measured $H_{ff'}$ ratio. A vibrational renumbering by one unit, and the corresponding reconstruction of the $f'\ ^1\Sigma_u^+$ state potential-energy curve, fails to reproduce the measured ratio. Thus the vibrational assignments estimated in Sec. IV A are confirmed. As we have already mentioned in Sec. IV B, however, the vibrational assignments for the significantly perturbed, more closely spaced levels with $v \geq 13$ are not as definite. Because of the strong mixing of the Rydberg and valence levels near the crossing point of the corresponding potential-energy curves, even the electronic assignments of the levels become uncertain in this energy region, particularly for the $f'(v=14)$ level of $^{18}O_2$, which is likely to be heavily mixed with $f(v=7)$. Nevertheless, all of the observed bands are $^1\Sigma_u^+ \leftarrow {}^3\Sigma_g^-$ transitions where the upper state has a considerable $f'\ ^1\Sigma_u^+$ valence character, as evidenced by the low measured rotational constants.

We have suggested previously in Sec. IV A 5 that the $v=1$ level of the $4p\pi_u j\ ^1\Sigma_u^+$ state for $^{16}O_2$ is rotationally perturbed by a high-lying level of the $f'\ ^1\Sigma_u^+$ valence state. From Fig. 14 it can be deduced that the $v=17$ level of $^{16}O_2$ (not shown) is likely to be the perturbing level. We have observed previously that the Rydberg-valence interaction is much smaller for the $4p\pi_u j\ ^1\Sigma_u^+(v=1) - f'\ ^1\Sigma_u^+(v=17)$ perturbation, where $H_{ff'} \approx 1.3\ \text{cm}^{-1}$, than for the $3p\pi_u f\ ^1\Sigma_u^+(v=4) - f'\ ^1\Sigma_u^+(v=5)$ perturbation, where $H_{ff'} \approx 5.3\ \text{cm}^{-1}$. The difference can be explained partially by a smaller vibrational overlap in the former case and also by noting that, according to quantum-defect theory [45], the electronic part H^e of the Rydberg-valence interaction is expected to fall off as $(n^*)^{-3/2}$. For the $3p\pi_u$ and $4p\pi_u$ Rydberg states of $^1\Sigma_u^+$ symmetry, it follows from the observed energy levels [8] that $n^*=2.28$ and 3.31, respectively, implying that the $n=4$ electronic interaction matrix element should be only 57% of the $n=3$ value, provided that we ignore the R dependence of H^e.

The other low-lying levels of the f' valence state that we have observed (the $v=7$ and 10 levels of $^{18}O_2$) lie slightly *below* the f Rydberg state levels $v=5$ and 6 of $^{18}O_2$, explaining why no rotational perturbations are evident in the latter levels. The proximity of the Rydberg to the valence level, however, is sufficient to enable the (7,0) and (10,0) bands of the $f' \leftarrow X$ system to gain enough strength to be observed. All other observed valence levels lie near or above the crossing point of the f' and f potential-energy curves and do not require the presence of a nearby level of the f state for the corresponding band to be observed.

In Fig. 15 we have combined the isotopic $f' \leftarrow X$ band origin data from Table V into an effective ΔG_v curve plotted as a function of the mass-reduced vibrational quantum number $\rho(v+1/2)$ [56,57]. The irregular perturbations in the measured vibrational term differences can be seen clearly in comparison with the smooth behavior of the unperturbed term differences calculated using the f' potential-energy curve of Fig. 14. The maximum vibrational perturbation occurs near the crossing point of the f' and f potentials where $\rho(v+1/2) \approx 12.8$.

In Fig. 16 we present isotopically reduced rotational constants B_v/ρ^2 [56] for the f' state as a function of the mass-reduced vibration. Once again, the rotational constants show significant irregular perturbation when compared with a smooth curve calculated using the f' potential-energy curve of Fig. 14. The measured rotational constants are all larger than the unperturbed values since the perturbations caused

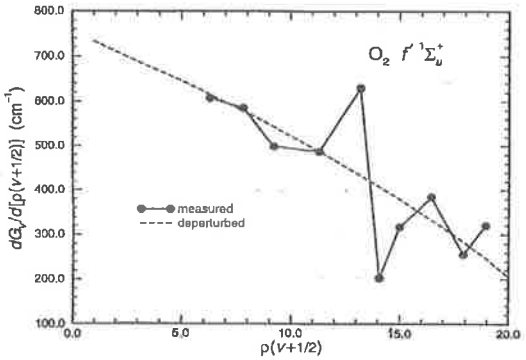

FIG. 15. Measured isotopically combined vibrational differences for the $f'\,^1\Sigma_u^+$ state of O_2, compared with estimated deperturbed values.

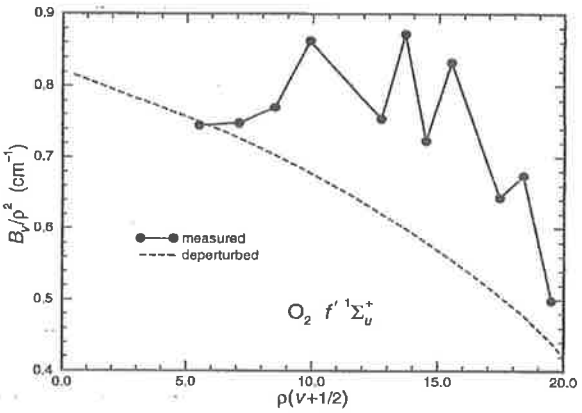

FIG. 16. Measured isotopically combined rotational constants for the $f'\,^1\Sigma_u^+$ state of O_2, compared with estimated deperturbed values.

by the Rydberg states result in the valence-state wave functions borrowing some of the characteristics of the perturbing states.

The predissociation linewidths, effective oscillator strengths, and line-shape parameters for the $f' \leftarrow X$ bands also exhibit irregular perturbations that show maximum effects near the crossing point of the f' and f potentials. In particular, the Fano line-shape parameter q changes sign near the crossing point. Kim and Yoshihara [54] have also recently observed q reversal in the photofragment-yield spectrum of Cs_2.

In this section we have collected together all of our observations of the $f'\,^1\Sigma_u^+$ valence state and have attempted to explain them coherently in general terms. It is clear from the discussion that significant interactions occur between the $f'\,^1\Sigma_u^+$ valence state and the $np\pi_u\,^1\Sigma_u^+$ Rydberg states. In addition, it is necessary to consider several other electronic states in order to explain the strength, predissociation, and asymmetry of the observed bands. An accurate treatment of the problem requires more than the normal techniques of perturbation theory. Therefore, in an associated work [58], we provide a CSE interpretation of the $f'\,^1\Sigma_u^+ \leftarrow X\,^3\Sigma_g^-$ system that puts our previous descriptive framework onto a more quantitative basis. Also, the semiempirical information resulting from the CSE treatment is compared with an *ab initio* treatment of the $f'\,^1\Sigma_u^+$ state.

VI. CONCLUSIONS

The lowest valence state of O_2 with $^1\Sigma_u^+$ symmetry, $f'\,^1\Sigma_u^+$, has been observed experimentally. Using a high-resolution monochromator-based system with excellent signal-to-noise performance, we have found a total of nine bands from the system $f'\,^1\Sigma_u^+ \leftarrow X\,^3\Sigma_g^-$ in the photoabsorption spectra of the isotopic molecules $^{16}O_2$ and $^{18}O_2$. The bands are found to be predissociating resonances that exhibit Beutler-Fano line shapes, rarely observed in molecular photodissociation. The observed line-shape asymmetries vary widely, an example of a window resonance in dissociation occurring for the (13,0) band of $^{18}O_2$. Irregular perturbations observed in the spectroscopic constants of the $f'\,^1\Sigma_u^+$ state are attributed to strong electrostatic interactions with the $np\pi_u\,^1\Sigma_u^+$ Rydberg states.

Using a combination of monochromator-based and very narrow-bandwidth laser-based measurements of the $f\,^1\Sigma_u^+ \leftarrow X\,^3\Sigma_g^-$ Rydberg transitions of isotopic O_2, we have found rotational perturbations in the $v=4$ level of $^{16}O^{18}O$ and the $v=5$ level of $^{16}O_2$ and have observed extra lines associated with the rotational perturbations in the $v=4$ and 5 levels of $^{16}O_2$. These observations have enabled us to show that the valence state $f'\,^1\Sigma_u^+$ reported here is responsible for the rotational perturbation of the Rydberg states $3p\pi_u f\,^1\Sigma_u^+$ and $4p\pi_u j\,^1\Sigma_u^+$ through the same electrostatic valence-Rydberg interactions responsible for the vibrational perturbations observed in the f' state.

The weakness of the bands of the $f' \leftarrow X$ system of O_2 precludes any significant influence on the transmission of solar vuv radiation through the terrestrial atmosphere. However, the agreement between our results and the recent *ab initio* calculations by Guberman and Giusti-Suzor [9] of the $f'\,^1\Sigma_u^+$ valence potential-energy curve and Rydberg-valence coupling supports their view of the importance of the $f'\,^1\Sigma_u^+$ valence state as a channel for the production of ionospheric $O(^1S)$ during the dissociative recombination of O_2^+ with electrons in the atmosphere.

ACKNOWLEDGMENTS

The authors thank Dr. S. L. Guberman for supplying unpublished calculations of the strength of the Rydberg-valence interaction for the $^1\Sigma_u^+$ states of O_2 and a tabulated *ab initio* potential-energy curve for the $f'\,^1\Sigma_u^+$ state. We are also grateful to Professors H. Lefebvre-Brion and J. H. Carver for critical readings of the manuscript and Professor M. L. Ginter for his assistance, comments, and suggestions made during visits to ANU sponsored by the National Science Foundation (U.S.) through a U.S.–Australian Cooperative Research Grant. Valuable technical assistance was provided by K. J. Lonsdale and C. J. Dedman.

[1] In this work, all energies (in eV) are referred to the minimum of the $X\,^3\Sigma_g^-$ potential-energy curve, while all term values (in cm^{-1}) are referred to the virtual level $X\,^3\Sigma_g^-(v=0, J=0, F_2)$.
[2] F. R. Gilmore, J. Quant. Spectrosc. Radiat. Transfer **5**, 369 (1965).
[3] H. F. Schaefer and F. E. Harris, J. Chem. Phys. **48**, 4946 (1968).
[4] B. J. Moss and W. A. Goddard III, J. Chem. Phys. **63**, 3523 (1975).
[5] N. H. F. Beebe, E. W. Thulstrup, and A. Andersen, J. Chem. Phys. **64**, 2080 (1976).
[6] R. P. Saxon and B. Liu, J. Chem. Phys. **67**, 5432 (1977).
[7] H. H. Michels, Adv. Chem. Phys. **45**, 225 (1981).
[8] D. H. Katayama, S. Ogawa, M. Ogawa, and Y. Tanaka, J. Chem. Phys. **67**, 2132 (1977).
[9] S. L. Guberman and A. Giusti-Suzor, J. Chem. Phys. **95**, 2602 (1991).
[10] J. Kaplan, Phys. Rev. **38**, 1048 (1931).
[11] M. Nicolet, Phys. Rev. **93**, 633 (1954).
[12] S. L. Guberman, Int. J. Quantum Chem. **13**, 531 (1979).
[13] S. L. Guberman, in *Physics of Ion-Ion and Electron-Ion Collisions*, edited by F. Brouillard (Plenum, New York, 1983), pp. 167–200.
[14] S. L. Guberman, Nature **327**, 408 (1987).
[15] S. L. Guberman, Planet. Space Sci. **36**, 47 (1988).
[16] S. L. Guberman, in *Dissociative Recombination: Theory, Experiment, and Applications*, edited by J. B. A. Mitchell and S. L. Guberman (World Scientific, Singapore, 1989), p. 151.
[17] V. J. Abreu, S. C. Solomon, W. E. Sharp, and P. B. Hays, J. Geophys. Res. **88**, 4140 (1983).
[18] J.-H. Yee and T. L. Killeen, Planet. Space Sci. **36**, 47 (1988).
[19] J.-H. Yee, V. J. Abreu, and W. B. Colwell, in *Dissociative Recombination: Theory, Experiment, and Applications*, Ref. [16], p. 286.
[20] S. L. Guberman (private communication).
[21] R. J. Buenker and S. D. Peyerimhoff, Chem. Phys. Lett. **34**, 225 (1975).
[22] J. Wang, D. G. McCoy, A. J. Blake, and L. Torop, J. Quant. Spectrosc. Radiat. Transfer **38**, 19 (1987).
[23] J. Wang, A. J. Blake, D. G. McCoy, and L. Torop, J. Quant. Spectrosc. Radiat. Transfer **40**, 501 (1988).
[24] B. R. Lewis, S. T. Gibson, M. Emami, and J. H. Carver, J. Quant. Spectrosc. Radiat. Transfer **40**, 1 (1988).
[25] B. R. Lewis, S. T. Gibson, M. Emami, and J. H. Carver, J. Quant. Spectrosc. Radiat. Transfer **40**, 469 (1988).
[26] J. Berkowitz, *Photoabsorption, Photoionization, and Photoelectron Spectroscopy* (Academic, New York, 1979), p. 413.
[27] B. R. Lewis, Appl. Opt. **22**, 1546 (1983).
[28] S. G. Tilford and J. D. Simmons, J. Phys. Chem. Ref. Data **1**, 147 (1972).
[29] C. R. Vidal, Adv. At. Mol. Phys. **23**, 1 (1988).
[30] R. Hilbig and R. Wallenstein, IEEE J. Quantum Electron. **QE-19**, 194 (1983).
[31] K. Miyazaki, H. Sakai, and T. Sato, Appl. Opt. **28**, 699 (1989).
[32] K. G. H. Baldwin, S. T. Gibson, B. R. Lewis, J. H. Carver, and T. J. McIlrath, *Proceedings on Short Wavelength Coherent Radiation*, edited by P. H. Bucksbaum and N. M. Ceglio (Optical Society of America, Washington, D.C., 1991), Vol. 11, p. 12.
[33] B. R. Lewis and S. T. Gibson, Can. J. Phys. **68**, 231 (1990).
[34] L. Veseth and A. Lofthus, Mol. Phys. **27**, 511 (1974).
[35] W. Steinbach and W. Gordy, Phys. Rev. A **8**, 1753 (1973).
[36] J. K. G. Watson, Can. J. Phys. **46**, 1637 (1968).
[37] U. Fano and J. W. Cooper, Rev. Mod. Phys. **40**, 441 (1968).
[38] We use the symbol ξ, rather than the normal ρ, to denote the Fano overlap parameter in order to avoid confusion with the isotopic parameter $\rho_i = \sqrt{\mu/\mu_i}$.
[39] The Watson [36] rotational line strengths and the constant-parameter assumption are expected to apply accurately only in the case of a relatively distant perturber. Allowing the parameters to vary with rotation according to Eq. (3) provides some generalization to the case of a closer perturber.
[40] Throughout this work, we follow Herzberg [44] in using the term "rotational perturbation" to describe irregularities in rotational term series. This should not be taken to indicate that the perturbation matrix element is J dependent.
[41] M. Ogawa and K. R. Yamawaki, Can. J. Phys. **47**, 1805 (1969).
[42] The subscript x in a rotational-branch notation denotes an extra line that arises from a transition to the electronic state that perturbs the f state.
[43] In the case of a homonuclear molecule with nuclear spin $I=0$, such as $^{16}O_2$, the even-J levels of a $^1\Sigma_u^+$ state have zero statistical weight [44]. Thus only odd-J levels are observable.
[44] G. Herzberg, *Molecular Spectra and Molecular Structure I. Spectra of Diatomic Molecules* (Van Nostrand, New York, 1950), pp. 133–145 and 282–283.
[45] H. Lefebvre-Brion and R. W. Field, *Perturbations in the Spectra of Diatomic Molecules* (Academic, Orlando, 1986), pp. 39, 166–168, 196, 247–254, and 387–411.
[46] B. R. Lewis, S. S. Banerjee, and S. T. Gibson, J. Chem. Phys. **102**, 6631 (1995).
[47] Strictly speaking, since the approximately 1.7 Å internuclear distance has been deduced from the rotational constant for the $v \approx 5$ (see later) level of the $f'\,^1\Sigma_u^+$ state, the corresponding *equilibrium* distance will be somewhat smaller.
[48] M. Ogawa, Can. J. Phys. **53**, 2703 (1975).
[49] W. Steinbach and W. Gordy, Phys. Rev. A **11**, 729 (1975).
[50] M. Ogawa, K. R. Yamawaki, A. Hashizume, and Y. Tanaka, J. Mol. Spectrosc. **55**, 425 (1975).
[51] Y. Tanaka, J. Chem. Phys. **20**, 1728 (1952).
[52] G. Herzberg, in *Topics in Modern Physics—A Tribute to E. U. Condon*, edited by W. E. Brittin and H. Odabasi (Colorado Association University Press, Boulder, Colorado, 1971), p. 191.
[53] M. Glass-Maujean, J. Breton, and P. M. Guyon, Chem. Phys. Lett. **63**, 591 (1979).
[54] B. Kim and K. Yoshihara, J. Chem. Phys. **99**, 1433 (1993).
[55] A weak, diffuse feature that we have observed in the spectrum of $^{18}O_2$ near 86 412 cm^{-1} appears to be the (6,0) band of the $f \leftarrow X$ system.
[56] W. C. Stwalley, J. Chem. Phys. **63**, 3062 (1975).
[57] Although the *perturbed* parameters presented in Figs. 15 and 16 are *not* expected to lie on a single curve, this remains a convenient method of presenting a limited amount of isotopic data.
[58] B. R. Lewis, S. T. Gibson, J. P. England, and S. L. Guberman (unpublished).

4.21 Assignment of the $^3\Pi_u - X^3\Sigma_g^-$ bands of O_2 observed in the region 1040–1200 Å

[41] J. P. England, B. R. Lewis, S. T. Gibson, and M. L. Ginter,
Journal of Chemical Physics **104**, 2765–2772 (1996).

Assignment of the $^3\Pi_u \leftarrow X\ ^3\Sigma_g^-$ bands of O_2 observed in the region 1040–1200 Å

J. P. England, B. R. Lewis, and S. T. Gibson
Research School of Physical Sciences and Engineering, The Australian National University, Canberra, ACT 0200, Australia

M. L. Ginter
Institute for Physical Science and Technology, University of Maryland, College Park, Maryland 20742

(Received 24 August 1995; accepted 9 November 1995)

A comprehensive vibronic assignment of the $^3\Pi_u$ states in the energy region approaching the first ionization threshold of O_2 is presented for the first time. Measurements of seventeen $^3\Pi_u \leftarrow X\ ^3\Sigma_g^-$ bands in the 85 800–93 000 cm^{-1} region of the ground-state photoabsorption spectra of $^{16}O_2$ and $^{18}O_2$ at 79 K are reported, including six bands in the spectrum of $^{18}O_2$ for the first time. Irregularities in vibrational spacings and in the extent of broadening by predissociation are shown to result from Rydberg-valence interactions. The observed transitions have been assigned, using semiempirical modeling of the $^3\Pi_u$ Rydberg-valence interactions based on the coupled-channel Schrödinger equations technique, to two vibrational progressions with upper states which we call $F\ ^3\Pi_u$ and $F'\ ^3\Pi_u$. The F and F' states are formed from the avoided crossings of the $np\sigma_u$ ($n=3$–5) Rydberg potential-energy curves by the lowest repulsive $^3\Pi_u$ valence potential-energy curve. © *1996 American Institute of Physics.* [S0021-9606(96)01607-8]

I. INTRODUCTION

The O_2 ground-state photoabsorption spectrum in the vacuum ultraviolet (VUV) region at energies below the first ionization threshold (12.07 eV)[1] has been the subject of much investigation,[2] largely because of its importance in atmospheric photochemistry.[3] In spite of these efforts, very few vibrational progressions have been convincingly assigned in the region 9.5–12.0 eV. In particular, only a small fraction of the expected Rydberg-state progressions converging on the ionic ground state have been identified.

The O_2 ground $X\ ^3\Sigma_g^-$ state and the metastable $a\ ^1\Delta_g$ and $b\ ^1\Sigma_g^+$ states are associated with the molecular-orbital configuration $(1\sigma_g)^2(1\sigma_u)^2(2\sigma_g)^2(2\sigma_u)^2(3\sigma_g)^2(1\pi_u)^4(1\pi_g)^2$. The lowest-energy Rydberg states are those built on the $(1\sigma_g)^2(1\sigma_u)^2(2\sigma_g)^2(2\sigma_u)^2(3\sigma_g)^2(1\pi_u)^4(1\pi_g)^1$ $X\ ^2\Pi_g$ ground state of O_2^+. The addition of an s or d Rydberg orbital to this ground-state ion core gives rise to *gerade* states which cannot be observed in single-photon absorption from the X, a, or b states. However, these *gerade* Rydberg states have been studied using two-photon absorption spectroscopy,[4,5] electron energy-loss spectroscopy[6] and translational spectroscopy,[7] and are now reasonably well understood. In contrast, the *ungerade* Rydberg states: $^1\Pi_u$ and $^3\Pi_u$ from the configurations $(1\sigma_g)^2(1\sigma_u)^2(2\sigma_g)^2(2\sigma_u)^2(3\sigma_g)^2(1\pi_u)^4(1\pi_g)^1np\sigma_u$; and $^1\Sigma_u^\pm$, $^3\Sigma_u^\pm$, $^1\Delta_u$, and $^3\Delta_u$ from the configurations $(1\sigma_g)^2(1\sigma_u)^2(2\sigma_g)^2(2\sigma_u)^2(3\sigma_g)^2(1\pi_u)^4(1\pi_g)^1np\pi_u$ ($n=3,4,5,\ldots$), are poorly understood. The only regular *ungerade* Rydberg progressions which have been definitively identified in ground- and metastable-state absorption spectra involve the lower vibrational levels of the $3p\pi_u\ f\ ^1\Sigma_u^+$, $4p\pi_u\ j\ ^1\Sigma_u^+$ and $3p\pi_u\ D\ ^3\Sigma_u^+$ states.[8,9]

Dipole-allowed transitions to $^3\Sigma_u^-$ and $^3\Pi_u$ states from the ground state are expected to give the strongest features in the absorption spectrum of O_2. Although ample experimental data on such states exists, many of the observed spectral features have not been definitively identified, probably because of the complications introduced by large interactions between Rydberg and valence states of the same symmetry. Currently, there is agreement among many theoretical[10–14] and experimental[15,16] workers that the three strong bands known as Tanaka's longest, second and third bands[17] (1244, 1206 and 1173 Å) result from transitions to the first three vibrational levels of the mixed Rydberg-valence $E\ ^3\Sigma_u^-$ state. The E state can be associated with the upper potential-energy well formed by the avoided crossing of the lowest valence and $3p\pi_u$ Rydberg potential-energy curves, while the lower potential-energy curve, labeled $B\ ^3\Sigma_u^-$, is the upper state of the Schumann–Runge system. Higher-energy states of this symmetry have not yet been definitely identified.

Less is known about the $^3\Pi_u$ states in this energy region. *Ab initio* calculations by Buenker and Peyerimhoff[18] gave an interaction matrix element of 1.06 eV, at an internuclear distance $R=2.38a_0$, between the $3p\sigma_u\ ^3\Pi_u$ Rydberg and valence $(1\sigma_g)^2(1\sigma_u)^2(2\sigma_g)^2(2\sigma_u)^2(3\sigma_g)^2(1\pi_u)^4(1\pi_g)^1(3\sigma_u)^1\ 1\ ^3\Pi_u$ states, which is about twice that calculated for the corresponding states of $^3\Sigma_u^-$ symmetry.[18] The diabatic potential-energy curve of the valence state crosses the Rydberg curve at an internuclear distance slightly larger than the equilibrium value for the Rydberg diabatic curve.[18] The lower adiabatic $^3\Pi_u$ potential curve formed by this avoided crossing has a plateau or weak minimum[18] for $2.0a_0<R<2.2a_0$ and transitions to this region of the potential give a significant contribution to the O_2 absorption cross section in the region of the Schumann–Runge continuum near 1356 Å.[19–21] At higher energies, the upper adiabatic

 0021-9606/96/104(8)/2765/8/$10.00

potential produced by the avoided crossing gives rise to a bound state. Buenker *et al.*[11] have made tentative assignments of peaks observed in electron energy loss spectra[22] based on their *ab initio* calculations of the potential-energy curve of this bound state.[18] However, their assignments are inconsistent with those based on optical measurements. Chang[23] and Chang and Ogawa[24] have identified $^3\Pi_u \leftarrow X\ ^3\Sigma_g^-$ bands at 1163 Å (86 000 cm^{-1}), 1137 Å (88 000 cm^{-1}), 1122 Å (89 200 cm^{-1}), and 1089 Å (91 800 cm^{-1}) by rotational analysis, and more recent work by Ito *et al.*[25] has led to the identification of two additional bands at 1065 Å (93 900 cm^{-1}) and 1049 Å (95 400 cm^{-1}). In addition, there has been some confusion about the identification of a band at 1153 Å (86 700 cm^{-1}),[23,26] presumably because its triplet structure is perturbed, but recent work[27] has led to a definitive assignment of this band as another $^3\Pi_u \leftarrow X\ ^3\Sigma_g^-$ transition. The anomalously small upper-state rotational constant of the 1163 Å band led Chang and Ogawa[24] to suggest that the upper state of the band is a mixed Rydberg-valence state, later called $F\ ^3\Pi_u$ by Huber and Herzberg,[28] but there have been no convincing electronic and vibrational assignments for the upper states of the other observed bands.

The aim of this study is a comprehensive vibronic analysis and assignment of all $^3\Pi_u \leftarrow X\ ^3\Sigma_g^-$ bands observed below the first ionization threshold. To this end, we present new absorption measurements of seventeen $^3\Pi_u \leftarrow X\ ^3\Sigma_g^-$ bands in the region 1075–1165 Å (85 800–93 000 cm^{-1}), eight for $^{16}O_2$ and nine for $^{18}O_2$. Vibronic assignments for all of these bands, and the two bands observed by Ito *et al.*,[25] are made by means of semiempirical calculations, based on the coupled-channel Schrödinger equations technique, which take account of the coupling between the $1\ ^3\Pi_u$ valence state and the $np\sigma_u\ ^3\Pi_u$ (n=3–7) Rydberg states. The use of a diabatic basis set for the calculations leads to the determination of deperturbed Rydberg potential-energy curves, associated quantum defects and Rydberg-valence couplings.

II. EXPERIMENTS

A. Methods

Two different methods of generating tunable VUV radiation have been used in this study. The first, described in detail elsewhere,[29] uses an argon dimer continuum discharge lamp with a 2.2 m scanning monochromator to give radiation with a bandwidth of ~0.030 Å (2.5 cm^{-1}) full width at half maximum (FWHM). The monochromator wavelength was calibrated using known emission lines[30] of Kr I, N I and II, O I and C I, and absorption lines from the $A\ ^1\Pi \leftarrow X\ ^1\Sigma^+$, $B\ ^1\Sigma^+ \leftarrow X\ ^1\Sigma^+$ and $C\ ^1\Sigma^+ \leftarrow X\ ^1\Sigma^+$ bands of CO,[31] and the $B\ ^1\Sigma_u^+ \leftarrow X\ ^1\Sigma_g^+$ Lyman bands of H_2,[32] and is expected to be accurate to within ~0.01 Å (0.8 cm^{-1}).

In the second method, also described in detail elsewhere,[27] tunable VUV radiation in the range 1118–1167 Å was produced by third harmonic generation[33] using radiation from an excimer-pumped dye laser focussed into a cell containing Kr or Xe at pressures in the range 5–100 Torr. A 0.2 m monochromator was used to remove the fundamental radiation. The VUV bandwidth, estimated from measurements of Xe and H_2 (0,0) Lyman-band absorption lines near 1130 Å, was found to be ~0.006 Å (0.5 cm^{-1}) FWHM. The wavelengths of the O_2 absorption measurements were calibrated to within ~0.003 Å (0.25 cm^{-1}) using measurements of CO absorption lines[31] and lines of the (1,0) band of the O_2 $j^1\Sigma_u^+ \leftarrow X\ ^3\Sigma_g^-$ system[34] near 1120 Å.

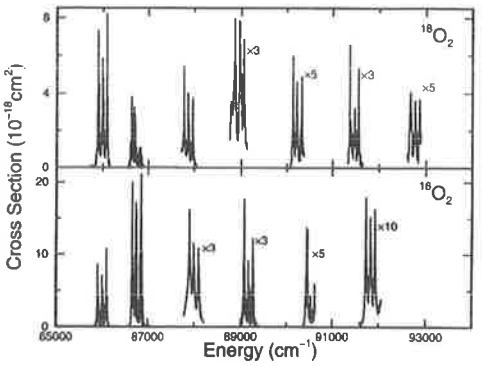

FIG. 1. The measured photoabsorption cross section (T=79 K) in the regions of thirteen $^3\Pi_u \leftarrow X\ ^3\Sigma_g^-$ bands of O_2. All measurements were taken using the monochromator apparatus except the four lowest-energy bands for $^{16}O_2$. The outer sub-bands of the $^{16}O_2$ band near 90 500 cm^{-1} are overlapped by stronger features due to another transition.

The O_2 absorption cell for each apparatus had LiF windows and gave an absorption path length of 10.9 cm. The cells were cooled by filling sleeves with liquid N_2, resulting in an effective gas temperature of 79±0.5 K. The use of low temperatures enabled clearer identification of the measured bands because of a reduction in the associated rotational structure. Samples of oxygen (BOC 99.9%, containing 99.8 atom% ^{16}O, or ICON, containing 99.5 atom% ^{18}O, 0.2 atom% ^{17}O and 0.3 atom% ^{16}O) were used at pressures between 0.1 and 10 Torr. The incident and transmitted radiation was detected photoelectrically using solar-blind photomultipliers equipped with LiF windows. Absolute cell transmittances were obtained by normalizing the measurements using the empty-cell values.

For both experimental systems, photoabsorption cross sections were determined from the measured cell transmittances using the Beer–Lambert law. However, the rotational linewidths of a number of the bands are less than the bandwidth of the monochromator-based apparatus and the cross section in these cases is pressure dependent and may be subject to some errors. This is not the case for measurements taken with the laser-based apparatus which yield absolute cross sections. Despite the limited resolution, the monochromator results are still useful in band identification.

B. Results

Figure 1 shows the measured photoabsorption cross section for thirteen of the $^3\Pi_u \leftarrow X\ ^3\Sigma_g^-$ bands identified in this work. Four weaker $^3\Pi_u \leftarrow X\ ^3\Sigma_g^-$ bands are shown in Fig. 2. The bands in the $^{18}O_2$ spectrum at energies >88 500 cm^{-1} and the $^{16}O_2$ band at 92 700 cm^{-1} have not been reported

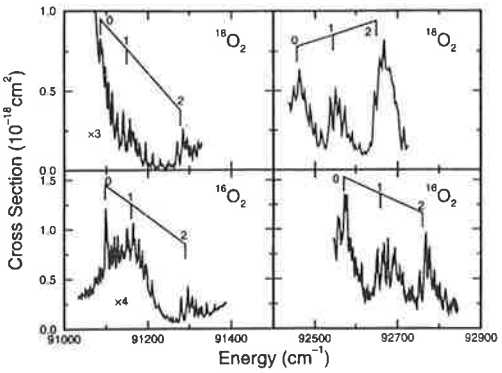

FIG. 2. The measured photoabsorption cross section ($T=79$ K) in the regions of four weak $^3\Pi_u \leftarrow X\ ^3\Sigma_g^-$ bands of O_2. The upper-state Ω values are shown for each $^3\Pi_{\Omega u} \leftarrow X\ ^3\Sigma_g^-$ sub-band origin. All measurements were taken using the monochromator apparatus. The bands at 91 200 cm^{-1} coincide with broad features due to another transition. The bands near 92 600 cm^{-1} are complicated on the left by sharp lines due to transitions to another state and on the right for $^{18}O_2$ by the lowest-energy sub-band of the band near 92 700 cm^{-1}, shown in Fig. 1.

previously. In addition, Chang's assignments[23] of the bands near 86800, 90500 and 91200 cm^{-1} in the $^{16}O_2$ spectrum appear incorrect in the light of the present work (see Sec. III C).

It is plausible that all of the bands shown in Fig. 1 are part of a vibrational progression. Most of the bands form a series having roughly constant spacings (~1200 cm^{-1}) which are less than those of the $X\ ^2\Pi_g$ ground state of O_2^+ (~1800 cm^{-1}), but the lowest two bands have an anomalously small separation of 753 cm^{-1} ($^{16}O_2$) and 730 cm^{-1} ($^{18}O_2$). All except two of the bands in Figs. 1 and 2 show triplet structure characteristic of a $^3\Pi_u \leftarrow X\ ^3\Sigma_g^-$ transition with the upper state close to Hund's case (a). The total splitting of ~190 cm^{-1} is close to the spin-splitting of the ground state of O_2^+.[28] The sub-bands from transitions to the $^3\Pi_{1u}$ components are not always centrally located because of spin–orbit coupling with nearby levels of the $^1\Pi_{1u}$ state of the same configuration, as previously demonstrated for the $^{16}O_2$ band near 86800 cm^{-1}.[27] The 90 500 cm^{-1} band of $^{16}O_2$ does not resemble the other bands because it coincides with stronger features from other transitions (possibly the $4f$ complex[23]), but its central $^3\Pi_{1u} \leftarrow X\ ^3\Sigma_g^-$ sub-band is isolated and of comparable intensity to the corresponding band of $^{18}O_2$. The $^{18}O_2$ band near 86 700 cm^{-1} has very narrow rotational lines and the measured cross section is pressure dependent, giving different apparent intensities for each of the different sub-bands.

Some of the bands in Fig. 1 show significant broadening by predissociation, the linewidths varying in an irregular fashion up to a maximum of ~10 cm^{-1} FWHM. Measured predissociation linewidths, extrapolated to zero rotation, are given in Table I for the four $^{16}O_2$ bands examined using the laser-based apparatus. It has not been possible to obtain precise values for the other bands because of either insufficient instrumental resolution or excessive overlap of other transitions. However, the results in Table I and qualitative results for the other bands in Fig. 1 show that the narrowest-linewidth bands ($\lesssim$2 cm^{-1} FWHM) occur near 86 700 cm^{-1} for $^{16}O_2$ and near 86 700 and 91 500 cm^{-1} for $^{18}O_2$, while the broadest linewidth bands ($\gtrsim$5 cm^{-1} FWHM) are those near 87 900 and 91 800 cm^{-1} for $^{16}O_2$. The predissociation linewidths for the weaker bands in Fig. 2 are estimated to be $\lesssim$2 cm^{-1} FWHM.

The vibronic analysis of the $^3\Pi_u \leftarrow X\ ^3\Sigma_g^-$ bands requires values for the vibrational energies. Therefore, we have derived effective rotationless term values for the $^3\Pi_{0u}$ and $^3\Pi_{2u}$ sub-levels from the present measurements by rotational analysis, and these values are given in Table II. Values for the $^3\Pi_{1u}$ sub-levels have not been included because, in general, they are strongly perturbed by spin–orbit coupling with $^1\Pi_{1u}$ states. The $^3\Pi_{1u} - {}^1\Pi_{1u}$ interactions will be discussed in detail elsewhere.[35] The assignments given in Table II are based on calculations discussed in Sec. III.

The rotationless term values have been determined using the ground-state energies given by Amiot and Verges[36] which are referenced to the non-existent F_2 ground-state level with $N''=J''=0$. In terms of the effective Hamiltonian given by Brown and Merer,[37] the rotationless term values are

$$T_v(^3\Pi_{0u}) = T_v - A + 2(B - A_D + 2\lambda_D/3) + 2\lambda/3 - 2\gamma - 4D, \quad (1)$$

TABLE I. Measured and calculated (CSE) rotational constants B', predissociation linewidths Γ and oscillator strengths f for the (0,0)–(3,0) $F\ ^3\Pi_u \leftarrow X\ ^3\Sigma_g^-$ bands of $^{16}O_2$. Measured parameters were obtained from fitting a band model, based on the Voigt line shape, to cross sections measured using the laser-based apparatus, and assignments are based on the discussion given in Sec. III C.

	B' (cm^{-1})[a]		Γ (cm^{-1} FWHM)[a,b]		$f(10^{-4})$[b]	
Band	Meas.	CSE	Meas.	CSE	Meas.	CSE
(0,0)	1.394±0.005	1.404	2.2±0.1	2.4	5.8±0.3	6.0
(1,0)	1.562±0.005	1.590	1.6±0.1	0.9	14.2±0.7	13.1
(2,0)[c]	1.475±0.005	1.509	6.4±0.8	7.6	2.9±0.8	4.1
(3,0)[c]	1.530±0.005	1.517	2.3±0.3	1.1	2.6±0.6	1.3

[a]Experimental parameter inherently includes effects of interactions with other electronic states whereas the calculated parameter includes only effects of $^3\Pi_u$ Rydberg-valence interactions.
[b]Extrapolated to zero rotation.
[c]Experimental cross sections corrected for contributions from other transitions.

TABLE II. Measured and calculated (CSE and first-order adiabatic) rotationless upper-state term values (to nearest cm^{-1}) for the $(v',0)\ ^3\Pi_u \leftarrow X\ ^3\Sigma_g^-$ bands. Rotationless term values for the $^3\Pi_{0u}$ and $^3\Pi_{2u}$ components given are defined by Eqs. (1) and (2) in the text and are referred to the virtual level $X\ ^3\Sigma_g^-$ ($v=0$, $J=0$, F_2). Unless otherwise stated, experimental uncertainties are $\lesssim 1.5\ cm^{-1}$.

		$^{16}O_2$				$^{18}O_2$			
		Measured		CSE	Adia.	Measured		CSE	Adia.
State[a]	v' [a]	$T_v(^3\Pi_2)$	$T_v(^3\Pi_0)$	$T_v(^3\Pi_0)$	$T_v(^3\Pi_0)$	$T_v(^3\Pi_2)$	$T_v(^3\Pi_0)$	$T_v(^3\Pi_0)$	$T_v(^3\Pi_0)$
$F\ ^3\Pi_u$	0	86 086[b]	85 902[b]	85 903	85 723	86 075[c]	85 892[c]	85 893	85 732
	1	86 842[b]	86 652[b]	86 654	86 623	86 808[c]	86 619[c]	86 618	86 587
	2	88 090[b]	87 904[b]	87 902	87 832	87 955[c]	87 768[c]	87 768	87 699
	3	89 258[b]	89 072[b]	89 069	89 083	89 046[c]	88 857[c]	88 858	88 866
	4	90 617[c,d]	90 428[c,d]	90 424	90 444	90 313[c]	90 126[c]	90 123	90 137
	5	91 914[c]	91 729[c]	91 727	91 822	91 549[c]	91 361[c]	91 360	91 427
	6			93 102	93 239	92 856[c]	92 667[c,d]	92 672	92 755
	7			94 554	94 668			94 031	94 096
	8							95 431	95 452
$F'\ ^3\Pi_u$	0	91 290[c]	91 097[c]	91 097	90 988	91 279[c]	91 086[c]	91 085	90 993
	1	92 760[c]	92 570[c]	92 573	92 292	92 650[c,d]	92 457[c]	92 455	92 217
	2	93 949[e]	93 761[e]	93 763	93 809			93 566	93 626
	3	95 474[e]	95 285[e]	95 283	95 437			94 950	95 158

[a]Assignments given in Sec. III C.
[b]Laser results.
[c]Monochromator results.
[d]Due to overlapping features, uncertainty $\sim 3\ cm^{-1}$.
[e]Results derived from Ref. 25.

and

$$T_v(^3\Pi_{2u}) = T_v + A - 2(B + A_D + 2\lambda_D/3) + 2\lambda/3, \qquad (2)$$

where T_v is the band origin, A is the spin–orbit constant, B is the rotational constant, λ is the spin–spin constant (including second-order spin–orbit effects), γ is the spin-rotation constant, and A_D, λ_D, and D are second-order centrifugal distortion constants. A preliminary report of band profile and rotational analyses for the four lowest-energy bands of $^{16}O_2$ has been presented elsewhere,[38] and the resulting rotational constants, oscillator strengths and predissociation linewidths for these bands are given in Table I. The results of Ito *et al.*[25] for bands at 93 900 and 95 400 cm^{-1} were used with Eqs. (1) and (2) to obtain rotationless term values which are included in Table II.

The bands at 86 000, 88 000, 89 200, and 91 800 cm^{-1} in the $^{16}O_2$ spectrum were correctly identified as $^3\Pi_u \leftarrow X\ ^3\Sigma_g^-$ transitions by Chang[23] and Chang and Ogawa[24] using spectrographic measurements. Their measured rotationless term values differ from the present ones by $<1.5\ cm^{-1}$ for the bands at 89 200 and 86 000 cm^{-1} which have narrow rotational lines, while their values for the more diffuse bands differ by $\lesssim 3\ cm^{-1}$.

III. SEMIEMPIRICAL MODELING

A. Method of calculation

The coupled-channel Schrödinger equations[39,40] (CSE) method was used to calculate the cross section for photoabsorption into the Rydberg-valence manifold of $^3\Pi_{0u}$ states. From calculations performed for different values of the rotation J, it was possible to determine resonance energies, oscillator strengths, linewidths, and rotational constants[41] for comparison with the available experimental data.

The input data required for the calculations were diabatic potential-energy curves representing the $\Omega=0$ components of the $np\sigma_u\ ^3\Pi_u$ Rydberg states for $n=3$–7 and the repulsive valence $1\ ^3\Pi_u$ state, electrostatic couplings between the Rydberg and valence states, and electric-dipole moments for transitions to each of these states from the $X\ ^3\Sigma_g^-$ state. Figure 3 shows the final diabatic potential-energy curves for the states included in our calculations. We chose to use the diabatic electronic-state basis because the corresponding potential-energy curves, electronic transition moments and Rydberg-valence couplings may be taken to vary smoothly

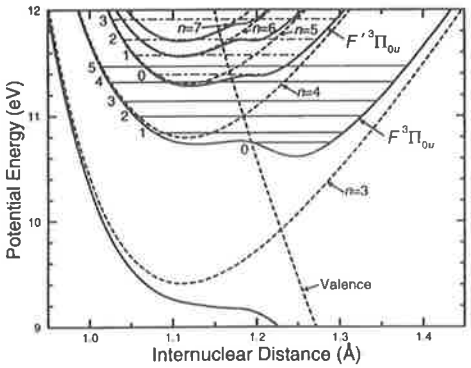

FIG. 3. Potential-energy curves for the $^3\Pi_{0u}$ states used to model the observed bands. Energies are given relative to the minimum of the ground-state $X\ ^3\Sigma_g^-$ potential-energy curve. Shown are the diabatic curves (dashed lines) for the repulsive valence state and the bound $np\sigma_u$ Rydberg states ($n=3$–7), and the corresponding adiabatic curves (solid lines) calculated using the Rydberg-valence couplings given in Table III. The observed vibrational levels of $^{16}O_2$ are also shown, associated with the second and third adiabatic potential-energy curves $F\ ^3\Pi_{0u}$ and $F'\ ^3\Pi_{0u}$ (Ref. 55).

TABLE III. Diabatic model parameters used in calculation of $^3\Pi_u \leftarrow X\ ^3\Sigma_g^-$ resonance energies. Values for the electronic term T_e, effective quantum number $n^* = n - \delta$, quantum defect δ, Rydberg-valence coupling H^e, and the coupling scaled by $(n^*)^{3/2}$ are given for each $np\sigma_u$ Rydberg state. Also given are electric dipole moments M^e for transitions from the O_2 ground state to each diabatic state.

State	T_e (eV)[a]	n^*	δ	H^e (cm^{-1})[a]	$(n^*)^{3/2}H^e$ (cm^{-1})	M^e (a.u.)[a]
$n=3$	9.409±0.006	2.270	0.730	7110±50	24 300	0.191±0.006
$n=4$	10.796±0.002	3.291	0.709	3540±20	21 150	0.081±0.009
$n=5$	11.307±0.001	4.279	0.721	2050±40	18 150	0.064[b]
$n=6$	11.568[b]	5.320	0.680	950±60	11 700	0.046[b]
$n=7$	11.711[b]	6.334	0.666	650[b]	10 400	0.036[b]
Valence						−0.056±0.010

[a]Uncertainties (3σ) are those obtained in the fitting process.
[b]Parameter fixed in fitting process.

with R. For these calculations we assumed that the couplings and transition moments were independent of R. An additional advantage of the use of a diabatic basis is that the parameters associated with the deperturbed Rydberg states can be compared with the analogous values obtained for unperturbed Rydberg states of other molecules.

Selected model parameters, described in Sec. III B, were varied to fit the experimental $T_v(^3\Pi_{0u})$ values shown in Table II, as well as the oscillator strengths, predissociation linewidths and rotational constants[41] listed in Table I. In addition, measured cross sections for the 1327 and 1356 Å continuum features[19,21] were used to constrain the problem in the energy region of the lowest potential-curve crossing.

B. Model parameters

The potential-energy curves chosen for the initial calculations were an *ab initio* diabatic curve for the valence state[42] and Rydberg curves with the same shape as that of the $X\ ^2\Pi_g$ state of the ion to which the series converges.[2] The general formula for the energy of Rydberg states is

$$E_n = E_\infty - \frac{\mathcal{R}}{n^{*2}}, \tag{3}$$

where E_∞ is the ionization limit (in this case[1] 97 348 cm^{-1}), $\mathcal{R} = \mathcal{R}_\infty/(1+m_e/M)$, $\mathcal{R}_\infty = 109\,737.315$ cm^{-1} is the Rydberg constant, m_e and M are the electron and molecule masses, respectively, $n^* = n - \delta$ is the effective quantum number and δ is the quantum defect. Initially, the Rydberg potentials were fixed to give $\delta = 0.7$, a value consistent with the value calculated *ab initio* by Betts and McKoy[43] and values for $np\sigma$ orbitals in a number of other molecules.[44–47] The δ values for $n=3$–5 were then allowed to vary and, in subsequent iterations, the potentials for the $n=6$–7 Rydberg states were fixed assuming a smooth variation of δ with n. In addition, the slope and crossing points of the valence potential-energy curve were allowed to vary along with the shapes of the $3p\sigma_u$ and $4p\sigma_u$ Rydberg curves and the equilibrium internuclear distance of the $5p\sigma_u$ Rydberg curve. The final values for δ, given in Table III, decrease slightly with increasing n, a behavior consistent with that calculated for the $np\sigma_u$ states of O_2 by Betts and McKoy,[43] and that measured[44,46,47] for the $np\sigma$ states of NO and CO. The quantum defects do not appear to be completely deperturbed, possibly due to the neglect of interactions with the $2\ ^3\Pi_u$ valence state[42] which crosses the $3p\sigma_u$ Rydberg potential-energy curve near 1.4 Å.

The Rydberg-valence electrostatic coupling matrix elements H^e are expected to scale with $(n^*)^{-3/2}$.[48] In our calculations, only the couplings for $n=3$–6 were varied while that for $n=7$ was fixed to give a smooth variation of $(n^*)^{3/2}H^e$ with n. Our value for the $n=3$ Rydberg-valence coupling, ~7100 cm^{-1}, is in rough agreement with the *ab initio* results of Buenker and Peyerimhoff[18] who obtained 8550 cm^{-1} at $R = 2.38a_0$. The couplings, shown in Table III, decrease as n increases more rapidly than expected, possibly indicating a dependence of H^e on R.

The electric dipole moments M^e for transitions to the valence state and to the $n=3$ and $n=4$ Rydberg states, given in Table III, were chosen to give agreement with the observed intensities of the 1327 and 1356 Å continuum features[21] and with the oscillator strengths of the $^3\Pi_u \leftarrow X\ ^3\Sigma_g^-$ bands measured with the laser apparatus (see Table I) which are not subject to errors due to inadequate instrumental resolution. The transition moments for the higher Rydberg states were set to values which decrease from the $n=3$ and $n=4$ values according to the usual $(n^*)^{-3/2}$ dependence.[48] The small value for the valence transition moment is consistent with the absence of a $^3\Pi_u \leftarrow X\ ^3\Sigma_g^-$ continuum underlying the Schumann–Runge bands.[49,50] While the signs of the individual electronic matrix elements M^e and H^e, listed in Table III, have no absolute significance, the observed intensities of the fitted $^3\Pi_u \leftarrow X\ ^3\Sigma_g^-$ features can only be explained if the product M^e (valence) $H^e M^e$ (Rydberg)<0.

C. Results and discussion

The final calculated rotationless cross section for each isotopomer in the range 85 500–95 500 cm^{-1} is shown in Fig. 4. The $T_v(^3\Pi_{0u})$ values determined from the cross sections agree with the experimental values to within ~5 cm^{-1}, as can be seen in Table II. In addition, the calculations reproduce the qualitative predissociation linewidths of the bands without requiring any other dissociative states in the model. Reasonable agreement is also obtained between the

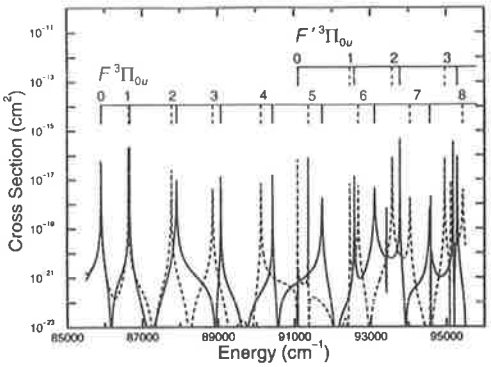

FIG. 4. The calculated rotationless photoabsorption cross section for $^3\Pi_{0u} \leftarrow X\ ^3\Sigma_g^-$ transitions of $^{16}O_2$ (solid line) and $^{18}O_2$ (dashed line). Assignments to $(v',0)\ F\ ^3\Pi_{0u} \leftarrow X\ ^3\Sigma_g^-$ and $(v',0)\ F'\ ^3\Pi_{0u} \leftarrow X\ ^3\Sigma_g^-$ transitions are indicated. Three resonances due to transitions to higher-lying states are also present.

calculated and measured parameters listed in Table I for the lowest-energy bands of $^{16}O_2$. Thus, although the measured term values and linewidths are quite irregular, the relatively simple model presented above has been able to simulate them quite accurately. This remarkable achievement implies that previous difficulties with assignments of the bands have been primarily due to the coupling of the Rydberg and valence $^3\Pi_u$ states.

Adiabatic potential-energy curves have been calculated from the diabatic curves and their couplings and are shown in Fig. 3. The electronic state formed by the crossings of the $n=3$ and $n=4$ Rydberg curves by the valence curve has been labeled $F\ ^3\Pi_u$, to be consistent with the label used by Huber and Herzberg,[28] and the label $F'\ ^3\Pi_u$ has been used for the state formed by the crossing of the $n=4$ and $n=5$ Rydberg curves by the valence curve. First-order adiabatic eigenenergies have been calculated for the F and F' states and are given as rotationless term values in Table II.

The adiabaticity parameter[51] $\zeta = H^e/\Delta G^{ad}$, where ΔG^{ad} is the separation of the first vibrational levels of the higher member of a pair of adiabatic states resulting from an avoided crossing, has been suggested as a measure of the applicability of the adiabatic or diabatic representations. Near-adiabatic behavior occurs for $\zeta \gg 1$, near-diabatic behavior occurs for $\zeta \ll 1$, while for cases where $\zeta \sim 1$ the amount of mixing of states in either representation is large. For example, $\zeta \approx 1.3$ for the $E\ ^3\Sigma_u^-$ state,[51] considered to be intermediate between adiabatic and diabatic.[52] For the $F\ ^3\Pi_u$ state, we calculate $\zeta \approx 2.9$,[53] suggesting that the behavior of this state is close to that of the adiabatic representation. This behavior is confirmed by the comparatively small rotational linewidths,[54] and by a comparison of the calculated first-order adiabatic rotationless term values for the F state with the results from the full coupled-channel calculations (Table II). The root-mean-square differences between the adiabatic and CSE energies of ~ 100 and ~ 70 cm^{-1} for $^{16}O_2$ and $^{18}O_2$, respectively, are much smaller than either the Rydberg-valence coupling of ~ 7100 cm^{-1} or the mean vibrational spacing of ~ 1200 cm^{-1}, supporting the adiabatic picture.[55] The diabatic energies, which can be deduced approximately from the diabatic electronic term values in Table III by assuming an ionic shape for the Rydberg potential-energy curves, bear no resemblance to the CSE energies.

Assignments of the observed bands were made by omitting various of the Rydberg states from the CSE models and studying the resulting calculated cross sections. The adiabatic potential curves, when considered with the calculated cross section shown in Fig. 4, are valuable for visualizing the assignments of the bands and for understanding the origin of the irregular characteristics.[55] All of the bands shown in Fig. 1 were unambiguously assigned to the state formed by the coupling of the diabatic $3p\sigma_u$ and $4p\sigma_u$ Rydberg and valence states and the upper levels can be represented by levels in the $F\ ^3\Pi_u$ adiabatic potential-energy well with $v'=0$–6. The CSE calculations also predict $F \leftarrow X$ bands with higher v' in the energy region shown in Fig. 4 and term values for these levels have been included in Table II. The double minimum of the $F\ ^3\Pi_u$ potential well (see Fig. 3) explains the irregular level structure, including the anomalously small separation between the lowest two levels. The first level $F(0)$ is in the right-hand part of the minimum which accounts for its anomalously small rotational constant (Table I). Higher levels show a more regular behavior with a mean vibrational spacing which is smaller than that of the ion[28] because the potential well of the $F\ ^3\Pi_u$ state is much wider than that of the ion.

By including the $5p\sigma_u$ Rydberg state in our model, we can account for all of the other observed bands. We assign the two bands observed near 91 200 and 92 600 cm^{-1} shown in Fig. 2 and the bands observed by Ito *et al.*[25] to transitions to the first four vibrational levels of the $F'\ ^3\Pi_u$ state. The $F'\ ^3\Pi_u$ adiabatic potential well, like the $F\ ^3\Pi_u$ well, has a strangely shaped minimum, but, in contrast to $F(0)$, $F'(0)$ is in the left-hand part of the well. As for the F state, much of the anomalous and irregular vibrational spacing for the F' state can be explained by the unusual shape of the corresponding potential-energy curve.

All of the observed bands have been assigned by considering only $np\sigma_u\ ^3\Pi_u$ Rydberg states with $n=3$–5. However, the $n=6$ and 7 Rydberg states were included in the final calculations because they produce three resonances in the region of the measurements (i.e., $<95\,400$ cm^{-1}) which have not been observed and produce shifts in the positions of resonances associated with the lower Rydberg states through coupling via the valence intermediary. In fact, one of these additional levels lies just below $F'(3)$ (see Fig. 4) which, therefore, may have some admixture of $n=6$ Rydberg character. This unobserved level may be responsible for the perturbations of the $F' \leftarrow X$ (3,0) sub-band rotational structure observed by Ito *et al.*[25] and may partly explain their suggestion that two different electronic states are responsible for the $F' \leftarrow X$ (2,0) and (3,0) bands that they analyzed. The calculations shown in Fig. 4 are consistent with the observation of Ito *et al.*[25] that the two bands they selected for analysis were among the strongest in this energy region. The unobserved

bands are predicted to be weaker and have narrower lines than the other bands in this region. Inclusion of Rydberg states beyond $n=7$ has no significant effect on the calculated energies other than relatively small overall shifts.

Further improvements in our understanding of the $^3\Pi_u$ states will require both experimental and theoretical advances. First, high-resolution measurements of the absorption cross section for all bands are needed to give more accurate values for rotational constants, predissociation linewidths and intensities. Second, more accurate CSE modeling of rotational effects will require a consideration of many additional interactions, such as the $^3\Pi_{1u}-{}^3\Pi_{0,2u}$ rotational interactions, $^3\Pi_{1u}-{}^1\Pi_{1u}$ spin–orbit interactions, and $^3\Pi_u-{}^3\Sigma_u^{\pm}$ and $^3\Pi_u-{}^3\Delta_u$ rotational interactions, most of which are poorly characterized experimentally at present. Third, further restraint of the parameters for the $n=5$–7 Rydberg states, will require measurements of bands which should exist in the high-energy region but which have not yet been observed. However, none of these refinements are expected to change the assignments of the $^3\Pi_u$ features discussed above or the basic features of the Rydberg-valence interactions present in our model.

IV. SUMMARY

The first comprehensive vibronic assignment of the $^3\Pi_u$ states of O_2 in the energy region below 95 400 cm^{-1} has been carried out using semiempirical modeling of the $^3\Pi_u$ Rydberg-valence interactions. To facilitate the assignments, measurements of seventeen $^3\Pi_u \leftarrow X\ ^3\Sigma_g^-$ bands in the region 85 800–93 000 cm^{-1} of the ground-state spectra of $^{16}O_2$ and $^{18}O_2$ have been presented. The six bands of $^{18}O_2$ at energies >88 500 cm^{-1} and the $^{16}O_2$ band near 92 700 cm^{-1} have been reported for the first time. Previous assignments[23] for three of the $^{16}O_2$ bands have been corrected. The irregular behavior of the observed bands, which has caused previous difficulties with their interpretation, has been found to be caused principally by strong Rydberg-valence interactions. Our final CSE calculations reproduce the measured band origins to within ~5 cm^{-1} and reproduce the irregular behavior of the line broadening due to predissociation. We have assigned the observed transitions to two vibrational progressions with upper levels in the $F\ ^3\Pi_u$ and $F'\ ^3\Pi_u$ adiabatic potential-energy curves, formed from the avoided crossing of the diabatic $(3p\sigma_u, 4p\sigma_u)$ and $(4p\sigma_u, 5p\sigma_u)$ Rydberg potential-energy curves by the diabatic valence potential-energy curve, respectively.

The use of CSE calculations performed with a diabatic electronic-state basis has enabled us to obtain deperturbed Rydberg-state parameters. The derived quantum defects of ~0.7 are consistent with expectations for $np\sigma$ orbitals and decrease slightly with increasing n, in agreement with *ab initio* calculations[43] and measurements for other molecules.[44,46,47] The derived $3p\sigma_u$ Rydberg-valence coupling $H^e \approx 7100$ cm^{-1} is in reasonable agreement with *ab initio* calculations,[18] but the couplings between the valence and the higher Rydberg states fall off faster than the expected $(n^*)^{-3/2}$ dependence,[48] possibly indicating a variation of H^e with R.

ACKNOWLEDGMENTS

The authors wish to acknowledge financial support from the Australian Research Council through a Post-Doctoral Research Fellowship (J.P.E.) and partial sponsorship (M.L.G.) from the United States National Science Foundation through a US–Australia Cooperative Research Grant. We also wish to thank Professors H. Lefebvre-Brion and J. H. Carver for a critical reading of the manuscript. Valuable technical assistance was provided by K. J. Lonsdale and C. J. Dedman.

[1] R. G. Tonkyn, J. W. Winniczek, and M. G. White, Chem. Phys. Lett. **164**, 137 (1989).
[2] P. H. Krupenie, J. Phys. Chem. Ref. Data **1**, 423 (1972).
[3] K. Watanabe, Adv. Geophys. **5**, 153 (1958).
[4] R. J. Yokelson, R. J. Lipert, and W. A. Chupka, J. Chem. Phys. **97**, 6153 (1992), and references therein.
[5] S. T. Pratt, J. L. Dehmer, and P. M. Dehmer, J. Chem. Phys. **93**, 3072 (1990).
[6] T. A. York and J. Comer, J. Phys. B **16**, 3627 (1983), and references therein.
[7] W. J. van der Zande, W. Koot, and J. Los, J. Chem. Phys. **91**, 4597 (1989), and references therein.
[8] M. Ogawa and K. R. Yamawaki, Can. J. Phys. **47**, 1805 (1969).
[9] D. H. Katayama, S. Ogawa, M. Ogawa, and Y. Tanaka, J. Chem. Phys. **67**, 2132 (1977).
[10] M. Yoshimine, K. Tanaka, H. Tatewaki, S. Obara, F. Sasaki, and K. Ohno, J. Chem. Phys. **64**, 2254 (1976).
[11] R. J. Buenker, S. D. Peyerimhoff, and M. Perić, Chem. Phys. Lett. **42**, 383 (1976).
[12] J. Wang, D. G. McCoy, A. J. Blake, and L. Torop, J. Quant. Spectrosc. Radiat. Transfer **38**, 19 (1987).
[13] J. Wang, A. J. Blake, D. G. McCoy, and L. Torop, J. Quant. Spectrosc. Radiat. Transfer **40**, 501 (1988).
[14] Y. Li, M. Honigmann, K. Bhanuprakash, G. Hirsch, R. J. Buenker, M. A. Dillon, and M. Kimura, J. Chem. Phys. **96**, 8314 (1992).
[15] B. R. Lewis, S. T. Gibson, M. Emami, and J. H. Carver, J. Quant. Spectrosc. Radiat. Transfer **40**, 1 (1988); **40**, 469 (1988).
[16] P. J. Miller, L. Li, W. A. Chupka, and S. D. Colson, J. Chem. Phys. **88**, 2972 (1988).
[17] Y. Tanaka, J. Chem. Phys. **20**, 1728 (1952).
[18] R. J. Buenker and S. D. Peyerimhoff, Chem. Phys. Lett. **34**, 225 (1975).
[19] L. C. Lee, T. G. Slanger, G. Black, and R. L. Sharpless, J. Chem. Phys. **67**, 5602 (1977).
[20] A. C. Allison, S. L. Guberman, and A. Dalgarno, J. Geophys. Res. **87**, 923 (1982).
[21] S. T. Gibson, B. R. Lewis, and J. H. Carver (unpublished).
[22] R. H. Huebner, R. J. Celotta, S. R. Mielczarek, and C. E. Kuyatt, J. Chem. Phys. **63**, 241 (1975).
[23] H. C. Chang, Ph.D. dissertation thesis, University of Southern California, 1973.
[24] H. C. Chang and M. Ogawa, J. Mol. Spectrosc. **44**, 405 (1972).
[25] K. Ito, K. P. Huber, K. Yoshino, M. Ogawa, and Y. Morioka, J. Mol. Spectrosc. **171**, 1 (1995).
[26] M. Ogawa, K. R. Yamawaki, A. Hashizume, and Y. Tanaka, J. Mol. Spectrosc. **55**, 425 (1975).
[27] J. P. England, B. R. Lewis, and M. L. Ginter, J. Chem. Phys. **103**, 1727 (1995).
[28] K. P. Huber and G. Herzberg, *Molecular Spectra and Molecular Structure, IV. Constants of Diatomic Molecules* (Van Nostrand Reinhold, New York, 1979), pp. 494 and 504.
[29] B. R. Lewis, J. P. England, R. J. Winkel, Jr., S. S. Banerjee, P. M. Dooley, S. T. Gibson, and K. G. H. Baldwin, Phys. Rev. A **52**, 2717 (1995).
[30] R. L. Kelly and L. J. Palumbo, *Atomic and Ionic Emission Lines Below 2000 Angstroms: Hydrogen Through Krypton*, Naval Research Laboratory Report No. 7599 (U.S. GPO, Washington D.C., 1973).
[31] S. G. Tilford and J. D. Simmons, J. Phys. Chem. Ref. Data **1**, 147 (1972).

[32] P. G. Wilkinson, Can. J. Phys. **46**, 1225 (1968).
[33] R. Mahon, T. J. McIlrath, V. P. Myerscough, and D. W. Koopman, IEEE J. Quantum Electron. **15**, 444 (1979).
[34] Line positions for the (1,0) $j\ ^1\Sigma_u^+ \leftarrow X\ ^3\Sigma_g^-$ band were determined from the measurements of the (1,0) $j\ ^1\Sigma_u^+ \leftarrow b\ ^1\Sigma_g^+$ band by Katayama *et al.* (Ref. 9), the $b\ ^1\Sigma_g^+(v=0)$ rotational term values calculated from the spectroscopic constants of D. L. Albritton, W. J. Harrop, A. L. Schmeltekopf, and R. N. Zare [J. Mol. Spectrosc. **46**, 103 (1973)], and the $X\ ^3\Sigma_g^-(v=0)$ rotational term values of Amiot and Verges (Ref. 36).
[35] J. P. England, B. R. Lewis, and S. T. Gibson (unpublished).
[36] C. Amiot and J. Verges, Can. J. Phys. **59**, 1391 (1981).
[37] J. M. Brown and A. J. Merer, J. Mol. Spectrosc. **74**, 488 (1979).
[38] J. P. England, B. R. Lewis, and S. T. Gibson, International Quantum Electronics Conference, Anaheim, California, 1994 (unpublished).
[39] E. F. van Dishoeck, M. C. van Hemert, A. C. Allison, and A. Dalgarno, J. Chem. Phys. **81**, 5709 (1984).
[40] L. Torop, D. G. McCoy, A. J. Blake, J. Wang, and T. Scholz, J. Quant. Spectrosc. Radiat. Transfer **38**, 9 (1987).
[41] While the principal aim of this work is the study of the vibronic energies, the inclusion of oscillator-strength data in the fit allows the determination of approximate diabatic electronic transition moments, and the inclusion of rotational constants and predissociation linewidths provides additional constraints on the determined potential-energy curves. Only the oscillator strengths, rotational constants, and predissociation linewidths derived from laser-based measurements were used in the fit because the data from monochromator-based measurements were considered less reliable due to insufficient instrumental resolution.
[42] R. P. Saxon and B. Liu, J. Chem. Phys. **67**, 5432 (1977).
[43] T. Betts and V. McKoy, J. Chem. Phys. **54**, 113 (1971).
[44] E. Miescher, J. Mol. Spectrosc. **20**, 130 (1966).
[45] P. K. Carroll and K. Yoshino, J. Phys. B **5**, 1614 (1972).
[46] M. Ogawa and S. Ogawa, J. Mol. Spectrosc. **41**, 393 (1972).
[47] M. Eidelsberg and F. Rostas, Astron. Astrophys. **235**, 472 (1990).
[48] H. Lefebvre-Brion and R. W. Field, *Perturbations in the Spectra of Diatomic Molecules* (Academic, Orlando, 1986), pp. 84, 211, and 385.
[49] B. R. Lewis, L. Berzins, J. H. Carver, and S. T. Gibson, J. Quant. Spectrosc. Radiat. Transfer **33**, 627 (1985).
[50] In contrast, the opposite situation occurs for the $^3\Sigma_u^-$ states of O_2 where the valence $B\ ^3\Sigma_u^- - X\ ^3\Sigma_g^-$ transition moment, which gives rise to the strong Schumann–Runge system, greatly exceeds the Rydberg transition moment [B. R. Lewis, S. S. Banerjee, and S. T. Gibson, J. Chem. Phys. **102**, 6631 (1995)]. The small valence $1\ ^3\Pi_u - X\ ^3\Sigma_g^-$ transition moment found here is consistent with the *ab initio* calculations of P. S. Julienne, D. Neumann, and M. Krauss, [J. Chem. Phys. **64**, 2990 (1976)], S. L. Guberman and A. Dalgarno [J. Geophys. Res. **84**, 4437 (1979)], and H. Partridge (private communication), but differs from those of Buenker *et al.* (Ref. 11) who appear to have reversed the labels on their Fig. 2(b).
[51] K. Dressler, Ann. Isr. Phys. Soc. **6**, 141 (1983).
[52] L. Torop, J. Wang, D. G. McCoy, and A. J. Blake, J. Quant. Spectrosc. Radiat. Transfer **43**, 457 (1990).
[53] The value of the adiabaticity parameter was obtained from a separate CSE calculation which included only the valence $^3\Pi_u$ state and lowest Rydberg $^3\Pi_u$ state. This calculation yielded $\Delta G^{ad}=2430\ cm^{-1}$, and $\zeta=7110/2430=2.9$.
[54] In the adiabatic picture, the predissociation broadening is primarily due to coupling of the adiabatic $^3\Pi_u$ bound states to the repulsive state through nonadiabatic interactions. If the widths are small, then the nonadiabatic coupling is small and the adiabatic representation adequately describes the states. In contrast, linewidths for levels of the $E\ ^3\Sigma_u^-$ state are generally large, indicating significant nonadiabatic coupling with the $B\ ^3\Sigma_u^-$ state at energies above the dissociation limit of the B state.
[55] It should be made clear that neither the diabatic nor the adiabatic potential-energy curves exactly represent the observed energy levels (Ref. 48). Nevertheless, since the adiabatic approximation is good, we have adopted the practice throughout this work of associating observed levels with the adiabatic F and F' potential-energy curves.

4.22 Spin-orbit interactions between Rydberg states of O_2

[42] J. P. England, B. R. Lewis, and M. L. Ginter,
Journal of Electron Spectroscopy and Related Phenomena **79**, 449–452 (1996).

Journal of Electron Spectroscopy and Related Phenomena 79 (1996) 449–452

Spin-orbit interactions between Rydberg states of O_2

J. P. England,[a] B. R. Lewis,[a] and M. L. Ginter[b]

[a]Research School of Physical Sciences and Engineering, The Australian National University, Canberra, ACT 0200, Australia

[b]Institute for Physical Science and Technology, University of Maryland, College Park, Maryland 20742, USA

Spin-orbit interactions between Rydberg states of O_2 have been studied by observing the photoabsorption spectrum in the 1100 – 1200 Å region. The dominant interactions are between states having the same primary molecular orbital configuration and these give rise to perturbations in rotational-level structures and the appearance of nominally-forbidden absorption bands. Three examples are given showing the effects of $^3\Pi_u - {}^1\Pi_u$ and $^3\Sigma_u^+ - {}^3\Sigma_u^-$ interactions in the ground-state absorption spectrum.

1. INTRODUCTION

The window region (1100 – 1300 Å) of the O_2 photoabsorption spectrum has been the subject of a number of previous studies. However, there have been few definitive assignments of features in this region because of the large number of accessible excited electronic states and irregularities caused by strong Rydberg-valence interactions. An improved understanding of the spectrum is desirable because of its importance in determining the depth of penetration of solar vacuum ultraviolet (VUV) radiation in the terrestrial atmosphere.

Some diabatic potential-energy curves for O_2 are shown in Fig. 1. The important *ungerade* Rydberg states in this energy region are the first members of the $np\lambda$ complexes ($n = 3, 4, 5, \ldots$) built on the $X^2\Pi_g$ state of O_2^+. These complexes give rise to $^1\Pi_u$, $^3\Pi_u$, $^1\Sigma_u^\pm$, $^3\Sigma_u^\pm$, $^1\Delta_u$ and $^3\Delta_u$ molecular states. However, the only regular Rydberg progressions observed in O_2 single-photon absorption spectra are the lower vibrational levels of the $3p\pi_u$ $D\,^3\Sigma_u^+$, $3p\pi_u$ $f\,^1\Sigma_u^+$ and $4p\pi_u$ $j\,^1\Sigma_u^+$ states [1,2]. The crossing of the Rydberg potential-energy curves for many states by curves for valence states of the same symmetry gives rise to large perturbations from electrostatic interactions [3] which can be modelled using coupled-channel Schrödinger equations (CSE) calculations [4].

In addition, strong spin-orbit coupling between states from the same $np\lambda$ complex results in irregularities in the rotational structure of vibrational bands and the appearance of spin-forbidden bands in the absorption spectrum. A number of vibrational bands have, as a consequence, been incorrectly assigned in the work of Chang [5]. A study of the $^1\Sigma_u^+ - {}^3\Sigma_u^-$ spin-orbit interactions was recently presented by Lewis *et al.* [6]. In this paper, we present measurements of three bands in the ground-state photoabsorption cross section which illustrate the effects of $^3\Pi_u - {}^1\Pi_u$ and $^3\Sigma_u^- - {}^3\Sigma_u^+$ spin-orbit interactions. Large vibrational overlap factors between states with $\Delta v = \pm 1$ which are inferred from the measurements can only be explained by considering the Rydberg-valence mixing of states of the same symmetry.

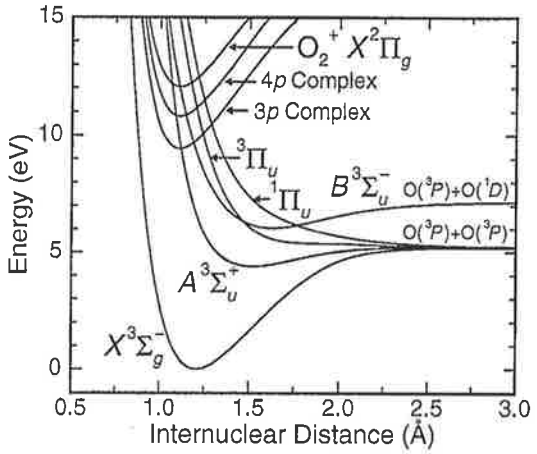

Figure 1. Diabatic potential-energy curves for O_2 relevant to a study of the $^3\Pi_u - {}^1\Pi_u$ and $^3\Sigma_u^- - {}^3\Sigma_u^+$ spin-orbit interactions.

PII S0368-2048 (96) 02892-7

2. EXPERIMENTAL METHODS

High-resolution measurements of the O_2 photoabsorption cross section have been taken using tunable vacuum-ultraviolet (VUV) radiation produced from third harmonic generation using excimer-pumped dye-laser radiation focussed in a cell containing Kr at pressures in the 5 – 100 Torr range. The VUV bandwidth, estimated from measurements of Xe and H_2 (0,0) Lyman-band absorption lines near 88500 cm^{-1}, was found to be $\sim$ 0.5 cm^{-1} full-width at half-maximum (FWHM), or $\sim$ 0.1 cm^{-1} FWHM with an intracavity étalon in the dye laser. Details of the apparatus and the wavelength calibration have been presented elsewhere [4,7].

The laser-based apparatus was limited to measurements for energies $\lesssim$ 89500 cm^{-1}. To access shorter wavelengths, a second apparatus based on an argon-dimer continuum discharge lamp with a 2.2 m scanning VUV monochromator was employed. This apparatus has been described in detail elsewhere [8]. Absorption measurements indicated that the radiation had a bandwidth of $\sim$ 2.5 cm^{-1} FWHM.

Absorption cells with LiF windows and path lengths of 10.9 cm were cooled by filling sleeves with liquid N_2, resulting in an effective gas temperature of 79 $\pm$ 0.5 K. Samples of oxygen (BOC 99.9%, containing 99.8 atom% ^{16}O were used at pressures between 0.1 Torr and 10 Torr. The incident and transmitted radiation was detected photoelectrically using solar-blind photomultipliers and absolute cell transmittances were obtained by normalizing the measurements using the empty-cell values. Photoabsorption cross sections were determined from the measured cell transmittances using the Beer-Lambert law.

3. THEORY

Strong spin-orbit interactions between states of the np Rydberg complexes of O_2 occur only between isoconfigurational states which interact through the l_{iz} s_{iz} terms of the spin-orbit operator [9]. Since interacting states must have the same value of Ω and the same e/f parity, for $^3\Pi_u - ^1\Pi_u$ and $^3\Sigma_u^+ - ^3\Sigma_u^-$ interactions, the only non-zero matrix elements are those between the sub-states $^3\Pi_{1u} - ^1\Pi_{1u}$ and $^3\Sigma_{1u}^- - ^3\Sigma_{1u}^+$.

The O_2 $np\sigma_u$ $^3\Pi_u$ and $^1\Pi_u$ Rydberg states have primary molecular-orbital configurations of the type $\ldots\pi_g\, np\sigma_u$. Matrix elements of the spin-orbit operator for these configurations are [9]

$$\langle {}^3\Pi_{1u}, v|\mathbf{H}^{SO}|{}^1\Pi_{1u}, v'\rangle = \frac{1}{2}a_{\pi_g}\langle v|v'\rangle,$$

where a_{π_g} is a molecular spin-orbit parameter. Similarly, the $np\pi_u$ $^3\Sigma_u^+$ and $^3\Sigma_u^-$ Rydberg states have primary configurations $\ldots\pi_g\, np\pi_u$ and the spin-orbit matrix elements are [10]

$$\langle {}^3\Sigma_{1u}^-, v|\mathbf{H}^{SO}|{}^3\Sigma_{1u}^+, v'\rangle = \frac{1}{2}\left(a_{\pi_g} + a_{np\pi_u}\right)\langle v|v'\rangle.$$

The Rydberg-orbital $a_{np\pi_u}$ parameter can be neglected in comparison with the valence-orbital a_{π_g} parameter [9].

In both of these cases, the matrix elements, apart from the $\langle v|v'\rangle$ factors, are essentially equal to the spin-orbit splitting $A \approx 96$ cm^{-1} of the $^3\Pi_u$ Rydberg state [9]. Normally, $\langle v|v'\rangle = \delta_{vv'}$ for isoconfigurational states. However, the mixing of Rydberg and valence states can result in differences between the potential-energy curves and, therefore, non-zero interactions between states with $\Delta v \neq 0$ [9].

4. RESULTS

4.1. $^3\Pi_{1u} - ^1\Pi_{1u}$ Interactions

Figure 2 shows measurements of the O_2 photoabsorption cross section in the range 86600 – 87300 cm^{-1} taken with the laser-based apparatus. The strong band is the (1,0) band of the $F\,^3\Pi_u \leftarrow$

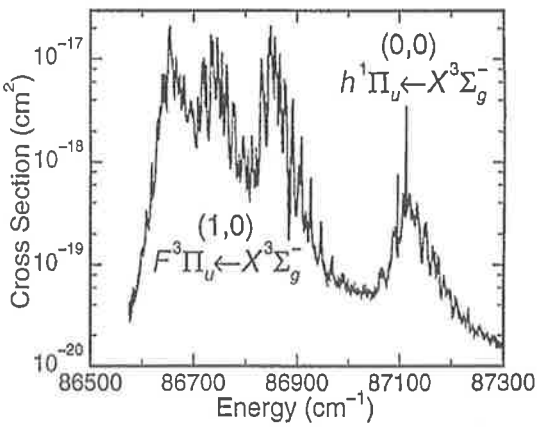

Figure 2. The O_2 photoabsorption cross section (T = 79 K) measured using the laser-based apparatus. A log scale has been used on the vertical axis to emphasize the weak band near 87100 cm^{-1}.

$X\,^3\Sigma_g^-$ system which was recently assigned by England *et al.* [4]. This band shows rotational structure characteristic of a $^3\Pi_u \leftarrow X\,^3\Sigma_g^-$ transition with the upper state close to Hund's case (a). The total splitting of the $^3\Pi_{0u} \leftarrow X\,^3\Sigma_g^-$ and $^3\Pi_{2u} \leftarrow X\,^3\Sigma_g^-$ sub-bands (196 $cm^{-1} \approx 2A$) is close to the spin-orbit splitting of the ground state of O_2^+ [11]. The band shows a shift (~ -20 cm^{-1}) of the central sub-band to lower energy which is consistent with a $^3\Pi_{1u} - {}^1\Pi_{1u}$ spin-orbit interaction, the $^1\Pi_{1u}$ level being higher in energy than the $^3\Pi_{1u}$ level.

A weak band which can be seen in Fig. 2 at higher energies than the (1,0) $F\,^3\Pi_u \leftarrow X\,^3\Sigma_g^-$ band has been definitively identified as a $^1\Pi_{1u} \leftarrow X\,^3\Sigma_g^-$ transition [7] on the basis of the observation of three narrow lines near its origin. Comparisons of the differences between their transition energies and the ground-state rotational term values [12] shows that the lines result from transitions to a $J' = 1$ level. Levels with $J' > 1$ are broadened by predissociation mediated by a coincident $^1\Delta_{2u}$ level [7].

Using two-level perturbation theory and measurements of the shift of the $^3\Pi_{1u}$ sub-level and the separation of the $^3\Pi_{1u}$ and $^1\Pi_{1u}$ levels, the strength of the weak band has been shown to result primarily from the $^3\Pi_{1u} - {}^1\Pi_{1u}$ spin-orbit interaction [7]. The calculated matrix element is 86 cm^{-1} which is approximately 90% of the spin-orbit splitting of the $^3\Pi_u$ state. Such a large value implies that the states have a large vibrational overlap. However, while the $^3\Pi_u$ level has $v = 1$, observations of the $b\,^1\Sigma_g^+$ metastable absorption spectrum [13] suggest that the $^1\Pi_{1u}$ level has $v = 0$. An explanation of the large vibrational overlap requires a treatment of the Rydberg-valence interactions and such work is in progress. Our studies have shown that the $F\,^3\Pi_u$ and $^1\Pi_u$ states observed in this work are formed from the interaction of the $3p\sigma_u$ and $4p\sigma_u$ Rydberg and lowest repulsive valence states, the potential-energy curves for each state having two minima.

4.2. $^3\Sigma_{1u}^- - {}^3\Sigma_{1u}^+$ Interactions

The O_2 photoabsorption cross section measured in the region of a strong band near 88900 cm^{-1} is shown in Fig. 3. This band was assigned by Chang [5] as two separate transitions to $^1\Pi_u$ and $^3\Sigma_u^+$ levels. However, such transitions are electric-dipole forbidden from the $X\,^3\Sigma_g^-$ state and would be expected to be weak. The rotational structure is clearly not that characteristic of the other strong and sharp transitions of this region

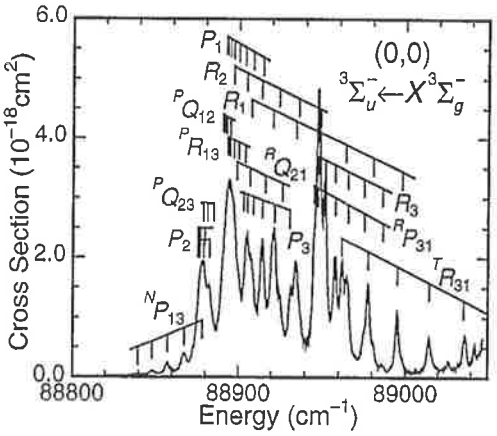

Figure 3. The O_2 photoabsorption cross section ($T = 79$ K) measured using the laser-based apparatus.

($^3\Pi_u \leftarrow X\,^3\Sigma_g^-$), as seen, for example, in Fig. 2. Our preliminary rotational analysis, giving the line assignments shown in Fig. 3, indicates that the band is a $^3\Sigma_u^- \leftarrow X\,^3\Sigma_g^-$ transition with highly perturbed structure. Other $^3\Sigma^-$ states of O_2 exhibit structure close to Hund's case (b) with second-order splitting of F_1, F_2 and F_3 components. In this case, however, the structure is closer to case (a) and the F_3 ($\sim {}^3\Sigma_{0u}^-$) and F_1, F_2 ($\sim {}^3\Sigma_{1u}^-$) components are separated by ~ 50 cm^{-1} indicating a large spin-orbit perturbation. Band modelling using the rotational-energy and line-strength formulae for an intermediate case (a) – (b) $^3\Sigma_u^- \leftarrow X\,^3\Sigma_g^-$ transition tending to case (c) [14] has shown that the $^3\Sigma_{1u}^- \leftarrow X\,^3\Sigma_g^-$ sub-bands are weaker than the $^3\Sigma_{0u}^- \leftarrow X\,^3\Sigma_g^-$ sub-band suggesting that the $\Omega' = 1$ components are the ones that are perturbed. It is likely, therefore, that the $^3\Sigma_{1u}^-$ components are spin-orbit coupled to a nearby $\Omega = 1$ state at higher energy. Unfortunately, a strong $F\,^3\Pi_u \leftarrow X\,^3\Sigma_g^-$ band falls in the region where we expect to see features from transitions to the perturbing state.

Preliminary results of CSE calculations for states of $^3\Sigma_u^\pm$ symmetry indicate that the level observed in this work is the $v = 0$ level in a potential-energy well formed from the avoided crossings of the $4p\pi_u$ and $5p\pi_u$ $^3\Sigma_u^-$ Rydberg and $B\,^3\Sigma_u^-$ valence states. It is perturbed by a nearby $v = 1$ level of the $4p\pi_u$ $^3\Sigma_u^+$ Rydberg state which is only weakly perturbed by Rydberg-valence interaction with the $A\,^3\Sigma_u^+$ valence state.

The second band ($v' = 1$) of the $^3\Sigma_u^- \leftarrow X\,^3\Sigma_g^-$ system has been observed at an energy near 90800 cm^{-1}, and is shown in Fig. 4. The rotational

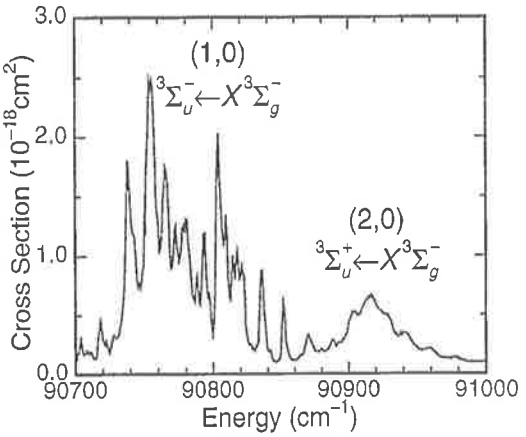

Figure 4. O_2 photoabsorption cross section measurements ($T = 79$ K) taken with the monochromator-based apparatus. The measurements are preliminary and are affected by limited instrumental resolution.

structure of this band is very similar to that of the (0,0) band. In this case, however, a weaker, diffuse band has been observed at higher energy and assigned to the (2,0) $4p\pi_u\ ^3\Sigma_u^+ \leftarrow X\,^3\Sigma_g^-$ transition. Band modelling using an effective Hamiltonian for the interacting $^3\Sigma_u^-$ and $^3\Sigma_u^+$ states has shown that the strength of the $^3\Sigma_u^+ \leftarrow X\,^3\Sigma_g^-$ band and the perturbation of the $^3\Sigma_u^- \leftarrow X\,^3\Sigma_g^-$ components can be explained using an interaction matrix element of ~ 70 cm^{-1}. The size of the this coupling implies a large vibrational overlap of wavefunctions with $\Delta v = 1$, as was found for the $^3\Pi_{1u} - {}^1\Pi_{1u}$ interaction.

5. CONCLUSIONS

We have provided three examples of Rydberg-state spin-orbit interactions observed in the O_2 photoabsorption spectrum. The interactions produce strong perturbations that have caused confusion in previous attempts to assign some of the allowed transitions. Detailed modelling of the spectrum is being carried out using coupled-channel Schrödinger equations calculations. Preliminary results have led to the vibrational assignments of the bands given in this work and have shown that it is necessary only to include the Rydberg-valence interactions and the spin-orbit interactions between isoconfigurational Rydberg states to enable all major observed effects to be explained.

In the cases where transitions to both spin-orbit interacting states have been observed, the spin-orbit matrix elements calculated from simple models are 70% and 90% of the value expected for Rydberg states of the same configuration. Contrary to expectations, the interacting levels have $\Delta v = 1$. The large overlap of the vibrational wavefunctions can be explained as being due to the unusual shapes of the $^3\Pi_u$, $^1\Pi_u$ and $^3\Sigma_u^-$ potential-energy curves caused by the Rydberg-valence couplings.

REFERENCES

1. M. Ogawa and K. R. Yamawaki, Can. J. Phys., 47 (1969) 1805.
2. D. H. Katayama, S. Ogawa, M. Ogawa, and Y. Tanaka, J. Chem. Phys., 67 (1977) 2132.
3. R. J. Buenker and S. D. Peyerimhoff, Chem. Phys. Lett., 34 (1975) 225.
4. J. P. England, B. R. Lewis, S. T. Gibson, and M. L. Ginter, J. Chem. Phys., submitted (1995).
5. H. C. Chang, Ph.D. dissertation thesis, University of Southern California, (1972).
6. B. R. Lewis, S. S. Banerjee, and S. T. Gibson, J. Chem. Phys., 102 (1995) 6631.
7. J. P. England, B. R. Lewis, and M. L. Ginter, J. Chem. Phys., 103 (1995) 1727.
8. B. R. Lewis, J. P. England, R. J. Winkel, Jr., S. S. Banerjee, P. M. Dooley, S. T. Gibson, and K. G. H. Baldwin, Phys. Rev. A, in press (1995).
9. H. Lefebvre-Brion and R. W. Field, Perturbations in the Spectra of Diatomic Molecules, Academic Press, Orlando, 1986.
10. R. Ogorzalek Loo, W. J. Marinelli, P. L. Houston, S. Arepalli, J. R. Wiesenfeld, and R. W. Field, J. Chem. Phys., 91 (1989) 5185.
11. K. P. Huber and G. Herzberg, Molecular Spectra and Molecular Structure, IV. Constants of Diatomic Molecules, Van Nostrand Reinhold, New York, 1979.
12. C. Amiot and J. Verges, Can. J. Phys., 59 (1981) 1391.
13. K. R. Yamawaki, Ph. D. dissertation thesis, University of Southern California (1972).
14. J. B. Tatum and J. K. G. Watson, Can. J. Phys., 49 (1971) 2693.

4.23 Understanding diatomic photodissociation with a coupled-channel Schrödinger equation model

[43] S. T. Gibson, and B. R. Lewis,
Journal of Electron Spectroscopy and Related Phenomena **80**, 9–12 (1996).

Journal of Electron Spectroscopy and Related Phenomena 80 (1996) 9–12

Understanding diatomic photodissociation with a coupled-channel Schrödinger equation model

S. T. Gibson and B. R. Lewis

Research School of Physical Sciences and Engineering, The Australian National University, Canberra ACT 0200, Australia

A coupled-channel Schrödinger equation model has been used to interpret the results of an experimental decomposition of the photoabsorption spectrum of O_2, covering the wavelength range from 1150 Å to 1750 Å. The model demonstrates that the main features of the spectrum, including many irregularities, arise from Rydberg-valence interactions.

1. INTRODUCTION

The photoabsorption spectra of diatomic molecules may appear quite complex due to perturbations which change the appearance of regular features [1]. Several theoretical calculations [2–4], which incorporate the coupling between electronic states, have demonstrated that discrete structures may interact with continua, resulting in complex spectral features. For O_2 [5], uncoupled models [6,7] have been shown to be inadequate to describe even the continuum.

In this work, a coupled-channel Schrödinger equation (CSE) model that treats the interactions between the radial wavefunctions of coupled electronic states, has been applied to the analysis of an experimentally-decomposed photoabsorption spectrum of O_2 [8]. This is the first CSE calculation to be compared with an experimentally-decomposed spectrum and the first to examine the complete O_2 spectrum over the wavelength range 1150 Å – 1750 Å. The model provides remarkable insight into the apparent complexities of the O_2 photoabsorption spectrum.

2. COUPLED-CHANNEL MODEL

The Schrödinger equation for the radial wavefunctions is given, in matrix form, by

$$\mathbf{F}''(R) + \frac{2\mu}{\hbar^2}\left[E\mathbf{1}^0 - \mathbf{W}(R)\right]\mathbf{F}(R) = \mathbf{0}^0, \qquad (1)$$

where μ is the reduced mass of the molecule, E is the energy and $\mathbf{W}$ is the interaction matrix, the diagonal elements of which are chosen to be the diabatic potential-energy curves, with the non-adiabatic couplings [1] as the off-diagonal elements [9]. This is the distorted-wave approximation [10].

2.1. Photoabsorption cross section

Equation (1) is solved using the numerical renormalization method of Johnson [11] and the wavefunctions are energy-normalized at the asymptotic limit [10]. The photoabsorption cross section for each open channel γ is given by

$$\sigma_\gamma = \frac{2\pi^2\nu}{3\epsilon_0}\left|\langle \mathbf{F}_\gamma|\mathbf{M}|F_i\rangle\right|^2, \qquad (2)$$

where ν is the photon energy in wavenumbers, F_i is the initial-state radial wavefunction, $\mathbf{F}$ is a vector of final-state radial wavefunctions and $\mathbf{M}$ is a vector of transition moments between the initial state and each channel, including rotational matrix elements [9].

An important consequence of this theory is that the wavefunctions in $\mathbf{F}$ have a mixed character and contain information about all of the coupled electronic states.

2.2. Intensity borrowing, resonance asymmetry and interference

Rewriting Eq. (2) in expanded form,

$$\sigma_\gamma \propto \left|\langle F_{\gamma 0}|M_0|F_i\rangle + \langle F_{\gamma 1}|M_1|F_i\rangle + \cdots\right|^2, \qquad (3)$$

reveals the origin of several spectral phenomena. If transitions into only one channel are optically allowed ($M_i = 0, i \neq 0$), then that one term determines the cross section. However, since the wavefunction $F_{\gamma 0}$ has a mixed character, structure associated with the other, optically-forbidden, states may appear in the absorption cross section. This is illustrated in Fig. 1. where only the continuum state (open channel) has a non-zero transition moment. The resonance appears in the calculated spectrum due to the mixed character of the wavefunction and borrows intensity from the

PII S0368-2048 (96) 02910-6

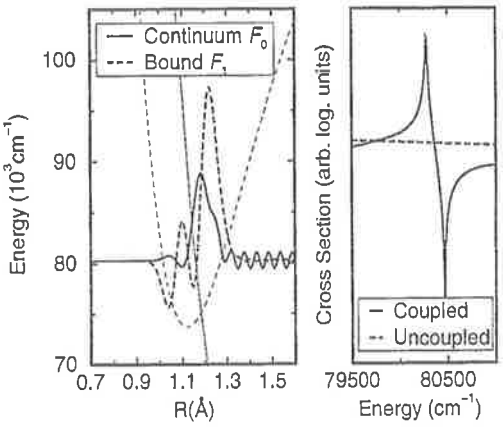

Figure 1. Coupled wavefunctions for a closed (bound) channel interacting with an open (continuum) channel, calculated at the energy of a resonance and shown with their respective potential energy curves. Note that the mixed character of each wavefunction causes the appearance of the resonance in the calculated cross section even if there is no transition moment between the closed channel and the initial state. The resonance is asymmetric.

continuum. Conversely, the continuum loses intensity. The resulting resonance profile is asymmetric.

If more than one term in Eq. (3) contributes to the cross section, then the individual terms may add or subtract, resulting in interference effects.

2.3. CSE model parameters

The CSE model was combined with a least-squares fitting program to match the calculated cross section, instrumentally degraded, to an experimental cross section and/or to the resonance positions and widths. Transition moments and the potential-energy curves of the interaction matrix were adjusted either by linear scaling, or through cubic-spline interpolation. In order to reduce the number of free parameters, it was assumed that the coupling function between each pair of states was independent of the internuclear distance R and transition moments were assumed to be linear functions of R. Initial shapes for potential energy curves were taken from Rydberg-Klein-Rees (RKR) curves or from *ab initio* calculations.

3. EXPERIMENTAL DATA

Gibson *et al.* [8] have experimentally decomposed the photoabsorption spectrum of O_2 into partial cross sections by measuring the fluorescence associated with the appearance of $O(^1D)$ following photodissociation of O_2. Their total and partial cross sections, measured with 2 Å full-width at half-maximum bandwidth, are shown in Fig. 2. The production

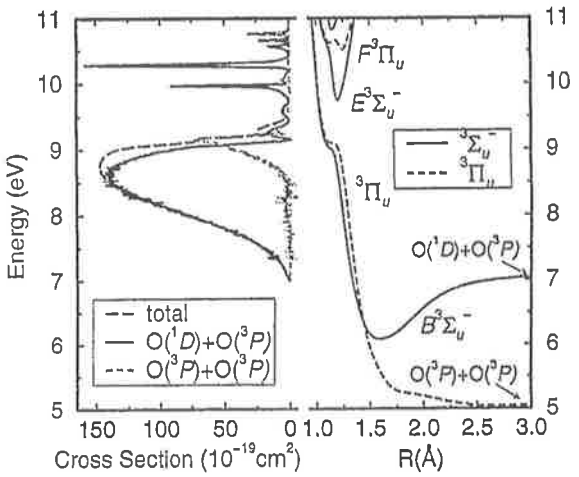

Figure 2. VUV photoabsorption spectrum of O_2 decomposed by measurement of the fluorescence associated with the appearance of $O(^1D)$. The qualitative features of each spectrum are readily associated with the structure of the corresponding adiabatic potential energy curves.

of $O(^1D)$ is predominantly associated with dissociation via $^3\Sigma_u^-$ states, while the difference cross section [total − $O(^1D)$] is associated with dissociation via $^3\Pi_u$ states [13]. These measurements indicate that the peak cross section of the Schumann-Runge continuum ($B^3\Sigma_u^- - X^3\Sigma_g^-$) occurs at a lower energy than would be indicated by the total cross section. The spectral features of the $^3\Pi_u - X^3\Sigma_g^-$ transition are similar in character to the $^3\Sigma_u^- - X^3\Sigma_g^-$ transition, with a short-wavelength sequence of bands of various widths and asymmmetries, and an oscillating continuum that intensifies towards intermediate wave-

lengths. However, the magnitude of the $^3\Pi_u - X^3\Sigma_g^-$ long-wavelength continuum is significantly less than its $^3\Sigma_u^- - X^3\Sigma_g^-$ counterpart.

Each spectrum may be interpreted qualitatively in terms of the adiabatic potential-energy curves shown in Fig. 2. However, for energies above 9 eV the spectra are complex due to the interactions between valence and Rydberg states and can only be explained accurately using the CSE picture.

For the $^3\Sigma_u^- - X^3\Sigma_g^-$ transition, in addition to the partial cross section measurements [8], the calculations were fitted to the temperature dependence of the cross section between 1480 Å and 1740 Å [12] in order to correctly define the inner limb of the $^3\Sigma_u^-$ valence-state potential-energy curve.

4. RESULTS

4.1. $^3\Sigma_u^- - X^3\Sigma_g^-$ CSE calculation

An optimised CSE rotationless ($J = 0$) calculation of the cross section yielding O(^1D) is shown in Fig. 3. together with the measurements [8]. The corresponding potential-energy curves and transition moments are shown in Fig. 4.

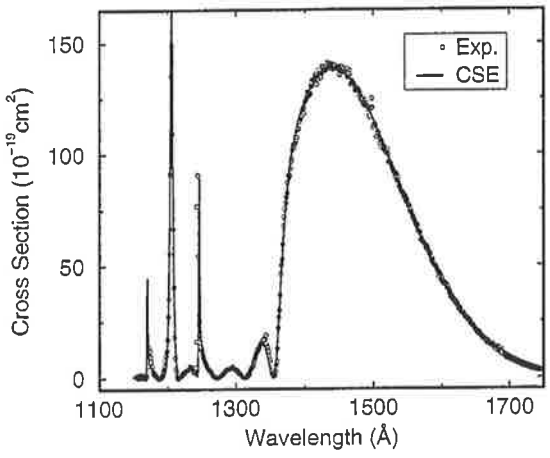

Figure 3. Measured [8] and calculated (CSE) partial photoabsorption cross sections yielding O(^1D). The smooth continuum and resonance structure below 1300 Å including asymmetry and linewidth variations, are reproduced.

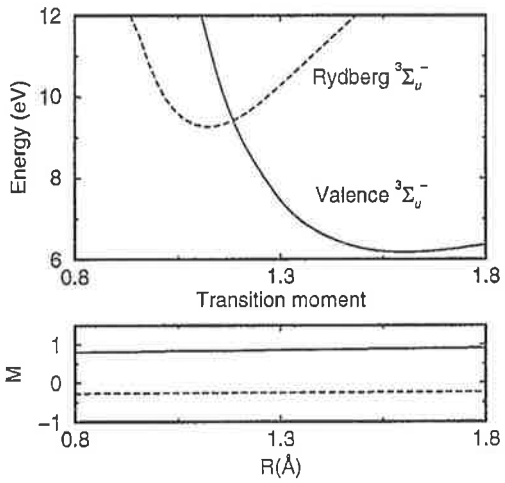

Figure 4. CSE model diabatic potential-energy curves and transition moments for the $^3\Sigma_u^- - X^3\Sigma_g^-$ transitions.

It was found that a single valence electronic state, electrostatically coupled to a single Rydberg electronic state, is sufficient to reproduce the main features of the spectrum. These features include the Schumann-Runge continuum, associated with the valence state, which maximizes near 1440 Å, the rapid fall off to a minimum at 1355 Å, the first subsidiary maximum at 1338 Å and the second maximum at 1293 Å. The resonances associated with the Rydberg state exhibit a large variety of widths and asymmetries which are well reproduced. The longest band at 1244 Å interferes with the underlying continuum and has opposite asymmetry to that of the second band at 1205 Å. For the third band at 1173 Å, the minimal model begins to fail due to the neglect of higher Rydberg states. This is also evidenced by changes in curvature of the deduced potential-energy curves which compensate for the neglected Rydberg states of higher principal quantum number.

The transition moment to the valence state is approximately 3 times the magnitude of the Rydberg-state moment. Thus, the bands associated with the Rydberg state gain intensity from the stronger valence transition.

4.2. $^3\Pi_u - X^3\Sigma_g^-$ CSE calculation

Rotationless CSE calculations fitted to the room-temperature difference cross section [8] are shown in

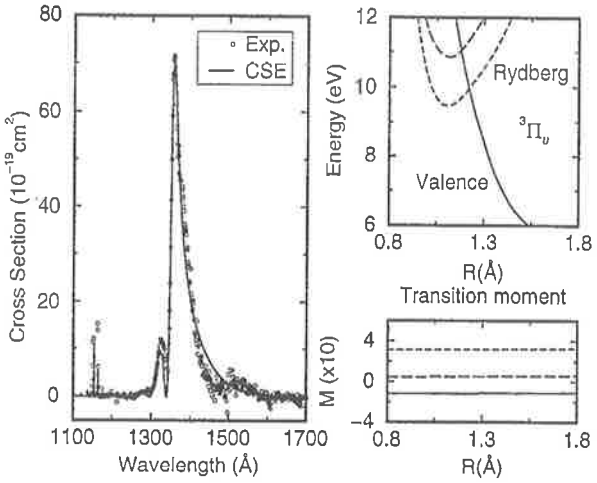

Figure 5. Measured [8] and calculated (CSE) partial photoabsorption cross sections yielding $O(^3P)+O(^3P)$, together with the associated model parameters.

Fig. 5. In this case, a minimum of two Rydberg states was required by the CSE model, otherwise anomalous structure was introduced into the deduced Rydberg potential-energy curve. The calculation matches the measured cross-section well, given the larger experimental uncertainties associated with the difference cross section data. The CSE model reproduces the main broad resonance at 1356 Å, the adjacent minimum at 1343 Å, the first subsidiary maximum at 1326 Å and the second at 1278 Å. The two narrow short-wavelength resonances at 1152 Å and 1162 Å are associated principally with the upper- and lower-energy Rydberg states, respectively.

In contrast to the $^3\Sigma_u^-$ case, the transition moment to the lowest energy Rydberg state is approximately 3 times the magnitude of the valence-state moment. Here, the valence continuum gains some intensity from the stronger Rydberg transition, but the small value for the valence transition moment results in a suppressed long-wavelength continuum relative to that of the $^3\Sigma_u^- - X^3\Sigma_g^-$ transition.

5. CONCLUSIONS

A coupled-channel Schrödinger equation model, which treats the coupling of vibrational wavefunctions that belong to different electronic states, has been fitted to an experimentally-decomposed photoabsorption spectrum of O_2 [8]. The CSE model demonstrates that interactions between electronic states of the molecule result in intensity borrowing, interference and resonance asymmetry.

The general features of the O_2 partial cross sections have been reproduced by simple Rydberg-valence CSE rotationless calculations that incorporate few electronic states. This minimal model has been used to demonstrate that much of the observed structure is simply a consequence of coupling between Rydberg and a valence states of the same symmetry. A more comprehensive calculation would match particular rotational features and fine-structure states and include a larger number of electronic states [14].

REFERENCES

1. H. Lefebvre-Brion and R. W. Field, Perturbations in the spectra of diatomic molecules, Academic Press, Orlando, 1986.
2. E. F. van Dishoeck, M. C. van Hemert, A. C. Allison, and A. Dalgarno, J. Chem. Phys., 81 (1984) 5709.
3. L. Torop, D. G. McCoy, A. J. Blake, J. Wang, and T. Scholz, J. Quant. Spectrosc. Radiat. Transfer, 38 (1987) 9.
4. B. Kim and K. Yoshihara, Phys. Rev. Lett., 73 (1994) 424.
5. J. Wang, D. G. McCoy, A. J. Blake, and L. Torop, J. Quant. Spectrosc. Radiat. Transfer, 38 (1987) 19.
6. A. C. Allison, S. L. Guberman, and A. Dalgarno, J. Geophys. Res., 87 (1982) 923.
7. A. C. Allison, S. L. Guberman, and A. Dalgarno, J. Geophys. Res., 91 (1986) 10193.
8. S. T. Gibson, B. R. Lewis, and J. H. Carver, (unpublished).
9. B. R. Lewis, S. S. Banerjee, and S. T. Gibson, J. Chem. Phys., 102 (1995) 6631.
10. F. H. Mies, Mol. Phys., 41 (1980) 953.
11. B. R. Johnson, J. Chem. Phys., 69 (1978) 4678.
12. S. T. Gibson, H. P. F. Gies, A. J. Blake, D. G. McCoy, and P. J. Rogers, J. Quant. Spectrosc. Radiat. Transfer, 30 (1983) 385.
13. L. C. Lee, T. G. Slanger, G. Black, and R. L. Sharpless, J. Chem. Phys., 67 (1977) 5602.
14. J. P. England, B. R. Lewis, S. T. Gibson and M. L. Ginter, J. Chem. Phys., (submitted 1995).

4.24 Indirect predissociation of the $3p\pi_u f^1\Sigma_u^+$ state of O_2

[44] S. S. Banerjee, B. R. Lewis, S. T. Gibson, J. P. England, and K. G. H. Baldwin, *Journal of Electron Spectroscopy and Related Phenomena* **80**, 17–20 (1996).

Journal of Electron Spectroscopy and Related Phenomena 80 (1996) 17–20

Indirect predissociation of the $3p\pi_u\ f\ ^1\Sigma_u^+$ state of O_2

S. S. Banerjee, B. R. Lewis, S. T. Gibson, J. P. England and K. G. H. Baldwin

Research School of Physical Sciences and Engineering, The Australian National University, Canberra, ACT 0200, Australia

Absolute photoabsorption cross sections for bands of the $3p\pi_u\ f\ ^1\Sigma_u^+ \leftarrow X\ ^3\Sigma_g^-$ transition of $^{16}O_2$ have been measured. The measurements were taken using narrow-bandwidth vacuum ultraviolet radiation generated by third-order frequency mixing in Xe and Kr of excimer-pumped dye laser radiation. The oscillator strengths and predissociation linewidths of the observed bands are found to vary irregularly with vibration, and some bands exhibit predissociation linewidths which increase rapidly with rotation. Theoretical modelling of the spectra using the coupled-channel Schrödinger equations technique shows that the principal channel for predissociation of the f state is the $^3\Sigma_u^-$ valence-state continuum, through an intermediate interaction between the f state and the neighbouring $3p\pi_u$ $^3\Sigma_u^-$ Rydberg state. We also show that there is a significant interference contribution to the strengths of these bands from the $f\ ^1\Sigma_u^+ \leftarrow b\ ^1\Sigma_g^+$ transition.

1. INTRODUCTION

Molecular oxygen plays an important role in the photochemistry of upper atmospheric reactions since it is a critical absorber in the vacuum ultraviolet (VUV) region of the spectrum (below 2000 Å). In the window region (1100 to 1300 Å), the absorption spectrum of O_2 shows complex structure, due to strong interactions between the closely-spaced high-lying molecular states.

In this study, we wish to investigate in detail the interactions of the $3p\pi_u\ f\ ^1\Sigma_u^+$ state of O_2. The diabatic potentials of the molecular states relevant to this study are shown in Fig. 1. Several vibrational bands in the $f\ ^1\Sigma_u^+ \leftarrow X\ ^3\Sigma_g^-$ and $f\ ^1\Sigma_u^+ \leftarrow b\ ^1\Sigma_g^+$ systems have been observed photographically and rotationally analysed previously [1–5]. This study represents the first measurement of the absolute photabsorption cross sections for the (1,0), (3,0) and (4,0) bands of the $f \leftarrow X$ system. The use of a laser system has enabled clear resolution of the rotational structure of these bands, and revealed significant anomalous behaviour. We interpret our measurements using a coupled-channel Schrödinger equations (CSE) model of the $f\ ^1\Sigma_u^+$ state predissociation.

2. EXPERIMENTAL METHOD

A laser based system was used to generate narrow-bandwidth VUV radiation from 1100 to 1300 Å in order to study bands of the $f \leftarrow X$ system. To produce the required VUV radiation, we used techniques of frequency tripling and two-photon resonant four-wave difference-frequency mixing in Xe and Kr, employing a XeCl excimer laser to pump synchronously two dye lasers. The details of this system have been published previously [6].

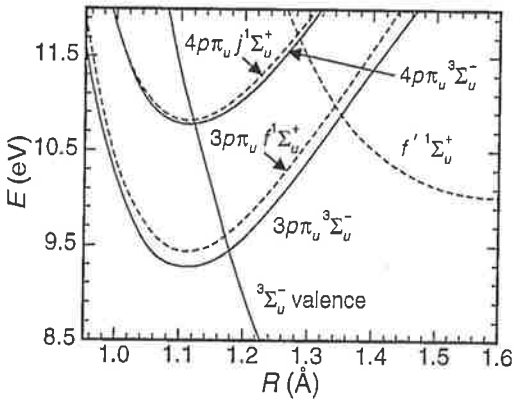

Figure 1. Diabatic potential-energy curves relevant to the predissociation of the $f\ ^1\Sigma_u^+$ state of O_2.

For each band, the wavelength was calibrated by measuring the positions of well known rotational lines of bands of the $A^1\Pi \leftarrow X^1\Sigma^+$ system of CO [7]. It was found that there was a significant periodic error in the wavelength calibration of the dye lasers, and it is believed that this error is due to imperfections in the drive screw for the grating in the laser.

PII S0368-2048 (96) 02912-X

The bandwidth of the generated VUV radiation, determined from measurements of Doppler-limited CO absorption lines, was in the range 0.25 – 0.5 cm^{-1} full-width at half-maximum (FWHM), a significant improvement over the monochromator system used for previous measurements [5].

The absorption cell was fitted with LiF windows and a cooling jacket which allowed measurements to be taken with the cell cooled by liquid nitrogen (effective sample gas temperature 79 ± 0.5 K) to simplify the rotational structure observed.

The incident and transmitted radiation was detected by solar-blind photomultipliers, and background normalisation was achieved using the results of an empty-cell scan taken between each pair of full-cell scans. Absolute photoabsorption cross sections were calculated using the Beer-Lambert law.

3. THEORY

It has previously been proposed [5] that the bound $f\,^1\Sigma_u^+$ state is indirectly predissociated by the $^3\Sigma_u^-$ valence-state continuum. In this basic model, the $f\,^1\Sigma_u^+$ state undergoes a spin-orbit interaction with the $3p\pi_u\,^3\Sigma_u^-$ Rydberg state, which in turn has a strong electrostatic coupling with the $^3\Sigma_u^-$ valence state continuum. It was suggested by Lewis *et al.* [5] that this basic model may be improved by introducing another source of oscillator strength whereby the forbidden $f\,^1\Sigma_u^+ \leftarrow X\,^3\Sigma_g^-$ transition borrows some strength from the dipole-allowed $f\,^1\Sigma_u^+ \leftarrow b\,^1\Sigma_g^+$ transition through strong spin-orbit coupling between the metastable b and ground X states, both arising from the $\ldots\pi_g^2$ configuration.

To obtain a model applicable over a wider energy range, it is necessary to include the effects of the $f'\,^1\Sigma_u^+$ valence state and the $4p\pi_u\,^3\Sigma_u^-$ and $4p\pi_u\,^1\Sigma_u^+$ Rydberg states. Potential-energy curves for the states of this extended six-potential model are shown in Fig. 1.

In a similar manner to the basic model [5], we do not include the $^3\Pi_u$ states in our extended model, since they do not predissociate the f state and the $^3\Pi_u \leftarrow X\,^3\Sigma_g^-$ transitions give only a small contribution to the continuum cross section in this energy range. However, although it is clear on energetic grounds that the f' state does not contribute to the predissociation of the f state [5], the f' state is responsible for a perturbation in the (4,0) band of the $f \leftarrow X$ transition [6], and thus should be included in the extended model. The couplings and the $^3\Sigma_u^- \leftarrow X\,^3\Sigma_g^-$ transition moments in the extended model were based on the previous study [5], with the values for the $4p$-complex states scaled according to $n^{*-3/2}$ [8], except for the spin-orbit couplings which were taken to be independent of n^*.

4. RESULTS

4.1. Absolute photoabsorption cross section measurements

Figure 2 shows the measured photoabsorption cross section for a typical band of the $f \leftarrow X$ transition. A

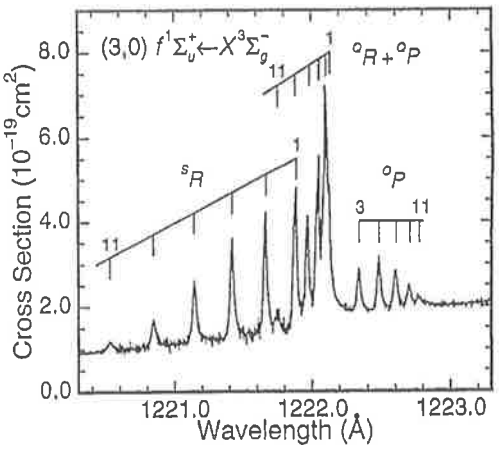

Figure 2. Photoabsorption cross section measurements (T = 79K).

striking feature of this and other bands of the $f \leftarrow X$ system is the observation of strongly asymmetric lineshapes for the rotationally resolved lines. In the example shown in Fig. 3, the Fano quantum-interference effect [9] is constructive at energies lower than the centre of the resonance, and destructive at higher energies.

4.2. Band-model fitting

Spectroscopic and lineshape parameters were obtained from the measured cross sections by fitting an empirical band model similar to that described previously [5]. For each rotational line, we used an asymmetric line profile based on the lineshape of Fano and Cooper [9]. After modification to allow for the

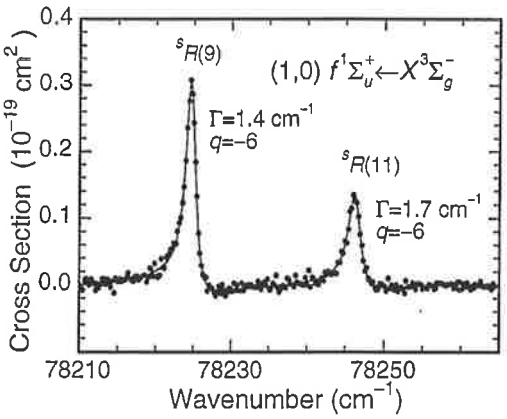

Figure 3. An example of asymmetric lineshapes in resolved rotational structure (T = 79K). A linear background has been subtracted.

Doppler contribution to the lineshapes, and convolution (in transmission) with a Gaussian instrument function, the model cross section appropriate to the experimental conditions was least-squares fitted to the measured cross section, enabling the determination of the spectroscopic and lineshape parameters associated with the bands of the $f \leftarrow X$ system.

The preliminary results of the band-model fitting are given in Table 1, where we have included the (2,0) band parameters of Lewis *et al.* [5]. For these fits, we assumed that the parameters were rotation-independent, except for the predissociation linewidth (discussed in Sec. 4.4). From Table 1, it is clear that the predissociation linewidths, oscillator strengths and lineshape asymmetries $(1/q)$ vary irregularly with v'. It should be noted that the (4,0) band shows exceptional behaviour, with extremely narrow and symmetric lines for low J'.

4.3. CSE calculations

The coupled-channel Schrödinger equations (CSE) approach used to develop the models presented in this paper has been described in detail elsewhere [5].

Initial calculations using the basic model for the predissociation of the f state [5] were unable to satisfactorily describe all of the bands of the $f \leftarrow X$ system, highlighting the need to use the extended six-potential model described in Sec. 3. Preliminary calculations using the extended model have confirmed, in support of the contention of Lewis *et al.* [5], that the $f \leftarrow b$ transition provides a significant source of strength to the $f \leftarrow X$ transition. The (1,0) band of the $f \leftarrow X$ system was particularly sensitive to this effect, with its calculated oscillator strength being halved when the effects of the $f \leftarrow b$ transition were included in the model.

Best agreement between the calculations and the measurements was found for spin-orbit couplings of 100 cm^{-1} between the $^1\Sigma_u^+$ and $^3\Sigma_u^-$ Rydberg states, and an effective transition moment borrowed from the $f \leftarrow b$ transition of 0.0045 a.u. The results of the CSE calculations are shown in Table 1, and are seen to be in good agreement with the measurements.

4.4. Rotational predissociation linewidths

It should be noted that the indirect predissociation of the $f^1\Sigma_u^+$ state by the $^3\Sigma_u^-$ valence-state continuum involves a sequence of homogeneous perturbations [8] and, thus, the interaction matrix elements have no explicit dependence on J'. However, it was found that some bands in the $f \leftarrow X$ system exhibit predissociation linewidths which increase rapidly with rotation, as illustrated in Fig. 4. Preliminary modelling

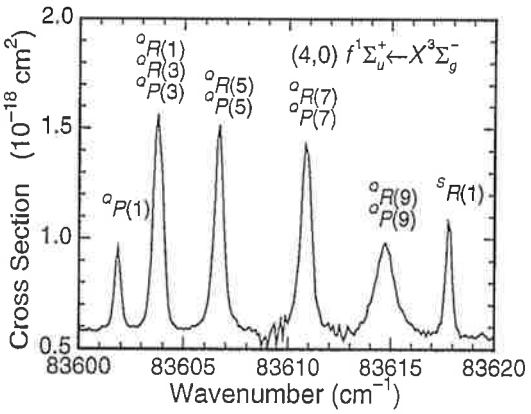

Figure 4. Rotationally resolved lines showing rapidly increasing predissociation linewidth with J' (T = 297 K).

suggests that there is an orbit-rotation interaction between the $f^1\Sigma_u^+$ state and the neighbouring Rydberg $^1\Pi_u$ state, which in turn has a strong electrostatic interaction with the dissociative valence $^1\Pi_u$ state. This represents an alternative predissociation pathway for the $f^1\Sigma_u^+$ state. Although this pathway does not contribute any strength to the $f \leftarrow X$ transition, it has a marked effect on the rotational predissociation

Table 1
Comparison of the measured and calculated rotationless predissociation linewidths, oscillator strengths and lineshape-asymmetries $(1/q)$ for the $(v',0)\ f\,^1\Sigma_u^+ \leftarrow X\,^3\Sigma_g^-$ bands of O_2. The results for $v' = 2$ have been given previously [5].

v'	Γ (cm^{-1} FWHM)		$f \times 10^6$		$1/q$	
	Meas.	Calc.	Meas.	Calc.	Meas.	Calc.
1	0.67±0.05	0.60	1.24±0.04	1.20	−0.20±0.01	−0.019
2	4.4±0.2	4.7	34±1	32	−0.33±0.01	−0.33
3	1.37±0.07	1.12	9.2±0.2	8.8	−0.090±0.007	−0.102
4	∼ 0	0.002	14±1	15	∼ 0	∼ 0

linewidths, since it can be shown [8] that the predissociation linewidth is expected to vary as $\Gamma = \Gamma_0 + \Gamma_J J(J+1)$ for an orbit-rotation interaction. We have found that the variation of predissociation linewidth with J' for the (4,0) band can be fitted very well using this quadratic functional form.

5. CONCLUSIONS

Absolute photoabsorption cross sections have been measured for bands of the $3p\pi_u f\,^1\Sigma_u^+ \leftarrow X\,^3\Sigma_g^-$ system. The use of a narrow-bandwidth laser system has enabled resolution of the rotational structure of these bands, revealing asymmetric lineshapes which can be described by Fano profiles. The $f \leftarrow X$ bands have oscillator strengths, lineshape asymmetries and predissociation linewidths which vary irregularly with vibration. In some of the bands, the predissociation linewidths were observed to increase rapidly with rotation.

The variation of oscillator strengths, lineshape asymmetries and predissociation linewidths with vibration can be explained by extending the previously published model [5] for indirect predissociation of the f state via the $^3\Sigma_u^-$ states to include the $f'\,^1\Sigma_u^+$ valence state and the $4p\pi_u\ ^1\Sigma_u^+$ and $^3\Sigma_u^-$ Rydberg states. Modelling of the measurements for the weaker bands confirms the suggestion [5] that lower-state spin-orbit mixing, whereby some of the $f \leftarrow X$ oscillator strength is borrowed from the $f\,^1\Sigma_u^+ \leftarrow b\,^1\Sigma_g^+$ transition leading to an interference effect, must be included for a complete description.

It is suggested that the strong dependence of the predissociation linewidth on J' can be explained by including a second indirect predissociation channel in the model, namely an interaction of the f state with the strongly mixed Rydberg and valence $^1\Pi_u$ states.

REFERENCES

1. M. Ogawa and K. R. Yamawaki, Can. J. Phys., 47 (1969) 1805.
2. F. Alberti, R. A. Ashby, and A. E. Douglas, Can. J. Phys., 46 (1968) 337.
3. M. Ogawa, Can J. Phys., 53 (1975) 2703.
4. D. H. Katayama, S. Ogawa, M. Ogawa, and Y. Tanaka, J. Chem. Phys., 67 (1977) 2132.
5. B. R. Lewis, S. S. Banerjee, and S. T. Gibson, J. Chem. Phys., 102 (1995) 6631.
6. B. R. Lewis, J. P. England, R. J. Winkel, Jr., S. S. Banerjee, P. M. Dooley, S. T. Gibson, and K. G. H. Baldwin, Phys. Rev. A, (in press, 1995).
7. S. G. Tilford and J. D. Simmons, J. Phys. Chem. Ref. Data, 1 (1972) 147.
8. H. Lefebvre-Brion and R. W. Field, Perturbations in the Spectra of Diatomic Molecules, Academic Press, Orlando, 1986.
9. U. Fano and J. W. Cooper, Rev. Mod. Phys., 40 (1968) 441.

4.25 Narrow-bandwidth VUV laser measurements of fine-structure predissociation linewidths in the Schumann-Runge bands of O_2

[45] P. M. Dooley, B. R. Lewis, S. T. Gibson, and K. G. H. Baldwin, *Journal of Electron Spectroscopy and Related Phenomena* **80**, 29–32 (1996).

Journal of Electron Spectroscopy and Related Phenomena 80 (1996) 29–32

Narrow-bandwidth VUV laser measurements of fine-structure predissociation linewidths in the Schumann-Runge bands of O_2

P. M. Dooley, B. R. Lewis, S. T. Gibson, and K. G. H. Baldwin

Research School of Physical Sciences and Engineering, The Australian National University, Canberra, ACT 0200, Australia

Fine-structure predissociation linewidths have been measured for the Schumann-Runge bands of O_2 ($B\,^3\Sigma_u^- \leftarrow X\,^3\Sigma_g^-$). Using two excimer-pumped dye lasers, radiation was generated in the 1800 Å region by four-wave mixing in Xe, achieving a bandwidth of $\sim 0.10\ \mathrm{cm}^{-1}$ full-width at half-maximum, and resolving lines to the Doppler limit. The predissociation linewidths are found to vary significantly with vibration, rotation and fine-structure. A predissociation model which includes spin-orbit interactions between the $B\,^3\Sigma_u^-$ state and the repulsive $1\,^1\Pi_u$, $2\,^3\Sigma_u^+$ and $1\,^5\Pi_u$ states, and spin-orbit and L-uncoupling interactions with the repulsive $1\,^3\Pi_u$ state, provides a good description of the measurements.

1. INTRODUCTION

The Schumann-Runge (SR) system of O_2, $B\,^3\Sigma_u^- \leftarrow X\,^3\Sigma_g^-$, plays an important role in the photochemistry of the terrestrial atmosphere. It controls the depth of penetration of solar vacuum ultraviolet (VUV) radiation, and predissociation of the discrete levels of the $B\,^3\Sigma_u^-$ state is an important source of energetic oxygen atoms in the atmosphere. Accurate knowledge of the predissociation linewidths of the SR bands (1750 – 2050 Å) is essential for photochemical modelling of the upper atmosphere.

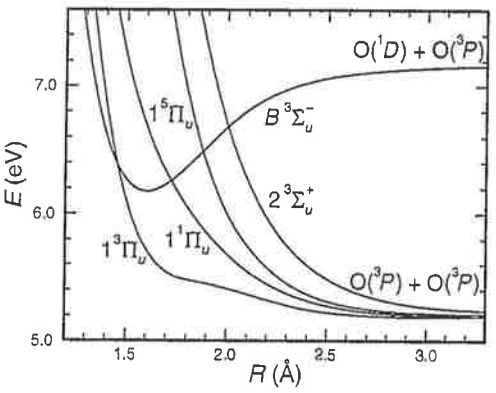

Figure 1. Potential-energy curves of O_2 relevant to the $B\,^3\Sigma_u^-$-state predissociation. Energies are given relative to the minimum in the $X\,^3\Sigma_g^-$ ground state potential-energy curve.

The SR bands have been the subject of much study; the many spectroscopic investigations have been reviewed by Yoshino *et al.* [1], while Lewis *et al.* [2] have recently reviewed work on the $B\,^3\Sigma_u^-$-state predissociation. Figure 1 shows potential-energy curves for the B state and the other states which perturb the B state leading to its predissociation. The B-state curve is a Rydberg-Klein-Rees (RKR) potential determined by Lewis *et al.* [3], while the repulsive curves are the *ab initio* calculations of Partridge *et al.* [4] ($1\,^3\Pi_u$, $1\,^5\Pi_u$) and Partridge [5] ($1\,^1\Pi_u$, $2\,^3\Sigma_u^+$).

The four repulsive states shown in Fig. 1 perturb the B state through spin-orbit interactions and the $1\,^3\Pi_u$ state also perturbs the B state via spin-electronic and L-uncoupling mechanisms [6,7]. These interactions cause predissociation of every vibrational level and are expected to produce irregular perturbations in the spectroscopic and triplet-splitting constants of the B state.

Although the SR predissociation rates are expected to vary significantly with the triplet fine-structure level [2], very few measurements of fine-structure-resolved predissociation linewidths have been reported [2,8]. The linewidths for the broader B-state levels with $v = 3 - 8$ are comparable with, or exceed, the fine-structure splittings, making it difficult to determine fine-structure widths, due to line overlap. However, most of the narrower levels, with $v > 12$, can be resolved with an experiment of sufficient resolving power. In this paper, following a suggestion by Lewis *et al.* [2], we present preliminary results of a

PII S0368-2048 (96) 02915-5

comprehensive study in which fine-structure-specific linewidths were measured for the B-state levels with $v = 9 - 18$.

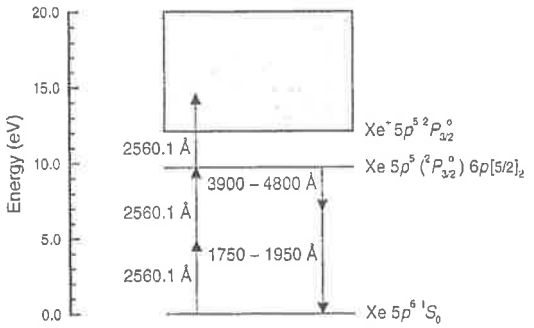

Figure 2. Xe energy level diagram, showing the four-wave mixing scheme.

2. EXPERIMENTAL METHOD

Radiation was generated using two-photon-resonant four-wave difference-frequency mixing (FWDFM) in Xe [9]. The corresponding energy-level diagram is shown in Fig. 2 and the experimental set up is shown in Fig. 3. The two lasers used were Lambda Physik FL3002 pulsed dye lasers pumped by an EMG201 Lambda Physik excimer laser. The output of one dye laser was frequency doubled in a BBO I crystal to reach the $6p[5/2]_2$ two-photon resonance in Xe, while the other laser was scanned between 3900 Å and 4800 Å, producing tunable VUV radiation between 1750 Å and 1950 Å. The two beams were focussed into the Xe cell using an off-axis lens of nominal focal length 25 cm. FWDFM can be phase-matched for either positive or negative dispersive media, and so a Xe pressure could always be chosen (usually in the range 70 – 90 Torr) to optimise phase-matching for any VUV wavelength. After the Xe cell the light passed through a 0.2 m monochromator which discriminated against non-VUV light. The VUV radiation was then divided by a beamsplitter. The reflected radiation was directed into a solar-blind photomultiplier tube (PMT) to monitor the incident intensity, while the transmitted beam passed through the absorption cell (which was filled with O_2 to pressures between 0.4 and 700 Torr) and was detected by a second PMT. The output pulses from the PMTs were processed by a boxcar gated integrator and the signals were averaged over fifty laser pulses. Each wavelength scan was done three times, with the absorption cell evacuated during the second scan to enable background correction. The detector signal was divided by the monitor signal to account for shot to shot variations, and slow drifts were compensated for by averaging the first and third (full) scans. The full-cell ratios were divided by the empty-cell ratios to give absolute cell transmittances and photoabsorption cross sections were calculated from the Beer–Lambert law.

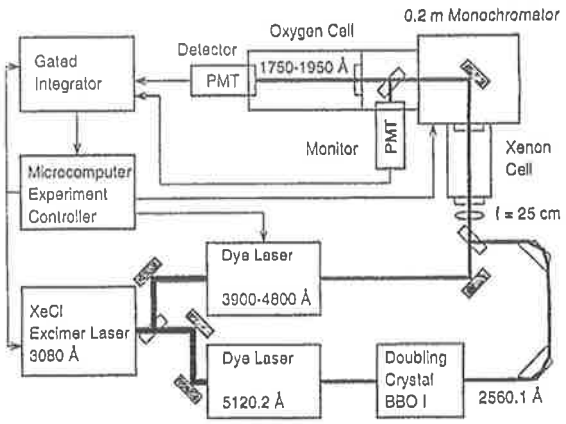

Figure 3. Experimental apparatus

Use of intracavity étalons reduced the nominal dye-laser bandwidth to 0.04 cm^{-1}, but it was found that the bandwidth of the resultant four-wave mixing signal (incorporating five fundamental dye-laser photons) was $\sim$ 0.10 cm^{-1} full-width at half-maximum (FWHM). This value varied significantly ($\pm$30%) from day to day, so it was necessary to monitor the bandwidth regularly using narrow reference lines. The instrumental bandwidth was deduced daily from a measurement of one of the reference lines, using a Voigt line-profile fitting program with the Doppler and predissociation linewidth components fixed at the known values. Two reference lines were used during this study. Their predissociation linewidths were determined using curve-of-growth analysis [10], which is independent of the instrumental bandwidth, and were found to be 0.051$\pm$0.007 cm^{-1} FWHM for the (14,0) $R_1(21)$ line and 0.069$\pm$0.010 cm^{-1} FWHM for

the (16,0) $R_1(23)$ line. Absolute wavenumber calibration was achieved by comparison with the measured wavenumbers of Yoshino *et al.* [1] for selected sharp, unblended lines of the SR system.

3. PREDISSOCIATION MODEL

The predissociation model used in this work is based on that developed by Julienne and Krauss [6] and Julienne [7] and optimised by Lewis *et al.* [2]. Briefly, the model employs a RKR potential for the B state and represents the four repulsive states in Fig. 1 as exponential potentials. Predissociation linewidths are calculated using the Golden rule. This results in a thirteen parameter model: four matrix elements for the spin-orbit interaction of the $B\,^3\Sigma_u^-$ state with each of the repulsive $1\,^1\Pi_u$, $2\,^3\Sigma_u^+$, $1\,^3\Pi_u$ and $1\,^5\Pi_u$ states; one for the **L**-uncoupling interaction with the $1\,^3\Pi_u$ state, and eight parameters for the crossing points and slopes of the four repulsive states. The matrix element for the **L**-uncoupling interaction is J-dependent and is expected to produce significant effects at high rotation.

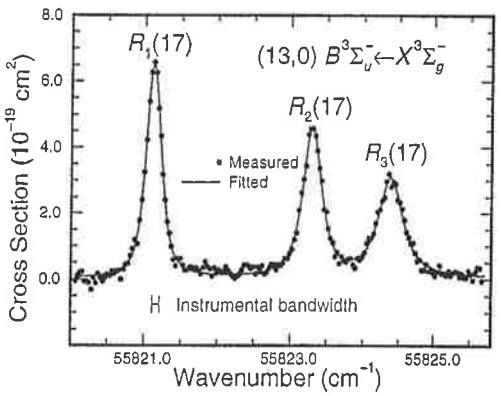

Figure 4. A representative experimental scan showing the measured photoabsorption cross section for the $(13,0)R(17)$ fine-structure triplet.

4. RESULTS

Figure 4 shows a representative experimental scan of the $(13,0)R(17)$ fine-structure triplet. The fine-structure is well resolved, and the difference in width between the fine-structure components is clearly visible. Lorentzian linewidths were deduced from such scans by fitting instrumentally-degraded Voigt profiles to each line, enabling specific account to be taken of the Doppler component (~ 0.012 cm^{-1} FWHM).

It was found that the Lorentzian component of the experimental linewidth had a pressure dependence due to collisional broadening. This was quantified by measuring absorption lines from the $v = 1$ vibrational level of the $X\,^3\Sigma_g^-$ ground state of O_2 ("hot bands") which were then compared with the corresponding lines from the $v = 0$ level of the ground state. As the population of the $v = 1$ level of the ground state is much lower than that of the $v = 0$ level, measurements of a given upper-state level could be made in very different pressure regimes at similar absorbances. This work gave a value for the collision-broadening coefficient of ~ 0.2 cm^{-1}/atm, confirming the result of Lewis *et al.* [11], which was determined at much higher pressures. It was necessary to correct the Lorentzian linewidths determined at high pressures for this effect.

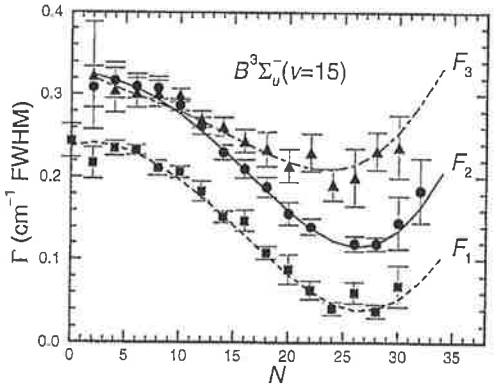

Figure 5. Measured and calculated fine-structure-specific predissociation linewidths as a function of rotation for the $v = 15$ level of the $B\,^3\Sigma_u^-$ state of O_2.

Figure 5 shows preliminary results for the fine-structure-specific linewidths of the (15,0) band as a function of rotation. These are the first comprehensive fine-structure-resolved measurements for this band and they exhibit strong dependence on N and fine-structure. It is particularly notable that the difference

between the F_1 and F_3 linewidths increases with rotation. This effect is specifically dependent on the interference term involving the vibronic L-uncoupling (η) and spin-orbit (ξ) interactions with the $1\,^3\Pi_u$ state [2]. The results in Fig. 5 indicate that $\eta\xi > 0$.

Figure 5 also shows good agreement between our experimental results and the predictions of the semi-empirical predissociation model. The model has been optimised to our preliminary results for $v = 9 - 18$ and the results of Lewis *et al.* [2] for $v = 0 - 8$, which were based on the measurements of Cosby *et al.* [8] and Yoshino *et al.* [12]. The model parameters were varied only slightly from previous values [2] to obtain this agreement, the most significant difference being an improved value for the ratio η/ξ of 0.025 compared with the previous value of 0.019 [2].

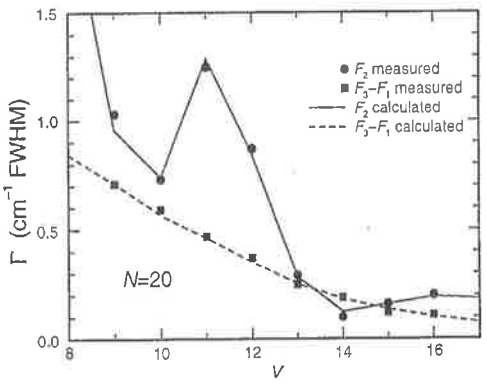

Figure 6. Vibrational dependence of the $N = 20$ F_2 and $F_3 - F_1$ predissociation linewidths.

Figure 6 shows the vibration dependence of the F_2 predissociation linewidths and the $F_3 - F_1$ difference-linewidths for N=20. For this rotation, the $B\,^3\Sigma_u^-$-state coupling is close to Hund's case (b) and the $F_3 - F_1$ widths are dominated by the smoothly varying $\eta\xi$ cross term associated with the inner-crossing $1\,^3\Pi_u$ state. Conversely, the F_2 widths are dominated by spin-orbit contributions, including those from the outer-limb crossings of the B state which result in rapid oscillation of linewidth with v. Figure 6 also shows the predictions of the present model which are in excellent agreement with the measurements.

5. CONCLUSIONS

Preliminary results are presented from the first detailed study of fine-structure-specific SR predissociation linewidths with $v' > 2$, measured using a narrow-bandwidth VUV laser source. We also present calculations based on the predissociation model of Lewis *et al.* [2] with slightly modified parameters, which are in good agreement with the experimental measurements presented. Our new value for η/ξ is 0.025, significantly higher than the previous value of 0.019 [2].

The measurements presented here, and further measurements in progress, are being undertaken as part of a collaborative project involving groups from SRI International, California, the Harvard–Smithsonian Centre for Astrophysics, Massachusetts and The Photon Factory, Tsukuba, in which predissociation linewidths obtained by three distinct narrow-bandwidth techniques (laser-based photoabsorption spectroscopy, laser-induced fluorescence spectroscopy, and VUV Fourier-transform spectroscopy) will be critically compared.

REFERENCES

1. K. Yoshino, D. E. Freeman, and W. H. Parkinson, J. Phys. Chem. Ref. Data, 13 (1984) 207.
2. B. R. Lewis, S. T. Gibson, and P. M. Dooley, J. Chem. Phys., 100 (1994) 7012.
3. B. R. Lewis, L. Berzins, J. H. Carver, and S. T. Gibson, J. Quant. Spectrosc. Radiat. Transfer, 36 (1986) 187.
4. H. Partridge, C. W. Bauschlicher, S. R. Langhoff, and P. R. Taylor, J. Chem. Phys., 95 (1991) 8292.
5. H. Partridge, (private communication, 1993).
6. P. S. Julienne and M. Krauss, J. Mol. Spectrosc., 56 (1975) 270.
7. P. S. Julienne, J. Mol. Spectrosc., 63 (1976) 60.
8. P. C. Cosby, H. Park, R. A. Copeland, and T. G. Slanger, J. Chem. Phys., 98 (1993) 5117.
9. R. Hilbig and R. Wallenstein, IEEE J. Quantum Electron., QE-19 (1983) 194.
10. I. M. Vardavas, J. Quant. Spectrosc. Radiat. Transfer, 49 (1993) 119.
11. B. R. Lewis, L. Berzins, C. J. Dedman, T. T. Scholz, and J. H. Carver, J. Quant. Spectrosc. Radiat. Transfer, 39 (1988) 271.
12. K. Yoshino, J. R. Esmond, A. S.-C. Cheung, D. E. Freeman, and W. H. Parkinson, Planet. Space Sci., 40 (1992) 185.

4.26 Electronic transition moments for the Herzberg I bands of O_2

[46] J. P. England, B. R. Lewis, and S. T. Gibson,
Canadian Journal of Physics **74**, 185–193 (1996).

Electronic transition moments for the Herzberg I bands of O_2

J.P. England, B.R. Lewis, and S.T. Gibson

Abstract: Recently published extensive high-resolution measurements of absolute integrated photoabsorption cross sections for rotational lines of the ($v' = 4 - 11$, $v'' = 0$) bands of the O_2 Herzberg I system have been fitted using general rotational line-strength formulae for $^3\Sigma_u^+ \leftarrow {}^3\Sigma_g^-$ transitions. Good fits were obtained using only three independent electronic transition-moment parameters that accounted for transition strength borrowed from electric-dipole-allowed transitions through spin-orbit and orbit-rotation interactions involving both upper and lower states of the transition. Absolute values of transition-moment parameters have been obtained, corresponding to R-centroids from 1.29 to 1.32 Å (1 Å = 10^{-10} m). Band oscillator strengths derived from the calculated integrated line strengths are in good agreement with most experimental measurements. Principal electronic matrix elements have been estimated by assuming that strength is borrowed from only two electric-dipole-allowed transitions.

Résumé : Une formule générale, basée sur l'intensité des lignes de rotation dans les transitions $^3\Sigma_u^+ - {}^3\Sigma_g^-$, est ajustée pour reproduire les sections efficaces intégrées de photoabsorption pour les lignes rotationnelles des bandes ($v' = 4 - 11$, $v'' = 0$) de O_2 (système de type Herzberg I) obtenues de mesures de haute résolution récemment publiées. On obtient un excellent accord en n'utilisant que trois paramètres indépendants, rattachés aux moments de transition électronique et qui rendent compte des forces de transition pour les transitions permises dipolaires électriques, en tenant compte des interactions spin-orbite rotation pour les états initial et final de la transition. Nous avons obtenu les valeurs absolues des paramètres de moment de transition. Ils correspondent à des centroïdes R de 1,29 à 1,32 Å(1 Å= 10^{-10}m). Les forces d'oscillateur déduites des intensités de ligne intégrées sont en bon accord avec les mesures. Les prinicipaux éléments de matrice électronique sont évalués en supposant que l'intensité découle simplement de deux transitions dipolaires permises.

[Traduit par la rédaction]

1. Introduction

The Herzberg I system, $A^3\Sigma_u^+ \leftarrow X^3\Sigma_g^-$, can be seen in the photoabsorption spectrum of O_2 as a series of weak bands from 2429 to 2700 Å (1 Å = 10^{-10} m) and as the major part of a weak continuum between 2000 and 2429 Å. The bands are a dominant feature of the ultraviolet night air-glow spectrum [1], while dissociation in the continuum provides an important source of atomic oxygen for the production of ozone in the stratosphere [2]. To model the photochemistry of the atmosphere, a knowledge of the $A^3\Sigma_u^+ \leftarrow X^3\Sigma_g^-$ transition strength is required.

Transitions $^3\Sigma^+ - {}^3\Sigma^-$ are electric-dipole forbidden by the $+ \not\rightarrow -$ symmetry selection rule, but they borrow strength from allowed transitions through the spin-orbit interactions $^3\Sigma^\pm - {}^3\Sigma^\mp$ and $^3\Pi - {}^3\Sigma^\pm$ with $\Delta\Omega = 0$, and through the orbit-rotation (L-uncoupling) interactions $^3\Pi - {}^3\Sigma^\pm$ with $\Delta\Omega = \pm 1$, involving both upper and lower states of the transition. Vibrational bands from these transitions consist of 13 branches, the relative intensities of the branches varying by orders of magnitude and depending on the relative strengths of the electronic interactions.

Received November 16, 1995. Accepted December 21, 1995.

J.P. England,[1] B.R. Lewis, and S.T. Gibson. Research School of Physical Sciences and Engineering, The Australian National University, Canberra, ACT 0200, Australia.

[1] Corresponding author: **Telephone:** (61) 6 249 3327; **FAX:** (61) 6 249 0390; **e-mail:** Julian.England@anu.edu.au

Can. J. Phys. **74**: 185–193 (1996). Printed in Canada / Imprimé au Canada

The first attempt to calculate rotational line strengths for the 13 branches of a $^3\Sigma^+ - {}^3\Sigma^-$ transition was carried out by Present [3] who considered pure Hund's case (b) $^3\Sigma^\pm$ states with transition strengths arising from either spin-orbit or rotational mixing with $^3\Pi$ states. More recently, line strengths were derived by Lewis and Gibson [4] for intermediate case (a) - (b) $^3\Sigma^\pm$ states in the presence of $^3\Sigma^\pm - {}^3\Sigma^\mp$ and $^3\Pi - {}^3\Sigma^\pm$ spin-orbit interactions, but neglecting orbit-rotation interactions. General formulae including effects of spin-orbit and orbit-rotation interactions have been derived by Bellary and Balasubramanian [5]. We used these formulae for the calculations of the present work. A computer program has been developed independently by Huestis et al. [6] to calculated rotational line intensities and energies for a number of electric-dipole-forbidden transitions, including $^3\Sigma^+ - {}^3\Sigma^-$ transitions.

Laboratory measurements of the $A^3\Sigma_u^+ \leftarrow X^3\Sigma_g^-$ absorption bands are difficult because of their small cross section and small rotational line widths. For many years, the only measurements of rotational line strength were relative values estimated from photographic plates (*a*) by Herzberg [7] for $N'' = 3$ and 13 lines of 11 branches of the (10,0) band,[2] and (*b*) by Hasson and Nicholls [9] for $N'' = 13$ lines of 7 branches of the same band. These two sets of data are in reasonable agreement. The data of Herzberg [7] have been used by Lewis and Gibson [4] ($N'' = 3$ and 13) and Huestis et al. [6] ($N'' = 13$) to obtain estimates of relative electronic

[2] The assignment of this band by Herzberg [7] as the (9, 0) band was corrected by Broida and Gaydon [8].

transition-moment parameters for the $A^3\Sigma_u^+ \leftarrow X^3\Sigma_g^-$ transition.

Recently, Yoshino et al. [10] measured integrated absorption cross sections for individual rotational lines of 10 branches of the (4,0)–(11,0) bands using high-resolution Fourier transform spectroscopy. In addition, integrated absorption cross sections for selected lines of the (8,0) and (9,0) bands have been measured by Bao et al. [11] using a laser-based apparatus. The results of Bao et al. [11] are in reasonable agreement with those of Yoshino et al. [10]. These are the only rotationally resolved absolute line-strength measurements for the $A^3\Sigma_u^+ \leftarrow X^3\Sigma_g^-$ bands of O_2.

In this paper, we present absolute electronic transition-moment parameters obtained by fitting the measurements of Yoshino et al. [10] using the general line-strength formulae of Bellary and Balasubramanian [5]. Comparisons are made with the ab initio transition moments of Klotz and Peyerimhoff [12] and the relative moments of Huestis et al. [6]. Room-temperature band oscillator strengths, determined from the calculated line strengths, are compared with the results from other studies, and values are presented for various electronic interaction matrix elements derived from the electronic transition-moment parameters by assuming that the transition strength is gained through interactions with only two other electronic states.

2. Rotational line-strength formulae

The $^3\Sigma^+ - {}^3\Sigma^-$ line-strength formulae given by Bellary and Balasubramanian (Tables 1 and 3 of ref. 5) are very general, having 13 independent electronic transition-moment parameters. In the case of the $A^3\Sigma_u^+ \leftarrow X^3\Sigma_g^-$ transition, the parallel moment Z models strength borrowed from $A^3\Sigma_u^+ \leftarrow {}^3\Sigma_g^+$ and $^3\Sigma_u^- \leftarrow X^3\Sigma_g^-$ transitions through $^3\Sigma_g^+ - X^3\Sigma_g^-$ and $A^3\Sigma_u^+ - {}^3\Sigma_u^-$ spin-orbit interactions, respectively, and includes second-order contributions from $^3\Pi_u \leftarrow {}^3\Pi_g$ transitions through $A^3\Sigma_u^+ - {}^3\Pi_u$ and $X^3\Sigma_g^- - {}^3\Pi_g$ spin-orbit interactions. The perpendicular moments X and Y model strength borrowed from $A^3\Sigma_u^+ \leftarrow {}^3\Pi_g$ and $^3\Pi_u \leftarrow X^3\Sigma_g^-$ transitions through $^3\Pi_g - X^3\Sigma_g^-$ and $A^3\Sigma_u^+ - {}^3\Pi_u$ spin-orbit interactions, respectively, and include second-order contributions from $^3\Pi_u \leftarrow {}^3\Sigma_g^+$ transitions through $A^3\Sigma_u^+ - {}^3\Pi_u$ and $^3\Sigma_g^+ - X^3\Sigma_g^-$ spin-orbit interactions, and from $^3\Sigma_u^- \leftarrow {}^3\Pi_g$ transitions through $A^3\Sigma_u^+ - {}^3\Sigma_u^-$ and $^3\Pi_g - X^3\Sigma_g^-$ spin-orbit interactions. Strength borrowed from $^3\Pi_u \leftarrow {}^3\Sigma_g^\pm$ and $^3\Sigma_u^\pm \leftarrow {}^3\Pi_g$ transitions through orbit-rotation effects is modelled using the parameters M_1, M_2, M_{ef}, M_{fe}, N_e, and N_f, while strength borrowed from $^3\Pi_u \leftarrow {}^3\Pi_g$ transitions through second-order interactions involving both orbit-rotation and spin-orbit coupling is represented by the moments η_0, η_1, ζ_0, and ζ_1.

Bellary and Balasubramanian [5] formulated their theory using Hund's case (a) basis functions. Since the $A^3\Sigma_u^+$ and $X^3\Sigma_g^-$ states are intermediate between Hund's cases (a) and (b), we require values for the mixing coefficients [13] c_J and s_J of the case (a) functions. These were determined from the spectroscopic constants recommended by Yoshino et al. [14] for the $A^3\Sigma_u^+$ state, and from the rotational energies of Amiot and Verges [15] for the ground $X^3\Sigma_g^-$ state.

Prior to our detailed calculations, we compared line strengths calculated using the formulae of Bellary and Balasubramanian [5] with the results of Huestis et al. [6] who assumed a model for the transition that used only three independent transition-moment parameters. In terms of the parameters of Bellary and Balasubramanian [5], their model corresponds to setting $X = Y$, $M_1 = M_2 = M_{ef} = M_{fe}$, and all other parameters apart from Z equal to zero.[3] Table 2 of Huestis et al. [6] contains calculated relative values for separate contributions to the line intensities from $^3\Sigma^\pm - {}^3\Pi$ spin-orbit, $^3\Sigma^\pm - {}^3\Pi$ orbit-rotation and $^3\Sigma^\pm - {}^3\Sigma^\mp$ spin-orbit interactions for the $N'' = 13$ lines of all 13 branches of the (10,0) band. Satisfactory agreement with the separate contributions of Huestis et al. [6] was obtained using the formulae of Bellary and Balasubramanian [5]; however, the comparison revealed differences in the signs of the rotational contributions to the ${}^QR_{23}$ and ${}^SR_{21}$ branches. Since these contributions are very small, the discrepancies do not affect significantly the final relative transition moments or oscillator strengths for the Herzberg I bands.

We have corrected the rotational line-strength formulae obtained by Bellary and Balasubramanian [5] for the special cases involving $J' = 0$ or $J'' = 0$. The $P_{i2}(1)$ lines ($i = 1$ or 3) should have strengths $2(X+\zeta_0)^2$ instead of $2(M_2+\zeta_0)^2$, while $R_{2j}(0)$ lines ($j = 1$ or 3) should have strengths $2(Y+\eta_0)^2$ instead of $2(M_1+\zeta_0)^2$. Only one such line, ${}^QR_{23}(1)$, exists in each band of the $A \leftarrow X$ system since symmetric rotational levels are absent for the homonuclear isotopomer $^{16}O_2$.

To relate the rotational line strengths $S_{J'J''}$ of Bellary and Balasubramanian [5] to the integrated line cross sections, we used expressions for the line oscillator strength:

$$f_{J'J''} = \frac{m_e c^2}{\pi e^2 N_{J''}} \int_{\text{line}} \sigma(\nu)\, d\nu$$

$$= \frac{8\pi^2 m_e c}{3he^2 g''} \left(\frac{\nu_{J'J''} q_{v'J'v''J''} S_{J'J''}}{2J''+1} \right) \qquad (1)$$

where $N_{J''}$ is the relative population of the J'' rotational level, $g'' = (2S''+1)(2-\delta_{0,\Lambda''}) = 3$ is the lower state statistical weight, m_e and e are the mass and charge of an electron, c is the speed of light, $\sigma(\nu)$ is the absorption cross section, ν and $\nu_{J'J''}$ are energies in wave numbers, h is Planck's constant, and $q_{v'J'v''J''}$ is the Franck–Condon factor. Here, $S_{J'J''}$ includes rotational and electronic parts of the dipole-moment matrix elements. Inserting values for the fundamental constants in (1) gives

$$\int_{\text{line}} \sigma(\nu)\, d\nu = 2.688 \times 10^8\, N_{J''} \left(\frac{\nu_{J'J''} q_{v'J'v''J''} S_{J'J''}}{2J''+1} \right) \qquad (2)$$

where the cross section is in cm^2, ν and $\nu_{J'J''}$ are in cm^{-1}, and $S_{J'J''}$ is in atomic units (1 au = 1 $(ea_0)^2$ = 7.188×10^{-59} C^2m^2).

Equation (2) has been used in the present work with two approximations. First, $\nu_{J'J''}$ varies by <1.5% across each vibrational band, so it has been replaced by an effective average value for each band.[4] Second, the variation of $q_{v'J'v''J''}$ with

[3] The parameters $\mu^{(t)}_{\Omega'\Omega''}$ used by Huestis et al. [6] in their model of the Herzberg I intensities are related to those of Bellary and Balasubramanian [5] as follows: $\mu^{(0)}_{10}/\mu^{(0)}_{11} = \mu^{(0)}_{01}/\mu^{(0)}_{11} = \sqrt{2}X/Z$; and $\mu^{(1)}_{11}/\mu^{(0)}_{11} = \mu^{(1)}_{00}/\mu^{(0)}_{11} = \mu^{(1)}_{1-1}/\mu^{(0)}_{11} = \sqrt{2}M_1/Z$. Absolute values were not given by Huestis et al. [6].

[4] The ${}^QR_{23}(9)$ line positions were used for all bands except the (11, 0) band for which the ${}^QR_{23}(5)$ line position was chosen.

Table 1. Calculated values for the rotationless Franck–Condon factor $q_{v'v''}$ and the relative rotational factor $\beta_{v'v''}$ for the $A^3\Sigma_u^+ \leftarrow X^3\Sigma_g^-$ $(v',0)$ bands.

Band	$q_{v'v''} \times 10^3$	$\beta_{v'v''} \times 10^4$
4,0	0.4309	−1.496
5,0	0.8149	−1.579
6,0	1.3245	−1.704
7,0	1.8884	−1.901
8,0	2.3796	−2.244
9,0	2.6290	−2.894
10,0	2.4494	−4.482
11,0	1.7080	−8.665

Note: Values for $q_{v'v''}$ and $\beta_{v'v''}$ were determined from calculated Franck–Condon factors $q_{v'J'v''J''}$ using the relation $q_{v'J'v''J''} = q_{v'v''}[1 + \beta_{v'v''}J''(J''+1)]$.

J' and J'' due to changes in the vibrational wave functions caused by the centrifugal terms in the Schrödinger equation is approximately linear, and, therefore, we have assumed

$$q_{v'J'v''J''} = q_{v'v''}[1 + \beta_{v'v''}J''(J''+1)] \tag{3}$$

where $q_{v'v''}$ and $\beta_{v'v''}$ depend only on the vibrational quantum numbers. This expression is similar to that used by Lewis et al. [16] to analyze the Schumann–Runge bands of O_2. Franck–Condon factors were calculated from RKR potential-energy curves of the A state derived from the spectroscopic constants suggested by Yoshino et al. [14], and the X state derived from the data of Cosby.[5] Values of $q_{v'v''}$ and $\beta_{v'v''}$, given in Table 1, were determined from calculations for $J' = J'' = 0$ and $J' = J'' = 20$ for all bands except the (11,0) band for which $J' = J'' = 0$ and $J' = J'' = 10$ were used. It was found that the rotational variation of the Franck–Condon factors increases from 6% at $v' = 4$ to 19% at $v' = 10$.

The $^3\Sigma^\pm - {}^3\Pi$ orbit-rotation coupling introduces strength to the bands in a way that causes the normal line-strength sum rules to be invalid. In addition, the Franck–Condon factors vary with J as described above. As a consequence, some definitions give band oscillator strengths [10] that are dependent on the gas temperature:

$$f_{v'v''} = \frac{m_e c^2}{\pi e^2 N_{v''}} \int_{\text{band}} \sigma(\nu)\, d\nu \tag{4}$$

where $N_{v''}$ is the relative population of the v'' vibrational level. A more fundamental quantity, the rotationless band oscillator strength $f^{(0)}_{v'v''}$, can be determined using the relation

$$f^{(0)}_{v'v''} = \frac{8\pi^2 m_e c}{3he^2} \nu_0 q_{v'v''} \frac{\Sigma R_e^2}{g''}$$

$$= 1.0125 \times 10^{-6} \nu_0 q_{v'v''}(Z^2 + 4X^2) \tag{5}$$

where $\Sigma R_e^2 = Z^2 + 4X^2$ is the sum of the squares of electronic (rotationless) transition moments, as defined by Whiting and Nicholls [17], in atomic units, and ν_0 is the band origin in wave numbers (tabulated as T_0 by Yoshino et al. [14]). The parameter $f^{(0)}_{v'v''}$ is independent of temperature, is not affected by rotational perturbations, and, when correctly normalized, should be continuous across the dissociation limit with the differential oscillator strength for the continuum [18].

Finally, it should be noted that the transition-moment parameters defined by Bellary and Balasubramanian [5] do not follow the convention of Whiting and Nicholls [17] when used with the equations given in this section. The difference is a factor of $\sqrt{2}$ in the definition of the spin-orbit part of the parallel transition moment: $Z/\sqrt{2}$ is equal to the transition moment of Whiting and Nicholls [17].

3. Results

The integrated rotational-line absorption cross sections of Yoshino et al. [10] for each band were fitted with the formulae of Bellary and Balasubramanian [5] by iteratively adjusting the 13 transition-moment parameters to minimize the sum of the squared deviations. Each deviation was weighted by dividing by the corresponding experimental uncertainty.[6] Strengths of blended lines were excluded from the fits except those for which Yoshino et al. [10] estimated the strengths using observed branching ratios. Lines showing rotational perturbations, reported by Yoshino et al. [14] in the (4,0), (7,0), (9,0), and (11,0) bands, were also omitted.[7] The perturbation of the (11,0) band has a large effect on the measured line strengths: a satisfactory fit to the strengths of this band could only be obtained by omitting those lines having upper levels F_1' and F_2' with $N' > 7$, the perturbed lines having strengths lower than those predicted by the calculations.

We found that only three independent transition-moment parameters, Z, $X = Y$, and $M_1 = M_2 = M_{ef} = M_{fe}$ (we have denoted this parameter as M), were necessary for an accurate description of the rotational line-strength measurements. All other parameters could be set to zero with no loss in accuracy. Our final calculations were done with only these three parameters varied. This result implies that

(*i*) spin-multiplet intervals of the $^3\Pi$ states participating in the perturbations are small compared with the relevant electronic term separations [5], and

(*ii*) second-order cross terms can be neglected.

Huestis et al. [6] also limited their calculations to vary only these parameters in modelling the $N'' = 13$ lines of the $A \leftarrow X$ (10,0) band and suggested that the $A^3\Sigma_u^+ \leftarrow X^3\Sigma_g^-$ transition

[5] P.C. Cosby, private communication 1995.

[6] Yoshino et al. [10] give uncertainties of 2% for $S = 4 \times 10^{-24}$ cm^2 cm^{-1}, and 8% for $S = 2.5 \times 10^{-26}$ cm^2 cm^{-1} (actual value given was $S = 2.5 \times 10^{-27}$ cm^2 cm^{-1} but this is much less than any measured values, and, therefore, was assumed to contain a typographical error). We assumed that relative experimental uncertainties varied with the line strength S according to $\Delta S/S = 1/(aS) + b$, where $a = 6.625 \times 10^{26}$ cm^{-2}/cm^{-1} and $b = 0.0196$.

[7] It should also be noted that the $^QQ_3(1)$ lines assigned by Yoshino et al. [14] for all bands apart from (4, 0) and (11, 0) have been incorrectly assigned since they are forbidden by the $J = 0 \not\leftrightarrow J = 0$ selection rule.

Fig. 1. Comparison of fitted integrated line strengths (lines) with the experimental data of Yoshino et al. [10] (points) for ten branches of the $A^3\Sigma_u^+ \leftarrow X^3\Sigma_g^-$ (5, 0) band.

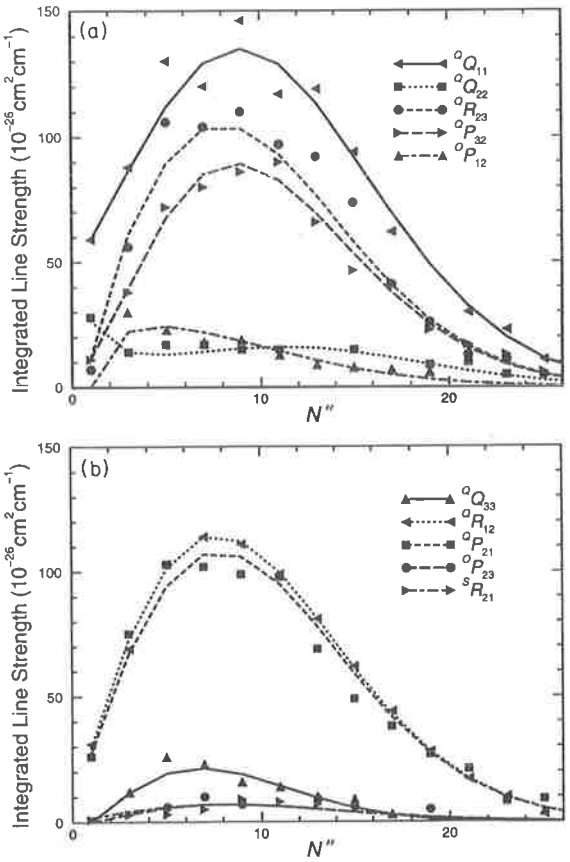

Fig. 2. Comparison of fitted integrated line strengths (lines) with the experimental data of Yoshino et al. [10] (points) for ten branches of the $A^3\Sigma_u^+ \leftarrow X^3\Sigma_g^-$ (10, 0) band.

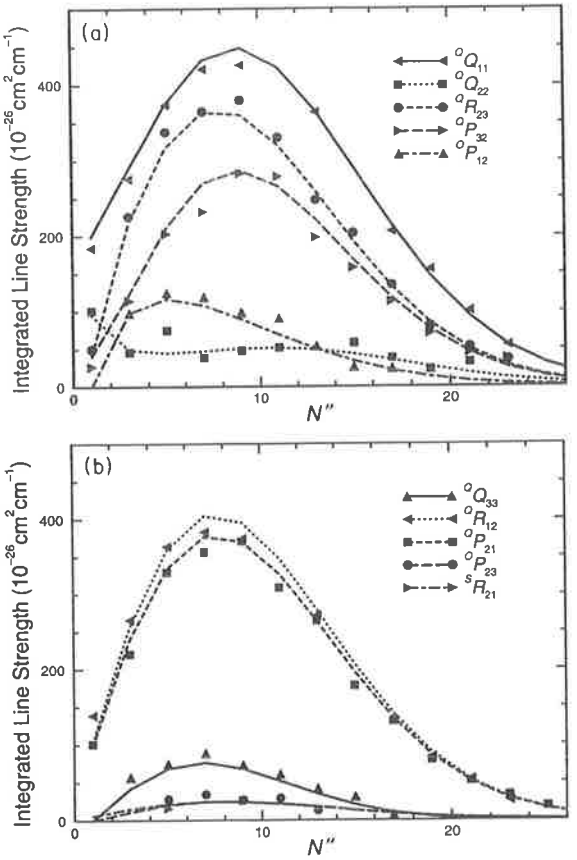

strength is borrowed from the electric-dipole-allowed transitions $B^3\Sigma_u^- \leftarrow X^3\Sigma_g^-$ and $A^3\Sigma_u^+ \leftarrow 1^3\Pi_g$, principally through the upper and lower state interactions $A^3\Sigma_u^+ - B^3\Sigma_u^-$ and $X^3\Sigma_g^- - 1^3\Pi_g$, respectively, as implied by the ab initio calculations of Klotz and Peyerimhoff [12].

In general, differences between the fitted and experimental values are larger than the experimental uncertainties and the χ^2 values are ~50 times the number of degrees of freedom. However, examination of the experimental data shows that the scatter in the measured line strengths is much larger than the estimated uncertainties of Yoshino et al. [10]. Figures 1 and 2 show integrated strengths for rotational lines of the (5,0) and (10,0) bands as examples of the results obtained from the fitting process, which included a total of 684 experimental line strengths for eight bands. The lines not reported by Yoshino et al. [10] generally have calculated line strengths $<15 \times 10^{-26}$ cm^2 cm^{-1}. However, we have found that the calculations give strengths for some lines of the $^sQ_{31}$ branches that are reasonably large ($>20 \times 10^{-26}$ cm^2 cm^{-1} for the (10,0) band) so that the lines should be observable experimentally. Lines of this branch were not reported by Yoshino et al. [14] or Borrell et al. [19], but were reported by Herzberg [7].

The transition-moment parameters obtained for each of the bands are given in Table 2 with corresponding R-centroids calculated from the RKR potentials described above. The moments Z and X show a slight increase as v' is increased or as the R-centroid is decreased, as can be seen in Fig. 3, in agreement with the variation predicted ab initio by Klotz and Peyerimhoff [12]. The values of Klotz and Peyerimhoff [12] are ~40% higher for Z and ~40% lower for X than the present values.[8] Values of the relative moments of Huestis et al. [6] for the (10,0) band, $X/Z = 0.369$ and $M/Z = 0.00953$ written in our notation, are in good agreement with our values of 0.407 ± 0.018 and 0.0098 ± 0.0009, respectively. This

[8] There is some confusion about the definitions of the transition-moment parameters. We have assumed the relations between the parameters of Klotz and Peyerimhoff [12] and those of Bellary and Balasubramanian [5] are $Z = \sqrt{2}U_9$ and $X = U_8 = U_{12}$, where U_9, U_8, and U_{12} represent the moments for $A^3\Sigma_u^+(\Omega = \pm 1) \leftarrow X^3\Sigma_g^-(\Omega = \pm 1)$, $A^3\Sigma_u^+(\Omega = \pm 1) \leftarrow X^3\Sigma_g^-(\Omega = 0)$, and $A^3\Sigma_u^+(\Omega = 0) \leftarrow X^3\Sigma_g^-(\Omega = \pm 1)$, respectively. Bates [20] seems to have interpreted the parameters of Klotz and Peyerimhoff [12] in the same way.

Table 2. Electronic transition-moment parameters and R-centroids for the $A^3\Sigma_u^+ \leftarrow X^3\Sigma_g^-$ $(v',0)$ bands.

Band	$Z(10^{-3}$ au)	$X(10^{-3}$ au)	$M(10^{-5}$ au)	R-centroid (Å)[a]
4,0	0.963 ± 0.046	0.363 ± 0.024	0.93 ± 0.15	1.3180
5,0	0.942 ± 0.027	0.385 ± 0.014	0.97 ± 0.10	1.3121
6,0	0.986 ± 0.037	0.379 ± 0.019	0.92 ± 0.12	1.3068
7,0	0.964 ± 0.030	0.388 ± 0.016	0.94 ± 0.10	1.3019
8,0	0.966 ± 0.032	0.388 ± 0.017	0.99 ± 0.10	1.2977
9,0	0.986 ± 0.022	0.390 ± 0.012	0.95 ± 0.08	1.2941
10,0	0.999 ± 0.027	0.407 ± 0.014	0.98 ± 0.09	1.2912
11,0	0.983 ± 0.052	0.405 ± 0.026	0.99 ± 0.23	1.2893
Average[b]	0.974 ± 0.011	0.389 ± 0.006	0.96 ± 0.04	1.3000

Note: Values for the electronic transition-moment parameters were obtained from fits to the integrated cross sections of rotational lines measured by Yoshino et al. [10]. Only the relative signs of the moments can be determined. Uncertainties ($\pm 3\sigma$) are statistical uncertainties derived from the fitting process.

[a] R-centroids have been calculated from the RKR potential-energy curves described in the text.

[b] Averages were weighted using the uncertainties given in the Table.

Table 3. Comparison of experimental and model integrated line strengths (10^{-26} cm^2 cm^{-1}) for the $N'' = 13$ lines of the $A^3\Sigma_u^+ \leftarrow X^3\Sigma_g^-$ (10,0) band.

Branch	Expt (Ref. 10)	Present work	Ref. 4[a]	Ref. 21[a]	Ref. 6[a]
$^QQ_{11}$	364	366		311	336
$^QQ_{22}$	66[b]	49.2		94	50
$^QQ_{33}$	42	34.5		63	26
$^QR_{12}$	272	280	298	254	277
$^QR_{23}$	248	260	203	193	282
$^QP_{21}$	265	264	210	197	255
$^QP_{32}$	198	222	231	253	218
$^OP_{12}$	54	49.9	60	126	54
$^OP_{23}$	13	17.8	47	32	24
$^OQ_{13}$		0.1	1	19	0.7
$^SQ_{31}$		7.7	11	9.7	5
$^SR_{21}$		17.5	51	32	23
$^SR_{32}$		2.1	5	4.3	6
RMS dev.[c]		6.7	35	28	11

[a] Values have been normalized by setting the sum of model strengths equal to the sum of experimental strengths for the branches where both columns have entries.

[b] Blended line, not included in the present fits.

[c] Root-mean-square deviations weighted by experimental uncertainties.

level of agreement is surprising considering the limited data upon which they [6] based their model.

Our fitted integrated line strengths for the $N'' = 13$ lines of the (10,0) band are given in Table 3 with the results from other line-strength models and the measured values of Yoshino et al. [10]. Relative intensities of the ^QQ lines were not calculated by Lewis and Gibson [4] because these

Fig. 3. Electronic transition-moment parameters (solid circles), derived from fits to the integrated line strengths of Yoshino et al. [10] for the $A^3\Sigma_u^+ \leftarrow X^3\Sigma_g^-$ $(v' = 4 - 11, 0)$ bands: (*a*) Z; (*b*) X; and (*c*) M. The ab initio results of Klotz and Peyerimhoff [12] for Z and X (continuous lines) have been normalized for comparison with the present values. (Footnote 8 gives the relation between the values of Klotz and Peyerimhoff [12] and the parameters Z and X).

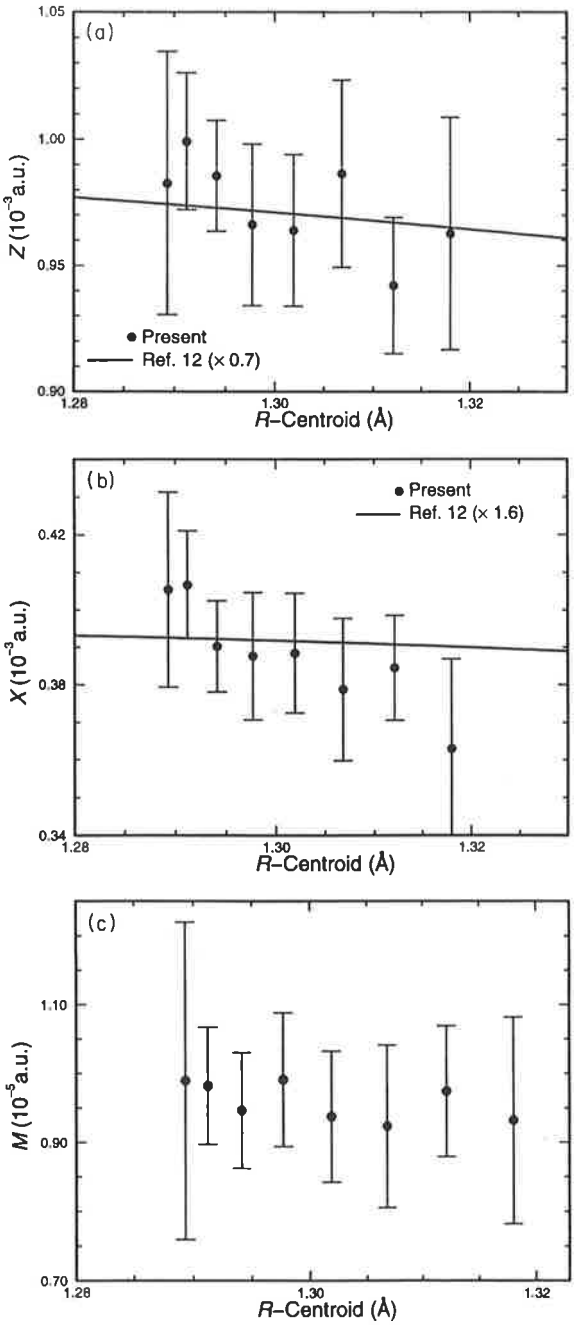

Table 4. Room-temperature band oscillator strengths $f_{v'v''}$ and rotationless band oscillator strengths $f^{(0)}_{v'v''}$ for the $A^3\Sigma_u^+ \leftarrow X^3\Sigma_g^-$ $(v',0)$ bands.

	$f_{v'v''} \times 10^{10}$						$f^{(0)}_{v'v''} \times 10^{10}$	
Band	Present[a]	Ref. 10[b]	Ref. 22	Ref. 9	Ref. 6[c]	Ref. 11[d]	Present[e]	Ref. 20[f]
4,0	0.252 ± 0.019	0.243	0.246	0.30 ± 0.06			0.240	0.344
5,0	0.496 ± 0.023	0.498	0.487	0.538 ± 0.08			0.470	0.686
6,0	0.846 ± 0.052	0.828	0.834	0.798 ± 0.12			0.812	1.17
7,0	1.212 ± 0.063	1.220	1.24	1.24 ± 0.19			1.16	1.71
8,0	1.549 ± 0.082	1.550	1.63	1.39 ± 0.21	0.88	1.71 ± 0.15	1.49	2.23
9,0	1.750 ± 0.068	1.710	1.85	1.4 ± 0.28	1.08	1.66 ± 0.15	1.71	2.64
10,0	1.687 ± 0.071	1.640	1.77	1.2 ± 0.24	0.93		1.68	2.42
11,0	0.94 ± 0.09	0.798	1.25	1.0 ± 0.3	0.68		1.16	0.840

[a] Uncertainties ($\pm 3\sigma$) are statistical.

[b] Uncertainties estimated at 2%.

[c] These are the experimental results of Ref. 6, not their recommended values. See the text footnote 10.

[d] Uncertainties ($\pm 3\sigma$) do not include uncertainties involved in the determination of $f_{v'v''}$ using a spectral simulation program.

[e] Uncertainties are the same as those given for the present values of $f_{v'v''}$.

[f] Values have been calculated from the spontaneous transition probabilities tabulated by Bates [20]. See the text footnote 8.

branches were known to be the most affected by the neglect of orbit-rotation interactions. The results of Cann and Nicholls [21] are based on an empirical adjustment of the formulae of Lewis and Gibson [4], made with no theoretical justification. Understandably, since ours are the only calculations explicitly fitted to the measurements of Yoshino et al. [10], the best agreement with the experimental values is obtained in the present work.

The band oscillator strength $f_{v'v''}$, which depends on temperature through the J''-dependent quantities, as described above, has been determined by summing the calculated integrated strengths of all rotational lines from the 13 branches[9] and using (4) with $N_{v''} = 0.9995$ at $T = 295$ K. Table 4 contains our oscillator strengths and those reported in other studies. Apart from the value for the (11,0) band, our oscillator strengths are close to, or slightly higher than, those of Yoshino et al. [10], presumably because of the inherent inclusion of weak lines not observed in the experimental work. Our oscillator strength for the (11,0) band, 18% higher than the value given by Yoshino et al. [10], includes strength lost through the perturbation of rotational lines with $N'' > 7$. The results of Hasson et al. [22] were obtained from the relative emission band strengths of Degen and Nicholls [23], normalized to their measured (7,0) absorption band strength. Apart from the (11,0) band, the differences between the present oscillator strengths and those of Hasson et al. [22] are <6%. The differences between our values and those of Hasson and Nicholls [9], based purely on absorption measurements, are larger, but still generally less than the combined errors. The experimental oscillator strengths of Huestis et al. [6] are significantly lower than the results from all other studies.[10] The results of Bao et al. [11] are based on measurements of only six peaks in the cross section for the (8,0) band and 17 peaks for the (9,0) band. Despite this, the agreement between their band oscillator strengths and the present values is satisfactory.

Band oscillator strengths were calculated at a number of different temperatures using the transition moments determined in this study. Differences from 295 K values are −1.6% at 77 K and +3.4% at 500 K for the (4,0) band, and +0.9% at 77 K and −1.9% at 500 K for the (10,0) band. These results show that the effects of the increase in the orbit-rotation contribution and the decrease in the relative Franck–Condon factor with increasing J'' partly cancel to produce only small variations of $f_{v'v''}$ with temperature.

Values for the rotationless band oscillator strength $f^{(0)}_{v'v''}$, included in Table 4, are, apart from the (11,0) value, less than the corresponding $f_{v'v''}$ values, with an average difference of ~4%. This is largely because $f^{(0)}_{v'v''}$ does not include strength gained through orbit-rotation interactions. For the (11,0) band, however, the value of $f^{(0)}_{v'v''}$ is larger than $f_{v'v''}$, which includes the effects of the reduction in the number of rotational lines due to the onset of dissociation near $N' = 15$. The rotationless oscillator strengths derived from spontaneous transition probabilities which Bates [20] calculated from the transition moments of Klotz and Peyerimhoff [12] are about 40% higher than the present results, reflecting the difference between the ab initio and present values for Z.[8]

4. Interaction matrix elements

The results of Klotz and Peyerimhoff [12] show that the

[9] The sum for the (11, 0) band included calculated integrated line strengths of rotational lines with upper levels $N' < 17$ for F_1' and F_2' levels, and $N' < 15$ for F_3' levels. According to Yoshino et al. [10], these are the only levels below the dissociation limit.

[10] These are not the recommended values of Huestis et al. [6]. More recent results obtained using the same experimental system with narrower laser bandwidths give larger oscillator strengths (private communication, T.G. Slanger, 1995).

dominant sources of transition strength for the $A^3\Sigma_u^+ \leftarrow X^3\Sigma_g^-$ transition are the allowed $B^3\Sigma_u^- \leftarrow X^3\Sigma_g^-$ and $A^3\Sigma_u^+ \leftarrow 1^3\Pi_g$ transitions, through the interactions $B^3\Sigma_u^- - A^3\Sigma_g^+$ and $1^3\Pi_g - X^3\Sigma_g^-$.[11] Therefore, the values of transition-moment parameters derived in this work, and given in Table 2, can be used to estimate values of the interaction matrix elements between these states. The present results show that Z, X, and M have the same sign; however, it must be noted that the signs of individual matrix elements cannot be determined because they depend on an arbitrary choice of phase in the molecular wave functions [25]. The moments and interaction elements are related through the equations [5]

$$Z = \sqrt{2}\,\frac{\langle B^3\Sigma_{1u}^- | \boldsymbol{H}^{SO} | A^3\Sigma_{1u}^+ \rangle}{E(B^3\Sigma_u^-) - E(A^3\Sigma_u^+)} \langle B^3\Sigma_u^- | \mu_z | X^3\Sigma_g^- \rangle \tag{6}$$

$$X = \frac{\langle 1^3\Pi_{1g} | \boldsymbol{H}^{SO} | X^3\Sigma_{1g}^- \rangle}{E(1^3\Pi_g) - E(X^3\Sigma_g^-)} \langle 1^3\Pi_g | \mu_+ | A^3\Sigma_u^+ \rangle \tag{7}$$

and

$$M = \frac{-\langle 1^3\Pi_{2g} | B\boldsymbol{L}^+ | X^3\Sigma_{1g}^- \rangle}{E(1^3\Pi_g) - E(X^3\Sigma_g^-)} \langle 1^3\Pi_g | \mu_+ | A^3\Sigma_u^+ \rangle \tag{8}$$

where $\boldsymbol{H}^{SO}$ is the spin-orbit operator, $B\boldsymbol{L}^+$ is the rotation-independent part of the orbit-rotation operator, E is the energy of the indicated electronic state, and μ_z and $\mu_+ = \mu_x + i\mu_y$ are molecule-fixed components of the electric-dipole operator. The following observations can be made.

1. The mean value of $|Z|$ determined in this work (0.974×10^{-3} au) is appropriate to an R-centroid of 1.30 Å. Since $|\langle B^3\Sigma_u^- | \mu_z | X^3\Sigma_g^- \rangle| = 0.81$ au (determined by Lewis and Gibson [4] from experimental work), and the $B - A$ energy separation of our RKR potentials is 1.83×10^4 cm^{-1} at $R = 1.30$ Å, the spin-orbit matrix element deduced from (6) is $|\langle B^3\Sigma_{1u}^- | \boldsymbol{H}^{SO} | A^3\Sigma_{1u}^+ \rangle| = 15.6$ cm^{-1}. This is in satisfactory agreement with the value of -20.7 cm^{-1} obtained by interpolation of the calculations of Klotz and Peyerimhoff [12], but differs substantially from the value calculated ab initio by Julienne [26] of 1.4 cm^{-1} at 1.588 Å.[12]

2. No experimental data exist for the $1^3\Pi_g$ state. However, using (7) and (8) with the average values of X and M from Table 2 appropriate to $R = 1.30$ Å, we obtain

$$\frac{X}{M} = \frac{\langle 1^3\Pi_{1g} | \boldsymbol{H}^{SO} | X^3\Sigma_{1g}^- \rangle}{-\langle 1^3\Pi_{2g} | B\boldsymbol{L}^+ | X^3\Sigma_{1g}^- \rangle} = 40.5 \tag{9}$$

This gives the ratio of spin-orbit and orbit-rotation matrix elements based solely on the experimental results and shows that the matrix elements have opposite signs.

3. If we use theoretical values [12] for the $1^3\Pi_g$ potential-energy curve and the $1^3\Pi_g - X$ spin-orbit matrix element, then we can obtain values for the orbit-rotation matrix elements and the unknown transition moment. Our best estimate of the separation of the X and $1^3\Pi_g$ states is the difference between the separation of the RKR potentials of the B and X states (5.797×10^4 cm^{-1} at 1.30 Å) and the separation of the B and $1^3\Pi_g$ states as determined from the potentials of Klotz and Peyerimhoff [12] (-3.5×10^3 cm^{-1} at 1.30 Å). Using with this the ab initio value [12] of 81.6 cm^{-1} for the spin-orbit interaction matrix element and $X/M = 40.5$, we get $|\langle 1^3\Pi_{2g} | B\boldsymbol{L}^+ | X^3\Sigma_{1g}^- \rangle| = 2.0$ cm^{-1} and $|\langle 1^3\Pi_g | \mu_+ | A^3\Sigma_u^+ \rangle| = 0.26$ au. Our estimated value for the orbit-rotation matrix element and the ab initio value for the spin-orbit matrix element are in surprisingly good agreement with values estimated using the single-configuration and pure-precession [27] approximations in the Appendix.

Finally, it should be re-emphasized that these estimates are based on the assumption that the $B^3\Sigma_u^- \leftarrow X^3\Sigma_g^-$ and $A^3\Sigma_u^+ \leftarrow 1^3\Pi_g$ transitions are the only major contributors to the strength of the Herzberg I bands.

5. Conclusions

Comprehensive high-resolution measurements [10] of absolute integrated photoabsorption cross sections for rotational lines of the Herzberg I $A^3\Sigma_u^+ \leftarrow X^3\Sigma_g^-$ ($v' = 4 - 11, 0$) bands of O_2 have been analyzed using appropriate rotational line-strength formulae [5] to obtain values of the parallel and perpendicular electronic transition-moment parameters. This is the first quantitative analysis of rotational line strengths to obtain absolute values for the transition moments and the first analysis to include data from more than one vibrational band. The measured line strengths were fitted accurately using only three independent transition-moment parameters to model the effects of spin-orbit (Z for the parallel component and X for the perpendicular component) and orbit-rotation (M) interactions. The values of Z and X show small variations with upper state vibration and R-centroid that are consistent with the variations present in ab initio calculations [12]. M does not vary significantly with R-centroid. The values of Z and X obtained in this work differ by -40% and $+40\%$ from the ab initio results [12] but the ratios X/Z and M/Z are in good agreement with the results of Huestis et al. [6], based on the experimental work of Herzberg [7].

Our room-temperature band oscillator strengths are in satisfactory agreement with results based on other experimental work [9–11, 22] except those of Huestis et al. [6]. When compared with most previous studies, the present analysis has the advantage that oscillator strengths inherently include contributions from weak lines that have not been observed while excluding weak lines from other transitions that fall in the region of the Herzberg I bands.

Finally, the assumption that the allowed $B^3\Sigma_u^- \leftarrow X^3\Sigma_g^-$ and $A^3\Sigma_u^+ \leftarrow 1^3\Pi_g$ transitions are the major contributors to the strength of the Herzberg I bands has enabled values for critical interaction matrix elements involving the $B^3\Sigma_u^-$ and $1^3\Pi_g$ states to be derived from the present electronic transition moments.

Acknowledgments

The authors wish to acknowledge helpful discussions with

[11] The contribution from the $1^3\Pi_u \leftarrow X^3\Sigma_g^-$ transition through the $1^3\Pi_u - A^3\Sigma_u^+$ interaction is negligible: at 1.300 Å the spin-orbit matrix element $\langle 1^3\Pi_u | \boldsymbol{H}^{SO} | A^3\Sigma_u^+ \rangle$ is only 0.9 cm^{-1} [12], the $1^3\Pi_u \leftarrow X^3\Sigma_g^-$ dipole transition moment is only 0.05 au [24] and the potential-energy separation is ~40 000 cm^{-1} [12], giving a contribution to X of only 1.1×10^{-6} au.

[12] The value obtained by extrapolation of the data of Klotz and Peyerimhoff [12] to this internuclear separation is -18.1 cm^{-1}.

Professor M.L. Ginter and Dr. D.L. Huestis and to thank Professors H. Lefebvre-Brion, M.L. Ginter, and J.H. Carver and Dr. T.G. Slanger for critically reading the manuscript.

References

1. J. Stegman and D.P. Murtagh. Planet. Space Sci. **36**, 927 (1988).
2. A. Horowitz, G. von Helden, W. Schneider, F.G. Simon, P.J. Crutzen, and G.K. Moortgat. J. Phys. Chem. **92**, 4956 (1988).
3. R.D. Present. Phys. Rev. **48**, 140 (1935).
4. B.R. Lewis and S.T. Gibson. Can. J. Phys. **68**, 231 (1990).
5. V.P. Bellary and T.K. Balasubramanian. J. Quant. Spectrosc. Radiat. Transfer, **45**, 283 (1991).
6. D.L. Huestis, R.A. Copeland, K. Knutsen, T.G. Slanger, R.T. Jongma, M.G.H. Boogaarts, and G. Meijer. Can. J. Phys. **72**, 1109 (1994).
7. G. Herzberg. Can. J. Phys. **30**, 185 (1952).
8. H.P. Broida and A.G. Gaydon. Proc. R. Soc. London, A, **222**, 181 (1954).
9. V. Hasson and R.W. Nicholls. J. Phys. B: At. Mol. Phys. **4**, 1778 (1971).
10. K. Yoshino, J.R. Esmond, J.E. Murray, W.H. Parkinson, A.P. Thorne, R.C.M. Learner, and G. Cox. J. Chem. Phys. **103**, 1243 (1995).
11. Z.-C. Bao, W. On Yu, and J.R. Barker. J. Chem. Phys. **103**, 6 (1995).
12. R. Klotz and S.D. Peyerimhoff. Mol. Phys. **57**, 573 (1986).
13. J.B. Tatum and J.K.G. Watson. Can. J. Phys. **49**, 2693 (1971).
14. K. Yoshino, J.E. Murray, J.R. Esmond, Y. Sun, W.H. Parkinson, A.P. Thorne, R.C.M. Learner, and G. Cox. Can. J. Phys. **72**, 1101 (1994).
15. C. Amiot and J. Verges. Can. J. Phys. **59**, 1391 (1981).
16. B.R. Lewis, L. Berzins, and J.H. Carver. J. Quant. Spectrosc. Radiat. Transfer, **36**, 209 (1986).
17. E.E. Whiting and R.W. Nicholls. Astrophys. J. Suppl. **27**, 1 (1974).
18. A.C. Allison, A. Dalgarno, and N.W. Pasachoff. Planet. Space Sci. **19**, 1463 (1971).
19. P.M. Borrell, P. Borrell, and D.A. Ramsay. Can. J. Phys. **64**, 721 (1986).
20. D.R. Bates. Planet. Space Sci. **37**, 881 (1989).
21. M.W. Cann and R.W. Nicholls. Can. J. Phys. **69**, 1163 (1991).
22. V. Hasson, R.W. Nicholls, and V. Degen. J. Phys. B: At. Mol. Phys. **3**, 1192 (1970).
23. V. Degen and R.W. Nicholls. J. Phys. B: At. Mol. Phys. **2**, 1240 (1969).
24. S.L. Guberman and A. Dalgarno. J. Geophys. Res. **84**, 4437 (1979).
25. H. Lefebvre-Brion and R.W. Field. Perturbations in the spectra of diatomic molecules. Academic Press, Orlando. 1986. pp. 58–64, 67, 95, 119, 177, 214, 221, 226, and 286.
26. P.S. Julienne. J. Mol. Spectrosc. **63**, 60 (1976).
27. J.H. Van Vleck. Phys. Rev. **33**, 467 (1929).
28. H.C. Chang and M. Ogawa. J. Mol. Spectrosc. **44**, 405 (1972).

Appendix

Relatively simple arguments can be used to obtain values for the $1^3\Pi_g - X^3\Sigma_g^-$ spin-orbit and orbit-rotation interaction matrix elements using the single-configuration and pure-precession [27] approximations. Because the same states are involved in the two matrix elements, it is possible to determine the relative signs of the matrix elements.

The X state arises from the configuration $\ldots(3\sigma_g)^2(1\pi_u)^4(1\pi_g)^2$. In the determinant notation of Lefebvre–Brion and Field [26], it is sufficient to represent the wave function as

$$|X^3\Sigma_{1g}^-\rangle = |\sigma_g\alpha\sigma_g\beta\pi_g^+\alpha\pi_g^-\alpha| \tag{10}$$

The $1^3\Pi_g$ state is affected by strong avoided crossings near 1.2 and 1.6 Å [12]. The region of interest in this work is between these avoided crossings where the dominant configuration is $\ldots(3\sigma_g)^1(1\pi_u)^4(1\pi_g)^3$. The wave functions necessary for our calculations are, therefore,

$$|1^3\Pi_{2g}\rangle = |\sigma_g\alpha\pi_g^+\alpha\pi_g^+\beta\pi_g^-\alpha| \tag{11}$$

and

$$|1^3\Pi_{1g}\rangle = \frac{1}{\sqrt{2}}\left[|\sigma_g\beta\pi_g^+\alpha\pi_g^+\beta\pi_g^-\alpha| + |\sigma_g\alpha\pi_g^+\alpha\pi_g^+\beta\pi_g^-\beta|\right] \tag{12}$$

The part of the spin-orbit operator giving nonzero matrix elements between Π and Σ states is $\frac{1}{2}\Sigma_i\hat{a}_i\boldsymbol{l}_i^{\pm}\cdot\boldsymbol{s}_i^{\mp}$ [26]. Therefore, using the wave functions given in (10) and (12), it follows that

$$\langle 1^3\Pi_{1g}|\boldsymbol{H}^{SO}|X^3\Sigma_{1g}^-\rangle = \frac{1}{2\sqrt{2}}\langle\pi_g^+|\hat{a}\boldsymbol{l}^+|\sigma_g\rangle \tag{13}$$

Similarly, using the microscopic form $\boldsymbol{L}^+ = \Sigma_i\boldsymbol{l}_i^+$ [26] and wave functions given in (10) and (11), we obtain

$$\langle 1^3\Pi_{2g}|B\boldsymbol{L}^+|X^3\Sigma_{1g}^-\rangle \approx -B(R)\langle\pi_g^+|\boldsymbol{l}^+|\sigma_g\rangle \tag{14}$$

where $B(R) = h/(8\pi^2\mu cR^2)$, μ is the reduced mass of the molecule, and the minus sign arises because an odd number of permutations has been carried out to match the order of appearance of the spin-orbitals in each wave function.

In general, the value of l for a molecular orbital is not well defined. However, there are two methods that will yield estimates of the matrix elements.

1. If we assume that the molecular orbitals can be expanded in terms of atomic orbitals [26] on each atom, A and B, such that

$$|\pi_g^+\rangle = \frac{1}{\sqrt{2}}|p\pi_A^+\rangle - \frac{1}{\sqrt{2}}|p\pi_B^+\rangle \qquad \text{and} \qquad |\sigma_g\rangle = \frac{1}{\sqrt{2}}|p\sigma_A\rangle - \frac{1}{\sqrt{2}}|p\sigma_B\rangle$$

then, using $l^+|p\sigma_K\rangle = \sqrt{2}\,|p\pi_K\rangle$ (where $K = A$ or B) and (13), we get an estimate of

$$\langle 1^3\Pi_{1g}|H^{SO}|X^3\Sigma_{1g}^-\rangle \approx \frac{1}{2}\langle p|\hat{a}|p\rangle = 76\ \text{cm}^{-1} \tag{15}$$

where the atomic spin-orbit parameter is $\langle p|\hat{a}|p\rangle = 151\ \text{cm}^{-1}$ [26]. This value for the matrix element is in good agreement with the value of Klotz and Peyerimhoff [12] (81.6 cm^{-1}).

2. We can obtain estimates of the matrix elements using the pure-precession approximation [27], not necessarily expected to be valid for valence states of O_2 [26], in which we associate a value of l with each orbital. If we assume the orbitals are atomic p-like ($l = 1$), then $l^+|\sigma_g\rangle = \sqrt{2}\,|\pi_g^+\rangle$. Therefore,

$$\langle 1^3\Pi_{1g}|H^{SO}|X^3\Sigma_{1g}^-\rangle = \frac{1}{2}\,a_{\pi_g} \approx 95\ \text{cm}^{-1} \tag{16}$$

where we have used a value for the molecular spin-orbit parameter $a_{\pi_g} = \langle \pi_g|\hat{a}|\pi_g\rangle \approx 190\ \text{cm}^{-1}$, estimated from the spin-orbit splitting of the $F^3\Pi_u$ state of O_2 [28]. This value for the interaction matrix element is in satisfactory agreement with the ab initio value of 81.6 cm^{-1} [12] and the value given above in (15).

Using the pure-precession approximation with (14) gives

$$\langle 1^3\Pi_{2g}|BL^+|X^3\Sigma_{1g}^-\rangle = -\sqrt{2}\,B(R) \approx -1.8\ \text{cm}^{-1} \text{ at } R = 1.30\ \text{Å} \tag{17}$$

The absolute value of this matrix element is in surprisingly good agreement with the value of 2.0 cm^{-1} obtained in Sect. 4. In addition, it should be noted that the relative signs of the spin-orbit and orbit-rotation matrix elements obtained here are the same as those in (9) implied by our analysis of the measured integrated line strengths.

4.27 Observation of the second $^3\Pi_u$ valence state of O_2

[47] B. R. Lewis, P. M. Dooley, J. P. England, K. Waring, S. T. Gibson, K. G. H. Baldwin, and H. Partridge,
Physical Review A **54**, 3923–3938 (1996).

Observation of the second $^3\Pi_u$ valence state of O_2

B. R. Lewis, P. M. Dooley, J. P. England, K. Waring, S. T. Gibson, and K. G. H. Baldwin
Research School of Physical Sciences and Engineering, The Australian National University, Canberra, Australian Capital Territory 0200, Australia

H. Partridge
NASA Ames Research Center, Moffett Field, California 94035
(Received 15 July 1996)

Rotational perturbations in the $B\ ^3\Sigma_u^-$ state of molecular oxygen are studied by measuring high-resolution vacuum ultraviolet laser photoabsorption cross sections of the (16,0)–(18,0) $B\ ^3\Sigma_u^- \leftarrow X\ ^3\Sigma_g^-$ Schumann-Runge bands of $^{16}O_2$. The observation of numerous extra lines in the spectrum, together with *ab initio* calculations of relevant potential-energy curves, enables the perturbing state to be assigned as the second valence state of $^3\Pi_u$ symmetry. This weakly bound state, which we name $C'^3\Pi_u$, is also likely to be principally responsible for the well-known rapid increase in the magnitudes of the B-state triplet-splitting constants λ_v and γ_v as the dissociation limit is approached. [S1050-2947(96)07911-5]

PACS number(s): 33.20.Ni, 33.70.Jg

I. INTRODUCTION

Molecular oxygen plays an important role in the photochemistry of the terrestrial atmosphere through its absorption of solar vacuum ultraviolet (VUV) radiation and subsequent (pre)dissociation. In particular, a precise knowledge of the spectroscopic parameters, oscillator strengths, and predissociation linewidths of the Schumann-Runge (SR) system, $B\ ^3\Sigma_u^- \leftarrow X\ ^3\Sigma_g^-$ is necessary for realistic photochemical modeling of the stratosphere and mesosphere [1,2].

The SR bands of O_2 have been the subject of much study. The many spectroscopic investigations have been reviewed by Yoshino *et al.* [3], while Lewis *et al.* [4] have recently reviewed work on the $B\ ^3\Sigma_u^-$-state predissociation. The B state is subject to a number of perturbations. Relevant potential-energy curves are shown in Fig. 1, where the $B\ ^3\Sigma_u^-$ curve is a Rydberg-Klein-Rees (RKR) potential determined by Lewis *et al.* [5] and the repulsive curves are the *ab initio* calculations of Partridge *et al.* [6] ($1\ ^3\Pi_u$, $1\ ^5\Pi_u$) and Partridge [7] ($1\ ^1\Pi_u$, $2\ ^3\Sigma_u^+$). As has been shown by Julienne and Krauss [8] and Julienne [9], the four repulsive states in Fig. 1 are responsible for the predissociation of every vibrational level of the B state and are also expected to produce irregular perturbations in the spectroscopic and triplet-splitting constants of the B state. In particular, the $1\ ^3\Pi_u$ state is expected to perturb G_v, B_v, λ_v, and γ_v through a combination of spin-orbit, spin-electronic, and L-uncoupling interactions. Irregular perturbations have indeed been observed in the second vibrational differences $\Delta^2 G_v$ of the B state for $v = 1-10$ and can be explained using the same model as that necessary to explain the observed predissociation [4,8,10].

In addition to the perturbations of the B-state vibrational structure caused by the repulsive states in Fig. 1, perturbations in the rotational structure of the B state have been observed for $v \geq 16$ in every O_2 isotopomer studied [3,10–12]. A few extra levels associated with the bound perturbing state(s) have been reported [3,11], but the level assignments are tentative, the perturbations remain unanalyzed, and no progress has been made in the identification of the perturbing state. Finally, for all O_2 isotopomers studied, the triplet-splitting constants λ_v and γ_v for $B\ ^3\Sigma_u^-$ ($v \gtrsim 11$) exhibit rapidly increasing smooth perturbations as the dissociation limit is approached [10]. Bergeman and Wofsy [13], using the unique-perturber approximation of Zare *et al.* [14], have invoked a spin-orbit interaction between the $B\ ^3\Sigma_u^-$ state and a $^3\Pi_u$ state correlating with the $O(^1D) + O(^3P)$ dissociation limit to explain this observed perturbation in λ_v. A similar approach has been followed by Cheung *et al.* [10], without assignment of the perturber.

In this work, we measure high-resolution photoabsorption cross sections for selected rotational lines from the (16,0)–(18,0) SR bands of $^{16}O_2$ and observe consistent sets of extra lines associated with the lowest-energy rotational perturbations of the F_2 levels of $B\ ^3\Sigma_u^-$ ($v = 16-18$). In addition, we perform *ab initio* calculations of possible perturbing states. A

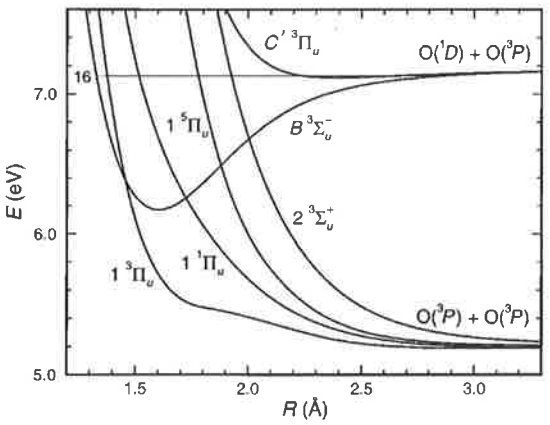

FIG. 1. Potential-energy curves for electronic states of O_2 relevant to perturbation of the $B\ ^3\Sigma_u^-$ state. Energies are given relative to the minimum of the ground-state $X\ ^3\Sigma_g^-$ potential-energy curve.

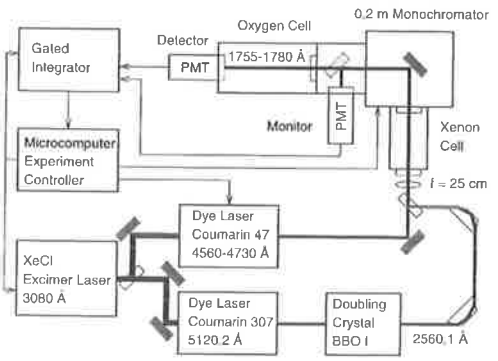

FIG. 2. Schematic diagram of the experimental apparatus.

full characterization of the perturbations, together with the *ab initio* calculations, leads to an assignment of the perturbing state as the second valence state of $^3\Pi_u$ symmetry, which we name $C'\,^3\Pi_u$. The calculated potential-energy curve for this state is shown in Fig. 1, where it can be seen that the $C'\,^3\Pi_u$ state is bound for energies near $B\,^3\Sigma_u^-(v \geq 16)$. In addition, we show that the C' state is also likely to be principally responsible for the rapidly increasing smooth perturbations observed in the B-state triplet-splitting constants λ_v and γ_v.

II. EXPERIMENTAL METHOD

The experimental apparatus, shown schematically in Fig. 2, is similar to that used in an earlier study of the $f\,^1\Sigma_u^+$ and $f'\,^1\Sigma_u^+$ states of O_2 and described in detail elsewhere [15]. Briefly, we used two-photon-resonant difference-frequency four-wave mixing (2PR-4WDM) in Xe [16,17] to generate narrow-bandwidth, tunable vacuum ultraviolet radiation in the range 1755–1780 Å in order to study rotational perturbations in $B\,^3\Sigma_u^-(v=16-18)$ by means of high-resolution photoabsorption spectroscopy.

One of the excimer-pumped dye lasers (Coumarin 307 in methanol) was tuned to a vacuum wavelength of 5120.2 Å so that its frequency-doubled output was two-photon resonant with the Xe transition $5p^5(^2P^o_{3/2})6p[\frac{5}{2}]_2 \leftarrow 5p^6\,^1S_0$. The doubled radiation was combined, after removal of the fundamental radiation, with the tunable radiation from the other dye laser (Coumarin 47 in methanol) and both beams were focussed into a cell containing Xe (US Services Inc., 99.999%) by a 25-cm focal-length quartz lens. VUV radiation generated by the 2PR-4WDM process was passed through a 0.2-m VUV monochromator which acted as a broad bandpass filter, tuned synchronously with the second dye laser and discriminating against the fundamental and doubled dye-laser radiation. The VUV radiation leaving the exit slit of the monochromator was divided into two beams by a slotted Al beam splitter. The reflected beam was monitored directly, while the transmitted beam passed through a 33-cm long, MgF_2-windowed absorption cell containing O_2 (BOC, 99.9%) before being detected. Output pulses from the solar-blind monitor and detector photomultipliers (EMI type 9413, CsI photocathode) were processed by a boxcar averaging system. A microcomputer was used to control the laser and monochromator scanning, the pressure of O_2 in the absorption cell, and the acquisition of the shot-averaged detector and monitor signals from the boxcar system.

In order to obtain the measurements presented here, scans were performed at room temperature (293 K) over ~0.3 Å ranges in the VUV from ~1755–1780 Å with wavelength increments of 0.001 Å. The phase matching for each scan was optimized by adjusting the pressure of Xe in the range 70–90 Torr to maximize the VUV signal. The monitor and detector signals were averaged over 50 laser shots for each datum point, during groups of three scans with the absorption cell alternately filled with a pressure of O_2 in the range 0.8–15 Torr, then evacuated, then refilled. This scheme allowed compensation for any slow drifts in detector sensitivity and correction for wavelength dependences in the generated signal which were not related to O_2 absorption [15]. Division of the detector signal by the monitor signal, after correction for scattered radiation, provided a measure of compensation for the shot-to-shot fluctuations inherent in the generated VUV signal. Absolute cell transmittances were obtained by dividing the full-cell ratios [(detector)/(monitor)] by the empty-cell ratios for each wavelength. Photoabsorption cross sections were calculated from the absolute transmittances using the Beer-Lambert law. Statistical uncertainties in the measured (peak) cross sections were ~3% and there was an additional systematic uncertainty of ~3% arising from uncertainties in O_2 pressure, temperature, and cell length.

Each dye laser was operated with an intracavity etalon, resulting in a nominal bandwidth of 0.04 cm^{-1} full-width at half-maximum (FWHM) for each fundamental beam. The average VUV bandwidth was estimated to be 0.08 ± 0.02 cm^{-1} FWHM by fitting an instrumentally degraded Voigt profile to the SR lines of narrowest predissociation linewidth ($v'=16$, F_1, high N') [18]. This value is consistent with the bandwidth of 0.06 ± 0.01 cm^{-1} FWHM reported by Yamanouchi and Tsuchiya [17] for 2PR-4WDM in Sr vapor. The nominal VUV wave number was given by

$$\nu_{\rm vuv} = \nu_{\rm 2p} - \nu_{\rm vis}, \tag{1}$$

where $\nu_{\rm 2p}$ was the wave number of the Xe two-photon resonance and $\nu_{\rm vis}$ was the vacuum-corrected wave number of the tunable dye laser. Absolute wave number calibration was achieved by comparison with the measured wave numbers of Yoshino *et al.* [3] for selected sharp, unblended lines of the SR system. The linearity and calibration of the dye-laser étalon scanning system were confirmed over the relatively small ($\lesssim 10$ cm^{-1}) ranges involved, by comparison of the measured combination differences between SR lines having a common upper level with accurately known O_2 ground-state energy levels [19]. The estimated absolute uncertainty in the wave number of a sharp, unblended line is ~0.1 cm^{-1}, while the relative uncertainty is $\sim 0.01-0.04$ cm^{-1}, the smaller value applying in the case of two sharp lines within the one etalon scan.

III. LINE-PROFILE ANALYSIS

SR absorption-line wave numbers, oscillator strengths, and predissociation linewidths were determined by a least-

squares fitting procedure. In this procedure, the measured photoabsorption cross sections were compared with model calculations, appropriate to the experimental conditions, in which the line parameters were allowed to vary independently. For unperturbed lines, or for well separated pairs of perturbed lines, the predissociation component of the line shape was taken as Lorentzian. The corresponding cross section for the ith line was given by

$$\sigma_i(\nu)=\frac{0.563\times10^{-12}s_i}{\Gamma_i\left[1+\left(\frac{\nu-\nu_i}{\Gamma_i/2}\right)^2\right]}\ \text{cm}^2, \tag{2}$$

where s_i is a strength factor related to the line oscillator strength, Γ_i (cm^{-1}) is the FWHM predissociation linewidth, and ν_i (cm^{-1}) is the wave number of the line center. As has been explained in detail elsewhere [20], Eq. (2) is inappropriate to describe the predissociation line shapes of perturbed pairs of lines whose separation does not greatly exceed their predissociation linewidths. In those cases, most noticeably for $v'=16$, destructive interference was observed for wave numbers between the centers of the perturbed and perturbing lines, and, therefore, the ith pair of perturbed main (m) and extra (x) lines was described by the coupled predissociation line shape [20]

$$\sigma_i(\nu)=\frac{0.563\times10^{-12}s_i\left(\frac{\Gamma_m/2}{\nu-\nu_m}+\frac{\Gamma_x/2}{\nu-\nu_x}\right)^2}{\Gamma_i\left[1+\left(\frac{\Gamma_m/2}{\nu-\nu_m}+\frac{\Gamma_x/2}{\nu-\nu_x}\right)^2\right]}\ \text{cm}^2, \tag{3}$$

where $\Gamma_i=\Gamma_m+\Gamma_x$ and s_i is the total strength for the pair of interfering lines. The Doppler component of the line shapes and the effects of the finite instrumental resolution were included in the model through appropriate convolution procedures and the underlying continuum was expressed as a low-order polynomial in ν.

IV. *AB INITIO* CALCULATIONS

The *ab initio* calculations followed the procedure reported in Ref. [6]. The orbitals were optimized using the state-averaged complete-active-space self-consistent-field (CASSCF) approach with the $2p$ orbitals active. The calculations were performed in D_{2h} symmetry with symmetry and equivalence restrictions imposed on the orbitals. All states of the specified spin and spatial symmetry which dissociate to the $O(^3P)+O(^3P)$ and $O(^1D)+O(^3P)$ asymptotes were included in the averaging; five states were included for the $^3\Pi_u$ (and $^3\Phi_u$) optimization and six were included for the $^3\Sigma_u^+$ and $^3\Delta_u$ states. External correlation was included using a multireference configuration-interaction (MRCI) procedure using the CASSCF reference and correlating both the $2s$ and $2p$ electrons. The effect of higher excitations was estimated using a multireference analog of the Davidson correction, denoted +Q. The basis set employed is the atomic natural orbitals (ANO) [21] basis set designated $[5s\ 4p\ (3+1)d\ 2f\ 1g]+(sp)$ [6]. The "$+sp$" indicates that the basis is augmented with diffuse s and p orbitals and the notation "$(3+1)d$" indicates that there are three ANO d functions and that the outer d primitive is uncontracted. This basis set provides an accurate description of the valence regions but does not contain the diffuse functions needed to describe Rydberg character. The potential-energy curves have not been corrected for basis-set superposition error (BSSE).

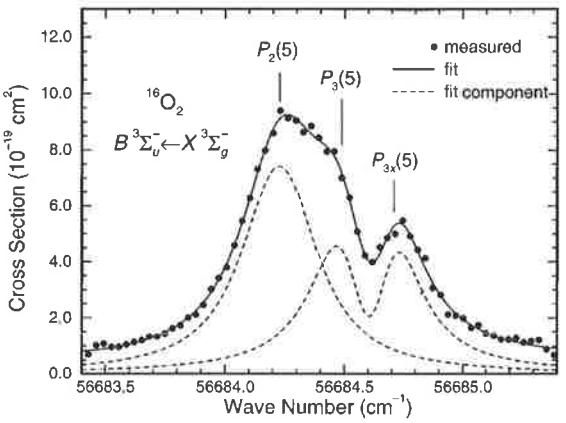

FIG. 3. Photoabsorption cross section for $^{16}O_2$ in the region of the $P_2(5)$ and $P_3(5)$ lines from the (16,0) band of the $B\,^3\Sigma_u^-\leftarrow X\,^3\Sigma_g^-$ system, measured at $T=293$ K with an instrumental resolution of $\sim0.06\ \text{cm}^{-1}$ FWHM. The fitted model cross section, and its components, which include the Doppler contribution, but not the instrumental degradation, are also shown. The $P_3(5)$ line is perturbed, a strong destructive interference being observed between the corresponding main and extra lines.

V. RESULTS AND DISCUSSION

A. Perturbations in $B\,^3\Sigma_u^-(v=16-18)$

A combination of high-resolution photoabsorption cross section measurements and the line-profile analysis technique described in Sec. III enabled the discovery and detailed characterization of many extra lines associated with rotational perturbations in $B\,^3\Sigma_u^-(v=16-18)$. It is usually not possible to obtain comparable information from spectrographic data alone, especially for blended spectral features, because of the difficulty in extracting reliable intensity information. In particular, we were able to measure the effects of the perturbations, not only on the term values, but also on the predissociation linewidths and oscillator strengths. Using this information, we were able to determine the J dependence of the perturbation matrix elements and thereby establish the symmetry of the perturbing state. While there are three fine-structure components associated with the $B\,^3\Sigma_u^-$ state, namely, the F_2 levels (f parity, $J=N$, $\Omega=1$) and the mixed F_1 and F_3 levels (e parity, $J=N\pm1$, $\Omega=0$ and 1), the F_1 levels for $v=16-18$ are well separted from the F_2 and F_3 levels and do not participate in the particular perturbations discussed here.

As an example of an observed perturbation, in Fig. 3 we show the measured photoabsorption cross section in the region of the $P_2(5)$ and $P_3(5)$ lines from the (16,0) SR band. It was not possible to obtain a convincing fit to the measured cross section when the predissociation line shapes of the

TABLE I. Wave numbers for main- (upper entries) and extra- (lower entries) branch lines from the $B\,^3\Sigma_u^-(v'=16,\ N',\ F_2$ and $F_3) \leftarrow X\,^3\Sigma_g^-(v''=0,\ N'')$ band of $^{16}O_2$, together with upper-state term values, all in cm^{-1}. Absolute uncertainties $\sim 0.1\ cm^{-1}$, relative uncertainties $\sim 0.01-0.03\ cm^{-1}$.

N''	$R_2(N'')$[a]	$P_2(N'')$	$R_3(N'')$	$P_3(N'')$	N'	$T_2(N')$[b]	$T_3(N')$[b]
1	56719.05[c]				2	56721.88	56720.66
3	56710.07[c]	56704.65	56710.42	56705.48[d]	4	56727.37	56725.60
	56711.44[e]		56710.65[d]			56728.70	56725.82
5	56692.80[d]	56684.23[c]	56693.32	56684.49	6	56735.94	56734.44
	56693.71	56685.58[c,e]		56684.71[d]		56736.85	
7	56666.87	56655.43	56667.85	56655.92	8	56747.39	56746.38
	56667.57[f]	56656.35				56748.08	
9	56633.26	56618.03	56634.06	56619.00[c]	10	56762.64	56761.48
	56632.12[f,g]	56618.74[d,f]				56761.49	
11	56590.64	56572.94	56591.89	56573.70	12	56780.33	56779.66
	56588.67	56571.78[f,g]				56778.37	
13	56539.41[h]	56518.82	56541.20	56520.05	14	56800.96	56800.82
15	56479.69	56456.19	56481.94	56457.91	16	56824.45	56824.85
17	56411.23	56384.96	56414.03	56387.20	18	56850.70	56851.63
19	56333.94	56305.10[h]	56337.48[c]	56307.84	20	56879.56	56881.21
21		56216.38		56219.87			

[a]The lines ${}^RQ_{21}(1)=56720.82\ cm^{-1}$[g], ${}^PQ_{23}(5)=56686.26\ cm^{-1}$, ${}^RQ_{32}(1)=56717.79\ cm^{-1}$, ${}^TR_{31}(1)=56724.60\ cm^{-1}$, and ${}^TR_{31_A}(1)=56724.83\ cm^{-1}$[c] were also observed.

[b]Weighted averages determined from the separate branch wave numbers.

[c]Blended with a weaker line.

[d]Shoulder.

[e]Weak.

[f]Extra line also reported by Brix and Herzberg [11].

[g]Extra line also reported by Yoshino *et al.* [3].

[h]Blended with a stronger line.

three component lines were represented by Eq. (2). However, when the two higher-energy lines were described by Eq. (3), the excellent fit shown in Fig. 3 resulted. Evidently, the $P_3(5)$ line is split into two mutually-interfering components due to a perturbation. Although the shift in energy due to the perturbation is small, almost total intensity sharing occurs between the main and extra lines. This conclusion is confirmed following an analysis of our measured cross sections near the $R_3(3)$ and ${}^TR_{31}(1)$ lines which, together with $P_3(5)$, share the common upper level $N'=4$, $J'=3$. Our assignments [22], $P_2(5)=56\,684.23\ cm^{-1}$, $P_3(5)=56\,684.49\ cm^{-1}$ and $P_{3x}(5)=56\,684.71\ cm^{-1}$, differ from those of Brix and Herzberg [11] and Yoshino *et al.* [3], neither of whom report a perturbation for this level. Our measured cross section for the region near the $P_2(11)$ perturbation in the (16,0) band, which also exhibits a particularly obvious interference effect, has been reported elsewhere [20].

Wave numbers for the lines observed in this work, together with the corresponding upper-state term values, are summarized in Tables I–III. Where possible, the term values are averages of the values determined from the P- and R-branch wave numbers for unblended lines. Thirty-four extra lines have been observed, only four of which, to our knowledge, have been reported previously in spectrographic studies [3,11]. As mentioned in Sec. II, wave numbers for the main-branch lines in Tables I–III are calibrated against those of Yoshino *et al.* [3] and are essentially indistinguishable for unblended, sharp lines. However, the wave numbers in Tables I–III for the many blended features at lower rotation should be more reliable than those of Yoshino *et al.* [3] because of superior instrumental resolution and a realistic line-profile analysis procedure.

The term values in Tables I–III are presented in Fig. 4 in such a way as to emphasize the perturbed main and extra levels in the F_2 and F_3 fine-structure components. It can be seen clearly in Fig. 4 that the F_2 levels for $v=16-18$ are perturbed by levels with smaller rotational constants. However, these perturbations fall into two classes. First, through the observation of the single extra level associated with the F_3 perturbation for $v=16$, $J=3$, it is apparent that the corresponding perturbing level has closely spaced e- and f-parity components, implying a perturbing state with $\Lambda \geqslant 1$ and a very small Λ doubling. Second, in contrast, the F_3 levels for $v=17$ and 18 are unperturbed in the range of rotation under consideration, implying that the F_2-level per-

TABLE II. Wave numbers for main- (upper entries) and extra- (lower entries) branch lines from the $B\ ^3\Sigma_u^-(v'=17, N',\ F_2$ and $F_3) \leftarrow X\ ^3\Sigma_g^-(v''=0,\ N'')$ band of $^{16}O_2$, together with upper-state term values, all in cm^{-1}. Absolute uncertainties $\sim 0.1\ cm^{-1}$, relative uncertainties $\sim 0.04\ cm^{-1}$.

N''	$R_2(N'')$	$P_2(N'')$	$R_3(N'')$	$P_3(N'')$	N'	$T_2(N')$[a]	$T_3(N')$[a]
1	56851.62				2	56854.50	56853.29
3	56842.11	56837.29[b]	56842.62[b]	56838.12	4	56859.35	56857.79
5	56823.78	56816.22	56824.25[b]	56816.67[c]	6	56866.92	56865.41
7	56796.63	56786.41	56797.44	56786.88	8	56877.16	56875.98
9	56760.69	56747.80	56761.96	56748.57	10	56890.06	56889.38
11	56715.78	56700.42[d]	56717.67[b]	56701.61	12	56905.49	56905.43
13	56661.94	56643.99	56664.48	56645.83	14	56923.42	56924.09
15	56598.82[b]	56578.63	56602.28	56581.16	16	56943.56	56945.21
	56606.92					56951.68	
17		56504.09	56530.89	56507.54[b]	18	56965.59	56968.51
	56531.88	56512.20				56971.36	
19	56448.56[b,c]	56419.98		56424.72[c]	20	56994.17	
	56443.11[c]	56425.76				56988.72	
21	56357.03[d]	56330.99[d]			22	57020.22	
	56349.59	56325.57[d]				57012.74	
23	56256.58	56228.09			24	57048.69	
		56220.58				57038.04	
25	56146.56	56116.21			26	57079.02	
	56132.52	56105.58				57064.96	
27							
		55980.81					

[a]Weighted averages determined from the separate branch wave numbers.
[b]Blended with a weaker line.
[c]Shoulder.
[d]Blended with a stronger line.
[e]Assignment differs from that of Yoshino *et al.* [3].

turber is either a Σ state, or a state with $\Lambda \geqslant 1$ and a very large Λ doubling.

The measured cross sections for perturbed pairs of lines from the (16,0) band were fitted using Eq. (3), allowing the determination of separate predissociation linewidths for the main and extra lines and the corresponding line-strength sums. These data are presented in Table IV as Γ_x/Γ_m, $\Gamma_x+\Gamma_m$, and $f_{v'm}+f_{v'x}(=f_{v'i})$. The line strengths have been converted into equivalent band oscillator strengths using the relation

$$f_{v'i}=s_i/(\alpha_i'' S_i), \tag{4}$$

where α_i'' and S_i are appropriately normalized Boltzmann and Hönl-London factors, respectively. For the (17,0) and (18,0) bands, where Eq. (2) was used to fit the measured cross sections, linewidth and oscillator-strength ratios were determined independently and the weighted average of these ratios is given in the Γ_x/Γ_m column of Table IV. Where possible, the data listed in Table IV were determined as weighted averages of separate P- and R-branch measurements. Predissociation linewidths and oscillator strengths are also shown in Figs. 5 and 6, respectively, for the F_2 main lines from the (16,0)–(18,0) bands, together with the corresponding main-extra sums. The effects of the perturbations on the main-line parameters are clearly evident. It is also apparent from Figs. 5 and 6 that the predissociation-linewidth and oscillator-strength sums in the perturbed regions join smoothly onto the values for the unperturbed levels. These observations confirm the validity of the two assumptions implicit in the use of Eq. (3): in the absence of perturbations, levels of the perturbing state are not predissociated and transitions into them from the ground state have insignificant strength [20]. With these assumptions, the measured term-value separations $\Delta T=|T_m-T_x|$ and predissociation-linewidth ratios $r=\Gamma_x/\Gamma_m(=f_{v'x}/f_{v'm})$ for the main- and extra-level pairs in Table IV can be used to calculate perturbation matrix elements and level shifts. Within the framework of standard two-level perturbation theory [23], it is easy to show that the perturbation matrix element is given by

TABLE III. Wave numbers for main- (upper entries) and extra- (lower entries) branch lines from the $B\,^3\Sigma_u^-(v'=18,\ N',\ F_2$ and $F_3)\leftarrow X\,^3\Sigma_g^-(v''=0,\ N'')$ band of $^{16}O_2$, together with upper-state term values, all in cm^{-1}. Absolute uncertainties $\sim 0.1\ cm^{-1}$, relative uncertainties $\sim 0.04\ cm^{-1}$.

N''	$R_2(N'')$[a]	$P_2(N'')$	$R_3(N'')$	$P_3(N'')$	N'	$T_2(N')$[b]	$T_3(N')$[b]
1	56953.52				2	56956.40	56955.40
3	56943.24	56939.15	56943.96[c]	56940.23	4	56960.48	56959.16
	56948.55[d]					56965.80	
5	56923.66[e]	56917.38[e]	56924.53	56918.05	6	56966.80	56965.64
	56928.34[c]	56922.67[d]				56971.53	
7	56894.65	56886.29	56896.18	56887.11	8	56975.15	56974.71
	56898.98	56891.02				56979.48	
9	56856.01	56845.77	56858.79	56847.28[e]	10	56985.35	56986.21
	56860.53	56850.10				56989.90	
11	56813.03	56795.62	56812.03[e]	56798.38[e]	12	57002.73	56999.78
	56807.62[e]	56800.20[e]				56997.32	
13	56756.44	56741.19[e]		56740.18	14	57017.94	
	56749.66	56735.82				57011.16	
15		56673.15[e]					
		56666.38					

[a]The lines $^RQ_{32}(1)=56952.52\ cm^{-1}$ and $^TR_{31}(3)=56950.35\ cm^{-1}$ were also observed.
[b]Weighted averages determined from the separate branch wave numbers.
[c]Blended with a stronger line.
[d]Weak.
[e]Blended with a weaker line.

$$|H_{mx}| = \sqrt{r}\,\Delta T/(1+r), \tag{5}$$

and the magnitude of the level shift by

$$|S| = r\,\Delta T/(1+r). \tag{6}$$

Values calculated using Eqs. (5) and (6) are included in Table IV and the perturbation matrix elements are also shown in Fig. 7. It is clear from Fig. 7 that the F_2 matrix elements for $v=16-18$ exhibit an essentially linear dependence on rotation and that the single F_3 perturbation matrix element for $v=16$, $J=3$ lies marginally below the line representing the $v=16$, F_2 data. These are key observations which help to determine the symmetry of the perturbing state.

The heterogeneous nature of the F_2-level perturbations shown in Fig. 7 ($\Delta\Omega=\pm 1$) confirms that the perturbing state is of *ungerade* symmetry with $\Omega=0$ or 2. If each perturbation results principally from interaction with a single state, then the first-order selection rules for perturbations [23] suggest that the perturber is a $^3\Pi_u$ state, interacting with $B\,^3\Sigma_u^-$ through the $\mathcal{L}$-uncoupling operator ($\Delta\Lambda=\Delta\Omega=\pm 1$). Only the $\Omega=0$ and $\Omega=2$ components of a $^3\Pi_u$ state with coupling approaching Hund's case (a) can produce a purely J-dependent interaction with $B\,^3\Sigma_{u1}^-(F_2, f)$ [4,24] and it is well known [24] that these components have completely different Λ-doubling characteristics, providing a possible explanation for the two classes of perturbation shown in Fig. 4. Using the more detailed arguments set out in the Appendix, we find that only the $\Omega=2$ component of the $^3\Pi_u$ perturber (small Λ doubling) can explain simultaneously the observed perturbation matrix elements for the F_2 and F_3 fine-structure components of $B(v=16)$, while only the $\Omega=0$ component (large Λ doubling) can explain the observed perturbations in the F_2 components of $B(v=17$ and $18)$ and the lack of perturbation of the nearby F_3 components.

It is advisable to consider whether a first-order picture of the perturbations is appropriate for the levels studied here. Near a dissociation limit, the separation in energy between electronic states can become small compared with the spin-orbit splittings, leading to a mixing of states with different Λ, Σ, and S values, and resulting in far-nuclei case (c) behavior [25] where only J and Ω are good quantum numbers. In the present case, the $B(16-18)$ levels lie $\sim 420-180\ cm^{-1}$ below the dissociation limit, respectively, while the off-diagonal spin-orbit interactions are expected to be less than the atomic spin-orbit parameter $\zeta_O(2p)=150\ cm^{-1}$. Thus, a case (a) description of the perturber levels in this energy region is reasonable, but a description intermediate between cases (a) and (c) may be more appropriate for the perturbers of $B(v\gtrsim 18)$.

B. Potential-energy curves

No Rydberg states of O_2 lie low enough in energy to produce bound-bound perturbations in $B\,^3\Sigma_u^-(v=16-18)$. However, the extensive *ab initio* calculations of Saxon and Liu [26] show several weakly bound *ungerade* valence states, correlating with the $O(^1D)+O(^3P)$ dissociation limit, some of which may be energetically capable of perturbing $B\,^3\Sigma_u^-(v=16-18)$. Since the first-order configuration-interaction (FOCI) calculations employed by Saxon and Liu [26] are expected to yield only qualitatively

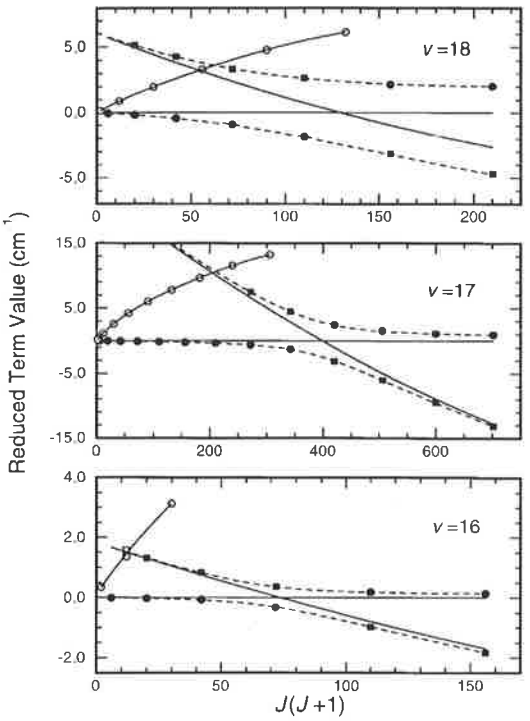

FIG. 4. Reduced term values for the main (circles) and extra (squares) levels associated with the lowest-energy rotational perturbations in the $F_2(f)$ (closed symbols) and $F_3(e)$ (open symbols) components of $B\ ^3\Sigma_u^-(v=16-18)$. Deperturbed energies of the respective F_2 levels (Table VII) have been subtracted from the absolute term values to enhance the visibility of the perturbations. The fitted perturbed (dashed lines) and deperturbed (solid lines) reduced term values were obtained using the two-level perturbation model described in the text and the respective model parameters given in Table VII. While the lowest-energy perturber level has closely spaced e- and f-parity components, resulting in a perturbation of $B\ ^3\Sigma_u^-(v=16,F_3)$, the F_3 levels for $v=17$ and 18 are unperturbed.

reliable binding energies for these states [6], we have performed MRCI + Q calculations according to the method described in Sec. IV, in order to assess more accurately the possible candidates for the perturbing state. Results for the three most strongly bound of these states are given in Table V. The corresponding potential-energy curves, formed by spline fitting the data of Table V and shifting in energy to be consistent with the experimental $O(^1D) + O(^3P)$ dissociation limit [27], are shown in Fig. 8. Spectroscopic constants, determined by fitting the G_v and B_v values obtained by numerical integration of the Schrödinger equation for these MRCI + Q potentials, are given in Table VI. The FOCI well depths calculated by Saxon and Liu [26] for these states exceed the MRCI + Q well depths by an average of 25%, somewhat less than, but in the same sense as, the discrepancy observed for other weakly bound states of O_2 correlating with the $O(^3P) + O(^3P)$ limit [6].

The MRCI + Q calculations, together with the evidence presented in Sec. V A, indicate that the second valence state of $^3\Pi_u$ symmetry, which we name $C'\ ^3\Pi_u$, is responsible for the perturbations that we have observed in $B\ ^3\Sigma_u^-(v=16-18)$. As can be seen in Fig. 8, vibrational levels of the C' potential-energy curve occur near the $v=16-18$ levels of the B state and the C'- and B-state outer limbs are nearly coincident for $v\gtrsim 18$, implying strong vibrational overlap. In addition, the large equilibrium internuclear distance for the C' potential ($R_e=2.386$ Å) explains the lack of predissociation of this state: no repulsive states correlating with the only lower limit, $O(^3P) + O(^3P)$, rise rapidly enough to cross the bound portion of the C' state. Despite the fact that the $C'\ ^3\Pi_u \leftarrow X\ ^3\Sigma_g^-$ transition is electric-dipole allowed, very poor Franck-Condon overlap between the X state ($R_e=1.208$ Å) and the C' state explains the negligible strength of the unperturbed $C' \leftarrow X$ lines.

Although ruled out as the principal perturber in a two-state interaction picture, it is possible that the $3\ ^3\Sigma_u^+$ and $2\ ^3\Delta_u$ states may produce other perturbations in the rotational structure of the B state. Energetically, the $3\ ^3\Sigma_u^+$ state could perturb $B(v\gtrsim 18)$ through the first-order spin-orbit interaction $^3\Sigma_{u1}^+ - {}^3\Sigma_{u1}^-$, but such perturbations are likely to be weak, since, as can be seen in Fig. 8, the outer limbs of the potential-energy curves for the two states are well separated, implying small vibrational-overlap factors. Energetically, the $2\ ^3\Delta_u$ state could perturb $B(v\gtrsim 16)$ through second-order interactions, principally of the type $^3\Sigma_u^- - {}^3\Pi_u - {}^3\Delta_u$, involving spin-orbit and/or $\mathcal{L}$-uncoupling interactions. These perturbations are also expected to be weak, not only because of their second-order nature, but also due to reasonably small vibrational-overlap factors. In addition, an examination of the calculated rotational constants in Table VI and those for the B-state levels in Table VII, indicates that such $2\ ^3\Delta_u$ perturbing levels would be likely to approach the perturbed levels from below, rather than above as is the case for the present observations. However, it is possible that some accidental perturbations involving coincidences between rovibrational levels of the B, C', and $2\ ^3\Delta_u$ states will be observable. In fact, we have found some multiple perturbations, as yet unanalyzed, in rotational levels of $B\ ^3\Sigma_u^-(v\gtrsim 16)$ higher than those discussed in this work. FOCI calculations [26] indicate that well depths for other weakly bound states correlating with the $O(^1D) + O(^3P)$ limit are $<100\ cm^{-1}$, implying that states other than the three discussed here are unlikely to play a role in the perturbation of $B\ ^3\Sigma_u^-(v\lesssim 20)$.

C. Deperturbation

We used a nonlinear least-squares fitting procedure and a simple two-level perturbation model [23] in which the unperturbed B- and C'-state term values were described by the usual polynomials in $J(J+1)$, with the additional assumption that the interaction matrix element was given by $|H_{BC'}| = |\eta_{BC'}|\sqrt{J(J+1)-\Omega_{C'}}$ (Fig. 7). For each level $B(v=16-18,F_2)$, we performed simultaneous fits to the measured main and extra term values listed in Tables I–III, respectively, and the width ratios $r=\Gamma_x/\Gamma_m$ listed in Table IV. The root-mean-square (RMS) term-value fitting deviations were only $\sim 0.01\ cm^{-1}$, $\sim 0.03\ cm^{-1}$, and $\sim 0.02\ cm^{-1}$, respectively, for $v=16$, 17, and 18, supporting the high relative accuracy claimed for the measurements. The

TABLE IV. Measured upper-state predissociation linewidths and equivalent band oscillator strengths for $B\ ^3\Sigma_u^-(v'=16-18,\ N',\ F_2$ and $F_3)\leftarrow X\ ^3\Sigma_g^-(v''=0)$. Measured width ratios and energy separations for the main (m) and extra (x) levels observed in association with perturbations in $B\ ^3\Sigma_u^-(v=16-18)$ are also shown, together with interaction matrix elements and level shifts estimated using Eqs. (5) and (6).

v'	Level	N'	$\lvert T_m-T_x\rvert$, cm^{-1}	Γ_x/Γ_m	$\Gamma_m+\Gamma_x$, cm^{-1}	$(f_{v'm}+f_{v'x})\times10^5$	$\lvert H_{mx}\rvert$, cm^{-1}	$\lvert S\rvert$, cm^{-1}
16	F_2	2			0.343±0.013	2.86±0.09		
		4	1.33±0.03	0.022±0.008	0.362±0.030	2.86±0.30	0.191±0.036	0.028±0.011
		6	0.91±0.02	0.095±0.015	0.357±0.017	2.80±0.13	0.256±0.017	0.079±0.011
		8	0.69±0.01	0.914±0.063	0.316±0.012	2.60±0.09	0.345±0.005	0.329±0.013
		10	1.15±0.01	0.181±0.010	0.313±0.005	2.61±0.03	0.414±0.010	0.176±0.008
		12	1.96±0.01	0.075±0.009	0.299±0.011	2.57±0.08	0.499±0.025	0.137±0.015
		14			0.273±0.011	2.44±0.07		
		16			0.254±0.006	2.34±0.04		
		18			0.225±0.008	2.14±0.06		
		20			0.197±0.014	1.98±0.10		
16	F_3	2			0.36±0.09	2.74±0.39		
		4	0.22±0.03	0.86±0.22	0.38±0.06	2.95±0.40	0.110±0.016	0.102±0.022
		6			0.335±0.025	2.89±0.12		
		8			0.324±0.016	2.83±0.16		
		10			0.304±0.005	2.66±0.03		
		12			0.311±0.010	2.70±0.07		
		14			0.273±0.010	2.55±0.07		
		16			0.265±0.007	2.37±0.05		
		18			0.255±0.010	2.25±0.06		
		20			0.238±0.023	2.13±0.15		
17	F_2	2			0.281±0.030	2.44±0.17		
		4			0.286±0.015	2.42±0.10		
		6			0.278±0.028	2.22±0.19		
		8			0.280±0.017	2.32±0.11		
		10			0.294±0.016	2.28±0.09		
		12			0.286±0.010	2.31±0.08		
		14			0.245±0.013	2.01±0.08		
		16	8.12±0.04	0.087±0.008	0.219±0.016	1.81±0.14	2.20±0.11	0.65±0.06
		18	5.77±0.04	0.281±0.027	0.189±0.008	1.49±0.04	2.39±0.10	1.27±0.11
		20	5.45±0.06	0.81±0.10	0.108±0.020	0.93±0.12	2.71±0.05	2.44±0.16
		22	7.48±0.04	0.245±0.032	0.122±0.024	1.30±0.18	2.97±0.12	1.47±0.16
		24	10.65±0.04	0.132±0.013	0.115±0.007	1.17±0.03	3.42±0.12	1.24±0.11
		26	14.06±0.04	0.080±0.012	0.088±0.009	1.02±0.05	3.68±0.23	1.04±0.14
17	F_3	2			0.282±0.102	2.24±0.71		
		4			0.280±0.036	2.48±0.14		
		6			0.304±0.032	2.32±0.18		
		8			0.276±0.012	2.38±0.09		
		10			0.284±0.009	2.31±0.06		
		12			0.259±0.010	2.11±0.05		
		14			0.235±0.010	2.12±0.07		
		16			0.251±0.014	2.01±0.07		
18	F_2	2			0.207±0.014	1.88±0.09		
		4	5.32±0.04	0.038±0.009	0.198±0.021	2.03±0.09	1.00±0.11	0.20±0.05
		6	4.73±0.05	0.10±0.02	0.192±0.029	1.75±0.25	1.36±0.12	0.43±0.09
		8	4.33±0.04	0.31±0.03	0.159±0.007	1.44±0.04	1.84±0.06	1.03±0.09
		10	4.55±0.04	0.70±0.04	0.123±0.009	1.05±0.04	2.24±0.03	1.87±0.08
		12	5.41±0.04	0.75±0.08	0.118±0.021	0.92±0.08	2.68±0.04	2.32±0.15
		14	6.78±0.04	0.47±0.05	0.140±0.011	1.07±0.06	3.16±0.08	2.17±0.16

TABLE IV. *(Continued).*

v'	Level	N'	$\lvert T_m - T_x\rvert$, cm^{-1}	Γ_x/Γ_m	$\Gamma_m+\Gamma_x$, cm^{-1}	$(f_{v'm}+f_{v'x})\times 10^5$	$\lvert H_{mx}\rvert$, cm^{-1}	$\lvert S\rvert$, cm^{-1}
18	F_3	2			0.211±0.027	1.94±0.19		
		4			0.217±0.017	1.87±0.10		
		6			0.221±0.009	2.02±0.07		
		8			0.209±0.010	2.03±0.07		
		10			0.209±0.009	1.91±0.05		

fitted width ratios agreed with the measured values within the experimental uncertainties, except for $v=17$, $J=24$, where the deviation slightly exceeded the uncertainty. The deperturbed spectroscopic constants [28] obtained for the $B\ ^3\Sigma_u^-$- and $C'\ ^3\Pi_u$-state levels are given in Table VII, together with the fitted interaction matrix-element slopes $|\eta_{BC'}|$. The fitting procedure indicates that the perturbations for $B(16-18)$ culminate [23] at $J=8.1$, $J=19.5$, and $J=10.9$, respectively. The deperturbed term values, predissociation linewidths, and oscillator strengths consistent with the model parameters of Table VII, together with the fitted perturbed values, are shown in Figs. 4, 5, and 6, respectively.

In Fig. 7, the model interaction matrix elements are compared with the values determined individually from the measurements using Eq. (5). It is seen in all cases that the simple perturbation model which we have used gives an excellent description of the observations.

The best agreement between the calculated and deperturbed perturber levels is obtained by assuming that $C'(0)$ perturbs $B(16)$, $C'(2)$ perturbs $B(17)$, and $C'(3)$ perturbs $B(18)$. While these vibrational assignments are likely, they cannot be regarded as definitive until further experimental information on perturber isotope shifts becomes available.

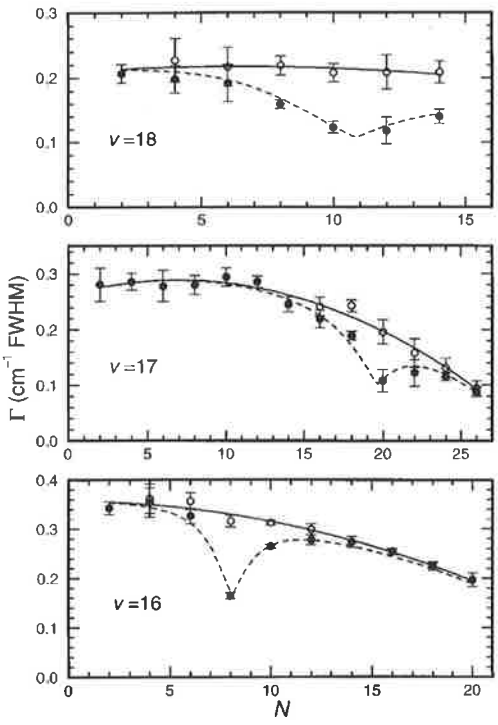

FIG. 5. Measured predissociation linewidths (closed circles) for the F_2 levels of $B\ ^3\Sigma_u^-(v=16-18)$ in the region of their lowest-energy rotational perturbations. In the case of the perturbed levels, the sum of the linewidths for the main and extra lines (open circles) is also shown. The deperturbed linewidths (solid lines) were obtained from a quadratic fit to the main-extra linewidth sums, while the corresponding perturbed linewidths (dashed lines) were calculated using the two-level perturbation model described in the text and the respective model parameters given in Table VII.

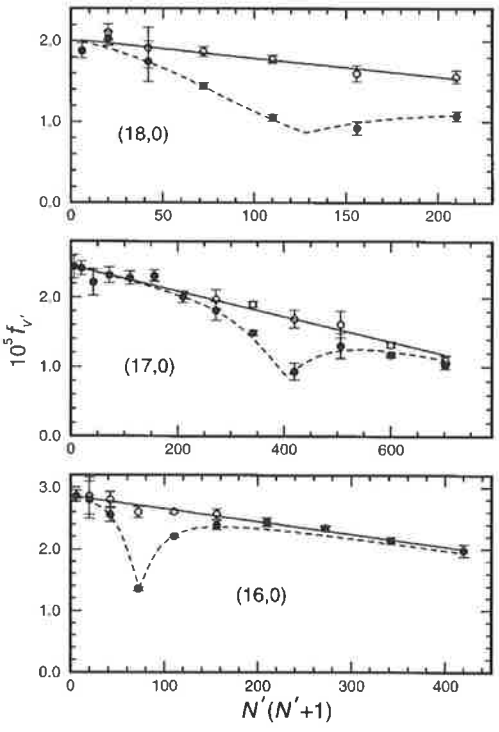

FIG. 6. Measured equivalent band oscillator strengths (closed circles) for the $B\ ^3\Sigma_u^-(v'=16-18,\ F_2)\leftarrow X\ ^3\Sigma_g^-(v''=0)$ bands in the region of their lowest-energy rotational perturbations. In the case of the perturbed levels, the oscillator-strength sum for the main and extra lines (open circles) is also shown. The deperturbed oscillator strengths (solid lines) were obtained from a linear fit to the main-extra oscillator-strength sums, while the corresponding perturbed oscillator strengths (dashed lines) were calculated using the two-level perturbation model described in the text and the respective model parameters given in Table VII.

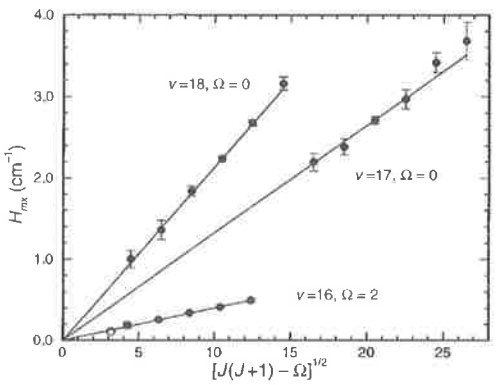

FIG. 7. Perturbation matrix elements for the interacting main and extra F_2 (closed circles) and F_3 (open circle) levels of $B\,^3\Sigma_u^-(v=16-18)$, obtained from the measurements given in Table IV using Eq. (5). Fitted matrix elements (solid lines) implied by the respective two-level perturbation-model parameters given in Table VII are also shown. In anticipation of later conclusions in this work, and for consistency with expressions given in the Appendix, the abscissa of the figure includes the Ω value for the perturbing level, which differs for the $B(16)$ and $B(17$ and $18)$ perturbations, respectively.

Cheung *et al.* [10,12] have reported rotational perturbations in the $B(16)$ level of $^{16}O^{18}O$ and the $B(18)$ and $B(19)$ levels of $^{18}O_2$, but their failure to observe extra lines makes it difficult to determine the perturber origins for these isotopomers. For comparative purposes, calculated MRCI + Q constants for the $C'\,^3\Pi_u$ perturber levels are included in Table VII. The agreement between the deperturbed and calculated band origins and rotational constants is good, especially when it is realized that the calculated values do not take into account the spin-splitting of the $C'\,^3\Pi_u$ state, and effectively refer to the $\Omega=1$ component, whereas the actual levels which perturb $B(16)$ and $B(17$ and $18)$ have $\Omega=2$ and $\Omega=0$, respectively. The calculated value of the centrifugal distortion constant D for the $C'(2)$ level agrees with the deperturbed value within the experimental uncertainty. However, since the $C'(3)$ level suffers a further perturbation from below for J values higher than those examined here, not removed by our two-level deperturbation procedure, the D value for this level is not fully deperturbed and cannot be compared with the calculated value.

The small discrepancies between the deperturbed and calculated perturber spectroscopic constants in Table VII can be reduced further by considering the spin-splitting of the $C'\,^3\Pi_u$ state. It follows, approximately, from the triplet term formulas discussed by Kovács [24] that the origins of the outer components of a regular $^3\Pi$ term with coupling intermediate between Hund's cases (a) and (b) are given by $\nu_0 \pm A$, and the effective rotational constants by $B(1\pm 2B/A)$, where ν_0 and B are the origin and rotational constant for the central component, $A>0$ is the spin-orbit constant, and the upper and lower signs refer to the $\Omega=2$ and $\Omega=0$ components, respectively. Qualitatively, the application of these relations to the calculated $\Omega=1$ values in Table VII simultaneously increases the ν_0 and B values for $C'\,^3\Pi_{u2}(v=0)$, while decreasing those for $C'\,^3\Pi_{u0}(v=2,3)$, providing better agreement with all of the deperturbed parameters. Quantitatively, invoking a regular $C'\,^3\Pi_u$ state having a spin-orbit constant $A\approx+30$ cm^{-1} minimizes the discrepancies between the deperturbed and calculated origins and rotational constants. The verification of this tentative conclusion, however, must await the observation of more Ω levels of the C' state than those reported here.

TABLE V. Energies (in cm^{-1}), calculated at the MRCI + Q level, for three weakly bound states of O_2 correlating with the $O(^1D) + O(^3P)$ limit. Energies are referred to the $O(^3P) + O(^3P)$ limit.

R (a.u.)	$C'\,^3\Pi_u$	$2\,^3\Delta_u$	$3\,^3\Sigma_u^+$
2.50		72827.54	
2.60		62190.18	
2.70		53250.23	80859.66
2.80		45817.28	68056.57
3.00	34170.16	34582.20	47896.91
3.20		26988.06	33595.93
3.25	27172.41		
3.40		22042.15	23487.62
3.50	21090.32		
3.60		17979.95	18897.54
3.75	17511.58		
3.80		16477.64	17120.72
4.00	16017.78	15758.97	16217.36
4.20		15490.76	15826.55
4.25	15540.28		
4.40		15447.00	15700.87
4.50	15454.00		
4.75	15490.94		
4.80		15575.29	15733.68
5.00	15556.66		
5.20		15719.54	15828.26
5.50	15679.83		
5.60		15815.67	15895.99
6.00	15771.80	15873.63	15936.25
6.50	15837.14	15915.26	
7.00	15882.77	15939.49	15976.41
7.50	15914.15	15954.84	15982.91
8.00	15935.53	15965.13	15986.18
9.00	15960.20	15976.85	15988.53
10.00	15966.93	15982.73	15989.28
11.00		15986.13	15989.86
100.0	15975.03		

We have estimated numerically the J-independent part of the $\mathcal{L}$-uncoupling interaction matrix elements between the RKR B-state potential and the calculated C'-state potential using Eq. (A3) with the electronic part replaced by the pure-precession [23] value, i.e., $|\eta_{BC'}| = \sqrt{2}|\langle v_B|\mathcal{B}|v_{C'}\rangle|$. The vibrational quantum number of the C' state was treated as a continuous variable and the values of $|\eta_{BC'}|$ for levels degenerate with the B-state levels were estimated by graphical interpolation. Agreement between the relative calculated and deperturbed values, which is only fair, can be improved by considering the spin-structure of the C' state, as demonstrated above for the spectroscopic constants. For a regular

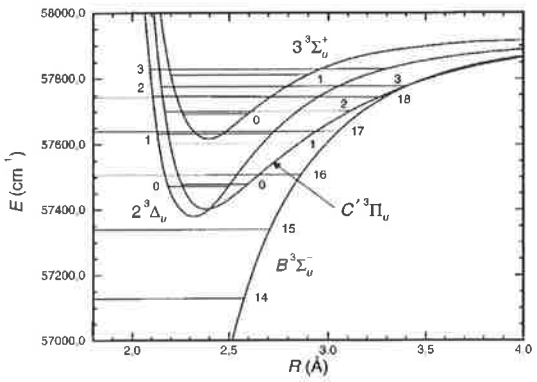

FIG. 8. Potential-energy curves for electronic states energetically capable of playing a role in the perturbation of $B\ ^3\Sigma_u^-(v=16-18)$. The B-state curve is a RKR potential, while the others were obtained from spline fits to the MRCI + Q calculations of Table V, following shifting in energy to be consistent with the experimental $O(^1D) + O(^3P)$ dissociation limit [27]: the $C'\ ^3\Pi_u$, $2\ ^3\Delta_u$, and $3\ ^3\Sigma_u^+$ curves were lowered by 106.5 cm^{-1}, 121.5 cm^{-1}, and 121.5 cm^{-1}, respectively. Energies are given relative to the minimum of the ground-state $X\ ^3\Sigma_g^-$ potential-energy curve.

$^3\Pi$ state, the effective potential-energy curves for the $\Omega=2$ and $\Omega=0$ components will lie a little above and below that for the $\Omega=1$ component, respectively, resulting in overlap factors $|\langle v_B|\mathcal{B}|v_{C'}\rangle|$ smaller for $\Omega=2$, and larger for $\Omega=0$, than those for $\Omega=1$. These variations are in such a sense as to improve agreement between the calculated and deperturbed relative values of $|\eta_{BC'}|$ given in Table VII. We do not pursue these considerations more quantitatively because of the great sensitivity of the overlap factors to the details of the calculated potential-energy curves, but merely note that the calculated MRCI + Q potential-energy curve for the C' state is broadly consistent with all of the deperturbed parameters of Table VII. In contrast, if, for example, we were to postulate that the level $B(18)$ were perturbed by either the $3\ ^3\Sigma_u^+$ or the $2\ ^3\Delta_u$ states, then the corresponding overlap factors result in numerical estimates of $|\eta|$ some 70 times and 15 times greater, respectively, than the tabulated value of $|\eta_{BC'}|$, clearly ruling out these states as the perturber.

Finally, from Tables I and IV, an estimate of the deperturbed term value for $C'\ ^3\Pi_{u2}(v=0,J=3,e)$ of 56 725.72±0.04 cm^{-1} can be determined. From our deperturbed spectroscopic constants for the C' state in Table VII, an estimated deperturbed term value for $C'\ ^3\Pi_{u2}(v=0,J=3,f)$ of 56 725.75±0.06 cm^{-1} is obtained [29]. The deperturbed Λ doubling for $J=3$ is thus $T_f - T_e = 0.03\pm0.08\approx0$ cm^{-1} within the experimental uncertainty. As discussed in the Appendix, such a small value is consistent with expectation for a $^3\Pi_2$ level approaching Hund's coupling case (a).

D. Perturbations in λ_v and γ_v for $B\ ^3\Sigma_u^-$

As noted in Sec. I, the spin-splitting constants for the $B\ ^3\Sigma_u^-$ state of O_2, λ_v and γ_v exhibit smooth perturbations which increase rapidly for high v as the B-state dissociation limit is approached. Bergeman and Wofsy [13] first suggested that the perturbation in λ_v could be explained by a spin-orbit interaction between the B state and a $^3\Pi_u$ state correlating with the same limit. Later, Julienne and Krauss [8] noted that the rotational constants B_v would also be affected by rotational interactions with such a $^3\Pi_u$ state, providing a possible explanation for the pathological turning in of the inner limbs of B-state RKR potential-energy curves derived from the experimental data. In this section, we investigate the consequences for λ_v and γ_v of the interactions between the $B\ ^3\Sigma_u^-$ state and the $C'\ ^3\Pi_u$ state, which, as we have seen in the previous sections, is responsible for rotational perturbations in the B-state levels with $v\geq16$.

Brown *et al.* [31] have developed an effective Hamiltonian for diatomic molecules and give a convenient set of expressions for the R-dependent electronic Hamiltonian parameters which includes both direct contributions and the effects of interaction with other electronic states through appropriate perturbation-theory terms. For example, the effective spin-spin parameter $\lambda(R)$ comprises two contributions:

$$\lambda(R)=\lambda^{(1)}(R)+\lambda^{(2)}(R), \tag{7}$$

where $\lambda^{(1)}(R)$ results from the direct spin-spin interaction $\mathcal{H}^{SS}$ and $\lambda^{(2)}(R)$ arises from second-order interactions involving the spin-orbit operator $\mathcal{H}^{SO}$. Thus, the effective spin-spin constant for the level v is given by

$$\lambda_v=\langle v|\lambda^{(1)}(R)|v\rangle+\langle v|\lambda^{(2)}(R)|v\rangle=\lambda_v^{(1)}+\lambda_v^{(2)}. \tag{8}$$

Field and Lefebvre-Brion [32] have estimated the direct component of λ_v for the B state of O_2 using the single-configuration approximation, obtaining $\lambda_v^{(1)}=1.38$ cm^{-1}. In

TABLE VI. Summary of spectroscopic constants for the three weakly bound states of Fig. 8 (in cm^{-1}, unless indicated otherwise), determined from fits to G_v and B_v values obtained by numerically integrating the Schrödinger equation for the MRCI + Q potential-energy curves of Fig. 8. Constants reproduce the G_v and B_v values to within ±1 cm^{-1} and ±0.002 cm^{-1}, respectively.

State	T_e	D_e	ω_e	$\omega_e x_e$	$\omega_e y_e$	R_e (Å)	B_e	α_e	γ_e[a]
$C'\ ^3\Pi_u$[b]	57406	518	154	16.0	0.63	2.386	0.370	0.0337	
$2\ ^3\Delta_u$[c]	57372	552	211	27.0	1.12	2.301	0.398	0.0306	−0.0025
$3\ ^3\Sigma_u^+$[d]	57621	303	158	20.9		2.401	0.366	0.0226	−0.0095

[a]Not to be confused with the effective spin-rotation constant γ_v.
[b]Constants determined from levels with $v=0-6$.
[c]Constants determined from levels with $v=0-5$.
[d]Constants determined from levels with $v=0-3$.

TABLE VII. Deperturbed spectroscopic constants and interaction matrix elements (in cm^{-1}) for levels of the $B\ ^3\Sigma_u^-$ and $C'\ ^3\Pi_u$ states, obtained from the measured term values of Tables I, II, and III and the width ratios of Table IV, together with comparable calculated constants for the $C'\ ^3\Pi_u$ levels.

State	Level	v	ν_0[a]	B	$D\times10^5$	$\lvert\eta_{BC'}\rvert$[b]
$B\ ^3\Sigma_u^-$	F_2, f	16	56719.53±0.03	0.3937±0.0004	3.10±0.08	
$C'\ ^3\Pi_u$	$\Omega=2, f$	0[c]	56721.35±0.06	0.3670±0.0015	~0.4	0.0402±0.0012
$C'\ ^3\Pi_u$	$\Omega=1$, calc.[d]	0	56691.5	0.3545	0.94	0.05[e]
$B\ ^3\Sigma_u^-$	F_2, f	17	56852.42±0.06	0.3474±0.0006	3.70±0.01	
$C'\ ^3\Pi_u$	$\Omega=0, f$	2[c]	56875.65±0.58	0.2808±0.0026	1.4±0.3	0.1325±0.0022
$C'\ ^3\Pi_u$	$\Omega=1$, calc.[d]	2	56913.8	0.2852	1.63	0.09[e]
$B\ ^3\Sigma_u^-$	F_2, f	18	56954.65±0.06	0.3016±0.0019	4.7±1.0	
$C'\ ^3\Pi_u$	$\Omega=0, f$	3[c]	56960.70±0.09	0.2460±0.0024	−1.9±1.1[f]	0.2137±0.0026
$C'\ ^3\Pi_u$	$\Omega=1$, calc.[d]	3	56988.5	0.2519	1.97	0.14[e]

[a]The unperturbed B- and C'-state term values were represented by the polynomial $\nu_0+BJ(J+1)-D[J(J+1)]^2$ in the deperturbation procedure.

[b]The interaction matrix elements are given by $|H_{BC'}|=|\eta_{BC'}|\sqrt{J(J+1)-\Omega_{C'}}$.

[c]Likely vibrational numbering from *ab initio* calculations. Absolute numbering is not definitive.

[d]Constants determined by numerical integration of the Schrödinger equation for the calculated C' potential-energy curve of Fig. 8.

[e]Pure-precession estimate $\sqrt{2}|\langle v_B|\mathcal{B}|v_{C'}\rangle|$ for degenerate levels.

[f]Anomalous sign for D reflects a further perturbation at higher J, not included in the present analysis.

the unique-perturber approximation, where we assume that the B state is perturbed only by the C' state, the expression for the indirect contribution given by Brown *et al.* [31] reduces to

$$\lambda^{(2)}(R)=-\frac{1}{2}\frac{|\xi(R)|^2}{V_B(R)-V_{C'}(R)}, \tag{9}$$

where

$$\xi(R)=\langle B\ ^3\Sigma_{u1}^-|\mathcal{H}^{SO}|C'\ ^3\Pi_{u1}\rangle, \tag{10}$$

and $V_B(R)$ and $V_{C'}(R)$ represent the potential-energy curves of the B and C' states, respectively.

Similarly, the effective spin-rotation parameter $\gamma(R)$ is given by

$$\gamma(R)=\gamma^{(1)}(R)+\gamma^{(2)}(R), \tag{11}$$

where the first-order term $\gamma^{(1)}(R)$ results from the direct spin-rotation interaction $\mathcal{H}^{SR}$ and is much smaller than the second-order term $\gamma^{(2)}(R)$ which arises from interactions with other states involving the product of the $\mathcal{L}$-uncoupling and spin-orbit operators. The effective spin-rotation constant for the level v is given by

$$\gamma_v=\langle v|\gamma^{(1)}(R)|v\rangle+\langle v|\gamma^{(2)}(R)|v\rangle=\gamma_v^{(1)}+\gamma_v^{(2)}. \tag{12}$$

With a unique-perturber view of the second-order contribution to the effective spin-rotation parameter of the B state, the expression given by Brown *et al.* [31] reduces to

$$\gamma^{(2)}(R)=-2\sqrt{2}\frac{\xi(R)\,\eta(R)}{V_B(R)-V_{C'}(R)}, \tag{13}$$

where

$$\eta(R)=\langle B\ ^3\Sigma_u^-|\mathcal{B}\mathcal{L}^-|C'\ ^3\Pi_u\rangle. \tag{14}$$

In principle, the sign of the interference cross-term $\xi(R)\,\eta(R)$ in Eq. (13), which is independent of the phase conventions for the molecular wave functions, can be determined experimentally by observing the sense of the perturbation in γ_v.

The expressions given by Julienne and Krauss [8] describing the perturbations in λ_v and γ_v for a $^3\Sigma$ state uniquely perturbed by a $^3\Pi$ state are equivalent to our treatment, but are computationally unattractive, involving perturbation sums over the discrete and continuum levels of the perturber. On the other hand, the expectation values of Eqs. (9) and (13) are easy to calculate and the resultant values of $\lambda_v^{(2)}$ and $\gamma_v^{(2)}$ should be accurate for levels in regions where the potential-energy curves of the B and C' states do not approach each other too closely. In this section, we consider only the B-state levels with $v\leq15$. From Fig. 8, it can be seen that the separation in energy of the B- and C'-state potential-energy curves is ~200 cm^{-1} near the outer turning point for $B(v=15)$. As we shall see, this is significantly greater than the B-C' interaction matrix elements and implies that Eqs. (9) and (13) are applicable.

Effective values of λ_v and γ_v for B-state levels with $v=0-15$, determined from the measurements of Yoshino *et al.* [3] by Lewis *et al.* [33], are shown in Fig. 9, where the rapidly increasing perturbations for $v\geq11$ can be seen readily. Using Eqs. (8), (9), (12), and (13), we have calculated values for $\lambda_v^{(2)}$ and $\gamma_v^{(2)}$ in the unique-perturber approximation. The RKR and calculated MRCI + Q potential-energy curves were used for $V_B(R)$ and $V_{C'}(R)$, respectively. In addition, it was assumed that $\xi(R)$ was R-independent [34] and that Eq. (14) could be rewritten as

$$\eta(R)=B(R)L^-(R), \tag{15}$$

where

$$B(R)=h/(8\pi^2\mu cR^2), \tag{16}$$

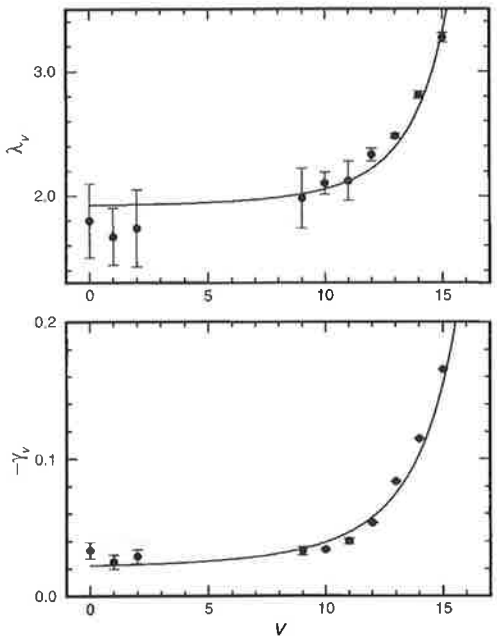

FIG. 9. Measured values (closed circles) of the spin-splitting parameters λ_v and γ_v for the $B\ ^3\Sigma_u^-$ state, emphasizing the rapidly increasing perturbations for $v \gtrsim 11$. Also shown are values of $1.8+\lambda_v^{(2)}$ and $-0.015+\gamma_v^{(2)}$ (lines) calculated in the unique-perturber approximation whereby it is assumed that only the $C'\ ^3\Pi_u$ state perturbs the B state, and that the corresponding spin-orbit and $\mathcal{L}$-uncoupling interactions are $\xi(R)=35\ \text{cm}^{-1}$ and $L^-(R)=-2.0$, respectively.

and

$$L^-(R)=\langle B\ ^3\Sigma_u^-|\mathcal{L}^-|C'\ ^3\Pi_u\rangle \tag{17}$$

was also taken to be R-independent [34]. The results obtained with $\xi(R)=35\ \text{cm}^{-1}$, $L^-(R)=-2.0$ and constant effective values $\lambda_v^{(1)}=1.8\ \text{cm}^{-1}$ and $\gamma_v^{(1)}=-0.015\ \text{cm}^{-1}$ are compared with the measurements in Fig. 9 where the agreement is seen to be very satisfactory. No allowance has been made for the small perturbations caused by the repulsive states, shown in Fig. 1, which are responsible for the B-state predissociation [8], but this will not affect our conclusions significantly. The character of the observed perturbations in λ_v and γ_v can be understood by referring to Fig. 8, where it can be seen that the energy denominator in Eqs. (9) and (13), $V_{C'}(R)-V_B(R)$, decreases for $R>R_e(C')=2.39$ Å, but increases very rapidly for $R<R_e$. Since the outer turning point for $B(v=12)$ is approximately equal to $R_e(C')$, this explains why the perturbations in the spin-splitting parameters have a rapid onset near $v=12$.

Our value for $\xi(R)$ is in satisfactory agreement with values of 40 cm^{-1} and 32 cm^{-1} determined by Bergeman and Wofsy [13] and Cheung *et al.* [10], respectively, by fitting the perturbation in λ_v using a simple unique-perturber formula which did not involve the potential-energy curves of the relevant electronic states. A spin-orbit matrix element of this size seems reasonable: a value of 31 cm^{-1} has been reported for the interaction between the B state and the first valence state of $^3\Pi_u$ symmetry [4]. There have been no previous estimates of $L^-(R)$.

As has been pointed out by Julienne and Krauss [8], whereas many electronic states can contribute to the perturbation of λ_v for the B state, only $^3\Pi_u$ states can contribute to the perturbation of γ_v (and B_v). The Wigner-Witmer correlation rules [35] imply that, in addition to the C' state, there are two other states of $^3\Pi_u$ symmetry associated with the $O(^1D)+O(^3P)$ limit. However, for the same electronic interaction strengths, our calculations show that these essentially repulsive states are expected to be 3–4 times less efficient than the C' state at perturbing the B state, due to greater separation in energy from the B-state potential. Of the other bound states shown in Fig. 8, only the $3\ ^3\Sigma_u^+$ state has a first-order-allowed spin-orbit interaction with the B state, $\langle ^3\Sigma_{u1}^+|\mathcal{H}^{SO}|^3\Sigma_{u1}^-\rangle$, resulting in a perturbation which decreases λ_v. This is in the opposite sense to the perturbation produced by the C' state and observed experimentally, where both the $\Omega=0$ and $\Omega=1$ components participate in spin-orbit interactions in which the $B\ ^3\Sigma_{u0}^-$ levels are depressed by twice as much as the $B\ ^3\Sigma_{u1}^-$ levels. Julienne [9] has estimated a semiempirical spin-orbit matrix element of 16 cm^{-1} at $R=2.117$ Å for the $3\ ^3\Sigma_{u1}^+-B\ ^3\Sigma_{u1}^-$ interaction. If we adopt this value, together with our MRCI + Q potential-energy curve for the $3\ ^3\Sigma_u^+$ state, then our estimate of the corresponding perturbation in λ_v is -15% of the observed value. Thus, the inclusion of this effect will change our conclusions only marginally. Despite all of the approximations in our analysis, it is likely that the interaction parameters obtained using the unique-perturber approximation will be qualitatively sound. Nevertheless, a complete *ab initio* study of the spin-orbit and $\mathcal{L}$-uncoupling matrix elements between all relevant electronic states correlating with the $O(^1D)+O(^3P)$ limit would be invaluable in refining our picture of the B-state perturbation.

Summarizing the results of this section, we concur with the suggestion of Bergeman and Wofsy [13] that the perturbation in λ_v for the B state is caused principally by a single $^3\Pi_u$ state. Moreover, our unique-perturber calculations indicate that the perturbing state is likely to be the same $C'\ ^3\Pi_u$ state that we have shown to be responsible for the rotational B-state perturbations reported in Sec. V A. The C' state is also principally responsible for the observed perturbations in γ_v. The negative sign determined for the electronic matrix-element product $L^-(R)\xi(R)$ is significant. In contrast, following a consideration of interference effects governing fine-structure-specific predissociation linewidths in the SR bands, Lewis *et al.* [4] found that the equivalent matrix-element product was positive for interactions between the B and $1\ ^3\Pi_u$ states. Although there are significant uncertainties, adopting the calculated MRCI + Q potential-energy curve for the C' state, and considering both the analysis of observed rotational perturbations presented in Sec. V C and the results of this section, it appears that the magnitude of the J-independent part of the electronic $\mathcal{L}$-uncoupling matrix element between the B and C' states is on the order of the pure-precession value $|L^-(R)|=\sqrt{2}$. This is not necessarily

to be expected for these mixed-configuration valence states [23] and suggests that an *ab initio* evaluation of this matrix element is desirable.

VI. CONCLUSIONS

Several rotational perturbations in the $B\ ^3\Sigma_u^-$ state of molecular oxygen have been studied by measuring high-resolution VUV laser photoabsorption cross sections of the (16,0)–(18,0) Schumann-Runge bands of $^{16}O_2$. The observation of many extra lines in the spectrum, a line-profile analysis procedure which allows for non-Lorentzian line shapes due to interference between the main and extra lines, and state-of-the-art *ab initio* calculations have enabled the perturbing state to be identified as the second valence state of $^3\Pi_u$ symmetry, $C'\ ^3\Pi_u$.

In particular, we have located three vibrational levels of the C' state which perturb $B(v=16-18, F_2)$ through an $\mathcal{L}$-uncoupling interaction. We have also shown that the C' state is likely to be responsible for much of the well-known rapid increase in the magnitudes of the B-state triplet-splitting constants λ_v and γ_v as the dissociation limit is approached.

Further work is in progress to examine and analyze other rotational perturbations in $B\ ^3\Sigma_u^-(v\geq 16)$ which occur at higher energies, at higher rotational excitation, and in other fine-structure components. Eventually, with the aid of isotopic studies, we hope to make rigorous vibrational assignments and determine a realistic semiempirical potential-energy curve and spin-orbit constant for $C'\ ^3\Pi_u$. In addition, it may be possible to clarify the roles of the $2\ ^3\Delta_u$ and $3\ ^3\Sigma_u^+$ states in the perturbation of the $B\ ^3\Sigma_u^-$ state. *Ab initio* calculations of the spin-orbit and $\mathcal{L}$-uncoupling interactions between the $B\ ^3\Sigma_u^-$ state and other states in this energy region would be extremely valuable in progressing towards a complete understanding of the $B\ ^3\Sigma_u^-$ perturbations.

ACKNOWLEDGMENTS

The authors are grateful to Professor H. Lefebvre-Brion, Professor J. H. Carver, and Dr. L. W. Torop for critical comments on the manuscript. We also thank Professor M. L. Ginter for his assistance, comments, and suggestions made during visits to the ANU sponsored by the National Science Foundation (U.S.) through a U.S.-Australian Cooperative Research Grant. Valuable technical assistance was provided by K. J. Lonsdale and C. J. Dedman.

APPENDIX: THE $^3\Sigma_u^- - ^3\Pi_u$ COUPLING

$^3\Sigma - ^3\Pi$ perturbations have been discussed in detail by Kovács [24,36,37] and are central to an understanding of Λ doubling in $^3\Pi$ states [24,38]. Here, we are concerned primarily with determining which $^3\Pi_\Omega$ substates are responsible for the perturbations observed in the $F_2(v=16-18)$ and $F_3(v=16)$ levels of the $B\ ^3\Sigma_u^-$ state.

If we express the molecular wave functions in the Hund's case (a) e/f-parity basis [23], then the nonzero $^3\Sigma - ^3\Pi$ interaction matrix elements are given by [4,8,39]

$$\langle {}^3\Sigma_0^-, v, J, e|\mathcal{H}|{}^3\Pi_0, v', J, e\rangle = \sqrt{2}(\xi + \sqrt{2}\,\eta), \quad \text{(A1a)}$$

$$\langle {}^3\Sigma_0^-, v, J, e|\mathcal{H}|{}^3\Pi_1, v', J, e\rangle = -\eta\sqrt{2J(J+1)}, \quad \text{(A1b)}$$

$$\langle {}^3\Sigma_1^-, v, J, {}^e_f|\mathcal{H}|{}^3\Pi_0, v', J, {}^e_f\rangle = \mp\eta\sqrt{J(J+1)}, \quad \text{(A1c)}$$

$$\langle {}^3\Sigma_1^-, v, J, {}^e_f|\mathcal{H}|{}^3\Pi_1, v', J, {}^e_f\rangle = \xi + \sqrt{2}\,\eta, \quad \text{(A1d)}$$

$$\langle {}^3\Sigma_1^-, v, J, {}^e_f|\mathcal{H}|{}^3\Pi_2, v', J, {}^e_f\rangle = -\eta\sqrt{J(J+1)-2}, \quad \text{(A1e)}$$

where

$$\xi(v,v',J) = \langle v, J|\langle {}^3\Sigma_1^-|\mathcal{H}^{SO}|{}^3\Pi_1\rangle|v', J\rangle, \quad \text{(A2)}$$

$$\eta(v,v',J) = \langle v, J|\langle {}^3\Sigma^-|\mathcal{BL}^-|{}^3\Pi\rangle|v', J\rangle, \quad \text{(A3)}$$

and $\mathcal{H}$, $\mathcal{H}^{SO}$, and $\mathcal{BL}^-$ represent the full molecular Hamiltonian, the spin-orbit operator, and the J-independent part of the $\mathcal{L}$-uncoupling operator, respectively.

Over the full range of rotation, appropriate wave functions for the $B\ ^3\Sigma_u^-$ state are intermediate between Hund's coupling cases (a) and (b) and can be expressed as [40,41]

$$|{}^3\Sigma_u^-, F_1, v, J\rangle = a|{}^3\Sigma_0^-, v, J, e\rangle + b|{}^3\Sigma_1^-, v, J, e\rangle, \quad \text{(A4a)}$$

$$|{}^3\Sigma_u^-, F_2, v, J\rangle = |{}^3\Sigma_1^-, v, J, f\rangle, \quad \text{(A4b)}$$

$$|{}^3\Sigma_u^-, F_3, v, J\rangle = b|{}^3\Sigma_0^-, v, J, e\rangle - a|{}^3\Sigma_1^-, v, J, e\rangle. \quad \text{(A4c)}$$

The mixing parameters a and b are given by

$$a(v,J) = \sqrt{[T_2(v,J) - T_1(v,J)]/[T_3(v,J) - T_1(v,J)]}, \quad \text{(A5a)}$$

$$b(v,J) = \sqrt{[T_3(v,J) - T_2(v,J)]/[T_3(v,J) - T_1(v,J)]}, \quad \text{(A5b)}$$

where $T_i(v,J)$ are the fine-structure term values, provided that centrifugal distortion is neglected [40].

First, we wish to consider the interactions of the F_2 levels of the B state. From Eqs. (A1c), (A1e) and (A4b), it can be seen that only the $^3\Pi_0$ and $^3\Pi_2$ substates can interact with a $^3\Sigma_1^-$ state in a way consistent with the J-dependent perturbation matrix element measured in this work. From Eqs. (A1) and (A4), the interactions of these $^3\Pi_{u\Omega}$ substates with $B\ ^3\Sigma_u^-(F_2$ and $F_3)$ are given by

$$\langle {}^3\Sigma_u^-, F_2, v, J|\mathcal{H}|{}^3\Pi_{u0}, v', J, f\rangle = \eta\sqrt{J(J+1)}, \quad \text{(A6a)}$$

$$\langle {}^3\Sigma_u^-, F_3, v, J|\mathcal{H}|{}^3\Pi_{u0}, v', J, e\rangle = \sqrt{2}b(\xi + \sqrt{2}\,\eta) + a\,\eta\sqrt{J(J+1)}, \quad \text{(A6b)}$$

and

$$\langle {}^3\Sigma_u^-, F_2, v, J|\mathcal{H}|{}^3\Pi_{u2}, v', J, f\rangle = -\eta\sqrt{J(J+1)-2}, \tag{A7a}$$

$$\langle {}^3\Sigma_u^-, F_3, v, J|\mathcal{H}|{}^3\Pi_{u2}, v', J, e\rangle = a\eta\sqrt{J(J+1)-2}. \tag{A7b}$$

In the case of $B\,{}^3\Sigma_u^-(v=16, J=3)$, substituting into Eq. (A5) the deperturbed term values $T_3(16,3)$ deduced from Tables I and IV, $T_2(16,3)$ deduced from Table VII, and the unperturbed $T_1(16,3)$ of Yoshino *et al.* [3], we find that $a(16,3)=0.92$ and $b(16,3)=0.38$. If the perturbing substate is $^3\Pi_{u0}$, from Eq. (A6) the ratio of the F_3 and F_2 perturbation matrix elements is

$$\frac{H_3(v,J)}{H_2(v,J)} = a + \frac{\sqrt{2}b(\xi+\sqrt{2}\eta)}{\eta\sqrt{J(J+1)}}. \tag{A8}$$

Thus, $H_3(16,3)/H_2(16,3)\approx 0.92+0.155\xi/\eta$, assuming that $\eta \ll \xi$. With this assumption, the second term (of either sign) will dominate and the ratio will be much greater than unity, inconsistent with our observations. For example, in the case of the interaction between the B state and the $1\,{}^3\Pi_u$ valence state, it has been reported by Lewis *et al.* [4] that $\eta/\xi=0.019$. In this case, $H_3(16,3)/H_2(16,3)\approx 9$. However, if the perturbing substate is $^3\Pi_{u2}$, from Eq. (A7) it follows that $H_3(v,J)/H_2(v,J)=-a$ and $H_3(16,3)/H_2(16,3) = -0.92$. Clearly, this is consistent with our observation, illustrated in Fig. 7, that $|H_3(16,3)/H_2(16,3)|\approx 1$ and demonstrates that the perturber of $B(16)$ is a $^3\Pi_{u2}$ state.

The above arguments, based on a case (a) picture of the $^3\Pi_u$ perturber, are essentially unchanged when we consider a $^3\Pi_u$ state with coupling intermediate between cases (a) and (b), but tending to case (a). This situation is expected to apply for rotational quantum numbers $J \ll Y = A/B$, where A and B are the diagonal spin-orbit and rotational constants of the $^3\Pi_u$ state, respectively. Applying this approximation to the triplet transformation matrix of Kovács [24], we can express the intermediate-coupled $^3\Pi_u$ wave functions in terms of the case (a) basis functions as follows:

$$|'{}^3\Pi_{u0}', v, J\rangle \approx |{}^3\Pi_{u0}, v, J\rangle + \frac{\sqrt{2J(J+1)}}{Y}|{}^3\Pi_{u1}, v, J\rangle, \tag{A9a}$$

$$|'{}^3\Pi_{u1}', v, J\rangle \approx -\frac{(J-1)\sqrt{2(J+1)}}{Y\sqrt{J}}|{}^3\Pi_{u0}, v, J\rangle + |{}^3\Pi_{u1}, v, J\rangle + \frac{J\sqrt{2(J+2)}}{Y\sqrt{(J-1)}}|{}^3\Pi_{u2}, v, J\rangle, \tag{A9b}$$

$$|'{}^3\Pi_{u2}', v, J\rangle \approx -\frac{\sqrt{2(J-1)(J+2)}}{Y}|{}^3\Pi_{u1}, v, J\rangle + |{}^3\Pi_{u2}, v, J\rangle. \tag{A9c}$$

Using Eqs. (A9a) and (A9c), it is easy to show that the form of Eqs. (A6a) and (A7a) remains unchanged when the $^3\Pi_u$ state has intermediate coupling with $J \ll Y$, but the parameter η must be replaced by an effective value given by $\eta_{\text{eff}} \approx \eta + \sqrt{2}\xi/(Y\eta)$. In other words, the conclusion that only $^3\Pi_{u2}$ or $^3\Pi_{u0}$ states can produce purely J-dependent perturbations in the F_2 levels of the B state remains valid for coupling intermediate between cases (a) and (b), but tending to case (a). Thus, the observation that the experimental perturbation matrix elements shown in Fig. 7 do not deviate significantly from a linear J dependence for $J \lesssim 25$ implies that the value of Y for the perturber is significantly greater than 25. Similarly, although Eqs. (A6b) and (A7b) are slightly modified in the case of intermediate coupling, both by the appearance of terms weakly dependent on J^2 and by the introduction of effective values for η in the J-dependent terms, the conclusion, based on a consideration of the ratio $H_3(16,3)/H_2(16,3)$, that the perturber of $B(16)$ is a $^3\Pi_{u2}$ state remains valid.

Support for these conclusions can be obtained from a consideration of Λ doubling in $^3\Pi$ states. For a $^3\Pi$ state conforming to Hund's case (a) coupling ($Y \to \infty$), the Λ-doubling expressions given by Brown and Merer [38] reduce to

$$\Delta T_{fe}({}^3\Pi_0) = 2(o_v + p_v + q_v), \tag{A10a}$$

$$\Delta T_{fe}({}^3\Pi_1) = q_v J(J+1), \tag{A10b}$$

$$\Delta T_{fe}({}^3\Pi_2) = 0, \tag{A10c}$$

where o_v, p_v, and q_v are the normal Λ-doubling parameters [31,38]. The parameter o_v includes the effect of the direct spin-spin interaction and the effects of spin-orbit interactions with other electronic states. The second-order parameters q_v and p_v represent the effects of interactions with other states through the $\mathcal{L}$-uncoupling operator, and through the product of the $\mathcal{L}$-uncoupling and spin-orbit operators, respectively. Broadly speaking, the Λ-doubling parameters for a $^3\Pi$ state embody the same interactions as those responsible for the perturbations in λ_v, γ_v, and B_v for a $^3\Sigma$ state and mathematical inter-relationships can be demonstrated in the case of the unique-perturber approximation and further simplifying assumptions [38].

An examination of Eq. (A10) indicates that the Λ-doubling characteristics for the $^3\Pi_0$ and $^3\Pi_2$ components differ considerably. The lack of doubling expected for a $^3\Pi_2$ level supports the classification of the $B(16)$ perturber as a $^3\Pi_{u2}$ level, since an inspection of Fig. 4 shows minimal splitting between the e and f levels of this perturber. The nonzero doubling expected for a $^3\Pi_0$ level is consistent with the classification of the $B(17$ and $18)$ perturbers as $^3\Pi_{u0}$ levels, since we have observed no e-level perturbers for these B-state levels, implying that the Λ doubling in these cases is large, i.e., beyond the scale of Fig. 4. This can be understood by anticipating the results of Sec. V D in which it is proposed that the B state and the perturbing $^3\Pi_u$ state are in a unique-perturber relationship, resulting in large pertur-

bationsin λ_v for the B-state levels with $v \geq 17$. Under these conditions, it is expected that the magnitude of o_v will be dominated by this unique spin-orbit interaction, and that the e levels of the $^3\Pi_{u0}$ perturber will be pushed to energies significantly higher than the corresponding f levels, since the B state has no $\Omega=0$ levels of f parity. This expectation is consistent with the lack of perturbation of the $F_3(e)$ levels of $B(v=17$ and $18)$ shown in Fig. 4.

[1] M. Nicolet and P. Mange, J. Geophys. Res. **59**, 15 (1954).
[2] M. Nicolet, J. Geophys. Res. **89**, 2573 (1984).
[3] K. Yoshino, D. E. Freeman, and W. H. Parkinson, J. Phys. Chem. Ref. Data **13**, 207 (1984).
[4] B. R. Lewis, S. T. Gibson, and P. M. Dooley, J. Chem. Phys. **100**, 7012 (1994).
[5] B. R. Lewis, L. Berzins, J. H. Carver, and S. T. Gibson, J. Quant. Spectrosc. Radiat. Transfer **36**, 187 (1986).
[6] H. Partridge, C. W. Bauschlicher, S. R. Langhoff, and P. R. Taylor, J. Chem. Phys. **95**, 8292 (1991).
[7] H. Partridge (unpublished).
[8] P. S. Julienne and M. Krauss, J. Mol. Spectrosc. **56**, 270 (1975).
[9] P. S. Julienne, J. Mol. Spectrosc. **63**, 60 (1976).
[10] A. S.-C. Cheung, K. Yoshino, D. E. Freeman, R. S. Friedman, A. Dalgarno, and W. H. Parkinson, J. Mol. Spectrosc. **134**, 362 (1989).
[11] P. Brix and G. Herzberg, Can. J. Phys. **32**, 110 (1954).
[12] A. S.-C. Cheung, K. Yoshino, D. E. Freeman, and W. H. Parkinson, J. Mol. Spectrosc. **131**, 96 (1988).
[13] T. H. Bergeman and S. C. Wofsy, Chem. Phys. Lett. **15**, 104 (1972).
[14] R. N. Zare, A. L. Schmeltekopf, W. J. Harrop, and D. L. Albritton, J. Mol. Spectrosc. **46**, 37 (1973).
[15] B. R. Lewis, J. P. England, R. J. Winkel, Jr., S. S. Banerjee, P. M. Dooley, S. T. Gibson, and K. G. H. Baldwin, Phys. Rev. A **52**, 2717 (1995).
[16] R. Hilbig and R. Wallenstein, IEEE J. Quantum Electron. **QE-19**, 194 (1983).
[17] K. Yamanouchi and S. Tsuchiya, J. Phys. B **28**, 133 (1995).
[18] The VUV bandwidth was found to be sensitive to the dye-laser pulse energies and the details of the dye-laser oscillator setup procedures. In normal operation, the pulse energies were reduced until the observed linewidths became constant, and temporal variations in bandwidth were monitored by the repeated measurement of a narrow reference line.
[19] L. Veseth and A. Lofthus, Mol. Phys. **27**, 511 (1974).
[20] B. R. Lewis, P. M. Dooley, J. P. England, S. T. Gibson, K. G. H. Baldwin, and L. W. Torop (unpublished).
[21] J. Almlöf and P. R. Taylor, J. Chem. Phys. **86**, 4070 (1987).
[22] The subscript x indicates an extra line associated with a transition into the perturbing state: for example, $P_{3x}(5)$ refers to the extra line which perturbs the main line $P_3(5)$.
[23] H. Lefebvre-Brion and R. W. Field, *Perturbations in the Spectra of Diatomic Molecules* (Academic, Orlando, 1986), pp. 39, 51–58, 196–197, 226–231, 247–248.
[24] I. Kovács, *Rotational Structure in the Spectra of Diatomic Molecules* (Hilger, London, 1969), pp. 68–70, 76–79, 258–261.
[25] R. S. Mulliken, Rev. Mod. Phys. **3**, 89 (1931).
[26] R. P. Saxon and B. Liu, J. Chem. Phys. **67**, 5432 (1977).
[27] S. T. Gibson, B. R. Lewis, K. G. H. Baldwin, and J. H. Carver, J. Chem. Phys. **94**, 1060 (1991).
[28] Due to the fragmentary observations of the C'-state levels, we used the simple polynomial form $\nu_0+BJ(J+1)-D[J(J+1)]^2$ to describe the unperturbed term values of the B and C' states. Thus, our deperturbed band origins will be defined differently from those obtained using a full molecular Hamiltonian in the deperturbation procedure.
[29] The deperturbed term value for $C'\ ^3\Pi_{u2}(J=3,f)$ must be estimated since this is a virtual level. In the case of a homonuclear molecule with nuclear spin $I=0$, such as $^{16}O_2$, the odd-J levels of a $^3\Pi_{u2}(f)$ state have zero statistical weight [30].
[30] G. Herzberg, *Molecular Spectra and Molecular Structure I. Spectra of Diatomic Molecules* (Van Nostrand, New York, 1950), pp. 133–140.
[31] J. M. Brown, E. A. Colbourn, J. K. G. Watson, and F. D. Wayne, J. Mol. Spectrosc. **74**, 294 (1979).
[32] R. W. Field and H. Lefebvre-Brion, Acta Phys. Hung. **35**, 51 (1974).
[33] B. R. Lewis, L. Berzins, and J. H. Carver, J. Quant. Spectrosc. Radiat. Transfer **36**, 209 (1986).
[34] The assumption of R-independent off-diagonal matrix elements between the B and C' states may not be very good due to R-dependent configuration mixing.
[35] E. Wigner and E. E. Witmer, Z. Phys. **51**, 859 (1928).
[36] I. Kovács, Z. Phys. **111**, 640 (1939).
[37] I. Kovács, Can. J. Phys. **36**, 309 (1958).
[38] J. M. Brown and A. J. Merer, J. Mol. Spectrosc. **74**, 488 (1979).
[39] K. F. Freed, J. Chem. Phys. **45**, 4214 (1966).
[40] J. K. G. Watson, Can. J. Phys. **46**, 1637 (1968).
[41] J. B. Tatum and J. K. G. Watson, Can. J. Phys. **49**, 2693 (1971).

4.28 Identification of two $^3\Sigma_u^- \leftarrow X\,^3\Sigma_g^-$ transitions of O_2 near 88930 and 90780 cm^{-1}

[48] J. P. England, B. R. Lewis, and M. L. Ginter,
Journal of Chemical Physics **105**, 1754–1763 (1996).

Identification of two $^3\Sigma_u^- \leftarrow X^3\Sigma_g^-$ transitions of $^{16}O_2$ near 88930 and 90780 cm^{-1}

J. P. England and B. R. Lewis
Research School of Physical Sciences and Engineering, The Australian National University, Canberra, ACT 0200, Australia

M. L. Ginter
Institute for Physical Science and Technology, University of Maryland, College Park, Maryland 20742

(Received 13 March 1996; accepted 19 April 1996)

New $^{16}O_2$ photoabsorption cross-section measurements are presented for two bands near 88930 cm^{-1} and 90780 cm^{-1}. We have assigned these bands as the (0,0) and (1,0) bands of the $E'^3\Sigma_u^- \leftarrow X^3\Sigma_g^-$ system, where the E' state is a mixed state resulting from the coupling of $4p\pi_u$ and $5p\pi_u$ $^3\Sigma_u^-$ Rydberg states with the lowest $^3\Sigma_u^-$ valence state. In contrast to the $E^3\Sigma_u^- \leftarrow X^3\Sigma_g^-$ bands seen at lower energies, these bands show resolved rotational structure. Spectroscopic parameters for the upper levels have been derived using an effective Hamiltonian and cross-section band models. The observed levels are perturbed by spin-orbit interactions with nearby levels ($v=1$ and 2) of the $4p\pi_u$ $D'^3\Sigma_u^+$ Rydberg state. In addition, transitions to the $v=2$ level of the perturber state have been observed near 90920 cm^{-1}. © *1996 American Institute of Physics.* [S0021-9606(96)02628-1]

I. INTRODUCTION

The O_2 ground-state photoabsorption spectrum in the vacuum ultraviolet (VUV) region at energies below the first ionization threshold (12.07 eV)[1] is important in atmospheric photochemistry.[2] Despite extensive studies of the spectrum,[3] many features in the region 9.5–12.0 eV (1030–1300 Å) remain unassigned. In general, difficulties in assigning features in this region are caused by the diffuseness of some bands and structural and intensity irregularities introduced by strong couplings between Rydberg and valence states.

Selected potential-energy curves for O_2 are shown in Fig. 1. The O_2 ground $X^3\Sigma_g^-$ state and the metastable $a^1\Delta_g$ and $b^1\Sigma_g^+$ states are associated with the molecular-orbital configuration $(1\sigma_g)^2(1\sigma_u)^2(2\sigma_g)^2(2\sigma_u)^2(3\sigma_g)^2(1\pi_u)^4 \times (1\pi_g)^2$. The lowest-energy Rydberg states are those built on the $X^2\Pi_g$ ground state of O_2^+, which has the configuration $(1\sigma_g)^2(1\sigma_u)^2(2\sigma_g)^2(2\sigma_u)^2(3\sigma_g)^2(1\pi_u)^4(1\pi_g)^1$. The np complexes formed by the addition of an electron in an $np\sigma_u$ or $np\pi_u$ orbital consist of *ungerade* states of symmetries $^1\Pi_u$, $^3\Pi_u$, $^1\Sigma_u^\pm$, $^3\Sigma_u^\pm$, $^1\Delta_u$ and $^3\Delta_u$. In the photoabsorption spectra of the ground and metastable states, the only regular *ungerade* Rydberg vibrational progressions which have been definitively identified involve the lower vibrational levels of the $3p\pi_u f^1\Sigma_u^+$, $4p\pi_u j^1\Sigma_u^+$ and $3p\pi_u D^3\Sigma_u^+$ states.[4,5]

Transitions to $^3\Sigma_u^-$ and $^3\Pi_u$ states from the ground state are electric-dipole-allowed and are, therefore, expected to give the strongest features in the O_2 ground-state absorption spectrum. Recent work by England *et al.*[6] has led to definitive assignments of vibrational bands of $^3\Pi_u \leftarrow X^3\Sigma_g^-$ transitions in the region 1040–1200 Å, with 10 bands identified for $^{16}O_2$ and 9 bands for $^{18}O_2$. The upper levels of these transitions have irregularities which were shown to result from the strong coupling of the repulsive $1\,^3\Pi_u$ valence state shown in Fig. 1 with Rydberg states having principal quantum numbers $n=3,4,\ldots,7$. Quantitative modelling[6] using coupled-channel Schrödinger equations (CSE) calculations gave values for the interaction matrix elements between $np\sigma_u$ $^3\Pi_u$ Rydberg states ($n=3,4,5$, and 6) and the $1\,^3\Pi_u$ valence state which decrease with n slightly more than the expected $(n^*)^{-3/2}$ dependence[7] ($n^*=n-\delta$ is the effective quantum number and δ is the quantum defect), with a matrix element of $H_3^e=7110\pm50$ cm^{-1} for the interaction between the $3p\sigma_u$-Rydberg and valence states.

Similar, but less extensive, CSE modelling has been carried out[8–10] for the interaction between the $3p\pi_u$ $^3\Sigma_u^-$ Rydberg state and the $1\,^3\Sigma_u^-$ valence state. Figure 1 shows adiabatic potential-energy curves for the $B^3\Sigma_u^-$ and $E^3\Sigma_u^-$ states resulting from this interaction. Transitions to the lower $B^3\Sigma_u^-$ state give rise to the Schumann–Runge bands and continuum (1300–2050 Å), and transitions to the first three vibrational levels of the $E^3\Sigma_u^-$ state give rise to the bands known as Tanaka's longest, second and third bands,[11] near 1244, 1206 and 1173 Å, respectively, which are all diffuse in the spectrum of $^{16}O_2$.[12] The interaction matrix element H_3^e between the $3p\pi_u$ Rydberg and valence states was estimated[9] to be 3780 cm^{-1} by fitting model calculations to the cross sections for the longest bands[9] of $^{16}O_2$, $^{16}O^{18}O$ and $^{18}O_2$, and to the temperature dependence of the Schumann–Runge continuum.[8] A similar value of $H_3^e=4038$ cm^{-1} was obtained by Lewis *et al.*[10] from fitting measurements of the longest and second bands[13,14] and the Schumann–Runge $O(^1D)+O(^3P)$ photodissociation continuum.[15,16] From the definition of the adiabaticity parameter,[17] the B and E states are intermediate between diabatic and adiabatic[17] in the region near the crossing of their diabatic counterparts, and their quantitative description requires CSE calculations.

Higher energy $^3\Sigma_u^- \leftarrow X^3\Sigma_g^-$ bands are expected to exist due to transitions to higher levels of the E state and to levels of higher-energy mixed $np\pi_u$ ($n\geq4$) Rydberg-valence

 0021-9606/96/105(5)/1754/10/$10.00

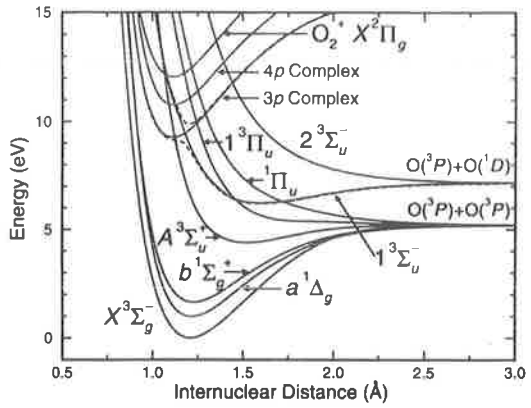

FIG. 1. Selected potential-energy curves for O_2. Curves for the states of np Rydberg complexes are drawn schematically. The adiabatic curves of Lewis *et al.* (Ref. 10) for the $B^3\Sigma_u^-$ and $E^3\Sigma_u^-$ states are shown as dashed lines.

states. However, no such bands have been identified with certainty. Chang[18] postulated that two bands at 86680 cm^{-1} and 90750 cm^{-1} were $^3\Sigma_u^- \leftarrow X^3\Sigma_g^-$ transitions. However, the band at 86680 cm^{-1} has since been reclassified as an $F^3\Pi_u \leftarrow X^3\Sigma_g^-$ transition,[6] while the band at 90750 cm^{-1} was described as diffuse and rotational lines were not definitively identified.[18]

In this paper, we present measurements of two bands at 88930 cm^{-1} and 90780 cm^{-1} in the $^{16}O_2$ spectrum that we have assigned to $^3\Sigma_u^- \leftarrow X^3\Sigma_g^-$ transitions on the basis of rotational analyses. These are the first $^3\Sigma_u^- \leftarrow X^3\Sigma_g^-$ bands with observable rotational structure found in the $^{16}O_2$ spectrum at energies higher than the Schumann–Runge bands.[12] The observed bands exhibit strong perturbations in their rotational structure. We discuss the origin of these perturbations, describe the nature of the observed electronic states, and make vibrational assignments.

II. EXPERIMENTS

This study has used two different methods for generating tunable VUV radiation. In the first method, described in detail by England *et al.*,[19] tunable VUV radiation in the range 1120–1130 Å was produced using third harmonic generation[20] by focussing radiation from an excimer-pumped dye laser into a cell containing Kr at a pressure of ~90 Torr. A 0.2 m monochromator was used to prevent the fundamental laser radiation, propagating collinearly with the VUV radiation, from entering the absorption cell. Measurements of Xe and H_2 (0,0) Lyman-band absorption lines near 1130 Å enabled us to estimate the VUV bandwidth to be ~ 0.006 Å (0.5 cm^{-1}) full width at half maximum (FWHM). The wavelengths of the O_2 absorption measurements were calibrated to within ~0.003 Å (0.25 cm^{-1}) using measurements of the (1,0) band of the CO $B^1\Sigma^+ \leftarrow X^1\Sigma^+$ system.[21] This apparatus was limited to wavelengths >1118 Å.

To access shorter wavelengths, an argon–dimer continuum discharge lamp was used with a 2.2 m scanning monochromator to give radiation with a bandwidth of ~0.030 Å (2.5 cm^{-1}) FWHM. This second apparatus has been described in more detail by Lewis *et al.*[22] The monochromator wavelengths in the region 1095–1110 Å were calibrated using emission lines[23] of N I and absorption lines

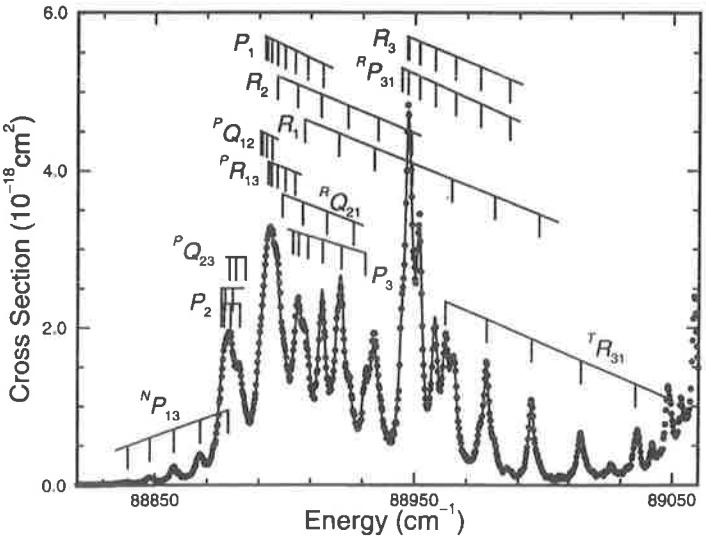

FIG. 2. The photoabsorption cross section (T=79 K) of the $^3\Sigma_u^- \leftarrow X^3\Sigma_g^-$ band of $^{16}O_2$ measured near 88930 cm^{-1} using the laser-based apparatus (solid circles). Also shown (solid line) is the result of the band-model fit to the cross section in the region 88813.8–89015.5 cm^{-1}. The positions of rotational lines indicated are those calculated from the spectroscopic parameters in Table V. Note that the $^RQ_{32}$ branch is not shown because the lines of this branch are predicted by our band model to be very weak. Some peaks on the high-energy side of the band are associated with a different transition.

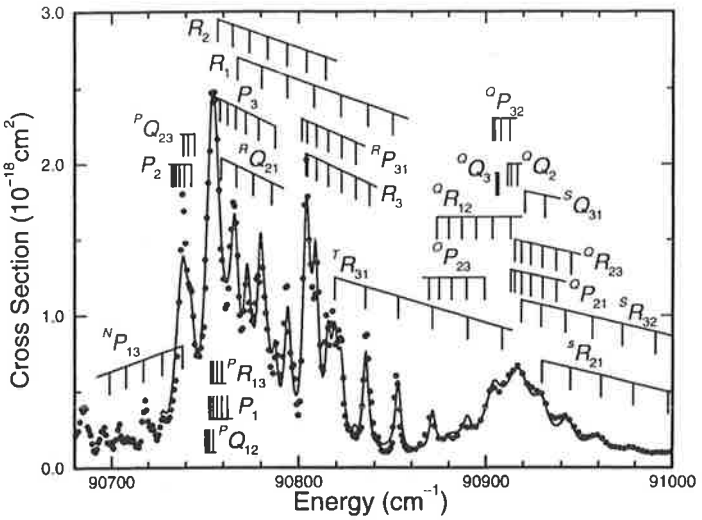

FIG. 3. The photoabsorption cross section ($T=79$ K) of the $^3\Sigma_u^- \leftarrow X^3\Sigma_g^-$ band of $^{16}O_2$ measured near 90780 cm^{-1} using the monochromator-based apparatus (solid circles). Note that the measured cross section is affected by the instrumental bandwidth. Also shown (solid line) is the result of the band model fit to the cross section in the region 90726.9–90991.0 cm^{-1} assuming coupled $^3\Sigma_{1u}^+$ and $^3\Sigma_{1u}^-$ upper states. The positions of rotational lines indicated are those calculated from the spectroscopic parameters in Table VI. Note that the $^RQ_{32}$ branch of the $^3\Sigma_u^- \leftarrow X^3\Sigma_g^-$ band and the $^QQ_1$, $^OP_{12}$, and $^OQ_{13}$ branches of the $^3\Sigma_u^+ \leftarrow X^3\Sigma_g^-$ band are not shown because the lines of these branches are predicted by our band model to be very weak. Some lines on the low-energy side of the spectrum are associated with a different transition.

from the $B^1\Sigma_u^+ \leftarrow X^1\Sigma_g^+$ Lyman bands of H_2,[24] and are expected to be accurate to within ~0.01 Å (0.8 cm^{-1}).

LiF windows were used on the O_2 absorption cells for each apparatus. The cells could be cooled to give an effective gas temperature of 79±0.5 K, in order to simplify the absorption cross section by reducing the rotational structure and the overlap with adjacent transitions. Samples of oxygen (BOC 99.9%, containing 99.8 at. % ^{16}O) were used at pressures of 0.15–10 Torr, and the absorption path length was 10.9 cm. The incident and transmitted radiation was detected photoelectrically using solar-blind photomultipliers equipped with LiF windows. Absolute cell transmittances were obtained by dividing the ratio of the transmitted and incident intensities measured with the cell full by the same ratio measured with the cell empty.

The Beer–Lambert law was used to convert measured cell transmittances into photoabsorption cross sections. The laser radiation has a bandwidth much less than the rotational linewidths of the measured bands and, therefore, the laser-based measurements yield absolute cross sections. However, the monochromator-based measurements give effective cross sections because rotational linewidths are less than the instrumental bandwidth.

III. RESULTS

Low-temperature $^{16}O_2$ photoabsorption cross sections for the two bands studied in this work are shown in Figs. 2 and 3. Both bands are strong compared with other bands in this region of the spectrum and show similar rotational structures with each having three band heads. Assignments of rotational lines were made with the aid of combination differences and the known ground-state rotational energies,[25] and the structure was found to be consistent with a

TABLE I. Measured transition energies (cm^{-1}) for the $^3\Sigma_u^- \leftarrow X^3\Sigma_g^-$ band near 88930 cm^{-1}. Uncertainties are ≤0.3 cm^{-1}, except where lines are blended.

N''	$^NP_{13}$	R_1	$P_1+^PR_{13}$	R_2	P_2	$^TR_{31}$	$R_3+^RP_{31}$	P_3
1		88907.5[a]		88897.0[a]		88961.9	88947.4[a] 88944.9[a]	
3	88878.8[a]	88921.3[a]		88905.0	88882.3[a]	88977.6	88947.4[a]	88931.4
5	88867.3	88934.3	88894.5[a]	88914.4[a]	88878.8	88995.1	88951.8	88921.3[a]
7	88857.5	88948.7[a]	88896.6[a]	88924.6[a]		89014.4	88957.7	88914.4[a]
9	88848.1	88963.9[a]	88899.7[a]	88936.4[a]		89036.3[a]	88965.2[a]	88908.7
11	88839.8	88980.7					88975.1[a]	88905.0[a]
13	88832.3	88998.1					88986.1	88903.8[a]
15	88825.9	89016.4[a]					88998.1[a]	
17	88820.2						89013.1[a]	

[a]Blended line.

TABLE II. Measured transition energies (cm^{-1}) for the $^3\Sigma_u^- \leftarrow X^3\Sigma_g^-$ band near 90780 cm^{-1}. Uncertainties are ≤ 1.0 cm^{-1}, except where lines are blended.

N''	$^NP_{13}$	R_1	$P_1+{}^PR_{13}$	R_2	P_2	$^TR_{31}$	$R_3+{}^RP_{31}$	P_3
1		90765.8[a]		90757.0[a]		90817.8[a]	90803.9[a]	
3	90738.3[a]	90779.4	90754.8[a]	90765.8[a]	90743.1	90835.8	90803.9[a]	90788.3
5	90727.8	90793.7	90754.8[a]	90772.6[a]		90852.0	90809.7[a]	90778.1[a]
7		90806.8[a]				90870.3	90814.6	90772.5[a]
9		90822.2[a]				90888.3		

[a]Blended line.

$^3\Sigma_u^- \leftarrow X^3\Sigma_g^-$ transition.[26] Of the 14 possible rotational branches for such a transition, we have identified lines from 9, including quite strong lines of the $^TR_{31}$ and $^NP_{13}$ branches [branches have been labelled using the notation $^{\Delta N}\Delta J(N'')$ with subscripts referring to the upper- and lower-state fine-structure levels, F_1, F_2 or F_3, respectively],[27] which are forbidden if the upper and lower states are pure Hund's case (b). One striking feature of both bands is the separation in energy of subbands for transitions to F_3 upper-state levels from those to F_1 and F_2 levels, indicating strong perturbations by other electronic states and resulting in a level structure reminiscent of Hund's case (a).

Measured wave numbers and rotational assignments are given in Tables I and II. The corresponding upper-state rotational term values, determined using the ground-state rotational energies of Amiot and Verges,[25] are given in Tables III and IV. The high N'' rotational lines given in Table I were identified from cross-section measurements obtained at a temperature of 297 K. Fewer lines were assigned for the 90780 cm^{-1} band than for the 88930 cm^{-1} band because of lower resolution and the presence of overlapping features from another band which prevents identification of the weaker rotational lines from the $^NP_{13}$ branch.

The only previous assignments of features in these bands are those of Chang,[18] who attributed the 88930 cm^{-1} band to $^3\Sigma_u^+ \leftarrow X^3\Sigma_g^-$ and $^1\Pi_u \leftarrow X^3\Sigma_g^-$ transitions with band origins of 88944.4 cm^{-1} and 88889.0 cm^{-1}, respectively, and the 90780 cm^{-1} band to $^3\Sigma_u^- \leftarrow X^3\Sigma_g^-$ and $^3\Sigma_u^+ \leftarrow X^3\Sigma_g^-$ transitions with band origins of 90748 cm^{-1} and 90805.2 cm^{-1}, respectively.[18] Only one branch of the $^1\Pi_u \leftarrow X^3\Sigma_g^-$ band had a significant number of identified lines, while two of the four branches for the $^3\Sigma_u^- \leftarrow X^3\Sigma_g^-$ band were not resolved and upper-state spin components were not identified. We have shown that it is not necessary to invoke multiple transitions to explain the observed bands and, in addition, the bands are too strong to be electric-dipole-forbidden transitions. Therefore, the previous assignments must be discarded.

TABLE III. Term values (cm^{-1}) for the upper state of the $^3\Sigma_u^- \leftarrow X^3\Sigma_g^-$ transition near 88930 cm^{-1} calculated from the measured transition energies of Table I and ground-state rotational energies of Amiot and Verges (Ref. 25). Uncertainties are $\lesssim 0.3$ cm^{-1}, except where lines are blended.

J'	$^3\Sigma_{1u}^-e$	$^3\Sigma_{1u}^-f$	$^3\Sigma_{0u}^-e$
1	88893.9[a]		88946.6
2		88899.7[a]	
3	88908.4		88962.9
4		88922.2	
5	88936.1		88992.9
6		88957.5	
7	88975.5		89036.2
8		89005.1	
9	89027.5		89092.9
10		89065.8	
11	89091.9		89163.3[a]
13	89168.6		89245.7
15	89257.7		89341.1[a]
17	89359.1[a]		89450.7[a]

[a]Estimated from blended lines.

IV. BAND MODELS

$^3\Sigma$ states are normally found to be close to Hund's coupling case (b) because first-order spin-orbit coupling in a $^3\Sigma$ state is zero. However, the effects of spin-orbit coupling with other electronic states (second-order effects[26]) and spin-spin interactions are similar to, although normally much smaller than, the effects of first-order spin-orbit coupling. This led Tatum and Watson[26] to describe $^3\Sigma^\pm$ states as intermediate between cases (a) and (b). In terms of symmetrized case (a) basis functions, the effective Hamiltonian for $^3\Sigma_u^-$ states of intermediate case (a)-(b) coupling is[28–30]

$$\begin{array}{c} \\ ^3\Sigma_{1u}^-, e \\ ^3\Sigma_{0u}^-, e \\ ^3\Sigma_{1u}^-, f \end{array} \begin{array}{c} \begin{array}{ccc} ^3\Sigma_{1u}^-, e & ^3\Sigma_{0u}^-, e & ^3\Sigma_{1u}^-, f \end{array} \\ \begin{pmatrix} H_{11} & H_{12} & 0 \\ H_{12} & H_{22} & 0 \\ 0 & 0 & H_{33} \end{pmatrix} \end{array}, \quad (1)$$

where

TABLE IV. Term values (cm^{-1}) for the upper state of the $^3\Sigma_u^- \leftarrow X^3\Sigma_g^-$ transition near 90780 cm^{-1} calculated from the measured transition energies of Table II and ground-state rotational energies of Amiot and Verges (Ref. 25). Uncertainties are $\lesssim 1.0$ cm^{-1}, except where lines are blended.

J'	$^3\Sigma_{1u}^-e$	$^3\Sigma_{1u}^-f$	$^3\Sigma_{0u}^-e$
1	90753.4[a]		90803.4
2		90760.4[a]	
3	90768.9		90819.1[a]
4		90783.0[a]	
5	90794.7		90851.2
6		90815.7[a]	
7	90834.8		90893.2
9	90885.2[a]		90948.7
11	90949.5[a]		91015.6

[a]Estimated from blended lines.

TABLE V. Spectroscopic parameters for the observed $^3\Sigma_u^- \leftarrow X^3\Sigma_g^-$ bands. Values of T, B, λ and γ are those obtained by fitting the upper-state term values given in Tables III and IV. Other parameters were obtained by fitting the band model to the measured cross section assuming a $^3\Sigma_u^-$ upper state which is tending to Hund's coupling case (c) (see Sec. IV).

Parameter	88930 cm^{-1} band	90780 cm^{-1} band
T (cm^{-1})	88908.3±0.3	90768.2±0.9
B (cm^{-1})	1.596±0.002	1.566±0.016
λ (cm^{-1})	−25.1±0.3	−24.0±1.1
γ (cm^{-1})	1.09±0.03	1.17±0.26
$f_{v'v''}\times 10^4$	2.13±0.06	1.5±0.3
μ_{11}/μ_{00}	0.78±0.08	0.87±0.15
$\Gamma(^3\Sigma_{0u}^-e)$ (cm^{-1} FWHM)	4.1±0.1	0.8±0.7
$\Gamma(^3\Sigma_{1u}^-e)$ (cm^{-1} FWHM)	5.8±0.2	4.0±1.1
$\Gamma(^3\Sigma_{1u}^-f)$ (cm^{-1} FWHM)	6.4±0.3	1.7±1.0

$$H_{11}=T+Bx-D(x^2+4x)+\tfrac{2}{3}(\lambda+\lambda_D x)-\gamma-3\gamma_D x,$$

$$H_{22}=T+B(x+2)-D(x^2+8x+4)-\tfrac{4}{3}[\lambda+\lambda_D(x+2)]-2\gamma-4\gamma_D(x+1),$$

$$H_{33}=T+Bx-Dx^2+\tfrac{2}{3}(\lambda+\lambda_D x)-\gamma-\gamma_D x,$$

and

$$H_{12}=-2\sqrt{x}\left[B-2D(x+1)-\frac{\gamma}{2}-\frac{\lambda_D}{3}-\frac{\gamma_D}{2}(x+4)\right],$$

with $x=J(J+1)$. Here, the parameter T is related to the band origin ν_0 of Brix and Herzberg[31] by $\nu_0=T+2\lambda/3-\gamma$, B is the rotational constant, λ accounts both for the effects of spin-spin and second-order spin-orbit interactions, γ accounts for spin-rotation effects, and D, λ_D and γ_D are centrifugal-distortion parameters. These parameters are effective parameters which include the effects of the coupling of other electronic states with the $^3\Sigma_u^-$ state being considered.

Spectroscopic constants given in Table V for each upper state were determined by fitting calculated eigenvalues of the Hamiltonian matrix in Eq. (1) to the experimental term values using a least-squares algorithm. The upper-state term values for the 88930 cm^{-1} and 90780 cm^{-1} bands were fitted to within 0.4 cm^{-1} and 0.9 cm^{-1}, respectively. The inclusion of the centrifugal distortion parameters did not improve the fits significantly, and, therefore, they were set to zero to obtain the final results. The constants obtained for each band are similar, reflecting the similarity of the structures of the bands.

The values of B are significantly lower than those expected for low vibrational levels of an unperturbed Rydberg state.[4] In addition, both upper levels have a large and negative value of λ (≈ -25 cm^{-1}) since the F_3 ($\sim{}^3\Sigma_{0u}^-,e$) component occurs at a higher energy than the F_1 ($\sim{}^3\Sigma_{1u}^-,e$) and F_2 ($\sim{}^3\Sigma_{1u}^-,f$) components, indicating that large spin-orbit interactions with other electronic states are present.

Values for predissociation linewidths and band oscillator strengths were derived by fitting an empirical band model directly to the measured absorption cross sections.[32] The band model employed was similar to models described previously,[10,13,14] except that Lorentzian functions were used in this work to represent the predissociation line shapes since the observed rotational lines exhibit no significant asymmetries. Rotational line centers were calculated using the ground-state rotational term values of Amiot and Verges[25] and eigenvalues of the effective Hamiltonian given in Eq. (1).

Rotational line strengths used in the band model were those of Tatum and Watson.[26] If the spin-orbit coupling is small, then only one electronic transition moment is necessary in the line-strength formulae. However, more general expressions for intensities tending to Hund's coupling case (c),[26] valid for larger spin-orbit mixing, contain four independent real transition moments: the parallel transition moments

$$\mu_{00}=\langle{}^3\Sigma_{0u}^-|\mu_z|X^3\Sigma_{0g}^-\rangle$$

and

$$\mu_{11}=\langle{}^3\Sigma_{1u}^-|\mu_z|X^3\Sigma_{1g}^-\rangle=\langle{}^3\Sigma_{-1u}^-|\mu_z|X^3\Sigma_{-1g}^-\rangle;$$

and the perpendicular transition moments

$$\mu_{01}=\frac{1}{\sqrt{2}}\langle{}^3\Sigma_{0u}^-|\mu_x-i\mu_y|X^3\Sigma_{1g}^-\rangle=-\frac{1}{\sqrt{2}}\langle{}^3\Sigma_{0u}^-|\mu_x+i\mu_y|X^3\Sigma_{-1g}^-\rangle,$$

and

$$\mu_{10}=\frac{1}{\sqrt{2}}\langle{}^3\Sigma_{1u}^-|\mu_x+i\mu_y|X^3\Sigma_{0g}^-\rangle=-\frac{1}{\sqrt{2}}\langle{}^3\Sigma_{-1u}^-|\mu_x-i\mu_y|X^3\Sigma_{0g}^-\rangle,$$

where μ_j ($j=x,y,z$) are molecule-fixed components of the electric-dipole operator, and the wave functions used here are unsymmetrized. Intermediate case (a)–(b) line strengths can be obtained from the Tatum and Watson formulae by setting $\mu_{00}=\mu_{11}$ and $\mu_{01}=\mu_{10}=0$. In the present band model, only the relative transition moments, μ_{11}/μ_{00}, μ_{01}/μ_{00}, μ_{10}/μ_{00}, are used, and an extra parameter is used to represent the band oscillator strength $f_{v',v''}=1.130\times 10^{12}\int_{\text{band}}\sigma(\nu)d\nu$, where the absorption cross section σ is in units of cm^2 and the transition energy ν is in wave numbers (cm^{-1}).

Other parameters included in the model were independent predissociation linewidths for the three case (a) basis states, $\Gamma(^3\Sigma_{0u}^-,e)$, $\Gamma(^3\Sigma_{1u}^-,e)$ and $\Gamma(^3\Sigma_{1u}^-,f)$ [actual predissociation linewidths were determined by summing the case (a) widths with coefficients being the squares of the basis-function mixing coefficients, c_J and s_J, obtained from eigenvectors of Eq. (1)], and three parameters to model an underlying continuum cross section varying quadratically with wavelength. To determine the model cross section to be

compared with experiment, the simulated spectrum is convolved with the Doppler function and then convolved, in transmission, with a Gaussian instrumental function.

A. The 88930 cm^{-1} band

The cross-section model fit to the $^3\Sigma_u^- \leftarrow X^3\Sigma_g^-$ band near 88930 cm^{-1}, shown in Fig. 2, was restricted to energies 88813.8–89015.5 cm^{-1} to avoid contributions from the nearby $F^3\Pi_u \leftarrow X^3\Sigma_g^-$ (3,0) band[6] at higher energy. An excellent fit was obtained, with the root-mean-square (rms) deviation being $\sim 6\times 10^{-20}$ cm^2. The spectroscopic parameters, T, B, λ and γ, derived from the fit agree with those obtained independently by fitting the term values in Table III only. Other non-zero parameters obtained from the band-model fit are given in Table V. Background parameters and μ_{01}/μ_{00} and μ_{10}/μ_{00} parameters were not required to obtain the high level of agreement with experiment indicated above. The derived parameters show that the $^3\Sigma_{0u}^-$ component has a significantly smaller predissociation width than the other components, and the $^3\Sigma_{1u}^- \leftarrow X^3\Sigma_g^-$ subbands of the transition are weaker than the $^3\Sigma_{0u}^- \leftarrow X^3\Sigma_g^-$ subband ($\mu_{11} < \mu_{00}$).

These effects, and the large splitting of the upper-state $^3\Sigma_{0u}^-$, e component from the $^3\Sigma_{1u}^-$, e and $^3\Sigma_{1u}^-$, f components, are all due to homogeneous perturbations (interacting electronic states with $\Delta\Omega = 0$).[7] Of the possible homogeneous interactions, $^3\Pi_u - {}^3\Sigma_u^-$ spin-orbit interactions would give non-zero values for μ_{01} and μ_{10} while μ_{11} and μ_{00} would remain equal. Also, $^3\Sigma_u^- - {}^3\Sigma_u^-$ interactions would neither produce a large value of $|\lambda|$ nor change the relative sizes of μ_{00} and μ_{11}. Thus, we can eliminate the only perturbations leading to an enhancement in the strength of any part of the transition, since only $^3\Sigma_u^- \leftarrow X^3\Sigma_g^-$ and $^3\Pi_u \leftarrow X^3\Sigma_g^-$ transitions are electric-dipole allowed. Therefore, the interaction must be one that leads to a decrease in the strength of the $^3\Sigma_{1u}^- \leftarrow X^3\Sigma_g^-$ subbands relative to the $^3\Sigma_{0u}^- \leftarrow X^3\Sigma_g^-$ subband. The only homogeneous interactions with the $^3\Sigma_{1u}^-$ components which do not also perturb the $^3\Sigma_{0u}^-$ component are spin-orbit interactions with $^1\Pi_{1u}$ and $^3\Sigma_{1u}^+$ states. Finally, since the $^3\Sigma_{1u}^-$ components are shifted down in energy, the preponderance of the perturbation must be produced by a level or levels at higher energy than the $^3\Sigma_u^-$ level under consideration. The relative linewidths of the $^3\Sigma_{1u}^- \leftarrow X^3\Sigma_g^-$ and $^3\Sigma_{0u}^- \leftarrow X^3\Sigma_g^-$ subbands imply that the perturber state has a relatively short lifetime compared with the $^3\Sigma_u^-$ state.

Due to experimental uncertainties, it is not possible to use the values of the parameters λ and μ_{11}/μ_{00} to predict reliably the position of the nearest perturber level. In addition, we have not been able to observe the transitions to the perturber level because the region 89030–89320 cm^{-1} is obscured by the presence of the relatively strong $F^3\Pi_u \leftarrow X^3\Sigma_g^-$ (3,0) band.

B. The 90780 cm^{-1} band

The fit to the cross section for this band (not shown in Fig. 3) was not as good as that for the lower-energy band. There are two main reasons for this. First, the measurements were taken at lower resolution and, therefore, they contain less information. Second, it is likely that there are features from other transitions [the $F^3\Pi_u \leftarrow X^3\Sigma_g^-$ (4,0) band[6] and the $4f$-complex[18]] in the cross section on the low-energy side of the band. Our best fits to the cross section in the energy range 90722.7–90867.8 cm^{-1} gave a rms deviation of $\sim 1.4\times 10^{-19}$ cm^2. The values of spectroscopic parameters ($T = 90767.1$ cm^{-1}, $B = 1.591$ cm^{-1}, $\lambda = -23.3$ cm^{-1} and $\gamma = 0.9$ cm^{-1}) obtained in this fit are slightly different from the values listed in Table V, presumably because of the extra information contained in the cross section data and because errors are introduced by a failure of the model to adequately account for features from other transitions in the cross section.

Overall, the spectroscopic parameters are similar to those obtained from the fit to the 88930 cm^{-1} band. In particular, the $^3\Sigma_{1u}^- \leftarrow X^3\Sigma_g^-$ subbands are, again, broader and less intense than the $^3\Sigma_{0u}^- \leftarrow X^3\Sigma_g^-$ subband. Therefore, as with the 88930 cm^{-1} band discussed in Sec. IVA, it is likely that the perturbing state is a short-lived $^1\Pi_{1u}$ or $^3\Sigma_{1u}^+$ state which interacts with the $^3\Sigma_{1u}^-$ state through spin-orbit coupling. In this case, however, there is no obscuring transition in the region where we expect to see transitions to the perturber state, and a weak, diffuse band can be seen near 90920 cm^{-1} (shown in Fig. 3).

A cross-section model for the case of a transition to a mixed $^3\Sigma_u^- - {}^3\Sigma_u^+$ upper state was developed to fit simultaneously the two bands near 90780 cm^{-1} and 90920 cm^{-1}. With case (a) basis functions, the effective Hamiltonian for the upper states contains the elements given in Eq. (1) for the $^3\Sigma_u^-$ state, with similar elements for the $^3\Sigma_u^+$ state (e and f labels interchanged), and a vibronic parameter $H_{\rm int} = \langle {}^3\Sigma_{1u}^+, e, v | \mathbf{H}^{\rm SO} | {}^3\Sigma_{1u}^-, e, v' \rangle = \langle {}^3\Sigma_{1u}^+, f, v | \mathbf{H}^{\rm SO} | {}^3\Sigma_{1u}^-, f, v' \rangle$ representing the effects of the $^3\Sigma_{1u}^- - {}^3\Sigma_{1u}^+$ spin-orbit interaction. Two parameters, used to represent the predissociation linewidths for transitions to the $^3\Sigma_u^-$ and $^3\Sigma_u^+$ states, were coupled in the calculations according to the spin-orbit mixing to obtain actual linewidths. We have obtained a satisfactory fit to the 90780 cm^{-1} band and the weak band at 90920 cm^{-1}, shown in Fig. 3, with a rms deviation of $\sim 9\times 10^{-20}$ cm^2. The fit shows that the spin-orbit interaction of the upper states can explain simultaneously the relative strengths of the two bands and the perturbation of the $^3\Sigma_{1u}^-$ components.

Values obtained for the parameters varied in the two-band fitting process are given in Table VI, apart from the wavelength-independent background cross section. These parameters are partially deperturbed and, therefore, cannot be compared directly with those in Table V. The T values for the $^3\Sigma_u^-$ and $^3\Sigma_u^+$ levels differ by $\Delta E^0 = 67$ cm^{-1}, which is of the same order as $H_{\rm int}$. It is, therefore, not surprising that intensity expressions[26] for states tending to Hund's case (c) were required to fit the 90780 cm^{-1} band using the single-state $^3\Sigma_u^- \leftarrow X^3\Sigma_g^-$ band model described above. Using two-level perturbation theory,[7] the shift δ of the $^3\Sigma_{1u}^-$ components, resulting from the interaction with the $^3\Sigma_{1u}^+$ components, is

TABLE VI. Deperturbed spectroscopic parameters for the $^3\Sigma_u^- \leftarrow X^3\Sigma_g^-$ band near 90780 cm^{-1} and the $^3\Sigma_u^+ \leftarrow X^3\Sigma_g^-$ band near 90920 cm^{-1} derived by assuming a model in which the upper states are coupled by a spin-orbit interaction.

Parameter	$^3\Sigma_u^-$	$^3\Sigma_u^+$
T (cm^{-1})	90797.3 ±0.4	90864.5 ±1.8
B (cm^{-1})	1.636±0.017	1.61±0.05
γ (cm^{-1})	0.57 ±0.13	0[a]
$D\times10^4$ (cm^{-1})	3.4 ±1.4	0[a]
Γ (cm^{-1} FWHM)	1.0 ±0.2	11 ±2
$f^{(0)}_{v'v''}\times10^4$	2.06 ±0.11	0[a]
$f^{(J)}_{v'v''}\times10^{4b}$	−6 ±3	0[a]
H_{int} (cm^{-1})	73.0 ± 0.6	

[a]Value fixed in fitting process.
[b]The band oscillator strength has been assumed to vary with J': $f_{v'v''}=f^{(0)}_{v'v''}+f^{(J)}_{v'v''}J'(J'+1)$.

$$\delta=\Delta E^0/2-[(\Delta E^0/2)^2+(H_{int})^2]^{1/2}=-47\text{cm}^{-1},$$

which is close to the expected value of $2\lambda=-48.0$ cm^{-1} derived from the uncoupled-model fit to the 90780 cm^{-1} band (Table V). The deperturbed $^3\Sigma_u^-$ predissociation linewidth agrees well with the width obtained for the $^3\Sigma_{0u}^-$ component (given in Table V) which is expected to be unaffected by the spin-orbit perturbation, while the much larger value for the deperturbed $^3\Sigma_u^+$ linewidth is consistent with the observed diffuseness of the 90920 cm^{-1} band and the large $^3\Sigma_{1u}^-$ widths obtained from the fit using the single-state band model (Table V).

It is difficult to assign independently the rotational lines of the diffuse 90920 cm^{-1} band in order to confirm its identification as a transition with upper state $^3\Sigma_u^+$. However, attempts to fit the cross section with a model of coupled $^3\Sigma_{1u}^-$ and $^1\Pi_{1u}$ states, the other likely possibility for the interacting states, were unsuccessful.

V. DISCUSSION

The characteristics of the $^3\Sigma_u^- \leftarrow X^3\Sigma_g^-$ bands observed at 88930 cm^{-1} and 90780 cm^{-1} are quite different from those of the longest and second bands,[13,14] the upper levels of which are the $v=0$ and $v=1$ levels of the $E^3\Sigma_u^-$ state, and from the $B^3\Sigma_u^- \leftarrow X^3\Sigma_g^-$ Schumann–Runge bands.[33] Compared with corresponding parameters for the $E^3\Sigma_u^- \leftarrow X^3\Sigma_g^-$ bands,[13,14] the measured oscillator strengths are much smaller, the rotational linewidths are much less, and upper-level B values are greater. Since no similar $^3\Sigma_u^- \leftarrow X^3\Sigma_g^-$ bands have been observed at energies lower than 88930 cm^{-1}, it is likely that the observed bands are (0,0) and (1,0) bands. We have attempted to obtain information on isotopic shifts in order to confirm these assignments; however, the spectra that we have measured for the corresponding bands of $^{18}O_2$ are diffuse and overlain by stronger transitions.

The assignments suggested above are supported by a qualitative consideration of the potential-energy curves, shown in Fig. 4. These curves are based on the model developed by Lewis *et al.*[10] to treat the coupling of the $3p\pi_u$ $^3\Sigma_u^-$ Rydberg and $^3\Sigma_u^-$ valence states, which we have extended to include higher Rydberg states. In general, the energy of the $v=0$ level of a Rydberg state is given by $E_n=E_\infty-\mathcal{R}/n^{*2}$, where E_∞ is the ionization limit, $\mathcal{R}$ is the Rydberg constant, $n^*=n-\delta$ is the effective quantum num-

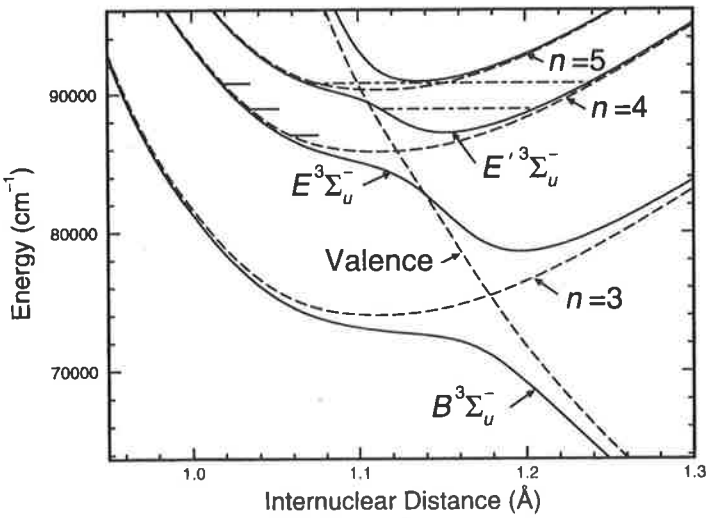

FIG. 4. Diabatic (dashed line) and adiabatic (solid line) potential-energy curves for $^3\Sigma_u^-$ states of O_2, determined as described in the text. Energies are referred to the $v=0$ level of the $X^3\Sigma_g^-$ ground state. Diabatic potential-energy curves are shown for $np\pi_u$ Rydberg $^3\Sigma_u^-$ states for $n=3-5$. These couple with the valence $^3\Sigma_u^-$ state to give the B, E and E' states, which are used here as labels for the corresponding adiabatic potential-energy curves. The energies of the observed $^3\Sigma_u^-$ levels are indicated by the dot-dashed lines. Note that, in this case where Rydberg-valence coupling is of intermediate strength, neither adiabatic nor diabatic representations quantitatively describe the actual levels. The approximate energies of the first three vibrational levels of the $D'^3\Sigma_u^+$ state, which has a potential-energy curve similar to that shown for the $4p\pi_u$ $^3\Sigma_u^-$ state, are indicated by solid lines.

ber, and δ is the quantum defect. For $^{16}O_2$, $\mathcal{R}=109733.583$ cm^{-1} and, for states converging to the O_2^+ $X^2\Pi_{1/2g}$ fine-structure component, $E_\infty=97348$ cm^{-1}.[1] (The zero of the energy scale is taken as the $v=0$ level of the $X^3\Sigma_g^-$ state.) The $3p\pi_u$ Rydberg state of Lewis *et al.*[10] has $E_3=74908$ cm^{-1} which corresponds to a quantum defect of 0.789. Since it is expected that the quantum defects will vary only slowly with n,[34] we have estimated the other Rydberg potential-energy curves shown in Fig. 4 by assuming a constant quantum defect and shifting the $3p\pi_u$ Rydberg potential up in energy to give $v=0$ energies $E_4=86708$ cm^{-1} and $E_5=91161$ cm^{-1}.

The interaction matrix elements H_n^e between the valence state and $np\pi_u$ Rydberg states are expected to scale with $(n^*)^{-3/2}$.[7] Therefore, from the value $H_3^e=4038$ cm^{-1} obtained by Lewis *et al.*,[10] we estimate matrix elements of $H_4^e\approx2310$ cm^{-1} and $H_5^e\approx1540$ cm^{-1}. The adiabatic potential-energy curves in Fig. 4 were derived from the diabatic curves and the above values for the interaction matrix elements using a matrix diagonalization routine. The electronic state formed by the coupling of the $4p\pi_u$ and $5p\pi_u$ Rydberg states with the valence state has been denoted as the E' state. Although neither adiabatic nor diabatic representations adequately describe the actual levels in this case where coupling is of intermediate strength, previous work has shown that a qualitative description of the states, adequate for vibrational assignments, can be gained from the adiabatic representation.[35] Comparison of the calculated adiabatic energies of 88460 cm^{-1} and 90660 cm^{-1} for the $v'=0$ and $v'=1$ bands of the $E'^3\Sigma_u^-\leftarrow X^3\Sigma_g^-$ system with the experimental T values of 88908.3 cm^{-1} and 90768.2 cm^{-1} supports our assignments of the bands as the (0,0) and (1,0) bands of the mixed Rydberg-valence $E'^3\Sigma_u^-\leftarrow X^3\Sigma_g^-$ system.

In the previous section, we concluded that the state which perturbs the E' state is likely to be a $^3\Sigma_{1u}^+$ state, but a $^1\Pi_{1u}$ state could not be definitively ruled out. On the basis of single-configuration estimates, summarized in the Appendix, it can be concluded that the matrix elements for the interactions of the $E'^3\Sigma_u^-$ state with the nearby $^3\Sigma_u^+$ states are likely to be in the range 65–95 cm^{-1}, whereas the spin-orbit matrix elements between the $E'^3\Sigma_u^-$ state and $^1\Pi_u$ states in this energy region are much smaller. Therefore, the vibronic matrix element of 73 cm^{-1} obtained from our modelling[36] of the perturber and perturbed bands near 90800 cm^{-1} can only be associated with an $E'^3\Sigma_u^- - {}^3\Sigma_u^+$ spin-orbit interaction, i.e. the perturber state is almost certainly a $^3\Sigma_u^+$ state.

At lower energies, transitions to the $3p\pi_u$ $D^3\Sigma_u^+$ Rydberg state have been observed by Ogawa *et al.*[37] in absorption from the ground state. Rotational structure of two of these bands has been analyzed by Ogawa and Yamawaki.[4] The low vibrational levels of the $D^3\Sigma_u^+$ state are relatively regular with separations and B values which are close to those of the $X^2\Pi_g$ state of the ion, showing that the D state behaves approximately as expected for an unperturbed $np\pi_u$ Rydberg state. Ogawa and Yamawaki[4] estimated an energy of 75450 cm^{-1} for the $D^3\Sigma_u^+\leftarrow X^3\Sigma_g^-$ (0,0) band which corresponds to $\delta=0.771$, assuming that the $^3\Sigma_{1u}^+$ Rydberg series converges to the $X^2\Pi_{3/2g}$ fine-structure component ($E_\infty=97545$ cm^{-1}). Since the $A^3\Sigma_u^+$ valence-state potential-energy curve,[38] which crosses the D-state potential-energy curve near its minimum (see Fig. 1), does not produce significant perturbations in the $D^3\Sigma_u^+$-state levels, higher $np\pi_u$ $^3\Sigma_u^+$ Rydberg states are likely to be even less perturbed by the valence state. If the quantum defect of the $4p\pi_u$ $^3\Sigma_u^+$ Rydberg state, denoted D', is the same as that of the D state, then predicted energies for the (1,0) and (2,0) bands of the $D'^3\Sigma_u^+\leftarrow X^3\Sigma_g^-$ system are ~88900 cm^{-1} and ~90700 cm^{-1}, respectively, as indicated in Fig 4. These energies, although slightly lower than the experimental T values for the perturbed levels, lead us to assign the perturber of the E' state as the Rydberg $D'^3\Sigma_u^+$ state, with the $v=1$ and $v=2$ levels of the D' state the dominant perturbers of the upper levels of the (0,0) and (1,0) $E'^3\Sigma_u^-\leftarrow X^3\Sigma_g^-$ bands, respectively, observed in this work. The latter assignment is supported by the deperturbed B value of 1.61 ± 0.05 obtained for the $^3\Sigma_u^+$ perturber (Table VI), a value consistent with the value of B ($v=2$, $X^2\Pi_g$, O_2^+) = 1.64 cm^{-1}.[3]

These assignments imply that there is a large spin-orbit interaction between levels with $\Delta v=1$, and, therefore, a large vibrational overlap between the corresponding wave functions. Such a large overlap can be explained by a shift of the $E'^3\Sigma_u^-$ ($v=0$ and 1) radial wave functions to larger internuclear distances as a result of the Rydberg-valence interaction so that the lobes of the wave functions are at internuclear distances similar to those of the $D'^3\Sigma_u^+$ ($v=1$ and 2) wave functions.[39] A similar effect was found by England *et al.*[19] for the spin-orbit interaction between $^1\Pi_{1u}$ ($v=0$) and $^3\Pi_{1u}$ ($v=1$) states of O_2.

VI. SUMMARY AND CONCLUSIONS

We have presented measurements of two intense $^3\Sigma_u^-\leftarrow X^3\Sigma_g^-$ bands near 88930 cm^{-1} and 90780 cm^{-1} in the $^{16}O_2$ photoabsorption spectrum. In contrast to the bands of the $E^3\Sigma_u^-\leftarrow X^3\Sigma_g^-$ system seen at lower energies, these bands show resolved rotational structure. The rotational lines have been assigned and term values of the upper levels have been fitted to obtain spectroscopic constants. The B values obtained are less than those expected for an unperturbed $np\pi_u$ Rydberg state. In addition, the $\Omega=1$ components exhibit shifts to lower energy caused by spin-orbit interactions with nearby levels of a higher-lying $^3\Sigma_{1u}^+$ state. A weaker band from transitions to the perturber state has been observed near 90920 cm^{-1}. A model which solves the coupled $^3\Sigma_u^- - {}^3\Sigma_u^+$ Hamiltonian has reproduced approximately both the strength of the weaker band and the perturbation of the stronger band.

The model of $^3\Sigma_u^-$ Rydberg-valence state interactions given by Lewis *et al.*[10] has been extended qualitatively to include $4p\pi_u$ and $5p\pi_u$ $^3\Sigma_u^-$ Rydberg states. Consideration of adiabatic potential-energy curves has enabled us to assign the observed intense bands as the (0,0) and (1,0) bands of transitions to a mixed state, $E'^3\Sigma_u^-$, resulting from the coupling of the $4p\pi_u$ and $5p\pi_u$ $^3\Sigma_u^-$ Rydberg states with the

lowest $^3\Sigma_u^-$ valence state. In addition, spin-orbit perturbations observed in the $v=0$ and $v=1$ levels of the $E'^3\Sigma_u^-$ state have been shown to result from interactions with the $v=1$ and $v=2$ levels of the $4p\pi_u$ $D'^3\Sigma_u^+$ Rydberg state, with the weak band near 90920 cm^{-1} corresponding to (2,0) $D' \leftarrow X$.

ACKNOWLEDGMENTS

The authors wish to acknowledge financial support from the Australian Research Council through a Post-Doctoral Research Fellowship (J.P.E.) and partial sponsorship (M.L.G.) from the United States National Science Foundation through a US–Australia Cooperative Research Grant. We thank Dr. S. T. Gibson for the use of his computer codes for transformation of diabatic to adiabatic potential-energy curves, and for calculation of energy eigenvalues. We also thank Professor H. Lefebvre-Brion for valuable discussions and Professor J. H. Carver, Professor H. Lefebvre-Brion and Dr. G. Stark for critically reading the manuscript. Valuable technical assistance was provided by K. J. Lonsdale and C. J. Dedman.

APPENDIX: ESTIMATES OF SPIN-ORBIT MATRIX ELEMENTS

We can estimate the values of spin-orbit matrix elements between relevant states using single-configuration calculations. In the determinant notation of Lefebvre-Brion and Field,[7] we represent the electronic wave functions of the $^3\Sigma_u^\pm$ Rydberg states arising from the $\pi_g np\pi_u$ molecular orbital (MO) configuration as

$$|^3\Sigma_{1u}^\pm\rangle = \frac{1}{\sqrt{2}}|(\pi_g^+ np\pi_u^- \pm \pi_g^- np\pi_u^+)\alpha\alpha|. \tag{A1}$$

The part of the spin-orbit operator giving non-zero matrix elements between states having the same values of Λ and Σ is $\Sigma_i \hat{a}_i \mathbf{l}_{iz}\cdot\mathbf{s}_{iz}$.[7] Therefore, it follows from Eq. (A1) that[40]

$$\langle ^3\Sigma_{1u}^+|\mathbf{H}^{SO}|^3\Sigma_{1u}^-\rangle = \tfrac{1}{2}(\langle\pi_g|\hat{a}|\pi_g\rangle - \langle np\pi_u|\hat{a}|np\pi_u\rangle). \tag{A2}$$

The Rydberg-orbital contribution to this matrix element is expected to be small because the Rydberg orbital is diffuse compared with the valence orbital and $\hat{a} \propto 1/r^3$, where r is the electron-nucleus distance.[7] We can estimate the value of $\langle\pi_g|\hat{a}|\pi_g\rangle$ by considering the spin-orbit splitting of the $^3\Pi_u$ states of O_2. The $F^3\Pi_u$ state consists of mixed Rydberg and valence states of $\pi_g np\sigma_u$ and $\pi_g\sigma_u$ configurations, respectively.[6] The spin-orbit matrix elements have the same value for these $^3\Pi_u$ configurations:[7]

$$\langle ^3\Pi_u|\mathbf{H}^{SO}|^3\Pi_u\rangle = \tfrac{1}{2}\langle\pi_g|\hat{a}|\pi_g\rangle.$$

Therefore, for $^3\Sigma_u^\pm$ Rydberg states from the $\pi_g np\pi_u$ MO configuration,

$$\langle ^3\Sigma_{1u}^+|\mathbf{H}^{SO}|^3\Sigma_{1u}^-\rangle \approx A(F^3\Pi_u)$$

and this has an experimental value of ~ 95 cm^{-1}.[6]

The $^3\Sigma_u^+$ states in this region are expected to be dominantly of Rydberg character (see Sec. V), whereas the $^3\Sigma_u^-$ states are of strongly mixed Rydberg and valence character. The valence $^3\Sigma_u^-$ state possesses the dominant MO configuration $\pi_g^3\pi_u^3$ which differs in two of the occupied orbitals from the $^3\Sigma_u^+$ Rydberg-state MO configuration. Thus, there are no non-zero matrix elements between this state and the Rydberg $^3\Sigma_u^+$ state.[7] The R-centroids for the interacting $E'^3\Sigma_u^-$ ($v=0$ and 1) and $D'^3\Sigma_u^+$ ($v=1$ and 2) levels, calculated for the adiabatic states shown in Fig. 4, are ~ 1.2 Å. It can be seen from Fig. 4 that this is to the right of the $^3\Sigma_u^-$ Rydberg-valence crossing and, in this region, the mixed E' state is dominantly $4p\pi_u$-Rydberg in character. Therefore, the spin-orbit matrix element between the $D'^3\Sigma_u^+$ Rydberg state and the Rydberg-valence mixed $E'^3\Sigma_u^-$ state is likely to be more than $1/\sqrt{2}$ of the Rydberg matrix element of 95 cm^{-1}.

The $^1\Pi_u$ states in this energy region[19] are expected to be mixtures of the Rydberg states,

$$|^1\Pi_{1u}\rangle = \frac{1}{\sqrt{2}}|\pi_g^+ np\sigma_u(\alpha\beta - \beta\alpha)|,$$

and the repulsive valence state,

$$|^1\Pi_{1u}\rangle = \frac{1}{\sqrt{2}}|\pi_g^+ \sigma_u(\alpha\beta - \beta\alpha)|.$$

The part of the spin-orbit operator giving non-zero matrix elements between states differing by $\Delta\Lambda = \pm 1$ and $\Delta\Sigma = \mp 1$ is $(1/2)\Sigma_i \hat{a}_i \mathbf{l}_i^\pm \cdot \mathbf{s}_i^\mp$.[7] Therefore, it follows that the Rydberg-Rydberg matrix element is

$$\langle ^1\Pi_{1u}|\mathbf{H}^{SO}|^3\Sigma_{1u}^-\rangle = \frac{1}{2\sqrt{2}}\langle np\pi_u|\hat{a}|np\pi_u\rangle,$$

where we have used $\mathbf{l}^+|np\pi_u^-\rangle = \sqrt{2}|np\sigma\rangle$ and $\mathbf{s}^-|\alpha\rangle = |\beta\rangle$. As in Eq. (A2), $\langle np\pi_u|\hat{a}|np\pi_u\rangle$ is expected to be very small compared with $\langle\pi_g|\hat{a}|\pi_g\rangle$ because of the $1/r^3$ dependence of $\hat{a}$. The interaction between the $\pi_g\sigma_u$ valence $^1\Pi_u$ state and the $\pi_g np\pi_u$ Rydberg $^3\Sigma_u^-$ state is also expected to be small compared with $\langle\pi_g|\hat{a}|\pi_g\rangle$.[41] Other terms in the mixed Rydberg-valence matrix element are zero since the valence and Rydberg $^1\Pi_u$ states differ from the $\pi_g^3\pi_u^3$ valence $^3\Sigma_u^-$ state by more than a single occupied orbital.

These single-configuration estimates show that the $D'^3\Sigma_u^+ - E'^3\Sigma_u^-$ spin-orbit matrix element is likely to be in the range 65–95 cm^{-1} while the $^1\Pi_u - ^3\Sigma_u^-$ spin-orbit matrix element is likely to be much smaller.

[1] R. G. Tonkyn, J. W. Winniczek, and M. G. White, Chem. Phys. Lett. **164**, 137 (1989).
[2] K. Watanabe, Adv. Geophys. **5**, 153 (1958).
[3] P. H. Krupenie, J. Phys. Chem. Ref. Data **1**, 423 (1972).
[4] M. Ogawa and K. R. Yamawaki, Can. J. Phys. **47**, 1805 (1969).
[5] D. H. Katayama, S. Ogawa, M. Ogawa, and Y. Tanaka, J. Chem. Phys. **67**, 2132 (1977).
[6] J. P. England, B. R. Lewis, S. T. Gibson, and M. L. Ginter, J. Chem. Phys. **104**, 2765 (1996).
[7] H. Lefebvre-Brion and R. W. Field, *Perturbations in the Spectra of Diatomic Molecules* (Academic, Orlando, 1986), pp. 39, 91, 92, 95, 108, 211, 247–248.
[8] J. Wang, D. G. McCoy, A. J. Blake, and L. Torop, J. Quant. Spectrosc. Radiat. Transfer **38**, 19 (1987).

[9] J. Wang, A. J. Blake, D. G. McCoy, and L. Torop, J. Quant. Spectrosc. Radiat. Transfer **40**, 501 (1988).
[10] B. R. Lewis, S. S. Banerjee, and S. T. Gibson, J. Chem. Phys. **102**, 6631 (1995).
[11] Y. Tanaka, J. Chem. Phys. **20**, 1728 (1952).
[12] Rotational structure consistent with a $^3\Sigma_u^- \leftarrow X^3\Sigma_g^-$ transition has been observed for the longest band of $^{18}O_2$ by M. Ogawa [Can. J. Phys. **53**, 2703 (1975)] and Lewis *et al.* (Ref. 13).
[13] B. R. Lewis, S. T. Gibson, M. Emami, and J. H. Carver, J. Quant. Spectrosc. Radiat. Transfer **40**, 1 (1988).
[14] B. R. Lewis, S. T. Gibson, M. Emami, and J. H. Carver, J. Quant. Spectrosc. Radiat. Transfer **40**, 469 (1988).
[15] L. C. Lee, T. G. Slanger, G. Black, and R. L. Sharpless, J. Chem. Phys. **67**, 5602 (1977).
[16] S. T. Gibson and B. R. Lewis (unpublished).
[17] K. Dressler, Ann. Isr. Phys. Soc. **6**, 141 (1983).
[18] H. C. Chang, Ph.D. dissertation thesis, University of Southern California, 1973.
[19] J. P. England, B. R. Lewis, and M. L. Ginter, J. Chem. Phys. **103**, 1727 (1995).
[20] R. Mahon, T. J. McIlrath, V. P. Myerscough, and D. W. Koopman, IEEE J. Quantum Electron. **15**, 444 (1979).
[21] S. G. Tilford and J. D. Simmons, J. Phys. Chem. Ref. Data **1**, 147 (1972).
[22] B. R. Lewis, J. P. England, R. J. Winkel, Jr., S. S. Banerjee, P. M. Dooley, S. T. Gibson, and K. G. H. Baldwin, Phys. Rev. A **52**, 2717 (1995).
[23] R. L. Kelly and L. J. Palumbo, *Atomic and Ionic Emission Lines Below 2000 Å: Hydrogen Through Krypton*, Naval Research Laboratory Report No. 7599 (U.S. GPO, Washington, D.C., 1973).
[24] P. G. Wilkinson, Can. J. Phys. **46**, 1225 (1968).
[25] C. Amiot and J. Verges, Can. J. Phys. **59**, 1391 (1981).
[26] J. B. Tatum and J. K. G. Watson, Can. J. Phys. **49**, 2693 (1971).
[27] For convenience, we use the conventional notation, based on a Hund's case (b) picture, to describe the branch structure of the $^3\Sigma_u^-$ state. Later, it becomes clear that the $^3\Sigma_u^-$ state is more accurately described as intermediate between cases (a) and (c), and we use case (a) notation.
[28] A. S.-C. Cheung, K. Yoshino, W. H. Parkinson, and D. E. Freeman, J. Mol. Spectrosc. **119**, 1 (1986).
[29] T. K. Balasubramanian and V. P. Bellary, Acta Phys. Hung. **63**, 249 (1988).
[30] Centrifugal terms in the effective Hamiltonian were given by Cheung *et al.* (Ref. 28), but we found that the off-diagonal term in λ_D should be $-\lambda_D/3$ rather than $-2\lambda_D/3$, in agreement with the result of Balasubramanian and Bellary (Ref. 29).
[31] P. Brix and G. Herzberg, Can. J. Phys. **32**, 110 (1954).
[32] The band model fits to the cross section included optimization of spectroscopic parameters describing the rotational energies of the upper states.
[33] B. R. Lewis, S. T. Gibson, and P. M. Dooley, J. Chem. Phys. **100**, 7012 (1994), and references therein.
[34] Quantum defects have been calculated *ab initio* by T. Betts and V. McKoy [J. Chem. Phys. **54**, 113 (1971)] for $np\pi_u$ and $np\sigma_u$ orbitals of O_2. Experimental results have been obtained for the O_2 $np\sigma_u$ orbital (Ref. 6) and for the NO $np\sigma_u$ and $np\pi_u$ orbitals [M. Eidelsberg and F. Rostas, Astron. Astrophys. **235**, 472 (1990)].
[35] L. Torop, D. G. McCoy, A. J. Blake, J. Wang, and T. Scholz, J. Quant. Spectrosc. Radiat. Transfer **38**, 9 (1987).
[36] This value for the interaction matrix element can be derived without assuming a symmetry for the perturber state. Relative to the energy of the $v=0$ level of the ground state, the unperturbed energy of the $^3\Sigma_u^-$ state is equal to the band origin of the $^3\Sigma_{0u}^- \leftarrow X^3\Sigma_g^-$ subband ($E_1^0 \sim 90800$ cm^{-1}), and the unperturbed energy of the perturber state is equal to the band origin of the 90920 cm^{-1} band minus the shift ($\delta = -2\lambda$) caused by the perturbation ($E_2^0 \sim 90910 - 48$ cm^{-1}). Using two-level perturbation theory, as discussed in Sec. IV B, the interaction matrix element is equal to $H_{\rm int} = [(\Delta E^0/2 + \delta)^2 - (\Delta E^0/2)^2]^{1/2} \sim 73$ cm^{-1}, where $\Delta E^0 = E_2^0 - E_1^0$.
[37] M. Ogawa, K. R. Yamawaki, A. Hashizume, and Y. Tanaka, J. Mol. Spectrosc. **55**, 425 (1975).
[38] R. P. Saxon and B. Liu, J. Chem. Phys. **67**, 5432 (1977).
[39] Calculations of the vibrational wave functions for the adiabatic E' ($v=0$ and 1) levels and the diabatic D' ($v=1$ and 2) levels give overlaps of ~ 0.6 between levels with $\Delta v = 1$. However, values of $H_{\rm int}$ and the spin-orbit matrix element determined in the Appendix suggest that the actual overlap could be even larger.
[40] R. Ogorzalek Loo, W. J. Marinelli, P. L. Houston, S. Arepalli, J. R. Wiesenfeld, and R. W. Field, J. Chem. Phys. **91**, 5185 (1989).
[41] H. Lefebvre-Brion (private communication, 1995).

4.29 Non-Lorentzian line shapes for interfering rotational resonances in the predissociation of O_2

[49] B. R. Lewis, P. M. Dooley, J. P. England, S. T. Gibson, K. G. H. Baldwin, and L. W. Torop,
Physical Review A **55**, 4164–4167 (1997).

Non-Lorentzian line shapes for interfering rotational resonances in the predissociation of O_2

B. R. Lewis, P. M. Dooley, J. P. England, S. T. Gibson, and K. G. H. Baldwin
Research School of Physical Sciences and Engineering, The Australian National University, Canberra, Australian Capital Territory 0200, Australia

L. W. Torop
Department of Physics and Mathematical Physics, The University of Adelaide, Adelaide, South Australia 5005, Australia
(Received 3 September 1996; revised manuscript received 27 December 1996)

Rotationally resolved measurements are presented of interacting predissociating resonances in the Schumann-Runge bands of O_2 that exhibit destructive quantum interference for energies between the line centers. The interacting resonances are described using a coupled line shape derived by treating simultaneously the perturbation and predissociation processes using the method of Fano [Phys. Rev. **124**, 1866 (1961)]. [S1050-2947(97)02206-3]

PACS number(s): 33.20.Ni, 33.70.Jg, 33.80.Gj

The concept of resonance is ubiquitous in physics. In particular, reactions involving particles with internal structure may lead to the formation of short-lived intermediate states (resonances) that profoundly affect the energy dependence of the reaction cross section. Resonant effects occur in nuclear reactions, electron scattering from atoms and molecules (negative-ion resonances) [1], atomic and molecular photoionization, and molecular photodissociation. When the widths of resonances are comparable with the spacing between resonances, interference effects may occur. Interacting resonances have received particular attention in the fields of nuclear reactions [2,3] and atomic and molecular autoionization [4,5], but there have been only two observations reported for molecular predissociation below the first ionization limit, using photoemission [6] and photofragmentation [7] spectroscopies.

In this work we present high-resolution photoabsorption measurements that show a particularly instructive example of closely interacting resonances in molecular predissociation. In the language of spectroscopy, a rotational level of a state that is predissociated is perturbed by a nearby rotational level of a different electronic state. This situation, apart from the narrow width of the perturber, is somewhat analogous to the "complex resonance" [8] of atomic and molecular autoionization, with the perturbing level playing the role of the "interloper" [8], and is amenable to theoretical treatment using either the configuration-interaction method of Fano [9] or the multichannel quantum-defect analysis (MCQDA) of Mies [10]. For the example reported here, the line-shape formula for the interacting resonances is particularly simple, containing only five adjustable parameters: the energies and widths of each resonance and an overall intensity factor.

The Schumann-Runge (SR) band system of O_2, $B\,^3\Sigma_u^- \leftarrow X\,^3\Sigma_g^-$ (1750–2050 Å), plays an important role in the photochemistry of the terrestrial atmosphere by controlling the depth of penetration of the solar vacuum ultraviolet (vuv) radiation necessary for the dissociation of many atmospheric species. The normal line-by-line techniques used by atmospheric modellers to describe SR band absorption assume that the predissociation component of the line shape is Lorentzian and that the actual line shape may be represented by a Voigt profile (the convolution of the predissociation and Doppler line shapes). These techniques have proven successful in reproducing the observed line shapes for energies not too far from the line centers. Here we show that, under certain conditions, interferences result in departures from the Lorentzian (Voigt) profile.

The mechanisms for the predissociation of $O_2(B\,^3\Sigma_u^-)$ were described fully by Julienne and Krauss [11] and Julienne [12]. They showed that a consideration of the coupling between the bound B state and four repulsive states whose potential-energy curves crossed the B-state potential allowed the experimental predissociation linewidths to be explained. The relevant potential-energy curves are shown in Fig. 1. The principal predissociative mechanism is spin-orbit coupling with the $1\,^5\Pi_u$ state, but spin-orbit coupling with the $1\,^1\Pi_u$ and $2\,^3\Sigma_u^+$ states and spin-orbit and orbit-rotation coupling with the $1\,^3\Pi_u$ state play significant roles. All vibrational levels of the B state are subject to predissociation, with

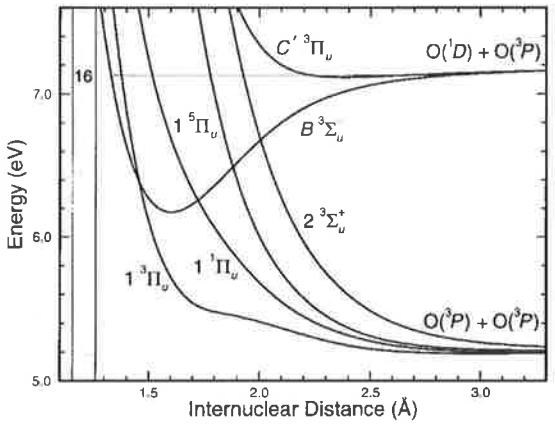

FIG. 1. Potential-energy curves for electronic states of O_2 relevant to the predissociation and perturbation of the $B\,^3\Sigma_u^-$ state. The Franck-Condon region for absorption from $X\,^3\Sigma_g^-(v=0)$ is shown shaded. Energies are given relative to the minimum of the X-state potential-energy curve.

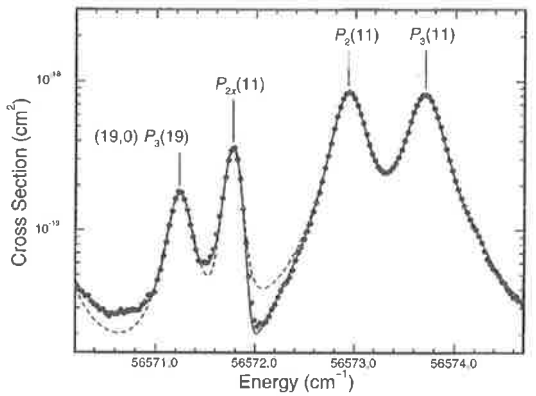

FIG. 2. Photoabsorption cross section for $^{16}O_2$ in the region of the $P_2(11)$ line from the (16,0) band of the $B\ ^3\Sigma_u^- \leftarrow X\ ^3\Sigma_g^-$ system, measured at $T=293$ K with an instrumental resolution of ~ 0.06 cm^{-1} FWHM (points). Also shown are fitted cross sections based on the Voigt line shape (dashed line) and the coupled line shape Eq. (20) for the interacting resonances $P_2(11)$ and $P_{2x}(11)$ (solid line).

linewidths in the range 0.03–4 cm^{-1} full width at half maximum (FWHM) [13].

Bound-bound perturbations occur for B-state levels with $v \geq 16$. In an associated work [14], we show that the perturber is the second valence state of $^3\Pi_u$ symmetry, $C'\ ^3\Pi_u$. An *ab initio* potential-energy curve for the C' state [14] is shown in Fig. 1. In Fig. 2 we present a high-resolution measurement of the room-temperature photoabsorption cross section for $^{16}O_2$ in the region of the perturbed rotational line $P_2(11)$ from the (16,0) SR band. The measurements were taken using tunable, narrow-bandwidth vuv radiation generated by the two-photon-resonant difference-frequency four-wave mixing of excimer-pumped dye-laser radiation in Xe [15,16]. A full description of the experimental apparatus is given elsewhere [14]. The resolution achieved (~ 0.06 cm^{-1} FWHM) is the highest reported in this spectral region. The perturbed extra line $P_{2x}(11)$, shown in Fig. 2, can be assigned on the basis of observed perturbations in the rotational term values of $B(v=16, F_2)$ and known combination differences. The measured cross section in Fig. 2 is notable for the unusually deep minimum between the main and extra lines $P_2(11)$ and $P_{2x}(11)$. An attempt to reproduce the measured cross section using a model in which each rotational line was described by a Voigt profile (Fig. 2, dashed line) failed completely for the minimum near 56 572 cm^{-1}. Apparently, destructive interference is occurring for energies between the centers of the main and extra lines that have interacting upper states sharing the common rotation $J'=10$. Since the symmetric Lorentzian predissociation line shape is unable to describe the measured cross section, we must develop a more appropriate theoretical treatment of the interacting predissociating resonances shown in Fig. 2.

To obtain an expression for the energy dependence of the cross section for photoabsorption into these coupled states, we employ the method of Fano [9] for treatment of the decay of bound states to continua, as formulated and extended by Mies [17]. It is convenient to start with a diabatic picture of

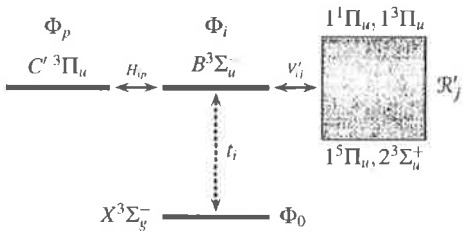

FIG. 3. Schematic diabatic picture of the transitions and interactions involving the $B\ ^3\Sigma_u^-$ state of O_2.

the relevant electronic states and interactions, summarized schematically in Fig. 3. In this picture, there is an electric-dipole-allowed transition between the $X\ ^3\Sigma_g^-$ ground state (Φ_0) and the B state (Φ_i), which is both perturbed by the C' state (Φ_p) and predissociated by four noninteracting dissociative continuum states ($\mathcal{R}_j$). In principle, transitions from the X state into the states of $^3\Pi_u$ symmetry are electric-dipole allowed. However, due to the location of the bound part of the $C'\ ^3\Pi_u$ potential at large internuclear distances R (Fig. 1), the corresponding Franck-Condon overlap with the X state is negligible. In addition, there are no repulsive states correlating with the lowest dissociation limit of O_2 that cross the C' potential. This allows two simplifying assumptions: there are no direct transitions into the C' state and there is no direct predissociation of the C' state. These assumptions have been verified experimentally [14]. Transitions from the X state into the predissociating continua are electric-dipole forbidden, except for those into the $1\ ^3\Pi_u$ state. However, the small Franck-Condon factors for the $1\ ^3\Pi_u \leftarrow X\ ^3\Sigma_g^-$ transition result in a negligible transition probability for energies in the region of the SR bands [18]. Thus it may be assumed that there are no transitions from the X state into the predissociating continua. This assumption leads to the conclusion that *unperturbed* lines of the SR system may be described accurately by Lorentzian predissociation line shapes [13]. Finally, the repulsive states that predissociate the B state are well separated in R and have only weak electronic interactions. Thus it may be assumed that the predissociating continua are noninteracting [19].

In the diabatic basis, the bound-state energies are

$$E_n = H_{nn} = \langle \Phi_n | \mathcal{H} | \Phi_n \rangle, \quad n = i, p, \tag{1}$$

where $\mathcal{H}$ is the total Hamiltonian and the Φ_n are real, normalized wave functions. Since there is a perturbation between the bound states in this basis, the interaction matrix element

$$H_{ip} = \langle \Phi_i | \mathcal{H} | \Phi_p \rangle \neq 0. \tag{2}$$

However, the bound basis states used in the development of the Fano-Mies theory [9,17], which we label 1 and 2, do not interact, i.e., $H_{12}=0$. Such states may be related to the diabatic states using standard bound-state perturbation formulas [20], which we write in the form

$$\Phi_1 = \Phi_i \cos\alpha + \Phi_p \sin\alpha,$$
$$\Phi_2 = -\Phi_i \sin\alpha + \Phi_p \cos\alpha, \tag{3}$$

where $\tan 2\alpha = 2H_{ip}/(E_i - E_p)$. The bound-state energies are related by

$$E_1 + E_2 = E_i + E_p \tag{4}$$

and

$$|E_1 - E_2| = \sqrt{|E_i - E_p|^2 + |2H_{ip}|^2}, \tag{5}$$

where $E_1 = H_{11}$ and $E_2 = H_{22}$.

The diabatic continua obey the relation

$$\langle \mathcal{R}_k'' | \mathcal{H} | \mathcal{R}_j' \rangle = E' \delta_{kj} \delta(E'' - E'), \tag{6}$$

where $\mathcal{R}_j'$ represents the real, energy-normalized wave function of energy E' for the continuum j. The amplitude for dissociation of state n to the energy E' continuum j is given by

$$V_{nj}' = \langle \mathcal{R}_j' | \mathcal{H} | \Phi_n \rangle, \quad n = 1,2, \tag{7}$$

and the total dissociation amplitude V_n' by $(V_n')^2 = \Sigma_j (V_{nj}')^2$. Since the perturber is not predissociated, $V_{pj}' = 0$ and it follows from Eq. (3) that

$$V_{1j}' = V_{ij}' \cos\alpha \text{ and } V_{2j}' = -V_{ij}' \sin\alpha. \tag{8}$$

The V_{nj}' are of the form $V_{nj}' = f_j' V_n'$, where $V_1' = V_i' \cos\alpha$, $V_2' = -V_i' \sin\alpha$, and the branching ratios $f_j' = V_{ij}'/V_i'$, where $\Sigma_j (f_j')^2 = 1$. These expressions emphasize that states 1 and 2 dissociate in the same way. Consequently, each state interacts only with that part of the energy E' continuum having the wave function

$$\mathcal{R}' = \sum_j f_j' \mathcal{R}_j'. \tag{9}$$

The dissociation amplitude of state n to $\mathcal{R}'$ is the total dissociation amplitude for that state

$$V_n' = \langle \mathcal{R}' | \mathcal{H} | \Phi_n \rangle. \tag{10}$$

Having found suitable basis states for the application of the Fano-Mies [9,17] theory, we note that there will be an energy E wave function Ψ that is a linear combination of Φ_1, Φ_2 and the $\mathcal{R}'$ of various energies E'. Although there are no direct interactions between basis states 1 and 2, they interact indirectly through $\mathcal{R}'$. Following Fano [9], we treat the predissociation by introducing modified orthonormal bound states $\hat{\Phi}_1$ and $\hat{\Phi}_2$, related to the diabatic and perturbed basis states by

$$\hat{\Phi}_1 = \Phi_1 \cos\beta + \Phi_2 \sin\beta = \Phi_i \cos\gamma + \Phi_p \sin\gamma,$$

$$\hat{\Phi}_2 = -\Phi_1 \sin\beta + \Phi_2 \cos\beta = -\Phi_i \sin\gamma + \Phi_p \cos\gamma, \tag{11}$$

where $\gamma = \alpha + \beta$, $\tan 2\beta = 2F_{12}/(F_{11} - F_{22})$ and

$$F_{nm} = E_n \delta_{nm} + \text{P} \int dE' \frac{1}{E - E'} V_n' V_m', \tag{12}$$

where P indicates a principal-part integral. The F matrix for the modified bound states is diagonal, i.e.,

$$\hat{F}_{mn} = \langle \hat{\Phi}_m | \mathcal{H} | \hat{\Phi}_n \rangle + \text{P} \int dE' \frac{1}{E - E'} \sum_j \hat{V}_{mj}' \hat{V}_{nj}'$$

$$= \hat{\varepsilon}_n \delta_{mn}, \tag{13}$$

where $\hat{\varepsilon}_n$ is the resonance energy of state $\hat{\Phi}_n$ and $\hat{V}_{nj}' = \langle \mathcal{R}_j' | \mathcal{H} | \hat{\Phi}_n \rangle$. $\hat{F}_{12}$, the amplitude for direct and indirect interactions between $\hat{\Phi}_1$ and $\hat{\Phi}_2$, is zero. The total dissociation amplitude $\hat{V}_n$ for state $\hat{\Phi}_n$ is given by $\hat{V}_n^2 = \Sigma_j \hat{V}_{nj}^2$.

Applying the method of Fano [9] to the modified orthonormal basis and energy normalizing the large-R form of the continuum wave function according to the usual scattering-theory techniques [2], it can be shown that the energy E wavefunction becomes

$$\Psi = \frac{1}{\sqrt{1 + \left(\sum_n 1/\hat{\epsilon}_n \right)^2}} \left(\sum_n \frac{\hat{\Upsilon}_n}{\pi \hat{V}_n \hat{\epsilon}_n} + \mathcal{R} \right), \tag{14}$$

where $\hat{\epsilon}_n = (E - \hat{\varepsilon}_n)/\pi \hat{V}_n^2$ and

$$\hat{\Upsilon}_n = \hat{\Phi}_n + \text{P} \int dE' \frac{1}{E - E'} \hat{V}_n' \mathcal{R}'. \tag{15}$$

As there is no photoabsorption into the continua, the photoabsorption amplitude from the initial state into the state Ψ may be written

$$t = \langle \Psi | \mathcal{T} | \Phi_0 \rangle = \frac{\sum_n \hat{t}_n/(\pi \hat{V}_n \hat{\epsilon}_n)}{\sqrt{1 + \left(\sum_n 1/\hat{\epsilon}_n \right)^2}}, \tag{16}$$

where $\hat{t}_n$ is the photoabsorption amplitude to state $\hat{\Phi}_n$ and $\mathcal{T}$ is the transition operator. From Eq. (11), since there is no absorption into the perturbing state p,

$$\hat{t}_1 = t_i \cos\gamma, \quad \hat{t}_2 = -t_i \sin\gamma, \tag{17}$$

and since state p does not dissociate,

$$\hat{V}_1 = V_i \cos\gamma \text{ and } \hat{V}_2 = -V_i \sin\gamma. \tag{18}$$

It follows from Eqs. (17) and (18) that

$$\hat{t}_1/\hat{V}_1 = \hat{t}_2/\hat{V}_2 = t_i/V_i. \tag{19}$$

The total photoabsorption cross section is the sum of the resonant cross section into Ψ and the nonresonant absorption into that part of the continuum space orthogonal to $\mathcal{R}$. As all photoabsorption into the continuua is negligible, the cross section is given by

$$\sigma(E) \propto \nu t^2 = \nu \left(\frac{t_i^2}{\pi V_i^2} \right) \frac{(1/\hat{\epsilon}_1 + 1/\hat{\epsilon}_2)^2}{1 + (1/\hat{\epsilon}_1 + 1/\hat{\epsilon}_2)^2}, \tag{20}$$

where ν is the transition energy. The dimensionless energy factors $\hat{\epsilon}_n$ may be expressed as

$$\hat{\epsilon}_n = 2(E - \hat{\varepsilon}_n)/\hat{\Gamma}_n , \tag{21}$$

where $\hat{\Gamma}_n = 2\pi \hat{V}_n^2$ is the resonance width of state $\hat{\Phi}_n$.

The line shape of Eq. (20) may be regarded as a special case of the two-bound-state, single-continuum expressions given elsewhere [4,9,17] and also follows from MCQDA [10]. Over the small range of energy applicable to the study of interacting predissociating resonances, the energy dependences of ν, t_i, V_i, and $\hat{\Gamma}_n$ can be neglected. In the case of a single bound state, Eq. (20) reduces to a Lorentzian line shape, appropriate for the case of an isolated predissociating resonance where there is no absorption into the continuum. For interacting resonances, we have an "interfering Lorentzian" profile. From Eq. (21), for energies between the resonance centers, $1/\hat{\epsilon}_1$ and $1/\hat{\epsilon}_2$ have opposite signs and the numerator of Eq. (20) must reach zero at some energy in this range. This prediction of destructive interference between the resonance centers is in agreement with our observations, but the measured cross section does not reach zero due to instrumental effects and contributions from other line wings. We have fitted the measured cross section of Fig. 2 using the coupled predissociation line shape of Eq. (20) to describe the interacting resonances $P_2(11)$ and $P_{2x}(11)$, allowing for the effects of the Doppler component of the line shape and the instrumental resolution. An excellent fit was obtained (Fig. 2, solid line) with resonance widths $\hat{\Gamma}_1 = 0.266$ cm^{-1} [$P_2(11)$] and $\hat{\Gamma}_2 = 0.046$ cm^{-1} [$P_{2x}(11)$] and a resonance separation $\hat{\varepsilon}_1 - \hat{\varepsilon}_2 = 1.155$ cm^{-1}.

Simple relationships between the physical observables associated with the resonances $\hat{\Phi}_n$ and the analogous (unobservable) quantities in the diabatic basis enable Eq. (20) to be used successfully to deperturb predissociated molecular spectra [14]. For example, from Eqs. (17) and (18) it follows that $\hat{\Gamma}_2/\hat{\Gamma}_1 = (\hat{t}_2/\hat{t}_1)^2 = \tan^2\gamma$, $\hat{\Gamma}_1 + \hat{\Gamma}_2 = 2\pi V_i^2 = \Gamma_i$, and $\hat{t}_1^2 + \hat{t}_2^2 = t_i^2$. In other words, the interloper "borrows" width and strength from the original predissociating resonance in an identical fashion such that the total width and strength is conserved. In addition, it can be shown that the effects of perturbation and dissociation act separately in a simple way on the resonance energies: the dissociation shifts the dissociating state as if it were isolated and the perturbation acts on the shifted energy as if it were a bound-state energy. This allows standard bound-state perturbation formulas [20] to be used in the deperturbation of rotational series of predissociating resonances and the determination of the interaction matrix elements H_{ip} [14].

The authors would like to thank Professor J. H. Carver, Professor M. L. Ginter, Professor A. R. P. Rau, Professor H. Lefebvre-Brion, Professor J.-P. Connerade, and Dr. F. Mies for critical comments on the manuscript.

[1] S. J. Buckman and C. W. Clark, Rev. Mod. Phys. **66**, 539 (1994).
[2] A. M. Lane and R. G. Thomas, Rev. Mod. Phys. **30**, 257 (1958).
[3] C. Mahaux, Nucl. Phys. **71**, 241 (1965); A. Lejeune, Nucl. Phys. A **116**, 72 (1968).
[4] J.-P. Connerade and A. M. Lane, Rep. Prog. Phys. **51**, 1439 (1988).
[5] C. H. Greene and Ch. Jungen, Adv. At. Mol. Phys. **21**, 51 (1985).
[6] C. Carlone, Phys. Rev. A **12**, 2464 (1975).
[7] B. Kim, K. Yoshihara, and S. Lee, Phys. Rev. Lett. **73**, 424 (1994).
[8] A. Giusti-Suzor and H. Lefebvre-Brion, Phys. Rev. A **30**, 3057 (1984).
[9] U. Fano, Phys. Rev. **124**, 1866 (1961).
[10] F. H. Mies, J. Chem. Phys. **80**, 2514 (1984); F. H. Mies and P. S. Julienne, *ibid.* **80**, 2526 (1984).
[11] P. S. Julienne and M. Krauss, J. Mol. Spectrosc. **56**, 270 (1975).
[12] P. S. Julienne, J. Mol. Spectrosc. **63**, 60 (1976).
[13] B. R. Lewis, S. T. Gibson, and P. M. Dooley, J. Chem. Phys. **100**, 7012 (1994).
[14] B. R. Lewis, P. M. Dooley, J. P. England, K. Waring, S. T. Gibson, K. G. H. Baldwin, and H. Partridge, Phys. Rev. A **54**, 3923 (1996).
[15] R. Hilbig and R. Wallenstein, IEEE J. Quantum Electron. **QE-19**, 194 (1983).
[16] K. Yamanouchi and S. Tsuchiya, J. Phys. B **28**, 133 (1995).
[17] F. H. Mies, Phys. Rev. **175**, 164 (1968).
[18] A. C. Allison, S. L. Guberman, and A. Dalgarno, J. Geophys. Res. **87**, 923 (1982).
[19] M. L. Sink and A. D. Bandrauk, J. Chem. Phys. **66**, 5313 (1977); R. Colle, *ibid.* **74**, 2910 (1981).
[20] H. Lefebvre-Brion and R. W. Field, *Perturbations in the Spectra of Diatomic Molecules* (Academic, Orlando, 1986), pp. 247–248.

4.30 Fine-structure-resolved collisional broadening in the Schumann-Runge bands of O_2

[50] P. M. Dooley, B. R. Lewis, K. Waring, S. T. Gibson, and K. G. H. Baldwin, *Journal of Quantitative Spectroscopy and Radiative Transfer* **58**, 93–100 (1997).

Pergamon

J. Quant. Spectrosc. Radiat. Transfer Vol. 58, No. 1, pp. 93–100, 1997

Printed in Great Britain

PII: S0022-4073(97)00024-1

0022-4073/97 $17.00 + 0.00

FINE-STRUCTURE-RESOLVED COLLISIONAL BROADENING IN THE SCHUMANN–RUNGE BANDS OF O_2

P. M. DOOLEY, B. R. LEWIS,† K. WARING, S. T. GIBSON, and K. G. H. BALDWIN

Research School of Physical Sciences and Engineering, The Australian National University, Canberra, ACT 0200, Australia

(Received 20 September 1996)

Abstract—Collisional self-broadening and shift coefficients are presented for selected fine-structure-resolved rotational lines from the $B^3\Sigma_u^- \leftarrow X^3\Sigma_g^-(v',1)$ bands of O_2. The coefficients were derived from high-resolution photoabsorption cross-sections measured using the tuneable, narrow-bandwidth, vacuum-ultraviolet radiation generated by the two-photon-resonant difference-frequency four-wave mixing of excimer-pumped dye-laser radiation in Xe. The results, obtained at room temperature and at pressures of less than 800 torr, are consistent with previous results derived from medium-resolution measurements of the $(v',0)$ bands at much higher pressures. © 1997 Elsevier Science Ltd

1. INTRODUCTION

The photoabsorption cross-sections of O_2 in the vacuum-ultraviolet (v.u.v.) are of importance in many applications, including atmospheric, combustion, explosion and shock-wave phenomena. Absorption in this spectral region is dominated by the Schumann–Runge (SR) transition, $B^3\Sigma_u^- \leftarrow X^3\Sigma_g^-$, comprising a strong continuum peaked near 1420 Å and a weaker band system from 1750 Å to 2050 Å. Potential-energy curves for the states participating in the SR transition are shown in Fig. 1, together with those for the four repulsive states which cross the B state and are responsible for its predissociation, principally through spin–orbit coupling.[1,2] A knowledge of the collision-broadening coefficients for lines in the SR bands is essential for the construction of accurate models of O_2 absorption, especially at elevated pressures.[3,4] In addition, the determination of accurate oscillator strengths and predissociation linewidths for the $B \leftarrow X$ bands from experimental cross-section measurements requires correction for collisional effects, even at pressures significantly less than 1 atm.[5–7] In particular, estimations of the strength of the continuum underlying the SR bands are very sensitive to the assumed value of the collision-broadening coefficient.[8]

There have been few measurements of collisional broadening in the SR bands. Cann et al[3] deconvolved the argon-broadened spectra of Bethke[9] to estimate a full-width at half-maximum (FWHM) broadening coefficient of $0.32\ cm^{-1}\ atm^{-1}$. They also extrapolated shocktube measurements[10–12] of O_2 self-broadening coefficients at temperatures near 3000 K to room temperature, assuming a $T^{-0.7}$ dependence, and obtained a FWHM broadening coefficient of $0.28\ cm^{-1}\ atm^{-1}$. The first comprehensive study of O_2 self-broadening in the SR bands was performed by Lewis et al,[13] who measured cross-sections for fine-structure-unresolved lines from the (2,0)–(15,0) bands at pressures in the range 10–60 atm with an instrumental resolution of $\sim 1.3\ cm^{-1}$ FWHM. They[13] observed significant collision-induced broadening, red shifting and asymmetry and analysed their results by means of a band model based on the Lindholm[14] lineshape, modified to allow a variable shift:width ratio. Finding little dependence of the collisional parameters on the rotational or upper-state vibrational quantum numbers, Lewis et al[13] concluded that a linearised FWHM collision-broadening parameter of $0.20\ cm^{-1}\ atm^{-1}$ and a shift:width ratio of -0.20 provided a good description of collisional effects in the SR bands. However, these results were inconsistent with those of Zhang and Ziegler,[15] who found no collisional broadening

†To whom all correspondence should be addressed.

in measurements of O- and S-branch $v'' = 6$ resonant Raman excitation profiles for excitation in the (5,0) SR band of O_2.

The only theoretical calculations of collision broadening in the SR bands are due to Breene,[16] who considered the resonance and van der Waals' broadening of O_2 by equilibrium air for temperatures $\geq$ 1000 K, treated in the impact approximation. Breene found that van der Waals' broadening was dominant, and, using his[16] calculated van der Waals' constants for the B and X states, Lewis et al[13] deduced collisional self-broadening and shift coefficients which were within $\sim$ 30% of their[13] measured values. In addition, Breene's calculations indicated that the collisional broadening was expected to be insensitive to rotation and relatively insensitive to the upper-state vibration. These predictions are consistent with the experimental findings of Lewis et al[13] and Treanor and Wurster.[10]

In this work, we present collisional self-broadening and shift coefficients for selected narrow fine-structure-resolved rotational lines from the $B \leftarrow X(v',1)$ SR bands. These hot-band lines occur conveniently in gaps between the $(v',0)$ bands and are sufficiently weak to provide unsaturated absorption in normal cells at pressures high enough (100–800 torr) to enable the measurement of collisional effects. When combined with predissociation linewidth components determined from high-resolution measurements of the equivalent $(v',0)$ transitions at low pressures, the hot-band measurements yield accurate broadening and shift coefficients which extend the measurements of Lewis et al[13] to significantly lower pressures.

2. EXPERIMENT

The experimental apparatus, shown schematically in Fig. 2, has been described in detail elsewhere.[17] Briefly, two-photon-resonant difference-frequency four-wave mixing[18] (2PR-4WDM) in Xe was used to generate tuneable narrow-bandwidth v.u.v. radiation from 1825 Å to 1850 Å, in order to measure high-resolution photoabsorption cross-sections for selected rotational lines from the $B \leftarrow X(v',1)$ system.

The output of one of the excimer-pumped dye lasers was frequency doubled in a BBO I crystal and the doubled output was tuned to be two-photon-resonant with the $6p_{[5/2]}^2$ level of Xe at 78,120 cm^{-1}. This beam was combined with the output of the tuneable dye laser and both beams were focused into a cell containing Xe by an off-axis lens. Tuneable v.u.v. radiation generated by the 2PR-4WDM process was passed through a low-resolution monochromator which discriminated

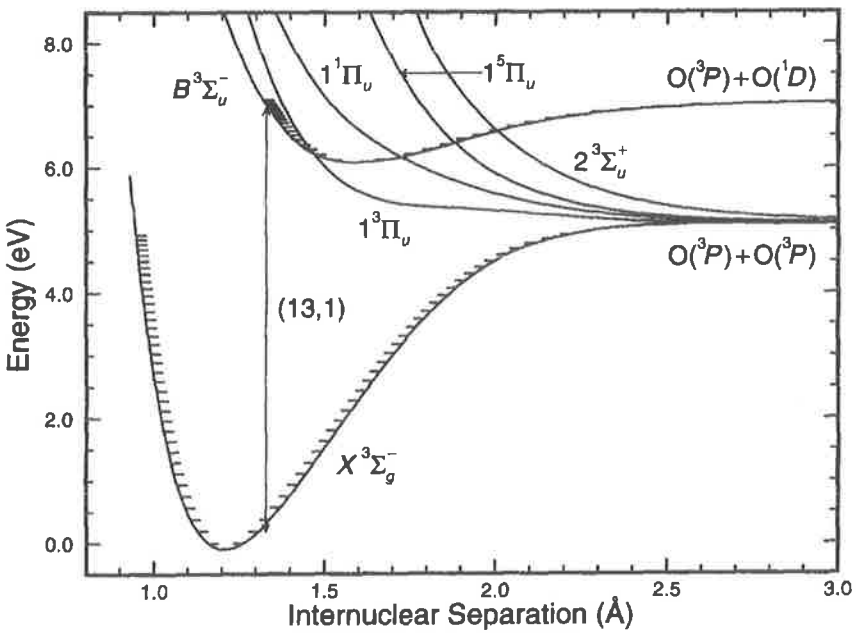

Fig. 1. Potential-energy curves of O_2 relevant to the Schumann–Runge system, $B^3\Sigma_u^- \leftarrow X^3\Sigma_g^-$, including those responsible for predissociation of the B state. Also shown is a transition representing the (13,1) hot band, typical of those studied in this work.

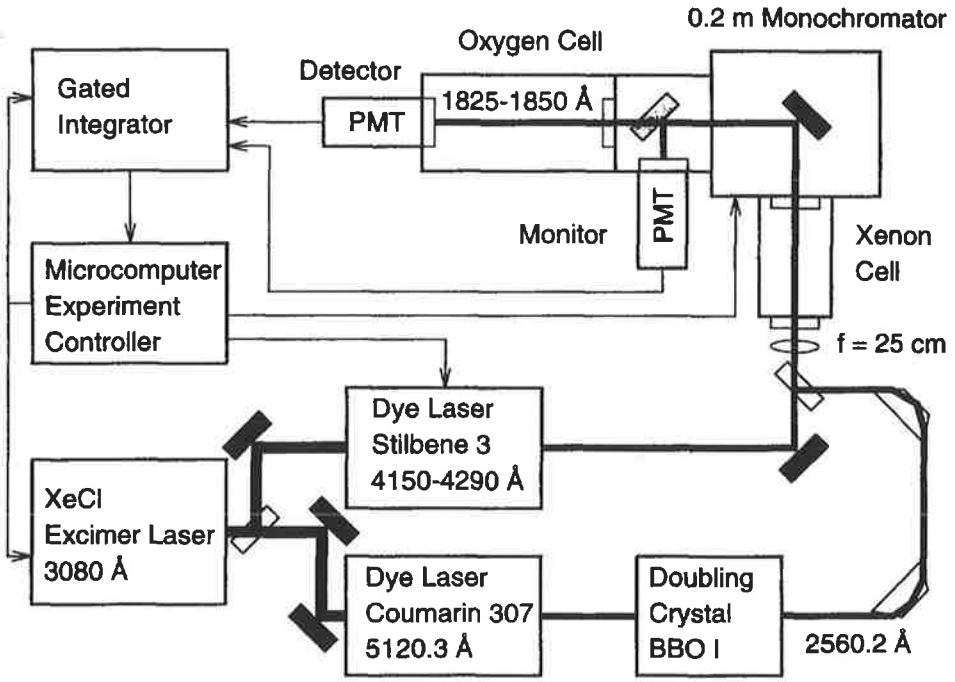

Fig. 2. Schematic diagram of the experimental apparatus.

against unwanted wavelengths. For measurements on the (v',1) SR bands, we used the dye Stilbene 3 and operated the tuneable dye laser in the range 4150–4290 Å, resulting in the production of v.u.v. radiation in the range 1825–1850 Å. For supporting measurements on the corresponding (v',0) bands, the dye was replaced by Coumarin 47, the laser was operated in the range 4460–4625 Å, and radiation in the range 1770–1795 Å was generated. The v.u.v. radiation leaving the monochromator was divided into two beams by a slotted Al beamsplitter. The reflected beam was monitored directly, while the transmitted beam passed through an absorption cell of length 33 cm, equipped with MgF_2 windows, before being detected. Output pulses from the solar-blind monitor and detector photomultipliers were processed by a boxcar averaging system.

The measurements presented here were all performed at room temperature (293 K). The phase matching for the 2PR-4WDM process was optimised by careful beam alignment and by adjusting the pressure of Xe, normally in the range 70–90 torr, to maximise the v.u.v. signal for the particular scan range. The monitor and detector signals were averaged over 50 laser shots for each datum point. Scans were performed in groups of three, with the absorption cell alternately filled with a pressure of O_2 in the range 1–800 torr, then evacuated, then refilled. This scheme compensated for drifts in photomultiplier sensitivity and the effects of wavelength structure in the photomultiplier signals which was not related to O_2 absorption.[19] Division of the detector signal by the monitor signal, after correction for scattered radiation, compensated for the shot-to-shot fluctuations inherent in the generated v.u.v. signal. Absolute cell transmittances were obtained by dividing the full-cell ratios (detector/monitor) by the empty-cell ratios at each wavelength. Photoabsorption cross-sections were calculated from the absolute transmittances by using the Beer–Lambert law.

Each dye laser was operated with an intra-cavity étalon, resulting in a nominal bandwidth of 0.04 cm^{-1} FWHM for each fundamental beam. The resultant v.u.v. bandwidth was determined to be ~ 0.09 cm^{-1} FWHM by examining the SR (v',0) lines of narrowest predissociation linewidth.[20] Absolute wavenumber calibration was achieved by comparison with the measured wavenumbers of Yoshino et al[21] for (v',0) lines in the vicinity of the hot-band lines being studied. It has been reported elsewhere[17] that the étalon scanning system of the dye laser is linear over the small scan ranges employed, and that uncertainties in the *relative* wavenumbers of sharp lines within the one étalon scan are $\lesssim 0.01$ cm^{-1}. The temporal stability of the laser system is also of critical importance to the reliability of the collisional shift measurements presented here which involved

successive scans over a given line at a number of different O_2 pressures. A laboratory air-conditioning system which used proportional control resulted in a temperature stability of $\sim \pm 0.2$°C and a corresponding wavenumber repeatability of $\lesssim 0.01$ cm^{-1}. This excellent system performance enabled the reliable measurement of the very small collisional shifts occurring for pressures < 1 atm.

3. ANALYSIS

The results of Lewis et al,[13] who measured collision-induced broadening, shift and asymmetry in the SR bands for pressures in the range 10–60 atm, imply a linear dependence of the observable collisional parameters on density for pressures $\lesssim 15$ atm (width), and $\lesssim 5$ atm (shift and asymmetry). Therefore, at the pressures employed in this work ($\lesssim 1$ atm), we expect to be in the binary-collision regime. We were unable to measure any statistically significant lineshape asymmetry for the rotational lines studied here, so we have adopted the Lorentzian approximation for the collisional part of the lineshape. Since all levels of the B state undergo predissociation, there is an additional broadening process which, to a high order of approximation, also results in a Lorentzian lineshape (predissociation linewidths 0.03–4 cm^{-1} FWHM[7]). In addition, it is necessary to consider the Doppler component of the lineshape which has a Gaussian profile (Doppler linewidth ~ 0.12 cm^{-1} FWHM). We assume no correlations between the broadening processes and adopt a Voigt profile to describe each rotational line in the analysis procedure: the Gaussian linewidth component is given by the well-defined Doppler width, while the Lorentzian linewidth component is the sum of the predissociation linewidth and the pressure-dependent collisional linewidth.

A non-linear least-squares procedure, in which a synthetic cross-section, based on this Voigt lineshape, is fitted to the measured cross-section, is used to determine the position, strength and Lorentzian linewidth component of each rotational line in a particular scan. The pseudo-continuum underlying the SR bands, comprising the wings of more distant lines, is represented by a quadratic polynomial in wavenumber, the coefficients of which are also determined in the fitting procedure. The instrumental bandpass function is represented by a Gaussian and is explicitly included in the synthetic cross-section through a convolution procedure, in transmittance space, which allows for the small degradation in cross-section due to finite instrumental resolution.

The very narrow bandwidth of the generated v.u.v. laser radiation (~ 0.09 cm^{-1} FWHM) enabled the full resolution of the individual rotational and fine-structure lines measured in this work, thus allowing the simple Voigt-lineshape fitting procedure, which included few assumptions, to be employed. In contrast, the limited experimental resolution of Lewis et al[13] (~ 1.3 cm^{-1} FWHM), together with greater collisional broadening at the higher pressures employed, necessitated the use of a band-model fitting procedure which included many assumptions regarding the relative positions, strengths and widths of the unresolved rotational and fine-structure components.

4. RESULTS AND DISCUSSION

The present study arose out of a comprehensive high-resolution study of fine-structure-specific predissociation linewidths in the (v',0) SR bands with $v' = 9$–18, and is limited to absorbing pressures $\lesssim 1$ atm in a cell of 33 cm length. For a number of reasons, it is not possible to perform a comprehensive study of collisional self-broadening under these conditions. First, the (v',0) bands become over-absorbed at pressures below those for which the collisional broadening is measurable; second, only for the narrower levels with $v' \geq 13$ will the collisional width become comparable with the predissociation width; and, third, since the weaker (v',1)-band lines are visible only in certain narrow regions between the (v',0) bands, the number of accessible rotational and fine-structure levels is limited. Nevertheless, the measurements of SR collisional self-broadening presented here are the first for pressures < 10 atm, and the first for fine-structure-resolved lines, providing a significant extension of the medium-resolution, high-pressure measurements of Lewis et al.[13]

Measured room-temperature cross-sections and Voigt lineshape-model fits for the (13,1)R_1(15) line are shown in Fig. 3 for two pressures of O_2, 99 torr and 717 torr, corresponding to weak and strong absorption, respectively. It is clear that significant broadening and red shifting has occurred

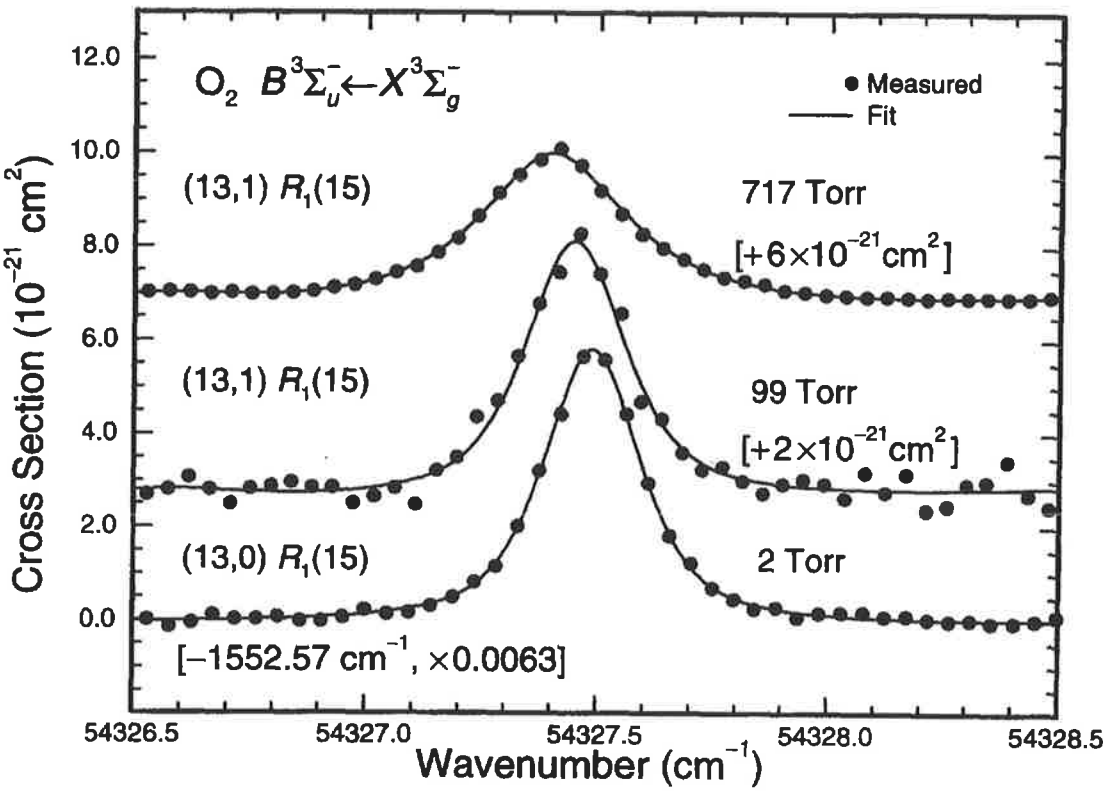

Fig. 3. Measured cross-sections and Voigt lineshape-model fits for two extreme pressures of O_2, illustrating the collision-induced broadening and red shift of the (13,1)R_1(15) line. For clarity, the cross-sections have been displaced upwards by the amounts indicated. For reference purposes, the measured cross-section for the (13,0)R_1(15) line is also shown, shifted in wavenumber by the appropriate ground-state rovibrational energy difference, and scaled down in intensity to enable convenient comparison with the equivalent hot-band cross-sections.

due to the increased pressure. For reference purposes, the measured cross-section and Voigt lineshape-model fit for the (13,0)R_1(15) line are also shown in Fig. 3, shifted in wavenumber by the appropriate ground-state rovibrational energy difference[22] of 1552.57 cm^{-1}, and scaled down in intensity by a factor of 0.0063 to enable convenient comparison with the hot-band cross-sections.

The fitted Lorentzian linewidth components for several fine-structure-resolved rotational lines, (13,1)R_1(15), (14,1)P_1(21), (15,1)P_2(15) and (15,1)P_3(15), are shown as a function of pressure (100–800 torr) in Fig. 4. In addition, the Lorentzian linewidths obtained from low-pressure measurements of the corresponding (v',0)-band lines, i.e., the predissociation linewidth components, are also shown. It is clear from Fig. 4 that the Lorentzian linewidths exhibit a linear dependence on pressure and that the slopes defined by the hot-band measurements are consistent with the predissociation linewidths determined separately from the (v',0)-band measurements. In addition, while the predissociation linewidths vary widely with vibration, rotation and fine-structure component, the collisional-linewidth slopes show little dependence on these quantities. The calculations of Breene,[16] who considers the effects of resonance and van der Waals' interactions, indicate that, at elevated temperatures, little dependence of the SR collisional-broadening coefficients on upper- or lower-state vibration or rotation is expected. This conclusion is supported by the measurements of Lewis et al[13] and is consistent with the present findings.

Collisional line shifts obtained by fitting the Voigt lineshape model to the cross-section measurements for the (13,1)R_1(15), (14,1)P_1(21) and (15,1)P_3(17) lines are shown as a function of pressure in Fig. 5. The measurements have been placed on a common scale by separately fitting a linear pressure dependence to the wavenumbers for each line and defining each fitted zero-pressure intercept to be a shift of zero. Although, due to the very small shifts involved for pressures of < 1 atm, the relative experimental uncertainties are considerably greater than those

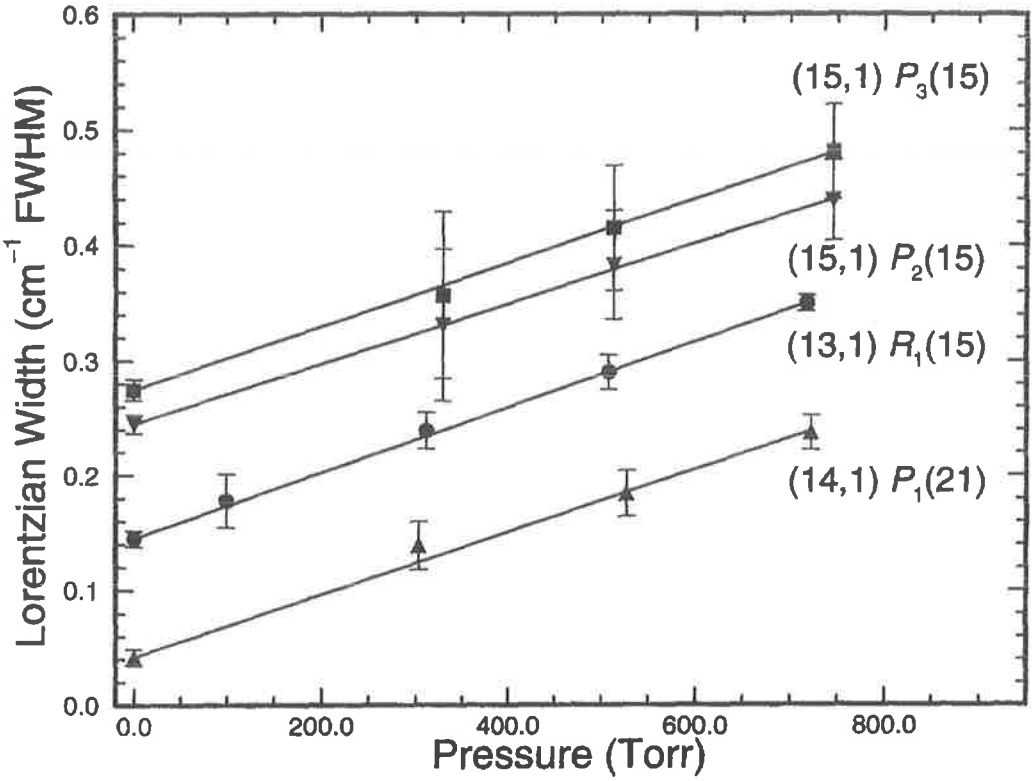

Fig. 4. Measured Lorentzian linewidth components (symbols) for several fine-structure-resolved transitions from the $B \leftarrow X(v',1)$ system. The lowest-pressure results for each line were obtained from measurements of the corresponding $(v',0)$ bands and represent the predissociation components of the Lorentzian linewidths. The weighted least-squares fits (lines) illustrate the similar magnitudes of the pressure dependence of the collisional linewidth for each transition.

pertaining to the widths, it can be seen in Fig. 5 that the collisional shifts exhibit an approximately linear dependence on pressure, with a similar slope for each line, within the experimental uncertainties. The global weighted linear least-squares fit to all of the shifts shown in Fig. 5 has a slope of $-0.056\ \mathrm{cm}^{-1}\ \mathrm{atm}^{-1}$.

A summary of the collision-broadening and shift coefficients obtained from weighted linear least-squares fits to the results shown in Figs. 4 and 5 is given in Table 1. The collisional linewidths and shifts are properties of both the upper and lower states of the $B \leftarrow X$ transition. However, as we have noted, little variation in these parameters is expected with rotation, or for a change of one unit in the ground-state vibrational quantum number.[13,16] Therefore, in Table 1, we compare our measured collisional coefficients for the $(v',1)$ bands with the high-pressure measurements of Lewis et al[13] for the $(v',0)$ bands. Neither work finds a significant variation with v'. The mean shift coefficients for the $v' = 13$–15 bands agree within the combined experimental uncertainties, while the present broadening coefficient exceeds that of Lewis et al[13] by $\sim 12\%$, a little outside the combined uncertainties. It should be noted, however, that the quoted uncertainties for both sets of measurements are statistical only, and do not include any systematic effects due to model or lineshape limitations. Overall the agreement is quite satisfactory, especially when one considers that the linearised coefficients of Lewis et al[13] were obtained from measurements taken at high pressures where the observable lineshape parameters mostly exhibited a non-linear dependence on pressure. Our confirmation of a room-temperature FWHM collisional self-broadening coefficient of $\sim 0.2\ \mathrm{cm}^{-1}\ \mathrm{atm}^{-1}$ in the SR bands of O_2 is at variance with the results of Zhang and Ziegler,[15] who, for pressures between 0.5 and 2 atm, found no collisional broadening in measured O- and S-branch $v'' = 6$ resonant Raman excitation profiles for excitation in the (5,0) SR band. Our results imply that an increase in collisional

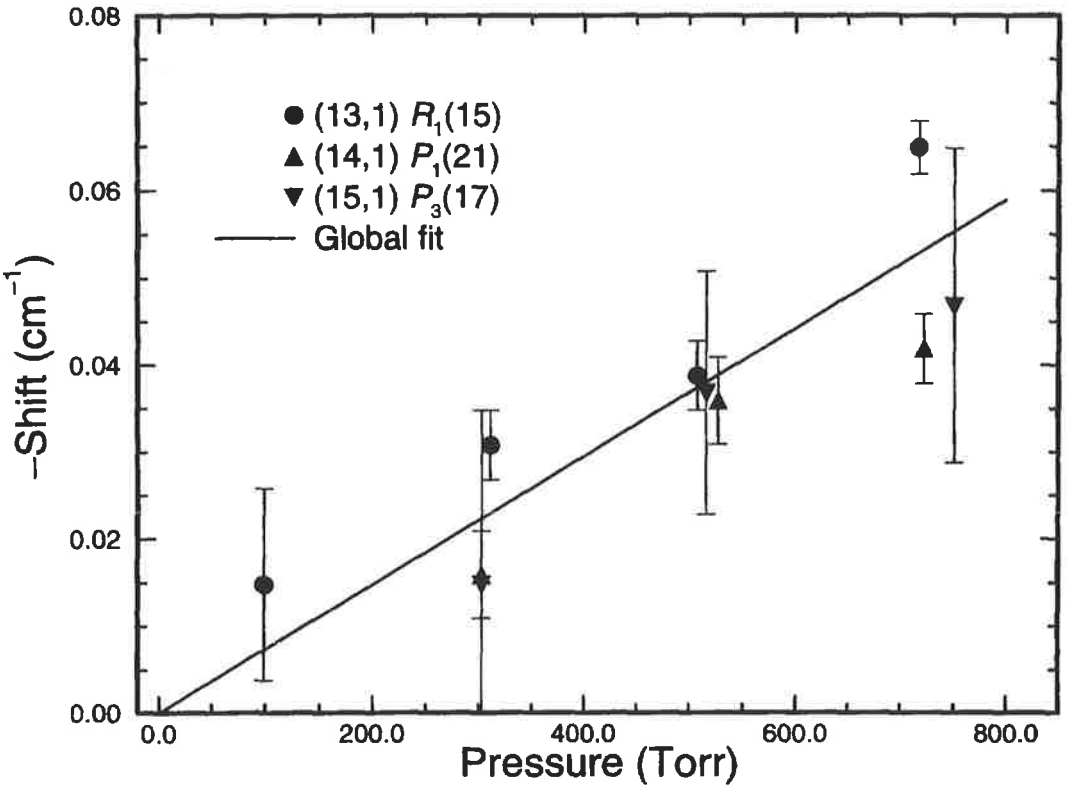

Fig. 5. Measured collisional line shifts for several fine-structure-resolved transitions from the $B \leftarrow X(v',1)$ system. The results have been placed on a common scale by separately fitting each set of results and defining each zero-pressure intercept to be a shift of zero. The resultant weighted least-squares global fit to the measurements provides a reasonable description of the pressure dependence of the collisional shift for each transition.

linewidth of $\sim 0.3\ cm^{-1}$ would have been expected over this pressure range, an $\sim 15\%$ increase in the $v' = 5$ predissociation linewidth of $\sim 2\ cm^{-1}$ FWHM, which should have been easily observable. Our experimental collisional shift:width ratio of -0.27 ± 0.04 agrees with that determined from the measurements of Lewis et al[13] for the same range of v', and is in fair agreement with the theoretical ratio -0.363 calculated by Lindholm[14] for purely van der Waals' interactions.

It is of some interest to compare the present results for the $B \leftarrow X$ system of O_2 with those obtained recently for the $A \leftarrow X(0,0)$ band of NO.[23,24] While the self-broadening coefficient for NO ($0.55\ cm^{-1}\ atm^{-1}$)[23] is considerably larger than is the case for O_2, the shift:width ratio (-0.31)[23] is in reasonable agreement. Similar broadening coefficients and shift:width ratios were found for Ar and N_2 colliders,[23,24] and, significantly, no dependence of the collisional parameters on rotation was found.[23] These observations are consistent with the calculations of Breene,[16] who found that similar interactions, principally van der Waals',[16] were likely to be responsible for collisional effects in the $B \leftarrow X$ system of O_2 and the $A \leftarrow X$ system of NO.

Table 1. Measured collision-broadening and shift coefficients.

	Broadening coefficient ($cm^{-1}\ atm^{-1}$)		Shift coefficient ($cm^{-1}\ atm^{-1}$)	
v'	This work	Ref. 13	This work	Ref. 13
13	0.217 ± 0.006	0.185 ± 0.004	-0.068 ± 0.011	-0.054 ± 0.004
14	0.206 ± 0.010	0.184 ± 0.005	-0.045 ± 0.012	-0.050 ± 0.004
15	0.203 ± 0.005†	0.189 ± 0.005	-0.051 ± 0.018	-0.047 ± 0.005
Ave.	0.208 ± 0.004	0.186 ± 0.003	-0.056 ± 0.008	-0.051 ± 0.003

†Weighted average over the $P_3(17)$, $P_2(15)$ and $P_3(15)$ lines.

5. CONCLUSIONS

Collisional self-broadening and shift coefficients, derived from high-resolution photoabsorption cross-sections measured using tuneable, narrow-bandwidth, v.u.v. laser radiation, have been presented for selected fine-structure-resolved rotational lines from the $B^3\Sigma_u^- \leftarrow X^3\Sigma_g^-(v',1)$ bands of O_2. These measurements of collisional effects in the SR bands are the first taken at pressures < 10 atm and are the first for resolved rotational and fine-structure features. The results, a mean FWHM self-broadening coefficient of $0.208\ cm^{-1}\ atm^{-1}$ and a mean shift coefficient of $-0.056\ cm^{-1}\ atm^{-1}$, with little dependence on rotation, upper-state vibration or fine-structure level (within the limited ranges of these parameters studied), are consistent with those of Lewis et al,[13] obtained from medium-resolution measurements of the $B^3\Sigma_u^- \leftarrow X^3\Sigma_g^-(v',0)$ bands at pressures in the range 10–60 atm. However, we differ markedly from Zhang and Ziegler,[15] who found no collisional broadening in resonant Raman excitation profiles for excitation in the (5,0) band.

While collisional coefficients of the magnitudes reported here are likely to be of only marginal significance in photochemical studies of the terrestrial atmosphere, it is necessary to take account of collisional effects in laboratory studies of the SR bands. In particular, Lorentzian linewidths for the weaker bands (0,0)–(2,0), which are normally measured at pressures of several hundred torr,[25] must be corrected for collisional broadening in order to obtain accurate estimates of the corresponding predissociation linewidths.[7]

Acknowledgements—The authors would like to thank Professor J. H. Carver for a critical assessment of the manuscript, and are grateful to K. J. Lonsdale and C. J. Dedman for valuable technical assistance.

REFERENCES

1. Julienne, P. S. and Krauss, M., *J. Mol. Spectrosc.*, 1975, **56,** 270.
2. Julienne, P. S., *J. Mol. Spectrosc.*, 1976, **63,** 60.
3. Cann, M. W. P., Nicholls, R. W., Evans, W. F. J., Kohl, J. L., Kurucz, R., Parkinson, W. H. and Reeves, E. M., *Appl. Opt.*, 1979, **18,** 964.
4. Cann, M. W. P., Shin, J. B. and Nicholls, R. W., *Can. J. Phys.*, 1984, **62,** 1738.
5. Lewis, B. R., Carver, J. H., Hobbs, T. I., McCoy, D. G. and Gies, H. P. F., *J. Quant. Spectrosc. Radiat. Transfer*, 1979, **22,** 213.
6. Lewis, B. R., Berzins, L., Carver, J. H. and Gibson, S. T., *J. Quant. Spectrosc. Radiat. Transfer*, 1986, **36,** 209.
7. Lewis, B. R., Gibson, S. T. and Dooley, P. M., *J. Chem. Phys.*, 1994, **100,** 7012.
8. Lewis, B. R., Berzins, L., Carver, J. H., Gibson, S. T. and McCoy, D. G., *J. Quant. Spectrosc. Radiat. Transfer*, 1985, **34,** 405.
9. Bethke, G. W., *J. Chem. Phys.*, 1959, **31,** 669.
10. Treanor, C. E. and Wurster, W. H., *J. Chem. Phys.*, 1960, **32,** 758.
11. Krindach, N. I., Sobolev, N. N. and Tunitskii, L. N., *Opt. Spectrosc.*, 1963, **15,** 326.
12. Buttrey, D. E., *J. Quant. Spectrosc. Radiat. Transfer*, 1969, **9,** 1527.
13. Lewis, B. R., Berzins, L., Dedman, C. J., Scholz, T. T. and Carver, J. H., *J. Quant. Spectrosc. Radiat. Transfer*, 1987, **39,** 271.
14. Lindholm, E., *Ark. Math. Astron. Fys.*, 1945, **32A,** 17.
15. Zhang, Y. P. and Ziegler, L. D., *J. Phys. Chem.*, 1989, **93,** 6665.
16. Breene, R. G., *Appl. Opt.*, 1967, **6,** 141.
17. Lewis, B. R., Dooley, P. M., England, J. P., Waring, K., Gibson, S. T., Baldwin, K. G. H. and Partridge, H., *Phys. Rev. A*, 1996, **54,** 3923.
18. Hilbig, R. and Wallenstein, R., *IEEE J. Quantum Electron.*, 1983, **QE19,** 194.
19. Lewis, B. R., England, J. P., Winkel, R. J. Jr., Banerjee, S. S., Dooley, P. M., Gibson, S. T. and Baldwin, K. G. H., *Phys. Rev. A*, 1995, **52,** 2717.
20. Dooley, P. M., Lewis, B. R., Gibson, S. T. and Baldwin, K. G. H., *J. Electron Spectrosc. Relat. Phenom.*, 1996, **80,** 29.
21. Yoshino, K., Freeman, D. E. and Parkinson, W. H., *J. Phys. Chem. Ref. Data*, 1984, **13,** 207.
22. Veseth, L. and Lofthus, A., *Mol. Phys.*, 1974, **27,** 511.
23. Chang, A. Y., DiRosa, M. D. and Hanson, R. K., *J. Quant. Spectrosc. Radiat. Transfer*, 1992, **47,** 375.
24. Vyrodov, A. O., Heinze, J. and Meier, U. E., *J. Quant. Spectrosc. Radiat. Transfer*, 1995, **53,** 277.
25. Cheung, A. S.-C., Yoshino, K., Esmond, J. R., Chiu, S. S.-L., Freeman, D. E. and Parkinson, W. H., *J. Chem. Phys.*, 1990, **92,** 842.

4.31 Angular distributions for photodissociation of O_2 in the Herzberg continuum

[51] B. Buijsse, W, J. van der Zande, A. T. J. B. Eppink, D. H. Parker, B. R. Lewis, and S. T. Gibson,
Journal of Chemical Physics **108**, 7229–7243 (1998).

Angular distributions for photodissociation of O_2 in the Herzberg continuum

B. Buijsse and W. J. van der Zande
FOM Institute for Atomic and Molecular Physics, Kruislaan 407, 1098 SJ Amsterdam, The Netherlands

A. T. J. B. Eppink and D. H. Parker
University of Nijmegen, Department of Molecular and Laser Physics, Toernooiveld 1, 6525 ED Nijmegen, The Netherlands

B. R. Lewis and S. T. Gibson
Research School of Physical Sciences and Engineering, The Australian National University, Canberra, ACT 0200, Australia

(Received 15 December 1997; accepted 27 January 1998)

Photodissociation in the Herzberg continuum of molecular oxygen has been studied at 236, 226 and 204 nm. Using ion-imaging and monitoring of $O(^3P_j)$, $j=0$, 1, and 2 product-atom angular distributions, the amount of parallel character of the transition was measured. In order to interpret these data, analyses of the photoabsorption oscillator strengths and the parallel-perpendicular nature of the Herzberg I, II and III bands, and extrapolation of these properties into the Herzberg-continuum region have been performed. Our measured fine-structure-averaged angular distributions are found to be consistent with this photoabsorption model. In addition, the dynamics of the dissociation process is discussed, based on the O-atom fine-structure distributions. © *1998 American Institute of Physics.* [S0021-9606(98)01317-8]

I. INTRODUCTION

Photodissociative reactions of diatomic molecules yield atoms that may either be in the ground state or in an excited state. Not only the quantum state of each atom, but also the photofragment angular distribution is an important observable. In particular, the angular distribution can elucidate the amount of parallel ($\Delta\Lambda=\Delta\Omega=0$) and perpendicular ($\Delta\Lambda=\Delta\Omega=\pm 1$) character in an electronic transition to a continuum state, information that is unattainable using conventional spectroscopic techniques. In contrast to the case of dipole-allowed transitions, where one matrix element dominates the transition probability, the situation is different for the weaker forbidden transitions. Here, intensity is borrowed from allowed transitions through one or several second-order pathways with either parallel or perpendicular character. If the nature of the optical excitation is a mixture of parallel and perpendicular, then this will be reflected in the photofragment angular distribution. In this way, angular distributions form a diagnostic tool which is of particular interest in the study of forbidden bound-free transitions. In this paper, we use this tool for investigation of the photodissociation of molecular oxygen in the Herzberg continuum.

The structure of molecular oxygen is complicated. This, for example, is reflected in the fact that oxygen has six bound states below the first dissociation limit, all correlating with ground-state $O(^3P_j)$ product atoms: the ground state $X\ ^3\Sigma_g^-$ and five metastable states, labelled $a\ ^1\Delta_g$, $b\ ^1\Sigma_g^+$, $A\ ^3\Sigma_u^+$, $c\ ^1\Sigma_u^-$, and $A'\ ^3\Delta_u$. The Herzberg transitions are electric-dipole-forbidden transitions from the O_2 $X\ ^3\Sigma_g^-$ ground state to the $A\ ^3\Sigma_u^+$, $c\ ^1\Sigma_u^-$, and $A'\ ^3\Delta_u$ states.[1–3] In our earth's atmosphere, the large abundance of oxygen compensates for the forbidden character of these transitions, and their importance to aeronomy[4] and atmospheric photochemistry[5] has made the Herzberg transitions the subject of considerable study. However, progress in characterizing the spectroscopy of these states has been slow, due to the weakness of the Herzberg I ($A\ ^3\Sigma_u^+ \leftarrow X\ ^3\Sigma_g^-$), Herzberg II ($c\ ^1\Sigma_u^- \leftarrow X\ ^3\Sigma_g^-$), and Herzberg III ($A'\ ^3\Delta_u \leftarrow X\ ^3\Sigma_g^-$) transitions, and also because of the strong pressure dependence of the Herzberg III transition intensity.[6,7] Understanding the spectroscopy requires detailed knowledge of the transition dipoles, to be discussed in detail in Sec. IV C. Briefly, the oscillator strength of the Herzberg transitions, including the corresponding dissociation continuum, is borrowed from dipole-allowed transitions through spin-orbit and orbit-rotation interactions, leading to an overall transition of mixed parallel and perpendicular character.

It is principally the Herzberg continuum that is responsible for photodissociation of O_2 in the 200–240 nm region. We have employed the technique of photofragment imaging to measure the angular distribution of the photofragments at 236, 226 and 204 nm. Hence, we have been able to determine the parallel-perpendicular nature of the transition to the Herzberg continuum at these wavelengths, assuming axial recoil for the (instantaneous) dissociation process. An expectation of the photofragment angular distributions can be obtained from an understanding of the discrete spectroscopy of the Herzberg systems. We have reviewed the current experimental and theoretical state of knowledge on the Herzberg transitions in O_2, employing the best available molecular parameters in the construction of a model of the corresponding O_2 photoabsorption, both for the bound and the continuous parts of the spectrum. Calculated cross sections based on this model are then used to independently assess our angular dis-

tributions, testing the quality of our knowledge of the Herzberg transitions.

In addition, we have investigated the *adiabaticity* of the dissociation process. The dynamics of diatomic molecular dissociation affects the relative population of the fine-structure states of the atomic photofragments. In particular, if a molecular Born-Oppenheimer state has fine structure, as is the case for the A and A' states, then the dissociation dynamics determines how the population of the molecular fine-structure states redistributes itself over the fine-structure states of the atoms.[8] Photodissociation in the Herzberg continuum produces only ground-state ^3P_j atoms, with j either 0, 1 or 2. Our experimental setup enables fine-structure-resolved measurements, not only of the rate at which $O(^3P_j)$ atoms are formed, but also of the corresponding angular distributions. Whether a molecule adiabatically follows a particular potential-energy curve to dissociation, or undergoes transitions to neighboring potentials correlating with different atomic fine-structure limits, is related to the velocity with which the dissociating molecule probes these potentials. In this way, the dissociation dynamics affects the branching ratio over the atomic multiplet. In addition, as our results will show, the angular distribution may also differ for each fine-structure component if the fine-structure levels of an excited molecular state do *not* contribute equally to a particular fine-structure state of the atomic fragments.[9]

The molecular photodissociation dynamics can be characterized by an adiabaticity parameter,[10,11] $\xi=\Delta R\Delta E_{SO}/\hbar v$ which compares the recoil time $\Delta R/v$, where ΔR is a characteristic recoil distance and v is the recoil velocity, with the characteristic time for spin-orbit coupling $\hbar/\Delta E_{SO}$, where ΔE_{SO} is the asymptotic spin-orbit coupling. Two limiting cases, the sudden-recoil limit ($\xi\rightarrow 0$), and the adiabatic limit ($\xi\rightarrow\infty$), correspond to high and low recoil velocity, respectively.

In the sudden-recoil limit, the atomic multiplet distribution is often close to a statistical one, i.e. proportional to $2j+1$, the degeneracy of each j state. However, for an exact calculation of the fine-structure distribution in this limit, a frame transformation in which molecular eigenstates are expanded in atomic eigenfunctions is required.[8]

The other extreme is fully adiabatic behavior. In this case, the projection Ω on the internuclear axis, of the total angular momentum of the initial Born-Oppenheimer state, is conserved during dissociation. At small internuclear separation R, the electrostatic forces between the nuclei are high and L and S are coupled to the internuclear axis [Hund's case (a)]. At greater R, the spin-orbit coupling becomes dominant over the electronic term in the Hamiltonian, and L and S couple to each other, but Ω remains a good quantum number [Hund's case (c)]. An adiabatic correlation diagram[11] can be used to find the specific atomic fine-structure state that connects with the fine-structure level of the molecule, this procedure amounting to ignoring any couplings between the noncrossing case (c) potential-energy curves.

Reality is often intermediate between the limiting cases. In this situation, the couplings between different electronic states must be known accurately. At short R, spin-orbit couplings may induce diabatic transitions between case (a) potentials, while at large R, where the spin-orbit term is diagonalized in the case (c) description, nonintersecting case (c) potentials may be coupled nonadiabatically by terms such as the radial kinetic-energy operator or the **L**-uncoupling operator.[10] Accurate knowledge of the potential-energy curves and the strengths of the couplings must be available for calculation of the fine-structure branching in this general case.[11]

Several authors have studied fine-structure branching in the dissociation of O_2. Matsumi and Kawasaki,[12] and Huang and Gordon,[11] using resonance-enhanced multi-photon ionization (REMPI), and laser-induced fluorescence (LIF) detection of the photofragments, respectively, performed fragmentation experiments at 157 nm in the Schumann-Runge (SR) continuum where they measured principally $O(^3P_j)$ fragments with $j=2$. Photodissociation of O_2 slightly above threshold in the SR continuum has been shown to be fully adiabatic.[13] Matsumi and Kawasaki[12] have also measured fine-structure branching ratios and Doppler profiles in the SR bands at 193 nm, obtaining results intermediate between the sudden-recoil and adiabatic limits. Leahy *et al.*,[14,15] using fast-beam photofragment translational spectroscopy, have measured *correlated* $O(^3P_{j_1})+O(^3P_{j_2})$ predissociation branching ratios for the SR bands, also obtaining results inconsistent with both the diabatic and adiabatic limits. Finally, Tonokura *et al.*[16] reached similar conclusions following the measurement of fine-structure branching ratios at 226 nm in the Herzberg continuum. Their results will be discussed in more detail in Sec. V A.

II. EXPERIMENT

Ion-imaging techniques have proven to be very valuable in the study of photodissociative processes. The full three-dimensional (3D) velocity distribution of recoiling fragments can be projected in one single image, revealing the kinetic-energy release in the dissociation process and the angular distribution of the photofragments. A detailed description of conventional ion imaging has been given in Ref. 17. A brief description of this technique and the experimental velocity-mapping setup that we used[18] will be presented here.

As depicted schematically in Fig. 1, the vacuum system consists of differentially-pumped source and ionization chambers. A cold, pulsed molecular beam is obtained by a supersonic expansion of 10%–20% O_2 in He as carrier gas at a stagnation pressure of 2 bar. We estimate the temperature of the beam to be between 5 and 10 K, implying an O_2 ground-state population predominantly in the lowest rotational level. Subsequently, the beam enters the ionization chamber through a 1 mm skimmer, passes a 1 mm hole in a repeller electrode, and is crossed at right angles by two pulsed, counter-propagating focused laser beams, one beam for pumping the Herzberg continuum, the other for probing the nascent oxygen atoms by means of REMPI. The atomic ions are formed in the presence of an electric field between the repeller and extractor plates ($V_E/V_R\approx 0.7$; $V_R\approx 4000$ V), and accelerated along the axis of a time-of-flight (TOF) tube towards the detector. These ions travel on expanding, nested

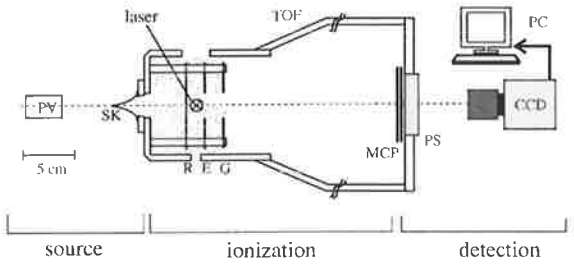

FIG. 1. Velocity-map imaging experimental setup: PV=pulsed valve; SK=1 mm skimmer; axially symmetric ion optics with Rm=repeller at voltage V_R, E=extractor at voltage V_E and G=ground electrode; a 15 mm spacing between the 0.2 mm thick plate electrodes is set using aluminum oxide tubes; E and G contain 20 mm apertures such that equipotential surfaces are bent as indicated; ⊗ denotes the laser focus, 108 mm downstream from the nozzle; TOF tube, 36 cm from laser focus to detector; dual MCP detector with PS=phosphor screen; CCD camera connected to the PC.

spherical surfaces, where the expansion speed of each surface is determined by the kinetic-energy release in the corresponding dissociation channel.

The extractor plate is part of the ion-lens optics, consisting of an axially symmetric three-plate assembly, with 20 mm apertures in the extractor and ground electrodes, thus forming an asymmetric immersion lens.[18] This lens guides all particles with the same initial velocity vector to the same point on the detector, irrespective of their initial distance from the ion-lens axis, a technique called *velocity-map imaging*.[18,19] The result is a better spatial resolution than in conventional ion imaging where an extracting wire-grid electrode is used. A good resolution is crucial in the two-laser experiments described here, in order to discriminate between the different images on the detector.

In the TOF tube, a separation takes place between ions of different masses. Simultaneously, the spherical distribution of fragment ions is flattened by the acceleration along the TOF axis in such a way that the spread in time-of-flight $\Delta t/t$ is very small ($<1\%$). This enables mass-selective ion detection with an imaging detector [dual 40 mm microchannel-plates (MCP) with a P-20 phosphor screen] by the application of a timed voltage pulse to the front MCP. The two-dimensional images appearing on the phosphor screen are recorded by a CCD camera equipped with a 25 mm focal-length objective lens. Images are integrated on the CCD chip over a preset number of laser pulses, and subsequent images are summed in a PC where further data analysis is performed. By choosing the polarization vector of the dissociation laser parallel to the image plane, the so-called inverse Abel-transform method[20] can be used to reconstruct the original 3D velocity distribution.

The Herzberg states, A, A', and c, all correlate with the $O(^3P_{j_1})+O(^3P_{j_2})$ dissociation limit. Adiabatically, these states connect to one fine-structure dissociation limit with $j_1=j_2=2$. State-selective detection of the individual $O(2p\ ^3P_j)$ atoms is achieved by (2+1) REMPI through the $O(3p\ ^3P_{j'})$ states, using wavelengths of 226.233, 226.059 and 225.656 nm for $j=0$, 1, and 2, respectively. For this purpose, a Nd:YAG-pumped dye laser (Spectra-Physics DCR-2A and PDL-2), operated with Coumarin-460 dye and frequency doubled in a BBO crystal, is used. In principle, about 0.5 mJ/5 ns UV power with vertical polarization (i.e., parallel to the detector face) can be focused onto the molecular beam with a lens of 20 cm focal-length. In order to avoid space-charge problems, the UV power is attenuated to about 0.1 mJ/5 ns. In spite of the considerable laser fluence, the one-photon transition is far from saturated. At the peak of the Herzberg continuum, where the absorption cross section is 7.35×10^{-24} cm^2, we dissociate about 1 in 10^5 molecules. Furthermore, the detection laser is scanned back and forth over the REMPI transition during image-data acquisition, thus probing all velocity groups at equal sensitivity and avoiding Doppler selection. Due to this scanning process, the fine-structure of the intermediate $O(3p\ ^3P)$ state is not resolved. The integrated two-photon line strengths are reported to yield equal sensitivity for the initial fine-structure states,[21–24] which simplifies the study of branching between these states. Since the $O(^3P_j)$ REMPI wavelengths are also suitable for excitation of O_2 into the Herzberg continuum, we performed, in the first instance, single-laser experiments. Images obtained with the molecular beam triggered after the laser pulse have been used to subtract the contribution of thermalized ambient background gas.

In the two-laser experiments, a second Nd:YAG-pumped dye laser (Spectra-Physics GCR-11 and PDL-2) is used to generate excitation wavelengths in the 203–240 nm range. The ~204 nm light is produced by frequency doubling and mixing in KDP and BBO crystals the output of the dye laser operated with Sulforhodamine 640 dye. Longer wavelengths are produced by direct frequency doubling in a BBO crystal, using the third harmonic of the YAG laser to pump, e.g., Coumarin-480 dye. In order to obtain vertical polarization, a Berek's compensator is used. Images from each laser separately are subtracted from the images with both lasers present, yielding the double-resonant signal free from background. The UV power was balanced and the focal points of the two laser beams were overlapped carefully in order to maximize the double-resonant signal while maintaining a homogeneous detection efficiency.

III. RESULTS

In Fig. 2(a), a raw O^+ ion image from $O(^3P_2)$ REMPI at 225.66 nm is shown. Three rings appear: the inner ring corresponding to one-photon excitation into the Herzberg continuum, leading to $O(^3P_2)+O(^3P_j)$; the middle ring and the outer ring due to two-photon excitation, leading to $O(^3P_2)+O(^1D_2)$ (second dissociation limit) and $O(^3P_2)+O(^3P_j)$, respectively. The reconstructed image, Fig. 2(b), represents a vertical section through the 3D distribution, and is obtained by an inverse Abel transform of the raw image. From this image, the 3D speed distribution in Fig. 3(a) is obtained by integrating over all angles, the results of which represent the branching between the three dissociation channels. The middle ring is strongest at this wavelength. In contrast, for the $j=0$ and $j=1$ images, the two-photon transition is much weaker. The reason for this rapid intensity variation with wavelength is the presence of quasi-bound Rydberg states at the two-photon energy.[19] At 225.66 nm, the $3d\delta\ ^3\Pi_{0,1}(v=2)$ state[25] enhances the two-photon excitation strength. This

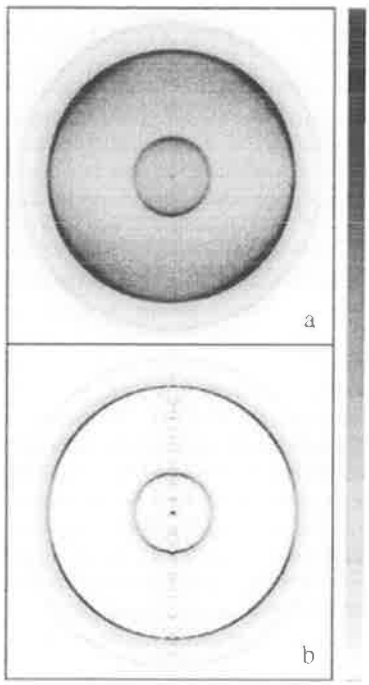

FIG. 2. (a) Raw $O(^3P_2)$ ion image obtained using a single laser at a wavelength near 225.67 nm. During 10 000 laser shots of data acquisition, the wavelength was scanned back and forth (by ~0.03 nm) across the REMPI transition. Laser polarization was vertical in the image, and the laser propagation direction was from left to right. The center dot corresponds to the O_2^+ signal at zero kinetic energy which is strong enough to be seen outside of the mass-selective gate for O^+. (b) Corresponding reconstructed image obtained by means of an inverse Abel transform. The 3D velocity distribution is recovered by revolution of the image around the vertical symmetry axis.

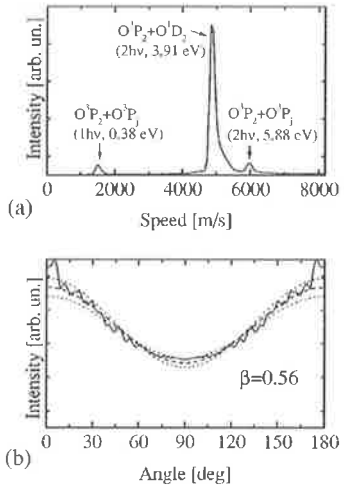

FIG. 3. Speed and angular distributions obtained from Fig. 2(b). (a) The speed distribution shows three channels, the outer two fast channels corresponding to two-photon excitations, and the slow channel to one-photon excitation into the Herzberg continuum. Dissociation limits and kinetic energy releases for each channel are indicated. (b) The angular distribution of the inner ring for this experimental run (solid curve) is fitted with $\beta=0.56$ (dashed curve), indicative of the dominance of parallel character in the excitation process. For comparison, curves with $\beta=0.46$ and 0.66 are shown also.

state subsequently predissociates to the $O(^3P_2)+O(^1D_2)$ dissociation limit. This channel shows a distinct quadrupolar angular distribution, indicative of $\Sigma\rightarrow\Sigma\rightarrow\Pi$ or $\Sigma\rightarrow\Pi\rightarrow\Pi$ two-photon transitions, for which the angular distribution is described by $I(\theta)\propto 1+\beta P_2(\cos\theta)+\gamma P_4(\cos\theta)$, where P_2 and P_4 represent second- and fourth-order Legendre polynomials, respectively, β and γ are anisotropy parameters, and θ is the angle between the recoil and laser-polarization directions. The outer ring is much weaker: apparently predissociation to the lower dissociation limit is weak.[26]

The inner ring corresponds to one-photon excitation into the Herzberg continuum, leading to $O(^3P_2)+O(^3P_j)$ at 0.38 eV kinetic-energy release. The angular distribution of these fragments is described by the simpler $I(\theta)\propto 1+\beta P_2(\cos\theta)$ distribution. This ring is quite weak due to the electric-dipole-forbidden nature of the Herzberg transitions. The character of the Herzberg transition will be discussed in detail in Sec. IV. Here, the statement that the transition borrows oscillator strength by mixing with other electronic states both in the ground and in the excited state will suffice. The transition strength comprises two types of contribution, parallel and perpendicular, for which $\beta=2$ and -1, respectively. Since the dissociation process takes place on a time scale much shorter than molecular rotation, the fragment angular anisotropy reflects directly the relative importance of the parallel and perpendicular contributions to the transition. In Fig. 3(b), the angular distribution measured for the inner ring is displayed, together with a fitted curve (dashed line) yielding an anisotropy parameter $\beta=0.56$ for this experimental run, and indicative curves (dotted lines) for $\beta=0.46$ and 0.66.

In this study, we concentrate solely on the Herzberg continuum, i.e. the one-photon signal. In Table I, the experimentally determined β parameters for the inner ring are listed. The tabulated values, classified according to three main excitation wavelengths (204, 226 and 236 nm), represent average fitted β parameters determined over a series of images. The uncertainty listed is, therefore, the standard deviation from the mean value, which is found to dominate the uncertainty resulting from the fitting procedure for a single image. The two main sources of error are believed to be associated with the method for background subtraction, and long- and short-term variations in detector sensitivity.

TABLE I. Measured anisotropy parameters β, characterizing the angular distribution of photofragments formed in the excitation of the O_2 Herzberg continuum at 204, 226, and 236 nm. Atoms are formed in three fine-structure states $O(^3P_j)$, with $j=0,1$ and 2.

λ nm	β $j=0$	$j=1$	$j=2$
204	0.35±0.15	0.53±0.15	0.87±0.10
226	0.37±0.24	0.61±0.09	0.64±0.08
236	-	0.31±0.15	-

For the one-laser experiment, the dissociation branching ratio over the different fine-structure states could only be determined at 226 nm. The measured $j=0:1:2$ branching ratio, normalized to the $j=0$ intensity, is $1.00\pm0.26:3.33\pm0.43:9.00\pm0.70$. These results have been corrected for the effects of the slight variation in laser intensity at the three detection wavelengths for $j=0$, 1, and 2. Reliable branching ratios could not be obtained for the two-laser experiments (dissociation at 204 nm and 236 nm, detection at 226 nm) because the signal in these cases relies on the precise overlap of the focal points of the two lasers: the three detection wavelengths lie relatively far apart, and when scanning the detection-laser wavelength, dispersive elements in the optics chain cause a significant displacement in the detection-laser focal position. Relative measurements, such as the angular distribution for different j states at 204 nm and 236 nm, are not affected by this overlap problem. For 236 nm measurements, however, the strong signal created by the 226 nm detection laser, especially for $j=2$, overwhelms the weak dissociation-laser signal. Only the $j=1$ signal from 236 nm dissociation could be extracted reliably from the detection-laser background.

IV. THE HERZBERG TRANSITIONS

A. Previous work

As explained in Sec. I, the angular distribution of the photofragments is closely related to the nature of the Herzberg continuum. Understanding the Herzberg continuum requires a thorough knowledge of the Herzberg bands. The discrete spectroscopy of the Herzberg states has been reviewed comprehensively by Slanger and Cosby,[27] with the review based principally on the high-resolution, multiple-reflection cell spectrographic measurements performed at the Herzberg Institute of Astrophysics, Ottawa.[28–31] Since the time of the Slanger and Cosby review, significant new high-resolution measurements have been performed by Yoshino *et al.*[32] and Slanger *et al.*,[33] using ultraviolet Fourier-transform spectroscopy (UVFTS) and cavity ring-down spectroscopy (CRDS), respectively. At present, the spectroscopic constants of the A state are known, from absorption spectra, for $v=0-12$, those of the c state for $v=1-18$, and those of the A' state for $v=2-13$.[34] Knowledge of the absolute and relative intensities of the Herzberg transitions is far from complete however, most of the early estimates being based on spectrographic data. Recently, Huestis *et al.*[35] published experimental oscillator strengths for the (8,0)–(11,0) bands of the $A\leftarrow X$ system, the (13,0), (14,0) and (16,0) bands of the $c\leftarrow X$ system, and the (9,0) and (11,0) bands of the $A'\leftarrow X$ system, based on CRDS in absorption, while Yoshino *et al.*[36] have measured oscillator strengths for the (4,0)–(11,0) bands of the $A\leftarrow X$ system using UVFTS. At present, it appears that the most reliable Herzberg I oscillator strengths are those of Yoshino *et al.*[36] However, the $c\leftarrow X$ and $A'\leftarrow X$ oscillator strengths of Huestis *et al.*[35] must be regarded as the only reasonable data available on the strengths of the Herzberg II and III transitions, despite the acknowledged shortcomings of CRDS in providing quantitative intensity information.[33,35] From their measured discrete oscillator strengths, Huestis *et al.*[35] concluded that the Herzberg I transition provides ~86% of the total strength of the Herzberg transitions.[37] To obtain an improved estimate of this quantity, it would be useful to have measurements of the Herzberg II and III oscillator strengths of the same resolution and quality as the Herzberg I UVFTS measurements of Yoshino *et al.*[36]

Measurement of the small Herzberg continuum cross section is a difficult problem, complicated not only by the necessity to extrapolate to zero pressure in order to remove the effects of collisional enhancement of the Herzberg III cross-section component, but also by corrections for the effects of Rayleigh scattering and the predissociation line wings of the nearby SR bands, $B\,{}^3\Sigma_u^-\leftarrow X\,{}^3\Sigma_g^-$. Direct, long-path measurements of stratospheric transmittances demonstrated that most of the early measurements had overestimated the cross section by as much as 40%.[38–40] This inspired new laboratory measurements[41–43] that confirmed a lower cross section. However, there remained differences between the results obtained in different laboratories from measurements taken with different path lengths and pressures, and it was not until the work of Yoshino *et al.*[44] that these differences were reconciled, resulting in a single recommendation for the Herzberg continuum cross section and its pressure dependence. In this work, we will adopt this recommendation for the absolute value of the Herzberg continuum cross section, but we note that more recent measurements[45,46] have resulted in even lower values. Thus, the question of the magnitude of the Herzberg continuum cross section cannot be regarded as settled completely.

There have been several *ab initio* studies of the potential-energy curves of the A, c, and A' states, with the recent multireference configuration-interaction with Davidson correction (MRCI+Q) calculations of Partridge *et al.*[47] expected to be the most accurate. These calculations show differences in equilibrium internuclear distance R_e from experiment of only ~0.005 Å, compared, for example, with first-order configuration-interaction calculations[48] which differ by ~0.04 Å. As far as we are aware, there has been only one *ab initio* study, by Klotz and Peyerimhoff,[49] on the origin of the electronic transition moments for the Herzberg transitions, a challenging theoretical problem. Their study, restricted to a consideration of transition-strength gain from dipole-allowed transitions through spin-orbit interactions, predicted that the $A\leftarrow X$ transition is of mixed parallel-perpendicular nature (principally parallel), while the $c\leftarrow X$ and $A'\leftarrow X$ transitions are entirely perpendicular. Further studies of rotational line strengths in the Herzberg I (Refs. 35, 50) and III (Refs. 31, 35) bands have shown that orbit-rotation couplings produce detectable J-dependent contributions to the corresponding effective electronic transition moments. Herzberg continuum cross sections[51] and transition probabilities[52] calculated using the electronic transition moments of Klotz and Peyerimhoff,[49] are in only fair agreement with the best experimental results.[50]

In summary, it is clear that, despite a considerable body of work on the Herzberg transitions, many uncertainties remain. In particular, it has not been possible, using traditional spectroscopic techniques, to make direct measurements of

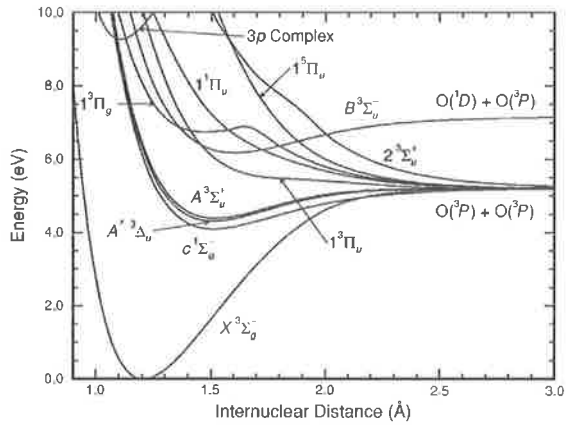

FIG. 4. Potential-energy curves of O_2 relevant to a discussion of the Herzberg transitions.

the branching ratios into the Herzberg I, II and III transitions which constitute the Herzberg continuum.

B. Potential-energy curves

Our adopted potential-energy curves for the A, A', and c states are shown in Fig. 4.[53] In principle, calculations of cross sections for the Herzberg continua, which peak near 6 eV, require significant extrapolations of the inner limbs of the potential-energy curves, away from the more accurately known bound-state potentials which have a common dissociation limit at ~5.2 eV. However, it is possible both to extrapolate reliably using information from *ab initio* calculations, and, in some cases, to reduce the reliance on extrapolation by incorporating knowledge gained from experimental information on the Rydberg-valence interactions involving the Herzberg states.

Our adopted potential-energy curve for the A state was obtained using the following three-stage procedure. First, a Rydberg-Klein-Rees (RKR) (Ref. 54) potential-energy curve was constructed using the spectroscopic constants of Borrell *et al.*,[28] for $v=0-3$, and Yoshino *et al.*,[32] for $v=4-11$.[55] Second, the RKR potential curve was extended smoothly beyond the experimentally known region. The outer-limb extension was of the form[56]

$$V(R)=V_\infty-C_n/R^n, \tag{1}$$

where the exponent n and the coefficient C_n were determined using the last two RKR turning points and the known dissociation limit $V_\infty=5.2141$ eV$(=D_e)$.[57] Due to irregularities in the upper part of the inner limb of the RKR potential, it was necessary to begin the inner-limb extension at ~5.05 eV ($v\approx9$). An initial extension was achieved by using the MRCI+Q potential of Partridge *et al.*,[47] shifted and scaled to agree as closely as possible with the RKR potential below $v=9$. The quality of this MRCI+Q potential can be judged by noting that it was necessary only to increase the well depth by 2.7%, shift to smaller R by 3.2 mÅ, and expand about R_e by 1.2% in order to obtain agreement with the RKR potential. Third, the inner limb of the A-state potential-energy curve in the 9–10 eV region was defined by using the results of a recent study of predissociation in the $3p\pi_u$ $D\,^3\Sigma_u^+$ Rydberg state,[58] represented qualitatively by the $3p$-complex potential-energy curve in Fig. 4. Briefly, the D state is predissociated *indirectly* by the $B\,^3\Sigma_u^-$ state, the upper state of the SR system, and *directly* by the A state. Banerjee[58] has performed a coupled-channel Schrödinger-equation analysis of the observed predissociation pattern which allows the repulsive limb of the A state, in the crossing region with the D state, to be defined quite accurately and the Rydberg-valence coupling between the A and D states of $^3\Sigma_u^+$ symmetry to be estimated. His results imply that the A-state potential-energy curve crosses that of the D state at $R=1.091$ Å, with a slope of -36 eV/Å, and that the Rydberg-valence coupling is 0.052 eV ($\simeq400$ cm^{-1}), much weaker than in the well-known case of the isoconfigurational $^3\Sigma_u^-$ states.[59] Finally, the MRCI+Q A-state inner limb, adjusted as described above, was extrapolated smoothly above ~7 eV in order to be consistent with these new results. It was found that a short spline extrapolation above 8.9 eV of the modified *ab initio* inner limb was almost identical in the 9–10 eV region with the potential determined independently from the D-state predissociation studies,[58] leading to confidence in our inner-limb extension procedures.

Our adopted potential-energy curves for the A' and c states were determined by a similar procedure. However, for these states there is insufficient experimental information available on the predissociation of Rydberg states of like symmetry to enable their inner limbs to be defined more accurately in the 9–10 eV region than is possible using the *ab initio* modification techniques described above.[60] In the case of the A' state, an RKR potential-energy curve was constructed using the spectroscopic constants of Coquart and Ramsay[30] for $v=2-11$.[55] The inner-limb extension above ~5.05 eV ($v\approx10$) was obtained by modifying the MRCI+Q A'-state potential of Partridge *et al.*[47] to optimize agreement with the RKR potential. This required an increase in well depth of 2.5%, a shift to smaller R by 4.1 mÅ, and an expansion about R_e by 0.8%. In the case of the c state, an RKR potential-energy curve was constructed using the spectroscopic constants of Ramsay[29] for $v=1-16$.[55] The inner-limb extension above ~5.05 eV ($v\approx15$) was obtained by modifying the MRCI+Q c-state potential of Partridge *et al.*[47] to optimize agreement with the RKR potential. This required an increase in well depth of 1.0%, a shift to smaller R by 7.8 mÅ, and a contraction about R_e by 1.2%.

C. Transition moments

The electric-dipole-forbidden Herzberg transitions borrow intensity from electric-dipole-allowed transitions of the oxygen molecule through, in principle, spin-orbit and orbit-rotation interactions with both the upper and lower states of each transition. In the general case, the effective electronic transition moment is of mixed parallel-perpendicular character, with a number of independent moments necessary to reproduce the observed rotational line strengths for the discrete transitions.

1. The $A\ ^3\Sigma_u^+ \leftarrow X\ ^3\Sigma_g^-$ transition

In a general treatment of $^3\Sigma^\pm \leftarrow ^3\Sigma^\mp$ transitions,[61] thirteen independent moments have been found to govern the rotational line strengths. In the particular case of the Herzberg I transition, $A\ ^3\Sigma_u^+ \leftarrow X\ ^3\Sigma_g^-$, however, England *et al.*[50] found that only three independent moments were necessary to explain the measured line strengths.[36] In their first-order picture, the dominant sources of $A \leftarrow X$ transition strength are the allowed transitions $B\ ^3\Sigma_u^- \leftarrow X\ ^3\Sigma_g^-$ (parallel) and $A\ ^3\Sigma_u^+ \leftarrow 1\ ^3\Pi_g$ (perpendicular), through the interactions $B\ ^3\Sigma_u^- - A\ ^3\Sigma_u^+$ [spin-orbit (SO)] and $1\ ^3\Pi_g - X\ ^3\Sigma_g^-$ [spin-orbit and orbit-rotation (OR)], respectively. This conclusion is essentially in agreement with the *ab initio* study of Klotz and Peyerimhoff,[49] which, however, considered only spin-orbit interactions, and also with the study of Huestis *et al.*[35] The independent moments Z, Y and M arise through the following interactions:[62]

$$X\ ^3\Sigma_{g,\pm 1}^- \overset{\parallel}{\rightarrow} B\ ^3\Sigma_{u,\pm 1}^- \overset{SO}{\leftrightarrow} A\ ^3\Sigma_{u,\pm 1}^+ : Z_1 = Z, \tag{2}$$

$$X\ ^3\Sigma_{g,0^+}^- \overset{SO}{\leftrightarrow} 1\ ^3\Pi_{g,0^+} \overset{\perp}{\rightarrow} A\ ^3\Sigma_{u,\pm 1}^+ : Y_1 = Y, \tag{3}$$

$$X\ ^3\Sigma_{g,\pm 1}^- \overset{SO}{\leftrightarrow} 1\ ^3\Pi_{g,\pm 1} \overset{\perp}{\rightarrow} A\ ^3\Sigma_{u,0^-}^+ : Y_0 = Y, \tag{4}$$

$$X\ ^3\Sigma_{g,0^+}^- \overset{OR}{\leftrightarrow} 1\ ^3\Pi_{g,\pm 1} \overset{\perp}{\rightarrow} A\ ^3\Sigma_{u,0^-}^+ : M_0 = M, \tag{5}$$

$$X\ ^3\Sigma_{g,\pm 1}^- \overset{OR}{\leftrightarrow} 1\ ^3\Pi_{g,\pm 2} \overset{\perp}{\rightarrow} A\ ^3\Sigma_{u,\pm 1}^+ : M_1 = M, \tag{6}$$

$$X\ ^3\Sigma_{g,\pm 1}^- \overset{OR}{\leftrightarrow} 1\ ^3\Pi_{g,0} \overset{\perp}{\rightarrow} A\ ^3\Sigma_{u,\pm 1}^+ : M_1 = M. \tag{7}$$

The sum rule for the $A \leftarrow X$ rotational line strengths, arising from all fine-structure levels of the lower state with a given J, implies that the square of the effective electronic transition moment is given by[63]

$$M_{\rm eff}^2 = [Z^2 + 4Y^2 - 4M^2 + 6M^2 J(J+1)]/g'', \tag{8}$$

where $g''=3$ is the lower-state degeneracy, and the perpendicular:parallel ratio by

$$M_\perp^2 / M_\parallel^2 = [4Y^2 - 4M^2 + 6M^2 J(J+1)]/Z^2. \tag{9}$$

The transition moments in Eqs. (2)–(9) depend parametrically on R, and some depend on J through the orbit-rotation coupling. For simplicity, these dependences have been suppressed in the transition-moment notation.

The effective electronic transition moment may be related to a (J-dependent) band oscillator strength by the relation

$$f_{v'v''} = 3.038\times 10^{-6} \nu |\langle \chi_{v'}(R)|M_{\rm eff}(R)|\chi_{v''}(R)\rangle|^2, \tag{10}$$

where $\chi_{v''}(R)$ and $\chi_{v'}(R)$ are the normalized discrete radial wavefunctions of the initial and final states, respectively, ν is the transition energy, in $\rm cm^{-1}$, and $M_{\rm eff}(R)$ is in a.u. In the R-centroid approximation,[64] Eq. (10) becomes

$$f_{v'v''} = 3.038\times 10^{-6} \nu q_{v'v''} M_{\rm eff}^2(R_{v'v''}), \tag{11}$$

where

$$q_{v'v''} = |\langle \chi_{v'}(R)|\chi_{v''}(R)\rangle|^2 \tag{12}$$

is the Franck-Condon factor, and

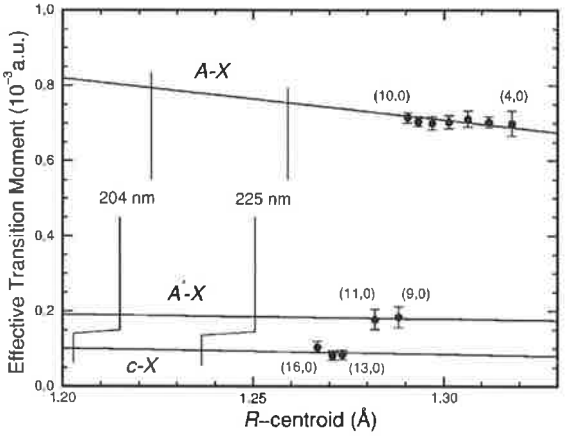

FIG. 5. Effective room-temperature electronic transition moments for the Herzberg transitions of O_2. Solid circles: values determined from measurements of the discrete oscillator strengths; $A \leftarrow X$ (4,0)–(10,0) (Ref. 50); $A' \leftarrow X$ (9,0), (11,0) and $c \leftarrow X$ (13,0), (14,0) and (16,0) (Ref. 35). Solid lines: adopted effective transition moments.

$$R_{v'v''} = \langle \chi_{v'}(R)|R|\chi_{v''}(R)\rangle / \langle \chi_{v'}(R)|\chi_{v''}(R)\rangle \tag{13}$$

is the R-centroid. Equation (11) can be used to determine an effective electronic transition moment, including an effective R dependence through association of R with the R-centroid, using experimental band oscillator strengths. As has been noted recently by Huestis,[65] there are complexities associated with degeneracy factors involved in the definition of transition moments for forbidden transitions. The effective electronic transition moments $M_{\rm eff}$, defined by Eq. (11) and used self-consistently throughout this work, implicitly contain degeneracy factors which may make their definition inconsistent with some other studies.

We have used the values of Z ($\sim 1.0\times 10^{-3}$ a.u.), Y ($\sim 0.4\times 10^{-3}$ a.u.) and M ($\sim 0.01\times 10^{-3}$ a.u.) determined by England *et al.*[50] from the measured absorption line oscillator strengths of Yoshino *et al.*[36] for the (4,0)–(10,0) $A \leftarrow X$ bands, with small adjustments to allow for the slightly different Franck-Condon factors arising from our A-state potential-energy curve, in Eq. (8) to determine values for the $A \leftarrow X$ effective electronic transition moment $M_{\rm eff}$. The dependence of $M_{\rm eff}$ on the rotational quantum number leads to a temperature dependence of the corresponding absorption oscillator strength. We have evaluated $M_{\rm eff}$ for $J=11$, appropriate for calculation of room-temperature cross sections, and for $J=0$, appropriate for interpretation of the measurements of this work taken at rotational temperatures in the range 5–10 K. Our results for $J=1$ are shown in Fig. 5 (solid circles), plotted as a function of the $A \leftarrow X$ R-centroid.[66] When going from room temperature to the 5–10 K region, $M_{\rm eff}^2$, and thus the absorption cross section, decreases by approximately 5% due to the J-dependent orbit-rotation coupling.

Calculations of the $A \leftarrow X$ photoabsorption continuum require a significant extrapolation of the effective transition moment towards smaller internuclear distances. Unfortunately, the precision with which such an extrapolation can be

performed, in the absence of other information, is limited. Therefore, as described further in Sec. IV D, we have chosen to use experimental information on the Herzberg continuum to further refine the transition-moment extrapolation. Our adopted effective $A \leftarrow X$ electronic transition moments are given by

$$M_{\mathrm{eff}}(R) = (2.154 - 1.112\ R) \times 10^{-3}\ \text{a.u.}, \tag{14}$$

for $T = 300$ K, and

$$M_{\mathrm{eff}}(R) = (2.104 - 1.087\ R) \times 10^{-3}\ \text{a.u.}, \tag{15}$$

for $T = 5 - 10\ K$, where R is in Å. Our room-temperature transition moment, shown in Fig. 5 (solid line), is seen to pass through the error bars of the points determined from the discrete spectrum and increases as R decreases, as predicted by the *ab initio* calculations.[49] The rate of increase, however, is significantly greater than that calculated by Klotz and Peyerimhoff[49] and also exceeds that implied from a linear least-squares fit to the discrete points.

2. The $A'\ ^3\Delta_u \leftarrow X\ ^3\Sigma_g^-$ transition

In a general treatment of $^3\Delta \leftarrow {}^3\Sigma$ transitions, Kerr and Watson[31] showed that the rotational line strengths are governed by six independent transition moments: one parallel (Z_1) and two perpendicular (Y_1 and Y_2) moments arising from spin-orbit perturbation, and three further perpendicular moments (M_1, M_2 and M_3) arising from low-order orbit-rotation couplings. In the specific case of the $A'\ ^3\Delta_u \leftarrow X\ ^3\Sigma_g^-$ transition of O_2, it was found necessary to retain all six moments in order to explain satisfactorily the observed rotational line strengths,[67] implying some departure from the first-order relations $Z_1 = 0$, $Y_1 = Y_2 = Y$, $M_1 = M_2 = M_3 = M$. Thus, the intensity-borrowing mechanism for the $A' \leftarrow X$ transition may involve perturbations by electronic states of many different symmetries and multiplicities. First-order transition moments for the $A' \leftarrow X$ system arise through interactions involving only $^3\Pi$ intermediaries and, in this approximation, values for Y have been calculated *ab initio* by Klotz and Peyerimhoff.[49]

It follows from the sum rule for the $A' \leftarrow X$ rotational line strengths[31] that the square of the effective electronic transition moment is given by

$$M_{\mathrm{eff}}^2 \propto Z_1^2 + Y_1^2 + Y_2^2 + 2J(J+1)[M_1^2 + M_2^2] + 2(J-1)(J+2)M_3^2. \tag{16}$$

Relative values for the individual transition moments deduced from limited experimental measurements on the (4,0), (7,0) and (9,0) $A' \leftarrow X$ bands[31,35] imply that the first term in Eq. (16) is negligible and that the $A' \leftarrow X$ transition is ~99% perpendicular. Hereafter, we will ignore the small parallel component of this transition.

We determined effective electronic transition moments for the (9,0) and (11,0) $A' \leftarrow X$ bands, shown in Fig. 5 plotted as a function of R-centroid, using the CRDS oscillator strengths of Huestis *et al.*[35] in Eq. (11), together with appropriate Franck-Condon factors calculated using our A'-state potential-energy curve, and transition energies given by Coquart and Ramsay.[30] Neither the precision nor the quantity of experimental data enables any conclusion to be made regarding the R-dependence of the transition moment. Therefore, we assume the relative slope implied by the *ab initio* calculations of Klotz and Peyerimhoff[49] and adopt a linear representation of the $A' \leftarrow X$ effective electronic transition moment, appropriate for room-temperature calculations,

$$M_{\mathrm{eff}}(R) = (3.461 - 1.285\ R) \times 10^{-4}\ \text{a.u.}, \tag{17}$$

shown in Fig. 5. Our adopted moment for low-temperature calculations was obtained by using the individual (7,0)-band transition moments determined by Kerr and Watson[31] in Eq. (16), in order to obtain the ratio between effective moments for $J = 0$ and $J = 11$, and then applying that ratio to the room-temperature moment of Eq. (17). Our adopted effective electronic transition moment for $T = 5 - 10$ K is given by

$$M_{\mathrm{eff}}(R) = (2.793 - 1.037\ R) \times 10^{-4}\ \text{a.u.} \tag{18}$$

3. The $c\ ^1\Sigma_u^- \leftarrow X\ ^3\Sigma_g^-$ transition

Watson[68] has given general treatments of $^1\Sigma^{\pm} \leftarrow {}^3\Sigma^{\pm}$ and $^1\Sigma^{\pm} \leftarrow {}^3\Sigma^{\mp}$ transitions, showing that only a single perpendicular transition moment is necessary for a description of rotational line strengths in $^1\Sigma^- \leftarrow {}^3\Sigma^-$ transitions. Thus, the Herzberg II system, $c\ ^1\Sigma_u^- \leftarrow X\ ^3\Sigma_g^-$, is free of the complexities involved in the triplet-triplet Herzberg I and III systems. To the first order, only spin-orbit interactions contribute to the $c \leftarrow X$ transition moment which is derived from mechanisms of the type:[49]

$$X\ ^3\Sigma_{g,\pm 1}^- \xrightarrow{\perp} {}^3\Pi_{u,0^-} \xleftrightarrow{\mathrm{SO}} c\ ^1\Sigma_{u,0^-}^-, \tag{19}$$

and

$$X\ ^3\Sigma_{g,\pm 1}^- \xleftrightarrow{\mathrm{SO}} {}^1\Pi_{g,\pm 1} \xrightarrow{\perp} c\ ^1\Sigma_{u,0^-}^-. \tag{20}$$

We have determined effective electronic transition moments for the (13,0), (14,0) and (16,0) $c \leftarrow X$ bands, shown in Fig. 5 plotted as a function of R-centroid, using the CRDS oscillator strengths of Huestis *et al.*[35] in Eq. (11), together with appropriate Franck-Condon factors calculated using our c-state potential-energy curve, and transition energies given by Ramsay.[29] Our adopted effective electronic transition moment for the $c \leftarrow X$ system, shown in Fig. 5, is consistent with these discrete points, but has a relative slope defined by the *ab initio* calculations of Klotz and Peyerimhoff:[49]

$$M_{\mathrm{eff}}(R) = (2.958 - 1.620\ R) \times 10^{-4}\ \text{a.u.} \tag{21}$$

Under the approximation whereby any second-order contributions arising from J-dependent orbit-rotation interactions have been neglected, Eq. (21) is assumed to apply at any temperature.

D. Cross sections

The cross section for photoabsorption from an initial discrete state into a continuum state is given by

$$\sigma(\nu, J) = 1.225 \times 10^{-23} \nu |\langle \chi'_{\nu J}(R) | M_{\mathrm{eff}}(R) | \chi''_{vJ}(R) \rangle|^2\ \text{cm}^2, \tag{22}$$

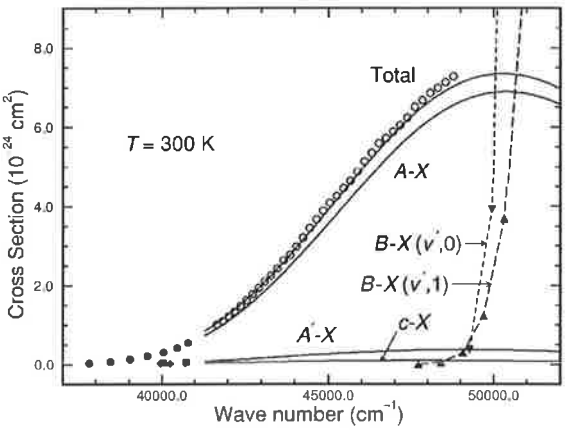

FIG. 6. Room-temperature photoabsorption cross sections in the Herzberg-continuum region. Solid lines: calculated cross sections for the Herzberg I, II, III and total Herzberg continua. Open circles: recommended experimental Herzberg continuum cross section (Ref. 44). Closed symbols: effective cross sections determined for discrete spectra from experimental oscillator-strength densities; $A\leftarrow X$ (4,0)–(10,0) (circles), oscillator strengths from Ref. 50; $A'\leftarrow X$ (9,0), (11,0) (squares) and $c\leftarrow X$ (13,0), (14,0) and (16,0) (diamonds), oscillator strengths from Ref. 35; $B\leftarrow X$ (v',0) (inverted triangles, dashed line) and (v',1) (triangles, long-dashed line), oscillator strengths from Refs. 73 and 74.

where ν is the transition energy in cm^{-1}, $\chi''_{vJ}(R)$ is the normalized discrete radial wavefunction of the initial state, $\chi'_{\nu J}(R)$ is the energy-normalized radial wavefunction of the final continuum state, and $M_{\rm eff}(R)$ is the effective electronic transition moment, with the transition matrix element evaluated in a.u. Temperature-dependent cross sections may be constructed by calculating cross sections for absorption from all relevant vibrational and rotational levels of the initial state using Eq. (22), weighting with appropriate normalized Boltzmann factors, and adding. Since it is not possible to resolve the structure of the final continuum state, it is unnecessary to consider the true branch structure of the transition and the single Q-branch model implied by Eq. (22) provides an accurate description of the cross section.

Room-temperature photoabsorption cross sections for the Herzberg I, II, III and total continua calculated using this method are shown in Fig. 6 (solid lines). The wavefunctions $\chi''_{vJ}(R)$ were determined by numerical integration of the radial Schrödinger equation for an RKR X-state potential, while the A-, A' and c-state potentials described in Sec. IV B were employed to determine the upper-state wave functions $\chi'_{\nu J}(R)$. As has been described in Sec. IV C, where necessary, effective electronic transition moments $M_{\rm eff}(R)$ evaluated for $J=11$ were used in calculations of the room-temperature cross sections.

The calculated Herzberg I ($A\leftarrow X$) cross section reaches a maximum of 6.89×10^{-24} cm^2 at 50 380 cm^{-1} (198 nm), while the Herzberg III ($A'\leftarrow X$) cross section reaches 0.38×10^{-24} cm^2 at 49 080 cm^{-1} (204 nm) and the Herzberg II ($c\leftarrow X$) cross section 0.10×10^{-24} cm^2 at 47 680 cm^{-1} (210 nm). The calculated total Herzberg continuum cross section reaches a maximum of 7.35×10^{-24} cm^2 at 50 280 cm^{-1} (199 nm) and is in good agreement with the recommended room-temperature Herzberg continuum cross section of Yoshino *et al.*[44] (open circles), reflecting our chosen method of optimizing the $A\leftarrow X$ transition-moment slope. The calculated total Herzberg continuum cross section is dominated by the Herzberg I contribution which rises from 86% at 41 300 cm^{-1} (242 nm) to 94% at the cross-section maximum. These Herzberg I cross-section branching ratios exceed those implied by the calculations of Saxon and Slanger,[51] which were based principally on the *ab initio* transition moments of Klotz and Peyerimhoff,[49] but, of course, are consistent with the discrete-spectrum branching ratio measured by Huestis *et al.*,[35] on which our adopted transition moments were partially based.

Also shown in Fig. 6 (solid circles, squares and diamonds) are effective cross sections related to the experimental oscillator-strength densities for the discrete Herzberg transitions, determined using the approximate expression

$$\sigma(\nu_{v'0})=1.77\times10^{-12}f_{v'0}/(\nu_{v'+1,0}-\nu_{v'-1,0}), \qquad (23)$$

where room-temperature band oscillator strengths $f_{v'0}$ were taken from England *et al.*[50] ($A\leftarrow X$) and Huestis *et al.*[35] ($A'\leftarrow X$ and $c\leftarrow X$), and the effective band wavenumbers $\nu_{v'0}$ were taken as the $^QQ_2(11)$ wavenumbers of Yoshino *et al.*[32] ($A\leftarrow X$), the $^QQ_2(11)$ wavenumbers of Coquart and Ramsay[30] ($A'\leftarrow X$), and the average of the $R(11)$ and $P(11)$ wavenumbers of Ramsay[29] ($c\leftarrow X$). The calculated individual Herzberg continuum cross sections are seen to be consistent with the corresponding discrete oscillator-strength densities, reflecting our choice of effective transition moments in Sec. IV C, and as required by the principle of continuity of oscillator-strength density across a dissociation limit.[69] It is worth noting that the experimental (total) Herzberg continuum cross section of Yoshino *et al.*[44] in the dissociation-limit region exceeds a rough extrapolation of the Herzberg I $\sigma(\nu_{v'0})$, within experimental uncertainty, by an amount consistent with the measured Herzberg I cross-section branching ratio of 86%, demonstrating the the mutual compatibility of our chosen experimental data sets for the discrete and continuous spectra. On the other hand, the Herzberg-continuum cross section measured recently by Amoruso *et al.*[46] is ~13% *lower* than the extrapolated Herzberg I $\sigma(\nu_{v'0})$, demonstrating the incompatibility between these data[46] and the best available measurements of the discrete spectrum.[36] This incompatibility has also been commented upon by Yoshino *et al.*[70]

Because of the relatively small contributions of the Herzberg II and III transitions to the total Herzberg continuum, it is the R-dependence of the effective Herzberg I transition moment that has the most important influence on the intensity and shape of the continuum. If, for example, the effective $A\leftarrow X$ transition moment is chosen to have a slope smaller than that of our adopted moment, consistent with a linear least-squares fit to the discrete points in Fig. 5, then the calculated Herzberg I cross section is found to have a maximum of only 5.69×10^{-24} cm^2, some 17% smaller than our calculated maximum $A\leftarrow X$ cross section, at 50 000 cm^{-1} (200 nm), some 2 nm longward of our calculated peak. This difference in cross section is larger than the experimental uncertainty in the Herzberg-continuum cross

section. Therefore, we have determined the final model $A \leftarrow X$ transition-moment slope by requiring that the calculated cross section reproduce approximately the measured cross section in Fig. 6, as foreshadowed in Sec. IV C. Small remaining differences in shape between the calculated and measured Herzberg cross sections suggest that the true $A \leftarrow X$ transition moment may be increasing as R decreases *faster* than linearly. The relative slope of our adopted $A \leftarrow X$ transition moment exceeds that calculated *ab initio* by Klotz and Peyerimhoff[49] for the principal parallel component by a factor of ~ 3. The explanation for this discrepancy remains unclear.[71]

The room-temperature Herzberg continuum is overlapped by the discrete SR ($B \leftarrow X$) transitions for $\nu > 47\,720$ cm^{-1}, inhibiting direct observation of the maximum in the continuum cross section. Therefore, we have considered only the long-wavelength continuum measurements[44] in constructing our absorption model.[72] Effective cross sections related to the room-temperature oscillator-strength densities due to the $(v',0)$ and $(v',1)$ SR bands, shown in Fig. 6 (solid triangles), emphasize the rapid onset of the stronger SR absorption. These cross sections were determined using Eq. (23) with the measured SR oscillator strengths of Lewis *et al.*[73] and Cheung *et al.*,[74] and the band wavenumbers of Yoshino *et al.*[75] and Cheung *et al.*,[74] with extrapolation where necessary. Coquart *et al.*[76] have measured O_2 photoabsorption cross sections for $T = 219$ K in the range 196.4–205 nm, correcting for the effects of SR-band predissociation line wings in obtaining estimates for the Herzberg continuum intensity. Their results imply a cross-section maximum of $8.1-8.2 \times 10^{-24}$ cm^2 in the range 198–199 nm. While this cross section is significantly larger than our calculated value, the position of the maximum is in good agreement. Other Herzberg photoabsorption models[44,76,77] predict cross-section maxima to occur in the range 196–205 nm.

E. Transition character

Having constructed a Herzberg photoabsorption model consistent with the best available experimental information, we are now in a position to consider the predictions of that model regarding the nature of the Herzberg continuum. As we have shown in Sec. IV C, the only significant source of parallel character is the Herzberg I transition. Under this circumstance, the relative perpendicular character of the total Herzberg photoabsorption is given by

$$r_{\mathrm{tot}}^{\perp} = r_{AX}^{\perp} r_{AX} + (1 - r_{AX}), \tag{24}$$

where $r_{AX}^{\perp} = M_{\perp}^2/(M_{\perp}^2 + M_{\parallel}^2)$ is the perpendicular branching ratio of the Herzberg I transition and $r_{AX} = \sigma_{AX}/\sigma_{\mathrm{tot}}$ is the Herzberg I cross-section branching ratio.

In Fig. 7, we show, plotted as a function of the $A \leftarrow X$ R-centroid, values of $r_{AX}^{\perp}$ (open circles) obtained using Eq. (9) with $J = 0$ and the $A \leftarrow X$ transition moments of England *et al.*,[50] obtained from the (4,0)–(10,0) band oscillator-strength measurements of Yoshino *et al.*[36] It can be seen in Fig. 7 that there is a tendency for $r_{AX}^{\perp}$ to increase as R decreases. Our adopted value for this branching ratio in the

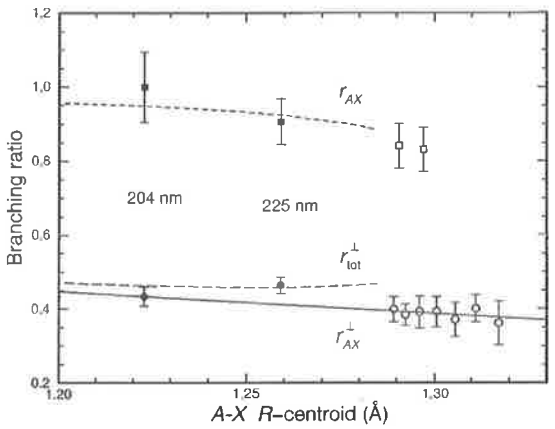

FIG. 7. Low-temperature branching ratios for the Herzberg systems. Open circles: discrete perpendicular branching ratios $r_{AX}^{\perp}$ for the $A \leftarrow X$ (4,0)–(10,0) bands, determined from the transition moments of Ref. 50. Solid line: adopted perpendicular branching ratio for the $A \leftarrow X$ system. Open squares: discrete $A \leftarrow X$ cross-section branching ratios r_{AX} determined from experimental (room-temperature) Herzberg I, II and III oscillator strengths (Refs. 35 and 50). Dashed line: calculated $A \leftarrow X$ cross-section branching ratio for the continuum. Long-dashed line: calculated perpendicular branching ratios $r_{\mathrm{tot}}^{\perp}$ for the total Herzberg continuum. Solid circles: experimental perpendicular branching ratios for the total Herzberg continuum, determined from the current photodissociation angular-distribution measurements. Solid squares: $A \leftarrow X$ cross-section branching ratios for the continuum, inferred from the current experimental perpendicular branching ratios and our adopted perpendicular branching ratio for the $A \leftarrow X$ system.

continuum has been obtained by extrapolation towards shorter R. A weighted least-squares fit to the discrete points yields the result:

$$r_{AX}^{\perp}(R) = 1.159 - 0.593\ R, \tag{25}$$

shown as a solid line in Fig. 7.

Also shown in Fig. 7 are values of the Herzberg I cross-section branching ratio r_{AX}, plotted as a function of the $A \leftarrow X$ R-centroid. The discrete points (open squares) were determined using the experimental oscillator-strength densities, described in Sec. IV D, for two regions where there were near coincidences of Herzberg I, II and III transitions. The results, 0.84 ± 0.06 near 40 740 cm^{-1}, and 0.83 ± 0.06 near 40 070 cm^{-1}, are consistent with the estimate due to Huestis *et al.*[35] of 0.86. Our model value for the Herzberg I cross-section branching ratio (dashed line) was determined following calculation of the Herzberg I, II and III continuum cross sections, using Eq. (22) with $J = 0$ and rotationless forms of the effective transition moments described in Sec. IV C. The model r_{AX}, as required, is consistent with values in the discrete spectrum[78] and rises slowly as R decreases. Finally, values of $r_{\mathrm{tot}}^{\perp}$ for the Herzberg continuum have been determined using our adopted values of $r_{AX}^{\perp}$ and r_{AX} in Eq. (24), and are shown as a long-dashed line in Fig. 7.

V. ANGULAR DISTRIBUTIONS

A. Fine-structure-averaged angular distributions

The photofragment angular distributions measured in this work at $T = 5-10$ K enable the mixture of perpendicular

and parallel character of the total Herzberg continuum to be established independently. It is, therefore, of great interest to compare values of $r_{\rm tot}^{\perp}$ obtained from these angular distributions with the low-temperature model predictions.

Using the fine-structure-specific angular-distribution parameters measured at 226 nm (Table I), and weighting according to the corresponding dissociation branching ratios, a fine-structure-averaged $\beta=0.612\pm0.065$ is obtained, implying that the dissociation has 54% parallel character ($\beta=2$) and 46% perpendicular character ($\beta=-1$), i.e. $r_{\rm tot}^{\perp}=0.463\pm0.022$. The corresponding model value is 0.457, in excellent agreement. Since we were unable to determine the dissociation branching ratios at 204 nm, we have estimated the fine-structure-averaged β at this wavelength by assuming that the fine-structure branching is statistical, justifying this assumption by noting that the recoil kinetic energy is 34× the spin-orbit splitting. This is not necessarily a good criterion for the suddenness of the dissociation. Huang *et al.*[11] mention a case where the recoil energy is 28 times the spin-orbit splitting, while the dissociation takes place nearly fully adiabatically. What matters is the characteristic recoil time, which must be short compared with the electronic precession time. In general, this is the case when the recoil energy is large compared with the spin-orbit splitting. From the estimated fine-structure-averaged $\beta=0.699\pm0.077$, it follows that $r_{\rm tot}^{\perp}=0.434\pm0.026$ at 204 nm, in reasonable agreement with our model value of 0.463. At 236 nm, we were only able to measure the $O(^3P_1)$ angular distribution, from which no conclusion can be drawn. Our experimental $r_{\rm tot}^{\perp}$ (solid circles) are shown in Fig. 7, compared with the model values, plotted at their respective $A\leftarrow X$ R-centroid values of 1.259 Å (226 nm) and 1.223 Å (204 nm). Tonokura *et al.*[16] have measured the anisotropy parameter for photodissociation of O_2 at 226 nm, together with corresponding fine-structure dissociation branching ratios. Their branching ratios ($^3P_0$:$^3P_1$:$^3P_2$=1.0:3.8:9.6) are in good agreement with ours, but their anisotropy parameter, $\beta=1.6\pm0.4$, differs considerably. Such a high value would imply that the Herzberg continuum has only ~13% perpendicular character, well below the known perpendicular branching ratio for the Herzberg I transition alone (Fig. 7). At present, we see no reason to doubt the transition character determined from detailed high-resolution optical rotational line-strength measurements in the discrete $A\leftarrow X$ spectrum. Furthermore, we note that the anisotropy parameter obtained by Tonokura *et al.*[16] was a result of a fitting process to Doppler profiles of photofragments. However, these profiles did not take into account any two-photon contributions, which should yield a broadband background. Our measurements clearly show this strong contribution, and for a reliable determination of the anisotropy parameter this contribution should not be neglected.

It is clear from Fig. 7 that the experimental $r_{\rm tot}^{\perp}$ are in reasonable agreement with our adopted $r_{AX}^{\perp}$, implying that the Herzberg continuum is dominated by the Herzberg I transition. Herzberg I cross-section branching ratios r_{AX} of 0.91 ± 0.07 (226 nm) and 1.00 ± 0.10 (204 nm), inferred using Eq. (24) with the experimental $r_{\rm tot}^{\perp}$ and the model $r_{AX}^{\perp}$, are shown in Fig. 7 (solid squares). Within the estimated uncertainty, which takes into account both the experimental uncertainty and the uncertainty involved in the model $r_{AX}^{\perp}$ extrapolation, the "experimental" r_{AX} are seen to be in good agreement with the model predictions.

B. Fine-structure-resolved angular distributions

Thus far, we have looked at fine-structure-averaged β parameters at 226 nm and 204 nm to obtain information on the nature of the optical transition, ignoring the fact that each of the $O(^3P_0$, $^3P_1$, and $^3P_2)$ photofragments has a different angular distribution, a surprising observation in itself. In this section, we focus on the individual angular distributions of the three fine-structure states. It is difficult to perform accurate calculations on these fine-structure-specific angular distributions without an intimate knowledge of the angular-momentum couplings of the electronic states participating in the transition, and the small- and large-R interactions with other states. Therefore, we restrict our considerations to the approximate cases defined by a case (a) description of the molecular states and adiabatic and sudden-recoil limits for the molecular dissociation dynamics. The approximations used make us very cautious in the drawing of conclusions. However, some qualitative features, such as the fine-structure dependence of the β-parameter in the case of a statistical dissociation, are of interest.

1. Adiabatic limit

From the adiabatic correlation diagram for $O(^3P)+O(^3P)$,[11] it can be seen that all three Herzberg states correlate with $O(^3P_2)+O(^3P_2)$. However, in our experiment we observe the formation of $^3P_1$ and $^3P_0$ fragments at 226 and 204 nm, and $^3P_1$ fragments at 236 nm. The presence of these fragments is inconsistent with adiabatic dissociation behavior.

It is easy to predict the angular distribution of the $^3P_2$ fragments measured at 226 and 204 nm in the case of adiabatic dissociation. Because only one type of fragment is formed in the adiabatic limit, the angular distribution reflects directly the mixed parallel-perpendicular character of the total Herzberg photoabsorption. Using the model of Sec. IV E to describe the relative perpendicular character of the Herzberg system, we find for the adiabatic anisotropy parameter:

$$\beta_{j=2}=r_{\rm tot}^{\perp}\beta^{\perp}+(1-r_{\rm tot}^{\perp})\beta^{\parallel}=2-3r_{\rm tot}^{\perp}, \tag{26}$$

where $\beta^{\perp}=-1$ and $\beta^{\parallel}=2$. From Sec. V A, the model $r_{\rm tot}^{\perp}=0.457$ at 226 nm and 0.463 at 204 nm. Thus, Eq. (26) gives $\beta_{j=2}=0.629$ and 0.611, respectively, at these two wavelengths. From Table I, the measured $\beta_{j=2}$ at 226 nm is 0.64 ± 0.08, in good agreement with the calculated adiabatic value. This agreement for $O(^3P_2)$ reflects the fact that this is the dominant fragmentation product, which contains the average information on the character of the dissociation. In this sense, the β-parameter for a dominant dissociation product provides a less sensitive indicator of the dissociation adiabaticity than do the dissociation branching ratios. Our experimental results show that the minority channels may have

TABLE II. Fine-structure branching ratios of $O(^3P_j)$, $j=0,1,2$, calculated in the sudden-recoil approximation, following excitation of O_2 into the $A\ ^3\Sigma_{u,0}(\Omega=0^-,\Omega=\pm1)$ sub-states. The parameters p and q are clarified in the text.

	$j=0$	$j=1$	$j=2$
$\Omega=0^-$	$4q$	$6p+6q$	$6p+14q$
$\Omega=\pm1$	$2p+2q$	$3p+9q$	$7p+13q$

very different anisotropy parameters. The fact that the measured β-parameter for $O(^3P_2)$ at 204 nm (0.87 ± 0.10) differs significantly from the adiabatic value suggests that the distribution over the fine-structure levels at this wavelength may not be as dominated by the $j=2$ fragments.

2. Sudden-recoil limit

The other extreme is the prompt dissociation process, described in the sudden-recoil limit. It is commonplace for a prompt dissociation to result in a statistical, or nearly statistical distribution over fine-structure states. The distribution can deviate from statistical when the optical excitations to the different molecular fine-structure states are of different strengths. Another exception occurs when it is not possible to conserve Ω in the dissociation process.[8] This is, for example, the case for the $A'\ ^3\Delta_u(\Omega=3)$ state that cannot connect to $^3P_0$ in any combination of $O(^3P_0)+O(^3P_j)$. As has been shown by Singer *et al.*,[8] the sudden-recoil case can be treated by writing the molecular wave function as a linear combination of atomic eigenstates, the suddenness of the dissociation "freezing" the angular part of the wavefunction. The squared coefficients in this expansion determine the branching over the different atomic fine-structure states. In Table II, derived from Table IV of Ref. 12, we collect these branching ratios for the A state. The coefficients p and q in Table II refer to so-called eigenvector coefficients $\langle\lambda_a\lambda_b|\Lambda\rangle$, factors that are used in the expansion of the orbital part of the molecular eigenstate $|\Lambda\rangle=|0\rangle$ into the orbital part of the atomic eigenstates $|l_a=1,\lambda_a\rangle$ and $|l_b=1,\lambda_b\rangle$: $p=\langle00|0\rangle$ and $q=\langle\pm1\mp1|0\rangle$. Calculation of these factors is not a straightforward process and we will use them as adjustable parameters, under the one restriction that the sum of each row in Table II is unity. This reflects that for $\Omega=0$, 1, and -1, the dissociation probability is unity ($12p+24q\equiv1$).

From an orientational point of view, two classes of molecules are formed following excitation of O_2 in the Herzberg continuum. On the one hand, molecules excited by perpendicular transitions into the electronic states $c\ ^1\Sigma_u^-$, $A'\ ^3\Delta_u$, and $A\ ^3\Sigma_{u,0^-}^+$ dissociate with an anisotropy parameter $\beta=\beta^\perp$. On the other hand, molecules are excited into the $A\ ^3\Sigma_{u,\pm1}^+$ states through transitions of mixed parallel and perpendicular character: we will label the corresponding anisotropy parameter $\beta_{AX}^{\pm1}$. The dissociation process influences the relative contributions of these two classes of molecules to specific atomic fine-structure states. Thus, in general, the $O(^3P_0,\ ^3P_1,$ and $^3P_2)$ photofragments may have different angular distributions. These fine-structure-specific angular distributions, as well as the fine-structure dissociation branching ratios, can be used, in principle, to obtain information on the correlation between molecular and atomic fine-structure levels, helping to elucidate the (a)diabaticity of the dissociation process.

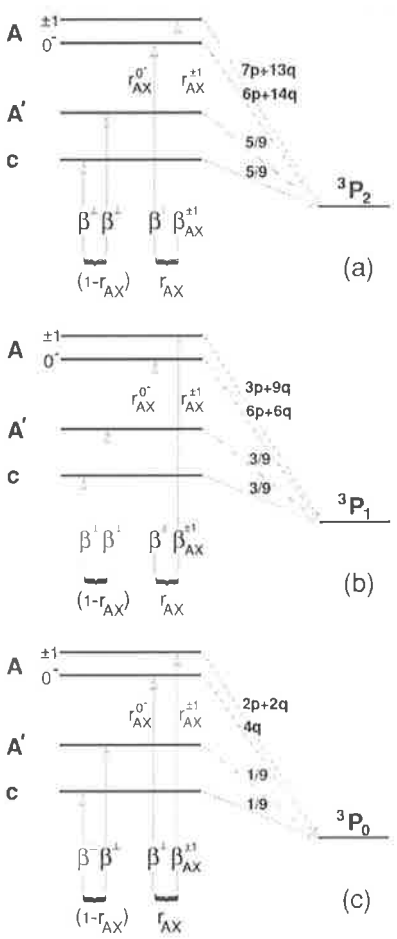

FIG. 8. Schematic diagrams used for the calculation of fine-structure-resolved angular distributions of $O(^3P_j)$ atoms resulting from photodissociation of O_2 in the Herzberg continuum. Indicated are the three Herzberg states A, A', and c. Transitions from the O_2 ground state to the $A(\Omega=0^-)$, A', and c states are perpendicular ($\beta=-1$), while the transition to the $A(\Omega=\pm1)$ state is of mixed parallel-perpendicular character. In panels (a), (b), and (c), the sudden-recoil limit is depicted where $^3P_2$ [panel (a)], $^3P_1$ [panel (b)], and $^3P_0$ [panel (c)] atoms are formed. For clarity, (a), (b), and (c) have not been incorporated into one scheme. The symbols are clarified in the text.

In Figs. 8(a)–8(c), we depict schematically the branching for the sudden-recoil dissociation forming $^3P_2$, $^3P_1$, and $^3P_0$ atomic fragments. The Ω-states of the molecule are shown only for the A state, because for this state different Ω-states are associated with different β parameters. The cross-section branching ratios for the $A(\Omega=0^-)$ and $A(\Omega=\pm1)$ states have been labelled $r_{AX}^{0^-}$ and $r_{AX}^{\pm1}$, respectively. Furthermore, we make the approximation that the A'-

and c-state dissociations result in a statistical fine-structure distribution. Using the notation adopted in Figs. 8(a)–8(c), we find:

$$\beta_{j=0}=\frac{r_{AX}r_{AX}^{0^-}(4q)\beta^{\perp}+r_{AX}r_{AX}^{\pm 1}(2p+2q)\beta_{AX}^{\pm 1}+\frac{1}{9}(1-r_{AX})\beta^{\perp}}{r_{AX}r_{AX}^{0^-}(4q)+r_{AX}r_{AX}^{\pm 1}(2p+2q)+\frac{1}{9}(1-r_{AX})}, \tag{27}$$

$$\beta_{j=1}=\frac{r_{AX}r_{AX}^{0^-}(6p+6q)\beta^{\perp}+r_{AX}r_{AX}^{\pm 1}(3p+9q)\beta_{AX}^{\pm 1}+\frac{3}{9}(1-r_{AX})\beta^{\perp}}{r_{AX}r_{AX}^{0^-}(6p+6q)+r_{AX}r_{AX}^{\pm 1}(3p+9q)+\frac{3}{9}(1-r_{AX})}, \tag{28}$$

and

$$\beta_{j=2}=\frac{r_{AX}r_{AX}^{0^-}(6p+14q)\beta^{\perp}+r_{AX}r_{AX}^{\pm 1}(7p+13q)\beta_{AX}^{\pm 1}+\frac{5}{9}(1-r_{AX})\beta^{\perp}}{r_{AX}r_{AX}^{0^-}(6p+14q)+r_{AX}r_{AX}^{\pm 1}(7p+13q)+\frac{5}{9}(1-r_{AX})}. \tag{29}$$

In order to calculate these sudden-recoil anisotropy parameters, it is convenient to express $r_{AX}^{0^-}$ and $r_{AX}^{\pm 1}\beta_{AX}^{\pm 1}$ in terms of $r_{AX}^{\perp}$, for which a model has been constructed in Sec. IV E. Using Table I of Ref. 61, it is possible to deduce sum rules for transitions into the $A(\Omega=0^-)$ and $A(\Omega=\pm 1)$ states. Under the approximation that rotational terms contributing to the transition moment may be neglected at the low beam temperature appropriate to this work, and neglecting M compared with Z and Y, it follows that $r_{AX}^{0^-}=2Y^2/(Z^2+4Y^2)=1-r_{AX}^{\pm 1}$. From this relation, Eq. (9) and the definition of $r_{AX}^{\perp}$ in Sec. IV E, it follows that $r_{AX}^{0^-}=\frac{1}{2}r_{AX}^{\perp}=1-r_{AX}^{\pm 1}$. Using alternative expressions for the average β parameter for the $A\leftarrow X$ transition, we can write $r_{AX}^{0^-}\beta^{\perp}+r_{AX}^{\pm 1}\beta_{AX}^{\pm 1}=r_{AX}^{\perp}\beta^{\perp}+(1-r_{AX}^{\perp})\beta^{\parallel}=2-3r_{AX}^{\perp}$. Thus, $r_{AX}^{\pm 1}\beta_{AX}^{\pm 1}=(2-\frac{5}{2}r_{AX}^{\perp})$. Accordingly, Eqs. (27)–(29) become:

$$\beta_{j=0}=\frac{-\frac{1}{2}r_{AX}r_{AX}^{\perp}(4q)+r_{AX}(2-\frac{5}{2}r_{AX}^{\perp})(2p+2q)-\frac{1}{9}(1-r_{AX})}{\frac{1}{2}r_{AX}r_{AX}^{\perp}(4q)+r_{AX}(1-\frac{1}{2}r_{AX}^{\perp})(2p+2q)+\frac{1}{9}(1-r_{AX})}, \tag{30}$$

$$\beta_{j=1}=\frac{-\frac{1}{2}r_{AX}r_{AX}^{\perp}(6p+6q)+r_{AX}(2-\frac{5}{2}r_{AX}^{\perp})(3p+9q)-\frac{3}{9}(1-r_{AX})}{\frac{1}{2}r_{AX}r_{AX}^{\perp}(6p+6q)+r_{AX}(1-\frac{1}{2}r_{AX}^{\perp})(3p+9q)+\frac{3}{9}(1-r_{AX})}, \tag{31}$$

and

$$\beta_{j=2}=\frac{-\frac{1}{2}r_{AX}r_{AX}^{\perp}(6p+14q)+r_{AX}(2-\frac{5}{2}r_{AX}^{\perp})(7p+13q)-\frac{5}{9}(1-r_{AX})}{\frac{1}{2}r_{AX}r_{AX}^{\perp}(6p+14q)+r_{AX}(1-\frac{1}{2}r_{AX}^{\perp})(7p+13q)+\frac{5}{9}(1-r_{AX})}. \tag{32}$$

Model values for both r_{AX} and $r_{AX}^{\perp}$ can be obtained from Fig. 7 for the different wavelengths of interest. We have used a least-squares procedure, varying the parameters p and q, to optimize our calculated β-parameters with respect to the measured values. Best agreement was obtained with $p=0.009$ and $q=0.037$. We have listed the calculated β-parameters in Table III. Comparing these values with the measured values in Table I, we can draw the following conclusions. At 236 nm, the dissociation is not of the sudden-recoil type, since the calculated $\beta_{j=1}=0.70$ is well outside the error bar of the measured value of 0.31 ± 0.15. In addition, at 204 nm the dissociation is still not sudden: although the calculated $\beta_{j=0}$ value falls within the error bar of the measured value, the measured and calculated $\beta_{j=1}$ and $\beta_{j=2}$ values are in disagreement. One would expect more parallel character in the observed $^3P_1$ angular distribution and more perpendicular character for $^3P_2$, in the case of a sudden-recoil dissociation. Hence it is likely that, also in the intermediate regime at 226 nm, the dissociation will not be in the sudden-recoil limit. Therefore, the relatively good agreement between the calculated and measured anisotropy parameters at this wavelength must be considered as fortuitous. This conclusion also follows, of course, from the nonstatistical fine-structure distribution observed at this wavelength.

We have also calculated the dissociation branching ratios over the fine-structure states, using the denominators of Eqs. (30)–(32). Normalizing the distribution on the $j=0$ intensity, we find the values collected in Table IV, which are not completely statistical. As remarked previously, sudden-recoil distributions can deviate from a perfect statistical distribution. However, these small calculated deviations cannot

TABLE III. Anisotropy parameters, calculated in the sudden-recoil approximation, characterizing the angular distribution of $O(^3P_j)$, $j=0,1,2$, photofragments formed in the excitation of the O_2 Herzberg continuum.

λ nm	β $j=0$	$j=1$	$j=2$
204	0.42	0.70	0.58
226	0.43	0.71	0.61
236	0.43	0.70	0.60

TABLE IV. Branching ratios, calculated in the sudden-recoil approximation, for $O(^3P_j)$, $j=0,1,2$, formation, following excitation of O_2 in the Herzberg continuum.

λ nm	Branching ratio $j=0$	$j=1$	$j=2$
204	1.0	3.3	5.3
226	1.0	3.3	5.3
236	1.0	3.3	5.3

explain the large deviation from a statistical distribution measured at 226 nm.

The approximate limiting calculations performed above suggest that the dissociation process is neither sudden nor fully adiabatic at the three wavelengths under consideration. Not being in one of the limiting cases, we need accurate knowledge of the couplings between different electronic states at short and large internuclear separation for the calculation of the β-parameters. From an adiabatic correlation diagram,[11] it can be seen which electronic states may be involved in the formation of $j<2$ atoms. The *ungerade* electronic states producing $O(^3P_0)$ are the $^5\Pi_u$ and $2\ ^3\Sigma_u^+$ states, while $O(^3P_1)$ can be formed by interaction with $^{1,3,5}\Pi_u$, $^5\Sigma_u^-$, and $2\ ^3\Sigma_u^+$ states. Theoretical calculations of the coupling strengths between the Herzberg states and these states are outside the scope of this paper.

VI. CONCLUSIONS

Velocity-map imaging has been used to measure $O(^3P_j)$, $j=0$, 1, and 2 atom angular distributions arising from the photodissociation of molecular oxygen at several wavelengths across the Herzberg continuum. The high image quality afforded by the method has allowed the determination of anisotropy parameters, even for such extremely weak transitions as those involved in the Herzberg systems. Previous attempts to obtain this information using Doppler-profile measurements[16] were possibly obstructed by strong signals arising from two-photon absorption, which have been observed clearly in this study.

We have described how photofragment angular distributions are related to the composition of the electronic transition moment between the ground state and the Herzberg continuum of molecular oxygen. The different components contributing to the oscillator strength of the Herzberg continuum can be established by extrapolation of parameters measured for the three Herzberg band systems. To this aim, a review of the current state of knowledge of these transitions has been given. This procedure has allowed for an independent determination of the relative Herzberg I cross section contribution (r_{AX}) to the total Herzberg continuum. The Herzberg I contribution is clearly dominant, rising from 86% at 242 nm to 94% at 198 nm. These numbers exceed the values implied by *ab initio* calculations.[49] Using the same parameters as in the cross-section calculations, the mixed parallel-perpendicular nature of the Herzberg I continuum ($r_{AX}^{\perp}$) and the total Herzberg continuum ($r_{\mathrm{tot}}^{\perp}$) have been determined.

The value of $r_{\mathrm{tot}}^{\perp}$ is crucial, because this quantity can be related to our photofragment angular-distribution measurements, providing an independent check on the quality of the Herzberg photoabsorption model. Comparing the model $r_{\mathrm{tot}}^{\perp}$ with two values obtained from our angular-distribution measurements, we found excellent agreement at 226 nm, and reasonable agreement at 204 nm. The slight discrepancy at 204 nm does not bring the photoabsorption model into dispute since we were unable to measure the branching over the fine-structure states of the atomic fragments at that wavelength and assumed the branching to be statistical, to get a better model. Thus, these two measurements add to the credibility of the model developed to explain the oscillator strength of the Herzberg continuum, but it is clear that more accurate angular-distribution measurements would allow the development of a significantly improved model.

Finally, we have attempted to understand the implications of our fine-structure-resolved angular distributions. Using our knowledge of the character the Herzberg transitions, and making various approximations and assumptions on the (a)diabaticity of the dissociation process, we have found that neither a fully adiabatic, nor a sudden-dissociation process could explain our observations at 204 and 226 nm. Apparently, the diabatic couplings at short R and the nonadiabatic coupling between the adiabatic potential-energy curves at large R play essential roles in the dissociation process, inhibiting both fully adiabatic and fully diabatic behavior. The measured anisotropy parameters will serve as a stringent test for any theoretical calculations that might be performed on the O_2 potential-energy curves and couplings in this region.

ACKNOWLEDGMENTS

This work is part of the research program of the "Stichting voor Fundamenteel Onderzoek der Materie (FOM)," which is financially supported by the "Nederlandse Organisatie voor Wetenschappelijk Onderzoek (NWO)." The authors wish to thank T. G. Slanger and D. L. Huestis for critical comments on the manuscript, and Cor Sikkens and Eugène van Leeuwen for technical support.

[1] G. Herzberg, Naturwissenschaften **20**, 577 (1932).
[2] G. Herzberg, Can. J. Phys. **30**, 185 (1952).
[3] G. Herzberg, Can. J. Phys. **31**, 657 (1953).
[4] R. R. Meier, Space Sci. Rev. **58**, 1 (1991).
[5] M. Nicolet and R. Kennes, Planet. Space Sci. **34**, 1043 (1986).
[6] A. J. Blake and D. G. McCoy, J. Quant. Spectrosc. Radiat. Transf. **38**, 113 (1987).
[7] G. Ya. Zelikina, V. V. Bertsev, and M. B. Kiseleva, Opt. Spectrosc. **77**, 513 (1994).
[8] S. J. Singer, K. F. Freed, and Y. B. Band, J. Chem. Phys. **79**, 6060 (1983).
[9] S. J. Singer, K. F. Freed, and Y. B. Band, J. Chem. Phys. **81**, 3091 (1984).
[10] L. L. Vahala, P. S. Julienne, and M. D. Havey, Phys. Rev. A **34**, 1856 (1986).
[11] Y.-L. Huang and R. J. Gordon, J. Chem. Phys. **94**, 2640 (1991).
[12] Y. Matsumi and M. Kawasaki, J. Chem. Phys. **93**, 2481 (1990).
[13] A. T. J. B. Eppink, D. H. Parker, M. H. M. Janssen, B. Buijsse, and W. J. van der Zande, J. Chem. Phys. **108**, 1305 (1998).
[14] D. J. Leahy, D. R. Cyr, D. L. Osborn, and D. M. Neumark, Chem. Phys. Lett. **216**, 503 (1993).
[15] D. J. Leahy, D. L. Osborn, D. R. Cyr, and D. M. Neumark, J. Chem. Phys. **103**, 2495 (1995).
[16] K. Tonokura, N. Shafer, Y. Matsumi, and M. Kawasaki, J. Chem. Phys. **95**, 3394 (1991).

[17] A. J. R. Heck and D. W. Chandler, Annu. Rev. Phys. Chem. **46**, 335 (1995).
[18] A. T. J. B. Eppink and D. H. Parker, Rev. Sci. Instrum. **68**, 3477 (1997).
[19] D. H. Parker and A. T. J. B. Eppink, J. Chem. Phys. **107**, 2357 (1997).
[20] C. J. Dash, Appl. Opt. **31**, 1146 (1992).
[21] W. K. Bischel, B. E. Perry, and D. R. Crosley, Appl. Opt. **21**, 1419 (1982).
[22] J. Bamford, L. E. Jusinski, and W. K. Bischel, Phys. Rev. A **34**, 185 (1986).
[23] R. P. Saxon and J. Eichler, Phys. Rev. A **34**, 199 (1986).
[24] Y.-L. Huang and R. J. Gordon, J. Chem. Phys. **93**, 868 (1990).
[25] R. J. Yokelson, R. J. Lipert, and W. A. Chupka, J. Chem. Phys. **97**, 6153 (1992).
[26] This observation is consistent with the results of van der Zande *et al.* [Chem. Phys. Lett. **140**, 175 (1987)] who found qualitatively similar branching in the predissociation of $O_2(3s\sigma\ ^3\Pi_g)$. It is likely that the lowest two valence states of $^3\Pi_g$ symmetry are responsible for the predissociation of both systems. The weaker predissociation to the lower limit supports diabatic behavior at the avoided crossing between the two valence states.
[27] T. G. Slanger and P. C. Cosby, J. Phys. Chem. **92**, 267 (1988).
[28] P. M. Borrell, P. Borrell, and D. A. Ramsay, Can. J. Phys. **64**, 721 (1986).
[29] D. A. Ramsay, Can. J. Phys. **64**, 717 (1986).
[30] B. Coquart and D. A. Ramsay, Can. J. Phys. **64**, 726 (1986).
[31] C. M. L. Kerr and J. K. G. Watson, Can. J. Phys. **64**, 36 (1986).
[32] K. Yoshino, J. E. Murray, J. R. Esmond, Y. Sun, W. H. Parkinson, A. P. Thorne, R. C. M. Learner, and G. Cox, Can. J. Phys. **72**, 1101 (1994).
[33] T. G. Slanger, D. L. Huestis, P. C. Cosby, H. Naus, and G. Meijer, J. Chem. Phys. **105**, 9393 (1996).
[34] The $\Omega=3$ component of the $A'\ ^3\Delta_u$ state is known, from absorption spectra, only for $v=4-11$.
[35] D. L. Huestis, R. A. Copeland, K. Knutsen, T. G. Slanger, R. T. Jongma, M. G. H. Boogaarts, and G. Meijer, Can. J. Phys. **72**, 1109 (1994).
[36] K. Yoshino, J. R. Esmond, J. E. Murray, W. H. Parkinson, A. P. Thorne, R. C. M. Learner, and G. Cox, J. Chem. Phys. **103**, 1243 (1995).
[37] Although the CRDS oscillator strengths for the $A\leftarrow X$ system are ~40% lower than the UVFTS values, Huestis *et al.* (Ref. 35) use recommended values close to those of Yoshino *et al.* (Ref. 36) in estimating the Herzberg I cross-section branching ratio. CRDS oscillator strengths for the weaker $A'\leftarrow X$ and $c\leftarrow X$ systems are expected to be significantly more accurate than those for the $A\leftarrow X$ system.
[38] J. E. Frederick and J. E. Mentall, Geophys. Res. Lett. **9**, 461 (1982).
[39] J. R. Herman and J. E. Mentall, J. Geophys. Res. **87**, 8967 (1982).
[40] G. P. Anderson and L. A. Hall, J. Geophys. Res. **88**, 6801 (1983).
[41] A. S.-C. Cheung, K. Yoshino, W. H. Parkinson, S. L. Guberman, and D. E. Freeman, Planet. Space Sci. **34**, 1007 (1986).
[42] A. Jenouvrier, B. Coquart, and M. F. Merienne, Planet. Space Sci. **34**, 253 (1986).
[43] A. Jenouvrier, B. Coquart, and M. F. Merienne, J. Quant. Spectrosc. Radiat. Transf. **36**, 349 (1986).
[44] K. Yoshino, A. S.-C. Cheung, J. R. Esmond, W. H. Parkinson, D. E. Freeman, S. L. Guberman, A. Jenouvrier, B. Coquart, and M. F. Merienne, Planet. Space Sci. **36**, 1469 (1988).
[45] K. Yoshino, J. R. Esmond, A. S.-C. Cheung, D. E. Freeman, and W. H. Parkinson, Planet. Space Sci. **40**, 185 (1992).
[46] A. Amoruso, L. Crescentini, M. S. Cola, and G. Fiocco, J. Quant. Spectrosc. Radiat. Transf. **56**, 145 (1996).
[47] H. Partridge, C. W. Bauschlicher, Jr., S. R. Langhoff, and P. R. Taylor, J. Chem. Phys. **95**, 8292 (1991).
[48] R. P. Saxon and B. Liu, J. Chem. Phys. **67**, 5432 (1977).
[49] R. Klotz and S. D. Peyerimhoff, Mol. Phys. **57**, 573 (1986).
[50] J. P. England, B. R. Lewis, and S. T. Gibson, Can. J. Phys. **74**, 185 (1996).
[51] R. P. Saxon and T. G. Slanger, J. Geophys. Res. **91**, 9877 (1986).
[52] D. R. Bates, Planet. Space Sci. **36**, 869 (1988).
[53] In this paper, potential energy, in eV, is referred to the minimum in the ground-state $X\ ^3\Sigma_g^-$ potential-energy curve.
[54] Except for the highest vibrational levels of the A state, which are perturbed significantly, our RKR procedure reproduces the experimental G_v and B_v values to within 0.7 cm^{-1} and 5×10^{-4} cm^{-1}, respectively, for each of the A, A', and c states.
[55] Extrapolation to $v=-0.5$ was performed by fitting a low-order Dunham polynomial to the lowest four known vibrational levels.
[56] R. J. LeRoy, J. Chem. Phys. **73**, 6003 (1980).
[57] P. C. Cosby and D. L. Huestis, J. Chem. Phys. **97**, 6108 (1992).
[58] S. S. Banerjee, Ph.D. dissertation thesis, The Australian National University, 1997.
[59] B. R. Lewis, S. S. Banerjee, and S. T. Gibson, J. Chem. Phys. **102**, 6631 (1995).
[60] Experimental information on the Rydberg-valence interaction for $^3\Delta_u$ symmetry can be obtained from the measured photoabsorption spectrum of metastable $O_2(a^1\Delta_g)$ (P. C. Hill, Ph.D. dissertation thesis, The Australian National University, 1991), but the predissociation pattern of the $^3\Delta_u$ Rydberg state is not well enough defined to enable an accurate repulsive limb of the $A'\ ^3\Delta_u$ state to be established. As far as can be determined, the A'-state potential-energy curve adopted here is consistent with the observed predissociation of the $^3\Delta_u$ Rydberg state. No experimental information is available on the Rydberg state of $^1\Sigma_u^-$ symmetry.
[61] V. P. Bellary and T. K. Balasubramanian, J. Quant. Spectrosc. Radiat. Transf. **45**, 283 (1991).
[62] Subscripts in the transition-moment notation adopted in this work refer to the value of Ω'. Equalities between the moments arise because of symmetry considerations, leading to the need for only three independent moments in the case of the $A\leftarrow X$ transition.
[63] Expressions given in Ref. 61 have been simplified and corrected to obtain Eqs. (8) and (9).
[64] P. A. Fraser, Can. J. Phys. **32**, 515 (1954).
[65] D. L. Huestis, in *Atomic, Molecular, and Optical Physics Handbook*, edited by G. W. F. Drake (AIP, New York, 1996), p. 403.
[66] $A\leftarrow X$ R-centroids associated with continuum wavelengths in Fig. 5 are determined using Eq. (13) with the radial part of the A-state continuum wavefunction replacing $\chi_{v'}(R)$.
[67] The rotational line strengths employed by Kerr and Watson (Ref. 31) were taken from the photographically recorded spectra of Coquart and Ramsay (Ref. 30).
[68] J. K. G. Watson, Can. J. Phys. **46**, 1637 (1968).
[69] A. C. Allison and A. Dalgarno, J. Chem. Phys. **55**, 4342 (1971).
[70] K. Yoshino, D. L. Huestis, and R. W. Nicholls, J. Quant. Spectrosc. Radiat. Transfer (to be published).
[71] In principle, it is possible to match the experimental cross section by making adjustments to the A-state potential-energy curve while retaining a smaller transition-moment slope. However, potential-energy curves determined in this way either exhibit anomalies in shape or are inconsistent with the known form in the Rydberg-valence region (Sec. IV B).
[72] We have made very minor corrections to the recommended continuum cross sections of Ref. 44 for $\nu>47\,720$ cm^{-1} to allow for the effects of the lowest $B\leftarrow X$ hot bands.
[73] B. R. Lewis, L. Berzins, and J. H. Carver, J. Quant. Spectrosc. Radiat. Transf. **36**, 209 (1986).
[74] A. S.-C. Cheung, K. Yoshino, W. H. Parkinson, and D. E. Freeman, Can. J. Phys. **62**, 1752 (1984).
[75] K. Yoshino, D. E. Freeman, and W. H. Parkinson, J. Phys. Chem. Ref. Data **13**, 207 (1984).
[76] B. Coquart, M. F. Merienne, and A. Jenouvrier, Planet. Space Sci. **38**, 287 (1990).
[77] M. Nicolet and R. Kennes, Planet. Space Sci. **36**, 1069 (1988), and references therein.
[78] Strictly speaking, since the discrete cross-section branching ratios are derived from room-temperature measurements and the model r_{AX} is calculated for $J=0$, the strong J-dependence of the $A'\leftarrow X$ transition moment leads to a small discrepancy (~2%).

4.32 Quantum interference in the Schumann-Runge bands of molecular oxygen

[52] B. R. Lewis, S. T. Gibson, L. W. Torop, and D. G. McCoy,
Geophysical Research Letters **25**, 2457–2460 (1998).

GEOPHYSICAL RESEARCH LETTERS, VOL. 25, NO. 13, PAGES 2457-2460, JULY 1, 1998

Quantum interference in the Schumann-Runge bands of molecular oxygen

B. R. Lewis and S. T. Gibson

Research School of Physical Sciences and Engineering, The Australian National University, Canberra, Australian Capital Territory, Australia

L. W. Torop and D. G. McCoy

Department of Physics and Mathematical Physics, The University of Adelaide, Adelaide, South Australia, Australia

Abstract. The photoabsorption cross section of O_2 in the Schumann-Runge bands is investigated theoretically using the coupled-channel Schrödinger-equations method. It is found that quantum interference between vibrational bands leads to significant asymmetry in the far line wings, a result supported by experimental evidence. Thus, Schumann-Runge cross sections calculated with the usual band models based on Voigt line shapes may be in error in regions of weak absorption between vibrational band heads, suggesting the need to re-evaluate aspects of atmospheric photochemistry sensitive to those regions.

Introduction

The Schumann-Runge (SR) bands of O_2, $B\,^3\Sigma_u^- \leftarrow X\,^3\Sigma_g^-$ (1750–2050 Å), play important direct and indirect roles in the photochemistry of the terrestrial atmosphere. Photodissociation in the SR bands provides a major source of odd oxygen in the stratosphere and the dominant source in the mesosphere. In addition, photoabsorption by O_2 in the SR bands controls the depth of penetration of solar vacuum ultraviolet (VUV) radiation into the atmosphere and, consequently, regulates the photodissociation rates of other species.

Complex structure in the SR-band spectrum results in the absorption of solar VUV radiation over a wide range of altitudes. However, absolute experimental cross sections are available for only a small range of wavelengths and temperatures[*Yoshino et al.*, 1983, 1987; *Cheung et al.*, 1996]. Therefore, in atmospheric applications, it is necessary to model the required temperature- and wavelength-dependent SR photoabsorption cross sections. This requires knowledge of the positions, strengths, widths and shapes of the many rovibrational lines in the SR bands. Extensive experimental measurements have yielded accepted values for the SR-band line positions[*Yoshino et al.*, 1984] and oscillator strengths[*Yoshino et al.*, 1983; *Lewis et al.*, 1986a]. Residual disagreements[*Lewis et al.*, 1994] in predissociation line widths[*Lewis et al.*, 1986b; *Cheung et al.*, 1990] are currently under investigation (P. M. Dooley et al., manuscript in preparation, 1998).

The usual basis for treating atmospheric problems involving the SR bands is the line-by-line model, whereby a synthetic spectrum is built up by summing contributions from individual rovibrational lines which are represented by Voigt profiles (convolutions of Lorentzian predissociation and Gaussian Doppler components). Underlying continua, due to the Herzberg transitions at long wavelengths and the SR transition at short wavelengths, must also be taken into account. For computational economy, before application to atmospheric problems, the high-resolution, temperature-dependent line-by-line cross sections are generally reduced to effective cross sections and transmittances for a few, relatively wide spectral intervals. Many such treatments, each based on the best experimental data available, have helped to develop an understanding of the photochemical implications of VUV absorption in the SR bands[*Fang et al.*, 1974; *Blake*, 1979; *Allen and Frederick*, 1982; *Murtagh*, 1988; *Nicolet and Kennes*, 1989].

In order to study photochemical processes which occur primarily over restricted wavelength ranges, however, it is necessary to retain the use of high-resolution cross sections. Recently, a polynomial representation of an improved SR line-by-line model has been developed which is well suited for atmospheric transmission calculations at high spectral resolution[*Minschwaner et al.*, 1992] and has been used in the calculation of NO photodissociation in the middle and upper atmosphere[*Minschwaner and Siskind*, 1993].

In this letter, we question one of the implicit assumptions of the line-by-line models, namely that the Voigt (Lorentzian) line shape provides a valid estimate of the cross section in the far line-wing. Using a coupled-channel Schrödinger equations (CSE) technique to calculate SR-band cross sections, we show that quantum interferences between vibrational bands result in significant far-wing lineshape asymmetries and discuss the consequences for atmospheric models.

Theoretical method

Photolysis in the SR bands occurs through predissociation of the $B\,^3\Sigma_u^-$ state, mediated by spin-orbit interactions between the B state and four repulsive states, $1\,^1\Pi_u$, $1\,^3\Pi_u$, $1\,^5\Pi_u$, and $2\,^3\Sigma_u^+$, and an additional rotational interaction with the $1\,^3\Pi_u$ state[*Julienne and Krauss*, 1975; *Julienne*, 1976]. In the usual theoretical treatment, predissociation line widths are calculated as the sums of partial widths for each interaction, obtained using the Fermi-Wentzel Golden Rule, and line shifts caused by the discrete-continuum perturbations are given by the sums of principal-part integrals[*Julienne and Krauss*, 1975]. Implicit in this

Paper number 98GL51783.
0094-8534/98/98GL-51783$05.00

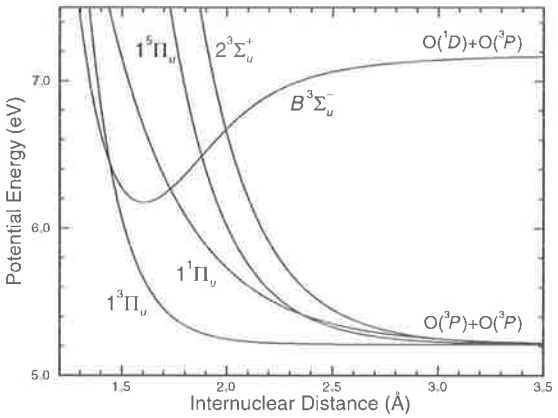

Figure 1. Model potential-energy curves for states involved in the $B\,^3\Sigma_u^-$-state predissociation. The energy scale is referred to the minimum in the ground-state $X\,^3\Sigma_g^-$ potential.

perturbative approach is the assumption of a Lorentzian predissociation line-shape component. While this assumption is valid near the line centres, the isolated-resonance Lorentzian line shape cannot be expected to describe the SR cross section accurately in the far wings.

We overcome this fundamental flaw of the line-by-line models by employing the CSE method, in which the techniques of scattering theory[*Mies*, 1980] are adapted to the calculation of molecular photodissociation cross sections for coupled states[*Torop et al.*, 1987]. In this method, Schrödinger equations for the motion of the nuclei in the various potential curves are coupled by terms representing transitions between the potentials. The potential curves, coupling strengths and photoabsorption amplitudes used are obtained by analysis of accurate, high-resolution measurements. Use of the quantum-mechanical CSE method enables the SR cross section to be calculated accurately at all wavelengths without any assumptions regarding individual line shapes. Effectively, the rovibrational line-by-line method is replaced by a rotation-by-rotation method, since the fundamental unit, or "line shape", in the CSE calculations is a rotational-branch cross section which *implicitly* contains all vibrational information. In addition, since the CSE model is derived from a physical picture of the molecular transition, rather than a mathematical parameterization, all of the detailed effects, such as the rotation, vibration, and fine-structure dependence of the predissociation linewidths, the rotation dependence of the effective band oscillator strengths, and the underlying SR continuum due to absorption from rovibrationally-excited X-state levels[*Gibson et al.*, 1991], are included implicitly. Self-consistent isotopic cross sections may be obtained simply by changing the molecular reduced mass in the calculations.

We use a diabatic CSE formulation which has been applied previously to a description of rovibronic photodissociation in O_2[*Lewis et al.*, 1995], together with a set of molecular parameters for the SR transition. Briefly, we use the X- and B-state Rydberg-Klein-Rees potential-energy curves and $B \leftarrow X$ electronic transition moment of *Lewis et al.* [1986a], and adopt the SR predissociation model of *Lewis et al.* [1986b] which assumes exponential potentials for the repulsive states and couplings which ignore the rotational interaction with the $1\,^3\Pi_u$ state. Our model potential-energy curves for the five coupled upper states are shown in Fig. 1. Rotational interactions between the $B\,^3\Sigma_u^-$-state sub-levels are taken into account explicitly, giving an accurate description of the transition fine structure, but fine-structure interactions within the repulsive states are ignored. The full SR cross section for a given temperature is built up from separate CSE calculations for individual rotational branches, followed by a properly weighted summation, taking into account the rotational line-strength and Boltzmann factors.

Results and discussion

In Fig. 2, our calculated *rotationless* CSE cross section for the SR band system is compared with an equivalent Lorentzian line-by-line calculation. For clarity, rotational and fine structure have been suppressed and the oscillator strength for each vibrational transition has been collapsed into a single line at the band origin. The line-by-line cross section has been constructed to yield lines of identical strength and width to the CSE calculations. There are significant differences in cross section between the two calculations in many of the absorption windows between vibrational bands. These differences arise because, unlike the line-by-line method, the CSE method includes the effects of quantum interference between vibrational resonances. Two regions are of particular interest. First, the line-by-line method grossly overestimates the SR cross section in the region $\lambda > 1925$ Å, due to the unphysical predominance of the Lorentzian wing of the strongly predissociated (4,0) band. Second, the quantum interference in the CSE SR-window regions changes dramatically from destructive for $v' = 10$–12, to constructive for $v' = 12$–14. Between the (13,0) and (14,0) bands, which have the *lowest* predissociation widths in the SR system, the CSE SR-window cross section reaches its *maximum* value, exceeding the line-by-line cross section by almost an order of magnitude. The

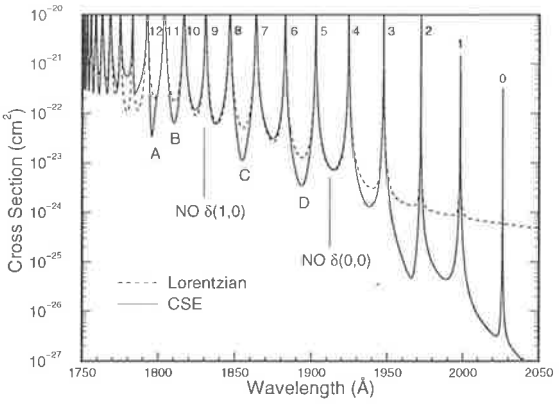

Figure 2. Comparison between rotationless SR-band cross sections calculated using the CSE and Lorentzian line-by-line methods, emphasizing significant differences occurring for some cross-section minima. Peaks are labelled with the vibrational quantum number of the $B\,^3\Sigma_u^-$-state.

CSE peaks are moderately well described by Lorentzians, but are described more accurately by Fano profiles[*Fano*, 1961]. For example, in the case of the (4,0) band, one of the most asymmetric resonances with a width of 3.5 cm^{-1}, the CSE-Lorentzian difference reaches 1% at ± 4 cm^{-1} from the line centre, while the difference from a Fano profile with a q-parameter of 452 reaches 1% at ± 32 cm^{-1}.

In Fig. 3, we compare the measured 79 K (12,0) SR-band cross section of *Yoshino et al.* [1987] with a full CSE calculation and a rudimentary Lorentzian line-by-line model which includes the effects of all wings from (11,0)–(13,0) lines. While both calculations provide a good description of the (12,0) line peaks, the CSE cross section is in much better agreement with the measurements in the regions of weak absorption (55560–55640 cm^{-1}, and >55800 cm^{-1}, but note that the experimental cross section includes isotopic lines in the former region which are not included in the calculations). Both the experimental and CSE (12,0) cross sections exhibit a pronounced asymmetry compared with the Lorentzian model, with a stronger blue band wing and a weaker red wing. Despite the noisy data and the clear need for further measurements concentrating on the SR windows, this result confirms the interference effects predicted by the CSE model.

Further evidence for the validity of the CSE-model predictions may be found by considering the characteristics of the continuum underlying the SR bands. Differences between experimental and SR band-model cross sections, have, in the past, been used to determine the underlying continuum. The hazards of using a Lorentzian line-by-line SR model in this procedure are illustrated with two examples. First, the 80 K underlying continuum of *Lewis et al.* [1985], deduced using a Lorentzian model, exhibits oscillatory structure, with very small, or negative, values of the continuum cross section in four SR windows (1800, 1812, 1858, 1892 Å). An inspection of Fig. 2 reveals that these wavelengths correspond to the four windows (A–D) where the CSE cross section is much less than the Lorentzian cross section. Thus,

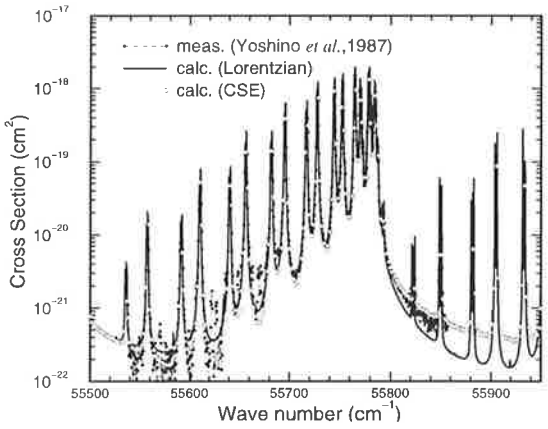

Figure 3. Comparison between a measured 79 K cross section for the (12,0) SR band and calculations using the CSE and Lorentzian line-by-line methods. The CSE calculations, with a stronger blue wing and a weaker red wing, are in better agreement with the measurements.

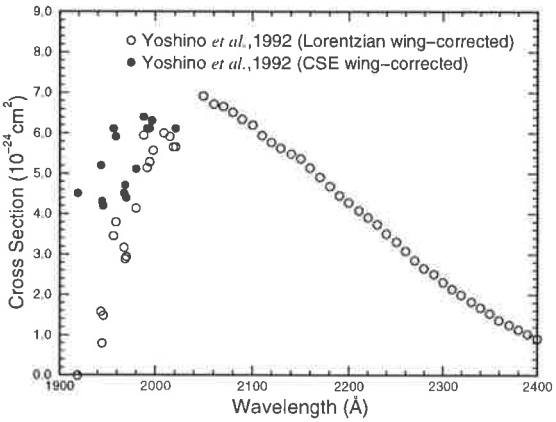

Figure 4. Experimental cross sections for the Herzberg continuum. Below 2030 Å, the measurements of *Yoshino et al.* [1992] have been SR Lorentzian-wing corrected (open circles). The CSE-wing correction yields more realistic estimates of the Herzberg continuum underlying the SR bands (filled circles).

this observation provides support for the CSE predictions and suggests that the oscillations in the underlying continuum are artifacts. Second, In Fig. 4, we show the experimental Herzberg continuum of *Yoshino et al.* [1992]. While the cross section for $\lambda > 2030$ Å is not subject to significant contamination by the SR bands, the results for shorter wavelengths, obtained by correction for SR line wings using a Lorentzian model, indicate anomalous behaviour, the imputed Herzberg cross section turning down and reaching zero near 1920 Å. *Yoshino et al.* [1992] interpret this result as indicating interference on the inner limb of the potential curve for the $A\,^3\Sigma_u^+$ state, but more recent evidence does not support this conclusion[*Buijsse et al.*, 1998]. On the other hand, if a CSE SR-wing correction is applied to the measurements, the deduced Herzberg continuum is more consistent with the expected bell shape, the rapid turn-down disappearing.

The CSE results will be of most significance to those atmospheric problems sensitive to the deeper penetration of solar VUV radiation in the SR-window regions, particularly where the windows coincide with regions of higher solar intensity, e.g. for longer SR-band wavelengths or for particular solar emission lines. In addition, the differences from the line-by-line results will be greatest at low temperatures where the window cross sections are more sensitive to the far wings of the strong band heads, including interference effects, rather than the near wings of local rotational lines. There may be some impact, for example, on calculations of the NO photodissociation profile. Many of the strongest lines of the NO $\delta(1,0)$ band lie in the window between the (9,0) and (10,0) SR bands where the basal cross section is determined largely by the blue wing of the (9,0) band head[*Minschwaner and Siskind*, 1993]. The rotationless CSE cross section (Fig. 2) is significantly higher than the Lorentzian cross section in this region, suggesting that a reevaluation of the NO photodissociation profile due to the $\delta(1,0)$ band may be warranted.

In conclusion, we have demonstrated the reality of quantum-interference effects in the SR bands. The full significance of our results to models of the atmospheric photochemistry requires further investigation.

Acknowledgments. This work was supported by DEETYA and the ARC.

References

Allen, M., and J. E. Frederick, Effective photodissociation cross sections for O_2 and NO in the Schumann-Runge bands, *J. Atmos. Sci., 39*, 2066-2075, 1982.

Blake, A. J., An atmospheric absorption model for the Schumann-Runge bands of O_2, *J. Geophys. Res., 84*, 3272-3282, 1979.

Buijsse, B., et al., Angular distributions for photodissociation of O_2 in the Herzberg continuum, *J. Chem. Phys., 108*, 7229-7243, 1998.

Cheung, A. S.-C., et al., Predissociation line widths of the (1,0)-(12,0) Schumann-Runge absorption bands of O_2 in the wavelength region 179-202 nm, *J. Chem. Phys., 92*, 842-849, 1990.

Cheung, A. S.-C., K. Yoshino, J. R. Esmond, and W. H. Parkinson, The Schumann-Runge bands of O_2 at 670 K and the spectroscopic constants of the ground state, $X\,^3\Sigma_g^-$, *J. Mol. Spectrosc., 178*, 66-77, 1996.

Fang, T. M., S. C. Wofsy, and A. Dalgarno, Opacity distribution functions and absorption in Schumann-Runge bands of O_2, *Planet. Space Sci., 22*, 413-425, 1974.

Fano, U., Effects of configuration interaction on intensities and phase shifts, *Phys. Rev., 124*, 1866-1878, 1961.

Gibson, S. T., B. R. Lewis, K. G. H. Baldwin, and J. H. Carver, Rotational features in the fluorescence excitation spectrum of $O(^1D_2)$ from vacuum ultraviolet laser photodissociation of O_2, *J. Chem. Phys., 94*, 1060-1068, 1991.

Julienne, P. S., $^3\Sigma_u^- - ^3\Sigma_u^+$ coupling in the O_2 $B\,^3\Sigma_u^-$ predissociation, *J. Mol. Spectrosc., 63*, 60-79, 1976.

Julienne, P. S., and M. Krauss, Predissociation of the Schumann-Runge bands of O_2, *J. Mol. Spectrosc., 56*, 270-308, 1975.

Lewis, B. R., et al., Decomposition of the photoabsorption continuum underlying the Schumann-Runge bands of $^{16}O_2$-II. Role of the $1\,^3\Pi_g$ state and collision-induced absorption, *J. Quant. Spectrosc. Radiat. Transfer, 34*, 405-415, 1985.

Lewis, B. R., L. Berzins, and J. H. Carver, Oscillator strengths for the Schumann-Runge bands of $^{16}O_2$, *J. Quant. Spectrosc. Radiat. Transfer, 36*, 209-232, 1986a.

Lewis, B. R., L. Berzins, J. H. Carver, and S. T. Gibson, Rotational variation of predissociation linewidth in the Schumann-Runge bands of $^{16}O_2$, *J. Quant. Spectrosc. Radiat. Transfer, 36*, 187-207, 1986b.

Lewis, B. R., S. T. Gibson, and P. M. Dooley, Fine-structure dependence of predissociation linewidth in the Schumann-Runge bands of O_2, *J. Chem. Phys., 100*, 7012-7034, 1994.

Lewis, B. R., S. S. Banerjee, and S. T. Gibson, Asymmetric line shapes in the indirect predissociation of the $f\,^1\Sigma_u^+$ Rydberg state of O_2, *J. Chem. Phys., 102*, 6631-6640, 1995.

Mies, F. H., A scattering theory of diatomic molecules: General formalism using the channel state representation, *Mol. Phys., 41*, 953-972, 1980.

Minschwaner, K., G. P. Anderson, L. A. Hall, and K. Yoshino, Polynomial coefficients for calculating O_2 Schumann-Runge cross sections at 0.5 cm^{-1} resolution, *J. Geophys. Res., 97*, 10103-10108, 1992.

Minschwaner, K., and D. E. Siskind, A new calculation of NO photolysis in the stratosphere, mesosphere, and lower thermosphere, *J. Geophys. Res., 98*, 20401-20412, 1993.

Murtagh, D. P., The O_2 Schumann-Runge system: New calculations of photodissociation cross sections, *Planet. Space Sci., 36*, 819-828, 1988.

Nicolet, M., and R. Kennes, Aeronomic problems of O_2 photodissociation-VI. Photodissociation frequency and transmittance in the spectral range of the Schumann-Runge bands, *Planet. Space Sci., 37*, 459-491, 1989.

Torop, L., et al., Effects of the close approach of potential curves in photoabsorption by diatomic molecules-I. Theory and computational procedures, *J. Quant. Spectrosc. Radiat. Transfer, 38*, 9-18, 1987.

Yoshino, K., D. E. Freeman, J. R. Esmond, and W. H. Parkinson, High resolution absorption cross section measurements and band oscillator strengths of the (1,0)-(12,0) Schumann-Runge bands of O_2, *Planet. Space Sci., 31*, 339-353, 1983.

Yoshino, K., D. E. Freeman, and W. H. Parkinson, Atlas of the Schumann-Runge bands of O_2 in the wavelength region 175-205 nm, *J. Phys. Chem. Ref. Data, 13*, 207-227, 1984.

Yoshino, K., D. E. Freeman, J. R. Esmond, and W. H. Parkinson, High resolution absorption cross sections and band oscillator strengths of the Schumann-Runge bands of O_2 at 79 K, *Planet. Space Sci., 35*, 1067-1075, 1987.

Yoshino, K., et al., High resolution absorption cross sections in the transmission window region of the Schumann-Runge bands and Herzberg continuum of O_2, *Planet. Space Sci., 40*, 185-192, 1992.

B. R. Lewis and S. T. Gibson, Research School of Physical Sciences and Engineering, The Australian National University, Canberra, ACT 0200, Australia. (e-mail: brenton.lewis@anu.edu.au; stephen.gibson@anu.edu.au)

L. W. Torop and D. G. McCoy, Department of Physics and Mathematical Physics, The University of Adelaide, Adelaide, SA 5005, Australia. (e-mail: ltorop@physics.adelaide.edu.au; dmccoy@physics.adelaide.edu.au)

(Received April 6, 1998; revised May 18, 1998; accepted May 20, 1998.)

4.33 A comparative high-resolution study of predissociation linewidths in the Schumann-Runge bands of O_2

[53] P. M. Dooley, B. R. Lewis, S. T. Gibson, K. G. H. Baldwin, P. C. Cosby, J. L. Price, R. A. Copeland, T. G. Slanger, A. P. Thorne, J. E. Murray, and K. Yoshino, *Journal of Chemical Physics* **109**, 3856–3867 (1998).

A comparative high-resolution study of predissociation linewidths in the Schumann-Runge bands of O_2

P. M. Dooley, B. R. Lewis, S. T. Gibson, and K. G. H. Baldwin
Research School of Physical Sciences and Engineering, The Australian National University, Canberra ACT 0200, Australia

P. C. Cosby, J. L. Price,[a] R. A. Copeland, and T. G. Slanger
Molecular Physics Laboratory, SRI International, Menlo Park, California 94025

A. P. Thorne and J. E. Murray
Blackett Laboratory, Imperial College of Science, Technology, and Medicine, London SW7 2BZ, United Kingdom

K. Yoshino
Harvard-Smithsonian Center for Astrophysics, Cambridge, Massachusetts 02138

(Received 10 April 1998; accepted 3 June 1998)

Results are presented of a comparative study in which three distinct high-resolution experimental techniques (vacuum-ultraviolet laser spectroscopy, laser-induced fluorescence spectroscopy and vacuum-ultraviolet Fourier-transform spectroscopy) were used to study predissociation in the Schumann-Runge bands of O_2 $B\ ^3\Sigma_u^-(v')\leftarrow X\ ^3\Sigma_g^-(v'')$ with $v'=13$ and 14. Our measurements are the first to be performed at high resolution for these levels and represent a significant advance on previous knowledge, characterizing completely the fine-structure and rotation dependencies of the $B\ ^3\Sigma_u^-(v=13$ and $14)$-state predissociation for the first time. The measured fine-structure-specific linewidths will result in significant improvements in the parameterization of models describing predissociation of the B-state and will have an impact on the development of realistic photochemical models of the terrestrial atmosphere. Good agreement was found between linewidths measured using vacuum-ultraviolet laser spectroscopy and laser-induced fluorescence spectroscopy, but unexpected difficulties arose in determining quantitative linewidths using vacuum-ultraviolet Fourier-transform spectroscopy. For each experimental technique, the instrumental resolution had to be carefully controlled and monitored in order to ensure reliable interpretation of the measured spectra. © *1998 American Institute of Physics.* [S0021-9606(98)00734-X]

I. INTRODUCTION

Photodissociation in the Schumann-Runge (SR) band system of molecular oxygen, $B\ ^3\Sigma_u^-\leftarrow X\ ^3\Sigma_g^-$ (175–205 nm), is a major source of odd oxygen in the stratosphere and the dominant one in the mesosphere. In addition, photoabsorption in the SR bands controls the depth of penetration of solar vacuum-ultraviolet (VUV) radiation into the atmosphere. Thus, due to their important role in terrestrial atmospheric photochemistry, the SR bands have been the subject of considerable study. The B state is predissociated by a number of repulsive states correlating with two ground-state oxygen atoms[1,2] and an accurate knowledge of the vibration, rotation and fine-structure dependence of the corresponding predissociation linewidths is essential,[3] both for the construction of realistic photochemical models,[4] and for the accurate parameterization of the predissociation mechanisms.[1,2]

Although there have been many attempts to measure predissociation linewidths in the $(v',0)$ SR bands, there remain significant disagreements between linewidths obtained in different laboratories.[5] This contrasts with the situation for the measured SR-band oscillator strengths[6,7] for which good agreement has been found. The most extensive measurements on the vibration and rotation dependence of the predissociation linewidths are those of Lewis *et al.*[8] and Cheung *et al.*[9] The results of Lewis *et al.*[8] $(v'=1-19)$ were obtained from equivalent-width measurements taken using a 2.2 m VUV monochromator with an instrumental resolution of 4.5 pm $(\sim 1.4\ \mathrm{cm}^{-1})$ full-width at half-maximum (FWHM), while those of Cheung *et al.*[9] $(v'=1-12)$ were obtained from the near-absolute photoabsorption cross-section measurements of Yoshino *et al.*,[7,10,11] taken using a 6.65 m scanning spectrometer with an instrumental resolution of 1.3 pm $(\sim 0.4\ \mathrm{cm}^{-1})$ FWHM. The ~20% discrepancy between these two sets of fine-structure-averaged linewidths for $v'=1-12$ has been reduced recently to ~8% by a reanalysis[5] of the measurements of Yoshino *et al.*, using cross sections of improved accuracy[12] and a less constrained method of data analysis.

In order to characterize accurately the B-state predissociation, it is preferable to measure fine-structure-specific linewidths. However, for many bands in the SR system, principally the broader bands with $v'=1-12$, the P- and R-branch triplets are incompletely resolved because the splittings of the ground- and upper-state triplet components F_1,

[a]Present address: Pacific Northwest National Laboratory, Richland, WA 99352.

F_2, F_3 are similar and the linewidths are comparable with the fine-structure splittings. In addition, near $v'=6$ the P and R branches in the $(v',0)$ spectra overlap, further inhibiting the confident determination of fine-structure-specific linewidths. A substantial improvement in the separation of fine-structure components was achieved by Cosby *et al.*,[13] using absorption from higher vibrational levels of the ground state $X\ ^3\Sigma_g^-$ to access the B-state. In addition, their use of laser-induced fluorescence (LIF) to detect the absorptions served to amplify[14-16] even small differences among the predissociation rates of the B-state fine-structure levels, allowing the measurement of fine-structure-specific predissociation rates for an extended range of rotational levels with $v'=0,2$ at high resolution ($\sim 0.06\ \mathrm{cm}^{-1} \approx 0.4-0.8$ pm FWHM).

For $(v',0)$ transitions, the fine-structure separation is sufficient for the narrower $v' \geqslant 13$ levels to allow the resolution of individual components with an instrument of sufficient resolving power, but such measurements are rare. Lewis *et al.*[17] have deduced predissociation linewidths for resolved F_1 levels with $v'=17$, $N'=2-26$ from high-resolution ($\sim 0.15\ \mathrm{cm}^{-1} \approx 0.5$ pm FWHM) photoabsorption spectra obtained using a coherent VUV source based on high-order anti-Stokes stimulated Raman scattering in H_2 of pulsed dye-laser radiation. In the absence of explicit spectral resolution, a determination of fine-structure-specific linewidths requires some form of synthetic spectral modeling. Indeed, the analysis by Lewis *et al.*[5] of the cross sections measured by Yoshino *et al.*[12] have enabled the determination of some fine-structure-specific widths for $v'=1$, 2, 5, 7–13, through such deconvolution procedures.

We have undertaken a collaborative study to address the lack of high-resolution measurements of fine-structure-specific predissociation linewidths in the SR bands, in order to characterize precisely the mechanisms for predissociation of the B state, and to provide accurate data for use in photochemical models of the terrestrial atmosphere. Three entirely different state-of-the-art high-resolution experimental techniques are used in different laboratories: vacuum-ultraviolet laser spectroscopy (VUVLS) at the Australian National University (ANU); laser-induced fluorescence spectroscopy (LIFS) at SRI International; and synchrotron-based vacuum-ultraviolet Fourier-transform spectroscopy (VUVFTS) at the Photon Factory. In this work, we compare critically these three experimental techniques and illustrate the comparison with rotation- and fine-structure-specific studies of the $B\ ^3\Sigma_u^-(v=13$ and $14)$ levels using each technique. These levels are among the narrowest in the SR system, providing an ideal testing ground for the high-resolution spectroscopies employed.

A preliminary report on the VUVLS measurements[18] and the results of a VUVLS study of perturbations in the high-v' SR bands[19] have appeared elsewhere. Details of an improved predissociation model for the B state, resulting from a combination of all of the new fine-structure-specific data, will appear in a further paper.

II. EXPERIMENTAL METHODS

A. Vacuum-ultraviolet laser spectroscopy

The experimental apparatus for VUVLS has been described in detail elsewhere.[19] Briefly, two-photon-resonant difference-frequency four-wave mixing[20,21] (2PR-DF4WM) of excimer-pumped dye-laser radiation in Xe was used to generate tunable narrow-bandwidth VUV radiation from 177.5 nm to 180.6 nm, in order to measure high-resolution photoabsorption cross sections for all accessible rotational lines from the (13,0) and (14,0) SR bands.

Two dye lasers (Lambda Physik FL3002E) were pumped by a common XeCl excimer laser (Lambda Physik EMG201). The output of the first dye laser, operated with the dye Coumarin 307, was frequency doubled in a BBO I crystal and the doubled output was tuned to be two-photon-resonant with the $6p[\frac{3}{2}]_2$ level of Xe at 78 120 cm^{-1}. This beam was combined with the tunable output of the second dye laser and both beams were focused into a cell containing Xe by an off-axis lens. Tunable VUV radiation generated by the 2PR-DF4WM process was passed through a low-resolution monochromator which discriminated against unwanted wavelengths. The dyes Coumarin 47 and 120 were used in the second dye laser, allowing tunability in the range 440–459 nm, and resulting in the production of VUV radiation in the range 177.5–180.6 nm. The VUV radiation leaving the monochromator was divided into two beams by a beam splitter. The reflected beam was monitored directly, while the transmitted beam passed through an absorption cell of length 33 cm, equipped with MgF_2 windows, before being detected. Output pulses from solar-blind monitor and detector photomultipliers were processed by a boxcar averaging system. The dynode-chain voltage of each photomultiplier was reduced, in order to limit the peak signal current to a value such that detector nonlinearity due to space-charge effects was $<1\%$. Most aspects of the experimental procedure were computer controlled, including triggering of the excimer laser, synchronous scanning of the dye laser and VUV monochromator, gas handling, pressure measurement and data acquisition.

All measurements were performed at room temperature (293 K). The phase matching for the 2PR-DF4WM process was optimized by careful beam alignment and by adjusting the pressure of Xe, normally in the range 70–90 Torr, to maximize the VUV signal for the particular scan range. The lasers were operated at a 10 Hz repetition rate and the monitor and detector signals were averaged over 50 laser shots for each datum point. The experimental scans varied from 1 cm^{-1} to 10 cm^{-1} in extent, with wave-number increments in the range 0.015–0.03 cm^{-1}. Scans were performed in groups of three, with the absorption cell alternately filled with a pressure of O_2 (99.9% purity) in the range 0.5–100 Torr, then evacuated, then refilled. This scheme compensated for drifts in photomultiplier sensitivity and the effects of wavelength structure in the photomultiplier signals which was not related to O_2 absorption.[22] Division of the detector signal by the monitor signal, after correction for scattered radiation, compensated for the shot-to-shot fluctuations inherent in the generated VUV signal. Absolute cell transmit-

tances were obtained by dividing the full-cell ratios (detector/monitor) by the empty-cell ratios at each wavelength. Photoabsorption cross sections were calculated from the absolute transmittances using the Beer–Lambert law.

Each dye laser was operated with an intracavity étalon to minimize the VUV bandwidth. The nominal VUV wave number was given by

$$\nu_{\mathrm{vuv}} = \nu_{2p} - \nu_{\mathrm{vis}}, \tag{1}$$

where ν_{2p} was the wave number of the Xe two-photon resonance and ν_{vis} was the vacuum-corrected wave number of the tunable dye laser. The measured wave numbers of Yoshino *et al.*[23] for selected sharp, unblended lines of the SR system (accuracy $\sim 0.1\ \mathrm{cm}^{-1}$) were used for absolute wavenumber calibration in the VUV. Linewidth uncertainties due to uncertainties in the relative wave-number calibration of an étalon scan are expected to be negligible.[19]

The spectral characteristics of the generated VUV radiation are of central importance in evaluating the reliability of linewidth measurements made with the VUVLS system, meriting discussion in some detail. The factors determining these spectral characteristics include: the bandwidth of the fundamental radiation produced by the two dye-laser oscillators; the modification to the oscillator spectral output by the two-stage pulse amplification and (in the case of the two-photon-resonant laser) by second-harmonic generation; the effect of the nonlinear four-wave mixing process; and, finally, modification of the nonlinear output due to the presence (under some circumstances) of intense laser fields.

The dye lasers used contain an oscillator and two amplifier stages. The oscillator cavity comprises a grating in Littrow configuration at one end and a dielectric mirror at the other. A series of prisms beam-expands the radiation from the pump region onto the grating to maximize the number of grating rulings illuminated. A specular reflection from one of the prisms forms the output-coupled beam, which is in turn reflected from a different portion of the grating to disperse any unwanted amplified spontaneous emission (ASE). The primary frequency-selective element is a Fabry–Perot étalon inserted into the cavity between the grating and the prisms. The étalon has a free spectral range of $1\ \mathrm{cm}^{-1}$ and modest finesse, yielding a bandwidth of $<0.04\ \mathrm{cm}^{-1}$ FWHM. The cavity length is ~ 30 cm which gives a longitudinal cavity-mode spacing of $0.016\ \mathrm{cm}^{-1}$, thereby enabling up to three cavity modes to be present within the étalon bandwidth. The oscillator is normally adjusted to favor a single cavity mode at the center of the étalon bandpass, with two much weaker longitudinal side modes being present. In practice, a combination of mode competition and thermal and mechanical instabilities results in shot-to-shot variations in the mode positions. Thus, the average spectral profile of the oscillator output resembles a series of mode peaks whose envelope is determined by the bandwidth of the étalon. Some gain narrowing may also occur, reducing the spectral intensity in the line wings. Such a narrow, multimode-envelope laser output has been observed in our laboratory using a pulsed spectrum analyzer (Burleigh PLSA3500).

The output from the oscillator is amplified twice in single-pass amplifiers, the latter of which is usually saturated. For the measurement of photoabsorption cross sections, however, the amplifier pump beams are attenuated to reduce the effects of ac Stark broadening in the Xe nonlinear medium. Nevertheless, some gain narrowing and chirping of the laser pulse is to be expected which will further modify the laser spectral output, although the relative frequency shifts involved are only of the order of 10^{-7}.[24] Spectral chirping may also occur in the frequency-doubling process as a result of the fact that the fundamental laser pulse is itself temporally asymmetric and chirped. The distortion of the temporal pulse shape due to the nonlinear response (proportional to the square of the instantaneous spectral intensity) thereby modifies the frequency distribution of the second harmonic.[25]

A similar frequency modification can occur in the four-wave mixing process. In particular, the two-photon-resonant process will exhibit the same type of sensitivity to the instantaneous phase of the fundamental radiation as occurs in second-harmonic generation. In addition, further modification of the VUV bandwidth may arise from ac Stark effects on the Xe energy levels, including broadening, shifting and asymmetry.

Thus, due to the complications described above, the VUV bandwidth is unlikely to be related simply to the fundamental laser bandwidths. Hepburn[26] has reported a VUV bandwidth of three times that of the input lasers ($0.16\ \mathrm{cm}^{-1}$ FWHM) for four-wave mixing in Hg and Mg vapor, once the tuning of the two-photon-resonant laser had been optimized. On the other hand, Yamanouchi and Tsuchiya[21] reported a VUV bandwidth of $0.06\ \mathrm{cm}^{-1}$ FWHM for 2PR-DF4WM in Sr vapor, not much greater than the input bandwidths. Our observed VUV bandwidths were intermediate between these values, varying significantly in the range $0.06–0.12\ \mathrm{cm}^{-1}$ FWHM according to the details of the particular experimental set-up adjustments.

In addition, it was found that ASE provided an unexpected means of instrumental distortion of the photoabsorption line shape. ASE from either dye laser, in combination with the other tuned beam, produced an untuned ASE pedestal in the generated VUV signal. Since the bandwidth of the VUV monochromator greatly exceeded that of the tuned component of the VUV signal, the broadband ASE VUV signal was favored disproportionately in the detection process, acting effectively as a scattered-light component. Thus, if the center of a narrow line were totally absorbed, the observed transmittance flattened off at a nonzero value, resulting in an underestimate of the peak photoabsorption cross section and a corresponding modification of the line shape.

In order to monitor the unpredictable instrumental bandwidth and eliminate the ASE problem, the following procedure was adopted. A narrow SR line, the $R_1(21)$ line from the (14,0) band, was chosen as a reference line. The oscillator strength for this line is well known from conventional spectroscopic measurements,[6] but independent knowledge of its predissociation linewidth was required for its full characterization. This was obtained by measuring the integrated absorptivity of the reference line for a range of O_2 pressures, yielding an experimental curve of growth.[27] A Voigt curve-of-growth analysis, using the known oscillator strength and a

Gaussian width Γ_G defined by the Doppler component, after correction for the effects of collision-induced broadening,[28,29] yielded a Voigt mixing parameter $a = \sqrt{\ln 2}\Gamma_L/\Gamma_G = 0.35$, implying a Lorentzian width Γ_L, due to predissociation, of 0.051 ± 0.007 cm^{-1} FWHM. Since equivalent width is independent of instrumental resolution,[27] this determination of the reference predissociation linewidth required no assumptions regarding the instrumental VUV bandwidth.

Once the reference line was characterized fully, it was scanned daily in order to optimize the experimental adjustments and determine the instrumental bandwidth. This was a difficult procedure. First, it was necessary to minimize the effects of ac Stark broadening by progressively reducing the dye-laser intensities until the apparent width of the reference line showed no intensity dependence. Second, it was essential to minimize ASE in the VUV signal. This was achieved by maximizing the apparent peak absorption of the reference line while iteratively adjusting the experimental system. These adjustments included: rotating the pump-beam line foci so as to be noncollinear with the laser beam; aligning the two laser beams into the Xe cell to maximize the efficiency of the 2PR-DF4WM process, thereby enabling operation at reduced laser intensities; and further attenuation of the pumping of the three dye-laser stages, as necessary. Following this system optimization, line-shape distortions due to ASE had been eliminated and it was possible to deduce a daily value for the VUV bandwidth using the least-squares fitting procedure described in Sec. III, together with the known strength and width parameters for the reference line. It was established that this bandwidth remained unaltered during the subsequent period of data taking. However, it was necessary to reoptimize the system daily, with a consequential change in bandwidth, unpredictable within the 0.06–0.12 cm^{-1} FWHM range.

As is apparent from the discussion above, it is difficult to define accurately the instrumental line shape *a priori*. Analyses of the reference line using a Gaussian profile to describe the shot-averaged instrumental line shape provided good fits to the experimental cross sections. Therefore, a Gaussian profile was assumed for the analysis of all measured cross sections.

B. Laser-induced fluorescence spectroscopy

The experimental protocol for LIFS has recently been described in detail,[13] so only the salient features and some important modifications will be discussed here. The O_2 B-state level is excited by single-photon absorption from an excited vibrational level of the O_2 $X\ ^3\Sigma_g^-$ ground state and is monitored by detecting the weak $B \rightarrow X$ fluorescence that competes with predissociation. Two laser beams, pump and probe, are required for the experiment. The pump-laser beam creates vibrationally excited O_2 by photolysis of O_3,[30] while the narrow-band probe-laser beam, temporally delayed with respect to the pump beam, is tuned in wavelength to excite the $B \leftarrow X$ absorption. All measurements were made at room temperature in a dilute mixture of O_3 in He at a total pressure in the range 20–30 Torr.

The probe-laser beam was generated by a dye laser (Lambda Physik LPD3000E) pumped by a XeCl excimer laser (Lambda Physik EMG102). When low powers were required, this dye laser was generally operated using only its oscillator and (attenuated) amplifier stages. A 3× beam-expanding telescope served to produce a collimated output beam which was further restricted by a 3 mm diameter aperture before entering the experimental cell. Two beam splitters between the laser and the cell directed portions of the excitation-laser beam to a monitor étalon, for verification of the laser-mode purity, and to an I_2 (LIF, $\lambda > 500$ nm) or Te_2 (absorption, $\lambda < 500$ nm) cell for wavelength calibration. For measurements of the SR (13,15), (13,16), and (14,16) bands, the frequency of the laser was doubled in a KDP crystal positioned between the beam splitters and the cell. Exalite 428 or Coumarin 120 dye solutions were used to generate the blue wavelengths for direct pumping of the SR (13,26), (13,27), and (14,26) bands, while Rhodamine 590 dye solution was used to generate the fundamental wavelengths for those bands requiring use of the doubling crystal. An intracavity étalon was used in the oscillator of the probe dye laser, which produced an (approximately Gaussian) instrumental bandwidth at the blue wavelengths in the range 0.04–0.05 cm^{-1} FWHM, as indicated both by the observed widths of the unblended peaks in the Te_2 absorption spectrum and by analysis of the SR absorption line shapes. The linewidth of the doubled laser was typically a factor of $\sqrt{2}$ larger than this, as verified by the observed (Doppler-corrected) widths of LIF peaks due to impurity OH absorptions in the O_3/He sample and by analysis of the SR absorption line shapes. Laser powers entering the cell were typically in the range 1–10 μJ, as required to minimize saturation broadening of the absorption lines. For the work reported here, the delay in the probe-laser pulse relative to the pump-laser pulse was in the range 1–10 μs, with the shortest delays favoring excitation from the higher ($v'' = 26$ and 27) vibrational levels of the O_2 X state.

The pump laser was the KDP-doubled output of a YAG-pumped dye laser (Quantel TDL-50), which provided a photolysis wavelength of 281 nm with pulse energies in the range 2–5 mJ. Although photolysis of O_3 is less efficient at this wavelength than at the excimer-laser-produced 248 nm used in previous work,[13] the pulse energy stability of the YAG-pumped system was found to be far superior in maintaining a uniform population of vibrationally excited O_2. The photolysis beam was apertured to 3 mm diameter, weakly focused through the cell, and precisely adjusted to counter-propagate collinearly with the probe beam, so as to maximize the LIF signal.

Fluorescence from the $B(v' = 13$ and $14)$ levels in the (13,3–6) and (14,3–6) emission bands was detected by a solar-blind photomultiplier through a MgF_2 window and an interference filter centered at 206 nm with a bandpass of 26 nm FWHM. A second photomultiplier with a blue-sensitive photocathode (R212), positioned at right angles to the first, simultaneously viewed the interaction region through a Suprasil window and a Wratten 18A filter (centered at 350 nm) with a bandpass of approximately 50 nm FWHM. Both the doubled pump beam and the probe beam were linearly polarized with the direction of polarization of the doubled ex-

citation beam and the photolysis beam orthogonal to the direction viewed by the solar-blind photomultiplier. In contrast, the polarization of the undoubled probe beam was in the direction viewed by this photomultiplier. However, no spatial inhomogeneity was observed in the detected fluorescence, such as might have been produced by alignment of the emitting O_2 with respect to the probe-laser polarization direction.

The amplified outputs of the photomultipliers were detected by boxcar integrators, whose digitized outputs were transferred to a laboratory computer after each laser shot, together with the signals from the monitor étalon, the wavelength calibration cell, and the probe-laser power meter. The computer also controlled the wavelength of the probe laser. Both lasers were operated at a repetition rate of 10 Hz and the probe laser was stepped in wavelength by 0.005–0.010 cm^{-1} after the accumulation of 10, 20, or 30 laser shots. Scans typically ranged from 6 cm^{-1} to 30 cm^{-1} in extent. All scans were wave-number calibrated using the I_2 (Ref. 31) or Te_2 (Ref. 32) reference lines, yielding accuracies of 0.013 cm^{-1} and 0.008 cm^{-1} for the doubled and undoubled probe beams, respectively.

The variation in 206 nm fluorescence intensity as a function of probe-laser wavelength constitutes the $B \leftarrow X$ absorption spectrum observed by LIFS. Prior to analysis, the raw fluorescence intensity at each wavelength was linearly corrected for small ($<10\%$) relative changes in the probe-laser power that may have occurred during the course of a scan and any wavelength-independent intensity contribution was subtracted. As discussed previously,[13] the absorption line shapes are subject to saturation broadening and (at much higher probe powers than used here) to a depletion in the population of the absorbing level of the X state of O_2. Therefore, the line shapes of selected rotational features in each of the SR bands were monitored as a function of probe-laser energy. These empirical changes in line shape were fully consistent with those expected from the measured (spatially averaged) laser energy densities and the stimulated emission coefficients of the various bands.[13] All measurements reported here were obtained with probe-laser energies that were sufficiently low that the required corrections for residual saturation broadening were $<10\%$ of the Lorentzian component in the Voigt line shape.

C. Vacuum-ultraviolet Fourier-transform spectroscopy

The spectral region of application of Fourier transform spectroscopy (FTS) has been extended into the VUV at Imperial College by means of an interferometer designed specifically to work at these shorter wavelengths.[33] The cut-off of the prototype interferometer was set at about 180 nm by the fused-silica beam splitter employed, but the substitution of a MgF_2 beam splitter has increased the range to about 140 nm.[34] The limiting resolution of this instrument is 0.025 cm^{-1} FWHM, more than sufficient to resolve the Doppler widths of the lines of the SR bands.

The attainment of a good signal-to-noise ratio (S/N) in high-resolution absorption spectroscopy is much more demanding than in emission spectroscopy because of the noise characteristics of the technique. Every spectral element seen by the detector contributes to the noise in the interferogram, and if the noise is "white" (independent of frequency) it is distributed evenly through the spectrum by the Fourier transform. In the UV, the dominant noise is photon noise, proportional to the square root of the signal. The S/N in the spectrum for a quasi-continuum is proportional to $(\phi t/W)^{1/2}$, where ϕ is the detected photon flux in photons $s^{-1}\,nm^{-1}$, t (s) is the total integration time and W (nm) is the bandwidth. There are, therefore, two requirements for high S/N: a background continuum source of high photon flux, and some means of limiting the spectral bandwidth to the region of interest to avoid all unnecessary contributions to the photon noise. Ordinary laboratory continuum sources (the high pressure Xe arc, the deuterium lamp and the argon mini-arc) fall off rapidly in radiance below 200 nm. The only alternative is synchrotron radiation. As this is intrinsically very broadband, the bandwidth must be limited either by optical filters or by a monochromator. Interference filters are inflexible and inefficient in the VUV, so the preferred option is a monochromator. Ideally, this should be a double monochromator with zero net dispersion, because the spread of angles passing through the interferometer from a single monochromator leads to small wavelength shifts and phase problems across the pass band.

Recent measurements of absorption cross sections of the $\delta(0,0)$ and $\beta(7,0)$ bands of NO by FTS at IC (Ref. 35) demonstrated these problems. With the continuum source used (a 500 mA positive-column discharge in hydrogen, similar to, but brighter than, a commercial deuterium lamp) the S/N obtainable for the $\delta(1,0)$ band at 183 nm was inadequate. The 0.3 m Czerny-Turner monochromator used as predisperser generated, as anticipated, uncomfortably large phase variations across the pass band. It was therefore decided to attempt to use synchrotron radiation as the background continuum for the absorption measurements on the SR bands. The particular choice of the Photon Factory was dictated by the availability on one of the beam lines of a zero-dispersion monochromator, normally used as the predisperser for the 6.65 m off-plane Eagle spectrograph of Dr. K. Ito,[36] who collaborated with us on the project.

Following shipment of the IC VUV FT spectrometer to Japan, the instrument was set up downstream of the monochromator. The rectangular beam normally falling on the entrance slit of the 6.65 m spectrograph was intercepted by a cylindrical mirror that focused it as an approximately circular patch of diameter 2 mm on the circular entrance aperture of the interferometer, after passing through an absorption cell 78 mm long. The pressure of O_2 was set at a value between 0.6 Torr and 10 Torr, depending on the spectral region observed. The bandwidth of the predisperser was normally set at 2.5 nm. Alignment of the interferometer axis with the synchrotron beam reflected by the cylindrical mirror proved to be a difficult task; good fine adjustments to position and rotation were not available during the limited period at Photon Factory, and the problems were accentuated by the fact that the VUV beam emerging from the double-grating monochromator was not coincident with the visible light beam when the gratings were turned to zero order. The possibility of small misalignments, or drifts in alignment, was a source

of some anxiety and is discussed further in Sec. III C. Most spectra were taken at a resolution of 0.06 cm^{-1} FWHM, but for some spectra the resolution was set at 0.12 cm^{-1} FWHM in order to maximize the S/N. This latter value matches the Doppler width for O_2 at room temperature. It should be noted that the S/N is proportional to the resolution if all other factors are held constant; if the maximum allowable entrance aperture is used and filled, the S/N in the photon-noise limit actually scales with the 3/2 power of the resolution. Thus, a factor of 2 in resolution requires a factor of 8 in integration time to recover the same S/N.

The synchrotron flux was attenuated by two mirror and two grating reflections plus transmission through four uncoated MgF_2 windows before entering the interferometer, where it underwent six further mirror reflections, one further window transmission, and a reflection/transmission at the beam splitter. The photon flux was estimated to be about 10^{10} photons nm^{-1} s^{-1} at the entrance to the interferometer, and about 10% of this on the detector (an R1220 photomultiplier with a solar-blind photocathode and a MgF_2 window). The S/N is proportional to the modulation efficiency of the interferogram as well as to the square root of the photon flux, and both modulation and mirror reflectivities fall off rather steeply with decreasing wavelength in the VUV. It was necessary to integrate for many hours to obtain a good S/N. The integration was performed by coadding interferograms (each of which involved a scan time of 6–8 min) in piles of 30 or so. The individual piles were coadded into larger piles whenever inspection showed no sign of a drift in phase between piles; otherwise each pile was transformed and phase-corrected separately, and the spectra were subsequently coadded. Typically, two or three spectra taken over two 12 h days went into producing a spectrum 2.5 nm wide at a resolution of 0.06 cm^{-1} with a S/N in the continuum of around 40.

In addition to the SR bands, we also measured absorption in NO from 190 nm down to 160 nm with a resolution of 0.06 cm^{-1}, except for the bands of shortest wavelength for which the resolution was 0.12 cm^{-1}.

III. ANALYSIS

In the general case, spanning the range of experimental conditions represented by the three experiments described in Sec. II, three broadening processes may make significant contributions to the instrument-free SR photoabsorption line shape.[37] First, for distances not too far from the line centers, the predissociation line shape for unperturbed lines may be taken as Lorentzian.[1,2,19] Second, for O_2 pressures that are not too high, the collisional line shape may also be described with sufficient accuracy by a Lorentzian.[28,29] Thus, the total Lorentzian linewidth is $\Gamma_L=\Gamma_p+\Gamma_c$, where Γ_p and Γ_c are the predissociation and collisional linewidths, respectively. For the most part, the O_2 pressures are low enough for collisional broadening to be neglected, but the VUVLS measurements for the weaker lines of higher rotational quantum number were taken at pressures up to 100 Torr, resulting in collisional linewidths up to 0.03 cm^{-1} FWHM.[28,29] Third, it is necessary to consider the Doppler component of the line shape which has a Gaussian profile (Doppler width Γ_D $\approx$0.12 cm^{-1} FWHM at room temperature). Thus, the Voigt profile, a convolution of Lorentzian and Gaussian line shapes, may be used to describe each rotational line in the analysis procedure:[38] the Gaussian linewidth component Γ_G is given by the well defined Doppler width, while the Lorentzian linewidth component Γ_L is the sum of predissociation and collisional components. For most of the results presented here, the very high experimental resolution, together with the relatively low predissociation linewidths, enabled full resolution of individual rotational and fine-structure lines, allowing a simple Voigt line shape fitting procedure to be employed, independent of any band-model assumptions.

A. VUVLS analysis

In the analysis of the VUVLS results, a nonlinear least-squares procedure, in which a synthetic cross section based on the Voigt line shape was fitted to the measured photoabsorption cross section, was used to determine independently the position, oscillator strength, and Lorentzian linewidth component for each rotational line in a particular scan. In a few cases, when the resolution of low-rotation F_2 and F_3 components was insufficient to enable independent fitting, the ratio of the strengths of these two fine-structure lines was held fixed at a readily calculable value[39] in the fitting procedure. In a few other cases, it was necessary to correct for the contributions of weak lines from other SR bands which were obscured completely by the lines of interest. The pseudo-continuum underlying the SR bands, comprising the wings of more distant lines, was represented by a quadratic polynomial in wave number, the coefficients of which were also determined in the fitting procedure. Normally, a constant or linear background was sufficient to obtain a good fit to the measured cross section. The Gaussian instrumental bandpass function was included explicitly in the synthetic cross section, through a convolution with the calculated transmittance spectrum, reproducing the small degradation in cross section due to the finite instrumental resolution.

B. LIFS analysis

A somewhat similar procedure was also followed in the analysis of the LIFS line shapes. However, a significant difference arises in that the relative fluorescence intensities are not only directly proportional to the photoabsorption cross sections, but are also inversely proportional to the lifetimes of the emitting levels. Thus, there is a correlation between the fluorescence intensity and the linewidth of the Lorentzian component of the Voigt line shape that describes each feature in the LIF excitation spectrum.[13] The linewidth Γ_G of the Gaussian component of the Voigt line shape was taken as a combination, in quadrature, of the instrumental width (Sec. II B) and the 300 K Doppler width of the absorption at the probe-laser wavelength.[40] Since much longer absorption wavelengths were used to produce the B-state levels in the LIFS studies, this Doppler contribution was relatively small in comparison with that applying to the two other experimental techniques, amounting to only 0.05 cm^{-1} FWHM and 0.09 cm^{-1} FWHM at the blue and frequency-doubled probe-laser wavelengths, respectively. The value of Γ_G was taken to be constant for all features within a given scan.

The line shapes for each of the three fine-structure components of a given LIFS rotational line multiplet were analyzed simultaneously, with the ratios of their individual photoabsorption line strengths held constant at the calculated values.[41] A nonlinear least-squares fit of the three coupled Voigt line shapes to the observed LIF spectrum yielded values for the line center and Lorentzian linewidth Γ_L of each of the three fine-structure components. In addition, values for the common background intensity of the LIF spectrum in the region of the multiplet and for the average relative absorption cross section of the multiplet were also determined in the fit. The relative magnitudes obtained for this latter parameter among the rotational lines in a given absorption band were found to be consistent with those calculated for a 300 K rotational temperature. The values of Γ_L obtained from these fits, following a small correction for saturation broadening (Sec. II B), are reported here as the predissociation level widths.

C. VUVFTS analysis

The peak absorption for the strong lines in the VUV FT spectra was well over the linear limit. The transmittance spectra were converted to absorbance spectra by taking the logarithm and manually fitting a smooth curve to the continuum between regions of strong absorption. It should then have been possible to fit a Voigt profile to each line in the manner described in Sec. III A for the VUVLS results. The fitting procedure used was part of the GREMLIN suite of programs written by J. W. Brault specifically for the analysis of FT spectra.[42] Compared with the calculated Doppler width of 0.12 cm^{-1} FWHM, the instrumental width should be negligible for the spectra taken with 0.06 cm^{-1} resolution, and for those taken at 0.12 cm^{-1} the instrumental contribution can be allowed for by convolving an appropriate sinc function with the Voigt. Although the instrumental function should properly be applied to the transmittance spectrum rather than the absorbance, checks showed that there was a negligible difference to the final fit over the range of absorbance recorded here.

The fitting of the lines showed two anomalies. First, the Doppler component of the best-fit Voigt function had a FWHM in the range 0.15–0.17 cm^{-1}, significantly greater than 0.12 cm^{-1}. Clamping the Doppler width at the expected value gave a worse fit to the line profiles. Second, since the narrowest lines in the high-resolution spectra had a measured FWHM of about 0.23 cm^{-1}, all the lines should have been fully resolved even in the lower-resolution (0.12 cm^{-1}) runs. The measured widths in both sets should therefore have been similar, whereas in fact they were on average greater by some 0.03 cm^{-1} in the lower-resolution spectra.

In an attempt to throw some light on these anomalies, we compared the NO absorption spectra taken at the Photon Factory with those taken previously at Imperial College with the FT spectrometer and a hydrogen discharge continuum background.[35] The intrinsic line shape of the the $\delta(0,0)$ and $\beta(7,0)$ bands of NO is almost pure Doppler. Whereas in the previous spectra, the Doppler widths were, as expected, about 0.12 cm^{-1} FWHM for the room-temperature measurements, the Photon Factory NO spectra appeared to have anomalous Gaussian widths similar to those in the O_2 spectra.

Comparison of the VUVFTS and VUVLS linewidths for a dozen well isolated O_2 lines showed that the FTS lines were consistently broader, on average by 0.06 cm^{-1} for the higher-resolution spectra and 0.09 cm^{-1} for the lower-resolution spectra. Taken together with the internal evidence, this suggests at first sight that the intrinsic resolution of the Photon Factory FT spectra was, for some reason, lower than the value determined by the length of the interferometer scan. We consider this explanation to be unlikely for two reasons. First, a broad instrumental function has less effect on a wide line than on a narrow one, whereas the VUVFTS-VUVLS differences for lines ranging in width from under 0.2 to 0.3 cm^{-1} FWHM (in the VUVLS spectra) show no dependence on linewidth. Second, to account for the observed broadening we have to postulate instrumental functions with widths of order 0.18 cm^{-1} and 0.21 cm^{-1} FWHM for the "high" and "low" resolution spectra, respectively. Convolution of the VUVLS spectra with sinc functions of these widths generates significant ringing, which is simply not observed in the VUVFTS spectra, so it is necessary to postulate further a smooth tapering off of the interferogram rather than a sharp termination. In that case the interferograms would be effectively truncated before the end of the shorter scans, and the additional scan length of the high-resolution interferograms would have no effect.

A possible explanation of the discrepancy is the "illumination shift" discussed by Learner and Thorne:[43] changes in the way in which the entrance aperture is illuminated affect the angular distribution of rays through the interferometer and result in small wave-number shifts. Given the inherent spatial instabilities of the synchrotron beam, the long optical path (two mirrors and two gratings) guiding it into the interferometer, the difficulties of aligning the latter and the many hours of coadding, it would indeed be surprising if there were not small illumination shifts. We have some evidence for them: if the separate piles of interferograms that make up one final spectrum are transformed separately, there are found to be small but significant wave-number shifts (0.01 to 0.03 cm^{-1}) between the piles in most cases. Unfortunately, the problem cannot be solved by simply correcting for these shifts because the lines within each pile are still anomalously wide, presumably due to shifts occurring during the accumulation of the pile. The maximum size of an illumination shift depends on the size of the entrance aperture and hence on the resolution. Illumination shifts of up to 0.03 cm^{-1} for the high-resolution, and somewhat more for the lower-resolution spectra would appear to be reasonable in the prevailing experimental conditions. However, the problem is that coadding a bunch of Voigt lines 0.2 cm^{-1} wide with displacements of up to 0.05 cm^{-1} or so does not broaden them enough to account for the observed widths.

We have to conclude that we do not have a satisfactory quantitative explanation for the anomalous widths of the VUVFTS lines. Since this problem has never before arisen over many years of use of the instrument on both emission and absorption spectra, it does appear to be related in some

way to the method of use at the Photon Factory. It has the unfortunate consequence that no reliable predissociation broadening parameters can be derived from the VUVFTS spectra without an independent measure of the effective instrumental resolution, although line strengths and relative wave numbers should not be affected.

IV. RESULTS AND DISCUSSION

Before proceeding further, it is pertinent to summarize some of the expected inherent advantages and disadvantages of each experimental technique. Both the VUVLS and VUVFTS techniques result in the measurement of photoabsorption cross sections, enabling absolute oscillator strengths, as well as predissociation linewidths, to be obtained from the measurements using the fitting technique described in Sec. III. VUVFTS has the advantage of simultaneous acquisition of the complete spectrum, but suffers from the need for a bright, controlled spectral-width continuum source in order to optimize the S/N. At present, this requires a synchrotron source. Both the VUVLS and LIFS methods require detailed, small step-size scans over the spectral features of interest and suffer from power-dependent bandwidths which must be controlled carefully. However, it is relatively easy to balance the conflicting requirements for a good S/N and a minimal power dependence of the bandwidth using the VUVLS method, since only moderate source intensity is required against which to measure the photoabsorption cross sections, whereas the LIF signal and S/N are directly related to the laser intensity. The LIFS technique has several unique advantages. First, as has been noted in Sec. III B, the photon energy is minimized by selecting a high vibrational level in the ground state as the origin of the absorbing transition. This, in turn, minimizes Doppler broadening of the transition, which scales directly with photon energy. Second, as mentioned in Sec. I, the ability to choose the lower-state level in the excitation allows a flexibility in controlling the separation of the fine-structure components in the absorption spectrum, which reflect the relative differences in the fine-structure levels of the B and X states. Third, the fluorescence intensity of the excited B-state level is inversely proportional to its lifetime. Thus, as we have noted in Sec. III B, the observed relative fluorescence intensities of the SR multiplets, in addition to their absorption line shapes, serve as another, more sensitive measure of their relative lifetimes. Finally, each B-state level can be accessed by absorption from two or more ground-state vibrational levels with different absorption cross sections, thus providing an important check on the influence of saturation broadening, or of unresolved line components, on the apparent line shape associated with the level. Overall, the high resolution provided by each experimental technique is expected to result in an important advance over all previous conventional measurements of SR linewidths.

We illustrate the observed characteristics of the different high-resolution experimental techniques in Fig. 1 which shows comparable measured and fitted spectra over the wave-number regions of the $B\ ^3\Sigma_u^-(v=14, N=12)$ fine-structure levels. Both the VUVLS and VUVFTS measurements are given in the form of effective photoabsorption cross sections σ for the (14,0) $R(11)$ fine-structure triplet, while the LIFS measurements are given in the form of relative fluorescence intensities I_f measured following excitation of the (14,16) and (14,26) $R(11)$ fine-structure triplets. The differential wave-number scales of each spectrum are identical, allowing meaningful visual comparisons of apparent linewidths. A comparison of the two photoabsorption spectra indicates that the VUVLS cross section has a greater S/N and a higher resolution, as evidenced by greater peak cross sections and smaller apparent linewidths. This lower effective resolution for the VUVFTS cross section is unexpected, as has been discussed in Sec. III C. While the LIF spectra have a smaller S/N, the greater flexibility allowed by excitation of vibrationally excited ground-state levels is evident in the increased separation of the $R_2(11)$ and $R_3(11)$ components when compared with the photoabsorption spectra. In addi-

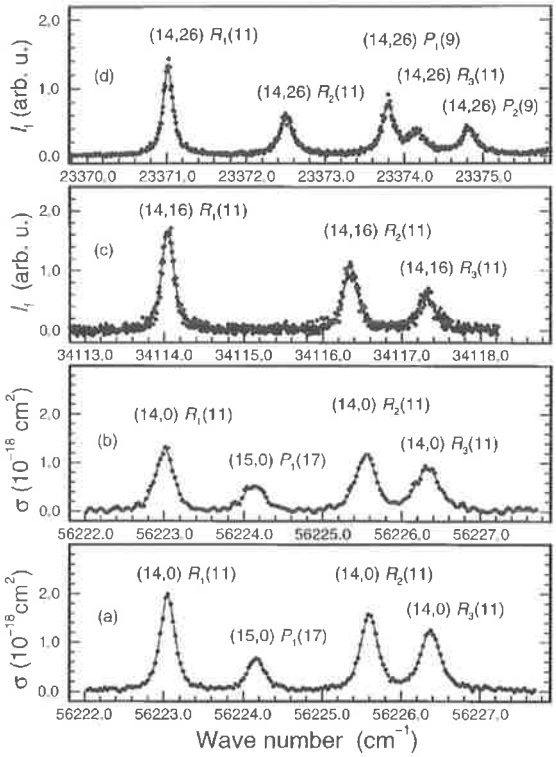

FIG. 1. Experimental scans (points) and fitted spectra (lines) over the region of the $B\ ^3\Sigma_u^-(v=14, N=12)$ fine-structure levels. (a) VUVLS cross section for (14,0) $R(11)$ triplet; Doppler width 0.12 cm^{-1}; instrumental resolution 0.10 cm^{-1}; apparent width for F_1 component 0.21 cm^{-1}; Lorentzian width 0.11 cm^{-1}. (b) VUVFTS cross section for (14,0) $R(11)$ triplet; Doppler width 0.12 cm^{-1}; instrumental resolution 0.19 cm^{-1}; apparent width for F_1 component 0.24 cm^{-1}; Lorentzian width 0.10 cm^{-1} (however, see the text). (c) LIFS scan for (14,16) $R(11)$ triplet; Doppler width 0.07 cm^{-1}; instrumental resolution 0.07 cm^{-1}; apparent width for F_1 component 0.18 cm^{-1}; Lorentzian width 0.12 cm^{-1}. (d) LIFS scan for (14,26) $R(11)$ triplet; Doppler width 0.05 cm^{-1}; instrumental resolution 0.05 cm^{-1}; apparent width for F_1 component 0.15 cm^{-1}; Lorentzian width 0.11 cm^{-1}. (All widths are FWHM values.) Each scan covers a similar range of wave numbers, but the lower transition energies for the LIFS scans result in smaller Doppler widths, and correspondingly smaller apparent linewidths.

tion, it is clear from Fig. 1 that the relative intensities of the fine-structure components vary much more widely in the LIF spectra than in the photoabsorption spectra. As discussed above, this is a consequence of the dependence of the LIF signal on the predissociation lifetime and indicates, more directly than do the apparent (total) relative linewidths, that the predissociation linewidths vary significantly with the fine-structure component, in the order $\Gamma_p(F_1)<\Gamma_p(F_2)<\Gamma_p(F_3)$. Of particular interest is a comparison of the apparent linewidths for the $R_1(11)$ transitions from the LIF and photoabsorption spectra. The LIFS linewidths are smaller for two reasons: smaller instrumental bandwidth and smaller Doppler width associated with the lower transition energy. The narrowest $R_1(11)$ line (apparent width 0.15 cm^{-1} FWHM) occurs for the (14,26) LIF spectrum which has the lowest transition energy ($\sim$23 000 cm^{-1}, Doppler width 0.05 cm^{-1} FWHM), followed by the (14,16) LIF spectrum (apparent width 0.18 cm^{-1} FWHM, transition energy $\sim$34 000 cm^{-1}, Doppler width 0.07 cm^{-1} FWHM), and the VUVLS and VUVFTS results for the (14,0) transition (apparent widths 0.21 cm^{-1} and 0.24 cm^{-1} FWHM, respectively, transition energy $\sim$56 000 cm^{-1}, Doppler width 0.12 cm^{-1} FWHM). Nevertheless, when analyzed using the procedures outlined in Sec. III with appropriate instrumental functions, each spectrum implies a consistent Lorentzian F_1 width of $\sim$0.11 cm^{-1} FWHM. Synthetic spectra fitted to each set of measurements, shown in Fig. 1, are seen to accurately reproduce the experimental results. However, we note here that, in order to obtain the fitted VUVFTS cross section in Fig. 1, it was necessary to vary the instrumental resolution from its nominal value. A resolution of 0.19 cm^{-1} FWHM resulted in VUVFTS predissociation linewidths and oscillator strengths in reasonable agreement with the VUVLS values for all three fine-structure components, in agreement with the general discussion in Sec. III C. It may be concluded from this example illustrated in Fig. 1 that, despite the diverse characteristics of the different experimental methods, each technique is capable of producing reliable predissociation linewidths, provided that the instrumental functions are well controlled and monitored. In the case of the VUVFTS measurements, the unexpected and unprecedented degradation of the effective resolution resulted in a lack of monitoring, preventing the independent deduction of a reliable set of linewidths.

The predissociation widths determined for all rotational and fine-structure levels of the B state with $v=13$ and 14, using the VUVLS and LIFS experimental techniques, are shown in Figs. 2 and 3 and are listed in Tables I and II, respectively. The results are given as a function of the B-state rotational quantum number N, where $N=J-1$, $N=J$, or $N=J+1$ for the F_1, F_2, or F_3 fine-structure levels, respectively. Unless indicated otherwise, each tabulated level width represents the average of values determined separately for $P(N+1)$ and $R(N-1)$ transitions terminating on the same B-state level.[44] In a few cases, particularly for lines near the band heads terminating on levels of low rotational quantum number, widths measured for satellite-branch lines have been included in the averages. The listed uncertainties in the level widths include statistical uncertainties reflecting

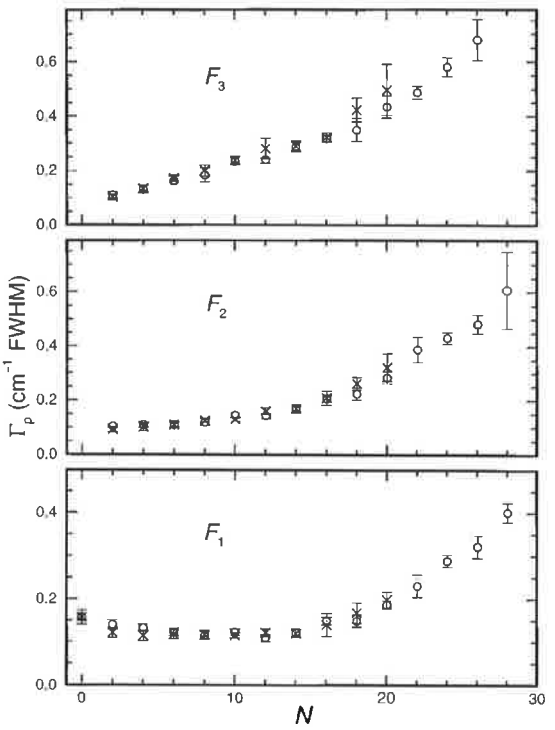

FIG. 2. Measured fine-structure-specific predissociation level widths for $B\ ^3\Sigma_u^-(v=13)$ as a function of B-state rotational quantum number N. Each point represents the average obtained from separate P- and R-branch measurements using the VUVLS (circles) and LIFS (crosses) techniques.

the S/N of the measurements and the sensitivity of the least-squares fitting procedure, together with a contribution reflecting incomplete knowledge of the instrumental linewidth. Uncertainty due to the instrumental contribution is smaller in the case of the LIFS results, but this is counterbalanced by an increased uncertainty due to smaller S/N. The VUVLS results cover a greater range of rotation, up to $N=28$ for $v=13$ and $N=30$ for $v=14$, primarily because of the larger S/N and the fact that measurements have been made using a greater range of O_2 pressures. The VUVLS measurements taken at pressures from 10 Torr to 100 Torr, the maximum employed, have been corrected for collisional broadening (0.2 cm^{-1}/atm),[28,29] as indicated in Tables I and II. The LIFS results require no such correction since they were taken at lower pressures.

There is excellent agreement between each set of results: only in the case of the $v=14$, F_1, $N=26$ level do the VUVFTS and LIFS linewidths differ by more than the combined experimental uncertainties. This agreement supports the applicability of these experimental techniques to the measurement of narrow linewidths, indicates that the calibrations of the instrumental resolutions have been performed properly, and supports the reliability of the predissociation level widths presented here. The complexity of the rotational and fine-structure dependence of the $B(v=13$ and 14) level widths is clearly evident from Figs. 2 and 3. The individual level widths vary over an order of magnitude, from

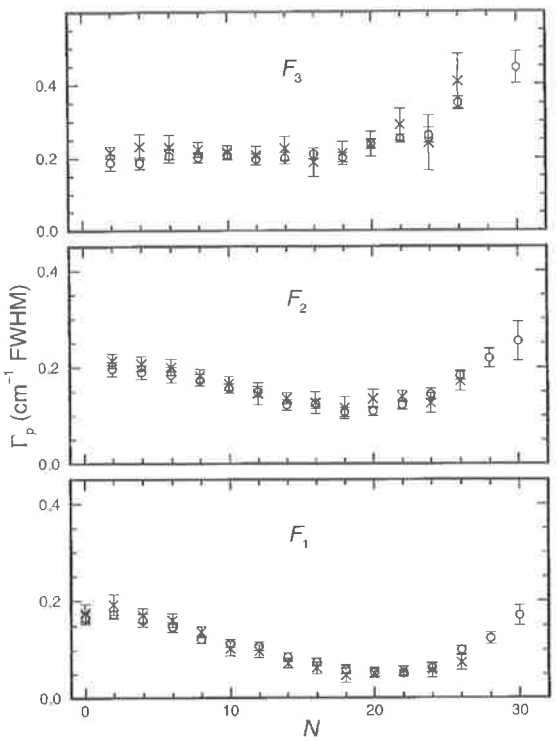

FIG. 3. Measured fine-structure-specific predissociation level widths for $B\ ^3\Sigma_u^-(v=14)$ as a function of B-state rotational quantum number N. Each point represents the average obtained from separate P- and R-branch measurements using the VUVLS (circles) and LIFS (crosses) techniques.

~ 0.05 cm^{-1} FWHM for $v=14$, F_1, $N\approx 20$, to ~ 0.6 cm^{-1} FWHM for $v=13$, F_3, $N=26$. While there is an essentially monotonic increase in level width with rotation for the F_2 and F_3 levels with $v=13$ and the F_3 levels for $v=14$, the remaining fine-structure levels at first decrease in width for increasing rotation, and then increase, passing through the minima near $N=10$ for F_1, $v=13$; $N=20$ for F_2, $v=14$; and $N=22$ for F_1, $v=14$. This general behavior is in good agreement with the predissociation-model predictions of Lewis *et al.*[5] In addition, although, for the reasons discussed in Sec. III C, we are unable to report quantitative VUVFTS linewidths, VUVFTS cross sections analyzed using the nominal instrumental resolution yield widths displaying the same rotational and fine-structure trends as in Figs. 2 and 3.

Prior to this work, there had been very few measurements of fine-structure-specific predissociation level widths for $B(v=13$ and $14)$, none of which was performed at high instrumental resolution. Lewis *et al.*[5] analyzed the photoabsorption cross sections of Yoshino *et al.*,[12] obtaining a few fine-structure-specific widths for $v=13$, $N=18-26$, while Lewis *et al.*[8] reported a few low-resolution fine-structure widths for $v=14$. It is clear from an inspection of Figs. 17 and 18 of Lewis *et al.*[5] that their[5,8] results are insufficient to establish the rotation and fine-structure dependence of the predissociation widths for these narrow vibrational levels. The present study rectifies this deficiency comprehensively,

TABLE I. Measured fine-structure-specific predissociation level widths for $B\ ^3\Sigma_u^-(v=13, N)$, in cm^{-1} FWHM.

Level	N	VUVLS	LIFS
F_1	0	0.157±0.008	0.157±0.017
	2	0.139±0.011	0.121±0.012
	4	0.132±0.008	0.114±0.012
	6	0.122±0.009	0.117±0.010
	8	0.114±0.009	0.116±0.011
	10	0.122±0.008	0.115±0.006
	12	0.109±0.008	0.121±0.009
	14	0.121±0.009	0.119±0.009
	16	0.149±0.009	0.140±0.027
	18	0.149±0.014[a]	0.168±0.024
	20	0.187±0.010	0.199±0.019
	22	0.231±0.026[b]	
	24	0.289±0.014[c]	
	26	0.322±0.026[c]	
	28	0.401±0.022[c]	
F_2	2	0.103±0.007	0.092±0.009
	4	0.109±0.010	0.100±0.014
	6	0.108±0.011	0.109±0.009
	8	0.118±0.012	0.125±0.007
	10	0.144±0.009	0.130±0.007
	12	0.143±0.009	0.159±0.013
	14	0.168±0.011	0.169±0.015
	16	0.206±0.012	0.209±0.026
	18	0.224±0.022[a]	0.262±0.023
	20	0.284±0.022[a]	0.322±0.052
	22	0.388±0.047[b]	
	24	0.431±0.022[c]	
	26	0.483±0.034[c]	
	28	0.608±0.141[a,c]	
F_3	2	0.110±0.011	0.102±0.010
	4	0.129±0.014	0.134±0.013
	6	0.162±0.017	0.171±0.013
	8	0.183±0.025	0.199±0.020
	10	0.233±0.012	0.237±0.014
	12	0.239±0.013	0.280±0.037
	14	0.286±0.017	0.288±0.021
	16	0.316±0.013	0.321±0.018
	18	0.348±0.042[a]	0.422±0.044
	20	0.433±0.041[a]	0.496±0.094
	22	0.486±0.024[a,c]	
	24	0.580±0.034[c]	
	26	0.678±0.075[c]	

[a]Determined from R-branch line only.
[b]Determined from P-branch line only.
[c]Corrected for collisional broadening.

providing a complete set of fine-structure-specific predissociation level widths for $B(v=13$ and $14)$.

V. CONCLUSIONS

In a comparative study using an array of state-of-the-art high-resolution spectroscopic techniques, the fine-structure and rotation dependencies of the predissociation of the O_2 $B\ ^3\Sigma_u^-(v=13$ and $14)$ levels have been characterized completely for the first time. The measurements presented here are the first to have been performed at high resolution for these levels and represent a significant advance on previous knowledge.[5] In combination with similar measurements for other vibrational levels, the present fine-structure-specific results will enable significant refinements in the parameters of

TABLE II. Measured fine-structure-specific predissociation level widths for $B\ ^3\Sigma_u^-(v=14, N)$, in cm^{-1} FWHM.

Level	N	VUVLS	LIFS
F_1	0	0.165±0.012[a]	0.175±0.018
	2	0.172±0.008	0.192±0.021
	4	0.160±0.013	0.170±0.014
	6	0.146±0.010	0.160±0.014
	8	0.121±0.008	0.136±0.011
	10	0.113±0.008	0.102±0.015
	12	0.107±0.009	0.097±0.013
	14	0.085±0.009	0.072±0.010
	16	0.074±0.008	0.062±0.013
	18	0.059±0.009	0.047±0.015
	20	0.053±0.009	0.051±0.009
	22	0.051±0.007[b]	0.056±0.010
	24	0.062±0.009[c]	0.057±0.016
	26	0.099±0.008[c]	0.073±0.015
	28	0.123±0.012[c]	
	30	0.170±0.020[b,c]	
F_2	2	0.196±0.015	0.213±0.015
	4	0.189±0.014	0.207±0.015
	6	0.184±0.016	0.200±0.017
	8	0.173±0.012	0.182±0.013
	10	0.156±0.010	0.166±0.014
	12	0.149±0.011	0.145±0.023
	14	0.122±0.011	0.136±0.011
	16	0.124±0.010	0.127±0.023
	18	0.107±0.010	0.116±0.023
	20	0.109±0.010[a]	0.135±0.019
	22	0.122±0.009[b]	0.139±0.012
	24	0.144±0.011[c]	0.126±0.020
	26	0.183±0.010[c]	0.171±0.020
	28	0.218±0.019[b,c]	
	30	0.253±0.040[b,c]	
F_3	2	0.186±0.022	0.215±0.016
	4	0.185±0.016	0.230±0.034
	6	0.205±0.019	0.229±0.033
	8	0.200±0.014	0.222±0.020
	10	0.207±0.013	0.215±0.018
	12	0.195±0.015	0.206±0.026
	14	0.198±0.015	0.225±0.033
	16	0.210±0.015	0.186±0.039
	18	0.200±0.013	0.211±0.032
	20	0.237±0.013	0.236±0.034
	22	0.251±0.011	0.289±0.044
	24	0.261±0.020[c]	0.239±0.076
	26	0.349±0.016[c]	0.406±0.076
	30	0.443±0.044[b,c]	

[a]Determined from P-branch line only.
[b]Determined from R-branch line only.
[c]Corrected for collisional broadening.

the standard model[1,2,5] for predissociation of the B state, resulting in greatly improved predictive capabilities and more reliable photochemical models of the terrestrial atmosphere. Although it was not possible to determine quantitative linewidths using the VUVFTS technique, the degree of agreement between the linewidths measured using the VUVLS and LIFS techniques is satisfying and gives confidence in the applicability of the experimental methods and the reliability of the results. However, the high-resolution performance provided by each technique was achieved at the cost of considerable experimental complexity and difficult adjustments and calibrations. In particular, each experimental technique suffers, to a greater or lesser extent, from ill definition of the instrumental resolution which must be carefully controlled and monitored. Further research into the detailed instrumental line shapes is warranted.

ACKNOWLEDGMENTS

The collaborative aspects of this research have been partially supported by reciprocal U.S.-Australian Cooperative Research Grants provided by the National Science Foundation (U.S.) and the Department of Industry, Technology and Commerce (Australia). The measurements at SRI International were partially supported by grants from the Atmospheric Sciences Division of NSF and from the Stratospheric Chemistry Division of NASA. The measurements at the Photon Factory were supported in part by a NSF Division of Atmospheric Sciences Grant No. ATM-91-16552 to Harvard College Observatory, and by the NASA Upper Atmospheric Research Program under Grant No. NAG5-484 to the Smithsonian Astrophysical Observatory. We also acknowledge the support of the Paul Instrument Fund of the Royal Society for the development of the VUV-FT spectrometer. The FTS measurements were made with the approval of the Photon Factory Advisory Committee (94G367). K.Y. thanks the Japan Society for the Promotion of Science for support.

[1] P. S. Julienne and M. Krauss, J. Mol. Spectrosc. **56**, 270 (1975).
[2] P. S. Julienne, J. Mol. Spectrosc. **63**, 60 (1976).
[3] M. Nicolet and P. Mange, J. Geophys. Res. **59**, 15 (1954).
[4] K. Minschwaner, G. P. Anderson, L. A. Hall, and K. Yoshino, J. Geophys. Res. **97**, 10103 (1992).
[5] B. R. Lewis, S. T. Gibson, and P. M. Dooley, J. Chem. Phys. **100**, 7012 (1994).
[6] B. R. Lewis, L. Berzins, and J. H. Carver, J. Quant. Spectrosc. Radiat. Transfer **36**, 209 (1986).
[7] K. Yoshino, D. E. Freeman, J. R. Esmond, and W. H. Parkinson, Planet. Space Sci. **31**, 339 (1983).
[8] B. R. Lewis, L. Berzins, J. H. Carver, and S. T. Gibson, J. Quant. Spectrosc. Radiat. Transfer **36**, 187 (1986).
[9] A. S.-C. Cheung, K. Yoshino, J. R. Esmond, S. S.-L. Chiu, D. E. Freeman, and W. H. Parkinson, J. Chem. Phys. **92**, 842 (1990).
[10] K. Yoshino, D. E. Freeman, J. R. Esmond, and W. H. Parkinson, Planet. Space Sci. **35**, 1067 (1987).
[11] A. S.-C. Cheung, K. Yoshino, W. H. Parkinson, and D. E. Freeman, Can. J. Phys. **62**, 1752 (1984).
[12] K. Yoshino, J. R. Esmond, A. S.-C. Cheung, D. E. Freeman, and W. H. Parkinson, Planet. Space Sci. **40**, 185 (1992).
[13] P. C. Cosby, H. Park, R. A. Copeland, and T. G. Slanger, J. Chem. Phys. **98**, 5117 (1993).
[14] R. A. Copeland, P. C. Cosby, D. R. Crosley, J. B. Jeffries, and T. G. Slanger, J. Chem. Phys. **86**, 2500 (1987).
[15] A. M. Wodtke, L. Hüwel, H. Schlüter, H. Voges, G. Meijer, and P. Andresen, J. Chem. Phys. **89**, 1929 (1988).
[16] X. Yang, A. M. Wodtke, and L. Hüwel, J. Chem. Phys. **94**, 2469 (1991).
[17] B. R. Lewis, S. T. Gibson, K. G. H. Baldwin, and J. H. Carver, J. Opt. Soc. Am. B **6**, 1200 (1989).
[18] P. M. Dooley, B. R. Lewis, S. T. Gibson, and K. G. H. Baldwin, J. Electron Spectrosc. Relat. Phenom. **80**, 29 (1996).
[19] B. R. Lewis, P. M. Dooley, J. P. England, K. Waring, S. T. Gibson, K. G. H. Baldwin, and H. Partridge, Phys. Rev. A **54**, 3923 (1996).
[20] R. Hilbig and R. Wallenstein, IEEE J. Quantum Electron. **QE19**, 194 (1983).
[21] K. Yamanouchi and S. Tsuchiya, J. Phys. B **28**, 133 (1995).
[22] B. R. Lewis, J. P. England, R. J. Winkel, Jr., S. S. Banerjee, P. M. Dooley, S. T. Gibson, and K. G. H. Baldwin, Phys. Rev. A **52**, 2717 (1995).
[23] K. Yoshino, D. E. Freeman, and W. H. Parkinson, J. Phys. Chem. Ref. Data **13**, 207 (1984).

[24] S. Gangopadhyay, N. Melikechi, and E. E. Eyler, J. Opt. Soc. Am. B **11**, 231 (1994).
[25] M. S. Fee, K. Danzmann, and S. Chu, Phys. Rev. A **45**, 4911 (1992).
[26] J. W. Hepburn, *Vacuum Ultraviolet Photoionization and Photodissociation of Molecules and Clusters*, edited by C. Y. Ng (World Scientific, Singapore, 1991), p. 446.
[27] R. M. Goody, *Atmospheric Radiation. I. A Theoretical Basis* (Clarendon, Oxford, 1964), pp. 125–138.
[28] B. R. Lewis, L. Berzins, C. J. Dedman, T. T. Scholz, and J. H. Carver, J. Quant. Spectrosc. Radiat. Transfer **39**, 271 (1987).
[29] P. M. Dooley, B. R. Lewis, K. Waring, S. T. Gibson, and K. G. H. Baldwin, J. Quant. Spectrosc. Radiat. Transfer **58**, 93 (1997).
[30] H. Park and T. G. Slanger, J. Chem. Phys. **100**, 287 (1994).
[31] S. Gerstenkorn and P. Luc, *Atlas du Spectre d'Absorption de la Molécule de l'Iode Entre 14800–20000 cm^{-1}* (Editions du C.N.R.S., Paris, 1978); *Atlas du Spectre d'Absorption de la Molécule de l'Iode Entre 14800–20000 cm^{-1}, Complément: Identification des Transitions du Système (B-X)* (Editions du C.N.R.S., Paris, 1980). A multiplicative correction factor of 0.999 999 62 was applied to the reported line positions as recommended by these authors.
[32] J. Cariou and P. Luc, *Atlas du Spectre d'Absorption de la Molécule de Tellure Partie 2: 18500–21200 cm^{-1} and Partie 5: 21100–23800 cm^{-1}* (Laboratoire Aime-Cotton, CNRS II, Orsay, 1980).
[33] A. P. Thorne, C. J. Harris, I. Wynne-Jones, R. C. M. Learner, and G. Cox, J. Phys. E **20**, 54 (1987).
[34] A. P. Thorne, Phys. Scr. **T65**, 31 (1996).
[35] J. E. Murray, K. Yoshino, J. R. Esmond, W. H. Parkinson, Y. Sun, A. Dalgarno, A. P. Thorne, and G. Cox, J. Chem. Phys. **101**, 62 (1994).
[36] K. Ito, T. Namioka, Y. Morioka, T. Sasaki, H. Noda, K. Goto, T. Katayama, and M. Koike, Appl. Opt. **25**, 837 (1986).
[37] While the effects of spontaneous radiative emission provide a negligible lifetime-broadening contribution to the Lorentzian linewidth, of course the LIFS experiment would not be possible without this process.
[38] It is assumed that there are no correlations between the individual broadening processes.
[39] Since the effective vibrational oscillator strength varies insignificantly with the fine-structure component for lines with a given N', the relative fine-structure photoabsorption line strengths are determined completely by the respective Boltzmann and Hönl-London factors. Both of these factors may be calculated to a high degree of accuracy: the Boltzmann factors may be derived from the well known ground-state term values for O_2 [L. Veseth and A. Lofthus, Mol. Phys. **27**, 511 (1974)], while expressions for the appropriate intermediate-coupling case [J. B. Tatum and J. K. G. Watson, Can. J. Phys. **49**, 2693 (1971)] may be used with the ground- and upper-state term values (Ref. 23) to calculate the Hönl-London factors.
[40] The attribution in Ref. 13 of unexpectedly large Gaussian linewidths to a relatively high translational temperature of the absorbing O_2 is incorrect. Subsequent studies of the LIFS line shapes as a function of pressure and of time delay between the pump and probe laser beams found that the O_2 was in thermal equilibrium with the buffer gas (300 K). A more likely explanation for these earlier results is an unexpectedly large probe-laser bandwidth.
[41] As described in Ref. 13, the relative absorption line strengths were calculated from the eigenvectors obtained in a diagonalization of the effective Hamiltonians for the B- and X-state levels, assuming a 300 K thermal population distribution in the X-state rotational levels. This procedure is equivalent to that described in Ref. 39.
[42] J. W. Brault (private communication).
[43] R. C. M. Learner and A. P. Thorne, J. Opt. Soc. Am. B **5**, 2045 (1988).
[44] Since LIFS measurements were made on several bands with various v'', the corresponding linewidth averages include multiple transitions accessing each upper-state level.

4.34 High-resolution oscillator-strength measurements for high-v' bands of the $A\,^1\Pi(v') - X\,^1\Sigma^+(v'' = 0)$ system of carbon monoxide

[54] G. Stark, B. R. Lewis, S. T. Gibson, and J. P. England,
The Astrophysical Journal **505**, 452–458 (1998).

THE ASTROPHYSICAL JOURNAL, 505:452–458, 1998 September 20

HIGH-RESOLUTION OSCILLATOR STRENGTH MEASUREMENTS FOR HIGH-v' BANDS OF THE $A\,^1\Pi(v')$–$X\,^1\Sigma^+(v''=0)$ SYSTEM OF CARBON MONOXIDE

GLENN STARK,[1] BRENTON R. LEWIS,[2] STEPHEN T. GIBSON,[2] AND JULIAN P. ENGLAND[2,3]
Received 1998 February 2; accepted 1998 April 21

ABSTRACT

Band oscillator strengths for six bands of the CO $A\,^1\Pi(v')$–$X\,^1\Sigma^+(v''=0)$ system with $13 \le v' \le 21$ have been determined from high-resolution (resolving power $\approx$750,000) absorption spectra recorded with a tunable vacuum ultraviolet (VUV) laser system. The instrumental bandwidth of the system, $\approx$0.11 cm^{-1} FWHM, was significantly less than the widths of the Doppler-broadened CO lines ($\approx$0.20 cm^{-1} FWHM). Integrated cross sections of individual rotational lines were determined by a least-squares fitting routine, taking into account the effects of the finite instrumental resolution on the measured absorption features. Our derived f-values for the $A(13)$–$X(0)$, $A(14)$–$X(0)$, and $A(16)$–$X(0)$ bands are consistent with other recent measurements, with the ab initio electronic transition moment calculations of Kirby & Cooper, and with f-values derived from the ab initio electronic transition moment calculations of Spielfiedel & Feautrier cited by Jolly et al. Our f-values for the $A(18)$–$X(0)$, $A(20)$–$X(0)$, and $A(21)$–$X(0)$ bands, the first directly measured values for these bands, progressively deviate from band oscillator strengths derived from the electronic transition moment function of Kirby & Cooper. In addition, a pressure-broadening coefficient of $(3.1 \pm 0.6) \times 10^{-4}$ cm^{-1} $torr^{-1}$ was determined for room-temperature CO–CO collisions.

Subject headings: molecular data — ISM: molecules — ultraviolet: ISM

1. INTRODUCTION

The capabilities of the Goddard High Resolution Spectrograph on the *Hubble Space Telescope* have led to new studies of interstellar $^{12}C^{16}O$ and its isotopic variants at vacuum ultraviolet (VUV) wavelengths. The rotationally resolved fourth positive $A\,^1\Pi(v')$–$X\,^1\Sigma^+(v''=0)$ systems of $^{12}C^{16}O$ and $^{13}C^{16}O$ have been observed in absorption in the line of sight to ζ Ophiuchi by Sheffer et al. (1992), Lambert et al. (1994), and Lyu, Smith, & Bruhweiler (1994). The rapid decrease in band oscillator strength for the $A(v')$–$X(0)$ bands as v' increases makes this system ideal for studying isotopic ratios; saturation effects in the astrophysical observations can be minimized by comparing $^{12}C^{16}O$ absorption features in weak high-v' bands with $^{13}C^{16}O$ absorption in the stronger low-v' bands. The interpretation of the new astrophysical observations requires accurate and reliable spectroscopic data. In this paper, we report oscillator strength measurements of six $^{12}C^{16}O$ $A(v')$–$X(0)$ bands with $13 \le v' \le 21$. Our measurements of the (13–0), (14–0), and (16–0) bands are compared with other experimental determinations and with theoretical predictions; our f-values for the (18–0), (20–0), and (21–0) bands are the first directly measured values for these bands.

The $A\,^1\Pi$–$X\,^1\Sigma^+$ electronic system of CO has been the subject of numerous laboratory investigations. Morton & Noreau (1994), in their compilation of fundamental spectroscopic data (wavelengths and oscillator strengths) for all CO transitions between 100 and 155 nm, provide a critically evaluated summary of the $A\,^1\Pi$–$X\,^1\Sigma^+$ database. Laboratory determinations of band f-values have utilized three independent approaches; radiative lifetime measurements (Field et al. 1983), optical absorption measurements (Eidelsberg et al. 1992; Smith et al. 1994; Jolly et al. 1997; Federman et al. 1997), and inelastic electron scattering (Chan, Cooper, & Brion 1993; Zhong et al. 1997). Ab initio calculations of the A–X electronic transition moment and associated band f-values have been reported by Kirby & Cooper (1989), Chantranupong et al. (1992), and A. Spielfiedel & N. Feautrier (1997, private communication, cited in Jolly et al. 1997).

The most recent laboratory determinations of $A(v')$–$X(0)$ band f-values are in quite good agreement for bands with $v' \le 7$; discrepancies between published results are typically no greater than about 10%. However, the laboratory results are significantly less consistent for A–X bands with $v' > 7$. For $8 \le v' \le 14$ the electron scattering measurements of Chan et al. (1993) and the optical absorption measurements of Smith et al. (1994) and Jolly et al. (1997) agree within the stated uncertainties and are consistent with the calculations of Kirby & Cooper (1989) and Spielfiedel & Feautrier (1997, private communication). The optical absorption measurements of Eidelsberg et al. (1992) are uniformly higher (by about 50%) than those of Chan et al. (1993), Smith et al. (1994), and Jolly et al. (1997), and the recent optical absorption measurements of Federman et al. (1997) are uniformly lower (by about 15%–20%). In their compilation of recommended A–X oscillator strengths for $0 \le v' \le 23$, Morton & Noreau (1994) adopted the measurements of Chan et al. (1993) for bands with $v' \le 12$ and extended them beyond $v' = 12$ by using the theoretical electronic transition moment of Kirby & Cooper (1989).

The relative merits of the inelastic electron scattering and optical absorption techniques are discussed by Chan et al. (1993) and Jolly et al. (1997). Briefly, the electron scattering technique has the advantage of not being susceptible to saturation effects despite its relatively low resolution ($\approx$0.65 nm FWHM at 130 nm). With well-separated band features, such as those of the $A(v')$–X(0) sequence, the low resolution

[1] Department of Physics, Wellesley College, 106 Central Street, Wellesley, MA 02181-8283; gstark@wellesley.edu.
[2] Research School of Physical Sciences and Engineering, Australian National University, Canberra A.C.T. 0200, Australia; brenton.lewis@anu.edu.au, stephen.gibson@anu.edu.au.
[3] Current address: Australian Bureau of Statistics, Belconnen, A.C.T. 2617, Australia; j.england@abs.gov.au.

of the technique does not introduce significant uncertainties; however, the extraction of absolute f-values from electron scattering measurements does require scaling by an independently determined calibration factor. Optical absorption measurements provide, in principle, a more direct determination of band f-values, although (as discussed by Hudson 1971, Stark et al. 1991, and Jolly et al. 1997) insufficient instrumental resolution leads to saturation effects, which, if not minimized or properly accounted for, can result in a systematic underestimation of band f-values (or band integrated cross sections).

The room-temperature Doppler broadening of CO A–X rotational lines results in line widths with a FWHM of ≈ 0.2 cm^{-1} (3 mÅ) at 120 nm. The instrumental resolutions used in the recent optical measurements of the A–X bands were ≈ 130 mÅ (Eidelsberg et al. 1992), 8 mÅ (Smith et al. 1994), 20 mÅ (Jolly et al. 1997), and 300 mÅ (Federman et al. 1997). Various experiment and analysis strategies can be used to correct for instrumental effects in an absorption measurement. Smith et al. (1994) restricted their measurements to small optical depths and used a spectral synthesis technique to apply 8%–16% corrections to their measured integrated cross sections; Federman et al. (1997) used an equivalent-width analysis to extract f-values; and Jolly et al. (1997) increased the CO line widths via pressure broadening in Ar and least-squares fitted their measured absorption spectra with CO A–X band models. While each of these analysis techniques can account for the effects of inadequate instrumental resolution, there are unavoidable uncertainties associated with such measurements; these uncertainties increase with decreasing instrumental resolving power. In practice, to avoid any significant instrumental effects in an absorption measurement, the instrument must be capable of resolving the actual line shapes. This requires an instrumental resolution significantly narrower than the FWHM of the absorbing features.

The absorption measurements described in this paper were carried out with a tunable VUV laser system with a resolution of ≈ 0.11 cm^{-1} FWHM (at 120 nm). This is significantly less than the Doppler width of CO rotational lines at room temperature (≈ 0.20 cm^{-1} FWHM), resulting in minimal systematic instrumental effects. Residual instrumental effects were treated by least-squares fitting Doppler-broadened CO line profiles, convolved with a Gaussian instrument profile, to the measured absorption profiles. Our measurements include f-values for the (13–0), (14–0), and (16–0) bands, allowing us to compare our results with those of Smith et al. (1994) and Jolly et al. (1997). We also report the first measured f-values for the (18–0), (20–0), and (21–0) bands. These are compared with theoretical f-values calculated from the ab initio electronic transition moment functions of Kirby & Cooper (1989) and with the f-values adopted by Morton & Noreau (1994) in their compilation of CO spectroscopic data.

2. EXPERIMENTAL PROCEDURE

Photoabsorption cross section measurements were made of individual rotational lines in six CO A–X absorption bands between 112 and 123 nm. VUV radiation was produced by a narrow-bandwidth, tunable laser system (England, Lewis, & Ginter 1995; England et al. 1996). A Lambda Physik EMG202 XeCl excimer laser (308 nm, 450 mJ per pulse) was used to pump a Lambda Physik FL2002 dye laser (p-terphenyl or DMQ in dioxane) equipped with an intracavity etalon. The near-UV output of the dye laser (339–369 nm) was focused into a cell containing Kr or Xe to generate third-harmonic radiation (Mahon et al. 1979). The rare gas pressures, in the range 5–100 torr, were determined by the phase-matching requirements needed to maximize the power of the tripled radiation. Radiation from the tripling cell was passed through a 0.2 m monochromator to remove the fundamental near-UV radiation. The bandwidth (FWHM) of the resulting VUV radiation was found to be ≈ 0.1 cm^{-1} (1.6 mÅ) via fits to the absorption-line shapes of individual CO rotational lines (see § 3).

VUV radiation leaving the exit slit of the monochromator was divided into two beams with a slotted aluminum beamsplitter. The reflected beam was monitored directly, while the transmitted beam passed through a 10.9 cm stainless steel absorption cell equipped with LiF windows before being detected. The reflected and transmitted beams were detected with solar-blind photomultiplier tubes (EMR type 541, KBr photocathode) operated at low gain to avoid dynode-saturation effects. The reflected beam served as a monitor of the laser intensity, while the transmitted beam was used to record CO absorption.

Samples of CO (Matheson 99.99%, natural abundance) were used at pressures between 0.5 and 300 torr, chosen to produce transmittances at line centers between 30% and 70%. Absolute CO pressures in the absorption cell were measured with variable-capacitance manometers; pressure uncertainties were typically on the order of 1% or less. Cell pressures were monitored continuously during each absorption scan. All measurements were carried out at room temperature except for selected scans of the $A(21)$–$X(0)$ band. Some low-rotational lines of this very weak band were measured at liquid nitrogen temperature to maximize their strengths relative to the underlying pseudocontinuum due to the pressure-broadened wings of the nearby strong (0, 0) and (1, 0) bands of the $B\,^1\Sigma^+$–$X\,^1\Sigma^+$ system. For these measurements, the absorption cell was cooled by filling the surrounding sleeve with liquid N_2, resulting in an effective gas temperature of 79 K.

Output pulses from the "monitor" and "detector" photomultiplier tubes were processed by a boxcar-averaging system. The monitor and detector signals were averaged over 100 laser shots for each datum point. The laser system was stepped with a wavelength increment (in the VUV) of 0.5 mÅ; a typical scan of an individual rotational line and the adjacent continuum consisted of 40 data points and required approximately 15 minutes of accumulation time. A 386-based microcomputer was used to control the laser and monochromator scanning, the pressure of CO in the absorption cell, and the acquisition of the shot-averaged detector and monitor signals from the boxcar system.

For each datum point, the averaged detector signal was divided by the averaged monitor signal to account for the shot-to-shot fluctuations inherent in the generated VUV signal. Before and after each absorption scan, empty-cell values of the monitor and detector signals were recorded; absolute-cell transmittances were obtained by dividing the full-cell ratios (detector/monitor) by the empty-cell ratios for each datum point. The resulting signal-to-noise ratio in a typical absorption scan was about 40:1.

The narrow-bandwidth VUV laser radiation was sometimes accompanied by a weak "quasi-continuum" associated with amplified stimulated emission (ASE) in the dye laser. This continuum radiation is comparable in its effect

on an absorption measurement to the broadband scattering that is often present in a grating spectrometer. If not properly accounted for, it can lead to a systematic underestimation of line strengths. The presence and strength of any ASE was monitored in our measurements by regularly observing very highly saturated absorption in rotational lines of the strong B–X (0–0) and (1–0) bands at 115 and 112 nm, respectively. In the measurement of a highly saturated line, any residual transmittance at line center can be attributed to broadband radiation. In practice, monitoring the residual transmittance in B–X rotational lines provided a convenient method of minimizing the ASE level via adjustments to the dye laser optics. The ASE level in our final set of measurements was normally less than 2% of the total signal and was not corrected for. The only exception to this was the measurement of absorption in the $A(14)$–$X(0)$ band, where the ASE level was determined to be 4% of the total signal. This broadband contribution was subtracted from the monitor and detector signals before further processing.

3. RESULTS AND DISCUSSION

A total of 100 absorption spectra were recorded of individual rotational lines in the six A–X vibrational bands studied. In the reduction of the data, each measured absorption feature was first converted to a measured photoabsorption cross section through application of the Beer-Lambert law,

$$\sigma_M(\nu) = \frac{1}{N} \ln\left[\frac{I_0(\nu)}{I(\nu)}\right], \quad (1)$$

where N is the column density of CO molecules, $I_0(\nu)$ is the incident intensity, and $I(\nu)$ is the transmitted intensity. The measured photoabsorption cross section, $\sigma_M(\nu)$, includes the effects of the laser bandwidth. A least-squares fitting routine, in which each rotatonal line was described by a Voigt profile comprising a well-defined Doppler contribution and, if necessary, a small Lorentzian contribution due to collision broadening, taking into account the effects of the finite instrumental resolution on the measured absorption, was used to determine values for the "true" integrated cross section of each line and the laser bandwidth, which was assumed to be described by a Gaussian. In the cases of the $A(20)$–$X(0)$ and $A(21)$–$X(0)$ bands, a continuous background photoabsorption term was allowed to vary in the fitting procedure to accommodate the effects of the pressure-broadened pseudocontinuum from the B–X bands. A representative photoabsorption cross section measurement, of the $R(10)$ and $Q(8)$ lines in the $A(16)$–$X(0)$ band, along with the modeled measured cross section determined by the parameters of the fit, is shown in Figure 1. The least-squares value of the laser bandwidth showed a small variation for individual rotational lines within any one vibrational band. An averaged value of this bandwidth was determined for each band and was held fixed in a subsequent iteration of the fitting routine. The averaged laser bandwidths vary from 0.11 cm^{-1} FWHM for the $A(13)$–$X(0)$, $A(16)$–$X(0)$, and $A(18)$–$X(0)$ bands to 0.15 cm^{-1} FWHM for the $A(20)$–$X(0)$ and $A(21)$–$X(0)$ bands. Table 1 summarizes the relevant experimental parameters, including the number of rotational lines and the range of J-values measured, for each band studied. Regions of significant local perturbation, for example, low-rotational lines in the $A(18)$–$X(0)$ band, were avoided in the measurements.

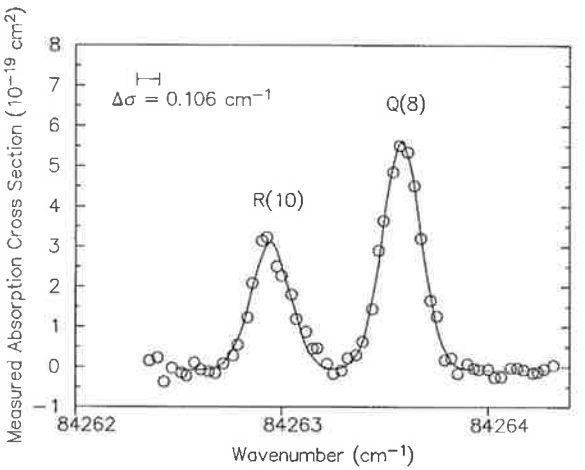

FIG. 1.—Measured photoabsorption cross section of the $R(10)$ and $Q(8)$ lines in the $A(16)$–$X(0)$ band along with the modeled measured cross section determined by a least-squares fit. The spectrum was sampled at wavelength intervals of 0.5 mÅ ($\approx$0.036 cm^{-1}). The instrumental resolution, determined by the fitting routine, was 0.106 cm^{-1} FWHM.

For each A–X vibrational band, the integrated cross sections of individual rotational lines, determined from the above fitting procedure, were converted into line oscillator strengths according to

$$f_{v'',J'',0,J''} = \frac{1.13 \times 10^{12} \int \sigma(\nu) d\nu}{\alpha_{J''}}, \quad (2)$$

where the integrated cross section is expressed in units of cm^2 cm^{-1} and $\alpha_{J''}$ is the fractional population of molecules in the J'' rotational level as determined by an appropriately normalized Boltzmann factor. In the framework of the

TABLE 1

EXPERIMENTAL PARAMETERS FOR BAND MEASUREMENTS

Band	ν_0[a] (cm^{-1})	Lines Measured	J''-range	Laser Bandwidth (cm^{-1} FWHM)	Cell Pressures (torr)
$A(13)$–$X(0)$.....	81320	17	1–19	0.11	0.45–6.5
$A(14)$–$X(0)$.....	82354	22	0–18	0.14	0.50–9.8
$A(16)$–$X(0)$.....	84315	12	1–10	0.11	4.0–22
$A(18)$–$X(0)$.....	86119	9	9–14	0.11	20–70
$A(20)$–$X(0)$.....	87741	21	2–14	0.15	40–300
$A(21)$–$X(0)$.....	88467	17	0–7	0.15	45–300

[a] Tilford & Simmons 1972.

Born-Oppenheimer approximation, the relation between a rotational line oscillator strength and the corresponding vibrational band oscillator strength for a $^1\Sigma$–$^1\Pi$ transition is (Larsson 1983)

$$f_{v',v''} = \frac{2(2J''+1)f_{v',J',v'',J''}}{S_{J',J''}}, \quad (3)$$

whre $S_{J',J''}$ is the Hönl-London factor. The band oscillator strength defined by equation (3) can have a small, but measurable, J-dependence (e.g., Lewis 1974; Lewis, Berzins, & Carver 1986). This is most easly seen from the relation between $f_{v',v''}$ and the vibrationally averaged transition dipole moment (Larsson 1983),

$$f_{v',v''} = 6.075 \times 10^{-6} \nu_{v',v''} |\langle \Psi_{v'} | R_e(R) | \Psi_{v''} \rangle|^2, \quad (4)$$

where $\nu_{v',v''}$ is the wavenumber of the band origin and R_e is expressed in atomic units. Centrifugal distortion effects associated with the molecular rotation slightly alter the potential energy curves of the upper and lower states and thereby alter the upper and lower state vibrational wave functions along with all vibrationally averaged parameters. Rotationless band oscillator strengths $[f_{v',v''}(J' = J'' = 0)]$ were derived from the rotationally dependent band oscillator strengths $[f_{v',v''}(J', J'')]$ determined above (eqs. [2] and [3]) by accounting for the rotational dependence of the vibrationally averaged transition dipole moment,

$$f_{v',v''}(J' = J'' = 0) = f_{v',v''}(J', J'')[r_{v',v''}(J', J'')], \quad (5)$$

where

$$r_{v',v''}(J', J'') = \frac{|\langle \Psi_{v'}(J'=0) | R_e(R) | \Psi_{v''}(J''=0) \rangle|^2}{|\langle \Psi_{v'}(J') | R_e(R) | \Psi_{v''}(J'') \rangle|^2}. \quad (6)$$

The appropriate ratios of the squares of vibrationally averaged transition dipole moments were calculated using the deperturbed A-state RKR potential curve of Field et al. (1972), an RKR curve determined from the ground-state molecular constants of Le Floch (1991), and the electronic transition moment of Kirby & Cooper (1989). These ratios, $r_{v',v''}(J', J'')$, treated as correction factors in determining rotationless band oscillator strengths from individual rotational-line measurements, are displayed in Figure 2 for the Q-branches of the six bands studied.

For each of the six bands studied, a final rotationless band oscillator strength was calculated from a weighted average of the band f-values derived, using the procedure described above, from individual rotational-line integrated cross sections. $A(13)$–$X(0)$ rotationless band f-values derived from measurements of 17 rotational lines, and an averaged rotationless band f-value, are displayed in Figure 3. The uncertainty in the integrated cross section of an individual line was typically about 6%–7%, resulting from a combination of uncertainties in the absorption cell pressure ($\approx$1%), the adopted value of the laser bandwidth (a 20% uncertainty in the laser bandwidth produced a 5% uncertainty in the integrated cross section), and the least-squares fitting parameters. For any one band, the scatter of the rotationless band oscillator strengths derived from individual line measurements was typically consistent with this 6%–7% uncertainty. The uncertainty in the final, averaged band f-values for $v' = 13$, 14, 16, and 18 is conservatively estimated to be 10%. The uncertainty in the band f-values for the $A(20)$–$X(0)$ and $A(21)$–$X(0)$ bands is estimated to be

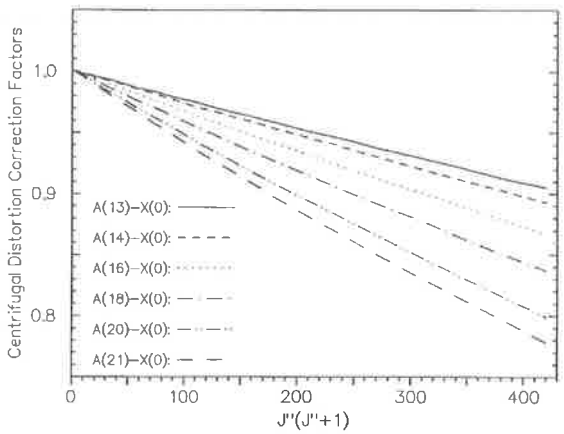

FIG. 2.—Centrifugal distortion correction factors, $r_{v',v''}(J', J'')$ (see eq. [6]), for the Q-branches of the six bands studied. For each band, the correction factor decreases approximately linearly with $J''(J''+1)$.

15%; this higher value is associated with pressure-broadening effects (see below) that complicate the analysis of the absorption features. Our rotationless band f-values are presented in Table 2. Note that all other measured band f-values presented in Table 2 are strictly appropriate only for room temperature.

The relatively small oscillator strengths of the high-v' bands of the A–X system necessitated the use of high absorption-cell pressures. The $A(20)$–$X(0)$ and $A(21)$–$X(0)$ bands were measured at cell pressures ranging from 40 to 300 torr; the $A(18)$–$X(0)$ band at pressures from 20 to 70 torr. At these pressures, the measured line widths were slightly pressure-broadened. The laser bandwidth for these bands was independently determined by scanning, at very low cell pressures, rotational lines in the nearby, strong CO $B(0)$–$X(0)$ and $B(1)$–$X(0)$ bands. Pressure-broadening in 23 rotational lines in the three bands was then determined through the least-squares fitting routine by allowing the

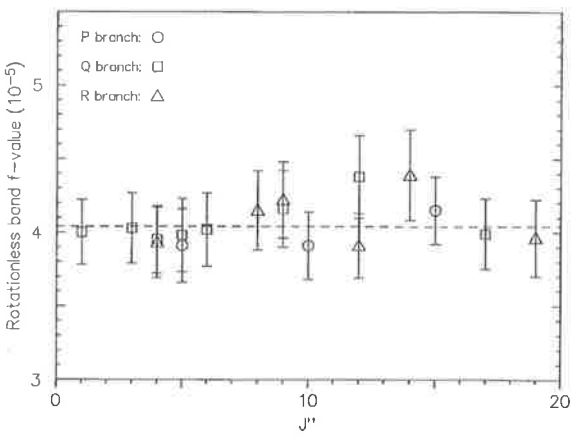

FIG. 3.—$A(13)$–$X(0)$ rotationless band f-values determined from 17 absorption spectra of individual rotational lines. The band f-values were determined using eqs. (3) and (5) in the text; i.e., the rotational dependence of the band f-values has been removed. The dotted line indicates the weighted average of the 17 measurements.

TABLE 2

BAND f-VALUES FOR $A(v')$–$X(0)$ BANDS OF CO (IN 10^{-5})[a]

v'	CCB93[b]	ERB92[c]	FML97[d]	SSY94[e]	JLB97[f]	This Work[g]	KC89[h]	MN94[i]	SF97[j]	$q_{v',0}$[k]
8	202(20)	290(30)	169(9)	...	...	...	193	202	183	6.89(−3)
9	95(9)	140(20)	78(5)	...	96(14)	...	92.4	95	87.5	3.02(−3)
10	41(4)	65(7)	35(2)	...	41.6(62)	...	43.0	41	40.8	1.29(−3)
11	18(2)	28(3)	13(2)	17(3)	20.2(30)	...	19.6	18	18.7	5.41(−4)
12	9(1)	13(2)	...	6.9(8)	...	...	8.84	9.00	8.47	2.24(−4)
13	...	...	...	3.7(4)	3.62(54)	4.04(40)	3.95	3.47	3.82	9.23(−5)
14	...	...	...	1.5(2)	1.66(25)	1.87(19)	1.76	1.44	1.72	3.79(−5)
15	...	...	...	...	0.71(1)	...	0.780	0.594	0.777	1.56(−5)
16	...	...	...	...	0.313(47)	0.386(39)	0.346	0.246	0.355	6.43(−6)
17	...	...	...	...	0.131(26)	...	0.154	0.102	0.165	2.68(−6)
18	...	...	...	...	...	0.085(13)	0.0686	0.0430	...	1.13(−6)
19	...	...	...	...	...	...	0.0307	0.0183	...	4.87(−7)
20	...	...	...	...	...	0.0187(28)	0.0137	0.0080	...	2.14(−7)
21	...	...	...	...	...	0.0099(15)	0.0062	0.0036	...	9.65(−8)

[a] Uncertainties in parentheses in units of last quoted decimal place.
[b] Chan et al. 1993.
[c] Eidelsberg et al. 1992.
[d] Federman et al. 1997.
[e] Smith et al. 1994.
[f] Jolly et al. 1997.
[g] Band f-values are "rotationless" (see text); all other measured f-values are strictly appropriate only for room temperature.
[h] Calculated from ab initio electronic transition moment of Kirkby & Cooper 1989.
[i] Morton & Noreau 1994; f-values for $8 \leq v' \leq 12$ adopted from Chan et al. 1993; f-values for $13 \leq v' \leq 21$ calculated from electronic transition moment of KC89 using R-centroid approximation.
[j] Spielfiedel & Feautrier 1997, tabulated in Jolly et al. 1997.
[k] Franck-Condon factors calculated from the deperturbed RKR $A\,^1\Pi$ potential curve of Field et al. 1972 and an RKR $X\,^1\Sigma^+$ potential curve constructed from the molecular constants of Le Floch 1991.

Lorentzian component of each Voigt line shape to be a free parameter; at the maximum absorption cell pressure used, 300 torr, the Lorentzian components of the line shapes reached 0.10 cm^{-1} FWHM. Figure 4 displays the FWHM of the pressure-broadened Lorentzians as a function of cell pressure. A linear fit to the data yields a pressure-broadening coefficient of $(3.1 \pm 0.6) \times 10^{-4}$ cm^{-1} $torr^{-1}$. To our knowledge, there are no other reports of pressure-broadening coefficients in the VUV for CO–CO collisions; Jolly et al. (1997) report a pressure-broadening coefficient of 1.8×10^{-4} cm^{-1} $torr^{-1}$ for CO–Ar collisions. In the final determination of the integrated cross sections for the pressure-broadened lines, the Lorentzian components of the line shapes were fixed at values determined by the derived CO–CO pressure-broadening coefficient. To access the lowest-J lines in the $A(21)$–$X(0)$ band, the absorption cell was cooled by liquid nitrogen to an effective temperature of 79 K. The pressure-broadening coefficient used in the analysis of these lines was assumed to scale with temperature as $T^{-0.7}$ (Cann et al. 1979), yielding a value of 7.8×10^{-4} cm^{-1} $torr^{-1}$ at 79 K.

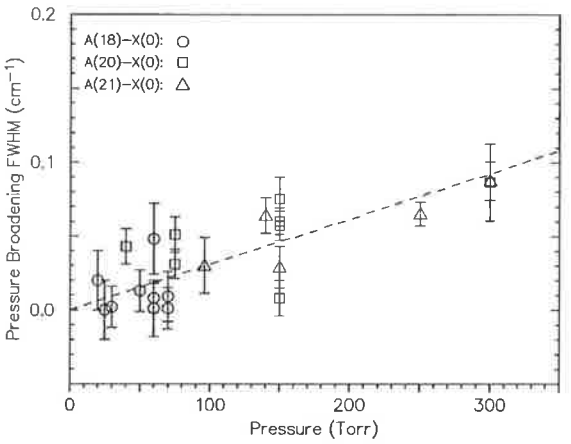

FIG. 4.—Pressure-broadening of rotational lines in the $A(18)$–$X(0)$, $A(20)$–$X(0)$, and $A(21)$–$X(0)$ bands at 295 K. A linear fit results in a pressure-broadening coefficient of $(3.1 \pm 0.6) \times 10^{-4}$ cm^{-1} $torr^{-1}$.

Our measured band oscillator strengths, as well as other published measured and calculated f-values, are displayed as a function of the $A\,^1\Pi$ vibrational level in Figure 5. The $A(v')$–$X(0)$ band oscillator strengths vary by over 4 orders of magnitude in the range $8 \leq v' \leq 21$. Following the lead of Jolly et al. (1997), to facilitate a visual comparison of the different data sets over this range, the f-values have been scaled by Franck-Condon factors; i.e., the "reduced band oscillator strengths" presented in Figure 5 are the ratios $f_{v',0}/q_{v',0}$. For this purpose $A(v')$–$X(0)$ Franck-Condon factors were calculated from the deperturbed RKR $A\,^1\Pi$ potential curve of Field et al. (1972) and an RKR $X\,^1\Sigma^+$ potential curve constructed from the molecular constants of Le Floch (1991). In the standard R-centroid approximation (Larsson 1983) the ratio $f_{v',v''}/q_{v',v}$ is proportional to the square of the electronic transition moment evaluated at the R-centroid for the vibrational band,

$$f_{v',v''} = 6.075 \times 10^{-6} \nu_{v',v''}\, q_{v',v''}\, R_e^2(R_{v',v''}) , \qquad (7)$$

where $\nu_{v',v''}$ is the wavenumber of the band origin, $R_{v',v}$ is the R-centroid, and R_e is expressed in atomic units; however, when the electronic transition moment, $R_e(R)$, exhibits curvature (e.g., Kirby & Cooper 1989) the R-centroid approximation is not appropriate and band oscillator strengths can only be directly related to the vibrationally averaged transition dipole moment (eq. [4]). In the case of the $A(v')$–$X(0)$ system, the R-centroid approx-

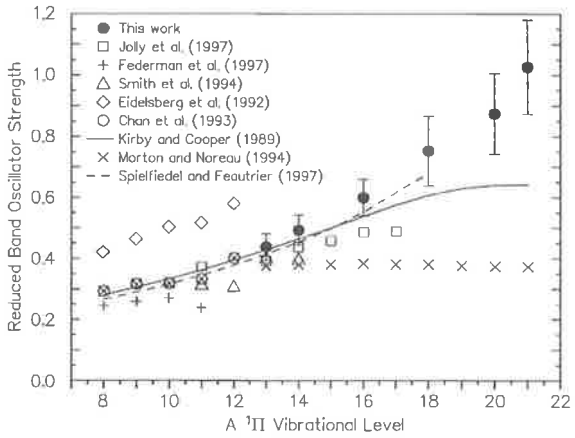

FIG. 5.—Measured and calculated band f-values for the $A(8 \leq v' \leq 21)$–$X(0)$ bands. To facilitate a visual comparison the f-values have been scaled by Franck-Condon factors; the "reduced" f-values are equal to $f_{v',0}/q_{v',0}$ (see text). The reduced f-values of Spielfiedel & Feautrier (1997) for $8 \leq v' \leq 17$ are determined from the f-values in Table 2 of Jolly et al. (1997) and our calculated $A(v')$–$X(0)$ Franck-Condon factors. The $A(18)$–$X(0)$ reduced f-value is taken directly from Fig. 14 of Jolly et al. (1997); it should be noted that the Franck-Condon factors used in the Jolly et al. (1997) reduced f-value determinations are generally slightly different from those used in our reduced f-value determinations.

imation breaks down for $v' > 12$, as has also been noted by Jolly et al. (1997). Thus, the $f_{v',0}/q_{v',0}$ ratios presented in Figure 5 are not equivalent to the square of the electronic transition moment; they are used only as an aid in representing the data.

Our measured oscillator strengths for the $A(13)$–$X(0)$ and $A(14)$–$X(0)$ bands are in reasonable agreement with the previous optical measurements of Smith et al. (1994) and Jolly et al. (1997); the three sets of measurements are consistent within their stated uncertainty limits. Our f-value for the $A(16)$–$X(0)$ band is also consistent with the measurement of Jolly et al. (1997), although just barely—the measured f-values differ by about 20% while the stated uncertainties are 10% (this work) and 15%. Our reduced f-values ($f_{v',0}/q_{v',0}$) for bands with $v' \geq 16$ increase steeply with increasing v', in contrast to the flattening off of the Jolly et al. (1997) results for $v' = 16$ and 17 (see Fig. 5).

Kirby & Cooper (1989) calculated theoretical $A(v')$–$X(0)$ band f-values for $0 \leq v' \leq 10$ based on their ab initio electronic transition-moment function. We have extended Kirby & Cooper's f-value calculations to include bands with $11 \leq v' \leq 21$; their ab initio electronic transition moment was used along with vibrational wave functions derived from the deperturbed $A\,^1\Pi$ RKR potential of Field et al. (1972) and an RKR $X\,^1\Sigma^+$ potential curve constructed from the ground-state molecular constants of Le Floch (1991) to determine the appropriate vibrationally averaged transition moments in equation (4). The results are presented in Table 2 and displayed in Figure 5. Theoretical f-values given by Jolly et al. (1997), derived from recent ab initio electronic transition moment calculations by Spielfiedel & Feautrier (1997), are also included in Table 2 and in Figure 5. With the exception of the optical measurements of Eidelsberg et al. (1992), the theoretical f-values based on the electronic transition moments of Kirby & Cooper (1989) and Spielfiedel & Feautrier (1997) are broadly consistent with recent experimental values for $v' \leq 15$. Our new measurements for higher vibrational levels deviate significantly from the Kirby & Cooper (1989) f-values, with that deviation growing progressively larger with larger v'. The rapid increase in our measured reduced band oscillator strengths for high-v' bands is consistent with the trend of f-values calculated from the electronic transition moment function of Spielfiedel & Feautrier (1997) (see Fig. 5, and Fig. 14 in Jolly et al. 1997).

It can be seen from Figure 5 that the adopted $A(v')$–$X(0)$ f-values of Morton & Noreau (1994) are significantly in error for $v' \geq 15$. Their adopted f-values in this range were derived from the electronic transition moment function of Kirby & Cooper (1989) under the assumption that the R-centroid approximation is valid. The progressive deviation of the Morton & Noreau f-values from the Kirby & Cooper f-values for high-v', presented in Table 2, is entirely due to the breakdown of the R-centroid approximation because of the curvature of the Kirby & Cooper (1989) electronic transition moment. Because the R-centroid approximation is not valid for $v' > 12$, it is not possible, with conventional techniques, to use our measured f-values to directly derive the behavior of the electronic transition moment.

4. CONCLUSIONS

We have measured oscillator strengths of six vibrational bands in the CO $A\,^1\Pi(v')$–$X\,^1\Sigma^+(v'' = 0)$ system with $13 \leq v' \leq 21$. The optical absorption measurements, performed with a tunable VUV laser system, were carried out with an instrumental resolution of ≈ 0.11 cm^{-1} FWHM (resolving power $\approx 750{,}000$). The instrumental bandwidth was significantly narrower than the width of the Doppler-broadened CO lines (FWHM ≈ 0.20 cm^{-1}). Integrated cross sections of individual rotational lines were determined by a least-squares fitting routine taking into account the effects of the finite instrumental resolution on the measured absorption features. Rotationless band oscillator strengths were derived from the rotational-line measurements; the small rotational dependence of the band oscillator strength was accounted for in the conversion from line strengths to band f-value. Our results for the $A(13)$–$X(0)$ and $A(14)$–$X(0)$ bands are consistent with the previous measurements of Smith et al. (1994) and Jolly et al. (1997). Our $A(16)$–$X(0)$ band f-values is consistent with the f-value reported by Jolly et al. (1997) within the combined uncertainties. Our measured band f-values for $v' = 18$, 20, and 21 cannot be reproduced using the electronic transition moment function of Kirby & Cooper (1989). Reduced band f-values calculated from the electronic transition moment function of Spielfiedel & Feautrier (1997) for $v' \geq 16$ (see Jolly et al. 1997) are consistent with our observation of a rapid increase in reduced band f-values with increasing v'.

The authors thank K. J. Lonsdale and C. J. Dedham for valuable technical assistance, G. S. gratefully acknowledges the support and hospitality of the Ultraviolet Physics Unit, Atomic and Molecular Physics Laboratories, at the Research School of Physical Sciences and Engineering, Australian National University, during his appointment as a Visiting Fellow. This project was supported in part by an NSF International Opportunities for Scientists and Engineers Program grant, INT-9513350.

REFERENCES

Cann, M. W. P., Nicholls, R. W., Evans, W. F. J., Kohl, J. L., Kurucz, R., Parkinson, W. H., & Reeves, E. M. 1979, Appl. Opt., 18, 964
Chan, W. F., Cooper, G., & Brion, C. E. 1993, Chem. Phys., 170, 123
Chantranupong, L., Bhanuprakash, K., Honigmann, M., Hirsch, G., & Buenker, R. J. 1992, Chem. Phys., 161, 351
Eidelsberg, M., Rostas, F., Breton, J., & Thieblemont, B. 1992, J. Chem. Phys., 96, 5585
England, J. P., Lewis, B. R., Gibson, S. T., & Ginter, M. L. 1996, J. Chem. Phys., 104, 2765
England, J. P., Lewis, B. R., & Ginter, M. L. 1995, J. Chem. Phys., 103, 1727
Federman, S. R., Menningen, K. L., Lee, W., & Stoll, J. B. 1997, ApJ, 477, L61
Field, R. W., Benoist D'Azy, O., Lavollée, M., Lopez-Delgado, R., & Tramer, A. 1983, J. Chem. Phys., 78, 2838
Field, R. W., Wicke, B. G., Simmons, J. D., & Tilford, S. G. 1972, J. Mol. Spectrosc., 44, 383
Hudson, R. D. 1971, Rev. Geophys., 9, 305
Jolly, A., Lemaire, J. L., Belle-Oudry, D., Edwards, S., Malmasson, D., Vient, A., & Rostas, F. 1997, J. Phys. B, 30, 4315
Kirby, K., & Cooper, D. L. 1989, J. Chem. Phys., 90, 4895
Lambert, D. L., Sheffer, Y., Gilliland, R. L., & Federman, S. R. 1994, ApJ, 420, 756
Larsson, M. 1983, A&A, 128, 291
Le Floch, A. 1991, Mol. Phys., 72, 133
Lewis, B. R. 1974, J. Quant. Spectrosc. Radiat. Transfer, 14, 723
Lewis, B. R., Berzins, L., & Carver, J. H. 1986, J. Quant. Spectrosc. Radiat. Transfer, 36, 209
Lyu, C., Smith, A. M., & Bruhweiler, F. C. 1994, ApJ, 426, 254
Mahon, R., McIlrath, T. J., Myerscough, V. P., & Koopman, D. W. 1979, IEEE J. Quantum Electron., 15, 444
Morton, D. C., & Noreau, L. 1994, ApJS, 95, 301
Sheffer, Y., Federman, S. R., Lambert, D. L., & Cardelli, J. R. 1992, ApJ, 397, 482
Smith, P. L., Stark, G., Yoshino, K., & Ito, K. 1994, ApJ, 431, L143
Stark, G., Yoshino, K., Smith, P. L., Ito, K., & Parkinson, W. H. 1991, ApJ, 369, 574
Tilford, S. G., & Simmons, J. D. 1972, J. Phys. Chem. Ref. Data, 1, 147
Zhong, Z. P., Feng, R. F., Xu, K. Z., Wu, S. L., Zhu, L. F., Zhang, X. J., Ji, Q., & Shi, Q. C. 1997, Phys. Rev. A, 55, 1799

4.35 The $O(^1D)$ yield from O_2 photodissociation near H Lyman-α (121.6 nm)

[55] J. Lacoursière, S. A. Meyer, G. W. Faris, T. G. Slanger, B. R. Lewis, and S. T. Gibson,
Journal of Chemical Physics **110**, 1949–1958 (1999).

JOURNAL OF CHEMICAL PHYSICS VOLUME 110, NUMBER 4 22 JANUARY 1999

The $O(^1D)$ yield from O_2 photodissociation near H Lyman-α (121.6 nm)

J. Lacoursière, S. A. Meyer,[a] G. W. Faris, and T. G. Slanger
Molecular Physics Laboratory, SRI International, Menlo Park, California 94025

B. R. Lewis and S. T. Gibson
Research School of Physical Sciences and Engineering, The Australian National University, Canberra, ACT 0200, Australia

(Received 4 September 1998; accepted 20 October 1998)

The solar H Lyman-α line is, through O_2 photodissociation, an important source of $O(^1D)$ production throughout the mesosphere and lower thermosphere. To ascertain the energy balance in this altitude region, it is necessary to know the $O(^1D)$ yield across the solar H Lyman-α feature, since H Lyman-α absorption by O_2 at ~80 km accounts for a substantial fraction of the solar radiation absorbed in the mesosphere. An earlier laboratory study had provided a value of 0.44 ± 0.05 for the $O(^1D)$ yield at the center of the solar H Lyman-α line, where the profile shows a minimum in intensity due to strong self-reversal of the line. Using tunable laser radiation, we have determined the $O(^1D)$ yield from O_2 photodissociation across the entire H Lyman-α profile from 121.2 to 121.9 nm, at a spectral resolution of 0.0015 nm (1 cm^{-1}). The results reveal a strongly wavelength-dependent window in the $O(^1D)$ yield, the origins of which are explained using calculations based on a coupled-channel Schrödinger-equations model of the O_2 photodissociation. The calculations, which show significant isotopic dependence near H Lyman-α, predict that the depth of the quantum-yield window will increase significantly as the temperature is lowered.
 [S0021-9606(99)00604-2]

I. INTRODUCTION

The coincidence in wavelength between the H Lyman-α line ($\lambda=121.6$ nm) and a deep window in the O_2 photoabsorption cross section has important consequences for the photochemistry of the terrestrial atmosphere. Atmospheric photodissociation of O_2 by solar Lyman-α radiation[1] contributes an important fraction of the total $O(^1D)$ production in the 75–82 km altitude region, with the remainder coming from O_3 photodissociation in the 200–300 nm Hartley band.[2] Schumann-Runge (SR) band absorption leads exclusively to $O(^3P)+O(^3P)$ products, whereas it has been known since the work of Lee *et al.*[3] that the quantum yield for $O(^1D)$ at Lyman-α is 0.44 ± 0.05.

Whether $O(^1D)$ or $O(^3P)$ is generated in a particular altitude region is an important question, as it affects both the chemistry and the energy balance in that region. The chemical reactivities of $O(^1D)$ and $O(^3P)$ are quite dissimilar, and the details of the processes by means of which the electronic energy of $O(^1D)$ and the translational energy of $O(^3P)$ are dissipated are also distinct. It is therefore essential to determine the yield of $O(^1D)$ at Lyman-α, and it is particularly important in an experimental determination to use radiation that has narrow-enough bandwidth to allow measurement of the wavelength dependence of the yield within the peculiar solar Lyman-α line shape.

Figure 1 shows the solar Lyman-α profile as parametrized by Chabrillat and Kockarts,[4] together with the O_2 absorption cross section at room temperature measured by Lewis *et al.*[5] The area of this Lyman-α profile is the usual value, $\Phi_\infty=3\times10^{11}$ photons cm^{-2} s^{-1}, which is representative of a quiet-Sun activity level.[6,7] The line has a minimum of intensity at line center due to absorption by geocoronal hydrogen.[8] The full width at half-maximum (FWHM) of the line is 0.08 nm (54 cm^{-1}) and the flux at its center is about one-quarter of its peak value. In the laboratory, a typical hydrogen-discharge lamp has an unreversed, or only slightly reversed, Lyman-α profile which is typically 0.0015 nm wide. To the extent that the $O(^1D)$ yield may vary across the 0.08 nm solar linewidth, conclusions about atmospheric $O(^1D)$ processes based on laboratory data obtained using such a source could be suspect. In the work of Lee *et al.*,[3] a value of 0.44 ± 0.05 was reported for the $O(^1D)$ yield at Lyman-α, obtained using a laboratory hydrogen-discharge lamp source. In the 120–130 nm spectral region, it was observed that the $O(^1D)$ yield showed sharp variations. However, it remains unclear whether the measured yield is relevant to O_2 photodissociation by actual solar Lyman-α, since the laboratory determination was made at exactly Lyman-α, i.e., in the core of the Lyman-α profile where the solar irradiance has a minimum. It was thus necessary to develop a light source with a tunability range of at least 0.1 nm, so that the entire width of the solar Lyman-α profile could be investigated. For that purpose, we used a tunable vacuum-ultraviolet (VUV) pulsed-laser light source with a bandwidth of ~1 cm^{-1} (0.0015 nm) FWHM and a tunability >10 nm. This source was designed by Meyer and Faris[9] and will be described briefly in Sec. II.

Selected potential-energy curves for O_2 are shown schematically in Fig. 2. When O_2 is excited from its ground state $X\,^3\Sigma_g^-$ into the so-called "window region" (110–130 nm,

[a]Present address: Tech Semiconductor, Woodlands, P.O. Box 0353, Singapore 917302.

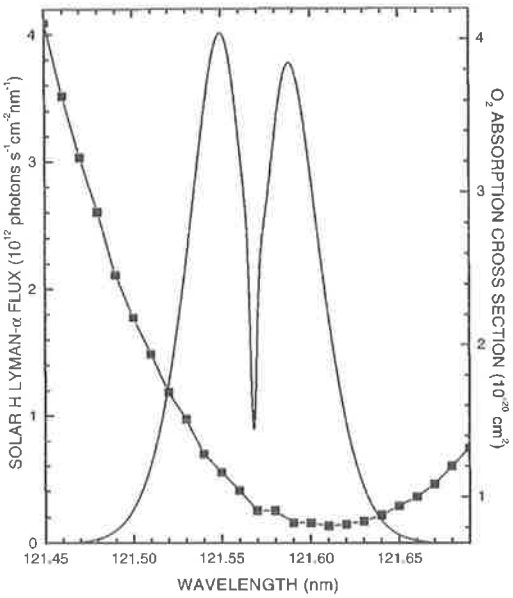

FIG. 1. Detailed view of the solar Lyman-α profile (the solid line, left axis), as parametrized by Chabrillat and Kockarts (Ref. 4) for a quiet-Sun activity level, showing its position near the minimum of the O_2 photoabsorption cross section (Ref. 5, connected squares, right axis).

9.6–11.4 eV),[10] an area of complex interactions between Rydberg and valence states, it is free to predissociate to a number of its lower dissociation limits. The energetically- and spin-allowed dissociation channels are

$$O_2(X\,^3\Sigma_g^-,\ v=0)+h\nu\rightarrow O(^3P)+O(^3P)$$
$$\rightarrow O(^3P)+O(^1D)$$
$$\rightarrow O(^3P)+O(^1S),$$

with dissociation thresholds of 242, 175, and 133 nm, respectively. In principle, fluorescence is also a possible relaxation mechanism, but Lee *et al.*[3] estimated from their experiment that the O_2 fluorescence yield after photoexcitation in this energy region was <0.001. Predissociation is therefore the dominant relaxation mechanism. Also, Ridley *et al.*[11] have determined experimentally an upper limit of 0.03 ± 0.01 for the $O(^3P)+O(^1S)$ dissociation yield at Lyman-α. Other works[12,13] have also reported a yield for this channel of <0.02, in general, between 116 and 125 nm. The channels $O(^3P)+O(^3P)$ and $O(^3P)+O(^1D)$ are, therefore, the only significant relaxation pathways available.[14]

The photoabsorption spectrum of O_2 in the window region is dominated by electric-dipole-allowed transitions from the $X\,^3\Sigma_g^-$ state into the strongly mixed Rydberg and valence states of $^3\Sigma_u^-$ and $^3\Pi_u$ symmetry. The $np\sigma_u\,^3\Pi_u$ states predissociate to the $O(^3P)+O(^3P)$ dissociation limit via the repulsive $\pi_g 3\sigma_u\,^3\Pi_u$ valence state, and the $np\pi_u\,^3\Sigma_u^-$ states predissociate principally to the $O(^1D)+O(^3P)$ limit via the $\pi_u^3\pi_g^3\,B\,^3\Sigma_u^-$ valence state, the upper state of the SR transition. For comparison with the experimental results, we have also estimated theoretically the $O(^1D)+O(^3P)$ yield by performing a coupled-channel Schrödinger-equations

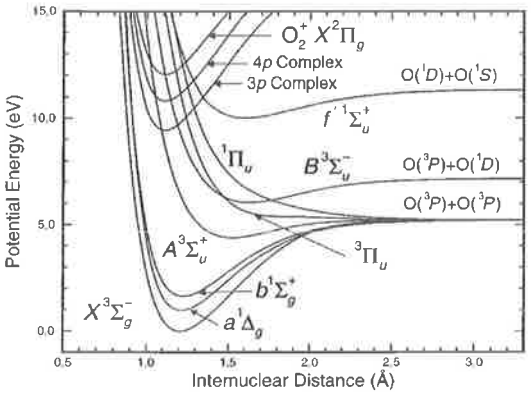

FIG. 2. Potential-energy curves of O_2, shown in a diabatic (crossing) representation. Energies are referred to the minimum in the ground-state $X\,^3\Sigma_g^-$ potential. The np Rydberg complexes, converging on the ionic ground state, contain $^{1,3}\Sigma_u^+$, $^{1,3}\Delta_u$, and $^{1,3}\Pi_u$ states.

(CSE) calculation of the partial $O_2\,^3\Sigma_u^-\leftarrow X\,^3\Sigma_g^-$ photodissociation cross section yielding $O(^1D)+O(^3P)$ and comparing it with the known experimental photoabsorption cross section.

This article is divided in two main sections: an experimental section (Sec. II), which includes a description of the data-analysis and presentation of the experimental results, and a theoretical section (Sec. III), where the $O(^1D)+O(^3P)$ quantum-yield calculation using the CSE method is described and compared with the experimental yield.

II. EXPERIMENT

A. $O(^1D)+O_2$ collisional energy transfer

We measured the relative $O(^1D)$ quantum yield from O_2 photodissociation between 121.2 and 121.9 nm at room temperature using O_2 of normal isotopic composition. The $O(^1D)$ population was monitored using the following energy-transfer reaction:

$$O(^1D)+O_2\rightarrow O_2(b\,^1\Sigma_g^+,\ v=0,1)+O(^3P), \qquad (1)$$

where about 40% of the $O_2(b\,^1\Sigma_g^+)$ molecules are formed in the $v=1$ vibrational level and the remaining fraction in $v=0$.[15,16] There is strong evidence that the efficient removal of $O_2(b\,^1\Sigma_g^+,\ v=1)$ by O_2 ($k=1.5\times10^{-11}$ cm^3 s^{-1})[17] produces principally $O_2(b\,^1\Sigma_g^+,\ v=0)$,[17] which is deactivated very inefficiently by O_2 ($k=3.9\times10^{-17}$ cm^3 s^{-1}).[15] This enables one to use the fluorescence of the $b\,^1\Sigma_g^+\rightarrow X\,^3\Sigma_g^-(0,0)$ transition at 762 nm as a measure of the $O(^1D)$ population. The radiative lifetime of the $b\,^1\Sigma_g^+(v=0)$ state is 11 s.[18] The reason for using reaction (1) for our measurement is that direct detection of $O(^1D)$ using the $O(^1D)\rightarrow O(^3P)$ emission at 630 nm is much more difficult since $O(^1D)$ has a radiative lifetime of 147 s (Ref. 18) and is deactivated very efficiently by O_2 ($k=4\times10^{-11}$ cm^3 s^{-1}).[15]

B. VUV generation

We photodissociated O_2 with tunable VUV laser light generated by a two-photon-resonant difference-frequency

(2PRDFM) mixing process using an ArF excimer laser and a Nd:YAG-pumped dye laser. Tuning of the VUV wavelength was provided by varying the dye-laser wavelength ($\nu_{VUV} = 2\nu_{ArF} - \nu_{dye}$). This VUV laser system has been described extensively in a recent article[9] and will be summarized here.

The ArF excimer-laser beam (10 Hz, ~20 mJ/pulse) and the Nd:YAG-pumped dye-laser beam (Coumarin 47, 10 Hz, ~9 mJ/pulse) were focused into a phase-matched gas mixture of H_2 and Kr (H_2:Kr=10:1) or Kr and Ar (Kr:Ar =1:4.1). The VUV generation efficiency was enhanced by tuning the ArF laser to a two-photon resonance of H_2 (103 487.08 cm^{-1}) when using the H_2:Kr mixture, or of Kr (103 363.43 cm^{-1}) when using the Kr:Ar mixture. For our measurements, the Kr:Ar mixture was necessary to generate VUV across the Lyman-α line because the use of H_2 produces H atoms which absorb VUV at that wavelength. The focal points of the two beams were spatially and temporally overlapped in the mixing cell whose exit window was a MgF_2 plano-convex lens ($R=20$ cm). The laser beams (VUV, ArF, and dye) struck the lens off-center and were thus dispersively separated (the lens also acted like a prism) in addition to being collimated over a distance of about 1.4 m *in vacuo*. At the end of this vacuum path, large (7 mm diam) and small (1.5 mm diam) apertures were used to select the VUV beam and suppress stray light from the ArF- and dye-laser beams. A red phosphor screen was used to locate the VUV beam and center it in the 1.5 mm aperture. The absolute intensity of the beam was eye-evaluated from the intensity of its spot on the phosphor screen. On the basis of a single measurement with a pyroelectric energy probe made immediately after the beam was observed on the phosphor screen, we estimated our VUV energy during this experiment to be <0.5 μJ/pulse. The relative VUV intensity was monitored between the 1.5 mm aperture and the O_2 flow cell by a solar-blind photomultiplier tube (PMT) (EMR model 542G-08-18) operated at 3.5 kV and mounted at right angles to the beam. This PMT has a CsI photocathode providing ~200× more sensitivity at Lyman-α than at the ArF wavelength (λ =193 nm). When the pulses from the dye and ArF lasers were not temporally overlapped, therefore preventing VUV production, the PMT did not generate any detectable signal. The output of the PMT was preamplified and fed to a boxcar averager, the dc output of which was voltage-to-frequency converted. In this form, the signal could be sent into the second channel of the photon counter used for the $O(^1D)$ yield measurement.

The VUV wavelength was tuned by varying the dye-laser wavelength manually via the position of its grating. We calibrated the VUV wavelength, and thus, indirectly, the dye-laser grating dial, using a VUV spectrometer and known VUV emission lines. We produced VUV emission lines around 120 nm by generating amplified spontaneous emission (ASE) in 50 Torr of H_2. When tuning the ArF laser to the $Q(1)$ line of the $E,F\,^1\Sigma_g^+ \leftarrow X\,^1\Sigma_g^+(6,0)$ two-photon transition of H_2, sufficient population was transferred from the ground state to produce ASE from the E,F state to the $B\,^1\Sigma_u^+$ state, and also subsequent ASE in the VUV from the B state to the ground state (the Lyman bands). First, we observed the $R(1)$ and $P(3)$ ASE lines of the $B\,^1\Sigma_u^+ \rightarrow X\,^1\Sigma_g^+(1,2)$ transition (83 438.44 and 82 909.46 cm^{-1}, respectively)[19] in order to calibrate the VUV spectrometer, and then VUV was produced using 2PRDFM. The VUV wavelength measured with the spectrometer defined the true dye-laser wavelength, since ν_{ArF} was tuned to a known two-photon resonance of H_2. This procedure yielded an accuracy of ± 0.01 nm (± 7 cm^{-1}) for VUV wavelengths near Lyman-α. The bandwidth of the VUV light is not known precisely, but is estimated to be on the order of 1 cm^{-1} (0.0015 nm) FWHM on the basis of a previous experiment using the same lasers and VUV generation scheme.[20]

C. O_2 flow cell

The VUV beam entered and exited the O_2 flow cell through MgF_2 windows situated 28 cm apart. Two pressure gauges (100 and 760 Torr ranges) measured the O_2 pressure in the cell. O_2 was flowed at 4.6 slpm (standard liters per minute) in order to prevent a build-up of O_3 concentration due to the production of O atoms from O_2 photodissociation. This is particularly important since the photodissociation of O_3 can lead to the production of $O(^1D)$ and $O_2(b\,^1\Sigma_g^+)$ via the spin-allowed dissociation channels $O(^1D)+O_2(a\,^1\Delta_g)$ and $O(^1D)+O_2(b\,^1\Sigma_g^+)$,[21] which have respective thresholds of 310.3 and 266.9 nm. Moreover, the O_3 to O_2 absorption cross-section ratio at Lyman-α is about 100. The use of a static cell is thus not acceptable for this experiment.

D. Fluorescence detection

Fluorescence at 762 nm from the $b\,^1\Sigma_g^+ \rightarrow X\,^3\Sigma_g^-(0,0)$ transition was detected in photon-counting mode by a cooled PMT (RCA C31034) operated at 1.9 kV and situated on the top face of the flow cell. From its point of emission in the center of the cell, the fluorescence passed successively through a fused-silica plano-convex lens ($f=5$ cm, 4 cm diam), a glass long-pass filter (Schott RG-715), and a Kodak Wratten 89-B filter. A spherical mirror ($R=3$ cm, 3.5 cm diam) was also placed at the bottom of the cell to enhance the fluorescence collection efficiency. The length of the VUV laser beam path seen by the PMT (the detection region) was 1.5 ± 0.5 cm. The distance between the beginning of this detection region and the entrance window of the flow cell was 8 ± 0.5 cm. The pulses from the PMT were preamplified 100× and sent to a dual-channel photon counter (Stanford SR400) whose second channel was used to measure the relative VUV intensity.

The $b\,^1\Sigma_g^+ \rightarrow X\,^3\Sigma_g^-(0,0)$ fluorescence counts were accumulated during a time gate open between 0.4 and 10.4 ms after the VUV laser pulse. The position and width of the time gate were determined by the lifetime of the $b\,^1\Sigma_g^+(v=0)$ state and the amount of stray light generated by the laser pulse. The fluorescence lifetime was measured in a simple preliminary laser-induced fluorescence (LIF) experiment. We excited the $b\,^1\Sigma_g^+ \leftarrow X\,^3\Sigma_g^-(1,0)$ transition of O_2 at 686.9 nm with a pulsed Nd:YAG-pumped dye laser and detected the $b\,^1\Sigma_g^+ \rightarrow X\,^3\Sigma_g^-(0,0)$ fluorescence at 762 nm. With 100 Torr of O_2 (99.995% purity) flowing in the cell, we observed a fluorescence lifetime of 2 ms, which is four times shorter than the value of 8 ms expected from the quenching of

$O_2(b\,^1\Sigma_g^+, v=0)$ by O_2.[15] We first thought that this shorter lifetime could be caused by water vapor or another contaminant coming from the O_2 cylinder. The rate constant for quenching of $O_2(b\,^1\Sigma_g^+, v=0)$ by H_2O is large enough ($k=5.4\times10^{-12}$ cm^3 s^{-1}) to cause this effect, at the specified impurity level for the O_2 cylinder. Since a longer fluorescence lifetime results in a better signal, we tried to condense the impurities by flowing O_2 through a bath of dry ice and isopropanol prior to its injection into the cell. Unfortunately, this lengthened the lifetime from 2 to only 2.2 ms. Interestingly, we also observed that the fluorescence lifetime depended on the flow cell used. The lifetime was 2 ms with the stainless-steel cell used for the experiment at Lyman-α, and only 0.83 ms with a black-anodized coated cell. It thus appears that most of the impurities shortening the fluorescence lifetime come from the cell walls, a black-anodized coating being a more efficient adsorber than stainless steel. As a precautionary measure during the experiment at Lyman-α, we installed a bath of dry ice and isopropanol between the mechanical pumping system and the output of the flow cell in order to trap pump-oil particles that might have been very efficient at quenching the $b\,^1\Sigma_g^+(v=0)$ state. We do not know, however, if this actually lengthened the fluorescence lifetime since the signal at Lyman-α was too low to permit an easy measurement.

In summary, with the setup described above, we detected an average of 13 O_2 $b\,^1\Sigma_g^+ \rightarrow X\,^3\Sigma_g^-(0,0)$ fluorescence events per VUV laser shot, with an average signal-to-background ratio of 2.7. The background counts most probably originate from the typical reddish fluorescence produced when the VUV laser beam, and to a lesser extent the ArF stray light, traverse the MgF_2 windows of the cell.

E. Data acquisition

The intensity $S(\lambda)$ (counts per laser pulse) of the $b\,^1\Sigma_g^+ \rightarrow X\,^3\Sigma_g^-(0,0)$ fluorescence signal at wavelength λ, which is proportional to the $O(^1D)$ quantum yield $\Phi_{^1D}(\lambda)$, is given by

$$S(\lambda)=\epsilon N_{\mathrm{abs}}(\lambda)\Phi_{^1D}(\lambda), \tag{2}$$

where ϵ is the $b\,^1\Sigma_g^+ \rightarrow X\,^3\Sigma_g^-(0,0)$ fluorescence detection efficiency, and $N_{\mathrm{abs}}(\lambda)$ is the number of photons absorbed per laser pulse in the detection region. If the number of photons per laser pulse entering the cell at wavelength λ is $f(\lambda)$, $N_{\mathrm{abs}}(\lambda)$ will be given by

$$N_{\mathrm{abs}}(\lambda)=f(\lambda)\exp[-\sigma(\lambda)\rho l_0]\{1-\exp[-\sigma(\lambda)\rho l_1]\}, \tag{3}$$

where $l_0=8\pm0.5$ cm defines the preabsorption region, i.e., the length between the entrance of the cell and the beginning of the detection region, $l_1=1.5\pm0.5$ cm is the length of the detection region, $\sigma(\lambda)$ is the absorption cross section (cm^2 molecule^{-1}) of O_2 at wavelength λ, and ρ is the O_2 number density (molecules cm^{-3}).

One of the difficulties in measuring the $O(^1D)$ quantum yield in the Lyman-α region is the fact that the O_2 absorption cross section increases very steeply when moving away from its minimum value near 121.6 nm (Fig. 1). This fact has two consequences. First, the wavelength dependence of the O_2 $b\,^1\Sigma_g^+ \rightarrow X\,^3\Sigma_g^-(0,0)$ fluorescence signal will depend not only on the wavelength dependence of the $O(^1D)$ yield, but also on the wavelength dependence of the O_2 absorption cross section, as shown by Eqs. (2) and (3). This dependence must be reflected in the data analysis. Second, it is clear that the pressure dependence of the signal intensity at a given wavelength will show a maximum. This is due to the tradeoff between having more absorbers in the detection region, and having more VUV power loss in the preabsorption region. As the VUV wavelength varies, the pressure giving the optimum signal will change due to the variation of the O_2 absorption cross section. Since our $b\,^1\Sigma_g^+ \rightarrow X\,^3\Sigma_g^-(0,0)$ fluorescence signal was not very large, it was difficult to measure the $O(^1D)$ yield across and beyond the solar Lyman-α profile at constant O_2 pressure without losing the signal. We therefore measured the $O(^1D)$ yield over a given wavelength region, and then changed the pressure to measure the yield over another region.

TABLE I. Characteristics and experimental conditions for each wavelength region used in the $O(^1D)$ quantum-yield measurements.

Region	λ-range (nm)	$P(O_2)$ (Torr)	No. of points	Nonlin. medium	P(med.) (Torr)
1	121.48–121.64	144±6	9	Kr:Ar	100:410
2	121.45–121.67	144±6	9	Kr:Ar	100:410
3	121.65–121.91	87±1	14	H_2:Kr	200:20
4	121.79–121.86	87±1	6	H_2:Kr	200:20
5	121.24–121.54	29±1	12	H_2:Kr	100:10
6	121.42–121.50	87±1	3	H_2:Kr	100:10

The data were acquired in the following way. After having manually set the VUV wavelength to a given value, the fluorescence counts and the VUV level were accumulated simultaneously for 600 laser shots under each of the following conditions: (1) with O_2 flowing in the cell; (2) without O_2 in the cell; (3) without O_2 in the cell and with the ArF- and dye-laser pulses desynchronized, thus preventing VUV production; (4) with O_2 in the cell and the ArF- and dye-laser pulses desynchronized. Condition (1) measured the signal proportional to the $O(^1D)$ production, or "$O(^1D)$ signal." Condition (2) measured the fluorescence background, which varied linearly with the relative VUV intensity. Condition (3) allowed measurement of the background in the VUV channel. The comparison of the fluorescence counts in steps (3) and (4) was important because it confirmed that stray light from the ArF laser ($\lambda=193$ nm) was not intense enough to produce fluorescence from its absorption by O_2, or, potentially, O_3. The data were taken in segments of six overlapping wavelength regions. Table I lists for each wavelength region the O_2 pressure, the number of points, and the nonlinear medium used to generate the VUV light.

F. Data analysis

We measured the *relative* wavelength dependence of the $O(^1D)$ quantum yield, which is proportional to the absolute $O(^1D)$ yield, $\Phi_{^1D}(\lambda)$ of Eq. (2). In other words, we did not calibrate ϵ, the $b\,^1\Sigma_g^+ \rightarrow X\,^3\Sigma_g^-(0,0)$ fluorescence detection efficiency. For each point of a given wavelength region, a

number directly proportional to $\Phi_{^1D}(\lambda)$ was extracted by normalizing the experimental signal $S(\lambda)$ using $N_{abs}(\lambda)$ [Eq. (3)]. In Eq. (3), the number $f(\lambda)$ of photons entering the cell per laser pulse was not measured, but was proportional to the measured relative VUV intensity I_{VUV}. From Eqs. (2) and (3), with $c(\lambda)=N_{abs}(\lambda)/f(\lambda)$ as the correction factor accounting for the variation of the absorption cross section of O_2, we obtain

$$\Phi_{^1D}(\lambda)\propto S(\lambda)/[c(\lambda)I_{VUV}]. \tag{4}$$

In the determination of $c(\lambda)$ we used the room-temperature O_2 absorption cross section of Lewis *et al.*,[5] corrected for pressure effects, for wavelength regions entirely contained between 121.4 and 121.9 nm (regions 1 and 2 in Table I), and the parametrized cross section of Dose *et al.*[22] for regions extending beyond this range (regions 3–6). The uncertainty of those cross sections is ~5%. With this correction procedure, the relative wavelength dependence of the $O(^1D)$ yield was determined within a single wavelength region. Since each of the six wavelength regions scanned partially overlapped the neighboring ones, the relative $O(^1D)$ yield across the entire wavelength range could be obtained by scaling the data so that they formed a single continuous curve.

On average, the uncertainty in the data points is ~8%, of which two-thirds arises from uncertainty in the correction factor $c(\lambda)$. An additional uncertainty of ~5% should be included to take into account the fact that the wavelength range of our experiment necessitated the use of experimental O_2 photoabsorption cross sections from two sources which differed slightly in their region of overlap.

G. Results and discussion

Our measured $O(^1D)$ quantum yields are shown in Fig. 3 and listed in Table II. The parametrized O_2 absorption cross section of Dose *et al.*[22] and the solar Lyman-α profile of Chabrillat and Kockarts[4] are reproduced in the bottom part of Fig. 3. The solid curve superimposed on the experimental data points is a Gaussian least-squares fit to equally weighted data points between 121.46 and 121.67 nm. It is important to recall that our yield measurements were not made absolutely. In the earlier study of Lee *et al.*,[3] it was possible to obtain a yield at Lyman-α relative to measurements in the Schumann–Runge continuum at 135–175 nm, where it is accepted that the $O(^1D)$ yield is unity. This was not possible in the present situation, with limited tunability of the laser system. We were therefore faced with two choices: either to use the earlier laboratory Lyman-α value, 0.44±0.05, as a point of normalization, or to use the results of our calculations (Sec. III) which indicate that, as the photodissociation wavelength approaches the peak of the 120.6 nm "second band" of O_2, the yield should become unity. Fortunately, these two choices do not lead to very different final results. Because the short-wavelength yield appears to reach a limiting value at the same time as the absorption cross section is rapidly increasing toward the 120.6 nm peak, it seems reasonable to judge that this limiting value is, in fact, unity. By normalizing in this manner, the laboratory Lyman-α value, at 121.57 nm, is increased from 0.44±0.05 to 0.53±0.05, which we believe does not do injustice to the earlier work.

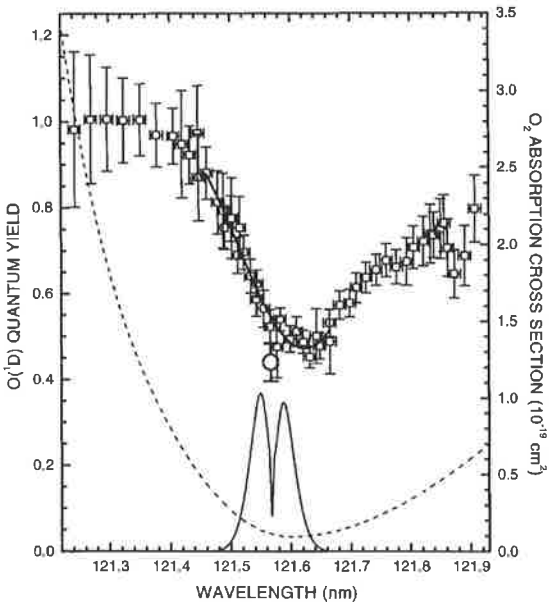

FIG. 3. Measured $O(^1D)$ quantum yield (squares, left axis). The parametrized O_2 absorption cross section of Dose *et al.* (Ref. 22, the dashed line, right axis) and the solar Lyman-α profile (Ref. 4) are reproduced in the bottom part of the figure. The solid line superimposed on the experimental data points is a Gaussian least-squares fit between 121.46 and 121.67 nm. The open circle is the previously measured value of 0.44±0.05 for the $O(^1D)$ yield (Ref. 3).

The quantity of interest for modeling the $O(^1D)$ production rate by solar Lyman-α in the mesosphere and lower thermosphere (MLT) is the weighted-mean quantum yield $\langle\Phi_{^1D}\rangle$ given by

$$\langle\Phi_{^1D}\rangle=\frac{\int\Phi_{^1D}(\lambda)J(\lambda)d\lambda}{\int J(\lambda)d\lambda}=\frac{\int\Phi_{^1D}(\lambda)F(\lambda)\sigma(\lambda)d\lambda}{\int F(\lambda)\sigma(\lambda)d\lambda}, \tag{5}$$

where integration takes place over the solar Lyman-α profile. In Eq. (5), $J(\lambda)$ is the photolysis rate of O_2, given by the product $F(\lambda)\sigma(\lambda)$, where $F(\lambda)$ is the solar Lyman-α flux. It will be shown in Sec. III that the $O(^1D)$ quantum yield $\Phi_{^1D}(\lambda)$ is also a function of temperature, as is the O_2 absorption cross section $\sigma(\lambda)$.[5] In the MLT, the weighted-mean $O(^1D)$ yield will therefore depend on altitude via the temperature dependence of $\sigma(\lambda)$ and $\Phi_{^1D}(\lambda)$. Interestingly, the wavelength distribution of the solar Lyman-α flux $F(\lambda)$ is also a function of altitude. As pointed out by Nicolet,[23] the shape of the O_2 absorption cross section within the solar Lyman-α profile (Fig. 1) will generate stronger absorption of the low-wavelength half of the profile than of the high-wavelength half, thus deforming the profile as the light penetrates the atmosphere. This deformation will cause the weighted-mean $O(^1D)$ yield to decrease with decreasing altitude.

Given the purpose of this work, here we will limit ourselves to calculating the weighted-mean $O(^1D)$ quantum yield at room temperature using the O_2 absorption cross section of Lewis *et al.*,[5] the parametrized profile of Chabrillat

TABLE II. Experimental $O(^1D)$ yield as a function of wavelength.

λ (nm)[a]	Region[b]	$O(^1D)$ yield[c]	λ (nm)[a]	Region[b]	$O(^1D)$ yield[c]
121.243	5	0.98±0.18	121.599	1	0.49±0.03
121.270	5	1.01±0.15	121.610	2	0.51±0.03
121.297	5	1.01±0.12	121.621	1	0.49±0.03
121.324	5	1.00±0.10	121.632	2	0.45±0.02
121.351	5	1.00±0.08	121.643	1	0.50±0.06
121.378	5	0.97±0.07	121.648	3	0.48±0.03
121.406	5	0.97±0.07	121.665	3	0.53±0.03
121.420	6	0.95±0.12	121.665	2	0.49±0.07
121.433	5	0.92±0.07	121.682	3	0.57±0.03
121.447	2	0.97±0.11	121.698	3	0.58±0.03
121.447	6	0.87±0.10	121.710	3	0.61±0.03
121.460	5	0.88±0.06	121.726	3	0.64±0.04
121.479	1	0.81±0.07	121.743	3	0.66±0.04
121.488	5	0.79±0.09	121.760	3	0.68±0.04
121.490	2	0.75±0.05	121.777	3	0.66±0.04
121.501	1	0.77±0.05	121.794	4	0.67±0.06
121.502	6	0.78±0.09	121.805	3	0.71±0.05
121.512	2	0.69±0.04	121.822	4	0.72±0.06
121.515	5	0.75±0.07	121.833	4	0.74±0.07
121.523	1	0.70±0.04	121.839	3	0.74±0.05
121.534	2	0.64±0.04	121.850	4	0.75±0.07
121.543	5	0.59±0.04	121.856	4	0.76±0.07
121.544	1	0.62±0.03	121.862	4	0.71±0.07
121.555	2	0.57±0.04	121.873	3	0.65±0.06
121.566	1	0.52±0.04	121.890	3	0.69±0.07
121.577	2	0.48±0.07	121.907	3	0.80±0.08
121.583	1	0.54±0.03			

[a]Wavelength calibration uncertainty ±0.01 nm (see the text).
[b]Scan region containing tabulated datum point (see Table I).
[c]Tabulated uncertainties are statistical, representing one standard deviation. An additional uncertainty of ~5% should be included to account for the use of two experimental O_2 photoabsorption cross sections which differ slightly in their range of overlap (see the text).

and Kockarts[4] representing the solar Lyman-α line shape at the top of the atmosphere, and our measured $O(^1D)$ yield. The weighted-mean $O(^1D)$ yield is calculated using Eq. (5), where the integration is performed on a grid defined by the experimental data points using the trapezoidal method. This calculation yields the result $\langle \Phi_{^1D} \rangle = 0.58 \pm 0.06$. It is verified easily that the same value is obtained when using the fitted Gaussian $O(^1D)$ yield shown in Fig. 3. This functional form of the yield, which may prove useful in atmospheric modeling, is given by

$$\Phi(\lambda) = 1.08 - \{0.168/[0.11(2\pi)^{1/2}]\} \times \exp\{-0.5[(\lambda - 121.623)/0.11]^2\}, \quad (6)$$

where λ is in the range 121.46–121.67 nm. It is also interesting to note that, when using only the numerator of Eq. (5), one finds that the low-wavelength half (λ<121.57 nm) of the solar Lyman-α profile at the top of the atmosphere (Fig. 1) produces two-thirds of the $O(^1D)$ generated by the full solar Lyman-α line.

In addition to being consistent with the previous value of the yield at exactly Lyman-α, our experimental wavelength-dependent $O(^1D)$ yield agrees well with the results of a semi-empirical CSE calculation. Section III explains how the calculations were performed and compares them with the experimental results.

III. THEORY

As implied in Sec. I, the total O_2 photodissociation cross section in the window region may be thought of as the sum of cross sections for the allowed transitions into the Rydberg-valence coupled $^3\Sigma_u^-$ and $^3\Pi_u$ states, the $O(^1D) + O(^3P)$ photofragments arising entirely from $^3\Sigma_u^-$ dissociations. In Sec. III A, we model the $O(^1D) + O(^3P)$ quantum yield in the window region near Lyman-α using the CSE method, and in Sec. III B the results are compared with our measured quantum yield.

A. Method of calculation

1. The CSE method

In the case of Rydberg and valence states of the same symmetry with molecular-orbital configurations differing in one or two of the occupied orbitals, such as the $^3\Pi_u$ and $^3\Sigma_u^-$ states of O_2, respectively, there may be strong interactions which invalidate the Born–Oppenheimer (BO) approximation.[24] This breakdown of the BO approximation may be addressed by using a CSE model in which the interactions between the BO basis states are included explicitly. In the adiabatic basis, the adiabatic potential-energy curves for the BO basis states exhibit an avoided crossing and these states interact nonadiabatically through an off-diagonal element of the nuclear kinetic-energy operator. In the diabatic basis, the diabatic BO basis-state potential-energy curves cross and interact through an off-diagonal element of the electrostatic Hamiltonian. Provided that a complete electronic-state basis is employed, then the results of CSE calculations are insensitive to the choice of an adiabatic or diabatic basis set. In practice, it is sufficient to include only enough interacting electronic states to accurately describe spectra in the energy region of interest. In this work, we choose the diabatic BO basis, as this has the attractive property that the wave functions, potential-energy curves, and coupling matrix elements can be expected to change smoothly with internuclear separation R.

The techniques of scattering theory[25] have been adapted to the calculation of molecular photodissociation cross sections. The CSE formalism, detailed by van Dishoeck *et al.*[26] and Torop *et al.*,[27] is particularly suitable for treatment of the strong Rydberg-valence interactions in O_2 and has been applied previously to explain unusual features in the spectrum of O_2.[28–31] Details of a CSE formulation suitable for the description of rovibronic photodissociation of O_2 have been given by Lewis *et al.*[29] Briefly, for a transition from a given rovibrational level of an initial uncoupled electronic state i into the n coupled states k, which include n_o open channels, the partial photodissociation cross section, in cm^2, to the open channel γ is given by

$$\sigma_{\gamma EJ \leftarrow iv''J''\Omega''} = 1.225 \times 10^{-23} g \nu \times |\langle \chi_{\gamma EJ}(R)|\mathbf{M}|\chi_{iv''J''\Omega''}(R)\rangle|^2, \quad (7)$$

and the total cross section by

$$\sigma_{EJ \leftarrow iv''J''\Omega''} = \sum_{\gamma=1}^{n_o} \sigma_{\gamma EJ \leftarrow iv''J''\Omega''}, \quad (8)$$

where E is the coupled-state energy, J is the rotational quantum number, ν is the transition energy in cm^{-1}, the degeneracy factor $g=(2-\delta_{0,\Lambda+\Lambda''})/(2-\delta_{0,\Lambda''})$, and the transition matrix elements are in atomic units. In Eq. (7), $\boldsymbol{\chi}_{\gamma EJ}(R)$ is the $n\times 1$ vector of coupled-channel radial wave functions with outgoing flux into channel γ, $\chi_{iv''J''\Omega''}(R)$ is the vibrational wave function of the initial state, and the elements of the $n\times 1$ rotronic transition-moment vector $\mathbf{M}$ are the products of appropriately normalized electronic transition moments $\mathcal{M}_k(R)$ and rotational matrix elements of the direction-cosine operator. The coupled-channel radial wavefunction vector $\boldsymbol{\chi}_{\gamma EJ}(R)$ is the solution of the diabatic-basis coupled Schrödinger equations, expressed in matrix form,

$$\left\{\mathbf{I}\frac{d^2}{dR^2}+\frac{2\mu}{\hbar^2}[E\mathbf{I}-\mathbf{V}(R)-\mathbf{V}^{\mathrm{rot}}(R)]\right\}\boldsymbol{\chi}_{\gamma EJ}(R)=0, \quad (9)$$

where μ is the molecular reduced mass, $\mathbf{I}$ is the identity matrix, $\mathbf{V}(R)$, of dimension $n\times n$, is the symmetric diabatic potential matrix, the diagonal elements of which are the diabatic electronic potential-energy curves $V_k(R)$, and $\mathbf{V}^{\mathrm{rot}}(R)$ is a diagonal matrix with elements given by matrix elements of the rotational part of the molecular Hamiltonian. The couplings between the interacting electronic states are given by the off-diagonal elements of $\mathbf{V}(R)$, containing the effects of electrostatic, rotational and spin-orbit interactions.

If the electronic wave functions are expressed in the Hund's case (a) e/f parity basis,[24] then the only nonzero elements $\mathcal{M}_k(R)$ arise from dipole-allowed parallel and perpendicular transitions between case (a) basis states and forbidden transitions borrow strength via the explicitly calculated upper-state mixing processes. For a finite temperature, the effective partial (or total) photodissociation cross sections can be expressed as the sums of cross sections into the upper-state e and f levels, each of which is calculated separately as a Boltzmann average of Eq. (7) [or Eq. (8)] over the initial distribution of v'',J'', and, in the case of a multiplet, Ω'' or F_i''.

2. The model implementation

In principle, the photodissociation of O_2 near Lyman-α at ~121.6 nm can be modeled by performing separate CSE calculations of the Rydberg-valence $^3\Pi_u \leftarrow X\,^3\Sigma_g^-$ and $^3\Sigma_u^- \leftarrow X\,^3\Sigma_g^-$ total photodissociation cross sections, which we denote as the "Π" and "Σ" cross sections, respectively. Since the Π_u dissociations yield only $O(^3P)+O(^3P)$ products, the total $O(^1D)+O(^3P)$ quantum yield would then be given by

$$\Phi_{^1D}(\lambda)=\sigma_{\Sigma_{^1D}}(\lambda)/[\sigma_\Sigma(\lambda)+\sigma_\Pi(\lambda)], \quad (10)$$

where $\sigma_{\Sigma_{^1D}}(\lambda)$ is the partial Σ cross section yielding $O(^1D)+O(^3P)$, denoted as "$\Sigma_{^1D}$." However, significant uncertainties result in the Π cross section and the quantum yield determined in this way. The nearest identifiable $^3\Pi_u \leftarrow X\,^3\Sigma_g^-$ features in the O_2 spectrum occur at ~135.5 and ~116.2 nm, associated, respectively, with the lower and upper adiabatic states formed due to the strong $^3\Pi_u$ Rydberg-valence interaction.[28] In the extensive energy region between these states, which includes Lyman-α, the calculated CSE Π cross section becomes weak and oscillatory, and, in the absence of experimental information enabling refinement of the $^3\Pi_u$ model parameters pertinent to this region, cannot be regarded as reliable. On the other hand, the strong Σ cross section which dominates this region of the spectrum can be characterized well by a CSE treatment. Lyman-α lies between the longest and second bands of O_2,[32] at ~124.4 and ~120.6 nm, respectively, very strong predissociating resonances associated with the $v=0$ and $v=1$ levels of the $E\,^3\Sigma_u^-$ state, the upper adiabatic state resulting from the $^3\Sigma_u^-$ Rydberg-valence interaction. Therefore, in this work we calculate only the partial and total Σ cross sections, estimating the total $O(^1D)+O(^3P)$ quantum yield in the Lyman-α region using the expression

$$\Phi_{^1D}(\lambda)=\sigma_{\Sigma_{^1D}}(\lambda)/\sigma(\lambda), \quad (11)$$

where, as in Sec. II, $\sigma(\lambda)$ is the O_2 photoabsorption cross section. It is important to note that it is assumed implicitly in Eq. (11) that the cross sections $\sigma_{\Sigma_{^1D}}(\lambda)$ and $\sigma(\lambda)$ refer to the same isotopic variant or mixture of O_2. For most wavelengths, cross sections for O_2 of normal isotopic composition are indistinguishable from those for $^{16}O_2$. However, as will be seen in Sec. III B, this does not apply to the cross-section minimum near Lyman-α where it is essential to use a $\Sigma_{^1D}$ cross section properly corrected for isotopic effects before estimating $O(^1D)$ quantum yields using Eq. (11).

Our CSE model, optimized using experimental information over the 110.0–140.0 nm range, provides an accurate description of a large number of Σ_u features in the window region of the O_2 spectrum. A detailed description of the optimization of the model parameters is given elsewhere.[33] Briefly, the model includes the $n=3$ and $n=4$ Rydberg states and the lowest valence states of $^3\Sigma_u^-$, $^3\Sigma_u^+$ and $^1\Sigma_u^+$ symmetry, and takes into account Rydberg-valence couplings for each symmetry, $^3\Sigma_{u1}^- - {}^3\Sigma_{u1}^+$ and $^3\Sigma_{u0}^- - {}^1\Sigma_{u0}^+$ Rydberg–Rydberg spin-orbit couplings (~100 cm^{-1}), and S-uncoupling in the triplet states ($2B_\Sigma\sqrt{J(J+1)}$). The $^3\Sigma_u^+$ and $^1\Sigma_u^+$ states have been included to allow a description of the forbidden band systems, $3p\pi_u\, f\,^1\Sigma_u^+ \leftarrow X\,^3\Sigma_g^-$ and $3p\pi_u\, D\,^3\Sigma_u^+ \leftarrow X\,^3\Sigma_g^-$, which are visible in the window region. Within the framework of the CSE model, these forbidden systems occur by borrowing strength from the allowed $^3\Sigma_u^- \leftarrow X\,^3\Sigma_g^-$ transition through spin-orbit interactions between components of the $3p$ Rydberg complex. As will be seen in Sec. III B, the inclusion of the $^3\Sigma_u^+$ states is particularly important for an accurate estimation of the $O(^1D)$ quantum yield near Lyman-α, since the $np\pi_u\,^3\Sigma_u^+$ Rydberg states, which are spin-orbit-coupled to the isoconfigurational $^3\Sigma_u^-$ states, are predissociated by the $\pi_u^3\pi_g^3 A\,^3\Sigma_u^+$ state, the upper state of the Herzberg I system, which correlates with the $O(^3P)+O(^3P)$ limit. Thus, in certain narrow spectral regions the $O(^1D)$ quantum yield pertaining to the Σ spectrum will fall below the value of unity expected for pure $^3\Sigma_u^-$ predissociation. Our calculated cross sections were obtained, formally, by summing separate upper-state e-level and f-level calculations. The e-level block included the twelve diabatic states of $^3\Sigma_{u0}^-$, $^3\Sigma_{u1}^-$, $^3\Sigma_{u1}^+$, and $^1\Sigma_{u0}^+$ symmetry,

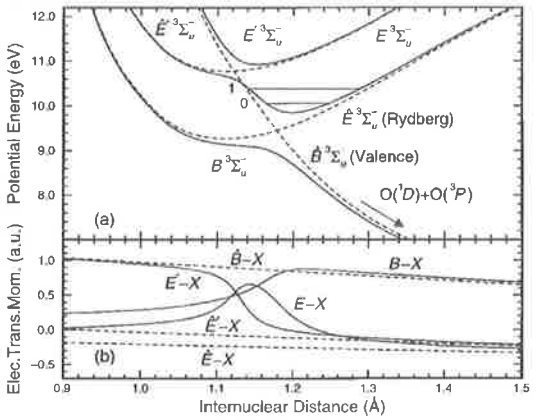

FIG. 4. (a) Diabatic CSE-model potential-energy curves $V_k(R)$ for the $^3\Sigma_u^-$ states of O_2 (dashed lines). The energy scale is defined relative to the minimum in the ground-state $X\,^3\Sigma_g^-$ potential-energy curve and the electronic-state nomenclature is discussed in Ref. 34. Strong Rydberg-valence coupling results in the corresponding adiabatic potential-energy curves (solid lines) exhibiting avoided crossings. The upper-state levels for the longest and second bands are indicated in relation to the adiabatic E-state potential, formed by the interaction of the pure valence and $n=3$ and $n=4$ Rydberg states. The Lyman-α region lies between these two levels. Predissociation of the E state occurs via the B state which correlates with the $O(^1D)+O(^3P)$ dissociation limit. (b) Diabatic CSE-model electronic transition moments $\mathcal{M}_k(R)$ for the $^3\Sigma_u^-\leftarrow X\,^3\Sigma_g^-$ transitions (dashed lines), together with the corresponding adiabatic moments (solid lines).

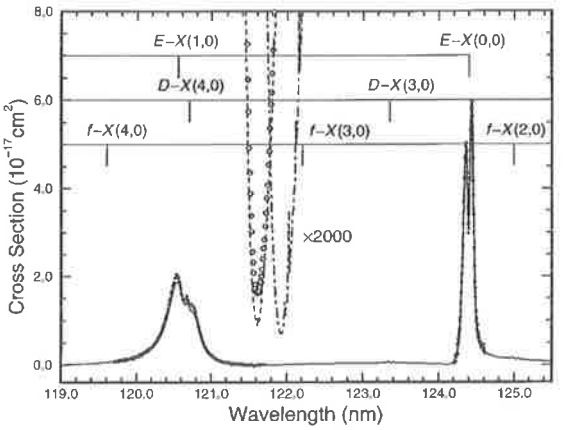

FIG. 5. Calculated and measured O_2 room-temperature cross sections. Experimental photoabsorption cross sections for the longest and second bands, $E\,^3\Sigma_u^-\leftarrow X\,^3\Sigma_g^-(0,0)$ and (1,0), (Refs. 40 and 41, solid circles) are compared with our calculated 297 K CSE Σ cross section for $^{16}O_2$ (the solid line). The positions of features arising from forbidden transitions into the $f\,^1\Sigma_u^+$ and $D\,^3\Sigma_u^+$ states are also indicated. In addition, with the aid of an expanded cross-section scale, the 288 K photoabsorption cross section of Lewis *et al.* (Ref. 5, open circles) is compared with our calculated 288 K CSE Σ cross section for $^{16}O_2$ (the dashed line). The calculated Σ cross section is significantly smaller than the measured total cross section at the cross-section minimum near 121.6 nm, indicating that the $O(^1D)+O(^3P)$ quantum yield is significantly less than unity (see the text). The calculated 288 K CSE Σ cross section for the $^{16}O^{18}O$ isotopomer (the dot-dashed line) is substantially greater than the $^{16}O_2$ cross section at Lyman-α and must be considered when estimating the quantum yield for normal O_2.

while the f-level block included the nine diabatic states of $^3\Sigma_{u1}^-$, $^3\Sigma_{u1}^+$, and $^3\Sigma_{u0}^+$ symmetry.

In this work, we concentrate mainly on a description of the $^3\Sigma_u^-$ model. In Fig. 4, the diabatic $^3\Sigma_u^-$ potential-energy curves $V_k(R)$ and $^3\Sigma_u^-\leftarrow X\,^3\Sigma_g^-$ electronic transition moments $\mathcal{M}_k(R)$ used in our CSE model are shown (dashed lines), together with the corresponding adiabatic potentials and transition moments (solid lines).[34] The diabatic electronic transition moments are taken to have a linear R dependence, while the Rydberg-valence couplings, 4033 and 2023 cm^{-1}, for $n=3$ and $n=4$, respectively, scaling approximately with $(n^*)^{-3/2}$,[24] are taken to be R independent.[35] While the diabatic $\hat{B}$-state valence potential-energy curve crosses the diabatic Rydberg curves, the strong electrostatic Rydberg-valence interaction in this basis results in adiabatic potential-energy curves which avoid crossing and are of heavily mixed character. In particular, the bound adiabatic E-state potential is a mixture of the pure valence and $n=3$ and $n=4$ Rydberg states. Conventionally, the lowest two vibrational levels of this *adiabatic* state are associated with the longest and second bands, the upper-state energies of which are shown in Fig. 4. However, it should be emphasized that neither the diabatic nor the adiabatic potential-energy curves exactly represent the observed energy levels and it is necessary to employ the CSE method to obtain realistic energies and cross sections. The adiabaticity parameter[36,37] for the lowest $^3\Sigma_u^-$ crossing is $\zeta\approx 1.3$, implying character intermediate between adiabatic and diabatic for the E-state levels in this region.

Initially, we calculated the room-temperature Σ cross section for $^{16}O_2$ defined by the CSE model described above, i.e., consisting essentially of the $^3\Sigma_u^-\leftarrow X\,^3\Sigma_g^-$ cross section, with minor features due to the $^3\Sigma_u^+$ and $^1\Sigma_u^+$ states, in the range 119.0–126.0 nm. First, using the diabatic upper-state potential-energy curves and couplings described above, the diabatic coupled-channel radial wave functions $\chi_{\gamma EJ}(R)$, normalized according to the method of Mies,[25] were calculated by solving Eq. (9) using the renormalized Numerov method of Johnson.[38] Second, ground-state vibrational wave functions $\chi_{X0J''\Omega''}$, calculated using a Rydberg–Klein–Rees potential-energy curve for the $X\,^3\Sigma_g^-$ state constructed from the spectroscopic constants of Cosby,[39] together with the diabatic electronic transition moments of Fig. 4 and appropriate rotational matrix elements, were used with Eqs. (7) and (8) to calculate the individual rotational cross sections into the e- and f-level coupled-channel blocks, $\sigma_{EJ\leftarrow X0J''\Omega''}$. Third, forming appropriate ground-state wave functions for a Hund's coupling case intermediate between (a) and (b), and adding the e- and f-level cross sections while performing a Boltzmann average over the ground-state fine-structure levels, the final room-temperature Σ cross section was formed.

B. Results and discussion

In Fig. 5, the $^{16}O_2$ Σ cross section calculated for a temperature of 297 K is shown (the solid line), compared with experimental O_2 room-temperature photoabsorption cross sections measured for the longest[40] and second[41] bands (solid circles), $E\leftarrow X(0,0)$ and (1,0), respectively. Agreement between the calculations and measurements is excellent for

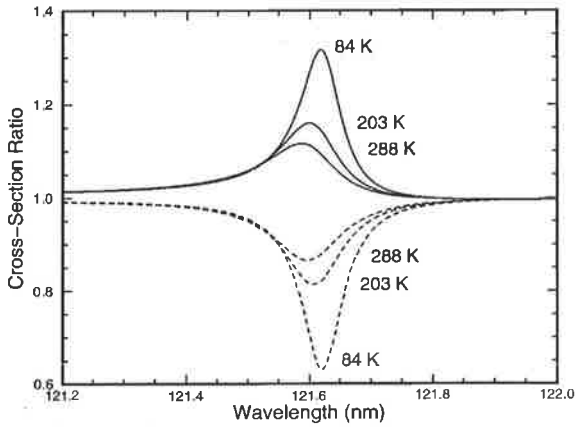

FIG. 6. The significance of second-order effects on the calculated cross sections for temperatures of 288, 203, and 84 K. Solid lines: Isotopic effect; ratios of the calculated Σ cross sections for normal O_2 and $^{16}O_2$. Dashed lines: Effect of indirect predissociation of the $^3\Sigma_u^-$ states by the $A\,^3\Sigma_u^+$ state; ratios of the calculated Σ_{1D} and Σ cross sections for $^{16}O_2$. Both effects are included in the calculated $O(^1D)$ quantum yields of Fig. 7.

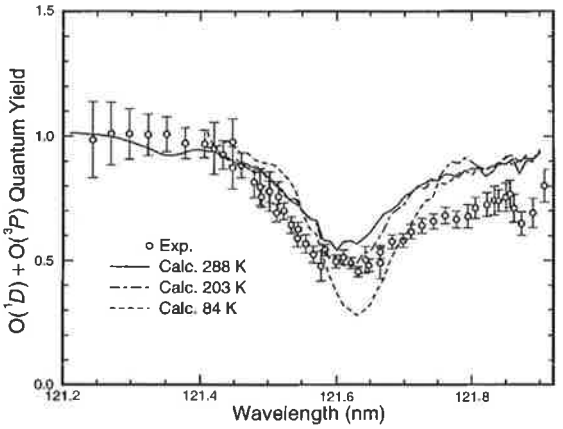

FIG. 7. Comparison between calculated and room-temperature experimental $O(^1D)+O(^3P)$ quantum-yield spectra for the photodissociation of O_2 near Lyman-α. Calculated quantum yields were obtained from our calculated CSE Σ_{1D} spectra, corrected for isotopic effects and shifted to longer wavelengths by 0.005 nm, and the experimental photoabsorption spectra of Refs. 5 and 22 (see the text for a discussion). The calculated minimum quantum yield, near 121.62 nm, decreases substantially as the temperature is lowered.

these very strong bands, with the largest discrepancy an ~5% underestimation of the cross section for the second band at ~120.6 nm. The positions of bands of the forbidden $f \leftarrow X$ and $D \leftarrow X$ systems are also indicated on Fig. 5. The most significant of these is the $D \leftarrow X(4,0)$ band which coincides with the second band, producing an interesting quantum-interference effect which will be discussed in detail elsewhere.[42] It is important to note that the excellent agreement between the calculated and measured structure on the long-wavelength wing of the second band would not have been possible without the inclusion of $^3\Sigma_u^+$ states in the CSE model.

Also shown in Fig. 5, with an expanded vertical scale, is the $^{16}O_2$ Σ cross section calculated for a temperature of 288 K in the region of Lyman-α (the dashed line), compared with the O_2 photoabsorption cross section, extrapolated to zero pressure, measured at the same temperature by Lewis *et al.*[5] (open circles). In this region, the measured cross section passes through a deep minimum, with a cross section some 10 000× smaller than at the peak of the longest band. The calculated Σ cross section also passes through a deep minimum at a similar wavelength, but this calculated minimum is significantly deeper than the measured minimum. This merely reflects the fact that we have calculated the Σ cross section, rather than the $\Sigma+\Pi$ cross section, and indicates that the $O(^1D)+O(^3P)$ quantum yield is significantly less than unity at the cross-section minimum. Rotational structure in the calculated Σ cross section at wavelengths longward of the minimum arises from the forbidden $f \leftarrow X(3,0)$ band.

The calculated $^{16}O^{18}O$ Σ cross section for $T=288$ K is also shown in Fig. 5 (the dot-dashed line). Due to a significant isotopic shift, the cross section for this isotopomer greatly exceeds that for $^{16}O_2$ at Lyman-α. The ratio of the calculated Σ cross sections for normal O_2 and $^{16}O_2$ is plotted in Fig. 6 (solid lines) as a function of wavelength near Lyman-α for temperatures of 84, 203, and 288 K.[43] The calculations show that, despite the low 0.408% abundance of $^{16}O^{18}O$, its effect on the photoabsorption of O_2 cannot be neglected, especially at low temperatures.

The effect of indirect predissociation of the $^3\Sigma_u^-$ states by the $A\,^3\Sigma_u^+$ state, foreshadowed in Sec. III A 2, can also be seen in Fig. 6 where the partial:total cross-section ratio $\sigma_{\Sigma_{1D}}(\lambda)/\sigma_{\Sigma}(\lambda)$ for $^{16}O_2$ is plotted (dashed lines). This "$O(^1D)$ Σ quantum yield" decreases to values significantly below unity near Lyman-α, confirming the necessity of including $^3\Sigma_u^+$ states in the CSE model for an accurate description of the O_2 photodissociation in this region, especially at low temperatures.

In Fig. 7, our calculated $T=288$ K isotopically corrected $O(^1D)+O(^3P)$ quantum yield for the dissociation of O_2 (solid line) is shown as a function of wavelength in the Lyman-α region, 121.2–121.9 nm, in comparison with the measured room-temperature yield (open circles). The calculated yield was obtained from our isotopically corrected CSE Σ_{1D} cross section and a photoabsorption cross section constructed from the cross sections of Lewis *et al.*[5] and Dose *et al.*,[22] extrapolated to zero pressure. The calculated cross section was shifted to longer wavelengths by 0.005 nm before applying Eq. (11), in order to improve agreement with the measured position for the quantum-yield minimum. Such a small shift is within the wavelength uncertainty expected for the CSE calculations, and is not unreasonable considering the difficulties inherent in comparing calculated and experimental cross sections, each with its own uncertainty, in regions of rapidly varying cross section. The calculated quantum yield varies from 1.0 near 121.2 nm, passes through a minimum of 0.56 near 121.61 nm, and rises to 0.91 near 121.9 nm, in good agreement with the behavior of the measured quantum yield.

We have also studied the temperature dependence of the $O(^1D)+O(^3P)$ quantum yield in the range 121.4–121.9 nm by performing CSE calculations of the isotopically corrected

Σ_{1D} cross section for temperatures of 203 and 84 K, shifting to longer wavelengths by 0.005 nm, as above, and comparing with the 203 and 84 K measured photoabsorption cross sections of Lewis *et al.*[5] As can be seen in Fig. 7, the calculated quantum yields (the dot-dashed line and dashed line, respectively) exhibit deeper minima than at room temperature, with a minimum yield of 0.28 at 121.63 nm for $T=84$ K. This effect occurs because the Σ (and Σ_{1D}) cross sections in the deep minimum near H Lyman-α are very sensitive to the behavior of the wings of the nearby strong spectral features, and, as is quite usual, these wings are very temperature dependent. On the other hand, the Π cross section is only broadly structured in this region and is much less temperature dependent. Thus, the strong temperature effect for the quantum yield arises principally from the Σ cross section.

IV. CONCLUSIONS

The measured room-temperature $O(^1D)+O(^3P)$ quantum yield near Lyman-α deviates significantly from unity, going from 1.0 at 121.35 nm through a minimum of 0.48 near 121.62 nm. This behavior is reproduced by a coupled-channel Schrödinger-equations calculation, based principally on the $^3\Sigma_u^- \leftarrow X\,^3\Sigma_g^-$ transitions. The low $O(^1D)+O(^3P)$ quantum yield near Lyman-α implies a significant contribution to the O_2 photodissociation from $^3\Pi_u \leftarrow X\,^3\Sigma_g^-$ transitions which yield $O(^3P)+O(^3P)$.

A strong temperature dependence of the calculated quantum yield has been found, with a minimum yield of 0.28 near 121.63 nm at a temperature of 84 K. This strong dependence arises principally due to the temperature dependence of the $^3\Sigma_u^- \leftarrow X\,^3\Sigma_g^-$ cross section. In addition, it has been found that the cross section for $^{16}O^{18}O$ substantially exceeds the $^{16}O_2$ cross section near Lyman-α, implying that the heteronuclear isotopomer plays a nonnegligible role in the photodissociation of normal O_2 in this wavelength region.

The results of the present work will help in modeling more accurately the effects of $O(^1D)$ generated from O_2 photodissociation by solar Lyman-α radiation in the mesosphere and lower thermosphere. It would be interesting to verify experimentally the temperature dependence of the $O(^1D)$ yield, given the broad temperature range (170–250 K) prevailing in the mesosphere and lower thermosphere.

ACKNOWLEDGMENTS

The experimental portion of this work was supported by NASA's Sun-Earth Connection Program. The authors thank Professor J. H. Carver for a critical reading of the manuscript.

[1] Throughout this work, Lyman-α is taken to mean H Lyman-α.
[2] G. Brasseur and S. Solomon, *Aeronomy of the Middle Atmosphere* (Reidel, Dordrecht, 1984), pp. 154–160.
[3] L. C. Lee, T. G. Slanger, G. Black, and R. L. Sharpless, J. Chem. Phys. **67**, 5602 (1977).
[4] S. Chabrillat and G. Kockarts, Geophys. Res. Lett. **24**, 2659 (1997).
[5] B. R. Lewis, I. M. Vardavas, and J. H. Carver, J. Geophys. Res. **88**, 4935 (1983).
[6] T. N. Woods and G. J. Rottman, J. Geophys. Res. **102**, 8769 (1997).
[7] W. K. Tobiska, W. R. Pryor, and J. M. Ajello, Geophys. Res. Lett. **24**, 1123 (1997).
[8] R. R. Meier and D. K. Prinz, J. Geophys. Res. **75**, 6969 (1970).
[9] S. A. Meyer and G. W. Faris, Opt. Lett. **23**, 204 (1998).
[10] In this work, energies in electron-volts are referred to the minimum in the ground-state $X\,^3\Sigma_g^-$ potential-energy curve.
[11] B. A. Ridley, R. Atkinson, and K. H. Welge, J. Chem. Phys. **58**, 3878 (1973).
[12] N. K. Bibinov, I. P. Vinogradov, and A. M. Pravilov, Opt. Spectrosc. **53**, 496 (1982).
[13] G. M. Lawrence and M. J. McEwan, J. Geophys. Res. **78**, 8314 (1973).
[14] One may, of course, speak of the "$O(^1D)$ yield" as a short form for the $O(^3P)+O(^1D)$ yield. These two forms are used interchangeably throughout this work.
[15] Chemical Kinetics and Photochemical Data for Use in Stratospheric Modeling, Evaluation Number 12, JPL Publication No. 97-4, NASA, January 15, 1997.
[16] M. J. E. Gauthier and D. R. Snelling, Can. J. Chem. **52**, 4007 (1974).
[17] H. I. Bloemink, R. A. Copeland, and T. G. Slanger, J. Chem. Phys. **109**, 4237 (1998).
[18] L. C. Lee and T. G. Slanger, J. Chem. Phys. **69**, 4053 (1978).
[19] I. Dabrowski, Can. J. Phys. **62**, 1639 (1984).
[20] G. W. Faris and M. J. Dyer, Opt. Lett. **18**, 382 (1993).
[21] M. R. Taherian and T. G. Slanger, J. Chem. Phys. **83**, 6246 (1985).
[22] V. Dose, U. Schmocker, and G. Sele, Z. Phys. A **274**, 1 (1975).
[23] M. Nicolet, Planet. Space Sci. **33**, 69 (1985).
[24] H. Lefebvre-Brion and R. W. Field, *Perturbations in the Spectra of Diatomic Molecules* (Academic, Orlando, 1986), pp. 56, 209–212.
[25] F. H. Mies, Mol. Phys. **41**, 953 (1980).
[26] E. F. van Dishoeck, M. C. van Hemert, A. C. Allison, and A. Dalgarno, J. Chem. Phys. **81**, 5709 (1984).
[27] L. Torop, D. G. McCoy, A. J. Blake, J. Wang, and T. Scholz, J. Quant. Spectrosc. Radiat. Transf. **38**, 9 (1987).
[28] J. P. England, B. R. Lewis, S. T. Gibson, and M. L. Ginter, J. Chem. Phys. **104**, 2765 (1996).
[29] B. R. Lewis, S. S. Banerjee, and S. T. Gibson, J. Chem. Phys. **102**, 6631 (1995).
[30] J. Wang, D. G. McCoy, A. J. Blake, and L. Torop, J. Quant. Spectrosc. Radiat. Transf. **38**, 19 (1987).
[31] J. Wang, A. J. Blake, D. G. McCoy, and L. Torop, J. Quant. Spectrosc. Radiat. Transf. **40**, 501 (1988).
[32] Y. Tanaka, J. Chem. Phys. **20**, 1728 (1952).
[33] B. R. Lewis, S. T. Gibson, J. P. England, and M. L. Ginter (unpublished).
[34] We use the *caret* to distinguish the pure diabatic electronic state (e.g., $\hat{B}$) from the corresponding adiabatic electronic state (e.g., B), with the convention that the diabatic and adiabatic states become indistinguishable at large R where the coupling is taken to approach zero.
[35] The $n=3$ Rydberg-valence couplings for the $^1\Sigma_u^+$ and $^3\Sigma_u^+$ states were ~1600 and ~400 cm^{-1}, respectively [S. S. Banerjee, Ph.D. dissertation thesis, The Australian National University, 1997.] These smaller couplings, and the high-energy location of the $^1\Sigma_u^+$ valence state, cause the lower vibrational structures of the $3p\pi_u f\,^1\Sigma_u^+$ and $3p\pi_u D\,^3\Sigma_u^+$ Rydberg states to be relatively unperturbed by the Rydberg-valence interactions, especially when compared with the highly perturbed $E\,^3\Sigma_u^-$ vibrational structure.
[36] K. Dressler, Ann. Isr. Phys. Soc. **6**, 141 (1983).
[37] The adiabaticity parameter $\zeta = V_{\hat{B}\hat{E}}/\Delta G_E$, where $V_{\hat{B}\hat{E}}$ is the electrostatic interaction matrix element between the diabatic electronic states, and ΔG_E is the separation of the first levels of the upper adiabatic state formed by the avoided crossing. This parameter provides a measure of the applicability of the adiabatic or diabatic picture to the mixed states. Near adiabatic behavior occurs for $\zeta \gg 1$, near-diabatic behavior for $\zeta \ll 1$, while for $\zeta \approx 1$, the amount of basis-state mixing in either representation is large.
[38] B. R. Johnson, J. Chem. Phys. **69**, 4678 (1978).
[39] P. C. Cosby (private communication).
[40] B. R. Lewis, S. T. Gibson, M. Emami, and J. H. Carver, J. Quant. Spectrosc. Radiat. Transf. **40**, 1 (1988).
[41] B. R. Lewis (unpublished).
[42] S. T. Gibson, B. R. Lewis, and D. G. McCoy (unpublished).
[43] The cross section for normal O_2 was estimated as an average of the Σ cross sections for $^{16}O_2$ and $^{16}O^{18}O$, weighted in the ratio 0.995 92:0.004 08, respectively.

4.36 Missing bands in the multiphoton excitation of coupled molecular states

[56] B. R. Lewis, S. T. Gibson, R. A. Copeland, and C. G. Bressler, *Physical Review Letters* **82**, 4212–4215 (1999).

Missing Bands in the Multiphoton Excitation of Coupled Molecular States

B. R. Lewis and S. T. Gibson
Research School of Physical Sciences and Engineering, The Australian National University, Canberra, ACT 0200, Australia

Richard A. Copeland and C. G. Bressler*
Molecular Physics Laboratory, SRI International, Menlo Park, California 94025
(Received 7 October 1998)

Measurements are reported of (3 + 1) resonance-enhanced multiphoton ionization of O_2 via the $F\,^3\Pi_u$ state which show near-vanishing intensity for F-$X(1,0)$, the strongest band in one-photon spectra. Using a coupled-channel treatment of the $^3\Pi_u$ Rydberg-valence interactions, this dramatic result is attributed to destructive interference between the amplitudes for transitions into the Rydberg and valence components of the heavily mixed F state, indicating a significant dependence of the relative transition amplitudes on the mode of excitation. Thus, "missing bands" in the multiphoton spectra of coupled states provide important information on relative multiphoton transition probabilities. [S0031-9007(99)09195-4]

PACS numbers: 33.80.Rv, 33.20.Ni, 33.70.Fd

Intensity anomalies in diatomic molecular excitation arise from interference effects occurring when there are nonzero probabilities for transitions into interacting electronic states. Such anomalies have been well documented [1], but there are few examples [1–3] involving the near-disappearance of a complete vibrational band. This dramatic phenomenon is most likely to occur in the excitation of strongly interacting Rydberg and valence states of the same symmetry [2,3], the configurations of which differ by one ("Rydbergization") or two orbitals [1]. Since one- and n-photon Rydberg:valence transition-moment ratios may well differ significantly, multiphoton excitation has the potential to produce specific missing bands which do not occur in one-photon spectra. However, the range of variation from the one-photon ratio would be expected to be smaller in the case of multiphoton excitation of a Rydbergized state, where there is a one-to-one correspondence between intermediate transition pathways to the final Rydberg and valence components. In this Letter, we report the first example of a missing band in multiphoton molecular excitation, a band which occurs strongly in one-photon spectra. This effect is observed in transitions to a Rydbergized state.

Strong Rydberg-valence (RV) interactions occurring in the $^3\Sigma_u^-$ and $^3\Pi_u$ states of O_2 [4] are responsible for a number of irregularities and unusual features [5–7] observed in one-photon-allowed transitions from the ground state $X\,^3\Sigma_g^-$. Although these transitions are also three-photon allowed, only the $E\,^3\Sigma_u^-(v = 0)$ state has been studied previously in three-photon experiments [8]. Below, we describe measurements of the (3 + 1) resonance-enhanced multiphoton-ionization (REMPI) spectrum of O_2, via the RV-mixed $F\,^3\Pi_u$ state, which contain a particularly dramatic example of a missing band. The three-photon and corresponding one-photon spectra are compared, and each is explained using a coupled-channel Schrödinger-equations (CSE) theoretical model of the $^3\Pi_u$ RV interactions.

The experimental apparatus was similar to that used in two-color pump-probe studies of collisional processes involving O_2 in the Herzberg states [9–11] and described in detail elsewhere [10], but only a single laser was employed for this work. Briefly, frequency-doubled, Nd:YAG-pumped dye-laser radiation [peak pulse energy ~5 mJ, bandwidth ~0.3 cm^{-1} full-width at half-maximum (FWHM)] was focused (lens focal length 20 cm) into a continuous-flow gas cell containing ~1 Torr of O_2 and the total positive-ion yield was recorded as a function of fundamental wavelength in the range 670–702 nm. An experimental room-temperature (3 + 1)-REMPI spectrum of O_2 in the region of the $F\,^3\Pi_u \longleftarrow X\,^3\Sigma_g^-(0,0)$–$(3,0)$ bands, corrected for variations in laser intensity and plotted as a function of the vacuum three-photon wavelength, is shown in Fig. 1(a). A corresponding one-photon spectrum, compiled from the laser-based absolute photoabsorption cross sections of Ref. [7] (resolution ~0.5 cm^{-1} FWHM), is shown in Fig. 1(b). The triplet structure of the F state is evident in both spectra [12], but there are vast differences in the relative intensities of the vibrational bands. In particular, while the (1,0) band is the strongest in the one-photon spectrum, it almost disappears from the three-photon spectrum which is dominated by the (0,0) band.

The F state of O_2 is a mixed state involving the bound $\ldots(3\sigma_g)^2(1\pi_u)^4(1\pi_g)\,np\sigma_u\,^3\Pi_u$ Rydberg states with $n = 3$ and 4, and the $\ldots(3\sigma_g)^2(1\pi_u)^4(1\pi_g)(3\sigma_u)1\,^3\Pi_u$ repulsive valence state [7]. Diabatic potential-energy curves for these interacting states are shown in Fig. 2 (dashed lines). Since the configurations of the Rydberg and valence states differ by a single orbital, in the diabatic basis there is a strong electrostatic RV interaction leading to adiabatic potential-energy curves (Fig. 2, solid

 0031-9007/99/82(21)/4212(4)$15.00

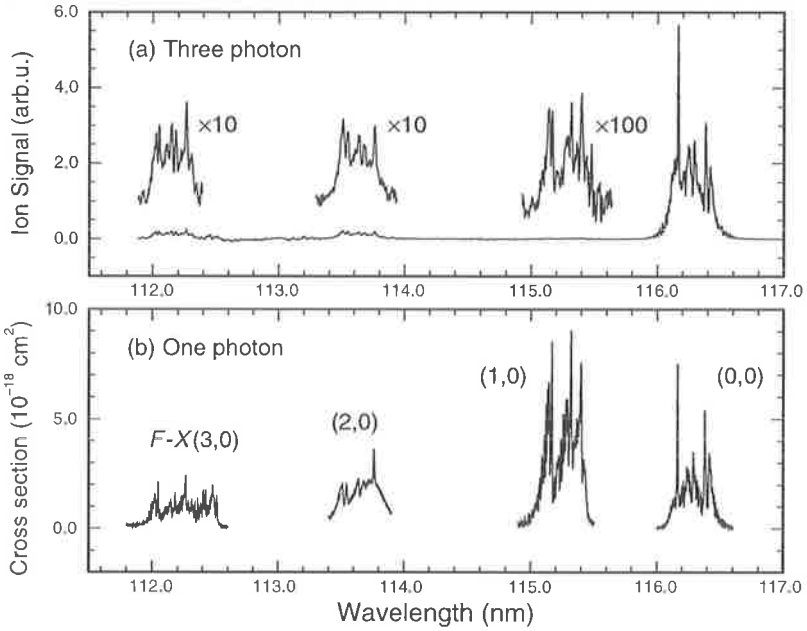

FIG. 1. Comparison of experimental spectra for one- and three-photon excitation of the $F\,^3\Pi_u$ state of O_2 at room temperature, plotted as a function of the vacuum transition wavelength. (a) (3 + 1)-REMPI spectrum for the $F \longleftarrow X(0,0)-(3,0)$ bands, corrected for variations in laser intensity. (b) Absolute one-photon absorption cross sections for the same bands, from Ref. [7]. Relative vibrational intensities vary markedly with the mode of excitation, the (1, 0) band almost disappearing in the three-photon case.

lines) which exhibit strongly avoided crossings. In the adiabatic picture, the lowest RV interaction is an example of Rydbergization, with the $3\sigma_u$ valence orbital becoming the $3p\sigma_u$ Rydberg orbital as the internuclear separation R decreases [1]. The double-minimum adiabatic potential in Fig. 2 may be associated with the F state. The adiabaticity parameter [13] for the $n = 3$ RV crossing, $\zeta = 2.9$ [7], is significantly greater than unity, suggesting near-adiabatic behavior for the F state. However, residual

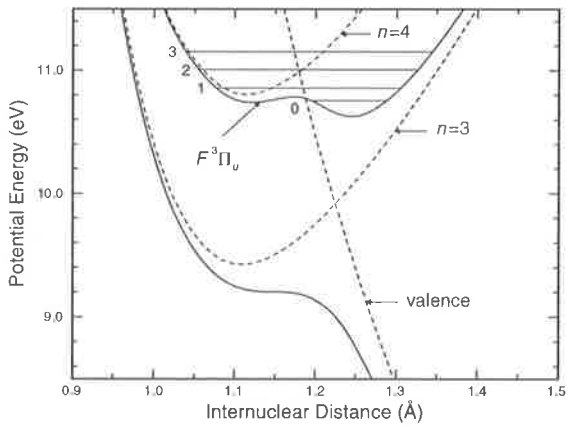

FIG. 2. Potential-energy curves for the $^3\Pi_u$ states of O_2, with energies referred to the minimum in the $X\,^3\Sigma_g^-$ potential. Diabatic curves (dashed lines) are shown for the repulsive valence state and the bound $np\sigma_u$ Rydberg states with $n = 3$ and 4, together with corresponding adiabatic curves (solid lines). Observed vibrational levels of $^{16}O_2$ are also indicated, associated with the second adiabatic potential $F\,^3\Pi_u$.

nonadiabatic coupling between the adiabatic states affects the F-state energy-level pattern and causes significant predissociation. Therefore, proper treatment of the $^3\Pi_u$ RV interaction requires coupled-state calculations in which the techniques of scattering theory [14] are applied to the calculation of molecular photodissociation cross sections [15], allowing the determination of vibrational intensities.

Here, we employ a simplified three-state diabatic CSE model, including the open valence channel and the closed $n = 3$ and $n = 4$ Rydberg channels, which is adapted from the six-state model of England *et al.* [7]. Briefly, ignoring rotation and the triplet structure of the $^3\Pi_u$ states, the cross section for photoabsorption from the $v'' = 0$ level of the ground state into the RV-coupled upper states at an energy E is given by

$$\sigma_{\rm abs}(\nu) \propto \nu |M^e_{\rm val}\langle \chi^E_{\rm val}(R) \mid \chi^0_X(R)\rangle + M^e_{n=3}\langle \chi^E_{n=3}(R) \mid \chi^0_X(R)\rangle + M^e_{n=4}\langle \chi^E_{n=4}(R) \mid \chi^0_X(R)\rangle|^2, \quad (1)$$

where ν is the transition energy, $\chi^0_X(R)$ is the ground-state vibrational wave function, the M^e are diabatic electronic transition moments, assumed to be independent of R, and the $\chi^E(R)$ are energy-normalized diabatic coupled-channel wave functions. These wave functions are elements of the vector $\boldsymbol{\chi}^E(R)$ which is the solution of the diabatic-basis coupled-channel Schrödinger equations, expressed in matrix form,

$$\left\{\mathbf{I}\,\frac{d^2}{dR^2} + \frac{2\mu}{\hbar^2}\,[E\mathbf{I} - \mathbf{V}(R)]\right\}\boldsymbol{\chi}^E(R) = 0, \quad (2)$$

where μ is the molecular reduced mass, $\mathbf{I}$ is the identity matrix, and the potential matrix

$$\mathbf{V}(R) = \begin{pmatrix} V_{\mathrm{val}}(R) & 0.872 & 0.422 \\ 0.872 & V_{n=3}(R) & 0 \\ 0.422 & 0 & V_{n=4}(R) \end{pmatrix}. \quad (3)$$

The diagonal elements of $\mathbf{V}(R)$ are the diabatic potential-energy curves shown in Fig. 2, and the nonzero off-diagonal elements, in eV, are the $n = 3$ and $n = 4$ RV couplings, assumed to be R independent, and scaling approximately with $(n^*)^{-3/2}$, where $n^* = n - a$ and a is the quantum defect [1]. The elements of $\mathbf{V}(R)$ differ slightly from those of Ref. [7] because of reoptimization for the three-state model.

In Eq. (1), there is the possibility of interference between the amplitudes for transitions into the coupled states. Elements of $\chi^E(R)$, calculated for energies near the $F(v = 0)$–$F(v = 3)$ levels by solving Eq. (2) using the renormalized Numerov method [16], are shown in Fig. 3, together with numbers proportional to the corresponding overlap factors with the ground-state wave function $\chi^0_X(R)$ [17], i.e., the constituent radial matrix elements of Eq. (1). To simplify the discussion, we assume that the Rydberg transition moments obey the $(n^*)^{-3/2}$ scaling rule [1] and take $M^e_{n=4}/M^e_{n=3} = 0.5$ [18]. Thus, the character of the interference effects is determined essentially by the ratio of the valence and Rydberg transition moments, $\mathcal{R} = M^e_{\mathrm{val}}/M^e_{n=3}$. Under certain conditions, the cross section defined by Eq. (1) vanishes. For example, the F-$X(0,0)$ band vanishes for $\mathcal{R} = -0.73$, while the $(1,0)$ band vanishes for $\mathcal{R} = -4.7$. Whether these conditions are achievable experimentally depends on the details of the excitation process.

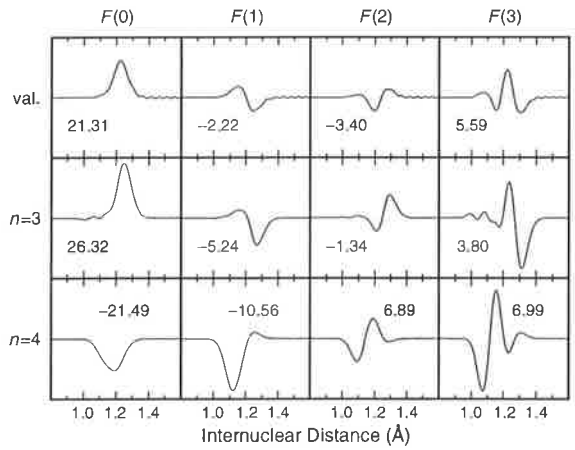

FIG. 3. Coupled-channel radial wave-function vectors $\chi^E(R)$ (columns) calculated at energies E corresponding to the $F(v = 0)$–$F(v = 3)$ levels. The wave functions (lines) are labeled according to the character of the corresponding diabatic state, i.e., valence, $n = 3$ Ry, and $n = 4$ Ry, respectively. Also shown are numbers proportional to the corresponding overlap factors between these wave functions and the ground-state $v'' = 0$ vibrational wave function, i.e., the constituent radial matrix elements of Eq. (1).

Vibrational band intensities may be obtained by integrating Eq. (1):

$$I^{v'0}_{\mathrm{abs}} \propto \int_{\mathrm{line}} \sigma_{\mathrm{abs}}(\nu)\, d\nu. \quad (4)$$

In the case of one-photon absorption, England *et al.* [7] found that a value of $\mathcal{R} \approx -0.3$ was necessary to explain the observed intensities [19]. Relative experimental intensities for the $F \leftarrow X(0,0)$–$(3,0)$ bands, obtained from the absorption oscillator strengths of Ref. [7], are shown in Table I compared with values calculated using Eqs. (1)–(4) with $\mathcal{R} = -0.35$. Good agreement is found between the experimental intensities and those calculated using our CSE model. The unusually small value of the diabatic valence transition moment necessary for this agreement is supported by *ab initio* calculations [20].

(3 + 1) REMPI may be regarded as a two-step process involving three-photon absorption to the resonant intermediate state, followed by one-photon ionization out of it [21]. When the resonant intermediate state is of mixed character, the vibrational REMPI intensities may be subject to interference effects in both the absorption and ionization steps [22]. However, it is impossible for a missing band to originate from interference in the ionization step when the *total* ionization signal, i.e., the sum over all vibrational levels of the ion, is recorded. Further, under normally applicable experimental conditions of weak excitation and saturated ionization, it is expected that observed REMPI intensities will reflect those in the three-photon absorption process [22]. However, in our case it is also necessary to allow for competition between predissociation and ionization, the alternative mechanisms leading to depopulation of the resonant intermediate state. Assuming that predissociation dominates ionization, relative three-photon absorption intensities may be deduced from the observed REMPI intensities using the relation

$$I^{v'0}_{\mathrm{abs}} \propto I^{v'0}_{\mathrm{REMPI}}\, \Gamma^{v'}_{\mathrm{pred}}, \quad (5)$$

where $\Gamma^{v'}_{\mathrm{pred}}$ is the predissociation linewidth [7].

TABLE I. Comparison of experimental and calculated $(v',0)$ intensities for one- and three-photon excitation of the $F\,^3\Pi_u$ state of O_2, normalized to unity for $v' = 0$.

	One-photon		Three-photon		
v'	Expt.[a]	Calc.[b]	REMPI[c]	Abs.[d]	Calc.[e]
0	1.0	1.0	1.0	1.0	1.0
1	2.4	2.4	0.007	0.005	0.004
2	0.50	0.69	0.075	0.22	0.24
3	0.45	0.39	0.067	0.070	0.040

[a]From experimental absorption oscillator strengths of Ref. [7].
[b]From CSE calculations with $\mathcal{R} = -0.35$.
[c]From experimental (3 + 1)-REMPI spectrum of Fig. 1(a).
[d]Relative three-photon absorption intensities obtained by correcting the REMPI intensities for competition between predissociation and ionization using the experimental predissociation linewidths of Ref. [7] in Eq. (5).
[e]From CSE calculations with $\mathcal{R} = -3.5$.

Relative (3 + 1)-REMPI vibrational intensities obtained by integrating the spectrum of Fig. 1(a) are shown in Table I, together with corresponding absorption intensities for the $F \leftarrow\leftarrow\leftarrow X(0,0)$–$(3,0)$ bands estimated using Eq. (5) with the known predissociation linewidths [7]. These experimental intensities have uncertainties of ~50%. Relative intensities calculated with $\mathcal{R} = -3.5$ and shown in Table I are in fairly good agreement with the experimental three-photon intensities.

These indicative calculations show that a CSE model of the $^3\Pi_u$ RV interaction in which only the single parameter $\mathcal{R}$ is varied is capable of explaining both the one- and three-photon relative intensities for four vibrational bands, including the near disappearance of the (1, 0) band in the three-photon spectrum. The dramatic behavior of the (0, 0) and (1, 0) intensities can be understood by substituting the radial matrix elements of Fig. 3 and the model transition moments into Eq. (1). In the one-photon case, there is partial destructive interference between the Rydberg and valence transition amplitudes for the (0, 0) band, while the (1, 0) intensity is dominated by a strong Rydberg contribution; in the three-photon case, the (0, 0) intensity is dominated by a stronger valence contribution, while there is near-complete destructive quantum interference between the valence and Rydberg amplitudes for the (1, 0) band.

Our principal conclusion is that the constituent Rydberg and valence transition amplitudes in Eq. (1) interfere in significantly different ways in one- and three-photon excitation. However, the explanation for the apparently increased importance of the valence transition moment in three-photon excitation is not clear. A near-resonance at the two-photon level with the lowest $^3\Pi_g$ valence state may lead to significant energy dependence of the transition moments. Interactions between the virtual intermediate states contributing to the three-photon transition moments [23] are likely to result in additional complexities. For example, strong RV interactions in the virtual intermediate states, e.g., the $E\,^3\Sigma_u^-$ state at the one-photon level, may play a significant role. We are unaware of any theoretical treatments of RV interactions in the virtual intermediate states of multiphoton transitions, but it is possible that such interactions in O_2 will lead to marked R dependence of the three-photon moments. Therefore, the empirical R-independent relative three-photon electronic transition moments described in this Letter should be regarded only as *effective* moments which implicitly include unmodeled effects such as residual energy dependence in the ionization step and the R and energy dependence of the actual three-photon transition moments. In addition, the role of autoionization requires clarification.

Nevertheless, observations that bands are missing in the multiphoton excitation of coupled states clearly have the potential to provide significant information on the relative multiphoton transition probabilities. In addition, the present study suggests that excitation processes in which the effective relative transition moments can be varied *continuously*, e.g., electron-impact excitation [24], would be of particular interest in tracing the development of missing bands in the excitation of coupled states.

The authors thank Professor H. Lefebvre-Brion and Dr. K. G. H. Baldwin for valuable discussions and critical readings of the manuscript. The experimental work was supported by NASA's Sun-Earth Connection and Planetary Atmospheres Programs.

*Current address: Institut de Physique Expérimentale, Université de Lausanne, CH-1015 Lausanne-Dorigny, Switzerland.

[1] H. Lefebvre-Brion and R. W. Field, *Perturbations in the Spectra of Diatomic Molecules* (Academic, Orlando, 1986), pp. 206–216, 257–283.
[2] Ch. Jungen, Can. J. Phys. **44**, 3197 (1966).
[3] J. Geiger and B. Schröder, J. Chem. Phys. **50**, 7 (1969).
[4] R. J. Buenker and S. D. Peyerimhoff, Chem. Phys. **8**, 324 (1975); Chem. Phys. Lett. **34**, 225 (1975).
[5] J. P. England, B. R. Lewis, and M. L. Ginter, J. Chem. Phys. **103**, 1727 (1995); **105**, 1754 (1996).
[6] B. R. Lewis, S. S. Banerjee, and S. T. Gibson, J. Chem. Phys. **102**, 6631 (1995).
[7] J. P. England, B. R. Lewis, S. T. Gibson, and M. L. Ginter, J. Chem. Phys. **104**, 2765 (1996).
[8] P. J. Miller, L. Li, W. A. Chupka, and S. D. Colson, J. Chem. Phys. **88**, 2972 (1988).
[9] R. A. Copeland, K. Knutsen, M. E. Onishi, and T. Yalçin, J. Chem. Phys. **105**, 10349 (1996).
[10] K. Knutsen, M. J. Dyer, and R. A. Copeland, J. Chem. Phys. **101**, 7415 (1994).
[11] R. A. Copeland, J. Chem. Phys. **100**, 744 (1994).
[12] The one-photon spectrum contains a broad feature underlying $F \leftarrow X(2,0)$ and another feature longward of $F \leftarrow X(3,0)$ arising from transitions to $^3\Sigma_u^-$ states.
[13] K. Dressler, Ann. Isr. Phys. Soc. **6**, 141 (1983).
[14] F. H. Mies, Mol. Phys. **41**, 953 (1980).
[15] E. F. van Dishoeck, M. C. van Hemert, A. C. Allison, and A. Dalgarno, J. Chem. Phys. **81**, 5709 (1984).
[16] B. R. Johnson, J. Chem. Phys. **69**, 4678 (1978).
[17] The X-state wave function was obtained using a Rydberg-Klein-Rees potential curve derived from the spectroscopic constants of P. C. Cosby (private communication).
[18] Using the quantum defects of Ref. [7], the scaling rule implies a ratio of 57% between the $n = 4$ and $n = 3$ Rydberg transition moments, while the fitted CSE model of Ref. [7] implies a ratio of 42 ± 5%.
[19] Signs of individual matrix elements have no meaning, but the observed intensities imply that $M^e_{\mathrm{val}} H^e_{n=3} M^e_{n=3} < 0$, where $H^e_{n=3}$ is the $n = 3$ RV coupling.
[20] P. S. Julienne, D. Neumann, and M. Krauss, J. Chem. Phys. **64**, 2990 (1976).
[21] S. N. Dixit and V. McKoy, J. Chem. Phys. **82**, 3546 (1985).
[22] J. Kimman, M. Lavollée, and M. J. van der Wiel, Chem. Phys. **97**, 137 (1985).
[23] J. B. Halpern, H. Zacharias, and R. Wallenstein, J. Mol. Spectrosc. **79**, 1 (1980).
[24] M. Dillon *et al.*, J. Chem. Phys. **102**, 1561 (1995).

4.37 The $B\,^3\Sigma_u^- \leftarrow b\,^1\Sigma_g^+$ transition of molecular oxygen

[57] B. R. Lewis, S. T. Gibson, T. G. Slanger, and D. L. Huestis,
Journal of Chemical Physics **110**, 11129–11132 (1999).

The $B\,^3\Sigma_u^- \leftarrow b\,^1\Sigma_g^+$ transition of molecular oxygen

B. R. Lewis and S. T. Gibson
Research School of Physical Sciences and Engineering, The Australian National University, Canberra, ACT 0200, Australia

T. G. Slanger and D. L. Huestis
Molecular Physics Laboratory, SRI International, Menlo Park, California 94025

(Received 8 March 1999; accepted 6 April 1999)

The origin of the intensity of the $B\,^3\Sigma_u^- \leftarrow b\,^1\Sigma_g^+$ transition of molecular oxygen, first observed recently by Eppink *et al.* [J. Chem. Phys. **108**, 1305 (1998)], is discussed. It is shown that the $B \leftarrow b$ transition borrows its intensity principally from the dipole-allowed $B \leftarrow X$ transition, through spin-orbit mixing between the $X\,^3\Sigma_g^-$ and $b\,^1\Sigma_g^+$ states. Estimated continuum photoabsorption cross sections and discrete oscillator strengths for the $B \leftarrow b$ system are presented. © *1999 American Institute of Physics.* [S0021-9606(99)01823-1]

Following their recent observation of maximally aligned $O(^1D)$ atoms produced in the photodissociation of a prepared rotational level of the metastable $b\,^1\Sigma_g^+(v=0)$ state of O_2, Eppink *et al.*[1] deduced that dissociation occurred adiabatically via the continuum of the $B\,^3\Sigma_u^-$ state. Although unremarked upon by the authors of Ref. 1, this observation represents the first experimental evidence for the $B \leftarrow b$ transition of O_2. Their experimental method involved a two-step process, with an initial $b\,^1\Sigma_g^+ \leftarrow X\,^3\Sigma_g^-$ excitation, followed by the $B\,^3\Sigma_u^- \leftarrow b\,^1\Sigma_g^+$ dissociation. Since both steps represent electric-dipole-forbidden transitions, it is somewhat surprising that sufficient photodissociation flux was observed to enable the successful completion of their experiment.[1] While the origin of the $b \leftarrow X$ transition probability is well-known,[2] there is no comparable information available for the $B \leftarrow b$ transition. In this communication, we discuss the likely origin of the $B \leftarrow b$ electronic transition moment (ETM) and estimate the corresponding photodissociation cross section.

If we consider only first-order spin-orbit interactions in a spin-forbidden transition between an initial state $|i\rangle$ and a final state $|f\rangle$, then the effective ETM is given approximately by[2]

$$\langle f|\boldsymbol{\mu}|i\rangle = \sum_{k\neq i} \frac{\langle f|\boldsymbol{\mu}|k\rangle\langle k|\mathbf{H}^{so}|i\rangle}{E_i - E_k} + \sum_{k\neq f} \frac{\langle f|\mathbf{H}^{so}|k\rangle\langle k|\boldsymbol{\mu}|i\rangle}{E_f - E_k}, \tag{1}$$

where $\mathbf{H}^{so}$ and $\boldsymbol{\mu}$ are the spin-orbit and electric-dipole operators, respectively, the $E_{i,k,f}$ are electronic-state energies, and the sums are over all states $|k\rangle$ that are dipole-connected to either the initial or final states. In the case of the $B \leftarrow b$ transition of O_2, lacking a full *ab initio* study of the relevant matrix elements and energies, it is instructive to consider specifically which terms in Eq. (1) are likely to be the major contributors to the ETM.

The $b\,^1\Sigma_g^+$ state is dipole-connected to $^1\Sigma_u^+$ and $^1\Pi_u$ states, the $B\,^3\Sigma_u^-$ state to $^3\Sigma_g^-$ and $^3\Pi_g$ states. Potential-energy curves (PECs) for the states of these symmetries having the lowest energy-denominators in Eq. (1) are shown in Fig. 1, together with PECs for the b and B states. All of the configurationally-excited states in Fig. 1 exhibit some degree of Rydberg-valence (RV) interaction,[3–7] and there is an electrostatic interaction[8] between the lowest two $^3\Pi_g$ valence states.[9] PECs for the strongly RV-interacting $^1\Pi_u$ and $^3\Sigma_u^-$ states are shown adiabatically in Fig. 1; those for the more weakly interacting $^1\Sigma_u^+$ and $^3\Pi_g$ states diabatically.

The PECs, shown in Fig. 1 and used here, have been constructed using a variety of Rydberg–Klein–Rees (RKR), semiempirical, and *ab initio* data. The X- and b-state PECs consist of RKR curves derived from the data of Cosby[10] and Slanger and Cosby,[11] respectively, with small- and large-R extensions based on the *ab initio* calculations of Partridge.[12] The B-state PEC consists of an RKR well obtained using the spectroscopic constants of Lewis *et al.*,[13] with an *ab initio* large-R extension[12] and a semiempirical small-R extension based on a coupled-channel treatment of the $^3\Sigma_u^-$ RV interaction.[4] The $1\,^1\Pi_u$ PEC is derived from an *ab initio* calculation,[12,14] with a semiempirical small-R extension based on a coupled-channel treatment of the $^1\Pi_u$ RV interaction.[3] Finally, the diabatic $^1\Sigma_u^+$ and $^3\Pi_g$ PECs in Fig. 1 represent the results of semiempirical coupled-channel studies, optimized to the available experimental information (Refs. 5 and 7, respectively).

First, in evaluating contributions to the $B \leftarrow b$ ETM arising from the states shown in Fig. 1, we consider the parallel term due to initial-state spin-orbit mixing,

$$R_{e\|}^{(1)}(R) = \frac{\langle B\,^3\Sigma_{u0}^-|\boldsymbol{\mu}|X\,^3\Sigma_{g0}^-\rangle\langle X\,^3\Sigma_{g0}^-|\mathbf{H}^{so}|b\,^1\Sigma_{g0}^+\rangle}{E_b - E_X}. \tag{2}$$

The terms on the right-hand side of Eq. (2) are fairly well-known, allowing a reasonable estimate of the magnitude of $R_{e\|}^{(1)}(R)$. We have constructed a semiempirical adiabatic $B \leftarrow X$ ETM, shown in Fig. 2(a), which is based on experimental Schumann–Runge (SR)-band oscillator strengths[13] in the $R=1.3$–1.4 Å region and the results of coupled-channel treatments of the SR continuum and avoided-crossing regions[4] at smaller R. When employed with the B- and X-state PECs of Fig. 1 , this ETM reproduces experimental intensities in the discrete and continuous SR regions to

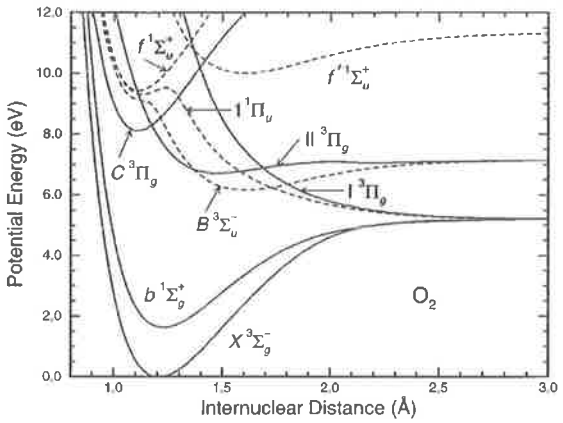

FIG. 1. Potential-energy curves for the *gerade* (solid lines) and *ungerade* (dashed lines) electronic states of O_2 of principal relevance to this study. The $^3\Pi_g$ and $^1\Sigma_u^+$ states are shown in a diabatic (crossing) representation.

within a few percent. Using this $B\leftarrow X$ ETM in Eq. (2), together with the *ab initio* X–b spin-orbit coupling of Minaev *et al.*[2] and an energy denominator determined from the b- and X-state PECs of Fig. 1, we obtain the estimate for $|R_{e\parallel}^{(1)}(R)|$ shown in Fig. 2(b). At $R=1.3$ Å, $|R_{e\parallel}^{(1)}(R)| = 0.011$ a.u., a relatively large value arising due to the simultaneously large $B\leftarrow X$ ETM (~0.81 a.u.) and X–b spin-orbit coupling (~170 cm^{-1}), together with the relatively small separation in energy between the b- and X-state PECs ($E_b - E_X \approx 12\,200\,cm^{-1}$).

Second, we consider the perpendicular term arising from initial-state mixing. Although, as noted above, there are three relatively low-lying $^3\Pi_g$ states complicated by significant RV and valence-valence interactions, a diabatic treatment of these states is appropriate. In the range of internuclear distance of principal importance to this study, $R=1.2$–1.4 Å, the strongest $^3\Pi_g$–b spin-orbit interaction[15] and the smallest energy-denominator are due to the $II\,^3\Pi_g$ state, the only $^3\Pi_g$ state considered in the contribution[16]

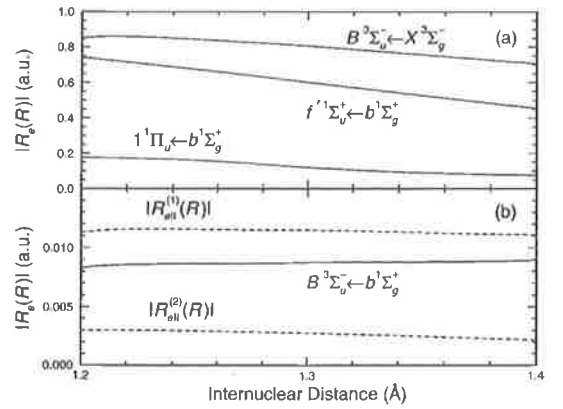

FIG. 2. Electronic transition moments for O_2. (a) Relevant dipole-allowed transitions. (b) The $B\leftarrow b$ transition and its parallel constituents which interfere destructively (see the text).

$$\sqrt{2}R_{e\perp}^{(1)}(R) = \frac{\langle B\,^3\Sigma_{u1}^-|\boldsymbol{\mu}|II\,^3\Pi_{g0}\rangle\langle II\,^3\Pi_{g0}|\mathbf{H}^{so}|b\,^1\Sigma_{g0}^+\rangle}{E_b - E_{^3\Pi}}. \tag{3}$$

No theoretical or experimental information appears to be available for the $B\leftarrow II\,^3\Pi_g$ ETM. However, from a study of rotational line strengths in the Herzberg I bands of O_2, England *et al.*[17] have determined $|\langle A\,^3\Sigma_u^+|\boldsymbol{\mu}|1\,^3\Pi_g\rangle|$ indirectly. Since the adiabatic $1\,^3\Pi_g$ state is equivalent to the diabatic $\ldots(3\sigma_g)(1\pi_u)^4(1\pi_g)^3II\,^3\Pi_g$ state[18] in the 1.2–1.4 Å range, and since both the $A\,^3\Sigma_u^+$ and $B\,^3\Sigma_u^-$ states are derived principally from the $\ldots(3\sigma_g)^2(1\pi_u)^3(1\pi_g)^3$ molecular-orbital (MO) configuration, both the $A\leftarrow 1\,^3\Pi_g$ and $B\leftarrow II\,^3\Pi_g$ transitions represent allowed $3\sigma_g\leftarrow 1\pi_u$ excitations, within the single-configuration approximation (SCA). It follows that $|\langle B\,^3\Sigma_u^-|\boldsymbol{\mu}|II\,^3\Pi_g\rangle| = |\langle A\,^3\Sigma_u^+|\boldsymbol{\mu}|1\,^3\Pi_g\rangle| = 0.26$ a.u.[17] Using this value in Eq. (3), together with a $II\,^3\Pi_g$–b spin-orbit coupling linearly interpolated from the *ab initio* values of Klotz and Peyerimhoff[15] (~70 cm^{-1}), and an energy denominator determined from the b- and $II\,^3\Pi_g$-state PECs in Fig. 1 ($E_b - E_{^3\Pi} \approx -43\,000\,cm^{-1}$), it follows that $|\sqrt{2}R_{e\perp}^{(1)}(R)| \approx 4\times10^{-4}$ a.u. at $R=1.3$ Å.

Third, we consider the parallel term arising from upper-state mixing. The $^1\Sigma_u^+\leftarrow b$ transitions are complicated by significant interaction between the diabatic Rydberg $f\,^1\Sigma_u^+$ and valence $f'\,^1\Sigma_u^+$ states and a significant transition probability into the f state,[19] which mixes noticeably ($H_{so} \approx 95\,cm^{-1}$)[4] with the Rydberg component of the B state. However, our indicative calculations suggest that the diabatic valence component dominates this part of the $B\leftarrow b$ cross section in the principal range of interest, $\lambda > 1800$ Å, and we consider only the term

$$R_{e\parallel}^{(2)}(R) = \frac{\langle B\,^3\Sigma_{u0}^-|\mathbf{H}^{so}|f'\,^1\Sigma_{u0}^+\rangle\langle f'\,^1\Sigma_{u0}^+|\boldsymbol{\mu}|b\,^1\Sigma_{g0}^+\rangle}{E_B - E_{f'}}. \tag{4}$$

Moss and Goddard[20] have calculated *ab initio* ETMs for the $B\leftarrow X$ and $f'\leftarrow b$ transitions, both of which represent $1\pi_g \leftarrow 1\pi_u$ excitations. Here, we adopt their $f'\leftarrow b$ ETM, lowered by 10% and shown in Fig. 2(a).[21] As far as we are aware, there have been no *ab initio* calculations of the B–f' spin-orbit coupling. However, since both states arise principally from the $\ldots(3\sigma_g)^2(1\pi_u)^3(1\pi_g)^3$ MO configuration, SCA arguments presented by Lefebvre-Brion and Field[22] suggest that the magnitude of this matrix element should be given approximately by the atomic spin-orbit parameter $\zeta_O(2p) \approx 150\,cm^{-1}$. Using these values in the numerator of Eq. (4), together with an energy denominator determined from the B- and f'-state PECs of Fig. 1, we obtain the estimate for $|R_{e\parallel}^{(2)}(R)|$ shown in Fig. 2(b), which has the value 0.0028 a.u. at $R=1.3$ Å.

Finally, we consider the perpendicular term due to upper-state mixing

$$\sqrt{2}R_{e\perp}^{(2)}(R) = \frac{\langle B\,^3\Sigma_{u1}^-|\mathbf{H}^{so}|1\,^1\Pi_{u1}\rangle\langle 1\,^1\Pi_{u1}|\boldsymbol{\mu}|b\,^1\Sigma_{g0}^+\rangle}{E_B - E_{^1\Pi}}. \tag{5}$$

The ETM for transitions between the b and $\ldots(3\sigma_g)^2(1\pi_u)^4(1\pi_g)(3\sigma_u)1\,^1\Pi_u$ states is not known.

However, both the $b\,^1\Sigma_g^+$ and $a\,^1\Delta_g$ metastable states of O_2 arise from the $\ldots(3\sigma_g)^2(1\pi_u)^4(1\pi_g)^2$ MO configuration, and the magnitude of the $1\,^1\Pi_u \leftarrow b$ ETM is expected to be related simply to the $1\,^1\Pi_u \leftarrow a$ ETM, both transitions corresponding to a $3\sigma_u \leftarrow 1\pi_g$ excitation.[23] We adopt an $R_e^{^1\Pi b}(R) = \langle 1\,^1\Pi_u|\boldsymbol{\mu}|b\,^1\Sigma_g^+\rangle/\sqrt{2}$, shown in Fig. 2(a), adapted from[24] the semiempirical adiabatic $1\,^1\Pi_u \leftarrow a$ ETM determined using a coupled-channel analysis of the available absolute experimental cross sections for excitation from the a state.[3] The $B-1\,^1\Pi_u$ spin-orbit coupling matrix element near $R=1.73$ Å has been determined to be $\sim 29\ \mathrm{cm}^{-1}$ from semiempirical analysis of SR-band predissociation line widths.[25] Here, we assume an R-independent value of 30 cm^{-1}. At $R=1.3$ Å, using the adopted ETM ($\sqrt{2}R_e^{^1\Pi b}(R) = 0.17$ a.u.) and spin-orbit coupling in Eq. (5), together with an energy denominator determined from the B- and $1\,^1\Pi_u$-state PECs of Fig. 1 ($E_B - E_{^1\Pi} \approx -13\,900\ \mathrm{cm}^{-1}$), it follows that $|\sqrt{2}R_{e\perp}^{(2)}(R)| \approx 4\times 10^{-4}$ a.u.

The foregoing analysis suggests that the $B \leftarrow b$ ETM is almost entirely parallel in character. In addition, an examination of the relative magnitudes of the two parallel terms contributing to the ETM shows that the $B \leftarrow b$ transition borrows its intensity principally from the dipole-allowed $B \leftarrow X$ transition, through spin-orbit mixing between the $X\,^3\Sigma_g^-$ and $b\,^1\Sigma_g^+$ states. This X–b spin-orbit mixing also plays an important role in determining the intensities of other forbidden transitions of O_2, including the magnetic-dipole $b \leftarrow X$ (Ref. 2) and the Rydberg $f \leftarrow X$ (Ref. 4) transitions. The magnitude of the effective $B \leftarrow b$ ETM is sensitive to the relative signs of the two parallel contributions [Eqs. (2) and (4)]. Using SCA arguments similar to those in the appendix of Ref. 4, it can be shown that, while the numerators have the same sign, these terms interfere destructively due to the opposite signs of the energy denominators. Thus, the effective $B \leftarrow b$ ETM, shown in Fig. 2(b), is given by

$$|R_e^{Bb}(R)| = |R_{e\parallel}^{(1)}(R) - R_{e\parallel}^{(2)}(R)|. \tag{6}$$

$B \leftarrow b$ photodissociation cross sections and discrete oscillator strengths calculated using this ETM and the B- and b-state PECs of Fig. 1 are shown in Fig. 3 and Table I, respectively. The calculations were performed using the well-known expressions[26]

$$\sigma^{Bb}(\lambda) = \frac{1.23\times 10^{-15} g}{\lambda}|\langle \chi_E^B(R)|R_e^{Bb}(R)|\chi_0^b(R)\rangle|^2 \tag{7}$$

and

$$f_{v'0}^{Bb} = \frac{304 g}{\lambda}|\langle \chi_{v'}^B(R)|R_e^{Bb}(R)|\chi_0^b(R)\rangle|^2, \tag{8}$$

where the cross section $\sigma^{Bb}(\lambda)$ is in cm^2, the transition wavelength λ is in Å, the transition matrix elements are in a.u., the degeneracy factor $g=1$ for the $B\,^3\Sigma_{u0}^- \leftarrow b\,^1\Sigma_{g0}^+$ transition, and $v''=J''=J'=0$. Radial wave functions for the initial discrete $[\chi_0^b(R)]$ and final discrete $[\chi_{v'}^B(R)]$ and continuum $[\chi_E^B(R)]$ states, the latter energy-normalized, were determined by numerical solution of appropriate Schrödinger equations.

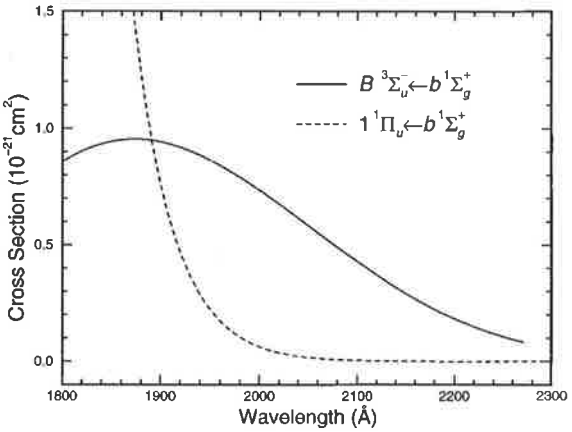

FIG. 3. Calculated photodissociation cross sections for the forbidden $B \leftarrow b$ and allowed $1\,^1\Pi_u \leftarrow b$ systems of O_2.

The peak $B \leftarrow b$ cross section, $\sim 9.5\times 10^{-22}\ \mathrm{cm}^2$ near 1870 Å, is at least two orders of magnitude larger than those for other forbidden transitions of O_2 in the same wavelength region,[27] but $B \leftarrow b$ photoabsorption is unlikely to play a significant role in the atmospheric photochemistry due to the low concentration of atmospheric $O_2(b\,^1\Sigma_g^+)$. It is also necessary to consider the allowed transitions contributing to the b-state photoabsorption in this region. While transitions to the high-lying $^1\Sigma_u^+$ states do not play a direct role, the $1\,^1\Pi_u \leftarrow b$ continuum cross section calculated[28] using the $1\,^1\Pi_u$ PEC of Fig. 1 and the $1\,^1\Pi_u \leftarrow b$ ETM of Fig. 2 is shown in Fig. 3. This perpendicular component of the b-state photoabsorption increases rapidly below ~ 2000 Å, but is insignificant at longer wavelengths where the cross section is

TABLE I. Calculated absorption oscillator strengths and origins for the $B \leftarrow b(v',0)$ bands of O_2.

v'	λ (Å)[a]	$f_{v'0}$
0	2759.60	4.8×10^{-13}
1	2708.23	4.8×10^{-12}
2	2660.29	2.6×10^{-11}
3	2615.67	9.5×10^{-11}
4	2574.11	2.7×10^{-10}
5	2535.51	6.5×10^{-10}
6	2499.90	1.3×10^{-9}
7	2466.99	2.4×10^{-9}
8	2436.93	4.0×10^{-9}
9	2409.57	5.9×10^{-9}
10	2384.92	8.0×10^{-9}
11	2363.05	1.0×10^{-8}
12	2343.92	1.2×10^{-8}
13	2327.50	1.3×10^{-8}
14	2313.77	1.3×10^{-8}
15	2302.57	1.2×10^{-8}
16	2293.65	1.1×10^{-8}
17	2286.68	9.0×10^{-9}
18	2281.35	7.3×10^{-9}
19	2277.42	5.5×10^{-9}
20	2274.70	3.8×10^{-9}
21	2273.04	2.1×10^{-9}

[a]Based on experimental origins for the $B \leftarrow X$ system [Refs. 13 and 29.]

dominated by the parallel $B \leftarrow b$ component. Thus, our results are consistent with the observation of parallel $B \leftarrow b$ photodissociation by Eppink *et al.*[1] At 2038 and 2250 Å, the wavelengths employed in the experiments of Ref. 1, we calculate $B \leftarrow b$ cross sections of $\sim 6 \times 10^{-22}$ and $\sim 1 \times 10^{-22}$ cm^2, respectively. These relatively high values may help to explain the success of those experiments.

The authors thank Professor H. Lefebvre-Brion and Dr. W. J. van der Zande for valuable discussions. We are pleased to acknowledge that, just prior to submission of this communication, we received information from B. Minaev regarding his *ab initio* calculations of the $B \leftarrow b$ transition probability. This work has now been submitted for publication to PCCP (U.K.).

[1] A. T. J. B. Eppink, D. H. Parker, M. H. M. Janssen, B. Buijsse, and W. J. van der Zande, J. Chem. Phys. **108**, 1305 (1998).
[2] B. Minaev, O. Vahtras, and H. Ågren, Chem. Phys. **208**, 299 (1996).
[3] P. C. Hill, Ph.D. thesis, The Australian National University (1991).
[4] B. R. Lewis, S. S. Banerjee, and S. T. Gibson, J. Chem. Phys. **102**, 6631 (1995).
[5] S. S. Banerjee, Ph.D. thesis, The Australian National University (1996).
[6] B. R. Lewis, J. P. England, R. J. Winkel, Jr., S. S. Banerjee, P. M. Dooley, S. T. Gibson, and K. G. H. Baldwin, Phys. Rev. A **52**, 2717 (1995).
[7] J. S. Morrill, M. L. Ginter, B. R. Lewis, and S. T. Gibson, J. Chem. Phys. (to be published).
[8] W. J. van der Zande, W. Koot, and J. Los, J. Chem. Phys. **91**, 4597 (1989).
[9] The RV interaction matrix elements are ~ 6300 cm^{-1} (Ref. 3), ~ 4000 cm^{-1} (Ref. 4), ~ 1600 cm^{-1} (Refs. 5 and 6), and ~ 620 cm^{-1} (Ref. 7), for the $^1\Pi_u$, $^3\Sigma_u^-$, $^1\Sigma_u^+$, and $^4\Pi_g$ states, respectively, while the $^3\Pi_g$ valence-valence matrix element is ~ 480 cm^{-1} (Ref. 8).
[10] P. C. Cosby (private communication, 1996).
[11] T. G. Slanger and P. C. Cosby, J. Phys. Chem. **92**, 267 (1988), and references therein.
[12] H. Partridge (private communications, 1993–1999); H. Partridge, C. W. Bauschlicher, Jr., S. R. Langhoff, and P. R. Taylor, J. Chem. Phys. **95**, 8292 (1991).
[13] B. R. Lewis, L. Berzins, and J. H. Carver, J. Quant. Spectrosc. Radiat. Transfer **36**, 209 (1986).
[14] The *ab initio* 1 $^1\Pi_u$ PEC crosses the B-state PEC at an R-value in excellent agreement with that implied by the Schumann–Runge predissociation study of Ref. 25.
[15] R. Klotz and S. D. Peyerimhoff, Mol. Phys. **57**, 573 (1986).
[16] The $R_e(R)$ of this work are defined according to the recommendations of E. E. Whiting, A. Schadee, J. B. Tatum, J. T. Hougen, and R. W. Nicholls, J. Mol. Spectrosc. **80**, 249 (1980).
[17] J. P. England, B. R. Lewis, and S. T. Gibson, Can. J. Phys. **74**, 185 (1996).
[18] In the molecular-orbital notation used here, the filled shells $(1\sigma_g)^2(1\sigma_u)^2(2\sigma_g)^2(2\sigma_u)^2$ are suppressed.
[19] D. H. Katayama, S. Ogawa, M. Ogawa, and Y. Tanaka, J. Chem. Phys. **67**, 2132 (1977).
[20] B. J. Moss and W. A. Goddard III, J. Chem. Phys. **63**, 3523 (1975).
[21] Since the *ab initio* $B \leftarrow X$ ETM of Ref. 20 must be lowered by 10% in order to agree with our adopted semiempirical moment, we lower their $f' \leftarrow b$ moment by a similar amount to preserve the calculated relativities.
[22] H. Lefebvre-Brion and R. W. Field, *Perturbations in the Spectra of Diatomic Molecules* (Academic, Orlando, 1986), pp. 107–108, 208–211, 216–217.
[23] This expectation is unaltered by the fact that the valence $3\sigma_u$ MO at large R in the Rydbergized 1 $^1\Pi_u$ state becomes the $3p\sigma_u$ Rydberg orbital at small R (Ref. 22).
[24] We take the 1 $^1\Pi_u \leftarrow b$ ETM to be equal to $1/\sqrt{2}\times$ the 1 $^1\Pi_u \leftarrow a$ ETM, as implied by SCA arguments.
[25] P. M. Dooley, Ph.D. thesis, The Australian National University (1997).
[26] K. P. Kirby and E. F. van Dishoeck, Adv. At. Mol. Phys. **25**, 437 (1988).
[27] R. P. Saxon and T. G. Slanger, J. Geophys. Res. **91**, 9877 (1986).
[28] Calculations of the 1 $^1\Pi_u \leftarrow b$ $^1\Sigma_g^+$ cross section using Eq. (7) require that $g=2$.
[29] P. Brix and G. Herzberg, Can. J. Phys. **32**, 110 (1954).

4.38 The $(X\,^2\Pi_g)\,ns\sigma_g\,^{1,3}\Pi_g$ Rydberg states of O_2: Spectra, structures and interactions

[58] J. S. Morrill, M. L. Ginter, B. R. Lewis, and S. T. Gibson,
Journal of Chemical Physics **111**, 173–185 (1999).

The $(X\,^2\Pi_g)\,ns\sigma_g\,^{1,3}\Pi_g$ Rydberg states of O_2: Spectra, structures, and interactions

J. S. Morrill[a)]
E. O. Hulburt Center for Space Research, Naval Research Laboratory, Washington, DC 20375–5352

M. L. Ginter
Institute for Physical Science and Technology, University of Maryland, College Park, Maryland 20742–2431

B. R. Lewis and S. T. Gibson
Research School of Physical Sciences and Engineering, The Australian National University, Canberra, ACT 0200, Australia

(Received 21 December 1998; accepted 6 April 1999)

The results of a critical reexamination of previous experimental observations of the $(X\,^2\Pi_g)\,ns\sigma_g\,^{1,3}\Pi_g$ Rydberg states of O_2 are employed to optimize a coupled-channel Schrödinger-equation (CSE) model describing rovibronic interactions among a number of $^{1,3}\Pi_g$ Rydberg and valence states. The results of calculations using this CSE model are compared with the experimental energy-level and predissociation linewidth data base. As a result of the optimization process, relevant potential-energy curves and Rydberg–valence, Rydberg–Rydberg, and valence–valence interactions are characterized for $^{1,3}\Pi_g$ states in the ~6.5–9.5 eV region above the ground state of O_2. The precision of these characterizations and the interpretation of the experimental observations are found to be limited by the quality of the existing data, which exhibit a number of inconsistencies that cannot be reconciled without new, well-characterized experimental studies. In spite of these difficulties, the present CSE model, as currently parametrized, represents a significant improvement over previous work, enabling identification of a number of previously unassigned spectral features associated with perturbation of the $3s\sigma_g\,d\,^1\Pi_g$ state by the $II\,^1\Pi_g$ valence state and an anomalous J sensitivity in predissociation branching ratios for the $d(v=1)$ level. In addition, the electronic structure and predissociation of the $ns\sigma_g$ states for $n \geqslant 4$ are found to be strongly influenced by $ns\sigma_g - (n-1)d\sigma_g$ Rydberg–Rydberg interactions. © *1999 American Institute of Physics.* [S0021-9606(99)00925-3]

I. INTRODUCTION

Molecular oxygen plays a prominent role in the photochemistry of the earth's atmosphere, in combustion, and in many other energetic processes. The last comprehensive review of the excited electronic states and spectra of O_2, by Krupenie in 1972,[1] contained very little information on the *gerade* (g) states lying between the dissociation limit of the $B\,^3\Sigma_u^-$ state and the ground electronic state $(X\,^2\Pi_g)$ of O_2^+ (the ~6.5–12 eV region above the $X\,^3\Sigma_g^-$ ground state of O_2). Since that time, there have been many studies, both experimental and theoretical, elucidating a variety of aspects of the g states in this energy region. However, much of the experimental data appears to be inferior to, and less analyzed than, corresponding data on the *ungerade* (u) states, and there is still significant need for improvement in our understanding of the structure and interactions of the g states lying above 6.5 eV.

Potential-energy curves for selected electronic states of O_2 are shown in Fig. 1, principally in a diabatic ("curve-crossing") representation. Curves for the valence states in Fig. 1 have been constructed from Rydberg–Klein–Rees (RKR) potentials[2] and adaptations of recent *ab initio* calculations.[3,4] The ground $X\,^3\Sigma_g^-$ state and the metastable $a\,^1\Delta_g$ and $b\,^1\Sigma_g^+$ states are associated with the $\ldots(3\sigma_g)^2(1\pi_u)^4(1\pi_g)^2$ molecular-orbital (MO) configuration.[5] These states, together with the more weakly bound $c\,^1\Sigma_u^-$, $A'\,^3\Delta_u$ and $A\,^3\Sigma_u^+$ Herzberg states, are well characterized[3,6–12] and dissociate to the $O(^3P)+O(^3P)$ ground-state separated-atom limit. The remaining twelve valence states[3,11] dissociating to $O(^3P)+O(^3P)$ are either weakly bound or unbound, with the $I\,^1\Pi_g$ and $I\,^3\Pi_g$ states of particular importance to this work.

The bound valence state $B\,^3\Sigma_u^-$, the upper state of the Schumann–Runge transition, dissociates to the lowest-excited separated-atom limit, $O(^3P)+O(^1D)$. There are seventeen additional states[11] dissociating to $O(^3P)+O(^1D)$, a few bound like $B\,^3\Sigma_u^-$, but many unbound. Of these states, the $II\,^3\Pi_g$ state, arising from the $\ldots(3\sigma_g)(1\pi_u)^4(1\pi_g)^3$ configuration, is of particular significance to this work, as is the bound $II\,^1\Pi_g$ valence state from the same MO configuration, which correlates with the third separated-atom limit, $O(^1D)+O(^1D)$.

The lowest-energy g Rydberg states are the first members of the $ns\sigma_g$ series (principal quantum number $n=3,4,5,\ldots$) built on the $X\,^2\Pi_g$-state core of O_2^+. These consist of Rydberg series of $^1\Pi_g$ and $^3\Pi_g$ molecular states

[a)]Work done at Department of Chemistry, University of Maryland, College Park, MD 20742.

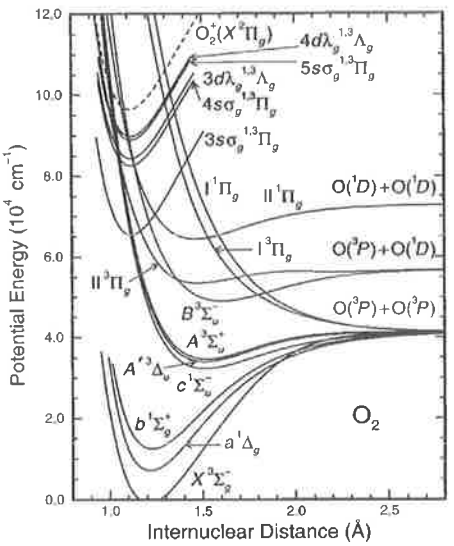

FIG. 1. Approximate diabatic representation of potential-energy curves for the lowest $(X\,^2\Pi_g)\,ns\sigma_g\,^{1,3}\Pi_g$- and $nd\lambda_g\,^{1,3}\Lambda_g$-state manifolds of O_2 in relation to the ground state $X\,^3\Sigma_g^-$, other well-known bound states, and four of the $^{1,3}\Pi_g$ valence states relevant to the perturbation and predissociation of the lower members of both Rydberg manifolds. The $X\,^2\Pi_g$ ground-state potential-energy curve of O_2^+ appears as a dashed line near the top of the figure.

from the $\ldots(3\sigma_g)^2(1\pi_u)^4(1\pi_g)\,ns\sigma_g$ MO configurations, which we denote as $(X\,^2\Pi_g)\,ns\sigma_g$. The next-lowest energy g Rydberg states are associated with the $(X\,^2\Pi_g)\,nd\lambda_g$ configurations $nd\sigma_g$, $nd\pi_g$ and $nd\delta_g$. The $(X\,^2\Pi_g)\,nd\sigma_g$ configurations produce $^1\Pi_g$ and $^3\Pi_g$ series; the $(X\,^2\Pi_g)\,nd\pi_g$ configurations produce $^1\Sigma_g^+$, $^3\Sigma_g^+$, $^1\Delta_g$, and $^3\Delta_g$ series; and the $(X\,^2\Pi_g)\,nd\delta_g$ configurations produce $^1\Pi_g$, $^3\Pi_g$, $^1\Phi_g$, and $^3\Phi_g$ series. At this time, no Rydberg configurations of the form $(X\,^2\Pi_g)\,nl\lambda_g$ which produce g states (l even) with $l>2$ have been observed experimentally.

Unperturbed Rydberg states fall into series of energy levels E_n converging on an ionization limit E_∞ ($=97\,348$ and $97\,546$ cm^{-1} for $v=0$ of the $X\,^2\Pi_{1/2g}$ and $X\,^2\Pi_{3/2g}$ core levels, respectively)[13] according to $E_\infty - E_n = \mathcal{R}(n^*)^{-2} = \mathcal{R}(n-\delta)^{-2}$, where $\mathcal{R}=109\,735.5$ cm^{-1} is the mass-corrected Rydberg constant for O_2, n^* is the effective quantum number and δ is the quantum defect. The lowest-energy members of the $(X\,^2\Pi_g)\,ns\sigma_g\,^{1,3}\Pi_g$ series are the $3s\sigma_g\,^{1,3}\Pi_g$ states whose $v=0$ levels are centered in the 8.2 eV=65 800 cm^{-1} ($n^*\approx1.86$) region above $X\,^3\Sigma_g^-$. The lowest-energy members of the $(X\,^2\Pi_g)\,nd\lambda_g$ series are $3d\lambda_g$, with the $3d\pi_g\,^{1,3}\Sigma_g^+$, $^{1,3}\Delta_g(v=0)$ levels centered in the 10.6 eV=85 300 cm^{-1} ($n^*\approx3.00$) region. Representative potential-energy curves for states associated with $ns\sigma_g(n=3-5)$ and $nd\lambda_g(n=3,4)$ orbitals illustrated in Fig. 1 have been constructed by displacing an RKR potential-energy curve for $O_2^+(X\,^2\Pi_g)$ downward to have $v=0$ levels near $n^*\approx1.86$, 2.80 and 3.79 for the $ns\sigma_g$ series and ≈3.00 and 4.02 for the $nd\lambda_g$ series.

The crossing of Rydberg-state potentials by valence-state potentials of the same symmetry may produce relatively strong homogeneous Rydberg–valence interactions which lead to perturbations, predissociations and, ultimately, noncrossing potential-energy curves in an adiabatic picture. In the case of particular interest to this work, the MO configurations of the $ns\sigma_g\,^{1,3}\Pi_g$ Rydberg and $II\,^{1,3}\Pi_g$ valence states differ by two electrons. The corresponding Rydberg–valence interactions are $\sim700-800$ cm^{-1} for $n=3$,[14] much less than those observed for the $(X\,^2\Pi_g)\,3p\pi_u\,^3\Sigma_u^-$ and $(X\,^2\Pi_g)\,3p\sigma_u\,^3\Pi_u$ states (~4000 and ~7000 cm^{-1}, respectively),[15,16] but sufficiently large to affect significantly the spectroscopy and predissociation of the $ns\sigma_g$ states.

Experimental observations of the $ns\sigma_g$ and other g states in the $\sim6.5-12$ eV range above $X\,^3\Sigma_g^-$ have resulted from studies which employed electron energy-loss (EEL),[17–19] resonance-enhanced multiphoton-ionization (REMPI),[20–40] REMPI-photoelectron (PE),[21,39] kinetic-energy-release (KER),[41–43] and single-photon absorption (SPA)[44] spectroscopies.[45] Theoretical treatments have included *ab initio*[3,4,11,14,46–51] and coupled-channel Schrödinger-equation (CSE) calculations.[52–54]

In order to maximize the utility of CSE models of interacting Rydberg and valence states, it is necessary to optimize the model parameters using comparisons between the calculations and as diverse a set of experimental observations as possible, covering a wide energy range. In this work, the results of a critical reexamination of previous experimental observations and analyses of the $ns\sigma_g\,^{1,3}\Pi_g$ Rydberg states of O_2 are used to optimize the parameters of a CSE model of the interacting $^{1,3}\Pi_g$ Rydberg and valence states in the $\sim6.5-9.5$ eV region above $X\,^3\Sigma_g^-$. Representative CSE-model calculations are presented, with particular emphasis on the vibronic aspects. Identification and analysis of numerous, mostly high-J, previously unidentified rotational perturbations[55] in the $3s\sigma_g\,^{1,3}\Pi_g$ states, which also support the CSE-model optimization, are the subjects of a companion paper in this issue.[56]

II. EXPERIMENTAL DATA BASE

A. Energies

Because atomic oxygen has a nuclear spin of zero, only totally symmetric levels exist in O_2.[57] Thus, only odd-N rotational levels exist in the $X\,^3\Sigma_g^-$ state of O_2, where each N level is split into three spin sublevels: F_1 ($J=N+1$), F_2 ($J=N$), and F_3 ($J=N-1$). As outlined by Slanger and Cosby,[10] several "absolute" scales have been used to describe the energy levels of O_2, and these scales differ from one another because of different definitions of the zero-energy reference (E_0) in the X state. The energy scale employed in this work is that preferred by Slanger and Cosby,[10] which is based on a specific Hamiltonian for the X state. This choice places E_0 in $X\,^3\Sigma_g^-$ 1.33 cm^{-1} below the extrapolated, nonexistent level taken as E_0 in many earlier works (F_2, $N=J=0$), or 0.25 cm^{-1} below the lowest existing level (F_3, $N=1$, $J=0$).

Since $g\leftarrow g$ single-photon transitions are dipole-forbidden from $X\,^3\Sigma_g^-$, the earliest experimental observations of the $ns\sigma_g\,^{1,3}\Pi_g$ Rydberg states arose from EEL measurements at various scattering angles. The most extensive

TABLE I. Representative experimentally determined level energies for the $d\,^1\Pi_g$ state, compared with the CSE model calculations.[a]

v	Ref. 25[b]	Ref. 56[c]	Ref. 43[d]	Ref. 42[e]	CSE[f]
0	66382	66358	66300		66356
1	68238	68226	68200		68226
2		70015	70108		70011
		70143[g]			70142[g]
3	71956	71950	71920		71950
4		73743		73760	73740
5			75710	75500	75485
6			77370	77185	77196
7			79140	78925	78924
8			80750	80550	80596

[a]Origins ν_0, in cm^{-1}, i.e., energies for hypothetical $J=0$ level in $d\,^1\Pi_g$. See Sec. II A for the E_0 reference used here.
[b]Refitting REMPI data from Ref. 25 using energy expression (1) in footnote 58 gave 66 380, 68 236, and 71 954 cm^{-1} for ν_0 for $v=0$, 1, and 3, respectively.
[c]From rotational analyses in Ref. 56 of REMPI spectra presented in Refs. 31 and 25.
[d]Estimated in Ref. 43 from KER spectra. Uncertainties ~100–200 cm^{-1}. See also footnote 59.
[e]Origins from simulation in Ref. 42 of KER spectra. Uncertainties increase from ~10 to ~100 cm^{-1} as v increases. See also footnote 59.
[f]Origins calculated using the present CSE model.
[g]Second entries for $v=2$ refer to the extra level II $^1\Pi_g(v=8)$.

recent experimental observations used two-photon techniques (where $g\leftarrow\leftarrow g$ transitions are allowed) and KER measurements (where charge exchange in collisions of O_2^+ beams with easily ionized species, such as Cs, produces O_2 in a number of Rydberg states). Overall, experimental observations of the $3s\sigma_g\,d\,^1\Pi_g$ and $C\,^3\Pi_g$ states fall into four categories: EEL,[17–19] REMPI,[24,25,30,31,33–36] KER,[41–43] and SPA.[44,45] All of these studies contain vibrationally-resolved information and some contain rotationally-resolved data. However, only a few partial rotational analyses are available,[25,33–36,42] although many studies present spectra which exhibit rotational structure but for which no rotational analyses are given.[24,30,31,33,35,40]

Representative data and spectra from the references above lead to the vibrational-level energies and rotational parameters of the $d\,^1\Pi_g$ and $C\,^3\Pi_g$ Rydberg states summarized in Tables I, II, and III.[58,59] Tables I–III also include results obtained from the CSE model (see Sec. IV) and the results of new rotational analyses of existing experimental data which appear in Ref. 56. Due to severe perturbations in the rotational structure of the $d\,^1\Pi_g(v=1-3)$ levels, rotational analyses prior to Ref. 56 were limited to the lowest rotational levels. Since the corresponding rotational parameters are strongly J dependent,[14,56] it is important to use a consistent and low-J restricted basis for the comparisons in Table II. Experiments with sufficient energy resolution reveal extensive rotationally resolved structure in transitions to the $d\,^1\Pi_g$ state. However, in most cases the highest-resolution observations of transitions to the $C\,^3\Pi_g$ state exhibit only partially resolved rotational structure because of relatively large linewidths produced by predissociation, the most notable exception being transitions to $C\,^3\Pi_g(v=2)$.

Compared with the $3s\sigma_g\,^{1,3}\Pi_g$ states, observations of higher-n members of the $ns\sigma_g\,^{1,3}\Pi_g$ series are relatively few and limited to the $n=4$ and 5 members. Available data for transitions to these states are derived from REMPI spectra[21,23,39] which show several sets of bands, the bands within each set separated approximately by the spin-orbit splitting of the O_2^+ ground state (~200 cm^{-1}). Representative spectroscopic information is summarized in Table IV. The values for $v=4$ are the result of a partial rotational analysis.[23] Approximate values for the $v=1-3$ levels of $4s\sigma_g$ states in Table IV are based on our estimates of the positions of features in spectral figures for the $4s\sigma_g\,^{1,3}\Pi_g \leftarrow\leftarrow X\,^3\Sigma_g^-(1,0)-(3,0)$ bands in Ref. 21. These $v>0$ assignments for $4s\sigma_g$ states are tentative because of lack of rotational analysis and complications due to interactions be-

TABLE II. Representative experimentally determined rotational parameters for the $d\,^1\Pi_g$ state, compared with CSE model calculations.[a]

v	Ref. 25[b]	Refs. 33[c], 42[d]	Ref. 56[e]	CSE[f]	Ion[g]
0	1.68 [19]		1.68_2 [30]	1.68	1.68
	$(4_{.34}\times10^{-6})$		$(7_{.7}\times10^{-6})$		
1	1.58 [12]		1.63 [10]	1.64	1.66
	$(1_{.14}\times10^{-3})$				
2			1.29 [6]	1.29	1.64
			1.15 [7][h]	1.12[h]	
3	1.15 [8]	1.16_9 [~15][c]	1.21_1 [15]	1.14	1.62
	$(1_{.76}\times10^{-5})$	$(9_{.00}\times10^{-5})$	$(4_{.9}\times10^{-4})$		
4		1.5_{85} [24][d]	1.59 [17–32]	1.59	1.60

[a]B_v and D_v values (D_v in parentheses), in cm^{-1}. Numbers in square brackets indicate the maximum J, or the range of J, for which the experimental rotational parameters were determined.
[b]Refitted values (see footnote b to Table I) of B_v (D_v) for $v=0$, 1 and 3 are 1.69_1 ($1_{.16}\times10^{-5}$), 1.60_5 ($1_{.83}\times10^{-5}$), and 1.17_7 ($1_{.76}\times10^{-4}$), respectively.
[c]From spectral simulation of $d\leftarrow\leftarrow a(3,0)$ band in Ref. 33.
[d]From simulation of high-resolution KER spectrum of $d\,^1\Pi_g(v=4)$ in Ref. 42.
[e]From rotational analyses in Ref. 56 of spectra presented in Refs. 31 and 25.
[f]Low-rotation B_v values calculated using present CSE model.
[g]B_v values for $O_2^+(X\,^3\Pi_g)$ from Ref. 9.
[h]Second entry refers to the extra level II $^1\Pi_g(v=8)$.

TABLE III. Representative experimentally determined energies for the $C\ ^3\Pi_g$ state, compared with CSE model calculations.[a]

v	Ω	Ref. 24[b]	Ref. 31[c]	Ref. 33[c]	Ref. 43[d]	CSE[e]
0	0	65573				
	1	65664	65645	65665	65740	65652
	2	65767				
1			67580	67650[i]	67580	67578
2	0	69366[g]	69372[h]			
	1	69445[g]	69451[h]	69440[i]	69400	69445
	2	69550[g]	69556[h]			
3	0	71189				
	1	71265	71255	71260	71260	71266
	2	71375				
4					72990	73021
5					74890	74787
6					76660	76520
7					78360	78201
8					79990	79840

[a]Diffuse-peak energies, in cm^{-1}, unless stated otherwise. See Sec. II A for E_0 reference used here.
[b]Our estimates from low-temperature REMPI spectra in Ref. 24.
[c]Average band head energy estimated by us from room-temperature REMPI spectra in Ref. 31.
[d]From KER spectra. Uncertainties ~100–200 cm^{-1}. See also Sec. II A and footnote 59.
[e]$^3\Pi_{1g}$ origins calculated using the present CSE model.
[f]Our rough estimate from room-temperature REMPI spectrum in Ref. 33.
[g]Origin from rotational reanalysis of spectrum in Refs. 35 and 24, in Ref. 56; $B_2(\Omega=0)=1.6_3$ cm^{-1}, $B_2(\Omega=1)=1.65_3$ cm^{-1}, $D_2(\Omega=1)=1.6\times10^{-5}$ cm^{-1}, $B_2(\Omega=2)=1.68_3$ cm^{-1}, $D_2(\Omega=2)=1.3\times10^{-5}$ cm^{-1}. Ref. 35 gives $\nu_0(\Omega=2)=69\,548$ cm^{-1}, $B_2(\Omega=2)=1.68$ cm^{-1}, and $D_2(\Omega=2)=1.7\times10^{-5}$ cm^{-1}.
[h]Our estimate of origin from low-temperature spectrum.
[i]Reported energy of $^3\Pi_{1g}$ bandhead in spectrum of metastable $O_2(a\ ^1\Delta_g)$.

TABLE IV. Experimental level energies and rotational constants of the $ns\sigma_g\ ^1\Pi_g$ and $^3\Pi_g$ states with $n=4$ and 5.[a]

				Ref. 23		Ref. 21	
n	v	State	Ω	ν_0	B_v	ν_0	B_v
4	0	$^3\Pi_g$	0	83361*		$83344._9$	1.5_5
			1	83373*		$83371._7$	1.7_4
			2	83541*		$83534._9$	1.6_2
		$^1\Pi_g$	1	83552*[b]		83578[c]	
	1	$^3\Pi_g$	0,1			85250[d]	
		$^{1,3}\Pi_g$	1,2			85420[d]	
	2	$^3\Pi_g$	0,1			87090[d]	
		$^{1,3}\Pi_g$	1,2			87260[d]	
	3	$^3\Pi_g$	0,1			88890[d]	
		$^{1,3}\Pi_g$	1,2			89070[d]	
	4	$^3\Pi_g$	0	$90648._0$	1.4_{53}		
			2	$90833._2$	1.5_{69}		
5	0	$^3\Pi_g$	0	$89718._4$	1.5_{58}[e]	$89718._7$	1.6_{26}[f]
			1	$89727._5$	1.9_{47}	$89726._7$	1.6_{81}[f]
			2	$89907._0$	1.6_{28}[e]	$89909._4$	1.6_{28}[f]
		$^1\Pi_g$	1	$89923._7$[b]	1.8_{23}	$89922._9$	1.7_{19}[f]
	1	$^3\Pi_g$	0	91621*			
			1	91615*			
			2	91798*			
		$^1\Pi_g$	1	91809*[b]			

[a]Energies in cm^{-1}. See footnote a to Table I, Sec. II A and footnote 58. Asterisks indicate the energies of the strongest features in the low-temperature spectrum, rather than origins.
[b]Tentative assignment in Ref. 23.
[c]Estimated by us from perturbation of $^3\Pi_g$ energies of Ref. 21. See Sec. IV C.
[d]Mean energy of strongest features, estimated by us from REMPI-PE spectra of Refs. 21 and 39. Uncertainties ±20 cm^{-1}.
[e]$\gamma_0=-0.6_{156}$ and 0.5_{556} cm^{-1} for the $^3\Pi_{0g}$ and $^3\Pi_{2g}$ levels, respectively.
[f]$\gamma_0=-1.0_9$, 1.2_1, -0.5_8, and 0.7_5 cm^{-1} for the $^3\Pi_{0g,1g,2g}$ and $^1\Pi_{1g}$ levels, respectively.

TABLE V. Representative linewidths Γ, in cm^{-1} FWHM, for experimentally observed v levels of the $ns\sigma_g\,^{1,3}\Pi_g$ states, compared with CSE-model calculations.[a]

n	State	v	Experimental			CSE[b] $J=1$	CSE[b] $J=15$
3	$d\,^1\Pi_g$	0	5[c]		2[d]	0.7	0.7
		1			4[d]	2.8	4.1
		2			7[e]	5.5	3.3
					16[e]	20	21
		3			4[d]	0.6	1.4
		4	10[f]		6[d]	7.8	4.8
		5	70[f]			100	100
		6	<30[f]			27	34
		7	<40[f]			5.5	3.1
3	$C\,^3\Pi_g$	0	50[g]		<20[h]	38	40
		1	320[g]		150[i]	150	150
		2	6[g]		2[j]	1.5	0.6
		3	90[g]		<50[h]	77	68
		4	60[g]			43	46
		5	2.6[k]			1.5	2.2
4	$^3\Pi_g$[l]	0	3.2[m]	4.0[n]	5.3[o]	5.3(8.3)[b]	5.4(8.5)[b]
		1	2.5[m]	1.3[n]		3.5(1.9)[b]	3.5(1.8)[b]
		2	1.4[m]	1.8[n]		6.4(5.7)[b]	6.2(5.4)[b]
		3	1.6[m,p]			5.0(7.5)[b]	5.0(5.3)[b]
		4	0.5[m]	1.1[n]		3.4(1.9)[b]	3.5(2.0)[b]
5	$^{1,3}\Pi_{1g}$	0	0.7[m,q]			0.7(0.7)[b]	0.6(1.5)[b]
		1	0.7[m,q]			0.5(0.7)[b]	0.5(0.7)[b]

[a]Where separately determined fine-structure linewidths are available, the tabulated values refer to the $\Omega=1$ component.

[b]$^{1,3}\Pi_1$ FWHM linewidths calculated using the present CSE model. For $n=4$ and 5, the $^1\Pi_1$ widths are in parentheses.

[c]References 25 and 36, from low-temperature REMPI spectra.

[d]FWHM estimated by us for narrowest lines in the REMPI spectrum of Ref. 31. $\Gamma(v=4)$ refers to $J\gtrsim 17$.

[e]From our simulation of the low-temperature REMPI spectrum of Ref. 25. Second entry refers to the extra level $II\,^1\Pi_g(v=8)$.

[f]Reference 42, from simulation of high-temperature KER spectrum. Tabulated width refers to low-J levels.

[g]Reference 24, from diffuse low-temperature REMPI spectrum.

[h]R. D. Johnson III, personal communication to Ref. 53.

[i]Reference 41, from simulation of high-temperature KER spectrum.

[j]Reference 40, from high-temperature REMPI spectrum.

[k]R. A. Copeland, experimental REMPI linewidth from personal communication to Ref. 14. Tabulated value for $^3\Pi_1$ component. $\Gamma(^3\Pi_0)=3.2\ cm^{-1}$, $\Gamma(^3\Pi_2)=1.8\ cm^{-1}$.

[l]Ω-component uncertain, unless indicated otherwise.

[m]Reference 23, FWHM for unassigned single line in low-temperature REMPI spectrum.

[n]Reference 39, FWHM for unassigned single line in low-temperature $^3\Pi_{0,1}$ REMPI-PE spectrum. $\Gamma(^3\Pi_2,{}^1\Pi_1)=3.8$, 1.7–2.1, 1.6–2.5, 2.0, 1.1 cm^{-1}, for $v=0$, 1, 2, 3, 4, respectively.

[o]Reference 21, $\Gamma(^3\Pi_{0,1})$ from simulation of low-temperature REMPI spectrum. $\Gamma(^3\Pi_2)=3.3\ cm^{-1}$.

[p]Possibly blended.

[q]Reference 23 gives $\Gamma(^3\Pi_{0,2})=0.5\ cm^{-1}$.

tween the $4s\sigma_g(v+1)$ and $3d\lambda_g(v)$ states which occur in the same energy region (see Sec. IV).

Difficulties were encountered in attempting to compare energies from the various data sets in the literature, due mainly to differences in experimental precision (often unspecified), underreporting of calibration and data-reduction techniques, and differing observational conditions (especially temperature). Attempts to reconcile these differences between data sets, demonstrably apparent in Tables I, II, and III, failed because only a few of the authors observing rotationally-resolved data reported (even in theses or reports) the spectral lines upon which their analyses were based and, subsequently, the original data have disappeared. These experimental uncertainties, which limit the extent and accuracy of quantitative characterization of the $ns\sigma_g\,^{1,3}\Pi_g$ states and their interactions with valence states, are described in greater detail in a review on the spectrum and structure of O_2 currently nearing completion.[60]

B. Linewidths

Experimentally based linewidth information, resulting from both REMPI and KER spectra, is fragmentary and even less documented than the energy-level data discussed in Sec. II A. Reported experimental values of linewidth Γ for transitions to the $ns\sigma_g\,^{1,3}\Pi_g$ states with $n=3-5$ in $^{16}O_2$ (a few values for other isotopic species appear in Ref. 24) are summarized in Table V. Table V also includes values for some

$d\,^1\Pi_g$ levels (footnote d) estimated in Ref. 56 from the spectra of Ogorzalek-Loo,[31] as well as CSE-based results from the present work to be discussed in Sec. IV. Linewidths for the more strongly predissociated levels have been derived, in general, from the simulation of partially resolved or unresolved band envelopes.[61] Tabulated widths for the narrower levels generally refer to the apparent widths of individual rotational lines, possibly blended, with no allowance for the instrumental resolution function. Significant discrepancies occur between linewidths from different sources. For example, the difference of a factor of three between the measured $C(v=2)$ linewidths[24,40] has been attributed by Tjossem and Smyth[40] to a combination of power broadening and higher probe linewidths in the Sur *et al.*[24,36] spectra. In view of the possibility of many undocumented effects, such as power broadening and other instrumental limitations in the REMPI spectra, it would seem prudent to consider most of the experimentally based linewidths in Table V as upper limits to the true values.

C. Unassigned spectra

The $(2+1)$ REMPI spectra of transitions to the C and d states show a series of unassigned "companion" structures at slightly shorter wavelengths from the $C\leftarrow\leftarrow X(2,0)$ and the $d\leftarrow\leftarrow a(0,0)$, (1,0), (2,0), and (3,0) bands,[31,33] all of which exhibit resolved rotational lines. For $C\leftarrow\leftarrow X(2,0)$, the structures appear in several groups, the stronger regions centered around $\sim 70\,200$ and $\sim 70\,270$ cm^{-1}. The structures in the $d\leftarrow\leftarrow a$ spectra are centered ~ 100 cm^{-1} to higher energy from each of the $d\leftarrow\leftarrow a(v',0)$ bands listed, except for the (2,0) band. The structure near $d\leftarrow\leftarrow a(0,0)$ is weak and poorly developed, while those structures near $d\leftarrow\leftarrow a(2,0)$ are relatively intense and complex, extending ~ 500 cm^{-1} towards higher transition energy in several groups which diminish in intensity with increasing energy. The structure near $d\leftarrow\leftarrow a(3,0)$ was previously attributed to the $C\leftarrow\leftarrow X(0,1)$ hot band,[33] an assignment disputed by Ogorzalek-Loo *et al.*[30]

Finally, SPA spectra[44] of supersonically-expanded and cooled O_2 indicate the presence of a weak band near "1545 Å"[44] ($64\,730\pm 170$ cm^{-1}) which remains unassigned. Reference to the figure presented in Ref. 44 implies that this wavelength should be 1555 Å ($64\,300$ cm^{-1}). If this transition originates from $X\,^3\Sigma_g^-(v=0)$, the upper level of the transition would be ~ 1600 and ~ 900 cm^{-1} below $d\,^1\Pi_g(v=0)$ and $C\,^3\Pi_g(v=0)$, respectively, using the 1545 Å value, while it would be ~ 2100 and ~ 1400 cm^{-1} below $d(v=0)$ and $C(v=0)$ using the 1555 Å value.

III. THEORETICAL TREATMENT

A. Previous work

There has been a significant amount of previous theoretical work treating the $ns\sigma_g\,^{1,3}\Pi_g$ Rydberg states and their interactions with valence states. *Ab initio* configuration-interaction calculations[14,48–51] have provided theoretical potential-energy curves and either direct or indirect indications of the magnitudes of the Rydberg–valence interactions. Semiempirical coupled-state modeling of predissociation linewidths[42] for selected isotopic rovibrational levels of the $d\,^1\Pi_g$ state and dissociative branching ratios[41] for $d\,^1\Pi_g$ and $C\,^3\Pi_g(v=0-2)$ has led to estimates for several Rydberg–valence and valence–valence interaction matrix elements. A subsequent full CSE treatment[54] of the $^1\Pi_g$ Rydberg–valence interaction compared B_v values for $d(v=0-3)$ with the results of the approximate treatment of Ref. 42, and also noted that there should be a bound valence level ~ 80 cm^{-1} above $d(v=2)$. Additional CSE calculations[52,53] considered the $^3\Pi_g$ Rydberg–valence interaction. Finally, in a comprehensive study, Li *et al.*[14] applied their *ab initio* $^{1,3}\Pi_g$ potential matrix to detailed calculations of predissociation in the $3s\sigma_g\,d\,^1\Pi_g$ and $C\,^3\Pi_g$ states, including a treatment of fine structure in the $^3\Pi_g$ states for the first time. Various semiempirical and theoretical Rydberg–valence, valence–valence, and Rydberg–Rydberg interaction matrix elements resulting from the above studies are summarized in Table VI, together with the parameters used in the present investigation.

TABLE VI. Representative semiempirical and *ab initio* Rydberg–valence (H_{Rv}), valence–valence (H_{vv}), and Rydberg–Rydberg (H_{RR}) coupling matrix elements for the $ns\sigma_g\,^{1,3}\Pi_g$ Rydberg and I,II $^{1,3}\Pi_g$ valence states, in cm^{-1}.

Mult.	Coupling	Ref. 52 [a]	Ref. 41 [a]	Ref. 14 [b]	CSE [c]
Singlet	$H_{Rv}(n=3)$		440[d]	660[e]	630[a]
	$H_{Rv}(n=4)$			470[e]	165[a]
	$H_{Rv}(n=5)$				75[a]
	H_{vv}			660	500[a]
Triplet	$H_{Rv}(n=3)$	500[f]	640	780[e]	620[a]
	$H_{Rv}(n=4)$			460[e]	165[g]
	$H_{Rv}(n=5)$				75[g]
	H_{vv}	440	480	660	500[h]
Sing.-Trip.	$H_{RR}(n=3)$			90[i]	95[j]
	$H_{RR}(n=4)$			90[i]	95[j]
	$H_{RR}(n=5)$				95[j]

[a]Semiempirical determination, from fit to experimental data.
[b]*Ab initio* calculation. Values corrected to diabatic Rydberg basis used here.
[c]Parameters of CSE model used here and in Ref. 56.
[d]Determined in Ref. 42.
[e]*R*-dependent calculation. Value at Rydberg-valence crossing point tabulated.
[f]Determined in Ref. 53. Reference 24 gives 520 cm^{-1}.
[g]Tied to corresponding singlet coupling in fitting procedure.
[h]Fixed at value determined for corresponding singlet coupling. This value leads to satisfactory estimates of the triplet branching ratios (see Table VII).
[i]*R*-dependent calculation. Value at R_c for $ns\sigma_g\,^{1,3}\Pi_g$ states tabulated.
[j]Fixed at a semiempirical value (Ref. 69) equal to half the $ns\sigma_g\,^3\Pi_{2g} - {}^3\Pi_{0g}$ splitting of ~ 190 cm^{-1} (see, e.g., Table IV).

B. The CSE method

Breakdown of the Born–Oppenheimer (BO) approximation produced by Rydberg–valence interactions may be addressed by using a CSE model in which interactions between BO basis states are included explicitly. In the adiabatic basis, the adiabatic potential-energy curves for the BO basis states exhibit an avoided crossing and these states interact nonadiabatically through off-diagonal elements of the nuclear kinetic-energy operator. In the diabatic basis, the diabatic potential-energy curves cross and interact through off-

diagonal elements of the electrostatic Hamiltonian. Provided that a complete electronic-state basis is employed, the results of CSE calculations are insensitive to the choice of an adiabatic or diabatic basis set. CSE formalisms have been detailed by van Dishoeck *et al.*[62] and Torop *et al.*[63] The CSE method is particularly suitable for treatment of Rydberg–valence interactions in O_2 and has been applied previously to explain unusual features in the spectrum of O_2 excited into the u states.[16,64,65]

The particular implementation of the CSE method employed here is described in more detail in Ref. 56 which deals principally with the specific problem of rotational perturbations in the $d\,^1\Pi_g$ state. Briefly, a diabatic coupled-channel basis is employed, including the $ns\sigma_g\,^1\Pi_{1g}$ and $^3\Pi_{1g}$ Rydberg states with $n=3-5$, together with the lowest-energy valence states of the same symmetry: $I\,^1\Pi_{1g}$, $II\,^1\Pi_{1g}$, $I\,^3\Pi_{1g}$, and $II\,^3\Pi_{1g}$. These basis states are coupled by electrostatic Rydberg–valence, valence–valence, and spin-orbit Rydberg–Rydberg interactions. Radial wave functions from a solution of the coupled-channel Schrödinger equations[56] are used to calculate partial and total excitation cross sections and the corresponding rovibrational energies, predissociation linewidths and dissociation branching ratios. The specific CSE model used here differs from that of Ref. 56 only in that the $n=4$ and 5 Rydberg states have been added to the basis.

C. CSE-model optimization

Potential-energy curves for the diabatic basis states and the assumed R-independent couplings between them were optimized using a weighted least-squares fitting procedure involving comparison between CSE-calculated and representative observed energy levels, rotational constants and predissociation linewidths from Tables I–V. Because of the diversity and inconsistency of the experimental data, it was necessary to choose particular data sets for use in the optimization process, without necessarily implying any superiority for those data. For the $d\,^1\Pi_g$ state, the main spectroscopic data employed were derived from the REMPI spectra of Ogorzalek-Loo[31] and Sur *et al.*[25] in Ref. 56 ($v=0-4$), and the KER spectra of van der Zande *et al.*[42] ($v=5-8$). For the $C\,^3\Pi_g$ state, data derived by us from the REMPI spectra of Sur *et al.*[24] were employed ($v=0-3$), together with the KER data of van der Zande *et al.*[43] ($v=4-8$). In the case of predissociation linewidths for the d and C states (Table V), when several estimates were available the smallest values were used in the optimization process.

Initial potential-energy curves for the $3s\sigma_g$ Rydberg states were formed by lowering an RKR curve for $O_2^+(X\,^2\Pi_g)$ to appropriate energies, while those for the valence states were derived from *ab initio* calculations.[3,4] The $I\,^{1,3}\Pi_g$ potentials were held fixed, while those for the d, C, and $II\,^{1,3}\Pi_g$ states were allowed to vary smoothly in the optimization procedure. The Rydberg–Rydberg spin-orbit coupling and the triplet valence–valence coupling were held fixed at the values given in Table VI, while the singlet and triplet Rydberg–valence couplings and the singlet valence–valence coupling were allowed to vary. These choices reflect the sensitivity to the various model parameters of the CSE calculations corresponding to available experimental data. In addition to the experimental data base described above, the inclusion in the fitting procedure of rovibrational energies for d-state levels near particular rotational perturbations[56] enabled detailed optimization of the $II\,^1\Pi_g$-state potential-energy curve, while REMPI intensity profiles[31] in spectral regions most influenced by valence levels enabled optimization of the singlet valence–valence interaction.[56]

In the case of the $ns\sigma_g\,^{1,3}\Pi_g$ Rydberg states with $n=4$ and 5, appropriate potential-energy curves were formed by lowering the ionic curve so that the $v=0$ energy levels of Table IV were reproduced, while the $n=4$ and 5 Rydberg–valence couplings were optimized by comparing CSE-calculated linewidths with the experimental $v=0$ predissociation linewidths of Yokelson *et al.*[21] and Yokelson *et al.*,[23] respectively (Table V). Since the predissociation problem for $n>3$ is somewhat underdetermined due to the paucity of reliable experimental linewidths, for this range of n the triplet and singlet Rydberg–valence couplings were taken as equal in the linewidth fitting procedure.

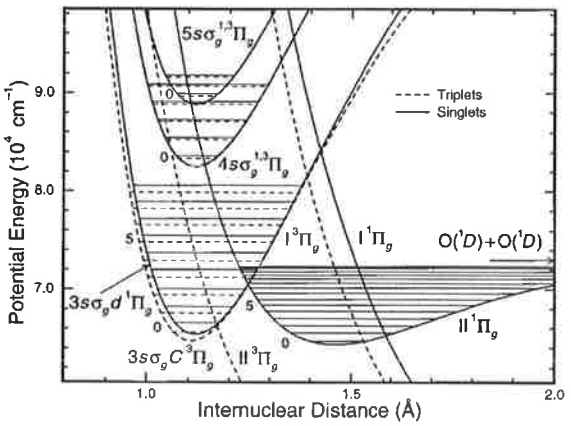

FIG. 2. Diabatic potential-energy curves for the $^{1,3}\Pi_g$ states used in the CSE-model calculations. The singlet and triplet $ns\sigma_g$ potential-energy curves for $n\geq 4$ are virtually indistinguishable on the scale of the figure. Coupled-channel vibrational eigenvalues for the bound states are also indicated as horizontal lines within their respective potentials.

IV. RESULTS AND DISCUSSION

A. CSE-model parameters

The resulting diabatic potential-energy curves for the $^{1,3}\Pi_g$ states modelled in Sec. III C are shown in Fig. 2, while the coupling matrix elements employed are given in Table VI. Using this parametric representation, energy levels, rotational parameters, predissociation linewidths and predissociation branching ratios were determined for selected $ns\sigma_g\,^{1,3}\Pi_g$ Rydberg states with $n=3-5$. These results are discussed in Secs. IV B and IV C.

Reliability of the potential-energy curves in Fig. 2 is limited by uncertainties in the experimental data. In addition, the $^3\Pi_g$ potentials are expected to be less reliable than the $^1\Pi_g$ potentials because they are based on analyses of spectra

which are significantly more diffuse. The small difference in R_e between the optimized potential-energy curves for the isoconfigurational $3s\sigma_g\, d\,^1\Pi_g$ and $C\,^3\Pi_g$ states likely arises because of the relative lack of experimental rotational constants for the C state. Nevertheless, the model $d\,^1\Pi_g$ Rydberg and $II\,^1\Pi_g$ valence potential-energy curves are expected to be significantly more accurate than those utilized in other semiempirical studies. In particular, detailed analysis of the d-state rotational perturbations in Ref. 56 has enabled the successful characterization of many $II\,^1\Pi_g$ vibrational levels indirectly through the effects of their strong perturbation of the d-state levels, leading to the reliable potential-energy curve for the $II\,^1\Pi_g$ state presented in Fig. 2.

Optimized values for the singlet and triplet $n=3$ Rydberg–valence interaction matrix elements in Table VI are in reasonable agreement with other semiempirical determinations and recent *ab initio* calculations.[14] Further refinement of these couplings is unlikely without significantly improved experimental measurements. The optimized value of the $n=4$ Rydberg–valence coupling (see Sec. III C) is in poor agreement with the *ab initio* values. However, because of uncertainties in the corresponding experimental linewidths, both the $n=4$ and $n=5$ couplings should be regarded as approximate. The optimized Rydberg–valence couplings decrease to ~27% from $n=3$ to $n=4$, and to ~45% from $n=4$ to $n=5$. However, this behavior contrasts with the slower and more regular decreases with n observed for the $np\sigma_u\,^3\Pi_u$ Rydberg series of O_2 (to ~50% from $n=3$ to $n=4$, to ~58% from $n=4$ to $n=5$).[16]

The valence–valence interaction matrix elements are more difficult to determine than the Rydberg–valence interaction matrix elements. As described in more detail in Ref. 56, certain regions of the REMPI spectra for transitions into the d state are sensitive to the $I\,^1\Pi_g$–$II\,^1\Pi_g$ interaction matrix element and have been used to obtain the optimized value presented in Table VI. This first semiempirical value of the singlet valence–valence interaction is significantly less than the *ab initio* value of Li *et al.*[14]

B. The $3s\sigma_g\, d\,^1\Pi_g$ and $C\,^3\Pi_g$ states

The several theoretical studies of the $^{1,3}\Pi_g$ Rydberg–valence interactions discussed in Sec. III A have treated many aspects of the $d\,^1\Pi_g$ and $C\,^3\Pi_g$ spectroscopies, including perturbation and predissociation mechanisms. The present and companion[56] works should be regarded as extensions of those studies.

1. Structure, intensities and assignments

Calculated vibrational energies and rotational parameters for the d and C states included in the columns headed CSE in Tables I, II, and III are in good agreement with the data base used to determine the model parameters, and satisfactory agreement with experiment overall, considering the large measurement uncertainties and significant differences between data sets. The CSE calculations show, in agreement with other studies, that the perturbation and predissociation occurring in the d- and C-state levels arise principally through Rydberg–valence interactions.

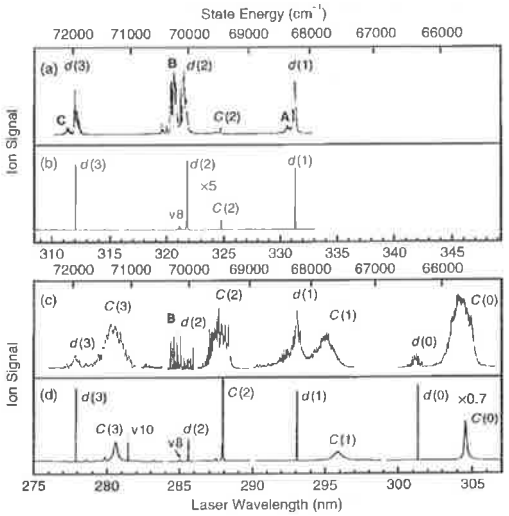

FIG. 3. Composite experimental (2+1) REMPI spectra of Johnson *et al.* (Ref. 33) for excitation from the $X\,^3\Sigma_g^-$ and $a\,^1\Delta_g$ states, together with corresponding transitions from CSE calculations for $J=1$. All data have been plotted on a common scale for the excited-state energy. Top panel: (a) Experimental spectrum from $O_2(a\,^1\Delta_g)$, indicating transitions to $3s\sigma_g\, d\,^1\Pi_g$ and $C\,^3\Pi_g$ levels and previously unassigned bands in regions A, B, and C. (b) Calculated REMPI spectrum, confirming the assignments in (a) and indicating the transition to the $II\,^1\Pi_g(v=8)$ valence level (v8), responsible for much of the spectral complexity in region B of (a). Bottom panel: (c) Experimental spectrum from $O_2(X\,^3\Sigma_g^-)$, indicating transitions to $3s\sigma_g\, d\,^1\Pi_g$ and $C\,^3\Pi_g$ levels and previously unassigned structure in region B. (d) Calculated REMPI spectrum, confirming assignments in (c) and indicating transitions to the $II\,^1\Pi_g(v=8$ and 10) valence levels (v8 and v10, respectively).

Aided by application of the CSE model, Ref. 56 has identified many previously unidentified perturbations in the rotational structure of the $d\,^1\Pi_g$-state levels, perturbations caused by a bound–bound Rydberg–valence interaction with the $II\,^1\Pi_g$ valence state. The effects of these perturbations are evident, for example, in the "anomalous" values of the low-J-based rotational parameters in Table II, values which differ markedly from the B_v values[9] expected for a member of an unperturbed Rydberg series converging on the ground state of the ion (see right-hand column in Table II).

While it is usually inadvisable to base detailed arguments and conclusions on intensity information in REMPI spectra, some general inferences may be drawn from broad intensity trends. In Fig. 3, the composite room-temperature (2+1) REMPI spectra of O_2 excited from the ground $X\,^3\Sigma_g^-$ [(c), lower panel] and metastable $a\,^1\Delta_g$ [(a), upper panel] states into the $3s\sigma_g\, d\,^1\Pi_g$ and $C\,^3\Pi_g$ states, recorded by Johnson *et al.*,[33] are shown plotted on a common excited-state energy scale. It is apparent from Fig. 3 that, while spin-forbidden two-photon transitions to the $d\,^1\Pi_g$ state occur quite strongly in excitation from $X\,^3\Sigma_g^-$, the opposite is the case for excitation from $a\,^1\Delta_g$, with only the $C\,^3\Pi_{1g} \leftarrow\leftarrow a\,^1\Delta_g(2,0)$ transition being visible.

These intensity trends can be understood through simple arguments involving intensity borrowing and competition between predissociation and ionization. The spin-orbit inter-

action between the $d\,^1\Pi_{1g}(v)$ and $C\,^3\Pi_{1g}(v)$ levels implies an effectively v-independent ~2% intensity borrowing by the spin-forbidden transition from the allowed transition in two-photon absorption spectra.[66] However, in the REMPI spectra this effect is strongly modified, in a way dependent on the relative linewidths, due to competition between predissociation and ionization.[56] As a result, transitions to $C\,^3\Pi_{1g}(v=2)$ are visible in Fig. 3 in excitation from the $a\,^1\Delta_g$ state [(a), upper panel] because this is the only triplet level to have a width narrow enough to be comparable with the corresponding singlet linewidth. On the other hand, transitions are observed to all singlet levels in the ground-state spectrum [(c), lower panel] because their widths are either much less than ($v=0$, 1, and 3), or comparable to ($v=2$), the triplet linewidths.

Semiquantitative support for these arguments follows from CSE calculations of the REMPI spectra.[56] Vibrational (2+1) REMPI spectra for excitation from $X\,^3\Sigma_g^-$ [(d), lower panel] and $a\,^1\Delta_g$ [(b), upper panel], calculated for $J=1$ using the current CSE model,[67] are also shown in Fig. 3. In Fig. 3, the ~316–326 nm segment of panel (b) has had its intensity scale expanded (×5) to illustrate better the calculated relative intensities of close-lying valence, allowed, and spin-forbidden transitions, while the ~299–307 nm segment of panel (d) has had its intensity scale reduced (×0.7) to keep its peaks on scale. Except for $v=2$, there is general agreement to within a factor of 2 between the observed and calculated relative intensities (i.e., the relative *areas* of the spectral features) for transitions from $X\,^3\Sigma_g^-$ to associated $d(v)$ and $C(v)$ levels.[68] The underestimate provided by the calculations for the exceptional $d(v=2):C(v=2)$ intensity ratio in each spectrum can be explained by noting that room-temperature REMPI spectra for transitions into the $d(v=2)$ level are dominated by high rotational levels since the $d(v=2)$ linewidth decreases markedly at high J,[56] whereas the calculated intensity ratio refers only to $J=1$.

Also evident in the experimental spectra of Fig. 3 are some of the unassigned companion features discussed in Sec. II C, labeled A, B, and C. It is apparent from a comparison between the experimental and calculated spectra in Fig. 3 that these features are too strong to be explained as transitions to the $II\,^1\Pi_g$ valence state, the most obvious suggestion for their origin. Detailed rotational CSE calculations in Ref. 56 show that these features represent transitions to high rotational levels of $d(v)$ and their band-like appearance is due to strong perturbations in the rotational structure of the $d\,^1\Pi_g$ Rydberg state caused by the bound valence state $II\,^1\Pi_g$. Transitions to this valence state are not seen in the experimental spectra of Fig. 3, but a transition to the $II\,^1\Pi_g(v=8)$ level[56] has been observed in a very-low-temperature ($T\lesssim 5$ K) $d\leftarrow\leftarrow X(2,0)$ (2+1) REMPI spectrum.[25] Transitions to this valence level appear in the calculated $J=1$ REMPI spectra at slightly shorter wavelengths than those to $d(v=2)$, with a relative valence:Rydberg intensity of 14%, in fairly good agreement with an observed ratio of ~11% deduced by us from Fig. 2 of Ref. 25.

Production of a REMPI signal following two-photon excitation of the $d\,^1\Pi_g(v=0)$ level from $a\,^1\Delta_g(v=0)$ requires a two-photon ionization step. The $d\leftarrow\leftarrow a(0,0)$ (2+2) REMPI spectrum appearing in Fig. 2 of Ref. 30 displays unusual satellite structure towards shorter wavelengths, as mentioned in Sec. II C. Since the $d(v=0)$ level is relatively unperturbed by the $II\,^1\Pi_g$ state, a different explanation is required for the existence of this particular satellite. It is likely that this explanation involves interferences at the three-photon level which modulate rotational intensities in the $d\leftarrow\leftarrow a(0,0)$ REMPI band. This interpretation is consistent with the fact that full and regular rotational development is observed in room-temperature $d\leftarrow\leftarrow X(0,0)$ (2+1) REMPI spectra.[31]

Finally, the unassigned SPA transition[44] described in Sec. II C has been shown to lie well below transitions to the lowest $3s\sigma_g$ Rydberg levels. However, the calculated $II\,^1\Pi_g(v=0)$ valence level (64 732 cm^{-1}) lies in the general region of the observed level (~64 730 cm^{-1} or ~64 300 cm^{-1}, see Sec. II C) and would be a tempting assignment[45] if it were not for the absence of a clear vibrational progression with the small characteristic valence-level spacing in the spectrum of Ref. 44.

2. Predissociation and predissociation branching ratios

Because of variability and uncertainty in the values of J pertinent to many of the experimental linewidths listed in Table V, predissociation linewidths calculated using the CSE model for both $J=1$ and 15 are also shown in the table. Calculated linewidths for the $3s\sigma_g\,C\,^3\Pi_g$ state exhibit the oscillatory vibrational pattern expected for an outer crossing between the $C\,^3\Pi_g$ Rydberg and $II\,^3\Pi_g$ valence states (crossing-point $R_x > R_e$, see Fig. 2), with maxima for $v=1$ and 3, and minima for $v=2$ (and 5), in agreement with the observations. However, quantitative agreement is hampered by the experimental uncertainties discussed in Sec. II B. In agreement with the *ab initio* study of Li *et al.*,[14] the CSE calculations indicate that the C-state linewidths are relatively J-independent, except for the narrower levels with $v=2$ and 5.

Predissociation of the $d\,^1\Pi_g$ state is complicated by bound–bound interactions with the $II\,^1\Pi_g$ valence state for energies below the $O(^1D)+O(^1D)$ dissociation limit (see Fig. 2), and, as pointed out by van der Zande *et al.*,[41] linewidths for the lowest vibrational levels are dominated by contributions from the triplet predissociation channel via spin-orbit interaction between the d and C states. Within the uncertainties of the diverse experimental data, calculated d-state predissociation linewidths in Table V reproduce the observed vibrational pattern, with a low-J linewidth maximum for $v=2$ and another maximum for $v=5$, and minima for $v=0$, 3 (and 7). While the general predissociation pattern for $v>3$ is consistent with expectation for an outer crossing between the $d\,^1\Pi_g$ Rydberg and $II\,^1\Pi_g$ valence states, the low-J linewidth maximum for $d(v=2)$ arises from a near degeneracy with the interacting $II\,^1\Pi_g(v=8)$ level which is heavily predissociated through $I\,^1\Pi_g - II\,^1\Pi_g$ valence–valence interaction. The calculated $J=1$ widths for $d(v=2)$ and the "extra" level $II\,^1\Pi_g(v=8)$ are in reasonable agreement with values derived by us from a simulation of the

TABLE VII. Measured and calculated dissociation branching ratios for the $3s\sigma_g\,{}^{1,3}\Pi_g(v=0-2)$ states.[a]

State	v	Meas.[b]	CSE ($J=1$)	CSE ($J=15$)
$d\,{}^1\Pi_g$	0	0.08	0.11	0.09
	1	0.28	0.13	0.43
	2	1.00	1.00	1.00
$C\,{}^3\Pi_g$	0	0.08	0.09	0.09
	1	0.07	0.09	0.09
	2	0.08	0.11	0.11

[a]The branching ratios represent the fraction predissociated to the ground-state dissociation limit $O(^3P)+O(^3P)$.
[b]From Ref. 41. Effective rotational temperature 550 K.

low-temperature spectrum in Fig. 2 of Sur *et al.*[25] The consequences of significant J dependence for some of the $d(v)$ linewidths are discussed in detail in Ref. 56.

Using CSE calculations of partial cross sections for dissociation into each open channel [$\mathrm{I}\,{}^{1,3}\Pi_g$, correlating with the $O(^3P)+O(^3P)$ dissociation limit; and $\mathrm{II}\,{}^3\Pi_g$, correlating with the limit $O(^1D)+O(^3P)$ (see Fig. 1)], the branching ratio representing the $O(^3P)+O(^3P)$ dissociation flux as a proportion of the total flux was determined for the $d\,{}^1\Pi_g$ and $C\,{}^3\Pi_g(v=0-2)$ levels. In the case of the C-state branching ratios, the $\Omega=1$ ratio was averaged with $\Omega=0$ and 2 ratios estimated using separate calculations in which the singlet states were omitted.

The branching ratios calculated for $J=1$ and 15 are compared in Table VII with observations based on the KER spectra of van der Zande *et al.*[41] The effective rotational temperature applicable to the measurements is 550 K,[41] corresponding to a most probable $J\approx 10$. Except for $d\,{}^1\Pi_g(v=1)$, the calculated branching ratios show little J dependence and are in reasonably good agreement with the measurements. Comparison between the calculations for $J=1$ and 15 in Table VII indicates that the $d(v=1)$ branching ratio has a strong J dependence. Additional, more detailed calculations show that the $d(v=1)$ branching ratio peaks sharply at $J=12$ with a value of 0.89, falling to 0.11 at $J=25$. Thus, the effective branching ratio for unresolved rotational levels will be critically dependent on the rotational distribution, suggesting that the $d(v=1)$ branching ratio in KER experiments will be anomalously sensitive to temperature.

Some qualitative justification for the behavior of the branching ratios in Table VII has been given by van der Zande *et al.*[41] In the interesting case of the $d\,{}^1\Pi_g$ state, $d(v=0)$ is coupled almost exclusively to $C(v=0)$, through the Rydberg–Rydberg spin-orbit interaction, and thus dissociates in the same way as $C(v=0)$. In contrast, $d(v=2)$ is strongly coupled to levels of the $\mathrm{II}\,{}^1\Pi_g$ state[56] and dissociates in the same way as this valence state, i.e., via the $\mathrm{I}\,{}^1\Pi_g$ valence state to the $O(^3P)+O(^3P)$ limit. The $d(v=1)$ level, however, lies in a critical region where its coupling to $C(v=1)$ competes with its coupling to $\mathrm{II}\,{}^1\Pi_g(v=5)$, the latter being extremely sensitive to the energy difference between the singlet Rydberg and valence rovibrational levels. It is shown in Ref. 56 that the $d(v=1)$ and $\mathrm{II}\,{}^1\Pi_g(v=5)$ levels coincide for $J\approx 12$, thus explaining the sensitivity of the calculated $d(v=1)$ branching ratio to J in this region. Because of this sensitivity, new, laser-based experiments in which the detailed J dependence of the $d(v=1)$ branching ratio is measured would be of value in refining models of the relevant Rydberg–valence, Rydberg–Rydberg, and valence–valence interactions.

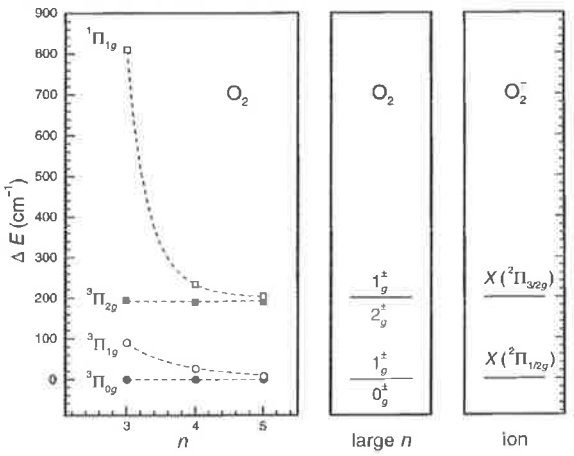

FIG. 4. Observed energy splittings $\Delta E=E(ns\sigma_g\,{}^{1,3}\Pi_{\Omega g})-E(ns\sigma_g\,{}^3\Pi_{0g})$ for the $v=0$ levels, illustrating the rapid transition from approximate (Λ,S) to (Ω,ω) coupling as n increases from 3 to 5, compared with the 3/2,1/2 splitting in the $X\,{}^2\Pi_g$ ground state of O_2^+.

C. The $ns\sigma_g\,{}^{1,3}\Pi_g$ states for $n=4$ and 5

1. Structure

As can be seen from Table IV, the $ns\sigma_g\,{}^{1,3}\Pi_g$ states with $n>3$ are not especially well characterized experimentally. Convincing rotational assignments exist only for the $v=0$ levels of the $n=4$ and $n=5$ states. Spectroscopic parameters and linewidths for the diffuse $4s\sigma_g\,{}^3\Pi_g(v=0)$ levels were determined by means of band simulation,[21] but none are available for $4s\sigma_g\,{}^1\Pi_g(v=0)$. The estimated origin for this level listed in Table IV was determined by us from the observed perturbation of the $4s\sigma_g\,{}^3\Pi_{1g}(v=0)$ level (presumably due to a $^3\Pi_{1g}-{}^1\Pi_{1g}$ interaction) using standard two-level perturbation expressions.[69] Weak, diffuse lines, not associated with the $^3\Pi_{2g}$ level, occur in the low-temperature $4s\sigma_g\,{}^3\Pi_{2g}, {}^1\Pi_{1g}\leftarrow\leftarrow X(0,0)$ spectrum[21,23,39] near the estimated position of the $^1\Pi_{1g}$ origin and are likely to be associated with this level. Spectroscopic parameters listed for the $5s\sigma_g\,{}^{1,3}\Pi_g(v=0)$ levels in Table IV were determined by rotational analysis[21,23] and include γ terms[58] attributed to increased S uncoupling for $n=5$.

As illustrated in Fig. 4, the variation with n of the splittings between the four Ω-components $^1\Pi_{1g}$, $^3\Pi_{2g}$, $^3\Pi_{1g}$, and $^3\Pi_{0g}$ in the $v=0$ levels of the known $ns\sigma_g$ states indicates a rapid and regular transition from (Λ,S) to (Ω,ω) coupling as n increases from 3 to 5. These observations, together with small variations in the corresponding quantum defects ($\delta=1.14$, 1.20, and 1.21 for the $ns\sigma_g\,{}^{1,3}\Pi_g(v=0)$ levels with $n=3$, 4, and 5, respectively) and relatively strong rates of decrease in the Rydberg–valence couplings (see Sec.

IV A) over the same range of n, combine to imply a much more rapid weakening of Rydberg-core electron interactions for the low-lying $ns\sigma_g$-based states of O_2 than has been reported[16] for $np\sigma_u$-based states with comparable n values. In addition, strong electronic interactions are expected between the $ns\sigma_g$ and $(n-1)d\sigma_g$ Rydberg states for $n \geq 4$. Unpublished *ab initio* calculations for the $^1\Pi_g$ states of O_2 by Lefebvre-Brion[70] support these expectations and give

$$``|4s\sigma_g\rangle'' = 0.73|4s\sigma_g\rangle + 0.67|3d\sigma_g\rangle \quad (1)$$

and

$$``|3d\sigma_g\rangle'' = 0.67|4s\sigma_g\rangle - 0.73|3d\sigma_g\rangle, \quad (2)$$

indicating very strong mixing of the ''pure'' $4s\sigma_g$ and $3d\sigma_g$ states.[71] Such strong mixing and the fact that the $4s\sigma_g\,^{1,3}\Pi_g(v+1)$ and $3d\sigma_g\,^{1,3}\Pi_g(v)$ level series lie very close to one another[21,39] are major contributing factors to the observation of extremely complex (and unanalyzed) spectra[21,39] associated with transitions to the $4s\sigma_g\,^{1,3}\Pi_g(v>0)$ levels. Analogous behavior can be expected for the $5s\sigma_g\,^{1,3}\Pi_g(v>0)$ levels, but the current lack of spectral data associated with transitions to these levels precludes further speculation.

2. Predissociation

The observed diffuseness of the $ns\sigma_g\,^{(1),3}\Pi_g$ levels decreases with n, as is expected if something like the $(n^*)^{-3/2}$ scaling rule[69] applies to the Rydberg–valence interaction matrix element. Simulation of the $4s\sigma_g\,^3\Pi_g \leftarrow\leftarrow X(0,0)$ spectrum by Yokelson *et al.*[21] yielded widths of 5.3 and 3.3 cm^{-1} full width at half maximum (FWHM) for the low-J $^3\Pi_{0,1g}$ and $^3\Pi_{2g}$ levels, respectively (see Table V). Widths quoted[23] for rotationally unassigned resolved transitions to the $^{1,3}\Pi_{1g}$ and $^3\Pi_{0,2g}$ levels in the $5s\sigma_g(0,0)$ and (1,0) bands are 0.7 and 0.5 cm^{-1}, respectively.

As described in Sec. III C, the experimental $v=0$, $\Omega=1$ linewidths (Table V) have been used in the optimization of the $^{1,3}\Pi_{1g}$ Rydberg–valence interaction matrix elements for $n=4$ and 5 in our CSE model. Therefore, the good agreement between these particular experimental and calculated linewidths in Table V is unsurprising. However, the predissociation channels contributing to the $ns\sigma_g\,^3\Pi_g(v)$ linewidths for $n=4$ and 5 are of interest. The CSE calculations indicate that both the $^1\Pi_{1g}$ and $^3\Pi_{1g}$ valence states contribute to the predissociation of the $^3\Pi_{1g}$ Rydberg levels through their respective Rydberg–valence interactions and the Rydberg–Rydberg spin-orbit interaction. For $n=4$, most of the triplet predissociation for $v=0$ is predicted to occur via the *singlet* valence states, while the reverse is true for $v=1-4$. For $n=5$, the triplet predissociation for $v=0$ and 1 is predicted to be dominated by the singlet valence channel.

While the calculated $^3\Pi_{1g}$ and $^1\Pi_{1g}$ linewidths listed in Table V are in satisfactory agreement with the measurements for the $4s\sigma_g\,^3\Pi_g(v=0)$ and $5s\sigma_g\,^3\Pi_g(v=0$ and 1) levels, those for the $4s\sigma_g\,^3\Pi_{1g}(v=1-4)$ levels are significantly larger than the experimental linewidths.[23,39] The linewidths quoted by Yokelson *et al.*[23] are for resolved, but unassigned lines in REMPI spectra which are attributed to transitions to $4s\sigma_g\,^3\Pi_g(v=1-4)$ levels, with Ω unspecified, except for $v=4$, where $\Omega=0$. Those measured by Wang[39] and listed in Table V are for resolved, but unassigned lines in REMPI-PE spectra, attributed to the $\Omega=0,1$ subbands of the same transitions. Since neither author gives rotational assignments for the lines in question, such attributions remain questionable. However, the vibrational pattern of the Wang linewidths[39] is consistent with the calculated pattern, with a minimum width for $v=1$. Such a pattern is a signature of the *singlet* predissociation (see calculated linewidths in Table V) which, to a certain extent, is reflected in the triplet linewidths because of the Rydberg–Rydberg spin-orbit interaction. The factor-of-three discrepancy between the experimental and calculated widths cannot be explained by uncertainty in the rotational assignments coupled with J dependence of the linewidths, since, for the most part, the calculated linewidths in Table V show little J dependence. If the experimental linewidths have been correctly attributed to the $4s\sigma_g\,^3\Pi_g(v=1-4)$ levels, then explanation of the discrepancy probably lies with the neglect of $4s\sigma_g(v+1)-3d\lambda_g(v)$ homogeneous and heterogeneous interactions in the present CSE model. However, at this time there is insufficient experimental information available to justify their inclusion.

V. SUMMARY AND CONCLUSIONS

Experimental data on the energies and linewidths of the $(X\,^2\Pi_g)\,ns\sigma_g\,^{1,3}\Pi_g(v)$ Rydberg states of O_2 exhibit a number of irreconcilable discrepancies. However, following some reanalysis, these data are sufficient to advance our understanding of the spectroscopy, predissociation, and perturbation of the $^{1,3}\Pi_g$ Rydberg and valence states in the ~6.5–9.5 eV region.

The results of a critical reexamination of the existing experimental data base on the $ns\sigma_g\,^{1,3}\Pi_g$ states have been employed to optimize the parameters of a CSE model of the $^{1,3}\Pi_g$ Rydberg and valence states and their interactions. Within the experimental uncertainties, the resulting CSE model has been found to give a good description of the experimental energies and linewidths (see Tables I–III, and V). The model optimization process also produces relevant potential-energy curves (see Fig. 2) and values for Rydberg–valence, Rydberg–Rydberg, and valence–valence interactions (see Table VI).

In addition, a number of previously unassigned spectral features have been associated with specific perturbations of the $3s\sigma_g d\,^1\Pi_g$ Rydberg-state levels by the $II\,^1\Pi_g$ valence-state levels, an anomalous J sensitivity in predissociation branching ratios for the $d(v=1)$ level has been identified (see Table VII), and the influence of $ns\sigma_g \sim (n-1)d\sigma_g$ Rydberg–Rydberg interactions on the electronic structure and predissociation of the $ns\sigma_g$ states for $n \geq 4$ discussed. Finally, we note that the precision of these characterizations has been limited by the quality of the existing experimental data, suggesting the need for further, less-uncertain measurements.

ACKNOWLEDGMENTS

The authors wish to thank Dr. R. R. Ogorzalek-Loo, Dr. R. J. Yokelson, Dr. S. T. Pratt, Dr. W. L. Glab, and Dr. R. D.

Johnson III for discussing and attempting to find original spectral line lists, Dr. R. J. Yokelson for providing Ref. 21 prior to publication, Professor H. Lefebvre-Brion for providing her unpublished calculations of the $3d-4s$ interaction, and Dr. W. J. van der Zande, Dr. T. G. Slanger, Dr. P. C. Cosby, Dr. R. A. Copeland, and Professor W. A. Chupka for helpful discussions. They also thank Dr. D. S. Ginter for her critical reading of the manuscript. J. S. Morrill would like to thank the Naval Research Laboratory for an Edison Memorial Graduate Fellowship which enabled him to pursue Ph.D. research at the University of Maryland. This work was supported in part by the National Science Foundation (US) (Grant Nos. INT 9512886 and PHY 9514413) and the Department of Industry, Science and Technology (Australia) (Grant No. 95/8769).

[1] P. H. Krupenie, J. Phys. Chem. Ref. Data **1**, 423 (1972).
[2] M. L. Ginter and R. Battino, J. Chem. Phys. **42**, 3222 (1965), and references therein.
[3] H. Partridge, C. W. Bauschlicher, Jr., S. R. Langhoff, and P. R. Taylor, J. Chem. Phys. **95**, 8292 (1991).
[4] H. Partridge (personal communications, 1995–1997).
[5] The fully occupied orbitals $(1\sigma_g)^2(1\sigma_u)^2(2\sigma_g)^2(2\sigma_u)^2$, common to all of the listed MO configurations, are suppressed in the notation used here.
[6] A. S.-C. Cheung, K. Yoshino, J. R. Esmond, and W. H. Parkinson, J. Mol. Spectrosc. **178**, 66 (1996).
[7] T. G. Slanger, D. L. Huestis, P. C. Cosby, H. Naus, and G. Meijer, J. Chem. Phys. **105**, 9393 (1996).
[8] D. L. Huestis, R. A. Copeland, K. Knutsen, T. G. Slanger, R. T. Jongma, M. G. H. Boogaarts, and G. Meijer, Can. J. Phys. **72**, 1109 (1994).
[9] R. R. Laher and F. R. Gilmore, J. Phys. Chem. Ref. Data **20**, 685 (1991).
[10] T. G. Slanger and P. C. Cosby, J. Phys. Chem. **92**, 267 (1988).
[11] R. P. Saxon and B. Liu, J. Phys. Chem. **67**, 5432 (1977).
[12] K. P. Huber and G. Herzberg, *Molecular Spectra and Molecular Structure: IV. Constants of Diatomic Molecules* (Van Nostrand Reinhold, New York, 1979), pp. 490–503.
[13] The E_v are effective origins, defined with respect to the zero-energy reference E_0 described in Sec. II A, and obtained using the $O_2^+[X\,^2\Pi_g(F_1, v=0, J=1/2)] \leftarrow O_2[X\,^3\Sigma_g^-(F_2, v=0, J=1)]$ ionization potential of R. G. Tonkyn, J. W. Winniczek, and M. G. White, Chem. Phys. Lett. **164**, 137 (1989), and the $O_2^+[X\,^2\Pi_g(v=0)]$ spin-orbit and rotational constants of E. A. Colbourn and A. E. Douglas, J. Mol. Spectrosc. **65**, 332 (1977).
[14] Y. Li, I. D. Petsalakis, H.-P. Liebermann, G. Hirsch, and R. J. Buenker, J. Chem. Phys. **106**, 1123 (1997).
[15] B. R. Lewis, S. S. Banerjee, and S. T. Gibson, J. Chem. Phys. **102**, 6631 (1995).
[16] J. P. England, B. R. Lewis, S. T. Gibson, and M. L. Ginter, J. Chem. Phys. **104**, 2765 (1996).
[17] T. A. York and J. Comer, J. Phys. B **16**, 3627 (1983).
[18] S. Trajmar, D. C. Cartwright, and R. I. Hall, J. Chem. Phys. **65**, 5275 (1976).
[19] D. C. Cartwright, W. J. Hunt, W. Williams, S. Trajmar, and W. A. Goddard III, Phys. Rev. A **8**, 2436 (1973).
[20] W. L. Glab, P. M. Dehmer, and J. L. Dehmer, J. Chem. Phys. **104**, 4937 (1996).
[21] R. J. Yokelson, Y. Wang, C. A. Woodward, and W. A. Chupka (unpublished).
[22] R. J. Yokelson, R. J. Lipert, and W. A. Chupka, J. Chem. Phys. **97**, 6144 (1992).
[23] R. J. Yokelson, R. J. Lipert, and W. A. Chupka, J. Chem. Phys. **97**, 6153 (1992).
[24] A. Sur, L. Nguyen, and N. Nikoi, J. Chem. Phys. **96**, 6791 (1992).
[25] A. Sur, R. S. Friedman, and P. J. Miller, J. Chem. Phys. **94**, 1705 (1991).
[26] H. Park, L. Li, and W. A. Chupka, J. Chem. Phys. **92**, 61 (1990).
[27] H. Park, L. Li, W. A. Chupka, and H. Lefebvre-Brion, J. Chem. Phys. **92**, 5835 (1990).
[28] S. T. Pratt, J. L. Dehmer, and P. M. Dehmer, J. Chem. Phys. **93**, 3072 (1990).
[29] H. Park, L. Li, and W. A. Chupka, Chem. Phys. Lett. **162**, 317 (1989).
[30] R. Ogorzalek-Loo, W. J. Marinelli, P. L. Huston, S. Arepalli, J. R. Wiesenfeld, and R. W. Field, J. Chem. Phys. **91**, 5185 (1989).
[31] R. R. Ogorzalek-Loo, Ph.D. thesis, Cornell University, 1989.
[32] H. Park, P. J. Miller, W. A. Chupka, and S. D. Colson, J. Chem. Phys. **89**, 6676 (1988).
[33] R. D. Johnson III, G. R. Long, and J. W. Hudgens, J. Chem. Phys. **87**, 1977 (1987).
[34] S. Katsumata, K. Sato, Y. Achiba, and K. Kimura, J. Electron Spectrosc. Relat. Phenom. **41**, 325 (1986).
[35] A. Sur, C. V. Ramana, W. A. Chupka, and S. D. Colson, J. Chem. Phys. **84**, 69 (1986).
[36] A. Sur, C. V. Ramana, and S. D. Colson, J. Chem. Phys. **83**, 904 (1985).
[37] H. Park, Ph.D. thesis, Yale University, 1990.
[38] R. J. Yokelson, Ph.D. thesis, Yale University, 1991.
[39] Y. Wang, Ph.D. thesis, Yale University, 1992.
[40] J. H. Tjossem and K. C. Smyth, Chem. Phys. Lett. **144**, 51 (1988).
[41] W. J. van der Zande, W. Koot, and J. Los, J. Chem. Phys. **91**, 4597 (1989).
[42] W. J. van der Zande, W. Koot, J. Los, and J. R. Peterson, J. Chem. Phys. **89**, 6758 (1988).
[43] W. J. van der Zande, W. Koot, J. Los, and J. R. Peterson, Chem. Phys. Lett. **140**, 175 (1987).
[44] E. Sominska, V. Kelner, and A. Gedanken, Chem. Phys. Lett. **213**, 117 (1993).
[45] The SPA spectra (Ref. 44) are for supersonically-expanded, cooled O_2, the nominally forbidden $g \leftarrow g$ transitions becoming visible through collision- or cluster-induced effects.
[46] S. Chung, C. C. Lin, and E. T. P. Lee, J. Phys. B **21**, 1155 (1988).
[47] R. Klotz and S. D. Peyerimhoff, Mol. Phys. **57**, 573 (1986).
[48] R. P. Saxon and B. Liu, J. Chem. Phys. **73**, 876 (1980).
[49] R. P. Saxon and B. Liu, J. Chem. Phys. **73**, 870 (1980).
[50] R. J. Buenker and S. D. Peyerimhoff, Chem. Phys. **8**, 324 (1975).
[51] R. J. Buenker and S. D. Peyerimhoff, Chem. Phys. Lett. **34**, 225 (1975).
[52] R. S. Friedman, M. L. Du, and A. Dalgarno, J. Chem. Phys. **93**, 2375 (1990).
[53] R. S. Friedman and A. Dalgarno, J. Chem. Phys. **93**, 2370 (1990).
[54] R. S. Friedman and A. Dalgarno, J. Chem. Phys. **90**, 7606 (1989).
[55] Here, the term "rotational perturbation" is used in its historical sense to indicate perturbation of the rotational structure of a band, rather than a perturbation caused by a rotation-dependent interaction.
[56] B. R. Lewis, S. T. Gibson, J. S. Morrill, and M. L. Ginter, J. Chem. Phys. **11**, 186 (1999).
[57] G. Herzberg, *Molecular Spectra and Molecular Structure: I. Spectra of Diatomic Molecules* (Van Nostrand, Princeton, 1950), pp. 130–139.
[58] Two types of energy expressions have been employed in the analysis of rotationally resolved data: (1) $E(v,J)=\nu_0+B_eJ(J+1)-D_v[J(J+1)]^2$, or (2) $E(v,J)=\nu_0+\gamma_vJ+B_vJ(J+1)$.
[59] Level energies from the KER data of Refs. 42 and 43 were corrected using newer D_0 values from P. C. Cosby and D. L. Huestis, J. Chem. Phys. **97**, 6108 (1992).
[60] J. S. Morrill, M. L. Ginter, B. R. Lewis, and S. T. Gibson (unpublished).
[61] In this work, the term "simulation" indicates a process whereby a parametric model is fitted to an experimental spectrum in order to obtain single-line spectroscopic information (e.g., line positions, widths, and strengths).
[62] E. F. van Dishoeck, M. C. van Hemert, A. C. Allison, and A. Dalgarno, J. Chem. Phys. **81**, 5709 (1984).
[63] L. Torop, D. G. McCoy, A. J. Blake, J. Wang, and T. Scholz, J. Quant. Spectrosc. Radiat. Transfer **38**, 9 (1987).
[64] J. Wang, D. G. McCoy, A. J. Blake, and L. Torop, J. Quant. Spectrosc. Radiat. Transfer **38**, 19 (1987).
[65] J. Wang, D. G. McCoy, A. J. Blake, and L. Torop, J. Quant. Spectrosc. Radiat. Transfer **40**, 501 (1988).
[66] The magnitude of the expected intensity borrowing was derived from the observed perturbation of the $C\,^3\Pi_{1g}$ level, due to the $C\,^3\Pi_{1g}-d\,^1\Pi_{1g}$ interaction, using standard two-level perturbation expressions (Ref. 69) and a coupling matrix element estimated from the $^3\Pi_{2g}-^3\Pi_{0g}$ splitting.
[67] The calculated spectra take into account competition between predissociation and ionization. The "ionization width" was taken to be $\Gamma^i=0.75$ cm^{-1}, as in Ref. 56, and convolution with an instrumental function of 3 cm^{-1} FWHM has been performed. Since the CSE model includes only $\Omega=1$ states, the calculated intensities of the $C\,^3\Pi_{1g}\leftarrow\leftarrow X$ peaks have been increased by a factor of 3 in an attempt to allow meaningful com-

parison between the calculated and observed singlet:triplet intensity ratios. However, the triplet structure of the C state is not otherwise included in the calculated spectra.

[68] Because of uncertainties regarding relative laser intensities for the different experimental scans in the composite spectra of Fig. 3, meaningful relative vibrational intensities cannot be obtained. However, the $d,C \leftarrow\leftarrow X(0,0)$, (1,0), and (3,0) pairs of bands in Fig. 3 [(c), lower panel] occur close together in single experimental scans and should yield more meaningful relative intensities.

[69] H. Lefebvre-Brion and R. W. Field, *Perturbations in the Spectra of Diatomic Molecules* (Academic, Orlando, 1986), pp. 92–93, 211, 247–248.

[70] H. Lefebvre-Brion (personal communication, 1998).

[71] Only the lower-energy members of the pairs of heavily mixed $ns\sigma_g$ and $(n-1)d\sigma_g$ states with $n \geq 4$ have been observed experimentally. In this work, we have followed Refs. 21, 23, and 39 in labeling these states as $ns\sigma_g$. In contrast, the theoretical studies, Refs. 19 and 46, label them as $(n-1)d\sigma_g$ and $nd\sigma_g$, respectively.

4.39 Perturbations in the $3s\sigma_g\,{}^{1,3}\Pi_g$ Rydberg states of O_2: bound-bound interactions with the second ${}^1\Pi_g$ and ${}^1\Delta_g$ valence states

[59] B. R. Lewis, S. T. Gibson, J. S. Morrill, and M. L. Ginter,
Journal of Chemical Physics **111**, 186–197 (1999).

Perturbations in the $3s\sigma_g\,{}^{1,3}\Pi_g$ Rydberg states of O_2: Bound–bound interactions with the second $^1\Pi_g$ and $^1\Delta_g$ valence states

B. R. Lewis and S. T. Gibson
Research School of Physical Sciences and Engineering, The Australian National University, Canberra, ACT 0200, Australia

J. S. Morrill[a)]
E. O. Hulburt Center for Space Research, Naval Research Laboratory, Washington, DC 20375–5352

M. L. Ginter
Institute for Physical Science and Technology, University of Maryland, College Park, Maryland 20742–2431

(Received 21 December 1998; accepted 6 April 1999)

Existing experimental (2+1) REMPI spectra for transitions into rotationally resolved levels of the $3s\sigma_g\,d\,^1\Pi_g$ and $3s\sigma_g\,C\,^3\Pi_g$ Rydberg states of O_2 have been rotationally analyzed, resulting in the first characterization of rotational perturbations in $d(v=1-3)$ and $C(v=2)$. In addition, the results of this analysis have been interpreted with the aid of a coupled-channel Schrödinger-equation (CSE) model of the interacting electronic states. The identification and characterization of perturbations in the d and C states have allowed the nature of the interactions between the $3s\sigma_g\,{}^{1,3}\Pi_g$ Rydberg states and the $II\,^1\Pi_g$ valence state to be clarified and a realistic empirical potential-energy curve for the $II\,^1\Pi_g$ state to be determined. While it is found that first- and second-order interactions with the $II\,^1\Pi_g$ valence state are responsible for the strongest perturbations observed in $d(v=1-3)$ and $C(v=2)$, additional weak perturbations found in $d(v=2$ and $3)$ are shown to result from a second-order interaction with the $II\,^1\Delta_g$ valence state. These weak perturbations, including an extra level observed for $d(v=3,\ J=17)$, appear to be the first experimental evidence for the $II\,^1\Delta_g$ state, long predicted theoretically. Finally, detailed comparisons between experimental spectra and $d\,^1\Pi_g\leftarrow\leftarrow a\,^1\Delta_g(1,0)$, (2,0) and (3,0) (2+1) REMPI spectra calculated using the CSE model are presented which support and illustrate these conclusions. © *1999 American Institute of Physics.* [S0021-9606(99)01025-9]

I. INTRODUCTION

Since the time of the last comprehensive review of the electronic structure of O_2 by Krupenie,[1] there have been many theoretical and experimental studies on the *gerade* states lying between the lowest dissociation limit (5.21 eV)[2] and the ground state of O_2^+ ($T_e=12.05$ eV). In particular, resonance-enhanced multiphoton-ionization (REMPI) spectroscopy has led to a number of interesting experimental studies on the $3s\sigma_g\,{}^{1,3}\Pi_g$ Rydberg states of O_2 ($T_e\approx 8.2$ eV).[3–10] As pointed out in a companion paper,[11] transition energies and linewidths resulting from these experimental studies were subject to significant uncertainties, limiting the accuracy of models developed to describe the spectroscopy and predissociation of the $3s\sigma_g\,{}^{1,3}\Pi_g$ states.

There have been relatively few rotational analyses of REMPI spectra involving excitation into the $3s\sigma_g\,d\,^1\Pi_g$ and $3s\sigma_g\,C\,^3\Pi_g$ states,[4,7,9,10] and those analyses have been limited to low rotational levels, either through the measurement of low-temperature spectra or the inability of previous workers to assign the spectral lines through regions of significant perturbation. In addition, features first reported by Johnson *et al.*[7] in (2+1) REMPI excitation spectra from the metastable $a\,^1\Delta_g$ state, and evident in several unpublished spectra,[6] have remained unassigned until now.

Rydberg–valence interactions play significant roles in the spectroscopy and predissociation of the d and C states and many theoretical studies have investigated these interactions using *ab initio*,[12–17] perturbative[3,18,19] and coupled-channel Schrödinger-equation (CSE)[4,20,21] techniques. The $II\,^1\Pi_g$ valence state[22] is bound in the energy region of the lower vibrational levels of the $3s\sigma_g\,{}^{1,3}\Pi_g$ states and is generally considered responsible for perturbing the d-state vibrational and rotational structure.[11] However, only a single $II\,^1\Pi_g$ valence level has been reported previously[4] and there have been no determinations of the interaction between the $I\,^1\Pi_g$ and $II\,^1\Pi_g$ valence states, other than estimates available from *ab initio* potential-energy curve calculations.

The unpublished thesis of Ogorzalek-Loo[6] contains a wealth of unanalyzed, well-resolved, room-temperature REMPI spectra which exhibit rich rotational structure. Analyses of these spectra in this work have enabled considerable progress to be made in remedying the deficiencies mentioned above. Presented below are the results of extensive rotational analyses of $d\,^1\Pi_g\leftarrow\leftarrow a\,^1\Delta_g$, $d\,^1\Pi_g\leftarrow\leftarrow X\,^3\Sigma_g^-$, and $C\,^3\Pi_g\leftarrow\leftarrow X\,^3\Sigma_g^-$ (2+1) REMPI spectra recorded by Ogorzalek-Loo[6] and by Sur *et al.*[4,9] These analy-

[a)]Work done at Department of Chemistry, University of Maryland, College Park, MD 20742.

ses have led to the identification and characterization of rotational perturbations in the d- and C-state levels.[23] In addition, CSE calculations of the d-state term values and $d \leftarrow\leftarrow a$ $(2+1)$ REMPI cross sections have been used to provide insight into the character of the Rydberg–valence and valence–valence interactions, the level structures of the $d\,^1\Pi_g$ and $II\,^1\Pi_g$ states, and the potential-energy curve of the $II\,^1\Pi_g$ valence state.

II. METHOD OF CALCULATION

A. The CSE method

The principal molecular-orbital (MO) configurations of the $\ldots(3\sigma_g)^2(1\pi_u)^4(1\pi_g)\,ns\sigma_g\,{}^{1,3}\Pi_g$ Rydberg and $\ldots(3\sigma_g)(1\pi_u)^4(1\pi_g)^3\,II\,{}^{1,3}\Pi_g$ valence states of O_2 differ by two orbitals, leading to significant Rydberg–valence interactions.[24] In addition, the principal MO configurations of the $II\,{}^{1,3}\Pi_g$ and $\ldots(3\sigma_g)^2(1\pi_u)^3(1\pi_g)^2(3\sigma_u)\,I\,{}^{1,3}\Pi_g$ states also differ by two orbitals, leading to significant valence–valence interactions. The corresponding breakdown of the Born–Oppenheimer (BO) approximation may be addressed by using the CSE technique,[25–27] in which interactions between BO basis states are included explicitly. The *diabatic* CSE basis is utilized in this work because of the attractive property that the associated wave functions, potential-energy curves, and coupling matrix elements can be expected to change smoothly with internuclear separation R.

Details of the CSE formulation employed can be found in Ref. 28. Briefly, the cross section for single-photon absorption[29] from a given rovibrational level of an initial uncoupled singlet electronic state into the n coupled states k, at an energy E, and with rotation J is given by

$$\sigma^{a}_{EJ;v''J''} \propto \nu |\langle \chi_{EJ}(R)|\mathbf{M}|\chi_{v''J''}(R)\rangle|^2. \tag{1}$$

In Eq. (1), ν is the transition energy, $\chi_{EJ}(R)$ is the coupled-channel radial wave-function matrix, and $\chi_{v''J''}(R)$ is the radial wave function of the initial state. In addition, the elements of the $n\times 1$ rotronic transition-moment vector $\mathbf{M}$ are the products of appropriately normalized electronic transition moments $\mathcal{M}_k(R)$ and rotational matrix elements of the direction-cosine operator. The coupled-channel radial wave-function matrix $\chi_{EJ}(R)$ is the solution of the diabatic-basis coupled Schrödinger equations, expressed in matrix form,

$$\left\{\mathbf{I}\frac{d^2}{dR^2} + \frac{2\mu}{\hbar^2}[E\mathbf{I} - \mathbf{V}(R) - \mathbf{V}^{\mathrm{rot}}(R)]\right\}\chi_{EJ}(R) = 0. \tag{2}$$

In Eq. (2), μ is the molecular reduced mass, $\mathbf{I}$ is the identity matrix, $\mathbf{V}(R)$ is the symmetric $n\times n$ diabatic potential matrix, the diagonal elements of which are the diabatic electronic potential-energy curves $V_k(R)$, and $\mathbf{V}^{\mathrm{rot}}(R)$ is a diagonal matrix with elements given by matrix elements of the rotational part of the molecular Hamiltonian. The couplings between the interacting electronic states are given by the off-diagonal elements of $\mathbf{V}(R)$, which contain the effects of electrostatic, rotational and spin-orbit interactions.

If the electronic wave functions are expressed in the Hund's case (a) e/f parity basis,[24] then the only nonzero elements $\mathcal{M}_k(R)$ arise from dipole-allowed transitions between case (a) basis states. For a specific temperature, the total cross section can be expressed as the sum of cross sections into the upper-state e and f levels, each of which is calculated separately as a Boltzmann average of Eq. (1) over the initial distribution of v'' and J''. As will be shown in Sec. II C, the CSE formulation summarized above may be readily adapted to a calculation of the $(2+1)$ REMPI spectra of coupled states.

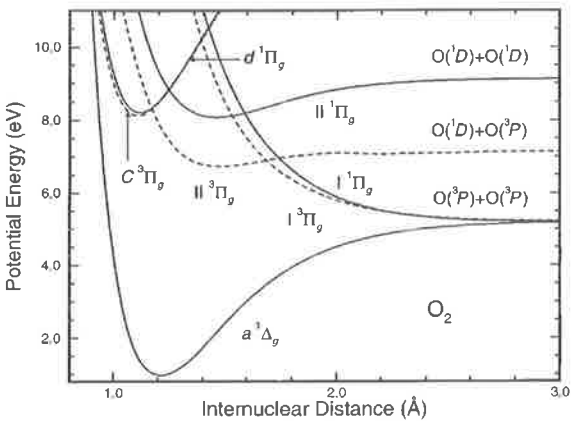

FIG. 1. Model singlet (solid lines) and triplet (dashed lines) potential-energy curves for O_2 used in CSE calculations of the $d\,^1\Pi_g \leftarrow\leftarrow a\,^1\Delta_g$ $(2+1)$ REMPI spectra. The energy scale is referred to the minimum in the ground-state $X\,^3\Sigma_g^-$ potential-energy curve (not shown). The valence–valence and Rydberg–valence-coupled states of $^1\Pi_g$ and $^3\Pi_g$ symmetry are shown in a diabatic representation which allows crossings between potential-energy curves of the same symmetry.

B. The CSE model implementation

The potential-energy curves and couplings, employed here and described below, were optimized in a least-squares fitting procedure. This procedure utilized a selection of the experimental $3s\sigma_g\,{}^{1,3}\Pi_g$ vibronic term values, rotational constants and predissociation linewidths summarized in Ref. 11, as well as rotational term values and intensity information taken from the analyses presented in Sec. III. Of primary concern are homogeneous interactions involving the $^1\Pi_{1g}$ states, so only $\Omega = 1$ states have been included in the model. The six-state coupled-channel model employed includes the $3s\sigma_g\,{}^1\Pi_{1g}$ and $3s\sigma_g\,{}^3\Pi_{1g}$ Rydberg states and the lowest two valence states of $^1\Pi_{1g}$ and $^3\Pi_{1g}$ symmetry. Our model diabatic potential-energy curves $V_k(R)$ for these states are shown in Fig. 1. In the fitting procedure, potential-energy curves for the valence states were obtained by smoothly adjusting the *ab initio* potentials of Partridge,[30] while those for the Rydberg states were obtained by adjusting initial curves with shapes similar to that for the ionic ground state $X\,^2\Pi_g$ to which the $ns\sigma_g$ series converges.[31]

The $^{1,3}\Pi_{1g}$-state manifold undergoes Rydberg–Rydberg, Rydberg–valence, and valence–valence interactions which are the principal mechanisms responsible for the perturbation and predissociation of these states. The nonzero off-diagonal elements of the potential matrix used here are the electro-

static Rydberg–valence interactions for the singlet and triplet states (630 and 620 cm^{-1}, respectively), the singlet and triplet valence–valence interactions (500 cm^{-1} for each multiplicity), and the spin-orbit singlet-triplet Rydberg–Rydberg interaction (95 cm^{-1}). The Rydberg–valence interactions are fairly well defined by the observed energy-level perturbations and predissociation patterns of the Rydberg states. The value adopted for the Rydberg–Rydberg interaction is similar to those used in CSE models of the O_2 *ungerade* states,[28] and is approximately half the spin-orbit splitting in the ionic ground state. The valence–valence interactions have only a second-order effect on the perturbation and predissociation of the Rydberg states, but they have a major effect on the dissociation branching ratios. The model value for the $^3\Pi_g$ valence–valence interaction is similar to the value determined by van der Zande *et al.*[18] from a translational spectroscopic study of the $^3\Pi_g$ branching ratios.

The semiempirical CSE model of the coupled $^{1,3}\Pi_{1g}$-state manifold employed here provides an accurate description of the chosen experimental data base, albeit within the significant measurement uncertainties. For example, the experimental and calculated $d\,^1\Pi_g$ rovibrational energies, which are of principal interest in this work, generally agree to within ± 5 cm^{-1}.

C. REMPI cross sections

The (2+1) REMPI process may be regarded as occurring in two steps: preparation of the excited state by two-photon absorption, followed by single-photon ionization.[32] Under experimental conditions of weak excitation and saturated ionization, and in the absence of competing processes depopulating the excited state, rotational structure in the REMPI spectrum should reflect that in the two-photon absorption spectrum.[33] The present theoretical treatment of the $d\,^1\Pi_g \leftarrow\leftarrow a\,^1\Delta_g$ (2+1) REMPI spectrum involves a CSE calculation of the cross section for two-photon absorption into the coupled $^{1,3}\Pi_{1g}$ states, together with a treatment of the single-photon ionization step which allows for competition between predissociation and photoionization of the excited-state manifold.

In the photoionization process, only the ground state of O_2^+ is accessible at the three-photon level using the laser wavelengths required to excite the $d \leftarrow\leftarrow a$ system. It is expected that the photoionization probability will be dominated by the contribution from the $3s\sigma_g d\,^1\Pi_g$ Rydberg state which undergoes a transition to the ionic ground state merely by the removal of the Rydberg electron, whereas ionization of the valence state is a two-electron process. Although two-photon transitions from the metastable $\ldots(3\sigma_g)^2(1\pi_u)^4(1\pi_g)^2\,a\,^1\Delta_g$ state are allowed into both the Rydberg and valence states of $^1\Pi_g$ symmetry, the low probability of ionization for the valence state makes it difficult to determine the relative magnitudes of the Rydberg and valence two-photon transition moments from a comparison between experimental and calculated REMPI spectra. However, the general absence of predominantly valence levels in recorded spectra and the relative intensities of the Rydberg and valence features in the low-temperature $d \leftarrow\leftarrow X(2,0)$ spectrum of Sur *et al.*[4] suggest that the valence transition moment is significantly smaller than the Rydberg moment.[34,35] Therefore, in calculations of the two-photon cross section, only the diabatic-basis electronic transition moment $\mathcal{M}_k$ associated with the $d \leftarrow\leftarrow a$ transition was assumed to be nonzero. This electronic transition moment was taken to have a value of unity and to be independent of R. The square of the corresponding element of the transition-moment vector $\mathbf{M}$ was then determined by the $\Delta\Omega = -1$ two-photon, rotational-line-strength expressions given by Bray and Hochstrasser.[36]

The CSE cross-section calculations were performed using the diabatic potential-energy curves and couplings described in Sec. II B. First, the diabatic coupled-channel wave-function matrix $\chi_{EJ}(R)$, normalized according to the method of Mies,[25] was calculated by solving Eq. (2) using the renormalized Numerov method of Johnson.[37] Second, these $\chi_{EJ}(R)$ wave functions, along with initial-state vibrational wave functions $\chi_{0J''}(R)$ calculated using a Rydberg–Klein–Rees (RKR) potential-energy curve for the $a\,^1\Delta_g$ state,[38] and the rotronic transition moments described above, were used in Eq. (1) to calculate individual rotational-branch cross sections $\sigma^{a}_{EJ;0J''}$.

In general, each two-photon rotational-branch cross section consists of at least two resonances, the strongest arising from transitions into $^1\Pi_g$ levels which are predominantly Rydberg in character, and the other(s) from valence transitions which borrow their strength from the Rydberg transitions. Because of the differing predissociation rates of the Rydberg and valence resonances and the J dependence of the predissociation, competition between predissociation and ionization must be taken into account in order to reproduce correctly the relative line strengths in the (2+1) REMPI band spectrum. In practice, this was accomplished by separately converting the two-photon cross sections calculated in the regions of individual resonances into corresponding (2+1) REMPI cross sections using the relation

$$\sigma^{i}_{EJ;0J''} = \phi^{i}_{J}\sigma^{a}_{EJ;0J''}, \tag{3}$$

where ϕ^{i}_{J} is the (resonance-dependent) ionization quantum yield, given by

$$\phi^{i}_{J} = \frac{k^{i}}{k^{i}+k^{d}_{J}} = \frac{\Gamma^{i}}{\Gamma^{i}+\Gamma^{d}_{J}}. \tag{4}$$

In Eq. (4), k^{i} and k^{d}_{J} are the ionization and predissociation rates, respectively, Γ^{i} and Γ^{d}_{J} the corresponding linewidths, and de-excitation by fluorescence has been neglected.

While Γ^{d}_{J} in Eq. (4) is given by the calculated predissociation linewidth, Γ^{i} is difficult to estimate and is taken as an adjustable parameter optimized, where appropriate, by comparison between the measured and calculated REMPI spectra.[39] Thus, in practice, the optimized values of Γ^{i} will include the effects of any other decay processes not specified in the CSE model. Finally, the total room-temperature (2+1) REMPI cross section was calculated by summing the individual rotational-branch e- and f-level REMPI cross sections, while performing an appropriate Boltzmann average over the initial-state distribution of v'' and J''.

III. RESULTS

In this section, experimentally based rotational term values for levels of the d state are presented, determined primarily through analysis of the $d \leftarrow\leftarrow a$ and $d \leftarrow\leftarrow X$ $(2+1)$ REMPI spectral figures originating in the thesis of Ogorzalek-Loo.[6] In addition, for the $d \leftarrow\leftarrow a$ transition, comparisons are made between experimental $(2+1)$ REMPI spectra[6] and spectra calculated using the CSE method described in Sec. II. It should be noted that the calibration history of the lasers used to obtain the Ogorzalek-Loo spectra[6] is unclear, leading to the possibility of significant term-energy uncertainties, especially in the *absolute* values of the terms.[11] Such uncertainties are not important here because this work is principally concerned with the explanation of REMPI band profiles and the identification of rotational perturbations, activities more dependent on the relative uncertainties of rotational terms within a given vibrational level.

While there are no obvious energy perturbations in the rotational structure of the $d(v=0$ and $4)$ levels, the $d(v=1-3)$ levels are significantly perturbed and are of major importance in establishing the nature of the $^1\Pi_g$ Rydberg–valence interaction. These levels are discussed in detail in the following subsections. In addition, new rotational analysis of the $C(v=2)$ level is reported in Sec. III E.

A. $d\,^1\Pi_g(v=0$ and $4)$

The $d \leftarrow\leftarrow a(0,0)$ $(2+2)$ REMPI spectrum presented by Ogorzalek-Loo[5,6] is not sufficiently well developed for rotational analysis. However, her $d \leftarrow\leftarrow X(0,0)$ $(2+1)$ REMPI spectrum displays sharp [apparent linewidths ≈ 2 cm^{-1} full-width at half-maximum (FWHM)], unperturbed rotational structure for $J \lesssim 30$ which yields, on analysis,[40] $\nu_0 = 66\,358$ cm^{-1}, $B = 1.682$ cm^{-1}, and $D = 7.7 \times 10^{-6}$ cm^{-1} for the $d(v=0)$ spectroscopic constants. The B value is similar to that for the O_2^+ $X\,^2\Pi_g(v=0)$ level (1.68),[41] as expected for an unperturbed Rydberg state built on this ionic core. Ogorzalek-Loo[6] also presents a partial spectrum for the $d \leftarrow\leftarrow a(4,0)$ band, consisting mainly of overlapping unperturbed S- and R-branch lines (apparent widths for narrowest features ≈ 6 cm^{-1} FWHM) with $J \gtrsim 17$. Tentative (extrapolated) spectroscopic constants deduced from this spectrum are $\nu_0 = 73\,743$ cm^{-1} and $B = 1.59$ cm^{-1}, assuming that $D = 0$. While the B value is in good agreement with the value of van der Zande *et al.*,[19] this agreement may be fortuitous considering the uncertainty in the rotational assignments of the partial spectrum.

B. $d\,^1\Pi_g(v=1)$

Rotational term values for $d(v=1)$ are shown in Fig. 2(a). The plotted values represent the averages of values determined from the $d \leftarrow\leftarrow a(1,0)$ spectrum,[6] lowered by 0.8 cm^{-1},[42] and values determined from the $d \leftarrow\leftarrow X(1,0)$ spectrum.[6] *Reduced* term values, obtained by subtracting $68\,227 + 1.66J(J+1)$ cm^{-1} from the term values, are shown in Fig. 2(b). Figure 2(b) emphasizes a rotational perturbation culminating at $J \approx 12$, with an effective interaction matrix element $H_{12} \approx 12$ cm^{-1},[43] which has not been reported previously. The rotational constant $B = 1.58$ cm^{-1} reported for $d(v=1)$ by Sur *et al.*[4] was derived from rotational levels assigned for $J \leqslant 12$ which are below the culmination of this perturbation. We find $\nu_0 = 68\,226$ cm^{-1} and $B = 1.63$ cm^{-1} for $J \leqslant 10$. However, it is evident from Fig. 2(b) that, overall, the reduced term values cluster around zero, indicating that the "deperturbed" $B \approx 1.66$ cm^{-1}, the value for O_2^+ $X\,^2\Pi_g(v=1)$.[41]

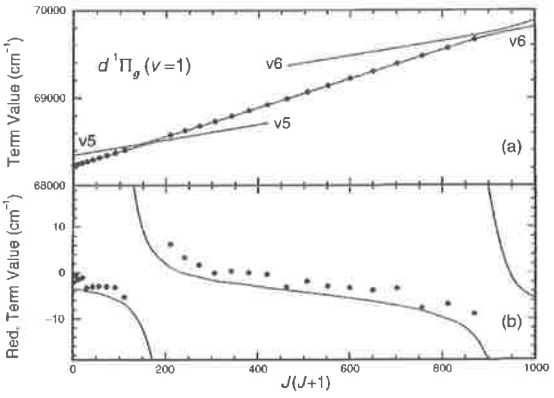

FIG. 2. (a) Comparison between term values for $d\,^1\Pi_g(v=1)$ (solid circles) derived in this work from analysis of the $d\,^1\Pi_g \leftarrow\leftarrow a\,^1\Delta_g$ and $d\,^1\Pi_g \leftarrow\leftarrow X\,^3\Sigma_g^-$ $(2+1)$ REMPI spectra of Ogorzalek-Loo (Ref. 6), and those calculated using the optimized CSE model (lines). The CSE calculations indicate that the $d(v=1)$ rotational terms are crossed by the $v=5$ and $v=6$ rotational terms of the $II\,^1\Pi_g$ valence state, labeled v5 and v6, respectively. (b) Plot of *reduced* term values, obtained by subtracting $68\,227 + 1.66J(J+1)$ cm^{-1} from the absolute term values of (a), which emphasize the rotational perturbation culminating at $J \approx 12$.

The calculated term values, shown in Fig. 2 as solid lines, are seen to be in good agreement with the measurements. These CSE calculations indicate that the $d(v=1)$ rotational terms are crossed by the $v=5$ and $v=6$ rotational terms of the $II\,^1\Pi_g$ valence state, the former causing the rotational perturbation at $J \approx 12$ and the latter leading to a second perturbation near $J \approx 30$, which lies just beyond the range of the measurements.[44]

The room-temperature $(2+1)$ REMPI spectrum recorded for the $d \leftarrow\leftarrow a(1,0)$ band by Ogorzalek-Loo[6] is shown in Fig. 3(a). The strongly blue-degraded rotational structure of this band (apparent linewidths ≈ 4 cm^{-1} FWHM) is anomalously weak in the 331 nm region, indicated by the arrow in Fig. 3(a). This structural minimum led Johnson *et al.*[7] to list two bands in this region, denoted A and B as indicated in Fig. 3(a). Johnson *et al.*[7] assigned band A to the $d \leftarrow\leftarrow a(1,0)$ transition and band B to a transition from the a state into a previously uncatalogued state.

The calculated CSE room-temperature $d \leftarrow\leftarrow a(1,0)$ $(2+1)$ REMPI spectrum in Fig. 3(b) is in reasonable agreement with the measured spectrum. The calculations were performed with $\Gamma^i = 0.75$ cm^{-1} FWHM and a Gaussian instrumental function of 3 cm^{-1} FWHM.[45] In agreement with experiment, the calculated spectrum displays a structural minimum near 331 nm, arising from the effects of the rotational perturbation near $J = 12$ discussed above. The band-intensity structure in this region arises not only from energy

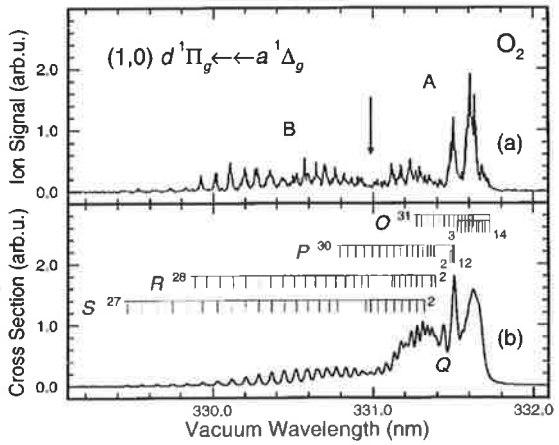

FIG. 3. (a) Room-temperature (2+1) REMPI spectrum measured for the (1,0) band of the $d\,^1\Pi_g \leftarrow\leftarrow a\,^1\Delta_g$ system by Ogorzalek-Loo (Ref. 6). The fundamental laser wavelengths have been air-vacuum corrected and the transition energy is given by twice the energy associated with the plotted vacuum wavelength. Despite a noisy spectrum, an anomalous intensity minimum, indicated by an arrow, can be discerned near 331 nm. The regions on either side of this minimum are labeled A and B, consistent with the two bands reported by Johnson *et al.* (Ref. 7). (b) The corresponding spectrum calculated using the CSE model, including rotational assignments for the significant spectral features. The calculated spectrum, degraded assuming an instrumental resolution of 3 cm^{-1} FWHM, reproduces the anomalous intensity minimum which results from regions of perturbation in the S and R branches due to crossing of the $d(v=1)$ rotational terms by the $v=5$ rotational terms of the $II\,^1\Pi_g$ valence state.

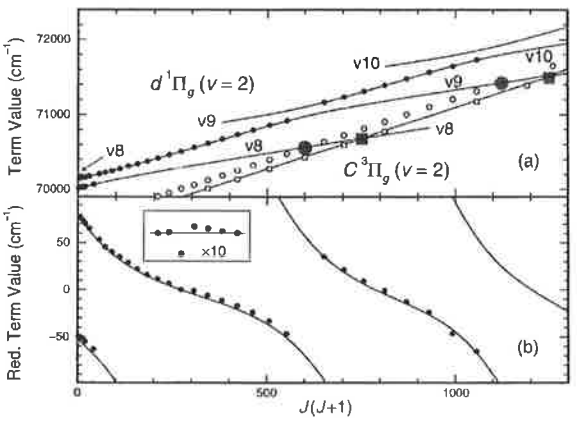

FIG. 4. (a) Comparison between term values for $d\,^1\Pi_g(v=2)$ (solid circles), $C\,^3\Pi_{1g}(v=2)$ (open squares) and $C\,^3\Pi_{2g}(v=2)$ (open circles), derived in this work from analysis of the $d\,^1\Pi_g \leftarrow\leftarrow a\,^1\Delta_g$, $d\,^1\Pi_g \leftarrow\leftarrow X\,^3\Sigma_g^-$ and $C\,^3\Pi_g \leftarrow\leftarrow X\,^3\Sigma_g^-$ (2+1) REMPI spectra of Ogorzalek-Loo (Ref. 6) and Sur *et al.* (Refs. 4 and 9), and term values calculated using the $\Omega=1$ CSE model (lines). Strong perturbations are caused by the crossing of the $d(v=2)$ rotational terms by the $v=8-10$ rotational terms of the $II\,^1\Pi_g$ valence state, labeled v8–10, respectively. Regions of weak perturbation in the C state (shaded) correspond to crossings by the $II\,^1\Pi_g(v=8$ and 9) valence-state rotational terms. (b) Plot of *reduced* term values for $d(v=2)$, obtained by subtracting $70\,063+1.64J(J+1)$ cm^{-1} from the absolute term values of (a), which emphasize the strong rotational perturbations culminating at $J\approx5$ and $J\approx24$. Inset: An energy-expanded, linearized view of the difference between the measured and calculated term values, highlighting an additional weak rotational perturbation in $d(v=2)$ near $J=16$ (see footnote 47).

shifts due to significant perturbations in the S and R branches, but also because increased mixing of the Rydberg (calculated widths ≈3 cm^{-1} FWHM) and valence (calculated widths ≈30 cm^{-1} FWHM) levels leads to increased broadening of the Rydberg levels and, consequently, lower ionization yields and REMPI intensities for the perturbed lines.

Comparison between Figs. 3(a) and 3(b) shows clearly that all of the observed structure can be associated with the $d\leftarrow\leftarrow a(1,0)$ transition, with only transitions into rotational levels of primarily Rydberg character being observed. However, there are some aspects of the measured branch intensities which are inconsistent with the calculated spectrum. For example, the intensity measured by Ogorzalek-Loo[6] for the upper S and R branches ("band B" region), relative to the intensity near the band head ("band A" region), is significantly larger than the corresponding calculated relative intensity and the experimental branch intensities in this region exhibit an additional structural minimum near 330.5 nm which is not reproduced by the CSE calculations. However, since the $d\leftarrow\leftarrow X(1,0)$ REMPI spectrum[6] does *not* exhibit these additional intensity anomalies, their explanation in the $d\leftarrow\leftarrow a(1,0)$ REMPI spectrum likely involves other factors, possibly including significant variation of laser intensity across the relevant tuning range, and/or the effects of interferences at the three-photon level.

C. $d\,^1\Pi_g(v=2)$

No rotational analyses of spectra involving the $d(v=2)$ level have been reported previously, most likely because of structural complexities produced by extensive perturbations, significant predissociation broadening of the low rotational levels, and the occurrence of levels of the $II\,^1\Pi_g$ valence state. Rotational term values for $d(v=2)$ are shown in Fig. 4(a). The plotted values represent the averages of values determined from the $d\leftarrow\leftarrow a(2,0)$ spectrum,[6] lowered by 2.1 cm^{-1},[42] and values determined from the $d\leftarrow\leftarrow X(2,0)$ spectrum,[6] supplemented at low J by values deduced from the low- and medium-temperature $d\leftarrow\leftarrow X(2,0)$ spectra of Sur *et al.*,[4] shifted downwards by 13.9 and 15.2 cm^{-1}, respectively, in order to be consistent with the relative wave-number scale of the Ogorzalek-Loo[6] data. The $d(v=2)$ level is heavily perturbed, as can be seen most clearly in Fig. 4(b), where *reduced* term values, obtained by subtracting $70\,063+1.64J(J+1)$ cm^{-1} from the experimentally determined term values, are plotted against $J(J+1)$. The lowest perturbation culminates at $J\approx5$, the second at $J\approx24$, each with an effective two-level interaction matrix element $H_{12}\approx62$ cm^{-1}. In addition, there is evidence of a third major perturbation in the region of $J\approx32$.

Spectroscopic constants $\nu_0=70\,015$ cm^{-1} and $B=1.29$ cm^{-1} ($J\leqslant6$), and $\nu_0=70\,143$ cm^{-1} and $B=1.15$ cm^{-1} ($J\leqslant7$), respectively, have been determined[40] for the lowest two rotational-term sequences in Fig. 4. These rotational constants are consistent with the accepted picture[4] of strongly mixed Rydberg and valence levels at low J in the case of the $d(v=2)$ level, with the upper level having the greater valence character. In terms of a "diabatic" picture,

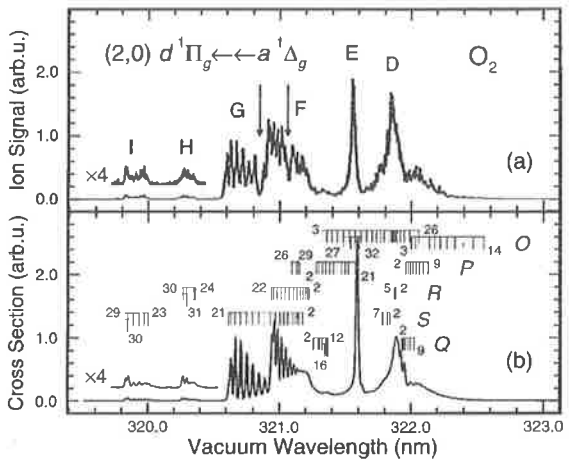

FIG. 5. (a) Room-temperature (2+1) REMPI spectrum measured for the (2,0) band of the $d\,^1\Pi_g \leftarrow\leftarrow a\,^1\Delta_g$ system by Ogorzalek-Loo (Ref. 6) [see caption of Fig. 3(a)]. Complex rotational structure is observed, with strong perturbations producing large displacements of portions of the rotational branches, and also weaker perturbations in the structure of those branches, indicated by arrows. Regions D through I correspond to bands reported by Johnson *et al.* (Ref. 7). (b) Corresponding spectrum calculated using the CSE model, including rotational assignments. The calculated spectrum, degraded assuming an instrumental resolution of 3 cm^{-1} FWHM, reproduces the strong perturbations caused by the $^1\Pi_g$ Rydberg–valence interaction. The origin of the weak perturbations is discussed in the text.

the "adiabatic" terms shown in Fig. 4(a) result from the crossing from above of the rotational term series for the $v=2$ level of the $d\,^1\Pi_g$ Rydberg state (origin near 70 080 cm^{-1}) by rotational term series for three successive vibrational levels of the $II\,^1\Pi_g$ valence state, near $J \approx 5$, 24, and 32, respectively, the B value for the Rydberg level being much larger than the B values for the valence levels in question (see Sec. IV A). With a few exceptions at low J, the observed rotational levels have primarily Rydberg character and are distributed around a reduced term value of zero in Fig. 4(b), indicating that the "deperturbed" $B \approx 1.64$ cm^{-1}, the value for $O_2^+\ X\,^2\Pi_g(v=2)$.[41] Finally, the calculated term values (solid lines in Fig. 4) are in good agreement with the measured values, including reproduction of the strong rotational perturbations which are found to be caused by the $v=8-10$ levels of the $II\,^1\Pi_g$ valence state.

One of the room-temperature (2+1) REMPI spectra for the $d \leftarrow\leftarrow a(2,0)$ band presented by Ogorzalek-Loo[6] is shown in Fig. 5(a). The great spectral complexity indicates why this band had not been rotationally analyzed until now. Johnson *et al.*[7] labeled six bands in their room-temperature spectra of this region D through I, a nomenclature we have preserved in Fig. 5(a). They[7] attributed part of the structure to the $d \leftarrow\leftarrow a(2,0)$ transition and parts of the remainder to transitions into other high-lying states, including the $II\,^1\Pi_g$ valence state. In addition, the low-temperature ($\lesssim 5$ K) $d \leftarrow\leftarrow X(2,0)$ (2+1) REMPI spectrum reported by Sur *et al.*[4] displays two distinct, well-separated features, one near D and the other near the low-energy limit of feature F in Fig. 5(a), with the low-energy feature narrower and more intense. Presumably, these low-rotation features lie near the low-J origins of structures in the room-temperature spectrum. Photoelectron spectra taken of these low-temperature features[4] showed similar electron-energy distributions, suggesting that they originated either from the same electronic state, or from strongly mixed states.

The calculated CSE room-temperature $d \leftarrow\leftarrow a(2,0)$ (2+1) REMPI spectrum, shown in Fig. 5(b), is in very good agreement with the measured spectrum in Fig. 5(a), reproducing semiquantitatively all of the main features and several other weaker, previously undesignated features. To obtain the spectrum in Fig. 5(b), Γ^i was taken as 0.75 cm^{-1} FWHM and the calculated spectrum was degraded with an instrumental resolution of 3 cm^{-1} FWHM, values obtained by minimizing the difference between the measured and calculated spectra for the narrow lines in the F and G regions.

The unusual structure of spectra associated with $d(v=2)$ arises principally from two effects. First, as indicated above and in Fig. 4, the $d(v=2)$ Rydberg level is crossed by successive vibrational levels of the $II\,^1\Pi_g$ valence state, producing significant perturbations which lead to rotational branches which appear segmented. Second, the CSE calculations indicate that predissociation linewidths of the observable, predominantly Rydberg-character levels vary significantly with rotation, passing through deep minima ($\lesssim 0.2$ cm^{-1} FWHM) near $J=21$ and $J=32$. This narrowing of linewidth increases the corresponding REMPI intensities through an enhanced photoionization quantum yield [Eq. (4)] and leads to the strongest features DEFG in Fig. 5 being associated with the O-, P-, R- and S-branch lines, respectively, with upper-state rotation J in the range 17–22. The weak features H and I in Fig. 5 are due to R- and S-branch lines with J in the range 25–32, near the higher-J linewidth minimum. The two-photon rotational line strengths of Bray and Hochstrasser[36] indicate that the Q-branch line strengths should fall off rapidly with increasing rotation for a $^1\Pi_g \leftarrow\leftarrow {}^1\Delta_g$ transition. This prediction is consistent with the observed spectrum which certainly has no high-rotation Q-branch structure, although a very weak, diffuse feature is observed in Fig. 5(a) near 321.35 nm, where a Q branch returning at $J=12$ is indicated in the calculated CSE spectrum.

Observation of valence features is difficult due to lower photoionization probability, greater competition through predissociation (calculated low-rotation predissociation linewidth ≈ 20 cm^{-1} FWHM, compared with ≈ 5 cm^{-1} FWHM for the comparable predominantly Rydberg levels), and low intrinsic transition moments. From the CSE calculations, the spectral regions of greatest valence character in Fig. 5 are the diffuse, low-J regions near 321.2 nm and $\gtrsim 322$ nm. The predissociation linewidths and REMPI intensities associated with these features in the calculated spectrum are significantly dependent on the inherent valence linewidth and are thus very sensitive to the strength of the CSE-model $^1\Pi_g$ valence–valence interaction.

Despite good agreement between the measured and calculated REMPI spectra, a close inspection of Fig. 5 reveals small irregularities in the measured spectrum which are not reproduced in the CSE calculations. Specifically, anomalously large spacings are observed between the $S(14)$ and

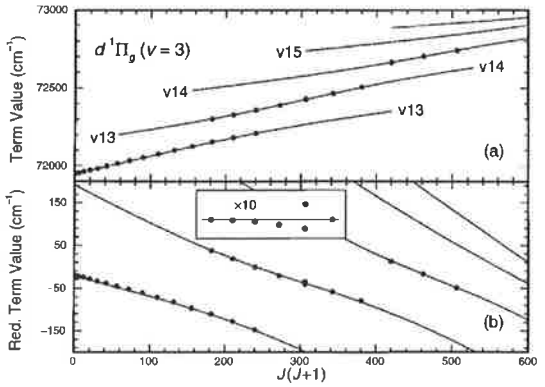

FIG. 6. (a) Comparison between term values for $d\,^1\Pi_g(v=3)$ (solid circles), derived in this work from analysis of the $d\,^1\Pi_g \leftarrow\leftarrow a\,^1\Delta_g$ and $d\,^1\Pi_g \leftarrow\leftarrow X\,^3\Sigma_g^-$ (2+1) REMPI spectra of Ogorzalek-Loo (Ref. 6), and term values calculated using the CSE model (lines). The CSE calculations indicate that the $d(v=3)$ rotational terms are crossed by the $v \geqslant 13$ rotational terms of the $II\,^1\Pi_g$ valence state. The lowest of these valence terms are labeled v13–15. (b) Plot of *reduced* term values, obtained by subtracting $71\,970+1.62J(J+1)$ cm^{-1} from the absolute term values of (a), which emphasize the strong rotational perturbations culminating at $J \approx 14$ and $J \approx 20$. Inset: An energy-expanded, linearized view of the difference between the measured and calculated term values, highlighting an additional weak perturbation near $J=17$ and the observation of an extra level associated with the perturbing state (see footnote 47).

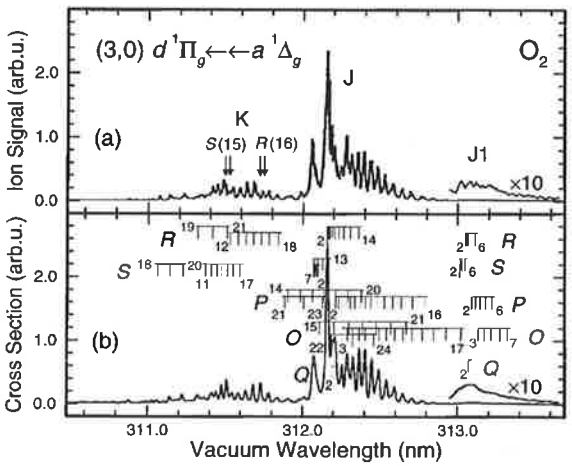

FIG. 7. (a) Room-temperature (2+1) REMPI spectrum measured for the (3,0) band of the $d\,^1\Pi_g \leftarrow\leftarrow a\,^1\Delta_g$ system by Ogorzalek-Loo (Ref. 6) [see caption of Fig. 3(a)]. As for the (2,0) band, complex rotational structure is observed, with strong perturbations producing large displacements of portions of the rotational branches. Weaker perturbations in the structure of those branches are indicated by arrows. Regions labeled K and J correspond to bands reported by Johnson *et al.* (Ref. 7). An additional weak, diffuse feature (J1) is observed near 313.1 nm. (b) Corresponding spectrum calculated using the CSE model, including rotational assignments for the significant spectral features [see caption of Fig. 5(b)]. Note that the branch label "*Q*" near 312.0 nm refers to the tick mark labeled "2" near 312.2 nm, *not* the nearby spectral feature which is actually a returning *S* branch. The origins of the weak perturbations and feature J1 are discussed in the text.

$S(15)$ lines in region G, and the $R(15)$ and $R(16)$ lines in region F, indicated by arrows in Fig. 5(a). These anomalies result from an additional weak rotational perturbation,[46] highlighted in Fig. 4(b) (inset),[47] where it can be seen that the maximum perturbation, corresponding to a downward shift of ~ 2.5 cm^{-1}, occurs for $J=16$. This perturbation has not been reported previously and a discussion of its origin will be postponed until Sec. IV.

D. $d\,^1\Pi_g(v=3)$

Rotational term values for $d(v=3)$ are shown in Fig. 6(a). The plotted values represent the averages of values determined from the $d \leftarrow\leftarrow a(3,0)$ spectrum,[6] raised by 0.5 cm^{-1},[42] and values determined from the $d \leftarrow\leftarrow X(3,0)$ spectrum.[6] As in the case of $d(v=2)$, the $d(v=3)$ level is heavily perturbed. The *reduced* term values plotted in Fig. 6(b), obtained by subtracting $71\,970+1.62J(J+1)$ cm^{-1} from the term values in Fig. 6(a), emphasize three major perturbations. The lowest culminates at $J \approx 14$ and has an effective two-level interaction matrix element $H_{12} \approx 74$ cm^{-1}. The second culminates at $J \approx 20$, with $H_{12} \approx 61$ cm^{-1}, while the third occurs in the region of $J \approx 23$. The experimentally based term values in Fig. 6 imply[40] spectroscopic constants $\nu_0 = 71\,950$ cm^{-1}, $B = 1.211$ cm^{-1}, and $D = 4.9 \times 10^{-4}$ cm^{-1}, for $J \leqslant 15$, which are consistent with the value $B = 1.15$ cm^{-1} reported by Sur *et al.*[4] from assignments for $J \leqslant 8$ only. Except in the region of the lowest-J perturbation, all of the observed rotational levels have primarily Rydberg character and are distributed around a reduced term value of zero in Fig. 6(b), indicating a "deperturbed" $B \approx 1.62$ cm^{-1}, the value for O_2^+ $X\,^2\Pi_g(v=3)$.[41]

As for $d(v=1$ and 2), the calculated term values for $d(v=3)$ (solid lines in Fig. 6) are in good agreement with the measurements, including reproduction of the rotational perturbations. The CSE calculations indicate that the $d(v=3)$ rotational terms are crossed by the $v \geqslant 13$ rotational terms of the $II\,^1\Pi_g$ valence state, causing the strong perturbations observed. As the dissociation limit of the valence state is approached at high J values in $d(v=3)$, the spacing between the valence levels decreases rapidly and the spectral complexity increases due to multiple level interactions.

One of the room-temperature (2+1) REMPI spectra for the $d \leftarrow\leftarrow a(3,0)$ band presented by Ogorzalek-Loo[6] is shown in Fig. 7(a). The calculated CSE room-temperature $d \leftarrow\leftarrow a(3,0)$ (2+1) REMPI spectrum in Fig. 7(b) is in excellent agreement with the experimental spectrum in almost all respects. The calculations were performed with $\Gamma^i = 0.75$ cm^{-1}, determined by optimizing agreement between the experimental and calculated spectra. In addition, the spectrum in Fig. 7(b) includes a convolution with a Gaussian instrumental function of 3 cm^{-1} FWHM.

Johnson *et al.*[7] labeled two bands in this region J and K. Band J was attributed[7] to the $d \leftarrow\leftarrow a(3,0)$ transition, while band K was assigned to the $C \leftarrow\leftarrow X(0,1)$ hot band, an assignment later disputed by Ogorzalek-Loo *et al.*[5] Band J (apparent linewidths ≈ 4 cm^{-1} FWHM) is strongly red-degraded, and, from a band simulation, Johnson *et al.*[7] noted

that the observed REMPI line strengths fell off at a significantly faster rate with increasing J than was implied by the theoretical line strengths.[36] In addition to the structures in regions J and K, the REMPI spectrum in Fig. 7(a) displays a weak, diffuse feature near 313.1 nm which we label J1. A careful inspection of Fig. 1 of Johnson *et al.*[7] reveals a similar feature.

Band J is associated with the low-J portion of Fig. 6, and, to that extent, can be analyzed as a separate band.[4,7] The low B and unusually large D values resulting from such analyses, together with the rapid falloff with increasing rotation of the REMPI intensities, result essentially from the perturbation of $d(v=3)$ by $II\,^1\Pi_g(v=13)$. As the culmination of the perturbation near $J=14$ is approached, increased mixing between the Rydberg (calculated width ≈ 0.6 cm^{-1} FWHM) and valence (calculated width ≈ 8 cm^{-1} FWHM) levels produces a rapid broadening of the Rydberg levels and an associated decrease in the REMPI intensity. The calculated Q branch, which, as we have mentioned in Sec. III C, is limited to the lower rotational levels in $^1\Pi_g \leftarrow\leftarrow {}^1\Delta_g$ transitions, is significantly more prominent for the (3,0) band than for the (2,0), simply because the low rotational levels for $d(v=3)$ are narrower than those for $d(v=2)$. However, no obvious Q-branch feature is visible in the experimental spectrum of Fig. 7(a).

The most prominent features in region K are associated with R- and S-branch transitions to levels with $J=13$–19. Their observed intensity envelopes result from linewidth narrowing, the calculated level widths passing through a minimum of ~ 0.5 cm^{-1} FWHM at $J=17$, approximately halfway between the crossings of $d(v=3)$ by the $v=13$ and 14 levels of the valence state (Fig. 6). Similarly, weaker structure observed in the spectrum in the vicinity of 311.2 nm is associated with transitions to levels with $J=20$–22.

As for the (1,0) and (2,0) bands discussed in Secs. III B and III C, most of the structure in Fig. 7(a) arises from transitions into levels of principally Rydberg character. However, a valence-state level is also observable in the spectrum of Fig. 7(a), as the weak, diffuse feature J1. This is only the second direct observation of a $^1\Pi_g$ valence-state level in the REMPI spectrum of O_2, following the earlier observation of a level just above $d(v=2)$ by Sur *et al.*[4] (Sec. III C). The CSE calculations imply that this feature arises from transitions into the $v=12$ level of the $II\,^1\Pi_g$ valence state which lies just *below* $d(v=3)$, the intensity of the valence feature being borrowed from the Rydberg transition. Assignments for the lowest calculated rotational lines in the $II\,^1\Pi_g \leftarrow\leftarrow a\,^1\Delta_g(12,0)$ band are given in Fig. 7(b).

Finally, a close inspection of Fig. 7 reveals small irregularities in the observed spectrum which are not reproduced in the CSE calculations. In particular, the $S(15)$ and $R(16)$ lines, indicated by arrows in Fig. 7(a), appear to be doubled. This additional weak rotational perturbation in $d(v=3)$ is highlighted in Fig. 6(b) (inset).[47] The observation of both main and extra $J=17$ levels leads to an effective two-level interaction matrix element of $H_{12}=2.6\pm0.3$ cm^{-1} for this weak perturbation which will be discussed in detail in Sec. IV B.

E. $C\,^3\Pi_g(v=2)$

The only low vibrational level of the $C\,^3\Pi_g$ state narrow enough to allow rotational analysis is the $v=2$ level. Using a combination of the $C\leftarrow\leftarrow X(2,0)$ spectrum of Sur *et al.*[9] and the $d,C\leftarrow\leftarrow X(2,0)$ spectrum of Ogorzalek-Loo,[6] the analysis of the $F_3(\Omega=2)$ sublevel by Sur *et al.*[9] has been extended to higher rotational levels and tentative rotational analyses of the $F_2(\Omega=1)$ and $F_1(\Omega=0)$ sublevels have been made. While the F_3 analysis is supported by combination differences, the F_2 analysis relies principally on S-branch lines and the F_1 analysis is possible only for the lowest-rotational lines in the F_1 subband of the $C\leftarrow\leftarrow X(2,0)$ spectrum.[9] The resultant $C(v=2)$ term values are shown in Fig. 4(a) in relation to the $d(v=2)$ term values.[40,48] On the surface, the $C(v=2)$ term values appear unexceptional, yielding spectroscopic constants:[49] $\nu_0=69\,550$ cm^{-1}, $B=1.68_3$ cm^{-1}, and $D=1.3\times10^{-5}$ cm^{-1} for the F_3 level; $\nu_0=69\,445$ cm^{-1}, $B=1.65_3$ cm^{-1}, and $D=1.6\times10^{-5}$ cm^{-1} for the F_2 level; and $\nu_0=69\,366$ cm^{-1} and $B=1.6_3$ cm^{-1} for the F_1 level. However, on closer inspection, the spectra reveal a number of possible anomalies, such as weakened or missing lines, which are suggestive of weak perturbations near $C\,^3\Pi_{2g}(v=2,\ J=24$ and 33) and $C\,^3\Pi_{1g}(v=2,\ J=27$ and 35), but it is not possible at this time to pursue a detailed analysis of these anomalies because of the sketchy nature of the experimental data.

The experimentally based term values for the F_2 levels of the C state are seen in Fig. 4(a) to be satisfactorily reproduced by the CSE calculations, but, due to the inclusion of only $\Omega=1$ states in our model, no term values have been calculated for the F_1 or F_3 levels. The possible weak perturbations in $C(v=2)$ are indicated as shaded areas in Fig. 4(a). Considered in conjunction with the strong perturbations in $d(v=2)$ discussed in Sec. III C, it is likely that the same levels of the $II\,^1\Pi_g$ valence state are responsible for both the d- and C-state perturbations.

IV. DISCUSSION

A. Rydberg–valence perturbations in $d\,^1\Pi_g$

The results of Sec. III demonstrate that a CSE model which includes significant Rydberg–valence interaction between the $^1\Pi_g$ states provides an excellent description of the strongly perturbed $d\,^1\Pi_g$ rovibrational term values and corresponding $d\leftarrow\leftarrow a\ (2+1)$ REMPI spectra. Figure 8 shows the model diabatic potential-energy curves for the strongly interacting $^1\Pi_g$ states in the energy range of interest, including the bound Rydberg levels and particular vibrational levels of the $II\,^1\Pi_g$ valence state for which evidence is found in this work.

The extended rotational analyses of the present work have led to the *indirect* characterization of many levels of the $II\,^1\Pi_g$ valence state, which, when combined with CSE-model analysis, has resulted in the determination of a realistic empirical potential-energy curve for this state. The good agreement found between the calculated and experimental term values (Sec. III), together with the relatively minor adjustments necessary to the diabatic curve for the $II\,^1\Pi_g$ state derived from the *ab initio* calculations of Partridge,[30] lead to

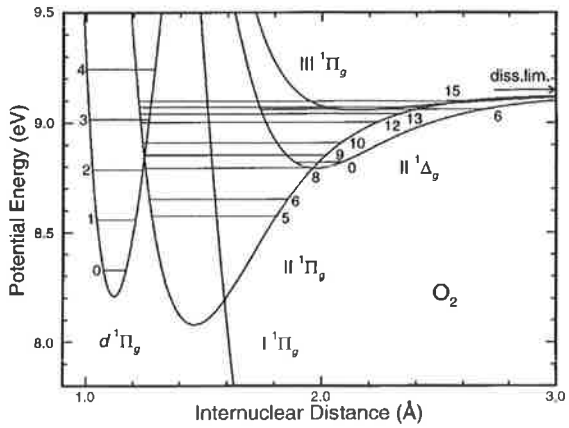

FIG. 8. Diabatic potential-energy curves of O_2 relevant to perturbation of the $d\,^1\Pi_g(v=1-3)$ Rydberg-state levels, indicating valence-state levels for which evidence is found in this work. The major perturbations evident in Figs. 2, 4, and 6 are caused by an electrostatic interaction between the bound Rydberg and valence states of $^1\Pi_g$ symmetry, while the minor perturbations observed for $d(v=2)$ and $d(v=3)$ result from a second-order effect involving an additional rotational interaction between the II $^1\Pi_g$ and II $^1\Delta_g$ valence states.

confidence in our empirical potential, which differs significantly from previous determinations.[4,12,19] Since the II $^1\Pi_g$ valence-state potential ($R_e=1.46$ Å) lies at a considerably larger internuclear distance than the $d\,^1\Pi_g$ Rydberg-state potential ($R_e=1.12$ Å), the rotational constants for the valence levels ($B_e=0.99$ cm^{-1}) are considerably smaller than those for the Rydberg levels ($B_e=1.69$ cm^{-1}). Thus, as J increases, in a relative sense the valence levels sweep down through the Rydberg levels, producing the many level crossings and perturbations analyzed in Sec. III, and explaining why, for the most part, the valence levels for $v\geqslant 5$ for which evidence has been found (Fig. 8) are those lying *above* the Rydberg levels which they perturb. Finally, we note that, while the vibrational numbering for the II $^1\Pi_g$ valence state is likely to be correct, this numbering cannot be regarded as completely rigorous in the absence of isotopic studies of the type foreshadowed by Sur *et al.*[4]

B. Weak perturbations in $d\,^1\Pi_g$

The weak perturbations in $d(v=2,\ J\approx 16)$ and $d(v=3,\ J\approx 17)$, reported in Secs. III C and III D, respectively, cannot be reproduced using the CSE diabatic-state $^1\Pi_{1g}$ basis described in Sec. II B. This situation does not change if the $3s\sigma_g\,^3\Pi_{0,2g}$ states are added to the basis. The observed $d(v=2)$ perturbation (Fig. 4), together with the $g\leftrightarrow g$ selection rule for perturbations, require the existence of a bound *gerade* electronic state of O_2 with $T_e\lesssim 8.8$ eV (Fig. 8). There are no Rydberg states other than the $3s\sigma_g\,^{1,3}\Pi_g$ states in this energy region. An inspection of complete sets of *ab initio* valence-state potential-energy curves[50,51] yields only one possible candidate perturber, the II $^1\Delta_g$ state, correlating with the same dissociation limit as the II $^1\Pi_g$ state, $O(^1D)+O(^1D)$. The multireference configuration-interaction with Davidson correction (MRCI+Q) *ab initio* potential-energy curve for the II $^1\Delta_g$ state, calculated by Partridge[30] and shown in Fig. 8, has $T_e=8.79$ eV and $R_e=1.97$ Å. This representation of the II $^1\Delta_g$ state is expected to be more accurate than previous calculations.[50,51] Energetically, the II $^1\Delta_g$ state is capable of perturbing both the $d(v=2)$ and $d(v=3)$ levels: calculated eigenvalues for the ($v=0$, $J=16$) and ($v=6$, $J=17$) levels of the MRCI+Q potential lie within ± 15 cm^{-1} of the $d(v=2,\ J=16)$ and $d(v=3,\ J=17)$ levels, respectively. In addition, the low rotational constants for the II $^1\Delta_g$-state levels (calculated $B_e=0.54$ cm^{-1}) are consistent with the observation (Figs. 4 and 6) that the $d(v=2)$ and $d(v=3)$ levels are perturbed from *above*.

Consideration of the selection rules for perturbations[24] shows that a $^1\Delta_{2g}$ state may interact heterogeneously with a $^1\Pi_{1g}$ state through the **L**-uncoupling operator ($\Delta\Lambda=\Delta\Omega=\pm 1$, $\Delta\Sigma=\Delta S=0$). However, a direct interaction between the II $^1\Delta_g$ and $d\,^1\Pi_g$ states is unlikely for two reasons. First, the principal MO configurations of these states, $\ldots(3\sigma_g)(1\pi_u)^3(1\pi_g)^3(3\sigma_u)$ and $\ldots(3\sigma_g)^2(1\pi_u)^4(1\pi_g)3s\sigma_g$, respectively, differ by three orbitals, implying a zero interaction matrix element in the single-configuration approximation.[24] Second, due to the wide separation in internuclear distance between the potential-energy curves for these two states (Fig. 8), the vibrational overlap factor is negligible. Nevertheless, an *indirect* interaction is possible between the II $^1\Delta_g$ and $d\,^1\Pi_g$ states, involving the II $^1\Pi_g$ intermediary. The principal MO configuration for the II $^1\Pi_g$ state, $\ldots(3\sigma_g)(1\pi_u)^4(1\pi_g)^3$, differs from that for the II $^1\Delta_g$ state by a single orbital ($\sigma_u\leftrightarrow\pi_u$), permitting a first-order-allowed **L**-uncoupling interaction between these two states.[24] Thus, a second-order interaction involving the homogeneous electrostatic interaction between the $d\,^1\Pi_g$ Rydberg and II $^1\Pi_g$ valence states (Sec. IV A), together with a heterogeneous **L**-uncoupling interaction between the II $^1\Pi_g$ and II $^1\Delta_g$ valence states, can be postulated to explain the observed weak perturbations in the $d\,^1\Pi_g$ state. These perturbations occur solely due to the valence admixture in the $d\,^1\Pi_g$ Rydberg-state wave function.

The rotronic part of the valence-state interaction has the form:[24]

$$H^{JL}(R)=\frac{hL^-(R)\sqrt{J(J+1)-2}}{8\pi^2\mu cR^2}, \tag{5}$$

where

$$L^-(R)=\langle \mathrm{II}\,^1\Pi_g|\mathbf{L}^-|\mathrm{II}\,^1\Delta_g\rangle. \tag{6}$$

The II $^1\Delta_g$-state potential-energy curve crosses the outer limb of the II $^1\Pi_g$-state curve (Fig. 8) in such a way that the vibrational overlap factors between near-degenerate levels are significant. In particular, the $d\,^1\Pi_g(v=2)-\mathrm{II}\,^1\Pi_g(v=8)-\mathrm{II}\,^1\Delta_g(v=0)$ interaction is expected to be the dominant indirect channel contributing to the weak $d(v=2)$ perturbation.

Further CSE calculations of the $d(v=2$ and 3) rovibrational term values have been performed, following the addi-

tion of the unmodified MRCI+Q $II\,^1\Delta_g$ state to the CSE-model diabatic basis, and including an **L**-uncoupling interaction between the basis $II\,^1\Delta_g$ and $II\,^1\Pi_g$ states. The value of $L^-(R)$ was taken as $\sqrt{2}$, consistent with the single-configuration pure-precession approximation,[24,52] which is expected to be an upper limit to the real interaction.[24] The calculated term values exhibit weak perturbations similar to those observed,[53] and an analysis of the calculated perturbations using standard two-level formulas[24] yields effective interaction matrix elements of 2.9 cm^{-1} for $d(v=2,\ J=16)$ and 1.7 cm^{-1} for $d(v=3,\ J=17)$, in satisfactory agreement with the rough values $\gtrsim$2.5 cm^{-1} and 2.6 cm^{-1}, respectively, estimated from the observations (Secs. III C and III D).

Thus, from energetic, configurational and interaction-strength considerations, the observed weak perturbations in the $d(v=2$ and $3)$ levels can be explained by an indirect interaction with the $II\,^1\Delta_g$ state. Although it cannot be ruled out that an additional, more weakly bound state is responsible for the $d(v=3)$ perturbation, it is not necessary to invoke this explanation. If the present interpretation is valid, the extra level observed in association with the $d(v=3)$ perturbation (Sec. III D) represents the first experimental observation of the $II\,^1\Delta_g$ state.

C. Valence–valence perturbations in $II\,^1\Pi_g$

Ab initio calculations of the $^1\Pi_g$ valence-state potential-energy curves[30] show that the adiabatic curves exhibit an avoided crossing which has the potential to affect the observed REMPI spectra. In a diabatic description, the repulsive $I\,^1\Pi_g$ potential crosses the bound $II\,^1\Pi_g$ potential low on its outer limb (Fig. 8), resulting in shifting and predissociation of the levels of the $II\,^1\Pi_g$ state. In principle, it should be possible to optimize the $I\,^1\Pi_g$ potential by adjusting its crossing point and slope, and the valence–valence interaction matrix element, until the experimental $II\,^1\Pi_g$ energy levels and predissociation pattern are reproduced. Unfortunately, the scarcity of predominantly valence levels observed in existing REMPI spectra makes such an approach impossible at present.

As pointed out in Sec. III, in addition to the obvious effects of the valence-level positions on the character of the Rydberg-state perturbation, there are certain spectral regions having particular sensitivity to the form of the $II\,^1\Pi_g$ valence-state predissociation. In particular, the predissociation widths of the $v=5$, 8, 12, and 13 levels of the $II\,^1\Pi_g$ state have significant effects on the appearance of the $d\leftarrow\leftarrow X(1,0)$, (2,0) and (3,0) spectra. In this work, we have fixed the $I\,^1\Pi_g$ potential and adjusted the $I\,^1\Pi_g - II\,^1\Pi_g$ interaction matrix element for best average agreement between the experimental and calculated spectra. The final result (500 cm^{-1}, see Sec. II B) is similar to the corresponding value for the $^3\Pi_g$ valence states,[18] in agreement with the prediction of van der Zande.[19] In principle, the outer-limb valence–valence crossing would be expected to result in an oscillatory dependence of the valence predissociation linewidth on the vibrational quantum number, leading to the possibility that some of the valence levels may be *narrow*. The future experimental detection of these levels may make it possible to better define the vibrational dependence of the predissociation, allowing optimization of the $I\,^1\Pi_g$-state potential-energy curve through adjustment of its crossing point and slope.

Finally, we note that the computed asymptotes[30] for the adiabatic $II\,^1\Pi_g$ and $III\,^1\Pi_g$ states (Fig. 8), both of which should correlate with the $O(^1D)+O(^1D)$ dissociation limit at 9.15 eV, are not degenerate, leading to the *appearance* of an avoided crossing. To overcome this problem, we used a diabatic description of the near-dissociation $II\,^1\Pi_g$ potential in the CSE calculations. Our adopted $II\,^1\Pi_g$ potential provides a good description of the perturbations in $d(v=3)$ and the spacing between the $II\,^1\Pi_g(v>13)$ energy levels (Fig. 6), both of which are sensitive to the near-dissociation potential.

V. SUMMARY AND CONCLUSIONS

Room-temperature $d\,^1\Pi_g\leftarrow\leftarrow a\,^1\Delta_g$ and $d\,^1\Pi_g\leftarrow\leftarrow X\,^3\Sigma_g^-$ (2+1) REMPI spectra of Ogorzalek-Loo[6] and low-temperature $d\,^1\Pi_g\leftarrow\leftarrow X\,^3\Sigma_g^-$ and $C\,^3\Pi_g\leftarrow\leftarrow X\,^3\Sigma_g^-$ spectra of Sur *et al.*[4,9] have been rotationally analyzed, significantly extending the range of rotationally characterized energies for the $3s\sigma_g\,d\,^1\Pi_g(v=0,1$ and $3)$ and $3s\sigma_g\,C\,^3\Pi_g(F_3,v=2)$ levels. In addition, for the first time, rotational level assignments for $d(v=2)$ and $C(F_1,F_2,v=2)$ have been determined and rotational perturbations in $d(v=1-3)$ and $C(v=2)$ have been characterized.

Using a coupled-channel Schrödinger-equation model, theoretical calculations of the $d\,^1\Pi_g\leftarrow\leftarrow a\,^1\Delta_g(1,0)$, (2,0) and (3,0) (2+1) REMPI spectra have been performed, yielding results in good agreement with the observed spectra, including a number of strongly perturbed regions. The identification and analysis of perturbations in the d and C states, together with the theoretical model calculations, have allowed the nature of the interactions between the $3s\sigma_g\,^{1,3}\Pi_g$ Rydberg states and the $II\,^1\Pi_g$ valence state to be clarified and a realistic empirical potential-energy curve for the $II\,^1\Pi_g$ state to be determined.

Finally, additional weak rotational perturbations found in $d(v=2$ and $3)$ can be attributed to a second-order effect involving not only a homogeneous electrostatic interaction between the $d\,^1\Pi_g$ Rydberg and the $II\,^1\Pi_g$ valence states, but also a heterogeneous rotational interaction between the $II\,^1\Pi_g$ and $II\,^1\Delta_g$ valence states. These weak perturbations, including an extra level observed for the $d(v=3,\ J=17)$ perturbation, represent the first experimental evidence for the $II\,^1\Delta_g$ valence state.

ACKNOWLEDGMENTS

The authors are grateful to Dr. H. Partridge for providing MRCI+Q *ab initio* potential-energy curves for the $^1\Pi_g$ and $^1\Delta_g$ valence states, and Dr. R. R. Ogorzalek-Loo for providing copies of her thesis and for several valuable discussions of its content. They would also like to thank Professor H. Lefebvre-Brion, Dr. D. S. Ginter, and Dr. W. J. van der Zande for critical readings of the manuscript, and Dr. P. C. Cosby, Dr. T. G. Slanger, and Dr. D. L. Huestis for valuable

discussions. J. S. Morrill would like to thank the Naval Research Laboratory for an Edison Memorial Graduate Fellowship which enabled him to pursue Ph.D. research at the University of Maryland. This work was supported in part by the National Science Foundation (US) (Grant Nos. INT 9512868 and PHY 9514413) and the Department of Industry, Science and Technology (Australia) (Grant No. 95/8769).

[1] P. H. Krupenie, J. Phys. Chem. Ref. Data **1**, 423 (1972).
[2] In this work, energies in eV are referred to the minimum in the ground-state $X\,^3\Sigma_g^-$ potential-energy curve.
[3] A. Sur, L. Nguyen, and N. Nikoi, J. Chem. Phys. **96**, 6791 (1992).
[4] A. Sur, R. S. Friedman, and P. J. Miller, J. Chem. Phys. **94**, 1705 (1991).
[5] R. Ogorzalek-Loo, W. J. Marinelli, P. L. Houston, S. Arepalli, J. R. Wiesenfeld, and R. W. Field, J. Chem. Phys. **91**, 5185 (1989).
[6] R. R. Ogorzalek-Loo, Ph.D. thesis, Cornell University, 1989.
[7] R. D. Johnson III, G. R. Long, and J. W. Hudgens, J. Chem. Phys. **87**, 1977 (1987).
[8] S. Katsumata, K. Sato, Y. Achiba, and K. Kimura, J. Electron Spectrosc. Relat. Phenom. **41**, 325 (1986).
[9] A. Sur, C. V. Ramana, W. A. Chupka, and S. D. Colson, J. Chem. Phys. **84**, 69 (1986).
[10] A. Sur, C. V. Ramana, and S. D. Colson, J. Chem. Phys. **83**, 904 (1985).
[11] J. S. Morrill, M. L. Ginter, B. R. Lewis, and S. T. Gibson, J. Chem. Phys. **111**, 173 (1999).
[12] Y. Li, I. D. Petsalakis, H.-P. Liebermann, G. Hirsch, and R. J. Buenker, J. Chem. Phys. **106**, 1123 (1997).
[13] R. Klotz and S. D. Peyerimhoff, Mol. Phys. **57**, 573 (1986).
[14] R. P. Saxon and B. Liu, J. Chem. Phys. **73**, 876 (1980).
[15] R. P. Saxon and B. Liu, J. Chem. Phys. **73**, 870 (1980).
[16] R. J. Buenker and S. D. Peyerimhoff, Chem. Phys. **8**, 324 (1975).
[17] R. J. Buenker and S. D. Peyerimhoff, Chem. Phys. Lett. **34**, 225 (1975).
[18] W. J. van der Zande, W. Koot, and J. Los, J. Chem. Phys. **91**, 4597 (1989).
[19] W. J. van der Zande, W. Koot, J. Los, and J. R. Peterson, J. Chem. Phys. **89**, 6758 (1988).
[20] R. S. Friedman and A. Dalgarno, J. Chem. Phys. **93**, 2370 (1990).
[21] R. S. Friedman and A. Dalgarno, J. Chem. Phys. **90**, 7606 (1989).
[22] In this work, the *diabatic* (crossing) states are labeled, e.g., I $^1\Pi_g$, II $^1\Pi_g$, III $^1\Pi_g$, etc., while the corresponding *adiabatic* states are labeled 1 $^1\Pi_g$, 2 $^1\Pi_g$, 3 $^1\Pi_g$, etc., with the convention that the ordered diabatic and adiabatic states become equivalent at large R.
[23] In this work, the term "rotational perturbation" is used in its historical sense to indicate perturbation of the rotational structure of a band, rather than a perturbation caused by a rotation-dependent interaction.
[24] H. Lefebvre-Brion and R. W. Field, *Perturbations in the Spectra of Diatomic Molecules* (Academic, Orlando, 1986), pp. 39, 56–58, 118–123, 208–216, 226–231, 247–254.
[25] F. H. Mies, Mol. Phys. **41**, 953 (1980).
[26] E. F. van Dishoeck, M. C. van Hemert, A. C. Allison, and A. Dalgarno, J. Chem. Phys. **81**, 5709 (1984).
[27] L. Torop, D. G. McCoy, A. J. Blake, J. Wang, and T. Scholz, J. Quant. Spectrosc. Radiat. Transfer **38**, 9 (1987).
[28] B. R. Lewis, S. S. Banerjee, and S. T. Gibson, J. Chem. Phys. **102**, 6631 (1995).
[29] In the Rydberg–valence region, where predissociation is the dominant deexcitation mechanism, the photoabsorption and photodissociation spectra are essentially equivalent.
[30] H. Partridge (personal communications, 1995–1997); H. Partridge, C. W. Bauschlicher, Jr., S. R. Langhoff, and P. R. Taylor, J. Chem. Phys. **95**, 8292 (1991).
[31] Smooth adjustments to the initial potential curves, where justified, were achieved through shifts in energy and internuclear distance, together with linear scaling of the well depths and widths. Dissociation limits for the valence states were held at the experimental values throughout this procedure.
[32] S. T. Pratt, P. M. Dehmer, and J. L. Dehmer, J. Chem. Phys. **81**, 3444 (1984).
[33] J. Kimman, M. Lavollée, and M. J. van der Wiel, Chem. Phys. **97**, 137 (1985).
[34] Despite a low ionization probability for the valence state, the admixture of Rydberg character in the valence wave functions would be expected to result in the observation of transitions to nominally valence levels in regions of favorable Franck–Condon overlap [near $d(v=2)$ and $d(v=3)$] if the valence two-photon transition moment were significantly larger than the Rydberg moment.
[35] Relative intensities of the Rydberg and valence features in the low-temperature $d\leftarrow\leftarrow X(2,0)$ spectrum of Ref. 4 are inconsistent with interference effects between the Rydberg and valence $^3\Pi_g\leftarrow\leftarrow X$ transition moments from which the $^1\Pi_g\leftarrow\leftarrow X$ transition moments are borrowed, suggesting that the Rydberg and valence moments differ significantly in magnitude. On configurational grounds, the same conclusion would be expected for the $^1\Pi_g\leftarrow\leftarrow a$ moments. Taken together with the conclusion of footnote 34, this suggests that $^1\Pi_g\leftarrow\leftarrow a$ absorption will be dominated by the Rydberg transition moment.
[36] R. G. Bray and R. M. Hochstrasser, Mol. Phys. **31**, 412 (1975).
[37] B. R. Johnson, J. Chem. Phys. **69**, 4678 (1978).
[38] The RKR potential-energy curve for the $a\,^1\Delta_g$ state was constructed using the G_v and B_v values given by T. G. Slanger and P. C. Cosby [J. Phys. Chem. **92**, 267 (1988)].
[39] The possibility of interference at the three-photon level is neglected and we take k^i and Γ^i to be wavelength and rotation independent for a given band.
[40] In this work, rotational terms for $a\,^1\Delta_g(v=0)$ were calculated using spectroscopic constants from Ref. 1, those for $X\,^3\Sigma_g^-(v=0)$ were taken from Veseth and Lofthus [L. Veseth and A. Lofthus, Mol. Phys. **27**, 511 (1974)], and d- and C-state terms were fitted to $T(J)=\nu_0+BJ(J+1)-D[J(J+1)]^2$. If insufficient rotational levels were available to define D, then D was taken as zero. All term values are referenced to an energy zero corresponding to a nonexistent level 0.25 cm^{-1} below the lowest real level of the X state (F_3, $N=1$, $J=0$), or 1.33 cm^{-1} below the extrapolated, nonexistent level (F_2, $N=J=0$) taken as an energy zero in many other studies.
[41] R. R. Laher and F. R. Gilmore, J. Phys. Chem. Ref. Data **20**, 685 (1991).
[42] Despite possible significant uncertainties in the term values of Ref. 6, results obtained from corresponding $d\leftarrow\leftarrow a$ and $d\leftarrow\leftarrow X$ spectra differed by a maximum of only 2 cm^{-1}. Nevertheless, it was necessary to remove this residual calibration difference before merging the two data sets to obtain a single set of term values which spanned a maximum range of d-state rotational quantum numbers.
[43] The effective two-level interaction matrix elements H_{12} were estimated as half the observed energy splittings at the level crossings, with some extrapolation where necessary.
[44] Additional small-scale variations (± 2 cm^{-1}) in the experimental reduced $d(v=1)$ term values in Fig. 2(b) arise from wavelength uncertainties associated with the very noisy spectrum of Fig. 3(a) and the effects of extensive line blending. Thus, there is no evidence for weak perturbations of the type reported in Secs. III C and III D for $d(v=2)$ and $d(v=3)$, respectively, which are based on clear spectral observations of resolved lines.
[45] The calculated (1,0) REMPI spectrum was relatively insensitive to the value of Γ^i, which was assumed to be the same as the value determined from the (2,0) and (3,0) spectra. The effective instrumental bandwidth was assumed to be the same as that deduced from the apparent widths of the narrowest lines in the (2,0) spectrum.
[46] There is the possibility of a further weak perturbation near $J=31$ [Fig. 4(b)], but term values in this region were estimated primarily from blended lines in the weak features H and I [Fig. 5(a)], implying the need for independent confirmation of this conclusion.
[47] In the inset, differences between experimental and calculated term values have been linearized by forcing the lowest- and highest-rotation points to zero, and plotting the results using the same horizontal scale, but an expanded vertical scale.
[48] Term values derived (footnote 40) from the spectrum of Sur *et al.* (Ref. 9) have been raised by 0.8 cm^{-1} to be consistent with those derived from the spectrum of Ogorzalek-Loo (Ref. 6) in the region of overlap. Thus, the relative relationship between d- and C-state term values shown in Fig. 4(a) is expected to be accurate.
[49] Maximum deviations in the fits for the $C(v=2)$ spectroscopic constants were significant ($\sim\pm 2$ cm^{-1}), due to a combination of weak perturbations, predissociation broadening, and blending of lines arising from different fine-structure levels of the X state.
[50] R. P. Saxon and B. Liu, J. Chem. Phys. **67**, 5432 (1977).

[51] H. H. Michels, Adv. Chem. Phys. **45**, 225 (1981).
[52] Apparent validity of the pure-precession approximation has been observed in other O_2 studies involving different valence states [B. R. Lewis, P. M. Dooley, J. P. England, K. Waring, S. T. Gibson, K. G. H. Baldwin, and H. Partridge, Phys. Rev. A **54**, 3923 (1996)].
[53] The culminations of the calculated perturbations do not coincide exactly with the measured values because the $II\,^1\Delta_g$ potential-energy curve has not been optimized.

4.40 High-resolution oscillator-strength measurements of the CO $B\,^1\Sigma^+ - X\,^1\Sigma^+$ (0,0) and (1,0) vibrational bands

[60] G. Stark, B. R. Lewis, S. T. Gibson, and J. P. England,
The Astrophysical Journal **520**, 732–736 (1999).

THE ASTROPHYSICAL JOURNAL, 520:732–736, 1999 August 1

HIGH-RESOLUTION OSCILLATOR STRENGTH MEASUREMENTS OF THE CO $B\,^1\Sigma^+$–$X\,^1\Sigma^+$ (0, 0) AND (1, 0) VIBRATIONAL BANDS

GLENN STARK,[1] BRENTON R. LEWIS,[2] STEPHEN T. GIBSON,[2] AND JULIAN P. ENGLAND[2,3]
Received 1998 December 14; accepted 1999 March 4

ABSTRACT

Large discrepancies in the published photoabsorption oscillator strengths of the vacuum-ultraviolet (VUV) bands of CO hamper the interpretation of VUV astronomical observations. We report new oscillator strength measurements of the (0, 0) and (1, 0) bands of the CO $B\,^1\Sigma^+$–$X\,^1\Sigma^+$ electronic system determined from high-resolution (resolving power $\approx$750,000) absorption spectra recorded with a tunable VUV laser system. The instrumental bandwidth ($\sim$0.14 cm^{-1} FWHM) was significantly less than the widths of the Doppler-broadened CO lines ($\sim$0.20 cm^{-1} FWHM). The $B(0)$–$X(0)$ and $B(1)$–$X(0)$ band oscillator strengths, derived from measurements of the photoabsorption cross sections of 36 individual rotational lines, are $(6.5 \pm 0.6) \times 10^{-3}$ and $(1.1 \pm 0.1) \times 10^{-3}$, respectively. Our results are compared with other recent laboratory measurements and with ab initio calculations.

Subject headings: ISM: molecules — molecular data — ultraviolet: ISM

1. INTRODUCTION

Carbon monoxide is the most abundant interstellar molecule after H_2, and, because it is much more readily observed than H_2, is used as a tracer of the large-scale distribution of molecular gas in our Galaxy. The capabilities of the Goddard High Resolution Spectrograph (GHRS) and the Space Telescope Imaging Spectrograph (STIS) on the *Hubble Space Telescope* (*HST*) have led to new studies of interstellar $^{12}C^{16}O$ and its isotopic variants at vacuum-ultraviolet (VUV) wavelengths. In addition, the expected launch of the NASA *Far Ultraviolet Spectroscopic Explorer* (*FUSE*) satellite, with an instrumental bandpass of 91–120 nm, will likely lead to new, high-resolution ($\lambda/\Delta\lambda \approx$ 30,000) astronomical measurements of CO absorption features, including the $B\,^1\Sigma^+$–$X\,^1\Sigma^+$ (0, 0) and (1, 0) bands at 115 and 112 nm, respectively. The interpretation of these new astrophysical observations will require accurate and reliable spectroscopic data.

The $B(0)$–$X(0)$ band of $^{12}C^{16}O$ was first observed in absorption in the line of sight to ζ Ophiuchi by the *Copernicus* satellite (Wannier, Penzias, & Jenkins 1982). Rotationally resolved spectra of the $B(0)$–$X(0)$ band were recorded by Sheffer et al. (1992) using the *HST* GHRS. Large discrepancies in the literature values of the photoabsorption oscillator strengths of the CO B–X bands have hampered the interpretation of these astronomical observations. As an illustration, the $B(0)$–$X(0)$ band oscillator strengths adopted by the above authors in their interpretations of the astronomical absorption spectra, $f = 0.015$ (Wannier et al. 1982) and $f = 0.0058$ (Sheffer et al. 1992), differ by almost a factor of 3. We report new oscillator strength measurements of the $B(0)$–$X(0)$ and $B(1)$–$X(0)$ bands of $^{12}C^{16}O$ determined from high-resolution (resolving power $\approx$750,000) absorption spectra recorded with a tunable VUV laser system. Our results are compared with other recent laboratory determinations and with recent theoretical calculations.

Morton & Noreau (1994), in their compilation of fundamental spectroscopic data for all CO transitions between 100 and 155 nm, critically evaluated the $B\,^1\Sigma^+$–$X\,^1\Sigma^+$ database. The B state has four known vibrational levels (Eidelsberg et al. 1987; Tchang-Brillet et al. 1992; Baker, Tchang-Brillet, & Julienne 1995). Transitions from the $X(0)$ level to the $B(0)$ and $B(1)$ levels are strong and have received the most attention from experimentalists and theorists. Three independent experimental approaches have been used in the determination of B–X band f-values; optical absorption measurements (Lee & Guest 1981; Eidelsberg et al. 1991), radiative lifetime measurements (Krishnakumar & Srivastava 1986; Drabbels, Meerts, & ter Meulen 1993), and inelastic electron-scattering measurements (Lassettre & Skerbele 1971; Chan, Cooper, & Brion 1993; Kanik, James, & Ajello 1995; Zhong et al. 1997). Ab initio calculations of the B–X electronic transition moment and B–X band oscillator strengths have been reported by Kirby & Cooper (1989), Chantranupong et al. (1992), and Rocha, Borges, & Bielschowsky (1998). Tchang-Brillet et al. (1992) used a semiempirical close-coupling model of the B–D' Rydberg valence interaction to calculate the $[B(0)$–$X(0)/B(1)$–$X(0)]$ f-value ratio. There is little agreement among the previously published results (see § 3), although one trend is apparent: the theoretical calculations produce B–X band f-values that are consistently lower than almost all of the experimentally determined f-values. In their compilation of recommended B–X band oscillator strengths, Morton & Noreau (1994) adopted the results of the measurements of Eidelsberg et al. (1991), but cautioned that, given the discrepant literature values, an uncertainty in the $B(0)$–$X(0)$ f-value on the order of a factor of 2 is appropriate.

Optical absorption measurements provide, in principle, a direct determination of band f-values. However, as discussed by Hudson (1971), Stark et al. (1991), and Jolly et al. (1997), insufficient instrumental resolution can lead to saturation effects, which, if not minimized or properly accounted for, result in a systematic underestimation of

[1] Department of Physics, Wellesley College, 106 Central Street, Wellesley, MA 02481; gstark@wellesley.edu.

[2] Research School of Physical Sciences and Engineering, Australian National University, Canberra, A.C.T. 0200, Australia; brenton.lewis@anu.edu.au, stephen.gibson@anu.edu.au.

[3] Current address: Australian Bureau of Statistics, Belconnen, A.C.T. 2617, Australia; j.england@abs.gov.au.

band f-values. The Doppler broadening of CO B–X rotational lines at 295 K results in line widths with a full width at half-maximum (FWHM) of 0.20 cm^{-1} (2.6 mÅ) at 115 nm. The instrumental resolutions used in previous optical measurements of B–X oscillator strengths were 300 mÅ (Lee & Guest 1981) and 130 mÅ (Eidelsberg et al. 1991). Various experimental and analytical strategies can be used to minimize, or correct for, instrumental effects in an absorption measurement. However, there are unavoidable uncertainties associated with extracting f-values from low-resolution absorption measurements, and these uncertainties increase with decreasing instrumental resolving power. In practice, to avoid significant instrumental effects in an absorption measurement, the instrument should be capable of resolving the actual line shapes. This requires an instrumental resolution narrower than the FWHM of the absorbing features. The absorption measurements described in this paper were carried out with a tunable VUV laser system with a resolution of ~ 0.14 cm^{-1} FWHM (at 115 nm), less than the Doppler width of the B–X rotational lines. Residual instrumental effects were treated by least-squares–fitting the measured absorption profiles to Doppler-broadened CO line profiles convolved in transmission with a Gaussian instrument profile.

2. EXPERIMENTAL PROCEDURE

Photoabsorption cross section measurements were made of individual rotational lines in the CO $B(0)$–$X(0)$ and $B(1)$–$X(0)$ bands at 115 and 112 nm, respectively. The experimental apparatus was similar to that used in our earlier study of the high-v' bands of the CO $A\ ^1\Pi$–$X\ ^1\Sigma^+$ ($v'' = 0$) system and has been described in detail by Stark et al. (1998). Briefly, VUV radiation was produced by a narrow-bandwidth, tunable laser system (England, Lewis, & Ginter 1995; England et al. 1996). A Lambda-Physik EMG202 XeCl excimer laser (308 nm, 450 mJ per pulse) was used to pump a Lambda-Physik FL2002 dye laser (p-terphenyl in dioxane) equipped with an intracavity etalon. The near-UV output of the dye laser (337–345 nm) was focused into a cell containing Kr, at pressures ranging from 40 to 100 torr, to generate third-harmonic radiation (Mahon et al. 1979). Radiation from the tripling cell was passed through a 0.2 m monochromator to remove the fundamental near-UV radiation. The bandwidth of the resulting VUV radiation was found to be ~ 0.14 cm^{-1} FWHM (~ 1.8 mÅ at 115 nm) via fits to the absorption-line shapes of individual Doppler-broadened CO rotational lines.

VUV radiation leaving the exit slit of the monochromator was divided into two beams with a slotted-aluminum beam splitter. The reflected beam served as a monitor of the laser intensity. The transmitted beam passed through a 10.9 cm stainless-steel absorption cell equipped with LiF windows before being detected. Both beams were detected with solar-blind photomultiplier tubes (EMR type 541; KBr photocathode). Samples of CO (Matheson 99.99%; natural isotopic abundance) were used at pressures between 0.004 and 0.700 torr, chosen to produce transmittances at line centers between 30% and 70%. Absolute CO pressures in the absorption cell were measured with a variable-capacitance manometer; cell pressures were monitored continuously during each absorption scan. All measurements were carried out at room temperature.

Output pulses from the "monitor" and "detector" photomultipliers were processed by a boxcar averaging system. The monitor and detector signals were averaged over 100 laser shots for each datum point. The laser system was stepped with a wavelength increment (in the VUV) of 0.5 mÅ; a typical scan of an individual rotational line and the adjacent continuum consisted of 40 datum points. For each datum point the averaged detector signal was divided by the averaged monitor signal to account for the shot-to-shot fluctuations inherent in the generated VUV signal. Before and after each absorption scan, empty-cell values of the monitor and detector signals were recorded; absolute cell transmittances were obtained by dividing the full-cell ratios (detector/monitor) by the empty-cell ratios for each datum point. The resulting signal-to-noise ratio in a typical absorption scan was about 40:1. The wavelength scales of the absorption scans were calibrated via the $B(0)$–$X(0)$ and $B(1)$–$X(0)$ rotational line positions of Eidelsberg et al. (1987).

The narrow-bandwidth VUV laser radiation was sometimes accompanied by a weak "quasi-continuum" associated with amplified stimulated emission (ASE) in the dye laser. This continuum radiation is comparable in its effect on an absorption measurement to the broadband scattering that is often present in a grating spectrometer. If not properly accounted for, it can lead to a systematic underestimation of line strengths. The presence and strength of any ASE were monitored in our measurements by regularly observing, at pressures of a few torr, highly saturated absorption in rotational lines of the B–X bands. In the measurement of a highly saturated line, any residual transmittance at line center can be attributed to broadband radiation. In practice, monitoring the residual transmittance in saturated B–X rotational lines provided a convenient method of minimizing the ASE level via adjustments to the dye-laser optics. The ASE level in our final set of measurements was always less than 3% of the total signal. This broadband contribution was subtracted from the monitor and detector signals before further data analysis.

3. RESULTS AND DISCUSSION

Thirty-six absorption spectra were recorded of individual rotational lines in the two B–X vibrational bands. The Beer-Lambert law was used to convert measured cell transmittances into measured photoabsorption cross sections:

$$\sigma_M(\nu) = \frac{1}{N} \ln\left[\frac{I_0(\nu)}{I(\nu)}\right], \tag{1}$$

where N is the column density of CO molecules, $I_0(\nu)$ is the incident intensity, and $I(\nu)$ is the transmitted intensity. The measured photoabsorption cross section, $\sigma_M(\nu)$, includes the effects of the laser VUV bandwidth. A least-squares fitting routine, taking into account the effects of the finite instrumental resolution on the measured absorption, was used to determine values for the "true" integrated cross section of each line and the laser VUV bandwidth, which was assumed to be described by a Gaussian. Eidelsberg et al. (1987) reported the onset of predissociation in the $B(0)$ and $B(1)$ levels of $^{12}C^{16}O$ at $J' = 37$ and $J' = 17$, respectively. To avoid uncertainties in the fitting routine associated with small but poorly constrained Lorentzian contributions to the line shapes, our measurements of predissociating rotational lines were not included in the determinations of band f-values. Because of the low pressures employed, collision-induced broadening (Stark et al. 1998) was negligible. In the

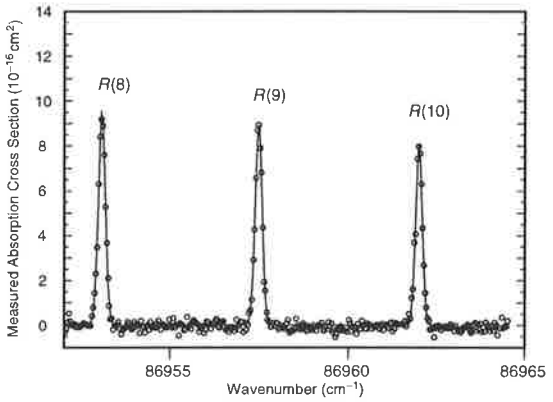

FIG. 1.—Measured photoabsorption cross section of the $R(8)$, $R(9)$, and $R(10)$ lines in the $B(0)$–$X(0)$ band, together with the modeled cross section determined by a least-squares fit. The spectrum was sampled at wavelength intervals of 0.5 mÅ (≈0.036 cm^{-1}).

fits of these lines, each feature was described by a Gaussian profile appropriate for Doppler broadening at 295 K.

The least-squares value of the laser VUV bandwidth showed a small variation for individual rotational lines within the two vibrational bands. An averaged value of this bandwidth was determined for each band and was held fixed in a subsequent iteration of the fitting routine. The resultant averaged laser VUV bandwidth was 0.14 cm^{-1} FWHM for the $B(0)$–$X(0)$ band and 0.12 cm^{-1} FWHM for the $B(1)$–$X(0)$ band. A representative photoabsorption cross section measurement, of the $R(8)$, $R(9)$, and $R(10)$ lines in the $B(0)$–$X(0)$ band, along with the modeled cross section determined by the parameters of the fit, is shown in Figure 1. An expanded view of the $R(9)$ line is shown in Figure 2, together with the fitted cross section and an indication of the fitted instrumental bandwidth.

The integrated cross sections of individual rotational lines, determined from the fitting procedure, were converted into line oscillator strengths according to

$$f_{v',J',0,J''} = \frac{1.13 \times 10^{12} \int \sigma(\nu) d\nu}{\alpha_{J''}}, \quad (2)$$

where the integrated cross section is expressed in units of cm^2 cm^{-1} and $\alpha_{J''}$ is the fractional population of molecules in the J'' rotational level as determined from an appropriately normalized Boltzmann factor (CO ground-state energy-level term values were taken from Le Floch 1991). Within the framework of the Born-Oppenheimer approximation, the relation between a rotational line oscillator strength and the corresponding vibrational band oscillator strength for a $^1\Sigma$–$^1\Sigma$ transition is (Larsson 1983)

$$f_{v',v''} = \frac{(2J'' + 1) f_{v',J',v'',J''}}{S_{J',J''}}, \quad (3)$$

where $S_{J',J''}$ is the Hönl-London factor (Herzberg 1950). For each band, a final band oscillator strength was calculated from a weighted average of the band f-values derived from individual rotational line f-values using equation (3). The $B(0)$–$X(0)$ and $B(1)$–$X(0)$ band f-values derived from measurements of individual rotational lines, and the final averaged band f-values, are displayed in Figures 3 and 4, respectively. Amiot, Roncin, & Verges (1986) reported small perturbations in the $J = 4$ and $J = 6$ rotational energies of the $B(0)$ level, with shifts of ~0.015 cm^{-1}. As can be seen in Figure 3, to within the experimental uncertainties, these perturbations have no noticeable effect on the strengths of the $R(3)$ and $R(5)$ absorption lines in the $B(0)$–$X(0)$ band. Therefore, these line oscillator strengths were included in the determination of the band f-value.

There are three contributions to the estimated fractional uncertainty in the integrated cross section of each individual line: (*a*) the fractional uncertainty in the absorbing column density of CO, ranging from ~1% for the highest pressure scans to ~8% for the lowest pressure scans; (*b*) the adopted value of the laser VUV bandwidth (a 20% change in the laser VUV bandwidth produces an ~5% change in each integrated cross section); and (*c*) the fractional uncertainty in the least-squares fitting value for the integrated cross section, typically ~2%. The total estimated fractional

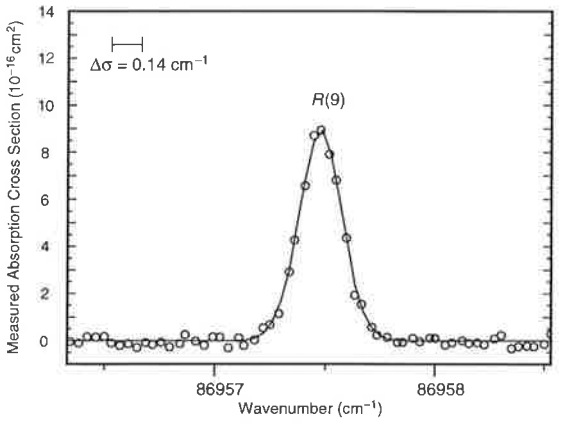

FIG. 2.—Enlargement of the fit to the $B(0)$–$X(0)$ $R(9)$ line. The instrumental resolution, determined by the fitting routine to be 0.14 cm^{-1} FWHM, is displayed in the upper left-hand corner.

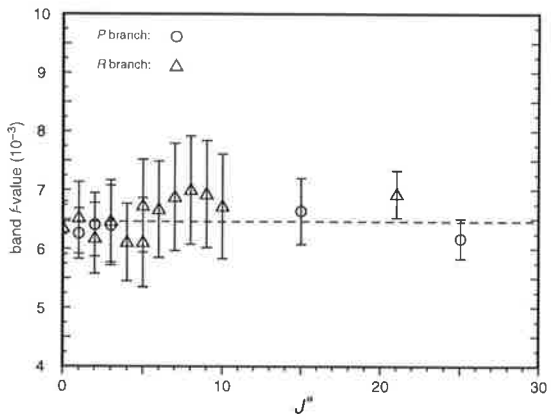

FIG. 3.—$B(0)$–$X(0)$ band f-values determined from 18 absorption spectra of individual rotational lines. The dotted line indicates the weighted average of the 18 measurements.

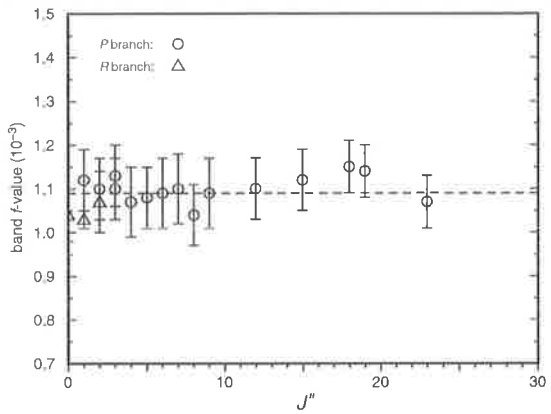

FIG. 4.—$B(1)$–$X(0)$ band f-values determined from absorption spectra of individual rotational lines. The dotted line indicates the weighted average of the measurements for $J' < 17$. The $P(18)$, $P(19)$, and $P(23)$ lines, originating from predissociating levels in the $B(1)$ state, were not included in the weighted average.

uncertainties in the integrated cross sections of individual lines, associated with the three contributions described above, vary from 6% to 12%. As can be seen in Figures 3 and 4, the scatters in the derived $B(0)$–$X(0)$ and $B(1)$–$X(0)$ band f-values are consistent with these 6%–12% uncertainties. The uncertainties in the two final, averaged band f-values are conservatively estimated to be 10%.

Our measured oscillator strengths for the $B(0)$–$X(0)$ and $B(1)$–$X(0)$ bands, as well as other published measured and calculated f-values, are presented in Table 1. Confidence in the accuracy of our measured B–X band f-values is supported by the status of our recent measurements of the CO $A(v')$–$X(0)$ band f-values (Stark et al. 1998) using the same experimental apparatus. For that band system, a consistent set of f-values has emerged: for the high-v' bands ($v' > 14$) there is agreement between the results our A–X optical measurements, the optical measurements of Jolly et al. (1997) and Eidelsberg et al. (1998), and the ab initio calculations of Spielfiedel (1998, private communication). For $11 \leq v' \leq 14$, our A–X results are also consistent with the optical measurements of Smith et al. (1994) and the electron-scattering measurements of Chan et al. (1993).

The $B(0)$–$X(0)$ band f-value derived from the low-resolution ($\Delta\lambda \approx 300$ mÅ) optical absorption measurements of Lee & Guest (1981) is approximately a factor of 3 smaller than our result. The $B(0)$–$X(0)$ and $B(1)$–$X(0)$ optical absorption measurements of Eidelsberg et al. (1991) ($\Delta\lambda \approx 130$ mÅ) are also inconsistent with our results; for both bands, the sets of measured f-values differ by about 50%, with our results being larger for each band. A scaling of the Eidelsberg et al. (1991) results by a factor of ~ 1.45 brings them into close agreement with our measured f-values. The difficulty of avoiding systematic line-saturation effects in low-resolution optical absorption measurements is a likely contributor to the discrepancies between our measured f-values and the f-values of Lee & Guest (1981) and Eidelsberg et al. (1991).

Our measured f-value for the $B(0)$–$X(0)$ band is also larger than those derived by Krishnakumar & Srivastava (1986) and by Drabbels et al. (1993) from their radiative lifetime measurements of the $B(0)$ level. However, the extraction of the $B(0)$–$X(0)$ band f-value from the radiative lifetime depends sensitively on a knowledge of the branching ratios from the $B(0)$ level. Drabbels et al. (1993) derived a $B(0) \rightarrow X(0)$ branching ratio from an analysis of radiative trapping in their measurements. An examination of Table IV in Drabbels et al. (1993) shows that there is significant disagreement in the literature regarding the $B(0)$ branching ratios. For example, the $B(0)$–$X(0)$ f-value derived by Krishnakumar & Srivastava (1986) is 35% larger than the f-value derived by Drabbels et al. (1993), while the respective radiative lifetime measurements differ by only 15%.

TABLE 1

B–X BAND f-VALUES ($\times 10^3$)[a]

Reference	$B(0)$–$X(0)$	$B(1)$–$X(0)$	$f(0, 0)/f(1, 0)$
Optical Absorption			
This work	6.5(6)	1.1(1)	5.9
Lee & Guest 1981	2.4(4)	...	...
Eidelsberg et al. 1991	4.52	0.72	6.3
Electron Energy Loss			
Lassettre & Skerbele 1971	15(3)	2.0(4)	7.6
Chan et al. 1993	8.03(41)	1.32(7)	6.1
Kanik et al. 1995	11.5(30)	...	...
Zhong et al. 1997	5.98(93)	...	...
Radiative Lifetime			
Krishnakumar & Srivastava 1986	5.2(4)	...	...
Drabbels et al. 1993	3.77(18)	...	...
Calculations			
Kirby & Cooper 1989	2.1	0.30	7.0
Chantranupong et al. 1992	5.08	0.52	9.8
Tchang-Brillet et al. 1992	...	...	6.7
Rocha et al. 1998	4.8	0.43	11.2

[a] Uncertainties in parentheses are in units of the last quoted decimal place.

The recent electron energy-loss measurements of Zhong et al. (1997) are consistent, within the stated uncertainties, with our measured f-value for the $B(0)$–$X(0)$ band. The electron-impact results of Chan et al. (1993) for the $B(0)$–$X(0)$ and $B(1)$–$X(0)$ bands are marginally inconsistent with our measured f-values, being about 15%–20% higher. The early electron-impact results of Lassettre & Skerbele (1971) and the recent electron-impact results of Kanik et al. (1995) are inconsistent with our measured f-values; it seems unlikely that our results can be reconciled with the results of these authors.

Our measured B–X f-values are significantly larger, by more than a factor of 3, than those derived from the ab initio calculations of Kirby & Cooper (1989), who stated that their calculations may have an uncertainty of as much as a factor of two. However, the $[B(0)$–$X(0)]/[B(1)$–$X(0)]$ f-value ratio calculated by Kirby & Cooper (1989), $\sim 7:1$, is in close accord with our measured f-value ratio of $\sim 6:1$. Our measured f-values are also larger than the calculated values of Chantranupong et al. (1992) and Rocha et al. (1998). In addition, both of these calculations predict an f-value ratio of $\sim 10:1$, significantly larger than our measured f-value ratio or that implied by any other published laboratory measurements. As pointed out by Eidelsberg et al. (1991) and Tchang-Brillet et al. (1992), calculated B–X f-values are sensitively dependent on the degree of mixing between the $B\ ^1\Sigma^+$ Rydberg state and the $D'\ ^1\Sigma^+$ valence state; this may explain the relatively large discrepancies between the measured and calculated B–X f-values. Tchang-Brillet et al. (1992) developed a semiempirical close-coupling model of the strong B–D' Rydberg-valence interaction that gives a 6.7:1 $[B(0)$–$X(0)]/[B(1)$–$X(0)]$ f-value ratio, much closer to the experimental result.

4. CONCLUSIONS

The oscillator strengths of the $^{12}C^{16}O$ $B(0)$–$X(0)$ and $B(1)$–$X(0)$ bands have been determined to be $(6.5 \pm 0.6) \times 10^{-3}$ and $(1.1 \pm 0.1) \times 10^{-3}$, respectively, from optical absorption measurements performed with a narrow-bandwidth tunable VUV laser system. Photoabsorption cross sections of 36 individual rotational lines in the two bands were measured with an instrumental bandwidth of ~ 0.14 cm^{-1} FWHM, narrower than the width of the Doppler-broadened CO lines (FWHM ≈ 0.20 cm^{-1}). Our measurements represent an approximate 70-fold increase in resolving power over previous optical absorption f-value measurements of the B–X bands.

We thank W. H. Parkinson and Peter L. Smith for useful discussions, and K. J. Lonsdale and C. J. Dedman for valuable technical assistance. G. S. gratefully acknowledges the support and hospitality of the Ultraviolet Physics Unit, Atomic and Molecular Physics Laboratories, at the Research School of Physical Sciences and Engineering, Australian National University, during his appointment as a Visiting Fellow. This project was supported in part by an NSF International Opportunities for Scientists and Engineers Program grant, INT-9513350, and by NASA grant NAG5-4348.

REFERENCES

Amiot, C., Roncin, J.-Y., & Verges, J. 1986, J. Phys. B, 19, L19
Baker, J., Tchang-Brillet, W.-U. L., & Julienne, P. S. 1995, J. Chem. Phys., 102, 3956
Chan, W. F., Cooper, G., & Brion, C. E. 1993, Chem. Phys., 170, 123
Chantranupong, L., Bhanuprakash, K., Honigmann, M., Hirsch, G., & Buenker, R. J. 1992, Chem. Phys., 161, 351
Drabbels, M., Meerts, W. L., & ter Meulen, J. J. 1993, J. Chem. Phys., 99, 2352
Eidelsberg, M., Roncin, J.-Y., Le Floch, A., Launay, F., Letezelter, C., & Rostas, J. 1987, J. Mol. Spectrosc., 121, 309
Eidelsberg, M., Benayound, J. J., Viala, Y., & Rostas, F. 1991, A&AS, 90, 231
Eidelsberg, M., Jolly, A., Lemaire, J. L., Tchang-Brillet, W.-U. L., Breton, J., & Rostas, F. 1998, A&A, in press
England, J. P., Lewis, B. R., Gibson, S. T., & Ginter, M. L. 1996, J. Chem. Phys., 104, 2765
England, J. P., Lewis, B. R., & Ginter, M. L. 1995, J. Chem. Phys., 103, 1727
Herzberg, G. 1950, Molecular Spectra and Molecular Structure (New York: Van Nostrand Reinhold)
Hudson, R. D. 1971, Rev. Geophys., 9, 305
Jolly, A., Lemaire, J. L., Belle-Oudry, D., Edwards, S., Malmasson, D., Vient, A., & Rostas, F. 1997, J. Phys. B, 30, 4315
Kanik, I., James, G. K., & Ajello, J. M. 1995, Phys. Rev. A, 51, 2067
Kirby, K., & Cooper, D. L. 1989, J. Chem. Phys., 90, 4895
Krishnakumar, E., & Srivastava, S. K. 1986, ApJ, 307, 795
Larsson, M. 1983, A&A, 128, 291
Lassettre, E. N., & Skerbele, A. 1971, J. Chem. Phys., 54, 1597
Lee, L. C., & Guest, J. A. 1981, J. Phys. B, 14, 3415
Le Floch, A. 1991, Mol. Phys., 72, 133
Mahon, R., McIlrath, T. J., Myerscough, V. P., & Koopman, D. W. 1979, IEEE J. Quantum Electron., 15, 444
Morton, D. C., & Noreau, L. 1994, ApJS, 95, 301
Rocha, A. B., Borges, I., & Bielschowsky, C. E. 1998, Phys. Rev. A, 57, 4394
Sheffer, Y., Federman, S. R., Lambert, D. L., & Cardelli, J. R. 1992, ApJ, 397, 482
Smith, P. L., Stark, G., Yoshino, K., & Ito, K. 1994, ApJ, 431, L143
Stark, G., Yoshino, K., Smith, P. L., Ito, K., & Parkinson, W. H. 1991, ApJ, 369, 574
Stark, G., Lewis, B. R., Gibson, S. T., & England, J. P. 1998, ApJ, 505, 452
Tchang-Brillet, W.-U. L., Julienne, P. S., Robbe, J.-M., Letzelter, C., & Rostas, F. 1992, J. Chem. Phys., 96, 6735
Wannier, P. G., Penzias, A. A., & Jenkins, E. B. 1982, ApJ, 254, 100
Zhong, Z. P., Feng, R. F., Xu, K. Z., Wu, S. L., Zhu, L. F., Zhang, X. J., Ji, Q., & Shi, Q. C. 1997, Phys. Rev. A, 55, 1799

4.41 Relations between Rydberg-valence interactions in the O_2 molecule

[62] B. R. Lewis, S. T. Gibson, S. S. Banerjee, and H. Lefebvre-Brion, *Journal of Chemical Physics* **113**, 2214–2223 (2000).

Relations between Rydberg-valence interactions in the O_2 molecule

B. R. Lewis, S. T. Gibson, and S. S. Banerjee
Research School of Physical Sciences and Engineering, The Australian National University, Canberra, ACT 0200, Australia

H. Lefebvre-Brion
Laboratoire de Photophysique Moléculaire, Bâtiment 213, Université de Paris-Sud, 91405 Orsay Cedex, France

(Received 7 March 2000; accepted 12 May 2000)

Using a single-configuration formulation, analytical expressions are derived for the $(X\,^2\Pi_g)\,ns\sigma_g$, $np\pi_u$, and $np\sigma_u$ Rydberg-valence interaction matrix elements in O_2. In addition, new results from diabatic, coupled-channel deperturbations of experimental data dependent on these interactions are reported for $n=3$ and 4. Using these results, the large differences in magnitude between the Rydberg-valence couplings for the constituent states of the $np\pi_u$ Rydberg complex that are predicted by the analytical expressions are verified experimentally. Effective values for several two-electron integrals are obtained semiempirically through comparison between analytical expressions and deperturbed experimental values for the Rydberg-state energies and Rydberg-valence couplings, allowing predictions to be made for the spectroscopy of the $np\pi_u\,^1\Sigma_u^-$ Rydberg states which have yet to be observed. © *2000 American Institute of Physics.* [S0021-9606(00)31530-6]

I. INTRODUCTION

Interactions between isosymmetric Rydberg and valence molecular electronic states occurring in the same energy region are responsible for a wide range of interesting spectral phenomena, including perturbations, predissociations, lineshape asymmetries, and intensity quantum-interference effects. The magnitudes of such Rydberg-valence interactions vary from small, where a *diabatic* picture is appropriate, through intermediate, to large, where an *adiabatic* picture applies and strongly avoided crossings occur between the pure Rydberg and valence states.

O_2 is one of the few molecules for which Rydberg-valence interactions have been extensively studied, both theoretically and experimentally. However, there have been no comprehensive studies of the relations between the interactions involving states of different symmetries associated with the various series of $nl\lambda$ Rydberg complexes converging on the $X\,^2\Pi_g$ state of O_2^+. *Ab initio* studies of the Rydberg-valence interactions in O_2 have been performed for the $3s\sigma_g\,^1\Pi_g$;[1] $3s\sigma_g$ and $4s\sigma_g\,^3\Pi_g$;[1,2] $3p\sigma_u$ and $4p\sigma_u\,^1\Pi_u$;[3] $3p\sigma_u$ and $4p\sigma_u\,^3\Pi_u$;[3,4] $3p\pi_u$ to $6p\pi_u\,^3\Sigma_u^-$;[4–8] $3p\pi_u$, $4p\pi_u$, $6p\pi_u$ and $7p\pi_u\,^1\Sigma_u^+$;[5,6,9] $3p\pi_u$ to $7p\pi_u\,^1\Delta_u$;[3,5,6] and $3p\pi_u\,^3\Delta_u$ states.[4] In addition, analyses of experimental spectra using effective-parameter, diabatic-basis theoretical treatments of the Rydberg-valence interactions have yielded semiempirical estimates of the interaction matrix elements for the $3s\sigma_g$ and $4s\sigma_g\,^1\Pi_g$,[10,11] $3s\sigma_g$ and $4s\sigma_g\,^3\Pi_g$,[11–14] $3p\pi_u\,^3\Sigma_u^-$,[15–17] and $3p\sigma_u$ to $6p\sigma_u\,^3\Pi_u$ states.[18] These estimates have resulted from the use of both perturbative[10,12,14] and coupled-channel[11,13,15–18] methods.

Two types of Rydberg-valence mixing can be described in terms of the single-configuration approximation.[19] First, in case (1), the configurations of the Rydberg and valence states differ by two orbitals. This is the case in O_2 for valence states of the $\cdots(1\pi_u)^3(1\pi_g)^3$ molecular-orbital configuration[20] and Rydberg states of the $\cdots(1\pi_u)^4(1\pi_g)(np\pi_u)$ configuration, shown schematically in a diabatic representation in Fig. 1(a), and also for the $\cdots(3\sigma_g)(1\pi_u)^4(1\pi_g)^3$ valence and $\cdots(3\sigma_g)^2(1\pi_u)^4(1\pi_g)(ns\sigma_g)$ Rydberg states, shown in Fig. 1(b). Second, in case (2), the configurations of the Rydberg and valence states differ by only one orbital. This is the case in O_2 for the $\cdots(1\pi_u)^4(1\pi_g)(np\sigma_u)$ Rydberg and $\cdots(1\pi_u)^4(1\pi_g)(3\sigma_u)$ valence states, shown in Fig. 1(c), which differ only in the last orbital.

In this work, we present analytical expressions for the $ns\sigma_g$, $np\pi_u$, and $np\sigma_u$ Rydberg-valence interaction matrix elements in O_2, based on a single-configuration formulation. New results from semiempirical, coupled-channel analyses of experimental spectra are also presented and compared with these expressions, other semiempirical data, and *ab initio* calculations. Finally, predictions are made for the spectroscopy of the $np\pi_u\,^1\Sigma_u^-$ Rydberg states which have yet to be observed.

II. THE SINGLE-CONFIGURATION APPROXIMATION

A. Rydberg energies

The single-configuration approximation has often been applied to the calculation of Rydberg states, in particular using the method pioneered by Lefebvre-Brion and Moser[21] (see also Ref. 22) and later used by Hunt and Goddard[23] under the improved virtual orbital (IVO) name. If the Rydberg states arising from the $\pi_g\,np\pi_u$ configuration are represented in the single-configuration approximation and if the

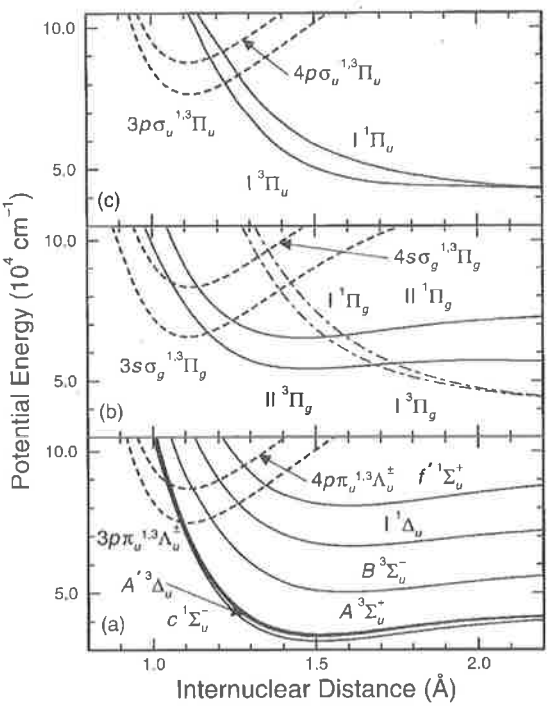

FIG. 1. Schematic diabatic potential-energy curves for the lower members of the ns and np Rydberg series converging on the $X\,{}^2\Pi_g$ state of O_2^+ (dashed lines), together with those for the interacting valence states (solid lines). The energy scale is referenced to the minimum in the $X\,{}^3\Sigma_g^-$ potential-energy curve (not shown) and the closely spaced constituent states of each Rydberg complex are represented by a single curve. (a) The $\cdots(1\pi_u)^3(1\pi_g)^3\,{}^{1,3}\Lambda_u^{\pm}$ valence and $\cdots(1\pi_u)^4(1\pi_g)(np\pi_u)\,{}^{1,3}\Lambda_u^{\pm}$ Rydberg states for $n=3$ and 4 (${}^{1,3}\Lambda_u^{\pm}={}^{1,3}\Sigma_u^{\pm},{}^{1,3}\Delta_u$). (b) The $\cdots(3\sigma_g)\times(1\pi_u)^4(1\pi_g)^3\,{}^{1,3}\Pi_g$ valence and $\cdots(3\sigma_g)^2(1\pi_u)^4(1\pi_g)(ns\sigma_g)\,{}^{1,3}\Pi_g$ Rydberg states for $n=3$ and 4. The $\cdots(3\sigma_g)^2(1\pi_u)^3(1\pi_g)^2(3\sigma_u)\,{}^{1,3}\Pi_g$ valence states are also indicated (dotted–dashed lines). (c) The $\cdots(1\pi_g)\times(3\sigma_u)\,{}^{1,3}\Pi_u$ valence and $\cdots(1\pi_g)(np\sigma_u)\,{}^{1,3}\Pi_u$ Rydberg states for $n=3$ and 4.

same orbitals are used for each of the states, the relative energies of these states are given by the Recknagel expressions:[24]

$$E({}^1\Sigma_u^-)=E-J^{(2)}+K^{(2)}, \tag{1a}$$

$$E({}^3\Delta_u)=E, \tag{1b}$$

$$E({}^3\Sigma_u^+)=E+J^{(2)}-K^{(2)}, \tag{1c}$$

$$E({}^3\Sigma_u^-)=E+2K^{(0)}-J^{(2)}-K^{(2)}, \tag{1d}$$

$$E({}^1\Delta_u)=E+2K^{(0)}, \tag{1e}$$

$$E({}^1\Sigma_u^+)=E+2K^{(0)}+J^{(2)}+K^{(2)}, \tag{1f}$$

where the exchange (K) and direct (J) integrals are given by

$$K^{(0)}=\int \pi_g^{+*}(1)np\pi_u^+(1)\frac{e^2}{r_{12}}np\pi_u^{-*}(2)\pi_g^-(2)d\tau_1\,d\tau_2, \tag{2a}$$

$$K^{(2)}=\int \pi_g^{+*}(1)np\pi_u^-(1)\frac{e^2}{r_{12}}np\pi_u^{-*}(2)\pi_g^+(2)d\tau_1\,d\tau_2, \tag{2b}$$

$$J^{(2)}=\int \pi_g^{+*}(1)\pi_g^-(1)\frac{e^2}{r_{12}}np\pi_u^{-*}(2)np\pi_u^+(2)d\tau_1\,d\tau_2. \tag{2c}$$

The magnitudes of these integrals depend on the atomic basis set used in the self-consistent calculations, but they are expected to be in the order $K^{(0)}>J^{(2)}>K^{(2)}$.

Diabatic observed values, i.e., deperturbed experimental values for the energies of the Rydberg states, can be fitted to the Recknagel expressions [Eq. (1)] and effective values for the integrals obtained. If one of the states has not been observed, knowledge of these integrals derived from the energies of the other states allows a value for its energy to be predicted semiempirically.

For the other Rydberg states treated in this paper, i.e., the ${}^{1,3}\Pi$ states arising from the $\pi_g ns\sigma_g$ and $\pi_g np\sigma_u$ configurations, the single-configuration approximation leads to the well-known expression

$$E({}^3\Pi)=E({}^1\Pi)-2K^{(0)}_{\pi_g,np\sigma}. \tag{3}$$

B. Rydberg-valence interactions

Using the single-configuration approximation for both the Rydberg and valence states, analytical expressions for the Rydberg-valence couplings can be obtained from the wave functions given in Table I in the form of the diagonals of the relevant determinants.

The electrostatic interactions between valence and Rydberg states of the same symmetry with the configurations $\cdots(1\pi_u)^3(1\pi_g)^3$ and $\cdots(1\pi_u)^4(1\pi_g)(np\pi_u)$, respectively, wave functions for which are given in the first part of Table I, can be expressed in terms of the two-electron integrals

$$M^{(0)}=\int \pi_u^{+*}(1)\pi_g^+(1)\frac{e^2}{r_{12}}np\pi_u^{-*}(2)\pi_g^-(2)d\tau_1\,d\tau_2, \tag{4a}$$

$$M^{(2)}=\int \pi_u^{+*}(1)\pi_g^-(1)\frac{e^2}{r_{12}}np\pi_u^{-*}(2)\pi_g^+(2)d\tau_1\,d\tau_2. \tag{4b}$$

These integrals have the same sign and $|M^{(0)}|>|M^{(2)}|$. Resulting expressions for the Rydberg-valence coupling matrix elements $H^{\rm cl}({}^{1,3}\Lambda_u^{\pm})=\langle\pi_u^3\pi_g^3\,{}^{1,3}\Lambda_u^{\pm}|\mathbf{H}^{\rm cl}|\pi_g\,np\pi_u\,{}^{1,3}\Lambda_u^{\pm}\rangle$ are

$$H^{\rm cl}({}^1\Sigma_u^-)=-2M^{(2)}=2H^{\rm cl}({}^3\Delta_u), \tag{5a}$$

$$H^{\rm cl}({}^3\Sigma_u^+)=0, \tag{5b}$$

$$H^{\rm cl}({}^3\Sigma_u^-)=2M^{(0)}, \tag{5c}$$

$$H^{\rm cl}({}^1\Delta_u)=2M^{(0)}-M^{(2)}, \tag{5d}$$

$$H^{\rm cl}({}^1\Sigma_u^+)=-2M^{(0)}+2M^{(2)}. \tag{5e}$$

As in the case of the two-electron integrals involved in the Recknagel energy expressions of Sec. II A, effective values for $|M^{(0)}|$ and $|M^{(2)}|$ can be obtained semiempirically through a comparison between the Rydberg-valence cou-

TABLE I. Electronic wave functions for interacting valence and Rydberg states of O_2 ($\Sigma=0$).[a]

Symmetry	Character	Ω	Wave function
$^3\Sigma_u^-$	Valence	0	$\frac{1}{2}\{\lvert\pi_u^+\alpha\,\pi_u^+\beta\,\pi_g^-\alpha\,\pi_g^-\beta[\pi_u^-\pi_g^+(\alpha\beta+\beta\alpha)]\rvert$ $-\lvert\pi_u^+\alpha\,\pi_u^-\beta\,\pi_g^+\alpha\,\pi_g^-\beta[\pi_u^+\pi_g^-(\alpha\beta+\beta\alpha)]\rvert\}$
	Rydberg	0	$\frac{1}{2}\{\lvert\pi_u^+\alpha\,\pi_u^+\beta\,\pi_u^-\alpha\,\pi_u^-\beta[\pi_g^+np\pi_u^-(\alpha\beta+\beta\alpha)]\rvert$ $-\lvert\pi_u^+\alpha\,\pi_u^+\beta\,\pi_u^-\alpha\,\pi_u^-\beta[\pi_g^-np\pi_u^+(\alpha\beta+\beta\alpha)]\rvert\}$
$^1\Sigma_u^+$	Valence	0	$\frac{1}{2}\{\lvert\pi_u^+\alpha\,\pi_u^+\beta\,\pi_g^-\alpha\,\pi_g^-\beta[\pi_u^-\pi_g^+(\alpha\beta-\beta\alpha)]\rvert$ $+\lvert\pi_u^-\alpha\,\pi_u^-\beta\,\pi_g^+\alpha\,\pi_g^+\beta[\pi_u^+\pi_g^-(\alpha\beta-\beta\alpha)]\rvert\}$
	Rydberg	0	$\frac{1}{2}\{\lvert\pi_u^+\alpha\,\pi_u^+\beta\,\pi_u^-\alpha\,\pi_u^-\beta[\pi_g^+np\pi_u^-(\alpha\beta-\beta\alpha)]\rvert$ $+\lvert\pi_u^+\alpha\,\pi_u^+\beta\,\pi_u^-\alpha\,\pi_u^-\beta[\pi_g^-np\pi_u^+(\alpha\beta-\beta\alpha)]\rvert\}$
$^3\Sigma_u^+$	Valence	0	$\frac{1}{2}\{\lvert\pi_u^+\alpha\,\pi_u^+\beta\,\pi_g^-\alpha\,\pi_g^-\beta[\pi_u^-\pi_g^+(\alpha\beta+\beta\alpha)]\rvert$ $+\lvert\pi_u^-\alpha\,\pi_u^-\beta\,\pi_g^+\alpha\,\pi_g^+\beta[\pi_u^+\pi_g^-(\alpha\beta+\beta\alpha)]\rvert\}$
	Rydberg	0	$\frac{1}{2}\{\lvert\pi_u^+\alpha\,\pi_u^+\beta\,\pi_u^-\alpha\,\pi_u^-\beta[\pi_g^+np\pi_u^-(\alpha\beta+\beta\alpha)]\rvert$ $+\lvert\pi_u^+\alpha\,\pi_u^+\beta\,\pi_u^-\alpha\,\pi_u^-\beta[\pi_g^-np\pi_u^+(\alpha\beta+\beta\alpha)]\rvert\}$
$^1\Sigma_u^-$	Valence	0	$\frac{1}{2}\{\lvert\pi_u^+\alpha\,\pi_u^+\beta\,\pi_g^-\alpha\,\pi_g^-\beta[\pi_u^-\pi_g^+(\alpha\beta-\beta\alpha)]\rvert$ $-\lvert\pi_u^+\alpha\,\pi_u^-\beta\,\pi_g^+\alpha\,\pi_g^+\beta[\pi_u^+\pi_g^-(\alpha\beta-\beta\alpha)]\rvert\}$
	Rydberg	0	$\frac{1}{2}\{\lvert\pi_u^+\alpha\,\pi_u^+\beta\,\pi_u^-\alpha\,\pi_u^-\beta[\pi_g^+np\pi_u^-(\alpha\beta-\beta\alpha)]\rvert$ $-\lvert\pi_u^+\alpha\,\pi_u^+\beta\,\pi_u^-\alpha\,\pi_u^-\beta[\pi_g^-np\pi_u^+(\alpha\beta-\beta\alpha)]\rvert\}$
$^3\Delta_u$	Valence	2	$\frac{1}{\sqrt{2}}\lvert\pi_u^+\alpha\,\pi_u^+\beta\,\pi_g^+\alpha\,\pi_g^+\beta[\pi_u^-\pi_g^-(\alpha\beta+\beta\alpha)]\rvert$
	Rydberg	2	$\frac{1}{\sqrt{2}}\lvert\pi_u^+\alpha\,\pi_u^+\beta\,\pi_u^-\alpha\,\pi_u^-\beta[\pi_g^+np\pi_u^+(\alpha\beta+\beta\alpha)]\rvert$
$^1\Delta_u$	Valence	2	$\frac{1}{\sqrt{2}}\lvert\pi_u^+\alpha\,\pi_u^+\beta\,\pi_g^+\alpha\,\pi_g^+\beta[\pi_u^-\pi_g^-(\alpha\beta-\beta\alpha)]\rvert$
	Rydberg	2	$\frac{1}{\sqrt{2}}\lvert\pi_u^+\alpha\,\pi_u^+\beta\,\pi_u^-\alpha\,\pi_u^-\beta[\pi_g^+np\pi_u^+(\alpha\beta-\beta\alpha)]\rvert$
$^3\Pi_g$	Valence	1	$\frac{1}{\sqrt{2}}\lvert 1\pi_g^+\alpha\,1\pi_g^+\beta[3\sigma_g\,1\pi_g^-(\alpha\beta+\beta\alpha)]\rvert$
	Rydberg	1	$\frac{1}{\sqrt{2}}\lvert 3\sigma_g\alpha\,3\sigma_g\beta[1\pi_g^+ns\sigma_g(\alpha\beta+\beta\alpha)]\rvert$
$^1\Pi_g$	Valence	1	$\frac{1}{\sqrt{2}}\lvert 1\pi_g^+\alpha\,1\pi_g^+\beta[3\sigma_g\,1\pi_g^-(\alpha\beta-\beta\alpha)]\rvert$
	Rydberg	1	$\frac{1}{\sqrt{2}}\lvert 3\sigma_g\alpha\,3\sigma_g\beta[1\pi_g^+ns\sigma_g(\alpha\beta-\beta\alpha)]\rvert$
$^3\Pi_u$	Valence	1	$\frac{1}{\sqrt{2}}\lvert 1\pi_g^+\,3\sigma_u(\alpha\beta+\beta\alpha)\rvert$
	Rydberg	1	$\frac{1}{\sqrt{2}}\lvert 1\pi_g^+\,np\sigma_u(\alpha\beta+\beta\alpha)\rvert$
$^1\Pi_u$	Valence	1	$\frac{1}{\sqrt{2}}\lvert 1\pi_g^+\,3\sigma_u(\alpha\beta-\beta\alpha)\rvert$
	Rydberg	1	$\frac{1}{\sqrt{2}}\lvert 1\pi_g^+\,np\sigma_u(\alpha\beta-\beta\alpha)\rvert$

[a]The determinantal wave functions use the notation of Ref. 19 for the spatial and spin parts of the one-electron orbitals.

pling expressions of Eq. (5) and diabatic observed values, obtained, e.g., using a coupled-channel analysis of experimental spectra.

The $^{1,3}\Pi_g$ states of O_2 provide another example of an interaction between Rydberg and valence states which differ by two orbitals. Wave functions for the Rydberg state with the configuration $\cdots(3\sigma_g)^2(1\pi_u)^4(1\pi_g)(ns\sigma_g)$ and the valence state with the configuration $\cdots(3\sigma_g)(1\pi_u)^4(1\pi_g)^3$ are given in the second part of Table I. The matrix elements for the electrostatic interactions between these valence and Rydberg states, expressed in terms of the integral

$$M=\int 3\sigma_g(1)1\pi_g^-(1)\frac{e^2}{r_{12}}ns\sigma_g(2)1\pi_g^+(2)d\tau_1\,d\tau_2, \tag{6}$$

are given by

$$H^{\mathrm{el}}(^1\Pi_g)=-H^{\mathrm{el}}(^3\Pi_g)=M. \tag{7}$$

In the case of configurations which differ by only one orbital, it is well known that, if the orbitals are solutions of the self-consistent Hamiltonian, the interaction between the states is exactly zero, corresponding to an interaction between monoexcited configurations (Brillouin's theorem).

The diabatic, or crossing, potentials must be defined in a lower-order approximation, assuming that the orbitals are not the self-consistent orbitals. The interaction matrix element is then nonzero. In this approximation, the couplings between the $\cdots(1\pi_u)^4(1\pi_g)(3p\sigma_u)$ Rydberg and $\cdots(1\pi_u)^4(1\pi_g)\times(3\sigma_u)$ valence $^{1,3}\Pi_u$ states obey the relation:

$$H^{el}(^3\Pi_u) = H^{el}(^1\Pi_u) - 2M', \tag{8}$$

where

$$M' = \int 1\pi_g^+{}^*(1)3\sigma_u(1)\frac{e^2}{r_{12}}np\sigma_u(2)1\pi_g^+(2)d\tau_1\, d\tau_2. \tag{9}$$

All quantities in Eq. (8) have the same sign with $|M'| \ll |H^{el}(^{1,3}\Pi_u)|$. The relation expressed in Eq. (8) can be understood by analogy, since, when the σ_u orbitals in Eq. (9) are identical, Eq. (8) represents the energy and it is well known that the energy of the triplet state is lower than that of the singlet state by just twice the exchange integral [see Eq. (3)].

C. Isoconfigurational spin–orbit interactions

Single-configuration estimates of the spin–orbit interaction are generally very good.[19] Using the electronic wave functions of Table I, together with the one-electron microscopic form of the spin–orbit operator $\mathbf{H}^{so} = \Sigma_i \hat{a}_i \mathbf{l}_i \cdot \mathbf{s}_i$, the isoconfigurational spin–orbit interactions can be deduced both for the Rydberg and for the valence states of interest to this work.

For both the $\pi_g np\sigma_u$ Rydberg and $\pi_g 3\sigma_u$ valence states, it follows that[25]

$$\langle ^3\Pi_{u1}|\mathbf{H}^{so}|^1\Pi_{u1}\rangle = a_{\pi_g}/2 = \langle ^3\Pi_{u2}|\mathbf{H}^{so}|^3\Pi_{u2}\rangle = A(^3\Pi_u), \tag{10}$$

where $a_{\pi_g} = \langle \pi_g|\hat{a}|\pi_g\rangle > 0$ is a single-electron integral expected to be roughly similar in magnitude to the atomic spin–orbit parameter $\zeta_O(2p) = 151\ cm^{-1}$, and $A(^3\Pi_u)$ is the diagonal spin–orbit constant. Since $A(^3\Pi_u)$ for the Rydberg state is known experimentally ($\approx 95\ cm^{-1}$),[18] single-configuration values for a_{π_g}, and all spin–orbit matrix elements expressible in terms of a_{π_g}, may be obtained easily. Similarly, for the $\pi_g ns\sigma_g$ Rydberg and $3\sigma_g\,\pi_g^3$ valence states,

$$\langle ^3\Pi_{g1}|\mathbf{H}^{so}|^1\Pi_{g1}\rangle = a_{\pi_g}/2 = \pm A(^3\Pi_g), \tag{11}$$

where the upper sign applies to the Rydberg state, the lower to the inverted valence state.

For the $\pi_g np\pi_u$ Rydberg states, we have

$$\langle ^3\Sigma_{u1}^-|\mathbf{H}^{so}|^3\Sigma_{u1}^+\rangle = (a_{\pi_g} - a_{np\pi_u})/2 \approx a_{\pi_g}/2, \tag{12a}$$

$$\langle ^3\Delta_{u2}|\mathbf{H}^{so}|^1\Delta_{u2}\rangle = (a_{\pi_g} - a_{np\pi_u})/2 \approx a_{\pi_g}/2, \tag{12b}$$

$$\langle ^3\Sigma_{u0}^{\pm}|\mathbf{H}^{so}|^1\Sigma_{u0}^{\mp}\rangle = (a_{\pi_g} + a_{np\pi_u})/2 \approx a_{\pi_g}/2, \tag{12c}$$

$$\langle ^3\Delta_{u3}|\mathbf{H}^{so}|^3\Delta_{u3}\rangle = (a_{\pi_g} + a_{np\pi_u})/2 = 2A(^3\Delta_u) \approx a_{\pi_g}/2. \tag{12d}$$

Since the operator $\mathbf{H}^{so}$ varies as $1/r_k^3$, where r_k represents the distance from an electron to the kth nucleus, $a_{np\pi_u}$ for the diffuse Rydberg orbital is relatively small compared with a_{π_g}, leading to the final approximations in Eq. (12). Similar expressions have been given in Ref. 26.

For the $\pi_u^3\pi_g^3$ valence states, it follows that

$$\langle ^3\Sigma_{u1}^-|\mathbf{H}^{so}|^3\Sigma_{u1}^+\rangle = (a_{\pi_g} - a_{\pi_u})/2 \approx 0, \tag{13a}$$

$$\langle ^3\Delta_{u2}|\mathbf{H}^{so}|^1\Delta_{u2}\rangle = (a_{\pi_g} - a_{\pi_u})/2 \approx 0, \tag{13b}$$

$$\langle ^3\Sigma_{u0}^{\pm}|\mathbf{H}^{so}|^1\Sigma_{u0}^{\mp}\rangle = -(a_{\pi_g} + a_{\pi_u})/2 \approx -a_{\pi_g}, \tag{13c}$$

$$\langle ^3\Delta_{u3}|\mathbf{H}^{so}|^3\Delta_{u3}\rangle = -(a_{\pi_g} + a_{\pi_u})/2 = 2A(^3\Delta_u) \approx -a_{\pi_g}. \tag{13d}$$

For homonuclear molecules, if the molecular π orbitals are expressed as linear combinations of atomic orbitals centered on each nucleus, and the atomic overlap integral is neglected, then $a_{\pi_u} \approx a_{\pi_g}$,[19] leading to the final approximations in Eq. (13).

Finally, we note that spin–orbit interactions between the valence and Rydberg states of interest here are zero in the single-configuration approximation.

III. SEMIEMPIRICAL ANALYSIS OF EXPERIMENT

The perturbations, predissociations, and other observable effects resulting from interactions between the Rydberg and valence states depicted in Fig. 1 enable the experimental characterization of those interactions for comparison with the expressions derived in Sec. II B. In this section, we summarize a comprehensive study of Rydberg-valence interactions in O_2 which uses the coupled-channel Schrödinger equations (CSE) method[27,28] to analyze available experimental data. Detailed aspects of this study have been,[11,17,18] or will be, reported elsewhere.

Reliable CSE analyses require access to a wide range of experimental data, covering as large an energy range as possible. In the case of the $^{1,3}\Pi_g$ states, (2+1)-photon resonance-enhanced multiphoton-ionization (REMPI) spectra involving excitation from the $X\,^3\Sigma_g^-$ and $a\,^1\Delta_g$ states were employed,[14,29,30] together with kinetic energy-release spectra,[10,31] as detailed in Ref. 11. For the $^3\Pi_u$ states, single-photon spectra for absorption from the X state, measured in this[18] and other[32] laboratories, were used, together with fluorescence-excitation spectra,[33,34] in the manner described in Ref. 18. For the $^3\Sigma_u^{\pm}$ and $^1\Sigma_u^+$, states, partially analyzed in Ref. 17, X-state photoabsorption spectra measured in this laboratory were employed,[17,35–38] supplemented by spectrographic data involving excitation from the $X\,^3\Sigma_g^-$ and $b\,^1\Sigma_g^+$ states,[39,40] and fluorescence-excitation spectra.[33,34] In the case of the $^1\Pi_u$ and $^{1,3}\Delta_u$ states, the prime sources of data were a-state photoabsorption spectra measured in this[41] and other[42] laboratories, together with spectrographic data.[43] The principal quantities reduced from these spectra for comparison with the CSE calculations were vibronic energies, rotational constants, predissociation linewidths, vibronic intensities, and absolute continuum photoabsorption cross sections.

The CSE formalism employed here has been described in detail in Ref. 17. Briefly, the interacting excited states were described in a diabatic basis and the coupled-channel

radial wave function obtained by solving the corresponding coupled equations was used, together with an initial-state vibrational wave function and diabatic electronic transition moments, to calculate the photodissociation cross section appropriate for comparison with the experimental data, either directly, or through derived parameters. For all symmetries considered, at least two Rydberg states ($n=3$ and 4) were included in the diabatic basis, as were the important Rydberg-valence and spin–orbit interactions discussed in Secs. II B and II C, respectively. These off-diagonal elements were assumed to be independent of the internuclear distance R. Initial Rydberg potential-energy curves were taken to have shapes similar to that of the ionic $X\,^2\Pi_g$ curve, appropriately displaced in energy, while *ab initio* calculations[44] and experimentally based Rydberg–Klein–Rees curves were employed for the initial valence potentials. In an iterative least-squares-fitting procedure, the CSE model parameters were adjusted[45] so as to optimize agreement with experiment. The particular model parameters of interest here are the optimized Rydberg potential-energy curves, together with the optimized Rydberg-valence and spin–orbit couplings. These deperturbed diabatic parameters are appropriate for comparison with the expressions derived in Sec. II.

Results of the CSE analyses are illustrated in Fig. 2 for two extreme cases of Rydberg-valence mixing. In Fig. 2(a), final potential-energy curves are shown for the $^3\Sigma_u^+$ states. In this case, the Rydberg-valence mixing is small ($|H^{el}|=420$ cm^{-1}) and a diabatic picture is appropriate, observed energy levels of the $D\,^3\Sigma_u^+$ and $G\,^3\Sigma_u^+$ states being most closely associated with the pure $3p\pi_u$ and $4p\pi_u$ Rydberg potentials, respectively. Spin–orbit interaction between the $np\pi_u\,^3\Sigma_{u1}^+$ and $^3\Sigma_{u1}^-$ Rydberg states ($H^{so}=95$ cm^{-1}) plays an important role, providing a perturbation mechanism additional to Rydberg-valence mixing, and, through $^3\Sigma_u^-$ Rydberg-valence mixing, a competing indirect predissociation channel. In addition, in spectra involving excitation from the $X\,^3\Sigma_g^-$ state, the same spin–orbit interaction provides the mechanism for the borrowing of intensity from allowed transitions into the $^3\Sigma_u^-$ states, leading to ready observation of the forbidden $^3\Sigma_u^+\leftarrow X\,^3\Sigma_g^-$ transitions. In Fig. 2(b), final potential-energy curves are shown for the $^1\Pi_u$ states. In this case, the Rydberg-valence mixing is very large ($|H^{el}|=6700$ cm^{-1}) and the adiabatic potentials (dashed lines) differ markedly from the diabatic potentials (solid lines). An adiabatic picture is appropriate here, with the observed levels of the $g\,^1\Pi_u$ and $h\,^1\Pi_u$ states being most closely associated with the bound portion of the lower adiabatic curve, and the double-minimum upper adiabatic curve, respectively. A similar situation applies to the isoconfigurational $^3\Pi_u$ states, but, since the Rydberg-valence crossing point for the triplet lies at a smaller R value than that for the singlet [see Fig. 1(c)], in this case, the lower adiabatic potential has a shoulder, rather than a bound portion, and the outer minimum of the upper double-minimum $F\,^3\Pi_u$ adiabatic potential is deeper than the inner minimum (see Fig. 3 of Ref. 18), in contrast to the case for the $h\,^1\Pi_u$ state. Spin–orbit interaction between the $np\sigma_u\,^1\Pi_{u1}$ and $^3\Pi_{u1}$ Rydberg states ($H^{so}=95$ cm^{-1}) also produces easily observable effects, most noticeably unequal triplet splittings through perturbation of the $^3\Pi_{u1}$ component, and also the appearance of some transitions to the $^1\Pi_u$ state in ground-state spectra,[46] through intensity borrowing from the $^3\Pi_u\leftarrow X\,^3\Sigma_g^-$ transitions.

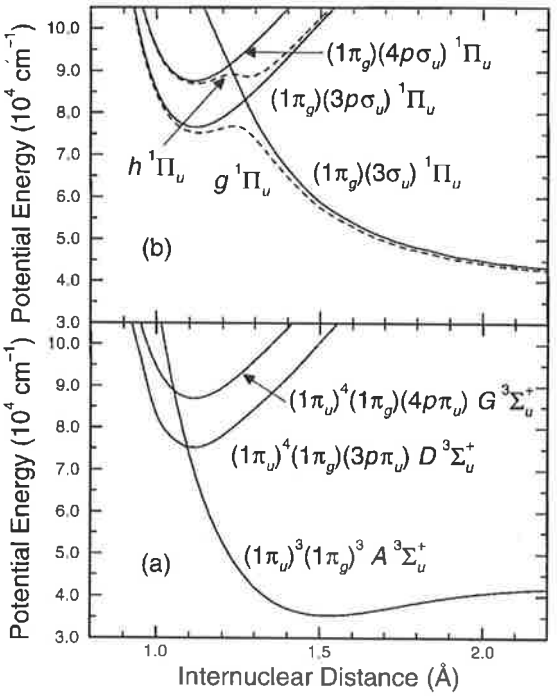

FIG. 2. Diabatic (solid lines) and adiabatic (dashed lines) potential-energy curves resulting from coupled-channel analyses of experiment for two extreme cases of Rydberg-valence interaction in O_2. The energy scale is referenced to the minimum in the $X\,^3\Sigma_g^-$ potential-energy curve. (a) The $^3\Sigma_u^+$ states. In this case, the interaction is small ($|H^{el}|=420$ cm^{-1} for $n=3$), the diabatic and adiabatic curves are indistinguishable on the scale of the figure, and a *diabatic* picture is appropriate. Observed vibrational levels of the $D\,^3\Sigma_u^+$ and $G\,^3\Sigma_u^+$ states can be associated with the diabatic $3p\pi_u$ and $4p\pi_u$ Rydberg potentials, respectively. (b) The $^1\Pi_u$ states. In this case, the interaction is large ($|H^{el}|=6700$ cm^{-1} for $n=3$), the diabatic and adiabatic curves differ greatly, and an *adiabatic* picture is appropriate. Observed vibrational levels of the $g\,^1\Pi_u$ and $h\,^1\Pi_u$ states can be associated with the bound portion of the lower adiabatic potential, and the double-minimum upper adiabatic potential, respectively.

IV. RESULTS AND DISCUSSION

A. Rydberg energies, Rydberg-valence and spin–orbit interactions

Observed diabatic energies for states from the $np\pi_u$, $ns\sigma_g$, and $np\sigma_u$ Rydberg series converging on the ground state of O_2^+, determined using the CSE analysis of experiment described in Sec. III, are summarized for $n=3$ and 4 in Table II, together with corresponding quantum defects δ and effective quantum numbers $n^*=n-\delta$ obtained using the Rydberg formula:

$$E_n=E_\infty-\frac{\mathcal{R}}{(n^*)^2}, \tag{14}$$

TABLE II. Diabatic energies, effective quantum numbers, and quantum defects for states from the $np\pi_u$, $ns\sigma_g$, and $np\sigma_u$ Rydberg series of O_2 converging on the $X\,^2\Pi_g$ state of O_2^+.[a]

		$n=3$					$n=4$				
Ryd. Orb.	Symm.	T_e(obs.)[b]	T_e(SC)[c]	T_e(IVO)[d]	n^*(obs.)	δ(obs.)	T_e(obs.)[b]	T_e(SC)[c]	T_e(IVO)[d]	n^*(obs.)	δ(obs.)
$np\pi_u$	$^1\Sigma_u^-$		74 280	74 530				86 630	87 110		
	$^3\Delta_u$	74 770(10)	74 770	75 170	2.208	0.792	86 790(20)	86 790	87 270	3.234	0.766
	$^3\Sigma_u^+$	75 260(20)	75 260	75 740	2.232	0.768	86 970(30)	86 950	87 430	3.262	0.738
	$^3\Sigma_u^-$	74 820(50)	74 790	75 980	2.210	0.790	86 880(40)	86 800	87 350	3.248	0.752
	$^1\Delta_u$	75 420(20)	75 450	76 780	2.240	0.760	87 030(30)	87 010	87 830	3.271	0.729
	$^1\Sigma_u^+$	76 130(10)	76 100	77 510	2.278	0.722	87 210(20)	87 220	87 990	3.300	0.700
$ns\sigma_g$	$^1\Pi_g$	65 550(20)		66 220	1.860	1.140	83 290(20)		83 640[f]	2.800	1.200
	$^1\Pi_g$	66 190(20)		67 110	1.879	1.121	83 340(20)		83 800[f]	2.805	1.195
$np\sigma_u$	$^3\Pi_u$	76 060(50)			2.274	0.726	87 170(30)			3.294	0.706
	$^1\Pi_u$	76 470(50)			2.296	0.704	87 500(30)			3.349	0.651

[a]Energies, in cm^{-1}, are T_e values referenced to the minimum of the $X\,^3\Sigma_g^-$ potential-energy curve.
[b]Diabatic, deperturbed energies from present CSE analysis of experiment (see Sec. III), with uncertainties in parentheses.
[c]From single-configuration (SC) expressions. Eq. (1), with $K^{(0)}=339\ cm^{-1}$, $J^{(2)}=573\ cm^{-1}$, $K^{(2)}=83\ cm^{-1}$, relative to the experimental $^3\Delta_u$ energy.
[d]*Ab initio* IVO calculations of Cartwright *et al.* (Ref. 52), corrected to give T_e values.
[e]From Eq. (1) with $K^{(0)}=108\ cm^{-1}$, $J^{(2)}=183\ cm^{-1}$, $K^{(2)}=27\ cm^{-1}$, i.e., the $n=3$ values scaled by $(n^*)^{-3}$, relative to the experimental $^3\Delta_u$ energy.
[f]Level labeled $3d\sigma_g$ in Ref. 52.

with $\mathcal{R}=109\,735.5\ cm^{-1}$ and $E_\infty=97\,284\ cm^{-1}$.[47] We emphasize that these observed quantities are deperturbed, i.e., the effects of both Rydberg-valence and spin–orbit interactions have been removed.

Quantum defects for the $3p$ states in Table II lie in the range 0.6–0.8 and are systematically smaller by ~4% for $n=4$. Similar behavior has been observed for the np states of other molecules.[48–50] Quantum defects for the $3s\sigma_g$ states are ~1.1, consistent with expectation, but those for $n=4$ are larger by ~6%. This increase in the quantum defect is accompanied by a rapid decrease in the singlet–triplet splitting from ~640 cm^{-1} for $n=3$, to ~50 cm^{-1} for $n=4$. These effects are discussed in more detail in Ref. 11, and may be attributed to the onset of strong $ns\sigma_g-(n-1)d\sigma_g$ interactions for $n\geqslant 4$ which are absent for $n=3$.[11,51]

The deperturbed energies may be appropriately compared with the results of single-configuration calculations, such as the IVO calculations of Cartwright *et al.*[52] which are also shown in Table II for the $np\pi_u$ and $ns\sigma_g$ states.[53] Fair agreement is found between the observed and calculated energies: the IVO values exceed the observed values by 400–1400 cm^{-1} for $n=3$, and by 400–800 cm^{-1} for $n=4$. However, the calculated separations between the $^1\Sigma_u^+$ and $^3\Delta_u$ states derived from the $np\pi_u$ Rydberg orbitals exceed the observed separations by approximately a factor of 2. In this respect, the preliminary configuration-mixing (CM) calculations of Buenker and Peyerimhoff,[54] which indicate that the $3p\pi_u$ states span a range of ~1600 cm^{-1}, are in much better agreement with the observations. However, neither the CM,[54] nor the IVO[52] calculations predict the correct energy ordering for the $3p\pi_u$ states, in particular, the observed order $T_e(^3\Sigma_u^+)>T_e(^3\Sigma_u^-)$. In addition, both calculations predict $3s\sigma_g\,^1\Pi_g-^3\Pi_g$ energy separations (~890 cm^{-1} for IVO,[52] ~810 cm^{-1} for MC[54]) significantly larger than observed (~640 cm^{-1}).

Although the IVO approximation gives a reasonable description of the Rydberg energies, it is insufficient to obtain very precise values. However, our analysis in Sec. II A suggests retaining the single-configuration formalism in order to be able to examine the relations between the energies of the various Rydberg states, while introducing *effective* values for the relevant integrals. Initially, it is of particular interest here to examine the utility of the single-configuration Recknagel[24] expressions [Eq. (1)] in descriptions of the $np\pi_u$ Rydberg energies. The relative $3p\pi_u$ IVO energies of Cartwright *et al.*,[52] where Gaussian orbitals have been used to describe the Rydberg orbitals, are well described using Eq. (1) with the following effective values for the integrals:

$$J^{(2)}=686\ cm^{-1},\ K^{(2)}=40\ cm^{-1},\ K^{(0)}=806\ cm^{-1}. \quad (15)$$

On the other hand, if the observed $3p\pi_u$ diabatic energies in Table II are fitted using Eq. (1), the following effective parameters are found:

$$J^{(2)}=573\ cm^{-1},\ K^{(2)}=83\ cm^{-1},\ K^{(0)}=339\ cm^{-1}. \quad (16)$$

Energies calculated using these parameters in Eq. (1), given in Table II, are seen to reproduce the observed values to within $\pm 30\ cm^{-1}$. If it is assumed that the Recknagel parameters scale with $(n^*)^{-3}$, then, using Eq. (16), the values

$$J^{(2)}=183\ cm^{-1},\ K^{(2)}=27\ cm^{-1},\ K^{(0)}=108\ cm^{-1} \quad (17)$$

are implied for the $4p\pi_u$ states. Energies calculated using these parameters in Eq. (1), also given in Table II, reproduce the observed values to within -10 and $+80\ cm^{-1}$. Such a degree of agreement between the observed energies and those implied by Eq. (1) is encouraging, considering that uncertainties in the observed energies are up to ~50 cm^{-1} for the more heavily deperturbed states. It is evident from Table II that no experimental data are available for the $np\pi_u\,^1\Sigma_u^-$ states. However, the analytical expressions, Eq. (1), enable energies for these states to be predicted (see Sec. IV B).

TABLE III. $np\pi_u$, $ns\sigma_g$, and $np\sigma_u$ Rydberg-valence couplings $|H^{el}|$, in cm^{-1}.

		$n=3$			$n=4$		
Ryd. Orb.	Symm.	Obs.[a]	SC[b]	*Ab initio*	Obs.[a]	SC[c]	*Ab initio*
$np\pi_u$	$^1\Sigma_u^-$		1800			1020	
	$^3\Delta_u$	770(50)	900	<320[d]	480(250)	510	
	$^3\Sigma_u^+$	420(40)	0		230(50)	0	
	$^3\Sigma_u^-$	4030(30)	3600	4100[e]	2020(30)	2040	
	$^1\Delta_u$	2640(30)	2700	2700[f]	1500(200)	1530	
	$^1\Sigma_u^+$	1600(100)	1800	1900[g]	840(270)	1020	
$ns\sigma_g$	$^3\Pi_g$	620(50)[h]		830/780[i]	170(70)[h,j]		180/460[i]
	$^1\Pi_g$	630(30)[h]		710/660[i]	170(70)[h,j]		170/480[i]
$np\sigma_u$	$^3\Pi_u$	7180(50)[k]		8400/7600[l]	3620(50)[k]		1840/5200[l]
	$^1\Pi_u$	6630(50)		8300/7000[l]	3570(50)		2000/4800[l]

[a]Diabatic, deperturbed couplings from present CSE analysis of experiment (see Sec. III), with uncertainties in parentheses.
[b]From single-configuration (SC) expressions, Eq. (5), with $M^{(0)}=1800\ cm^{-1}$, $M^{(2)}=900\ cm^{-1}$.
[c]From Eq. (5) with $M^{(0)}=1020\ cm^{-1}$, $M^{(2)}=510\ cm^{-1}$, i.e., the $n=3$ values scaled by $(n^*)^{-3/2}$.
[d]Reference 4; effective value from minimal splitting between adiabatic Rydberg and valence potentials.
[e]Reference 8; value at calculated Rydberg-valence crossing point.
[f]Reference 3; effective value from minimal splitting between adiabatic Rydberg and valence potentials.
[g]References 6 and 9; estimated value at Rydberg-valence crossing point ($R=1.34$ Å).
[h]Given in Ref. 11.
[i]Reference 1; value at calculated Rydberg-valence crossing point. Second value has been corrected by us to the diabatic basis employed here.
[j]Singlet and triplet values held equal in fitting procedure.
[k]From simultaneous fit to $^{1,3}\Pi_{u1}$ states. From fit to $^3\Pi_{u0}$ states, Ref. 18 gives 7110 cm^{-1} and 3540 cm^{-1} for $n=3$ and 4 couplings, respectively.
[l]Reference 3; value at calculated Rydberg-valence crossing point. Second value has been corrected by us to the diabatic basis employed here.

While the effective Recknagel parameters implied by the IVO calculations [Eq. (15)] are in accordance with the expected ordering $K^{(0)}>J^{(2)}>K^{(2)}$ (see Sec. II A), the observed effective parameters [Eq. (16)] do not satisfy the relation $K^{(0)}>J^{(2)}$, but satisfy the more important relations $K^{(0)}>K^{(2)}$ and $J^{(2)}>K^{(2)}$. It is interesting that, in a Recknagel study of the experimental energies for the $\pi_g nd\pi_g$ Rydberg states of O_2, Yokelson *et al.*[55] found the same qualitative relationships between the parameters. For the $3d\pi_g$ states, the following effective parameters were deduced:[55]

$$J^{(2)}=166\ cm^{-1},\ K^{(2)}=48\ cm^{-1},\ K^{(0)}=150\ cm^{-1}, \quad (18)$$

reasonably similar to the present $4p\pi_u$ parameters [see Eq. (17)].

Observed Rydberg-valence couplings involving the $np\pi_u$, $ns\sigma_g$, and $np\sigma_u$ Rydberg states, determined using the CSE analysis of experiment described in Sec. III, are summarized for $n=3$ and 4 in Table III, together with selected *ab initio* values. The present couplings for the $^3\Delta_u$, $^3\Sigma_u^+$, $^1\Delta_u$, $^1\Sigma_u^+$, and $^1\Pi_u$ states represent the first experimentally based values reported for those symmetries. As illustrated for two extreme cases in Fig. 2, Table III confirms that the magnitudes of the couplings are extremely variable. While the case (2) couplings for the $^{1,3}\Pi_u$ states are the largest, the case (1) couplings vary widely depending on the state symmetry. Overall, there is fairly good agreement between the observed and various *ab initio* couplings, with the observed values generally lower, but it should be emphasized that care needs to be taken with the comparisons. The observed couplings have been obtained using a CSE model which assumes no R dependence and results in values applicable principally in the region of the Rydberg-valence crossing points, which vary from $R_x=1.08$ Å to 1.35 Å for the $n=3$ states considered in this work. Thus, the observed couplings have been compared in Table III with *ab initio* values calculated for appropriate values of R_x, where possible. Furthermore, our diabatic potential-energy curves are somewhat dependent on the underlying assumptions of the CSE model, e.g., that of R-independent coupling, and similar problems arise because of differing theoretical definitions of the diabatic states: Spelsberg and Meyer[8] define the diabatic states as those obtained by diagonalization of the operator $\Sigma_i x_i^2$ in the space spanned by the states, whereas Li *et al.*[1,3] diagonalize the x^2+y^2 quadrupole-moment property. This latter method results in nonzero coupling between the $n=3$ and $n=4$ diabatic Rydberg states. In Table III, we give both the *ab initio* couplings calculated directly by Li *et al.*[1,3] and corresponding modified values which have been corrected by us to the diabatic basis employed here, i.e., a basis requiring zero interaction between the Rydberg states.

From Table III, it can be seen that the observed Rydberg-valence couplings for the np and ns states scale differently with n. For all of the $np\pi_u$ and $np\sigma_u$ states for which it has been possible to determine an $n=4$ coupling, the ratio $H^{el}(n=4)/H^{el}(n=3)$ lies in the range 0.50–0.62, consistent with the $(n^*)^{-3/2}$ scaling rule which predicts a

ratio of ~0.57. However, the observed ratio for the $ns\sigma_g$ states is ~0.27. This latter result can be attributed to the effects of the $3d-4s$ interactions invoked above to explain the rapid decrease in the singlet–triplet splitting for these states. While the scaling rule consequently fails in this case, it is interesting to note that the ratio of the observed $^1\Pi_g-{}^3\Pi_g$ splittings for $n=4$ and $n=3$ (~0.09) remains approximately equal to the *square* of the corresponding ratio of the couplings ($0.27^2=0.07$).

Although the Hartree–Fock approximation is not valid for the valence states of interest, the single-configuration expressions [Eq. (5)], based on the leading terms in the configuration-interaction expansions of these states, represent the principal new results obtained in Sec. II and enable an effective-parameter description of the relationships between the magnitudes of the Rydberg-valence couplings for the various states of the $np\pi_u$ complexes. Values calculated using Eq. (5) with the effective parameters $M^{(1)}=1800$ cm^{-1} and $M^{(2)}=900$ cm^{-1}, shown in Table III, are seen to provide a very good description of the observed couplings for $n=3$, certainly at the $\pm 400-500$ cm^{-1} level. In addition, values calculated assuming the scaling rule, i.e., with $M^{(1)}=1020$ cm^{-1} and $M^{(2)}=510$ cm^{-1}, also shown in Table III, reproduce the observed $n=4$ couplings to within ± 200 cm^{-1}. Just as for the energies discussed above, the analytical expressions for the Rydberg-valence couplings enable predictions to be made for the unobserved $np\pi_u\,{}^1\Sigma_u^-$ states (see Sec. IV B).

In the case of the $3s\sigma_g$ states, the observed equality between the magnitudes of the couplings for the $^1\Pi_g$ and $^3\Pi_g$ states (see Table III) is consistent with Eq. (7) with an effective $|M|=630$ cm^{-1}. However, the magnitude of the observed $3p\sigma_u\,{}^3\Pi_u$ coupling exceeds the corresponding $^1\Pi_u$ value by ~11%, inconsistent with Eq. (8) which predicts a larger value for the singlet. This apparent inconsistency can be explained by noting the different Rydberg-valence crossing points for the $^1\Pi_u$ and $^3\Pi_u$ states [see Fig. 1(c)], and postulating that the Rydberg-valence couplings decrease significantly with R. The detailed *ab initio* calculations of Li *et al.*[3] support this view: while, for a given R value, the *ab initio* $n=3$ singlet coupling indeed exceeds the triplet coupling, consistent with Eq. (8), at the relevant Rydberg-valence crossing points the calculated singlet coupling is ~8% *less* than the triplet value, consistent with our observations.[56]

Finally, we note that the off-diagonal spin–orbit interactions between the valence states, described in Sec. II C, have little effect on the spectroscopy of the Rydberg states, so it is not possible in general to determine values for these interactions through analysis of the current experimental data. However, as mentioned in Sec. III, the corresponding interactions among the Rydberg states produce noticeable effects. For the $\pi_g\,3p\pi_u$ Rydberg states, we have determined the values, $|\langle {}^3\Delta_{u2}|\mathbf{H}^{so}|{}^1\Delta_{u2}\rangle|=96\pm 6$ cm^{-1}, $|\langle {}^3\Sigma_{u0}^-|\mathbf{H}^{so}|{}^1\Sigma_{u0}^+\rangle|=99\pm 4$ cm^{-1}, and $|\langle {}^3\Sigma_{u1}^-|\mathbf{H}^{so}|{}^3\Sigma_{u1}^+\rangle|=92\pm 11$ cm^{-1}, from CSE analysis of experiment. For the other nonzero Rydberg spin–orbit matrix elements which have not been determined explicitly, values fixed at 95 cm^{-1} were found to provide good descriptions of experiment. In this way, most of the single-configuration expressions in Eqs. (10), (11), and (12) have been verified.

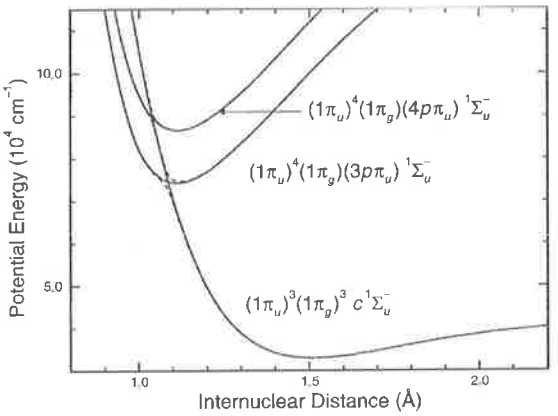

FIG. 3. Diabatic potential-energy curves (solid lines) employed in modeling the $np\pi_u$ Rydberg-valence interactions for the $^1\Sigma_u^-$ states, together with the corresponding adiabatic potentials (dashed lines). The energy scale is referenced to the minimum in the $X\,{}^3\Sigma_g^-$ potential-energy curve. In the region of the $n=3$ crossing, the behavior of the $^1\Sigma_u^-$ states is intermediate between diabatic and adiabatic.

B. Predictions for the $^1\Sigma_u^-$ states

Single-photon transitions to the $np\pi_u\,{}^1\Sigma_u^-$ Rydberg states are electric-dipole-forbidden from the ground $X\,{}^3\Sigma_g^-$ and metastable $a\,{}^1\Delta_g$ and $b\,{}^1\Sigma_g^+$ states of O_2. Furthermore, the first-order intensity-borrowing mechanism which leads to the experimental observation of forbidden transitions such as $3p\pi_u f\,{}^1\Sigma_{u0}^+\leftarrow X\,{}^3\Sigma_{g0}^-$ and $3p\pi_u D\,{}^3\Sigma_{u1}^+\leftarrow X\,{}^3\Sigma_{g1}^-$, through off-diagonal spin–orbit mixing within the $3p\pi_u$ Rydberg complex [see Eq. (12)], is not available in the case of the $np\pi_u\,{}^1\Sigma_{u0}^-$ states which are coupled only to the $np\pi_u\,{}^3\Sigma_{u0}^+$ states [see Eq. (12c)] which are also inaccessible in allowed transitions from the X, a, and b states. Thus, it is not surprising that transitions to the $np\pi_u\,{}^1\Sigma_u^-$ states have not been observed. However, the analytical expressions, Eqs. (1) and (5), in association with the CSE method summarized in Sec. III, enable some predictions to be made regarding the $^1\Sigma_u^-$ Rydberg-state spectroscopy.

Diabatic potential-energy curves used in the present CSE modeling of the $^1\Sigma_u^-$ Rydberg-valence interaction are shown in Fig. 3 as solid lines. The $c\,{}^1\Sigma_u^-$ valence potential was taken from Ref. 57, while the $3p\pi_u$ and $4p\pi_u\,{}^1\Sigma_u^-$ potentials were taken to have shapes identical to the corresponding $^1\Sigma_u^+$ potentials determined in the study of Sec. III, shifted in energy to have $T_e=74\,280$ cm^{-1} and $T_e=86\,630$ cm^{-1}, respectively, as implied by the single-configuration predictions of Table II. The Rydberg-valence interaction matrix elements were taken to be $H^{el}(n=3)=1800$ cm^{-1} and $H^{el}(n=4)=1020$ cm^{-1}, as implied by the single-configuration predictions of Table III, leading to the adiabatic potential-energy curves shown in Fig. 3 as dashed lines. In the region of the $n=3$ avoided crossing, the adiabaticity parameter[58] $\zeta=H^{el}(n=3)/\Delta G^{ad}$, where ΔG^{ad} is the separation of the first vibrational levels of the second adiabatic state, has a

TABLE IV. Indicative spectroscopic parameters, in cm^{-1}, for the $np\pi_u$ Rydberg-valence coupled $^1\Sigma_u^-$ states of O_2, calculated using the CSE method.

n[a]	v[a]	T_{v0}[b]	B_v	Γ_v[c]
3	0	74 850	1.64	560[d]
3	1	76 250	1.71	600[d]
3	2	78 150	1.64	78
3	3	80 110	1.61	14
3	4	81 960	1.62	180
3	5	83 650	1.64	330
3	6	85 300	1.58	240
4	0	86 860	1.69	33
3	7	87 030	1.54	65
3	8	88 690	1.59	52
4	1	88 810	1.58	10
3	9	90 420	1.52	2
4	2	90 620	1.61	110
3	10	92 120	1.49	20[d]
4	3	92 370	1.63	180[d]

[a]The mixed levels are labeled according to their *predominant* (n,v) character.
[b]Energies are referenced to the virtual level $X\,^3\Sigma_g^-(v=0,J=0,F_2)$.
[c]FWHM predissociation linewidth.
[d]Approximate value for blended feature.

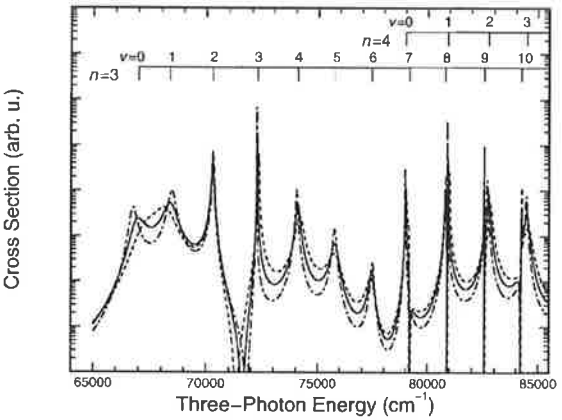

FIG. 4. Indicative rotationless three-photon absorption cross sections for the Rydberg-valence mixed $^1\Sigma_u^- \leftarrow\leftarrow\leftarrow a\,^1\Delta_g(v''=0)$ transitions of O_2, calculated using the CSE method. The solid line: with model parameters of Sec. IV B, including $H^{el}(n=3)=1800$ cm^{-1}, $H^{el}(n=4)=1020$ cm^{-1}. The dashed line: with $H^{el}(n=3)=2300$ cm^{-1}, $H^{el}(n=4)=1300$ cm^{-1}. The dotted–dashed line: with $H^{el}(n=3)=1300$ cm^{-1}, $H^{el}(n=4)=735$ cm^{-1}. The excited-state coupled-channel resonances are labeled according to the (n,v) character of the dominant diabatic Rydberg state.

value of ~0.8, implying behavior intermediate between diabatic and adiabatic. Hence, the coupled-channel energy levels will not be strictly associated with either set of potentials. In what follows, however, we will label levels according to their predominant diabatic character. Finally, we note that spin–orbit interactions have not been included in the CSE model employed here, since their inclusion is unlikely to affect the calculated $^1\Sigma_u^-$ energy-level structure significantly, at least at the modest level of uncertainty required for these predictions.

Vibronic energy levels, rotational constants and predissociation linewidths calculated for the Rydberg-valence coupled $^1\Sigma_u^-$ states using this CSE model are summarized in Table IV. Despite conservatively estimated uncertainties of $\sim\pm100$ cm^{-1} in the energy levels and $\sim\pm50\%$ in the linewidths due to unavoidable uncertainties in the model parameters, several general observations can be made. First, the Rydberg-valence interaction causes strong perturbation and predissociation: the calculated vibrational spacings and rotational constants show erratic variations; in particular, the $n=3$, $v=0$ and 1 levels are abnormally closely spaced and their widths are a significant proportion of that spacing. Second, with the present parameters, the $n=4$, v levels roughly coincide with the $n=3$, $v+7$ levels, leading to the possibility of interesting interference effects. Finally, the degree of predissociation is such that none of the calculated levels is particularly narrow: for $n=3$, there are linewidth minima of 14 cm^{-1} and 2 cm^{-1} full-width at half-maximum (FWHM), at $v=3$ and $v=9$, respectively. This predissociation will, no doubt, significantly hamper the experimental detection of these $^1\Sigma_u^-$ states using normal spectroscopic methods.

Nevertheless, we suggest a possible detection scheme. Transitions from the $a\,^1\Delta_g$ state to $^1\Sigma_u^-$ states are allowed in three-photon absorption, so it may be possible to detect some levels of the $np\pi_u\,^1\Sigma_u^-$ states in (3 + 1) REMPI experiments involving excitation from this metastable state.[59] In Fig. 4, we show a relative Rydberg-valence coupled $^1\Sigma_u^- \leftarrow\leftarrow\leftarrow a\,^1\Delta_g(v''=0)$ absorption spectrum (the solid line), calculated without rotational structure using the present CSE model with R-independent diabatic three-photon electronic transition moments for $n=3$ and 4.[60] Also shown in Fig. 4 are cross sections calculated for values of the Rydberg-valence couplings at the limits of the estimated uncertainty: [$H^{el}(n=3)=2300$ cm^{-1}, $H^{el}(n=4)=1300$ cm^{-1}, the dashed line]; [$H^{el}(n=3)=1300$ cm^{-1}, $H^{el}(n=4)=735$ cm^{-1}, the dotted–dashed line]. While the general observations of the previous paragraph are unchanged with these parameters, it is noticeable from Fig. 4 that, for the highest value of the coupling, transitions into the $n=3$, $v=0$ and 1 levels merge into a single broad predissociating resonance. In REMPI spectra, the detected ion signal suffers from competition between ionization and predissociation,[61] so the narrowest transitions in the absorption spectrum of Fig. 4 will be favored further in the associated REMPI spectrum. Hence, the best possibilities for REMPI detection appear to be the $n=3$, $v=3$ and 9 levels, together with the $n=4$, $v=1$ level.

V. SUMMARY AND CONCLUSIONS

Using a single-configuration formulation, analytical expressions have been derived for the $ns\sigma_g$, $np\pi_u$, and $np\sigma_u$ Rydberg-valence interaction matrix elements in O_2. In particular, new two-parameter expressions have been given for the Rydberg-valence couplings involving the six states arising from the $np\pi_u$ Rydberg orbital. In addition, the results of new, diabatic, coupled-channel deperturbations of experimental data dependent on these interactions have been summarized for $n=3$ and 4. The large differences in magnitude between the Rydberg-valence couplings for the constituent states of the $np\pi_u$ Rydberg complex that are predicted by

the analytical expressions have been verified experimentally, suggesting that these expressions may be of use in the study of Rydberg-valence interactions in isovalent molecules such as S_2 and SO. Effective values for several two-electron integrals have been obtained semiempirically through comparison between analytical expressions and deperturbed experimental values for the Rydberg-state energies and Rydberg-valence couplings, allowing predictions to be made for the spectroscopy of the $np\pi_u\,{}^1\Sigma_u^-$ Rydberg states which have yet to be observed. An experiment which might allow detection of these states has been suggested.

ACKNOWLEDGMENTS

This paper was prepared during the tenure of H.L.-B. as a Visiting Fellow in the Ultraviolet Physics Unit of the Atomic and Molecular Physics Laboratories at the Australian National University. B.R.L. would like to thank Professor R. J. Buenker for helpful discussions on *ab initio* matrix elements.

[1] Y. Li, I. D. Petsalakis, H.-P. Liebermann, G. Hirsch, and R. J. Buenker, J. Chem. Phys. **106**, 1123 (1997).
[2] Y. Li, M. Honigmann, G. Hirsch, and R. J. Buenker, Chem. Phys. Lett. **212**, 185 (1993).
[3] Y. Li, G. Hirsch, and R. J. Buenker, J. Chem. Phys. **108**, 8123 (1998).
[4] R. J. Buenker and S. D. Peyerimhoff, Chem. Phys. Lett. **34**, 225 (1975).
[5] S. L. Guberman, Planet. Space Sci. **36**, 47 (1987).
[6] S. L. Guberman (private communication).
[7] Y. Li, M. Honigmann, K. Bhanuprakash, G. Hirsch, and R. J. Buenker, J. Chem. Phys. **96**, 8314 (1992).
[8] D. Spelsberg and W. Meyer, J. Chem. Phys. **109**, 9802 (1998).
[9] S. L. Guberman and A. Giusti-Suzor, J. Chem. Phys. **95**, 2602 (1991).
[10] W. J. van der Zande, W. Koot, J. Los, and J. R. Peterson, J. Chem. Phys. **89**, 6758 (1988).
[11] J. S. Morrill, M. L. Ginter, B. R. Lewis, and S. T. Gibson, J. Chem. Phys. **111**, 173 (1999).
[12] W. J. van der Zande, W. Koot, and J. Los, J. Chem. Phys. **91**, 4597 (1989).
[13] R. S. Friedman and A. Dalgarno, J. Chem. Phys. **93**, 2370 (1990).
[14] A. Sur, L. Nguyen, and N. Nikoi, J. Chem. Phys. **96**, 6791 (1992).
[15] J. Wang, D. G. McCoy, A. J. Blake, and L. Torop, J. Quant. Spectrosc. Radiat. Transf. **38**, 19 (1987).
[16] J. Wang, A. J. Blake, D. G. McCoy, and L. Torop, J. Quant. Spectrosc. Radiat. Transf. **40**, 501 (1988).
[17] B. R. Lewis, S. S. Banerjee, and S. T. Gibson, J. Chem. Phys. **102**, 6631 (1995).
[18] J. P. England, B. R. Lewis, S. T. Gibson, and M. L. Ginter, J. Chem. Phys. **104**, 2765 (1996).
[19] H. Lefebvre-Brion and R. W. Field, *Perturbations in the Spectra of Diatomic Molecules* (Academic, Orlando, 1986), pp. 58–59, 208–211, 216–221.
[20] In the principal molecular-orbital notation used here, the filled shells $(1\sigma_g)^2(1\sigma_u)^2(2\sigma_g)^2(2\sigma_u)^2$, common to all states, are suppressed, as is the $(3\sigma_g)^2$ shell where appropriate.
[21] H. Lefebvre-Brion and C. M. Moser, J. Chem. Phys. **43**, 1394 (1965).
[22] H. Lefebvre-Brion, J. Mol. Struct. **19**, 103 (1973).
[23] W. J. Hunt and W. A. Goddard III, Chem. Phys. Lett. **6**, 414 (1969).
[24] A. Recknagel, Z. Phys. **87**, 375 (1934).
[25] Numerical subscripts in the electronic-state designations employed here refer to the value of $|\Omega|$.
[26] R. Ogorzalek-Loo *et al.*, J. Chem. Phys. **91**, 5185 (1989).
[27] E. F. van Dishoeck, M. C. van Hemert, A. C. Allison, and A. Dalgarno, J. Chem. Phys. **81**, 5709 (1984).
[28] L. Torop, D. G. McCoy, A. J. Blake, J. Wang, and T. Scholz, J. Quant. Spectrosc. Radiat. Transf. **38**, 9 (1987).
[29] R. R. Ogorzalek-Loo, Ph.D. thesis, Cornell University, 1989.
[30] A. Sur, R. S. Friedman, and P. J. Miller, J. Chem. Phys. **94**, 1705 (1991).
[31] W. J. van der Zande, W. Koot, J. Los, and J. R. Peterson, Chem. Phys. Lett. **140**, 175 (1987).
[32] K. Ito, K. P. Huber, K. Yoshino, M. Ogawa, and Y. Morioka, J. Mol. Spectrosc. **171**, 1 (1995).
[33] L. C. Lee, T. G. Slanger, G. Black, and R. L. Sharpless, J. Chem. Phys. **67**, 5602 (1977).
[34] S. T. Gibson and B. R. Lewis, J. Electron Spectrosc. Relat. Phenom. **80**, 9 (1996).
[35] B. R. Lewis, S. T. Gibson, M. Emami, and J. H. Carver, J. Quant. Spectrosc. Radiat. Transf. **40**, 1 (1988).
[36] B. R. Lewis, S. T. Gibson, M. Emami, and J. H. Carver, J. Quant. Spectrosc. Radiat. Transf. **40**, 469 (1988).
[37] S. S. Banerjee, Ph.D. thesis, The Australian National University, 1996.
[38] B. R. Lewis *et al.*, J. Chem. Phys. **52**, 2717 (1995).
[39] H. C. Chang, Ph.D. thesis, University of Southern California, 1973.
[40] D. H. Katayama, S. Ogawa, M. Ogawa, and Y. Tanaka, J. Chem. Phys. **67**, 2132 (1977).
[41] P. C. Hill, Ph.D. thesis, The Australian National University, 1991.
[42] S. Ogawa and M. Ogawa, Can. J. Phys. **53**, 1845 (1975).
[43] K. R. Yamawaki, Ph.D. thesis, University of Southern California, 1972.
[44] H. Partridge, C. W. Bauschlicher, Jr., S. R. Langhoff, and P. R. Taylor, J. Chem. Phys. **95**, 8292 (1991); H. Partridge (private communication).
[45] Depending on the quantity and quality of the available experimental data, the significant portions of the Rydberg and valence potential-energy curves were allowed to vary in either a constrained, or an unconstrained, fashion during the fitting procedure.
[46] J. P. England, B. R. Lewis, and M. L. Ginter, J. Chem. Phys. **103**, 1727 (1995).
[47] In Eq. (14), the Rydberg constant $\mathcal{R}$ is mass-corrected and the equilibrium–equilibrium ionization potential from the $X\,{}^3\Sigma_g^-$ state of O_2, E_∞, is averaged over both Ω-components of the $X\,({}^2\Pi_g)$ state of O_2^+.
[48] E. Miescher, J. Mol. Spectrosc. **20**, 130 (1966).
[49] M. Ogawa and S. Ogawa, J. Mol. Spectrosc. **41**, 393 (1972).
[50] M. Eidelsberg and F. Rostas, Astron. Astrophys. **235**, 472 (1990).
[51] S. Chung, C. C. Lin, and E. T. P. Lee, J. Phys. B **21**, 1155 (1988).
[52] D. C. Cartwright, W. J. Hunt, W. Williams, S. Trajmar, and W. A. Goddard III, Phys. Rev. A **8**, 2436 (1973).
[53] Since the IVO calculations (Ref. 52) inherently include the effects of strong Rydberg-valence interactions for the $np\sigma_u$ states, IVO energies for these states are not included for comparison in Table II.
[54] R. J. Buenker and S. D. Peyerimhoff, Chem. Phys. **8**, 324 (1975).
[55] R. J. Yokelson, R. J. Lipert, and W. A. Chupka, J. Chem. Phys. **97**, 6153 (1992).
[56] Note that the *modified* values of Ref. 3, i.e., those corrected to the diabatic basis used here, have been used in drawing this conclusion.
[57] B. Buijsse, W. J. van der Zande, A. T. J. B. Eppink, D. H. Parker, B. R. Lewis, and S. T. Gibson, J. Chem. Phys. **108**, 7229 (1998).
[58] K. Dressler, Ann. Isr. Phys. Soc. **6**, 141 (1983).
[59] A scheme involving three-photon excitation from the $b\,{}^1\Sigma_g^+$ state using a single laser would be unproductive since $\Sigma_u^- \leftarrow\leftarrow\leftarrow \Sigma_g^+$ transitions are identity-forbidden [D. M. Friedrich, J. Chem. Phys. **75**, 3258 (1981)].
[60] The Rydberg electronic transition moments were assumed to scale with $(n^*)^{-3/2}$ and the valence moment was taken as zero.
[61] B. R. Lewis, S. T. Gibson, J. S. Morrill, and M. L. Ginter, J. Chem. Phys. **111**, 186 (1999).